

**NIST Special Publication 1018-3  
Sixth Edition**

**Fire Dynamics Simulator  
Technical Reference Guide  
Volume 3: Validation**

Kevin McGrattan  
Simo Hostikka  
Jason Floyd  
Randall McDermott  
Marcos Vanella  
Eric Mueller

<http://dx.doi.org/10.6028/NIST.SP.1018>



**Fire Safety Research Institute**  
A UL Research Institute

**NIST**  
**National Institute of  
Standards and Technology**  
U.S. Department of Commerce

**EXHIBIT 1 - GORBETT**

**NIST Special Publication 1018-3  
Sixth Edition**

**Fire Dynamics Simulator  
Technical Reference Guide  
Volume 3: Validation**

Kevin McGrattan  
Randall McDermott  
Marcos Vanella  
Eric Mueller

*Fire Research Division, Engineering Laboratory, Gaithersburg, Maryland*

Simo Hostikka  
*Aalto University, Espoo, Finland*

Jason Floyd  
*Fire Safety Research Institute, UL Research Institutes, Columbia, Maryland*

<http://dx.doi.org/10.6028/NIST.SP.1018>

April 8, 2024  
Revision: FDS-6.9.1-0-g889da6a



U.S. Department of Commerce  
*Gina M. Raimondo, Secretary*

National Institute of Standards and Technology  
*Laurie E. Locascio, NIST Director and Undersecretary of Commerce for Standards and Technology*

Certain commercial entities, equipment, or materials may be identified in this document in order to describe an experimental procedure or concept adequately. Such identification is not intended to imply recommendation or endorsement by the National Institute of Standards and Technology, nor is it intended to imply that the entities, materials, or equipment are necessarily the best available for the purpose.

**National Institute of Standards and Technology Special Publication 1018-3  
Natl. Inst. Stand. Technol. Spec. Publ. 1018-3, 1217 pages (October 2013)  
CODEN: NSPUE2**

# FDS Developers

The Fire Dynamics Simulator and Smokeview are the products of an international collaborative effort led by the National Institute of Standards and Technology (NIST) and Fire Safety Research Institute, UL Research Institutes. Its developers and contributors are listed below.

## Principal Developers of FDS

Kevin McGrattan, NIST, Gaithersburg, Maryland

Simo Hostikka, Aalto University, Espoo, Finland

Jason Floyd, Fire Safety Research Institute, UL Research Institutes, Columbia, Maryland

Randall McDermott, NIST, Gaithersburg, Maryland

Marcos Vanella, NIST, Gaithersburg, Maryland

Eric Mueller, NIST, Gaithersburg, Maryland

## Principal Developer of Smokeview

Glenn Forney, NIST, Gaithersburg, Maryland

## Collaborators and Contributors

Anthony Hamins, NIST, Gaithersburg, Maryland

Jonathan Hodges, Jensen Hughes, Blacksburg, Virginia

Emanuele Gissi, Corpo Nazionale dei Vigili del Fuoco, Italy

William Mell, U.S. Forest Service, Seattle, Washington

Julio Cesar Silva, Rio on Fire, Orlando, Florida

Craig Weinschenk, Fire Safety Research Institute, UL Research Institutes, Columbia, Maryland

# About the Developers

**Kevin McGrattan** is a mathematician in the Fire Research Division of NIST. He received a bachelor of science degree from the School of Engineering and Applied Science of Columbia University in 1987 and a doctorate at the Courant Institute of New York University in 1991. He joined the NIST staff in 1992 and has since worked on the development of fire models, most notably the Fire Dynamics Simulator.

**Simo Hostikka** is an associate professor of fire safety engineering at Aalto University School of Engineering, since January 2014. Before joining Aalto, he worked as a Principal Scientist and Team Leader at VTT Technical Research Centre of Finland. He received a master of science (technology) degree in 1997 and a doctorate in 2008 from the Department of Engineering Physics and Mathematics of the Helsinki University of Technology. He is the principal developer of the radiation and solid phase sub-models within FDS.

**Jason Floyd** is a Lead Research Engineer at the Underwriters Laboratories Fire Safety Research Institute in Columbia, Maryland. He received a B.S. (1993), M.S. (1995), and a Ph.D. (2000) from the Nuclear Engineering Program of the University of Maryland. After graduating, he was awarded a National Research Council Post-Doctoral Fellowship at the Building and Fire Research Laboratory of NIST. He is a principal developer of the combustion, control logic, aerosol, droplet evaporation, and HVAC sub-models within FDS.

**Randall McDermott** joined the Fire Research Division at NIST in 2008. He received a B.S. from the University of Tulsa in Chemical Engineering in 1994 and a Ph.D. from the University of Utah in 2005. His research interests include subgrid-scale models and numerical methods for large-eddy simulation, turbulent combustion, immersed boundary methods, and Lagrangian particle methods.

**Marcos Vanella** joined the Fire Research Division at NIST in 2019. He received diplomas in Mechanical and Aeronautical Engineering from the National University of Cordoba, Argentina, and M.S. and Ph.D. degrees in Mechanical Engineering from the University of Maryland, College Park. His research interests include computer simulation and scientific software development applied to engineering systems, mainly in the areas of fluid flow and multiphysics interaction problems.

**Glenn Forney** is a computer scientist in the Fire Research Division of NIST. He received a bachelor of science degree in mathematics from Salisbury State College and a master of science and a doctorate in mathematics from Clemson University. He joined NIST in 1986 (then the National Bureau of Standards) and has since worked on developing tools that provide a better understanding of fire phenomena, most notably Smokeview, an advanced scientific software tool for visualizing Fire Dynamics Simulation data.

**Eric Mueller** joined the Fire Research Division at NIST in 2021. He received a B.S. in Engineering Physics from Tufts University (2010), an M.S. from Worcester Polytechnic Institute (2012), and a Ph.D. from the University of Edinburgh (2017), both in fire safety engineering. His research interests include the

development of sub-models relevant to heat and mass transfer in wildland and wildland-urban interface fires.

**Emanuele Gissi** is a professional fire chief of the Italian Fire and Rescue Service (CNVVF) since 2002. He received a Ph.D. in Engineering Physics from the University of Ancona, Italy, in 2000. In addition to managing fire brigades, his main interest is bridging the gap between fire research and fire safety engineering practice. He develops open source tools for FDS.

**Anthony Hamins** joined the Fire Research Division at NIST in 1989. He received his B.S. from the University of California, Berkeley, in Physics and is Ph.D. from U.C. San Diego in Engineering Physics in 1985. His research interests include fire model validation, fire dynamics, heat and mass transfer processes in fires of multiple scales, fire suppression, flame structure, wildland-urban interface fires, and micro-gravity combustion.

**Jonathan Hodes** is a Lead Engineer in the Research, Development, Testing, and Evaluation Division at Jensen Hughes in Blacksburg, Virginia. He received a B.S. (2012) and M.S. (2014) from Clemson University and Ph.D. (2018) from Virginia Tech in Mechanical Engineering. His research interests include compartment fire dynamics, heat transfer from fires to surfaces, predicting fire growth, wildland-urban interface fires, and the intersection of physics modeling and artificial intelligence.

**William (Ruddy) Mell** is an applied mathematician currently at the U.S. Forest Service in Seattle, Washington. He holds a B.S. degree from the University of Minnesota (1981) and doctorate from the University of Washington (1994). His research interests include the development of large-eddy simulation methods and sub-models applicable to the physics of large fires in buildings, vegetation, and the wildland-urban interface.

**Julio Cesar Silva** is a Lead Researcher at Rio on Fire. He worked in the Fire Research Division of NIST as a Guest Researcher from National Council for Scientific and Technological Development, Brazil. He received a M.Sc. in 2010 and a doctorate in 2014 from Federal University of Rio de Janeiro in Civil Engineering. His research interests include fire-structure interaction and he develops coupling strategies between FDS and finite-element codes.

**Craig Weinschenk** is a Lead Research Engineer at the Underwriters Laboratories Fire Safety Research Institute, in Columbia, Maryland. He worked in the Fire Research Division at NIST as a National Research Council Postdoctoral Research Associate in 2011. He received a B.S. from Rowan University in 2006 in Mechanical Engineering. He received an M.S. in 2007 and a doctorate in 2011 from The University of Texas at Austin in Mechanical Engineering. His research interests include numerical combustion, fire-structure interaction, and human factors research of fire-fighting tactics.

# Preface

This is Volume 3 of the FDS Technical Reference Guide. Volume 1 describes the mathematical model and numerical method. Volume 2 documents past and present model verification work. Instructions for using FDS are contained in a separate User's Guide [1].

The FDS Technical Reference Guide is based in part on the “Standard Guide for Evaluating the Predictive Capability of Deterministic Fire Models,” ASTM E 1355 [2]. ASTM E 1355 defines *model evaluation* as “the process of quantifying the accuracy of chosen results from a model when applied for a specific use.” The model evaluation process consists of two main components: verification and validation. *Verification* is a process to check the correctness of the solution of the governing equations. Verification does not imply that the governing equations are appropriate; only that the equations are being solved correctly. *Validation* is a process to determine the appropriateness of the governing equations as a mathematical model of the physical phenomena of interest. Typically, validation involves comparing model results with experimental measurement. Differences that cannot be explained in terms of numerical errors in the model or uncertainty in the measurements are attributed to the assumptions and simplifications of the physical model.

Evaluation is critical to establishing both the acceptable uses and limitations of a model. Throughout its development, FDS has undergone various forms of evaluation, both at NIST and beyond. This volume provides a survey of validation work conducted to date to evaluate FDS.

# Disclaimer

The US Department of Commerce makes no warranty, expressed or implied, to users of the Fire Dynamics Simulator (FDS), and accepts no responsibility for its use. Users of FDS assume sole responsibility under Federal law for determining the appropriateness of its use in any particular application; for any conclusions drawn from the results of its use; and for any actions taken or not taken as a result of analysis performed using these tools.

Users are warned that FDS is intended for use only by those competent in the fields of fluid dynamics, thermodynamics, heat transfer, combustion, and fire science, and is intended only to supplement the informed judgment of the qualified user. The software package is a computer model that may or may not have predictive capability when applied to a specific set of factual circumstances. Lack of accurate predictions by the model could lead to erroneous conclusions with regard to fire safety. All results should be evaluated by an informed user.

Throughout this document, the mention of computer hardware or commercial software does not constitute endorsement by NIST, nor does it indicate that the products are necessarily those best suited for the intended purpose.

# Acknowledgments

The following individuals and organizations played a role in the validation process of FDS.

- The US Nuclear Regulatory Commission Office of Research has funded key validation experiments, the preparation of the FDS manuals, and the development of various sub-models that are of importance in the area of nuclear power plant safety. Special thanks to Mark Salley, David Stroup, and Jason Dreisbach for their efforts and support.
- Anthony Hamins of NIST directed the NIST/NRC and WTC experiments, conducted smaller methane burner measurements, and quantified the experimental uncertainty of these and other experiments used in this study. Alex Maranghides was the Director of the Large Fire Laboratory at NIST at the time these tests were conducted, and he helped to design the experiments. Therese McAllister oversaw the instrumentation of the structural steel during the WTC experiments.
- Anthony Hamins of NIST developed the technique of evaluating experimental uncertainty that is used throughout this Guide. Blaza Toman of the Statistical Engineering Division of NIST developed the method of quantifying the model uncertainty.
- Rick Peacock of NIST assisted in the interpretation of results from the “NBS Multi-Room Test Series,” a set of three room fire experiments conducted at the National Bureau of Standards (now NIST) in the mid-1980’s.
- Bryan Klein, currently employed at Thunderhead Engineering, Inc., assisted in the development of techniques to automatically generate the plots that are found throughout this Guide.
- Bill Pitts, Nelson Bryner, and Erik Johnsson of NIST contributed and interpreted test data for the “NIST Reduced Scale Enclosure Experiments.” Matthew Bundy, Erik Johnsson, Paul Fuss, David Lenhart, Sung Chan Kim, and Andrew Lock of NIST contributed similar data collected within a full-scale standard compartment in 2010.
- Rodney Bryant of NIST contributed velocity profile data for the “Bryant Doorway” series.
- Anthony Putorti and Scott Bareham of NIST contributed temperature measurements from plate thermometer experiments in a cone calorimeter.
- David Sheppard, currently of the Bureau of Alcohol, Tobacco and Firearms (ATF), conducted the experiments referred to as the “UL/NFPRF Test Series” on behalf of the Fire Protection Research Foundation (then known as the National Fire Protection Research Foundation) while working at Underwriters Labs in Northbrook, Illinois. Sheppard, along with Bryan Klein, currently employed at Thunderhead Engineering, Inc., conducted the experiments referred to as the “ATF Corridors” series in 2008.

- Jerry Back, Craig Beyler and Phil DiNenno of Hughes Associates and Pat Tatem of the Naval Research Laboratory contributed experimental data for the “HAI/NRL Wall Fire” series. Thanks also to Craig Beyler for assistance with the data for the “Beyler Hood Experiments.”
- Ken Steckler provided details about the “Steckler Compartment Experiments” of 1979.
- Jianping Zhang at the University of Ulster contributed heat flux measurements from the SBI apparatus.
- At the University of Maryland, Professor Fred Mowrer and Phil Friday were the first to apply FDS to the NRC-sponsored experiments referred to in this document as the “FM/SNL Test Series” (Factory Mutual and Sandia National Laboratories conducted these experiments).
- Jukka Vaari of VTT, Finland, contributed the Cup Burner test cases.
- Steve Nowlen of Sandia National Laboratory provided valuable information about the FM/SNL series, and he also conducted the CAROLFIRE experiments.
- Ulf Wickström of SP, Sweden, contributed experimental data from a series of experiments (SP AST) that were designed to evaluate the feasibility of using plate thermometer measurements as boundary conditions for a heat conduction calculation within several types of steel beams. The adiabatic surface temperature concept was tested in both the experiments and model.
- Jeremy Thornock at the University of Utah provided data on the Sandia helium plume.
- Sheldon Teiszen at Sandia National Laboratories, Albuquerque, provided detailed statistics for the helium plume and pool fire experiments conducted in the Sandia FLAME facility.
- Taylor Myers, a student at the University of Maryland and a Summer Undergraduate Research Fellow (SURF) at NIST, analyzed the Vettori Flat and Sloped Ceiling sprinkler experiments. Thanks also to Bob Vettori of the U.S. Nuclear Regulatory Commission and formerly of NIST for his help in locating the original test data and laboratory notebooks.
- Hans la Cour-Harbo, a masters degree student at the Technical University of Denmark, provided guidance and insight on the NRCC Facade experiments. Scott Bareham of NIST provided the technical drawing of the test enclosure.
- Prof. Stanislav Stolarov and graduate students Mark McKinnon and Jing Li of the University of Maryland provided the properties of several polymers for the FAA Polymers example.
- Michael Spearpoint and masters degree students Roger Harrison and Rob Fleury of the University of Canterbury, New Zealand, supplied measurements of mass entrainment rates into spill plumes (Harrison Spill Plumes) and heat flux measurements from propane burner fires (Fleury Heat Flux).
- Ezti Oztekin of the Federal Aviation Administration (FAA) developed the FAA Cargo Compartments cases based on experiments sponsored by the FAA.
- Topi Sikanen of VTT, Finland, and Jonathan Wahlqvist of Lund University, Sweden, contributed FDS input files for the PRISME DOOR series.
- Paul Tyson, a student at the University of Ulster, Northern Ireland, contributed the input files and supporting documents for the NRCC Smoke Tower experiments.
- James White, a student at the University of Maryland, provided documentation and input files for the UMD Line Burner cases.

- Charlie Hopkin and Michael Spearpoint of Olsson Fire & Risk provided the data and FDS input files for experiments conducted by Adam Bittern at the University of Christchurch, New Zealand.
- The simulations of liquefied natural gas (LNG) dispersion experiments that are described in this report were originally designed by Jeffrey Engerer and Anay Luketa of Sandia National Laboratories on behalf of the Pipeline and Hazardous Materials Safety Administration of the U.S. Department of Transportation.
- Rahul Kallada Janardhan, a doctoral student at Aalto University, Finland, prepared the BST/FRS wood crib fire spread simulations.
- Deepak Paudel, a doctoral student at Aalto University, Finland, prepared the models and datasets for the Insulation Material Fire Resistance tests.
- Aleksi Rinta-Paavola, a doctoral student at Aalto University, Finland, carried out tests and prepared the simulations of Aalto Wood Experiments.

# Contents

|   |       |
|---|-------|
| <b>FDS Developers</b>   | i     |
| <b>About the Developers</b>                                       | iii   |
| <b>Preface</b>  | v     |
| <b>Disclaimer</b>   | vii   |
| <b>Acknowledgments</b>  | ix    |
| <b>Contents</b>   | xiii  |
| <b>List of Figures</b>  | xxiii |
| <b>List of Tables</b>   | xlv   |
| <b>List of Acronyms</b>   | xlix  |
| <b>1 What is Model Validation?</b>                                | 1     |
| 1.1 Blind, Specified, and Open Validation Experiments . . . . .   | 1     |
| 1.2 How to Use this Guide . . . . .                               | 2     |
| <b>2 Survey of Past Validation Work</b>                           | 5     |
| 2.1 Validation Work with Pre-Release Versions of FDS . . . . .    | 6     |
| 2.2 Validation of FDS since 2000 . . . . .                        | 7     |
| 2.2.1 Fire Plumes . . . . .                                       | 7     |
| 2.2.2 Pool Fires . . . . .  | 8     |
| 2.2.3 Air and Gas Movement in the Absence of Fire . . . . .       | 8     |
| 2.2.4 Wind Engineering . . . . .                                  | 9     |
| 2.2.5 Atmospheric Dispersion . . . . .                            | 9     |
| 2.2.6 Growing Fires . . . . .                                     | 10    |
| 2.2.7 Flame Spread . . . . .                                      | 10    |
| 2.2.8 Compartment Fires . . . . .                                 | 11    |
| 2.2.9 Sprinklers, Mist System, and Suppression by Water . . . . . | 12    |
| 2.2.10 Airflows in Fire Compartments . . . . .                    | 13    |
| 2.2.11 Tunnel Fires . . . . .                                     | 13    |
| 2.2.12 Smoke Detection . . . . .                                  | 14    |
| 2.2.13 Combustion Model . . . . .                                 | 14    |
| 2.2.14 Soot Deposition . . . . .                                  | 15    |
| 2.2.15 Wildfires . . . . .  | 15    |

|          |  |           |
|----------|--|-----------|
| 2.3      | Reconstructions of Actual Fires . . . . .            | 16        |
| <b>3</b> | <b>Description of Experiments</b>                    | <b>17</b> |
| 3.1      | Aalto Woods Experiments . . . . .                    | 17        |
| 3.2      | ArupFire Tunnel Fire Experiments . . . . .           | 18        |
| 3.3      | ATF Corridors Experiments . . . . .                  | 18        |
| 3.4      | Atmospheric Dispersion Correlations . . . . .        | 20        |
| 3.5      | Backward Facing Step . . . . .                       | 20        |
| 3.6      | Beyler Hood Experiments . . . . .                    | 20        |
| 3.7      | BGC/GRI LNG Fire Experiments . . . . .               | 22        |
| 3.8      | Bittern Sprinkler Experiments . . . . .              | 23        |
| 3.9      | Bouchair Solar Chimney . . . . .                     | 25        |
| 3.10     | BRE Spray Test for Radiation Attenuation . . . . .   | 26        |
| 3.11     | Bryant Doorway Velocity Measurements . . . . .       | 27        |
| 3.12     | BST/FRS Wood Crib Fire Experiments . . . . .         | 28        |
| 3.13     | Cable Response to Live Fire – CAROLFIRE . . . . .    | 29        |
| 3.14     | Crown Fires . . . . .                                | 30        |
| 3.15     | CSIRO Grassland Fires . . . . .                      | 30        |
| 3.16     | CSTB Tunnel Experiments . . . . .                    | 33        |
| 3.17     | Cup Burner Experiments . . . . .                     | 34        |
| 3.18     | DelCo Trainer Experiments . . . . .                  | 36        |
| 3.19     | DoJ/HAI Pool Fire Experiments . . . . .              | 38        |
| 3.20     | Droplet Evaporation . . . . .                        | 39        |
| 3.21     | Edinburgh Vegetation Drag . . . . .                  | 39        |
| 3.22     | FAA Cargo Compartments . . . . .                     | 40        |
| 3.23     | FAA Polymers . . . . .                               | 41        |
| 3.24     | Fleury Heat Flux Measurements . . . . .              | 41        |
| 3.25     | FM Burner Experiments . . . . .                      | 41        |
| 3.26     | FM/FPRF Data Center Experiments . . . . .            | 42        |
| 3.27     | FM Parallel Panel Experiments . . . . .              | 44        |
| 3.28     | FM/SNL Experiments . . . . .                         | 45        |
| 3.29     | FM Vertical Wall Flame Experiments . . . . .         | 47        |
| 3.30     | FPL Materials . . . . .                              | 47        |
| 3.31     | Frankman Vegetation Experiments . . . . .            | 48        |
| 3.32     | FSRI/NIJ Materials . . . . .                         | 48        |
| 3.33     | Hamins Gas Burner Experiments . . . . .              | 48        |
| 3.34     | Harrison Spill Plumes . . . . .                      | 48        |
| 3.35     | Heskestad Flame Height Correlation . . . . .         | 51        |
| 3.36     | Insulation Material Fire Resistance Tests . . . . .  | 51        |
| 3.37     | JH/FRA Rail Car Experiments . . . . .                | 51        |
| 3.38     | JH/NIJ Materials . . . . .                           | 55        |
| 3.39     | Lattimer Tilted Wall . . . . .                       | 55        |
| 3.40     | LEMTA Spray Test for Radiation Attenuation . . . . . | 56        |
| 3.41     | LEMTA Spray Cooling . . . . .                        | 57        |
| 3.42     | LEMTA/UGent Pool Fires . . . . .                     | 57        |
| 3.43     | LLNL Enclosure Experiments . . . . .                 | 58        |
| 3.44     | LNG Dispersion Experiments . . . . .                 | 61        |
| 3.45     | Loughborough Jet Fire Experiments . . . . .          | 63        |

|        |  |     |
|--------|--|-----|
| 3.46   | McCaffrey Plume Experiments . . . . .                    | 64  |
| 3.47   | Memorial Tunnel Experiments . . . . .                    | 67  |
| 3.48   | Montoir LNG Fires . . . . .                              | 69  |
| 3.49   | NBS Multi-Room Experiments . . . . .                     | 70  |
| 3.50   | NIST Composite Beam Experiments . . . . .                | 73  |
| 3.51   | NIST E119 Compartment Experiments . . . . .              | 77  |
| 3.52   | NIST Douglas Firs . . . . .                              | 81  |
| 3.53   | NIST Enclosure Experiments . . . . .                     | 82  |
| 3.53.1 | NIST Reduced Scale Enclosure Experiments, 1994 . . . . . | 82  |
| 3.53.2 | NIST Reduced Scale Enclosure Experiments, 2007 . . . . . | 82  |
| 3.53.3 | NIST Full-Scale Enclosure Experiments, 2008 . . . . .    | 82  |
| 3.53.4 | Modeling Notes . . . . .                                 | 83  |
| 3.54   | NIST Helium Experiments . . . . .                        | 85  |
| 3.55   | NIST/NRC Compartment Experiments . . . . .               | 86  |
| 3.56   | NIST/NRC Corner, Wall, and Cabinet Experiments . . . . . | 88  |
| 3.56.1 | Wall and Corner Effects . . . . .                        | 88  |
| 3.56.2 | Cabinet Effects . . . . .                                | 90  |
| 3.57   | NIST/NRC OLIVE-Fire Experiments . . . . .                | 93  |
| 3.58   | NIST/NRC Parallel Panel Experiments . . . . .            | 96  |
| 3.59   | NIST/NRC Transient Combustibles Experiments . . . . .    | 96  |
| 3.60   | NIST Polymers . . . . .                                  | 98  |
| 3.61   | NIST Pool Fire Experiments . . . . .                     | 98  |
| 3.62   | NIST Smoke Alarm Experiments . . . . .                   | 99  |
| 3.63   | NIST Soot Deposition Gauge . . . . .                     | 102 |
| 3.64   | NIST Structure Separation Experiments . . . . .          | 103 |
| 3.65   | NIST Vent Study . . . . .                                | 104 |
| 3.66   | NRCC Facade Heat Flux Measurements . . . . .             | 107 |
| 3.67   | NRCC Smoke Tower Experiments . . . . .                   | 108 |
| 3.68   | NRL/HAI Wall Heat Flux Measurements . . . . .            | 111 |
| 3.69   | Phoenix LNG Fires . . . . .                              | 111 |
| 3.70   | Pool Fires . . . . .                                     | 113 |
| 3.71   | PRISME Project . . . . .                                 | 114 |
| 3.72   | Purdue Flames . . . . .                                  | 114 |
| 3.73   | Ranz Marshall Droplet Experiments . . . . .              | 115 |
| 3.74   | Restivo Compartment Air Flow Experiment . . . . .        | 116 |
| 3.75   | Sandia Methane Burner . . . . .                          | 117 |
| 3.76   | Sandia Plume Experiments . . . . .                       | 118 |
| 3.77   | Scaling Pyrolysis . . . . .                              | 119 |
| 3.78   | SETCOM Wall Condensation Experiments . . . . .           | 120 |
| 3.79   | Shell LNG Fireball Experiments . . . . .                 | 121 |
| 3.80   | Sippola Aerosol Deposition Experiments . . . . .         | 122 |
| 3.81   | Smyth Slot Burner Experiment . . . . .                   | 125 |
| 3.82   | RISE Materials . . . . .                                 | 125 |
| 3.83   | SP Adiabatic Surface Temperature Experiments . . . . .   | 126 |
| 3.84   | SP Wood Crib Experiments . . . . .                       | 127 |
| 3.85   | Steckler Compartment Experiments . . . . .               | 129 |
| 3.86   | SWJTU Tunnel Experiments . . . . .                       | 132 |
| 3.87   | Theobald Hose Stream Experiments . . . . .               | 132 |

|          |   |            |
|----------|---|------------|
| 3.88     | UL/NIST Vent Experiments . . . . .                          | 132        |
| 3.89     | UL/NFPRF Sprinkler, Vent, and Draft Curtain Study . . . . . | 134        |
| 3.90     | UL/NIJ House Experiments . . . . .                          | 140        |
| 3.91     | Ulster SBI Corner Heat Flux Measurements . . . . .          | 145        |
| 3.92     | UMD Polymers . . . . .                                      | 145        |
| 3.93     | UMD Line Burner . . . . .                                   | 145        |
| 3.94     | UMD SBI Experiment . . . . .                                | 148        |
| 3.95     | USCG/HAI Water Mist Suppression Tests . . . . .             | 149        |
| 3.96     | USFS/Catchpole Experiments . . . . .                        | 149        |
| 3.97     | USFS/Corsica Experiments . . . . .                          | 149        |
| 3.98     | USN High Bay Hangar Experiments . . . . .                   | 150        |
| 3.99     | UWO Wind Tunnel Experiments . . . . .                       | 150        |
| 3.100    | Vettori Flat Ceiling Experiments . . . . .                  | 151        |
| 3.101    | Vettori Sloped Ceiling Experiments . . . . .                | 154        |
| 3.102    | VTT Large Hall Tests . . . . .                              | 154        |
| 3.103    | VTT Water Spray Experiments . . . . .                       | 157        |
| 3.104    | Waterloo Methanol Pool Fire Experiment . . . . .            | 157        |
| 3.105    | WTC Spray Burner Experiments . . . . .                      | 158        |
| 3.106    | Wu Bakar Tunnel Experiments . . . . .                       | 160        |
| 3.107    | Summary of Experiments . . . . .                            | 160        |
| <b>4</b> | <b>Quantifying Model Uncertainty</b>                        | <b>167</b> |
| 4.1      | Introduction . . . . .                                      | 167        |
| 4.2      | Sources of Model Uncertainty . . . . .                      | 169        |
| 4.3      | Experimental Uncertainty . . . . .                          | 170        |
| 4.3.1    | Uncertainty of Common Fire Measurements . . . . .           | 171        |
| 4.3.2    | Propagation of Input Parameter Uncertainty . . . . .        | 173        |
| 4.3.3    | Summary of Experimental Uncertainty Estimates . . . . .     | 177        |
| 4.4      | Calculating Model Uncertainty . . . . .                     | 177        |
| 4.5      | Example . . . . .   | 180        |
| 4.6      | Additional Considerations . . . . .                         | 181        |
| <b>5</b> | <b>HGL Temperature and Depth</b>                            | <b>183</b> |
| 5.1      | HGL Reduction Method . . . . .                              | 183        |
| 5.2      | ATF Corridors . . . . .                                     | 184        |
| 5.3      | CSTB Tunnel . . . . .                                       | 188        |
| 5.4      | DelCo Trainers . . . . .                                    | 191        |
| 5.5      | FM/SNL Test Series . . . . .                                | 199        |
| 5.6      | JH/FRA Experiments . . . . .                                | 204        |
| 5.7      | LLNL Enclosure Series . . . . .                             | 209        |
| 5.8      | NBS Multi-Room Test Series . . . . .                        | 218        |
| 5.9      | NIST Composite Beam . . . . .                               | 222        |
| 5.10     | NIST E119 Compartment . . . . .                             | 225        |
| 5.11     | NIST Full-Scale Enclosure (FSE), 2008 . . . . .             | 229        |
| 5.12     | NIST/NRC Test Series . . . . .                              | 236        |
| 5.13     | NIST/NRC Corner Effects Experiments . . . . .               | 241        |
| 5.14     | NIST Vent Study . . . . .                                   | 247        |
| 5.15     | NRCC Smoke Tower . . . . .                                  | 254        |

|          |  |            |
|----------|--|------------|
| 5.16     | PRISME DOOR Experiments . . . . .                          | 256        |
| 5.17     | PRISME SOURCE Experiments . . . . .                        | 260        |
| 5.18     | Steckler Compartment Experiments . . . . .                 | 263        |
| 5.19     | UL/NIST Vent Experiments . . . . .                         | 271        |
| 5.20     | UL/NIJ House Experiments . . . . .                         | 273        |
| 5.21     | VTT Test Series . . . . .                                  | 276        |
| 5.22     | WTC Test Series . . . . .                                  | 277        |
| 5.23     | Summary of Hot Gas Layer Temperature and Height . . . . .  | 280        |
| <b>6</b> | <b>Fire Plumes</b>   | <b>283</b> |
| 6.1      | Plume Temperatures . . . . .                               | 283        |
| 6.1.1    | FM Burner Experiments . . . . .                            | 284        |
| 6.1.2    | FM/SNL Experiments . . . . .                               | 287        |
| 6.1.3    | McCaffrey's Plume Correlation . . . . .                    | 290        |
| 6.1.4    | NIST/NRC Corner/Wall/Cabinet Effects Experiments . . . . . | 292        |
| 6.1.5    | NIST Pool Fires . . . . .                                  | 294        |
| 6.1.6    | NRCC Smoke Tower Experiments, Stairwell Plumes . . . . .   | 300        |
| 6.1.7    | Sandia Methane Burner Experiments . . . . .                | 302        |
| 6.1.8    | SP Adiabatic Surface Temperature Experiments . . . . .     | 306        |
| 6.1.9    | UMD Line Burner . . . . .                                  | 309        |
| 6.1.10   | USN High Bay Hangar Experiments . . . . .                  | 311        |
| 6.1.11   | VTT Large Hall Experiments . . . . .                       | 315        |
| 6.1.12   | Waterloo Methanol Pool Fire Experiment . . . . .           | 316        |
| 6.1.13   | Summary of Plume Temperature Predictions . . . . .         | 324        |
| 6.2      | Flame Height . . . . .                                     | 325        |
| 6.2.1    | Heskestad's Flame Height Correlation . . . . .             | 325        |
| 6.2.2    | UMD Line Burner . . . . .                                  | 329        |
| 6.2.3    | Flame Height Summary . . . . .                             | 330        |
| 6.3      | Flame Tilt . . . . .                                       | 331        |
| 6.4      | Harrison Spill Plumes/Entrainment Experiments . . . . .    | 332        |
| 6.5      | Sandia Plume Experiments . . . . .                         | 333        |
| 6.5.1    | Sandia 1 m Helium Plume . . . . .                          | 333        |
| 6.5.2    | Sandia 1 m Methane Pool Fire . . . . .                     | 338        |
| 6.5.3    | Sandia 1 m Hydrogen Pool Fire . . . . .                    | 344        |
| 6.6      | Purdue 7.1 cm Methane Flame . . . . .                      | 347        |
| 6.7      | FM Vertical Wall Flame Experiments . . . . .               | 351        |
| <b>7</b> | <b>Ceiling Jets and Device Activation</b>                  | <b>355</b> |
| 7.1      | Ceiling Jet Temperatures . . . . .                         | 355        |
| 7.1.1    | ATF Corridors Experiment . . . . .                         | 356        |
| 7.1.2    | Arup Tunnel Experiments . . . . .                          | 362        |
| 7.1.3    | DelCo Trainers . . . . .                                   | 363        |
| 7.1.4    | FAA Cargo Compartments . . . . .                           | 366        |
| 7.1.5    | FM/SNL Experiments . . . . .                               | 371        |
| 7.1.6    | NIST Composite Beam . . . . .                              | 374        |
| 7.1.7    | NIST Smoke Alarm Experiments . . . . .                     | 376        |
| 7.1.8    | NIST/NRC Experiments . . . . .                             | 378        |
| 7.1.9    | NIST/NRC Corner Effects Experiments . . . . .              | 381        |

|          |   |            |
|----------|---|------------|
| 7.1.10   | NIST Vent Study . . . . .   | 385        |
| 7.1.11   | NRCC Smoke Tower . . . . .  | 387        |
| 7.1.12   | PRISME DOOR Experiments . . . . .                                       | 389        |
| 7.1.13   | PRISME SOURCE Experiments . . . . .                                     | 391        |
| 7.1.14   | SP Adiabatic Surface Temperature Experiments . . . . .                  | 393        |
| 7.1.15   | UL/NFPRF Series I Experiments . . . . .                                 | 395        |
| 7.1.16   | UL/NIJ House Experiments . . . . .                                      | 398        |
| 7.1.17   | UL/NIST Vent Experiments . . . . .                                      | 399        |
| 7.1.18   | Vettori Flat Ceiling Experiments . . . . .                              | 401        |
| 7.1.19   | Vettori Sloped Ceiling Experiments . . . . .                            | 408        |
| 7.1.20   | WTC Experiments . . . . .   | 418        |
| 7.1.21   | Summary of Ceiling Jet Temperature Predictions . . . . .                | 419        |
| 7.2      | Sprinkler Activation Times . . . . .                                    | 420        |
| 7.2.1    | Time to First Sprinkler Activation . . . . .                            | 420        |
| 7.2.2    | Number of Sprinkler Activations . . . . .                               | 421        |
| 7.3      | Smoke Detector Activation Times . . . . .                               | 429        |
| 7.4      | Backlayering of Smoke in Tunnels . . . . .                              | 431        |
| 7.4.1    | Wu Bakar Tunnel Experiments . . . . .                                   | 431        |
| 7.4.2    | Memorial Tunnel Experiments . . . . .                                   | 432        |
| 7.4.3    | FHWA Tunnel Experiments . . . . .                                       | 468        |
| <b>8</b> | <b>Gas Velocity</b> . . . . .   | <b>473</b> |
| 8.1      | ATF Corridor Experiments . . . . .                                      | 473        |
| 8.2      | Backward Facing Step . . . . .  | 478        |
| 8.3      | Bryant Doorway Experiments . . . . .                                    | 481        |
| 8.4      | Edinburgh Vegetation Drag . . . . .                                     | 483        |
| 8.5      | FM/FPRF Datacenter Experiments . . . . .                                | 486        |
| 8.6      | JH/FRA Experiments . . . . .  | 488        |
| 8.7      | McCaffrey's Plume Correlation . . . . .                                 | 490        |
| 8.8      | NIST Pool Fires . . . . .   | 492        |
| 8.9      | PRISME DOOR Experiments . . . . .                                       | 493        |
| 8.10     | Restivo Experiment . . . . .  | 494        |
| 8.11     | Steckler Compartment Experiments . . . . .                              | 495        |
| 8.12     | UL/NIJ House Experiments . . . . .                                      | 503        |
| 8.13     | Waterloo Methanol Pool Fire Experiment . . . . .                        | 508        |
| 8.14     | WTC Experiments . . . . .   | 517        |
| 8.15     | Summary of Velocity Predictions . . . . .                               | 522        |
| <b>9</b> | <b>Gas Species and Smoke</b> . . . . .                                  | <b>523</b> |
| 9.1      | Major Combustion Products, O <sub>2</sub> and CO <sub>2</sub> . . . . . | 523        |
| 9.1.1    | DelCo Trainers . . . . .  | 524        |
| 9.1.2    | FAA Cargo Compartments . . . . .  | 527        |
| 9.1.3    | LLNL Enclosure . . . . .  | 528        |
| 9.1.4    | NIST/NRC Experiments . . . . .  | 545        |
| 9.1.5    | NRCC Smoke Tower . . . . .  | 549        |
| 9.1.6    | PRISME DOOR Experiments . . . . .                                       | 551        |
| 9.1.7    | PRISME SOURCE Experiments . . . . .                                     | 555        |
| 9.1.8    | WTC Experiments . . . . .   | 558        |

|           |   |            |
|-----------|---|------------|
| 9.1.9     | UMD Line Burner . . . . .   | 560        |
| 9.1.10    | Summary of Major Combustion Products Predictions . . . . .            | 561        |
| 9.2       | <b>Smoke . . . . .</b>  | <b>562</b> |
| 9.2.1     | FM Burner Experiments . . . . .                                       | 562        |
| 9.2.2     | FM/FPRF Data Center Experiments . . . . .                             | 571        |
| 9.2.3     | NIST/NRC Experiments . . . . .  | 572        |
| 9.2.4     | FAA Cargo Compartments . . . . .                                      | 576        |
| 9.3       | <b>Aerosols . . . . .</b>   | <b>578</b> |
| 9.3.1     | Sippola Aerosol Deposition Experiments . . . . .                      | 578        |
| 9.3.2     | NIST Soot Deposition Gauge Experiments . . . . .                      | 579        |
| 9.4       | <b>Droplet Evaporation . . . . .</b>                                  | <b>582</b> |
| 9.4.1     | Ranz and Marshall . . . . .   | 582        |
| 9.4.2     | Fujita et al. . . . .   | 584        |
| 9.4.3     | Gavin . . . . .   | 585        |
| 9.4.4     | Kolaitis and Founti . . . . .   | 586        |
| 9.4.5     | Maqua et al. . . . .  | 587        |
| 9.4.6     | Taflin Experiments . . . . .  | 588        |
| 9.5       | <b>Products of Incomplete Combustion . . . . .</b>                    | <b>589</b> |
| 9.5.1     | Smyth Slot Burner Experiment . . . . .                                | 589        |
| 9.5.2     | Beyler Hood Experiments . . . . .                                     | 593        |
| 9.5.3     | NIST Reduced Scale Enclosure (RSE) Experiments, 1994 . . . . .        | 595        |
| 9.5.4     | NIST Reduced-Scale Enclosure (RSE) Experiments, 2007 . . . . .        | 597        |
| 9.5.5     | NIST Full-Scale Enclosure (FSE) Experiments, 2008 . . . . .           | 609        |
| 9.5.6     | NIST Pool Fires . . . . .   | 636        |
| 9.5.7     | Summary, Products of Incomplete Combustion . . . . .                  | 643        |
| 9.6       | <b>Helium Release in a Reduced Scale Garage Geometry . . . . .</b>    | <b>644</b> |
| <b>10</b> | <b>Pressure</b>   | <b>649</b> |
| 10.1      | FM/FPRF Datacenter Experiments . . . . .                              | 649        |
| 10.2      | NIST/NRC Experiments . . . . .  | 649        |
| 10.3      | LLNL Enclosure Experiments . . . . .                                  | 653        |
| 10.4      | PRISME DOOR Experiments . . . . .                                     | 662        |
| 10.5      | PRISME SOURCE Experiments . . . . .                                   | 667        |
| 10.6      | Prétrel/IRSN Water Spray Experiments . . . . .                        | 670        |
| 10.7      | UL/NIJ House Experiments . . . . .                                    | 672        |
| 10.8      | Summary of Pressure Predictions . . . . .                             | 679        |
| <b>11</b> | <b>Surface Temperature</b>  | <b>681</b> |
| 11.1      | Wall, Ceiling and Floor Temperatures . . . . .                        | 682        |
| 11.1.1    | FAA Cargo Compartments . . . . .                                      | 682        |
| 11.1.2    | NIST Composite Beam . . . . .   | 683        |
| 11.1.3    | NIST Full-Scale Enclosure (FSE), 2008 . . . . .                       | 690        |
| 11.1.4    | NIST/NRC Experiments . . . . .  | 698        |
| 11.1.5    | PRISME DOOR Experiments . . . . .                                     | 711        |
| 11.1.6    | PRISME SOURCE Experiments . . . . .                                   | 715        |
| 11.1.7    | WTC Experiments . . . . .   | 718        |
| 11.1.8    | Insulation Materials Fire Resistance Tests . . . . .                  | 732        |
| 11.1.9    | Summary of Wall, Ceiling, and Floor Temperature Predictions . . . . . | 737        |

|           |  |            |
|-----------|--|------------|
| 11.2      | Target Temperature . . . . .                                       | 738        |
| 11.2.1    | NIST Composite Beam . . . . .                                      | 738        |
| 11.2.2    | NIST E119 Compartment . . . . .                                    | 740        |
| 11.2.3    | NIST/NRC Experiments . . . . .                                     | 741        |
| 11.2.4    | NIST/NRC Corner Effects Experiments . . . . .                      | 756        |
| 11.2.5    | SP Adiabatic Surface Temperature Experiments . . . . .             | 769        |
| 11.2.6    | WTC Experiments . . . . .  | 797        |
| 11.2.7    | CAROLFIRE Experiments . . . . .                                    | 809        |
| 11.2.8    | Frankman Vegetation Experiments . . . . .                          | 815        |
| 11.2.9    | PRISME Experiments . . . . .                                       | 816        |
| 11.2.10   | Summary of Target Temperature Predictions . . . . .                | 824        |
| 11.2.11   | Time to Failure . . . . .  | 825        |
| 11.3      | Liquid Pool Surface Temperature . . . . .                          | 826        |
| 11.3.1    | Pool Fires . . . . .   | 826        |
| 11.3.2    | NIST Pool Fires and Waterloo Methanol . . . . .                    | 828        |
| 11.3.3    | Summary of Liquid Pool Surface Temperature Predictions . . . . .   | 829        |
| <b>12</b> | <b>Heat Flux</b> . . . . .   | <b>831</b> |
| 12.1      | Heat Flux to Walls, Ceiling, and Floor . . . . .                   | 832        |
| 12.1.1    | FAA Cargo Compartments . . . . .                                   | 832        |
| 12.1.2    | FM Parallel Panel Experiments . . . . .                            | 833        |
| 12.1.3    | JH/FRA Experiments . . . . .                                       | 834        |
| 12.1.4    | FM Vertical Wall Flame Experiments . . . . .                       | 837        |
| 12.1.5    | NIST E119 Compartment . . . . .                                    | 839        |
| 12.1.6    | NIST/NRC Experiments . . . . .                                     | 840        |
| 12.1.7    | NIST/NRC Parallel Panel Experiments . . . . .                      | 853        |
| 12.1.8    | NIST Reduced-Scale Enclosure (RSE) Experiments, 2007 . . . . .     | 854        |
| 12.1.9    | NRCC Facade Experiments . . . . .                                  | 856        |
| 12.1.10   | NRL/HAI Experiments . . . . .                                      | 860        |
| 12.1.11   | PRISME DOOR Experiments . . . . .                                  | 863        |
| 12.1.12   | PRISME SOURCE Experiments . . . . .                                | 869        |
| 12.1.13   | Ulster SBI Experiments . . . . .                                   | 873        |
| 12.1.14   | UMD SBI Experiment . . . . .                                       | 874        |
| 12.1.15   | WTC Experiments . . . . .  | 876        |
| 12.1.16   | Summary of Wall, Ceiling and Floor Heat Flux Predictions . . . . . | 880        |
| 12.2      | Heat Flux to Targets . . . . .                                     | 881        |
| 12.2.1    | Fleury Experiments . . . . .                                       | 881        |
| 12.2.2    | Hamins Gas Burner Experiments . . . . .                            | 887        |
| 12.2.3    | BGC/GRI LNG Fires . . . . .  | 912        |
| 12.2.4    | Loughborough Jet Fire Experiments . . . . .                        | 915        |
| 12.2.5    | Montoir LNG Fires . . . . .  | 920        |
| 12.2.6    | NIST Douglas Firs . . . . .  | 924        |
| 12.2.7    | NIST/NRC Experiments . . . . .                                     | 925        |
| 12.2.8    | NIST Pool Fires . . . . .  | 934        |
| 12.2.9    | NIST Structure Separation Verification . . . . .                   | 937        |
| 12.2.10   | Phoenix LNG Fires . . . . .  | 939        |
| 12.2.11   | Sandia Methane Burner Experiments . . . . .                        | 941        |
| 12.2.12   | Shell LNG Fireballs . . . . .                                      | 949        |

|           |   |             |
|-----------|---|-------------|
| 12.2.13   | UMD SBI Experiment . . . . .                                    | 950         |
| 12.2.14   | UMD Line Burner . . . . .                                       | 951         |
| 12.2.15   | WTC Experiments . . . . .                                       | 953         |
| 12.2.16   | Summary of Target Heat Flux Predictions . . . . .               | 957         |
| 12.3      | Attenuation of Thermal Radiation in Water Spray . . . . .       | 958         |
| 12.3.1    | BRE Spray Experiments . . . . .                                 | 958         |
| 12.3.2    | LEMTA Spray Experiments . . . . .                               | 958         |
| 12.4      | Water Spray Cooling . . . . .                                   | 960         |
| 12.4.1    | LEMTA Spray Cooling Experiments . . . . .                       | 960         |
| 12.5      | Convective Heat Flux . . . . .                                  | 961         |
| 12.5.1    | Bouchair Solar Chimney . . . . .                                | 961         |
| 12.6      | Radiation Source Term . . . . .                                 | 968         |
| 12.6.1    | FM Burner Experiments . . . . .                                 | 968         |
| 12.7      | Condensation Heat Flux . . . . .                                | 971         |
| 12.7.1    | SETCOM Experiments . . . . .                                    | 971         |
| <b>13</b> | <b>Suppression</b>  | <b>973</b>  |
| 13.1      | Minimum Agent Concentration Experiments . . . . .               | 973         |
| 13.1.1    | Cup Burner Experiments . . . . .                                | 973         |
| 13.1.2    | FM Burner Experiments . . . . .                                 | 975         |
| 13.1.3    | UMD Line Burner . . . . .                                       | 976         |
| 13.2      | Compartment Fire Extinction . . . . .                           | 977         |
| 13.2.1    | LLNL Enclosure Experiments . . . . .                            | 977         |
| 13.2.2    | NIST/NRC OLIVE-Fire Experiments . . . . .                       | 982         |
| 13.2.3    | SWJTU Tunnel Experiments . . . . .                              | 988         |
| 13.2.4    | USCG/HAI Water Mist Suppression Tests . . . . .                 | 989         |
| 13.2.5    | Summary, Flame Extinction Time . . . . .                        | 995         |
| 13.3      | Theobald Hose Stream Experiments . . . . .                      | 996         |
| 13.4      | VTT Water Spray Experiments . . . . .                           | 998         |
| <b>14</b> | <b>Burning Rate and Fire Spread</b>                             | <b>1001</b> |
| 14.1      | FAA Polymers . . . . .  | 1001        |
| 14.1.1    | Glossary of Terms . . . . .                                     | 1001        |
| 14.1.2    | Non-Charring Polymers, HDPE, HIPS, and PMMA . . . . .           | 1003        |
| 14.1.3    | Complex Non-Charring Polymers: PP, PA66, POM, and PET . . . . . | 1005        |
| 14.1.4    | Polycarbonate (PC) . . . . .                                    | 1007        |
| 14.1.5    | Poly(vinyl chloride) (PVC) . . . . .                            | 1009        |
| 14.1.6    | Poly(aryl ether ether ketone)) (PEEK) . . . . .                 | 1011        |
| 14.1.7    | Poly(butylene terephthalate) (PBT) . . . . .                    | 1014        |
| 14.1.8    | PBT with Glass Fibers (PBT-GF) . . . . .                        | 1016        |
| 14.2      | NIST Polymers . . . . .   | 1018        |
| 14.3      | UMD Polymers . . . . .  | 1020        |
| 14.3.1    | One-Step Degradation: ABS, HIPS, and PMMA . . . . .             | 1020        |
| 14.3.2    | Two-Step Degradation: Kydex . . . . .                           | 1023        |
| 14.3.3    | Three-Step Degradation: PEI, PET, and POM . . . . .             | 1025        |
| 14.4      | Corrugated Cardboard . . . . .                                  | 1028        |
| 14.5      | Wood Cribs and Similar Wood/Paper Combustibles . . . . .        | 1032        |
| 14.5.1    | Aalto Woods . . . . .   | 1033        |

|                     |  |             |
|---------------------|--|-------------|
| 14.5.2              | BST/FRS Wood Crib Experiments . . . . .                | 1037        |
| 14.5.3              | NIST/NRC Transient Combustibles . . . . .              | 1040        |
| 14.5.4              | SP Wood Crib Experiments . . . . .                     | 1043        |
| 14.6                | Liquid Pool Fires . . . . .                            | 1045        |
| 14.6.1              | DoJ/HAI Pool Fires . . . . .                           | 1045        |
| 14.6.2              | LEMTA/UGent Pool Fires . . . . .                       | 1053        |
| 14.6.3              | Pool Fire Measurements . . . . .                       | 1056        |
| 14.6.4              | NIST Pool Fires . . . . .                              | 1058        |
| 14.6.5              | Waterloo Methanol Pool Fire . . . . .                  | 1058        |
| 14.7                | Vertical Flame Spread . . . . .                        | 1059        |
| 14.7.1              | NIST/NRC Parallel Panel Experiments . . . . .          | 1059        |
| 14.7.2              | UMD SBI Experiment . . . . .                           | 1060        |
| 14.8                | Scaling Pyrolysis (SPyro) . . . . .                    | 1061        |
| 14.8.1              | Aalto Woods Experiments . . . . .                      | 1061        |
| 14.8.2              | FAA Polymers Experiments . . . . .                     | 1062        |
| 14.8.3              | FPL Wood Experiments . . . . .                         | 1066        |
| 14.8.4              | FSRI/NIJ Experiments . . . . .                         | 1068        |
| 14.8.5              | JH Experiments . . . . .                               | 1082        |
| 14.8.6              | RISE Experiments . . . . .                             | 1085        |
| 14.9                | Compartment Fires . . . . .                            | 1099        |
| 14.9.1              | JH/FRA Reduced Scale Compartment Experiments . . . . . | 1099        |
| 14.10               | Wildland Fire Burning and Spread Rates . . . . .       | 1101        |
| 14.10.1             | Crown Fires . . . . .                                  | 1101        |
| 14.10.2             | CSIRO Grassland Fires . . . . .                        | 1102        |
| 14.10.3             | USFS/Catchpole Experiments . . . . .                   | 1104        |
| 14.10.4             | USFS/Corsica Fire Spread Experiments . . . . .         | 1150        |
| 14.10.5             | Burning Trees (NIST Douglas Firs) . . . . .            | 1152        |
| 14.11               | Summary of Burning and Spread Rates . . . . .          | 1154        |
| <b>15</b>           | <b>Wind Engineering and Atmospheric Dispersion</b>     | <b>1157</b> |
| 15.1                | UWO Wind Tunnel Experiments . . . . .                  | 1157        |
| 15.2                | LNG Dispersion Experiments . . . . .                   | 1167        |
| 15.3                | Stack Emission Plume Rise . . . . .                    | 1175        |
| <b>16</b>           | <b>Conclusion</b>                                      | <b>1179</b> |
| 16.1                | Summary of FDS Model Uncertainty Statistics . . . . .  | 1179        |
| 16.2                | Normality Tests . . . . .                              | 1180        |
| 16.3                | Summary of FDS Validation Git Statistics . . . . .     | 1186        |
| <b>Bibliography</b> |  | <b>1189</b> |

# List of Figures

|      |   |     |
|------|---|-----|
| 3.1  | Geometry of the ATF Corridors Experiments . . . . .                                     | 19  |
| 3.2  | Geometry of the Backward Facing Step experiments . . . . .                              | 20  |
| 3.3  | Sketch of Beyler Hood cross section . . . . .   | 21  |
| 3.4  | Plan view of the Bittern Sprinkler Experiments . . . . .                                | 24  |
| 3.5  | Geometry of the Bouchair Solar Chimney experiment . . . . .                             | 26  |
| 3.6  | Geometry of Bryant's compartment . . . . .  | 28  |
| 3.7  | Snapshots of the simulation of CSIRO Grassland Fire F19 . . . . .                       | 32  |
| 3.8  | Instrumentation of the single level DelCo training structure . . . . .                  | 36  |
| 3.9  | Instrumentation of the two level DelCo training structure . . . . .                     | 37  |
| 3.10 | Geometry of the Edinburgh Vegetation Drag experiments . . . . .                         | 40  |
| 3.11 | Sketch of the FM/FPRF enclosure . . . . .   | 43  |
| 3.12 | Sketch of the FM parallel panel apparatus . . . . .                                     | 44  |
| 3.13 | Geometry of the FM/SNL Experiments . . . . .  | 46  |
| 3.14 | Geometry of the Harrison Spill Plumes Experiments . . . . .                             | 50  |
| 3.15 | Combustible lining configuration in scaled compartment fire experiments . . . . .       | 54  |
| 3.16 | Instrumentation plan from compartment fire experiments . . . . .                        | 54  |
| 3.17 | Lattimer tilted wall apparatus . . . . .  | 56  |
| 3.18 | Geometry of the LLNL Enclosure Experiments . . . . .                                    | 60  |
| 3.19 | Photograph of a jet fire experiment at the Spadeadam Test Site . . . . .                | 63  |
| 3.20 | McCaffrey Plume Centerline Temperature and Velocity Correlations . . . . .              | 65  |
| 3.21 | McCaffrey Plume Burner Surface Temperatures . . . . .                                   | 66  |
| 3.22 | Memorial Tunnel cross section . . . . .   | 67  |
| 3.23 | Geometry of the NBS Multi-Room Experiments . . . . .                                    | 72  |
| 3.24 | Elevation view of NIST Composite Beam experiments . . . . .                             | 74  |
| 3.25 | Plan view of NIST Composite Beam experiments . . . . .                                  | 75  |
| 3.26 | Side view of NIST Composite Beam experiments . . . . .                                  | 76  |
| 3.27 | Plan view of NIST E119 Compartment experiment . . . . .                                 | 78  |
| 3.28 | Elevation view of NIST E119 Compartment experiment . . . . .                            | 79  |
| 3.29 | Elevation view of NIST E119 Compartment experiment . . . . .                            | 80  |
| 3.30 | Geometry of the compartment used in the NIST Full-Scale Enclosure experiments . . . . . | 84  |
| 3.31 | Geometry of the NIST/NRC Experiments . . . . .  | 87  |
| 3.32 | Diagram of thermocouple layout for NIST/NRC Corner Effects experiments . . . . .        | 89  |
| 3.33 | Large cabinet drawing, NIST/NRC Corner Effects Experiments . . . . .                    | 91  |
| 3.34 | Medium-sized cabinet drawing, NIST/NRC Corner Effects Experiments . . . . .             | 92  |
| 3.35 | Cabinet grill, NIST/NRC Corner Effects Experiments . . . . .                            | 93  |
| 3.36 | NIST/NRC OLIVE-Fire enclosure photographs . . . . .                                     | 95  |
| 3.37 | Description of test items . . . . .   | 97  |
| 3.38 | Geometry of the manufactured home from the NIST Smoke Alarm Experiments . . . . .       | 101 |
| 3.39 | NFRL 8 MW calibration burner assembly drawing . . . . .                                 | 103 |

|      |  |     |
|------|--|-----|
| 3.40 | Structure Separation Verification setup . . . . .  | 104 |
| 3.41 | FDS particle model of NFRL 8 MW burner . . . . .   | 104 |
| 3.42 | Geometry of the compartment from the NIST Vent Study . . . . .                           | 106 |
| 3.43 | Geometry of the NRCC Facade Experiments . . . . .  | 108 |
| 3.44 | Geometry of the NRCC Smoke Tower Experiments . . . . .                                   | 110 |
| 3.45 | Photograph of Phoenix LNG Fire Test 2 . . . . .  | 112 |
| 3.46 | Geometry of Restivo's compartment . . . . .  | 117 |
| 3.47 | Cutaway view of the Sandia FLAME test cell . . . . .                                     | 118 |
| 3.48 | Photographs of the Shell LNG Fireball experiments . . . . .                              | 121 |
| 3.49 | Geometry of the SP/AST compartment for Test 2 . . . . .                                  | 127 |
| 3.50 | Geometry of the Steckler Compartment Experiments . . . . .                               | 131 |
| 3.51 | Geometry of the UL/NIST Experiments . . . . .  | 133 |
| 3.52 | Plan view of the UL/NFPRF heptane spray experiments, Series I . . . . .                  | 135 |
| 3.53 | Plan view of the UL/NFPRF heptane spray experiments, Series II . . . . .                 | 136 |
| 3.54 | Plan view of the UL/NFPRF plastic commodity Test P-3 . . . . .                           | 137 |
| 3.55 | Layout of the one story ranch-style house in the UL/NIJ experiments . . . . .            | 141 |
| 3.56 | Geometry of UL NIJ Colonial-style House . . . . .  | 142 |
| 3.57 | UMD Line Burner isometric view of burner and oxidizer assembly . . . . .                 | 147 |
| 3.58 | Schematic diagram of the UMD SBI experiment . . . . .                                    | 148 |
| 3.59 | Geometry of the Vettori Flat Ceiling compartment . . . . .                               | 152 |
| 3.60 | Geometry of the VTT Large Fire Test Hall . . . . .                                       | 156 |
| 3.61 | Geometry of the WTC Experiments . . . . .  | 159 |
| 4.1  | Demonstration of model uncertainty . . . . .   | 168 |
| 4.2  | Sample scatter plot . . . . .  | 170 |
| 4.3  | Sample time history plots . . . . .  | 178 |
| 5.1  | ATF Corridors, HGL temperature and height, first floor, 50 kW, 100 kW, 240 kW . . . . .  | 184 |
| 5.2  | ATF Corridors, HGL temperature and height, first floor, 250 kW, 500 kW, mixed . . . . .  | 185 |
| 5.3  | ATF Corridors, HGL temperature and height, second floor, 50 kW, 100 kW, 240 kW . . . . . | 186 |
| 5.4  | ATF Corridors, HGL temperature and height, second floor, 250 kW, 500 kW, mixed . . . . . | 187 |
| 5.5  | CSTB Tunnel, Test 2, temperatures at 4, 8, 12 and 24 m downstream of fire . . . . .      | 189 |
| 5.6  | CSTB Tunnel, Test 27, temperatures at 4, 8, 12 and 24 m downstream of fire . . . . .     | 190 |
| 5.7  | DelCo Trainers, HGL Temperature and Height, Test 2 . . . . .                             | 192 |
| 5.8  | DelCo Trainers, HGL Temperature and Height, Test 3 . . . . .                             | 193 |
| 5.9  | DelCo Trainers, HGL Temperature and Height, Test 4 . . . . .                             | 194 |
| 5.10 | DelCo Trainers, HGL Temperature and Height, Test 5 . . . . .                             | 195 |
| 5.11 | DelCo Trainers, HGL Temperature and Height, Test 6 . . . . .                             | 196 |
| 5.12 | DelCo Trainers, HGL Temperature, Tests 22-23 . . . . .                                   | 197 |
| 5.13 | DelCo Trainers, HGL Temperature, Tests 24-25 . . . . .                                   | 198 |
| 5.14 | FM/SNL experiments, HGL temperature and height, Tests 1, 2, 3 . . . . .                  | 199 |
| 5.15 | FM/SNL experiments, HGL temperature and height, Tests 4, 5, 6, 7 . . . . .               | 200 |
| 5.16 | FM/SNL experiments, HGL temperature and height, Tests 8, 9, 10, 11 . . . . .             | 201 |
| 5.17 | FM/SNL experiments, HGL temperature and height, Tests 12, 13, 14, 15 . . . . .           | 202 |
| 5.18 | FM/SNL experiments, HGL temperature and height, Tests 16, 17, 21, 22 . . . . .           | 203 |
| 5.19 | JH/FRA experiments, HGL temperature and height, 1:4 scale inert lining . . . . .         | 204 |
| 5.20 | JH/FRA experiments, HGL temperature and height, 1:4 scale combustible lining . . . . .   | 205 |
| 5.21 | JH/FRA experiments, HGL temperature and height, 1:2 scale inert lining . . . . .         | 206 |

|      |   |     |
|------|---|-----|
| 5.22 | JH/FRA experiments, HGL temperature and height, 1:2 scale combustible lining . . . . .  | 207 |
| 5.23 | JH/FRA experiments, HGL temperature and height, 1:1 scale inert lining . . . . .        | 208 |
| 5.24 | LLNL Enclosure experiments, HGL temperature, Tests 1-8 . . . . .                        | 210 |
| 5.25 | LLNL Enclosure experiments, HGL temperature, Tests 9-16 . . . . .                       | 211 |
| 5.26 | LLNL Enclosure experiments, HGL temperature, Tests 17-24 . . . . .                      | 212 |
| 5.27 | LLNL Enclosure experiments, HGL temperature, Tests 25-32 . . . . .                      | 213 |
| 5.28 | LLNL Enclosure experiments, HGL temperature, Tests 33-40 . . . . .                      | 214 |
| 5.29 | LLNL Enclosure experiments, HGL temperature, Tests 41-48 . . . . .                      | 215 |
| 5.30 | LLNL Enclosure experiments, HGL temperature, Tests 49-56 . . . . .                      | 216 |
| 5.31 | LLNL Enclosure experiments, HGL temperature, Tests 57-64 . . . . .                      | 217 |
| 5.32 | NBS Multi-Room experiments, HGL temperature and height, Test 100A . . . . .             | 219 |
| 5.33 | NBS Multi-Room experiments, HGL temperature and height, Test 100O . . . . .             | 220 |
| 5.34 | NBS Multi-Room experiments, HGL temperature and height, Test 100Z . . . . .             | 221 |
| 5.35 | NIST Composite Beam, mid-compartment HGL temperatures . . . . .                         | 223 |
| 5.36 | NIST Composite Beam, end-compartment HGL temperatures . . . . .                         | 224 |
| 5.37 | NIST E119 Compartment Test 1, upper layer gas temperatures temperatures . . . . .       | 226 |
| 5.38 | NIST E119 Compartment Test 2, upper layer gas temperatures temperatures . . . . .       | 227 |
| 5.39 | NIST E119 Compartment Test 3, upper layer gas temperatures temperatures . . . . .       | 228 |
| 5.40 | NIST FSE, HGL temperature and height, Tests 8-11 . . . . .                              | 230 |
| 5.41 | NIST FSE, HGL temperature and height, Tests 12-15 . . . . .                             | 231 |
| 5.42 | NIST FSE, HGL temperature and height, Tests 16-19 . . . . .                             | 232 |
| 5.43 | NIST FSE, HGL temperature and height, Tests 20-23 . . . . .                             | 233 |
| 5.44 | NIST FSE, HGL temperature and height, Tests 24-27 . . . . .                             | 234 |
| 5.45 | NIST FSE, HGL temperature and height, Tests 28-30, 32 . . . . .                         | 235 |
| 5.46 | NIST/NRC experiments, HGL temperature and height, Tests 1-2, 7-8 . . . . .              | 237 |
| 5.47 | NIST/NRC experiments, HGL temperature and height, Tests 4, 10, 13, 16 . . . . .         | 238 |
| 5.48 | NIST/NRC experiments, HGL temperature and height, Tests 3, 9, 17 . . . . .              | 239 |
| 5.49 | NIST/NRC experiments, HGL temperature and height, Tests 5, 14, 15, 18 . . . . .         | 240 |
| 5.50 | NIST/NRC Corner Effects, HGL temperature and height, corner experiments . . . . .       | 242 |
| 5.51 | NIST/NRC Corner Effects, HGL temperature and height, wall experiments . . . . .         | 243 |
| 5.52 | NIST/NRC Corner Effects, HGL temperature and height, cabinet experiments 1-4 . . . . .  | 244 |
| 5.53 | NIST/NRC Corner Effects, HGL temperature and height, cabinet experiments 5-8 . . . . .  | 245 |
| 5.54 | NIST/NRC Corner Effects, HGL temperature and height, cabinet experiments 9-12 . . . . . | 246 |
| 5.55 | NIST Vent Study, HGL temperature and height, Tests 1 and 2 . . . . .                    | 248 |
| 5.56 | NIST Vent Study, HGL temperature and height, Tests 3 and 4 . . . . .                    | 249 |
| 5.57 | NIST Vent Study, HGL temperature and height, Tests 5 and 6 . . . . .                    | 250 |
| 5.58 | NIST Vent Study, HGL temperature and height, Tests 7 and 8 . . . . .                    | 251 |
| 5.59 | NIST Vent Study, HGL temperature and height, Tests 9 and 13 . . . . .                   | 252 |
| 5.60 | NIST Vent Study, HGL temperature and height, Tests 14 and 15 . . . . .                  | 253 |
| 5.61 | NRCC Smoke Tower experiments, HGL temperature in the fire room and stair vestibule . .  | 255 |
| 5.62 | PRISME DOOR experiments, HGL temperature and height, Room 1, Tests 1-3 . . . . .        | 256 |
| 5.63 | PRISME DOOR experiments, HGL temperature and height, Room 1, Tests 4-6 . . . . .        | 257 |
| 5.64 | PRISME DOOR experiments, HGL temperature and height, Room 2, Tests 1-3 . . . . .        | 258 |
| 5.65 | PRISME DOOR experiments, HGL temperature and height, Room 2, Tests 4-6 . . . . .        | 259 |
| 5.66 | PRISME SOURCE experiments, HGL temperature and height, Room 2, Tests 1-4 . . . . .      | 261 |
| 5.67 | PRISME SOURCE experiments, HGL temperature and height, Room 2, Tests 5-6 . . . . .      | 262 |
| 5.68 | Steckler experiments, HGL temperature, Tests 10, 11, 12, 13, 14, 18, 612, 710 . . . . . | 264 |
| 5.69 | Steckler experiments, HGL temperature, Tests 16, 17, 19, 22, 23, 30, 41, 810 . . . . .  | 265 |

|      |   |     |
|------|---|-----|
| 5.70 | Steckler experiments, HGL temperature, Tests 20, 21, 114, 144, 210, 212, 242, 410 . . .                     | 266 |
| 5.71 | Steckler experiments, HGL temperature, Tests 116, 122, 220, 221, 224, 240, 310, 324 . . .                   | 267 |
| 5.72 | Steckler experiments, HGL temperature, Tests 510, 512, 514, 517, 540, 542, 544, 610 . . .                   | 268 |
| 5.73 | Steckler experiments, HGL temperature, Tests 160, 513, 520, 521, 522, 524, 541, 622 . . .                   | 269 |
| 5.74 | Steckler experiments, HGL temperature, Tests 161, 162, 163, 164, 165, 166, 167 . . . . .                    | 270 |
| 5.75 | UL/NIST experiments, HGL temperature and height, Tests 1-4 . . . . .  | 272 |
| 5.76 | UL/NIJ Experiments, HGL temperature and height, Tests 1, 2, and 5 . . . . .                                 | 274 |
| 5.77 | UL/NIJ Experiments, HGL temperature and height, Tests 1, 4, and 6 . . . . .                                 | 275 |
| 5.78 | VTT experiments, HGL temperature and height, Tests 1-3 . . . . .  | 276 |
| 5.79 | WTC experiments, HGL temperature and height, Tests 1-3 . . . . .  | 277 |
| 5.80 | WTC experiments, HGL temperature and height, Tests 4-6 . . . . .  | 278 |
| 5.81 | Summary, HGL temperature, natural and forced ventilation . . . . .  | 280 |
| 5.82 | Summary, HGL temperature, unventilated compartments; HGL depth . . . . .                                    | 281 |
| 6.1  | FM Burner experiments, plume mean and rms temperatures . . . . .  | 284 |
| 6.2  | FM Burner experiments, plume mean and rms temperatures . . . . .  | 285 |
| 6.3  | FM Burner experiments, temperature PDFs . . . . .   | 286 |
| 6.4  | FM/SNL experiments, plume temperature, Tests 1-4 . . . . .  | 287 |
| 6.5  | FM/SNL experiments, plume temperature, Tests 5-12 . . . . .   | 288 |
| 6.6  | FM/SNL experiments, plume temperature, Tests 13-17, 21-22 . . . . .   | 289 |
| 6.7  | McCaffrey experiments, plume temperature . . . . .  | 290 |
| 6.8  | McCaffrey experiments, plume temperature, Froude scaling . . . . .  | 291 |
| 6.9  | NIST/NRC Corner Effects experiments, plume temperature . . . . .  | 293 |
| 6.10 | NIST Pool Fires, centerline temperature, acetone, ethanol, methane . . . . .                                | 295 |
| 6.11 | NIST Pool Fires, centerline temperature, methanol and propane . . . . .                                     | 296 |
| 6.12 | NIST Pool Fires, 30 cm methanol, radial profiles of mean and rms temperature . . . . .                      | 297 |
| 6.13 | NIST Pool Fires, 100 cm methanol, plume mean and rms temperatures . . . . .                                 | 298 |
| 6.14 | NIST Pool Fires, 100 cm methanol fire, radial profiles of mean and rms temperature . . . . .                | 299 |
| 6.15 | NRCC Smoke Tower, stairwell temperatures . . . . .  | 301 |
| 6.16 | Sandia Methane Burner, plume temperature, Tests 1-4 . . . . .   | 302 |
| 6.17 | Sandia Methane Burner, plume temperature, Tests 5-12 . . . . .  | 303 |
| 6.18 | Sandia Methane Burner, plume temperature, Tests 13-20 . . . . .   | 304 |
| 6.19 | Sandia Methane Burner, plume temperature, Tests 21-28 . . . . .   | 305 |
| 6.20 | SP AST experiments, plume temperature, 1.1 m diesel fire . . . . .  | 307 |
| 6.21 | SP AST experiments, plume temperature, 1.9 m diesel and 1.1 m heptane fires . . . . .                       | 308 |
| 6.22 | UMD_Line_Burner temperature profiles . . . . .  | 309 |
| 6.23 | UMD_Line_Burner temperature contours . . . . .  | 310 |
| 6.24 | USN Hangar experiments, Iceland, plume temperature, Tests 1-6 . . . . .                                     | 311 |
| 6.25 | USN Hangar experiments, Iceland, plume temperature, Tests 7, 9-13 . . . . .                                 | 312 |
| 6.26 | USN Hangar experiments, Iceland, plume temperature, Tests 14-15, 17-20 . . . . .                            | 313 |
| 6.27 | USN Hangar experiments, Hawaii, plume temperature, Tests 1-7, 11 . . . . .                                  | 314 |
| 6.28 | VTT experiments, plume temperature . . . . .  | 315 |
| 6.29 | Waterloo Methanol, centerline profile, mean temperature, 2 cm to 60 cm above burner . . .                   | 316 |
| 6.30 | Waterloo Methanol, radial mean and rms temperature, 2 cm to 8 cm above burner . . . .                       | 317 |
| 6.31 | Waterloo Methanol, radial mean and rms temperature, 10 cm to 16 cm above burner . . . .                     | 318 |
| 6.32 | Waterloo Methanol, radial mean and rms temperature, 18 cm to 40 cm above burner . . . .                     | 319 |
| 6.33 | Waterloo Methanol, radial mean and rms temperature, 50 cm to 60 cm above burner . . . .                     | 320 |
| 6.34 | Waterloo Methanol, radial profiles of $\bar{T}'w'$ and $\bar{T}'u'$ , 2 cm to 8 cm above the burner . . . . | 321 |

|      |   |     |
|------|---|-----|
| 6.35 | Waterloo Methanol, radial profiles of $\overline{T'w'}$ and $\overline{T'u'}$ , 10 cm to 16 cm above the burner . . . . . | 322 |
| 6.36 | Waterloo Methanol, radial profiles of $\overline{T'w'}$ and $\overline{T'u'}$ , 18 cm to 30 cm above the burner . . . . . | 323 |
| 6.37 | Summary of plume temperature predictions . . . . .  | 324 |
| 6.38 | Verification of the heat release rate for Heskestad Flame Height cases . . . . .  | 326 |
| 6.39 | Summary of flame height predictions, Heskestad correlation . . . . .  | 327 |
| 6.40 | Flame height uncertainty, multiple correlations and flame height definitions . . . . .                                    | 327 |
| 6.41 | Predicted HRR as a function of height above the burner . . . . .  | 328 |
| 6.42 | UMD_Line_Burner flame height . . . . .  | 329 |
| 6.43 | Summary of flame height predictions . . . . .   | 330 |
| 6.44 | Summary of flame tilt angle predictions . . . . .   | 331 |
| 6.45 | Summary of plume entrainment predictions . . . . .  | 332 |
| 6.46 | Sandia 1 m helium plume image . . . . .   | 334 |
| 6.47 | Sandia 1 m helium plume vertical velocity profiles . . . . .  | 335 |
| 6.48 | Sandia 1 m helium plume radial velocity profiles . . . . .  | 336 |
| 6.49 | Sandia 1 m helium plume mean and RMS mass fraction profiles . . . . .   | 337 |
| 6.50 | Sandia 1 m methane pool fire instantaneous temperature contours . . . . .   | 338 |
| 6.51 | Sandia 1 m methane pool fire (Test 14) mean velocity profiles . . . . .   | 339 |
| 6.52 | Sandia 1 m methane pool fire (Test 24) mean velocity profiles . . . . .   | 340 |
| 6.53 | Sandia 1 m methane pool fire (Test 24) turbulent kinetic energy . . . . .   | 341 |
| 6.54 | Sandia 1 m methane pool fire (Test 17) mean velocity profiles . . . . .   | 342 |
| 6.55 | Sandia 1 m methane pool fire velocity signal and power spectrum . . . . .   | 343 |
| 6.56 | Sandia 1 m hydrogen pool fire instantaneous temperature contours . . . . .  | 344 |
| 6.57 | Sandia 1 m hydrogen pool fire (Test 35) mean velocity profiles . . . . .  | 345 |
| 6.58 | Sandia 1 m hydrogen pool fire (Test 25) turbulent kinetic energy . . . . .  | 346 |
| 6.59 | Purdue 7.1 cm methane flame mean mixture fraction profiles . . . . .  | 347 |
| 6.60 | Purdue 7.1 cm methane flame mean temperature profiles . . . . .   | 348 |
| 6.61 | Purdue 7.1 cm methane flame mean velocity profiles . . . . .  | 349 |
| 6.62 | Purdue 7.1 cm methane flame rms velocity profiles . . . . .   | 350 |
| 6.63 | FM Vertical Wall Flame mean temperature profiles . . . . .  | 352 |
| 6.64 | FM Vertical Wall Flame soot depth measurements . . . . .  | 353 |
| 7.1  | ATF Corridors experiments, ceiling jet, 50 kW . . . . .   | 357 |
| 7.2  | ATF Corridors experiments, ceiling jet, 100 kW . . . . .  | 358 |
| 7.3  | ATF Corridors experiments, ceiling jet, 250 kW . . . . .  | 359 |
| 7.4  | ATF Corridors experiments, ceiling jet, 500 kW . . . . .  | 360 |
| 7.5  | ATF Corridors experiments, ceiling jet, mixed HRR . . . . .   | 361 |
| 7.6  | Arup Tunnel experiments, ceiling jet . . . . .  | 362 |
| 7.7  | DelCo Trainers, ceiling jet temperature, Tests 2-4 . . . . .  | 363 |
| 7.8  | DelCo Trainers, ceiling jet temperature, Tests 5 and 6 . . . . .  | 364 |
| 7.9  | DelCo Trainers, ceiling jet temperature, Tests 22-25 . . . . .  | 365 |
| 7.10 | Layout of ceiling TCs, FAA Cargo Compartments . . . . .   | 366 |
| 7.11 | FAA Cargo Compartment experiments, ceiling jet, Test 1 . . . . .  | 367 |
| 7.12 | FAA Cargo Compartment experiments, ceiling jet, Test 1 and 2 . . . . .  | 368 |
| 7.13 | FAA Cargo Compartment experiments, ceiling jet, Test 2 and 3 . . . . .  | 369 |
| 7.14 | FAA Cargo Compartment experiments, ceiling jet, Test 3 . . . . .  | 370 |
| 7.15 | FM/SNL experiments, ceiling jet, Tests 1-6 . . . . .  | 371 |
| 7.16 | FM/SNL experiments, ceiling jet, Tests 7-14 . . . . .   | 372 |
| 7.17 | FM/SNL experiments, ceiling jet, Tests 15-17, 21-22 . . . . .   | 373 |

|      |   |     |
|------|---|-----|
| 7.18 | NIST Composite Beam, ceiling jet temperatures . . . . .                                 | 375 |
| 7.19 | NIST Smoke Alarm experiments, ceiling jet . . . . .                                     | 377 |
| 7.20 | NIST/NRC experiments, ceiling jet, Tests 1, 2, 4, 7, 8, 10, 13, 16 . . . . .            | 379 |
| 7.21 | NIST/NRC experiments, ceiling jet, Tests 3, 5, 9, 14, 15, 17, 18 . . . . .              | 380 |
| 7.22 | NIST/NRC Corner Effects experiments, ceiling jet temperature . . . . .                  | 382 |
| 7.23 | NIST/NRC Corner Effects experiments, ceiling jet temperature, large cabinet . . . . .   | 383 |
| 7.24 | NIST/NRC Corner Effects experiments, ceiling jet temperature, medium-sized cabinet . .  | 384 |
| 7.25 | NIST Vent Study, ceiling jet temperature, Tests 1-6 . . . . .                           | 385 |
| 7.26 | NIST Vent Study, ceiling jet temperature, Tests 7-9, 13-15 . . . . .                    | 386 |
| 7.27 | NRCC Smoke Tower experiments, ceiling jet . . . . .                                     | 387 |
| 7.28 | NRCC Smoke Tower, upper floor temperatures . . . . .                                    | 388 |
| 7.29 | PRISME DOOR experiments, ceiling jet, Room 1 . . . . .                                  | 389 |
| 7.30 | PRISME DOOR experiments, ceiling jet, Room 2 . . . . .                                  | 390 |
| 7.31 | PRISME SOURCE experiments, ceiling jet, Room 2 . . . . .                                | 392 |
| 7.32 | SP AST experiments, ceiling jet, Test 1 . . . . .                                       | 393 |
| 7.33 | SP AST experiments, ceiling jet, Tests 2 and 3 . . . . .                                | 394 |
| 7.34 | UL/NFPPRF experiments, ceiling jet, Series I, Tests 1-6 . . . . .                       | 395 |
| 7.35 | UL/NFPPRF experiments, ceiling jet, Series I, Tests 7-14 . . . . .                      | 396 |
| 7.36 | UL/NFPPRF experiments, ceiling jet, Series I, Tests 15-22 . . . . .                     | 397 |
| 7.37 | UL/NIJ Experiments, ceiling jet temperature . . . . .                                   | 398 |
| 7.38 | UL/NIST Vents experiments, ceiling jet . . . . .  | 400 |
| 7.39 | Vettori Flat Ceiling experiments, ceiling jet, Tests 1-8 . . . . .                      | 402 |
| 7.40 | Vettori Flat Ceiling experiments, ceiling jet, Tests 9-16 . . . . .                     | 403 |
| 7.41 | Vettori Flat Ceiling experiments, ceiling jet, Tests 17-24 . . . . .                    | 404 |
| 7.42 | Vettori Flat Ceiling experiments, ceiling jet, Tests 25-32 . . . . .                    | 405 |
| 7.43 | Vettori Flat Ceiling experiments, ceiling jet, Tests 33-40 . . . . .                    | 406 |
| 7.44 | Vettori Flat Ceiling experiments, ceiling jet, Tests 41-45 . . . . .                    | 407 |
| 7.45 | Vettori Sloped Ceiling experiments, ceiling jet, Tests 1-8 . . . . .                    | 409 |
| 7.46 | Vettori Sloped Ceiling experiments, ceiling jet, Tests 9-16 . . . . .                   | 410 |
| 7.47 | Vettori Sloped Ceiling experiments, ceiling jet, Tests 17-24 . . . . .                  | 411 |
| 7.48 | Vettori Sloped Ceiling experiments, ceiling jet, Tests 25-32 . . . . .                  | 412 |
| 7.49 | Vettori Sloped Ceiling experiments, ceiling jet, Tests 33-40 . . . . .                  | 413 |
| 7.50 | Vettori Sloped Ceiling experiments, ceiling jet, Tests 41-48 . . . . .                  | 414 |
| 7.51 | Vettori Sloped Ceiling experiments, ceiling jet, Tests 49-56 . . . . .                  | 415 |
| 7.52 | Vettori Sloped Ceiling experiments, ceiling jet, Tests 57-64 . . . . .                  | 416 |
| 7.53 | Vettori Sloped Ceiling experiments, ceiling jet, Tests 65-72 . . . . .                  | 417 |
| 7.54 | WTC experiments, ceiling jet, Tests 1-6 . . . . .                                       | 418 |
| 7.55 | Summary of ceiling jet temperature predictions . . . . .                                | 419 |
| 7.56 | Comparison of measured and predicted sprinkler actuation times . . . . .                | 420 |
| 7.57 | UL/NFPPRF experiments, number of sprinkler activations, Series I, Tests 1-8 . . . . .   | 422 |
| 7.58 | UL/NFPPRF experiments, number of sprinkler activations, Series I, Tests 9-16 . . . . .  | 423 |
| 7.59 | UL/NFPPRF experiments, number of sprinkler activations, Series I, Tests 17-22 . . . . . | 424 |
| 7.60 | UL/NFPPRF experiments, number of sprinkler activations, Series II, Tests 1-6 . . . . .  | 425 |
| 7.61 | UL/NFPPRF experiments, number of sprinkler activations, Series II, Tests 7-12 . . . . . | 426 |
| 7.62 | UL/NFPPRF experiments, no. of sprinkler activations, Group A Commodity, Tests 1-5 . .   | 427 |
| 7.63 | Comparison of the number of predicted and measured sprinkler activations . . . . .      | 428 |
| 7.64 | Summary of smoke detector activation times (temperature rise), NIST Smoke Alarms . .    | 429 |
| 7.65 | Summary of activation times, smoke detector model, NIST Smoke Alarms . . . . .          | 430 |

|       |   |     |
|-------|---|-----|
| 7.66  | Wu and Bakar critical velocity correlation with FDS results added . . . . .                   | 431 |
| 7.67  | Volume flow in Memorial Tunnel as a function of the number of jet fans . . . . .              | 432 |
| 7.68  | Summary of Memorial Tunnel Test 501 . . . . .   | 433 |
| 7.69  | Summary of Memorial Tunnel Test 502 . . . . .   | 434 |
| 7.70  | Summary of Memorial Tunnel Test 605 . . . . .   | 435 |
| 7.71  | Summary of Memorial Tunnel Test 606A . . . . .  | 436 |
| 7.72  | Summary of Memorial Tunnel Test 607 . . . . .   | 437 |
| 7.73  | Summary of Memorial Tunnel Test 608 . . . . .   | 438 |
| 7.74  | Summary of Memorial Tunnel Test 610 . . . . .   | 439 |
| 7.75  | Summary of Memorial Tunnel Test 611 . . . . .   | 440 |
| 7.76  | Summary of Memorial Tunnel Test 612B . . . . .  | 441 |
| 7.77  | Summary of Memorial Tunnel Test 615B . . . . .  | 442 |
| 7.78  | Summary of Memorial Tunnel Test 617A . . . . .  | 443 |
| 7.79  | Summary of Memorial Tunnel Test 618A . . . . .  | 444 |
| 7.80  | Summary of Memorial Tunnel Test 621A . . . . .  | 445 |
| 7.81  | Summary of Memorial Tunnel Test 622B . . . . .  | 446 |
| 7.82  | Summary of Memorial Tunnel Test 623B . . . . .  | 447 |
| 7.83  | Summary of Memorial Tunnel Test 624B . . . . .  | 448 |
| 7.84  | Summary of Memorial Tunnel Test 625B . . . . .  | 449 |
| 7.85  | Back-layer, Full Transverse Ventilation, Sequence 1 . . . . .                                 | 451 |
| 7.86  | Back-layer, Full Transverse Ventilation, Sequence 1 . . . . .                                 | 452 |
| 7.87  | Back-layer, Full Transverse Ventilation, Sequence 1 . . . . .                                 | 453 |
| 7.88  | Back-layer, Full Transverse Ventilation, Sequence 1 . . . . .                                 | 454 |
| 7.89  | Back-layer, Partial Transverse Exhaust Ventilation, Sequence 3 . . . . .                      | 455 |
| 7.90  | Back-layer, Partial Transverse Exhaust Ventilation, Sequence 3 . . . . .                      | 456 |
| 7.91  | Back-layer, Partial Transverse Exhaust Ventilation, Sequence 3 . . . . .                      | 457 |
| 7.92  | Back-layer, Partial Transverse Supply Ventilation, Sequences 4 and 5 . . . . .                | 458 |
| 7.93  | Back-layer, Two-Zone Partial Transverse Ventilation, Sequence 6 . . . . .                     | 459 |
| 7.94  | Back-layer, Two-Zone Partial Transverse Ventilation, Sequence 6 . . . . .                     | 460 |
| 7.95  | Back-layer, Two-Zone Partial Transverse Ventilation, Sequence 6 . . . . .                     | 461 |
| 7.96  | Back-layer, Partial Transverse Ventilation with Single Point Extraction, Sequence 8 . . . . . | 462 |
| 7.97  | Back-layer, Partial Transverse Ventilation with Single Point Extraction, Sequence 8 . . . . . | 463 |
| 7.98  | Back-layer, Partial Transverse Ventilation with Single Point Extraction, Sequence 8 . . . . . | 464 |
| 7.99  | Back-layer, Partial Transverse Ventilation with Single Point Extraction, Sequence 8 . . . . . | 465 |
| 7.100 | Back-layer, Point Supply Operation, Sequence 9 . . . . .                                      | 465 |
| 7.101 | Back-layer, Point Exhaust Operation, Sequence 10 . . . . .                                    | 466 |
| 7.102 | Back-layer, Partial Transverse with Oversize Exhaust Ports, Sequence 13 and 14 . . . . .      | 467 |
| 7.103 | Summary of FHWA Tunnel experiments 7, 8, 9 and 10 . . . . .                                   | 469 |
| 7.104 | Summary of FHWA Tunnel experiments 11, 13, 14 and 15 . . . . .                                | 470 |
| 7.105 | Summary of FHWA Tunnel experiments 19, 22 and 24 . . . . .                                    | 471 |
| 8.1   | ATF Corridors, gas velocity, first level, Location H . . . . .                                | 474 |
| 8.2   | ATF Corridors, gas velocity, first level, Location I . . . . .                                | 475 |
| 8.3   | ATF Corridors, gas velocity, second level, Location J . . . . .                               | 476 |
| 8.4   | ATF Corridors, gas velocity, second level, Location K . . . . .                               | 477 |
| 8.5   | Instantaneous contours of velocity magnitude . . . . .  | 478 |
| 8.6   | Friction coefficient and pressure coefficient . . . . .                                       | 479 |
| 8.7   | Backward facing step flow profiles . . . . .  | 480 |

|      |  |     |
|------|--|-----|
| 8.8  | Bryant Doorway experiments, gas velocity profiles . . . . .  | 482 |
| 8.9  | Edinburgh Vegetation Drag, gas velocity profiles, low bulk density . . . . .                       | 483 |
| 8.10 | Edinburgh Vegetation Drag, gas velocity profiles, medium bulk density . . . . .                    | 484 |
| 8.11 | Edinburgh Vegetation Drag, gas velocity profiles, high bulk density . . . . .                      | 485 |
| 8.12 | FM/FPRF experiments, gas velocity, low fan rate . . . . .  | 486 |
| 8.13 | FM/FPRF experiments, gas velocity, high fan rate . . . . .   | 487 |
| 8.14 | JH/FRA experiments, gas velocity, 1:4 scale inert lining configurations . . . . .                  | 488 |
| 8.15 | JH/FRA experiments, gas velocity, 1:4 scale combustible lining configurations . . . . .            | 488 |
| 8.16 | JH/FRA experiments, gas velocity, 1:2 scale inert lining configurations . . . . .                  | 488 |
| 8.17 | JH/FRA experiments, gas velocity, 1:2 scale combustible lining configurations . . . . .            | 489 |
| 8.18 | JH/FRA experiments, gas velocity, 1:1 scale inert lining configurations . . . . .                  | 489 |
| 8.19 | JH/FRA experiments, gas velocity, 1:1 scale combustible lining configurations . . . . .            | 489 |
| 8.20 | McCaffrey Plumes, centerline plume velocity . . . . .  | 490 |
| 8.21 | McCaffrey Plumes, centerline plume velocity, Froude scaling . . . . .                              | 491 |
| 8.22 | NIST Pool Fires, centerline velocity . . . . .   | 492 |
| 8.23 | PRISME DOOR experiments, gas velocity . . . . .  | 493 |
| 8.24 | Restivo experiment, gas velocity . . . . .   | 494 |
| 8.25 | Steckler experiments, velocity profiles, Tests 10, 11, 12, 13, 14, 18, 612, 710 . . . . .          | 496 |
| 8.26 | Steckler experiments, velocity profiles, Tests 16, 17, 19, 22, 23, 30, 41, 810 . . . . .           | 497 |
| 8.27 | Steckler experiments, velocity profiles, Tests 20, 21, 114, 144, 210, 212, 242, 410 . . . . .      | 498 |
| 8.28 | Steckler experiments, velocity profiles, Tests 116, 122, 220, 221, 224, 240, 310, 324 . . . . .    | 499 |
| 8.29 | Steckler experiments, velocity profiles, Tests 510, 512, 514, 517, 540, 542, 544, 610 . . . . .    | 500 |
| 8.30 | Steckler experiments, velocity profiles, Tests 160, 513, 520, 521, 522, 524, 541, 622 . . . . .    | 501 |
| 8.31 | Steckler experiments, velocity profiles, Tests 161, 162, 163, 164, 165, 166, 167 . . . . .         | 502 |
| 8.32 | UL/NIJ Experiments, Velocity, single story house, Tests 1, 2, and 5 . . . . .                      | 504 |
| 8.33 | UL/NIJ Experiments, Velocity, two-story house, Test 1 . . . . .                                    | 505 |
| 8.34 | UL/NIJ Experiments, Velocity, two-story house, Test 4 . . . . .                                    | 506 |
| 8.35 | UL/NIJ Experiments, Velocity, two-story house, Test 6 . . . . .                                    | 507 |
| 8.36 | Waterloo Methanol, radial mean and rms vert. vel., 2 cm to 8 cm above burner . . . . .             | 509 |
| 8.37 | Waterloo Methanol, radial mean and rms vert. vel., 10 cm to 16 cm above burner . . . . .           | 510 |
| 8.38 | Waterloo Methanol, radial mean and rms vert. vel., 18 cm to 30 cm above burner . . . . .           | 511 |
| 8.39 | Waterloo Methanol, radial mean and rms horz. vel., 2 cm to 8 cm above burner . . . . .             | 512 |
| 8.40 | Waterloo Methanol, radial mean and rms horz. vel., 10 cm to 16 cm above burner . . . . .           | 513 |
| 8.41 | Waterloo Methanol, radial mean and rms horz. vel., 18 cm to 30 cm above burner . . . . .           | 514 |
| 8.42 | Waterloo Methanol, radial profiles of $\overline{u'w'}$ , 2 cm to 12 cm above the burner . . . . . | 515 |
| 8.43 | Waterloo Methanol, radial profiles of $u'w'$ , 14 cm to 30 cm above the burner . . . . .           | 516 |
| 8.44 | Layout of velocity probes, WTC Experiments . . . . .   | 517 |
| 8.45 | WTC experiments, inlet velocity, Points 1-3 . . . . .  | 518 |
| 8.46 | WTC experiments, inlet velocity, Points 6-8 . . . . .  | 519 |
| 8.47 | WTC experiments, outlet velocity, Points 1-5 . . . . .   | 520 |
| 8.48 | WTC experiments, outlet velocity, Points 6-10 . . . . .  | 521 |
| 8.49 | Summary of velocity predictions . . . . .  | 522 |
| 9.1  | DelCo Trainers, CO <sub>2</sub> and O <sub>2</sub> concentration, Tests 2-4 . . . . .              | 524 |
| 9.2  | DelCo Trainers, CO <sub>2</sub> and O <sub>2</sub> concentration, Tests 5-6 . . . . .              | 525 |
| 9.3  | DelCo Trainers, CO <sub>2</sub> and O <sub>2</sub> concentration, Tests 22-25 . . . . .            | 526 |
| 9.4  | FAA Cargo Compartment experiments, CO <sub>2</sub> and O <sub>2</sub> concentration . . . . .      | 527 |
| 9.5  | LLNL Enclosure, O <sub>2</sub> and CO <sub>2</sub> concentration, Tests 1-4 . . . . .              | 529 |

|      |  |     |
|------|--|-----|
| 9.6  | LLNL Enclosure, O <sub>2</sub> and CO <sub>2</sub> concentration, Tests 5-8 . . . . .                    | 530 |
| 9.7  | LLNL Enclosure, O <sub>2</sub> and CO <sub>2</sub> concentration, Tests 9-12 . . . . .                   | 531 |
| 9.8  | LLNL Enclosure, O <sub>2</sub> and CO <sub>2</sub> concentration, Tests 13-16 . . . . .                  | 532 |
| 9.9  | LLNL Enclosure, O <sub>2</sub> and CO <sub>2</sub> concentration, Tests 17-20 . . . . .                  | 533 |
| 9.10 | LLNL Enclosure, O <sub>2</sub> and CO <sub>2</sub> concentration, Tests 21-24 . . . . .                  | 534 |
| 9.11 | LLNL Enclosure, O <sub>2</sub> and CO <sub>2</sub> concentration, Tests 25-28 . . . . .                  | 535 |
| 9.12 | LLNL Enclosure, O <sub>2</sub> and CO <sub>2</sub> concentration, Tests 29-32 . . . . .                  | 536 |
| 9.13 | LLNL Enclosure, O <sub>2</sub> and CO <sub>2</sub> concentration, Tests 33-36 . . . . .                  | 537 |
| 9.14 | LLNL Enclosure, O <sub>2</sub> and CO <sub>2</sub> concentration, Tests 37-40 . . . . .                  | 538 |
| 9.15 | LLNL Enclosure, O <sub>2</sub> and CO <sub>2</sub> concentration, Tests 41-44 . . . . .                  | 539 |
| 9.16 | LLNL Enclosure, O <sub>2</sub> and CO <sub>2</sub> concentration, Tests 45-48 . . . . .                  | 540 |
| 9.17 | LLNL Enclosure, O <sub>2</sub> and CO <sub>2</sub> concentration, Tests 49-52 . . . . .                  | 541 |
| 9.18 | LLNL Enclosure, O <sub>2</sub> and CO <sub>2</sub> concentration, Tests 53-56 . . . . .                  | 542 |
| 9.19 | LLNL Enclosure, O <sub>2</sub> and CO <sub>2</sub> concentration, Tests 57-60 . . . . .                  | 543 |
| 9.20 | LLNL Enclosure, O <sub>2</sub> and CO <sub>2</sub> concentration, Tests 61-64 . . . . .                  | 544 |
| 9.21 | NIST/NRC experiments, CO <sub>2</sub> and O <sub>2</sub> concentration, Tests 3, 9, 17 . . . . .         | 545 |
| 9.22 | NIST/NRC experiments, CO <sub>2</sub> and O <sub>2</sub> concentration, Tests 5, 14, 15, 18 . . . . .    | 546 |
| 9.23 | NIST/NRC experiments, CO <sub>2</sub> and O <sub>2</sub> concentration, Tests 1, 2, 7, 8 . . . . .       | 547 |
| 9.24 | NIST/NRC experiments, CO <sub>2</sub> and O <sub>2</sub> concentration, Tests 4, 10, 13, 16 . . . . .    | 548 |
| 9.25 | NRCC Smoke Tower, CO <sub>2</sub> and O <sub>2</sub> concentration, Tests BK-R and COMP-R . . . . .      | 549 |
| 9.26 | NRCC Smoke Tower, CO <sub>2</sub> and O <sub>2</sub> concentration, Tests CLC-I-R and CLC-II-R . . . . . | 550 |
| 9.27 | PRISME DOOR experiments, CO <sub>2</sub> and O <sub>2</sub> concentration, Room 1, Tests 1-3 . . . . .   | 551 |
| 9.28 | PRISME DOOR experiments, CO <sub>2</sub> and O <sub>2</sub> concentration, Room 1, Tests 4-6 . . . . .   | 552 |
| 9.29 | PRISME DOOR experiments, CO <sub>2</sub> and O <sub>2</sub> concentration, Room 2, Tests 1-3 . . . . .   | 553 |
| 9.30 | PRISME DOOR experiments, CO <sub>2</sub> and O <sub>2</sub> concentration, Room 2, Tests 4-6 . . . . .   | 554 |
| 9.31 | PRISME SOURCE experiments, CO <sub>2</sub> and O <sub>2</sub> concentration, Room 2, Tests 1-4 . . . . . | 556 |
| 9.32 | PRISME SOURCE experiments, CO <sub>2</sub> and O <sub>2</sub> concentration, Room 2, Tests 5-6 . . . . . | 557 |
| 9.33 | WTC experiments, CO <sub>2</sub> and O <sub>2</sub> concentration, Tests 1-3 . . . . .                   | 558 |
| 9.34 | WTC experiments, CO <sub>2</sub> and O <sub>2</sub> concentration, Tests 4-6 . . . . .                   | 559 |
| 9.35 | UMD_Line_Burner oxygen concentration profiles . . . . .  | 560 |
| 9.36 | Summary of major gas species predictions . . . . .   | 561 |
| 9.37 | FM Burner experiments, plume mean and rms soot volume fraction, 20.9 % O <sub>2</sub> . . . . .          | 562 |
| 9.38 | FM Burner experiments, plume mean and rms soot volume fraction, 20.9 % O <sub>2</sub> . . . . .          | 563 |
| 9.39 | FM Burner experiments, plume mean and rms soot volume fraction, 16.8 % O <sub>2</sub> . . . . .          | 564 |
| 9.40 | FM Burner experiments, plume mean and rms soot volume fraction, 16.8 % O <sub>2</sub> . . . . .          | 565 |
| 9.41 | FM Burner experiments, plume mean and rms soot volume fraction, 15.2 % O <sub>2</sub> . . . . .          | 566 |
| 9.42 | FM Burner experiments, plume mean and rms soot volume fraction, 15.2 % O <sub>2</sub> . . . . .          | 567 |
| 9.43 | FM Burner experiments, soot volume fraction PDFs, 20.9 % O <sub>2</sub> . . . . .                        | 568 |
| 9.44 | FM Burner experiments, soot volume fraction PDFs, 16.8 % O <sub>2</sub> . . . . .                        | 569 |
| 9.45 | FM Burner experiments, soot volume fraction PDFs, 15.2 % O <sub>2</sub> . . . . .                        | 570 |
| 9.46 | FM/FPRF Data Center, smoke concentration, propylene and cable sources . . . . .                          | 571 |
| 9.47 | NIST/NRC experiments, smoke concentration, closed door experiments . . . . .                             | 573 |
| 9.48 | NIST/NRC experiments, smoke concentration, open door experiments . . . . .                               | 574 |
| 9.49 | Summary of smoke concentration predictions . . . . .   | 575 |
| 9.50 | FAA Cargo Compartments experiments, smoke obscuration . . . . .  | 576 |
| 9.51 | Summary of smoke obscuration predictions . . . . .   | 577 |
| 9.52 | Predicted and measured aerosol deposition velocities, Sippola experiments . . . . .                      | 578 |
| 9.53 | Summary of aerosol deposition velocity predictions . . . . .   | 579 |

|       |  |     |
|-------|--|-----|
| 9.54  | Predicted and measured aerosol deposited mass, NIST Soot Deposition Gauge exp . . . . .                            | 580 |
| 9.55  | Summary of aerosol deposited mass predictions . . . . .  | 581 |
| 9.56  | Droplet diameter for the Ranz and Marshall experiment . . . . .  | 582 |
| 9.57  | Evaporation rates for the Ranz and Marshall experiments . . . . .  | 583 |
| 9.58  | Summary of evaporation rates for the Ranz and Marshall experiments . . . . .                                       | 583 |
| 9.59  | Normalized droplet area for the Fujita experiments . . . . .   | 584 |
| 9.60  | Droplet temperature change, Fujita et al. experiments . . . . .  | 585 |
| 9.61  | Droplet terminal velocity for the Gavin experiments . . . . .  | 585 |
| 9.62  | Square of the droplet diameter, Kolaitis and Founti . . . . .  | 586 |
| 9.63  | Droplet surface temperature, Kolaitis and Founti . . . . .   | 587 |
| 9.64  | Droplet surface temperature for the Maqua et al. experiments . . . . .   | 587 |
| 9.65  | Droplet diameter for the Taflin experiments . . . . .  | 588 |
| 9.66  | Temperature predictions at 7 mm, 9 mm, and 11 mm above burner, Smyth experiment . . . . .                          | 589 |
| 9.67  | CH <sub>4</sub> and O <sub>2</sub> volume fractions at 11 mm, 9 mm, and 7 mm above burner, Smyth burner . . . . .  | 590 |
| 9.68  | CO <sub>2</sub> and CO volume fractions at 11 mm, 9 mm, and 7 mm above burner, Smyth burner . . . . .              | 591 |
| 9.69  | H <sub>2</sub> O and H <sub>2</sub> volume fractions at 11 mm, 9 mm, and 7 mm above burner, Smyth burner . . . . . | 592 |
| 9.70  | Summary of gas species predictions, Beyler hood experiments . . . . .  | 594 |
| 9.71  | Comparison of measured and predicted CO concentration, NIST RSE experiments . . . . .                              | 595 |
| 9.72  | Comparison of measured and predicted CO <sub>2</sub> concentration, NIST RSE experiments . . . . .                 | 595 |
| 9.73  | Comparison of measured and predicted O <sub>2</sub> concentration, NIST RSE experiments . . . . .                  | 596 |
| 9.74  | Comparison of measured and predicted H <sub>2</sub> O concentration, NIST RSE experiments . . . . .                | 596 |
| 9.75  | Comparison of measured and predicted temperature, NIST RSE experiments . . . . .                                   | 596 |
| 9.76  | Summary of Test 1, NIST RSE 2007 . . . . .   | 597 |
| 9.77  | Summary of Test 2, NIST RSE 2007 . . . . .   | 598 |
| 9.78  | Summary of Test 3, NIST RSE 2007 . . . . .   | 599 |
| 9.79  | Summary of Test 4, NIST RSE 2007 . . . . .   | 600 |
| 9.80  | Summary of Test 5, NIST RSE 2007 . . . . .   | 601 |
| 9.81  | Summary of Test 6, NIST RSE 2007 . . . . .   | 602 |
| 9.82  | Summary of Test 7, NIST RSE 2007 . . . . .   | 603 |
| 9.83  | Summary of Test 10, NIST RSE 2007 . . . . .  | 604 |
| 9.84  | Summary of Test 11, NIST RSE 2007 . . . . .  | 605 |
| 9.85  | Summary of Test 12, NIST RSE 2007 . . . . .  | 606 |
| 9.86  | Summary of Test 15, NIST RSE 2007 . . . . .  | 607 |
| 9.87  | Summary of Test 16, NIST RSE 2007 . . . . .  | 608 |
| 9.88  | Summary of ISONG3, NIST FSE 2008 . . . . .   | 609 |
| 9.89  | Summary of ISOHept4, NIST FSE 2008 . . . . .   | 610 |
| 9.90  | Summary of ISOHept5, NIST FSE 2008 . . . . .   | 611 |
| 9.91  | Summary of ISOHept8, NIST FSE 2008 . . . . .   | 612 |
| 9.92  | Summary of ISOHept9, NIST FSE 2008 . . . . .   | 613 |
| 9.93  | Summary of ISONylon10, NIST FSE 2008 . . . . .   | 614 |
| 9.94  | Summary of ISOPP11, NIST FSE 2008 . . . . .  | 615 |
| 9.95  | Summary of ISOHeptD12, NIST FSE 2008 . . . . .   | 616 |
| 9.96  | Summary of ISOHeptD13, NIST FSE 2008 . . . . .   | 617 |
| 9.97  | Summary of ISOPropD14, NIST FSE 2008 . . . . .   | 618 |
| 9.98  | Summary of ISOProp15, NIST FSE 2008 . . . . .  | 619 |
| 9.99  | Summary of ISOStyrene16, NIST FSE 2008 . . . . .   | 620 |
| 9.100 | Summary of ISOStyrene17, NIST FSE 2008 . . . . .   | 621 |
| 9.101 | Summary of ISOPP18, NIST FSE 2008 . . . . .  | 622 |

|       |  |     |
|-------|--|-----|
| 9.102 | Summary of ISOHept19, NIST FSE 2008 . . . . .  | 623 |
| 9.103 | Summary of ISOToluene20, NIST FSE 2008 . . . . .                                       | 624 |
| 9.104 | Summary of ISOStyrene21, NIST FSE 2008 . . . . .                                       | 625 |
| 9.105 | Summary of ISOHept22, NIST FSE 2008 . . . . .  | 626 |
| 9.106 | Summary of ISOHept23, NIST FSE 2008 . . . . .  | 627 |
| 9.107 | Summary of ISOHept24, NIST FSE 2008 . . . . .  | 628 |
| 9.108 | Summary of ISOHept25, NIST FSE 2008 . . . . .  | 629 |
| 9.109 | Summary of ISOHept26, NIST FSE 2008 . . . . .  | 630 |
| 9.110 | Summary of ISOHept27, NIST FSE 2008 . . . . .  | 631 |
| 9.111 | Summary of ISOHept28, NIST FSE 2008 . . . . .  | 632 |
| 9.112 | Summary of ISOToluene29, NIST FSE 2008 . . . . .                                       | 633 |
| 9.113 | Summary of ISOPropanol30, NIST FSE 2008 . . . . .                                      | 634 |
| 9.114 | Summary of ISONG32, NIST FSE 2008 . . . . .  | 635 |
| 9.115 | NIST Pool Fires, centerline product species, acetone . . . . .                         | 637 |
| 9.116 | NIST Pool Fires, centerline product species, ethanol . . . . .                         | 638 |
| 9.117 | NIST Pool Fires, centerline product species, methanol . . . . .                        | 639 |
| 9.118 | NIST Pool Fires, centerline product species, methane . . . . .                         | 640 |
| 9.119 | NIST Pool Fires, centerline product species, propane, 20 kW . . . . .                  | 641 |
| 9.120 | NIST Pool Fires, centerline product species, propane, 34 kW . . . . .                  | 642 |
| 9.121 | Summary of carbon monoxide predictions . . . . .                                       | 643 |
| 9.122 | Results of the NIST_He_2009 experiments . . . . .                                      | 645 |
| 9.123 | Results of the NIST_He_2009 experiments . . . . .                                      | 646 |
| 9.124 | Results of the NIST_He_2009 experiments . . . . .                                      | 647 |
| 9.125 | Summary of species concentration predictions . . . . .                                 | 648 |
| 10.1  | FM/FPRF Data Center, differential pressure . . . . .                                   | 649 |
| 10.2  | NIST/NRC experiments, compartment pressure, Tests 1, 2, 4, 7, 8, 10, 13, 16 . . . . .  | 651 |
| 10.3  | NIST/NRC experiments, compartment pressure, Tests 3, 5, 9, 14, 15, 17, 18 . . . . .    | 652 |
| 10.4  | LLNL Enclosure experiments, compartment pressure, Tests 1-8 . . . . .                  | 654 |
| 10.5  | LLNL Enclosure experiments, compartment pressure, Tests 9-16 . . . . .                 | 655 |
| 10.6  | LLNL Enclosure experiments, compartment pressure, Tests 17-24 . . . . .                | 656 |
| 10.7  | LLNL Enclosure experiments, compartment pressure, Tests 25-32 . . . . .                | 657 |
| 10.8  | LLNL Enclosure experiments, compartment pressure, Tests 33-40 . . . . .                | 658 |
| 10.9  | LLNL Enclosure experiments, compartment pressure, Tests 41-48 . . . . .                | 659 |
| 10.10 | LLNL Enclosure experiments, compartment pressure, Tests 49-56 . . . . .                | 660 |
| 10.11 | LLNL Enclosure experiments, compartment pressure, Tests 57-64 . . . . .                | 661 |
| 10.12 | PRISME DOOR, compartment pressure and supply/exhaust, Room 1, Tests 1-3 . . . . .      | 663 |
| 10.13 | PRISME DOOR, compartment pressure and supply/exhaust, Room 1, Tests 4-6 . . . . .      | 664 |
| 10.14 | PRISME DOOR, compartment pressure and supply/exhaust, Room 2, Tests 1-3 . . . . .      | 665 |
| 10.15 | PRISME DOOR, compartment pressure and supply/exhaust, Room 2, Tests 4-6 . . . . .      | 666 |
| 10.16 | PRISME SOURCE, pressure and supply/exhaust flow rates, Tests 1, 2, 3 and 4 . . . . .   | 668 |
| 10.17 | PRISME SOURCE, pressure and supply/exhaust flow rates, Tests 5, 5a, 6 and 6a . . . . . | 669 |
| 10.18 | Plan view of the Prétrel water spray experiments . . . . .                             | 670 |
| 10.19 | Various measurements from the Prétrel water spray experiment . . . . .                 | 671 |
| 10.20 | UL/NIJ Experiments, Pressure, Single-Story (Ranch) House, Test 1 . . . . .             | 673 |
| 10.21 | UL/NIJ Experiments, Pressure, Single-Story (Ranch) House, Test 2 . . . . .             | 674 |
| 10.22 | UL/NIJ Experiments, Pressure, Single-Story (Ranch) House, Test 5 . . . . .             | 675 |
| 10.23 | UL/NIJ Experiments, Pressure, Two-Story (Colonial) House, Test 1 . . . . .             | 676 |

|       |  |     |
|-------|--|-----|
| 10.24 | UL/NIJ Experiments, Pressure, Two-Story (Colonial) House, Test 4               | 677 |
| 10.25 | UL/NIJ Experiments, Pressure, Two-Story (Colonial) House, Test 6               | 678 |
| 10.26 | Summary of pressure predictions  | 679 |
| 11.1  | FAA Cargo Compartment experiments, ceiling surface temperatures                | 682 |
| 11.2  | NIST Composite Beam, under-deck temperatures, Sections 3 and 4                 | 684 |
| 11.3  | NIST Composite Beam, under-deck temperatures, Sections 5 and 6                 | 685 |
| 11.4  | NIST Composite Beam, inside-deck temperatures, Sections 1 and 2                | 686 |
| 11.5  | NIST Composite Beam, inside-deck temperatures, Sections 3 and 4                | 687 |
| 11.6  | NIST Composite Beam, inside-deck temperatures, Sections 5 and 6                | 688 |
| 11.7  | NIST Composite Beam, inside-deck temperatures, Sections 7 and 8                | 689 |
| 11.8  | NIST FSE experiments, floor and ceiling temperatures, Tests 3-4, 8             | 691 |
| 11.9  | NIST FSE experiments, floor and ceiling temperatures, Tests 9-12               | 692 |
| 11.10 | NIST FSE experiments, floor and ceiling temperatures, Tests 13-16              | 693 |
| 11.11 | NIST FSE experiments, floor and ceiling temperatures, Tests 17-20              | 694 |
| 11.12 | NIST FSE experiments, floor and ceiling temperatures, Tests 21-24              | 695 |
| 11.13 | NIST FSE experiments, floor and ceiling temperatures, Tests 25-28              | 696 |
| 11.14 | NIST FSE experiments, floor and ceiling temperatures, Tests 29, 30, 32         | 697 |
| 11.15 | NIST/NRC experiments, north wall temperatures, Tests 1, 2, 4, 7, 8, 10, 13, 16 | 699 |
| 11.16 | NIST/NRC experiments, north wall temperatures, Tests 3, 5, 9, 14, 15, 18       | 700 |
| 11.17 | NIST/NRC experiments, south wall temperatures, Tests 1, 2, 4, 7, 8, 10, 13, 16 | 701 |
| 11.18 | NIST/NRC experiments, south wall temperatures, Tests 3, 5, 9, 14, 15, 18       | 702 |
| 11.19 | NIST/NRC experiments, east wall temperatures, Tests 1, 2, 4, 7, 8, 10, 13, 16  | 703 |
| 11.20 | NIST/NRC experiments, east wall temperatures, Tests 3, 5, 9, 14, 15, 18        | 704 |
| 11.21 | NIST/NRC experiments, west wall temperatures, Tests 1, 2, 4, 7, 8, 10, 13, 16  | 705 |
| 11.22 | NIST/NRC experiments, west wall temperatures, Tests 3, 5, 9, 14, 15, 18        | 706 |
| 11.23 | NIST/NRC experiments, ceiling temperatures, Tests 1, 2, 4, 7, 8, 10, 13, 16    | 707 |
| 11.24 | NIST/NRC experiments, ceiling temperatures, Tests 3, 5, 9, 14, 15, 18          | 708 |
| 11.25 | NIST/NRC experiments, floor wall temperatures, Tests 1, 2, 4, 7, 8, 10, 13, 16 | 709 |
| 11.26 | NIST/NRC experiments, floor temperatures, Tests 3, 5, 9, 14, 15, 18            | 710 |
| 11.27 | PRISME DOOR experiments, wall temperatures, vertical array, Room 1             | 711 |
| 11.28 | PRISME DOOR experiments, wall temperatures, four sides, Room 1                 | 712 |
| 11.29 | PRISME DOOR experiments, wall temperatures, vertical array, Room 2             | 713 |
| 11.30 | PRISME DOOR experiments, wall temperatures, four sides, Room 2                 | 714 |
| 11.31 | PRISME SOURCE experiments, wall temperatures, vertical array, Room 2           | 716 |
| 11.32 | PRISME SOURCE experiments, wall temperatures, four sides, Room 2               | 717 |
| 11.33 | WTC experiments, ceiling temperatures, north array                             | 719 |
| 11.34 | WTC experiments, ceiling temperatures, south array                             | 720 |
| 11.35 | WTC experiments, ceiling temperatures, east array, Points 1-4                  | 721 |
| 11.36 | WTC experiments, ceiling temperatures, east array, Points 5-7                  | 722 |
| 11.37 | WTC experiments, ceiling temperatures, west array, Points 1-4                  | 723 |
| 11.38 | WTC experiments, ceiling temperatures, west array, Points 5-8                  | 724 |
| 11.39 | WTC experiments, ceiling temperatures, diagonal array                          | 725 |
| 11.40 | WTC experiments, wall temperatures, Points 98, 100, 102                        | 726 |
| 11.41 | WTC experiments, wall temperatures, Points 103, 105, 106                       | 727 |
| 11.42 | WTC experiments, wall temperatures, Points 107, 109, 110                       | 728 |
| 11.43 | WTC experiments, inner ceiling temperatures, north-south axis                  | 729 |
| 11.44 | WTC experiments, inner ceiling temperatures, east-west axis                    | 730 |

|       |  |     |
|-------|--|-----|
| 11.45 | WTC experiments, inner wall temperatures . . . . .   | 731 |
| 11.46 | Insulation material cold side temperatures, Tests 1-6 . . . . .                              | 733 |
| 11.47 | Insulation material cold side temperatures, Tests 7-14 . . . . .                             | 734 |
| 11.48 | Insulation material cold side temperatures, Tests 15-22 . . . . .                            | 735 |
| 11.49 | Insulation material cold side temperatures, Tests 23-30 . . . . .                            | 736 |
| 11.50 | Summary of compartment surface temperature predictions . . . . .                             | 737 |
| 11.51 | NIST Composite Beam, beam temperatures . . . . .   | 738 |
| 11.52 | NIST Composite Beam, beam temperatures . . . . .   | 739 |
| 11.53 | NIST E119 Compartment, Plate temperatures . . . . .  | 740 |
| 11.54 | NIST/NRC experiments, Cable A temperatures, Tests 1, 2, 4, 7, 8, 10, 13, 16 . . . . .        | 742 |
| 11.55 | NIST/NRC experiments, Cable A temperatures, Tests 3, 5, 9, 14, 15, 18 . . . . .              | 743 |
| 11.56 | NIST/NRC experiments, Cable B temperatures, Tests 1, 2, 4, 7, 8, 10, 13, 16 . . . . .        | 744 |
| 11.57 | NIST/NRC experiments, Cable B temperatures, Tests 3, 5, 9, 14, 15, 18 . . . . .              | 745 |
| 11.58 | NIST/NRC experiments, Cable Ca temperatures, Tests 1, 2, 4, 7, 8, 10, 13, 16 . . . . .       | 746 |
| 11.59 | NIST/NRC experiments, Cable Ca temperatures, Tests 3, 5, 9, 14, 15, 18 . . . . .             | 747 |
| 11.60 | NIST/NRC experiments, Cable Cb temperatures, Tests 1, 2, 4, 7, 8, 10, 13, 16 . . . . .       | 748 |
| 11.61 | NIST/NRC experiments, Cable Cb temperatures, Tests 3, 5, 9, 14, 15, 18 . . . . .             | 749 |
| 11.62 | NIST/NRC experiments, Cable D temperatures, Tests 1, 2, 4, 7, 8, 10, 13, 16 . . . . .        | 750 |
| 11.63 | NIST/NRC experiments, Cable D temperatures, Tests 3, 5, 9, 14, 15, 18 . . . . .              | 751 |
| 11.64 | NIST/NRC experiments, Cable F temperatures, Tests 1, 2, 4, 7, 8, 10, 13, 16 . . . . .        | 752 |
| 11.65 | NIST/NRC experiments, Cable F temperatures, Tests 3, 5, 9, 14, 15, 18 . . . . .              | 753 |
| 11.66 | NIST/NRC experiments, Cable G temperatures, Tests 1, 2, 4, 7, 8, 10, 13, 16 . . . . .        | 754 |
| 11.67 | NIST/NRC experiments, Cable G temperatures, Tests 3, 5, 9, 14, 15, 18 . . . . .              | 755 |
| 11.68 | NIST/NRC Corner Effects, plate and cabinet temperatures, Test 1 . . . . .                    | 757 |
| 11.69 | NIST/NRC Corner Effects, plate and cabinet temperatures, Test 2 . . . . .                    | 758 |
| 11.70 | NIST/NRC Corner Effects, plate and cabinet temperatures, Test 3 . . . . .                    | 759 |
| 11.71 | NIST/NRC Corner Effects, plate and cabinet temperatures, Test 4 . . . . .                    | 760 |
| 11.72 | NIST/NRC Corner Effects, plate and cabinet temperatures, Test 5 . . . . .                    | 761 |
| 11.73 | NIST/NRC Corner Effects, plate and cabinet temperatures, Test 6 . . . . .                    | 762 |
| 11.74 | NIST/NRC Corner Effects, plate and cabinet temperatures, Test 7 . . . . .                    | 763 |
| 11.75 | NIST/NRC Corner Effects, plate and cabinet temperatures, Test 8 . . . . .                    | 764 |
| 11.76 | NIST/NRC Corner Effects, plate and cabinet temperatures, Test 9 . . . . .                    | 765 |
| 11.77 | NIST/NRC Corner Effects, plate and cabinet temperatures, Test 10 . . . . .                   | 766 |
| 11.78 | NIST/NRC Corner Effects, plate and cabinet temperatures, Test 11 . . . . .                   | 767 |
| 11.79 | NIST/NRC Corner Effects, plate and cabinet temperatures, Test 12 . . . . .                   | 768 |
| 11.80 | SP AST experiments, Station A plate, adiabatic surface, and steel temperatures, Test 1 . . . | 770 |
| 11.81 | SP AST experiments, Station B plate, adiabatic surface, and steel temperatures, Test 1 . . . | 771 |
| 11.82 | SP AST experiments, Station C plate, adiabatic surface, and steel temperatures, Test 1 . . . | 772 |
| 11.83 | SP AST experiments, Station A plate, adiabatic surface, and steel temperatures, Test 2 . . . | 773 |
| 11.84 | SP AST experiments, Station B plate, adiabatic surface, and steel temperatures, Test 2 . . . | 774 |
| 11.85 | SP AST experiments, Station C plate, adiabatic surface, and steel temperatures, Test 2 . . . | 775 |
| 11.86 | SP AST experiments, Station A plate, adiabatic surface, and steel temperatures, Test 3 . . . | 776 |
| 11.87 | SP AST experiments, Station B plate, adiabatic surface, and steel temperatures, Test 3 . . . | 777 |
| 11.88 | SP AST experiments, Station C plate, adiabatic surface, and steel temperatures, Test 3 . . . | 778 |
| 11.89 | SP AST experiments, steel temperatures, 1.1 m diesel fire . . . . .                          | 780 |
| 11.90 | SP AST experiments, steel temperatures, 1.1 m and 1.9 m diesel, 1.1 m heptane fires . . .    | 781 |
| 11.91 | SP AST experiments, steel temperatures, 1.1 m heptane fire . . . . .                         | 782 |
| 11.92 | SP AST experiments, Insulated Room, Test A1 . . . . .  | 784 |

|        |   |     |
|--------|---|-----|
| 11.93  | SP AST experiments, Insulated Room, Test A2   | 785 |
| 11.94  | SP AST experiments, Insulated Room, Test A3   | 786 |
| 11.95  | SP AST experiments, Insulated Room, Test A4   | 787 |
| 11.96  | SP AST experiments, Insulated Room, Test A5   | 788 |
| 11.97  | SP AST experiments, Insulated Room, Test B1   | 789 |
| 11.98  | SP AST experiments, Insulated Room, Test B2   | 790 |
| 11.99  | SP AST experiments, Insulated Room, Test C1   | 791 |
| 11.100 | SP AST experiments, Insulated Room, Test C2   | 792 |
| 11.101 | SP AST experiments, Insulated Room, Test C3   | 793 |
| 11.102 | SP AST experiments, Insulated Room, Test D1   | 794 |
| 11.103 | SP AST experiments, Insulated Room, Test D2   | 795 |
| 11.104 | Drawing of a plate thermometer  | 796 |
| 11.105 | Predictions of plate thermometer temperatures in a cone calorimeter                 | 796 |
| 11.106 | WTC experiments, steel temperatures, upper column                                   | 798 |
| 11.107 | WTC experiments, steel temperatures, middle column                                  | 799 |
| 11.108 | WTC experiments, steel temperatures, lower column                                   | 800 |
| 11.109 | WTC experiments, steel temperatures, upper Truss A                                  | 801 |
| 11.110 | WTC experiments, steel temperatures, middle Truss A                                 | 802 |
| 11.111 | WTC experiments, steel temperatures, lower Truss A                                  | 803 |
| 11.112 | WTC experiments, steel temperatures, upper Truss B                                  | 804 |
| 11.113 | WTC experiments, steel temperatures, middle Truss B                                 | 805 |
| 11.114 | WTC experiments, steel temperatures, lower Truss B                                  | 806 |
| 11.115 | WTC experiments, steel temperatures, Bar 1  | 807 |
| 11.116 | WTC experiments, slug temperatures  | 808 |
| 11.117 | CAROLFIRE, electrical cable temperatures, Penlight Tests 1, 2, 3, 7, 9, 11-13       | 810 |
| 11.118 | CAROLFIRE, electrical cable temperatures, Penlight Tests 17, 19-20, 22-24, 27-28    | 811 |
| 11.119 | CAROLFIRE, electrical cable temperatures, Penlight Tests 4-6, 8, 10, 14-16          | 812 |
| 11.120 | CAROLFIRE, electrical cable temperatures, Penlight Tests 21, 25-26, 29-30, 63, 65   | 813 |
| 11.121 | CAROLFIRE, electrical cable temperatures, Penlight Tests 18, 31, 62, 64             | 814 |
| 11.122 | Frankman vegetation experiments, fuel temperatures                                  | 815 |
| 11.123 | PRISME LEAK experiments, cable temperature, Tests 1 and 2                           | 817 |
| 11.124 | PRISME LEAK experiments, cable temperature, Tests 3 and 4                           | 818 |
| 11.125 | PRISME DOOR experiments, cable temperature, Room 1, Cable BW                        | 819 |
| 11.126 | PRISME DOOR experiments, cable temperature, Room 1, Cable HW                        | 820 |
| 11.127 | PRISME DOOR experiments, cable temperature, Room 2, Cable BE                        | 821 |
| 11.128 | PRISME DOOR experiments, cable temperature, Room 2, Cable HE                        | 822 |
| 11.129 | PRISME DOOR experiments, cable temperature, Room 2, Cable HW                        | 823 |
| 11.130 | Summary of target temperature predictions   | 824 |
| 11.131 | Summary of time to failure predictions for electrical cables                        | 825 |
| 11.132 | ASTM E2058 water evaporation 50 kW/m <sup>2</sup> , surface temperature             | 826 |
| 11.133 | VTT heptane pool fire surface temperatures  | 826 |
| 11.134 | Pool fire experiments, surface temperatures   | 827 |
| 11.135 | NIST 1 m and Waterloo 30 cm methanol pool fires, surface temperature                | 828 |
| 11.136 | Summary of liquid pool surface temperature predictions                              | 829 |
| 12.1   | FAA Cargo Compartment experiments, heat flux to ceiling                             | 832 |
| 12.2   | FM Parallel Panel experiments, side wall heat flux                                  | 833 |
| 12.3   | JH/FRA corner exp, HF to ceiling, wall, and floor 1:4 scale inert lining, Tests 1-2 | 835 |

|       |   |     |
|-------|---|-----|
| 12.4  | JH/FRA corner exp, HF to ceiling, wall, and floor, Tests 3 and 3A . . . . .         | 835 |
| 12.5  | JH/FRA corner exp, heat flux to ceiling, wall, and floor Tests, Tests 6-7 . . . . . | 835 |
| 12.6  | JH/FRA corner exp, HF to ceiling, wall, and floor, Tests 8 . . . . .                | 835 |
| 12.7  | JH/FRA corner exp, HF to the ceiling, wall, and floor, Tests 11-12 . . . . .        | 836 |
| 12.8  | JH/FRA corner exp, HF to ceiling, wall, and floor, Test 13 . . . . .                | 836 |
| 12.9  | FM Vertical Wall Flame experiments, flame radiance . . . . .                        | 837 |
| 12.10 | FM Vertical Wall Flame experiments, centerline heat flux . . . . .                  | 838 |
| 12.11 | NIST E119 Compartment, wall heat fluxes . . . . .                                   | 839 |
| 12.12 | NIST/NRC experiments, heat flux to north wall, Tests 1, 2, 4, 7, 8, 10 . . . . .    | 841 |
| 12.13 | NIST/NRC experiments, heat flux to north wall, Tests 3, 5, 9, 14, 15, 18 . . . . .  | 842 |
| 12.14 | NIST/NRC experiments, heat flux to south wall, Tests 1, 2, 4, 7, 8, 10 . . . . .    | 843 |
| 12.15 | NIST/NRC experiments, heat flux to south wall, Tests 3, 5, 9, 14, 15, 18 . . . . .  | 844 |
| 12.16 | NIST/NRC experiments, heat flux to east wall, Tests 1, 2, 4, 7, 8, 10 . . . . .     | 845 |
| 12.17 | NIST/NRC experiments, heat flux to east wall, Tests 3, 5, 9, 14, 15, 18 . . . . .   | 846 |
| 12.18 | NIST/NRC experiments, heat flux to west wall, Tests 1, 2, 4, 7, 8, 10 . . . . .     | 847 |
| 12.19 | NIST/NRC experiments, heat flux to west wall, Tests 3, 5, 9, 14, 15, 18 . . . . .   | 848 |
| 12.20 | NIST/NRC experiments, heat flux to the floor, Tests 1, 2, 4, 7, 8, 10 . . . . .     | 849 |
| 12.21 | NIST/NRC experiments, heat flux to the floor, Tests 3, 5, 9, 14, 15, 18 . . . . .   | 850 |
| 12.22 | NIST/NRC experiments, heat flux to the ceiling, Tests 1, 2, 4, 7, 8, 10 . . . . .   | 851 |
| 12.23 | NIST/NRC experiments, heat flux to the ceiling, Tests 3, 5, 9, 14, 15, 18 . . . . . | 852 |
| 12.24 | NIST/NRC Parallel Panel experiments, heat flux profiles . . . . .                   | 853 |
| 12.25 | Summary of Test 1, NIST RSE 2007 . . . . .  | 854 |
| 12.26 | Summary of Test 2, NIST RSE 2007 . . . . .  | 855 |
| 12.27 | Smokeview rendering of NRCC Facade experiment . . . . .                             | 856 |
| 12.28 | NRCC Facade experiments, heat flux, window configuration 1 and 2 . . . . .          | 857 |
| 12.29 | NRCC Facade experiments, heat flux, window configuration 3 and 4 . . . . .          | 858 |
| 12.30 | NRCC Facade experiments, heat flux, window configuration 5 . . . . .                | 859 |
| 12.31 | NRL/HAI experiments, heat flux to the wall, Tests 1-5 . . . . .                     | 861 |
| 12.32 | NRL/HAI experiments, heat flux to the wall, Tests 6-9 . . . . .                     | 862 |
| 12.33 | PRISME DOOR experiments, total heat flux, vertical array, Room 1 . . . . .          | 863 |
| 12.34 | PRISME DOOR experiments, radiative heat flux, vertical array, Room 1 . . . . .      | 864 |
| 12.35 | PRISME DOOR experiments, total heat flux, four walls, Room 1 . . . . .              | 865 |
| 12.36 | PRISME DOOR experiments, total heat flux, vertical array, Room 2 . . . . .          | 866 |
| 12.37 | PRISME DOOR experiments, radiative heat flux, vertical array, Room 2 . . . . .      | 867 |
| 12.38 | PRISME DOOR experiments, total heat flux, four walls, Room 2 . . . . .              | 868 |
| 12.39 | PRISME SOURCE experiments, total heat flux, vertical array, Room 2 . . . . .        | 870 |
| 12.40 | PRISME SOURCE experiments, radiative heat flux, vertical array, Room 2 . . . . .    | 871 |
| 12.41 | PRISME SOURCE experiments, total heat flux, four walls, Room 2 . . . . .            | 872 |
| 12.42 | Ulster SBI experiments, corner fire heat flux . . . . .                             | 873 |
| 12.43 | UMD SBI heat flux to PMMA panel . . . . .   | 875 |
| 12.44 | WTC experiments, heat flux to the floor . . . . .                                   | 877 |
| 12.45 | WTC experiments, heat flux to the ceiling . . . . .                                 | 878 |
| 12.46 | WTC experiments, heat flux to the ceiling . . . . .                                 | 879 |
| 12.47 | Summary of compartment surface heat flux predictions . . . . .                      | 880 |
| 12.48 | Fleury Heat Flux, 100 kW fires . . . . .  | 882 |
| 12.49 | Fleury Heat Flux, 150 kW fires . . . . .  | 883 |
| 12.50 | Fleury Heat Flux, 200 kW fires . . . . .  | 884 |
| 12.51 | Fleury Heat Flux, 250 kW fires . . . . .  | 885 |

|       |  |     |
|-------|--|-----|
| 12.52 | Fleury Heat Flux, 300 kW fires . . . . .   | 886 |
| 12.53 | Heat flux predictions, Hamins methane burner Tests 1-4 . . . . .                           | 889 |
| 12.54 | Heat flux predictions, Hamins methane burner Tests 5-8 . . . . .                           | 890 |
| 12.55 | Heat flux predictions, Hamins methane burner Tests 9-12 . . . . .                          | 891 |
| 12.56 | Heat flux predictions, Hamins methane burner Tests 13-16 . . . . .                         | 892 |
| 12.57 | Heat flux predictions, Hamins methane burner Tests 17-20 . . . . .                         | 893 |
| 12.58 | Heat flux predictions, Hamins methane burner Tests 21-24 . . . . .                         | 894 |
| 12.59 | Heat flux predictions, Hamins methane burner Tests 25-28 . . . . .                         | 895 |
| 12.60 | Heat flux predictions, Hamins methane burner Tests 29-30 . . . . .                         | 896 |
| 12.61 | Heat flux predictions, Hamins propane burner Tests 1-4 . . . . .                           | 898 |
| 12.62 | Heat flux predictions, Hamins propane burner Tests 5-8 . . . . .                           | 899 |
| 12.63 | Heat flux predictions, Hamins propane burner Tests 9-12 . . . . .                          | 900 |
| 12.64 | Heat flux predictions, Hamins propane burner Tests 13-16 . . . . .                         | 901 |
| 12.65 | Heat flux predictions, Hamins propane burner Tests 17-20 . . . . .                         | 902 |
| 12.66 | Heat flux predictions, Hamins propane burner Tests 21-24 . . . . .                         | 903 |
| 12.67 | Heat flux predictions, Hamins propane burner Tests 25-28 . . . . .                         | 904 |
| 12.68 | Heat flux predictions, Hamins propane burner Tests 29-32 . . . . .                         | 905 |
| 12.69 | Heat flux predictions, Hamins propane burner Tests 33-34 . . . . .                         | 906 |
| 12.70 | Heat flux predictions, Hamins acetylene burner Tests 1-4 . . . . .                         | 908 |
| 12.71 | Heat flux predictions, Hamins acetylene burner Tests 5-8 . . . . .                         | 909 |
| 12.72 | Heat flux predictions, Hamins acetylene burner Tests 9-12 . . . . .                        | 910 |
| 12.73 | Heat flux predictions, Hamins acetylene burner Tests 13-16 . . . . .                       | 911 |
| 12.74 | Schematic diagram of BGC/GRI test facility . . . . .                                       | 912 |
| 12.75 | BGC/GRI LNG Fires, heat flux profiles for Tests 1-8 . . . . .                              | 913 |
| 12.76 | BGC/GRI LNG Fires, heat flux profiles for Tests 9-13 . . . . .                             | 914 |
| 12.77 | Location of heat flux gauges, Loughborough Jet Fires . . . . .                             | 915 |
| 12.78 | Loughborough Jet Fires, heat flux to pipe, Test 1 . . . . .                                | 916 |
| 12.79 | Loughborough Jet Fires, heat flux to pipe, Test 2 . . . . .                                | 917 |
| 12.80 | Loughborough Jet Fires, heat flux to pipe, Test 3 . . . . .                                | 918 |
| 12.81 | Loughborough Jet Fires, far-field radiometers . . . . .                                    | 919 |
| 12.82 | Layout of the Montoir LNG Fires . . . . .  | 920 |
| 12.83 | Montoir LNG Fires, far-field radiometers, Test 1 . . . . .                                 | 921 |
| 12.84 | Montoir LNG Fires, far-field radiometers, Test 2 . . . . .                                 | 922 |
| 12.85 | Montoir LNG Fires, far-field radiometers, Test 3 . . . . .                                 | 923 |
| 12.86 | NIST Douglas Firs, heat flux . . . . .   | 924 |
| 12.87 | NIST/NRC experiments, heat flux to Cable B, Tests 1, 2, 4, 7, 8, 10, 13, 16 . . . . .      | 926 |
| 12.88 | NIST/NRC experiments, heat flux to Cable B, Tests 3, 5, 9, 14, 15, 18 . . . . .            | 927 |
| 12.89 | NIST/NRC experiments, heat flux to Cable D, Tests 1, 2, 4, 7, 8, 10, 13, 16 . . . . .      | 928 |
| 12.90 | NIST/NRC experiments, heat flux to Cable D, Tests 5, 9, 14 . . . . .                       | 929 |
| 12.91 | NIST/NRC experiments, heat flux to Cable F, Tests 1, 2, 4, 7, 8, 10, 13, 16 . . . . .      | 930 |
| 12.92 | NIST/NRC experiments, heat flux to Cable F, Tests 3, 5, 9, 14, 15, 18 . . . . .            | 931 |
| 12.93 | NIST/NRC experiments, heat flux to Cable G, Tests 1, 2, 4, 7, 8, 10, 13, 16 . . . . .      | 932 |
| 12.94 | NIST/NRC experiments, heat flux to Cable G, Tests 3, 5, 9, 14, 15, 18 . . . . .            | 933 |
| 12.95 | NIST Pool Fires, 30 cm methanol, radial profiles heat flux near surface . . . . .          | 934 |
| 12.96 | NIST Pool Fires, 30 cm methanol, radial and vertical profiles of total heat flux . . . . . | 935 |
| 12.97 | NIST Pool Fires, 100 cm methanol, radial and vertical profiles of heat flux . . . . .      | 935 |
| 12.98 | NIST Pool Fires, 100 cm methanol, radial profiles of heat flux . . . . .                   | 936 |
| 12.99 | NIST Structure Separation Verification heat flux (4 MW) . . . . .                          | 937 |

|  |     |
|--|-----|
| 12.100 NIST Structure Separation Verification heat flux (8 MW) . . . . .                     | 938 |
| 12.101 Layout of the Phoenix LNG Fires . . . . .   | 939 |
| 12.102 Phoenix LNG Fires, radial profiles of wide-angle heat flux . . . . .                  | 940 |
| 12.103 Phoenix LNG Fires, vertical profiles of narrow-angle heat flux . . . . .              | 940 |
| 12.104 Sandia Methane Burner, heat flux, Tests 1-4 . . . . .                                 | 942 |
| 12.105 Sandia Methane Burner, heat flux, Tests 5-8 . . . . .                                 | 943 |
| 12.106 Sandia Methane Burner, heat flux, Tests 9-12 . . . . .                                | 944 |
| 12.107 Sandia Methane Burner, heat flux, Tests 13-16 . . . . .                               | 945 |
| 12.108 Sandia Methane Burner, heat flux, Tests 17-20 . . . . .                               | 946 |
| 12.109 Sandia Methane Burner, heat flux, Tests 21-24 . . . . .                               | 947 |
| 12.110 Sandia Methane Burner, heat flux, Tests 25-28 . . . . .                               | 948 |
| 12.111 Shell LNG Fireballs, heat flux . . . . .  | 949 |
| 12.112 UMD SBI, radiative heat flux at six vertical locations . . . . .                      | 950 |
| 12.113 UMD Line Burner contour of integrated radiation intensity. . . . .                    | 951 |
| 12.114 UMD Line Burner radiative fraction and radiative heat flux . . . . .                  | 952 |
| 12.115 WTC experiments, heat flux at Station 2, high position . . . . .                      | 953 |
| 12.116 WTC experiments, heat flux at Station 2, low position . . . . .                       | 954 |
| 12.117 WTC experiments, heat flux to upper column . . . . .                                  | 955 |
| 12.118 WTC experiments, heat flux to lower column . . . . .                                  | 956 |
| 12.119 Summary of target heat flux predictions . . . . .                                     | 957 |
| 12.120 Droplet speeds and mean diameters for the three nozzles . . . . .                     | 958 |
| 12.121 Comparison of radiation attenuation, BRE and LEMTA Spray experiments . . . . .        | 959 |
| 12.122 LEMTA Spray Cooling steel plate temperatures . . . . .                                | 960 |
| 12.123 Bouchair Solar Chimney, 0.1 m thermal cavity . . . . .                                | 962 |
| 12.124 Bouchair Solar Chimney, 0.2 m thermal cavity . . . . .                                | 963 |
| 12.125 Bouchair Solar Chimney, 0.3 m thermal cavity . . . . .                                | 964 |
| 12.126 Bouchair Solar Chimney, 0.5 m thermal cavity . . . . .                                | 965 |
| 12.127 Bouchair Solar Chimney, 1.0 m thermal cavity . . . . .                                | 966 |
| 12.128 Summary of Bouchair Solar Chimney results . . . . .                                   | 967 |
| 12.129 FM Burner experiments, mean and rms vertical heat flux profiles . . . . .             | 969 |
| 12.130 FM Burner experiments, radiant fraction . . . . .                                     | 970 |
| 12.131 Summary of SETCOM results . . . . .   | 971 |
| <br>13.1 Results of Cup Burner experiments . . . . .   | 974 |
| 13.2 FM Burner combustion efficiency . . . . .   | 975 |
| 13.3 UMD Line Burner combustion efficiency . . . . .   | 976 |
| 13.4 LLNL Extinction Time, Tests 1-8 . . . . .   | 978 |
| 13.5 LLNL Extinction Time, Tests 22, 24, 25, 27, 28, 29, 32, 37 . . . . .                    | 979 |
| 13.6 LLNL Extinction Time, Tests 39, 41, 43-48 . . . . .                                     | 980 |
| 13.7 LLNL Extinction Time, Test 49 . . . . .   | 981 |
| 13.8 NIST/NRC OLIVE-Fire maximum HRR and gas concentrations, Tests 3, 4, 8, 9 . . . . .      | 983 |
| 13.9 NIST/NRC OLIVE-Fire maximum HRR and gas concentrations, Tests 12, 13, 15, 16 . . . . .  | 984 |
| 13.10 NIST/NRC OLIVE-Fire maximum HRR and gas concentrations, Tests 17, 19, 22, 23 . . . . . | 985 |
| 13.11 NIST/NRC OLIVE-Fire maximum HRR and gas concentrations, Tests 24, 26, 27, 29 . . . . . | 986 |
| 13.12 NIST/NRC OLIVE-Fire maximum HRR and gas concentrations, Tests 30, 31 . . . . .         | 987 |
| 13.13 SWJTU Tunnel experiments, extinction time . . . . .                                    | 988 |
| 13.14 USCG/HAI experiments, extinction time . . . . .  | 990 |
| 13.15 USCG/HAI experiments, extinction time . . . . .  | 991 |

|       |   |      |
|-------|---|------|
| 13.16 | USCG/HAI experiments, extinction time . . . . .   | 992  |
| 13.17 | USCG/HAI experiments, extinction time . . . . .   | 993  |
| 13.18 | USCG/HAI experiments, extinction time . . . . .   | 994  |
| 13.19 | Extinguishment times for the USCG/HAI water mist suppression tests . . . . .                        | 995  |
| 13.20 | Theobald Hose Stream max range . . . . .  | 996  |
| 13.21 | Theobald Hose Stream max height . . . . .   | 997  |
| 13.22 | Theobald Hose Stream distance to max height . . . . .   | 997  |
| 13.23 | Droplet speed, flux, and mean diameter profiles of the LN-2 nozzle . . . . .                        | 999  |
| 14.1  | Results of FAA Polymers, non-charring, comparison . . . . .   | 1004 |
| 14.2  | Results of FAA Polymers, complex, non-charring, comparison . . . . .                                | 1006 |
| 14.3  | Heat release rate of polycarbonate (PC) . . . . .   | 1008 |
| 14.4  | Heat release rate of poly(vinyl chloride) (PVC) . . . . .   | 1010 |
| 14.5  | Heat release rate of poly(aryl ether ether ketone) (PEEK) . . . . .                                 | 1013 |
| 14.6  | Mass loss rate of poly(butylene terephthalate) (PBT) . . . . .                                      | 1015 |
| 14.7  | Mass loss rate of poly(butylene terephthalate) with glass fibers (PBT-GF) . . . . .                 | 1017 |
| 14.8  | NIST Polymers, TGA, MCC and DSC analysis of black PMMA . . . . .                                    | 1019 |
| 14.9  | NIST Polymers, PMMA in the Cone and Gasification Apparatus . . . . .                                | 1019 |
| 14.10 | Mass loss rate of ABS and HIPS . . . . .  | 1021 |
| 14.11 | Mass loss rate of PMMA . . . . .  | 1022 |
| 14.12 | Mass loss rate of Kydex . . . . .   | 1024 |
| 14.13 | Mass loss rate of PEI and PET . . . . .   | 1026 |
| 14.14 | Mass loss rate of POM . . . . .   | 1027 |
| 14.15 | Mass loss rate of corrugated cardboard . . . . .  | 1031 |
| 14.16 | Aalto Woods heat release rates . . . . .  | 1034 |
| 14.17 | Aalto Woods mass loss rates . . . . .   | 1035 |
| 14.18 | Heat release in room corner tests, Aalto Woods model . . . . .                                      | 1036 |
| 14.19 | BST/FRS Wood Cribs temperatures, Tests 1 and 2 . . . . .  | 1037 |
| 14.20 | BST/FRS Wood Cribs temperatures, Tests 3 and 4 . . . . .  | 1038 |
| 14.21 | BST/FRS Wood Cribs temperatures, Tests 5 and 6 . . . . .  | 1039 |
| 14.22 | NIST/NRC Transient Combustibles: wood cribs . . . . .   | 1040 |
| 14.23 | NIST/NRC Transient Combustibles: boxes . . . . .  | 1041 |
| 14.24 | NIST/NRC Transient Combustibles: pallets . . . . .  | 1042 |
| 14.25 | SP Wood Cribs heat release rates, Tests 1-6 . . . . .   | 1043 |
| 14.26 | SP Wood Cribs heat release rates, Tests 7-12 . . . . .  | 1044 |
| 14.27 | DoJ/HAI Pool Fires, Tests 1-8 . . . . .   | 1047 |
| 14.28 | DoJ/HAI Pool Fires, Tests 9-16 . . . . .  | 1048 |
| 14.29 | DoJ/HAI Pool Fires, Tests 17-22 . . . . .   | 1049 |
| 14.30 | DoJ/HAI Pool Fires, Tests 25-32 . . . . .   | 1050 |
| 14.31 | DoJ/HAI Pool Fires, Tests 33-40 . . . . .   | 1051 |
| 14.32 | DoJ/HAI Pool Fires, Tests 41-46 . . . . .   | 1052 |
| 14.33 | LEMTA/UGent Pool Fires burning rate and sub-surface temperature, heptane . . . . .                  | 1054 |
| 14.34 | LEMTA/UGent Pool Fires burning rate and sub-surface temperature, methanol . . . . .                 | 1055 |
| 14.35 | ASTM E2058 fire propagation apparatus water evaporation at 50 kW/m <sup>2</sup> heat flux . . . . . | 1056 |
| 14.36 | VTT Large Hall Test burning rate . . . . .  | 1056 |
| 14.37 | Comparison of burning rates for various liquid pool fires . . . . .                                 | 1057 |
| 14.38 | NIST 1 m methanol burning rate . . . . .  | 1058 |
| 14.39 | Waterloo Methanol mass loss rate . . . . .  | 1058 |

|       |  |      |
|-------|--|------|
| 14.40 | NIST/NRC Parallel Panels experiments . . . . .   | 1059 |
| 14.41 | UMD SBI experiment, heat release rate . . . . .  | 1060 |
| 14.42 | HRRPUA of Aalto Woods using scaling model . . . . .                                      | 1061 |
| 14.43 | HRRPUA of FAA Polymers using scaling model . . . . .                                     | 1063 |
| 14.44 | HRRPUA of FAA Polymers using scaling model . . . . .                                     | 1064 |
| 14.45 | HRRPUA of FAA Polymers using scaling model . . . . .                                     | 1065 |
| 14.46 | HRRPUA of FPL Materials using scaling model . . . . .                                    | 1067 |
| 14.47 | HRRPUA of FSRI Materials using scaling model, other materials . . . . .                  | 1069 |
| 14.48 | HRRPUA of FSRI Materials using scaling model, others materials . . . . .                 | 1070 |
| 14.49 | HRRPUA of FSRI Materials using scaling model, others materials . . . . .                 | 1071 |
| 14.50 | HRRPUA of FSRI Materials using scaling model, others materials . . . . .                 | 1072 |
| 14.51 | HRRPUA of FSRI Materials using scaling model, polymer materials . . . . .                | 1074 |
| 14.52 | HRRPUA of FSRI Materials using scaling model, polymer materials . . . . .                | 1075 |
| 14.53 | HRRPUA of FSRI Materials using scaling model, polymer materials . . . . .                | 1076 |
| 14.54 | HRRPUA of FSRI Materials using scaling model, polymer materials . . . . .                | 1077 |
| 14.55 | HRRPUA of FSRI Materials using scaling model, wood-based materials . . . . .             | 1079 |
| 14.56 | HRRPUA of FSRI Materials using scaling model, wood-based materials . . . . .             | 1080 |
| 14.57 | HRRPUA of FSRI Materials using scaling model, wood-Based materials . . . . .             | 1081 |
| 14.58 | HRRPUA of JH Materials using scaling model . . . . .                                     | 1083 |
| 14.59 | HRRPUA of JH Materials using scaling model . . . . .                                     | 1084 |
| 14.60 | HRRPUA of RISE Materials using scaling model, mixtures materials . . . . .               | 1087 |
| 14.61 | HRRPUA of RISE Materials using scaling model, mixtures materials . . . . .               | 1088 |
| 14.62 | HRRPUA of RISE Materials using scaling model, mixtures materials . . . . .               | 1089 |
| 14.63 | HRRPUA of RISE Materials using scaling model, mixtures materials . . . . .               | 1090 |
| 14.64 | HRRPUA of RISE Materials using scaling model, mixtures materials . . . . .               | 1091 |
| 14.65 | HRRPUA of RISE Materials using scaling model, other materials . . . . .                  | 1093 |
| 14.66 | HRRPUA of RISE Materials using scaling model, polymer materials . . . . .                | 1095 |
| 14.67 | HRRPUA of RISE Materials using scaling model, polymer materials . . . . .                | 1096 |
| 14.68 | HRRPUA of RISE Materials using scaling model, wood-based materials . . . . .             | 1098 |
| 14.69 | JH/FRA experiments, HRR, 1:4 scale plywood half lining configuration, Test 3 . . . . .   | 1099 |
| 14.70 | JH/FRA experiments, HRR, 1:4 scale plywood full lining configuration, Test 3A . . . . .  | 1099 |
| 14.71 | JH/FRA experiments, HRR, 1:2 scale plywood half lining configuration, Test 8 . . . . .   | 1100 |
| 14.72 | JH/FRA experiments, HRR, 1:1 scale plywood half lining configuration, Test 13 . . . . .  | 1100 |
| 14.73 | Comparison observed and predicted rates of spread for a variety of crown fires . . . . . | 1101 |
| 14.74 | Measured and predicted fire front position for the CSIRO Grassland Fires . . . . .       | 1103 |
| 14.75 | Flame front, USFS/Catchpole experiments . . . . .  | 1105 |
| 14.76 | Flame front, USFS/Catchpole experiments . . . . .  | 1106 |
| 14.77 | Flame front, USFS/Catchpole experiments . . . . .  | 1107 |
| 14.78 | Flame front, USFS/Catchpole experiments . . . . .  | 1108 |
| 14.79 | Flame front, USFS/Catchpole experiments . . . . .  | 1109 |
| 14.80 | Flame front, USFS/Catchpole experiments . . . . .  | 1110 |
| 14.81 | Flame front, USFS/Catchpole experiments . . . . .  | 1111 |
| 14.82 | Flame front, USFS/Catchpole experiments . . . . .  | 1112 |
| 14.83 | Flame front, USFS/Catchpole experiments . . . . .  | 1113 |
| 14.84 | Flame front, USFS/Catchpole experiments . . . . .  | 1114 |
| 14.85 | Flame front, USFS/Catchpole experiments . . . . .  | 1115 |
| 14.86 | Flame front, USFS/Catchpole experiments . . . . .  | 1116 |
| 14.87 | Flame front, USFS/Catchpole experiments . . . . .  | 1117 |

|        |   |       |
|--------|---|-------|
| 14.88  | Flame front, USFS/Catchpole experiments . . . . .                         | .1118 |
| 14.89  | Flame front, USFS/Catchpole experiments . . . . .                         | .1119 |
| 14.90  | Flame front, USFS/Catchpole experiments . . . . .                         | .1120 |
| 14.91  | Flame front, USFS/Catchpole experiments . . . . .                         | .1121 |
| 14.92  | Flame front, USFS/Catchpole experiments . . . . .                         | .1122 |
| 14.93  | Flame front, USFS/Catchpole experiments . . . . .                         | .1123 |
| 14.94  | Flame front, USFS/Catchpole experiments . . . . .                         | .1124 |
| 14.95  | Flame front, USFS/Catchpole experiments . . . . .                         | .1125 |
| 14.96  | Flame front, USFS/Catchpole experiments . . . . .                         | .1126 |
| 14.97  | Flame front, USFS/Catchpole experiments . . . . .                         | .1127 |
| 14.98  | Flame front, USFS/Catchpole experiments . . . . .                         | .1128 |
| 14.99  | Flame front, USFS/Catchpole experiments . . . . .                         | .1129 |
| 14.100 | Flame front, USFS/Catchpole experiments . . . . .                         | .1130 |
| 14.101 | Flame front, USFS/Catchpole experiments . . . . .                         | .1131 |
| 14.102 | Flame front, USFS/Catchpole experiments . . . . .                         | .1132 |
| 14.103 | Flame front, USFS/Catchpole experiments . . . . .                         | .1133 |
| 14.104 | Flame front, USFS/Catchpole experiments . . . . .                         | .1134 |
| 14.105 | Flame front, USFS/Catchpole experiments . . . . .                         | .1135 |
| 14.106 | Flame front, USFS/Catchpole experiments . . . . .                         | .1136 |
| 14.107 | Flame front, USFS/Catchpole experiments . . . . .                         | .1137 |
| 14.108 | Flame front, USFS/Catchpole experiments . . . . .                         | .1138 |
| 14.109 | Flame front, USFS/Catchpole experiments . . . . .                         | .1139 |
| 14.110 | Flame front, USFS/Catchpole experiments . . . . .                         | .1140 |
| 14.111 | Flame front, USFS/Catchpole experiments . . . . .                         | .1141 |
| 14.112 | Flame front, USFS/Catchpole experiments . . . . .                         | .1142 |
| 14.113 | Flame front, USFS/Catchpole experiments . . . . .                         | .1143 |
| 14.114 | Flame front, USFS/Catchpole experiments . . . . .                         | .1144 |
| 14.115 | Flame front, USFS/Catchpole experiments . . . . .                         | .1145 |
| 14.116 | Flame front, USFS/Catchpole experiments . . . . .                         | .1146 |
| 14.117 | Flame front, USFS/Catchpole experiments . . . . .                         | .1147 |
| 14.118 | Flame front, USFS/Catchpole experiments . . . . .                         | .1148 |
| 14.119 | Flame front, USFS/Catchpole experiments . . . . .                         | .1149 |
| 14.120 | HRR, USFS/Corsica experiments . . . . .                                   | .1150 |
| 14.121 | Rate of Spread, USFS/Corsica experiments . . . . .                        | .1151 |
| 14.122 | Snapshots of a 2 m Douglas fir fire simulation . . . . .                  | .1152 |
| 14.123 | Measured and predicted MLR for the Douglas fir tree experiments . . . . . | .1153 |
| 14.124 | Summary of heat release rate predictions . . . . .                        | .1154 |
| 14.125 | Summary of burning rate predictions . . . . .                             | .1154 |
| 14.126 | Summary of liquid pool burning rate predictions . . . . .                 | .1155 |
| 14.127 | Summary of scaling heat release rate per unit area predictions . . . . .  | .1155 |
| 14.128 | Summary, Wildfire Rate of Spread . . . . .                                | .1156 |
| 15.1   | UWO Wind Tunnel schematic drawings . . . . .                              | .1158 |
| 15.2   | UWO Wind Tunnel, SS20-Test 7 pressure coefficients, 180° . . . . .        | .1159 |
| 15.3   | UWO Wind Tunnel, SS20-Test 7 pressure coefficients, 180° . . . . .        | .1160 |
| 15.4   | UWO Wind Tunnel, SS20-Test 7 pressure coefficients, 270° . . . . .        | .1161 |
| 15.5   | UWO Wind Tunnel, SS20-Test 7 pressure coefficients, 270° . . . . .        | .1162 |
| 15.6   | UWO Wind Tunnel, SS21-Test 6 pressure coefficients, 0° . . . . .          | .1163 |

|       |  |       |
|-------|--|-------|
| 15.7  | UWO Wind Tunnel, SS21-Test 6 pressure coefficients, 0° . . . . .                     | .1164 |
| 15.8  | UWO Wind Tunnel, SS21-Test 6 pressure coefficients, 45° . . . . .                    | .1165 |
| 15.9  | UWO Wind Tunnel, SS21-Test 6 pressure coefficients, 45° . . . . .                    | .1166 |
| 15.10 | LNG Dispersion experiments, Burro velocity and temperature profiles . . . . .        | .1168 |
| 15.11 | LNG Dispersion experiments, Coyote velocity and temperature profiles . . . . .       | .1169 |
| 15.12 | LNG Dispersion experiments, Falcon velocity and temperature profiles . . . . .       | .1170 |
| 15.13 | LNG Dispersion experiments, Maplin Sands velocity and temperature profiles . . . . . | .1171 |
| 15.14 | LNG Dispersion experiments, Burro and Coyote . . . . .                               | .1172 |
| 15.15 | LNG Dispersion experiments, Falson and Maplin Sands . . . . .                        | .1173 |
| 15.16 | Summary of LNG Dispersion predictions . . . . .                                      | .1174 |
| 15.17 | Images of Plume Height simulations . . . . .   | .1176 |
| 15.18 | Atmospheric Dispersion, Plume Height results . . . . .                               | .1177 |

# List of Tables

|      |   |     |
|------|---|-----|
| 3.1  | Summary of simulated Beyler Hood experiments . . . . .                                    | 22  |
| 3.2  | BGC/GRI LNG Fires test parameters . . . . .   | 23  |
| 3.3  | Summary of results, Bittern experiments . . . . .   | 25  |
| 3.4  | Properties of sprinklers used in Bittern Experiments . . . . .                            | 25  |
| 3.5  | BST/FRS test cases . . . . .  | 29  |
| 3.6  | Measured properties for the CSIRO Grassland Fire cases . . . . .                          | 31  |
| 3.7  | Assumed properties for dry grass and soil . . . . .                                       | 33  |
| 3.8  | Summary of Cup Burner Data . . . . .  | 35  |
| 3.9  | Gasoline and kerosene components . . . . .  | 38  |
| 3.10 | Summary of FM/SNL Experiments . . . . .   | 47  |
| 3.11 | Summary of JH/FRA Materials . . . . .   | 52  |
| 3.12 | Summary of JH/FRA Rail Car Experiments . . . . .  | 53  |
| 3.13 | Summary of JH/FRA Rail Car Experiments . . . . .  | 55  |
| 3.14 | Liquid properties used in the LEMTA/Ugent Pool Fires simulations . . . . .                | 57  |
| 3.15 | Summary of LLNL Enclosure Experiments . . . . .   | 59  |
| 3.16 | Summary of LNG Dispersion Experiments . . . . .   | 62  |
| 3.17 | Summary of the Loughborough Jet Fire Experiments . . . . .                                | 64  |
| 3.18 | Summary of McCaffrey Plume Experiments . . . . .  | 65  |
| 3.19 | Summary of Memorial Tunnel Experiments . . . . .  | 68  |
| 3.20 | Summary of Memorial Tunnel Experiments . . . . .  | 69  |
| 3.21 | Summary of the Montoir LNG Fire Experiments . . . . .                                     | 70  |
| 3.22 | Measured properties for the NIST Douglas Fir Experiments . . . . .                        | 81  |
| 3.23 | Assumed properties for the NIST Douglas Fir Experiments . . . . .                         | 82  |
| 3.24 | Summary of NIST Reduced-Scale Experiments, 2007. . . . .                                  | 83  |
| 3.25 | Summary of NIST FSE Experiments selected for model validation . . . . .                   | 85  |
| 3.26 | Summary of NIST/NRC Cabinet Experiments. . . . .  | 93  |
| 3.27 | Average heat and product yields of the various test items . . . . .                       | 96  |
| 3.28 | Summary of NIST Smoke Alarm Experiments selected for model validation . . . . .           | 100 |
| 3.29 | Experiment Details for Gravimetric Measurements of Soot Deposition . . . . .              | 102 |
| 3.30 | Heights of the thermocouples above the floor of each level of the enclosure . . . . .     | 105 |
| 3.31 | Vent State by Experiment: Time Opened . . . . .   | 107 |
| 3.32 | Liquid fuel properties . . . . .  | 114 |
| 3.33 | Summary of Ranz and Marshall droplet evaporation experiments . . . . .                    | 115 |
| 3.34 | Summary of Materials . . . . .  | 119 |
| 3.35 | Summary of SETCOM condensation experiments selected for model validation . . . . .        | 120 |
| 3.36 | Summary of Sippola aerosol deposition experiments selected for model validation . . . . . | 124 |
| 3.37 | Parameters for SP Wood Cribs simulations . . . . .  | 129 |
| 3.38 | Summary of Steckler compartment experiments . . . . .                                     | 130 |
| 3.39 | Summary of UL/NIST Vent experiments . . . . .   | 134 |

|       |   |      |
|-------|---|------|
| 3.40  | Results of the UL/NFPRF heptane spray experiments, Series I . . . . .                         | 138  |
| 3.41  | Results of the UL/NFPRF heptane spray experiments, Series II . . . . .                        | 139  |
| 3.42  | Locations of measurement devices in the UL/NIJ ranch-style house . . . . .                    | 143  |
| 3.43  | Locations of measurement devices in the UL/NIJ colonial-style house . . . . .                 | 143  |
| 3.44  | Sequence of events for the one story ranch-style house in the UL/NIJ experiments . . . . .    | 143  |
| 3.45  | Sequence of events for the two story colonial-style house in the UL/NIJ experiments . . . . . | 144  |
| 3.46  | Test matrix for the USFS/Corsica Experiments . . . . .  | 150  |
| 3.47  | Heat release rate profiles for the Vettori experiments . . . . .                              | 153  |
| 3.48  | Summary of important experimental parameters . . . . .  | 162  |
| 3.49  | Summary of important numerical parameters . . . . .   | 165  |
| 4.1   | Summary of uncertainty estimates . . . . .  | 177  |
| 6.1   | Summary of parameters for the flame height predictions . . . . .                              | 326  |
| 9.1   | Test parameters of the NIST_He_2009 experiments . . . . .                                     | 644  |
| 11.1  | Wall measurement positions for the NIST/NRC series . . . . .                                  | 698  |
| 11.2  | Ceiling surface measurement locations for the WTC series . . . . .                            | 718  |
| 11.3  | Property of Insulation Materials . . . . .  | 732  |
| 12.1  | Summary of the NRL/HAI Wall Heat Flux Measurements . . . . .                                  | 860  |
| 12.2  | Heat flux gauge positions relative to the center of the fire pan in the WTC series . . . . .  | 876  |
| 12.3  | Parameters of the Hamins methane burner experiments . . . . .                                 | 888  |
| 12.4  | Parameters of the Hamins propane burner experiments . . . . .                                 | 897  |
| 12.5  | Parameters of the Hamins acetylene burner experiments . . . . .                               | 907  |
| 12.6  | Radiometer positions, Loughborough Jet Fires . . . . .  | 915  |
| 13.1  | Summary of NIST/NRC OLIVE-Fire Experiments . . . . .  | 982  |
| 13.2  | USCG/HAI water mist suppression extinguishment times . . . . .                                | 989  |
| 14.1  | FAA non-charring polymer properties . . . . .   | 1003 |
| 14.2  | FAA complex non-charring polymer properties . . . . .   | 1005 |
| 14.3  | Properties of polycarbonate (PC) . . . . .  | 1007 |
| 14.4  | Properties of poly(vinyl chloride) (PVC) . . . . .  | 1009 |
| 14.5  | Properties of poly(aryl ether ether ketone) (PEEK) . . . . .                                  | 1012 |
| 14.6  | Properties of poly(butylene terephthalate) (PBT) . . . . .                                    | 1014 |
| 14.7  | Properties of poly(butylene terephthalate) with glass fibers (PBT-GF) . . . . .               | 1016 |
| 14.8  | NIST PMMA properties . . . . .  | 1018 |
| 14.9  | Properties of ABS, HIPS, and PMMA . . . . .   | 1020 |
| 14.10 | Properties of Kydex . . . . .   | 1023 |
| 14.11 | Properties of PEI, PET, and POM . . . . .   | 1025 |
| 14.12 | Properties of corrugated cardboard . . . . .  | 1028 |
| 14.13 | Cardboard composition and dimensions . . . . .  | 1030 |
| 14.14 | Properties of spruce and pine . . . . .   | 1033 |
| 14.15 | Summary of DoJ/HAI Diked Fire Tests . . . . .   | 1046 |
| 14.16 | Properties of Aalto Woods . . . . .   | 1061 |
| 14.17 | Properties of FAA Polymers . . . . .  | 1062 |
| 14.18 | Properties of FPL Materials . . . . .   | 1066 |

|       |  |      |
|-------|--|------|
| 14.19 | Properties of FSRI Materials, other materials . . . . .      | 1068 |
| 14.20 | Properties of FSRI Materials, polymer materials . . . . .    | 1073 |
| 14.21 | Properties of FSRI Materials, Wood-Based materials . . . . . | 1078 |
| 14.22 | Properties of JH Materials . . . . .                         | 1082 |
| 14.23 | Properties of RISE Materials, mixture materials . . . . .    | 1085 |
| 14.24 | Properties of RISE Materials, mixture materials . . . . .    | 1086 |
| 14.25 | Properties of RISE Materials, other materials . . . . .      | 1092 |
| 14.26 | Properties of RISE Materials, polymer materials . . . . .    | 1094 |
| 14.27 | Properties of RISE Materials, Wood-Based materials . . . . . | 1097 |
| 16.1  | Summary statistics . . . . .                                 | 1179 |
| 16.2  | Validation Git Statistics . . . . .                          | 1186 |

# List of Acronyms

|           |  |
|-----------|--|
| ALOFT     | A Large Outdoor Fire plume Trajectory model                            |
| AST       | Adiabatic Surface Temperature  |
| ASTM      | American Society for Testing and Materials                             |
| ATF       | Bureau of Alcohol, Tobacco, Firearms, and Explosives                   |
| BRE       | British Research Establishment   |
| CAROLFIRE | Cable Response to Live Fire Test Program                               |
| CFAST     | Consolidated Model of Fire Growth and Smoke Transport                  |
| CFT       | Critical Flame Temperature   |
| DNS       | Direct Numerical Simulation  |
| FAA       | Federal Aviation Administration  |
| FDS       | Fire Dynamics Simulator  |
| FLAME     | Fire Laboratory for Accreditation of Models by Experimentation         |
| FM        | Factory Mutual Global  |
| FSE       | Full-Scale Enclosure   |
| HAI       | Hughes Associates, Inc.  |
| HDPE      | high density polyethylene  |
| HGL       | Hot Gas Layer  |
| HIPS      | high-impact polystyrene  |
| HRR       | Heat Release Rate  |
| ISO       | International Standards Organization                                   |
| LEMTA     | Laboratoire d'Energétique et de Méchanique Théorique et Appliquée      |
| LES       | Large Eddy Simulation  |
| LLNL      | Lawrence Livermore National Laboratory                                 |
| LNG       | Liquified Natural Gas  |
| MEC       | Minimum Extinguishing Concentration                                    |
| NBS       | National Bureau of Standards (former name of NIST)                     |
| NFPRF     | National Fire Protection Research Foundation                           |
| NIST      | National Institute of Standards and Technology                         |
| NRC       | Nuclear Regulatory Commission  |
| NRCC      | National Research Council of Canada                                    |
| NRL       | Naval Research Laboratory  |
| PDPA      | Phase Doppler Particle Analyzer  |
| PIV       | Particle Image Velocimetry   |
| PMMA      | poly(methyl methacrylate)  |
| PRISME    | Propagation d'un incendie pour des scénarios multi-locaux élémentaires |
| PVC       | Polyvinyl chloride   |
| RANS      | Reynolds Averaged Navier-Stokes  |

|       |   |
|-------|---|
| RSE   | Reduced-Scale Enclosure   |
| SBI   | Single Burning Item   |
| SNL   | Sandia National Laboratory  |
| SP    | Statens Provningsanstalt (Technical Research Institute of Sweden)         |
| TGA   | Thermal Gravimetric Analysis  |
| THIEF | Thermally-Induced Electrical Failure                                      |
| UL    | Underwriters Laboratories   |
| USN   | United States Navy  |
| VTFRL | Virginia Tech Fire Research Laboratory                                    |
| VTT   | Valtion Teknillinen Tutkimuskeskus (Technical Research Centre of Finland) |
| WTC   | World Trade Center  |

# Chapter 1

## What is Model Validation?

Although there are various definitions of model validation, for example the one contained in ASTM E 1355 [2], most define it as the process of determining how well the mathematical model predicts the actual physical phenomena of interest. Validation typically involves (1) comparing model predictions with experimental measurements, (2) quantifying the differences in light of uncertainties in both the measurements and the model inputs, and (3) deciding if the model is appropriate for the given application. This guide only does (1) and (2). Number (3) is the responsibility of the end user. To say that FDS is “validated” means that the end user has quantified the model uncertainty for a given application and decided that the model is appropriate. Although the FDS developers spend a considerable amount of time comparing model predictions with experimental measurements, it is ultimately the end user who decides if the model is adequate for the job at hand.

This Guide is merely a collection of calculation results. As FDS develops, it will expand to include new experimental measurements of newly modeled physical phenomena. With each minor release of FDS (version 5.2 to 5.3, for example), the plots and graphs are all regenerated to ensure that changes to the model have not decreased the accuracy of a previous version.

The following sections discuss key issues that must be considered when deciding whether or not FDS is appropriate for a given application. It depends on (a) the scenarios of interest, (b) the predicted quantities, and (c) the desired level of accuracy. FDS can be used to model most any fire scenario and predict almost any quantity of interest, but the prediction may not be accurate because of limitations in the description of the fire physics, and also because of limited information about the fuels, geometry, and so on.

### 1.1 Blind, Specified, and Open Validation Experiments

ASTM E 1355 [2] describes three basic types of validation calculations – *Blind*, *Specified*, and *Open*.

**Blind Calculation:** The model user is provided with a basic description of the scenario to be modeled.

For this application, the problem description is not exact; the model user is responsible for developing appropriate model inputs from the problem description, including additional details of the geometry, material properties, and fire description, as appropriate. Additional details necessary to simulate the scenario with a specific model are left to the judgment of the model user. In addition to illustrating the comparability of models in actual end-use conditions, this will test the ability of those who use the model to develop appropriate input data for the models.

**Specified Calculation:** The model user is provided with a complete detailed description of model inputs, including geometry, material properties, and fire description. As a follow-on to the blind calculation, this

test provides a more careful comparison of the underlying physics in the models with a more completely specified scenario.

**Open Calculation:** The model user is provided with the most complete information about the scenario, including geometry, material properties, fire description, and the results of experimental tests or benchmark model runs which were used in the evaluation of the blind or specified calculations of the scenario. Deficiencies in available input (used for the blind calculation) should become most apparent with comparison of the open and blind calculation.

The calculations presented in this Guide all fall into the *Open* category. There are several reasons for this, the first being the most practical:

- All of the calculations presented in this Guide are re-run with each minor release of FDS (i.e., 5.3 to 5.4). The fact that the experiments have already been performed and the results are known qualify these calculations as *Open*.
- Some of the calculations described in this Guide did originally fall into the *Specified* category because they were first performed before the experiments were conducted. However, in almost every case, the experiment was not conducted exactly as specified, and the pre-calculated results were not particularly useful in determining the accuracy of the model.
- None of the calculations were truly *Blind*, even those performed prior to the experiments. The purpose of a *Blind* calculation is to assess the degree to which the choice of input parameters affects the outcome. However, in such cases it is impossible to discern the uncertainty associated from the choice of input parameters from that associated with the model itself. The primary purpose of this Guide is to quantify the uncertainty of the model itself, in which case *Blind* calculations are of little value.

## 1.2 How to Use this Guide

When considering whether to use FDS for a given application, do the following:

1. Survey Chapter 2 to learn about past efforts by others to validate the model for similar applications. Keep in mind that most of the referenced validation exercises have been performed with older versions of FDS, and you may want to obtain the experimental data and the old FDS input files and redo the simulations with the version of FDS that you plan to use.
2. Identify in Chapter 3 the experimental data sets appropriate for your application. In particular, the summary of the experiments found in Sec. 3.107 contains a table listing various non-dimensional quantities that characterize the parameters of the experiments. For example, the equivalence ratio of a compartment fire experiment indicates the degree to which the fire was over or under-ventilated. To say that the results of a given experiment are relevant to your scenario, you need to demonstrate that its parameters “fit” within the parameter space outlined in Table 3.48.
3. Search the Table of Contents to find comparisons of FDS simulations with the relevant experiments. For a given experiment, there may be numerous measurements of quantities like the gas temperature, heat flux, and so on. It is a challenge to sort out all the plots and graphs of all the different quantities and come to some general conclusion. For this reason, this Guide is organized by output quantity, not by individual experiment or fire scenario. In this way, it is possible to assess, over a range of different experiments and scenarios, the performance of the model in predicting a given quantity. Overall trends and biases become much more clear when the data is organized this way.

4. Determine the accuracy of the model for given output quantities of interest listed in Table 16.1. An explanation of the accuracy metrics is given in Chapter 4.

The experimental data sets and FDS input/output files described in this Guide are all managed via the [project repository](#). You might want to re-run examples of interest to better understand how the calculations were designed, and how changes in the various parameters might affect the results. This is known as a *sensitivity study*, and it is difficult to document all the parameter variations of the calculations described in this report. Thus, it is a good idea to determine which of the input parameters are particularly important.

## Chapter 2

# Survey of Past Validation Work

In this chapter, a survey of FDS validation work is presented. Some of the work has been performed at NIST, some by its grantees and some by engineering firms using the model. Because each organization has its own reasons for validating the model, the referenced papers and reports do not follow any particular guidelines. Some of the works only provide a qualitative assessment of the model, concluding that the model agreement with a particular experiment is “good” or “reasonable.” Sometimes, the conclusion is that the model works well in certain cases, not as well in others. These studies are included in the survey because the references are useful to other model users who may have a similar application and are interested in even qualitative assessment. It is important to note that some of the papers point out flaws in early releases of FDS that have been corrected or improved in more recent releases. Some of the issues raised, however, are still subjects of active research. The research agenda for FDS is greatly influenced by the feedback provided by users, often through publication of validation efforts.

It is useful to divide the various validation exercises described in this chapter into two classes – those for which the heat release rate (HRR) of the fire is *specified* as an input to the model and those for which the HRR is *predicted* by the model. The former is often the case for a design application, the latter for a forensic reconstruction.

Design applications typically involve an existing building or a building under design. A so-called “design fire” is specified either by a regulatory authority or by the engineers performing the analysis. Because the fire’s heat release rate is specified, the role of the model is to predict the transport of heat and combustion products throughout the room or rooms of interest. Ventilation equipment is often included in the simulation, like fans, blowers, exhaust hoods, HVAC ducts, smoke management systems, etc. Sprinkler and heat and smoke detector activation are also of interest. The effect of the sprinkler spray on the fire is usually less of interest since the heat release rate of the fire is specified rather than predicted. Detailed descriptions of the contents of the building are usually not necessary because these items are assumed to not contribute to the fire, and even if they are, the burning rate will be specified, not predicted. Sometimes, it is necessary to predict the heat flux from the fire to a nearby “target,” and even though the target may heat up to some specified ignition temperature, the subsequent spread of the fire usually goes beyond the scope of the analysis because of the uncertainty inherent in object to object fire spread.

Forensic reconstructions require the model to simulate an actual fire based on information that is collected after the event, such as eye witness accounts, unburned materials, burn signatures, etc. The purpose of the simulation is to connect a sequence of discrete observations with a continuous description of the fire dynamics. Usually, reconstructions involve more gas/solid phase interaction because virtually all objects in a given room are potentially ignitable, especially when flashover occurs. Thus, there is much more emphasis on such phenomena as heat transfer to surfaces, pyrolysis, flame spread, and suppression. In general, forensic reconstructions are more challenging simulations to perform because they require more detailed

information about the room contents, and there is much greater uncertainty in the total heat release rate as the fire spreads from object to object.

Validation studies of FDS to date have focused more on design applications than reconstructions. The reason is that design applications usually involve specified fires and demand a minimum of thermo-physical properties of real materials. Transport of smoke and heat is the primary focus, and measurements can be limited to well-placed thermocouples, a few heat flux gauges, gas samplers, etc. Phenomena of importance in forensic reconstructions, like second item ignition, flame spread, vitiation effects and extinction, are more difficult to model and more difficult to study with well-controlled experiments. Uncertainties in material properties and measurements, as well as simplifying assumptions in the model, often force the comparison between model and measurement to be qualitative at best. Nevertheless, current validation efforts are moving in the direction of these more difficult issues.

## 2.1 Validation Work with Pre-Release Versions of FDS

FDS was officially released in 2000. However, for two decades various CFD codes using the basic FDS hydrodynamic framework were developed at NIST for different applications and for research. In the mid 1990s, many of these different codes were consolidated into what eventually became FDS. Before FDS, the various models were referred to as LES, NIST-LES, LES3D, IFS (Industrial Fire Simulator), and ALOFT (A Large Outdoor Fire Plume Trajectory).

The NIST LES model describes the transport of smoke and hot gases during a fire in an enclosure using the Boussinesq approximation, where it is assumed that the density and temperature variations in the flow are relatively small [3, 4, 5, 6]. Such an approximation can be applied to a fire plume away from the fire itself. Much of the early work with this form of the model was devoted to the formulation of the low Mach number form of the Navier-Stokes equations and the development of the basic numerical algorithm. Early validation efforts compared the model with salt water experiments [7, 8, 9], and fire plumes [10, 11, 12, 13]. Clement validated the hydrodynamic model in FDS by measuring salt water flows using Laser Induced dye Fluorescence (LIF) [14]. An interesting finding of this work was that the transition from a laminar to a turbulent plume is very difficult to predict with any technique other than DNS.

Eventually, the Boussinesq approximation was dropped and simulations began to include more fire-specific phenomena. Simulations of enclosure fires were compared to experiments performed by Steckler [15]. Mell et al. [16] studied small helium plumes, with particular attention to the relative roles of baroclinic torque and buoyancy as sources of vorticity. Cleary et al. [17] used the LES model to simulate the environment seen by multi-sensor fire detectors and performed some simple validation work to check the model before using it. Large fire experiments were performed by NIST at the FRI test facility in Japan, and at US Naval aircraft hangars in Hawaii and Iceland [18]. Room airflow applications were considered by Emmerich and McGrattan [19, 20].

These early validation efforts were encouraging, but highlighted the need to improve the hydrodynamic model by introducing the Smagorinsky form of large eddy simulation. This addition improved the stability of the model because of the relatively simple relation between the local strain rate and the turbulent viscosity. There is both a physical and numerical benefit to the Smagorinsky model. Physically, the viscous term used in the model has the right functional form to describe sub-grid mixing processes. Numerically, local oscillations in the computed flow quantities are damped if they become large enough to threaten the stability of the entire calculation.

## 2.2 Validation of FDS since 2000

There is an on-going effort at NIST and elsewhere to evaluate FDS as new capabilities are added. To date, most of this work has focused on the model's ability to predict the transport of heat and exhaust products from a fire through an enclosure. In these studies, the heat release rate is usually prescribed, along with the production rates of various products of combustion. More recently, validation efforts have moved beyond just transport issues to consider fire growth, flame spread, suppression, sprinkler/detector activation, and other fire-specific phenomena.

The validation work discussed below can be organized into several categories: Comparisons with full-scale tests conducted especially for the chosen evaluation, comparisons with previously published full-scale test data, comparisons with standard tests, comparisons with documented fire experience, and comparisons with engineering correlations. There is no single method by which the predictions and measurements are compared. Formal, rigorous validation exercises are time-consuming and expensive. Most validation exercises are done simply to assess if the model can be used for a very specific purpose. While not comprehensive on their own, these studies collectively constitute a valuable assessment of the model.

### 2.2.1 Fire Plumes

There are several examples of fire flows that have been extensively studied, so much so that a set of engineering correlations combining the results of many experiments have been developed. These correlations are useful to modelers because of their simplicity. The most studied phenomena include fire plumes, ceiling jets, and flame heights.

Although much of the early validation work before FDS was released involved fire plumes, it remains an active area of interest. One study by Chow and Yin [21] surveys the performance of various models in predicting plume temperatures and entrainment for a 470 kW fire with a diameter of 1 m and an unbounded ceiling. They compare the FDS results with various correlations and a RANS (Reynolds-Averaged Navier-Stokes) model.

Battaglia et al. [22] used FDS to simulate fire whirls. First, the model was shown to reproduce the McCaffrey correlation of a fire plume, then it was shown to reproduce qualitatively certain features of fire whirls. At the time, FDS used Lagrangian elements to introduce heat from the fire (no longer used), and this combustion model could not replicate the extreme stretching of the core of the flame zone.

Quintiere and Ma [23, 24] compared predicted flame heights and plume centerline temperatures to empirical correlations. For plume temperature, the Heskestad correlation [25] was chosen. Favorable agreement was found in the plume region, but the results near the flame region were found to be grid-dependent, especially for low  $Q^*$  fires. At this same time, researchers at NIST were reaching similar conclusions, and it was noticed by both teams that a critical parameter for the model is  $D^*/\delta x$ , where  $D^*$  is the characteristic fire diameter and  $\delta x$  is the grid cell size. If this parameter is sufficiently large, the fire can be considered well-resolved and agreement with various flame height correlations was found. If the parameter is not large enough, the fire is not well-resolved and adjustments must be made to the combustion routine to account for it.

Gutiérrez-Montes et al. [26] simulated 1.3 MW and 2.3 MW fires in a 20 m cubic atrium using FDS version 4. Similar experiments were conducted at VTT, Finland, in a 19 m tall test hall with similar sized fires. These results are included in Sec. 6.1.11.

Hurley and Munguia [27, 28] compared FDS (version 4) simulations with plume and ceiling jet measurements from a series of full-scale tests conducted by Underwriters Laboratories. The tests were conducted in a 36.6 m by 36.6 m compartment with ceiling heights ranging from 3 m to 12.2 m. Heat release rates followed a modified t-squared growth profile. Thermocouples attached to brass disks were used to simulate thermal detectors.

## 2.2.2 Pool Fires

Xin et al. [29] used FDS to model a 1 m diameter methane pool fire. The computational domain was 2 m by 2 m by 4 m with a uniform grid size of 2.5 cm. The predicted results were compared to experimental data and found to qualitatively and quantitatively reproduce the velocity field. The same authors performed a similar study of a 7.1 cm methane burner [30] and a helium plume [31].

The 7.1 cm diameter buoyant diffusion flame has been extensively studied both experimentally and computationally. Zhou and Gore [32] reported radial profiles of mixture fraction and vertical velocity for estimation of thermal expansion for natural gas buoyant diffusion flames stabilized on a 7.1 cm diameter diffuser burner. Xin et al. [33] used a Lagrangian thermal element based combustion model to simulate this flame. The authors noted that the simulations were sensitive to the burnout time utilized by the combustion model. To gain further insight into the species distribution inside the fire, Xin et al. [30] performed fire dynamics simulations using a mixture fraction based combustion model. Xin and Gore [34] used laser-induced incandescence to determine soot distributions in vertical and horizontal planes for methane and ethane turbulent buoyant flames. Biswas et al. [35] utilized a novel time series model to simulate the scalar concentrations and temperature fields for these flames.

Hostikka et al. [36] modeled small pool fires of methane, natural gas and methanol to test the FDS radiation solver for low-sooting fires. They conclude that the predicted radiative fluxes are higher than measured values, especially at small heat release rates, due to an over-prediction of the gas temperature. These tests are also included in the Heat Flux section of this report.

Hietaniemi, Hostikka and Vaari [37] considered heptane pool fires of various diameters. Predictions of the burning rate as a function of diameter follow the trend observed in a number of experimental studies. Their results show an improvement in the model over the earlier work with methanol fires, due to improvements in the radiation routine and the fact that heptane is more sooty than methanol, simplifying the treatment of radiation. The authors point out that reliable predictions of the burning rate of liquid fuels require roughly twice as fine a grid spanning the burner than would be necessary to predict plume velocities and temperatures. The reason for this is the prediction of the heat feedback to the burning surface necessary to *predict* rather than to *specify* the burning rate.

## 2.2.3 Air and Gas Movement in the Absence of Fire

The low Mach number assumption in FDS is appropriate not only to fire, but to most building ventilation scenarios. An example of how the model can be used to assess indoor air quality is presented by Musser et al. [38]. The test compartment was a displacement ventilation test room that contained computers, furniture, and lighting fixtures as well as heated rectangular boxes intended to represent occupants. A detailed description of the test configuration is given by Yuan et al. [39]. The room is ventilated with cool supply air introduced via a diffuser that is mounted on a side wall near the floor. The air rises as it is warmed by heat sources and exits through a return duct located in the upper portion of the room. The flow pattern is intended to remove contaminants by sweeping them upward at the source and removing them from the room. Sulphur hexafluoride, SF<sub>6</sub>, was introduced into the compartment during the experiment as a tracer gas near the breathing zone of the occupants. Temperature, tracer concentration, and velocity were measured during the experiments.

In another study, Musser and Tan [40] used FDS to assess the design of ventilation systems for facilities in which train locomotives operate. Although there is only a limited amount of validation, the study is useful in demonstrating a practical use of FDS for a non-fire scenario.

Mniszewski [41] used FDS to model the release of flammable gases in simple enclosures and open areas. In this work, the gases were not ignited.

Kerber and Walton [42] provided a comparison between FDS version 1 and experiments on positive

pressure ventilation in a full-scale enclosure without a fire.

## 2.2.4 Wind Engineering

Most applications of FDS involve fires within buildings. However, it can be used to model thermal plumes in the open and wind impinging on the exterior of a building. Rehm, McGrattan, Baum and Simiu [43] used the LES solver to estimate surface pressures on simple rectangular blocks in a crosswind, and compared these estimates to experimental measurements. In a subsequent paper [44], they considered the qualitative effects of multiple buildings and trees on a wind field.

A different approach to wind was taken by Wang and Joulain [45]. They considered a small fire in a wind tunnel 0.4 m wide and 0.7 m tall with flow speeds of 0.5 m/s to 2.5 m/s. Much of the comparison with experiment is qualitative, including flame shape, lean, length. They also use the model to determine the predominant modes of heat transfer for different operating conditions. To assess the combustion, they implemented an “eddy break-up” combustion model [46] and compared it to the mixture fraction approach used by FDS. The two models performed better or worse, depending on the operating conditions. Some of the weaknesses of the mixture fraction model as implemented in FDS version 2 were addressed in subsequent versions.

Chang and Meroney [47] compared the results of FDS with the commercial CFD package FLUENT in simulating the transport of pollutants from steady point sources in an idealized urban environment. FLUENT employs a variety of RANS (Reynolds Averaged Navier-Stokes) closure methods, whereas FDS employs large eddy simulation (LES). The results of the numerical models were compared with wind tunnel measurements within a 1:50 scale physical model of an urban street “canyon.”

FDS has recently been applied to urban canopy modeling [48] and wind engineering. Le et al. [49] modeled flow over a backward facing step using DNS with a Reynolds number of 5,100. To verify the results, Jovic and Driver [50] supplemented the DNS simulation with an identically proportioned wind tunnel experiment. Together, the data sets from these two studies have provided the baseline for analysis of recent simulations of flow over a backward facing step that are documented in this guide.

Sarwar et al. [51] used FDS to compare SGS eddy viscosity models. The constant Smagorinsky model performed the best, although the dynamic Smagorinsky and Deardorff models, nearly equivalent in accuracy, were found to perform better than the Vreman model. To avoid explicit specification of inlet turbulence conditions, the authors created an extremely long inlet section to allow turbulence to develop.

## 2.2.5 Atmospheric Dispersion

During the 1980s and 1990s, the Building and Fire Research Laboratory at NIST studied the burning of crude oil under the sponsorship of the US Minerals Management Service. The aim of the work was to assess the feasibility of using burning as a means to remove spilled oil from the sea surface. As part of the effort, Rehm and Baum developed a special application of the LES model called ALOFT. The model was a spin-off of the two-dimensional LES enclosure model, in which a three-dimensional steady-state plume was computed as a two-dimensional evolution of the lateral wind field generated by a large fire blown in a steady wind. The ALOFT model is based on large eddy simulation in that it attempts to resolve the relevant scales of a large, bent-over plume. Validation work was performed by simulating the plumes from several large experimental burns of crude oil in which aerial and ground sampling of smoke particulate was performed [52]. Yamada [53] performed a validation of the ALOFT model for 10 m oil tank fire. The results indicate that the prediction of the plume cross section 500 m from the fire agree well with the experimental observations.

Mouilleau and Champassith [54] performed a validation study to assess the ability of FDS (version 4) to model atmospheric dispersion. They concluded that the best results were obtained for simulations done with

explicitly-modeled wind fluctuations. Specific atmospheric flow characteristics were evaluated for passive releases in open and flat fields.

## 2.2.6 Growing Fires

Floyd [55, 56] compared FDS predictions with measurements from fire tests at the Heiss-Dampf Reaktor (HDR) facility in Germany. The structure was originally the containment building for a nuclear power reactor. The cylindrical structure was 20 m in diameter and 50 m in height topped by a hemispherical dome 10 m in radius. The building was divided into eight levels. The total volume of the building was approximately 11,000 m<sup>3</sup>. From 1984 to 1991, four fire test series were performed within the HDR facility. The T51 test series consisted of eleven propane gas tests and three wood crib tests.

FDS predictions of fire growth and smoke movement in large spaces were performed by Kashef [57]. The experiments were conducted at the National Research Council Canada. The tests were performed in a compartment with dimensions of 9 m by 6 m by 5.5 m with 32 exhaust inlets and a single supply fan. A burner generated fires ranging in size from 15 kW to 1000 kW.

## 2.2.7 Flame Spread

Although FDS simulations have been compared to actual and experimental large-scale fires, it is difficult to quantify the accuracy because of the uncertainty associated with material properties. Most quantified validation work associated with flame spread have been for small, laminar flames with length scales ranging from millimeters to a few centimeters.

For example, FDS (or its core algorithms) have been used at a grid resolution of roughly 1 mm to look at flames spreading over paper in a micro-gravity environment [58, 59, 60, 61, 62, 63], as well as “g-jitter” effects aboard spacecraft [64]. Simulations have been compared to experiments performed aboard the Space Shuttle. The flames are laminar and relatively simple in structure, and the materials are relatively well-characterized.

FDS flame spread predictions were compared to experiments over a 5 m slab of PMMA performed by Factory Mutual Research Corporation (FMRC) [23, 24].

A charring model was implemented in FDS by Hostikka and McGrattan [65]. The model was a simplification of work done at NIST by Ritchie et al. [66]. The charring model was first used to predict the burning rate of a small wooden sample in the cone calorimeter. Full-scale room tests with wood paneling were modeled, but the results were grid-dependent. This was likely a consequence of the gas phase spatial resolution, rather than the solid phase.

Kwon et al. [67] performed three simulations to evaluate the capability of FDS, version 4, in predicting upward flame spread. The FDS predictions were compared with empirical correlations and experimental data for upward flame spread on a 5 m PMMA panel. A simplified flame spread model was also applied to assess the simulation results.

An extensive amount of flame spread validation work with FDS version 4 has been performed by Hi- etaniemi, Hostikka, and Vaari at VTT, Finland [37]. The case studies are comprised of fire experiments ranging in scale from the cone calorimeter (ISO 5660-1, 2002) to full-scale fire tests such as the room corner test (ISO 9705, 1993). Comparisons are also made between FDS 4 results and data obtained in the SBI (Single Burning Item) Euro-classification test apparatus (EN 13823, 2002) as well as data obtained in two ad hoc experimental configurations: one is similar to the room corner test but has only partial linings and the other is a space to study fires in building cavities. In the study of upholstered furniture, the experimental configurations are the cone and furniture calorimeters, and the ISO room. For liquid pool fires, comparison is made to data obtained by numerous researchers. The burning materials include spruce timber, MDF (Medium Density Fiber) board, PVC wall carpet, upholstered furniture, cables with plastic sheathing, and

heptane. The scope of the VTT work is considerable. Assessing the accuracy of the model must be done on a case by case basis. In some cases, predictions of the burning rate of the material were based solely on its fundamental properties, as in the heptane pool fire simulations. In other cases, some properties of the material are unknown, as in the spruce timber simulations. Thus, some of the simulations are true predictions, some are calibrations. The intent of the authors was to provide guidance to engineers using the model as to appropriate grid sizes and material properties. In many cases, the numerical grid was made fairly coarse to account for the fact that in practice, FDS is used to model large spaces of which the fuel may only comprise a small fraction.

Mangs and Hostikka [68] carried out experiments and simulations (FDS 5.4.3) of the vertical flame spread on the surface of thin birch wood cylinders at different ambient temperatures. The parameters for the pyrolysis model were estimated from TGA and cone calorimeter experiments. The gas phase flow was calculated in the DNS mode with 1.0 mm grid cells in axi-symmetric geometry. The simulation model was able to predict the flame spread rates within the uncertainties associated with the experiments and postsimulation analysis of the spread rate.

Moinuddin et al. [69] conducted numerical simulations of coupled solid-phase reactions (pyrolysis) and gas-phase reaction (combustion). FDS was used for simulating the PMMA (non-charring), pine (charring), wool (charring) and cotton (charring) flaming fire experiments conducted with a cone calorimeter at 50 kW/m<sup>2</sup> and 30 kW/m<sup>2</sup>. The inputs of chemical kinetics and the heat of reaction were obtained from sample mass change and enthalpy data in TGA and differential scanning calorimetry (DSC) tests and the flammability parameters were obtained from cone calorimeter experiments.

## 2.2.8 Compartment Fires

As part of the NIST investigation of the World Trade Center fires and collapse, a series of large scale fire experiments were performed specifically to validate FDS [70]. The tests were performed in a rectangular compartment 7.2 m long by 3.6 m wide by 3.8 m tall. The fires were fueled by heptane for some tests and a heptane/toluene mixture for the others. The results of the experiments and simulations are included in detail in this Guide.

A second set of experiments to validate FDS for use in the World Trade Center investigation is documented in Ref. [71]. The experiments are not described as part of this Guide. The intent of these tests was to evaluate the ability of the model to simulate the growth of a fire burning three office workstations within a compartment of dimensions 11 m by 7 m by 4 m, open at one end to mimic the ventilation of windows similar to those in the WTC towers. Six tests were performed with various initial conditions exploring the effect of jet fuel spray and ceiling tiles covering the surface of the desks and carpet. Measurements were made of the heat release rate and compartment gas temperatures at four locations using vertical thermocouple arrays. Six different material samples were tested in the NIST cone calorimeter: desk, chair, paper, computer case, privacy panel, and carpet. Data for the carpet, desk and privacy panel were input directly into FDS, with the other three materials lumped together to form an idealized fuel type. Open burns of single workstations were used to calibrate the simplified fuel package. Details of the modeling are contained in Ref. [72].

Moinuddin et al. [73] conducted experiments to measure the temperature rise of protected and unprotected structural steel during a fire within a small enclosure (an ISO 9705 room). The fuel (wood crib) was placed at two locations (front and back) within the room. The temperature of six steel columns and two steel beams was measured. Predictions by FDS were compared with the measurements.

The BRE Centre for Fire Safety Engineering at the University of Edinburgh conducted a series of large-scale fire tests in a real high rise building in Dalmarnock, Glasgow, Scotland [74, 75]. The experiments took place in July, 2006, with the close collaboration of the Strathclyde Fire Brigade and other partners. These experiments attempted to create realistic scenario in which a wide range of modern fire safety engineering tools could be put to a test. Jahn, Rein and Torero assessed the sensitivity of FDS when applied to these

experiments [76]. Fire size and location, convection, radiation and combustion parameters were varied in order to determine the associated degree of sensitivity. Emphasis was put in the prediction of secondary ignition and time to flashover. In this context and while keeping the HRR constant, simulations of fire growth were significantly sensitive to location of the heat release rate, fire area, flame radiative fraction, and material thermal and ignition properties.

Students at Stord/Haugesund University College in Norway simulated full-scale experiments of temperature and smoke spread in a realistic multi-room setting using both CFAST and FDS [77]. Data from the top 0.5 m of the compartments was compared with measurements. The simulations were found to provide satisfying results in CFAST, as an alternative to FDS.

Drean et al. [78] measured the fire exposure to an exterior facade of a two-level test facility operated by the engineering firm Efectis in Saint-Aubin, France. The objective was to evaluate the ability of FDS, version 6, to predict the gas temperatures and heat fluxes at the exterior wall.

Chaudhari et al. [79] simulated controlled fire experiments using a gas burner conducted in a purpose-built, two-story, moderately air-tight residential structure. Temperatures, gas concentrations (oxygen, water vapor, carbon dioxide), and differential pressures were monitored throughout the structure. HVAC status and stairwell door openings to the fire room were varied for the experiments.

Moinuddin et al. [80] used FDS to simulate fires in a deep enclosure with a depth of 4 m, width of 2 m, and opening heights of 0.6 m, 0.8 m, and 1.0 m. The results were compared to various empirical methods.

## 2.2.9 Sprinklers, Mist System, and Suppression by Water

Vettori [81] modeled sprinkler activation patterns in a room with an obstructed ceiling. In a follow-up report, Vettori [82] extended his study to include sloped ceilings, with and without obstructions. Both of these experimental series are included within the current validation guide and are referred to the Vettori Flat and Sloped Ceiling Experiments.

A significant validation effort for sprinkler activation and suppression was a project entitled the International Fire Sprinkler, Smoke and Heat Vent, Draft Curtain Fire Test Project organized by the National Fire Protection Research Foundation [83]. Thirty-nine large scale fire tests were conducted at Underwriters Laboratories in Northbrook, IL. The tests were aimed at evaluating the performance of various fire protection systems in large buildings with flat ceilings, like warehouses and “big box” retail stores. All the tests were conducted under a 30 m by 30 m adjustable-height platform in a 37 m by 37 m by 15 m high test bay. At the time, FDS had not been publicly released and was referred to as the Industrial Fire Simulator (IFS), but it was essentially the same as FDS version 1. The first and second series of heptane spray burner fires are included in this guide under the heading “UL/NFPRF Sprinkler, Vent, and Draft Curtain Study.” Most of the full-scale experiments performed during the project used a heptane spray burner to generate controlled fires of 1 MW to 10 MW. However, five experiments were performed with 6 m high racks containing the Factory Mutual Standard Plastic Commodity, or Group A Plastic. To model these fires, bench scale experiments were performed to characterize the burning behavior of the commodity, and larger test fires provided validation data with which to test the model predictions of the burning rate and flame spread behavior [84, 85]. Two to four tier configurations were evaluated.

High rack storage fires of pool chemicals were modeled by Olenick et al. [86] to determine the validity of sprinkler activation predictions of FDS. The model was compared to full-scale fires conducted in January, 2000 at Southwest Research Institute in San Antonio, Texas.

FDS has been used to study the behavior of a fire undergoing suppression by a water mist system. Kim and Ryoo [87, 88] compared FDS predictions to results of compartment fire tests with and without the application of a water mist. The cooling and oxygen dilution were predicted to within about 10 % of the measurements, but the simulations failed to predict the complete extinguishment of a hexane pool fire. The authors suggest that this is a result of the combustion model rather than the spray or droplet model.

Another study of water mist suppression using FDS was conducted by Hume at the University of Canterbury, Christchurch, New Zealand [89]. Full-scale experiments were performed in which a fine water mist was combined with a displacement ventilation system to protect occupants and electrical equipment in the event of a fire. Simulations of these experiments with FDS showed qualitative agreement, but the version of the model used in the study (version 3) was not able to predict accurately the decrease in heat release rate of the fire.

Hostikka and McGrattan [90] evaluated the absorption of thermal radiation by water sprays. They considered two sets of experimental data and concluded that FDS has the ability to predict the attenuation of thermal radiation “when the hydrodynamic interaction between the droplets is weak.” However, modeling interacting sprays would require a more costly coalescence model. They also note that the results of the model were sensitive to grid size, angular discretization, and droplet sampling.

O’Grady and Novozhilov [91] compared the predictions of FDS version 4 against full-scale fire tests performed at SP Sweden involving a 1.5 MW steady-state fire with two different sprinkler flow rates [92]. The authors reported results for gas temperatures and the tangential flow velocity in the ceiling jet. Sensitivity of the model to a range of input parameters was investigated. The model demonstrated moderate sensitivity to the spray parameters, such as spray cone configuration, initial droplet velocities, and droplet sizes. On the other hand, the sensitivity to other parameters such as sprinkler atomization length and rms of droplet size distribution was low.

Xiao [93] compared FDS simulations with real scale compartment measurements for unsprinklered and sprinklered experiments. Numerical results for doorway mass flow rate and temperature are compared with the experimental data for three fire sizes.

Zhao and Zhang [94, 95] have simulated the effect of water sprays on vertical flame spread.

Mahmud et al. [96] conducted a study on the characterization of water mists, in terms of distribution of flux density of sprays, produced by a single and a multi-orifice high-pressure jet nozzle. Full-scale experiments were conducted and the distributions of volume flux density of sprays were measured. The sprays were also modeled using FDS to investigate the capability of the model in predicting the distribution behaviour of the spray.

### **2.2.10 Airflows in Fire Compartments**

Friday and Mowrer [97] studied the use of FDS in large scale mechanically ventilated spaces. The ventilated enclosure was provided with air injection rates of 1 to 12 air changes per hour and a fire with heat release rates ranging from 0.5 MW to 2 MW. The test measurements and model output were compared to assess the accuracy of FDS. These simulations have been repeated with the latest version of FDS and reported in this guide under the heading “FM/SNL Test Series.”

Zhang et al. [98] utilized the FDS model to predict turbulence characteristics of the flow and temperature fields due to fire in a compartment. The experimental data was acquired through tests that replicated a half-scale ISO Room Fire Test. Two cases were explored – the heat source in the center of the room and the heat source adjacent to a wall. In both cases, the heat source was a heating element with an output of 12 kW/m<sup>2</sup>.

### **2.2.11 Tunnel Fires**

Cochard [99] used FDS to study the ventilation within a tunnel. He compared the model results with a full-scale tunnel fire experiment conducted as part of the Massachusetts Highway Department Memorial Tunnel Fire Ventilation Test Program. The test consisted of a single point supply of fresh air through a 28 m<sup>2</sup> opening in a 135 m tunnel.

McGrattan and Hamins [100] also applied FDS to simulate two of the Memorial Tunnel Fire Tests as validation for the use of the model in studying an actual fire in the Howard Street Tunnel, Baltimore,

Maryland, July 2001. The experiments chosen for the comparison were unventilated. One experiment was a 20 MW fire; the other a 50 MW fire.

Piergoirgio et al. [101] provided a qualitative analysis of FDS applied to a truck fire within a tunnel. The goal of their analysis was to describe the spread of the toxic gases within the tunnels, to determine the places not involved in the spreading of combustion products and to quantify the oxygen, carbon monoxide and hydrochloric acid concentrations during the fire.

Edwards et al. [102, 103] used FDS to determine the critical air velocity for smoke reversal in a tunnel as a function of the fire intensity, and his results compared favorably with experimental results. In a further study, Edwards and Hwang [104] applied FDS to study fire spread along combustibles in a ventilated mine entry. Analyses such as these are intended for planning and implementation of ventilation changes during mine fire fighting and rescue operations.

Bilson et al. [105] used FDS to evaluate the interaction of a deluge system with a tunnel ventilation and smoke exhaust system.

Harris [106] used FDS to determine the heat flux from a tunnel fire under varying water application rates. These results were qualitatively consistent with experimental results of Arvidson [107], who conducted burn tests for shielded and unshielded standard plastic commodities under a variety of spray conditions.

Trelles and Mawhinney [108, 109] simulated with FDS 4 a series of full-scale fire suppression experiments conducted at the San Pedro de Anes test tunnel near Gijon, Asturias, Spain in February, 2006. The fuel consisted of wooden and polyethylene pallets, and the suppression system consisted of different configurations of water mist nozzles.

## 2.2.12 Smoke Detection

The ability of version 1 of FDS to accurately predict smoke detector activation was studied by D'Souza [110]. The smoke transport model within FDS was tested and compared with UL 217 test data. The second step in this research was to further validate the model with full-scale multi-compartment fire tests. The results indicated that FDS is capable of predicting smoke detector activation when used with smoke detector lag correlations that correct for the time delay associated with smoke having to penetrate the detector housing. A follow-up report by Roby et al. [111] and paper by Zhang et al. [112] describes the implementation and validation of the smoke detector algorithm currently incorporated in FDS.

Another study of smoke detector activation was carried out by Brammer at the University of Canterbury, New Zealand [113]. Two fire tests from a series performed in a two-story residence were simulated, and smoke detector activation times were predicted using three different methods. The methods consisted of either a temperature correlation, a time-lagged function of the optical density, or a thermal device much like a heat detector. The purpose was to identify ways to reliably predict smoke detector activation using typical model output like temperature and smoke concentration. It was remarked that simulating the early stage of the fire is critical to reliable prediction.

Cleary [114] also provided a comparison between FDS computed gas velocity, temperature and concentrations at various detector locations. The research concluded that multi-room fire simulations with the FDS model can accurately predict the conditions that a sensor might experience during a real fire event.

## 2.2.13 Combustion Model

A few studies have been performed comparing direct numerical simulations (DNS) of a simple burner flame to laboratory experiments [115]. Another study compared DNS calculations of a counterflow diffusion flames to experimental measurements and the results of a one-dimensional multi-step kinetics model [116].

Bundy, Dillon and Hamins [117, 118] studied the use of FDS in providing data and correlations for fire investigators to support their investigations. A paraffin wax candle was placed within a small plexi-glass

enclosure. The heat flux from the candle flame was modeled with FDS.

Floyd et al. [119, 56] compared the radiation model of FDS version 2 with full-scale data from the Virginia Tech Fire Research Laboratory (VTFRL). The test compartment was outfitted with equipment capable of taking temperature, air velocity, gas concentrations, unburned hydrocarbon and heat flux measurements. The test facility consisted of a single compartment geometrically similar to the ISO 9705 standard compartment with dimensions of 1.2 m by 1.8 m by 1.2 m in height. The ceiling and walls were constructed of fiberboard over a steel shell with a floor of concrete. Three baseline experiments were completed with fires ranging in size from 90 kW to 440 kW.

Xin and Gore [120] compared FDS predictions and measurements of the spectral radiation intensities of small fires. The fuel flow rates for methane and ethylene burners were selected so that the Froude numbers matched that of liquid toluene pool fires. The heat release rate was 4.2 kW for the methane flame and 3.4 kW for the ethylene flame. Line of sight spectral radiation intensities were measured at six downstream locations. The spectral radiation intensity calculations were performed by post-processing the transient scalar distributions provided by FDS.

Zhang et al. [121] compared the experimental results of a circular methane gas burner to predictions computed by FDS. The compartment was 2.8 m by 2.8 m by 2.2 m high with natural ventilation from a standard door.

## 2.2.14 Soot Deposition

Several studies have been conducted that indicate soot deposition is an important factor in compartment fires for the accurate prediction of smoke concentrations, smoke detector activations, and visibility. Gottuk et al. [122] reported that smoke concentrations predicted by FDS near smoke alarms in a corridor were two to five times greater than measured smoke concentrations. Hamins et al. [123] conducted full-scale compartment fire experiments for use in validation studies of various fire models, including FDS. The results indicated that smoke concentrations predicted by FDS were up to five times greater than measured smoke concentrations. Floyd and McDermott [124] implemented thermophoretic and turbulent diffusion soot deposition mechanisms in FDS and compared predicted soot densities and concentrations to measurements from small- and large-scale experiments. Riahi [125] conducted bench-scale experiments to measure soot densities and soot deposition patterns on walls for various fuels. Riahi identified thermophoretic deposition as an important soot deposition mechanism in the hot gas layer. Cohan [126] used FDS to simulate select cases from the Gottuk [122] corridor tests, Hamins et al. [123] NRC experiments, and Riahi [125] hood experiments with thermophoretic and turbulent diffusion soot deposition mechanisms. Overholt and Ezekoye [127] implemented gravitational settling of soot in the gas-phase in FDS and quantified the effects of gravitational settling/deposition compared to thermophoretic and turbulent diffusion deposition for small- and large-scale validation cases.

## 2.2.15 Wildfires

Work began in the early 2000's to adapt FDS to wildland fire spread. Mell et al. [128, 129] simulated fire spread over grassland and the burning of Douglas fir trees. Perez-Ramirez et al. [130] simulated small-scale fire spread experiments under a laboratory calorimeter. All of these studies used a variant of FDS referred to as Wildland-FDS or WFDS. Since that time, these studies have been redone and the results are included in this guide under the headings "CSIRO Grassland Fires," "NIST Douglas Firs," and "USFS Corsica."

Wadhwani et al. [131, 132] conducted experiments using a device that produces controlled and repeatable sets of firebrands, and validated FDS for firebrand transport against this set of experiments.

## 2.3 Reconstructions of Actual Fires

ASTM E 1355 states that a model may be evaluated by comparing it with “Documented Fire Experience” which includes:

- eyewitness accounts of real fires,
- known behavior of materials in fires (for example, melting temperatures of materials), and
- observed post-fire conditions, such as the extent of fire spread.

Often the term “reconstruction” is applied to this type of simulation, because the model is used to reconstruct events based on evidence collected during and after the fire. Some of the more notable studies performed at NIST include:

- McGrattan, Bouldin, and Forney simulated the fires within the World Trade Center towers and Building 7 on September 11, 2001 [72].
- Grosshandler et al. investigated the fire that occurred at the Station Nightclub in Rhode Island in February, 2003 [133].
- Madrzykowski and Vettori examined a fire in a townhouse in Washington, D.C., where two fire fighters were killed and one severely injured in 1999 [134].
- Vettori, Madrzykowski, and Walton simulated a fire in a Houston restaurant that killed two fire fighters in 2000 [135].
- Madrzykowski, Forney and Walton simulated a fire that killed three children and three fire fighters in a two story duplex house in Iowa in 1999 [136].
- Madrzykowski and Walton investigated the fire in the Cook County (Chicago) Administration Building in October, 2003, that killed six people trapped in a stairwell [137].
- Bryner et al. simulated a fire in a large furniture store that occurred in June, 2007, killing nine fire fighters [138].

Outside of NIST, FDS has been used to investigate many actual fires, but very few of these studies are documented in the literature. Exceptions include:

- A large fire in a “cash & carry” warehouse in the UK was studied by Camp and Townsend using both hand calculations and FDS (version 1) [139].
- A study by Rein et al. [140] looked at several fire events using an analytical fire growth model, the NIST zone model CFAST, and FDS.
- A similar study was performed several years earlier by Spearpoint et al. [141] as a class exercise at the University of Maryland.
- During the SFPE Professional Development Week in the fall of 2001, a workshop was held in which several engineers related their experiences using FDS as a forensic tool [142].
- The role of carbon monoxide in the deaths of three fire fighters was studied by Christensen and Icove [143].

Icove and May [144] discuss the benefits of computer fire models in forensic fire investigations, historical and pending legal case law, and methods to use modeling results within expert reports and testimony. Particular issues reviewed are the use of animations versus simulations, evidentiary guidelines, and authentication using verification and validation studies.

## Chapter 3

# Description of Experiments

This chapter contains a brief description of the experiments that were used for model validation. Only enough detail is included here to provide a general understanding of the model simulations. Anyone wishing to use the experimental measurements for validation ought to consult the cited test reports or other publications for a comprehensive description.

### 3.1 Aalto Woods Experiments

Rinta-Paavola et al. developed a material model for Norway spruce and Scots pine woods to predict char front progress and heat release in burning timber [145]. The material models are calibrated using temperature, mass loss rate and heat release rate measurements of wood specimens in a cone calorimeter. The model is intended for a number of different fire scenarios, such as fully developed fire with only little oxygen in the compartment, or the decay period after flaming with exposed char still smoldering. Cone calorimeter measurements were conducted under flaming, inert, and smoldering conditions to replicate these scenarios. The estimated material models are able to predict the experiments in the scale of cone calorimeter.

The material model for spruce developed using cone calorimeter measurements is tested in prediction of heat release rates in two previously existing experiments: an ISO 9705 room corner test [146] (test code M12 in the original source) and a modified room corner test originally reported in Finnish in [147]. English description of the modified test is available in [37].

In a room corner test, the walls and the ceiling of a 2.4 m by 3.6 m by 2.4 m (width, length, height) test compartment are lined with the tested material. The 2.4 m wide front wall has a 0.8 m wide, 2.0 m high door opening in the middle, and the back corner adjacent to the wall opposite to the door has a gas burner with an output of 100 kW for the first ten minutes of the test. If flashover does not occur during this time, the burner heat release is increased to 300 kW for another ten minutes. The test is terminated after 20 minutes or when flashover occurs.

In the test M12 [146] the walls and the ceiling are lined with 10 mm thick spruce timber, whereas in the modified test [147] the walls and ceiling only in the proximity of the gas burner was lined with 22 mm thick spruce timber, elsewhere being exposed concrete. In both of the studied tests the flashover occurred within the first ten minutes, so the burner heat release was 100 kW over the entire duration of the test.

#### Modeling Notes

In the simulations of flaming cone calorimeter experiments, the computational domain is 20 cm in length and width and 30 cm in height, with a grid resolution of 1 cm. For the inert and smoldering experiments the domain is 30 cm by 30 cm by 30 cm with the resolution of 10 cm, as the gaseous phase was not directly

modelled. In the simulations of room corner tests, the computational domain continued for 1.5 m outside after the 20 cm thick front wall. In the corner where the burner was located, the grid resolution was 2 cm over a volume that extends for 0.5 m from the corner at x-, and y directions, and spans the entire height from floor to the ceiling. Elsewhere, a resolution of 10 cm was used.

Neither [146] nor [147] reported the initial moisture content of the timbers, so a moisture mass fraction of 0.09 similar to the cone calorimeter specimens in [145], was assumed in the beginning of room corner tests. This is a relevant moisture content for timber in normal room air.

The parameters in the original research of Rinta-Paavola et al. [145] were estimated for FDS 6.7.7, but in FDS 6.7.8 and later the reaction rate equation for solid pyrolysis is different, possibly requiring scaling of the pre-exponential factor when parameters are carried from a FDS version with the old reaction rate definition to a newer one. See [145] for greater detail. Table 14.14 presents appropriately scaled parameters that yield results consistent to the original simulations in [145] when initial moisture mass fraction is 0.09. If a different initial moisture content is used, re-scaling of the frequency factor would be necessary to gain most accurate possible agreement with the model presented in [145].

## 3.2 ArupFire Tunnel Fire Experiments

Gabriele Vigne and Jimmy Jönsson of ArupFire conducted a series of fire experiments within a tunnel with a 50 m<sup>2</sup> cross section. The tunnel is located in La Ribera del Folgoso, Spain. It is approximately 6.5 m high, 8 m wide and 300 m long. Five replicate tests were conducted using a 1 m by 2 m steel pan filled with heptane on water. Near-ceiling temperatures were measured 2 m, 4 m, 6 m and 8 m from the plume centerline. The peak heat release rate was approximately 5.3 MW.

## 3.3 ATF Corridors Experiments

A series of eighteen experiments were conducted in a two-story structure with long hallways and a connecting stairway in the large burn room of the ATF Fire Research Laboratory in Ammendale, Maryland, in 2008 [148]. The test enclosure consisted of two 17.0 m long hallways connected by a stairway consisting of two staircases and an intermediary landing. There was a door at the opposite end of the first floor hallway, which was closed during all tests. The end of the second floor hallway was open with a soffit near the ceiling.

The walls and ceilings of the test structure were constructed of 1.2 cm gypsum wallboard. The flooring throughout the structure, including the stairwell landing floor, consisted of one layer of 1.3 cm thick cement board on one layer of 1.9 cm thick plywood supported by wood joists. The first set of stairs, which had eight risers, led from the first floor up to the landing area. The second set of stairs, which had nine risers, led from the landing area up to the second floor. The stairs were constructed of 2.5 cm thick clear pine lumber. The two set of stairs were separated by an approximately 0.42 m wide gap in the middle of the stairwell. This gap was separated from the stairs by a 0.91 m tall barrier constructed of a single piece of gypsum board. The flue space was open to the first floor. The flue space was separated from the second floor by a 0.9 m tall barrier constructed of gypsum board. There was a metal exterior type door at the end of the first floor near the burner. The door was closed during all experiments.

The fire source was a natural gas diffusion burner. The burner surface was horizontal, square and 0.45 m on each side, its surface was 0.37 m above the floor, and it was filled with gravel. The burner was located near the end of the first floor away from the stairs. A diagram of the test structure is displayed in Figure 3.1.

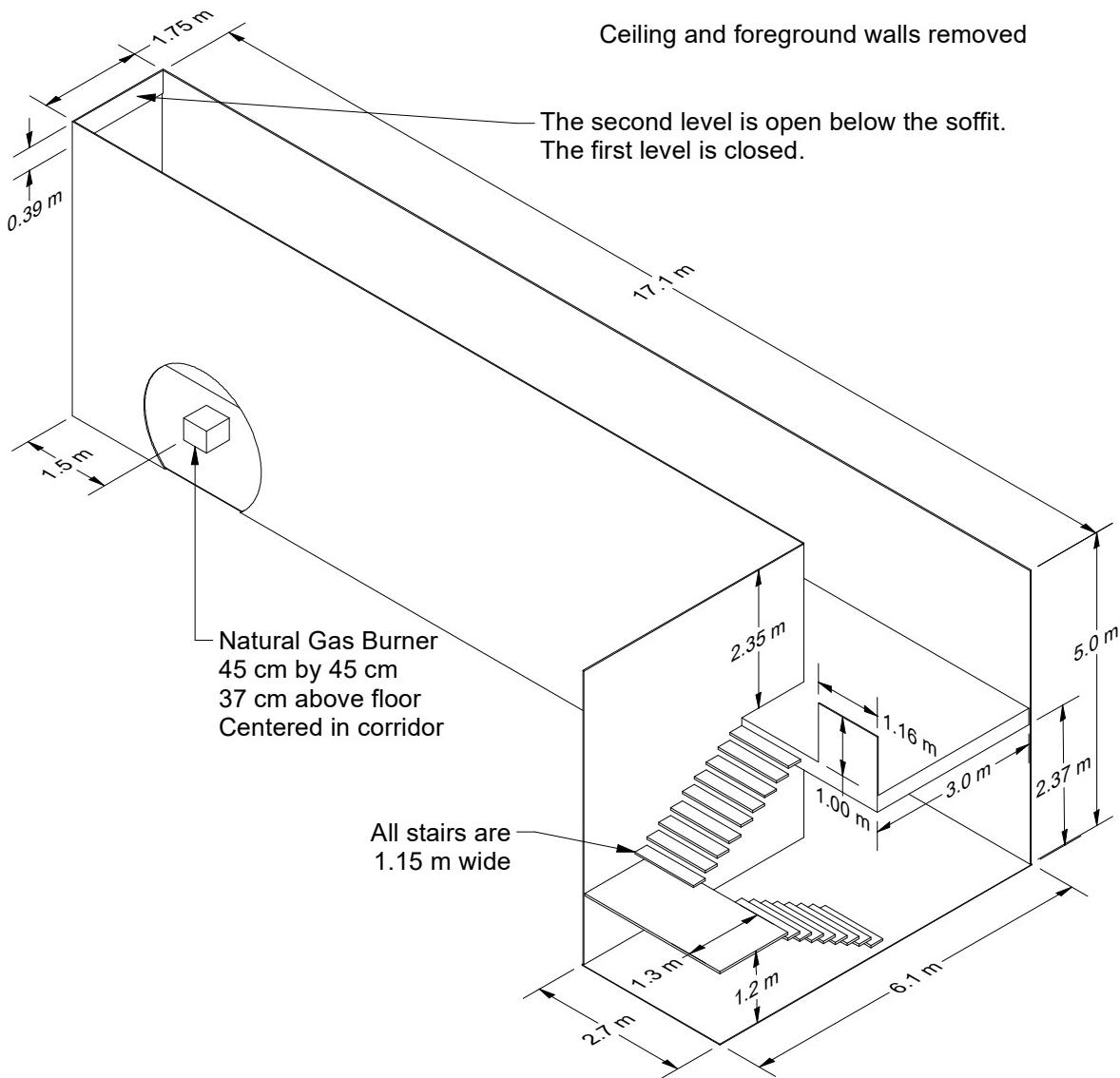


Figure 3.1: Geometry of the ATF Corridors Experiments.

### 3.4 Atmospheric Dispersion Correlations

A common exercise in atmospheric dispersion modeling is predicting the plume rise height of stack emissions. Stull [149] presents an empirical correlation for plume rise height from a smoke stack in a stable atmospheric boundary layer. Details of the correlation and simulation are found in Sec. 15.3.

### 3.5 Backward Facing Step

A common validation experiment for CFD codes involves flow through a channel with a backward facing step. These experiments are designed to test the influence of grid resolution, inlet turbulence, wall boundary treatments, and eddy viscosity models. One set of experiments has been conducted by Jovic and Driver [50]. A schematic view of the experiment is shown in Fig. 3.2. The dimensions of the channel are based on step height  $h = 0.0098$  m. The length of the channel is  $24h$ . The width of the channel is  $4h$ . The height of the inlet section is  $5h$ , and the height of the channel downstream of the step is  $6h$ . The expansion ratio is thus 1.2. The inlet is split into three sub-inlets to permit localized variation of inlet turbulence. The Reynolds number of the flow is 5100, based on the free-stream velocity (7.2 m/s) and the step height.

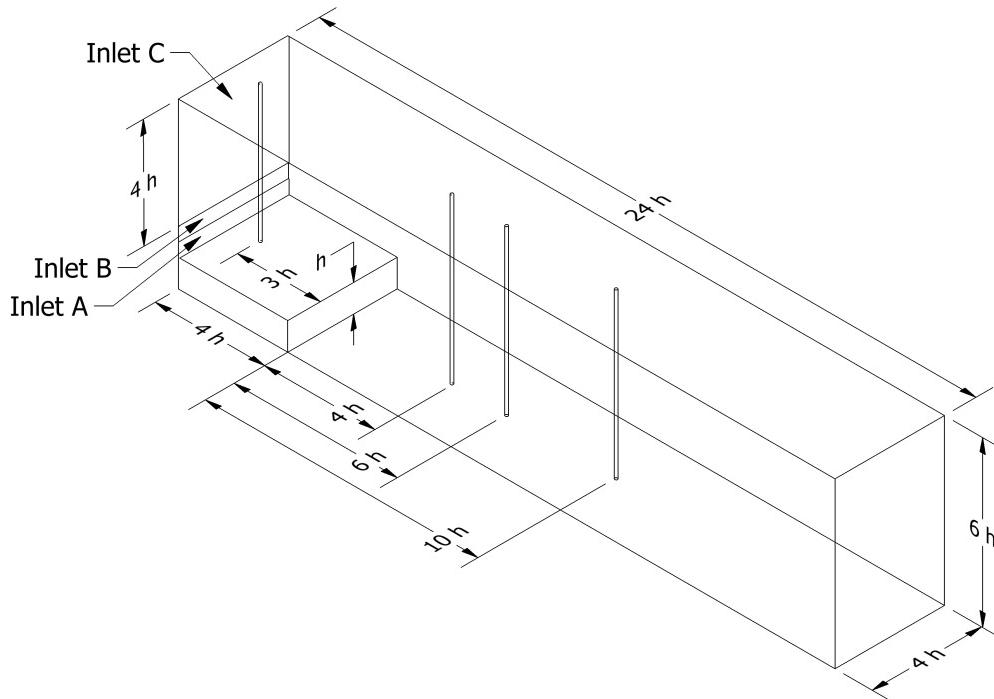


Figure 3.2: Geometry of the Backward Facing Step experiments.

### 3.6 Beyler Hood Experiments

Craig Beyler performed small-scale fire experiments where a variety of circular gas burners were centered at various heights underneath a closed, cylindrical hood, 100 cm in diameter and 48 cm in height [150]. The hood consisted of two concentric cylinders separated by an air gap, as shown in Fig. 3.3. The inner cylinder

was shorter than the outer and this allowed combustion products to be removed uniformly from the hood perimeter. The exhaust gases were then analyzed to determine species concentrations. The burner could be raised and lowered with respect to the bottom edge of the hood. The reported relative standard uncertainty of the measured gas species mass fractions was 6 %. The fuels consisted of acetone, ethanol, isopropanol, methanol, propane, propylene, and toluene. Hood equivalence ratios varied from 0.2 to 1.7. A subset of 47 of the original 148 experiments spanning the equivalence ratio range for each fuel were simulated for validation, see Table 3.1.

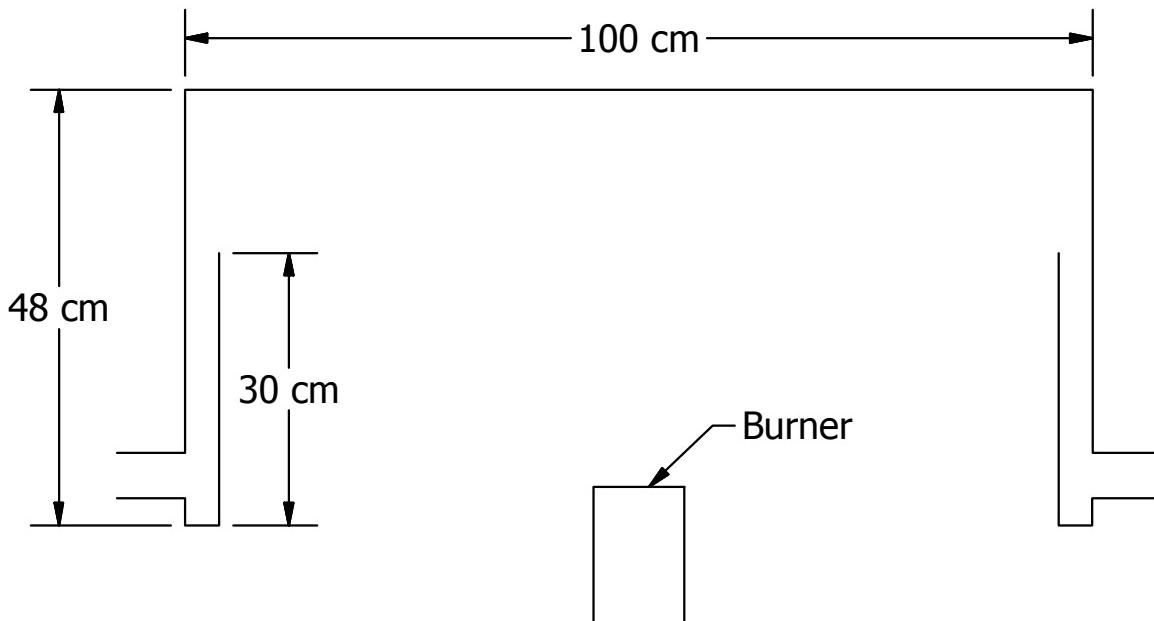


Figure 3.3: Sketch of Beyler Hood cross section.

### Modeling Notes

Simulations of the Beyler Hood experiments are performed at 3 cm resolution within a fairly simple facsimile of the actual hood. The boundary conditions are set to adiabatic to allow for a relatively quick ramp up to steady-state conditions.

The two-step simple chemistry combustion scheme is applied, where an infinitely fast reaction converts the fuel to CO, soot, and water vapor, followed sequentially by a second fast reaction that converts the soot and CO to CO<sub>2</sub>. Some of the soot and CO does not convert to CO<sub>2</sub>, based on post-flame yields listed by Tewarson [151].

A minimum auto-ignition temperature is specified for each fuel [152] to prevent the fuel vapor from igniting at the layer interface. This restriction is relaxed in the grid cells just above the burner surface to allow for ignition without a secondary heat source. In addition, a critical flame temperature of 500 °C is applied in all cases to account for local flame extinction. The grid is too coarse to support the actual values, and the chosen value is a placeholder until a better flame extinction model is developed.

Table 3.1: Summary of simulated Beyler Hood experiments. A negative value of Separation Distance indicates the burner top is below the lower rim of the hood.

| Exp. No. | Fuel Gas    | HRR (kW) | Burner (cm) | Sep. Dist. (cm) | Exp. No. | Fuel Gas  | HRR (kW) | Burner (cm) | Sep. Dist. (cm) |
|----------|-------------|----------|-------------|-----------------|----------|-----------|----------|-------------|-----------------|
| 117      | Acetone     | 18.0     | 22.6        | -12             | 232      | Propane   | 13.5     | 19.5        | -5              |
| 119      | Acetone     | 16.4     | 22.6        | -1              | 257      | Propane   | 8.2      | 19.5        | -15             |
| 122      | Acetone     | 16.4     | 22.6        | 4               | 287      | Propane   | 7.9      | 19.5        | 5               |
| 142      | Acetone     | 12.1     | 22.6        | 4               | 303      | Propane   | 18.3     | 19.5        | 5               |
| 145      | Acetone     | 12.7     | 22.6        | 4               | 307      | Propane   | 21.4     | 19.5        | 5               |
| 106      | Ethanol     | 17.3     | 22.6        | -9              | 318      | Propane   | 18.3     | 19.5        | -20             |
| 107      | Ethanol     | 21.3     | 22.6        | -4              | 322      | Propane   | 21.4     | 19.5        | -20             |
| 108      | Ethanol     | 17.3     | 22.6        | 4               | 334      | Propane   | 21.4     | 19.5        | -15             |
| 110      | Ethanol     | 13.5     | 22.6        | 4               | 355      | Propane   | 18.3     | 19.5        | 0               |
| 115      | Ethanol     | 13.5     | 22.6        | 4               | 359      | Propane   | 21.4     | 19.5        | 0               |
| 130      | Isopropanol | 12.4     | 22.6        | 4               | 371      | Propane   | 21.4     | 19.5        | -5              |
| 132      | Isopropanol | 12.4     | 22.6        | 4               | 389      | Propane   | 18.3     | 19.5        | 0               |
| 133      | Isopropanol | 12.4     | 22.6        | 4               | 429      | Propane   | 28.1     | 19.5        | -10             |
| 136      | Isopropanol | 12.4     | 22.6        | -1              | 433      | Propane   | 31.5     | 19.5        | -10             |
| 141      | Isopropanol | 12.4     | 22.6        | 4               | 445      | Propane   | 31.5     | 19.5        | -15             |
| 942      | Methanol    | 11.0     | 22.6        | 0               | 780      | Propylene | 7.5      | 19.5        | -10             |
| 943      | Methanol    | 11.0     | 22.6        | 0               | 805      | Propylene | 7.5      | 19.5        | -10             |
| 945      | Methanol    | 11.0     | 22.6        | -5              | 859      | Propylene | 31.4     | 19.5        | -10             |
| 947      | Methanol    | 11.0     | 22.6        | 0               | 870      | Propylene | 19.0     | 19.5        | -2              |
| 951      | Methanol    | 9.8      | 22.6        | 0               | 882      | Propylene | 19.1     | 19.5        | -10             |
| 160      | Toluene     | 11.5     | 22.6        | -6              | 886      | Propylene | 19.1     | 19.5        | -5              |
| 162      | Toluene     | 11.5     | 22.6        | -1              | 910      | Propylene | 31.4     | 19.5        | -11             |
| 165      | Toluene     | 11.5     | 22.6        | 4               |          |           |          |             |                 |
| 166      | Toluene     | 11.5     | 22.6        | 5               |          |           |          |             |                 |
| 170      | Toluene     | 11.5     | 22.6        | 4               |          |           |          |             |                 |

### 3.7 BGC/GRI LNG Fire Experiments

In 1982 and 1983, P.A. Croce and K.S. Mudan of Arthur D. Little, Inc., and J. Moorhouse of the British Gas Corporation (BGC) supervised 13 liquified natural gas (LNG) trench fire experiments conducted by BGC on behalf of the Gas Research Institute (GRI) [153]. Thirteen experiments were performed with nominal trench sizes ranging from 0.8 m by 4.4 m to 3.9 m by 52 m and aspect ratios ranging from approximately 5 to 30. Wind speeds varied from approximately 1 m/s to almost 10 m/s. Measurements made during the tests included flame geometry, radiative heat flux, emissive power, burning rate, LNG liquid and vapor compositions, and meteorological data. The fires were observed to exhibit substantial flame drag and flame breakup, unlike low aspect ratio pools. Steady burning was achieved in all tests.

The key parameters for each experiment are listed in Table 3.2. The Flame Tilt angle is the measured deflection of the flame from the vertical. The Flame Drag Ratio is the distance that the flame drags along the ground outside of the trench added to the trench width, and then divided by the trench width. The Avg. Flame Length denotes the time-averaged flame length, while the Max. Flame Length refers to the time-averaged extent of the fluctuating flame tips.

Table 3.2: BGC/GRI LNG Fires test parameters.

| Test No. | Trench Length (m) | Trench Width (m) | Aspect Ratio | Wind Speed (m/s) | Burning Rate (kg/m <sup>2</sup> /s) | Flame Tilt (deg) | Flame Drag Ratio | Avg. Flame Length (m) | Max. Flame Length (m) |
|----------|-------------------|------------------|--------------|------------------|-------------------------------------|------------------|------------------|-----------------------|-----------------------|
| 1        | 23.53             | 1.81             | 13.00        | 3.8              | 0.064                               | 56.3             | 2.57             | 4.4                   | 8.9                   |
| 2        | 15.52             | 1.81             | 8.57         | 1.5              | 0.069                               | 56.1             | 2.30             | 3.8                   | 7.3                   |
| 3        | 9.23              | 1.83             | 5.04         | 1.0              | 0.098                               | 45.2             | 1.21             | 7.1                   | 11.4                  |
| 4        | 23.50             | 1.83             | 12.84        | 8.36             | 0.054                               | 56.8             | 2.96             | 3.4                   | 7.3                   |
| 5        | 9.05              | 1.82             | 4.97         | 9.31             | 0.060                               | 60.5             | 2.96             | 4.2                   | 8.2                   |
| 6        | 23.45             | 3.94             | 5.95         | 4.98             | 0.082                               | 59.6             | 2.62             | 6.9                   | 16.8                  |
| 7        | 23.45             | 0.82             | 28.60        | 3.80             | 0.049                               | 48.3             | 3.98             | 2.0                   | 4.3                   |
| 8        | 11.82             | 0.82             | 14.41        | 2.05             | 0.058                               | 49.8             | 3.77             | 2.1                   | 4.6                   |
| 9        | 9.10              | 0.82             | 11.10        | 5.40             | 0.051                               | 47.0             | 3.68             | 1.5                   | 3.7                   |
| 10       | 52.05             | 3.89             | 13.38        | 7.05             | 0.060                               | 61.3             | 2.83             | 7.9                   | 20.3                  |
| 11       | 4.37              | 0.81             | 5.40         | 5.90             | 0.052                               | 49.9             | 4.16             | 1.8                   | 3.6                   |
| 12       | 52.15             | 1.82             | 28.65        | 8.60             | 0.046                               | 61.3             | 3.70             | 3.3                   | 8.1                   |
| 13       | 23.10             | 0.77             | 30.00        | 3.69             | 0.043                               | 55.7             | 4.23             | 2.1                   | 5.3                   |

### Modeling Notes

The experiments are simulated using the specified fuel burning rate. The fuel is assumed to be methane. The atmosphere is assumed to be neutral with a large Obukhov length,  $L = 1000000$ , and the ground surface is flat with an assumed aerodynamic roughness,  $z_0 = 0.1$  m. The relative humidity, ambient temperature and pressure, and wind speed at 9 m are specified in the report. The radiative fraction is assumed to 0.25 and the radiative path length is assumed to be 50 m; that is, the effective absorption coefficients of the various gas mixtures are evaluated over a distance of 50 m. The radiation source term is taken directly as 25 % of the combustion energy release rate. The soot yield is assumed to be 0.005.

**Flame Height Results:** Sec. 6.2.3

**Flame Tilt Results:** Sec. 6.3

**Heat Flux Results:** Sec. 12.2.3

## 3.8 Bittern Sprinkler Experiments

In 2004, a set of 22 fire experiments was conducted at the University of Canterbury, New Zealand, by Adam Bittern [154, 155]. In each experiment, a single chair was burned within an enclosure with two sprinklers installed. The sprinklers were not charged with flowing water during the experiments, but pressure gauges were installed immediately upstream of each sprinkler to indicate activation. The sprinkler actuation time, chair mass loss rate, and gas temperature profile were measured. The HRR was estimated from the measured mass loss rate and heat of combustion of the fuel.

The experiments incorporated four different types of sprinklers, two fire locations (the center and corner of the enclosure), and two ventilation conditions (open or closed door). The enclosure was timber-framed and lined with 10 mm thick gypsum plasterboard. The door was made of plywood and was 0.8 m wide by 2.1 high. The compartment layout, dimensions and experimental arrangement are shown in Figure 3.4.

The chair used as fuel for each experiment was made of flexible polyurethane foam slabs, where each slab measured approximately 0.5 m by 0.4 m by 0.1 m. The seat was ignited using a solid petroleum lighter.

Table 3.3 reports the sprinkler actuation times of each sprinkler.

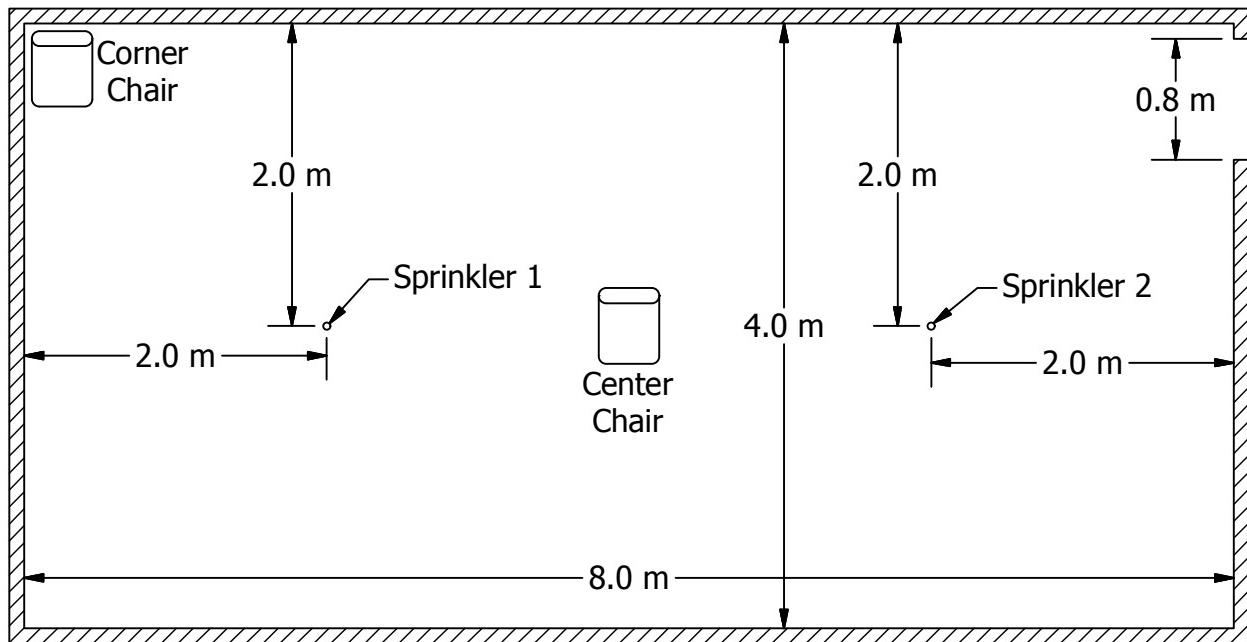


Figure 3.4: Plan view of the Bittern Sprinkler Experiments.

### Modeling Notes

The assumptions given in this section were used in the original analysis of the experiments [154].

The gypsum board had a thickness of 1 cm, density of  $731 \text{ kg/m}^3$ , specific heat of  $0.90 \text{ kJ/(kg}\cdot\text{K)}$ , conductivity of  $0.17 \text{ W/(m}\cdot\text{K)}$ , and emissivity of 0.88. The concrete floor was assumed to have a thickness of 10 cm, density of  $2300 \text{ kg/m}^3$ , specific heat of  $0.88 \text{ kJ/(kg}\cdot\text{K)}$ , conductivity of  $1.2 \text{ W/(m}\cdot\text{K)}$ , and emissivity of 0.5.

The properties of the sprinklers are shown in Table 3.4. These properties are based on the manufacturer's specification where available or otherwise estimated based on measured values of comparable sprinklers. For modeling purposes, the sprinkler offset, 2 cm, was selected based on an approximate 2 cm glass bulb length, and the C-factor selected was based on a sensitivity analyses undertaken in the original study.

The average heat of combustion of the upholstery was measured in a cone calorimeter to be 21.9 MJ/kg (Exp. 1-10) and 20.4 MJ/kg (Exp. 12-22). Since the primary fuel used in the experiments was flexible polyurethane foam, the radiant loss fraction assumed in the fire model was 0.46. Other combustion parameters were as for polyurethane foam, and all parameters selected are consistent with those used in the original BRANZFIRE study [155]. For the "simple chemistry" combustion model, inputs for stoichiometric yields have been selected from literature based on GM23 foam, with an effective molecular formula of  $\text{CH}_{1.8}\text{O}_{0.35}\text{N}_{0.06}$ . The soot yield was assumed to be 0.227 kg/kg. The area of the fire was taken to be 0.4 m by 0.5 m. The height of the fire was assumed to be 0.65 m above the floor.

Table 3.3: Summary of results, Bittern experiments. Note that Exp. 11 has been excluded because of a failed mass loss measurement.

| Exp. | Spr. 1 | Time (s) | Spr. 2 | Time (s) | $T_0$ (°C) | Door   | Fire Position |
|------|--------|----------|--------|----------|------------|--------|---------------|
| 1    | Res A  | 210      | Res A  | 250      | 23.7       | Open   | Center        |
| 2    | Res A  | 225      | Res A  | 211      | 25.5       | Open   | Center        |
| 3    | Res B  | 192      | Res B  | 192      | 25.5       | Open   | Center        |
| 4    | SS68   | 226      | SS68   | 226      | 25.7       | Open   | Center        |
| 5    | SS68   | 266      | SS68   | 272      | 27.5       | Open   | Center        |
| 6    | SS68   | 216      | SS68   | 211      | 27.7       | Open   | Center        |
| 7    | Res A  | 182      | Res A  | 186      | 28.2       | Open   | Center        |
| 8    | Res B  | 182      | Res B  | 187      | 27.9       | Open   | Center        |
| 9    | Res B  | 233      | Res B  | 230      | 28.9       | Open   | Center        |
| 10   | Res A  | 183      | Res B  | 184      | 29.4       | Open   | Center        |
| 12   | SS68   | 246      | Res B  | 228      | 24.0       | Closed | Center        |
| 13   | SS68   | 204      | Res B  | 194      | 24.5       | Closed | Center        |
| 14   | SS68   | 203      | Res B  | 187      | 24.2       | Closed | Center        |
| 15   | SS68   | 270      | Res B  | 253      | 23.7       | Closed | Center        |
| 16   | Res B  | 178      | Res A  | 224      | 20.6       | Closed | Corner        |
| 17   | Res B  | 181      | Res A  | 228      | 23.8       | Closed | Corner        |
| 18   | SS68   | 187      | Res A  | 221      | 25.0       | Closed | Corner        |
| 19   | SS68   | 189      | Res A  | 223      | 26.4       | Closed | Corner        |
| 20   | SS68   | 205      | Res A  | DNA      | 25.3       | Closed | Corner        |
| 21   | SS93   | 216      | SS93   | 330      | 25.2       | Closed | Corner        |
| 22   | SS93   | 205      | SS93   | 263      | 25.2       | Closed | Corner        |

Table 3.4: Properties of sprinklers used in Bittern Experiments.

| Short Name | Description                        | RTI<br>(m·s) <sup>1/2</sup> | C-Factor<br>(m/s) <sup>1/2</sup> | Act. Temp.<br>°C |
|------------|------------------------------------|-----------------------------|----------------------------------|------------------|
| Res A      | Residential, 3 mm glass bulb       | 36                          | 0.4                              | 68               |
| Res B      | Residential, 3 mm glass bulb       | 36                          | 0.4                              | 68               |
| SS68       | Standard Response, 5 mm glass bulb | 95                          | 0.4                              | 68               |
| SS93       | Standard Response, 5 mm glass bulb | 95                          | 0.4                              | 93               |

For experiments 11 to 22, the door to the compartment was closed. The estimated leakage area was assumed based on data for loose-fitting internal walls. An area of 0.053 m<sup>2</sup> was evenly distributed across the door.

### 3.9 Bouchair Solar Chimney

To evaluate solar-induced ventilation systems in desert climates, Bouchair [156] constructed a simple test apparatus shown in Fig. 3.5. A compartment with interior dimensions of approximately 1.6 m long, 1.8 m, and 2.0 m high had a window on one side and an air inlet slot on the other, leading into a 1.5 m wide cavity with two heating panels spanning the long dimension. The panels were heated to 10 °C, 20 °C, 30 °C, or 40 °C above ambient, drawing air through the compartment and into the thermal cavity. The mass flow rate

of air through the cavity was measured. The inlet slot was either 0.1 m or 0.4 m high, and 1.4 m wide. The thermal cavity was 1.5 m wide, and the hot panels were separated by 0.1 m, 0.2 m, 0.3 m, 0.5 m, or 1.0 m. In all, there were 40 different sets of test parameters.

In addition to the results presented in this guide, simulations of this experiment were performed by Shi and Zhang [157]. The objective of the simulations is to predict the mass flow rate by accurately modeling the convective heat transfer between the air and hot panels.

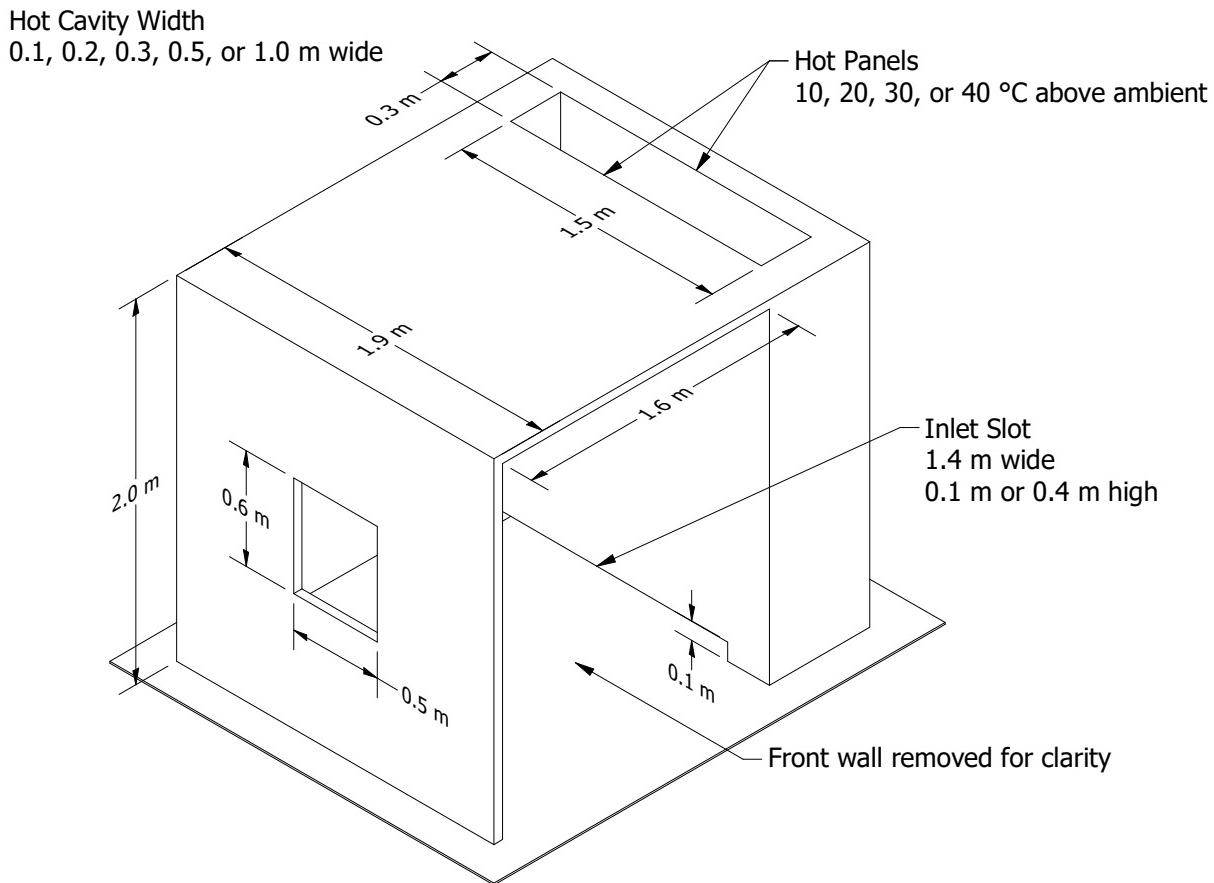


Figure 3.5: Geometry of the Bouchar Solar Chimney experiment.

### 3.10 BRE Spray Test for Radiation Attenuation

Murrel et al. [158] measured the attenuation of thermal radiation passing through a water spray using a heat flux gauge. The radiation was produced by a heat panel, one meter square, at 900 °C. The horizontal distance from the radiation panel to the spray nozzle was 2 m and to the measurement point 4 m. The nozzles were positioned at a height 0.24 m above the panel upper edge. The heat flux gauge was positioned at the line passing through the center of the panel. The attenuation of radiation was defined as  $(q_0 - q_s)/q_0$ , where  $q_0$  is the initial radiative heat flux, measured without a spray, and  $q_s$  is the heat flux measured during the spray operation.

Experimental results are used from three full-cone type nozzles, labeled A, B and D. The opening angles of the nozzles were between 90 and 108 degrees. The purpose of the simulation is to compare the measured and simulated attenuation of radiation at different flow conditions. The nozzles were specified in terms of median droplet size and mean vertical velocity using PDPA measurement in a single position, 0.7 m below the nozzle. The droplet boundary conditions were determined by assuming  $d_m \propto p^{-1/3}$  and  $v \propto p^{1/2}$  type of dependencies between the droplet size, speed and pressure.

### **3.11 Bryant Doorway Velocity Measurements**

Rodney Bryant of the Fire Research Division at NIST performed a series of velocity measurements of the gas velocity within the doorway of a standard ISO 9705 compartment for fires ranging from 34 kW to 511 kW [159, 160, 161]. A doorway served as the only vent for the enclosure. It included a jamb of 37 cm extending outward to facilitate the laser measurements. The entire compartment was elevated 0.3 m off the floor of the laboratory (see Fig. 3.6). The measurements were made using both bi-directional probes and PIV (Particle Image Velocimetry). The PIV measurements only cover the lower two-thirds of the doorway because of difficulties in seeding the hot outflow gases. The bi-directional probe measurements span the entire height of the doorway, but Bryant reports that these measurements were up to 20 % greater than the PIV measurements in certain regions of the flow. Consequently, only the PIV data was used for comparison to the model.

Note: All values refer to inner dimension.

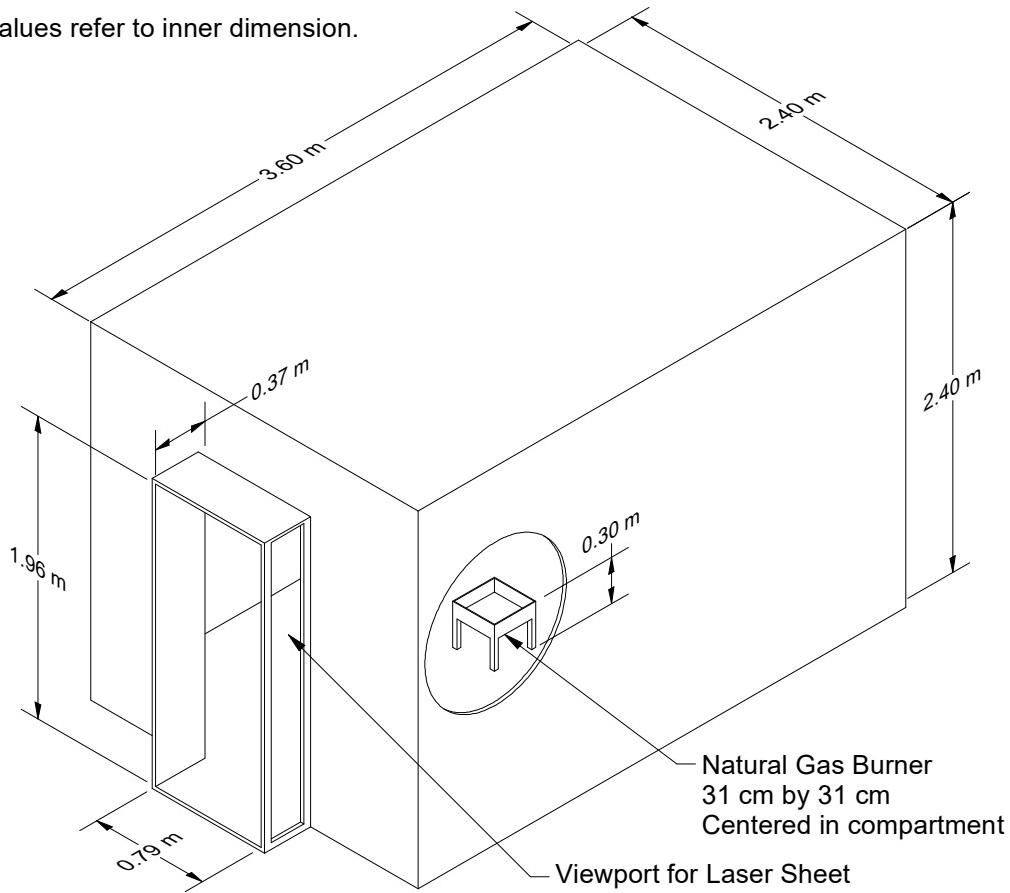


Figure 3.6: Geometry of Bryant's compartment.

### 3.12 BST/FRS Wood Crib Fire Experiments

In 1993, British Steel Technical, Swinden Laboratories, in collaboration with the Building Research Establishment (BRE), Fire Research Station, conducted nine fire experiments inside the BRE ex-airship hangar testing facility at Cardington, Bedfordshire, England [162]. The objective of the experiments was to examine the influence of combustible loading and ventilation on fire severity.

The roof of the test compartment was made of 20 cm thick reinforced aerated concrete slabs with a density of  $450 \text{ kg/m}^3$ . The walls were made of 215 mm thick lightweight concrete blocks with a density of  $1375 \text{ kg/m}^3$ . The floor was covered with a 125 mm deep layer of sand with a density of  $1750 \text{ kg/m}^3$ . Both the roof and walls were lined with two 25 mm thick layers of standard grade ceramic fiber blanket with a density of  $128 \text{ kg/m}^3$ . Taking into account the lining materials, the compartment was 22.9 m long, 5.6 m deep, and 2.8 m high.

Ventilation was provided at one end of the compartment through a full-width, variable height opening. Lightweight concrete blocks were used to construct temporary walls to reduce the ventilation from fully open to an eighth of the available area.

The combustibles consisted of 33 1 m square wood cribs in 11 rows. Each crib was constructed of 1 m long and 5 cm square cross section sticks of Western Hemlock softwood (density  $400 \text{ kg/m}^3$ ), dried to 10 % moisture content. The sticks were stacked with 5 cm gaps. Table 3.5 lists the fire load densities

and ventilation areas. The rear-most three cribs at the back of the compartment were ignited simultaneously. Temperatures were measured along crib lines 2 (back), 6 (middle) and 10 (front), using 3 mm thermocouples placed 300 mm below the ceiling. The average of three thermocouples at the same longitudinal position is used for model validation.

Table 3.5: Fire load densities and relative ventilation areas in the BST/FRS experiments [162].

| Test number                                 | 1   | 2   | 3   | 4   | 5   | 6   |
|---|-----|-----|-----|-----|-----|-----|
| Combustible load ( $\text{kg}/\text{m}^2$ ) | 40  | 20  | 20  | 40  | 20  | 20  |
| Relative Ventilation Area                   | 1/1 | 1/1 | 1/2 | 1/2 | 1/4 | 1/8 |

### Modeling Notes

The fire spread on wood cribs is modeled as a combination of simple and complex pyrolysis models. The unresolved surface area of the wood cribs is compensated using an area multiplicator input parameter. Modeling is reported in [163].

## 3.13 Cable Response to Live Fire – CAROLFIRE

CAROLFIRE was a project sponsored by the U.S. Nuclear Regulatory Commission to study the thermal response and functional behavior of electrical cables [164]. The primary objective of CAROLFIRE was to characterize the various modes of electrical failure (e.g., hot shorts, shorts to ground) within bundles of power, control and instrument cables. A secondary objective of the project was to develop a simple model to predict thermally-induced electrical failure (THIEF). The measurements used for these purposes were conducted at Sandia National Laboratories and are described in Volume II of the CAROLFIRE test report. In brief, there were two series of experiments. The first were conducted within a heated cylindrical enclosure. Single and bundled cables were exposed to various heat fluxes and the electrical failure modes recorded. The second series of experiments involved cables within trays in a semi-enclosed space under which a gas-fueled burner created a hot layer to force cable failure. Only results from the first series are used here.

Petra Andersson and Patrick Van Hees of the Swedish National Testing and Research Institute (SP) proposed that a cable's thermally-induced electrical failure can be predicted via a one-dimensional heat transfer calculation, under the assumption that the cable can be treated as a homogenous cylinder [165]. Their results for PVC cables were encouraging and suggested that the simplification of the analysis is reasonable and that it should extend to other types of cables. The assumptions underlying the THIEF model are as follows:

1. The heat penetration into a cable of circular cross section is primarily in the radial direction.
2. The cable is homogeneous in composition. In reality, a cable is constructed of several different types of polymeric materials, cellulosic fillers, and a conducting metal, most often copper.
3. The thermal conductivity, specific heat, and density of the assumed homogeneous cable are independent of temperature. In reality, both the thermal conductivity and specific heat of polymers are temperature-dependent, but this information is not easily obtained from manufacturers.
4. It is assumed that no decomposition reactions occur within the cable during its heating, and ignition and burning are not considered in the model. In fact, thermoplastic cables melt, thermosets form a char layer, and both release volatile gases up to and beyond the point of electrical failure.

5. Electrical failure occurs when the temperature just inside the cable jacket reaches an experimentally determined value.

### 3.14 Crown Fires

The term “crown fire” refers to a wildfire that spreads from the ground surface into the tree canopy. Alexander and Cruz [166] compiled a data set of 57 crown fires that occurred in the U.S. and Canada between 1965 and 2003. For each fire, the relative humidity, ambient temperature, and dominant vegetation type are reported, along with estimated values for the vegetation moisture content, *canopy*<sup>1</sup> bulk density, and open 10 m wind speed. The vegetation consists mainly of coniferous trees, like pines and spruces, and dry undergrowth and ground cover, i.e. scrub brush and dry pine needles. The reported relative humidity ranges between 5 % and 50 %, the estimated moisture content ranges between 5 % and 10 %, the estimated *canopy* bulk density ranges between 0.1 kg/m<sup>3</sup> and 0.2 kg/m<sup>3</sup>, the estimated wind speed ranges between 10 km/h and 50 km/h, and the observed rate of spread ranges between 10 m/min and 110 m/min.

#### Modeling Notes

It is not possible to compare directly the model simulations with the observed fires because of lack of information about the number, spacing, and height of the trees; and the depth, mass, and composition of the ground cover. Instead, Ziegler et al. [167, 168, 169, 170] developed tree maps based on various forests found in the western region of the U.S. The maps contain the location and rough dimensions of each tree in a 4 ha area. Eight maps were developed based on four specific locations and pre- or post-treated conditions. In addition, Ziegler et al. suggest that the moisture content of the trees is approximately 100 %, and the ground cover 5 %. The *crown* bulk density for all simulations is 1.2 kg/m<sup>3</sup>, and the surface density is 0.72 kg/m<sup>2</sup> with a depth of 6 cm. The simulated fires are ignited along a strip, and the rate of spread is calculated based on the position of peak temperature.

The simulations are performed with a numerical grid that has a resolution of 1 m by 1 m by 0.5 m near the ground, and the vertical dimension increases gradually with height. Because of this relatively coarse resolution, the burning rate of the vegetation is limited to ensure that any given patch of surface vegetation or volume of canopy vegetation cannot burn completely in less than 30 s.

### 3.15 CSIRO Grassland Fires

In July and August of 1986, the Commonwealth Scientific and Industrial Research Organisation (CSIRO) of Australia conducted controlled grassland fire experiments near Darwin, Northern Territory [171]. July and August are in the middle of the dry season when the grasses are fully cured (dried) and the weather is warm and dry. The experiments were conducted on flat plots measuring 100 m by 100 m, 200 m by 200 m, or 200 m by 300 m. Two cases have been simulated. Case C064 was conducted on a 100 m by 100 m plot of kerosene grass (*Eriachne burkittii*); Case F19 was conducted on a 200 m by 200 m plot of kangaroo grass (*Themeda australis*).

#### Modeling Notes

Two of these experiments were originally simulated with FDS by Mell et al. [128]. These simulations modeled the grass as a collection of cylindrical Lagrangian particles. The pyrolysis model assigned to the

---

<sup>1</sup>Note the difference between *canopy* bulk density and *crown* bulk density, both of which are abbreviated CBD. The former is the bulk density over the entire forested area, whereas the latter refers to the bulk density within the crown of an individual tree.

particles is described in the FDS User’s Guide [1], chapter “Wildland Fire Spread,” Sec. 17.1, “Thermal Degradation Model for Vegetation.”

Now these two experiments are also simulated using the Boundary Fuel Model (BFM) [130] and the Rothermel-Albini fire spread algorithm [172, 173]. For the experiment labelled Case C064, fuel index 1 (Short Grass) is used, with a modified moisture fraction of 0.063. For F19, fuel index 3 (Tall Grass) is used, with a modified moisture fraction of 0.058.

Measured properties for the specific types of grasses burned in the two experiments are listed in Table 3.6. Properties that were not measured are listed in Table 3.7. These assumed properties are typically for wood or cellulosic fuels. The moisture is modeled as water. The grass is assumed to be composed primarily of cellulose.

Snapshots of the Lagrangian particle simulation of Case F19 is shown in Fig. 3.7. The computational domain in this case is 240 m by 240 m by 20 m. The grid cells are 0.5 m cubes. The domain is subdivided into 36 individual meshes and run in parallel. The grass is represented 1 simulated blade per grid cell. The radius of the cylinder is derived from the measured surface area to volume ratio. Each simulated blade of grass represents many more actual blades of grass. The weighting factor is determined from the measured bulk mass per unit area. The fires in the experiments were ignited by two men carrying drip torches walking in opposite directions along the upwind boundary of the plot (the red strip in Fig. 3.7). In FDS, this action was modeled using a specified spread rate along the strip.

Table 3.6: Measured properties for the CSIRO Grassland Fire cases [171].

| Property                     | Units                  | Case F19 | Case C064 |
|------------------------------|------------------------|----------|-----------|
| Wind Speed                   | m/s                    | 4.8      | 4.6       |
| Ambient Temperature          | °C                     | 34       | 32        |
| Surface Area to Volume Ratio | $\text{m}^{-1}$        | 12240    | 9770      |
| Grass Height                 | m                      | 0.51     | 0.21      |
| Bulk Mass per Unit Area      | $\text{kg}/\text{m}^2$ | 0.313    | 0.283     |
| Moisture Fraction            | %                      | 5.8      | 6.3       |

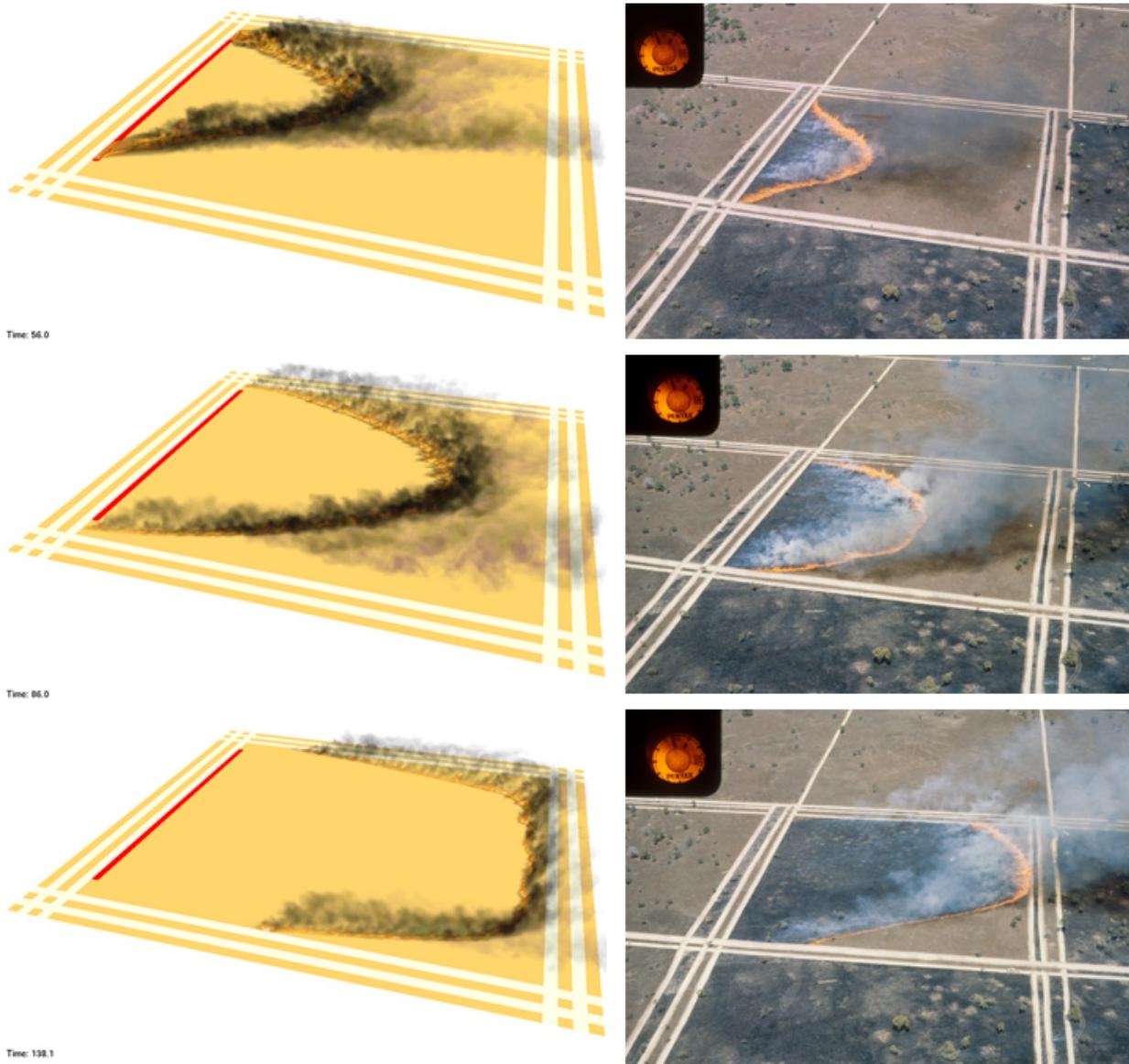


Figure 3.7: Snapshots of the simulation of CSIRO Grassland Fire F19 compared to photographs of the fire.

Table 3.7: Assumed properties for various types of dried grass and soil.

| Property                     | Units             | Value   | Reference       |
|------------------------------|-------------------|---|-----------------|
| Chemical Composition         | –                 | C <sub>6</sub> H <sub>10</sub> O <sub>5</sub> | Assumption      |
| Heat of Combustion           | kJ/kg             | 15600   | [174]           |
| Soot Yield                   | kg/kg             | 0.015   | [151]           |
| Char Yield                   | kg/kg             | 0.2   | [174]           |
| Specific Heat                | kJ/(kg·K)         | 1.5   | Various sources |
| Conductivity                 | W/(m·K)           | 0.1   | Assumption      |
| Density                      | kg/m <sup>3</sup> | 512   | [172]           |
| Heat of Pyrolysis            | kJ/kg             | 418   | [175]           |
| Obukhov Length               | m                 | -500  | Assumption      |
| Aerodynamic Roughness Length | m                 | 0.03  | Assumption      |
| Drag Coefficient             | –                 | 2.8   | [176]           |
| Soil Specific Heat           | kJ/(kg·K)         | 2.0   | [177]           |
| Soil Conductivity            | W/(m·K)           | 0.25  | [177]           |
| Soil Density                 | kg/m <sup>3</sup> | 1300  | [177]           |

### 3.16 CSTB Tunnel Experiments

Between 2005 and 2008, the French building research laboratory, Centre Scientifique et Technique du Bâtiment (CSTB) cooperated with the French Tunnel Study Center (CETU), the French National Centre for Scientific Research (CNRS, Institut PPRIME) and the French Directorate for Civil Security (DSC) to conduct fire experiments in a tunnel, some of which involved a water mist system [178, 179]. The first aim was to improve the understanding of the interaction between water mist and a tunnel fire. The second was to develop a database for model validation. A one-third scale was selected with the objective of studying realistic fire phenomena in an affordable way. Twenty-eight experiments were conducted (20 with and 8 without water mist) with varying fuels (heptane pool, wood crib, and wood pallet) and longitudinal velocities (with and without back layering).

The tunnel was 43 m long, with a semi-circular cross section whose area was approximately 4 m<sup>2</sup>. The walls were covered by a fire resistant mortar cement with well known thermal properties. The floor was made of concrete. A fan was mounted at the downstream side of the tunnel. Measurements were made of the following: fuel mass, gas temperature, air velocity, radiative heat flux and gas concentration (CO, CO<sub>2</sub> and O<sub>2</sub>). Sensors were located at 11 longitudinal positions.

Tests 2 and 27 have been selected because neither exhibited back layering. The longitudinal velocity in Test 2 was approximately 2.2 m/s and in Test 27 it was 3.1 m/s. Both experiments involved a 0.5 m<sup>2</sup> area heptane pool. In Test 2, the HRR was deduced from the fuel mass loss rate only. In Test 27, the HRR was deduced from both the mass loss rate and from oxygen consumption calorimetry.

In Test 27, a water mist system was manually activated 300 s after ignition. The water mist system was composed of six nozzles along the centerline of the tunnel, from 4 m upstream to 3.5 m downstream of the fire, 1.5 m apart. The operating pressure was approximately 90 bar. The water flow rate injected at each nozzle was close to 5.5 L/min, corresponding to a total mist discharge rate of approximately 33 L/min. Test 27 is interesting because it involved a very low water injection rate. The main consequence is that the HRR actually increased slightly after the nozzles were activated, and the fire did not extinguish. The experiment stopped when the fuel was exhausted. This allowed for an assessment of the model's ability to predict the gas cooling and radiation attenuation.

### Modeling Notes

The simulations of these experiments are performed using 12 meshes. To prevent numerical instability due to oscillations in pressure, a common problem for tunnel fire simulations, the `VELOCITY_TOLERANCE` and `PRESSURE_TOLERANCE` are reduced to 0.01 m/s and 400 s<sup>-2</sup>, respectively, and the `MAX_PRESSURE_ITERATIONS` is increased to 50. The multi-port mist nozzles are each modeled as a collection of single nozzles with varying orientations.

## 3.17 Cup Burner Experiments

The cup-burner is a widely used experimental apparatus for studying the effectiveness of flame extinguishing agents. Typically, these experiments feature a steady fuel-air co-flow diffusion flame that is established above the cup. The extinguishing agent is gradually introduced into the air stream to determine the minimum concentration of the agent that leads to lift off. One hundred and ten experimental data sets are examined. The data sets include sixteen fuels: acetone, acetylene, benzene, butane, dodecane, ethanol, ethylene, heptane, hexane, hydrogen, methane, methanol, octane, propanol, and toluene, and five inert gases: argon (Ar), carbon dioxide (CO<sub>2</sub>), helium (He), and nitrogen (N<sub>2</sub>), and sulfur hexafluoride (SF<sub>6</sub>). A STANJAN<sup>2</sup> calculation has been performed to determine the equilibrium temperature using the measured minimum extinguishing concentration for each experiment. The calculation assumes constant pressure and enthalpy using a stoichiometric mixture of fuel and air plus agent. For combinations of fuel and agent with multiple experiments, the average extinguishing concentration and the average flame temperature is taken, resulting in forty-six unique combinations of fuel and agent listed in Table 3.8.

### Modeling Notes

Cup burner dimensions, fuel inlet velocity, and co-flow inlet velocity vary slightly amongst the researchers; however, extinguishing concentrations have been shown to be fairly insensitive over the range of typical values. The cup burner model was implemented as a 2D, cylindrical geometry with a 1 cm radius for the burner and a 4 cm radius for the tube. A 1 mm grid resolution was used. For gaseous fuels a 1 cm/s inlet velocity was used for the burner. Liquid fuels used burning rates from the SFPE Handbook; fuels without published burning rates scaled the burning rate of a chemically similar fuel (e.g. alcohol, alkane) using the heat of vaporization for the fuel. The fuel temperature boundary condition was ambient for gaseous fuels and one-half of the boiling point for liquid fuels. The co-flow was set to 12 cm/s. The agent mass fraction was ramped from approximately 10 % below to 10 % above the values shown in Table 3.8. The `CRITICAL_FLAME_TEMPERATURE` was set to the values in Table 3.8.

---

<sup>2</sup>STANJAN is a program for chemical equilibrium calculations.

Table 3.8: Summary of Cup Burner Data

| Fuel      | Agent           | MEC  | CFT  | References  |
|-----------|-----------------|------|------|---|
| Acetone   | Ar              | 34.0 | 1729 | [180, 181]  |
| Acetone   | CO <sub>2</sub> | 19.0 | 1678 | [182]   |
| Acetone   | N <sub>2</sub>  | 28.0 | 1670 | [180, 182]  |
| Acetylene | CO <sub>2</sub> | 45.0 | 1338 | [182]   |
| Acetylene | N <sub>2</sub>  | 58.0 | 1312 | [182]   |
| Benzene   | CO <sub>2</sub> | 20.1 | 1691 | [182, 183]  |
| Benzene   | N <sub>2</sub>  | 30.3 | 1683 | [180, 182, 183]   |
| Butane    | N <sub>2</sub>  | 31.0 | 1594 | [182]   |
| Butane    | CO <sub>2</sub> | 19.0 | 1639 | [182]   |
| Dodecane  | N <sub>2</sub>  | 33.0 | 1577 | [180]   |
| Ethanol   | Ar              | 36.5 | 1654 | [180, 181]  |
| Ethanol   | CO <sub>2</sub> | 23.7 | 1542 | [182, 183]  |
| Ethanol   | N <sub>2</sub>  | 34.6 | 1529 | [180, 182, 183]   |
| Ethylene  | CO <sub>2</sub> | 32.0 | 1471 | [182]   |
| Ethylene  | N <sub>2</sub>  | 45.0 | 1441 | [182]   |
| Heptane   | Ar              | 39.5 | 1643 | [180, 184, 181, 185, 186, 187, 188, 189, 190]                     |
| Heptane   | N <sub>2</sub>  | 31.2 | 1617 | [180, 184, 191, 181, 192, 185, 186, 187, 182, 183, 188, 189, 190] |
| Heptane   | CO <sub>2</sub> | 21.4 | 1617 | [181, 192, 185, 186, 187, 182, 183]                               |
| Heptane   | He              | 31.5 | 1763 | [185, 186]  |
| Heptane   | SF <sub>6</sub> | 11.0 | 1531 | [185]   |
| Hexane    | Ar              | 33.0 | 1740 | [181]   |
| Hexane    | CO <sub>2</sub> | 20.0 | 1647 | [182]   |
| Hexane    | N <sub>2</sub>  | 29.0 | 1646 | [180, 182]  |
| Hydrogen  | CO <sub>2</sub> | 60.0 | 913  | [182]   |
| Hydrogen  | N <sub>2</sub>  | 72.0 | 870  | [182]   |
| Methane   | Ar              | 33.8 | 1659 | [180, 193, 181]   |
| Methane   | N <sub>2</sub>  | 24.2 | 1663 | [193, 182, 194]   |
| Methane   | CO <sub>2</sub> | 14.4 | 1694 | [182, 183]  |
| Methane   | He              | 26.7 | 1746 | [193]   |
| Methanol  | Ar              | 45.0 | 1494 | [180, 181]  |
| Methanol  | CO <sub>2</sub> | 29.2 | 1410 | [182, 183]  |
| Methanol  | N <sub>2</sub>  | 40.8 | 1395 | [180, 182, 183]   |
| Octane    | Ar              | 27.0 | 1790 | [181]   |
| Octane    | CO <sub>2</sub> | 24.0 | 1542 | [182]   |
| Octane    | N <sub>2</sub>  | 33.0 | 1564 | [180, 182]  |
| Propane   | Ar              | 37.5 | 1652 | [180, 181]  |
| Propane   | CO <sub>2</sub> | 21.0 | 1600 | [182]   |
| Propane   | N <sub>2</sub>  | 32.3 | 1573 | [191, 182, 194]   |
| Propanol  | Ar              | 28.0 | 1781 | [181]   |
| Propanol  | CO <sub>2</sub> | 22.0 | 1584 | [182]   |
| Propanol  | He              | 30.0 | 1755 | [185]   |
| Propanol  | N <sub>2</sub>  | 30.0 | 1608 | [182, 185]  |
| Propanol  | SF <sub>6</sub> | 11.0 | 1515 | [185]   |
| Toluene   | Ar              | 27.0 | 1854 | [181]   |
| Toluene   | CO <sub>2</sub> | 17.0 | 1744 | [182, 183]  |
| Toluene   | N <sub>2</sub>  | 24.4 | 1755 | [182, 183]  |

MEC Minimum Extinguishing Concentration (mol/mol)

CFT Critical Flame Temperature (°C)

### 3.18 DelCo Trainer Experiments

The NIST Fire Fighting Technology Group conducted a series of experiments in two structures of similar design located at the Delaware County (“DelCo”) Emergency Services Training Center in Sharon Hill, Pennsylvania [195]. Three propane burners were used to provide the fire source for all experiments, and various sensors were used to collect gas temperature, gas velocity, heat flux, and gas concentration measurements throughout the structure.

The single level structure was instrumented with five bare-bead thermocouple arrays and two gas sample inlet pipes at the locations shown in Fig. 3.8. Both floors of the two level structure were instrumented with three bare-bead thermocouple arrays and one gas sample inlet pipe at the locations shown in Fig. 3.9.

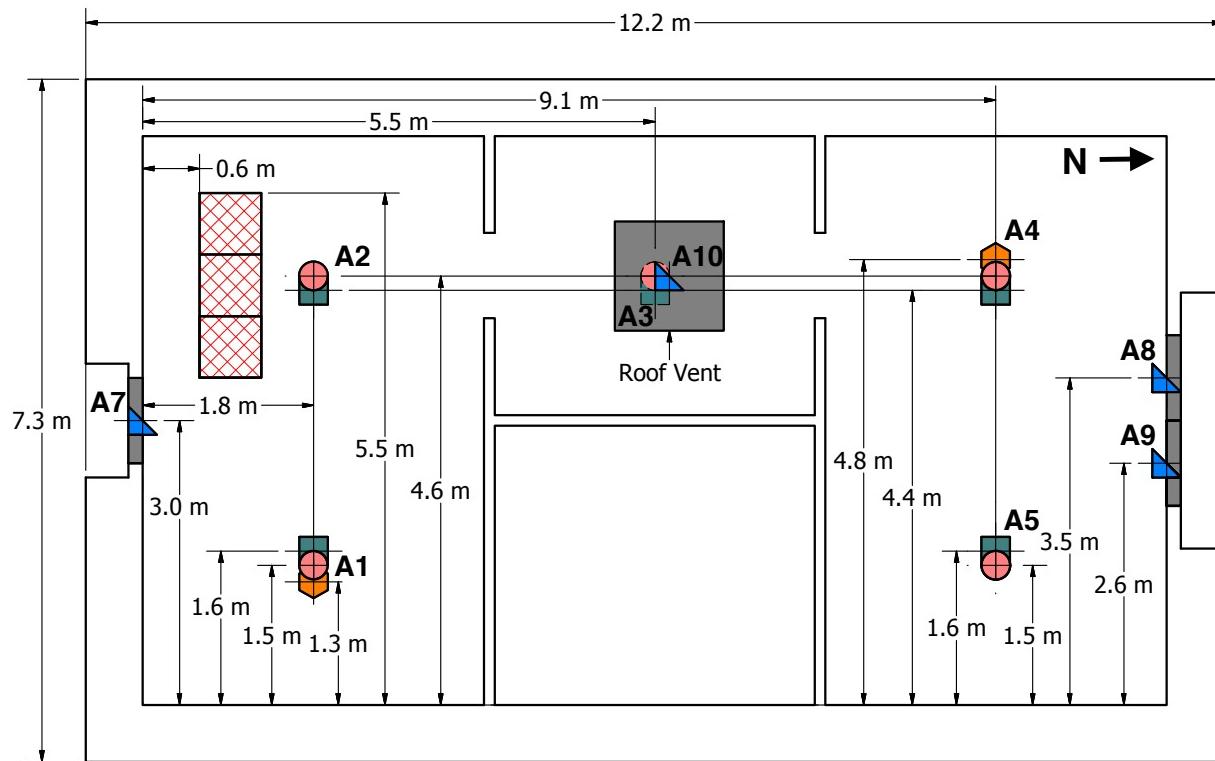


Figure 3.8: Instrumentation of the single level DelCo training structure. The thermocouple arrays are denoted by crossed circles and the gas sampling measurement locations are denoted by hexagons at locations A1 and A4. The burner is denoted by three cross-hatched squares.

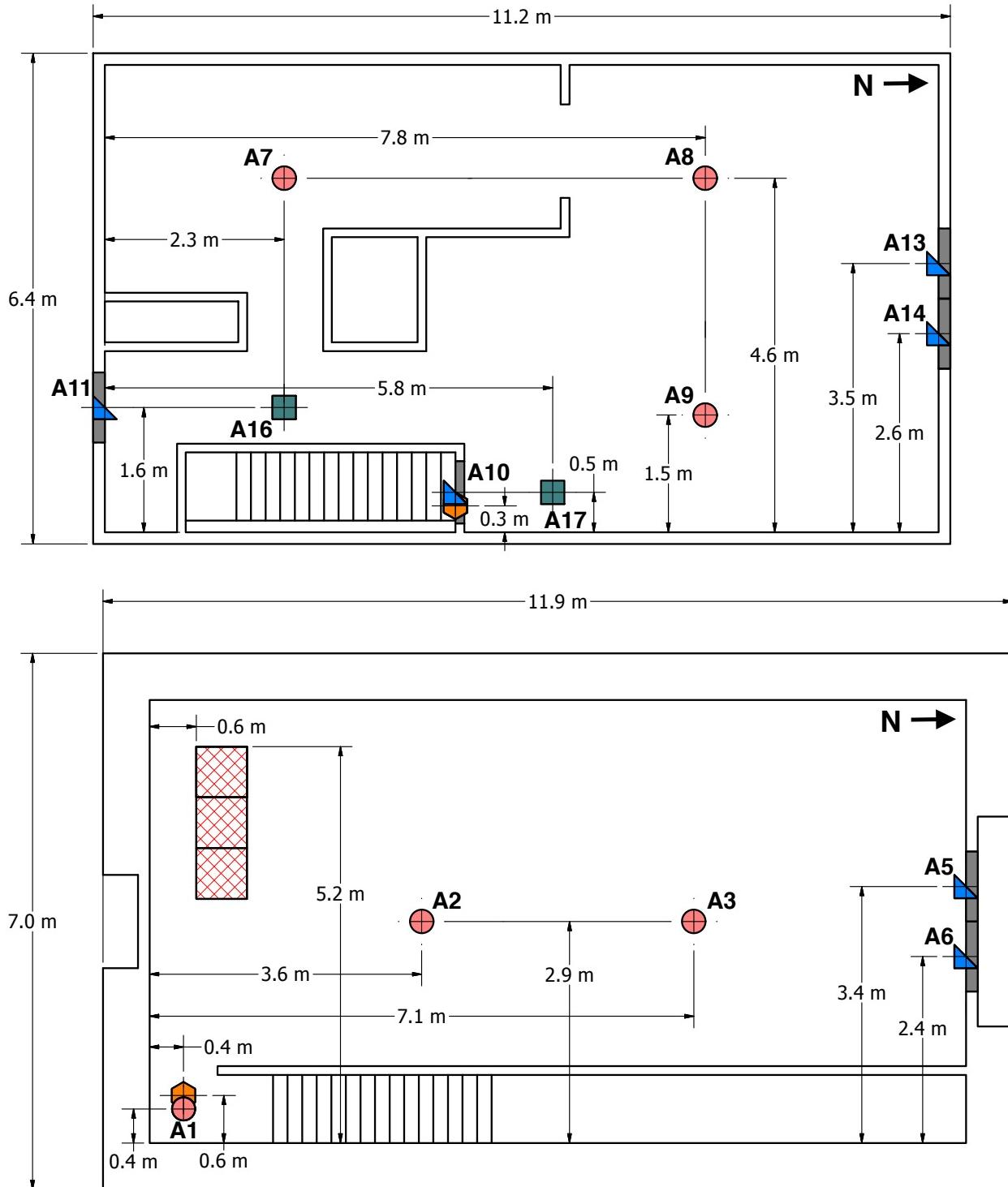


Figure 3.9: Instrumentation of the second floor (top) and first floor (bottom) of the two level DelCo training structure. The thermocouple arrays are denoted by crossed circles and the gas sampling measurement locations are denoted by hexagons at locations A1 and A10. The burner is denoted by three cross-hatched squares.

### 3.19 DoJ/HAI Pool Fire Experiments

The U.S. Department of Justice sponsored a series of liquid pool fire experiments performed by Hughes Associates, Inc. [196]. Hundreds of experiments were performed, involving six different liquid fuels, eight different substrates, a variety of pan sizes and pool depths. Of these, 44 experiments were chosen from the “Diked Fire Test Series,” where gasoline or kerosene was burned within 0.3 m, 0.6 m, or 1.2 m square pans with liquid depths ranging from 1 mm to 20 mm. The substrate was either coated concrete or vinyl, each of which was designed to avoid liquid absorption. The vinyl flooring material had a nominal thickness of 1.2 mm applied to a 14.7 mm plywood using a vinyl adhesive. Table 14.15 provides a summary of the experimental parameters.

#### Modeling Notes

The test report for the experiments does not explicitly list the components of the gasoline or kerosene. Rather, distillation curves are provided showing that the initial and final boiling points for gasoline are 45 °C and 212 °C, and for kerosene 170 °C and 257 °C. The density of the gasoline is 742 kg/m<sup>3</sup> and the kerosene 798 kg/m<sup>3</sup>. From various industry documents, it is postulated that the gasoline is a mixture of n-hexane (0.521 by mass), n-heptane (0.054), n-octane (0.063), n-decane (0.023), benzene (0.20), and toluene (0.139). The kerosene is assumed to be a mixture of iso-octane (0.04), n-nonane (0.19), iso-nonane (0.12), n-decane (0.15), iso-decane (0.11), n-undecane (0.09), and cis-decalin (0.30). The relevant properties of these liquids are listed in Table 3.32.

A few additional assumptions are made concerning the mixtures. First, that the absorption coefficient of all components is set to 150 m<sup>-1</sup>, a value that is typical of heavy hydrocarbon liquids. Seconds, the thermal conductivity of the components is set to an artificially low value of 0.02 W/m/K to roughly account for the buoyancy that drives heated liquid upwards towards the surface. Third, all liquid components are assumed to evaporate into a single gas phase species, n-hexane. If this were not assumed, additional transport equations and combustion reactions would be needed for all liquid components.

Finally, to simulate the ignition of the liquid pools, an external flux is imposed at the surface for 10 s in the case of gasoline and 25 s for kerosene.

Table 3.9: Gasoline and kerosene components [197].

| Fuel Component | Chemical Formula                | W (g/mol) | $\rho$ (kg/m <sup>3</sup> ) | $c_p$ (kJ/(kg·K)) | $h_v$ (kJ/kg) | $T_b$ °C |
|----------------|---------------------------------|-----------|-----------------------------|-------------------|---------------|----------|
| Benzene        | C <sub>6</sub> H <sub>6</sub>   | 78.1      | 879                         | 1.72              | 393           | 80.1     |
| cis-Decalin    | C <sub>10</sub> H <sub>18</sub> | 138.3     | 897                         | 1.68              | 297           | 195.8    |
| iso-Decane     | C <sub>10</sub> H <sub>22</sub> | 142.3     | 728                         | 2.20              | 269           | 167.0    |
| n-Decane       | C <sub>10</sub> H <sub>22</sub> | 142.3     | 730                         | 2.21              | 278           | 174.1    |
| n-Heptane      | C <sub>7</sub> H <sub>16</sub>  | 100.2     | 684                         | 2.24              | 317           | 98.4     |
| n-Hexane       | C <sub>6</sub> H <sub>14</sub>  | 86.2      | 659                         | 2.27              | 335           | 68.7     |
| iso-Nonane     | C <sub>9</sub> H <sub>20</sub>  | 128.3     | 708                         | 2.34              | 350           | 143.0    |
| n-Nonane       | C <sub>9</sub> H <sub>20</sub>  | 128.3     | 718                         | 2.22              | 290           | 150.8    |
| iso-Octane     | C <sub>8</sub> H <sub>18</sub>  | 114.2     | 692                         | 2.09              | 270           | 99.2     |
| n-Octane       | C <sub>8</sub> H <sub>18</sub>  | 114.2     | 702                         | 2.23              | 301           | 125.6    |
| Toluene        | C <sub>7</sub> H <sub>8</sub>   | 92.1      | 867                         | 1.67              | 360           | 110.6    |
| n-Undecane     | C <sub>11</sub> H <sub>24</sub> | 156.3     | 740                         | 2.21              | 268           | 195.9    |

## 3.20 Droplet Evaporation

Five sets of experiments have been selected for validation of the evaporation of liquid droplets.

### Fujita, Kurose, and Komori Experiments

Fujita, Kurose, and Komori performed a series of experiments that suspended a water drop in a heated, vertical wind tunnel [198]. Four experiments were modeled with relative humidity values of 0 % and 30 % and droplet Reynolds numbers of 60 and 150 (approximately 0.8 m/s and 2.0 m/s). Droplet size and surface temperature were recorded as functions of time.

### Gavin Experiments

Gavin performed two experiments of a single water drop falling in dry air [199]. The test apparatus was a vertical wind tunnel. A drop was injected into the wind tunnel and the vertical air stream velocity was changed over time to maintain the drop at a constant elevation in the wind tunnel. The first droplet was 769  $\mu\text{m}$  with an initial temperature of 23.0 °C. The second droplet was 557  $\mu\text{m}$  with an initial temperature of 24.3 °C.

### Kolaitis and Founti Experiments

Kolaitis and Founti measured the diameter and temperature of suspended liquid fuel droplets in a heated air stream [200]. Four experiments were chosen: a 1.26 mm droplet of ethanol at an initial temperature of 34.2 °C in 94 °C quiescent air, a 1.13 mm droplet of decane at an initial temperature of 73.8 °C in 94 °C quiescent air, a 1.15 mm droplet of heptane at an initial temperature of 49.0 °C in 94 °C quiescent air, and a 1.42 mm droplet of heptane at an initial temperature of 15.5 °C in 94 °C air at 0.146 m/s.

### Maqua, Castanet, and Lemoine Experiments

Maqua, Castanet, and Lemoine measured the temperature of falling droplets of ethanol and acetone mixtures in a heated plume [201]. Because the temperature and velocity of the plume was not well-characterized, only the experiments involving a droplet falling in quiescent air were modeled. As FDS does not currently have a sub-model for the evaporation of a multi-component fuel, only the experiments for a pure ethanol droplet (140  $\mu\text{m}$ ) and a pure acetone droplet (140  $\mu\text{m}$ ) were modeled. The initial droplet temperature in both experiments was 45 °C in 20 °C air.

### Taflin Experiments

Taflin measured the diameter of suspended water droplets in dry air [202]. One droplet was initially 43.9  $\mu\text{m}$  and the other was 56.6  $\mu\text{m}$ .

## 3.21 Edinburgh Vegetation Drag

Mueller et al. [203] characterized the pressure drop through beds of randomly oriented pine needles and used the results to parameterize a drag model following the form of the Forchheimer equation. They then measured the development of velocity profiles within and above these pine needle beds, using a hotwire anemometer, and compared the results to FDS predictions using the parameterized model. Fuel beds with

bulk densities of  $20 \text{ kg/m}^3$ ,  $40 \text{ kg/m}^3$ , and  $60 \text{ kg/m}^3$  were tested, with inlet velocities in the range of 0.5–2.0 m/s. A condensed version of the comparison is reproduced in this guide, which serves to test the ability of the model to represent the general features of flow in sparse multiphase media.

### Modeling Notes

In the experiment, the test section extended 400 mm beyond the vegetation layer. This extent of the domain is reproduced in the simulations in order to avoid possible influence of the downstream boundary condition. The upstream boundary condition is set using the measurements located at  $x = -75 \text{ mm}$ , which allows for the reproduction of a slight non-uniformity in the flowfield. Due to difficulties in compacting the high bulk density case, the fuel layer is set to extend to 55 mm in the  $60 \text{ kg/m}^3$  simulations.

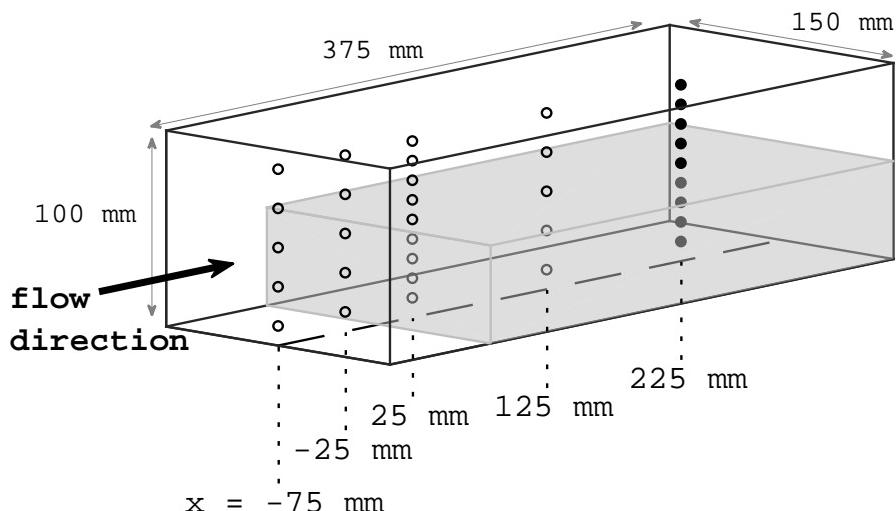


Figure 3.10: Geometry of the wind tunnel test section for the Edinburgh Vegetation Drag experiments. Vegetation filled the lower half of the  $150 \text{ mm} \times 100 \text{ mm}$  test section, starting from  $x = 0 \text{ mm}$ . Circles indicate the locations of velocity measurements, with the filled circles corresponding to those used for comparison in this guide.

## 3.22 FAA Cargo Compartments

The U.S. Federal Aviation Administration (FAA) has sponsored experiments and modeling of smoke transport within aircraft storage compartments [204, 205]. Two types of compartments were used; one from a Boeing 707 and one from a McDonnell Douglas DC-10. The 707 compartment was 6.7 m in length, 3.2 m in width, and 1.4 m in height. The DC-10 compartment was 14 m in length, 4.4 m in width, and 1.7 m in height. The fire for all experiments was fueled by a 0.1 m by 0.1 m tray of plastic resin producing a peak HRR of 5 kW [206]. The long walls of the compartments were barrel-shaped to conform to the shape of the aircraft fuselage. The fire was placed in different locations, and measurements of gas and ceiling temperature, heat flux, gas concentration, and smoke obscuration were made at a variety of locations, mostly near the ceiling.

### 3.23 FAA Polymers

As part of their efforts to characterize the burning behavior of commonly used plastics, the U.S. Federal Aviation Administration (FAA) conducted measurements of the thermal properties of charring and non-charring polymers with the specific purpose of providing input data for numerical pyrolysis models [207, 208]. The study aimed to determine whether a one-dimensional conduction/reaction model could be used as a practical tool for prediction and/or extrapolation of the results of fire calorimetry tests. The non-charring polymers included poly(methyl methacrylate) (PMMA), high-impact polystyrene (HIPS), and high density polyethylene (HDPE). The charring polymers included polycarbonate (PC) and polyvinyl chloride (PVC).

### 3.24 Fleury Heat Flux Measurements

Rob Fleury, a master's degree student at the University of Canterbury in Christchurch, New Zealand, measured the heat flux from a variety of propane fires [209]. The objective of the work was to evaluate a variety of empirical heat flux calculation methods. For the measurements, heat flux gauges were mounted on moveable dollies that were placed in front of, and to the side of, burners with dimensions of 0.3 m by 0.3 m (1:1 burner), 0.6 m by 0.3 m (2:1 burner), and 0.9 m by 0.3 m (3:1 burner). The heat release rates were set to 100 kW, 150 kW, 200 kW, 250 kW, and 300 kW. The gauges were mounted at heights of 0 m, 0.5 m, 1.0 m, and 1.5 m relative to the top edge of the burner.

### 3.25 FM Burner Experiments

A series of gas burner experiments was conducted by Zeng and Wang at FM Global in which the co-flow air stream was gradually diluted with nitrogen until flame extinction was achieved [210]. Numerical simulations were subsequently performed by Ren et al. [211]. In the experiments, a cylindrical, water-cooled steel burner (15.2 cm O.D., 13.7 cm I.D.) was placed near the floor of a 1.22 m by 1.22 m by 1.83 m tall compartment. Four fuels were used: ethylene ( $C_2H_4$ ), methane ( $CH_4$ ), propane ( $C_3H_8$ ), and propylene ( $C_3H_6$ ). The heat release rate in each experiment was 10 kW with a 1 kW ring of premixed ethylene pilot burners to stabilize the flame. At the start of each experiment, air was pumped through the floor at a rate sufficient to supply the fire with approximately 10 times the stoichiometric requirement. Subsequently, nitrogen was slowly added to the air stream until the fire was extinguished.

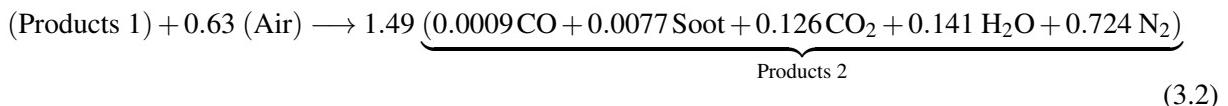
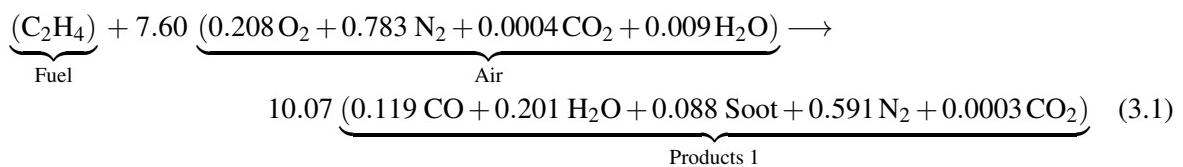
In the same enclosure and using the same burner, Ren et al. [212] made high-frequency mean and rms temperature measurements along six radial profiles above a 15 kW ethylene fire. Soot measurements were made at similar locations. The co-flow air stream at the floor was set to 20.9 %, 16.8 %, and 15.2 % oxygen volume fraction. Additional experiments were performed at 19 %, 17 %, and 15 % oxygen in which global radiation measurements were made, including total radiative fraction and the vertical distribution of radiative emission.

#### Modeling Notes

The FDS simulations of the 10 kW ethylene, methane, propane and propylene fires are run for 65 s, in which time the oxygen concentration in the co-flow stream is ramped down linearly from 21 % to 8 %. The volume flow of the co-flow stream has been increased tenfold compared to the experiments to prevent a downwash of ambient air into the sealed compartment. The 15 kW ethylene fire simulations at the various fixed oxygen levels are performed for 20 s. For these simulations, the oxygen volume fraction is specified directly, as is the co-flow stream.

The 10 kW variable fuel cases examining combustion efficiency and extinction are modeled using a two-step reaction scheme. In the first step, fuel is converted to CO, soot, and water vapor, and in the second step, the CO and Soot are oxidized to form CO<sub>2</sub>. Both reactions are fast, but the oxidation step follows the first reaction in serial. That is, in a given time step, all available oxygen first converts fuel to CO and Soot, assumed to be C<sub>0.9</sub>H<sub>0.1</sub>. Any leftover oxygen is then used to oxidize existing CO and Soot. There are two assumptions: (i) the ratio of fuel C that is converted to CO in the first reaction step (the remainder goes to Soot) and (ii) the post-flame yields of CO and Soot. For the first assumption (the intermediate step), we assume that 95 % of the carbon goes to CO for a clean fuel like methane, we assume 85 % goes to CO for propane, and that 60 % goes to CO for both ethylene and propylene. The post flame yields for each fuel are taken from Tewarson's measurements reported in the SFPE Handbook [151].

Under the assumption that Air contains 383 ppm CO<sub>2</sub> and water vapor corresponding to 40 % humidity, the full two-step reaction scheme for ethylene is written in terms of "lumped" species as follows:



The pilot ring is modeled with a "pilot fuel model". We use 36 particles arranged in a uniform ring around the burner. The mass flow rate of ethylene from each particle is set to achieve the total 1 kW from the pilot ring. In the pilot fuel model, the fuel stream from the pilot particles sees an auto-ignition temperature (AIT) of 0 K. That is, fuel emanating from the pilot particles is not subject to an ignition temperature threshold. Further, this fuel undergoes simple 1-step, fast chemistry. The fuel emanating from the main burner (for each different fuel type, including ethylene) undergoes 2-step, fast chemistry as discussed above and is subject to an ignition temperature threshold with the AIT for each fuel taken from Beyler's chapter in the SFPE Handbook [152]. Likewise, the critical flame temperatures for each fuel are taken from [152]. While there are now 3 chemical reactions for each case (a pilot fuel reaction plus the two main fuel reactions), each with its own "fuel", the CFT for the extinction model is based on the fuel for the main burner first step reaction, either methane, ethylene, propylene, or propane.

The burner surface temperature was modeled by specifying a 2.54 cm thick surface made of sand. The back side temperature was held constant at 25 °C to match the water cooled burner in the experiment.

The radiative fraction has been predicted rather than specified in all simulations.

### 3.26 FM/FPRF Data Center Experiments

The Fire Protection Research Foundation funded a series of large-scale experiments involving smoke detection in high airflow data centers as part of a research project on behalf of the NFPA 75 and NFPA 76 Technical Committees [213]. The test enclosure consisted of a data center mockup that was 4.9 m high, 4.8 m wide, and 7.3 m deep (Fig. 3.11). The mockup was divided into a 0.9 m tall subfloor with air supplied via a natural vent opening on one short wall, a 0.9 m tall ceiling plenum with air removed via a mechanical vent opening on one short wall, two 2 m tall by 0.6 m wide by 5.3 m long enclosed cold aisles located along the outer walls, and a 3.1 m tall hot aisle. Flow from the subfloor to the cold aisles occurred through grated floor tiles, flow from the cold aisles to the hot aisle was through two rows of empty equipment cabinets

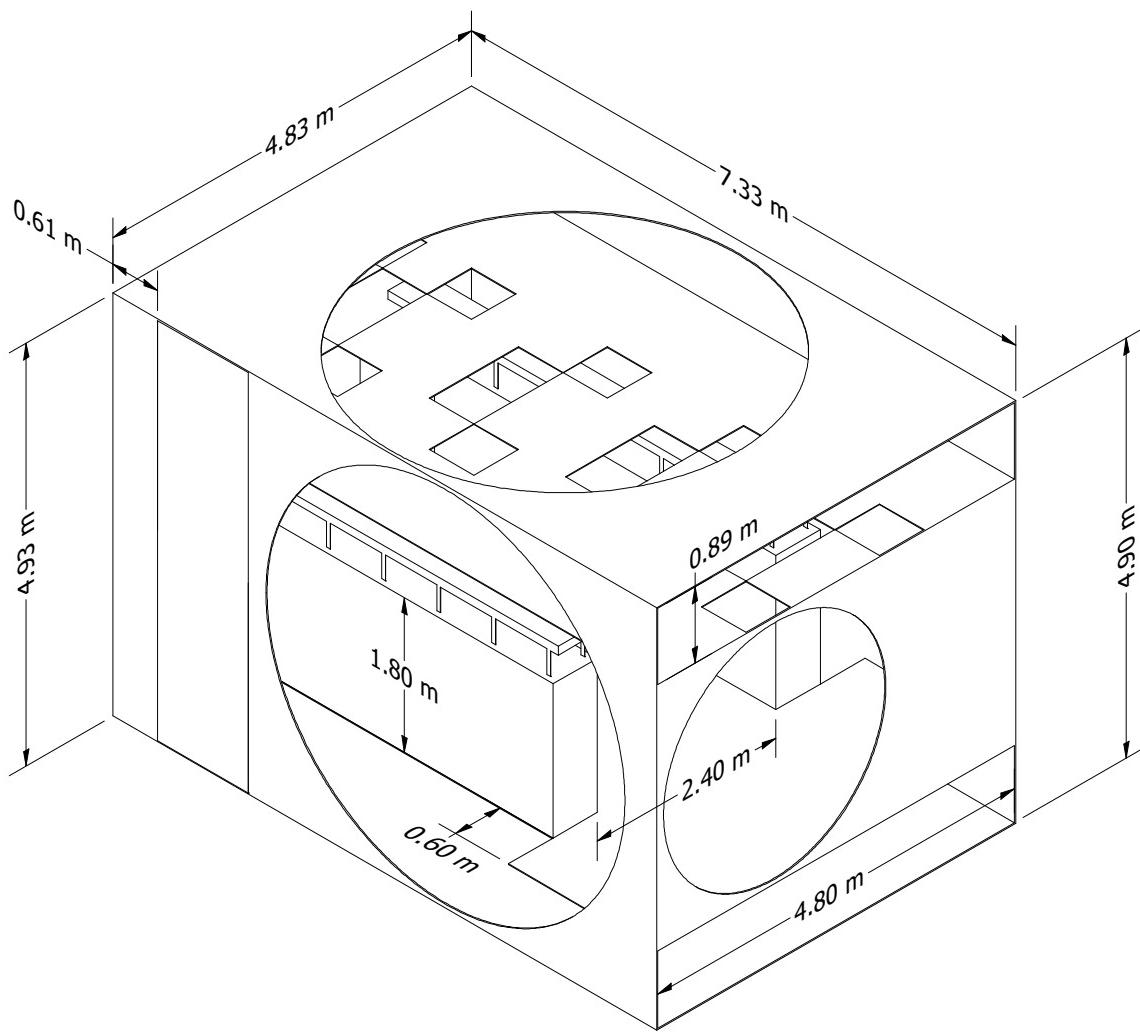


Figure 3.11: Sketch of the FM/FPRF enclosure.

with perforated metal doors, and flow from the hot aisle to the ceiling plenum was through perforated metal ceiling tiles.

Two sets of experiments were performed. The first made use of a sonic anemometer to map the flow field resulting from 78 air changes per hour (ACH) and 265 ACH. Additional measurements were made of the pressure drops through the floor and ceiling tiles. The second set of experiments measured smoke detection response to a variety of detectors from a range of typical smoke sources plus propylene (used for its ease of characterization and repeatability).

### **Modeling Notes**

The FDS model of the facility makes use of the particle screen drag model to create the pressure losses through the various metal meshes and grates. The FDS model also uses the specified leakage location model to model leakage through the seams of floor and ceiling tiles. The actual leakage area was not measured.

Instead the area was estimated using the measured pressure drop compared to the manufacturer's reported pressure drop. A description of the process used to create the FDS model and the test uncertainties can be found in a companion report documenting modeling of the tests with FDS 6.0.0 [214].

### 3.27 FM Parallel Panel Experiments

Patricia Beaulieu of Worcester Polytechnic Institute made heat flux measurements within a set of vertical parallel panels as part of a cooperative research program between Worcester Polytechnic Institute and FM Global (Factory Mutual) [215]. The experimental apparatus consisted of two vertical parallel panels, 2.4 m high and 0.6 m wide, with a sand burner at the base. The objective of the project was to measure the flame spread rate over various composite wall lining materials, but there were also experiments conducted with inert walls for the purpose of measuring the heat flux from fires fueled by propane and propylene at heat release rates of 30 kW, 60 kW, and 100 kW. A sketch of the apparatus is shown in Fig. 3.12.

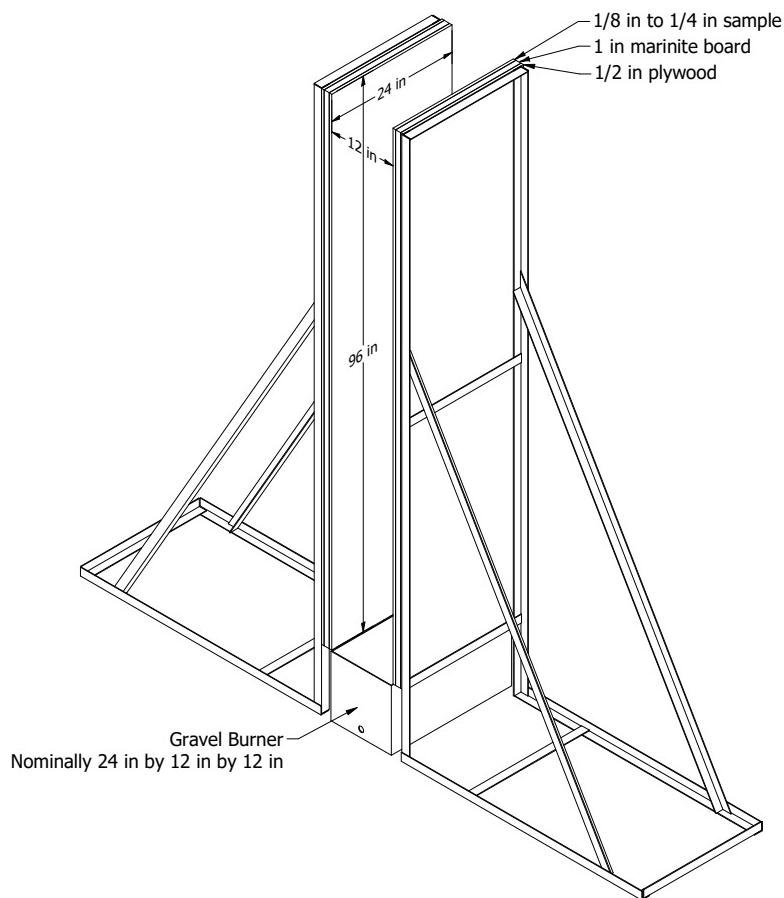


Figure 3.12: Sketch of the FM parallel panel apparatus.

## 3.28 FM/SNL Experiments

The Factory Mutual and Sandia National Laboratories (FM/SNL) test series consists of 25 compartment fire experiments conducted in 1985 for the U.S. Nuclear Regulatory Commission (NRC) by Factory Mutual Research Corporation (FMRC), under the direction of Sandia National Laboratories (SNL) [216, 217]. The primary purpose of these experiments was to provide data with which to validate computer models for various types of compartments typical of nuclear power plants. The experiments were conducted in an enclosure measuring approximately 18 m long by 12 m wide by 6 m high, constructed at the FMRC fire test facility in Rhode Island. A drawing is included in Fig. 3.13. All of the experiments included forced ventilation to simulate typical power plant conditions. Six of the experiments were conducted with a full-scale control room mock-up in place. Parameters varied during the experiments included fire intensity, enclosure ventilation rate, and fire location. Only data from nineteen experiments (Tests 1-17, 21, and 22) is used in the current study. In these experiments, the fires were fueled by a propylene gas burner, and heptane and methanol liquid pools. In the experiments not selected, the heat release was not reported and could not be estimated with confidence. Table 3.10 lists the test parameters.

The following information was provided by the test director, Steve Nowlen of Sandia National Laboratory. In particular, Tests 4, 5, and 21 were given extra attention.

**Heat Release Rate:** The HRR was determined using oxygen consumption calorimetry in the exhaust stack with a correction applied for the carbon dioxide in the upper layer of the compartment. The uncertainty of the fuel mass flow was not documented. Several tests selected for this study had the same target peak heat release rate of 516 kW following a 4 min “t-squared” growth profile. The test report contains time histories of the measured HRR, for which the average, sustained HRR following the ramp up for Tests 4, 5, and 21 have been estimated as 510 kW, 480 kW, and 470 kW, respectively. Once reached, the peak HRR was maintained essentially constant during a steady-burn period of 6 min in Tests 4 and 5, and 16 min in Test 21. Note that in Test 21, Nowlen reports a “significant” loss of effluent from the exhaust hood that could lead to an under-estimate of the HRR towards the end of the experiment.

**Radiative Fraction:** The radiative fraction was not measured during the experiment, but in this study it is assumed to equal 0.35, which is typical for a smoky hydrocarbons. It was further assumed that the radiative fraction was about the same in Test 21 as the other tests, as fuel burning must have occurred outside of the electrical cabinet in which the burner was placed.

**Measurements:** Four types of measurements were conducted during the FM/SNL test series that are used in the current model evaluation study, including the HGL temperature and depth, and the ceiling jet and plume temperatures. Aspirated thermocouples (TCs) were used to make all of the temperature measurements. Generally, aspirated TC measurements are preferable to bare-bead TC measurements, as systematic radiative exchange measurement error is reduced.

**HGL Depth and Temperature:** Data from all of the vertical TC trees were used when reducing the HGL height and temperature. For the majority of the tests, Sectors 1, 2, and 3 were used, all weighted evenly. For Tests 21 and 22, Sectors 1 and 3 were used, evenly weighted. Sector 2 was partially within the fire plume.

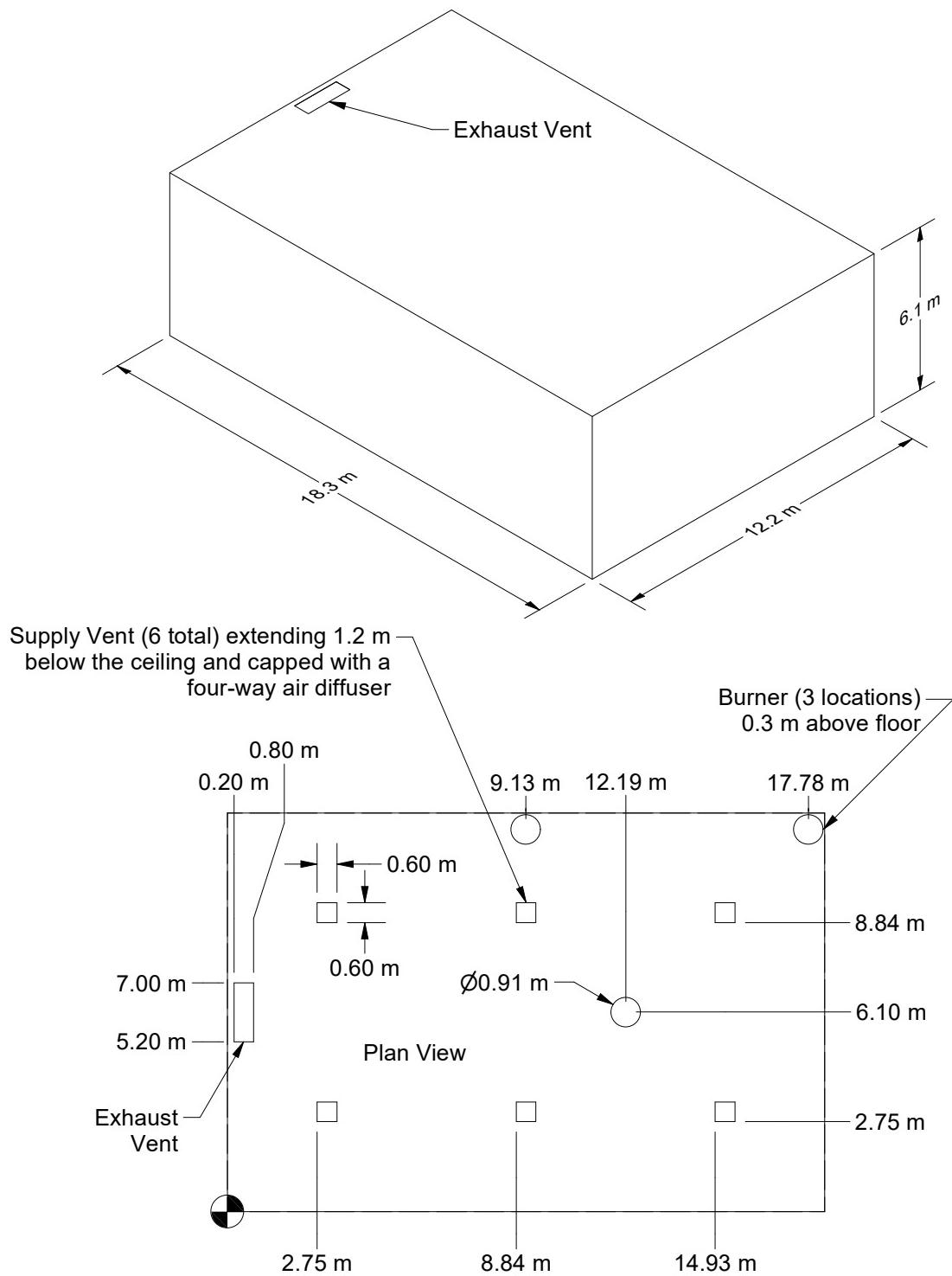


Figure 3.13: Geometry of the FM/SNL Experiments.

Table 3.10: Summary of FM/SNL Experiments. ACH stands for Air Changes per Hour.

| Test No. | Fuel Type        | Nominal Peak HRR (kW) | Fire Position | Ventilation Rate (ACH) | Room Configuration |
|----------|------------------|-----------------------|---------------|------------------------|--------------------|
| 1        | Propylene Burner | 516                   | Center        | 10                     | Empty              |
| 2        | Propylene Burner | 516                   | Center        | 10                     | Empty              |
| 3        | Propylene Burner | 2000                  | Center        | 10                     | Empty              |
| 4        | Propylene Burner | 516                   | Center        | 1                      | Empty              |
| 5        | Propylene Burner | 516                   | Center        | 10                     | Empty              |
| 6        | Heptane Pool     | 500                   | Wall          | 1                      | Empty              |
| 7        | Propylene Burner | 516                   | Center        | 1                      | Empty              |
| 8        | Propylene Burner | 1000                  | Center        | 1                      | Empty              |
| 9        | Propylene Burner | 1000                  | Center        | 8                      | Empty              |
| 10       | Heptane Pool     | 1000                  | Wall          | 4.4                    | Empty              |
| 11       | Methanol Pool    | 500                   | Wall          | 4.4                    | Empty              |
| 12       | Heptane Pool     | 2000                  | Wall          | 4.4                    | Empty              |
| 13       | Heptane Pool     | 2000                  | Wall          | 8                      | Empty              |
| 14       | Methanol Pool    | 500                   | Wall          | 1                      | Empty              |
| 15       | Heptane Pool     | 1000                  | Wall          | 1                      | Empty              |
| 16       | Heptane Pool     | 500                   | Corner        | 1                      | Empty              |
| 17       | Heptane Pool     | 500                   | Corner        | 10                     | Empty              |
| 21       | Propylene Burner | 500                   | Cabinet       | 1                      | Furnished          |
| 22       | Propylene Burner | 1000                  | Cabinet       | 1                      | Furnished          |

### 3.29 FM Vertical Wall Flame Experiments

A series of experiments was conducted by FM Global [218] in which turbulent flames were generated by flowing various gases through a vertical, water-cooled burner, 1.32 m tall and 0.38 m wide, with 0.152 m side walls. Measurements of soot depth, temperature, radiative heat flux, and radiance were made at various heights.

### 3.30 FPL Materials

The Forest Products Laboratory (FPL) of the United States Department of Agriculture maintains a public domain repository of data from cone calorimeter experiments conducted at FPL [219]. The data contains primarily wood and wood-based products tested in a variety of thicknesses tested at multiple heat fluxes. Data from eight materials tested at multiple heat fluxes are used in validation of the scaling-based pyrolysis model.

#### Modeling Notes

This database does not provide thermal properties of the materials. Thermal conductivity, specific heat capacity, and ignition temperature for these materials are specified based on data available in the literature [151].

### 3.31 Frankman Vegetation Experiments

Experiments were performed by Frankman et al. [220] at Brigham Young University in 2010 in which small wood shavings and pine needles were exposed to various levels of heat flux from a ceramic burner. Small thermocouples recorded the steady state temperatures. The fuel elements were positioned 15 cm, 25 cm, 35 cm, and 45 cm from the 23 cm by 15 cm rectangular ceramic burner with a radiative heat flux of approximately 37 kW/m<sup>2</sup>. The fuel elements were suspended by a wire with a horizontal orientation. The hydraulic diameters of the small excelsior, large excelsior and Ponderosa pine samples were reported to be 0.44 mm, 1.29 mm, and 0.70 mm, respectively.

#### Modeling Notes

These calculations are performed with a relatively crude grid because typical wildland fire simulations cannot employ fine grids. A free convection correlation for horizontal cylinders is employed for the convective heat transfer coefficient of the fuel samples. Cylindrical Lagrangian particles are used to represent the fuels with diameters equal to the reported hydraulic diameters. The burner is modeled as a hot plate with a radiative heat flux of 37 kW/m<sup>2</sup>. Nominal values of 0.1 W/m/K, 1 kJ/kg/K, and 450 kg/m<sup>3</sup> are assumed for the thermal conductivity, specific heat, and density of the vegetation. The emissivity is assumed to be 1. The results are relatively insensitive to the thermal properties because the final temperatures are largely determined via the balance of radiation heat flux on to and convective heat flux off of the fuel samples. The temperature rise of all samples does not exceed 100 °C.

### 3.32 FSRI/NIJ Materials

The National Institute of Justice (NIJ) sponsored a series of experiments to develop a database of material and reaction properties [221]. The research focused on systematically quantifying the physical conditions of each material prior to the fire, how the material will respond to the exposure of heat, and how it will perform once it has ignited [222]. The database includes 134 materials with data from cone calorimeter, Fourier transform infrared spectrometer (FTIR), Heat Flow Meter (HFM), Micro-scale Combustion Calorimeter (MCC), and Simultaneous Thermal Analyzer (STA). Technical details on each experimental method can be found in [223]. Note that not all materials in the database have data for each experiment. Cone calorimeter data at multiple heat fluxes is included for 54 materials. These data are used in validation of the scaling-based pyrolysis model.

### 3.33 Hamins Gas Burner Experiments

Anthony Hamins of NIST measured the heat flux at various points around gas burner fires [36]. Three different sized circular burners were used, with diameters of 0.10 m, 0.38 m, and 1.0 m. Three different gases were used, acetylene, methane, and propane. The heat release rates ranged from 2 kW to 200 kW, and values of  $\dot{Q}^*$  ranged from 0.04 to 10.6.

### 3.34 Harrison Spill Plumes

Roger Harrison, a student at the University of Canterbury, New Zealand, performed a series of one-tenth scale experiments to characterize thermal spill plume entrainment [224, 225, 226, 227]. The dimensions of the fire compartment were 1 m by 1 m by 0.5 m high. The height of the compartment opening was equal to the height of the compartment. The width of the opening was varied from 0.2 m to 1 m. A 0.3 m balcony

was attached to the top of the compartment opening. The balcony extended 0.5 m beyond each side of the fire compartment. The heat release rate of the fire varied from 5 kW to 15 kW. The plume entrainment rate was measured at different heights by varying the exhaust rate of gases from a hood above the compartment. Two different test configurations were used to model both detached and adhered spill plumes. A diagram of the test structure is displayed in Figure 3.14.

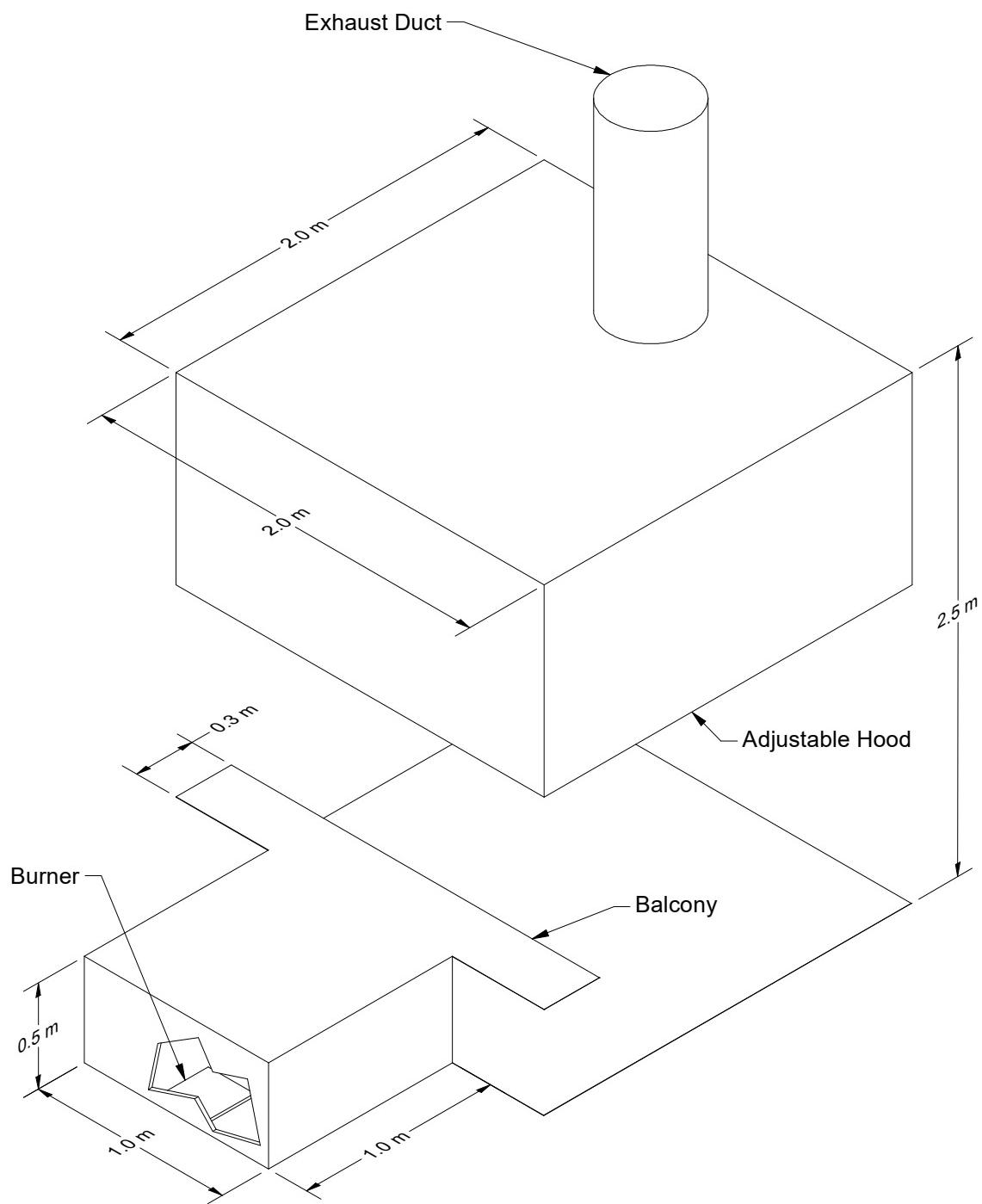


Figure 3.14: Geometry of the Harrison Spill Plumes Experiments.

### 3.35 Heskestad Flame Height Correlation

A widely used experimental correlation for flame height is given by the expression [228, 25]:

$$\frac{L_f}{D} = 3.7 (\dot{Q}^*)^{2/5} - 1.02 \quad ; \quad \dot{Q}^* = \frac{\dot{Q}}{\rho_\infty c_p T_\infty \sqrt{g} D^{5/2}} \quad (3.3)$$

where  $\rho_\infty$ ,  $c_p$ , and  $T_\infty$  are the ambient density, specific heat, and temperature.  $\dot{Q}^*$  is a non-dimensional quantity that relates the fire's heat release rate,  $\dot{Q}$ , with the diameter of its base,  $D$ . The greater the value of  $\dot{Q}^*$ , the higher the flame height relative to its base diameter.

### 3.36 Insulation Material Fire Resistance Tests

Paudel et al. [229] studied small-scale fire resistance tests for 30 different types of stone wool insulation varying in density, thickness, and organic content. During each test, a 60 cm square sample of insulation covered by a 1 mm thick steel plate was mounted to the opening of a small combustion chamber. Thus, one side of the sample was exposed to ambient ( $T_\infty$ ) conditions, and the other side was attached to the steel plate whose temperature followed the ISO 834 standard fire curve,

$$T_h(t) = T_\infty + 345 \log_{10}(8t + 1) \quad (3.4)$$

with time,  $t$ , in minutes and exposure temperature,  $T_h$ , in °C. The temperature measurements were made using K-type thermocouples covered with 30 mm square inorganic insulating pads. The pads were attached to the back side of the sample using heat-resistant glue or pins.

#### Modeling Notes

The numerical simulation is explained in Ref. [229]. Because detailed kinetic properties of the material are currently not available, the chemical decomposition parameters ( $A$ ,  $E_a$  and  $n$ ) were optimized based on the cold-side measured temperatures. Unlike in Ref. [229], the optimized values in the simulation are constant,  $A = 0.0028 \text{ s}^{-1}$ ,  $E_a = 21700 \text{ J/mol}$ , and  $n = 0.71$ . The optimization used a Monte Carlo method of 1000 Latin hypercube samples, where the sampling range was 0.001 to 1000  $\text{s}^{-1}$  for  $A$ ,  $1 \times 10^4$  to  $1 \times 10^5 \text{ J/mol}$  for  $E_a$ , and 0.1 to 1 for  $n$ .

### 3.37 JH/FRA Rail Car Experiments

The Federal Railroad Administration (FRA) in the U.S. sponsored a series of small to large-scale enclosure experiments to evaluate the impact of modern materials on HRRs in fully-developed railcar fires.

Luo, Kraft, DiDomizio, McKinnon, Hodges, Yazdani, and Lattimer [230] aggregated existing data from standard tests on historic railcar materials. Based on an analysis of the results, the authors identified a set of new materials representative of modern materials in use in railcars which had not been extensively tested. A set of 7 materials were identified for bench-scale and full-scale testing. Each material was tested in a TGA in nitrogen and air environments, a cone calorimeter at three heat fluxes in accordance with ASTM E1354, radiant panel testing in accordance with ASTM E162, and room-corner testing in accordance with NFPA 286. The 7 materials included in this test series are summarized in Table 3.11. Optimized material properties for modeling these materials were subsequently presented by Yang, Hodges, Rippe, Kraft, and Lattimer in [231]. Data from cone calorimeter and NFPA 286 experiments from these materials are used in

Table 3.11: Summary of JH/FRA Rail Car Experiments. [230]

| Sample   | Identifying Name      | Description and End-Use   |
|----------|-----------------------|---|
| Sample 1 | PVC Blend             | Opaque thermoplastic material, nominally 3.81 mm thick, used for seat backs, wall panels, window masks, partitions, and ceiling panels.                                   |
| Sample 2 | Plywood Composite     | Composite material consisting of a layer of plywood sandwiched between layers of aluminum, nominally 12.7 mm thick, used for wall panels, ceiling panels, and closets.    |
| Sample 3 | Balsa Composite       | Composite material consisting of a layer of balsa wood sandwiched between layers of aluminum, nominally 15.9 mm thick, used for wall panels, ceiling panels, and closets. |
| Sample 4 | Acrylic               | Translucent thermoplastic material 4.5 mm thick, used for light fixtures.   |
| Sample 5 | PC Blend              | Opaque thermoplastic material, nominally 4.75 mm thick, used for seat backs, wall panels, window masks, partitions, and ceiling panels.                                   |
| Sample 6 | Vinyl Ester Resin FRP | Fiberglass material, nominally 7.0 mm thick, used for wall lining, window masks, and seat components.   |
| Sample 7 | Phenolic Resin FRP    | Fiberglass material, nominally 3.27 mm thick, used for wall lining.   |

validating the scaling-based pyrolysis model. Note that two of the NFPA 286 experiments are not included in the validation (samples 1 and 5) due to significant material deformation and detachment occurring during testing.

In a follow-up study, Hodges, DiDomizio, Lattimer, and Kapahi [232] conducted a series of seventeen scaled compartment fire tests consisting of fourteen unique configurations and three repeated tests. Tests were conducted at three scales including full-scale, half-scale, and quarter-scale. The baseline full-scale compartment design was based on a standard size National Fire Protection Association (NFPA) 286 fire room, which is 2.44 m wide, 2.44 m tall, and 3.66 m deep with a single door opening which is 0.9 m wide, and 2.0 m tall. The initiating fire was a propane burner in the back-left corner of the compartment except in tests 5 and 10 which used a kerosene-type jet fuel, JP-5. The reduced-scale compartment designs were geometrically scaled except for the ventilation, which was non-linearly scaled to maintain the equivalence ratio of the compartment. The lining material thickness was kept the same at each scale to preserve the burning duration.

Six tests used combustible lining with either plywood (note, bare plywood rather than the composite used in the prior study) or the vinyl ester resin FRP from the prior study (note, 3.5 mm thickness used instead of 7.0 mm). A reduced fraction of the surfaces were covered in the combustible lining cases to control the peak HRR from the testing. The first lining configuration covered a 2.44 m x 2.44 m section on the back wall, left wall, and ceiling closest to the fire. This configuration was used for all FRP experiments, and for one plywood experiment at the quarter scale. The second lining configuration covered a 1.22 m wide x 2.44 m tall section on the left and back walls nearest the burner, and a 1.22 m x 1.22 m section on the ceiling above the burner. This configuration was used in quarter, half, and full-scale plywood experiments. The two lining configurations are shown in Figure 3.15. Note the lining coverage numbers are provided for the full-scale and were geometrically scaled down in the half and quarter scales.

Table 3.12 provides a summary of the experiments. Each HRR listed for cases with non-combustible

lining (NC) corresponded to a separate 5-minute exposure level (i.e., test 2 had 3 stages each 5 minutes long starting at 20 kW, then increasing the burner to 45 kW, then a final 5-minute stage at 50 kW). The instrumentation plan from the test series is shown in Figure 3.15 and Figure 3.16.

Data from these experiments are used in validating the thermal environment (HGL Temperature and Depth, heat flux to the surface), velocity through the ventilation, and fire growth (HRR). The tests with FRP lining are omitted from validation due to a lack of bench-scale data at the thickness used in the testing (data is available of the vinyl ester resin FRP at a 7.0 mm thickness but a 3.5 mm thickness was used in this study).

Table 3.12: Summary of JH/FRA Rail Car Experiments. [232]

| Test No. | Scale Config. | Lining Material | Initiating HRR (kW) | Peak HRR (kW) | Ventilation   | Fuel Type |
|----------|---------------|-----------------|---------------------|---------------|---------------|-----------|
| 1        | Quarter       | NC              | 20/40               | 20/40         | Door          | Propane   |
| 2        | Quarter       | NC              | 20/45/50            | 20/45/50      | Door + Window | Propane   |
| 3        | Quarter       | Plywood         | 40                  | 113           | Door          | Propane   |
| 3A       | Quarter       | Plywood Full    | 40                  | 246           | Door          | Propane   |
| 4        | Quarter       | FRP             | 40                  | 87            | Door          | Propane   |
| 5        | Quarter       | NC              | -                   | 60            | Door          | JP-5      |
| 6        | Half          | NC              | 80/160              | 80/160        | Door          | Propane   |
| 7        | Half          | NC              | 80/160/200          | 80/160/200    | Door + Window | Propane   |
| 8        | Half          | Plywood         | 160                 | 466           | Door          | Propane   |
| 9        | Half          | FRP             | 160                 | 400           | Door          | Propane   |
| 10       | Half          | NC              | -                   | 110           | Door          | JP-5      |
| 11       | Full          | NC              | 720/1,430           | 720/1,430     | Door          | Propane   |
| 12       | Full          | NC              | 720/1,610           | 720/1,610     | Door + Window | Propane   |
| 13       | Full          | Plywood         | 1,430               | 5,500         | Door          | Propane   |
| 14       | Full          | FRP             | 1,430               | 4,500         | Door          | Propane   |

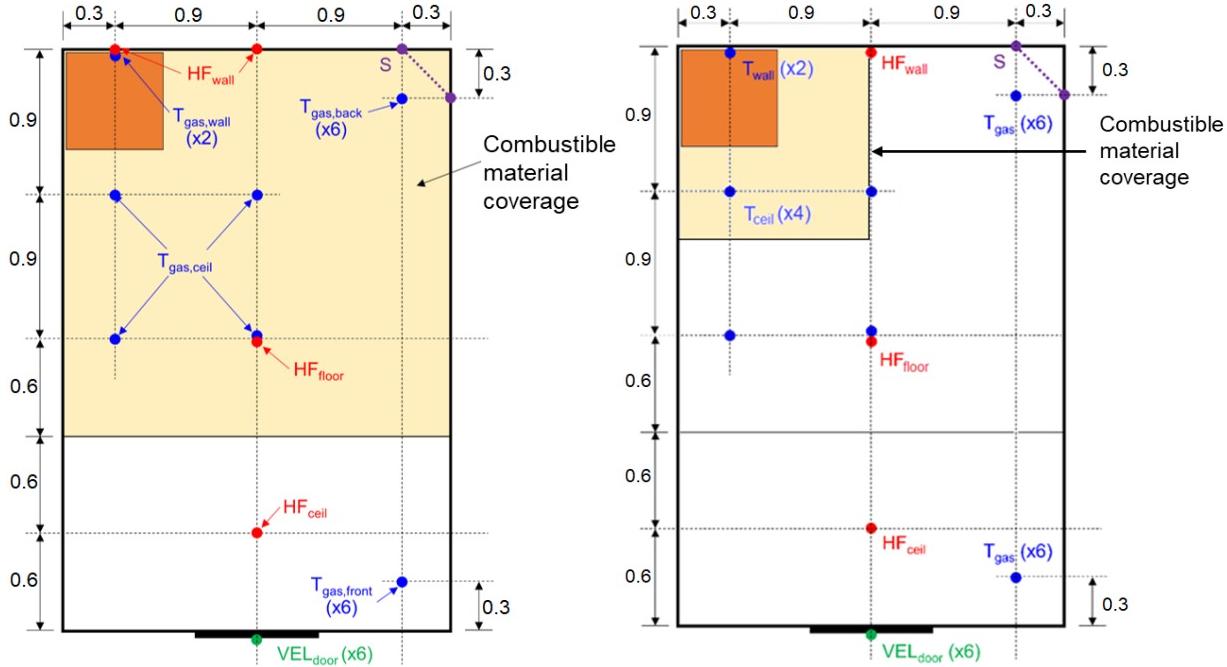


Figure 3.15: Combustible lining configuration in scaled compartment fire experiments (left) lining configuration 1 (right) lining configuration 2. Dimensions are in meters and correspond to the full-scale compartment.

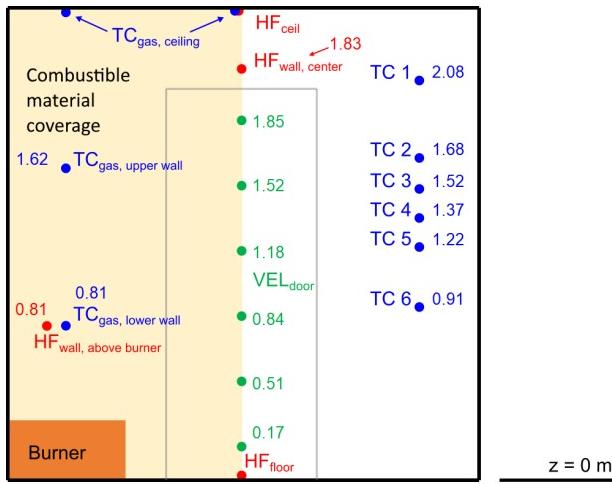


Figure 3.16: Instrumentation plan from compartment fire experiments, front view. Dimensions are in meters and correspond to the full-scale compartment.

## Modeling Notes

The simulations are performed with a spatial resolution of 2 cm for the quarter-scale, 4 cm for the half scale, and 8 cm for the fullscale.

The combustion reaction is assumed to be propane using the simple chemistry single-step combustion model. Extinction is modeled using the “Extinction 2” algorithm in which the reactions are assumed to occur if (1) the local gas temperature exceeds the `AUTO IGNITION TEMPERATURE` of 450 °C, and (2) the local oxygen concentration exceeds a temperature-dependent lower limit. The value of 450 °C is reported

for propane in Beyler's chapter of the SFPE Handbook [152].

The combustible lining experiments in this study are used to evaluate a scaling-based simplified pyrolysis model. The model input parameters used in simulating these experiments are summarized in Section 14.8.5. Additional detail on these properties can be found in previous test reports [230, 233].

Note that the full-scale test with plywood lining is included in the validation but there is uncertainty in the material thickness used. The test plan and report indicate a 6.35 mm thickness of plywood, but the total energy consumed during the test and the duration of the peak indicates a 12.7 mm thickness of plywood was more plausible. The full-scale plywood is modeled with a 12.7 mm thickness.

### 3.38 JH/NIJ Materials

The National Institute of Justice (NIJ) sponsored a series of experiments to develop a systematic approach to quantify material and reaction property inputs for accurate computer fire models [233]. The research focused on identifying the optimal experiments to use in determining these properties to minimize the variability in the determination through optimization. TGA experiments at three heating rates, cone calorimeter experiments at three thermal exposures in accordance with ASTM E1354, and MCC experiments with four oxygen concentrations in accordance with ASTM D7309-13 were conducted on seven diverse materials. The materials studied in this work included black poly(methyl methacrylate) (PMMA), fiberglass reinforced plastic (FRP), medium-density fibreboard (MDF), white pine, white spruce, cardboard, and oriented strand board (OSB). The cone calorimeter experiments from this study are used in validation of the scaling-based pyrolysis model.

### 3.39 Lattimer Tilted Wall

Lattimer with Fire Science Solutions measured the heat flux and gas temperatures from a propane fire against to a tilted wall. The experiments were sponsored by Fire Science Solutions, LLC. and were conducted at Virginia Tech in Blacksburg, VA. The wall was 1.5 m high and 0.60 m wide, with the sand burner centered on the wall. All experiments used a square sand burner with a side length of 0.30 m. The fires ranged in size from 20 kW to 75 kW. Heat fluxes and gas temperatures were measured every 0.15 m along the vertical centerline of the wall. The wall was tilted through a linear actuator attached to the back of the mounting frame. The majority of tests moved the wall during exposure to evaluate the impacts on flame separation. A picture of the apparatus is provided in Figure 3.17. A summary of the experiments conducted in this study is provided in Table 3.13.

Table 3.13: Summary of Lattimer Tilted Wall Experiments.

| Test No. | HRR (kW) | Angles (degrees)      | Delay Before Movement (s) | Movement Time Between Angles (s) | Delay at Each Angle (s) | Test Duration (s) |
|----------|----------|-----------------------|---------------------------|----------------------------------|-------------------------|-------------------|
| 1        | 35       | 0-67                  | 75                        | 24                               | 0                       | 155               |
| 2        | 50       | 0-67                  | 75                        | 23                               | 0                       | 130               |
| 3        | 75       | 0-67                  | 75                        | 23                               | 0                       | 145               |
| 4        | 50       | 0, 11, 23, 35, 49, 67 | 255                       | 4                                | 296                     | 1800              |
| 5        | 20       | 0, 10, 20             |                           |                                  |                         |                   |

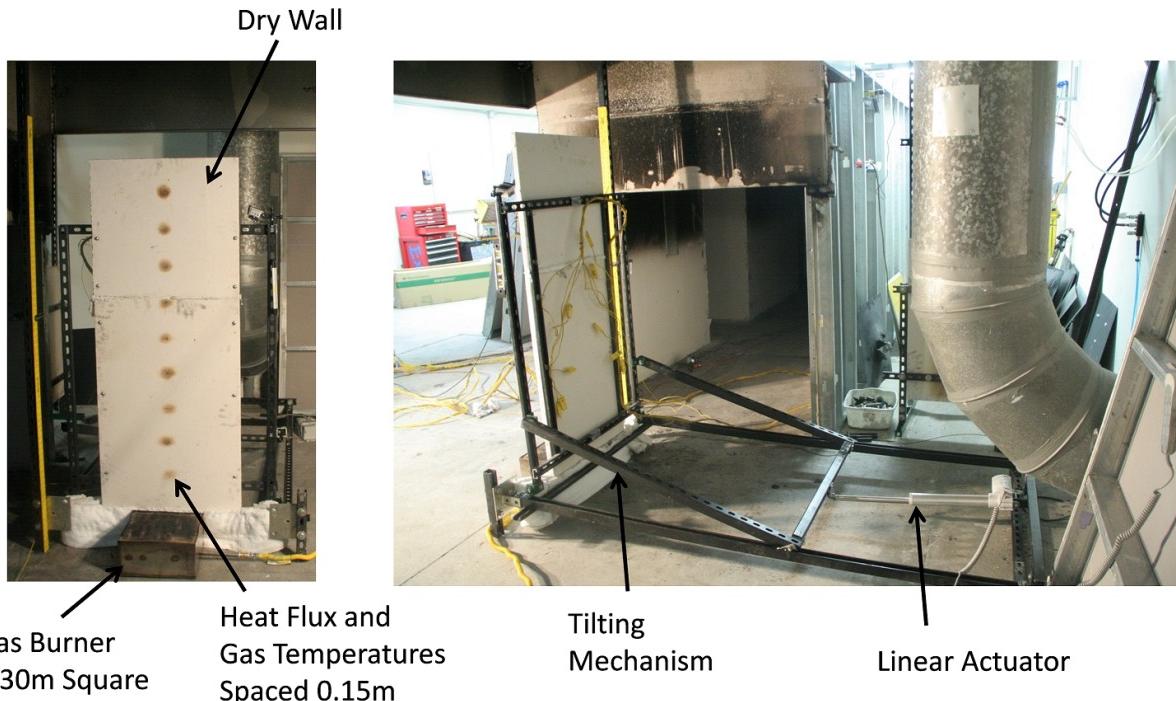


Figure 3.17: Lattimer tilted wall apparatus.

### Modeling Notes

The main case from this study used at this time is case 4 since the wall was held at each angle for close to 5 minutes. Each of these tilt angles are simulated neglecting the time history before arriving at the angle. The other cases are simulated at the start and end angles since the wall was held at that point for at least 30 seconds.

### 3.40 LEMTA Spray Test for Radiation Attenuation

Lechene et al. [234] measured the attenuation of thermal radiation passing through a water spray using a heat flux gauge. The radiation was produced by a 30 cm by 35 cm heat panel whose emission was close to a black body at 500 °C. The horizontal distance from the radiation panel to the spray nozzle was 1.5 m and to the measurement point 3 m. The heat flux gauge was positioned at the line passing through the center of the panel. Seven nozzles were arranged in a row, 10 cm apart. They were positioned 1.5 m high. The heat panel was translated vertically during the experiment, the distance between the panel upper edge and the nozzle row varying between 20 cm and 100 cm. The attenuation of radiation is defined as previously described for the BRE Spray experiments. The purpose of the simulations is to compare the measured and simulated attenuation of radiation at different heights. The water mist nozzle has been characterized by Lechene by measuring the spray angles and the water flow rate. The droplet size is set by using a PDPA measurement in a single position, 20 cm below the injection point.

### 3.41 LEMTA Spray Cooling

A series of experiments was conducted at the Laboratoire Énergies and Mécanique Théorique et Appliquée (LEMTA) to measure the temperature of a hot steel plate cooled by a water spray [235]. The 1 m by 1 m by 2 mm thick steel plate, in either a horizontal or vertical configuration, was heated by a radiant panel either 20 cm below or to the side. The 50 cm by 50 cm heater delivered a total power of approximately 50 kW with a radiative component estimated to be 25 kW, producing a radiative heat flux near 100 kW/m<sup>2</sup>. After the plate reached a steady temperature, the radiant panel was switched off and a water spray nozzle 50 cm above or to the side of the plate was activated. Three different nozzle designs were tested: (1) a single Protectospray D3 (PSD3) conical nozzle from Tyco flowing at 34.5 L/min, (2) a single SU42 conical jet nozzle from Spraying Systems flowing at 4.6 L/min, and (3) four TPU400067 flat jet nozzles from Spraying Systems flowing for a total of 1.6 L/min.

Each experiment was performed in a horizontal and vertical orientation. The steel plate temperature was measured at the center on top and bottom in order to assess the heat transfer across the plate.

#### Modeling Notes

For the simulations, the heat flux from the radiant panel is adjusted so as to approximately match the measured steady-state plate temperature at the time of spray activation. Droplet and spray parameters are taken from Ref. [235]. It is estimated that the droplets move laterally over the plate at 2 m/s. The heat conduction in the steel plate is performed in 3-D, with extra cells added in the normal direction to capture the thermal gradient in depth.

### 3.42 LEMTA/UGent Pool Fires

Beiji et al. [236] conducted pool fire experiments using methanol and heptane in square pans measuring 5.5 cm, 8.0 cm, 10.5 cm, and 15.0 cm. The depth of the liquid in each experiment was approximately 4.6 cm, and thermocouples were positioned at 9 vertical locations near the pan center, ranging from 5 mm to 45 mm above the pan floor and spaced 5 mm apart.

#### Modeling Notes

Properties of the liquid fuels are listed in Table 3.14. The thermal conductivity has been increased by a factor of 12 for heptane and 4.5 for methanol to account for the fact that FDS does not model the convection of the liquid within the pan. Details are found in Ref. [236]. Also note that the mass transfer coefficient is fixed and not calculated based on local conditions. For heptane, its value is 1.5 mm/s and for methanol, 10 mm/s.

Table 3.14: Liquid properties used in the LEMTA/UGent Pool Fires simulations [237]. “Eff. Cond.” is an effective value of the thermal conductivity that accounts for liquid convection.

| Fuel     | Liquid Density (kg/m <sup>3</sup> ) | Eff. Cond. (W/m/K) | Spec. Heat (kJ/kg/K) | Heat of Vap. (kJ/kg) | Heat of Comb. (kJ/kg) | Boiling Temp. (°C) | Soot Yield (-) | CO Yield (-) | Rad. Frac. (-) |
|----------|-------------------------------------|--------------------|----------------------|----------------------|-----------------------|--------------------|----------------|--------------|----------------|
| Heptane  | 675                                 | 1.68               | 2.24                 | 317                  | 43610                 | 98.5               | 0.037          | 0.01         | 0.29           |
| Methanol | 796                                 | 0.90               | 2.48                 | 1099                 | 21060                 | 64.8               | 0.001          | 0.001        | 0.16           |

### 3.43 LLNL Enclosure Experiments

Sixty-four compartment experiments were conducted at Lawrence Livermore National Laboratory (LLNL) in 1986 to study the effects of ventilation on enclosure fires [238]. These experiments are the basis of the Foote, Pagni, Alvares compartment temperature correlation [239].

The test enclosure was 6 m long, 4 m wide, and 4.5 m high (Fig. 3.18) with a methane rock burner in the center of the space positioned at various elevations. For most of the experiments the burner was placed on the floor. The fires varied in size,  $\dot{Q}$ , from 50 kW to 400 kW. The burner was 0.57 m in diameter and 0.23 m height. A single door was closed and sealed for most experiments, and air was pulled through the compartment at rates,  $\dot{m}$ , varying from 100 g/s to 500 g/s. In some tests the enclosure included a plenum space, where make-up air could be injected from above or below. The test matrix is listed in Table 3.15.

#### Modeling Notes

The LLNL Enclosure is modeled using a single mesh spanning the interior of the test compartment. The heat release rate of the methane burner and the thermal properties of the walls, ceiling and floor are specified based on information provided in the test report.

The test report of the LLNL Enclosure experiments lists the mass flow rate,  $\dot{m}$ , through the exhaust duct during the experiment. This mass flow rate is specified explicitly in the model. The make-up air into the compartment is supplied by an inlet duct and compartment leakage, both of which are modeled. The inlet duct is modeled as a 7 m long, 30 cm diameter circular duct with a loss coefficient of 25.6. The leakage area is then calculated based on the reported compartment under or over-pressure,  $\Delta p$ , during the experiment. The leak area is computed based on the following formulae:

$$\frac{\dot{m}}{\rho} = A_L \sqrt{\frac{2|\Delta p|}{\rho}} \quad ; \quad A_L = A_{L,\text{ref}} \left( \frac{|\Delta p|}{|\Delta p_{\text{ref}}|} \right)^{n-0.5} \quad (3.5)$$

The reference leakage area,  $A_{L,\text{ref}}$ , is estimated to be 0.0033 m<sup>2</sup>,  $n = 0.6311$ ,  $\Delta p_{\text{ref}} = 50$  Pa.

In some of the experiments, the fire was reported to have self-extinguished, in which case the model employs the relatively simple Mowrer extinction model along with the one-step fast chemistry model of combustion. The Mowrer model predicts local flame extinction when the oxygen concentration within a grid cell is less than that required to raise the cell temperature to the critical flame temperature, which is 1507 °C for methane [152].

Table 3.15: Summary of LLNL Enclosure Experiments.

| Test No. | Room Config. | $h_0$ m | $\dot{Q}$ kW | $\dot{m}$ g/s | $T_\infty$ °C | $t_{end}$ s | Test No. | Room Config. | $h_0$ m | $\dot{Q}$ kW | $\dot{m}$ g/s | $T_\infty$ °C | $t_{end}$ s |
|----------|--------------|---------|--------------|---------------|---------------|-------------|----------|--------------|---------|--------------|---------------|---------------|-------------|
| 1        | TL           | 0       | 200          | 0             | 23            | 560         | 33       | PH           | 0       | 100          | 200           | 23            | 5100        |
| 2        | TL           | 0       | 200          | 0             | 27            | 545         | 34       | PH           | 0       | 100          | 300           | 34            | 4280        |
| 3        | TL           | 0       | 400          | 0             | 27            | 300         | 35       | PH           | 0       | 100          | 400           | 22            | 4110        |
| 4        | TL           | 0       | 300          | 0             | 24            | 385         | 36       | PH           | 0       | 100          | 500           | 29            | 4060        |
| 5        | TL           | 0       | 50           | 0             | 28            | 2770        | 37       | PH           | 0       | 200          | 100           | 20            | 520         |
| 6        | TL           | 0       | 100          | 0             | 29            | 1295        | 38       | PH           | 0       | 200          | 300           | 29            | 4100        |
| 7        | TL           | 0       | 100          | 0             | 35            | 1240        | 39       | PH           | 0       | 250          | 100           | 18            | 430         |
| 8        | TL           | 0       | 200          | 0             | 35            | 555         | 40       | PH           | 0       | 200          | 400           | 28            | 4290        |
| 9        | TL           | 0       | 200          | 500           | 33            | 4220        | 41       | PH           | 0       | 150          | 100           | 20            | 970         |
| 10       | TL           | 0       | 200          | 100           | 28            | 6050        | 42       | PHE          | 2       | 200          | 180           | 30            | 5120        |
| 11       | TL           | 0       | 200          | 200           | 18            | 4780        | 43       | PHE          | 2       | 200          | 0             | 32            | 570         |
| 12       | TL           | 0       | 200          | 300           | 21            | 5440        | 44       | PHE          | 1       | 200          | 180           | 19            | 2670        |
| 13       | TL           | 0       | 200          | 400           | 28            | 5150        | 45       | PHE          | 1       | 200          | 0             | 30            | 810         |
| 14       | TL           | 0       | 200          | 400           | 28            | 5090        | 46       | PHE          | 0.6     | 200          | 180           | 19            | 960         |
| 15       | TL           | 0       | 100          | 300           | 24            | 4070        | 47       | PHE          | 0.6     | 200          | 0             | 19            | 730         |
| 16       | TL           | 0       | 200          | 300           | 21            | 6560+       | 48       | PHE          | 0.3     | 200          | 0             | 21            | 520         |
| 17       | PL           | 0       | 200          | 500           | 26            | 3980        | 49       | PHE          | 0.3     | 200          | 180           | 26            | 970         |
| 18       | PL           | 0       | 200          | 400           | 21            | 4840        | 50       | PHE          | 1       | 200          | 180           | 21            | 4730        |
| 19       | PL           | 0       | 200          | 300           | 18            | 5110        | 51       | PNE          | 1       | 200          | NAT           | 33            | 3360        |
| 20       | PL           | 0       | 200          | 200           | 16            | 6570        | 52       | PN           | 0       | 200          | NAT           | 23            | 4680        |
| 21       | PL           | 0       | 200          | 100           | 23            | 6570        | 53       | PHGS         | 0       | 200          | 185           | 33            | 1540        |
| 22       | PH           | 0       | 200          | 190           | 30            | 950         | 54       | PHGS         | 0       | 200          | 215           | 21            | 4180        |
| 23       | PH           | 0       | 200          | 215           | 28            | 4260        | 55       | PN           | 0       | 100          | NAT           | 31            | 4120        |
| 24       | PH           | 0       | 200          | 205           | 26            | 1480        | 56       | PHGW         | 0       | 200          | 190           | 20            | 1240        |
| 25       | PH           | 0       | 200          | 205           | 25            | 2050        | 57       | PHGW         | 0       | 200          | 215           | 29            | 5390        |
| 26       | PH           | 0       | 200          | 500           | 24            | 4100        | 58       | PHX          | 0       | 200          | 190           | 18            | 4090        |
| 27       | PH           | 0       | 200          | 100           | 23            | 540         | 59       | PHXE         | 1       | 200          | 190           | 24            | 4090        |
| 28       | PH           | 0       | 150          | 150           | 31            | 1870        | 60       | PN           | 0       | 400          | NAT           | 22            | 2680        |
| 29       | PH           | 0       | 250          | 250           | 28            | 1520        | 61       | TN           | 0       | 200          | NAT           | 31            | 2730        |
| 30       | PH           | 0       | 250          | 300           | 34            | 4080        | 62       | TN           | 0       | 400          | NAT           | 22            | 2660        |
| 31       | PH           | 0       | 250          | 500           | 36            | 4160        | 63       | TN           | 0       | 50           | NAT           | 28            | 3240        |
| 32       | PH           | 0       | 100          | 100           | 33            | 4110        | 64       | TN           | 0       | 100          | NAT           | 17            | 3570        |

T full compartment  
 P plenum configuration  
 L low inlet duct  
 H high inlet duct  
 E elevated fire,  $h_0$

N natural ventilation (door open)  
 X 3 ft extension on inlet opening  
 GS grate on inlet, north/south configuration  
 GW grate on inlet, east/west configuration

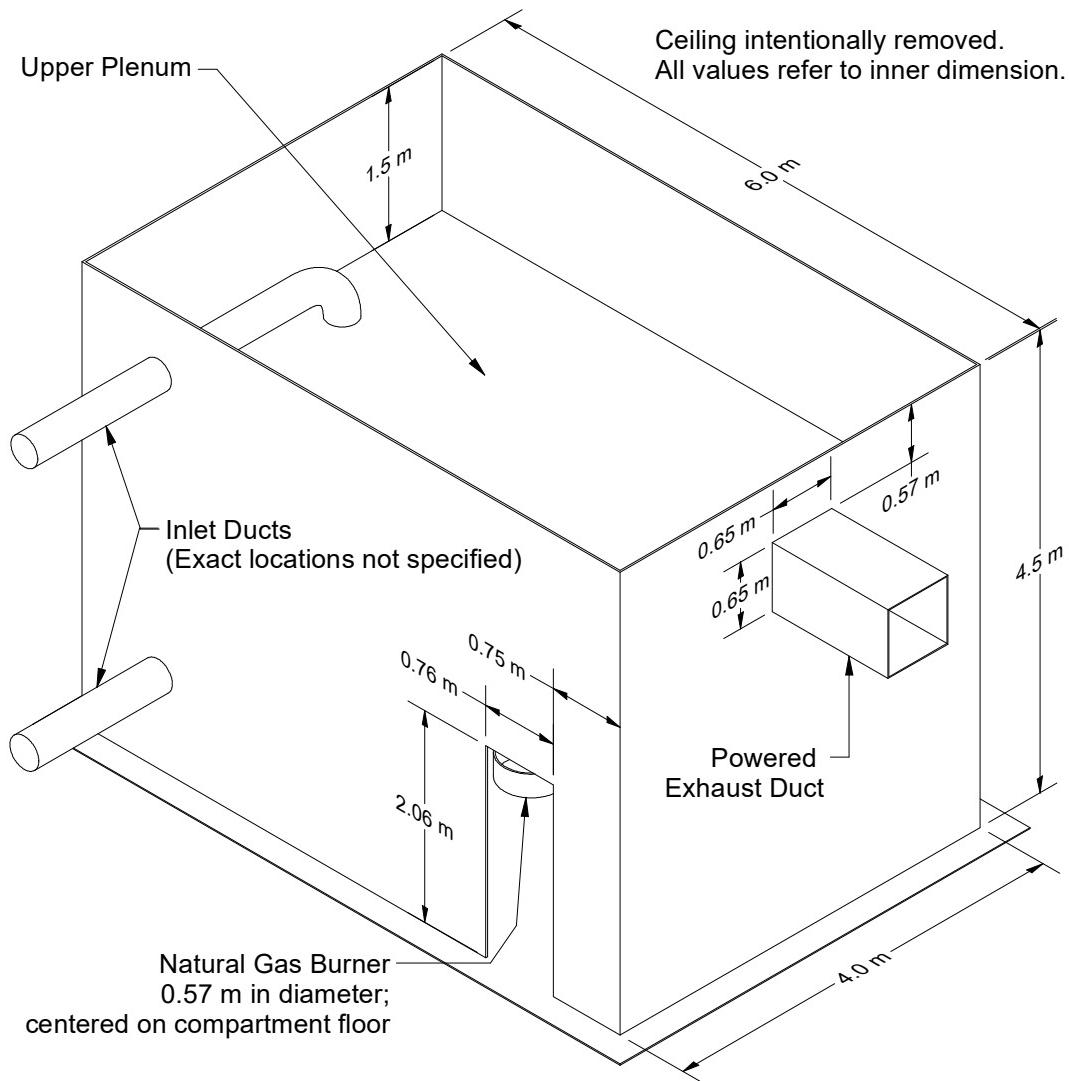


Figure 3.18: Geometry of the LLNL Enclosure Experiments.

## 3.44 LNG Dispersion Experiments

In 2006, the Fire Protection Research Foundation (FPRF) undertook a research project for the National Fire Protection Association (NFPA) Liquefied Natural Gas (LNG) Technical Committee to develop tools for evaluating LNG dispersion models. The work was carried out by the Health and Safety Laboratory (HSL), a directorate of the UK Health and Safety Executive (HSE). HSL developed the LNG Model Evaluation Protocol (MEP), which contained a structure for complete evaluation of LNG dispersion models [240]. The experiments are described in Ref. [241].

### Modeling Notes

The simulations of liquefied natural gas (LNG) dispersion experiments that are described in this report were originally designed by Jeffrey Engerer and Anay Luketa of Sandia National Laboratories on behalf of the Pipeline and Hazardous Materials Safety Administration of the U.S. Department of Transportation.

Parameters for the LNG dispersion experiments are given in Table 3.16. In some cases, values of the Monin-Obukhov parameters are taken directly from the test reports. However, for some of the experiments, these parameters were not derived using the same similarity functions as those presented above, in which case the parameters have been recomputed to best fit the measured velocity and temperature profiles. In the table,  $u_*$  is the friction velocity,  $\kappa = 0.41$  is the Von Kármán constant,  $z_0$  is the *aerodynamic* roughness length,  $\theta_*$  is the scaling potential temperature,  $\theta_0$  is the ground level potential temperature,  $L$  is the Monin-Obukhov length, and the similarity functions are those proposed by Dyer [242] and discussed in the report of the Falcon field experiments [243].

In the experiments, a fixed mass,  $m$ , of LNG was spilled onto water, forming a pool of increasing radius. For modeling purposes, it is assumed that the mass flux of natural gas from the circular pool is fixed at  $\dot{m}_{\max}'' = 0.167 \text{ kg}/(\text{m}^2 \cdot \text{s})$ , and the temperature of the gas is  $-162^\circ\text{C}$ , as suggested in the testing protocols. The diameter of the pool,  $D$ , is calculated using the assumed mass flux per unit area, the reported mass of LNG,  $m$ , and the spill duration,  $\Delta t$ .

$$D = \sqrt{\frac{4m}{\pi \dot{m}_{\max}'' \Delta t}} \quad (3.6)$$

The values of  $D$  are given in Table 3.16.

Table 3.16: Summary of LNG Dispersion Experiments.

| Series<br>Number                    | Burro  |        |        |        | Coyote |        |        |        | Falcon |       |        |         | Maplin Sands |         |  |  |
|-------------------------------------|--------|--------|--------|--------|--------|--------|--------|--------|--------|-------|--------|---------|--------------|---------|--|--|
|                                     | 3      | 7      | 8      | 9      | 3      | 5      | 6      | 1      | 3      | 4     | 27     | 34      | 35           |         |  |  |
| Parameters supplied by test reports |        |        |        |        |        |        |        |        |        |       |        |         |              |         |  |  |
| Fuel Mass, $m$ (kg)                 | 14712  | 17289  | 12453  | 10730  | 6532   | 12676  | 10139  | 28074  | 21435  | 18984 | 3714   | 2094    | 3658         |         |  |  |
| Spill Duration, $\Delta t$ (s)      | 167    | 174    | 107    | 79     | 65     | 98     | 82     | 131    | 154    | 301   | 160    | 95      | 135          |         |  |  |
| $p_0$ (mbar)                        | 948    | 940    | 941    | 940    | 936    | 939    | 942    | 908.9  | 900.8  | 906.3 | —      | —       | —            |         |  |  |
| $T_0$ (°C)                          | 34.5   | 33.8   | 32.9   | 35.4   | 39.6   | 29.3   | 24.1   | 32.2   | 35.0   | 30.8  | 14.9   | 15.2    | 16.1         |         |  |  |
| RH (%)                              | 5.2    | 7.4    | 4.5    | 14.4   | 11.3   | 22.1   | 22.8   | —      | 4.0    | 12.0  | 53     | 90      | 77           |         |  |  |
| Computed parameters                 |        |        |        |        |        |        |        |        |        |       |        |         |              |         |  |  |
| $L$ (m)                             | -9.49  | -111   | 16.2   | -142   | -8.56  | -33.2  | 82.5   | 4.96   | -422   | 69.4  | -14.4  | -75.5   | -81.2        |         |  |  |
| $u_*$ (m/s)                         | 0.255  | 0.372  | 0.074  | 0.252  | 0.310  | 0.480  | 0.210  | 0.061  | 0.305  | 0.369 | 0.190  | 0.280   | 0.315        |         |  |  |
| $z_0$ (m)                           | 0.0002 | 0.0002 | 0.0002 | 0.0002 | 0.0002 | 0.0002 | 0.0002 | 0.0002 | 0.008  | 0.008 | 0.008  | 0.0003‡ | 0.0003‡      | 0.0003‡ |  |  |
| $\theta_*$ (K)                      | -0.532 | -0.097 | 0.026  | -0.035 | -0.890 | -0.520 | 0.039  | 0.058  | -0.018 | 0.152 | -0.180 | -0.075  | -0.088       |         |  |  |
| $q''$ (W/m <sup>2</sup> )           | -154   | -41    | 2      | -10    | -314   | -284   | 9      | 4      | -5     | 58    | -39    | -24     | -32          |         |  |  |
| $D$ (m)                             | 25.9   | 27.5   | 29.9   | 32.2   | 27.7   | 31.4   | 30.6   | 19.5†  | 16.0†  | 10.8† | 13.3   | 12.8    | 14.4         |         |  |  |

‡ The roughness length was changed to 0.00002 m to better match the measured velocity and temperature profiles

† The Falcon experiments involved 4 separated spills

### 3.45 Loughborough Jet Fire Experiments

Researchers at Loughborough University, UK, conducted a series of six large-scale, high pressure jet fire experiments using natural gas and natural gas/hydrogen mixtures at the GL Noble Denton Spadeadam Test Site in Cumbria, UK [244]. For each fuel, the gas was released horizontally at high pressure (approximately 60 bar) through 20 mm, 35 mm and 50 mm diameter holes at the end of a 15 cm diameter pipe. The jet fires engulfed a 0.9 m diameter, 16 m long pipe section perpendicular to the flow direction. Heat flux measurements were made at various locations on the pipe and further afield. A typical jet fire experiment at the facility is shown in Fig. 3.19.



Figure 3.19: Photograph of a jet fire experiment at the Spadeadam Test Site.

Table 3.17 lists the key parameters for the natural gas experiments which have been chosen for this study. Note that the direction of the jet was nominally to the east, parallel to the prevailing wind. The wind deviated slightly in each experiment, as indicated in the table.

#### Modeling Notes

FDS is a low Mach number code and cannot model directly the supersonic flow at the pipe orifice. Instead, cold (-160 °C) droplets with a median volumetric diameter of 1000  $\mu\text{m}$  are injected with an initial velocity of 1000 m/s and spray angle of 10°. These droplets evaporate readily to form methane gas. No attempt is made to model the stand-off distance because there is no mechanism in FDS to account for flame suppression due to high shear.

Table 3.17: Summary of the Loughborough Jet Fire Experiments.

| Test No. | Fuel Type | Hole Diam. (mm) | Dist. to Pipe (m) | Wind Dir. (°) | Wind Speed (m/s) | Mass Flow (kg/s) | Heat Rel. Rate (MW) | Flame Length (m) | Stand-Off Distance (m) | Rad. Frac. (%) |
|----------|-----------|-----------------|-------------------|---------------|------------------|------------------|---------------------|------------------|------------------------|----------------|
| 1        | Nat. Gas  | 20              | 9.45              | 271           | 6.3              | 2.9              | 140                 | 19.8             | 6.0                    | 13.7           |
| 2        | Nat. Gas  | 35              | 15.45             | 297           | 6.2              | 9.6              | 462                 | 37.8             | 7.5                    | 17.9           |
| 3        | Nat. Gas  | 50              | 21.61             | 267           | 3.6              | 19.5             | 939                 | 49.9             | 8.7                    | 20.2           |

The grid resolution is 20 cm; thus, the circular pipe is modeled as a collection of 20 cm square rods with a cross section that is 0.8 m by 0.8 m, but with the corners removed. The velocity boundary condition is assumed to be free-slip because otherwise the polygonally-shaped obstruction would exert a fictitiously high drag force on the flow. The empirical heat transfer coefficient for the pipe is calculated using parameters appropriate for a cylindrical rather than a flat plate. The Nusselt number is taken as

$$\text{Nu} = 0.027 \text{Re}^{0.805} \text{Pr}^{1/3} \quad ; \quad \text{Re} = \frac{\rho D \|\mathbf{u}_t\|}{\mu} \quad ; \quad \text{Pr} = 0.7 \quad (3.7)$$

This correlation is appropriate for  $40,000 < \text{Re} < 400,000$  [245].

The values of radiative fraction in the model are based on the measured values reported in Table 3.17. To resolve the radiation field at the far-field radiometers, 600 angles are used in solving the radiation transport equation rather than the default 100. The radiation absorption coefficients are calculated by RadCal assuming a path length of 100 m rather than the default value of 0.1 m.

The wind profile is based on measurements made 10.85 m above the relatively flat terrain. The aerodynamic roughness length,  $z_0$ , is set to 0.03 m, appropriate for relatively flat grasslands, prairies, farms, etc. The Obukhov length,  $L$ , is set to 100,000 m, typical of a neutral atmosphere. Synthetic turbulence is generated at the upstream boundary of the computational domain, with a characteristic eddy length scale of 1 m and root-mean-square velocity fluctuation of 0.1 m/s.

**Flame Length Results:** Sec. 6.2.3

**Heat Flux Results:** Sec. 12.2.4

## 3.46 McCaffrey Plume Experiments

In 1979, at the National Bureau of Standards (now NIST), Bernard McCaffrey measured centerline temperature and velocity profiles above a porous, refractory burner. There were five distinct heat release rates, ranging from 14 kW to 57 kW. The fuel was natural gas (35 kJ/L [45 MJ/kg assuming 19 kg/kmol as mole weight for natural gas]). The burner was square, 0.3 m on each side. The results of the experiments are reported in Reference [246]. Along the centerline of the burner, velocity and temperature were measured using bi-directional probes and thermocouples, respectively. The centerline data collapses when scaled by the Froude number as shown in Fig. 3.20. Radiant fraction measurements for natural gas were made in [247]. For convenience, we have extracted the data from that report for the heat release rates reported in [246]. See Table 3.18. The burner surface temperatures are extrapolated to the surface location from a least squares fit of the temperature data below  $z/Q^{2/5} = 0.05 \text{ m} \text{W}^{-2/5}$ . The extrapolations for each power are shown in Fig. 3.21.

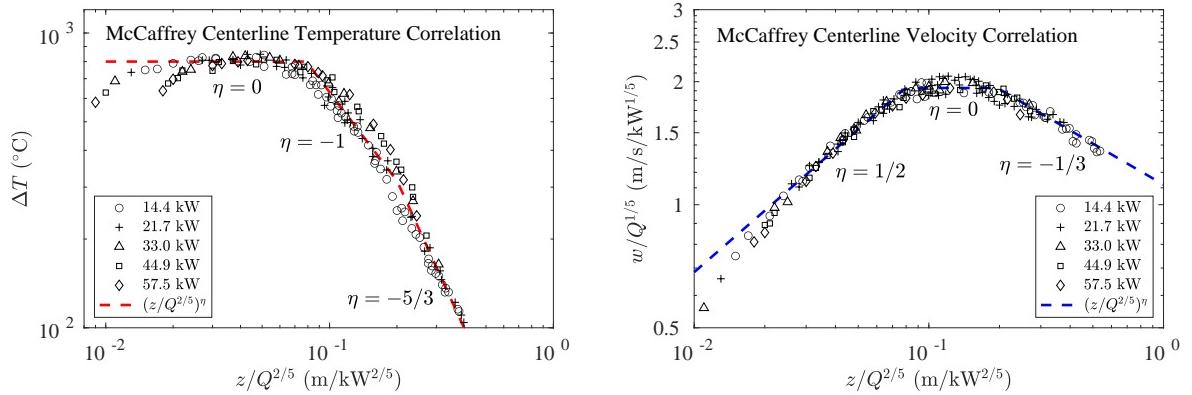


Figure 3.20: McCaffrey Plume Centerline Temperature and Velocity Correlations (dashed lines) and raw data (symbols).

Table 3.18: Summary of McCaffrey Plume Experiments, 1979.

| $Q$ (kW) | $Q^*$ | $D^*$ (m) | HRRPUA (kW/m <sup>2</sup> ) | $\chi_r$ | $T_{\text{surf}}$ (°C) |
|----------|-------|-----------|-----------------------------|----------|------------------------|
| 14.4     | 0.270 | 0.178     | 160                         | 0.17     | 750                    |
| 21.7     | 0.407 | 0.209     | 241                         | 0.21     | 716                    |
| 33.0     | 0.618 | 0.248     | 367                         | 0.25     | 630                    |
| 44.9     | 0.841 | 0.280     | 499                         | 0.27     | 608                    |
| 57.5     | 1.07  | 0.309     | 639                         | 0.27     | 534                    |

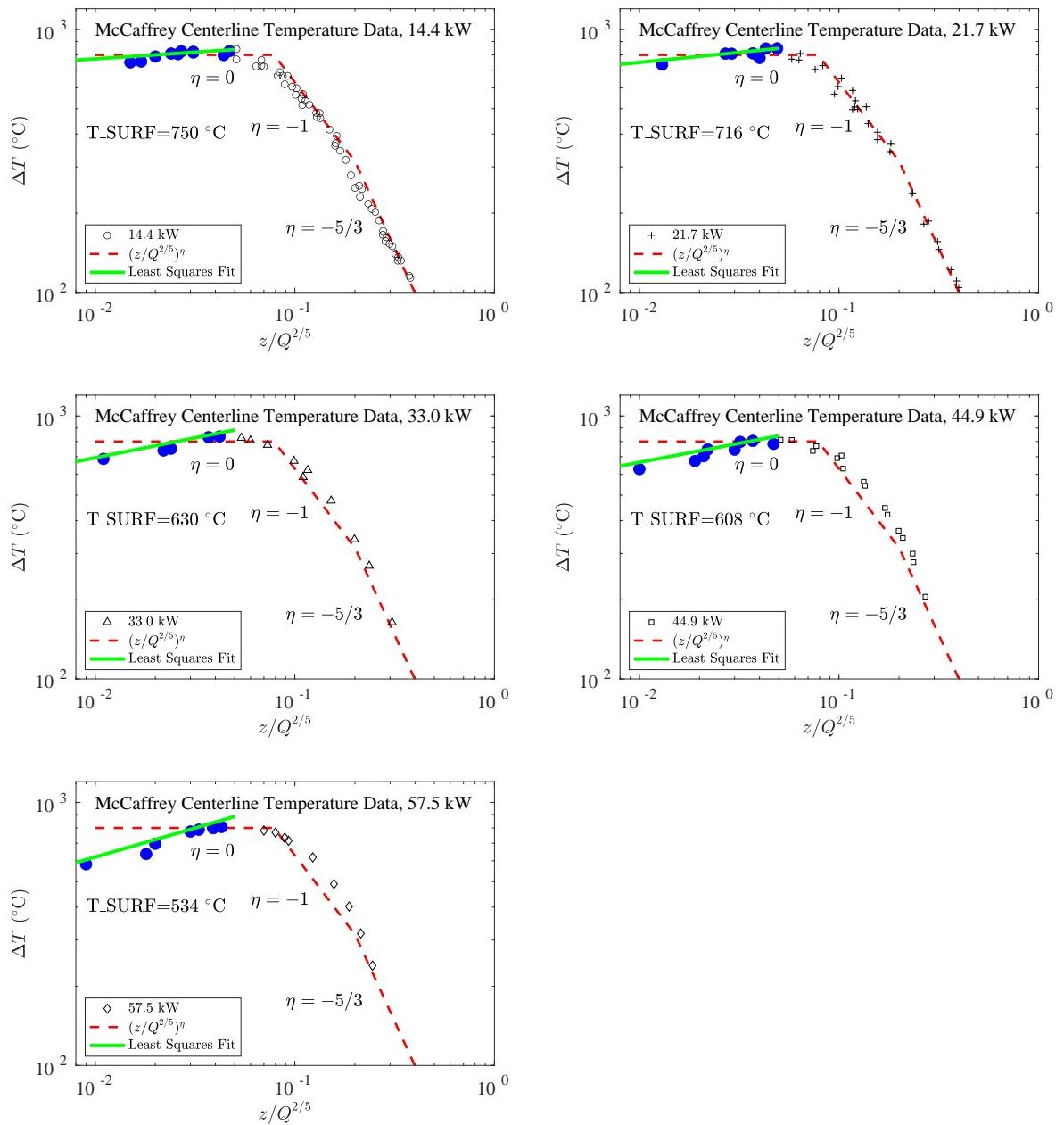


Figure 3.21: McCaffrey Plume Burner Surface Temperatures.

### 3.47 Memorial Tunnel Experiments

Between 1993 and 1995, 98 fire ventilation experiments were conducted in a decommissioned road tunnel near Charlestown, West Virginia [248]. The experiments were intended to support the design of the ventilation system for the Central Artery Tunnel Project in Boston, Massachusetts.

The Memorial Tunnel is approximately 854 m long, 8.8 m wide, and 7.9 m tall at the peak of its semi-circular ceiling, with a 3.2 % grade uphill from its south to north portal. At each portal, a fan room 4.3 m above the roadway extends 21.3 m into the tunnel. There is also a walkway along the west tunnel wall.

The fuel used in the experiments is described in the report as a “low sulfur No. 2 fuel oil.” The fuel was pumped into pans sized to produce nominally 50 MW, 20 MW, 10 MW, and 30 MW fires. Using a combination of pans, fires of 10 MW, 20 MW, 50 MW or 100 MW were produced.

Eighty-one experiments employed *transverse* ventilation; that is, a ceiling was mounted 4.4 m above the roadway and fans at both ends of the tunnel supplied or exhausted air from the tunnel via vents in the ceiling or along the west wall near the roadway. The other seventeen experiments employed *longitudinal* ventilation in which the ceiling was removed and jet fans were installed in sets of three at various positions along the length of the tunnel. Tables 3.19 and 3.20 list the nominal parameters of each experiment.

The experiments employing longitudinal ventilation, listed in Table 3.20, are identified in the test report as Sequence 15 (natural ventilation), Sequence 17 (15 fans installed uphill of the fuel pans), and Sequence 18 (9 additional fans installed downhill of the fuel pans). A sketch of the tunnel cross-section is shown in Fig. 3.22. The fans were installed in sets of three, with each fan centerline a distance of 2.3 m from the curved ceiling and 2.4 m apart. Each fan had an inner diameter of 1.26 m and a volume flow of 42.9 m<sup>3</sup>/s (91 000 cfm). Varying numbers of fans were operated during each experiment to determine the “critical velocity” required to prevent smoke “backlayering;” that is, the spread of smoke in the uphill direction against the flow of air in the downhill direction.

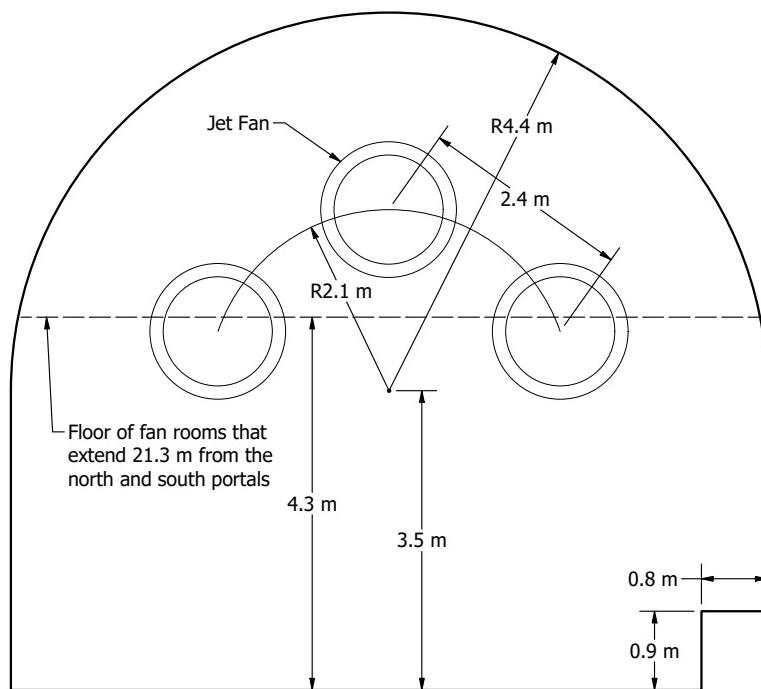


Figure 3.22: Sketch of the Memorial Tunnel cross section.

Table 3.19: Summary of Memorial Tunnel Experiments. Note that the “Sequence” refers to a set of experiments with a similar ventilation configuration.

| Test Number | Sequence Number | Heat Release Rate (MW) | Test Number | Sequence Number | Heat Release Rate (MW) |
|-------------|-----------------|------------------------|-------------|-----------------|------------------------|
| 101CR       | 1               | 10                     | 239         | 6               | 100                    |
| 102         | 1               | 20                     | 244B        | 5               | 20                     |
| 102R1       | 1               | 20                     | 245B        | 6               | 20                     |
| 102R        | 1               | 20                     | 246B        | 6               | 20                     |
| 103         | 1               | 20                     | 247B        | 3               | 20                     |
| 104         | 1               | 20                     | 248B        | 3               | 20                     |
| 105         | 1               | 20                     | 249B        | 3               | 20                     |
| 106         | 1               | 20                     | 250B        | 6               | 20                     |
| 107         | 1               | 20                     | 251B        | 6               | 20                     |
| 108         | 1               | 20                     | 252B        | 3               | 20                     |
| 109         | 1               | 20                     | 301A        | 8               | 20                     |
| 110         | 1               | 50                     | 302A        | 8               | 20                     |
| 111         | 1               | 50                     | 303A        | 8               | 20                     |
| 112A        | 1               | 20                     | 305A        | 8               | 20                     |
| 113A        | 1               | 50                     | 306A        | 8               | 20                     |
| 115A        | 1               | 50                     | 309A        | 8               | 50                     |
| 126B        | 1               | 20                     | 312A        | 8               | 50                     |
| 126BR1      | 1               | 20                     | 313A        | 8               | 50                     |
| 128B        | 1               | 20                     | 314         | 9               | 10                     |
| 202         | 3               | 20                     | 315A        | 101             | 10                     |
| 203         | 3               | 20                     | 316         | 9               | 20                     |
| 205         | 3               | 20                     | 317A        | 102             | 10                     |
| 207A        | 3               | 20                     | 318A        | 101             | 10                     |
| 208A        | 3               | 20                     | 319A        | 102             | 10                     |
| 210         | 3               | 20                     | 320A        | 102             | 10                     |
| 212         | 3               | 20                     | 321A        | 9               | 50                     |
| 214A        | 3               | 50                     | 338B        | 8               | 20                     |
| 215A        | 3               | 50                     | 339B        | 8               | 20                     |
| 216A        | 3               | 50                     | 340B        | 8               | 20                     |
| 217A        | 3               | 50                     | 341B        | 8               | 20                     |
| 218B        | 3               | 20                     | 342B        | 8               | 20                     |
| 223         | 4               | 20                     | 343B        | 8               | 20                     |
| 226         | 5               | 20                     | 344B        | 8               | 20                     |
| 227A        | 5               | 20                     | 345B        | 8               | 20                     |
| 229         | 6               | 20                     | 346B        | 8               | 20                     |
| 230         | 6               | 20                     | 401A        | 13              | 50                     |
| 231         | 6               | 20                     | 403A        | 13              | 20                     |
| 233         | 6               | 20                     | 404A        | 14              | 20                     |
| 235         | 6               | 50                     | 407B        | 13              | 20                     |
| 236         | 6               | 50                     | 408B        | 13              | 20                     |
| 238A        | 6               | 50                     |             |                 |                        |

Table 3.20: Summary of Memorial Tunnel Experiments.

| Test Number | Sequence Number | Heat Release Rate (MW) | Number of Fans | Fan Start Time (min) |
|-------------|-----------------|------------------------|----------------|----------------------|
| 501         | 15              | 20                     | 0              | N/A                  |
| 502         | 15              | 50                     | 0              | N/A                  |
| 605         | 17              | 10                     | 1-15           | 0                    |
| 606A        | 17              | 10                     | 0-3            | 5                    |
| 607         | 17              | 20                     | 2-3            | 0                    |
| 608         | 17              | 20                     | 0-4            | 2                    |
| 610         | 17              | 50                     | 4-6            | 0                    |
| 611         | 17              | 50                     | 0-6            | 2                    |
| 612B        | 17              | 50                     | 0-10           | 5                    |
| 615B        | 17              | 100                    | 0-6            | 2                    |
| 617A        | 17              | 10                     | 1-5            | 0                    |
| 618A        | 17              | 20                     | 0-4            | 2                    |
| 621A        | 17              | 100                    | 2-8            | 0                    |
| 622B        | 17              | 50                     | 0-10           | 0                    |
| 623B        | 18              | 20                     | 1-6            | 0                    |
| 624B        | 18              | 50                     | 0-7            | 2                    |
| 625B        | 18              | 100                    | 3-7            | 0                    |

### Modeling Notes

The simulations of the Memorial Tunnel experiments are performed with a 0.28 m uniform grid. This grid size is chosen so that the exit area of the jet fans can be approximated by a four by four array of cells. The jet fans are modeled as rectangular ducts with a specified volume flow of 42.9 m<sup>3</sup>/s (91 000 cfm). The fan speed is ramped up or down in approximately 10 s.

The 854 m tunnel is divided into 84 equal lengths. Rectangular obstructions approximate the semi-circular tunnel ceiling, vehicle silhouettes, and instrumentation packages.

The fuel is assumed to be n-heptane with a soot yield of 3.7 % and CO yield of 1.0 % [151]. The heat release rates of the fires are specified as functions of time following the measured curves found in the test report.

The results of the simulations are found in Sec. 7.4.2.

## 3.48 Montoir LNG Fires

In 1987, British Gas, British Petroleum, Shell, Elf Aquitaine, Total CFP, and Gaz de France conducted 35 m diameter LNG pool fire experiments [249]. The construction of the test facility was carried out by Gaz de France near the Montoir de Bretagne methane terminal. Three fire experiments were performed under different wind conditions. The Montoir site was selected because the ground is level and obstruction free. Wide angle radiation measurements were made at various locations around the fires, extending outwards approximately 300 m. A bund constructed of lightweight concrete and sand, approximately 1 m tall, surrounded the 35 m pool.

A summary of the key test parameters is given in Table 3.21. Note that results were compiled for specific time intervals during each experiment.

Table 3.21: Summary of the Montoir LNG Fire Experiments.

| Test | Time Interval (s) | Burning Rate (kg/m <sup>2</sup> /s) | Wind Direction (deg) | 9 m Wind Speed (m/s) | Amb. Temp. (°C) | Rel. Hum. (%) | Atm. Pres. (mbar) |
|------|-------------------|-------------------------------------|----------------------|----------------------|-----------------|---------------|-------------------|
| 1    | 60-100            | 0.12                                | 59                   | 2.5                  | 25              | 53            | 1022              |
|      | 130-170           | 0.13                                | 70                   | 4.8                  |                 |               |                   |
| 2    | 35-50             | 0.14                                | 268                  | 6.8                  | 21              | 54            | 1015              |
|      | 65-85             | 0.15                                | 263                  | 9.8                  |                 |               |                   |
|      | 100-130           | 0.16                                | 260                  | 10.3                 |                 |               |                   |
|      | 165-185           | 0.15                                | 257                  | 9.1                  |                 |               |                   |
| 3    | 57-70             | 0.11                                | 87                   | 1.9                  | 14              | 85            | 1009              |
|      | 90-120            | 0.13                                | 79                   | 3.5                  |                 |               |                   |
|      | 130-160           | 0.13                                | 82                   | 4.2                  |                 |               |                   |

### Modeling Notes

The experiments are simulated using the specified fuel burning rates for the several time periods during each experiment. The fuel is assumed to be methane. The atmosphere is assumed to be unstable with an Obukhov length,  $L = -350$ , and the ground surface is roughly open with an assumed aerodynamic roughness,  $z_0 = 0.1$  m. The relative humidity, ambient temperature and pressure, and wind speed at 9 m are specified in Table 3.21.

The radiative fraction is assumed to 0.14 based on field estimates and the radiative path length is assumed to be 300 m; that is, the effective absorption coefficients of the various gas mixtures are evaluated over a distance of 300 m. 600 solid angles, rather than the default 100, are used to solve the radiative transport equation. The soot yield is assumed to be 0.01.

**Flame Height Results:** Sec. 6.2.3

**Flame Tilt Results:** Sec. 6.3

**Heat Flux Results:** Sec. 12.2.5

## 3.49 NBS Multi-Room Experiments

The National Bureau of Standards (NBS, which is now called the National Institute of Standards and Technology, NIST) Multi-Room Experiments consisted of 45 fire tests representing 9 different sets of conditions were conducted in a three-room suite (see Fig. 3.23). The experiments were conducted in 1985 and are described in detail in Ref. [250]. The suite consisted of two relatively small rooms, connected via a relatively long corridor. The fire source, a gas burner, was located against the rear wall of one of the small compartments. Fire tests of 100 kW, 300 kW and 500 kW were conducted. For the current study, only three 100 kW fire experiments have been used, including Test 100A from Set 1, Test 100O from Set 2, and Test 100Z from Set 4. These tests were selected because they had been used in prior validation studies, and because these tests had the steadiest values of measured heat release rate during the steady-burn period.

Following is additional information provided by the test director, Richard Peacock of NIST:

**Heat Release Rate:** In the two tests for which the door was open, the HRR during the steady-burn period measured via oxygen consumption calorimetry was 110 kW with an uncertainty of about 15 %, consistent with the replicate measurements made during the experimental series and the uncertainty typical of oxygen consumption calorimetry. It was assumed that the closed door test (Test 100O) had the same HRR as the open door tests.

**Radiative Fraction:** Natural gas was used as the fuel in Test 100A. In Tests 100O and 100Z, acetylene was added to the natural gas to increase the smoke yield, and as a consequence, the radiative fraction increased. The radiative fraction of natural gas has been studied previously, whereas the radiative fraction of the acetylene/natural gas mixture has not been studied. The radiative fraction for the natural gas fire was assigned a value of 0.20, whereas a value of 0.30 was assigned for the natural gas/acetylene fires.

**Measurements:** Only two types of measurements conducted during the NBS test series were used in the evaluation considered here, because there was less confidence in the other measurements. The measurements considered here were the HGL temperature and depth, in which bare bead TCs were used to make these measurements. Single point measurements of temperature within the burn room were not used in the evaluation of plume or ceiling jet algorithms. This is because the geometry was not consistent in either case with the assumptions used in the model algorithms of plumes or jets. Specifically, the burner was mounted against a wall, and the room width-to-height ratio was less than that assumed by the various ceiling jet correlations.

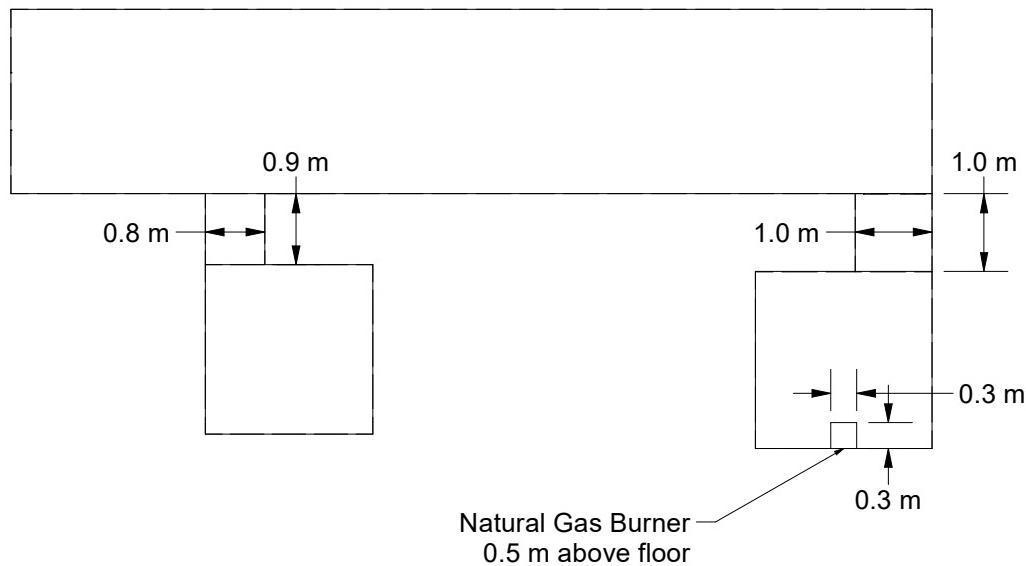
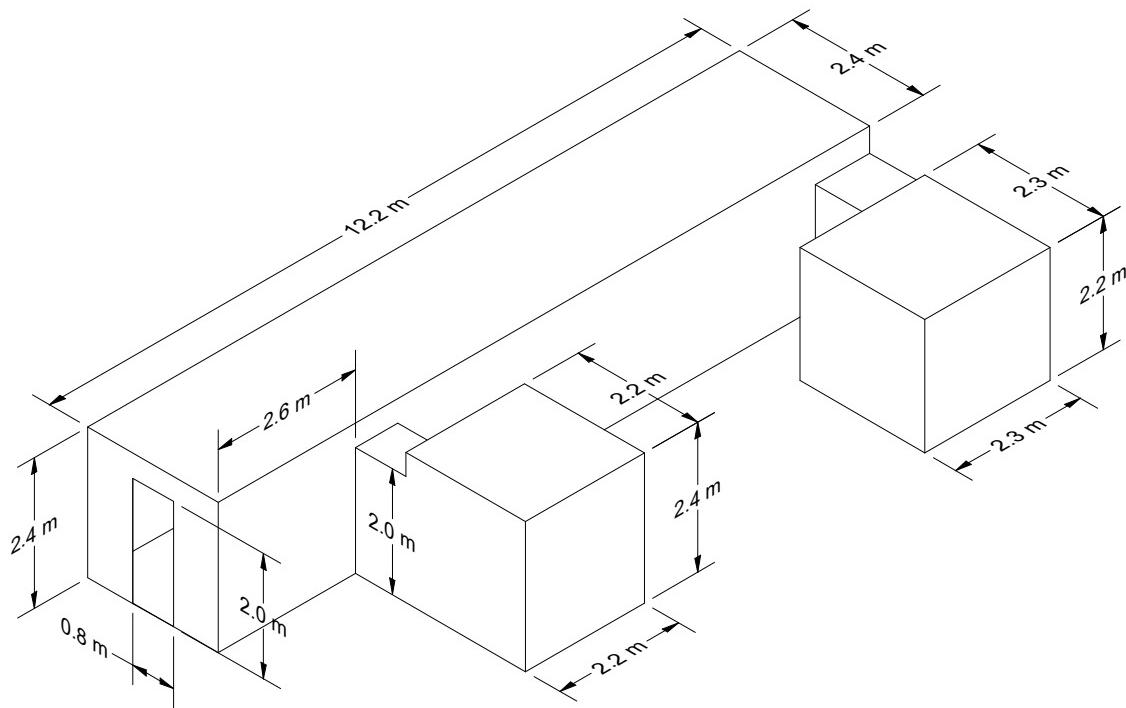


Figure 3.23: Geometry of the NBS Multi-Room Experiments.

## 3.50 NIST Composite Beam Experiments

A set of experiments was conducted in the Large Fire Laboratory at NIST to study the behavior of long-span steel-concrete composite floor beams designed and constructed following U.S. building codes and standards [251]. The composite beam consisted of a 12.8 m long W18×35 steel beam and an 16 cm thick lightweight concrete slab cast on top of 7.6 cm deep ribbed steel decking. Drawings of the compartment are shown in Figs. 3.24 through 3.26.

Simultaneous mechanical and fire loading was applied to the specimens. The measurements focused on evaluation of the characteristics of the fire loading, temperatures, and structural responses of the specimens to fires.

### Modeling Notes

The simulations of the NIST Composite Beam experiments are performed with 5 cm grid cells and 32 meshes. The calculations are sped up by a factor of 10 using `TIME_SHRINK_FACTOR=10`, whereby a 60 min experiment is simulated in 6 min of real time because the heat release rate is held steady for most of the experiment. The specific heats of all solid materials are reduced by a factor of 10 automatically to account for the change in time scale.

Because these experiments involve a global equivalence ratio of approximately 1, the two-step simple chemistry model is used, where soot and CO are produced when the fire becomes under-ventilated.

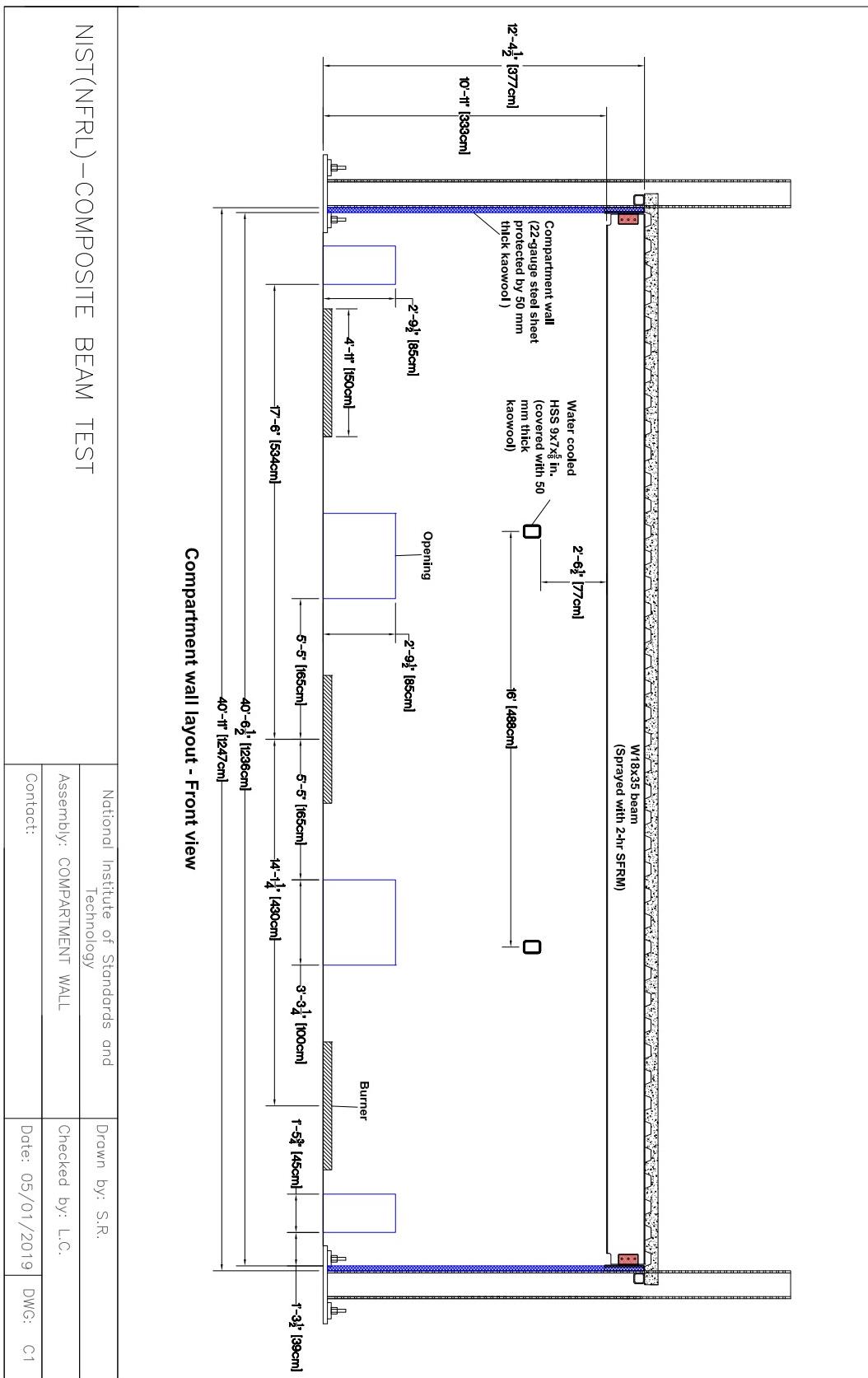


Figure 3.24: Elevation view of NIST Composite Beam experiments.

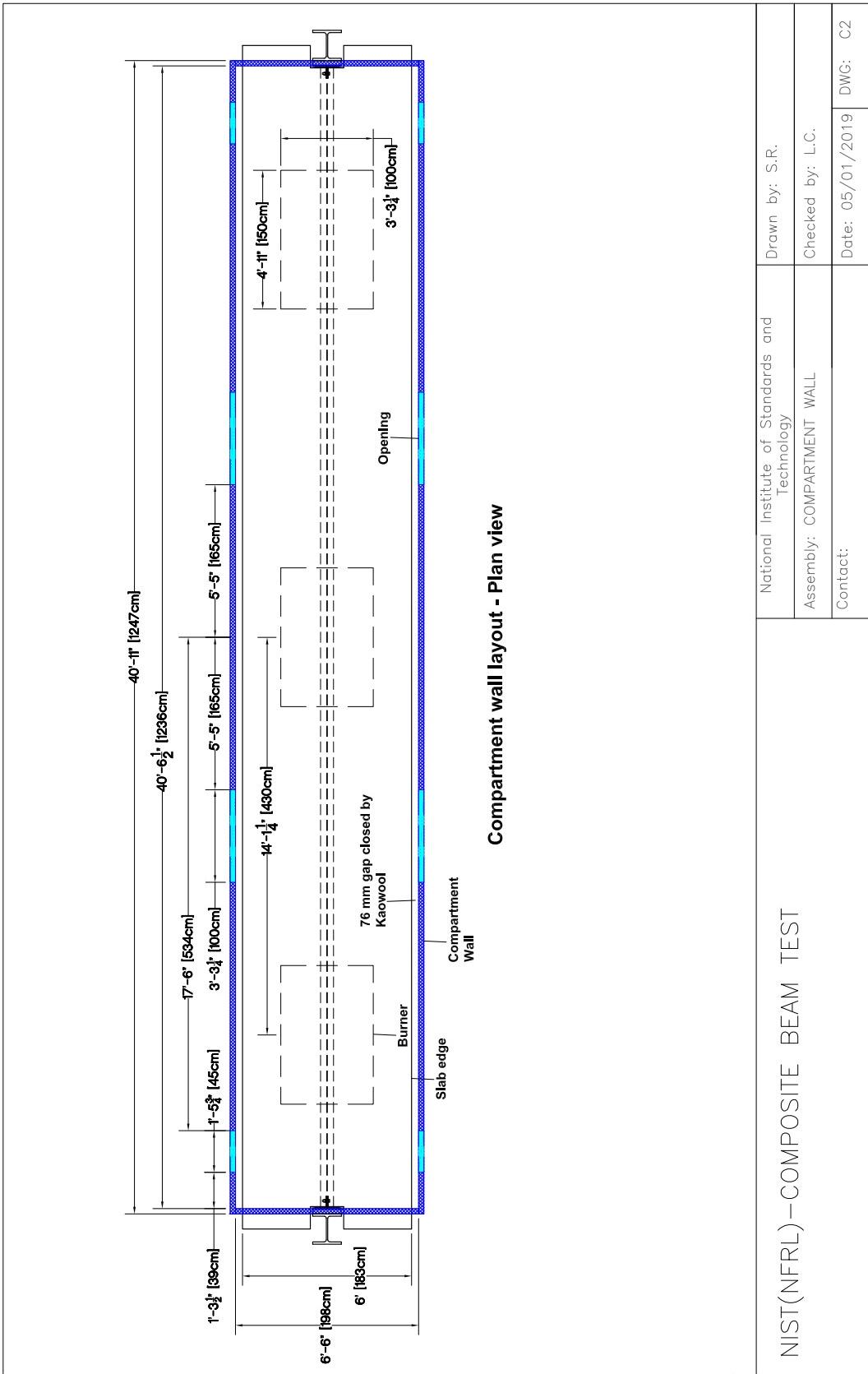


Figure 3.25: Plan view of NIST Composite Beam experiments.

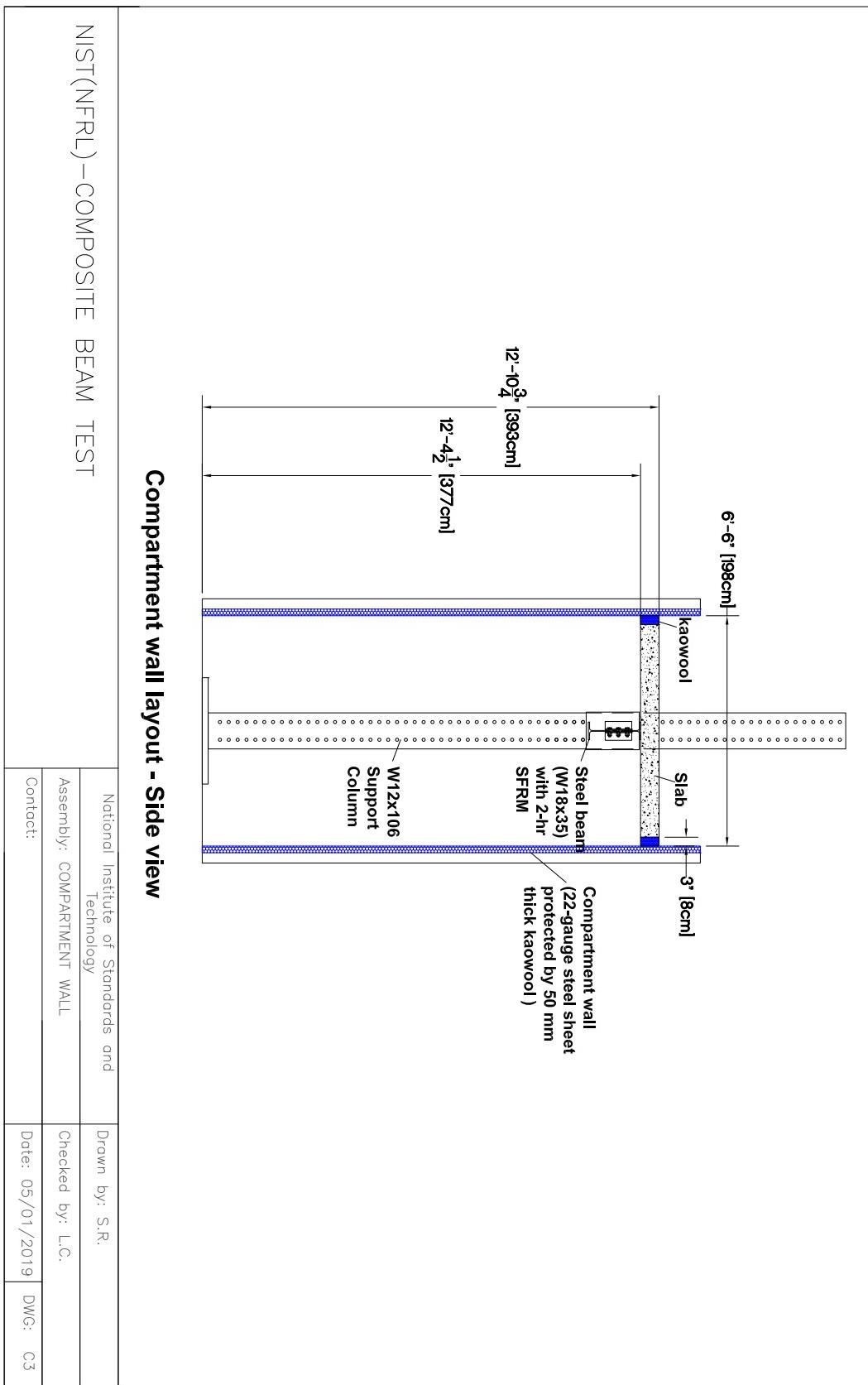
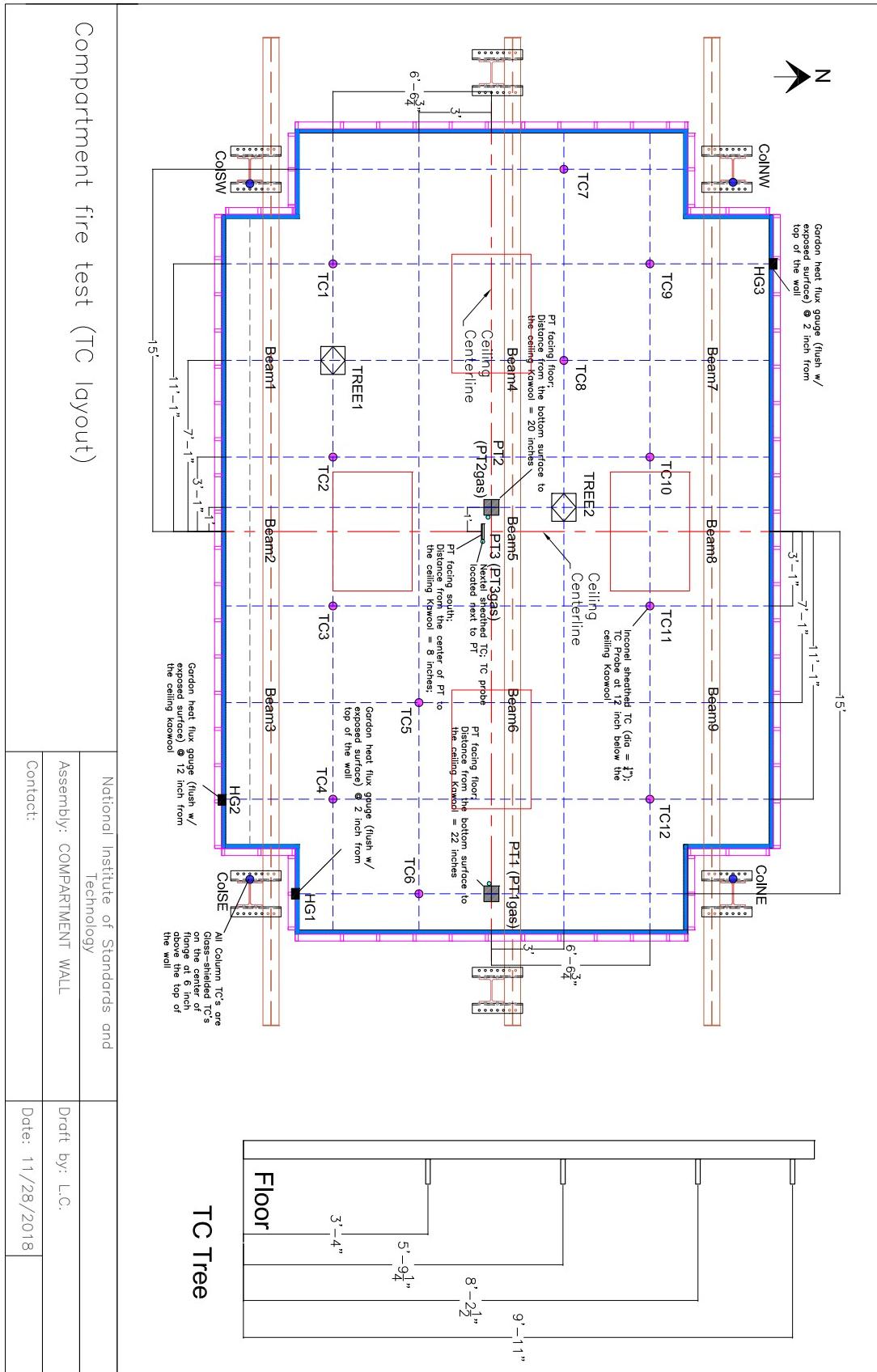


Figure 3.26: Side view of NIST Composite Beam experiments.

### 3.51 NIST E119 Compartment Experiments

In December 2018, three fire experiments were conducted in a compartment approximately 10.8 m wide, 7.0 m deep and 3.8 m high, constructed in the Large Fire Laboratory of NIST [252]. The experiments were designed to test different types of floor assemblies. Two experiments, designed as replicates, lasted 15 min, and the third lasted 75 min. Four natural gas burners generated a peak heat release rate of approximately 10 MW in the 75 min experiments. The measured average upper layer gas temperature was comparable with that prescribed in the ASTM E119 standard [253]. Drawings of the compartment are shown in Figs. 3.27 through 3.29.



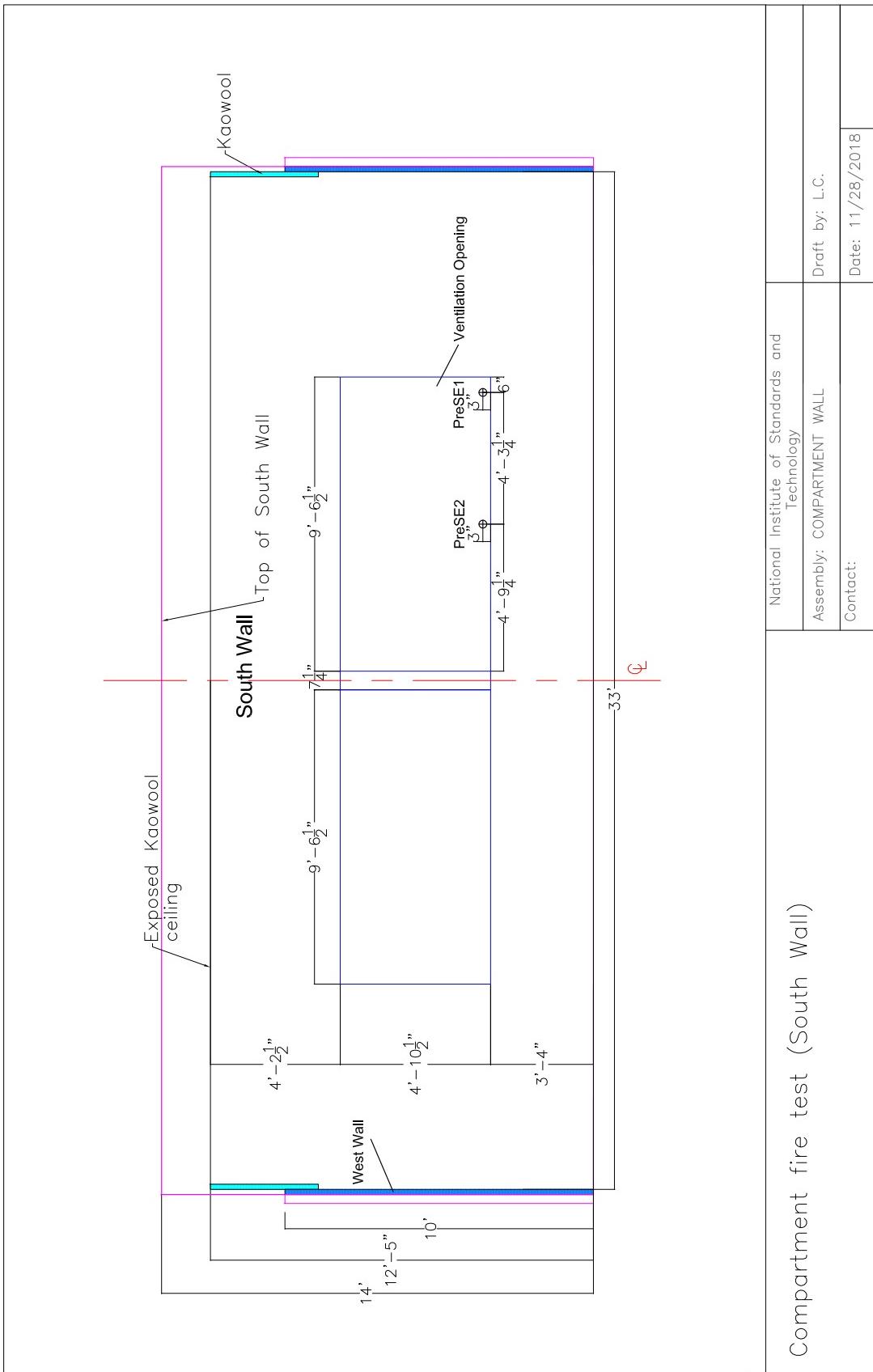


Figure 3.28: Elevation view of NIST E119 Compartment experiment.

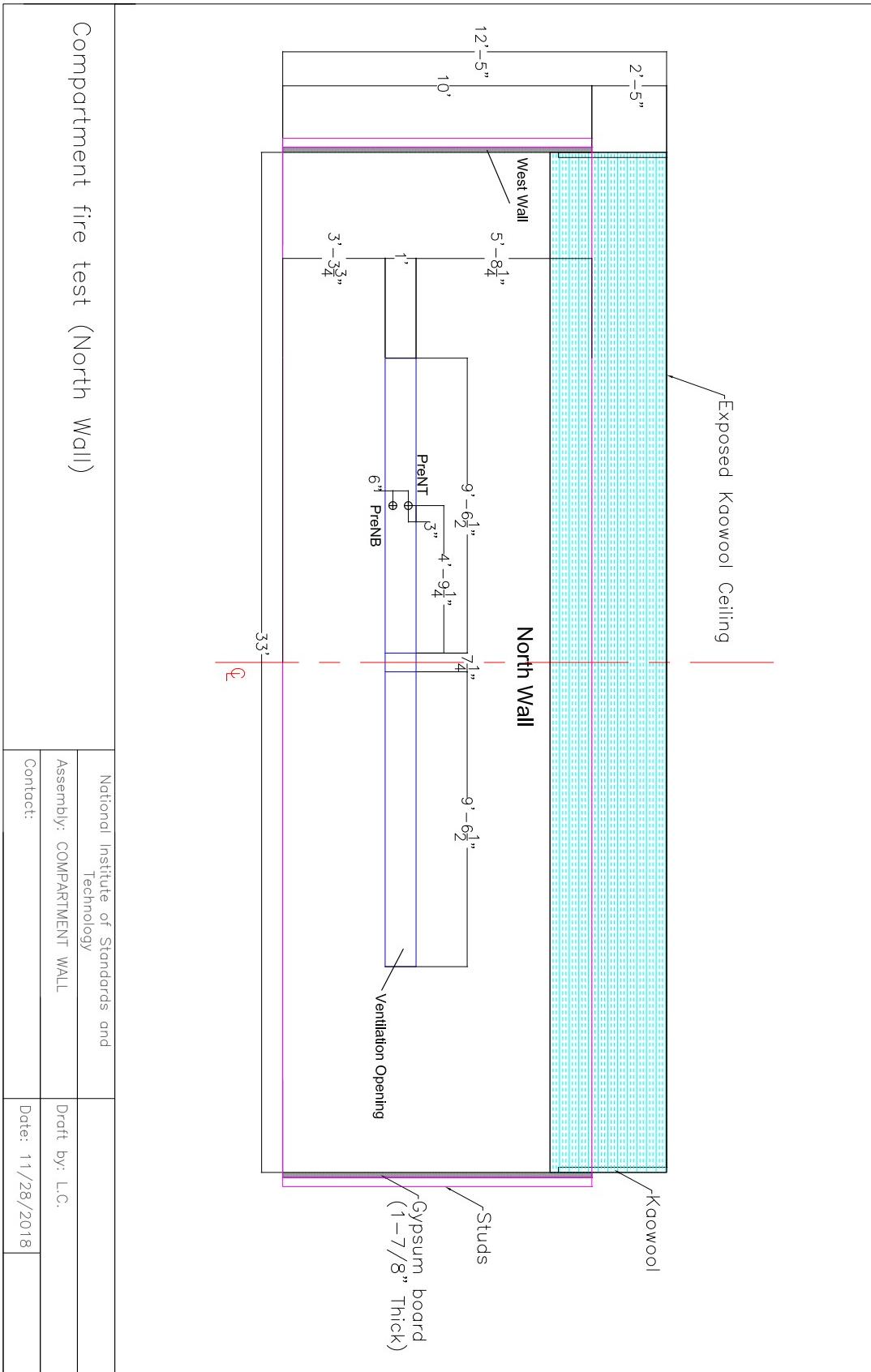


Figure 3.29: Elevation view of NIST E119 Compartment experiment.

## 3.52 NIST Douglas Firs

In 2009, Mell et al. measured the burning rate and heat fluxes from individual Douglas fir trees of various sizes and moisture contents [129]. Nine of the trees were approximately 2 m tall, and three were approximately 5 m tall. The results were presented as averages: the three 5 m trees had an average moisture content of 26 %, three of the 2 m trees had an average moisture content of 49 %, and the remaining six 2 m trees had a moisture content of 14 %. The 2 m trees were ignited with a natural gas ring burner with a diameter of 80 cm and a heat release rate of 30 kW. The trees with a moisture content of 14 % were exposed to the burner for 10 s and the 49 % trees were exposed for 30 s. The 5 m trees were exposed to a hexagonal burner with a span of 122 cm and HRR of 130 kW for 30 s.

### Modeling Notes

The trees are modeled as a collection of cylindrical Lagrangian particles. Mell et al. [129] group the particles into three size classes. The pyrolysis model applied to the particles is described in the FDS User's Guide [1], chapter "Wildland Fire Spread," Sec. 17.1, "Thermal Degradation Model for Vegetation."

Measured properties of the trees are listed in Table 3.22, and assumed properties are listed in Table 3.23. These assumed properties are typically for wood or cellulosic fuels. The moisture is modeled as water. The vegetation is assumed to be composed primarily of cellulose. Reference [129] provides an estimate of the distribution of mass for the foliage, roundwood less than 3 mm in diameter, roundwood 3 mm to 6 mm, and roundwood 6 mm to 10 mm. For the 2 m trees, the distribution is approximately 64 %, 11 %, 10 %, and 15 %, respectively. For the 5 m trees, it is 60 %, 17 %, 12 %, and 11 %, respectively.

Table 3.22: Measured properties for the NIST Douglas Fir Experiments [129].

| Property                             | Units                  | Case 1 | Case 2 | Case 3 |
|--------------------------------------|------------------------|--------|--------|--------|
| Replicate Experiments                | –                      | 6      | 3      | 3      |
| Avg. Crown Height                    | m                      | 1.9    | 1.9    | 4.2    |
| Avg. Base Height                     | m                      | 0.15   | 0.15   | 0.3    |
| Avg. Base Width                      | m                      | 1.7    | 1.7    | 2.9    |
| Foliage Surface Area to Volume Ratio | $\text{m}^{-1}$        | 3940   | 3940   | 3940   |
| Avg. Initial Mass                    | kg                     | 9.7    | 13.5   | 57.9   |
| Avg. Moisture Fraction               | %                      | 14     | 49     | 26     |
| Assumed Bulk Mass per Unit Volume    | $\text{kg}/\text{m}^3$ | 3.2    | 4.6    | 2.7    |

Table 3.23: Assumed properties for the NIST Douglas Fir Experiments.

| Property             | Units             | Value                   | Reference  |
|----------------------|-------------------|-------------------------|------------|
| Chemical Composition | –                 | $C_{3.4}H_{6.2}O_{2.5}$ | [66]       |
| Heat of Combustion   | kJ/kg             | 17700                   | [174]      |
| Soot Yield           | kg/kg             | 0.02                    | [129]      |
| Char Yield           | kg/kg             | 0.26                    | [174]      |
| Specific Heat        | kJ/(kg·K)         | $1.1 + 0.0037T$         | [254]      |
| Conductivity         | W/(m·K)           | 0.2                     | Assumption |
| Density              | kg/m <sup>3</sup> | 514                     | [172]      |
| Heat of Pyrolysis    | kJ/kg             | 416                     | [175]      |

## 3.53 NIST Enclosure Experiments

A variety of reduced-scale and full-scale compartment fire experiments have been performed at NIST over the past few decades. The main objective of each series is to measure the concentrations of oxygen, carbon dioxide, carbon monoxide, soot, and unburned hydrocarbons in an under-ventilated compartment. These data sets also provide extreme temperature and heat flux measurements.

### 3.53.1 NIST Reduced Scale Enclosure Experiments, 1994

The NIST Reduced Scale Enclosure (RSE) was a 40 % scale version of the ISO 9705 compartment [255]. It measured 0.98 m wide by 1.46 m deep by 0.98 m tall. A door, centered on the smaller wall, was 0.48 m wide by 0.81 m tall. A 15 cm diameter natural gas burner was positioned in the center of the compartment. The burner was on a stand so that its top was 15 cm above the floor. The fires ranged from 50 kW to 600 kW. Species measurements, including CO concentration, were made near the ceiling in the front and back of the compartment.

### 3.53.2 NIST Reduced Scale Enclosure Experiments, 2007

Another set of reduced-scale compartment experiments was conducted in 2007 at NIST [256]. The compartment was similar in dimension: 0.95 m wide by 1.42 m deep by 0.98 m tall with the exact same door dimensions. Four different burner types were used: a 13 cm square sand burner, a 25 cm square liquid fuel burner, a spray nozzle into 0.4 m diameter circular pan, and a 60 cm diameter circular pan. Six different fuels were used: natural gas; heptane, methanol, ethanol and toluene liquids; and solid polystyrene beads. The fires ranged from 15 kW to 425 kW, but only fires greater than 190 kW were used for comparison because the smaller fires produced no significant CO. Measurements of O<sub>2</sub>, CO<sub>2</sub>, CO, soot, and unburned hydrocarbon concentration were made near the ceiling in the front and back of the compartment.

### 3.53.3 NIST Full-Scale Enclosure Experiments, 2008

The NIST FSE (2008) Experiments were conducted in an ISO 9705 compartment [257]. The compartment was 2.4 m wide by 3.6 m long by 2.4 m high with a 2 m high door at one end (Fig. 3.30). The door width varied between 0.1 m and 0.8 m. The experiments were designed to study the effects of fuel type, fuel distribution, and vent size on under-ventilated compartment fires. Twenty-seven of the thirty experiments

Table 3.24: Summary of NIST Reduced-Scale Experiments, 2007.

| Test No. | Fuel Type   | Fuel Formula                    | Peak HRR (kW) | Burner Size (m <sup>2</sup> ) | Doorway Opening (cm) |
|----------|-------------|---------------------------------|---------------|-------------------------------|----------------------|
| 1        | Natural Gas | CH <sub>4</sub>                 | 190           | 0.017                         | 48                   |
| 2        | Natural Gas | CH <sub>4</sub>                 | 395           | 0.017                         | 48                   |
| 3        | Natural Gas | CH <sub>4</sub>                 | 410           | 0.017                         | 48                   |
| 4        | Heptane     | C <sub>7</sub> H <sub>16</sub>  | 375           | 0.063                         | 48                   |
| 5        | Heptane     | C <sub>7</sub> H <sub>16</sub>  | 220           | 0.063                         | 24                   |
| 6        | Natural Gas | CH <sub>4</sub>                 | 420           | 0.063                         | 24                   |
| 7        | Heptane     | C <sub>7</sub> H <sub>16</sub>  | 340           | 0.063                         | 48                   |
| 10       | Toluene     | C <sub>7</sub> H <sub>8</sub>   | 340           | 0.063                         | 48                   |
| 11       | Ethanol     | C <sub>2</sub> H <sub>6</sub> O | 335           | 0.126                         | 48                   |
| 12       | Methanol    | CH <sub>4</sub> O               | 305           | 0.126                         | 48                   |
| 15       | Heptane     | C <sub>7</sub> H <sub>16</sub>  | 375           | 0.126                         | 48                   |
| 16       | Polystyrene | C <sub>8</sub> H <sub>8</sub>   | 360           | 0.283                         | 48                   |

were simulated, which included 7 different fuels, 3 fuel sources, and 4 ventilation openings. The three experiments not simulated had several malfunctions of equipment such that the data could not be trusted.

Peak heat release rates ranged from approximately 100 kW to 2.5 MW. Table 3.25 provides a summary of the experiments. Species concentrations and temperature measurements were made at the front and rear of the compartment.

### 3.53.4 Modeling Notes

In the simulations of all of the NIST enclosure experiments, it is assumed that the combustion can be simplified to two fast reactions, the first converting fuel to CO and soot, and the second converting CO and soot to CO<sub>2</sub>. By default, 2/3 of the carbon in the fuel is converted to CO in the first step, the remaining 1/3 to soot. The heats of combustion for the reactions are calculated directly from the heats of formation of the individual molecules. For cases where the fuel molecule is not pre-defined in FDS (e.g., styrene), the fuel's enthalpy of formation is specified. For cases where the fuel's enthalpy of formation is not known (e.g. nylon), the heat of combustion that is reported for complete combustion is specified in a single reaction test case, from which an effective enthalpy of formation is reported<sup>3</sup> and then used in the actual two-step reaction scheme.

In the experiments, the heat release rate was measured via oxygen consumption calorimetry. In the simulations, the mass loss rate of fuel was specified by taking the measured HRR and dividing by the heats of combustion listed in Ref. [151].

In all simulations, the model geometry included the compartment interior plus a comparable volume at the exterior to allow for a natural flow into and out of the compartment.

Also, in all simulations, the fire suppression algorithm has been turned off (SUPPRESSION=.FALSE.). The reason for this is that the suppression algorithm is not able to distinguish viability of a fire that is close

<sup>3</sup>The FDS diagnostic output (.out) file contains detailed information about the reaction stoichiometry, heats of combustion, and enthalpies of formation.

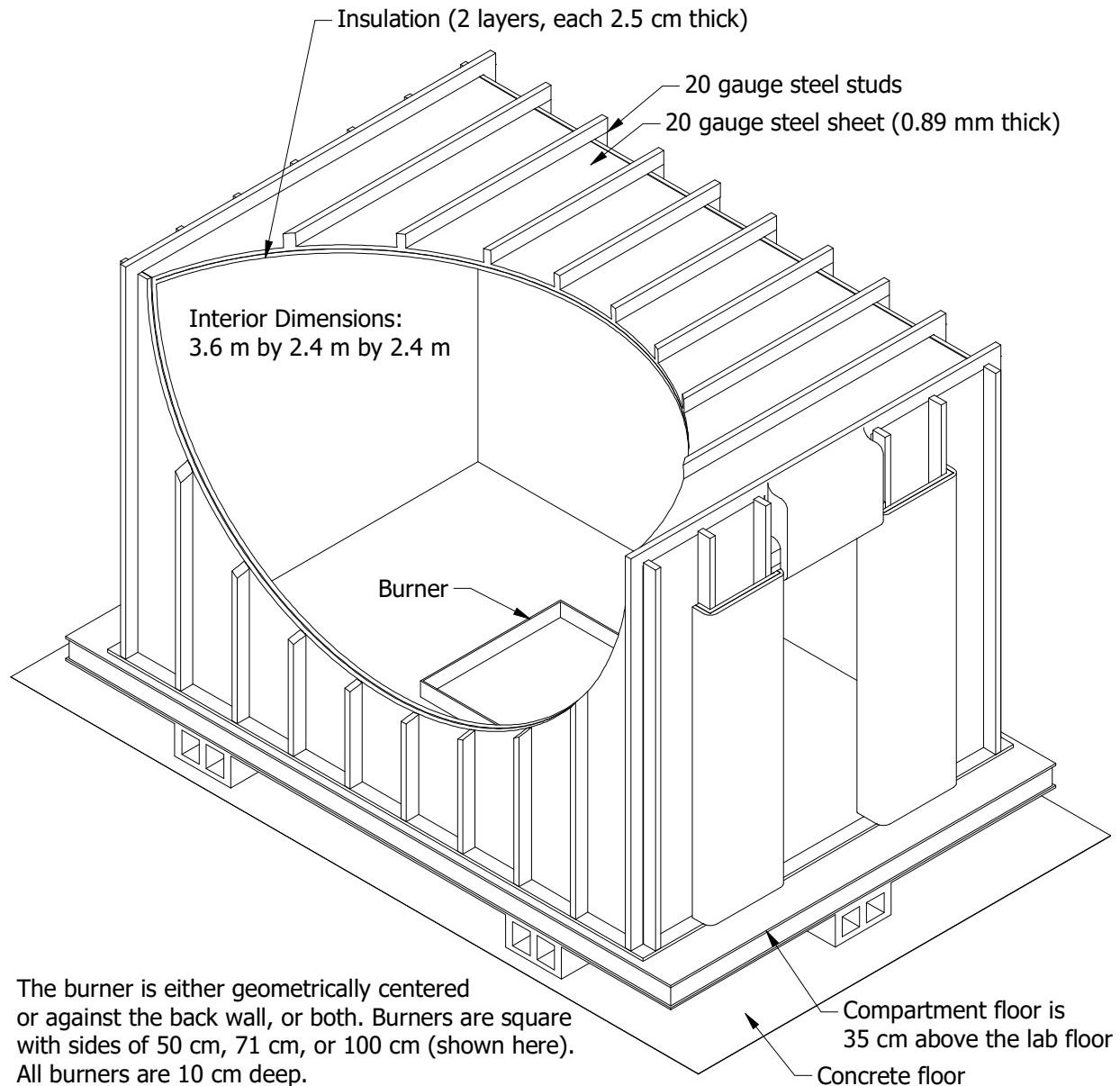


Figure 3.30: Geometry of the compartment used in the NIST Full-Scale Enclosure (FSE) experiments.

to the point of extinction. Research continues in this area.

Table 3.25: Summary of NIST FSE Experiments selected for model validation.

| Test Name     | Fuel Type   | Fuel Formula                      | Fuel Mass (kg) | No. of Burners | Burner Size (m <sup>2</sup> ) | Doorway Opening (cm) |
|---------------|-------------|-----------------------------------|----------------|----------------|-------------------------------|----------------------|
| ISONG3        | Natural Gas | CH <sub>4</sub>                   |                | 1              | 1.0                           | 80                   |
| ISOHept4      | Heptane     | C <sub>7</sub> H <sub>16</sub>    | Pool Fed       | 1              | 1.0                           | 80                   |
| ISOHept5      | Heptane     | C <sub>7</sub> H <sub>16</sub>    | Pool Fed       | 1              | 1.0                           | 40                   |
| ISOHept8      | Heptane     | C <sub>7</sub> H <sub>16</sub>    | 10             | 1              | 0.5                           | 20                   |
| ISOHept9      | Heptane     | C <sub>7</sub> H <sub>16</sub>    | 20             | 1              | 0.5                           | 20                   |
| ISONylon10    | Nylon       | C <sub>6</sub> H <sub>11</sub> NO | 10             | 1              | 0.5                           | 20                   |
| ISOPP11       | Propylene   | C <sub>3</sub> H <sub>6</sub>     | 10             | 1              | 0.5                           | 20                   |
| ISOHeptD12    | Heptane     | C <sub>7</sub> H <sub>16</sub>    | 20             | 2              | 0.25                          | 20                   |
| ISOHeptD13    | Heptane     | C <sub>7</sub> H <sub>16</sub>    | 20             | 2              | 0.25                          | 20                   |
| ISOPropD14    | Propanol    | C <sub>3</sub> H <sub>8</sub> O   | 24             | 2              | 0.25                          | 20                   |
| ISOProp15     | Propanol    | C <sub>3</sub> H <sub>8</sub> O   | 24             | 1              | 0.5                           | 20                   |
| ISOStyrene16  | Styrene     | C <sub>8</sub> H <sub>8</sub>     | 10             | 1              | 0.5                           | 20                   |
| ISOStyrene17  | Styrene     | C <sub>8</sub> H <sub>8</sub>     | 30             | 1              | 1.0                           | 20                   |
| ISOPP18       | Propylene   | C <sub>3</sub> H <sub>6</sub>     | 20             | 2              | 0.5                           | 20                   |
| ISOHept19     | Heptane     | C <sub>7</sub> H <sub>16</sub>    | 20             | 1              | 0.5                           | 20                   |
| ISOToluene20  | Toluene     | C <sub>7</sub> H <sub>8</sub>     | 17             | 1              | 0.5                           | 20                   |
| ISOStyrene21  | Styrene     | C <sub>8</sub> H <sub>8</sub>     | 15             | 1              | 0.5                           | 20                   |
| ISOHept22     | Heptane     | C <sub>7</sub> H <sub>16</sub>    | Spray          | 1              | 0.5                           | 20                   |
| ISOHept23     | Heptane     | C <sub>7</sub> H <sub>16</sub>    | Spray          | 1              | 0.5                           | 10                   |
| ISOHept24     | Heptane     | C <sub>7</sub> H <sub>16</sub>    | Spray          | 1              | 0.5                           | 10                   |
| ISOHept25     | Heptane     | C <sub>7</sub> H <sub>16</sub>    | Spray          | 1              | 0.5                           | 40                   |
| ISOHept26     | Heptane     | C <sub>7</sub> H <sub>16</sub>    | Spray          | 1              | 0.5                           | 40                   |
| ISOHept27     | Heptane     | C <sub>7</sub> H <sub>16</sub>    | Spray          | 1              | 0.5                           | 10                   |
| ISOHept28     | Heptane     | C <sub>7</sub> H <sub>16</sub>    | Spray          | 1              | 0.5                           | 20                   |
| ISOToluene29  | Toluene     | C <sub>7</sub> H <sub>8</sub>     | Spray          | 1              | 0.5                           | 20                   |
| ISOPropanol30 | Propanol    | C <sub>3</sub> H <sub>8</sub> O   | Spray          | 1              | 0.5                           | 20                   |
| ISONG32       | Natural Gas | CH <sub>4</sub>                   |                | 1              | 0.28                          | 20                   |

### 3.54 NIST Helium Experiments

Eighteen experiments were conducted at NIST in which helium was released over a lengthy time period inside of a 1.5 m by 1.5 m by 0.75 m plexiglass box with one or two small leakage holes [258]. The experiments were intended to represent the release of hydrogen from passenger vehicle fuel cell inside of a residential garage. Test parameters included the release rate and length, the location of the release, and the size and location of the leakage. Measurements were made of the helium concentration in a rake at seven locations over the height of the compartment during the release and for a period of up to 11 hours post-release.

Test variables included all permutations of the leak rate and time (14.8 L/min over 3600 s or 3.71 L/min over 14400 s), leak location (on the floor at the center of the compartment, on the floor at the center of the rear wall, and 2.5 cm below the ceiling at the center of the compartment), and the leak area (2.4 cm by 2.4 cm at the center of the front wall, 3.05 cm by 3.05 cm at the center of the front wall, and a pair of

2.15 cm by 2.15 cm centered on the front wall 2.5 cm from the floor and ceiling).

Leakage areas were square holes under  $10 \text{ cm}^2$  in area. Attempting to resolve flows through these holes would have required very small grid cells in the vicinity of the holes. Instead, the FDS HVAC model was used. For each leakage hole a pair of HVAC ducts was defined over a height of two grid cells (one grid cell height for each vent). Each duct was assigned one-half the leakage area and the experimentally determined orifice flow coefficient. This approach enabled bi-directional flow to occur at the leakage vent as occurred during each test following the termination of the helium release.

### 3.55 NIST/NRC Compartment Experiments

These experiments, sponsored by the US NRC and conducted at NIST, consisted of 15 large-scale experiments performed in June 2003. All 15 tests were included in the validation study. The experiments are documented in Ref. [123]. The fire sizes ranged from 350 kW to 2.2 MW in a compartment with dimensions 21.7 m by 7.1 m by 3.8 m high, designed to represent a compartment in a nuclear power plant containing power and control cables. A diagram of the test structure is displayed in Figure 3.31.

The walls and ceiling were covered with two layers of marinate boards, each layer 0.0125 m thick. The floor was covered with one layer of gypsum board on top of a layer of plywood. Thermo-physical and optical properties of the marinate and other materials used in the compartment are given in Ref. [123]. The room had one door and a mechanical air injection and extraction system. Ventilation conditions, the fire size, and fire location were varied. Numerous measurements (approximately 350 per test) were made including gas and surface temperatures, heat fluxes and gas velocities.

Following are some notes provided by Anthony Hamins, who conducted the experiments:

**Natural Ventilation:** The compartment had a 2 m by 2 m door in the middle of the west wall. Some of the tests had a closed door and no mechanical ventilation (Tests 2, 7, 8, 13, and 17), and in those tests the measured compartment leakage was an important consideration. The test report lists leakage areas based on measurements performed prior to Tests 1, 2, 7, 8, and 13. For the closed door tests, the leakage area used in the simulations was based on the last available measurement. The chronological order of the tests differed from the numerical order. For Test 4, the leakage area measured before Test 2 was used. For Tests 10 and 16, the leakage area measured before Test 7 was used.

**Mechanical Ventilation:** The mechanical ventilation and exhaust was used during Tests 4, 5, 10, and 16, providing about 5 air changes per hour. The door was closed during Test 4 and open during Tests 5, 10, and 16. The supply duct was positioned on the south wall, about 2 m off the floor. An exhaust duct of equal area to the supply duct was positioned on the opposite wall at a comparable location. The flow rates through the supply and exhaust ducts were measured in detail during breaks in the testing, in the absence of a fire. During the tests, the flows were monitored with single bi-directional probes during the tests themselves.

**Heat Release Rate:** A single nozzle was used to spray liquid hydrocarbon fuels onto a 1 m by 2 m fire pan that was about 0.1 m deep. The test plan originally called for the use of two nozzles to provide the fuel spray. Experimental observation suggested that the fire was less unsteady with the use of a single nozzle. In addition, it was observed that the actual extent of the liquid pool was well-approximated by a 1 m circle in the center of the pan. For safety reasons, the fuel flow was terminated when the lower-layer oxygen concentration dropped to approximately 15 % by volume. The fuel used in 14 of the tests was heptane, while toluene was used for one test. The HRR was determined using oxygen consumption calorimetry. The recommended uncertainty values were 17 % for all of the tests.

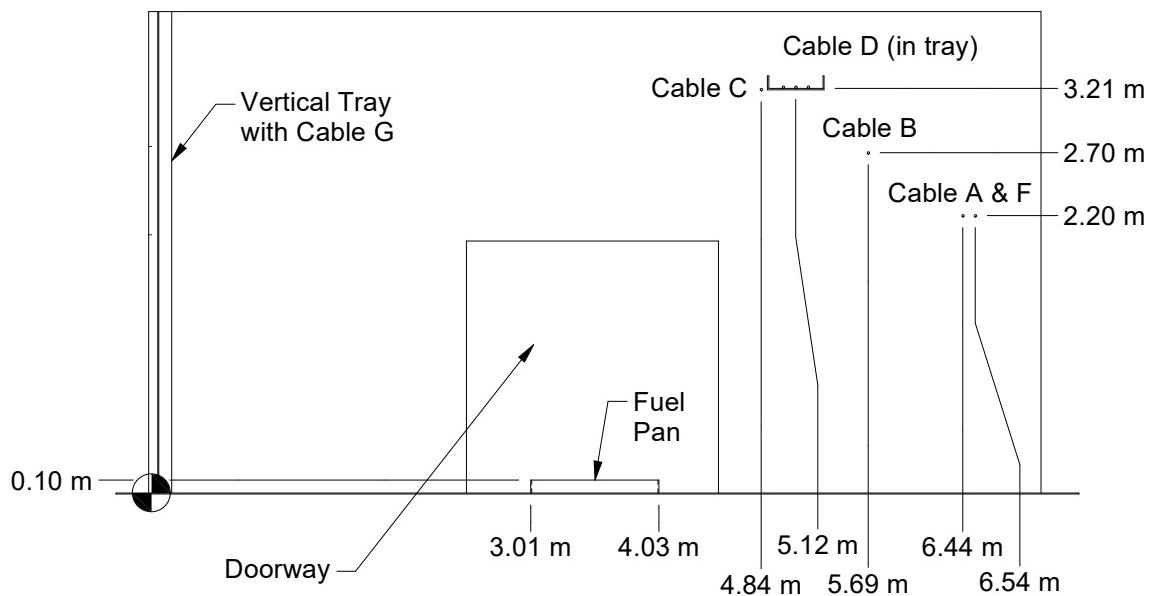
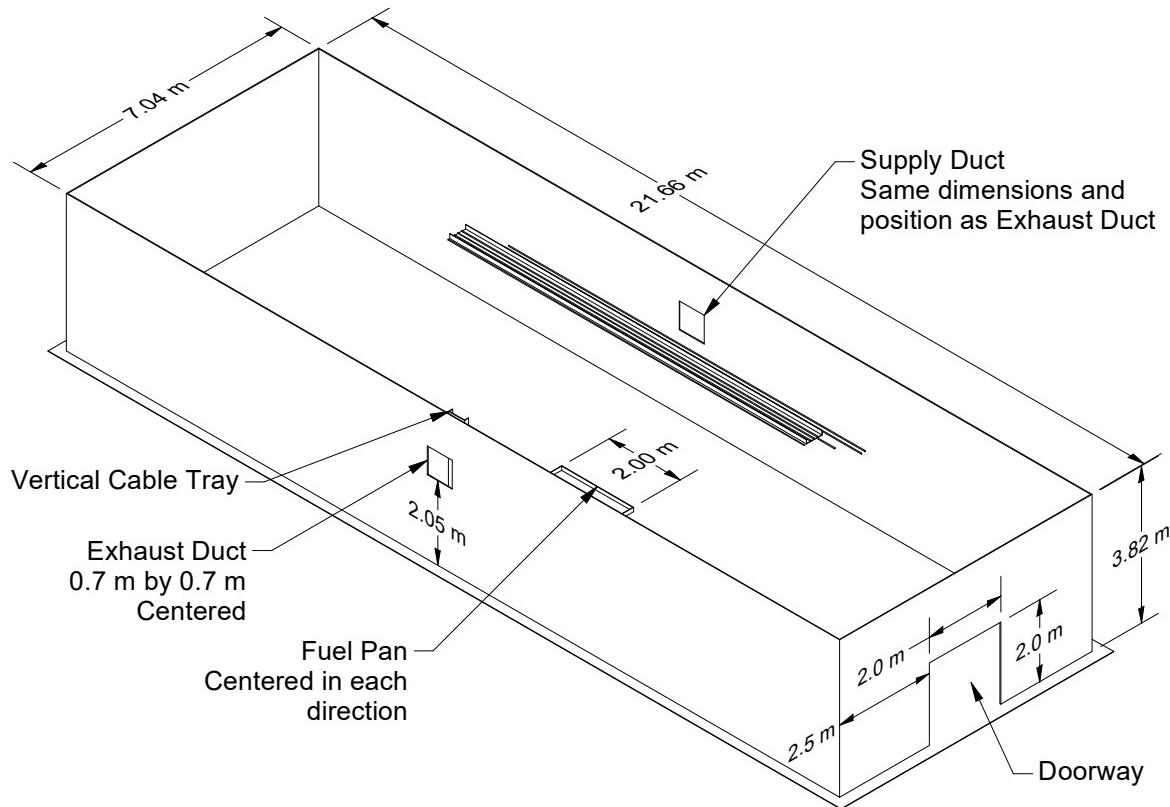


Figure 3.31: Geometry of the NIST/NRC Experiments.

**Radiative Fraction:** The values of radiative fraction and its uncertainty were reported as 0.44(7) and 0.40(9) for heptane and toluene, respectively.

**Soot Yield:** The values of the soot yield and its uncertainty were reported as 0.0149(33) kg/kg and 0.195(52) kg/kg for heptane and toluene, respectively.

## 3.56 NIST/NRC Corner, Wall, and Cabinet Experiments

In the summer of 2017, experiments were conducted in a large compartment in the NIST large fire laboratory on behalf of the U.S. Nuclear Regulatory Commission. There were two sets of experiments. In the first set, conducted in July, 2017, a natural gas burner was positioned either in a corner or against a wall, and gradually moved outward. In the second set of experiments, conducted in September, 2017, a natural gas burner was placed inside one of two steel cabinets meant to represent typical industrial-scale electrical enclosures.

The compartment for all experiments was 11 m long, 7 m wide, and 3.8 m high. The long dimension of the compartment ran east-west. A 1.8 m wide, 2.4 m high door was centered on the east (short) wall.

All of the fires were fueled by one or more 30.5 cm (1 ft) square natural gas burners. Each burner was essentially a steel box, 30.5 cm square in plan and 15 cm deep, fueled from below. The lip of the burner was 2.5 cm (1 in) wide. A 2.5 cm thick piece of Kawool insulation was placed under a steel mesh to form the surface of the burner.

### 3.56.1 Wall and Corner Effects

Six large compartment experiments [259] were conducted in July, 2017, where four natural gas burners were positioned (1) in a corner and (2) against a wall, and then moved outward in stages until the corner or wall effect became negligible. The quad burner was 60 cm by 60 cm and the burner surface was 54 cm above the floor. The corner fire was located in the southwest corner of the large compartment. The wall fire was centered on the south (long) wall.

The experiments began with the quad burner in the corner or against the wall for the first 30 min. At 30 min, the burner was moved so that its edge(s) was 10 cm away from the wall(s). It remained for 15 min, after which it was moved to 20 cm, 30 cm, 50 cm, 100 cm, and 160 cm, each time remaining 15 min for a total experiment time of 2 h.

A three-dimensional array of thermocouples was positioned on a track mounted to the ceiling above the burner. The purpose of this array was to measure maximum plume temperatures at heights of 2.1 m, 2.7 m, and 3.4 m above the floor. As the burner moved, the thermocouple array moved with it. For the corner fire experiments, when the burner was at the 0 cm, 10 cm, and 20 cm positions, the thermocouple array overhead remained at its original location in the corner. As the burner moved beyond 20 cm, the thermocouple array was moved the same amount so that the burner was always below the array in the same position. In other words, for the corner fire experiments, after the center point of the burner reached the point directly below the position 18 on the diagram below, the burner and array moved together, maintaining their relative position.

The experimental data consists primarily of thermocouple measurements. The key to the column names are as follows:

- TC-AG-01 through TC-AG-29 are the thermocouples at the top of the cage, 46 cm below the ceiling (see pattern below).
- TC-BG-01 through TC-BG-29 are the thermocouples at the mid-level of the cage, 107 cm below the ceiling (see pattern below).

- TC-CG-01 through TC-CG-29 are the thermocouples at the bottom of the cage, 168 cm below the ceiling (see pattern below).
- TC-WT-01 through TC-WT-13 are the thermocouples of the vertical array called the West Tree. The array was 2.75 m from the west (short) wall and 3.5 m from the south (long) wall. TC-WT-01 was located 2 cm below the ceiling, and the rest were spaced 30 cm apart.
- TC-ET-01 through TC-ET-13 are the thermocouples of the East Tree. The array was 2.75 m from the east (short) wall and 3.5 m from the south (long) wall. TC-ET-01 was located 2 cm below the ceiling, and the rest were spaced 30 cm apart.
- TC-C-01 through TC-C-11 are the thermocouples 2 cm from the corner above the corner fire. TC-C-01 was located 2 cm below the ceiling, and the rest were spaced 30 cm apart.
- TC-W-01 through TC-W-11 are the thermocouples 2 cm from the wall above the wall fire. TC-W-01 was located 2 cm below the ceiling, and the rest were spaced 30 cm apart.
- HRR (cal) is the heat release rate of the fire as measured using oxygen consumption calorimetry. HRR (NG) is the heat release rate determined from the mass flow rate of natural gas.

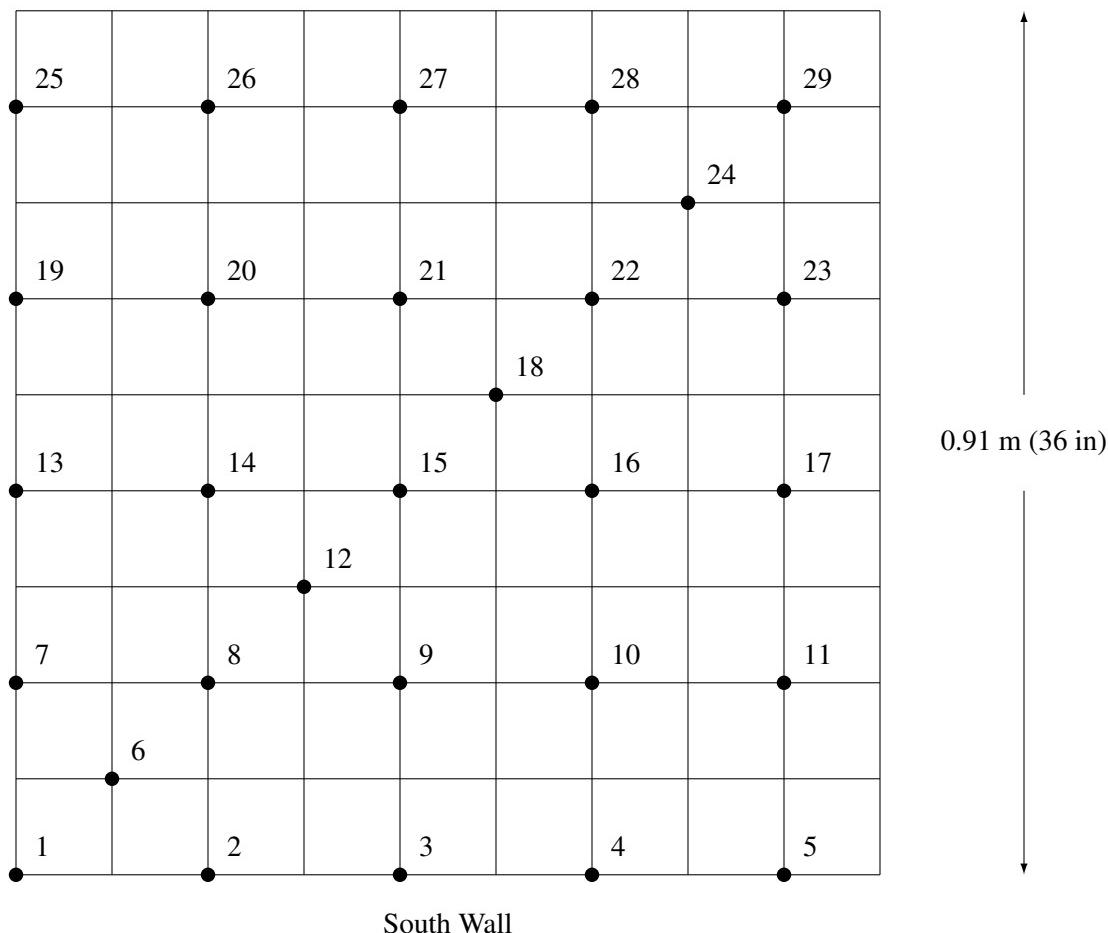


Figure 3.32: Diagram of thermocouple layout for NIST/NRC Corner Effects experiments.

The East and West Tree thermocouples were used to estimate the height of the hot gas layer (HGL), and the average temperatures of the upper and lower layers. Also, the three horizontal arrays of thermocouples above the burner were processed by first taking a 2 min running average of each TC, and then choosing the maximum value for each of the three elevations above the fire. These were taken as approximate centerline plume temperatures at each height. These experimental files are labelled with “HGL” and “Plume”, respectively.

### 3.56.2 Cabinet Effects

In this second series of experiments, conducted in September, 2017, two different mock steel cabinets were used. Each cabinet was constructed of 12 gauge (2.8 mm or 7/64 in) steel plate with openings as shown in Figs. 3.33 and 3.34. The large cabinet was nominally 0.9 m by 0.9 m by 2.1 m and the medium size cabinet was 0.6 m by 0.6 m by 2.1 m. The openings near the top of each cabinet were sometimes covered with a steel grill, shown in Fig. 3.35.

For the first set of experiments (1-6), the large cabinet was positioned with its front opening facing eastward towards the opening of the test compartment. Its left side was 1.8 m from the south wall and its front side was 5.8 m from the east wall. Two 0.3 m by 0.3 m natural gas burners were placed side by side in the cabinet from the perspective of the cabinet front opening. The top of the burner was 50 cm above the floor of the cabinet. For Tests 1-4, the front door of the cabinet was closed, and the heat release rate was initially set to 50 kW for 30 min, then it was increased to 100 kW for 15 min, 200 kW for 15 min, and 400 kW for 15 min. For Tests 5-6, the front door was opened, and the heat release rate was set to 200 kW, 400 kW, and 700 kW for 15 min each, and then 1000 kW for 5 min, a total of 50 min.

In the second set of experiments (7-10), the medium-sized cabinet was positioned so that its front was the same distance from the east wall as the large cabinet, and its left side was 2.0 m (6.5 ft) from the south wall. A single 30 cm by 30 cm gas burner was centered within. For the closed door tests, the heat release rate was 25 kW, 50 kW, 100 kW, and 200 kW, each for 15 min. For the open door tests, the heat release rate was 40 kW, 80 kW, 200 kW, and 325 kW, each for 15 min.

In the third set of experiments (11-12), the cabinet was removed, and two 30 cm by 30 cm burners were spaced 0.9 m (3 ft) apart, side to side. One of the burners was centered under the array of thermocouples. Both burners were 2.0 m from the south wall. These experiments used the same heat release rate sequence as the open and closed door large cabinet experiments.

The data files for these experiments are labelled, `NIST_NRC_Cabinet_Test_n.csv`. These files contain the same measurement positions as the corner and wall experiments, with the following additional measurements:

- PT-1 through PT-8 are plate thermometers positioned 0.6 m (2 ft) from each side of the cabinet at heights of 0.8 m (2.5 ft) and 1.4 m (4.5 ft). PT-1 is the upper plate on the left side. PT-2 is lower left. PT-3 is upper back. PT-4 is lower back. PT-5 is upper front. PT-6 is lower front. PT-7 is upper right. PT-8 is lower right.
- STC-1 through STC-6 are sheathed thermocouples within the cabinet, 15 cm (6 in) from the left side, centered. STC-1 is 6 cm (2.5 in) from the top. STC-2 through STC-6 are 30 cm, 60 cm, 90 cm, 120 cm, and 150 cm from the top, respectively.
- TC-Cab is a single 24 gauge Type K thermocouple welded to the center of the back side on the outside of the cabinet. For Test 11, this TC was placed just under the Kaowool surface of the burner, and for Test 12, it was placed just above the surface.

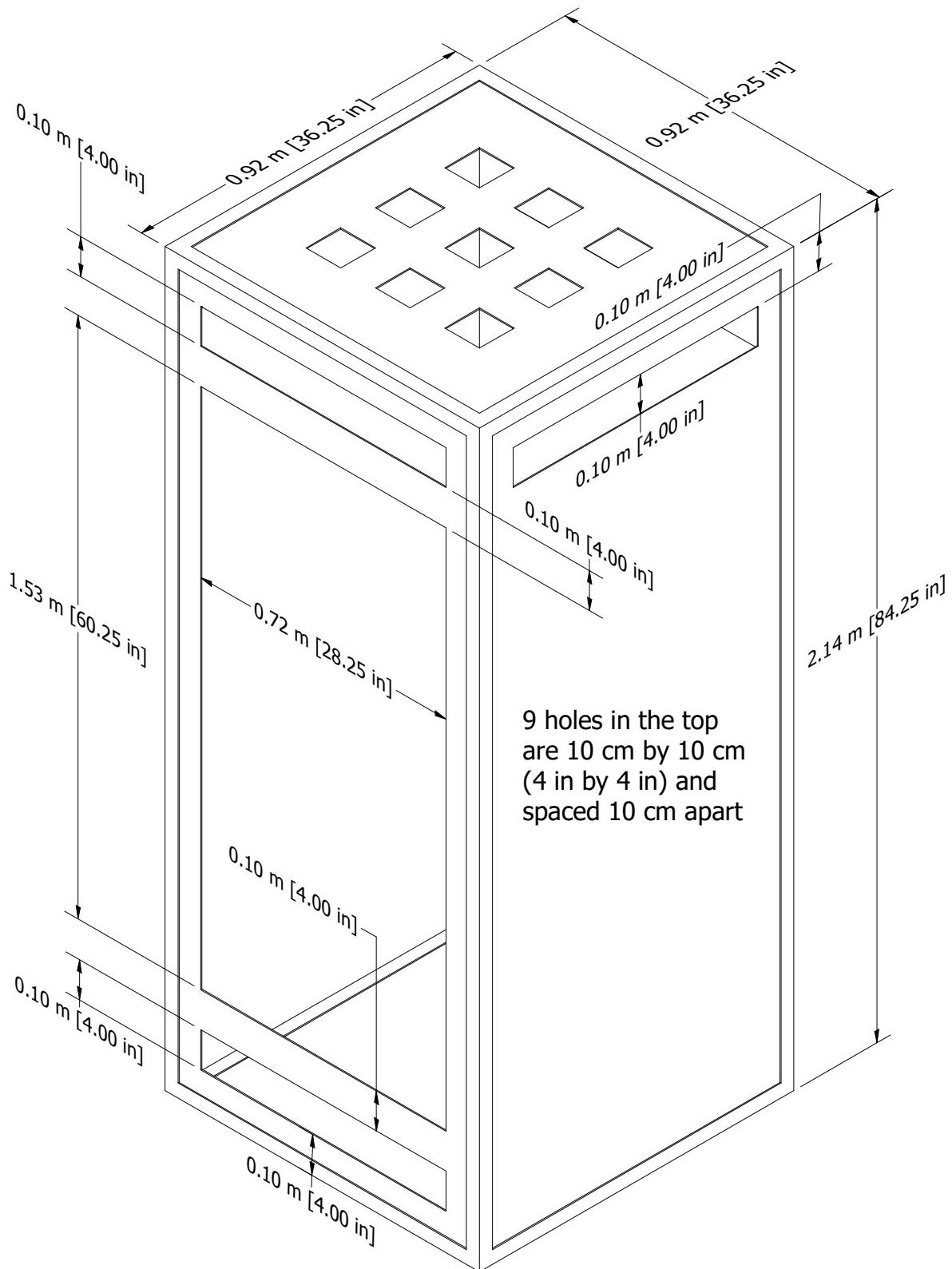


Figure 3.33: Large cabinet drawing, NIST/NRC Corner Effects Experiments.

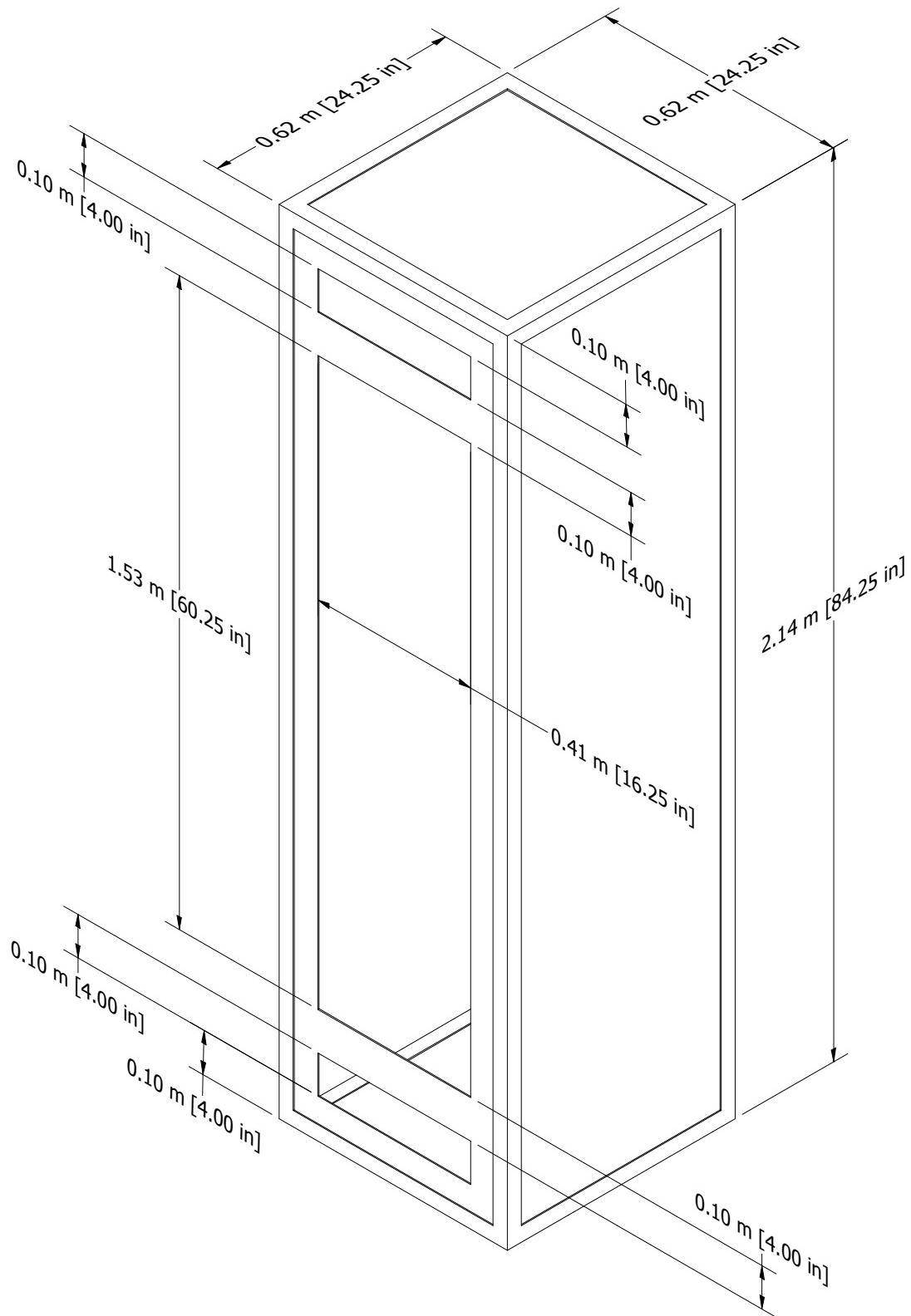


Figure 3.34: Medium-sized cabinet drawing, NIST/NRC Corner Effects Experiments.

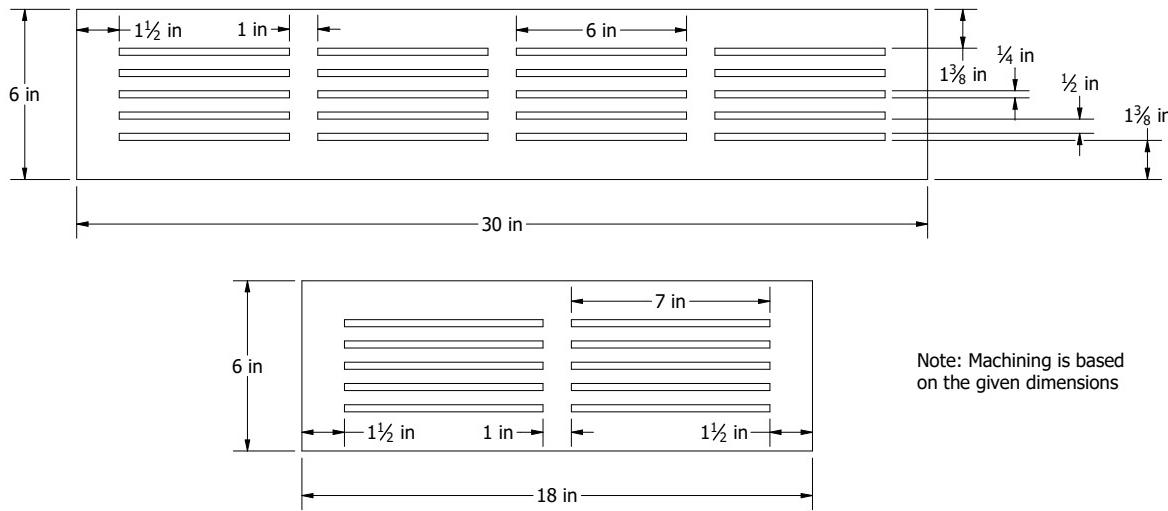


Figure 3.35: Cabinet grill, NIST/NRC Corner Effects Experiments.

The three dimensional array of thermocouples used in the wall and corner experiments was positioned over the front of the cabinet, such that TC positions 1, 7, 13, 19, and 25 in Fig. 3.32 were just above the upper front edge of the cabinet.

The test matrix is as follows:

Table 3.26: Summary of NIST/NRC Cabinet Experiments.

| Test | Cabinet | Front Door | Top Vents | Upper Side Vents                   | HRR (kW)            |
|------|---------|------------|-----------|------------------------------------|---------------------|
| 1    | Large   | Closed     | Closed    | Grill                              | 50, 100, 200, 400   |
| 2    | Large   | Closed     | All open  | Grill                              | 50, 100, 200, 400   |
| 3    | Large   | Closed     | Closed    | Front open, all others closed      | 50, 100, 200, 400   |
| 4    | Large   | Closed     | Closed    | Front and back open, others closed | 50, 100, 200, 400   |
| 5    | Large   | Open       | Closed    | Front and back open, others closed | 200, 400, 700, 1000 |
| 6    | Large   | Open       | Open      | All open                           | 200, 400, 700, 1000 |
| 7    | Medium  | Closed     | Closed    | Grill                              | 25, 50, 100, 200    |
| 8    | Medium  | Closed     | Closed    | Open                               | 25, 50, 100, 200    |
| 9    | Medium  | Open       | Closed    | Open                               | 40, 80, 200, 325    |
| 10   | Medium  | Open       | Closed    | Closed                             | 40, 80, 200, 325    |
| 11   | None    | N/A        | N/A       | N/A                                | 200, 400, 700, 1000 |
| 12   | None    | N/A        | N/A       | N/A                                | 50, 100, 200, 400   |

### 3.57 NIST/NRC OLIVE-Fire Experiments

In March, 2022, experiments were conducted at NIST to determine the maximum heat release rate that a fire can reach within steel electrical enclosures [260]. OLIVE is an acronym for Oxigen-Limited Ifires Inside

Under-Ventilated Enclosures. Photographs of the enclosures are shown in Fig. 3.36. The enclosures were pressure-tested before and after the experiments to determine the leakage and vent opening areas. These opening areas are a key parameter in the numerical modeling.

Thirty-two experiments were conducted; twenty-one of which were fueled by a natural gas burner. The others involved a variety of plastics and electrical cables. Eighteen of the natural gas experiments were chosen for simulation. The natural gas cases not chosen had unexpectedly large gaps between the steel panels open up during the experiment. The leakage through these gaps could not be measured.

### Modeling Notes

The simulations are performed with a spatial resolution of 4 cm. The enclosures are modeled simply as rectangular steel boxes with no internal partitions included. Both leakage and vents are modeled in the same way by using the “localized leakage” methodology in FDS where the volume flow rate,  $\dot{V}$ , through a vent or a crack is a function of the pressure difference,  $\Delta p$ :

$$\dot{V} = CA \left( \frac{2\Delta p}{\rho_0} \right)^{0.5} \left( \frac{\Delta p}{\Delta p_{ref}} \right)^{0.1} \quad (3.8)$$

The discharge coefficient,  $C = 0.61$ , is recommended by the manufacturer of the calibrated fan used for determining the leakage area,  $A$ . The extra pressure term in the expression represents a weak relationship between the discharge coefficient and the pressure rise. The pressure exponent of 0.6 best fits the leakage data. The reference pressure,  $\Delta p_{ref}$ , is taken as 1 Pa to maintain unit consistency. The measured leakage is applied using four “patches,” two above the neutral plane and two below. Because there is no way to determine the exact distribution of the leakage, the specification of the leakage area to the upper and lower patches is based on roughly matching the gas concentrations early in the simulation when the enclosure is well-ventilated. There is still considerable uncertainty in the leakage distribution and the amount of leakage because during the experiments the gaps and seams of the enclosures tended to open up as the gases within heated.

The combustion of natural gas (assumed to be methane) within the enclosures is modeled using the two-step simple chemistry algorithm. That is, the first reaction converts methane to CO, soot, and water vapor, and the second step converts the CO and soot to CO<sub>2</sub>, assuming enough oxygen is present following the first reaction. By default, two-thirds of the carbon atoms in the fuel molecule are converted to CO in the first step; the rest to soot.

Extinction is modeled using the “Extinction 1” algorithm in which the reactions are assumed to occur if (1) the local gas temperature exceeds the AUTO IGNITION TEMPERATURE of 540 °C, and (2) the local oxygen concentration exceeds a temperature-dependent lower limit. The value of 540 °C is reported in Beyler’s chapter of the SFPE Handbook [152].



Figure 3.36: Photographs of the eight electrical enclosures used for the NIST/NRC OLIVE-Fire experiments. The enclosures are numbered 1 through 8 in sequence. Enclosure #1 and #2 (top row) have the same exterior design.

## 3.58 NIST/NRC Parallel Panel Experiments

As part of a Nuclear Regulatory Commission (NRC) research project to assess fire behavior in electrical enclosures, rate of spread and heat release rate measurements were made on various plastics lining a parallel panel apparatus. The panels were 0.6 m (2 ft) wide, 2.4 m (8 ft) tall, and separated by 0.3 m (1 ft). A 60 kW propane sand burner was positioned at the base of the two panels. Plastics tested to date include PMMA, PVC, and PBT, cut into 6.4 mm (0.25 in) thick panels. A sketch of the apparatus, originally developed by Factory Mutual, is shown in Fig. 3.12.

The Parallel Panel experiment involving black PMMA is part of the suite of cases contributed to the MaCFP (Measurements and Computation of Fire Phenomena) working group of the IAFSS. Its properties are listed in Section 14.2.

## 3.59 NIST/NRC Transient Combustibles Experiments

In December, 2019 and February, 2020, 40 calorimetry experiments were conducted at the National Fire Research Laboratory at NIST on behalf of the U.S. Nuclear Regulatory Commission. The experiments were conducted under a 6.1 m (20 ft) by 6.1 m hood with a nominal capacity of 3 MW. The full report on the experiments can be found in Ref. [261].

The items burned are described briefly in Fig. 3.37. These consist of commercially available materials constructed mainly of wood and paper. Each item was weighed before and after the experiment on a load cell accurate to 10 g.

The fires were all ignited using one or more 7.5 cm (3 in) segments of approximately 1 cm (0.5 in) diameter cotton rope soaked in approximately 10 mL of acetone. For some items like the wood cribs and pallets, a small amount of shredded craft or “crinkle” paper was used to sustain the ignition until steady burning was achieved.

The floor beneath the burning item was protected with a single layer of gypsum board covered by a single layer of concrete board.

The heats of combustion and product yields of the various items burned are given in Table 3.27. These values are derived from the measured initial and final mass, and an assumed value of 13.61 MJ/kg for the energy released per unit mass of oxygen consumed.

Table 3.27: Average heat and product yields of the various test items.

| Item   | $\Delta H$ (MJ/kg) | CO Yield          | CO <sub>2</sub> Yield | Soot Yield          | Residue Yield     |
|--------|--------------------|-------------------|-----------------------|---------------------|-------------------|
| Box #1 | $14.8 \pm 0.5$     | $0.039 \pm 0.001$ | $1.48 \pm 0.05$       | $0.0014 \pm 0.0003$ | $0.031 \pm 0.016$ |
| Pallet | $17.2 \pm 0.5$     | $0.031 \pm 0.001$ | $1.66 \pm 0.06$       | $0.0033 \pm 0.0006$ | $0.059 \pm 0.024$ |
| Crib   | $16.7 \pm 0.5$     | $0.023 \pm 0.001$ | $1.63 \pm 0.06$       | $0.0020 \pm 0.0003$ | $0.053 \pm 0.034$ |

### Modeling Notes

The combustible items are modeled as collections of Lagrangian particles that undergo a three-step decomposition process consisting of moisture evaporation, pyrolysis, and char oxidation. The moisture content,  $M$ , of the conditioned materials was less than the 0.05 lower limit of the moisture meter, and this value is used in the calculations.

**Box #1:** Single-wall corrugated box with nominal dimensions 61 cm by 61 cm by 46 cm (24 in by 24 in by 18 in) filled with “crinkle paper,” a common packing material made by shredding craft paper. The box alone had a mass of approximately 1.6 kg (3.5 lb), and the box and paper combined had a mass of 8.0 kg (18 lb). The box top flaps were closed, end over end, but not sealed with tape.



**Pallet:** Pine wood pallet with dimensions 122 cm by 102 cm by 12 cm (48 in by 40 in by 4.75 in). Its mass was approximately 16.0 kg (35 lb). Its moisture content was less than 5 %. Shown at right are two pallets, which were ignited with 1 kg (2.2 lb) of crinkle paper distributed evenly throughout the lower pallet.



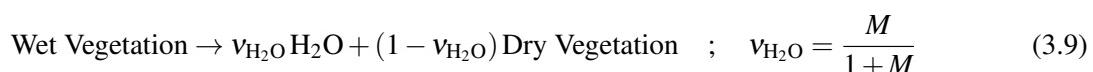
**Crib:** Pine wood crib with dimensions 56 cm by 56 cm by 46 cm (22 in by 22 in by 18 in) constructed of slats with a cross-section 3.8 cm (1.5 in) square. Its mass was approximately 39 kg (86 lb). Its moisture content was less than 5 %. It was ignited with 0.75 kg (1.7 lb) of crinkle paper stuffed in the space below the first row of slats.



Figure 3.37: Description of test items.

In the model, all of the wood and paper materials are assumed to be made up of cellulose,  $C_6H_{10}O_5$ , with a net heat of combustion of 16.12 MJ/kg [262]. It is also assumed that the materials have a char yield of 20 %, meaning that 20 % of the dry mass is converted into char that undergoes an exothermic oxidation reaction generating 32.12 MJ/kg of char consumed. The decomposition reactions are as follows:

1. Endothermic moisture evaporation



2. Endothermic pyrolysis of dry vegetation



### 3. Exothermic char oxidation



Note that the fuel gas is taken as cellulose with 20 % of its molecular mass decreased to account for the residual char, which is assumed to be pure carbon. The heat of combustion of this modified fuel gas is 12120 MJ/kg. The yield of residual Ash is based on the measured residual mass.

The crinkle paper is assumed to consist of 3 cm long, 4 mm wide strips with a surface area to volume ratio of  $10000 \text{ m}^{-1}$  (approximately 0.2 mm thick). The length and width are important only in defining the mass and volume of each particle. The thermal and kinetic properties of the paper are assumed to be similar to those of corrugated cardboard given in Table 14.12. The cardboard that makes up the box that holds the crinkle paper has a mass of  $0.62 \text{ kg/m}^2$  and the box itself has a mass of 1.6 kg. The corrugated paper has an assumed dry density of  $350 \text{ kg/m}^3$ , yielding an effective thickness of 1.8 mm. In the model, the box does not undergo char oxidation but rather “burns away” to expose the crinkle paper inside.

The wood crib is made up of 104 56 cm (22 in) long, 3.8 cm (1.5 in) square interlacing pine wood strips. The particles used to model the crib are assumed to be cylindrical in shape but with a surface area to volume ratio of  $69 \text{ m}^{-1}$  based on a direct measurement of the actual crib geometry. The dry density of the wood has been measured to be  $463 \text{ kg/m}^3$ , its peak pyrolysis temperature is taken to be  $320^\circ\text{C}$  [263], its char yield assumed to be 20 %, and its heat of reaction is taken to be  $418 \text{ kJ/kg}$  [264]. Other property values are based on the default vegetation pyrolysis model described in the FDS User’s Guide.

The pine wood pallets are constructed of 1.6 cm (5/8 in) thick planks and modeled as a collection of flat particles with a thickness of 8 mm and the same thermal and kinetic properties as the cribs, except that the wood making up the pallets has a dry density of  $414 \text{ kg/m}^3$ .

The drag per unit volume exerted by the particles is given by

$$\mathbf{f} = \frac{\rho}{2} C_d \kappa \mathbf{u} |\mathbf{u}| \quad ; \quad \kappa = C_s \sigma \beta \quad (3.12)$$

where  $\rho$  is the gas density,  $C_d$  is a drag coefficient,  $\mathbf{u}$  is the local velocity vector,  $C_s$  is a shape factor,  $\sigma$  is the surface area to volume ratio, and  $\beta$  is the packing ratio; that is the ratio of particle volume to cell volume. The shape factor is taken as 0.25 for all particle types. The packing ratio is determined by the measured mass of the item and the volume it occupies. The drag coefficient for the wood crib is 65, a value obtained by simulating a finely-resolved wood crib in a wind tunnel and calibrating the drag of the equivalent “crib particles” accordingly. The drag coefficient of the crinkle paper is taken as 1, and that of the pallet is taken as 3. These are only order of magnitude estimates and have not been verified.

## 3.60 NIST Polymers

Researchers at NIST have conducted measurements on various polymers as part of the MaCFP (Measurements and Computation of Fire Phenomena). The Condensed Phase Subgroup has focussed initially on PMMA. Measurements include TGA (Thermo-Gravimetric Analysis), DSC (Differential Scanning Calorimetry, MCC (Micro-Combustion Calorimeter), the NIST Gasification Apparatus, and the Cone Calorimeter.

## 3.61 NIST Pool Fire Experiments

The NIST Pool Fire Experiments include temperature, species concentration, velocity, and heat flux measurements of 30 cm and 100 cm diameter circular liquid fuel fires, and 37 cm gaseous burner fires.

The 30 cm burner is 15 cm deep and has a wall thickness of 1.6 mm. The burner is fitted with legs such that the burner rim is positioned 30 cm above the floor. The bottom of the burner is maintained at a constant temperature by flowing tap water (nominally  $20^\circ\text{C}$ ) through a 3 cm section on the bottom of the

fuel pan. The dimensions of the circular burner are similar to Weckman's methanol experiment described in Sec. 3.104.

The 100 cm burner is also 15 cm deep, has a wall thickness of 1.6 mm, and is water-cooled.

The 37 cm burner is actually 38 cm in diameter with an effective diameter of 37 cm. It is water cooled, and the surface temperature is maintained at approximately 40 °C. The measured fuel flow rate for the methane fire was 0.69 g/s and its estimated HRR was 34.5 kW. The heat release rates of the two propane fires were 20 kW and 34 kW.

Details and references with regard to the plume temperature measurements are given in Sec. 6.1.5. Details on the heat flux measurements are given in Sec. 12.2.8. Details on the gas species measurements is given in Sec. 9.5.6. Details on the velocity measuremnts is given in Sec. 8.8.

### **Modeling Notes**

The 30 cm pool fires are modeled at three different grid resolutions—2 cm, 1 cm, and 0.5 cm. The 100 cm pool fires are modeled at 4 cm, 2 cm, and 1 cm resolution. The mass loss rate of the fuel is specified.

A two-step reaction mechanism is implemented. In the first reaction, fuel is converted to CO, soot, H<sub>2</sub>, and H<sub>2</sub>O. In the second reaction, the CO, soot, and H<sub>2</sub> are converted to CO<sub>2</sub> and H<sub>2</sub>O. Both reactions employ fast kinetics, but proceed in series, not in parallel. The relative amounts of CO, soot, and H<sub>2</sub> produced in the first step are still subjects of study, and for the moment have been estimated based on measured results. The fractions of carbon atoms converted to CO in the first step are as follows—0.85 for acetone; 0.95 for ethanol; 0.97 for methane; 1.0 for methanol; 0.85 for propane. For all fuels, one half of the hydrogen atoms are converted to H<sub>2</sub> in the first step.

The radiative fractions are specified based on measured values—0.31 for acetone; 0.26 for ethanol; 0.15 for methane; 0.21 for 1 m methanol; 0.22 for 30 cm methanol; 0.22 for propane.

## **3.62 NIST Smoke Alarm Experiments**

A series of experiments was conducted by NIST to measure the activation time of ionization and photoelectric smoke alarms in a residential setting [265]. Tests were conducted in actual homes with representative sizes and floor plans, utilized actual furnishings and household items for fire sources, and tested actual smoke alarms sold in retail stores at that time. Thirty-six tests were conducted in two homes; 27 in a single-story manufactured home, and 8 in a two-story home. Eight experiments that were conducted in the single-story manufactured home were selected for model validation. Only tests that used a flaming ignition source with a couch or mattress fuel package were considered; the cooking oil fires and tests that used a smoldering ignition source were not considered. The flaming ignition tests used a moderate flame source to quickly ignite the fuel package.

The primary partitioning of the single-story floor plan consisted of three bedrooms, one full bathroom, one kitchen/dining area, one living room, and two hallways (see Fig. 3.38). For testing, the doors to Bedroom 3 and the bathroom were always closed. The ceiling was peaked on the long axis, reaching a height of 2.4 m. The outside walls were approximately 2.1 m in height. The slope of the ceiling was approximately 8.4°. Groups of smoke alarms were located in the room of fire origin, at least one bedroom, and in a central location. Five stations (Station A through Station E) containing smoke alarm<sup>4</sup> arrays were mounted parallel to the ceiling.

Although a load cell was used in the experiments to measure the mass loss rate of the fuel package, the mass loss data were not reliable enough to reconstruct the HRR curves for each test. Instead, the HRR

---

<sup>4</sup>Note that, in the FDS Guides, smoke detectors and smoke alarms are collectively referred to as smoke detectors because the same smoke detection algorithm is used to predict activation of either type of device.

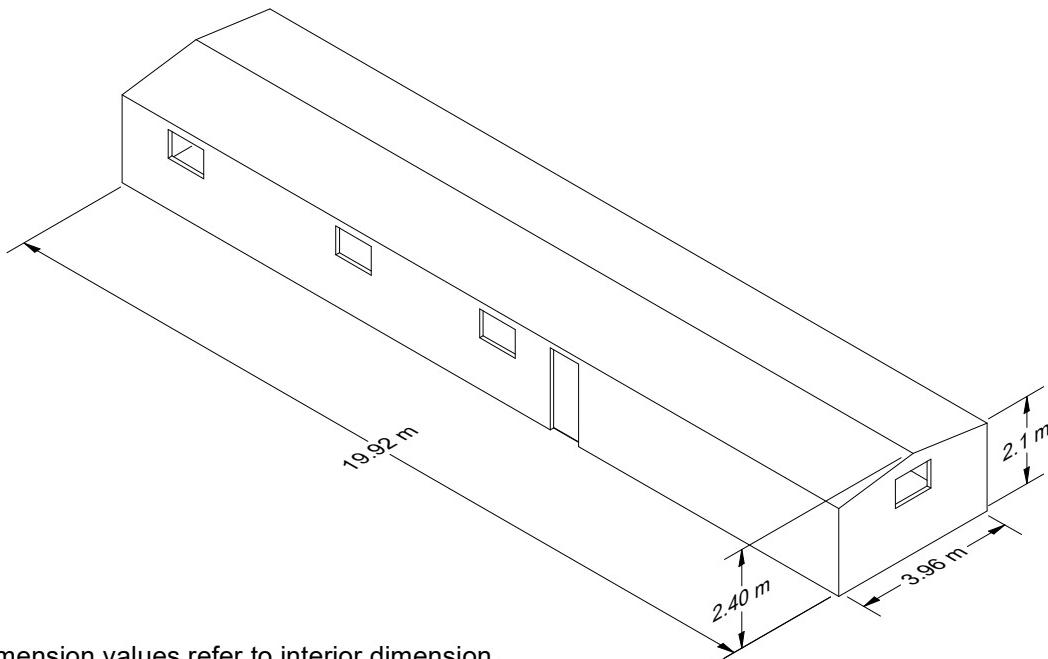
curves were determined by approximating the fire growth using a  $t$ -squared ramp, as in Eq. (3.13). The parameters for the  $t$ -squared ramp were calibrated in FDS by using the temperature measured at the highest thermocouple in the tree (2 cm below the ceiling) in the fire room.

$$\dot{Q} = \dot{Q}_0 \left( \frac{t}{\tau} \right)^2 \quad (3.13)$$

A time offset was used to align the predicted ceiling thermocouple temperatures with the measured temperatures. This offset is reported as the time at which the  $t$ -squared ramp begins. The  $t$ -squared calibration parameters and time offsets for the HRR ramps are shown in Table 3.28. Additionally, the ignition source had a small effect on the measured ceiling thermocouple temperatures. Therefore, the size of the ignition source was approximated as either 3 kW or 7 kW, and the time offset of the ignition source was also calibrated by using the measured ceiling thermocouple temperatures. The resulting HRR curve was input into FDS as a fire ramp. A summary of the eight tests selected for model validation is shown in Table 3.28.

Table 3.28: Summary of NIST Smoke Alarm Experiments selected for model validation.

| Test No. | Fire Source | Fire Location | $\dot{Q}_0$ (kW) | $\tau$ (s) | Time Offset (s) |
|----------|-------------|---------------|------------------|------------|-----------------|
| SDC02    | Chair       | Living Room   | 150              | 180        | 20              |
| SDC05    | Mattress    | Bedroom       | 200              | 180        | 20              |
| SDC07    | Mattress    | Bedroom       | 350              | 180        | 50              |
| SDC10    | Chair       | Living Room   | 150              | 180        | 40              |
| SDC33    | Chair       | Living Room   | 100              | 180        | 10              |
| SDC35    | Chair       | Living Room   | 100              | 180        | 10              |
| SDC38    | Mattress    | Bedroom       | 120              | 180        | 25              |
| SDC39    | Mattress    | Bedroom       | 200              | 180        | 25              |



**Notes:**

1. All dimension values refer to interior dimension.
2. The letters A-E refer to detector locations.
3. All walls are 10 cm thick.
4. All exterior doors and windows were closed during testing.
5. Doors to Bath and Bedroom #3 closed during testing.

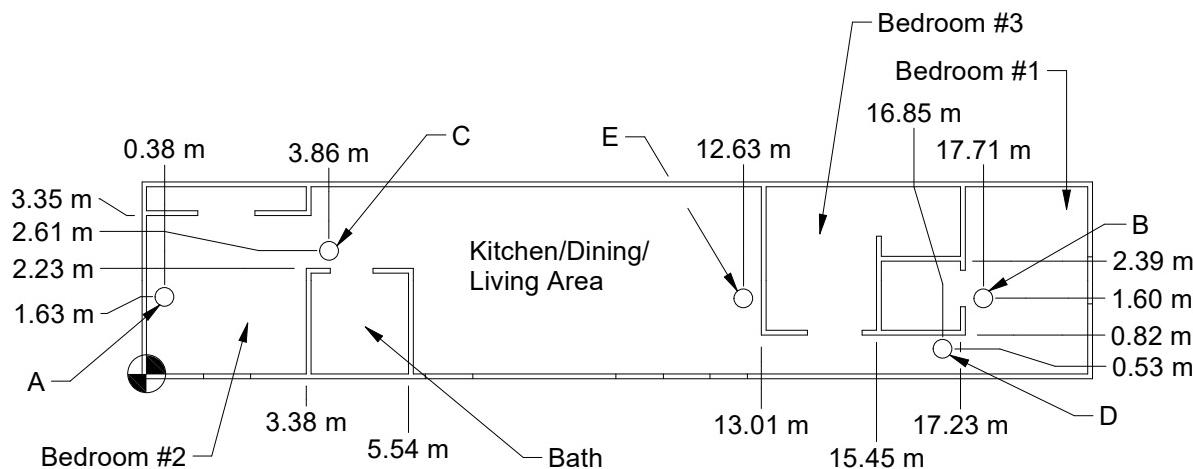


Figure 3.38: Geometry of the manufactured home from the NIST Smoke Alarm Experiments.

### 3.63 NIST Soot Deposition Gauge

A series of tests were performed as part of an effort to develop a gauge capable of making real time measurements of soot deposition [266]. The test apparatus consisted of a hot plate and cold plate measuring 8 cm wide by 41 cm long and separated by 1 cm. The hot plate was electrically heated and the cold plate was water cooled. A laminar diffusion flame burner using propene as the fuel was used to generate soot. A portion of the effluent from the burner was sent through the test apparatus. In addition to tests using the new gauge, a series of gravimetric tests were performed using 47 mm diameter pieces of aluminum foil attached to the cold plate in four locations. Tests with the aluminum foil used nominal flowrates of 2.5, 5.0, and 10.0 SLPM and nominal temperature differences of 100 °C and 200 °C. The test channel was mounted vertically to avoid gravitational settling and with the laminar flow speeds the device essentially creates only thermophoretic deposition. Four replicate tests were performed for the 2.5 and 5.0 SLPM flowrates and three for the 10.0 SLPM flowrate. A summary of the 22 tests modeled is given in the table below.

Table 3.29: Experiment Details for Gravimetric Measurements of Soot Deposition

| Test no. | Flow Speed<br>(SLPM) | ΔT<br>(K) | Inlet Soot Conc.<br>(mg/m <sup>3</sup> ) |
|----------|----------------------|-----------|--|
| 1        | 2.5                  | 94        | 67.6                                     |
| 2        | 2.5                  | 94        | 69.2                                     |
| 3        | 2.5                  | 96        | 64.2                                     |
| 4        | 2.5                  | 96        | 64.2                                     |
| 5        | 5.0                  | 96        | 65.5                                     |
| 6        | 5.0                  | 95        | 62.7                                     |
| 7        | 5.0                  | 92        | 61.9                                     |
| 8        | 5.0                  | 94        | 68.4                                     |
| 9        | 10.0                 | 97        | 25.9                                     |
| 10       | 10.0                 | 98        | 27.4                                     |
| 11       | 10.0                 | 99        | 25.5                                     |
| 12       | 2.5                  | 187       | 60.2                                     |
| 13       | 2.5                  | 190       | 61.5                                     |
| 14       | 2.5                  | 189       | 64.2                                     |
| 15       | 2.5                  | 187       | 59.1                                     |
| 16       | 5.0                  | 188       | 59.7                                     |
| 17       | 5.0                  | 186       | 58.5                                     |
| 18       | 5.0                  | 187       | 60.7                                     |
| 19       | 5.0                  | 187       | 55.5                                     |
| 20       | 10.0                 | 191       | 23.5                                     |
| 22       | 10.0                 | 188       | 24.4                                     |
| 21       | 10.0                 | 189       | 22.6                                     |

### 3.64 NIST Structure Separation Experiments

Maranghides et al. [267, 268] have developed a series of tests designed to understand safe structure separation distances for sheds, fences, and other combustible materials, with and without wind, in the wildland-urban interface (WUI).

#### Verification Tests

Prior to modeling heat fluxes to surfaces with attached flames or modeling ignition of siding material, a relatively simple test was carried out to record heat fluxes from a known fire source to targets in the proximity to the flame. The 8 MW NFRL calibration burner [269] (see Fig. 3.39) is positioned on a raised platform under the medium scale hood in NFRL. Three heat flux gauge towers are positioned 1, 2, and 3 m from the burner edge (or 2, 3, and 4 m from the burner center). Figure 3.40 shows a photograph from [268] (courtesy Matt Hoehler).

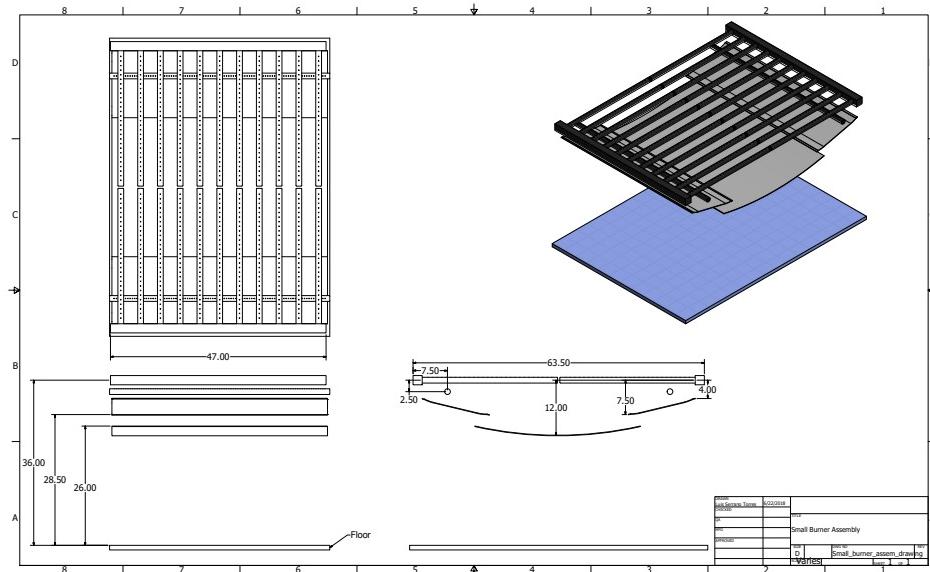


Figure 3.39: NFRL 8 MW calibration burner assembly drawing produced by NIST SURF student Louis Serrano Torres. Units in inches.

#### Modeling Notes

The burner is roughly  $1 \text{ m} \times 1.5 \text{ m}$  with 802 fuel ports  $1/8\text{th}$  inch in diameter (see Fig. 3.39). The FDS model of the burner is built from particles (see Fig. 3.41). Each particle has a radius set to give a spherical area equivalent to a  $1/8\text{th}$  inch diameter fuel port. The time ramp in the FDS simulation is compressed by a factor of 10. The “gauge heat flux” is recorded in an orientation pointing toward the burner ( $+x$  direction). The burner flow baffle plates are made from thin OBST. Fictitious manifolds are made from thickened OBST. The number of radiation angles is increased to 400. The radiation path length is set to 2 m. Ambient conditions are taken from historical weather data for the day of the experiment. The natural gas composition is taken from NFRL records on the day. A radiant fraction of 0.25 is prescribed, which is both consistent with a methane flame with additional ethane and the heat flux data farthest from the fire source under the

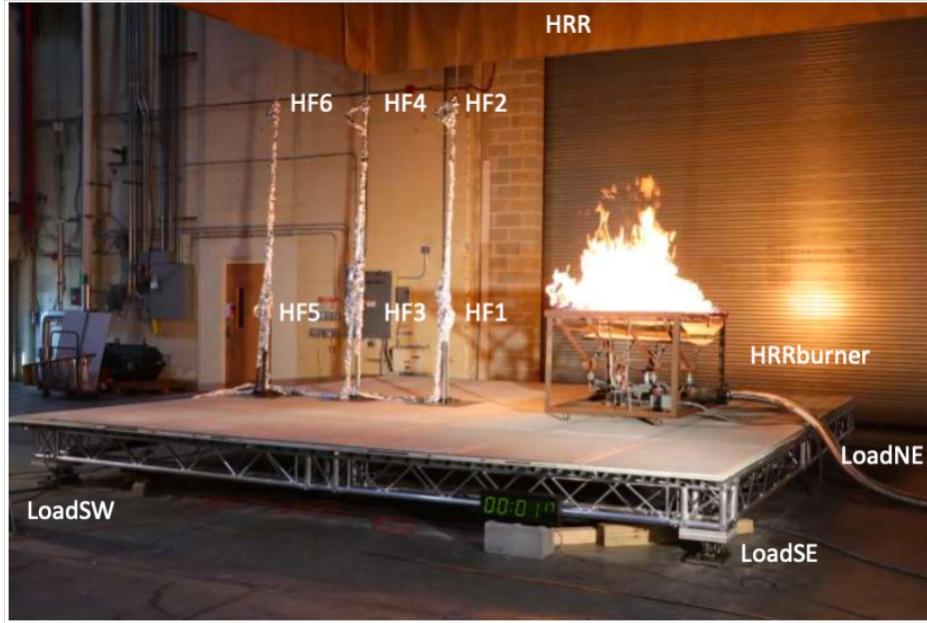


Figure 3.40: Structure Separation Verification setup showing natural gas burner and heat flux gauge positions.

assumption of a point source model. The burner has a  $D^*$  of approximately 2.2. As a baseline, a grid resolution of 5 cm provides a  $D^*/\Delta x = 44$ . Reasonably high resolution may be necessary if near-flame heat flux values are of interest. However, we also provide FDS results for 10 cm resolution.

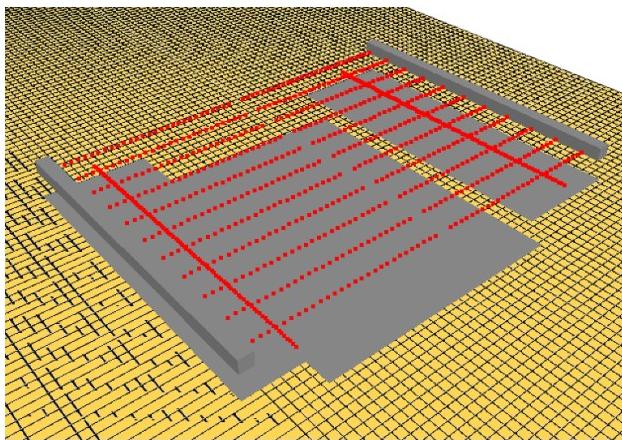


Figure 3.41: Image of the FDS particle model for the 8 MW NFRL burner.

### 3.65 NIST Vent Study

A series of 15 reduced-scale enclosure experiments were conducted during the summer of 2017 by Summer Undergraduate Research Fellows (SURF) Fateema Farzana and Cory Schovanec. There is no test report or paper describing these experiments; only what is included here.

## Enclosure Geometry

A drawing of the enclosure is given in Fig. 3.42. The enclosure consisted of two compartments stacked one on top of the other. The interior lateral dimensions of each compartment were 119 cm by 121 cm. The height of the lower compartment was 59 cm, and the upper was 61 cm. The enclosure was located within a vented laboratory space that was approximately 3 m by 3 m by 2.8 m high. The floor of this space was tiled, but a single sheet of gypsum board served as the lower floor of the test enclosure.

The front door was open in all experiments. For some portion of some of the experiments, the second floor was completely sealed. The leakage area was approximately 18 cm<sup>2</sup>, measured at an over-pressure of 25 Pa.

## Material Properties

The walls, ceiling and floor of each compartment was 1.6 cm (5/8 in) Type X gypsum board. Wood studs formed the exterior frame. Thermo-physical properties of the gypsum board were taken from Ref. [270] and manufacturer literature. It was assumed that the specific heat was 1.089 kJ/(kg · K), thermal conductivity 0.15 W/m/K, and density 673 kg/m<sup>3</sup>. Additionally, a layer of kaowool, shown in Fig. 3.42 was used to seal the gap between the removable roof and the second story walls. Aluminum tape was used to seal all other seams.

## Burner

For all experiments, a 10 cm square propane burner fueled at a rate of 1.65 L/min generated a 2.5 kW fire according to the following calculation:

$$1.65 \frac{\text{L}}{\text{min}} \times \frac{1}{60} \frac{\text{min}}{\text{s}} \times \frac{1}{1000} \frac{\text{m}^3}{\text{L}} \times 1.967 \frac{\text{kg}}{\text{m}^3} \times 46,300 \frac{\text{kJ}}{\text{kg}} = 2.50 \text{ kW} \quad (3.14)$$

Note that the mass flow controller (Sierra Instruments SmartTrak 50) assumed standard conditions to be 0 °C and 101325 Pa. For Tests 13-15, a Dwyer flow meter was used in place of the mass flow controller. The flow meter had a flow range of 4 L/min air.

## Thermocouples

Eight Type-K thermocouples were inserted at each level to measure the vertical temperature profile. The thermocouples formed a vertical array at 84 cm from the left wall of the enclosure, and 17 cm from the front wall. TC-1 was defined as the uppermost thermocouple, with heights defined as the vertical distance from the compartment specific floor.

Table 3.30: Heights of the thermocouples above the floor of each level of the enclosure

| Floor 2 TC's | 1    | 2    | 3     | 4    | 5     | 6    | 7    | 8    |
|--------------|------|------|-------|------|-------|------|------|------|
| Height (cm)  | 56.5 | 50.8 | 45.5  | 41.0 | 36.0  | 29.8 | 19.8 | 10.5 |
| Floor 1 TC's | 9    | 10   | 11    | 12   | 13    | 14   | 15   | 16   |
| Height (cm)  | 51.8 | 47.0 | 40.64 | 35.6 | 30.48 | 25.7 | 16.5 | 7.0  |

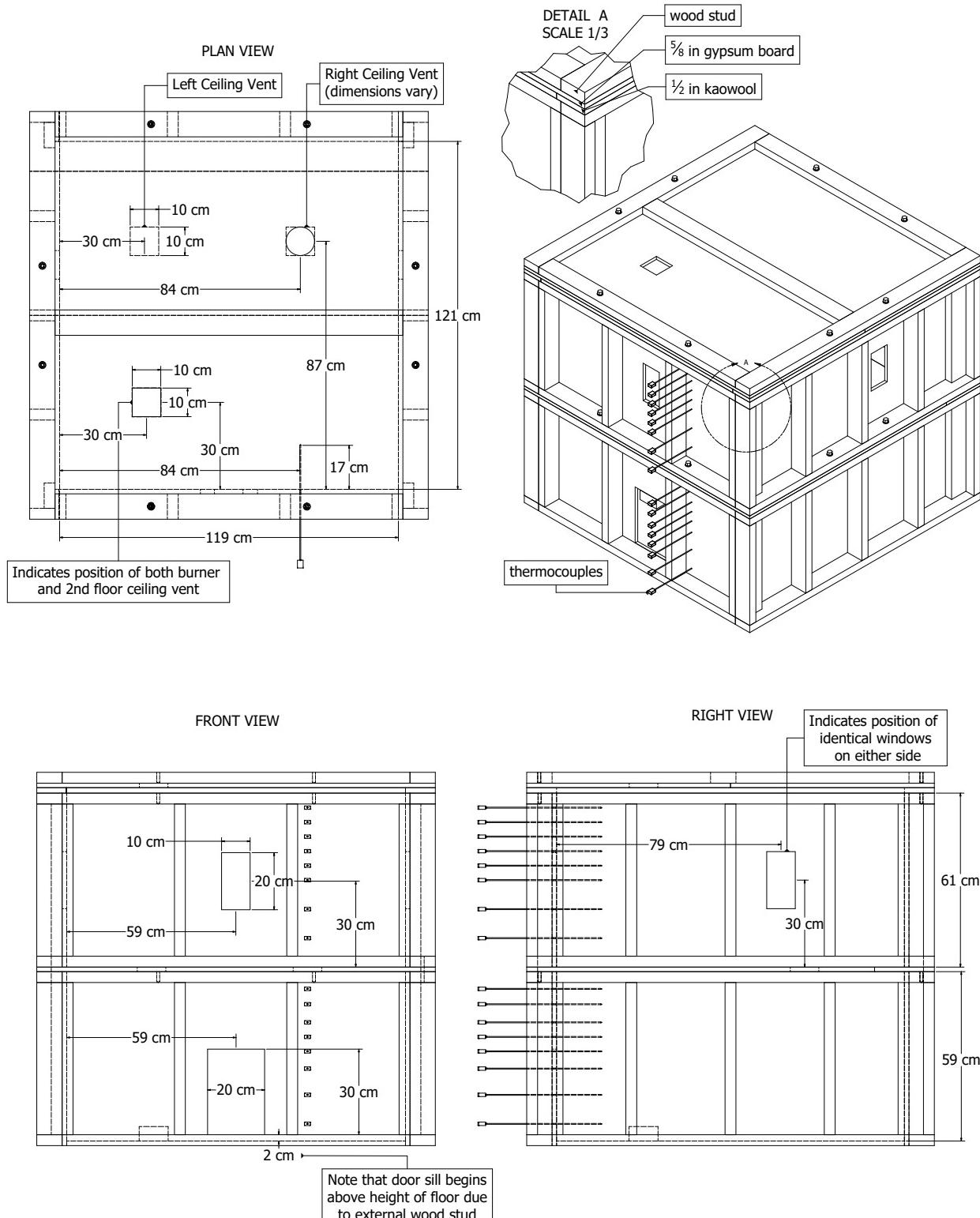


Figure 3.42: Geometry of the compartment from the NIST Vent Study

### Test Procedure

Each experiment lasted 100 min with a 5 min cool down period. Table 3.31 indicates the times when vents and windows were opened after the start of each experiment. For Test No. 1-4, two trials were performed. In each case, the difference in temperature remained within 3 percent, a difference of less than 1 °C. For this reason, no further replicates were conducted.

Table 3.31: Vent State by Experiment: Time Opened

| Test No. | Front Window (min) | Left Window (min) | Right Window (min) | Left Vent (min) | Right Vent (min) | Left Vent Area (cm <sup>2</sup> ) | Right Vent Area (cm <sup>2</sup> ) | Right Vent Shape | Roof Vent (min) |
|----------|--------------------|-------------------|--------------------|-----------------|------------------|-----------------------------------|------------------------------------|------------------|-----------------|
| 1        | 0                  | 0                 | 0                  | Closed          | 0                | 0                                 | 100                                | Square           | Closed          |
| 2        | 0                  | 0                 | 0                  | Closed          | 20               | 0                                 | 100                                | Square           | Closed          |
| 3        | 60                 | 40                | Closed             | Closed          | 20               | 0                                 | 100                                | Square           | Closed          |
| 4        | 0                  | 0                 | 0                  | Closed          | 0                | 0                                 | 400                                | Square           | Closed          |
| 5        | 0                  | 0                 | 0                  | Closed          | 20               | 0                                 | 400                                | Square           | Closed          |
| 6        | 60                 | 40                | Closed             | Closed          | 20               | 0                                 | 400                                | Square           | Closed          |
| 7        | 0                  | 0                 | 0                  | 0               | 0                | 100                               | 400                                | Square           | Closed          |
| 8        | 0                  | 0                 | 0                  | 20              | 40               | 100                               | 400                                | Square           | Closed          |
| 9        | 80                 | 60                | Closed             | 20              | 40               | 100                               | 400                                | Square           | Closed          |
| 10       | 0                  | 0                 | 0                  | Closed          | 0                | 0                                 | 100                                | Circle           | Closed          |
| 11       | 0                  | 0                 | 0                  | Closed          | 20               | 0                                 | 100                                | Circle           | Closed          |
| 12       | 60                 | 40                | Closed             | Closed          | 20               | 0                                 | 100                                | Circle           | Closed          |
| 13       | 0                  | 0                 | 0                  | 0               | 0                | 100                               | 400                                | Square           | 0               |
| 14       | 0                  | 0                 | 0                  | 20              | 40               | 100                               | 400                                | Square           | 60              |
| 15       | Closed             | Closed            | Closed             | 20              | 40               | 100                               | 400                                | Square           | 60              |

### 3.66 NRCC Facade Heat Flux Measurements

A series of experiments was conducted by the Fire Research Section of the Institute for Research in Construction, National Research Council of Canada (NRCC), to measure the heat flux to a mock exterior building facade due to a fire within a compartment [271, 272]. The experiments selected for model validation were conducted using a series of propane line burners within a compartment whose interior dimensions were 5.95 m wide, 4.4 m deep, and 2.75 m high (see Fig. 3.43). There were five different door/window sizes:

1. 0.94 m by 2.00 m high
2. 0.94 m by 2.70 m high (door)
3. 2.60 m by 1.37 m high (shown in Fig. 3.43)
4. 2.60 m by 2.00 m high
5. 2.60 m by 2.70 m high (door)

There were four fire sizes: 5.5 MW, 6.9 MW, 8.6 MW, and 10.3 MW. In all, 19 experiments were conducted, with the exception of the 10.3 MW fire with Window 1. In each experiment, heat flux measurements were made 0.5 m, 1.5 m, 2.5 m, and 3.5 m above the top of the door/window.

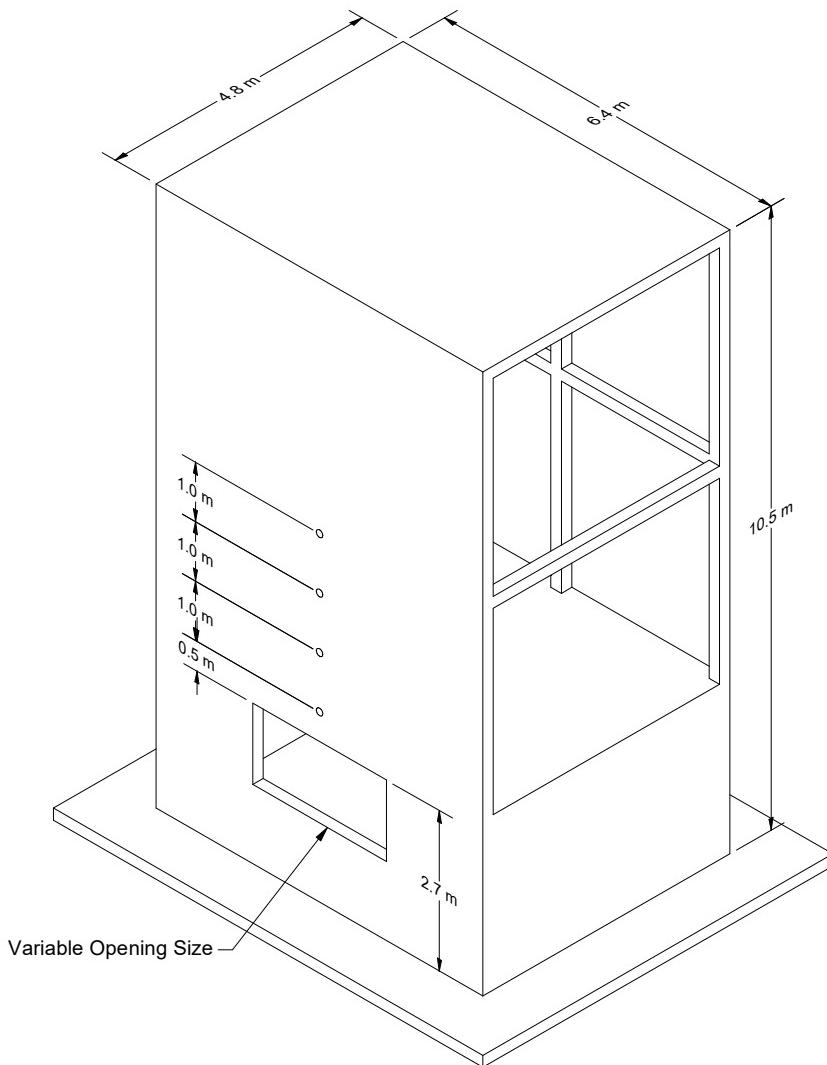


Figure 3.43: Geometry of the NRCC Facade Experiments.

### 3.67 NRCC Smoke Tower Experiments

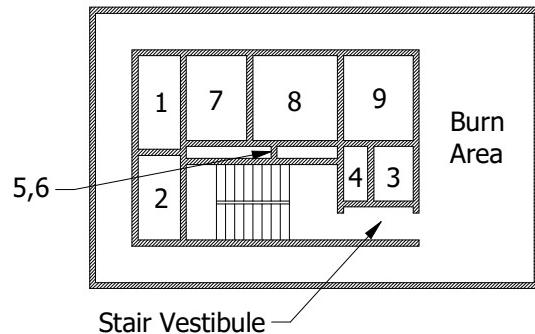
In 2006 and 2007, the National Research Council of Canada (NRCC) conducted 10 fire experiments in a 10 story experimental facility in Almonte, Ontario to study smoke movement through the stair shaft to the upper floors of the building. Four of these experiments utilized actual commodities as fuel, and six utilized a propane burner. Four of the six propane fires were intended to reproduce the heat release of the commodity fires, and these experiments (BK-R, CMP-R, CLC-I-R, and CLC-II-R) have been chosen for this guide.

Details of the experiments are included in a master's thesis and paper by Yan Wang [273, 274]. A description of FDS simulations of the propane experiments not included in this guide is given by Hadjisophocleous and Jia [275]. The analysis of the propane burner experiments discussed in this guide are based on the work of Paul Tyson at Ulster University as part of his master's thesis [276].

The tower was designed as a test bed for the center core of a high-rise building. It includes a compartment and corridor on each floor, a stair shaft, elevator shaft and service shafts [277]. Figure 3.44 displays the geometry of the building as modeled in FDS. All walls and floor slabs are taken to be 0.2 m thick. The first two floors are 3.4 m high, slab to slab. The upper eight floors are 2.4 m, slab to slab. The propane burner was located on the second floor and the smoke flowed through open doors to the stair vestibule and stair shaft itself. In the four experiments considered in this guide, the stair shaft was open on the fourth, sixth, eighth, and tenth floors. The other floors were closed off to the stair shaft. The ventilation system was turned off. A single door was opened on the first floor, and there were no other openings to the outside save natural building leakage. The referenced documents do not explicitly include estimates of leakage areas, but for the sake of modeling, the leakage for each floor was concentrated at a single 1.5 m by 1.5 m exterior window. The leakage area was specified based on an estimate of a "loose" building exterior in NFPA 92 [278]. This is a very important consideration in modeling because it determines the extent to which the smoke rising up the stair shaft encounters an opposing downward flow.

Thermocouples and gas analyzers were placed at various locations to measure temperature and O<sub>2</sub>, CO<sub>2</sub> and CO concentrations. A vertical array of TCs was located in the fire compartment and the doorway leading into the stair shaft on the second floor. TCs were also placed at each floor in the stair shaft. The gas analyzers were located in the stair shaft at the second floor, just outside the door to the fire compartment.

1. Building Supply Shaft
2. Building Return/Exhaust Shaft
3. Smoke Shaft
4. Elevator/Stair Vestibule Supply Shaft
5. Stair Supply Shaft
6. Stair Exhaust Shaft
7. Service Shaft
8. Elevator Shaft
9. Elevator Vestibule



SECTION F-F

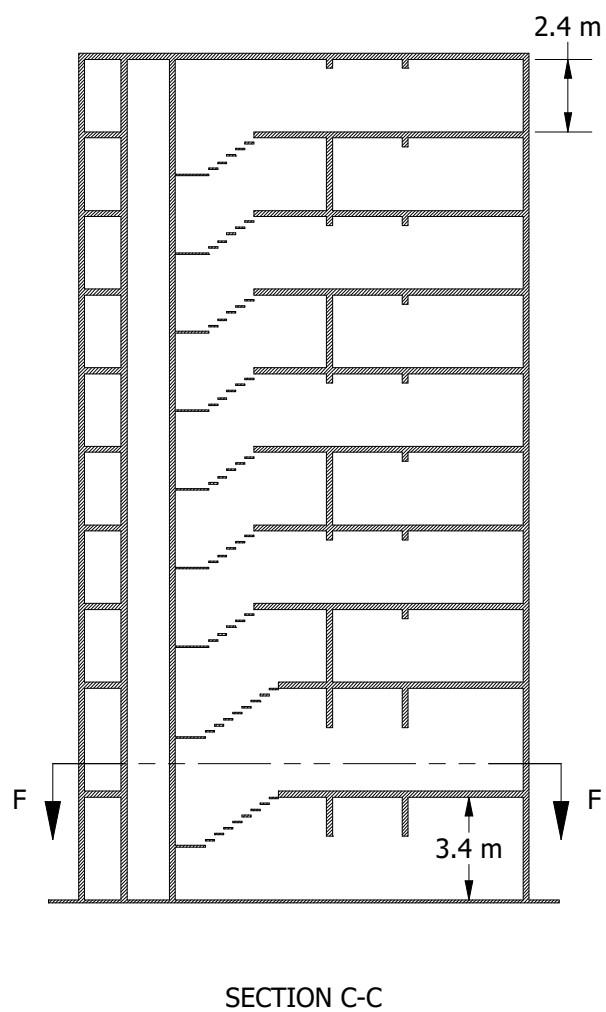
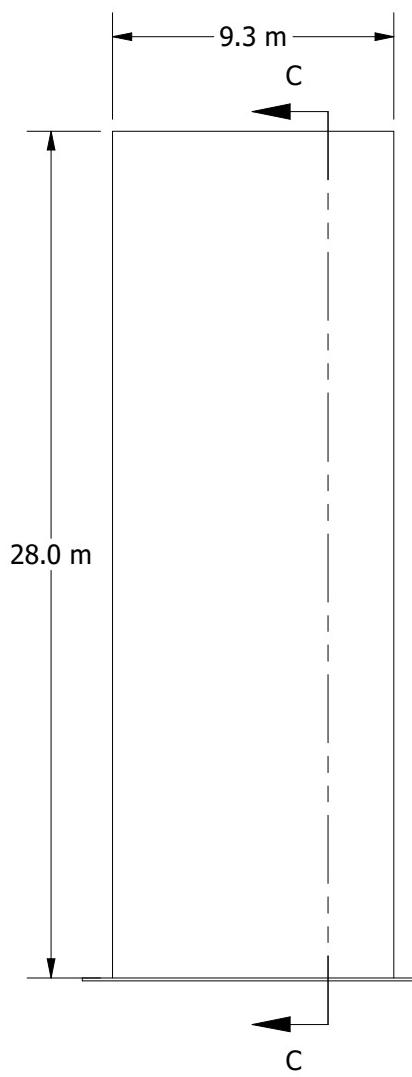


Figure 3.44: Geometry of the NRCC Smoke Tower Experiments.

## 3.68 NRL/HAI Wall Heat Flux Measurements

Back, Beyler, DiNenno and Tatem [279] measured the heat flux from 9 different sized propane fires set up against a wall composed of gypsum board. The experiments were sponsored by the Naval Research Laboratory and conducted by Hughes Associates, Inc., of Baltimore, Maryland. The square sand burner ranged in size from 0.28 m to 0.70 m, and the fires ranged in size from 50 kW to 520 kW.

## 3.69 Phoenix LNG Fires

In 2009, Sandia National Laboratories conducted two large-scale LNG pool fire experiments in a 120 m diameter pond in its Area III test complex in Albuquerque, New Mexico [280]. The fires were approximately 21 m and 83 m in diameter. Measurements of flame height, smoke production, burn rate, and heat flux were performed. A photograph of Test 2 is shown in Fig. 3.45.

### Modeling Notes

The simulation of Test 1 uses 1 m grid cells, while Test 2 uses 2 m cells. The computational domain for both simulations forms the shape of a cross that includes the fire and the radiometers to the north, south, east and west. Methane is the specified fuel, with a soot yield of 0.01 and radiative fraction of 0.25. Both values are estimates.

There are 1200 solid angles, rather than the default 100, used in the radiative transport equation to uniformly distribute the fire's radiative energy outward approximately 250 m. The value of 1200 is based on an assessment of the contours of the integrated radiative intensity. Also, both wide and narrow-angle radiometer measurements were made at distances ranging from 100 m to 250 m from the pool center, with various inclination angles. For the narrow-angle measurements, FDS chooses the nearest discrete radiation angle to represent the narrow-angle heat flux. At such large distances, it is difficult to "find" an angle that emanates from the fire to the location of the device.

**Flame Height Results:** Sec. 6.2.3

**Flame Tilt Results:** Sec. 6.3

**Heat Flux Results:** Sec. 12.2.10

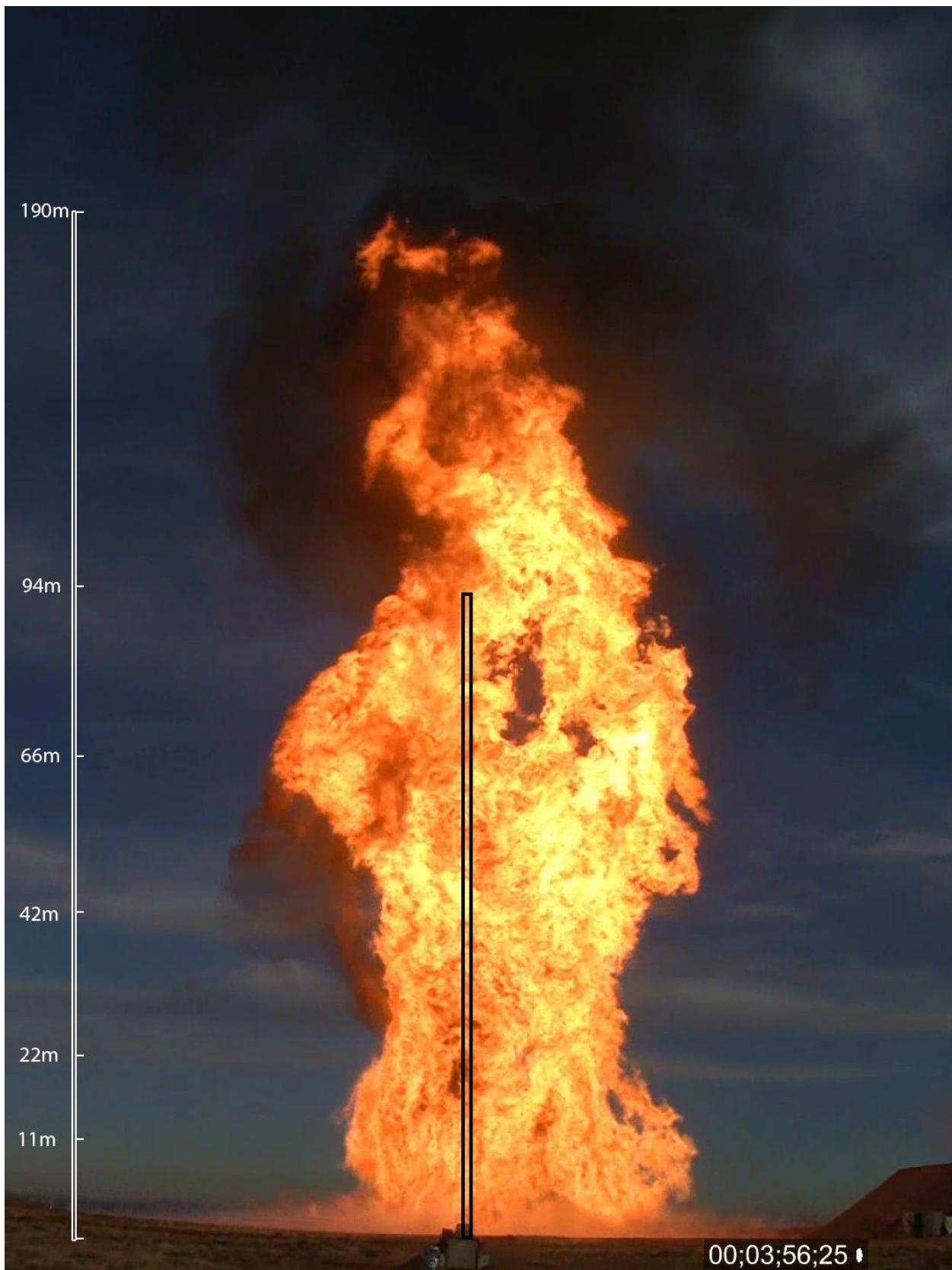


Figure 3.45: Photograph of Phoenix LNG Fire Test 2 [280].

## 3.70 Pool Fires

The “Pool Fires” cases include a variety of flammable and non-flammable liquid evaporation experiments:

1. A variety of pure liquid pool fires compiled by Gottuk and White [281] based on earlier compilations such as that by Mudan [282]. The liquids are listed in Table 3.32.
2. A single experiment involving the evaporation of water under a 50 kW/m<sup>2</sup> heat flux in the ASTM E2058 fire propagation apparatus, reported in Ref. [151].
3. Two heptane pool fire experiments described in Ref. [237].

### Modeling Notes

Because there are few details concerning the burning rates cited by Gottuk and White [281], the pans for the fuels listed in Table 3.32, with the exception of water, are assumed to be 1 m square with a fuel depth of 10 cm.

The simulations of the VTT heptane pool fires are performed in a 4 m by 4 m by 6 m domain with open boundaries, and a circular pool with steel (one cell high and thick) lip. The pool surface is 1 m above the floor.

The burning rate of liquid hydrocarbon fuels has been found to correlate well with the ratio of the heat of combustion,  $\Delta h_c$ , and the heat of gasification,  $\Delta h_g$ :

$$\dot{m}'' = 0.001 \frac{\Delta h_c}{\Delta h_g} \quad ; \quad \Delta h_g = \Delta h_v + \int_{T_0}^{T_b} c_p dT \quad (3.15)$$

where  $\Delta h_v$  is the latent heat of vaporization,  $T_0$  is the initial temperature,  $T_b$  is the boiling temperature, and  $c_p$  is the specific heat of the liquid fuel. The heat of gasification is the amount of energy required to raise the fuel from its initial temperature to its boiling temperature and evaporate it.

Table 3.32 lists the liquid fuel properties used in the simulations. Note that the heats of vaporization are evaluated at the liquid boiling temperature. The thermal conductivities,  $k$ , are found in Ref. [283], except for butane, which is found in Ref. [284]. The heats of combustion,  $\Delta h_c$ , are computed in FDS based on the heats of formation of the reactants and products listed in Ref. [285]. The heats of combustion account for the presence of products of incomplete combustion, like CO and soot.

The effective absorption coefficients,  $\kappa$ , for benzene and ethanol are based on curve fits to experimental data as explained in Appendix K of the FDS Technical Reference Guide. The absorption coefficient for methanol presented in Appendix K is calculated with the assumption that the incoming radiation is approximately blackbody radiation. The absorption coefficient for ethanol is calculated based on experimentally determined spectrum of an ethanol flame. Since both methanol and ethanol flames are low sooting, the blackbody radiation assumption is not correct. Instead it is assumed that the absorption coefficient for methanol should be of similar magnitude as that for ethanol. For heptane, butane and acetone the absorption coefficients are simple order of magnitude estimates.

Table 3.32: Liquid fuel properties.

| Fuel     | $\rho$<br>kg/m <sup>3</sup><br>[286] | $c_p$<br>kJ/(kg K)<br>[287] | $k$<br>W/(m K)<br>[283] | $\Delta h_v$<br>kJ/kg<br>[284] | $\Delta h_c$<br>kJ/kg<br>See text | $\chi_r$<br>[151] | $y_{CO}$<br>g/g<br>[151] | $y_s$<br>g/g<br>[151] | $T_b$<br>°C<br>[288] | $\kappa$<br>m <sup>-1</sup><br>See text |
|----------|--------------------------------------|-----------------------------|-------------------------|--------------------------------|-----------------------------------|-------------------|--------------------------|-----------------------|----------------------|---|
| Acetone  | 791                                  | 2.13                        | 0.20                    | 501                            | 28555                             | 0.27              | 0.003                    | 0.014                 | 56.15                | 100                                     |
| Benzene  | 874                                  | 1.74                        | 0.14                    | 393                            | 33823                             | 0.60              | 0.067                    | 0.181                 | 80.15                | 123                                     |
| Butane   | 573                                  | 2.28                        | 0.12                    | 385                            | 44680                             | 0.31              | 0.007                    | 0.029                 | 0                    | 100                                     |
| Ethanol  | 794                                  | 2.44                        | 0.17                    | 837                            | 27474                             | 0.25              | 0.001                    | 0.008                 | 78.35                | 1534.3                                  |
| Heptane  | 675                                  | 2.24                        | 0.14                    | 317                            | 43580                             | 0.33              | 0.010                    | 0.037                 | 98.35                | 187.5                                   |
| Methanol | 796                                  | 2.48                        | 0.20                    | 1099                           | 20934                             | 0.16              | 0.001                    | 0.001                 | 64.65                | 1500                                    |
| Water    | 1000                                 | 4.18                        | 0.60                    | 2260                           | N/A                               | N/A               | N/A                      | N/A                   | 100.0                | 140                                     |

### 3.71 PRISME Project

PRISME is the name of a fire test program conducted under the auspices of the Organization for Economic Cooperation and Development, Nuclear Energy Agency (OECD/NEA). The experiments were conducted at the French Institut de radioprotection et de sûreté nucléaire (IRSN) at Cadarache. A variety of experiments were conducted to study ventilation effects, electrical cable failure, and leakage. The test reports are not publicly available, but an entire edition of *Fire Safety Journal* documented various experimental and modeling studies [289].

The PRISME DOOR series consisted of six experiments, five of which involving two compartments connected by an open door (Tests 1-5) and one involving a third compartment (Test 6). The compartments were 5 m by 6 m by 4 m high. A well-instrumented ventilation system supplied air and exhausted combustion products at specified rates, but the thermal expansion of the gases caused these rates to change, a phenomenon that was intended to test the ventilation capabilities of the models. Wahlqvist and van Hees [290] modeled these experiments using FDS and contributed the input files for the cases documented in this guide.

The PRISME LEAK series consisted of experiments where smoke and heat flowed through various types of leaks between the test compartments. Instrumented cables were placed at various locations, and gas and solid phase temperatures were measured. FDS was used to simulate the heating up of the cables using the measured gas temperature several centimeters from the cables [291].

While not technically a part of the PRISME project, one of a series of experiments [292] conducted within the same facility was analyzed by Beji and Prétrel [293]. In this experiment, two water spray nozzles were activated during a fire in a sealed, mechanically-ventilated compartment. The change in pressure and ventilation flow rates induced by the water spray can be used to assess the amount of energy extracted by the water droplets.

### 3.72 Purdue Flames

A turbulent buoyant diffusion flame is established on a diffuser burner with an exit diameter of 7.1 cm. The diverging angle of the burner is 7° such that the gaseous fuel (methane) is decelerated and forms a uniform velocity distribution at the burner exit [30]. The methane (CH<sub>4</sub>) mass flow rate (84.3 mg/s) The buoyant diffusion flame burns in a quiescent atmospheric pressure environment. The flame is surrounded by a screened enclosure to minimize flame disturbance. The Froude number of the flame is 0.109 and matches that of a 7.1 cm diameter liquid toluene pool fire [30, 32]. The total heat release rate of the methane flame is 4.2 kW under the assumption of complete combustion, and the visible flame height is approximately

36 cm [30]. Measured and computed vertical and horizontal velocity, mixture fraction, and temperature values for this flame have been reported by Xin et al. [30, 294] and Zhou et al. [32, 295]. The mean temperatures have been inferred from the measured species concentrations [30] by assuming an adiabatic flame. The interdependencies between species concentrations, temperature and specific heat have been ignored for determining the mean temperature.

### 3.73 Ranz Marshall Droplet Experiments

In 1952, Ranz and Marshall performed a set of droplet evaporation experiments that ultimately led to the development of Nusselt and Schmidt number correlations for droplets [296]. The experiments documented in Figure 8 and Tables 1-4 in the paper have been modeled with FDS. For Figure 8 of the paper, a 1043  $\mu\text{m}$  water droplet was suspended in still dry air at an ambient temperature and pressure of 24.9 °C and 98792 Pa, and its diameter was measured over time. For the experiments in Tables 1-4 in the paper, droplets were suspended in a dry air stream. Experimental parameters include the fluid type (water or benzene), initial droplet diameter, ambient temperature, and velocity of the air stream. The evaporation rate in the simulations is calculated based the time required for the droplet to decrease in size to 350  $\mu\text{m}$ , the minimum reported diameter. Table 3.33 summarizes the experiments.

Table 3.33: Summary of Ranz and Marshall droplet evaporation experiments.

| Table No. | Test No. | Fluid | Diameter ( $\mu\text{m}$ ) | Air Temperature (°C) | Pressure (Pa) | Velocity (m/s) |
|-----------|----------|-------|----------------------------|----------------------|---------------|----------------|
| 1         | 1        | Water | 954                        | 19.9                 | 99059         | 2.46           |
| 1         | 2        | Water | 954                        | 24.6                 | 98659         | 2.1            |
| 1         | 3        | Water | 954                        | 24.9                 | 98659         | 1.723          |
| 1         | 4        | Water | 954                        | 25.3                 | 98659         | 1.532          |
| 1         | 5        | Water | 954                        | 25.4                 | 98659         | 1.197          |
| 1         | 6        | Water | 954                        | 24.3                 | 98392         | 0.952          |
| 1         | 7        | Water | 954                        | 24.4                 | 98392         | 0.762          |
| 1         | 8        | Water | 954                        | 24.5                 | 98392         | 0.571          |
| 1         | 9        | Water | 954                        | 24.5                 | 98392         | 0.571          |
| 1         | 10       | Water | 954                        | 24.6                 | 98392         | 0.285          |
| 1         | 11       | Water | 954                        | 24.7                 | 98392         | 0.1513         |
| 1         | 12       | Water | 954                        | 24.8                 | 98392         | 0.1718         |
| 1         | 13       | Water | 954                        | 24.9                 | 98392         | 0.0841         |
| 1         | 14       | Water | 954                        | 25.0                 | 98392         | 0.0337         |
| 1         | 15       | Water | 954                        | 23.2                 | 98392         | 2.86           |
| 1         | 16       | Water | 954                        | 23.6                 | 99459         | 2.67           |
| 1         | 17       | Water | 954                        | 23.7                 | 99459         | 2.28           |
| 1         | 18       | Water | 954                        | 24.0                 | 99459         | 3.06           |
| 1         | 19       | Water | 954                        | 24.9                 | 98792         | 0              |
| 2         | 1        | Water | 950                        | 90.0                 | 98792         | 2.3            |
| 2         | 2        | Water | 950                        | 77.5                 | 98792         | 1.1            |
| 2         | 3        | Water | 950                        | 78.7                 | 98792         | 1.1            |
| 2         | 4        | Water | 950                        | 78.7                 | 98792         | 1.1            |
| 2         | 5        | Water | 950                        | 84.0                 | 98792         | 1.83           |
| 2         | 6        | Water | 950                        | 82.5                 | 98792         | 1.14           |

Table 3.33: Continued

| Table No. | Test No. | Fluid   | Diameter ( $\mu\text{m}$ ) | Air Temperature ( $^{\circ}\text{C}$ ) | Pressure (Pa) | Velocity (m/s) |
|-----------|----------|---------|----------------------------|--|---------------|----------------|
| 2         | 7        | Water   | 950                        | 83.0                                   | 98792         | 1.14           |
| 2         | 8        | Water   | 950                        | 66.4                                   | 98792         | 0.55           |
| 2         | 9        | Water   | 950                        | 71.4                                   | 98792         | 0.176          |
| 3         | 1        | Water   | 850                        | 115.0                                  | 98792         | 1.84           |
| 3         | 2        | Water   | 710                        | 115.0                                  | 98792         | 1.84           |
| 3         | 3        | Water   | 560                        | 85.0                                   | 98792         | 0.188          |
| 3         | 4        | Water   | 460                        | 85.0                                   | 98792         | 0.188          |
| 3         | 5        | Water   | 960                        | 221.0                                  | 98792         | 1.84           |
| 3         | 6        | Water   | 580                        | 221.0                                  | 98792         | 1.84           |
| 3         | 7        | Water   | 880                        | 193.0                                  | 98792         | 0.77           |
| 3         | 8        | Water   | 600                        | 193.0                                  | 98792         | 0.77           |
| 3         | 9        | Water   | 1010                       | 125.0                                  | 98792         | 0.21           |
| 4         | 1        | Benzene | 1100                       | 24.4                                   | 97592         | 0.051          |
| 4         | 2        | Benzene | 1100                       | 26.4                                   | 97592         | 0.153          |
| 4         | 3        | Benzene | 1100                       | 27.1                                   | 98125         | 0.289          |
| 4         | 4        | Benzene | 1100                       | 17.9                                   | 98525         | 0.748          |
| 4         | 5        | Benzene | 1100                       | 17.5                                   | 98525         | 1.124          |
| 4         | 6        | Benzene | 1100                       | 17.7                                   | 97725         | 1.5            |
| 4         | 7        | Benzene | 1100                       | 20.7                                   | 97725         | 0.188          |
| 4         | 8        | Benzene | 1100                       | 20.4                                   | 97725         | 0.283          |
| 4         | 9        | Benzene | 1100                       | 19.9                                   | 97725         | 0.755          |
| 4         | 10       | Benzene | 1100                       | 20.0                                   | 97725         | 1.13           |
| 4         | 11       | Benzene | 1100                       | 20.2                                   | 97725         | 1.516          |
| 4         | 12       | Benzene | 1100                       | 20.2                                   | 97725         | 1.9            |
| 4         | 13       | Benzene | 1100                       | 20.4                                   | 97725         | 2.88           |

### 3.74 Restivo Compartment Air Flow Experiment

Velocity measurements for forced airflow within a 9 m by 3 m by 3 m high compartment (Fig. 3.46) were made by Restivo [297]. These measurements have been widely used to validate CFD models designed for indoor air quality applications. It was also used to assess early versions of FDS [19, 20, 38]. In the experiment, air was forced into the compartment through a 16.8 cm vertical slot along the ceiling running the width of the compartment with a velocity of 0.455 m/s. A passive exhaust was located near the floor on the opposite wall, with conditions specified such that there was no buildup of pressure in the enclosure. The component of velocity in the lengthwise direction was measured in four arrays: two vertical arrays located 3 m and 6 m from the inlet along the centerline of the room, and two horizontal arrays located 8.4 cm above the floor and below the ceiling, respectively. These measurements were taken using hot-wire anemometers. While data on the specific instrumentation used are not readily available, hot-wire systems tend to have limitations at low velocities, with typical thresholds of approximately 0.1 m/s.

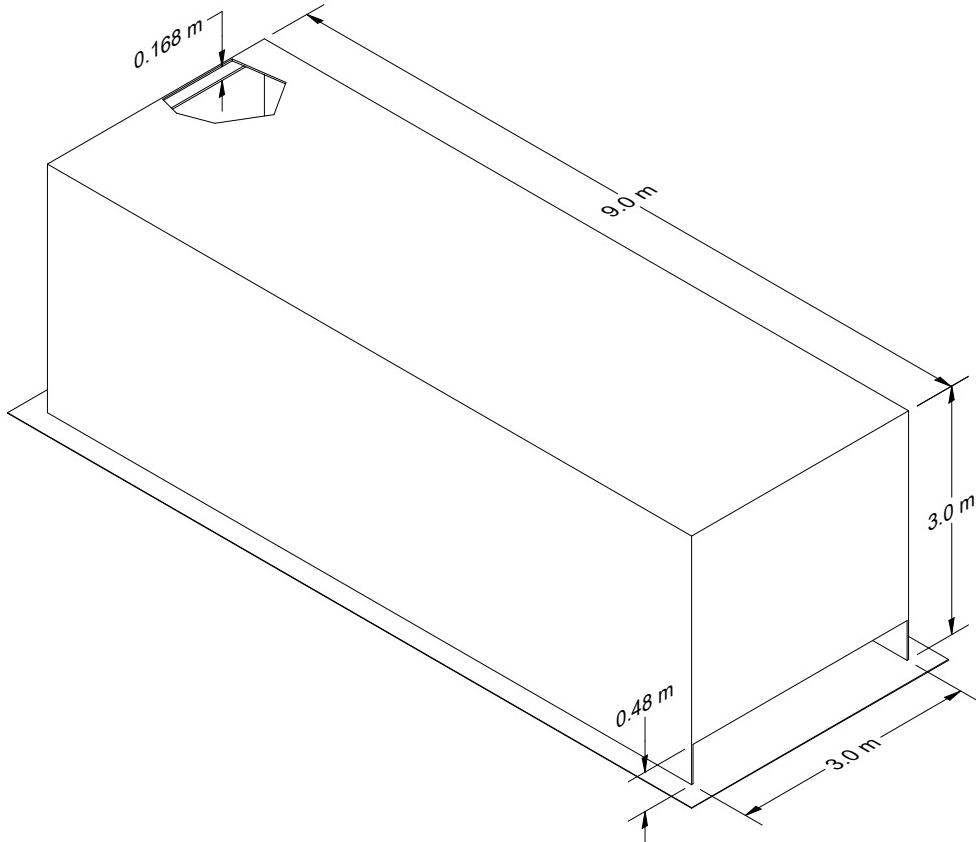


Figure 3.46: Geometry of Restivo's compartment.

### 3.75 Sandia Methane Burner

A series of 3 m diameter methane gas burner experiments were conducted in the Fire Laboratory for Accreditation of Models and Experiments (FLAME) facility in the Thermal Test Complex at Sandia National Laboratories [280]. The test chamber (Fig. 3.47) is cylindrical with an inner diameter of 18.3 m and a height of 13.1 m at the perimeter. The ceiling slopes upwards to a height of 15.2 m at the center. The perimeter walls are made of steel channel sections that are water-cooled. The gas burner is surrounded by a 12.7 m diameter steel spill plate. Beyond the spill plate is steel grating through which air can flow from the basement.

#### Modeling Notes

The simulations of the 3 m methane fires are done with 10 cm grid resolution in an open domain. That is, the walls of the cylindrical test cell are not modeled.

The radiative fraction is specified at 0.35 rather than the default 0.20 for methane because the large fire is far more sooty and luminous than a small methane flame. 600 solid angles are used to solve the radiative transport equation rather than the default 100 so as to resolve the radiative flux 9 m from the fire.

**Flame Height Results:** Sec. 6.2.3

**Heat Flux Results:** Sec. 12.2.11

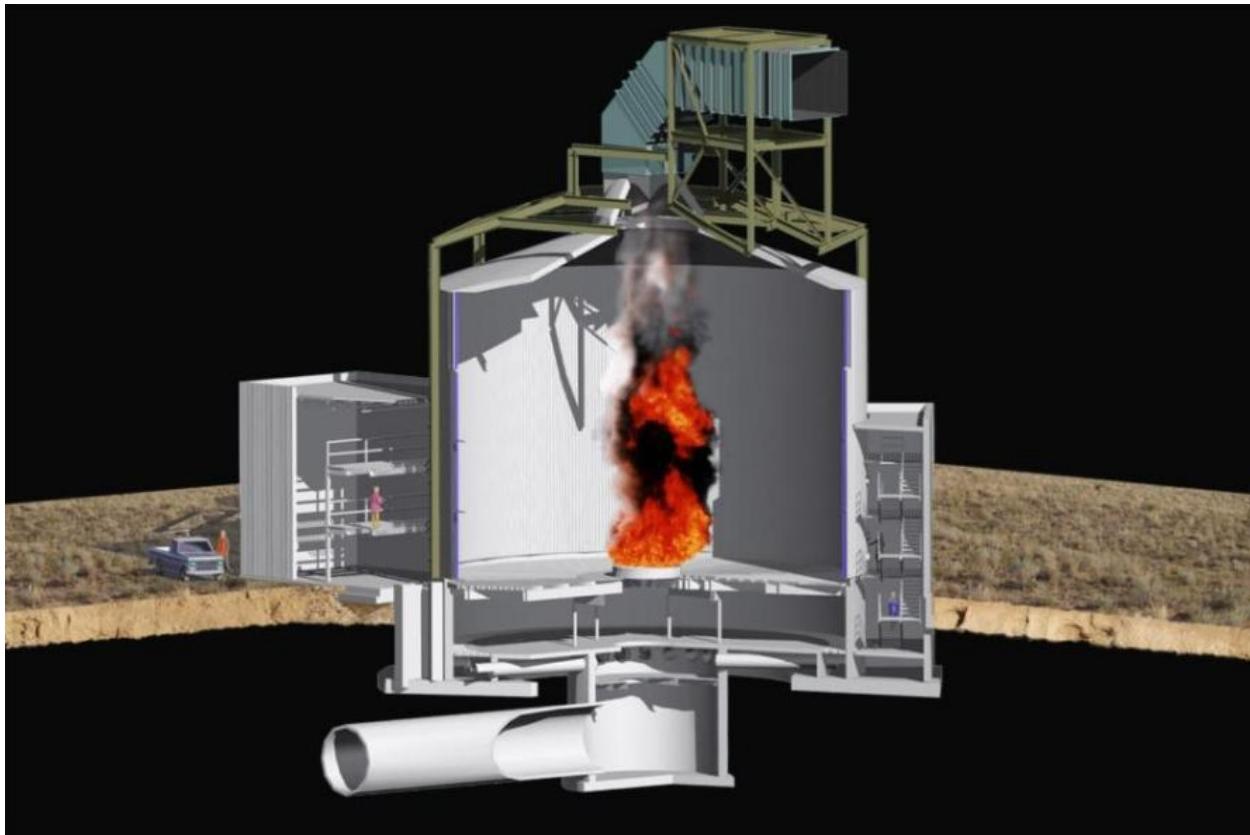


Figure 3.47: Cutaway view of the Sandia FLAME test cell.

### 3.76 Sandia Plume Experiments

The Fire Laboratory for Accreditation of Models by Experimentation (FLAME) facility [298, 299] at Sandia National Laboratories in Albuquerque, New Mexico, is designed specifically for validating models of buoyant fire plumes. The plume source is 1 m in diameter surrounded by a 0.5 m steel ‘ground plane’. O’Hern et al. [298] studied a turbulent buoyant helium plume in the FLAME facility. PIV/PLIF techniques are used to obtain instantaneous joint scalar and velocity fields and thus obtain Favre averaged velocity fields. Earlier work to model this experiment has been performed by DesJardin et al. [300]. Tieszen et al. [301, 302] studied methane and hydrogen pool fires.

#### Modeling Notes

The data in the experimental repository for the helium plume is Favre averaged. The “helium” was actually a mixture of 96.4 vol % (0.7075 mass fraction) helium, 1.7 vol % (0.1809 mass fraction) acetone, and 1.9 vol % (0.1116 mass fraction) oxygen; this mixture is referred to as the “plume fluid” [298]. The data for “mass fraction” in the experimental repository is for Favre averaged plume fluid mass fraction. To account for any effect of differential diffusion, we separately transport helium, acetone, and oxygen in the simulations. Then the plume fluid mass fraction is obtained using the conversion  $Y_{\text{plume fluid}} = Y_{\text{acetone}}/0.1809$ .

Note that the velocity fields in the methane and hydrogen fire plumes were obtained directly from PIV and are therefore ensemble averaged [301, 302].

### 3.77 Scaling Pyrolysis

FDS has a scaling-based pyrolysis model which dynamically scales a reference heat release rate per unit area curve based on the energy absorbed on the surface. These cases include cone calorimeter experiments conducted at multiple heat transfer levels. The robustness of the approach is evaluated using cone calorimeter data for 166 materials available in public datasets. These materials include:

1. Fifteen materials from studies conducted by Jensen Hughes, Inc. (JH) located in Baltimore, MD, USA [230, 233].
2. Eight materials from the U.S. Federal Aviation Administration (FAA) Polymers experiments [207, 303].
3. Two materials from the Aalto Wood experiments conducted at Aalto University in Finland [145].
4. Seventy-one materials from the material testing database provided by the Fire Safety Research Institute (FSRI) at the UL Research Institutes [221].
5. Eight materials from the Forest Products Laboratory (FPL) of the U.S. Department of Agriculture database [219].
6. Sixty-one materials from the Research Institutes of Sweden (RISE) database [304].

Table 3.34 summarizes the materials by source and composition category. The polymers category includes pure polymers, polymer blends, polymers with coating (e.g., scratch resistance), and polymers with non-fibrous additives. The wood material category includes natural wood species and wood-based products such as plywood, hardboard, and particleboard (with and without fire resistant treatment). The mixtures category includes polymers with fibrous additives, multi-layered materials, and assemblies. The other material category includes other natural and synthetic materials such as asphalt shingles, cardboard, rubbers, felts, and gypsum wallboards. Approximately half of the materials are polymers, with the remaining half split across the other three material categories.

Table 3.34: Summary of Materials

| Dataset        | Mixtures | Others | Polymers | Wood-Based | Total |
|----------------|----------|--------|----------|------------|-------|
| Aalto Woods    | 0        | 0      | 0        | 2          | 2     |
| FAA Polymers   | 0        | 0      | 8        | 0          | 8     |
| FPL Materials  | 0        | 0      | 0        | 8          | 8     |
| FSRI Materials | 0        | 26     | 30       | 15         | 71    |
| JH Materials   | 5        | 1      | 4        | 5          | 15    |
| RISE Materials | 37       | 3      | 16       | 5          | 61    |
| Total          | 42       | 30     | 58       | 35         | 165   |

#### Modeling Notes

Each case is modeled using the solid phase only solver in FDS. An empirical model is used to account for the thermal exposure after ignition based on the estimated flame heat flux. The empirical model requires soot yield,  $Y_s$ , data. Materials which  $Y_s$  was measured to be zero or less than zero were set to a minimum value of 0.001 g/g. Materials for which data was not available in the original studies used a  $Y_s$  of 0.05 g/g.

Note that the RISE and FPL databases did not provide ignition properties or information on specific material conditioning or modifications to test procedures. For these materials, a thermal conductivity of 0.4 W/(m · K), specific heat capacity of 1.0 kJ/(kg · K), and an emissivity of unity was assumed. The ignition temperature of each material was calculated based on measured time to ignitions across all tests using either properties provided by the authors or these assumed properties. The ignition temperature is provided for reference; however, in the models the time to ignition in each case is fixed based on experimental data (i.e., the validation focuses on what happens after ignition).

### 3.78 SETCOM Wall Condensation Experiments

The Separate Effect Test for Condensation Modeling (SETCOM) facility is located in Jülich, Germany [305]. The facility is a recirculating duct containing a flow conditioning section for establishing temperature and humidity and a test section for performing condensation experiments. The condensation section contains a 4 m or 5 m long, water-cooled, aluminum plate for its floor with the remaining walls adiabatic. The condensation section can be tilted from horizontal to vertical to investigate the effects of orientation on condensation. A set of five experiments were performed using the 4 m test section that measured the condensation heat flux from hot, high humidity air. Temperature, humidity, and flow rate were varied.

#### Modeling Notes

Prior to running the validation cases, a set of five scoping simulations were run with no condensation. These simulations used a short length of the test section with `PERIODIC` boundary conditions. These cases were used to determine the rms velocity as a function of the mean velocity.

The condensation simulations included a 4 m portion of duct upstream to allow for flow development, and a 1 m portion of duct downstream to avoid boundary effects on the test section. The upstream boundary condition was set with the conditions shown in the table below along with synthetic eddy method inputs using the rms velocity determine from the scoping simulations. The outlet was defined as an `OPEN` boundary. The experiments measured temperature 1.5 cm into the aluminum plate along the plate centerline. The test measured condensation heat transfer was used with the inside plate temperature to derive the plate surface temperature. The condensation plate `TMP_FRONT` was set to derived temperature as a function of length along the plate.

Table 3.35: Summary of SETCOM condensation experiments selected for model validation.

| Test No. | Air Speed (m/s) | Temperature (°C) | Humidity (%) |
|----------|-----------------|------------------|--------------|
| 1        | 0.8             | 86               | 69           |
| 2        | 1.8             | 84               | 57           |
| 3        | 3.7             | 79               | 59           |
| 4        | 4.2             | 78               | 71           |
| 5        | 5.2             | 75               | 71           |

### 3.79 Shell LNG Fireball Experiments

Shell Research Ltd. commissioned four large-scale BLEVE (Boiling Liquid Expanding Vapor Explosion) experiments using LNG (Liquified Natural Gas) at the DNV (Det Norske Veritas) GL test facility at Spadeadam, UK [306]. For Experiments 2-4, the cylindrical containment vessel (Fig. 3.48) was constructed of 6 mm stainless steel plates and had a length of approximately 6.5 m and diameter of approximately 1 m, with a total volume of 5.055 m<sup>3</sup>. The mass of LNG for Experiments 2-4 was approximately 681 kg, 1306 kg, and 1251 kg, respectively. The LNG consisted of 96.7 % methane, 3.0 % ethane, 0.2 % nitrogen, and 0.1 % propane, by volume. The reservoir pressure for Experiments 2-4 was maintained at 13.01 bar, 6.07 bar, and 13.62 bar; and the temperatures were –115 °C, –131 °C, and –115 °C, respectively.



Figure 3.48: (Top) Pressure vessel used in the Shell LNG Fireball experiments. (Bottom) Photographs of Tests 2, 3, and 4, respectively [306].

The rupture of the vessels was initiated by an explosive cutting charge designed to rip open the vessel from end to end. Commercial fireworks were ignited just prior to the explosive charge to ensure ignition of the released gas.

Radiometers and pressure transducers were positioned at various distances from the vessel. Only a fraction of the data has been made public, including radiometer measurements at distances of 40 m, 70 m, and 100 m.

### **Modeling Notes**

The FDS simulations of the three BLEVE experiments are performed with 1 m resolution spanning a volume that is 200 m long, 120 m wide, and 200 m high. The specified mass of LNG is injected uniformly for 0.2 s at the ground over an area 4 m long and 4 m wide. An inert obstruction that is 1 m long by 1 m wide and 1 m tall is suspended 1 m above the spill region to represent the remains of the containment vessel. No attempt is made to model the destruction of the vessel or the subsequent spill of LNG.

Approximately 600 angles are used in the radiative transport solver rather than the default 100. A radiative fraction of 30 % is used, rather than the default of 20 % for methane.

### **Heat Flux Results:** Sec. 12.2.12

## **3.80 Sippola Aerosol Deposition Experiments**

Mark Sippola, a doctoral student at the University of California, Berkeley, measured aerosol deposition velocities for various sizes of monodisperse fluorescent particles and various air velocities in a duct [307, 308]. The experimental facility consisted of a duct loop with a section for injecting fluorescent aerosol particles. The loop contained four measurement sections with two sections located after a long segment of straight duct such that fully-developed flow profiles existed. The experiments considered here include tests with measurements in the fully-developed flow test sections. Tests included 16 test for straight smooth steel duct and 15 tests in a straight duct lined with insulation. Based upon pressure drop measurements made in the duct, the roughness of the insulated duct was estimated as 1.5 mm. Both ducts had dimensions of 15 cm by 15 cm. The particle diameters were nominally 1  $\mu\text{m}$ , 3  $\mu\text{m}$ , 5  $\mu\text{m}$ , 9  $\mu\text{m}$ , and 16  $\mu\text{m}$ . The air velocities in the duct were nominally 2.2 m/s, 5.3 m/s, and 9.0 m/s. In each test section, a total of twelve panels (20 cm by 10 cm) were cut from the duct section to measure the amount of particles deposited to the duct surfaces; four panels each from the duct ceiling, wall, and floor surfaces. Fluorescent measurement techniques and aerosol concentration measurements were used to calculate the deposition velocities of the particles to duct surfaces (ceiling, wall, and floor) in each of the two straight duct sections where the turbulent flow profile was fully developed. The experiments are summarized in Table 3.36.

### **Modeling Notes**

FDS treats smoke particulate and aerosols in a similar way to other gaseous combustion products, basically a tracer gas whose production rate is a fixed fraction of the fuel consumption rate. However, there is an option in the model to allow smoke or aerosols to deposit on solid surfaces, thus reducing its concentration in the product stream. The particle deposition velocity,  $u_{\text{dep}}$ , is calculated by

$$u_{\text{dep}} = \frac{J_1 + J_2 + J_3 + J_4}{4 C_{\text{avg}}} \quad (3.16)$$

where  $J_1$  through  $J_4$  are the deposition fluxes ( $\text{kg}/(\text{m}^2 \text{s})$ ) for duct panels 1 through 4 given by

$$J = \frac{m_d}{A_d \Delta t} \quad (3.17)$$

where  $m_d$  is the mass of particles on the duct panel (kg),  $A_d$  is the area of the duct panel ( $\text{m}^2$ ), and  $\Delta t$  is the duration over which the aerosol deposits onto the panel (s).  $C_{\text{avg}}$  is the average aerosol concentration in the duct test section ( $\text{kg}/\text{m}^3$ ) and is given by

$$C_{\text{avg}} = \frac{C_{\text{upstream}} + C_{\text{downstream}}}{2} \quad (3.18)$$

Table 3.36: Summary of Sippola aerosol deposition experiments selected for model validation.

| Test No. | Air Speed (m/s) | Particle Diameter ( $\mu\text{m}$ ) | Particle Density ( $\text{kg/m}^3$ ) |
|----------|-----------------|-------------------------------------|--------------------------------------|
| 1        | 2.2             | 1.0                                 | 1350                                 |
| 2        | 2.2             | 2.8                                 | 1170                                 |
| 3        | 2.1             | 5.2                                 | 1210                                 |
| 4        | 2.2             | 9.1                                 | 1030                                 |
| 5        | 2.2             | 16                                  | 950                                  |
| 6        | 5.3             | 1.0                                 | 1350                                 |
| 7        | 5.2             | 1.0                                 | 1350                                 |
| 8        | 5.2             | 3.1                                 | 1170                                 |
| 9        | 5.4             | 5.2                                 | 1210                                 |
| 10       | 5.3             | 9.8                                 | 1030                                 |
| 11       | 5.3             | 16                                  | 950                                  |
| 12       | 9.0             | 1.0                                 | 1350                                 |
| 13       | 9.0             | 3.1                                 | 1170                                 |
| 14       | 8.8             | 5.4                                 | 1210                                 |
| 15       | 9.2             | 8.7                                 | 1030                                 |
| 16       | 9.1             | 15                                  | 950                                  |
| 17       | 2.2             | 1.0                                 | 1350                                 |
| 18       | 2.2             | 3.0                                 | 1170                                 |
| 19       | 2.2             | 5.3                                 | 1190                                 |
| 20       | 2.2             | 8.4                                 | 1090                                 |
| 21       | 2.2             | 13                                  | 960                                  |
| 22       | 5.3             | 1.0                                 | 1350                                 |
| 23       | 5.2             | 2.9                                 | 1170                                 |
| 24       | 5.2             | 4.9                                 | 1190                                 |
| 25       | 5.3             | 8.2                                 | 1090                                 |
| 26       | 5.3             | 13                                  | 960                                  |
| 27       | 8.9             | 1.0                                 | 1350                                 |
| 28       | 8.7             | 2.8                                 | 1170                                 |
| 29       | 8.8             | 5.0                                 | 1190                                 |
| 30       | 8.9             | 8.4                                 | 1090                                 |
| 31       | 8.9             | 13                                  | 960                                  |

## 3.81 Smyth Slot Burner Experiment

Kermit Smyth et al. conducted diffusion flame experiments at NIST using a methane/air Wolfhard-Parker slot burner. The experiments are described in detail in Refs. [309, 310]. The Wolfhard-Parker slot burner consists of an 8 mm wide central slot flowing fuel surrounded by two 16 mm wide slots flowing dry air with 1 mm separations between the slots. The slots are 41 mm in length. Measurements were made of all major species and a number of minor species along with temperature and velocity. Experimental uncertainties have been reported as 5 % for temperature and 10 % to 20 % for the major species.

### Modeling Notes

A two-step combustion scheme (a modified version of the mechanism by Andersen et al. [311]) is used to simulate the Smyth Slot Burner Experiment. A 2D DNS calculation is run at two different grid resolutions: 0.250 mm and 0.125 mm. In the modified mechanism, the hydrocarbon/oxygen reaction to CO is assumed to be infinitely fast (mixed is burnt) to avoid complications of modeling ignition. The reversible CO to CO<sub>2</sub> reaction is modeled with Arrhenius kinetics. As discussed by Westbrook and Dryer [312], the kinetic constants for the reduced CO mechanism may be model dependent. Here, the Arrhenius constant for the forward CO to CO<sub>2</sub> reaction is tuned to match the Smyth experimental data.

A second set of simulations is run at the same two spatial resolutions, but in these cases both the first and second reactions are infinitely fast. However, the first reaction, where fuel is converted to CO and H<sub>2</sub>O, proceeds before the second, where the CO is converted to CO<sub>2</sub>. That is, the reactions are run serially rather than in parallel to illustrate that while both reactions are relatively fast compared to the mixing time scale, the first reaction is faster than the second. This assumption breaks down when the mixing time scale drops below approximately  $3 \times 10^{-4}$  s, which is on the order of  $\delta/s_L$ , the flame thickness divided by the laminar flame speed. For this reason, a lower limit on the time-scale (TAU\_CHEM=3E-4) is imposed. This same modeling strategy is used in the large eddy simulations of the NIST Reduced Scale Enclosure (RSE) experiments of 1994 (Sec. 3.53.1), RSE 2007 (Sec. 3.53.2), Full-Scale Enclosure (FSE) 2008 (Sec. 3.53.3), UMD Line Burner experiments 3.93, and Waterloo Methanol Experiments (Sec. 3.104). Note that in these LES simulations, the parameter TAU\_CHEM is irrelevant—it is only needed when the grid resolution is on the order of 0.1 mm or less.

Comparisons of the simulations with measurements can be found in Sec. 9.5.1.

## 3.82 RISE Materials

The Research Institutes of Sweden (RISE) maintains a database of public measurement data from fire tests in various method and areas as well as from specific research projects [304]. The database contains cone calorimeter experiments from 156 combinations of materials and different thicknesses. A total of 74 materials tested at multiple heat fluxes with sufficient information on the materials tested are included in validation of the scaling-based pyrolysis model.

### Modeling Notes

This database does not provide thermal properties of the materials. Thermal conductivity, specific heat capacity, and ignition temperature for these materials are specified based on data available in the literature [151].

### 3.83 SP Adiabatic Surface Temperature Experiments

In 2008, three compartment experiments were performed at SP Technical Research Institute of Sweden under the sponsorship of Brandforsk, the Swedish Fire Research Board [313]. The objective of the experiments was to demonstrate how plate thermometer measurements in the vicinity of a simple steel beam can be used to supply the boundary conditions for a multi-dimensional heat conduction calculation for the beam. The adiabatic surface temperature was derived from the plate temperatures.

The experiments were performed inside a standard compartment designed for corner fire testing (ISO 9705). The compartment is 3.6 m deep, 2.4 m wide and 2.4 m high and includes a door opening 0.8 m by 2.0 m (Fig. 3.49). The room was constructed of 20 cm thick light weight concrete blocks with a density of  $600 \text{ kg/m}^3 \pm 100 \text{ kg/m}^3$ . The heat source was a gas burner run at a constant power of 450 kW. The top of the burner, with a square opening 30 cm by 30 cm, was placed 65 cm above the floor, 2.5 cm from the walls. A single steel beam was suspended 20 cm below the ceiling along the centerline of the compartment. There were three measurement stations along the beam at lengths of 0.9 m (Position A), 1.8 m (Position B), and 2.7 m (Position C) from the far wall where the fire was either positioned in the corner (Tests 1 and 2), or the center (Test 3). The beam in Test 1 was a rectangular steel tube filled with an insulation material. The beam in Tests 2 and 3 was an I-beam. A diagram of the room used in Test 2 is displayed in Figure 3.49.

A second series of experiments involving plate thermometers was carried out in 2011 [314]. A 6 m long, 20 cm diameter vertical steel column was positioned in the center of 1.1 m and 1.9 m diesel fuel and 1.1 m heptane pool fires. Gas, plate thermometer, and surface temperatures were measured at heights of 1 m, 2 m, 3 m, 4 m, and 5 m above the pool surface. These experiments are notable because the column is partially engulfed in flames.

A third series of experiments involving plate thermometers was conducted in 2015 [315]. A simple compartment with a single door was constructed and instrumented primarily with plate thermometers. The compartment was 2.7 m long, 1.8 m wide, and 1.8 m tall, with a 0.6 m by 1.5 m door centered on one of the short walls. The PTs were affixed to the walls. The 12 experiments were conducted with four different wall linings. In Series A, the compartment was lined with a 10 cm thick light concrete block. In Series B, the compartment was lined with a 5 cm thick layer of insulation backed by a 3 mm thick plate of steel. In Series C, the compartment was lined with an uninsulated 3 mm thick steel plate. In Series D, the compartment was lined with a 3 mm thick steel plate backed by a 5 cm thick layer of insulation (the opposite of Series B). The fires were fueled by a 0.3 m by 0.3 m propane burner located in the center of the room except for Test A3, where it was centered on the back wall. For most of the experiments, the heat release rate was 1000 kW, except for A2 and C1, which were 500 kW, and A4 and C3, which employed linear ramp-ups to 1250 kW.

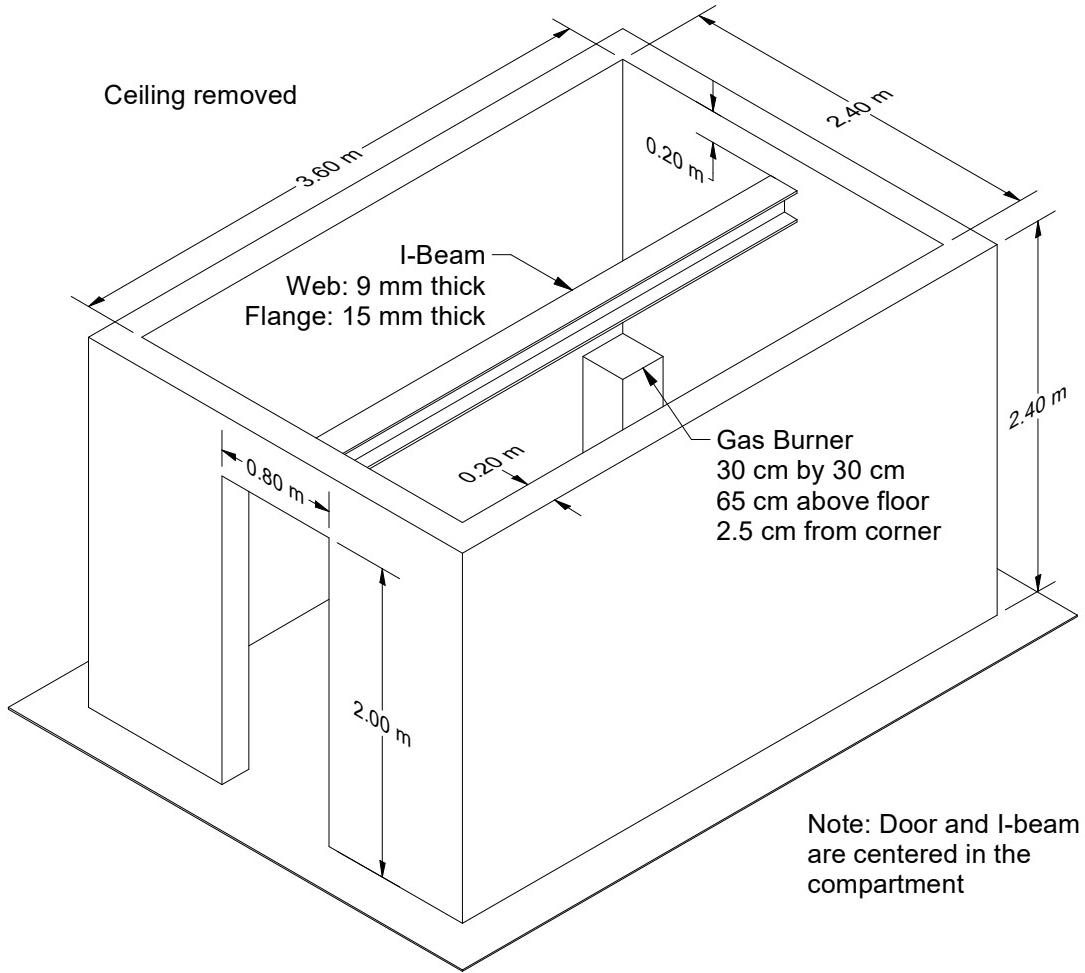


Figure 3.49: Geometry of the SP/AST compartment for Test 2.

### 3.84 SP Wood Crib Experiments

Hansen and Ingason burned piles of reduced-scale wood pallets in a reduced-scale wind tunnel to develop a simple model that predicts the heat release rate of multiple objects separated by varying distances [316, 317]. The tunnel was 10 m long with a rectangular cross section 0.6 m wide by 0.4 m tall. Four piles of 1:4 scale pallets were placed at various positions in the tunnel. Each pile of 5 pallets was 0.3 m long, 0.2 m wide and 0.18 m tall. The fire was ignited on the windward side of the upwind pile with a 3 cm by 3 cm by 2.4 cm block of fiberboard soaked in 9 mL of heptane. The HRR was measured, along with temperature, heat flux, and oxygen concentration at various locations.

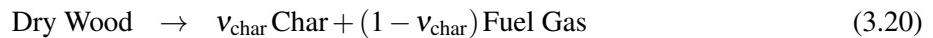
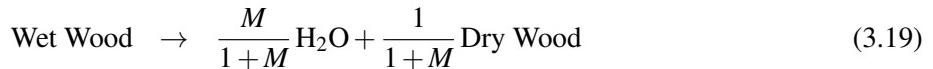
#### Modeling Notes

The FDS simulations of these experiments were originally performed by Janardhan and Hostikka [318, 163] using a variety of pyrolysis models in which the pallets are partially resolved. Here, however, the piles of pallets are modeled as an array of Lagrangian particles in lieu of solid obstructions so that a relatively coarse grid of 4 cm can be used. The modeling strategy is very similar to that used for vegetation in wildfire

simulations. The wood planks are characterized as a homogenous collection of flat disks with a surface area to volume ratio  $\sigma = 460 \text{ m}^{-1}$  and a packing ratio  $\beta = 0.42$ . The packing ratio is the bulk crib mass per unit volume divided by the density of the wood,  $m'''/\rho_{\text{wood}}$ . The average mass of a pile of pallets is 1.7 kg.

The radiation absorption coefficient is taken as  $\kappa = C_s \sigma \beta$ , where the shape factor, or ratio of plate surface area to projected area, is  $C_s = 0.25$ . The absorption coefficient,  $\kappa$ , also appears in the formula for wind drag, where the pressure drop,  $\Delta p$ , over a distance,  $L$ , is given by  $\Delta p/L = 0.5\rho C_d \kappa u^2$ . The drag coefficient,  $C_d = 2.8$ , was measured by Falkenstein-Smith et al. [176] in a study of vegetation. Its application to wood cribs has not been validated.

The wood is assumed to pyrolyze, forming  $\text{C}_{3.4}\text{H}_{6.2}\text{O}_{2.5}$  [66] with a heat of combustion of 18.1 MJ/kg [316], according to the following reaction scheme [163]:



(3.21)

The reaction rates are given by [163]:

$$r_{\text{H}_2\text{O}} = \left( \frac{\rho_{\text{s,H}_2\text{O}}}{\rho_{\text{s,0}}} \right)^{3.31} A_{\text{H}_2\text{O}} \exp \left( -\frac{E_{\text{H}_2\text{O}}}{RT} \right) \quad (3.22)$$

$$r_{\text{wood}} = \left( \frac{\rho_{\text{s,wood}}}{\rho_{\text{s,0}}} \right)^{1.69} A_{\text{wood}} \exp \left( -\frac{E_{\text{wood}}}{RT} \right) \quad (3.23)$$

The equation governing the temperature of the solid is

$$\rho_s c \frac{\partial T}{\partial t} = -\rho_{\text{s,0}} (\Delta h_{\text{H}_2\text{O}} r_{\text{H}_2\text{O}} + \Delta h_{\text{wood}} r_{\text{wood}}) + \nabla \cdot \dot{\mathbf{q}}_{\text{c}}'' + \nabla \cdot \dot{\mathbf{q}}_{\text{r}}'' \quad (3.24)$$

The parameters for the pyrolysis model are listed in Table 3.37.

Table 3.37: Parameters for SP Wood Cribs simulations [163].

| Property                        | Units             | Value                    |
|---------------------------------|-------------------|--------------------------|
| $M$                             | kg/kg             | 0.016                    |
| $\rho_{\text{H}_2\text{O}}$     | kg/m <sup>3</sup> | 1000                     |
| $c_{\text{H}_2\text{O}}$        | kJ/kg/K           | 4.18                     |
| $k_{\text{H}_2\text{O}}$        | W/m/K             | 0.1                      |
| $A_{\text{H}_2\text{O}}$        |                   | $9.57 \times 10^{22}$    |
| $E_{\text{H}_2\text{O}}$        | J/mol             | 136000                   |
| $\Delta h_{\text{H}_2\text{O}}$ | kJ/kg             | 2500                     |
| $\rho_{\text{wood}}$            | kg/m <sup>3</sup> | 393                      |
| $c_{\text{wood}}$               | kJ/kg/K           | $0.85 + 0.00241(T - 20)$ |
| $k_{\text{wood}}$               | W/m/K             | $0.07 + 0.00038(T - 20)$ |
| $\varepsilon_{\text{wood}}$     |                   | 0.95                     |
| $A_{\text{wood}}$               |                   | 141000                   |
| $E_{\text{wood}}$               | J/mol             | 89700                    |
| $\Delta h_{\text{wood}}$        | kJ/kg             | 250                      |
| $\rho_{\text{char}}$            | kg/m <sup>3</sup> | 135                      |
| $c_{\text{char}}$               | kJ/kg/K           | (see Ref. [163])         |
| $k_{\text{char}}$               | W/m/K             | $0.11 + 0.00031(T - 20)$ |
| $\varepsilon_{\text{char}}$     |                   | 1.0                      |
| $v_{\text{char}}$               | g/g               | 0.195                    |

### 3.85 Steckler Compartment Experiments

Steckler, Quintiere and Rinkinen performed a set of 55 compartment fire tests at NBS in 1979. The compartment was 2.8 m by 2.8 m by 2.13 m high<sup>5</sup>, with a single door of various widths, or alternatively a single window with various heights. A 30 cm diameter methane burner was used to generate fires with heat release rates of 31.6 kW, 62.9 kW, 105.3 kW and 158 kW. Vertical profiles of velocity and temperature were measured in the doorway, along with a single vertical profile of temperature within the compartment. A full description and results are reported in Reference [319]. The basic test matrix is listed in Table 3.38. Note that the test report does not include a detailed description of the compartment. However, an internal report<sup>6</sup> by the test sponsor, Armstrong Cork Company, reports that the compartment floor was composed of 19 mm calcium silicate board on top of 12.7 mm plywood on wood joists. The walls and ceiling consisted of 12.7 mm ceramic fiber insulation board over 0.66 mm aluminum sheet attached to wood studs. A diagram of the compartment is displayed in Fig. 3.50.

<sup>5</sup>The test report gives the height of the compartment as 2.18 m. This is a misprint. The compartment was 2.13 m high.

<sup>6</sup>Technical Research Report, Fire Induced Flows Through Room Openings - Flow Coefficients, Project 203005-003, Armstrong Cork Company, Lancaster, Pennsylvania, May, 1981.

Table 3.38: Summary of Steckler compartment experiments.

| Test | Door Width (m) | Door Height (m) | HRR $\dot{Q}$ (kW) | Burner Location | Test            | Door Width (m) | Door Height (m) | HRR $\dot{Q}$ (kW) | Burner Location |
|------|----------------|-----------------|--------------------|-----------------|-----------------|----------------|-----------------|--------------------|-----------------|
| 10   | 0.24           | 1.83            | 62.9               | Center          | 224             | 0.74           | 0.92            | 62.9               | Back Corner     |
| 11   | 0.36           | 1.83            | 62.9               | Center          | 324             | 0.74           | 0.92            | 62.9               | Back Corner     |
| 12   | 0.49           | 1.83            | 62.9               | Center          | 220             | 0.74           | 1.83            | 31.6               | Back Corner     |
| 612  | 0.49           | 1.83            | 62.9               | Center          | 221             | 0.74           | 1.83            | 105.3              | Back Corner     |
| 13   | 0.62           | 1.83            | 62.9               | Center          | 514             | 0.24           | 1.83            | 62.9               | Back Wall       |
| 14   | 0.74           | 1.83            | 62.9               | Center          | 544             | 0.36           | 1.83            | 62.9               | Back Wall       |
| 18   | 0.74           | 1.83            | 62.9               | Center          | 512             | 0.49           | 1.83            | 62.9               | Back Wall       |
| 710  | 0.74           | 1.83            | 62.9               | Center          | 542             | 0.62           | 1.83            | 62.9               | Back Wall       |
| 810  | 0.74           | 1.83            | 62.9               | Center          | 610             | 0.74           | 1.83            | 62.9               | Back Wall       |
| 16   | 0.86           | 1.83            | 62.9               | Center          | 510             | 0.74           | 1.83            | 62.9               | Back Wall       |
| 17   | 0.99           | 1.83            | 62.9               | Center          | 540             | 0.86           | 1.83            | 62.9               | Back Wall       |
| 22   | 0.74           | 1.38            | 62.9               | Center          | 517             | 0.99           | 1.83            | 62.9               | Back Wall       |
| 23   | 0.74           | 0.92            | 62.9               | Center          | 622             | 0.74           | 1.38            | 62.9               | Back Wall       |
| 30   | 0.74           | 0.92            | 62.9               | Center          | 522             | 0.74           | 1.38            | 62.9               | Back Wall       |
| 41   | 0.74           | 0.46            | 62.9               | Center          | 524             | 0.74           | 0.92            | 62.9               | Back Wall       |
| 19   | 0.74           | 1.83            | 31.6               | Center          | 541             | 0.74           | 0.46            | 62.9               | Back Wall       |
| 20   | 0.74           | 1.83            | 105.3              | Center          | 520             | 0.74           | 1.83            | 31.6               | Back Wall       |
| 21   | 0.74           | 1.83            | 158.0              | Center          | 521             | 0.74           | 1.83            | 105.3              | Back Wall       |
| 114  | 0.24           | 1.83            | 62.9               | Back Corner     | 513             | 0.74           | 1.83            | 158.0              | Back Wall       |
| 144  | 0.36           | 1.83            | 62.9               | Back Corner     | 160             | 0.74           | 1.83            | 62.9               | Center*         |
| 212  | 0.49           | 1.83            | 62.9               | Back Corner     | 163             | 0.74           | 1.83            | 62.9               | Back Corner*    |
| 242  | 0.62           | 1.83            | 62.9               | Back Corner     | 164             | 0.74           | 1.83            | 62.9               | Back Wall*      |
| 410  | 0.74           | 1.83            | 62.9               | Back Corner     | 165             | 0.74           | 1.83            | 62.9               | Left Wall*      |
| 210  | 0.74           | 1.83            | 62.9               | Back Corner     | 162             | 0.74           | 1.83            | 62.9               | Right Wall*     |
| 310  | 0.74           | 1.83            | 62.9               | Back Corner     | 167             | 0.74           | 1.83            | 62.9               | Front Center*   |
| 240  | 0.86           | 1.83            | 62.9               | Back Corner     | 161             | 0.74           | 1.83            | 62.9               | Doorway*        |
| 116  | 0.99           | 1.83            | 62.9               | Back Corner     | 166             | 0.74           | 1.83            | 62.9               | Front Corner*   |
| 122  | 0.74           | 1.38            | 62.9               | Back Corner     | * Raised burner |                |                 |                    |                 |

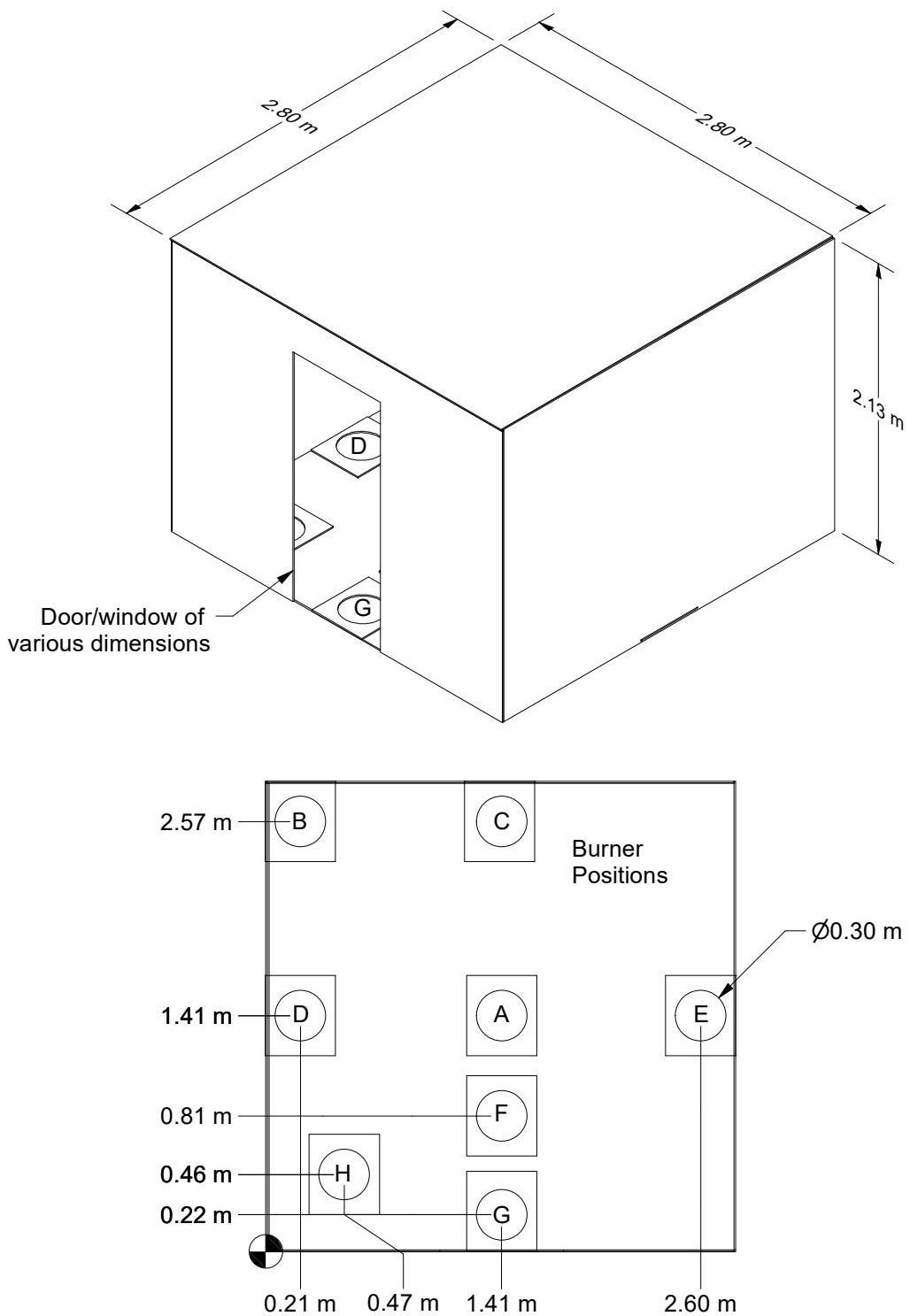


Figure 3.50: Geometry of the Steckler Compartment Experiments.

### 3.86 SWJTU Tunnel Experiments

Fires fueled by methanol and propane ranging from 5.6 kW to 16.8 kW were conducted in a 1:20 reduced-scale tunnel at Southwest Jiaotong University, Chengdu, China [320]. The tunnel was 0.45 m wide, 0.23 m high and 20.8 m long. The burner was located at the center of the tunnel and both ends were open. Temperatures and gas concentrations (i.e., O<sub>2</sub>, CO and CO<sub>2</sub>) were measured. The results showed that both methanol and propane fires self-extinguished in the 20.8 m long tunnel within approximately 10 min, except for the 5.6 kW methanol fire. The larger the heat release rate, the faster the self-extinction of the fire. The oxygen concentrations in the 20.8 m long tunnel decreased to approximately 12 % except for the 5.6 kW methanol fire, which remained well above the limiting oxygen concentration. Self-extinction was not observed for fires of the same heat release rates in a 10 m long tunnel of the same cross section. The oxygen concentrations in the 10 m long tunnel decreased to approximately 17 %. In the long tunnel with large fire sizes, the smoke layer descended to the floor, inhibiting the supply of fresh air reaching the fire.

### 3.87 Theobald Hose Stream Experiments

Fire hose nozzle jets with nominal diameters of 1.3 cm up to 2.5 cm were studied over a range of operating pressures and jet orientation angles. The maximum throw distance was recorded as well as the max height of the ballistic arc and the distance to the max height. Details of the experiments are presented in [321]. In the paper, the *primary breakup length* is correlated as a function of Weber number (We) and Reynolds number (Re) of the water jet.

#### Modeling Notes

FDS models liquid water by means of Lagrangian particles. This is the same model used to describe sprinkler droplets. A key difference between sprinklers and hose streams, however, is that sprinkler nozzles purposely atomize the water jet immediately as the water is introduced into the computational domain. To model hose streams, FDS introduces two new parameters to the PART class: PRIMARY\_BREAKUP\_LENGTH and PRIMARY\_BREAKUP\_DRAG\_REDUCTION\_FACTOR. The particles enter the domain and for the time period before the particle has traveled the distance PRIMARY\_BREAKUP\_LENGTH, the particle drag coefficient is multiplied by the specified PRIMARY\_BREAKUP\_DRAG\_REDUCTION\_FACTOR, which may be zero. In this way, FDS can mimic the jet core, which experiences little to no drag before the jet goes unstable.

To calibrate the FDS results (this case is a calibration exercise more than a validation), the PRIMARY\_BREAKUP\_LENGTH was set to twice the value of Z (the value of 50 % jet breakup) in the paper and the PRIMARY\_BREAKUP\_DRAG\_REDUCTION\_FACTOR was set to zero.

### 3.88 UL/NIST Vent Experiments

In 2012, the Fire Fighting Technology Group at NIST conducted experiments at Underwriters Laboratories (UL) in Northbrook, Illinois, to assess the change in compartment temperature due to the opening of one or two 1.2 m square ceiling vents [322]. Four experiments were conducted using a natural gas burner in a 6.1 m by 4.3 m by 2.4 m compartment with a single door opening. The fires ranged in size from 500 kW to 2 MW, and the vents were opened and closed such that during the four experiments there were 31 discrete time intervals in which model predictions could be compared to quasi-steady conditions. The compartment contained two vertical arrays of thermocouples, and the door and vents were instrumented with thermocouples and bi-directional velocity probes. Only the thermocouple data has been used in the

validation study. A diagram of the compartment is displayed in Figure 3.51. The major test parameters are listed in Table 3.39.

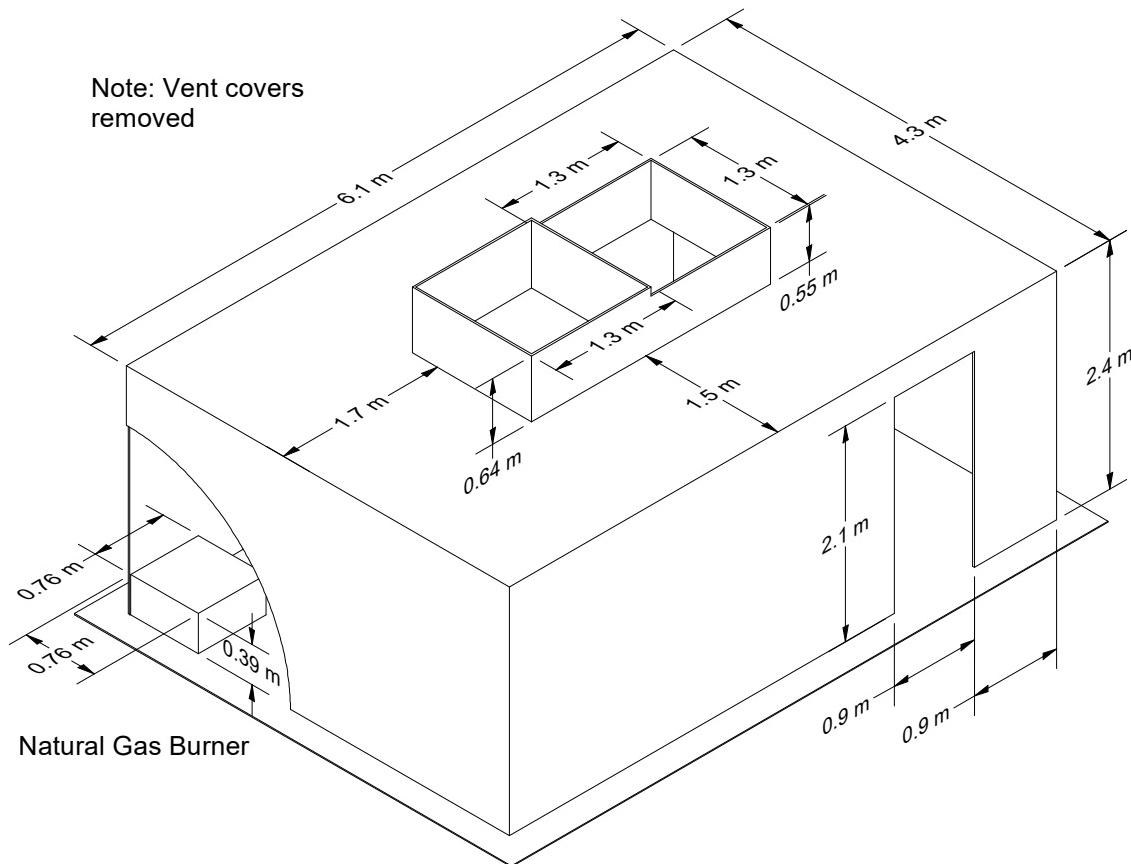


Figure 3.51: Geometry of the UL/NIST Experiments.

Table 3.39: Summary of UL/NIST Vent experiments. Note that the 31 “experiments” are actually discrete time intervals during the course of four separate fires.

| Exp. No. | End Time (s) | HRR (kW) | No. of Vents | Exp. No. | End Time (s) | HRR (kW) | No. of Vents |
|----------|--------------|----------|--------------|----------|--------------|----------|--------------|
| Fire 1   |              |          |              | Fire 3   |              |          |              |
| 1        | 1215         | 430      | 0            | 14       | 453          | 476      | 0            |
| 2        | 1840         | 430      | 1            | 15       | 816          | 476      | 1            |
| 3        | 2168         | 430      | 2            | 16       | 1153         | 476      | 2            |
| 4        | 2474         | 430      | 0            | 17       | 1640         | 1002     | 0            |
| 5        | 2955         | 1011     | 0            | 18       | 1936         | 1002     | 1            |
| 6        | 3170         | 1011     | 1            | 19       | 2233         | 1002     | 2            |
| 7        | 3604         | 1011     | 2            | Fire 4   |              |          |              |
| 8        | 3840         | 1011     | 0            | 20       | 519          | 1011     | 0            |
| 9        | 4153         | 2188     | 0            | 21       | 967          | 1011     | 1            |
| 10       | 4284         | 2188     | 1            | 22       | 1325         | 1011     | 2            |
| Fire 2   |              |          |              | 23       | 1559         | 470      | 2            |
| 11       | 565          | 2144     | 0            | 24       | 1653         | 470      | 1            |
| 12       | 833          | 2144     | 1            | 25       | 2013         | 470      | 0            |
| 13       | 931          | 2144     | 2            | 26       | 2411         | 470      | 1            |
|          |              |          |              | 27       | 2910         | 470      | 2            |
|          |              |          |              | 28       | 3399         | 2188     | 2            |
|          |              |          |              | 29       | 3586         | 2188     | 0            |
|          |              |          |              | 30       | 3803         | 2188     | 1            |
|          |              |          |              | 31       | 4035         | 2188     | 2            |

### 3.89 UL/NFPRF Sprinkler, Vent, and Draft Curtain Study

In 1997, thirty-four heptane spray burner and five racked commodity experiments were conducted at the Large Scale Fire Test Facility at Underwriters Laboratories (UL) in Northbrook, Illinois [323, 83]. The spray burner experiments were divided into two test series. Series I consisted of 22 4.4 MW experiments. Series II consisted of 12 10 MW experiments. The objective of the spray burner experiments was to characterize the temperature and flow field for fire scenarios with a controlled heat release rate in the presence of sprinklers, draft curtains, and smoke & heat vents.

The Large Scale Fire Test Facility at UL contains a 37 m by 37 m (120 ft by 120 ft) main fire test cell, equipped with a 30.5 m by 30.5 m (100 ft by 100 ft) adjustable height ceiling. The UL/NFPRF test results (Series I) are summarized in Table 3.40. The UL/NFPRF test results (Series II) are summarized in Table 3.41. The layout of the experiments is shown in Figs. 3.52, 3.53, and 3.54.

**Ceiling:** The ceiling was raised to a height of 7.6 m and instrumented with thermocouples and other measurement devices. The ceiling was constructed of 0.6 m by 1.2 m by 1.6 cm UL fire-rated Armstrong

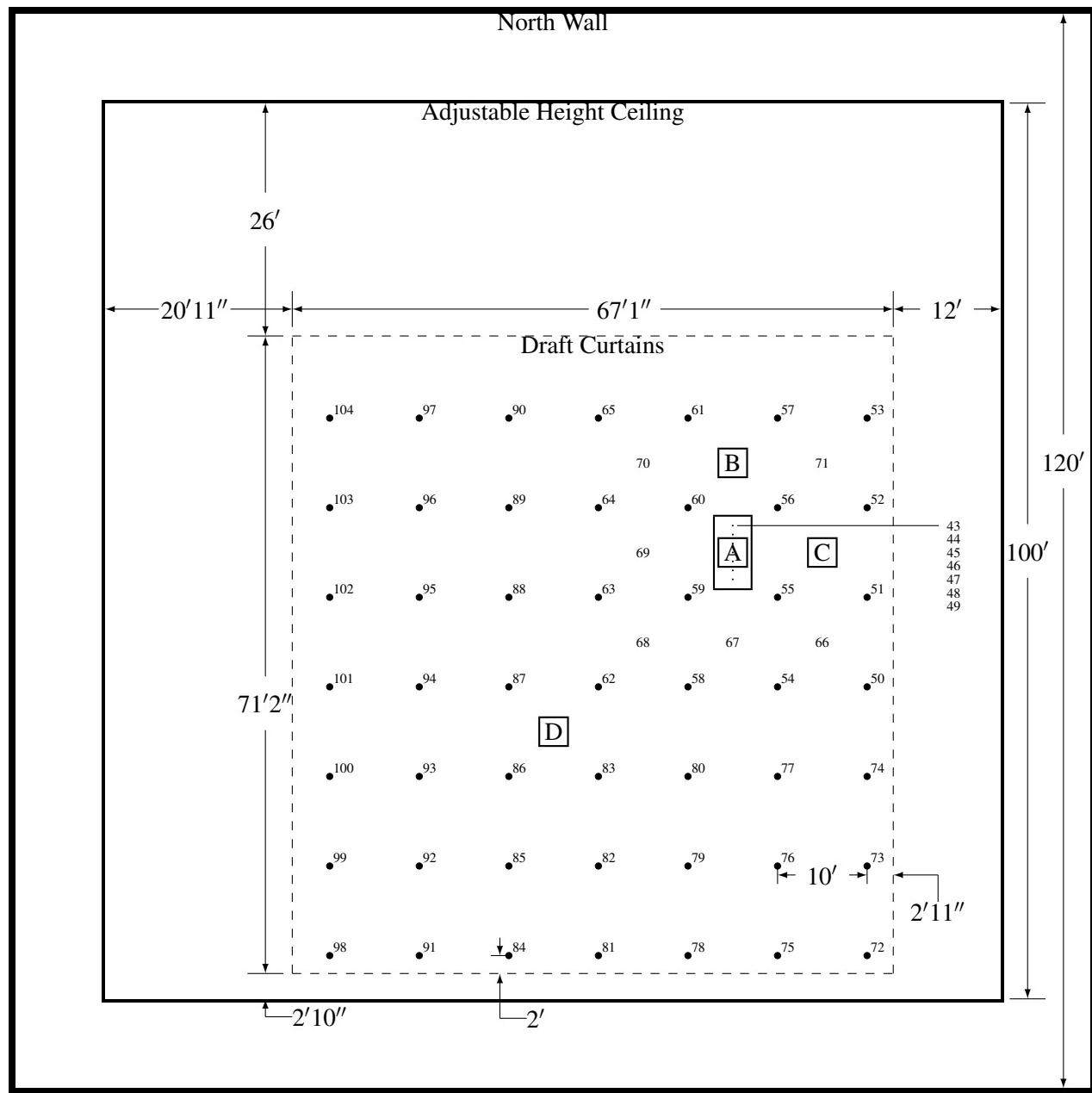


Figure 3.52: Plan view of the UL/NFPRF heptane spray experiments, Series I. The sprinklers are indicated by the solid circles and are spaced exactly 10 ft apart. The number beside each sprinkler location indicates the channel number of the nearest thermocouple. The vent dimensions are 4 ft by 8 ft. The boxed letters A, B, C and D indicate burner positions. Corresponding to each burner position is a vertical array of thermocouples. Thermocouples 1–9 hang 7, 22, 36, 50, 64, 78, 92, 106 and 120 in from the ceiling, respectively, above Position A. Thermocouples 10 and 11 are positioned above and below the ceiling tile directly above Position B, followed by 12–20 that hang at the same levels below the ceiling as 1–9. The same pattern is followed at Positions C and D, with thermocouples 21–31 at C and 32–42 at D.

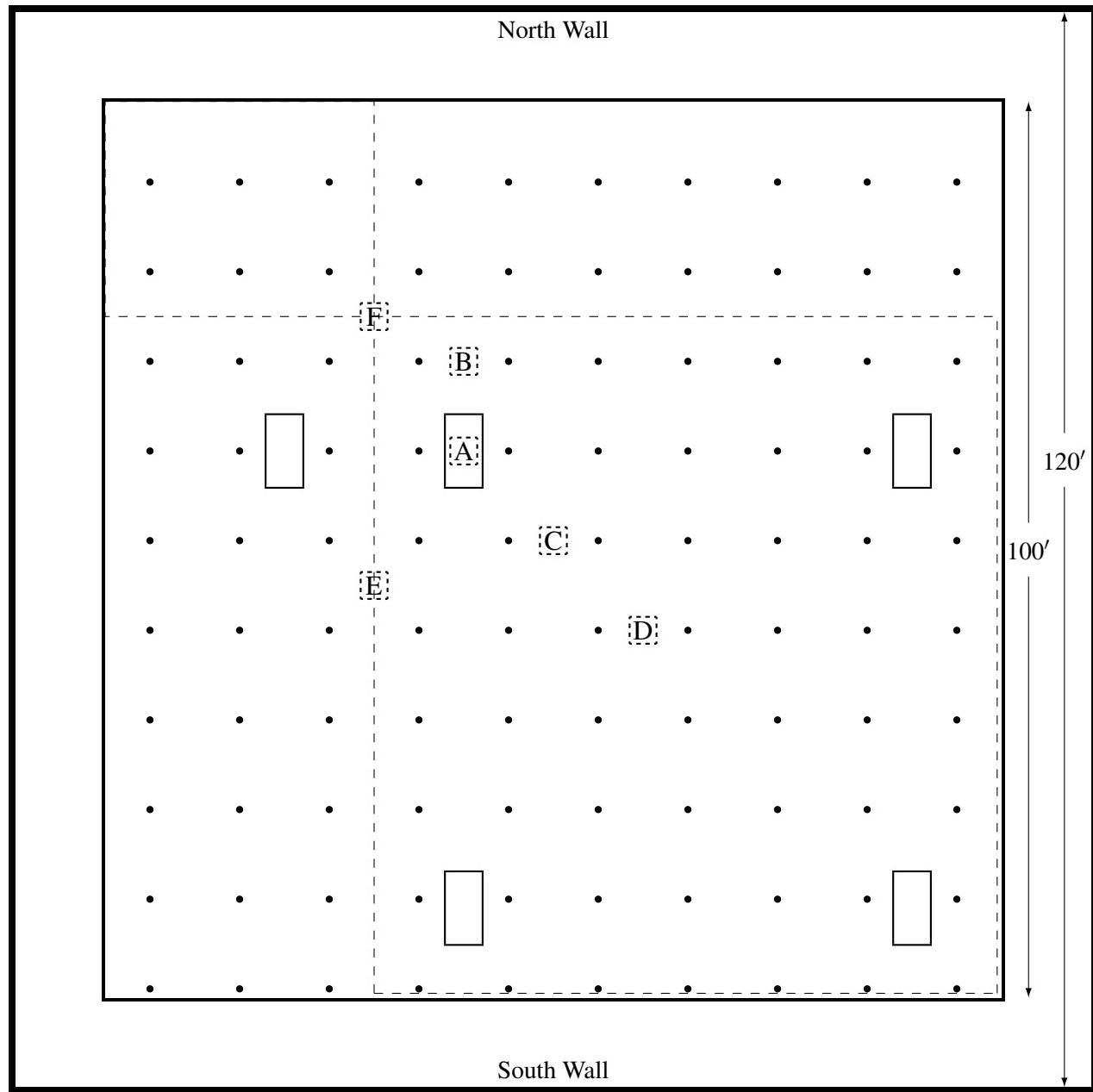


Figure 3.53: Plan view of the UL/NFPRF heptane spray experiments, Series II. The boxed letters A, B, C, D, E and F indicate burner positions. The sprinklers are indicated by the solid circles and are spaced exactly 10 ft apart. The vents are 4 ft by 8 ft.

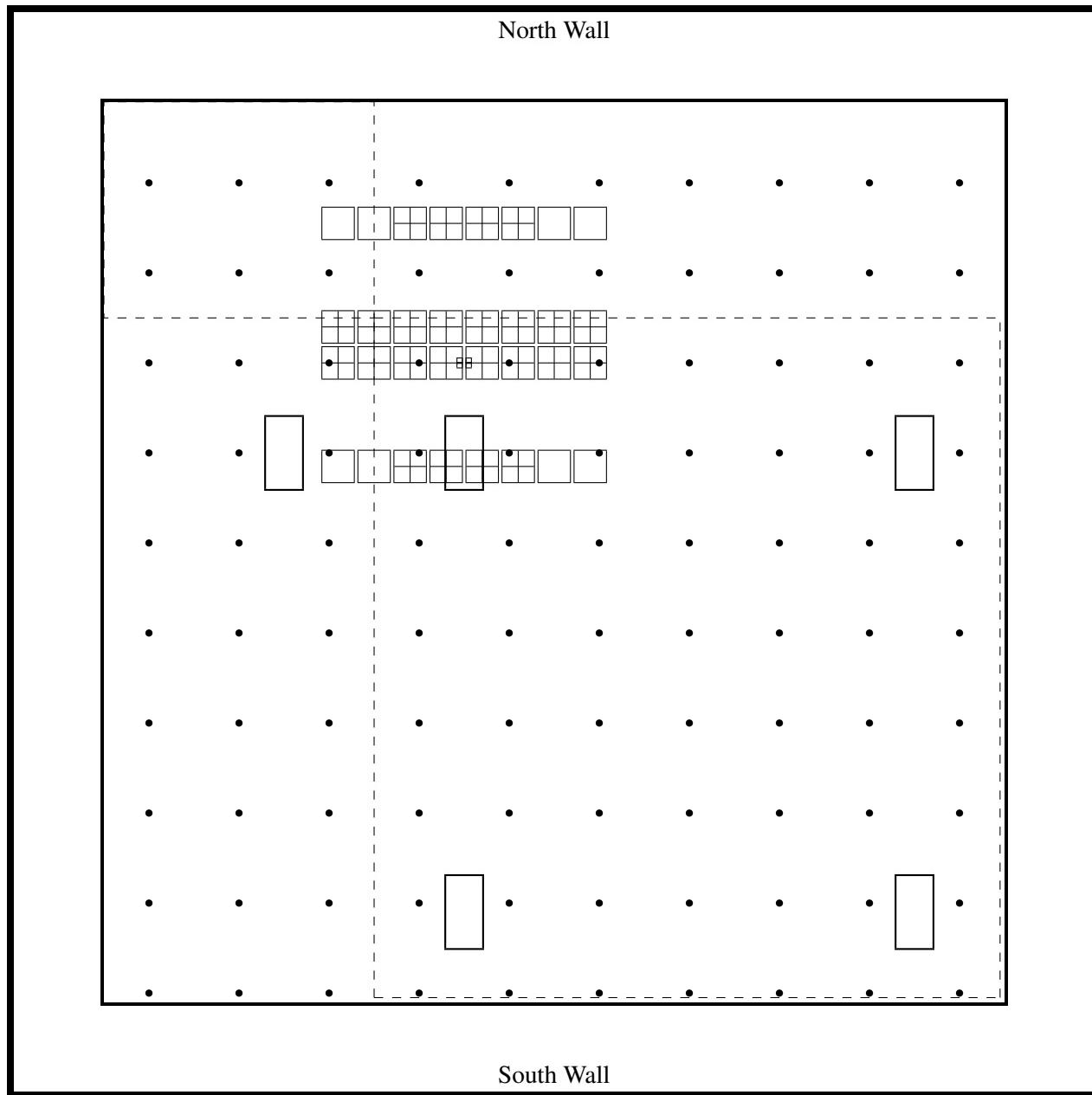


Figure 3.54: Plan view of the UL Large Scale Fire Test Facility with the layout of plastic commodity Test P-3. Tests P-1 and P-2 did not include the draft curtains (dashed lines). The sprinklers (dots) were separated by exactly 10 ft. The racks were located 30 ft south and 20 ft east of the position shown in Tests P-1, P-4, and P-5. The racks were located 10 ft south of the position shown in Test P-2. Each pallet load of boxed plastic commodity is represented by a square subdivided into four smaller squares to depict the individual boxes. Pallets containing empty boxes are represented by empty squares. Roof vents are represented by rectangles.

| Heptane Spray Burner Test Series I |             |                    |                     |                  |                |                          |
|------------------------------------|-------------|--------------------|---------------------|------------------|----------------|--------------------------|
| Test No.                           | Burner Pos. | Vent Operation     | First Actuation (s) | Total Actuations | Draft Curtains | Heat Release Rate MW @ s |
| I-1                                | B           | Closed             | 65                  | 11               | Yes            | 4.4 @ 50                 |
| I-2                                | B           | Manual (0:40)      | 66                  | 12               | Yes            | 4.4 @ 50                 |
| I-3                                | B           | Manual (1:30)      | 64                  | 12               | Yes            | 4.4 @ 50                 |
| I-4                                | C           | Closed             | 60                  | 10               | Yes            | 4.4 @ 50                 |
| I-5                                | C           | Manual (0:40)      | 72                  | 9                | Yes            | 4.4 @ 50                 |
| I-6                                | C           | Manual (1:30)      | 62                  | 8                | Yes            | 4.4 @ 50                 |
| I-7                                | C           | 74°C link (DNO)    | 70                  | 10               | Yes            | 4.4 @ 50                 |
| I-8                                | B           | 74°C link (9:26)   | 60                  | 11               | Yes            | 4.4 @ 50                 |
| I-9                                | D           | 74°C link (DNO)    | 70                  | 12               | Yes            | 4.4 @ 50                 |
| I-10                               | D           | Manual (0:40)      | 72                  | 13               | Yes            | 4.4 @ 50                 |
| I-11                               | D           | 74°C link (4:48)   | N/A                 | N/A              | Yes            | 4.4 @ 50                 |
| I-12                               | A           | Closed             | 68                  | 14               | Yes            | 4.4 @ 50                 |
| I-13                               | A           | 74°C link (1:04)   | 69                  | 5                | Yes            | 6.0 @ 60                 |
| I-14                               | A           | Manual (0:40)      | 74                  | 7                | Yes            | 5.8 @ 60                 |
| I-15                               | A           | Manual (1:30)      | 64                  | 5                | Yes            | 5.8 @ 60                 |
| I-16                               | A           | 74°C link (1:46)   | 106                 | 4                | Yes            | 5.0 @ 110                |
| I-17                               | B           | 100°C link (DNO)   | 58                  | 4                | No             | 4.6 @ 50                 |
| I-18                               | C           | 100°C link (DNO)   | 58                  | 4                | No             | 3.7 @ 50                 |
| I-19                               | A           | 100°C link (10:00) | 56                  | 10               | No             | 4.6 @ 50                 |
| I-20                               | A           | 74°C link (1:20)   | 54                  | 4                | No             | 4.2 @ 50                 |
| I-21                               | C           | 74°C link (7:00)   | 58                  | 10               | No             | 4.6 @ 50                 |
| I-22                               | D           | 100°C link (DNO)   | 60                  | 6                | No             | 4.6 @ 50                 |

Table 3.40: Results of Series I of the UL/NFPRF heptane spray experiments. Note that DNO means “Did Not Open”. Also note, the fires grew at a rate proportional to the square of the time until a certain flow rate of fuel was achieved at which time the flow rate was held steady. Thus, the “Heat Release Rate” was the size of the fire at the time when the fuel supply was leveled off.

Ceramaguard (Item 602B) ceiling tiles. The manufacturer reported the thermal properties of the material to be: specific heat 753 J/(kg·K), thermal conductivity 0.0611 W/(m·K), and density 313 kg/m<sup>3</sup>.

**Draft Curtains:** Sheet metal, 1.2 mm thick and 1.8 m deep, was suspended from the ceiling for 16 of the 22 Series I tests, enclosing an area of about 450 m<sup>2</sup> and 49 sprinklers. The curtains were in place for all of the Series II tests.

**Sprinklers:** Central ELO-231 (Extra Large Orifice) uprights were used for all the tests. The orifice diameter of this sprinkler is reported by the manufacturer to be nominally 1.6 cm (0.64 in), the reference actuation temperature is reported by the manufacturer to be 74°C (165°F). The RTI (Response Time Index) and C-factor (Conductivity factor) were reported by UL to be 148 (m·s)<sup>½</sup> and 0.7 (m/s)<sup>½</sup>, respectively [323]. When installed, the sprinkler deflector was located 8 cm below the ceiling. The thermal element of the sprinkler was located 11 cm below the ceiling. The sprinklers were installed with nominal 3 m by 3 m (exact 10 ft by 10 ft) spacing in a system designed to deliver a constant 0.34 L/(s·m<sup>2</sup>) (0.50 gpm/ft<sup>2</sup>) discharge density when supplied by a 131 kPa (19 psi) discharge pressure

| Heptane Spray Burner Test Series II (10 MW Fires) |                 |                   |                   |                  |                 |                 |       |
|---|-----------------|-------------------|-------------------|------------------|-----------------|-----------------|-------|
| Test No.  | Burner Position | Vent Operation    | Sprinklers Opened | First Activation | Last Activation | Avg. Peak Temp. |       |
|   |                 |                   |                   |                  |                 | °C              | °F    |
| II-1  | D               | 74°C link (DNO)   | 27                | 1:15             | 6:13            | 129.4           | 264.9 |
| II-2  | D               | All Open at Start | 28                | 1:05             | 5:53            | 128.8           | 263.8 |
| II-3  | A               | 74°C link (1:15)  | 12                | 1:08             | 4:00            | 101.8           | 215.2 |
| II-4  | B               | 74°C link (1:48)  | 16                | 1:03             | 5:54            | 108.8           | 227.8 |
| II-5  | D               | 74°C link (DNO)   | 28                | 1:10             | 7:07            | 130.0           | 266.0 |
| II-6  | D               | All Open at Start | 27                | 1:10             | 5:21            | 127.5           | 261.5 |
| II-7  | A               | Closed            | 18                | 1:09             | 4:11            | 117.2           | 243.0 |
| II-8  | B               | 74°C link (1:12)  | 13                | 1:10             | 3:34            | 107.7           | 225.9 |
| II-9  | E               | 74°C link (DNO)   | 23                | 1:07             | 3:28            | 115.8           | 240.4 |
| II-10   | F               | 74°C link (3:20)  | 19                | 1:14             | 3:01            | 108.4           | 227.1 |
| II-11   | C               | 74°C link (DNO)   | 23                | 1:02             | 3:56            | 123.4           | 254.1 |
| II-12   | C               | All Open at Start | 23                | 0:58             | 4:55            | 119.0           | 246.2 |

Table 3.41: Results of the UL/NFPRF heptane spray experiments, Series II. Note that all fires were ramped up to 10 MW in 75 s following a *t-squared* curve.

**Vent:** UL-listed double leaf fire vents with steel covers and steel curb were installed in the adjustable height ceiling in the position shown in Figs. 3.52 and 3.53. The vent is designed to open manually or automatically. The vent doors were recessed into the ceiling about 0.3 m (1 ft).

**Heptane Spray Burner:** The heptane spray burner consisted of a 1 m by 1 m square of 1.3 cm pipe supported by four cement blocks 0.6 m off the floor. Four atomizing spray nozzles were used to provide a free spray of heptane that was then ignited. For all but one of the Series I tests, the total heat release rate from the fire was manually ramped up following a “*t-squared*” curve to a steady-state in 75 s (150 s was used in Test I-16). The fire was ramped to 10 MW in 75 s for the Series II tests. The fire growth curve was followed until a specified fire size was reached or the first sprinkler activated. After either of these events, the fire size was maintained at that level until conditions reached roughly a steady state, i.e., the temperatures recorded near the ceilings remained steady and no more sprinkler activations occurred. The heat release rate from the burner was confirmed by placing it under the large product calorimeter at UL, ramping up the flow of heptane in the same manner as in the tests, and measuring the total and convective heat release rates. It was found that the convective heat release rate was  $0.65 \pm 0.02$  of the total.

**Plastic Commodity:** The Factory Mutual Research Corporation (FMRC) standard “Group A Plastic” test commodity served as the fuel for the rack storage experiments [324]. The cartoned plastic commodity consists of rigid crystalline polystyrene cups packaged in compartmented, single-wall, corrugated paper cartons. Each carton is a cube 0.53 m (21 in) on a side. Eight boxes comprise a pallet load. Two-way, slatted deck hardwood pallets support the loads. A pallet load weighs approximately 80 kg (170 lb), of which about 36 % is plastic, 35 % is wood, and 29 % is corrugated paper [324]. Each storage array consisted of a main (ignition) double-row rack at the center, flanked on two sides by single row target racks. The rows were separated by 8 ft wide aisles. Each of the two rows of the main array consisted of four 2.4 m (8 ft) long bays; a 0.15 m (6 in) flue separated the rows. Longitudinal flues of 0.2 m (7.5 in) were used to separate the pallets within a row. The overall loaded area of the double-row rack measured approximately 2.3 m (7.5 ft) wide by 10 m (33 ft) long. The racks were divided vertically into 4 tiers;

the overall loaded height was 5.8 m (19 ft). The fire was ignited with 2 standard igniters which consisted of 8 cm (3 in) long by 8 cm diameter cylinders of rolled cotton material, each soaked in 120 mL (4 oz) of gasoline and enclosed in a polyethylene bag. The rolls were placed against the carton surfaces in the first tier, just above the pallet. The igniters were lit with a flaming propane torch at the start of each test.

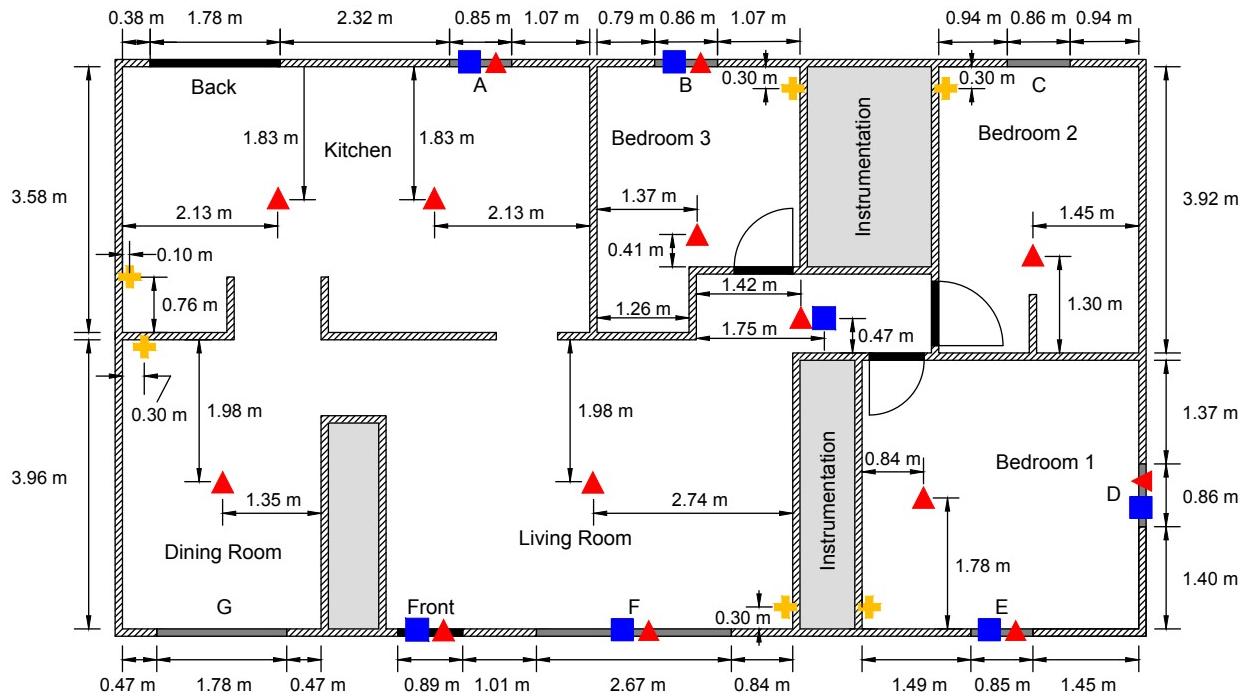
**Instrumentation:** The instrumentation for the tests consisted of thermocouples, gas analysis equipment, and pressure transducers. The locations of the instrumentation are referenced in the plan view of the facility (Fig. 3.52). Temperature measurements were recorded at 104 locations. Type K 0.0625 in diameter Inconel sheathed thermocouples were positioned to measure (i) temperatures near the ceiling, (ii) temperatures of the ceiling jet, and (iii) temperatures near the vent.

### 3.90 UL/NIJ House Experiments

The Firefighter Safety Research Institute (FSRI) of Underwriters Laboratory (UL), with support from the National Institute of Justice (NIJ), conducted fire experiments in a one-story ranch-style house and a two-story colonial-style house in the large fire facility at Northbrook, Illinois, in 2016 and 2017 [325]. In addition to this validation guide, modeling of the experiments is also reported in [326]. The goal of the experiments was to determine the effect of ventilation on fire patterns in fully-furnished homes. As part of the project, a natural gas burner was positioned within the unfurnished structures to evaluate changes in flow patterns as various doors and windows were opened and closed. The test structures were instrumented with thermocouple trees, pressure transducers, and bi-directional probes. The floor plan for the single story ranch-style house is included in Fig. 3.55, and plans for the two story colonial-style house in Fig. 3.56. The ceiling was 2.4 m above the floor in the ranch-style house. The colonial-style house featured an atrium with a 5.6 m ceiling height. The first story ceiling in the colonial-style house was 2.5 m above the floor, and the second story ceiling was 2.8 m above the floor.

The leakage area in the single story structure was measured to be 0.08 m<sup>2</sup> at 10 Pa. The leakage area in the two story structure was measured to be 0.18 m<sup>2</sup> at 10 Pa.

The natural gas burner in each set of experiments had dimensions of 0.6 m by 0.6 m, and the surface of the burner was approximately 0.6 m above the floor. The heat release rate for the single story ranch house was 250 kW, and 500 kW for the two story colonial. The locations of the burner in each house are indicated in the floor plans. The labels for the measurement devices in the one and two story houses are listed in Tables 3.42 and 3.43, respectively. Three experiments with unique sequences of events (e.g. opening doors and windows) were conducted in each style of house. All experiments began with all exterior doors and windows closed and the times at which each door and window was opened are listed Table 3.44 and 3.45.



| Icon | Instrumentation    |
|------|--------------------|
| ▲    | Thermocouple Array |
| ■    | Gas Velocity       |
| ✚    | Pressure Tap       |

Figure 3.55: Layout of the one story ranch-style house in the UL/NIJ experiments.

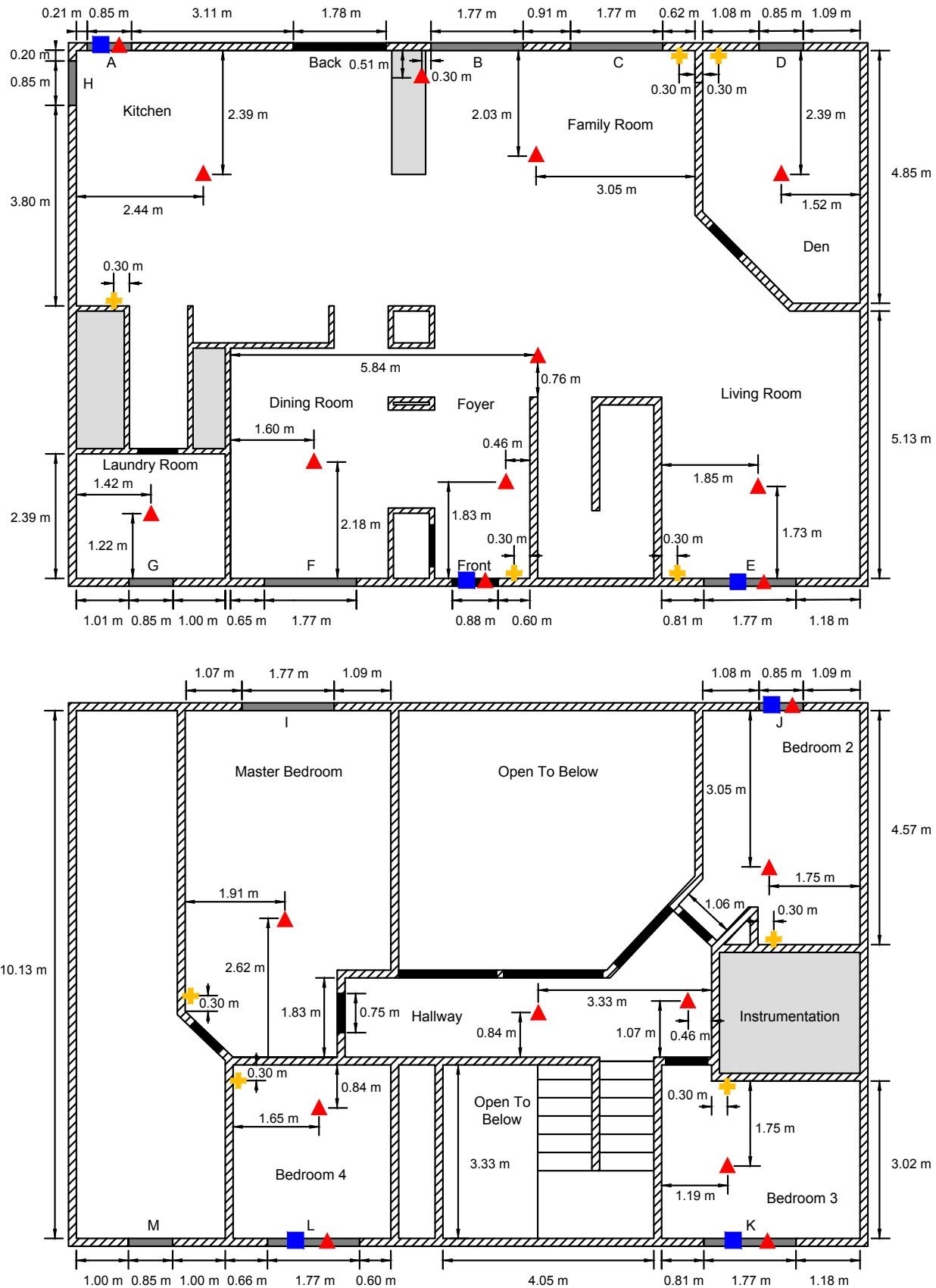


Figure 3.56: Geometry of UL NIJ Colonial-style House  
142

| Temp. | Location       | Pressure | Location    | Velocity | Location   |
|-------|----------------|----------|-------------|----------|------------|
| 1TC   | Bedroom 1      | 1PT      | Bedroom 1   | 1BDP     | Window E   |
| 2TC   | Bedroom 2      | 2PT      | Bedroom 2   | 2BDP     | Window D   |
| 3TC   | Bedroom 3      | 3PT      | Bedroom 3   | 3BDP     | Window B   |
| 4TC   | Hallway        | 4PT      | Living Room | 4BDP     | Hallway    |
| 5TC   | Living Room    | 5PT      | Kitchen     | 5BDP     | Window F   |
| 6TC   | Dining Room    | 6PT      | Dining Room | 6BDP     | Front Door |
| 7TC   | Kitchen (East) |          |             | 7BDP     | Window A   |
| 8TC   | Kitchen (West) |          |             |          |            |

Table 3.42: Locations of measurement devices in the UL/NIJ ranch-style house.

| Temp. | Location                   | Pressure | Location       | Velocity | Location   |
|-------|----------------------------|----------|----------------|----------|------------|
| 1TC   | Master Bedroom             | 1PT      | Master Bedroom | 1BDP     | Front Door |
| 2TC   | Bedroom 2                  | 2PT      | Bedroom 2      | 2BDP     | Window J   |
| 3TC   | Bedroom 3                  | 3PT      | Bedroom 3      | 3BDP     | Window K   |
| 4TC   | Bedroom 4                  | 4PT      | Bedroom 4      | 4BDP     | Window L   |
| 5TC   | 2nd Floor Hallway (East)   | 5PT      | Front Corridor | 5BDP     | Window E   |
| 6TC   | 2nd Floor Hallway (Middle) | 6PT      | Living Room    | 6BDP     | Window A   |
| 7TC   | Family Room (West Corner)  | 8PT      | Den            |          |            |
| 8TC   | Family Room (Center)       | 9PT      | Family Room    |          |            |
| 9TC   | Den                        | 10PT     | Kitchen        |          |            |
| 10TC  | Living Room                |          |                |          |            |
| 11TC  | Under 2nd Floor Hallway    |          |                |          |            |
| 12TC  | Foyer                      |          |                |          |            |
| 13TC  | Dining Room                |          |                |          |            |
| 14TC  | Laundry Room               |          |                |          |            |
| 15TC  | Kitchen                    |          |                |          |            |

Table 3.43: Locations of measurement devices in the UL/NIJ colonial-style house.

| Event           | Test 1 | Test 2 | Test 5 |
|-----------------|--------|--------|--------|
| Front Door Open | 300 s  | 1200 s | 1290 s |
| Back Door Open  | 1275 s | 1860 s | 300 s  |
| Window A Open   | 1260 s | 1845 s | -      |
| Window B Open   | 1245 s | 1830 s | -      |
| Window C Open   | 1230 s | 900 s  | -      |
| Window D Open   | 1215 s | -      | 600 s  |
| Window E Open   | 600 s  | 600 s  | -      |
| Window F Open   | 1200 s | 1815 s | 1200 s |
| Window G Open   | 1300 s | 1875 s | -      |
| Burner Off      | 900 s  | 1500 s | 900 s  |

Table 3.44: Sequence of events for the one story ranch-style house in the UL/NIJ experiments.

| Event           | Test 1 | Test 4 | Test 6 |
|-----------------|--------|--------|--------|
| Front Door Open | 600 s  | 600 s  | 1200 s |
| Back Door Open  | -      | -      | -      |
| Window A Open   | -      | -      | 900 s  |
| Window B Open   | -      | 900 s  | -      |
| Window C Open   | -      | -      | -      |
| Window D Open   | -      | -      | -      |
| Window E Open   | -      | -      | -      |
| Window F Open   | -      | -      | -      |
| Window G Open   | -      | -      | -      |
| Window H Open   | -      | -      | -      |
| Window I Open   | -      | -      | -      |
| Window J Open   | -      | -      | -      |
| Window K Open   | 900 s  | 1260 s | 600 s  |
| Window L Open   | 1200 s | 1320 s | -      |
| Window M Open   | -      | -      | -      |
| Burner Off      | 1500 s | 1200 s | 1500 s |

Table 3.45: Sequence of events for the two story colonial-style house in the UL/NIJ experiments.

### 3.91 Ulster SBI Corner Heat Flux Measurements

Zhang et al. [327] measured the heat flux and flame heights from fires in the single burning item (SBI) enclosure at the University of Ulster, Northern Ireland. Thin steel plate probes were used to measure the surface heat flux, and flame heights were determined by analyzing the instantaneous images extracted from the videos of the experiments by a CCD camera. Three heat release rates were used – 30 kW, 45 kW, and 60 kW.

### 3.92 UMD Polymers

Stoliarov et al. conducted measurements of the thermal properties of charring and non-charring polymers with the specific purpose of providing input data for numerical pyrolysis models [328, 329, 330, 331]. The study aimed to determine whether a one-dimensional conduction/reaction model could be used as a practical tool for prediction and/or extrapolation of the results of fire calorimetry tests. The non-charring polymers included poly(methyl methacrylate) (PMMA), high-impact polystyrene (HIPS), and polyoxymethylene (POM). The charring polymers included acrylonitrile butadiene styrene (ABS), polyethylene terephthalate (PET), Kydex, and polyethylenimine (PEI).

### 3.93 UMD Line Burner

**James P. White, University of Maryland, College Park**

The University of Maryland (UMD) Line Burner experimental facility provides for the study of a low-strain, buoyancy-driven, fully-turbulent diffusion flame in a canonical line-fire configuration. This facility provides well-controlled inlet and boundary conditions while introducing the complicating effects of buoyancy and turbulence characteristic of large-scale accidental fires. A variety of non-intrusive diagnostics are employed to measure local and integral flame characteristics. The facility comprises a slot burner centrally located within a surrounding, uniform co-flowing oxidizer. Controlled suppression of the flame is achieved via the introduction of either excess nitrogen gas or a fine water mist into the oxidizer stream. A detailed description of this facility is presented in White et al. [332].

An illustration of the burner and oxidizer assembly is presented in Fig. 3.57. The burner features a sand-filled, stainless-steel fuel port, measuring 5 cm wide by 50 cm long, with 1.5 mm thick side walls. Methane gas (99.5 % purity) or propane gas (99.5 % purity) are the primary burner fuels. A methane flow rate of  $1.00 \pm 0.02$  g/s (nominal 5.4 cm/s) or a propane flow rate of  $1.08 \pm 0.02$  g/s (nominal 2.1 cm/s) is utilized, measured using a mass flow controller. Assuming complete combustion, the total heat-release rate is roughly 50 kW for either fuel.

The burner is centrally located at the mouth of a surrounding oxidizer port, measuring 50 cm wide by 75 cm long, with 10 cm thick side walls. Flow conditioning elements ensure that the oxidizer is well-mixed and exits the oxidizer port with a uniform, flat velocity profile. The co-flowing oxidizer is provided at a fixed flow rate of  $75 \pm 5$  g/s (total, including variable suppressant flow, nominal 22 cm/s), measured using a calibrated pitot-static probe.

Sitting on top of the oxidizer port and surrounding the fuel port is a thin, 5 mm tall, 5 cm wide annulus of ceramic fiberboard, positioned so the top of the board is 10 mm below the lip of the fuel port (and 5 mm above the oxidizer port). This board serves as a flow blockage to reduce the oxidizer velocity near the flame base, forcing the onset of buoyancy-generated turbulence upstream toward the fuel port and reducing the tendency to form laminar structures at the base of the flame.

For nitrogen-dilution suppression experiments, the flame is suppressed via the introduction of a variable flow of gaseous nitrogen into the oxidizer. Suppression potential is characterized by the oxygen mole-fraction in the oxidizer,  $X_{O_2}$ . This quantity is measured using a paramagnetic oxygen analyzer via a probe located in the oxidizer port. The analyzer provides a measurement accuracy of  $\pm 0.125$  in the volume percentage of  $O_2$  and a response time of 5 s. An additional transport delay of approximately 20 s is compensated to provide synchronous data collection with other measurements.

Visible flame height is measured using a video camera, defined based on a 50 % intermittent flame height [332]. These image-based measurements rely on visible flame emissions, including the incandescence of soot particles, and do not strictly locate the stoichiometric flame sheet. The uncertainty in each flame height measurement is less than  $\pm 1.5$  cm.

Infrared radiative emissions are measured using a water-cooled Schmidt-Boelter heat-flux transducer. The sensor is positioned 100 cm radially outward from the burner centroid, 18 cm above the fuel port, facing perpendicular to the long axis of the burner. This device has a hemispherical absorptance of 0.94 for a spectral range between 0.6-15.0  $\mu\text{m}$ , a maximum viewing angle of 90°, and a response time of 0.25 s. Measurement accuracy is  $\pm 3$  %. The convective portion of the measured heat flux is neglected and sans-flame measurements are applied to correct for background irradiation.

Heat flux data are converted to radiative loss fraction,  $\chi_r$ , using a weighted multi-point radiation source model, whereby the measured heat flux is assumed to be received from an array of isotropic point sources uniformly distributed over a two-dimensional plane oriented across the visible flame surface. The uncertainty in each  $\chi_r$  measurement is less than  $\pm 4.5$  %.

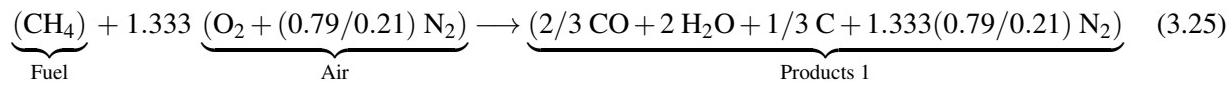
Mean and RMS (root mean square) temperature data are recorded using an array of R-Type thermocouple probes positioned at selected locations along the centerline of the flame. These probes are constructed using 50  $\mu\text{m}$  diameter wires with exposed, bead-welded junctions. Combustion products are collected in an exhaust evacuation system, wherein a gas sampling system provides measurement of the molar concentrations of oxygen ( $\pm 0.25$  mol %  $O_2$ ), carbon dioxide ( $\pm 1000$  ppm  $CO_2$ ), carbon monoxide ( $\pm 100$  ppm CO), water vapor ( $\pm 3$  % RH), and total hydrocarbons ( $\pm 10$  ppm THC) in the exhaust stream. From these measurements, integral heat release rate and combustion efficiency measurements are derived using species-based calorimetry techniques.

### Modeling Notes

The simulations of the UMD Line Burner experiments are performed for a duration of 80 s. The first 10 s allow the flame to stabilize at ambient conditions. At 10 s, nitrogen is introduced in the co-flow air stream and linearly increased so that the oxygen concentration decreases to 10 % at 80 s. When the oxygen concentration drops to 18 %, the nitrogen ramp up is delayed for 10 s in order to collect steady-state profiles of oxygen and temperature at heights of 12.5 cm and 25 cm above the burner.

The calculations are performed at three grid resolutions: 12.5 mm, 6.25 mm, and 3.125 mm, using 24, 164, and 204 meshes respectively.

The combustion and extinction are modeled using a two-step reaction scheme. In the first step, fuel is converted to CO, soot, and water vapor, and in the second step, the CO and soot are oxidized to form  $CO_2$ . Both reactions are fast, but the oxidation step follows the first reaction. That is, in a given time step, all available oxygen first forms CO and soot. Any leftover oxygen is then used to oxidize existing CO and soot. The methane reaction is written in terms of “lumped” species as follows:



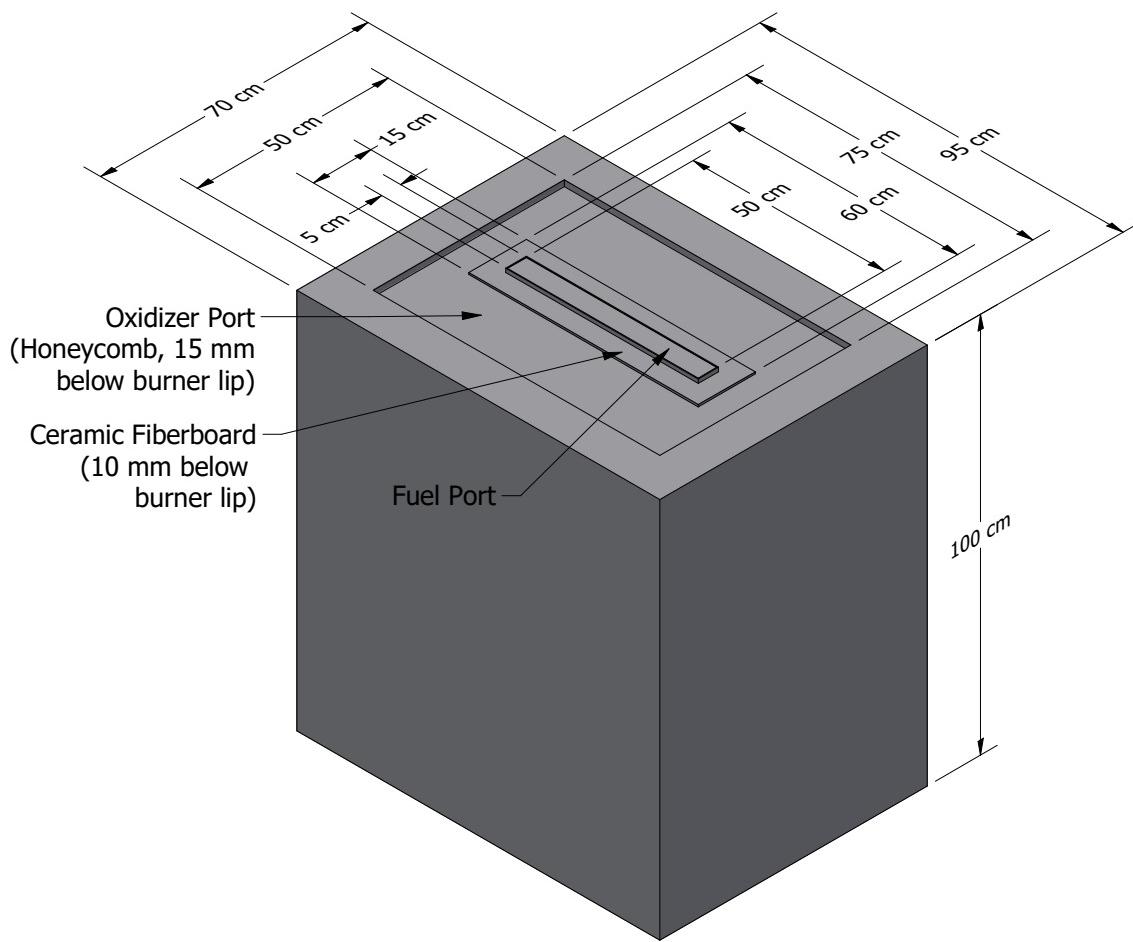
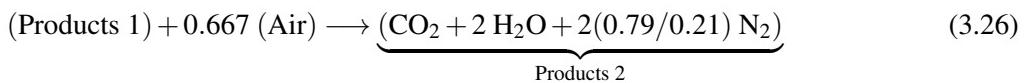
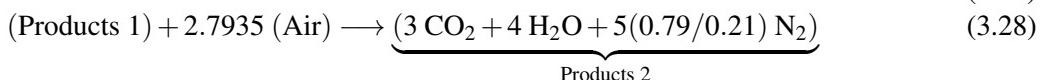
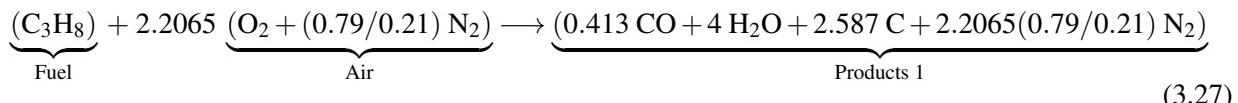


Figure 3.57: UMD Line Burner isometric view of burner and oxidizer assembly.



The propane reaction is:



The stoichiometry is dictated by the composition of the fuel molecule except for the stoichiometric coefficients of CO and soot in the first step. By default, 2/3 of the carbon in the fuel molecule is converted to CO, and 1/3 to soot. No better strategy has yet emerged for determining this. For both methane and propane, soot is generated in the first step, and as the co-flow is diluted with nitrogen, the flame color changes from yellow to blue as the in-flame soot volume fraction decreases. The simple two-step reaction scheme cannot predict the distribution of soot and CO in the first step; thus, the stoichiometric coefficients for CO and soot

(C) in Eq. (3.25) are chosen somewhat arbitrarily. The choice *does* affect the predicted radiative fraction of the fire and the heat flux to the radiometer.

Extinction of the fire is achieved using the *critical flame temperature* concept, which is the default extinction model in FDS. The CFT is 1507 °C for methane and 1447 °C for propane [152]. In addition, combustion is suppressed below the auto-ignition temperatures of 540 °C and 450 °C for methane and propane, respectively, except in a small volume just above the burner where the fuel is allowed to burn on contact with oxygen. This is a simple way to simulate the effect of a spark igniter.

### 3.94 UMD SBI Experiment

Researchers at the University of Maryland measured the flame spread over two perpendicular panels of black PMMA [333]. The experimental setup, shown in Fig. 3.58, was based on the Single Burning Item (SBI) test [334], but with symmetric panels. Two 50 cm wide and 5.8 mm thick black cast poly (methyl methacrylate) (PMMA) panels having a total height of 146 cm were mounted onto Marinite I calcium silicate board (1.27 cm thick, 60 cm wide). The properties of both materials can be found in Ref. [333].

The panels were ignited by a triangular propane sandbox burner (side length 25 cm; height 3.5 cm), that was placed 4 cm away from both panels. The burner flame was sustained throughout the experiment, with a heat release rate (HRR) of 30 kW.

A set of seven experiments was performed. The flame was allowed to spread until the HRR reached 300 kW. Once the HRR exceeded this threshold value, the propane burner was turned off and the flame was extinguished.

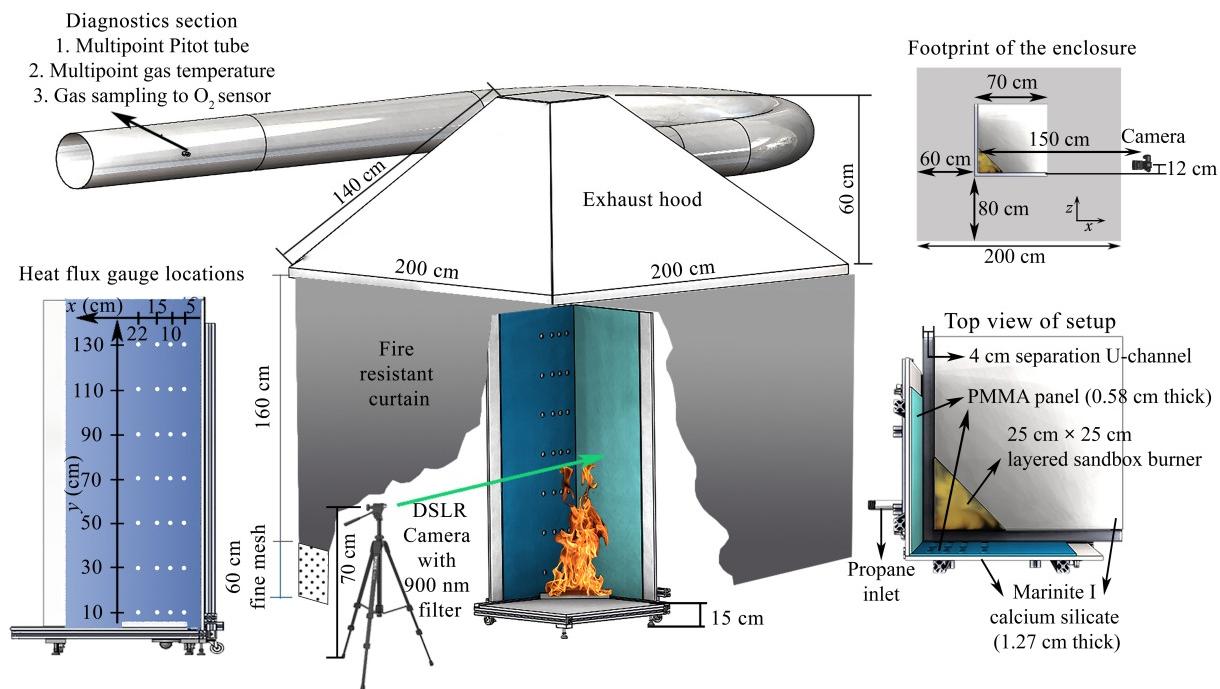


Figure 3.58: Schematic diagram of the UMD SBI experiment.

### **3.95 USCG/HAI Water Mist Suppression Tests**

The U.S. Coast Guard sponsored a series of experiments to assess the fire suppression capabilities of a variety of water mist systems in a variety of ship board configurations. The experiments were conducted in 1999 by Hughes Associates, Inc., in a simulated machinery space aboard the test vessel *State of Maine* at the USCG Fire and Safety Test Detachment, Mobile, Alabama [335]. The space had nominal dimensions of 7 m by 5 m by 3 m, containing two steel engine mock-ups each measuring 3 m by 1 m by 1.5 m. The space was equipped with a door for natural ventilation and a forced ventilation system providing approximately 15 air changes per hour. Five commercially available water mist systems were evaluated. The obstructed heptane spray fires ranged in size from approximately 250 kW to 1 MW.

### **3.96 USFS/Catchpole Experiments**

The U.S. Forest Service and collaborators from the University of New South Wales, Australia, conducted 354 fire experiments in a wind tunnel with a cross section of 3 m by 3 m [336]. The tunnel is part of the Intermountain Fire Sciences Laboratory in Missoula, Montana. The fires involved four different fuel species, a range of fuel bed depths, packing ratios, moisture contents and wind speeds. The fuels were regular and coarse excelsior (*Populus tremuloides*), and pine needles and heartwood sticks (*Pinus ponderosa*). The vegetation was placed in a 1 m wide and 8 m long tray. An approximately 5 cm wide tray of ethanol liquid was positioned at one end, and the fire spread rate was measured using photocells and video analysis.

#### **Modeling Notes**

The vegetation is modeled as a collection of cylindrical Lagrangian particles. The pyrolysis model assigned to the particles is described in the FDS User's Guide [1], chapter "Wildland Fire Spread," Sec. 17.1, "Thermal Degradation Model for Vegetation." The parameters for each experiment are listed in a table in Ref. [336].

### **3.97 USFS/Corsica Experiments**

Perez-Ramirez et al. at the University of Corsica, France, and Mell at the U.S. Forest Service's Pacific Wildland Fire Science Laboratory in Seattle, Washington, simulated six bench-scale fires spreading over a 1 m wide by 2 m long bed of pine needles [130]. The heat release rates from the spreading fires were measured in a furniture calorimeter. The fuel beds were made up of *Pinus pinaster* needles, and three different fuel loadings (0.6, 0.9 and 1.2 kg/m<sup>2</sup>) were tested under no-slope and up-slope conditions (20°).

#### **Modeling Notes**

The pine needles are modeled as a collection of cylindrical Lagrangian particles. The pyrolysis model assigned to the particles is described in the FDS User's Guide [1], chapter "Wildland Fire Spread," Sec. 17.1, "Thermal Degradation Model for Vegetation."

The test parameters for these experiments are given in Table 3.46.

| Exp. No. | Dry Fuel Loading (kg/m <sup>2</sup> ) | Slope (deg.) | Dry Mass per Volume (kg/m <sup>3</sup> ) | Packing Ratio | Bed Depth (cm) |
|----------|---------------------------------------|--------------|--|---------------|----------------|
| 1_0      | 0.6                                   | 0            | 17                                       | 0.033         | 3.5            |
| 2_0      | 0.9                                   | 0            | 16                                       | 0.031         | 5.5            |
| 3_0      | 1.2                                   | 0            | 18                                       | 0.035         | 6.5            |
| 1_20     | 0.6                                   | 20           | 17                                       | 0.033         | 3.5            |
| 2_20     | 0.9                                   | 20           | 16                                       | 0.031         | 5.5            |
| 3_20     | 1.2                                   | 20           | 18                                       | 0.035         | 7.5            |

Table 3.46: Test matrix for the USFS/Corsica Experiments.

### 3.98 USN High Bay Hangar Experiments

The U.S. Navy sponsored a series of 33 tests within two hangars examining fire detection and sprinkler activation in response to spill fires in large enclosures. Experiments were conducted using JP-5 and JP-8 fuels in two Navy high bay aircraft hangars located in Naval Air Stations in Barber's Point, Hawaii and Keflavik, Iceland [337].

The Hawaii tests were conducted in a 15 m high hangar measuring 97.8 m in length and 73.8 m in width. Of the 13 tests conducted in the facility 11 were conducted in pans ranging from .09 m<sup>2</sup> to 4.9 m<sup>2</sup> in area with heat release rates varying from 100 kW to 7.7 MW. The burner was placed in the center of the room on a scale that continuously recorded the pans weight. The facility was equipped with a number of detection devices including thermocouples, electronic smoke and spot heat detectors, projected beam smoke detectors, combination UV/IR optical flame detectors, line-type heat detectors, as well as sprinklers. Measurements were recorded at a large number of locations allowing for a thorough profile of compartment behavior.

It was suspected that fire plume behavior and response of detection devices in a cold building may not have been well replicated by the experiments held in the warm hangar in Hawaii. The Iceland tests were conducted under a 22 m barrel vaulted ceiling in a hangar measuring 45.7 m by 73.8 m. 22 tests in total were conducted. The majority of these tests fires burned JP-5 fuel with the remainder burning JP-8. The jet fuel fires ranged in size from .06 m<sup>2</sup> to 20.9 m<sup>2</sup> and in heat release rate from 100 kW to approximately 33 MW. The facility was equipped similarly to the Hawaii hangar.

### 3.99 UWO Wind Tunnel Experiments

Wind tunnel measurements were conducted at the University of Western Ontario (UWO) [338] on a 1:100 scale model of the Texas Tech Wind Engineering Field Research Laboratory (WERFL) building which has approximate dimensions of 9.1 m by 13.7 m by 4 m and a slightly pitched roof. In the test report, this experiment is referred to as Test 7. Pressure measurements were made for 22 wind directions for this scale model.

#### Modeling Notes

The 1:100 scale model of the building is approximately 14 cm long, 9 cm wide, and 4 cm tall. The simulations use 5.0 mm, 2.5 mm, and 1.25 mm cubic grid cells, uniformly spanning the computational domain of dimensions 1.12 m × 0.56 m × 0.28 m. The 4 cm height of the scale model is spanned by 8, 16, and 32 grid cells. The grid resolution was assessed by checking that the values of  $y^+$ , a non-dimensional distance, never

exceed 150 for any mesh resolution.  $y^+$  values are dependent on turbulence model wall laws and a value of 150 means that the first grid point is well within the logarithmic region.

Only two wind directions are chosen for validation,  $180^\circ$  and  $270^\circ$ , representing right angles formed with the long and short sides of the building. For each angle, 3 lines of pressure measurements running up the windward side, along the roof, and down the leeward side are used for comparison to the simulation. One line of pressure measurements along the side of the scale model is also used.

The incoming flow assigned at the inflow boundary is characterized by its mean wind speed profile and turbulent fluctuations. For consistency with the UWO experiments, the mean wind speed profile was modeled by the power law:

$$U(z) = 9.144 \left( \frac{z}{0.0396} \right)^p \quad (3.29)$$

where 9.144 m/s is the reference wind speed at the 0.0396 m roof height of the scale model and the power law exponent  $p = 0.1173$  was fit to the experimental data.

Fluctuations at the inlet boundary are generated by the Synthetic Eddy Method (SEM) of Jarrin [339]. The desired value of `N_EDDY` (the number of eddies generated at the inlet) is the largest possible value that does not slow down the simulation. This value is determined by running a number of simulations for the same time while varying the `N_EDDY` input and recording the total run time. The other turbulence parameters, `L_EDDY` (characteristic eddy length) and `REYNOLDS_STRESS`, are set based on the turbulence intensity data from the UWO experiments. The Reynolds stresses are found by multiplying the turbulence intensity in each direction by the wind velocity at roof height to determine the root mean square of the velocity fluctuations, and then squaring the root mean square values.

The side walls and roof of the wind tunnel are set to free-slip. The roughness length at the ground is specified to be 0.0001 m, 1/100 the full-scale value of 0.01 m. The outlet of the wind tunnel is set to an “open” boundary condition, where pressure is set to the ambient pressure.

### 3.100 Vettori Flat Ceiling Experiments

Vettori [81] analyzed a series of 45 experiments conducted at NIST that were intended to compare the effects of different ceiling configurations on the activation times of quick response residential pendent sprinklers. The two ceiling configurations used consisted of an obstructed ceiling, with parallel beams 0.038 m wide by 0.24 m deep placed 0.41 m on center, and a smooth ceiling configuration, in which the beams were covered by a sheet of gypsum board. In addition to the two ceiling configurations, there were also three fire growth rates and three burner locations used – a total of 18 test configurations. The fire growth rate was provided by a computer controlled methane gas burner to mimic a standard t-squared<sup>7</sup> fire growth rate with either a slow, medium, or fast ramp up. The burner was placed in a corner of the room, then against an adjacent wall, and then in a location removed from any wall. Measurements were taken to record sprinkler activation time, temperatures at varying heights and locations within the room, and the ceiling jet velocities at several other locations. A diagram of the test structure is displayed in Figure 3.59.

---

<sup>7</sup>The actual heat release rate are presented in Table 3.47.

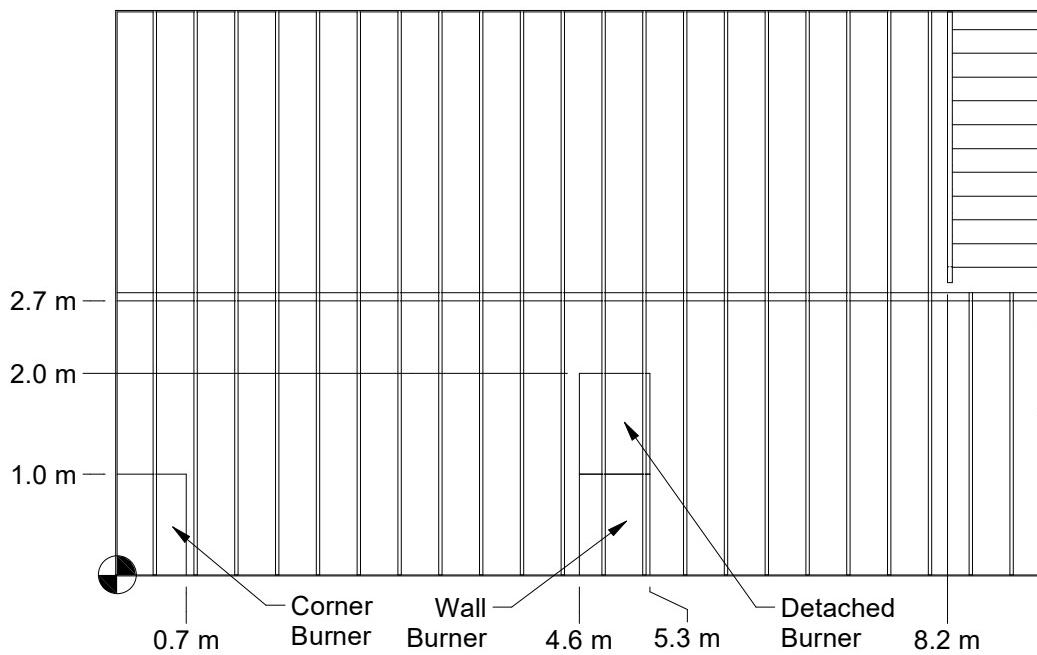
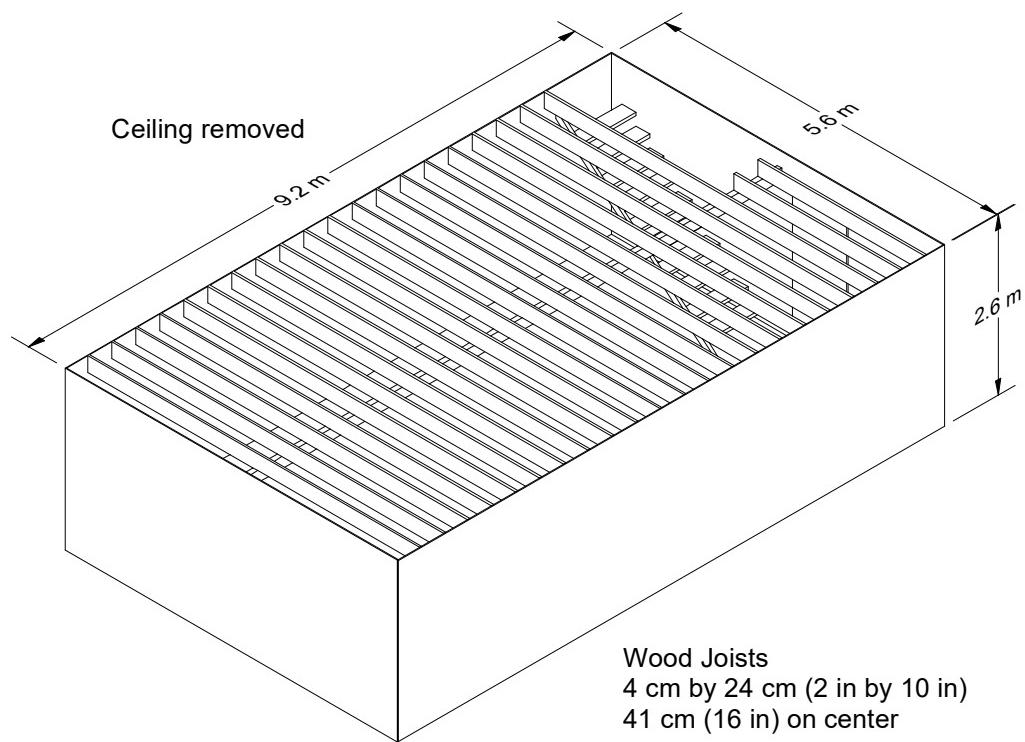


Figure 3.59: Geometry of the Vettori Flat Ceiling compartment.

Table 3.47: Heat release rate profiles for the Vettori experiments.

| Time<br>(s) | Slow<br>(kW) | Medium<br>(kW) | Fast<br>(kW) |
|-------------|--------------|----------------|--------------|
| 0           | 0            | 0              | 0            |
| 10          | 9            | 20             | 75           |
| 20          | 16           | 34             | 127          |
| 30          | 23           | 51             | 173          |
| 40          | 30           | 67             | 196          |
| 50          | 35           | 83             | 271          |
| 60          | 42           | 104            | 379          |
| 70          | 52           | 125            | 515          |
| 80          | 62           | 143            | 673          |
| 90          | 68           | 162            | 852          |
| 100         | 78           | 174            | 1053         |
| 110         | 85           | 192            |              |
| 120         | 94           | 239            |              |
| 130         | 100          | 279            |              |
| 140         | 109          | 325            |              |
| 150         | 115          | 373            |              |
| 160         | 125          | 424            |              |
| 170         | 137          | 479            |              |
| 180         | 148          | 537            |              |
| 190         | 163          | 599            |              |
| 200         | 179          | 663            |              |
| 210         | 195          |                |              |
| 220         | 213          |                |              |
| 230         | 231          |                |              |
| 240         | 250          |                |              |
| 250         | 269          |                |              |
| 260         | 290          |                |              |
| 270         | 311          |                |              |
| 280         | 333          |                |              |
| 290         | 354          |                |              |
| 300         | 378          |                |              |
| 310         | 402          |                |              |
| 320         | 427          |                |              |
| 330         | 453          |                |              |
| 340         | 479          |                |              |
| 350         | 506          |                |              |
| 360         | 534          |                |              |
| 370         | 562          |                |              |

### 3.101 Vettori Sloped Ceiling Experiments

Vettori [82] performed a series of 72 compartment experiments to measure the activation times of quick-response residential pendent sprinklers mounted under a ceiling with an adjustable slope. There were 36 unique configurations (2 replicates of each) combining the following parameters:

- Flat, 13°, or 24° Ceiling Slope
- Smooth or Obstructed Ceiling Surface
- Fast or Slow Growth Fire
- Corner, Wall, or Detached Burner Location

Note that the Slow and Fast fire growth profiles were the same as those reported in Table 3.47.

### 3.102 VTT Large Hall Tests

The experiments are described in Ref. [340]. The series consisted of 8 experiments, but because of replicates only three unique fire scenarios. The experiments were undertaken to study the movement of smoke in a large hall with a sloped ceiling. The tests were conducted inside the VTT Fire Test Hall, with dimensions of 19 m high by 27 m long by 14 m wide. Each test involved a single heptane pool fire, ranging from 2 MW to 4 MW. Four types of predicted output were used in the present evaluation – the HGL temperature and depth, average flame height and the plume temperature. Three vertical arrays of thermocouples (TC), plus two thermocouples in the plume, were compared to FDS predictions. The HGL temperature and height were reduced from an average of the three TC arrays using the standard algorithm described in Chapter 5. The ceiling jet temperature was not considered, because the ceiling in the test hall is not flat, and the standard model algorithm is not appropriate for this geometry.

The VTT test report lacks some information needed to model the experiments, which is why some information was based on private communications with the principal investigator, Simo Hostikka.

**Surface Materials:** The walls and ceiling of the test hall consist of a 1 mm thick layer of sheet metal on top of a 5 cm layer of mineral wool. The floor was constructed of concrete. The report does not provide thermal properties of these materials.

**Natural Ventilation:** In Cases 1 and 2, all doors were closed, and ventilation was restricted to infiltration through the building envelope. Precise information on air infiltration during these tests is not available. The scientists who conducted the experiments recommend a leakage area of about  $2 \text{ m}^2$ , distributed uniformly throughout the enclosure. By contrast, in Case 3, the doors located in each end wall (Doors 1 and 2, respectively) were open to the external ambient environment. These doors are each 0.8 m wide by 4 m high, and are located such that their centers are 9.3 m from the south wall.

**Mechanical Ventilation:** The test hall has a single mechanical exhaust duct, located in the roof space, running along the center of the building. This duct had a circular section with a diameter of 1 m, and opened horizontally to the hall at a distance of 12 m from the floor and 10.5 m from the west wall. Mechanical exhaust ventilation was operational for Case 3, with a constant volume flow rate of  $11 \text{ m}^3/\text{s}$  drawn through the exhaust duct.

**Heat Release Rate:** Each test used a single liquid fuel pan with its center located 16 m from the west wall and 7.4 m from the south wall. For all tests, the fuel was heptane in a circular steel pan that was partially filled with water. The pan had a diameter of 1.17 m for Case 1 and 1.6 m for Cases 2 and 3. In

each case, the fuel surface was 1 m above the floor. The trays were placed on load cells, and the HRR was calculated from the mass loss rate. For the three cases, the fuel mass loss rate was averaged from individual replicate tests. In the HRR estimation, the heat of combustion (taken as 44,600 kJ/kg) and the combustion efficiency for n-heptane was used. Hostikka suggests a value of 0.8 for the combustion efficiency. Tewarson reports a value of 0.93 for a 10 cm pool fire [151]. For the calculations reported in the current study, a combustion efficiency of 0.85 is assumed. In general, an uncertainty of 15 % has been assumed for the reported HRR of most of the large scale fire experiments used.

**Radiative Fraction:** The radiative fraction was assumed to be 0.35, similar to many smoky hydrocarbons.

A diagram of the test structure is displayed in Figure 3.60.

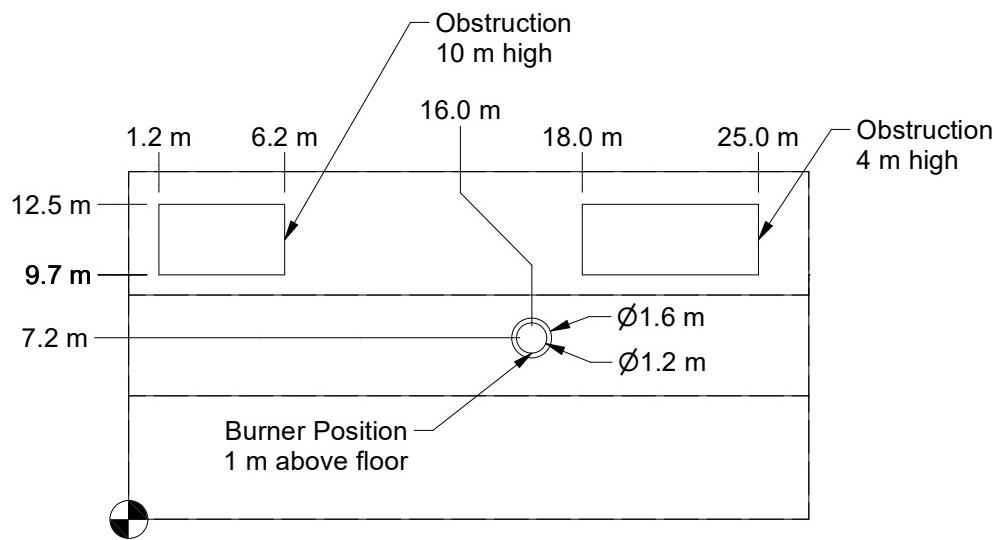
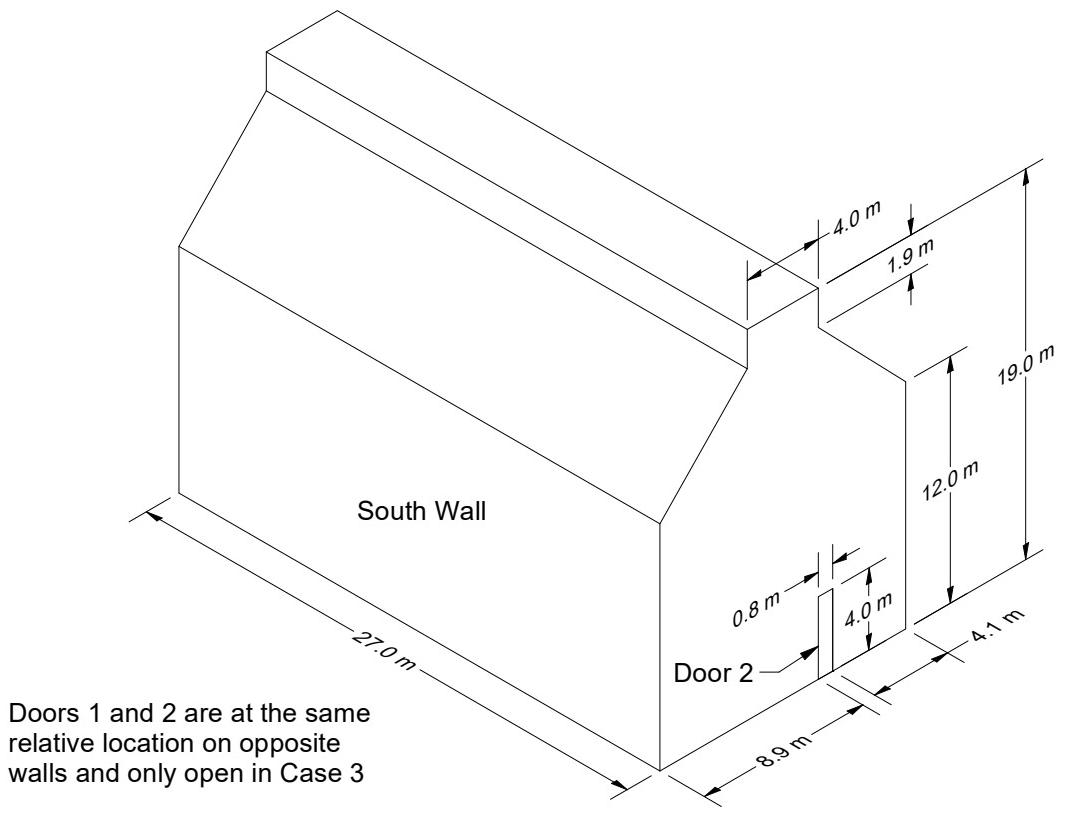


Figure 3.60: Geometry of the VTT Large Fire Test Hall.

### 3.103 VTT Water Spray Experiments

The spray from a single water mist nozzle was measured at Tampere University of Technology using a direct imaging technique [341]. The model number of the nozzle is LN-2, manufactured by the Spraying Systems Company. It is a fine spray hydraulic atomizing nozzle of the standard spray, small capacity type. Measurements were made 40 cm and 62 cm below the nozzle. Measured quantities include the average droplet velocity, droplet flux, and median diameter.

### 3.104 Waterloo Methanol Pool Fire Experiment

Beth Weckman measured near-field temperatures and velocities of a 30.5 cm diameter methanol pool fire at the University of Waterloo, Ontario, Canada [342]. The methanol fuel flow rate was maintained at  $1.35 \text{ cm}^3/\text{s}$  to maintain a burner rim height of 1 cm. Assuming complete combustion, the heat release rate was approximately 24.6 kW.

The burner was mounted on a traversing stand that allowed for radial and axial traverses of the fire flow field. The vapor core, continuous flame zone and fluctuating regions of the fire plume were characterized via profiles of axial and radial velocity and temperature taken at 2 cm intervals from the pool centerline to 16 cm from the centerline in the radial direction, and at heights from 2 cm to 20 cm above the fuel surface. A final radial profile was taken at a height of 30 cm. Measurements were made by moving the burner while the velocity and temperature transducers were held at a fixed point. To shield the fire from drafts, the entire system was enclosed by panels of wire mesh that was covered with an aluminum window screen.

Time resolved velocity measurements were performed using a two component laser doppler anemometer. Time resolved temperature data was measured using  $50 \mu\text{m}$  diameter, bare-wire thermocouples (Pt vs Pt-10% Rh) with known bead diameters in the range of  $75 \mu\text{m}$  to  $100 \mu\text{m}$ .

Additional measurements of a 30.5 cm diameter methanol pool fire were made by Hamins et al., including the heat flux to the pool surface [343], centerline profiles of temperature and species concentrations [344], and an additional radial profile of temperature 60 cm above the pool surface [344].

#### Modeling Notes

The methanol pool fire is modeled at three different grid resolutions—2 cm, 1 cm, and 0.5 cm. Two sets of simulations are performed, one in which the mass loss rate of fuel is specified, and one in which it is predicted. The gas phase measurements are compared with the simulations for which the burning rate is specified.

Because measurements of CO were made within the flame envelop, a two-step reaction mechanism is implemented. In the first reaction, fuel is converted to CO and  $\text{H}_2\text{O}$ , and in the second reaction, CO is converted to  $\text{CO}_2$ . Both reactions employ fast kinetics and performed serially. It is assumed that no soot is formed in either reaction.

Physical properties of methanol are taken from a data sheet published by the Methanol Institute [345]: boiling temperature,  $64.6^\circ\text{C}$ , heat of vaporization at  $64.6^\circ\text{C}$ ,  $1098.3 \text{ kJ/kg}$ , thermal conductivity,  $0.2 \text{ W}/(\text{m}\cdot\text{K})$ , specific heat at  $25^\circ\text{C}$ ,  $2.53 \text{ kJ}/(\text{kg}\cdot\text{K})$ , density at  $20^\circ\text{C}$ ,  $792 \text{ kg/m}^3$ . The heat of combustion is given as  $19.9 \text{ kJ/g}$ , but this value is not input directly, but rather calculated based on the heats of formation of the reactants and products of combustion.

The radiative fraction is *predicted* by the model, not specified by the user, for all cases. The path length used by RadCal to compute the table of effective radiative absorption coefficients for the gas mixture is set to 10 cm, the default value. The absorption coefficient of the liquid methanol is given as  $1140 \text{ m}^{-1}$ .

The modeled thermocouple has a bead diameter of  $100 \mu\text{m}$  to match the experiments.

For the simulations where the burning rate is not specified, a liquid fuel evaporation model is used with a boiling temperature of 64.6 °C.

### 3.105 WTC Spray Burner Experiments

As part of its investigation of the World Trade Center disaster, the Building and Fire Research Laboratory at NIST conducted several series of fire experiments to both gain insight into the observed fire behavior and also to validate FDS for use in reconstructing the fires. The first series of experiments involved a relatively simple compartment with a liquid spray burner and various structural elements with varying amounts of sprayed fire-resistive materials (SFRM). A diagram of the compartment is shown in Fig. 3.61. A complete description of the experiments can be found in the NIST WTC report NCSTAR 1-5B [70]. A complete description of the SFRM can be found in the NIST WTC report NCSTAR 1-6A [346]. The overall enclosure was rectangular, as were the vents and most of the obstructions. The compartment walls and ceiling were made of 2.54 cm thick marinite. The manufacturer provided the thermal properties of the material used in the calculation. The density was 737 kg/m<sup>3</sup>, conductivity 0.12 W/m/K. The specific heat ranged from 1.17 kJ/kg/K at 93 °C to 1.42 kJ/kg/K at 425 °C. This value was assumed for higher temperatures. The steel used to construct the column and truss flanges was 0.64 cm thick. The density of the steel was assumed to be 7,860 kg/m<sup>3</sup>; its specific heat 0.45 kJ/kg/K.

Two fuels were used in the tests. The properties of the fuels were obtained from measurements made on a series of unconfined burns that are referenced in the test report. The first fuel was a blend of heptane isomers, C<sub>7</sub>H<sub>16</sub>. Its soot yield was set at a constant 1.5 %. The second fuel was a mixture (40 % - 60 % by mass) of toluene, C<sub>7</sub>H<sub>8</sub>, and heptane. Because FDS only considers the burning of a single hydrocarbon fuel, the mixture was taken to be C<sub>7</sub>H<sub>12</sub> with a soot yield of 11.4 %. The radiative fraction for the heptane blend was 0.44; for the heptane/toluene mixture it was 0.39. The heat release rate of the simulated burner was set to that which was measured in the experiments. The spray burner was modeled using reported properties of the nozzle and liquid fuel droplets.

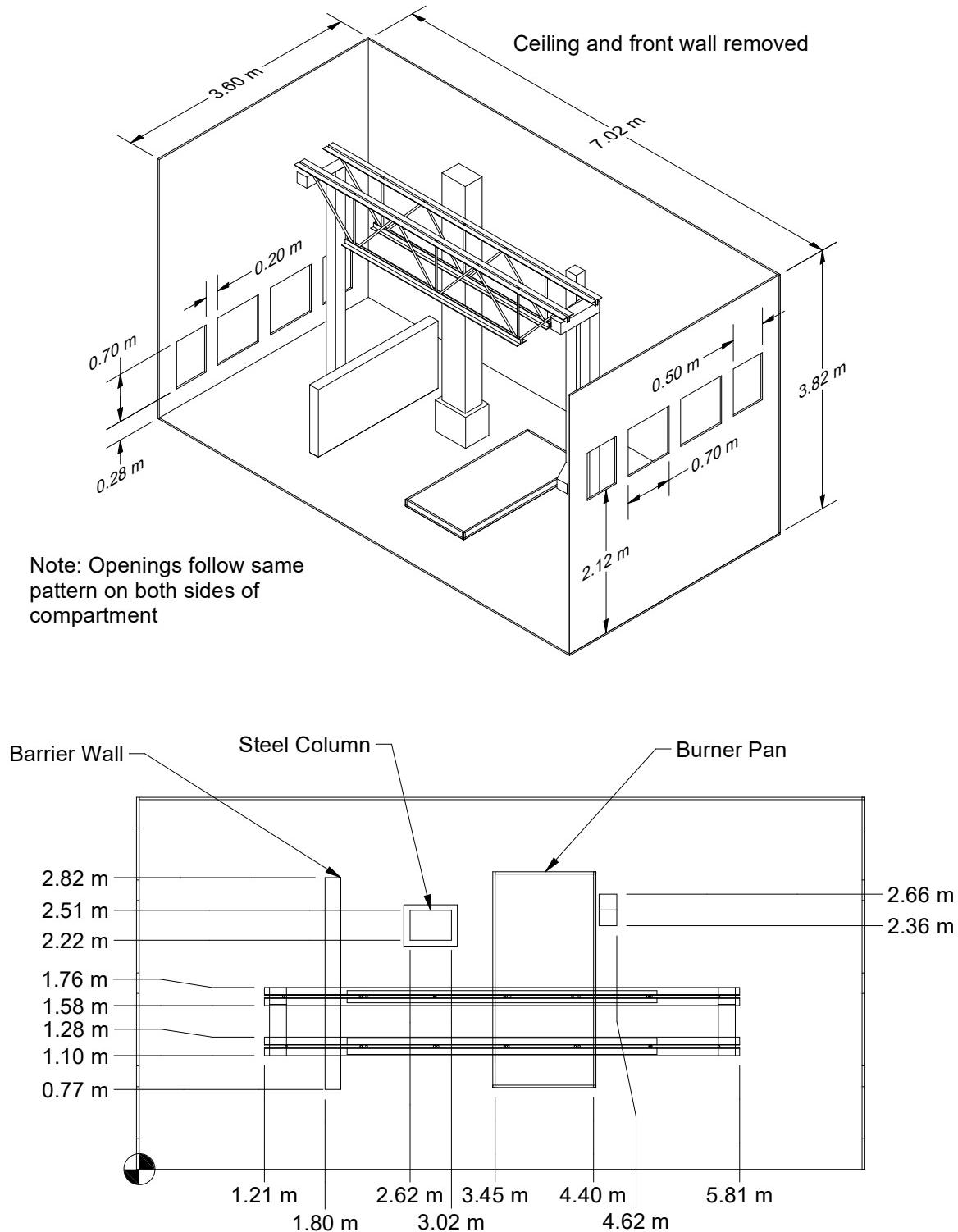


Figure 3.61: Geometry of the compartment used for the WTC Experiments.

### 3.106 Wu Bakar Tunnel Experiments

An important issue in road tunnel design with respect to fire safety is *back-layering*. In the event of a fire in a tunnel, a common strategy is to blow the smoke in one direction to allow occupants to escape and first responders to find the fire. The extent to which smoke from the fire spreads against imposed ventilation is known as back-layering. Experiments to quantify back-layering have been conducted at both small and full-scale. One important set of small-scale experiments was performed by Wu and Bakar [347]. The experiments were conducted in 15 m long tunnels with 5 different cross sections. Tunnels A, B, C, and D were rectangular in cross section with a height of 25 cm and widths of 13.6 cm, 25 cm, 50 cm, and 100 cm, respectively. Tunnel E was 24.4 cm high, 27.4 cm wide at the base, with walls slanted inwards 7° from the vertical leading to a circular arch ceiling.

A 12 cm diameter circular propane burner was placed flush with the floor at a distance of approximately 6 m from the upstream opening. For a range of fire sizes, the air velocity through the tunnel was ramped up until the back-layer length was reduced to zero; that is, the upstream extent of the smoke layer coincided with the upstream edge of the burner. These results were then used to develop an empirical correlation relating the *critical velocity*, tunnel cross section, and heat release rate.

#### Modeling Notes

Five simulations are conducted; one for each tunnel type. In each, the heat release rate is stepped over from the lowest to highest reported value in 20 s increments. During each steady period, the near-ceiling temperatures are recorded and used to infer the location of the back-layer; that is, the back-layer extent coincides with a drop in the ceiling jet temperature to within 10 °C of ambient. The surface roughness of the tunnel walls is estimated to be 1 mm. The wall material is taken as generic steel.

### 3.107 Summary of Experiments

Table 3.48 presents a summary of all the experiments described in this chapter in terms of parameters commonly used in fire protection engineering. This “parameter space” outlines the range of applicability of the validation studies performed to date. In other words, if this guide is to be cited as justification for using FDS to simulate a given fire scenario, that scenario must be similar to these experiments in the sense of having comparable physical parameters. These parameters are explained below:

**Heat Release Rate,  $\dot{Q}$ ,** is the range of peak heat release rates of the fires in the test series.

**Fire Diameter,  $D$ ,** is the equivalent diameter of the base of the fire, calculated  $D = \sqrt{4A/\pi}$ , where  $A$  is the area of the base.

**Ceiling Height,  $H$ ,** is the distance from floor to ceiling.

**Fire Froude Number,  $\dot{Q}^*$ ,** is a useful non-dimensional quantity for plume correlations and flame height estimates.

$$\dot{Q}^* = \frac{\dot{Q}}{\rho_\infty c_p T_\infty \sqrt{g D D^2}} \quad (3.30)$$

It is essentially the ratio of the fuel gas exit velocity and the buoyancy-induced plume velocity. Jet fires are characterized by large Froude numbers. Typical accidental fires have a Froude number near unity.

**Flame Height relative to Ceiling Height,  $L_f/H$ ,** is a convenient way to express the physical size of the fire relative to the size of the room. The height of the visible flame, based on Hesketh's correlation, is

estimated by:

$$L_f = D \left( 3.7 (\dot{Q}^*)^{2/5} - 1.02 \right) \quad (3.31)$$

**Global Equivalence Ratio,  $\phi$ ,** is the ratio of the mass flux of fuel to the mass flux of oxygen into the compartment, divided by the stoichiometric ratio.

$$\phi = \frac{\dot{m}_f}{r \dot{m}_{O_2}} = \frac{\dot{Q} \text{ (kW)}}{13,100 \text{ (kJ/kg)} \dot{m}_{O_2}} \quad ; \quad \dot{m}_{O_2} = \begin{cases} \frac{1}{2} 0.23 A_0 \sqrt{H_0} & : \text{Natural Ventilation} \\ 0.23 \rho \dot{V} & : \text{Mechanical Ventilation} \end{cases} \quad (3.32)$$

Here,  $r$  is the stoichiometric ratio,  $A_0$  is the area of the compartment opening,  $H_0$  is the height of the opening,  $\rho$  is the density of air, and  $\dot{V}$  is the volume flow of air into the compartment. If  $\phi < 1$ , the compartment is considered “well-ventilated” and if  $\phi > 1$ , the compartment is considered “under-ventilated.”

**Compartment Aspect Ratios,  $W/H$  and  $L/H$ ,** indicate if the compartment is shaped like a hallway, typical room, or vertical shaft.

**Relative Distance along the Ceiling,  $r_{cj}/H$ ,** indicates the distance from the fire plume of a sprinkler, smoke detector, etc., relative to the compartment height,  $H$ .

**Relative Distance from the Fire,  $r_{rad}/D$ ,** indicates whether a “target” is near or far from the fire.

Table 3.48: Summary of important experimental parameters.

| Test Series            | $\dot{Q}$<br>(kW)                 | $D$<br>(m)  | $H$<br>(m)  | $\dot{Q}^*$                        | $L_f/H$   | $\phi$      | $W/H$ | $L/H$ | $r_{ci}/H$ | $r_{rad}/D$ |
|------------------------|-----------------------------------|-------------|-------------|------------------------------------|-----------|-------------|-------|-------|------------|-------------|
| Arup Tunnel            | 5344                              | 1.6         | 7           | 1.5                                | 0.8       | 0.0         | 1.1   | 43    | 0.0 – 1.1  | N/A         |
| ATF Corridors          | 50 – 500                          | 0.5         | 2.4         | 0.3 – 3.3                          | 0.3 – 0.9 | 0.0 – 0.1   | 0.8   | 7.1   | 0.8 – 6.0  | N/A         |
| Beyler Hood            | 8 – 30                            | 0.2         | 0.5         | 0.5 – 1.1                          | 0.7 – 1.3 | 0.2 – 1.7   | 2.0   | 2.0   | N/A        | N/A         |
| Bittern Sprinklers     | 150                               | 0.5         | 2.4         | 0.8                                | 0.5       | 0.04        | 1.7   | 3.3   | 0.8        | N/A         |
| Bryant Doorway         | 34 – 511                          | 0.3         | 2.4         | 0.5 – 6.9                          | 0.2 – 1.0 | 0.0 – 0.2   | 1.0   | 2.1   | 0.6 – 0.8  | N/A         |
| DelCo Trainers         | 440 – 1190                        | 0.7 – 1.2   | 2.4         | 0.7 – 1.0                          | 0.8 – 1.1 | 0.1 – 0.3   | 1.5   | 2.5   | 0.4 – 3.8  | N/A         |
| FAA Cargo              | 5                                 | 0.1         | 1.4         | 1.4                                | 0.2       | 0.2         | 2.3   | 4.8   | 0.1 – 4.8  | N/A         |
| Fleury Heat Flux       | 100 – 300                         | 0.3 – 0.6   | Open        | 0.3 – 5.5                          | Open      | Open        | Open  | Open  | Open       | 1.7 – 3.3   |
| FM Panels              | 30 – 100                          | 0.5         | Open        | 0.2 – 0.5                          | Open      | Open        | Open  | Open  | Open       | 0           |
| FM/SNL                 | 470 – 516                         | 0.9         | 6.1         | 0.6 – 2.4                          | 0.3 – 0.6 | 0.0 – 0.2   | 2.0   | 3.0   | 0.2 – 0.3  | N/A         |
| Hamins CH <sub>4</sub> | 0.4 – 162                         | 0.1 – 1.0   | Open        | 0.1                                | Open      | Open        | Open  | Open  | N/A        | 0.1 – 12    |
| Harrison Plumes        | 5 – 15                            | 0.16        | 0.5         | 0.5 – 1.4                          | 0.5 – 1.0 | Open        | Open  | Open  | N/A        | N/A         |
| Heskestad              | 10 <sup>2</sup> – 10 <sup>7</sup> | 1.1         | Open        | 10 <sup>-1</sup> – 10 <sup>4</sup> | Open      | Open        | Open  | Open  | N/A        | N/A         |
| JH/FRA                 | 20 – 5,500                        | 0.15 – 0.61 | 0.61 – 2.44 | 1.5 – 5.2                          | 0.8 – 3.7 | 0.08 – 0.42 | 1     | 1.5   | N/A        | N/A         |
| LLNL Enclosure         | 50 – 400                          | 0.6         | 4.5         | 0.2 – 1.5                          | 0.1 – 0.4 | 0.1 – 0.4   | 0.9   | 1.3   | 0.3 – 1.0  | N/A         |
| McCaffrey Plume        | 14 – 57                           | 0.3         | Open        | 0.2 – 0.8                          | Open      | Open        | Open  | Open  | N/A        | N/A         |
| NBS Multi-Room         | 110                               | 0.3         | 2.4         | 1.5                                | 0.5       | 0.0         | 1.0   | 5.1   | N/A        | N/A         |
| NIST Composite Beam    | 4000                              | 1.4         | 3.7         | 0.5                                | 0.7       | 0.6         | 0.5   | 3.5   | N/A        | N/A         |
| NIST FSE               | 100 – 2500                        | 0.6 – 1.1   | 2.4         | 0.5 – 1.8                          | 0.4 – 1.7 | 0.2 – 5.9   | 1.0   | 1.5   | 0.4 – 0.8  | N/A         |
| NIST/NRC               | 350 – 2200                        | 1.0         | 3.8         | 0.3 – 2.0                          | 0.3 – 1.0 | 0.0 – 0.3   | 1.9   | 5.7   | 0.3 – 2.1  | 2.0 – 4.0   |
| NIST/NRC Cabinet       | 200 – 400                         | 0.3 – 0.5   | 2.1         | 0.3 – 3.7                          | 0.2 – 0.9 | 1.3 – 12    | 0.3   | 0.4   | N/A        | 1.2 – 2.0   |
| NIST/NRC Corner        | 200 – 400                         | 0.7         | 3.8         | 0.4 – 0.9                          | 0.3 – 0.5 | <0.1        | 1.8   | 2.9   | 0.5 – 2.3  | N/A         |
| NIST RSE               | 50 – 600                          | 0.15        | 1.0         | 5.2 – 63                           | 0.9 – 2.8 | 0.1 – 1.1   | 1.0   | 1.5   | N/A        | N/A         |
| NIST Smoke Alarms      | 100 – 350                         | 1.0         | 2.4         | 0.2 – 0.3                          | 0.2 – 0.5 | N/A         | 1.7   | 8.3   | 1.3 – 8.3  | N/A         |
| NIST Vent Study        | 2.5                               | 0.1         | 0.6         | 0.7                                | 0.4       | 0.05        | 2.0   | 2.0   | 1.0        | N/A         |
| NRCC Facade            | 5000 – 10300                      | 4.3         | 2.8         | 0.1 – 0.2                          | 0.9 – 1.7 | 0.6 – 1.2   | 1.6   | 2.2   | N/A        | 0           |
| NRCC Smoke Tower       | 3000                              | 2.2         | 3.4         | 0.4                                | 1.0       | 0.7         | 0.1   | 0.2   | 1.2        | N/A         |
| NRL/HAI                | 50 – 520                          | 0.3 – 0.7   | Open        | 1.1 – 1.2                          | Open      | Open        | Open  | Open  | N/A        | 0           |
| PRISME                 | 480 – 1600                        | 0.7 – 1.1   | 4.0         | 1.1                                | 0.5 – 0.8 | 0.5         | 1.3   | 1.5   | 0.0 – 0.5  | 2.3 – 5.7   |

Table 3.48: Summary of important experimental parameters (continued).

| Test Series    | $\dot{Q}$<br>(kW) | $D$<br>(m) | $H$<br>(m) | $\dot{Q}^*$ | $L_f/H$   | $\phi$    | $W/H$ | $L/H$ | $r_{ci}/H$ | $r_{rad}/D$ |
|----------------|-------------------|------------|------------|-------------|-----------|-----------|-------|-------|------------|-------------|
| Sandia Plume   | 1500 – 2250       | 1.0        | Open       | 1.4 – 2.0   | Open      | Open      | Open  | Open  | N/A        | N/A         |
| SP AST         | 450               | 0.3        | 2.4        | 6.1         | 1.1       | 0.1       | 1.0   | 1.5   | N/A        | N/A         |
| Steckler       | 31.6 – 158        | 0.3        | 2.1        | 0.8 – 3.8   | 0.3 – 0.7 | 0.0 – 0.6 | 1.3   | 1.3   | N/A        | N/A         |
| UL/NFPRF       | 4400 – 10000      | 1.0        | 7.6        | 4.0 – 9.1   | 0.7 – 1.0 | Open      | 4.9   | 4.9   | 0.6 – 3.9  | N/A         |
| UL/NIST Vents  | 500 – 2000        | 0.9        | 2.4        | 0.7 – 2.6   | 0.8 – 1.6 | 0.2 – 0.6 | 1.8   | 2.5   | 1.0 – 2.3  | N/A         |
| Ulster SBI     | 30 – 60           | 0.2        | Open       | 1.5 – 3.0   | Open      | Open      | Open  | Open  | N/A        | 0           |
| USCG/HAI       | 250 – 1000        | 0.3        | 3.0        | 6.0 – 24    | 0.6 – 1.1 | 0.3 – 1.0 | 1.7   | 2.3   | N/A        | N/A         |
| USN Hawaii     | 100 – 7700        | 0.3 – 2.5  | 15         | 0.7 – 1.3   | 0.1 – 0.4 | Open      | 4.9   | 6.5   | 0 – 1.2    | N/A         |
| USN Iceland    | 100 – 15700       | 0.3 – 3.4  | 22         | 0.7 – 1.3   | 0.0 – 0.3 | Open      | 2.1   | 3.4   | 0 – 1.0    | N/A         |
| Vettori Flat   | 1055              | 0.7        | 2.6        | 2.5         | 1.1       | 0.3       | 2.1   | 3.5   | 0.8 – 2.9  | N/A         |
| Vettori Sloped | 1055              | 0.7        | 2.5        | 2.5         | 1.2       | 0.3       | 2.2   | 2.9   | N/A        | N/A         |
| VTT Large Hall | 1860 – 3640       | 1.4 – 1.8  | 19         | 0.7         | 0.2       | 0         | 1.0   | 1.4   | 0 – 0.6    | N/A         |
| WTC            | 1970 – 3240       | 1.6        | 3.8        | 0.6 – 0.9   | 0.8 – 1.1 | 0.3 – 0.5 | 0.9   | 1.8   | 0.0 – 0.8  | 0.3 – 1.3   |

Table 3.49 lists a few important parameters related to the numerical resolution of the calculation.

**Characteristic Fire Diameter,  $D^*$ ,** is a useful length scale that incorporates the heat release rate of the fire.

$$D^* = \left( \frac{\dot{Q}}{\rho_\infty c_p T_\infty \sqrt{g}} \right)^{2/5} \quad (3.33)$$

**Plume Resolution Index,  $D^*/\delta x$ ,** is the number of grid cells of length  $\delta x$  that span the characteristic diameter of the fire. The greater its value, the more “resolved” are the fire dynamics.

**Ceiling Height relative to Fire Diameter,  $H/D^*$ ,** is the non-dimensional height of the smoke plume.

Note that the calculations performed for the various validation studies described in this Guide use a wide range of values of the Plume Resolution Index,  $D^*/\delta x$ . There are several reasons for this. First, typical applications of FDS often involve relatively small fires in relatively large spaces, and it is impractical to use a very fine grid that captures the detailed fire dynamics. Second, for some applications the accuracy of calculation is highly dependent on resolving the plume well, but for others, it is less important. For those citing the validation studies in this Guide, it is important that both the physical and numerical parameters are comparable to the given application.

Table 3.49: Summary of important numerical parameters.

| Test Series       | $D^*$ (m)  | $D^*/\delta x$ | $H/D^*$     |
|-------------------|------------|----------------|-------------|
| Arup Tunnel       | 1.8        | 9              | 3.8         |
| ATF Corridors     | 0.3 – 0.7  | 3 – 7          | 3.4 – 8.5   |
| Beyler Hood       | 0.1 – 0.2  | 5 – 8          | 2.1 – 3.5   |
| Bryant Doorway    | 0.2 – 0.7  | 5 – 14         | 3.4 – 9.9   |
| DelCo Trainers    | 0.7 – 1.0  | 6.9 – 10       | 2.3 – 3.5   |
| FAA Cargo         | 0.1        | 5.6            | 12          |
| Fleury Heat Flux  | 0.4 – 0.6  | 8 – 12         | Open        |
| FM Panels         | 0.2 – 0.4  | 12 – 19        | Open        |
| FM/SNL            | 0.7        | 7              | 8.5 – 8.8   |
| Hamins Burner     | 0.04 – 0.5 | 6              | Open        |
| Harrison Plumes   | 0.1 – 0.2  | 5 – 7          | 2.8 – 4.4   |
| Heskstad          | 0.4 – 44   | 5 – 20         | Open        |
| JH/FRA            | 0.2 – 1.2  | 8.8 – 15.6     | 2.0 – 3.5   |
| LLNL Enclosure    | 0.3 – 0.6  | 1 – 3          | 6.9 – 15.9  |
| McCaffrey Plume   | 0.2 – 0.3  | 5 – 20         | Open        |
| NBS Multi-Room    | 0.4        | 4              | 6.2         |
| NIST FSE          | 0.4 – 1.4  | 3.8 – 14       | 1.7 – 6.3   |
| NIST/NRC          | 0.6 – 1.3  | 5 – 11         | 3.1 – 6.5   |
| NIST/NRC Cabinets | 0.2 – 0.7  | 2.2 – 6.7      | 3.1 – 9.5   |
| NIST/NRC Corner   | 0.5 – 0.7  | 5.1 – 6.7      | 5.7 – 7.5   |
| NIST RSE          | 0.3 – 0.8  | 12 – 32        | 1.3 – 3.5   |
| NIST Smoke Alarms | 0.4 – 0.6  | 3.8 – 6.3      | 3.8 – 6.3   |
| NIST Vent Study   | 0.1        | 3.5            | 6.8         |
| NRCC Facade       | 1.8 – 2.4  | 18 – 24        | 1.2 – 1.5   |
| NRCC Smoke Tower  | 1.5        | 15             | 18.6        |
| NRL/HAI           | 0.3 – 0.7  | 9 – 10         | Open        |
| PRISME            | 0.7 – 1.2  | 7 – 12         | 3.4 – 5.6   |
| Sandia Plume      | 1.2 – 1.8  | 20 – 118       | Open        |
| SP AST            | 0.7        | 14             | 3.5         |
| Steckler          | 0.2 – 0.4  | 5 – 9          | 4.8 – 9.1   |
| UL/NFPRF          | 1.7 – 2.4  | 8 – 12         | 3.2 – 4.5   |
| UL/NIST           | 0.7 – 1.2  | 7 – 12         | 1.9 – 3.4   |
| Ulster SBI        | 0.2 – 0.3  | 12 – 15        | Open        |
| USCG/HAI          | 0.5 – 0.9  | 5 – 9          | 3.2 – 5.6   |
| USN Hawaii        | 0.4 – 2.1  | 2 – 11         | 7.1 – 40.3  |
| USN Iceland       | 0.4 – 2.8  | 2 – 14         | 7.8 – 59    |
| Vettori Flat      | 1.0        | 12             | 2.8         |
| Vettori Sloped    | 1.0        | 10             | 2.6         |
| VTT Large Hall    | 1.2 – 1.6  | 5 – 6          | 12.1 – 15.8 |
| WTC               | 0.9 – 1.1  | 9 – 11         | 3.5 – 4.1   |

## Chapter 4

# Quantifying Model Uncertainty

This chapter describes a method to estimate the model uncertainty using comparisons of model predictions with experimental measurements whose uncertainty has been quantified. The method is ideal for complex numerical models like FDS for which a systematic analysis of sub-components is impractical, but for which there exists a relatively large amount of experimental data with which to evaluate the accuracy of the model predictions. If the uncertainty in the experiments can be quantified, the uncertainty in the model can then be expressed in the form of a normal distribution whose mean and standard deviation are estimated from the relative difference between the predicted and measured values.

This method only addresses model uncertainty. It does not account for the uncertainty associated with the model input parameters. How the *parameter uncertainty* is treated depends greatly on the type of application. Regardless of how the parameter uncertainty is calculated, the model uncertainty needs to be addressed independently. In fact, it is incumbent on the model developers to express the uncertainty of the model in as simple a form as possible to enable the end user to assess the impact of parameter uncertainty and then combine the two forms of uncertainty into a final result.

### 4.1 Introduction

The most effective way of introducing the subject of uncertainty in fire modeling is by way of an example. Suppose that a fire model is used to estimate the likelihood that an electrical control cable could be damaged by a fire. It is assumed that the cable loses functionality when its surface temperature reaches 200 °C, and the model predicts that the cable temperature could reach as high as 175 °C. Does this mean that there is no chance of damage? The answer is no, because the input parameters, like the heat release rate of the fire, and the model assumptions, like the way the cables are modeled, are uncertain. The combination of the two – the *parameter uncertainty* and the *model uncertainty* – leave open the possibility that the cable temperature could exceed 200 °C.

This chapter addresses *model uncertainty* only and suggests a simple method to quantify it. While parameter uncertainty is certainly an important consideration in fire modeling, its treatment varies considerably depending on the particular application. For example, in what is often referred to as a “bounding analysis,” the model input parameters are chosen so as to simulate a “maximum credible” or “worst case” fire. In other cases, mean values of the input parameters constitute a “50th percentile” design scenario. Sometimes entire statistical distributions, rather than individual values, of the input parameters are “propagated” through the model in a variety of ways, leading to a statistical distribution of the model output. Notarianni and Parry survey these techniques in the SFPE Handbook [348]. Regardless of the method that is chosen for assessing the impact of the input parameters on the model prediction, there needs to be a way of quantifying the uncertainty of the model itself. In other words, how good is the prediction for a given set of input parameters?

The issue of model uncertainty has been around as long as the models themselves. The scenario above, for example, was considered by Siu and Apostolakis in the early 1980s [349] as part of their development of risk models for nuclear power plants. The fire models at the time were relatively simple. In fact, many were engineering correlations in the form of simple formulae. This made the methods for quantifying their uncertainty reasonably tractable because each formula consisted of only a handful of physical parameters. Over the past thirty years, however, both fire modeling and the corresponding methods of uncertainty analysis have become far more complex. The current generation of computational fluid dynamics (CFD) based fire models require such a large number of physical and numerical parameters that it is considered too cumbersome to estimate model uncertainty by systematically assessing their combined effect on the final prediction. The more practical approach is to compare model predictions with actual fire experiments in a validation study, the conclusions of which typically come in the form of statements like: “The model generally over-predicts the measured temperatures by about 10 %,” or “The model predictions are within about 20 % of the measured heat fluxes.” This information is helpful, at the very least to demonstrate that the model is appropriate for the given application. However, even the statement that the model over-predicts measured temperatures by 10 % is useful not only to gain acceptance of the model but also to provide a better sense of the model’s accuracy, and a greater level of assurance in answering the question posed above. Knowing that the model not only predicted a temperature of 175 °C, but also that the model tends to over-predict temperatures by a certain amount, increases the confidence that the postulated fire would not cause the cable to fail. The probability of cable failure could be quantified further via a statistical distribution like the one shown in Fig. 4.1. The area indicated by the shaded region is the probability that the temperature will exceed 200 °C, even though the model has predicted a peak temperature of only 175 °C.

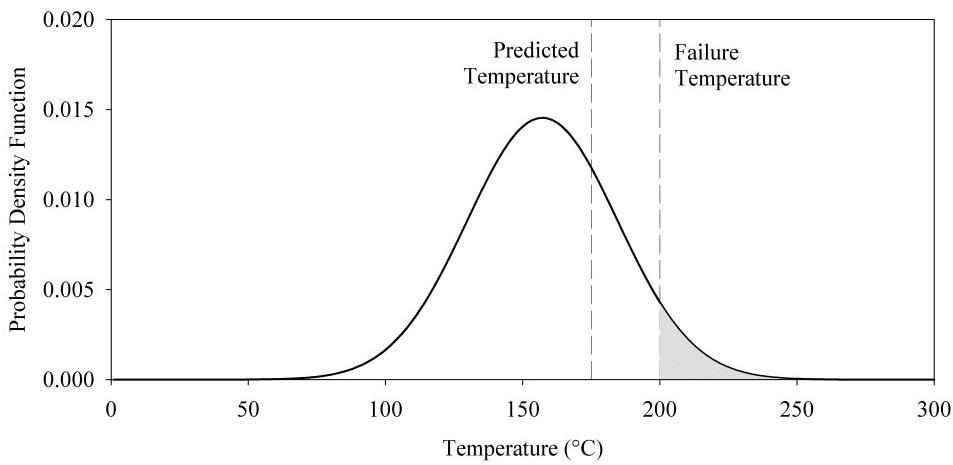


Figure 4.1: Plot showing a possible way of expressing the uncertainty of the model prediction.

This chapter describes a method for expressing *model uncertainty* by way of a distribution like the one shown in Fig. 4.1. The procedure is not a dramatic departure from the current practice of fire model validation in that it relies entirely on comparisons of model predictions and experimental measurements. The advantage of the approach is that it does not demand advanced knowledge of statistics or details of the numerical model. The parameters of the distribution shown in Fig. 4.1, namely the mean and standard deviation, are not generated by the model user. Rather, they are reported as the results of the validation study. The calculation of the probability of exceeding some critical threshold (i.e., the area under the curve) is a simple table look-up or function call in data analysis software like Microsoft Excel®.

## 4.2 Sources of Model Uncertainty

A deterministic fire model is based on fundamental conservation laws of mass, momentum and energy, applied either to entire compartments or smaller control volumes that make up the compartments. A CFD model may use millions of control volumes to compute the solution of the Navier-Stokes equations. However, it does not actually solve the Navier-Stokes equations, but rather an approximate form of these equations. The approximation involves simplifying physical assumptions, like the various techniques for treating subgrid-scale turbulence. One critical approximation is the discretization of the governing equations. For example, the partial derivative of the density,  $\rho$ , with respect to the spatial coordinate,  $x$ , can be written in approximate form as:

$$\frac{\partial \rho}{\partial x} = \frac{\rho_{i+1} - \rho_{i-1}}{2 \delta x} + \mathcal{O}(\delta x^2) \quad (4.1)$$

where  $\rho_i$  is the average value of the density in the  $i$ th grid cell and  $\delta x$  is the spacing between cells. The second term on the right represents all of the terms of order  $\delta x^2$  and higher in the Taylor series expansion and are known collectively as the *discretization error*. These extra terms are simply dropped from the equation set, the argument being that they become smaller and smaller with decreasing grid cell size,  $\delta x$ . The effect of these neglected terms is captured, to some extent, by the subgrid-scale turbulence model, but that is yet another approximation of the true physics. What effect do these approximations have on the predicted results? It is very difficult to determine based on an analysis of the discretized equations. One possibility for estimating the magnitude of the discretization error is to perform a detailed convergence analysis, but this still does not answer a question like, “What is the uncertainty of the model prediction of the gas temperature at a particular location in the room at a particular point in time?”

To make matters worse, there are literally dozens of subroutines that make up a CFD-based fire model, from its transport equations, radiation solver, solid phase heat transfer routines, pyrolysis model, empirical mass, momentum and energy transfer routines at the wall, and so on. It has been suggested by some that a means to quantify the model uncertainty is to combine the uncertainties of all the model components. However, such an exercise is very difficult, especially for a CFD model, for a number of reasons. First, fire involves a complicated interaction of gas and solid phase phenomena that are closely coupled. Second, grid sensitivity in a CFD model or the error associated with a two-layer assumption in a zone model are dependent on the particular fire scenario. Third, fire is an inherently transient phenomenon in which relatively small changes in events, like a door opening or sprinkler actuation, can lead to significant changes in outcome.

Rather than attempt to decompose the model into its constituent parts and assess the uncertainty of each, the strategy adopted here is to compare model predictions to as many experiments as possible. This has been the traditional approach for quantifying model uncertainty in fire protection engineering because of the relative abundance of test data. Consider, for example, the plot shown in Fig. 4.2. This is the typical outcome of a validation study, where in this case a series of heat flux measurements are compared with model predictions. The diagonal line indicates where the prediction and measurement agree. But because there is uncertainty associated with each, it cannot be said that the model is perfect if its predictions agree exactly with measurements. There needs to be a way of quantifying the uncertainties of each before any conclusions can be drawn. Such an exercise would result in the uncertainty bars<sup>1</sup> shown in the figure. The horizontal bar associated with each point represents the uncertainty in the measurement itself. For example, the heat flux gauge is subject to uncertainty due to its design and fabrication. Because the horizontal bar represents the experimental uncertainty, it is assumed that the vertical bar represents the model uncertainty. This is only partially true. In fact the vertical bar represents the total uncertainty of the prediction, which is a combination of the *model* and *parameter* uncertainties. The physical input parameters, like the heat release rate and material properties, are based on measurements that are reported in the documentation of

---

<sup>1</sup>The data in Fig. 4.2 was extracted from Ref. [350]. The uncertainty bars are for demonstration only.

the experiment. The total *experimental uncertainty* is represented by all of the horizontal bar and part of the vertical. If the *experimental uncertainty* can be quantified, then the *model uncertainty* can be obtained as a result.

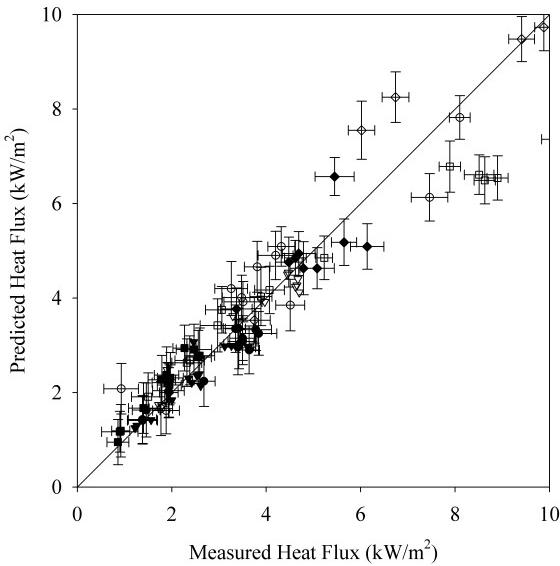


Figure 4.2: Example of a typical scatter plot of model predictions and experimental measurements.

### 4.3 Experimental Uncertainty

The difference between a model prediction and an experimental measurement is a combination of three components: (1) uncertainty in the measurement of the predicted quantity, (2) uncertainty in the model input parameters, and (3) uncertainty in the model physics and numerics. The first two components are related to uncertainty in the measured input and output quantities. For example, consider the hot gas layer (HGL) temperature. First, the thermocouple measurements used to calculate the HGL temperature have uncertainty. Second, the measurement of the heat release rate of the fire has uncertainty, and this uncertainty affects the predicted HGL temperature. Third, the model itself, including its physical assumptions and numerical approximations, has uncertainty. The objective of the validation study is to quantify this third component, the model uncertainty. To do this, the first two components of uncertainty related to the experimental measurements must be quantified. The combination of these two, the experimental uncertainty, is the objective of this section.

For many of the experiments considered in this guide, the uncertainty of the measurements was not documented. Instead, estimates of measurement uncertainty are made based on those few experiments that do include uncertainty estimates, and this information is supplemented by engineering judgment. In the following two subsections, each component of the experimental uncertainty is considered separately. First, the uncertainty in the measurement of the predicted quantity of interest, like the surface temperature of the compartment. Second, the uncertainties of the most important input parameters are propagated through simple models to quantify their effect on the predicted quantity. Then, the uncertainties are combined via simple quadrature to estimate the total experimental uncertainty.

Note that in this guide, all uncertainties are expressed in relative form, as a percentage. The uncertainty

of a measurement is a combination of the systematic uncertainty associated with the various underlying measurements and assumptions; and the random uncertainty associated with the conduct of the experiment. Following the recommended guidelines for evaluating and expressing the uncertainty of measurements [351], the systematic and random uncertainty values are combined via quadrature resulting in a combined relative standard uncertainty.

### **4.3.1 Uncertainty of Common Fire Measurements**

Because most of the experiments described in this guide have little or no information about the uncertainty of the measurements, much of this section is based on the uncertainty analysis contained in the test report of the NIST/NRC Experiments<sup>2</sup>. The types of measurements described in this report are the ones most commonly used in large scale fire experiments. They include thermocouples for gas and surface temperature measurements, heat flux gauges, smoke and gas analyzers, and pressure sensors.

#### **Thermocouples**

Thermocouples are used to measure both gas and surface temperatures. They come in a variety of sizes and are constructed of different types of metals. Some are shielded or aspirated to limit the influence of thermal radiation from remote sources. In Ref. [123], Hamins et al. estimate the uncertainty of the various thermocouple measurements. Estimates of the combined relative standard uncertainty fall in a range between 2.5 % and 7.5 %. Because it is not possible to analyze the thousands of thermocouple measurements made in the experiments, the relative standard uncertainty applied to all thermocouple measurements is 5 %.

#### **Heat Flux Gauges**

For the NIST/NRC experiments, four types of heat flux gauges were used, some of which measured the total heat flux, and some of which measured only the radiation heat flux. The uncertainty associated with a heat flux measurement depends on many factors, including gauge characteristics, the calibration conditions and accuracy, as well as the incident flux modes (convective, radiative, conductive). Typically, the reported relative standard uncertainty of heat flux gauges varies from about 2.5 % to 5 %, with the measurement uncertainty dominated by uncertainty in the calibration and repeatability of the measurement. Repeatability of the various heat flux measurements in the NIST/NRC experiments was determined by examining measurements by the same instruments for different pairs of repeat tests. The difference between the measurements was about 3.5 %, on average, for both the radiative flux measurements and the total flux measurements. For all of the experiments described in this guide, a combined relative standard uncertainty of 5 % is suggested based on the measurement repeatability and calibration uncertainties reported for the NIST/NRC experiments.

#### **Gas Analyzers**

Gas concentrations were measured in two sets of experiments conducted at NIST, the NIST/NRC and the WTC experiments. The volume fractions of the combustion products, carbon monoxide (CO) and carbon dioxide (CO<sub>2</sub>), were measured using gas sampling in conjunction with non-dispersive infrared analyzers, while the oxygen (O<sub>2</sub>) volume fraction was typically measured using a paramagnetic analyzer. Gases were extracted through stainless steel or other types of lines and were pumped from the compartment and passed

---

<sup>2</sup>Note that the uncertainties in Ref. [123] are reported in the form of 95 % confidence intervals, or “2-sigma”. This is referred to as the expanded uncertainty with a coverage factor of 2. To avoid confusion, in this report the uncertainty of all measurements and model predictions shall be reported in terms of a relative standard uncertainty; that is, the estimated standard deviation of the measured or predicted quantity.

through the analyzers. For several reasons, water in the sample was typically filtered, so the reported results are denoted as “dry”. Analyzers were calibrated through the use of standard gas mixtures, with low relative uncertainties. Problems with the technique may involve instrument drift, analyzer response, incomplete and partial drying of sample gases, or (in the case when drying is not used) undetermined amounts of water vapor in the oxygen cell, which result in inaccurate readings.

For the NIST/NRC experiments, the species were measured in both the upper and lower layers. The relative standard uncertainty in the measured values was about 1.5 % for both the O<sub>2</sub> depletion and the CO<sub>2</sub> measurements. The largest contributors were the uncertainty in the composition of the calibration gas and the possibility of an undetermined amount of water vapor in the sample. The difference between the repeat measurements was about 1 %, on average, for both the O<sub>2</sub> depletion and the CO<sub>2</sub> measurements. Therefore, the combined relative standard uncertainty is estimated to be 2 % for measurements of both the O<sub>2</sub> decrease and the CO<sub>2</sub> increase.

### **Smoke Light Extinction Calculations**

The smoke concentration was measured in the NIST/NRC experiments using laser transmission at 632.8 nm. The reported mass concentration of smoke,  $m_s'''$ , was computed using the following expression:

$$m_s''' = \frac{\ln(I_0/I)}{\phi_s L} \quad (4.2)$$

where  $L$  is the path length,  $I$  and  $I_0$  are the laser signal and reference signal, respectively, and  $\phi_s$  is the specific extinction coefficient, which has a nearly universal value of 8.7 m<sup>2</sup>/g ± 5 % for hydrocarbons [352]. The systematic relative standard uncertainty of this measurement was reported to be 9 % in Ref. [123], with the dominant contribution to the uncertainty coming from drift in the laser measurement. Repeatability of the smoke measurement was investigated for the NIST/NRC experiments. The mean difference between replicate measurements was about 11 %. Therefore, a combined relative standard uncertainty of 14 % is suggested.

### **Pressure Gauges**

The uncertainty in pressure measurements is typically small, but depends on the sensor type and calibration. In the NIST/NRC experiments, the differential pressure gauge used was temperature compensated, highly linear, and very stable. The estimated relative standard uncertainty is 0.5 %.

### **Bi-Directional Probes**

Gas velocity is typically measured in fire experiments using bi-directional probes. These devices work like pitot tubes but have much larger openings. Bryant [159] estimates that the standard relative uncertainty of this measurement, assuming that the probe is aligned well with the flow, is approximately 7 %.

### **Oxygen Consumption Calorimeters**

For all of the experiments described in this guide, the heat release rate (HRR) is determined either via oxygen consumption calorimetry or via the mass loss rate multiplied by the fuel heat of combustion. The accuracy of each method varies roughly between 2.5 %, where the fire is small and the fuel stoichiometry is well understood, and 13 %, where the fire is large or the smoke is not completely captured or the fuel stoichiometry is not well understood. In Ref. [123], the relative standard uncertainty of a 2 MW heptane spray fire is estimated to be 7.5 %. It is assumed that the uncertainty of the HRR for the other experiments is comparable.

## Device Activation or Failure Time

Fire models are often used to predict the time to activation of devices like sprinklers and smoke detectors, and time to failure of critical equipment like electrical cables. Measuring activation or failure times in experiments is fairly precise, and, thus, the uncertainty of such measurements is essentially zero. Almost all of the uncertainty associated with these times is in the measurement or characterization of the mechanism of activation or failure. For example, the activation of a sprinkler is based on its measured RTI (Response Time Index) and activation temperature. Estimates of the uncertainty of these parameters are discussed in the next section.

### 4.3.2 Propagation of Input Parameter Uncertainty

Empirical correlations for basic fire phenomena provide a convenient way to assess the propagation of the uncertainty of the model input parameters. The more complex fire models may require dozens of physical and numerical input parameters for a given fire scenario. However, only a few of these parameters, when varied over their plausible range of values, significantly impact the results. For example, the thermal conductivity of the compartment walls does not significantly affect a predicted cable surface temperature, but the HRR of the fire does. The relatively simple empirical models identify the key parameters that impact the predicted quantity, and they provide the means to quantify the functional relationship between model inputs and outputs.

## Gas and Surface Temperatures

According to the McCaffrey, Quintiere, and Harkleroad (MQH) correlation, the HGL temperature rise,  $T - T_0$ , in compartment fire is proportional to the HRR,  $\dot{Q}$ , raised to the two-thirds power:

$$T - T_0 = C \dot{Q}^{\frac{2}{3}} \quad (4.3)$$

The constant,  $C$ , involves a number of geometric and thermo-physical parameters that are unique to the given fire scenario. By way of differentials, this empirical relationship can be expressed in the form:

$$\frac{\Delta T}{T - T_0} \approx \frac{2}{3} \frac{\Delta \dot{Q}}{\dot{Q}} \quad (4.4)$$

This is a simple formula with which one can readily estimate the relative change in the temperature rise due to the relative change in the HRR. The uncertainty in the HRR of the validation experiments was estimated to be 7.5 %. Equation (4.4) indicates that a 7.5 % increase in the HRR should lead to a 5 % increase in the HGL temperature.

## HGL Depth

Most of the experiments for which the HGL depth was predicted had at least one open door or window that effectively determined the steady-state HGL depth. Unlike all of the other predicted quantities, the HGL depth is relatively insensitive to the fire's HRR. It is largely determined by the height of the opening, and for this reason there is essentially no uncertainty associated with the model inputs that affect the layer depth.

## Gas and Smoke Concentration

Most fire models assume that combustion product gases and soot, once beyond the flaming region of the fire, are passively transported throughout the compartment. The major products of combustion, like CO<sub>2</sub>

and water vapor, plus the major reactant, O<sub>2</sub>, are generated, or consumed, in direct proportion to the burning rate of the fuel, which is directly proportional to the HRR. The mass fraction of any species in the HGL is directly proportional to the product of its yield and the HRR.

For many of the experiments described in this guide, the yields of the major product gases like O<sub>2</sub> and CO<sub>2</sub> from pure fuels like methane gas and heptane liquid are known from the basic stoichiometry to a high level of accuracy. Thus, the relative uncertainty in the concentration of major products gases is the same as that of the HRR, 7.5 %. The uncertainty in the smoke concentration, however, is a combination of the uncertainty of the HRR and the soot yield. The relative standard uncertainty of the soot yield of heptane reported in Ref. [123] is 11 %. The uncertainties for HRR and soot yield are combined via quadrature and the resulting expanded relative uncertainty is 13 %.

## Pressure

In a closed, ventilated compartment, the average pressure,  $p$ , is governed by the following equation:

$$\frac{dp}{dt} = \frac{\gamma - 1}{V} (\dot{Q} - \dot{Q}_{\text{loss}}) + \frac{\gamma p}{V} (\dot{V} - \dot{V}_{\text{leak}}) \quad (4.5)$$

where  $\gamma$  is the ratio of specific heats (about 1.4),  $V$  is the compartment volume,  $\dot{Q}$  is the HRR,  $\dot{Q}_{\text{loss}}$  is the sum of all heat losses to the walls,  $\dot{V}$  is the net ventilation rate into the compartment, and  $\dot{V}_{\text{leak}}$  is the leakage rate out of the compartment. The leakage rate is a function of the compartment over-pressure:

$$\dot{V}_{\text{leak}} = A_{\text{leak}} \sqrt{\frac{2(p - p_{\infty})}{\rho_{\infty}}} \quad (4.6)$$

The maximum compartment pressure is achieved when the pressure rise term in Eq. (4.5) is set to zero. Rearranging terms yields an estimate for the maximum pressure:

$$(p - p_{\infty})_{\text{max}} \approx \frac{\rho_{\infty}}{2} \left( \frac{(\gamma - 1)(\dot{Q} - \dot{Q}_{\text{loss}}) + \gamma p_{\infty} \dot{V}}{\gamma p_{\infty} A_{\text{leak}}} \right)^2 \quad (4.7)$$

The test report for the NIST/NRC experiments contains estimates of the uncertainty in the HRR, ventilation rate and leakage area. To calculate the uncertainty in the maximum pressure rise resulting from the uncertainty in these three parameters, the pressure rise estimate in Eq. (4.7) was calculated using 1000 randomly selected sets of values of the HRR, ventilation rate, and leakage area. These parameters were assumed to be randomly distributed with mean values of 1000 kW, 1 m<sup>3</sup>/s, and 0.06 m<sup>2</sup> and relative standard uncertainties of 75 kW, 0.1 m<sup>3</sup>/s, and 0.0021 m<sup>2</sup>. The mean values of these parameters were typical of the NIST/NRC experiments, and the uncertainties were reported in the test report. The resulting relative standard uncertainty in the pressure of a closed compartment due to the uncertainty in the HRR, ventilation rate, and leakage area is 21 %.

For an open compartment, in which the ventilation rate and leakage area have much less influence, the relative standard uncertainty in the pressure is twice that of the HRR, 15 %.

## Velocity

Fire-induced velocities, as in a plume or ceiling jet, are roughly proportional to the HRR to the 1/3 power [353]. Given that the relative standard uncertainty in the HRR is 7.5 %, the uncertainty in gas velocity due to the propagated effect of the uncertainty in the HRR is 2.5 %.

## Heat Flux

The heat flux to a target or wall is a combination of direct thermal radiation from the fire and convective and thermal radiation from the HGL. If the heat flux is predominantly due to the thermal radiation of the fire, it can be approximated using the point source radiation model:

$$\dot{q}'' = \frac{\chi_r \dot{Q}}{4\pi r^2} \quad (4.8)$$

where  $\chi_r$  is the radiative fraction,  $\dot{Q}$  is the HRR, and  $r$  is the distance from the fire. The relative standard uncertainty of the heat flux is a combination of the uncertainty in the radiative fraction and the HRR:

$$\frac{\delta \dot{q}''}{\dot{q}''} \approx \frac{\delta \dot{Q}}{\dot{Q}} + \frac{\delta \chi_r}{\chi_r} \quad (4.9)$$

Reference [123] estimates the relative standard uncertainty of the radiative fraction of a heptane pool fire to be 8 %. Combined with the 7.5 % uncertainty in the HRR (via quadrature) yields a 11 % relative standard uncertainty in the heat flux directly from a fire.

The heat flux to a cold surface due to the exposure to hot gases and not necessarily the fire itself is the sum of radiative and convective components:

$$\dot{q}'' = \epsilon \sigma (T_{\text{gas}}^4 - T_{\infty}^4) + h (T_{\text{gas}} - T_{\infty}) \quad (4.10)$$

where  $\epsilon$  is the surface emissivity,  $\sigma$  is the Stefan-Boltzmann constant,  $T_{\text{gas}}$  is the gas temperature,  $T_{\infty}$  is the ambient temperature, and  $h$  is the convective heat transfer coefficient. From the discussion above, the relative standard uncertainty in the gas temperature rise above ambient is 5 % resulting from an estimated uncertainty in the HRR of 7.5 %. There is also uncertainty in the convective heat transfer coefficient, but this is attributed to the model, not the experimental measurements. Thus, the uncertainty in the heat flux is largely a function of the uncertainty in the gas temperature which is largely a function of the HRR. As was done for the pressure, 1000 randomly selected values of gas temperature with a mean of 300 °C above ambient and an relative uncertainty of 5 % resulted in a corresponding uncertainty of 9 % in the heat flux.

In actual compartment fires, the heat flux to surfaces is a combination of direct thermal radiation from the fire and indirect radiation and convection from the hot gases. Given that the calculation of the former incurs a 11 % relative standard uncertainty and the latter 9 %, to simplify the analyses, a value of 10 % is used for all heat flux predictions.

## Sprinkler Activation Time

The uncertainty in the reported sprinkler activation times is due mainly to uncertainties in the measured HRR, RTI (Response Time Index), and activation temperature. There is a negligible uncertainty in the measured activation time itself, which is typically determined with a pressure transducer. To determine the effect of the uncertainties in the HRR, RTI and activation temperature, consider the ordinary differential equation governing the temperature,  $T_{\text{link}}$ , of a conventional glass bulb of fusible link sprinkler:

$$\frac{dT_{\text{link}}}{dt} = \frac{\sqrt{u}}{\text{RTI}} (T_{\text{gas}} - T_{\text{link}}) \quad (4.11)$$

Here,  $u$  and  $T_{\text{gas}}$  are the velocity and the temperature of the ceiling jet, respectively. According to Alpert's ceiling jet correlation [353], the ceiling jet temperature and velocity are proportional to the HRR raised to the power of 2/3 and 1/3, respectively. Given the relative standard uncertainty in the HRR of 7.5 %, the uncertainty in the ceiling jet temperature and velocity are, thus, 5 % and 2.5 %, respectively. As for the RTI

and activation temperature, these values are measured experimentally and the uncertainties differ depending on the test procedure. Vettori [81] reports that the RTI of the sprinklers used in his experiments is  $56 \text{ (m}\cdot\text{s)}^{1/2}$  with a relative standard uncertainty of 11 %, and that the activation temperature is  $68^\circ\text{C} \pm 2.4^\circ\text{C}$ . This latter uncertainty estimate is assumed to represent one standard deviation. Assuming an ambient temperature of approximately  $20^\circ\text{C}$ , the relative standard uncertainty in the activation temperature is assumed to be 5 %.

To determine how the uncertainties in the measured parameters affect the sprinkler activation time, Eq. (4.11) was integrated 1000 times using random selections of the ceiling jet temperature and velocity, RTI, and activation temperature. The mean ceiling jet temperature was increased linearly at rates varying from  $0.5^\circ\text{C/s}$  to  $2^\circ\text{C/s}$ , consistent with the variety of growth rates measured by Vettori. The mean ceiling jet velocity was assumed to be 1 m/s. This procedure yielded a relative standard uncertainty in the sprinkler activation time of 6 %.

The activation times recorded by Vettori include two or three replicates for each configuration. The standard deviation of the 45 measured activation times, normalized by the mean of each set of replicates, was 6 %, consistent with the result obtained above.

### Number of Activated Sprinklers

Alpert's ceiling jet correlation [353] predicts the temperature rise,  $T - T_\infty$  ( $^\circ\text{C}$ ), as a function of the HRR,  $\dot{Q}$  (kW), and radial distance,  $r$  (m), from the plume centerline:

$$T - T_\infty = 5.38 \frac{\dot{Q}^{2/3}/H^{5/3}}{(r/H)^{2/3}} \quad ; \quad r/H > 0.18 \quad (4.12)$$

For a given ceiling height,  $H$ , the radial extent of the sprinkler activation temperature is directly proportional to  $\dot{Q}$ . The number of activated sprinklers is roughly proportional to the square of this radial distance, assuming the sprinklers are uniformly spaced on a rectangular grid. Thus, the uncertainty in the number of activated sprinklers due to the uncertainty in the HRR is 15 %.

### Electrical Cable Failure Time

The uncertainty in the reported cable failure times is due mainly to uncertainties in the measured exposing temperature, cable diameter, and jacket thickness. The uncertainty in the measured mass per unit length of the cable is assumed to be negligible. To determine the uncertainty in the cable failure time, the heat conduction equation in the THIEF model was solved numerically using 10,000 random selections of the exposing temperature, cable diameter, and jacket thickness. The cable diameter was varied from 16.25 mm to 16.35 mm, and the jacket thickness was varied from 1.45 mm to 1.55 mm. The uncertainty in the exposing temperature of the cylindrical heater was assumed to be 2.5 %, the lower bound of the range of uncertainty estimates for thermocouple measurements. The mass per unit length of the cable was assumed to be 0.529 kg/m, and the ambient temperature was assumed to be  $20^\circ\text{C}$ . This procedure yielded an estimated relative standard uncertainty in the cable failure time of 12 %.

### Smoke Detector Activation Time

There is a single set of experiments with which to evaluate model predictions of smoke detector activation time, the NIST Home Smoke Alarm Experiments. The test report [265] does not include detailed information about the alarm mechanism within the various smoke detectors used in the experiments. Thus, from a modeling standpoint, these devices are “black boxes” and their activation can only be discerned from a variety of empirical techniques, the most popular of which is to assume that the smoke detector behaves like a sprinkler or heat detector whose activation is governed by Eq. (4.11) with a low activation temperature and

RTI, Bukowski and Averill [354] suggest an activation temperature of 5 °C to be typical of many residential smoke alarms. The propagated uncertainty of this estimate is difficult to determine because temperature rise is not particularly well-correlated with smoke concentration within the sensing chamber of the detector. Nevertheless, the relative standard deviation of the normalized activation times for the NIST Home Smoke Alarm Experiments is 34 %. Without more detailed information about the activation criteria, the models cannot predict the activation times more accurately than this value.

### 4.3.3 Summary of Experimental Uncertainty Estimates

Table 4.1 summarizes the estimated uncertainties of the major output quantities. The right-most column in the table represents the total experimental uncertainty, denoted as  $\tilde{\sigma}_E$ , a combination of the uncertainty in the measurement of the output quantity itself, along with the propagated uncertainties of the key measured input quantities. This total experimental uncertainty is obtained by taking the square root of the sum of the squares of the measurement and propagation uncertainties that have been estimated in the previous two sections. It is assumed that the two forms of uncertainty are independent.

Table 4.1: Summary of uncertainty estimates. All values are expressed in the form of a standard relative uncertainty.

| Output Quantity              | Measurement Uncertainty | Propagated Input Uncertainty | Combined Uncertainty, $\tilde{\sigma}_E$ |
|------------------------------|-------------------------|------------------------------|--|
| Gas and Solid Temperatures   | 0.05                    | 0.05                         | 0.07                                     |
| HGL Depth                    | 0.05                    | 0.00                         | 0.05                                     |
| Gas Concentrations           | 0.02                    | 0.08                         | 0.08                                     |
| Smoke Concentration          | 0.14                    | 0.13                         | 0.19                                     |
| Pressure, Closed Compartment | 0.01                    | 0.21                         | 0.21                                     |
| Pressure, Open Compartment   | 0.01                    | 0.15                         | 0.15                                     |
| Velocity                     | 0.07                    | 0.03                         | 0.08                                     |
| Heat Flux                    | 0.05                    | 0.10                         | 0.11                                     |
| No. Activated Sprinklers     | 0.00                    | 0.15                         | 0.15                                     |
| Sprinkler Activation Time    | 0.00                    | 0.06                         | 0.06                                     |
| Cable Failure Time           | 0.00                    | 0.12                         | 0.12                                     |
| Smoke Alarm Activation Time  | 0.00                    | 0.34                         | 0.34                                     |

## 4.4 Calculating Model Uncertainty

This section describes a method for calculating the *model uncertainty* [355]. Specifically, this entails developing formulae for the mean and standard deviation of a statistical distribution like the one shown in Fig. 4.1. These formulae are functions solely of the model predictions and the experimental measurements against which the model is compared. The objective is to characterize the performance of the model in predicting a given quantity of interest (e.g., the hot gas layer temperature) with two parameters; one that expresses the tendency for the model to under or over-predict the true value of the quantity and one that expresses the degree of scatter about the true value.

The predicted and measured values of the quantity of interest are obtained from one or more validation studies. Figure 4.3 is a typical example of a comparison of model and measurement. Given that usually dozens of such measurements are made during each experiment, and potentially dozens of experiments are conducted as part of a test series, hundreds of such plots can be produced for any given quantity of interest. Usually, the data is condensed into a more tractable form by way of a single metric with which to compare

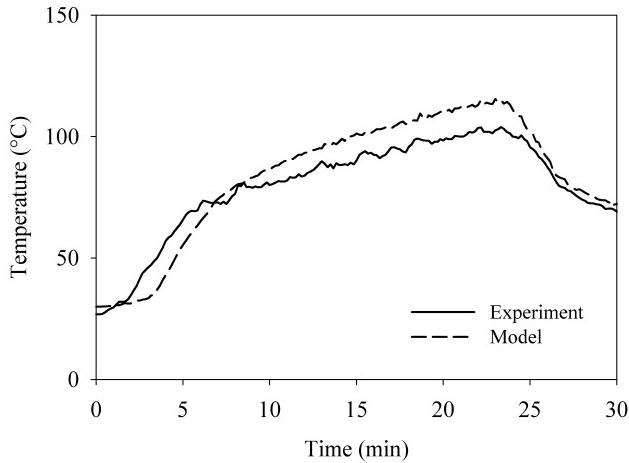


Figure 4.3: Example of a typical time history comparison of model prediction and experimental measurement.

the two curves, like the ones shown in Fig. 4.3. Peacock et al. [356] discuss various possible metrics. The metric most often used in the FDS validation process is the difference between the peak values of the time-averaged predicted and measured time histories. Thus, for each measurement point,  $i$ , there is a pair of Experimental and Modeled values,  $(E_i, M_i)$ , where  $i$  ranges from 1 to  $n$  and both  $E_i$  and  $M_i$  are positive numbers expressing the greatest rise in the value of the measured/predicted quantity above its ambient. Here,  $n$  is the total number of measurement points of a particular quantity of interest from all the experiments.

As mentioned above, measurements from full-scale fire experiments often lack uncertainty estimates. In cases where the uncertainty is reported, it is usually expressed as either a standard deviation or confidence interval about the measured value. In other words, there is rarely a reported systematic bias in the measurement because if a bias can be quantified, the reported values are adjusted accordingly. For this reason, assume that a given experimental measurement,  $E_i$ , is normally distributed about the “true” value,  $\theta_i$ , and there is no systematic bias:

$$E \mid \theta \sim N(\theta, \sigma_E^2) \quad (4.13)$$

The notation<sup>3</sup>  $E \mid \theta$  means that  $E$  is conditional on a particular value of  $\theta$ . This is the usual way of defining a likelihood function. It is convenient to use the so-called delta method<sup>4</sup> to obtain the approximate distribution

$$\ln E \mid \theta \sim N\left(\ln \theta - \frac{\tilde{\sigma}_E^2}{2}, \tilde{\sigma}_E^2\right) \quad (4.14)$$

The purpose of applying the natural log to the random variable is so that its variance can be expressed in terms of the relative uncertainty,  $\tilde{\sigma}_E = \sigma_E / \theta$ . This is the way that experimental uncertainties are reported.

<sup>3</sup>Note that the subscript,  $i$ , has been dropped merely to reduce the notational clutter.

<sup>4</sup>Given the random variable  $X \sim N(\mu, \sigma^2)$ , the delta method [357] provides a way to estimate the distribution of a function of  $X$ :

$$g(X) \sim N\left(g(\mu) + g''(\mu) \sigma^2 / 2, (g'(\mu) \sigma)^2\right)$$

In addition, the results of past validation exercises, when plotted as shown in Fig. 4.2, form a wedge-shaped pattern that suggests that the difference between predicted and measured values is roughly proportional to the magnitude of the measured value.

It cannot be assumed, as in the case of the experimental measurements, that the model predictions have no systematic bias. Instead, it is assumed that the model predictions are normally distributed about the true values multiplied by a bias factor,  $\delta$ :

$$M | \theta \sim N(\delta \theta, \sigma_M^2) \quad (4.15)$$

The standard deviation,  $\sigma_M$ , and the bias factor,  $\delta$ , represent the model uncertainty. Again, the delta method renders a distribution for  $\ln M$  whose parameters can be expressed in terms of a relative standard deviation:

$$\ln M | \theta \sim N\left(\ln \delta + \ln \theta - \frac{\tilde{\sigma}_M^2}{2}, \tilde{\sigma}_M^2\right) ; \quad \tilde{\sigma}_M = \frac{\sigma_M}{\delta \theta} \quad (4.16)$$

Combining Eq. (4.14) with Eq. (4.16) yields:

$$\ln M - \ln E = \ln(M/E) \sim N\left(\ln \delta - \frac{\tilde{\sigma}_M^2}{2} + \frac{\tilde{\sigma}_E^2}{2}, \tilde{\sigma}_M^2 + \tilde{\sigma}_E^2\right) \quad (4.17)$$

To estimate the mean and standard deviation of the distribution<sup>5</sup>, first define:

$$\overline{\ln(M/E)} = \frac{1}{n} \sum_{i=1}^n \ln(M_i/E_i) \quad (4.18)$$

The least squares estimate of the standard deviation of the combined distribution is defined as:

$$\tilde{\sigma}_M^2 + \tilde{\sigma}_E^2 \approx \frac{1}{n-1} \sum_{i=1}^n \left[ \ln(M_i/E_i) - \overline{\ln(M/E)} \right]^2 \quad (4.19)$$

Recall that  $\tilde{\sigma}_E$  is known and the expression on the right can be evaluated using the pairs of measured and predicted values. Equation (4.19) imposes a constraint on the value of the experimental uncertainty,  $\tilde{\sigma}_E$ . A further constraint is that  $\tilde{\sigma}_M$  cannot be less than  $\tilde{\sigma}_E$  because it is not possible to demonstrate that the model is more accurate than the measurements against which it is compared. Combining the two constraints leads to:

$$\tilde{\sigma}_E^2 < \frac{1}{2} \text{Var}(\ln(M/E)) \quad (4.20)$$

An estimate of  $\delta$  can be found using the mean of the distribution:

$$\delta \approx \exp\left(\overline{\ln(M/E)} + \frac{\tilde{\sigma}_M^2}{2} - \frac{\tilde{\sigma}_E^2}{2}\right) \quad (4.21)$$

Taking the assumed normal distribution of the model prediction,  $M$ , in Eq. (4.15) and using a Bayesian argument<sup>6</sup> with a non-informative prior for  $\theta$ , the posterior distribution can be expressed:

$$\delta \theta | M \sim N(M, \sigma_M^2) \quad (4.22)$$

---

<sup>5</sup>The assumption that  $\ln(M/E)$  is normally distributed has been tested for each quantity of interest discussed in the chapters ahead. The results are shown in Sec. 16.2.

<sup>6</sup>The form of Bayes theorem used here states that the posterior distribution is the product of the prior distribution and the likelihood function, normalized by their integral:  $f(\theta|M) = p(\theta)f(M|\theta)/\int p(\theta)f(M|\theta)d\theta$ . A constant prior is also known as a Jeffreys prior [358].

The assumption of a non-informative prior implies that there is not sufficient information about the prior distribution (i.e., the true value) of  $\theta$  to assume anything other than a uniform<sup>7</sup> distribution. This is equivalent to saying that the modeler has not biased the model input parameters to compensate for a known bias in the model output. For example, if a particular model has been shown to over-predict compartment temperature, and the modeler has reduced the specified heat release rate to better estimate the true temperature, then it can no longer be assumed that the prior distribution of the true temperature is uniform. Still another way to look at this is by analogy to target shooting. Suppose a particular rifle has a manufacturers defect such that, on average, it shoots 10 cm to the left of the target. It must be assumed that any given shot by a marksman without this knowledge is going to strike 10 cm to the left of the intended target. However, if the marksman knows of the defect, he or she will probably aim 10 cm to the right of the intended target to compensate for the defect. If that is the case, it can no longer be assumed that the intended target was 10 cm to the right of the bullet hole.

The final step in the derivation is to rewrite Eq. (4.22) as:

$$\theta | M \sim N\left(\frac{M}{\delta}, \tilde{\sigma}_M^2 \left(\frac{M}{\delta}\right)^2\right) \quad (4.23)$$

This formula has been obtained<sup>8</sup> by dividing by the bias factor,  $\delta$ , in Eq. (4.22). To summarize, given a model prediction,  $M$ , of a particular quantity of interest (e.g., a cable temperature), the true (but unknown) value of this quantity is normally distributed. The mean value and variance of this normal distribution are based solely on comparisons of model predictions with past experiments that are similar to the particular fire scenario being analyzed. The performance of the model is quantified by the estimators of the parameters,  $\delta$  and  $\tilde{\sigma}_M$ , which have been corrected to account for uncertainties associated with the experimental measurements.

When computing the relative error between measured and predicted values, an additional step is performed to ensure that the bias factor,  $\delta$ , is not skewed by a large number of data points at any particular region in the scatter plot. The approach used for this procedure is called a regressogram, i.e., a bin-smoothed estimator function [359]. This approach accounts for cases in which small measured values are compared to small predicted values, which can result in a large relative error. In these cases, the calculated bias factor might not be representative of the overall model bias, especially for larger measured and predicted values. Alternatively, a regressogram treats the average values throughout the scatter plot equally by subdividing the scatter plot into bins and normalizing each bin by the number of local data points. The regressogram estimator function is implemented as follows. For each scatter plot, the  $x$ -axis is subdivided into 10 equally spaced bins. Each bin is assigned a weight that is inversely proportional to the number of points in the bin; a bin with more points is assigned a smaller weight, and a bin with fewer points is assigned a larger weight. Finally, when the relative error is calculated, each bin is multiplied by its respective bin weight.

## 4.5 Example

This section describes how to make use of Eq. (4.23). Referring to the sample problem given above, suppose a fire model is being used to estimate the likelihood that electrical control cables could be damaged due to a fire in a compartment. Damage is assumed to occur when the surface temperature of any cable reaches 200 °C. What is the likelihood that the cables would be damaged if the model predicts that the maximum surface temperature of the cables is 175 °C. Assuming that the input parameters are not in question, the following procedure is suggested:

---

<sup>7</sup>A uniform distribution means that for any two equally sized intervals of the real line, there is an equal likelihood that the random variable takes a value in one of them.

<sup>8</sup>Note that if  $X \sim N(\mu, \sigma^2)$ , then  $cX \sim N(c\mu, (c\sigma)^2)$ .

1. Assemble a collection of model predictions,  $M_i$ , and experimental measurements,  $E_i$ , from past experiments involving objects with similar thermal characteristics as the cables in question. How “similar” the experiment is to the hypothetical scenario under study can be quantified by way of various parameters, like the thermal inertia of the object, the size of the fire, the size of the compartment, and so on. Obtain estimates of the experimental uncertainty from those who conducted the experiments or follow the procedure outlined by Hamins [350]. Express the experimental uncertainty in relative terms,  $\tilde{\sigma}_E$ .
2. Calculate the bias factor,  $\delta$ , and relative standard deviation,  $\tilde{\sigma}_M$ , from Eqs. (4.21) and (4.19), respectively.

Consider the distribution, Eq. (4.23), of the “true” temperature,  $\theta$ , shown graphically in Fig. 4.1. The vertical lines indicate the “critical” temperature at which damage is assumed to occur ( $T_c = 200^\circ\text{C}$ ), and the temperature predicted by the model ( $175^\circ\text{C}$ ). Given an ambient temperature of  $20^\circ\text{C}$ , the predicted temperature rise,  $M$ , is  $155^\circ\text{C}$ . The mean and standard deviation in Eq. (4.23) are calculated:

$$\mu = 20 + \frac{M}{\delta} = 20 + \frac{155}{1.13} = 157^\circ\text{C} ; \quad \sigma = \tilde{\sigma}_M \frac{M}{\delta} = 0.20 \times \frac{155}{1.13} = 27^\circ\text{C} \quad (4.24)$$

respectively. The shaded area beneath the bell curve is the probability that the “true” temperature can exceed the critical value,  $T_c = 200^\circ\text{C}$ , which can be expressed via the *complimentary error function*:

$$P(T > T_c) = \frac{1}{2} \operatorname{erfc} \left( \frac{T_c - \mu}{\sigma \sqrt{2}} \right) = \frac{1}{2} \operatorname{erfc} \left( \frac{200 - 157}{27 \sqrt{2}} \right) \approx 0.06 \quad (4.25)$$

This means that there is a 6 % chance that the cables could become damaged, assuming that the model’s input parameters are not subject to uncertainty.

## 4.6 Additional Considerations

Keep in mind that for any fire experiment, FDS might predict a particular quantity accurately (within the experimental uncertainty bounds, for example), but another quantity less accurately. For example, in a series of 15 full-scale fire experiments conducted at NIST in 2003, sponsored by the U.S. Nuclear Regulatory Commission, the average hot gas layer (HGL) temperature predictions were nearly within the accuracy of the measurements themselves, yet the smoke concentration predictions differed from the measurements by as much as a factor of 3. Why? Consider the following issues associated with various types of measurements:

- Is the measurement taken at a single point, or averaged over many points? In the example above, the HGL temperature is an average of many thermocouple measurements, whereas the smoke concentration is based on the extinction of laser light over a short length span. Model error tends to be reduced by the averaging process, plus most fire models, including FDS, are based on global mass and energy conservation laws that are expressed as spatial averages.
- Is the measured quantity time-averaged or instantaneous? For example, a surface temperature prediction is less prone to error in comparison to a heat flux prediction because the former is, in some sense, a time-integral of the latter.
- In the case of a point measurement, how close to the fire is it? The terms “near-field” and “far-field” are used throughout this Guide to describe the relative distance from the fire. In general, predictions of near-field phenomena are more prone to error than far-field. There are exceptions, however. For example, a prediction of the temperature directly within the flaming region may be more accurate than that made just a fire diameter away because of the fact that temperatures tend to stabilize at about  $1000^\circ\text{C}$  within the fire itself, but then rapidly decrease away from the flames. Less accurate predictions typically occur in regions of steep gradients (rapid changes, both in space and time).

## Chapter 5

# HGL Temperature and Depth

FDS, like any CFD-based fire model, does not perform a direct calculation of the HGL temperature or height. These are constructs unique to two-zone models. Nevertheless, FDS does make predictions of gas temperature at the same locations as the thermocouples in the experiments, and these values can be reduced in the same manner as the experimental measurements to produce an “average” HGL temperature and height. Regardless of the validity of the reduction method, the FDS predictions of the HGL temperature and height ought to be representative of the accuracy of its predictions of the individual thermocouple measurements that are used in the HGL reduction. The temperature measurements from the experiments reported in this chapter are used to compute an HGL temperature and height with which to compare to FDS. The same layer reduction method, described in the next section, is used for all the data presented in this chapter.

### 5.1 HGL Reduction Method

Fire protection engineers often need to estimate the location of the interface between the hot, smoke-laden upper layer and the cooler lower layer in a burning compartment. Relatively simple fire models, often referred to as *two-zone models*, compute this quantity directly, along with the average temperature of the upper and lower layers. In a CFD-based fire model like FDS, there are not two distinct zones, but rather a continuous profile of temperature. Nevertheless, there are methods that have been developed to estimate layer height and average temperatures from a continuous vertical profile of temperature. One such method [360] is as follows: Consider a continuous function  $T(z)$  defining temperature  $T$  as a function of height above the floor  $z$ , where  $z = 0$  is the floor and  $z = H$  is the ceiling. Define  $T_u$  as the upper layer temperature,  $T_\ell$  as the lower layer temperature, and  $z_{\text{int}}$  as the interface height. Compute the quantities:

$$(H - z_{\text{int}}) T_u + z_{\text{int}} T_\ell = \int_0^H T(z) dz = I_1$$

$$(H - z_{\text{int}}) \frac{1}{T_u} + z_{\text{int}} \frac{1}{T_\ell} = \int_0^H \frac{1}{T(z)} dz = I_2$$

Solve for  $z_{\text{int}}$ :

$$z_{\text{int}} = \frac{T_\ell(I_1 I_2 - H^2)}{I_1 + I_2 T_\ell^2 - 2 T_\ell H} \quad (5.1)$$

Let  $T_\ell$  be the temperature in the lowest mesh cell and, using Simpson’s Rule, perform the numerical integration of  $I_1$  and  $I_2$ .  $T_u$  is defined as the average upper layer temperature via

$$(H - z_{\text{int}}) T_u = \int_{z_{\text{int}}}^H T(z) dz \quad (5.2)$$

Further discussion of similar procedures can be found in Ref. [361].

## 5.2 ATF Corridors

The ATF Corridors experiments consisted of two corridors one on top of the other and connected by a stairwell. HGL temperature and depth reductions were carried out using three arrays of thermocouples in the lower corridor (Trees A, B, and C) and two arrays in the upper corridor (Trees G and H).

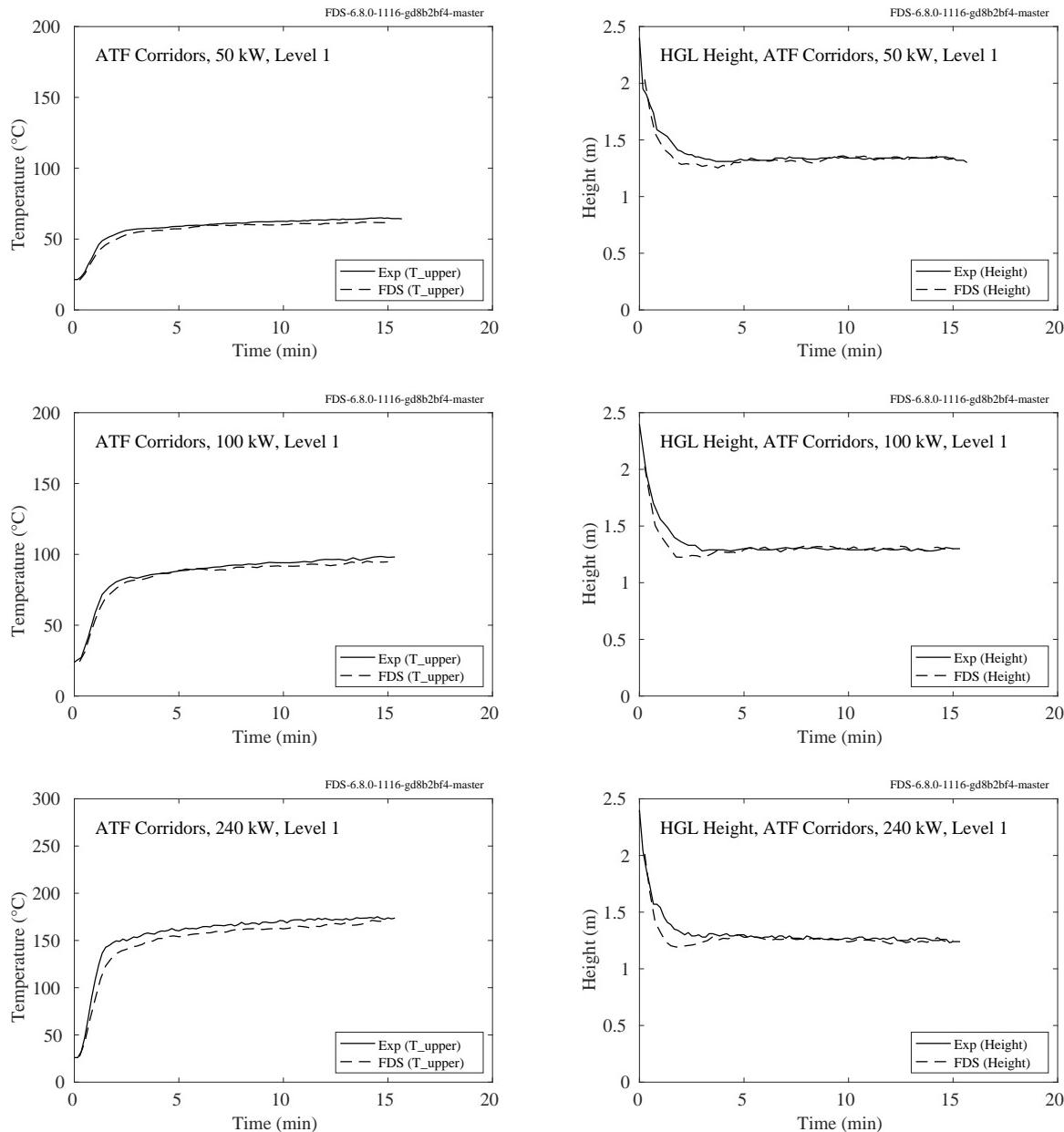


Figure 5.1: ATF Corridors, HGL temperature and height, first floor, 50 kW, 100 kW, 240 kW.

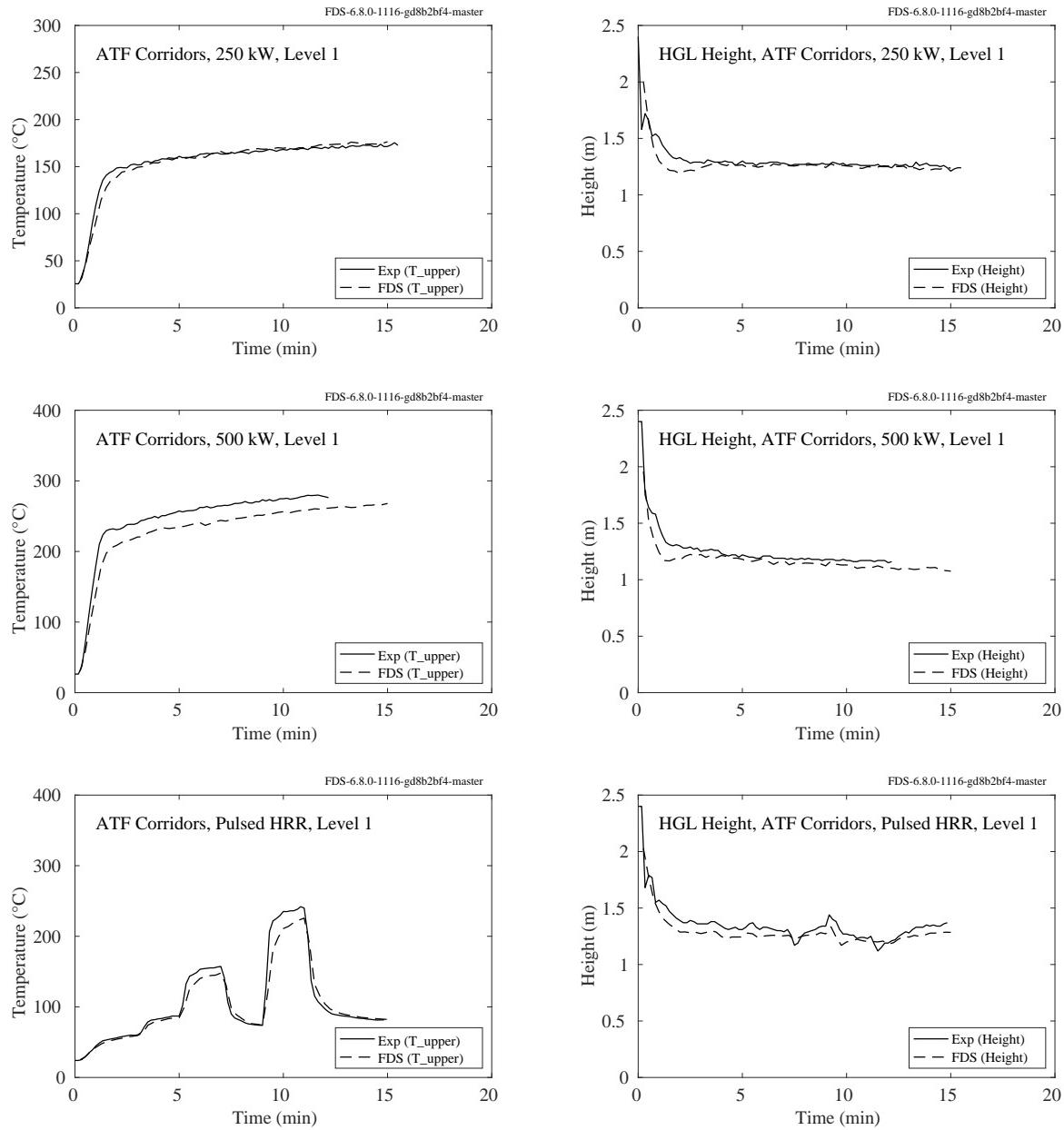


Figure 5.2: ATF Corridors, HGL temperature and height, first floor, 250 kW, 500 kW, mixed.

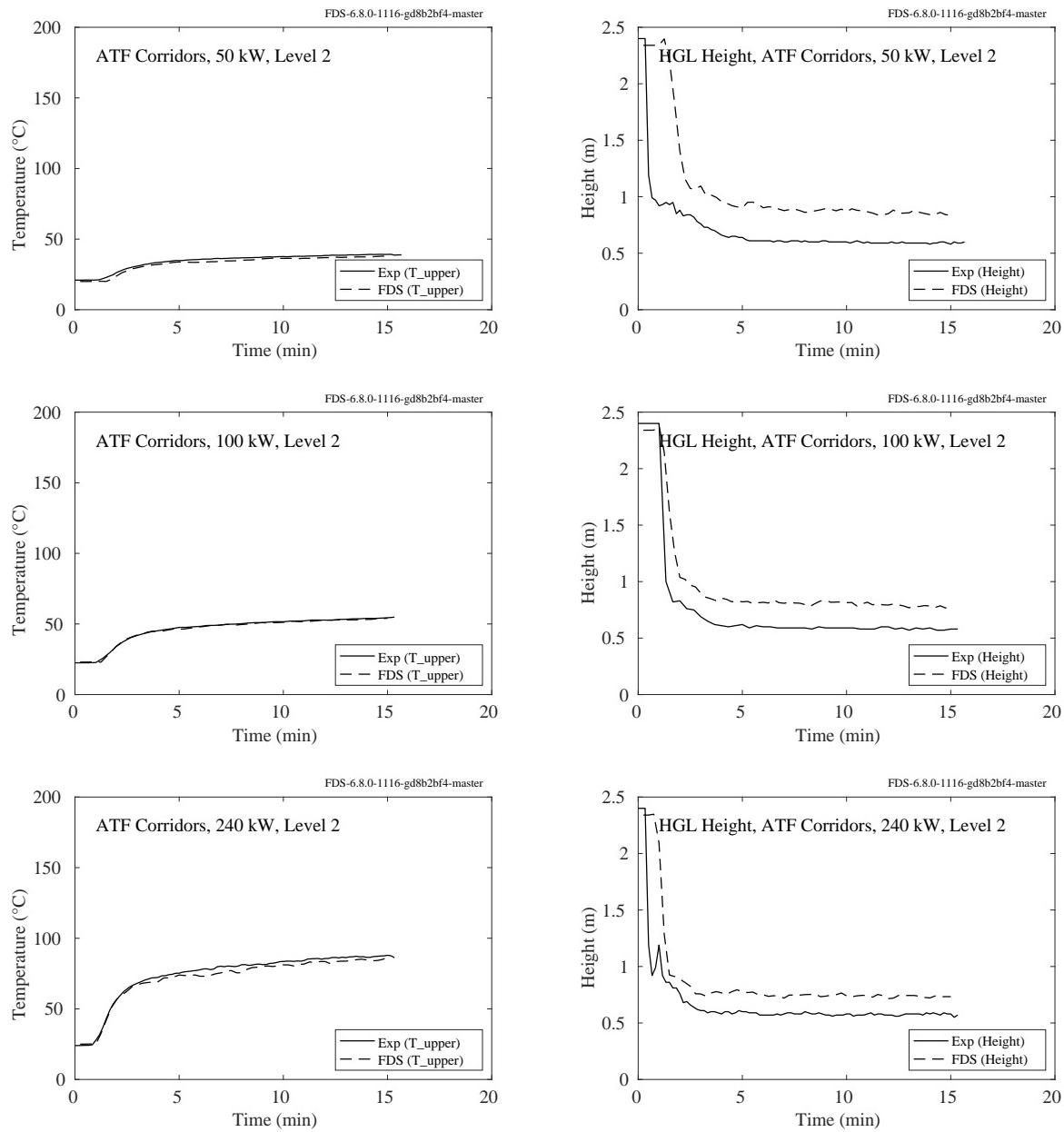


Figure 5.3: ATF Corridors, HGL temperature and height, second floor, 50 kW, 100 kW, 240 kW.

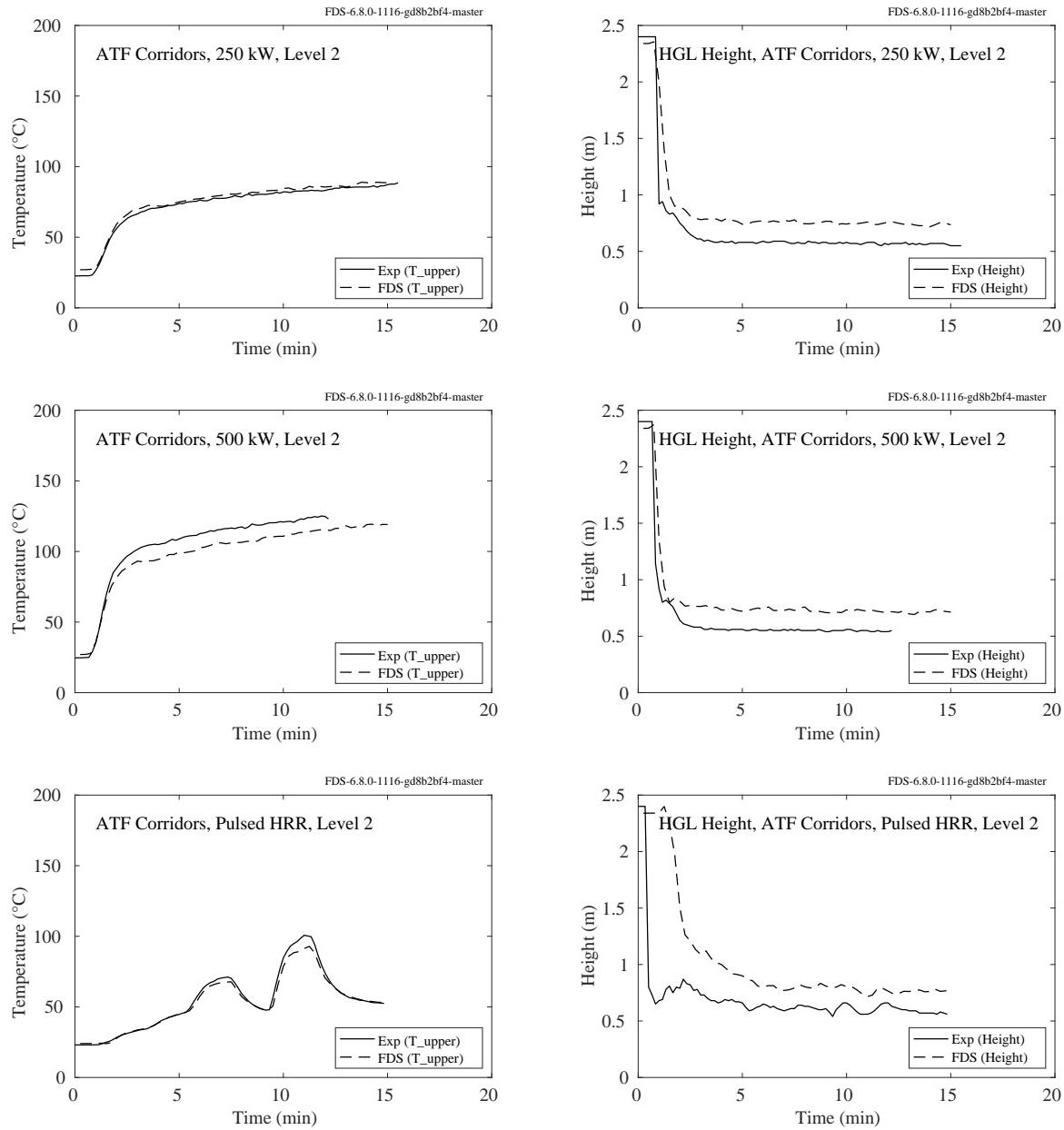


Figure 5.4: ATF Corridors, HGL temperature and height, second floor, 250 kW, 500 kW, mixed.

### 5.3 CSTB Tunnel

The CSTB Tunnel experiments include thermocouple measurements at various locations in a small-scale tunnel equipped with a water mist system. Two experiments (Tests 2 and 27) are simulated; the former with no mist activation and the latter with activation after 5 min. The tunnel is approximately 43 m long and the fire is located 17.5 m from the upstream opening.

On the following pages, thermocouple measurements at downwind distances of 4 m, 8 m, 12 m, and 24 m are compared to the predicted values. For a given label, say T+2411, the T denotes Temperature, the +24 means 24 m downwind of the fire, and the final two digits denote the particular thermocouple within an array at that location. The chosen TCs are located along the vertical centerline.

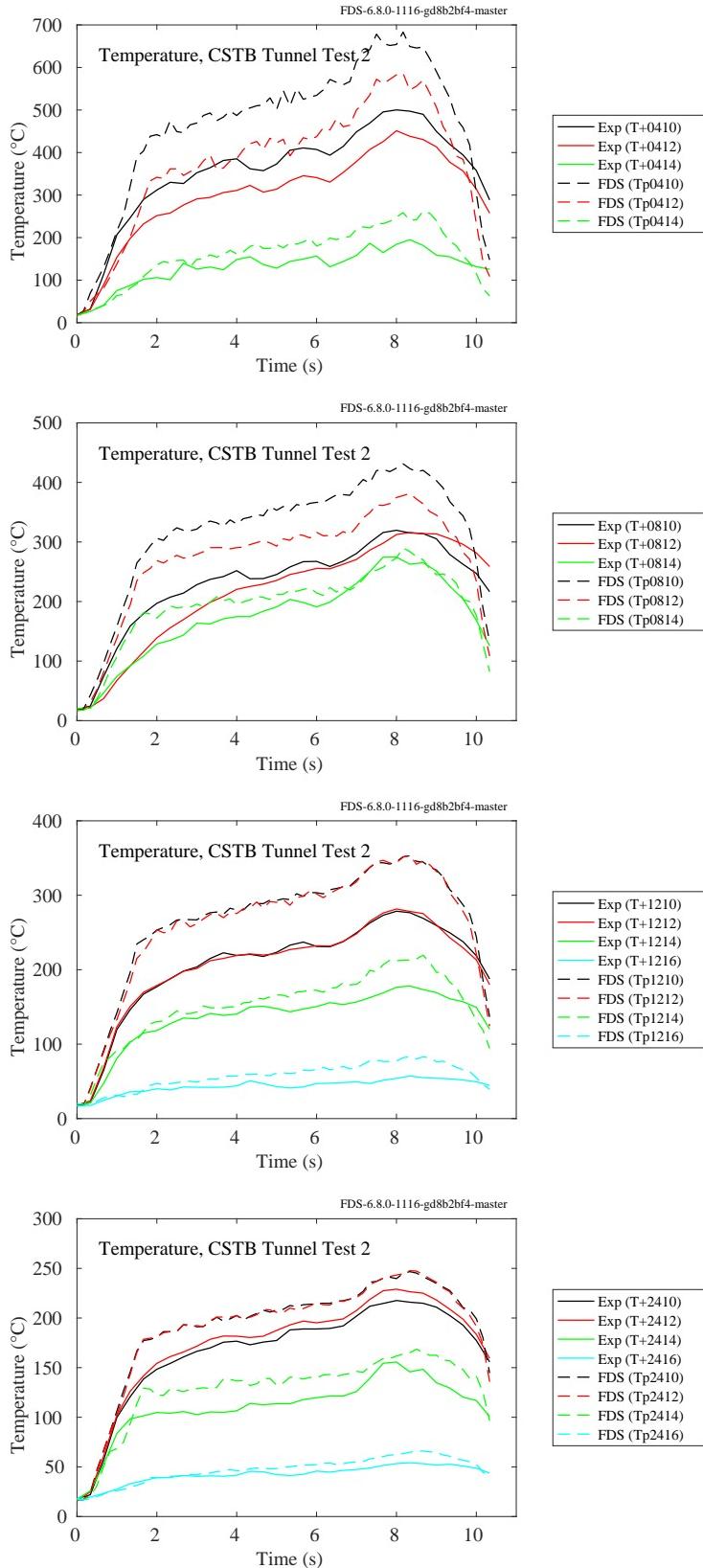


Figure 5.5: CSTB Tunnel, Test 2, temperatures at 4, 8, 12 and 24 m downstream of fire.

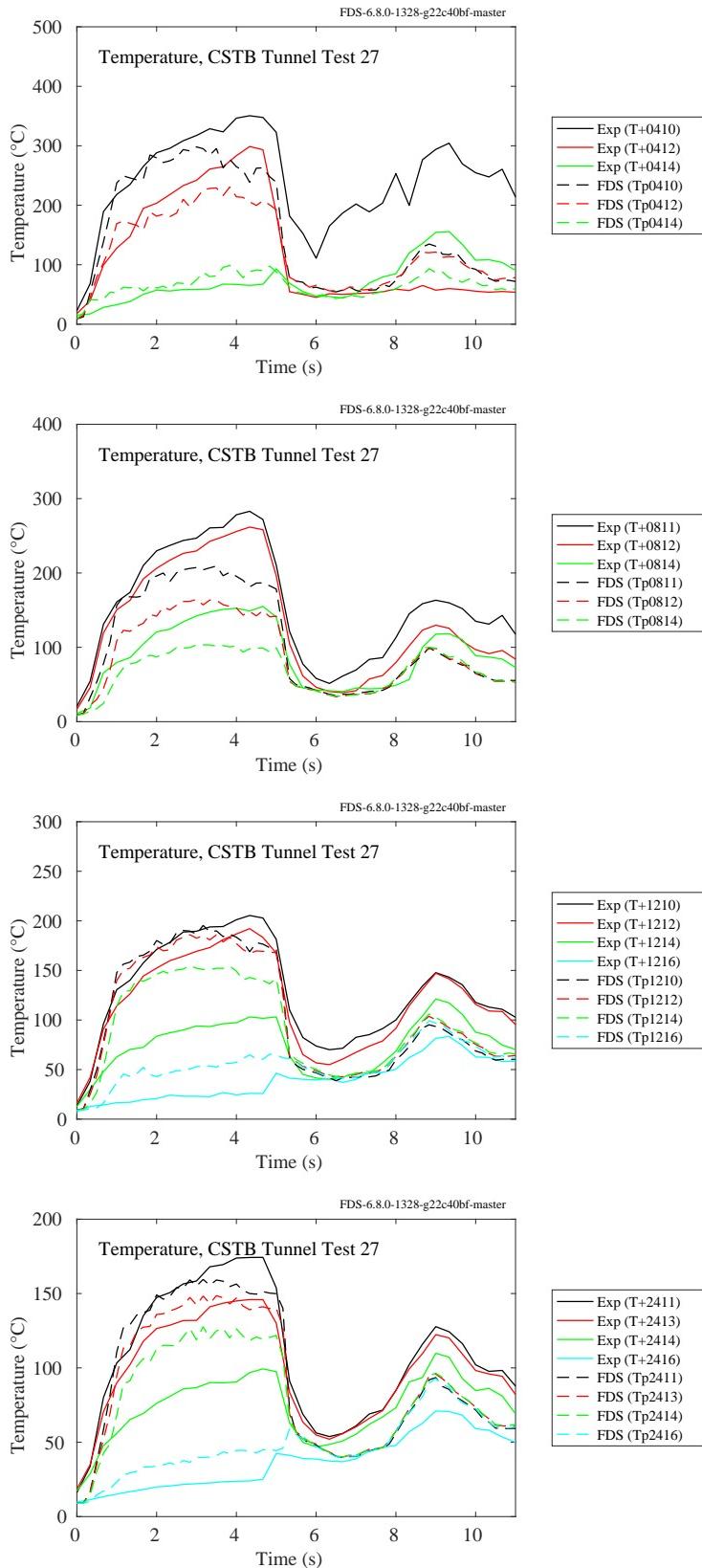


Figure 5.6: CSTB Tunnel, Test 27, temperatures at 4, 8, 12 and 24 m downstream of fire.

## 5.4 DelCo Trainers

The DelCo Trainer experiments were conducted in two different structures. Tests 2-6 were conducted in a single level structure consisting of three rooms. Rooms 1 and 3 had two thermocouple trees and Room 2 had one. Tests 22-25 were conducted in a two level structure. Floors 1 and 2 each had three thermocouple arrays. See Sec. 3.18 for their exact locations.

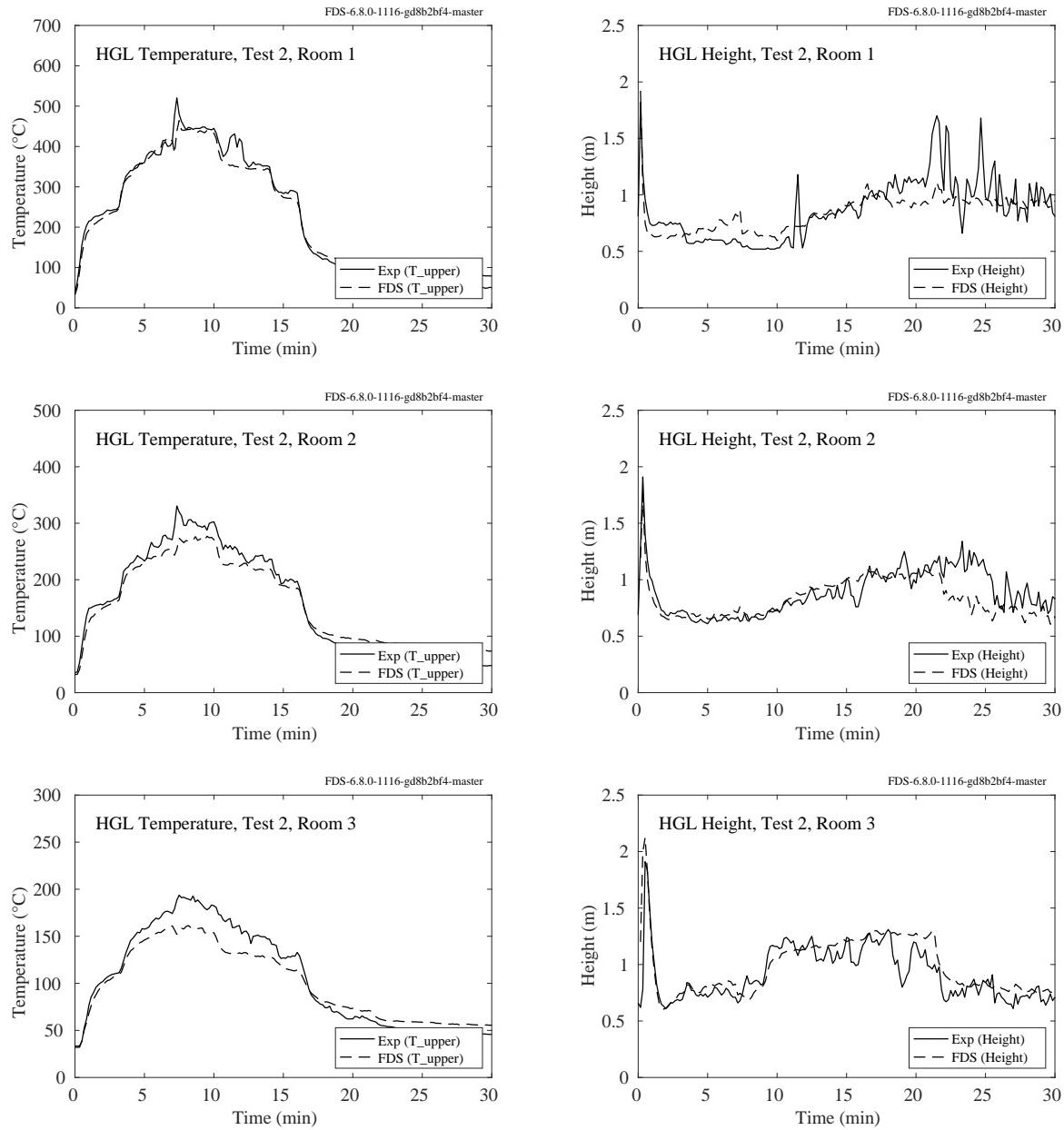


Figure 5.7: DelCo Trainers, HGL Temperature and Height, Test 2.

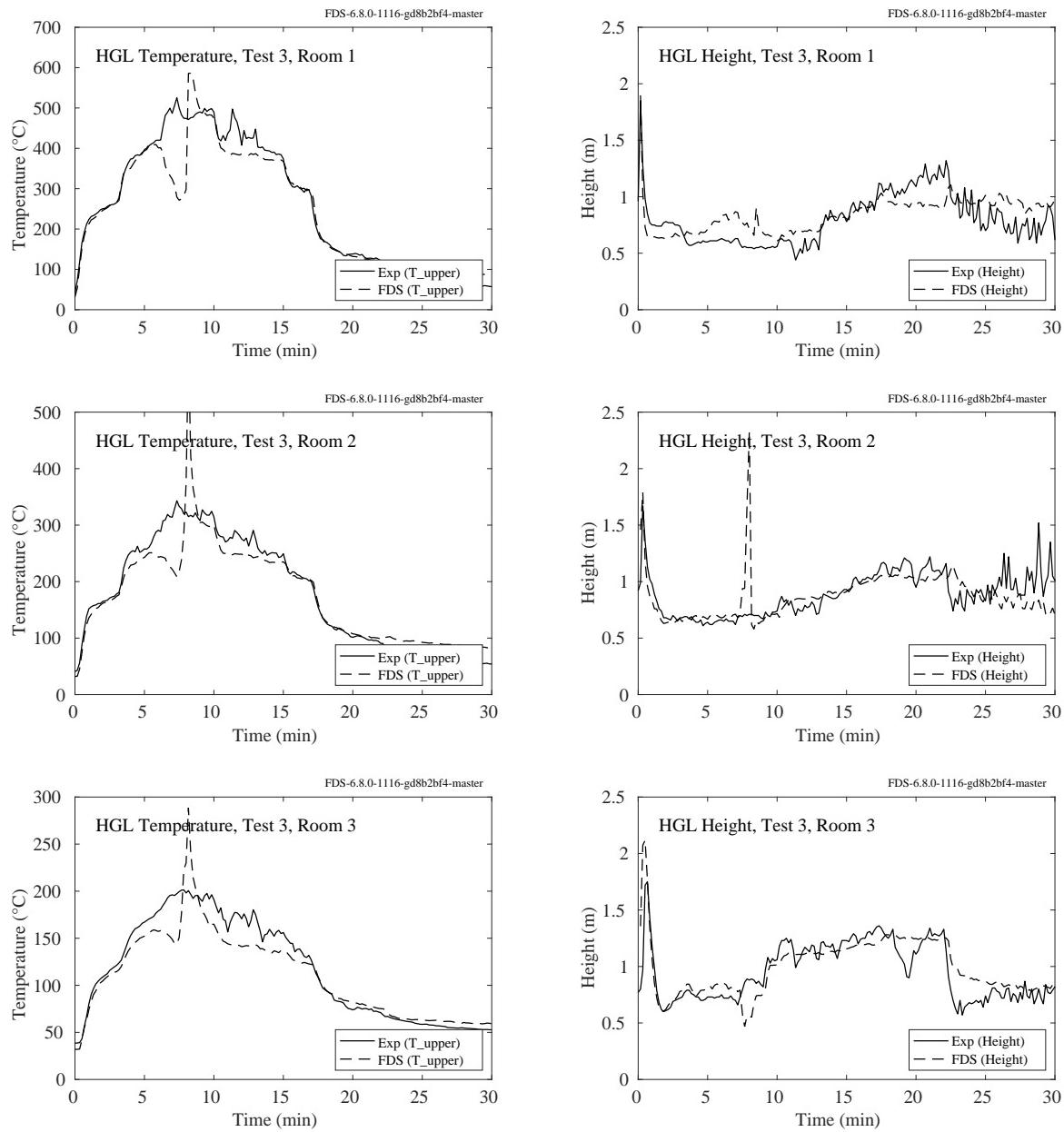


Figure 5.8: DelCo Trainers, HGL Temperature and Height, Test 3.

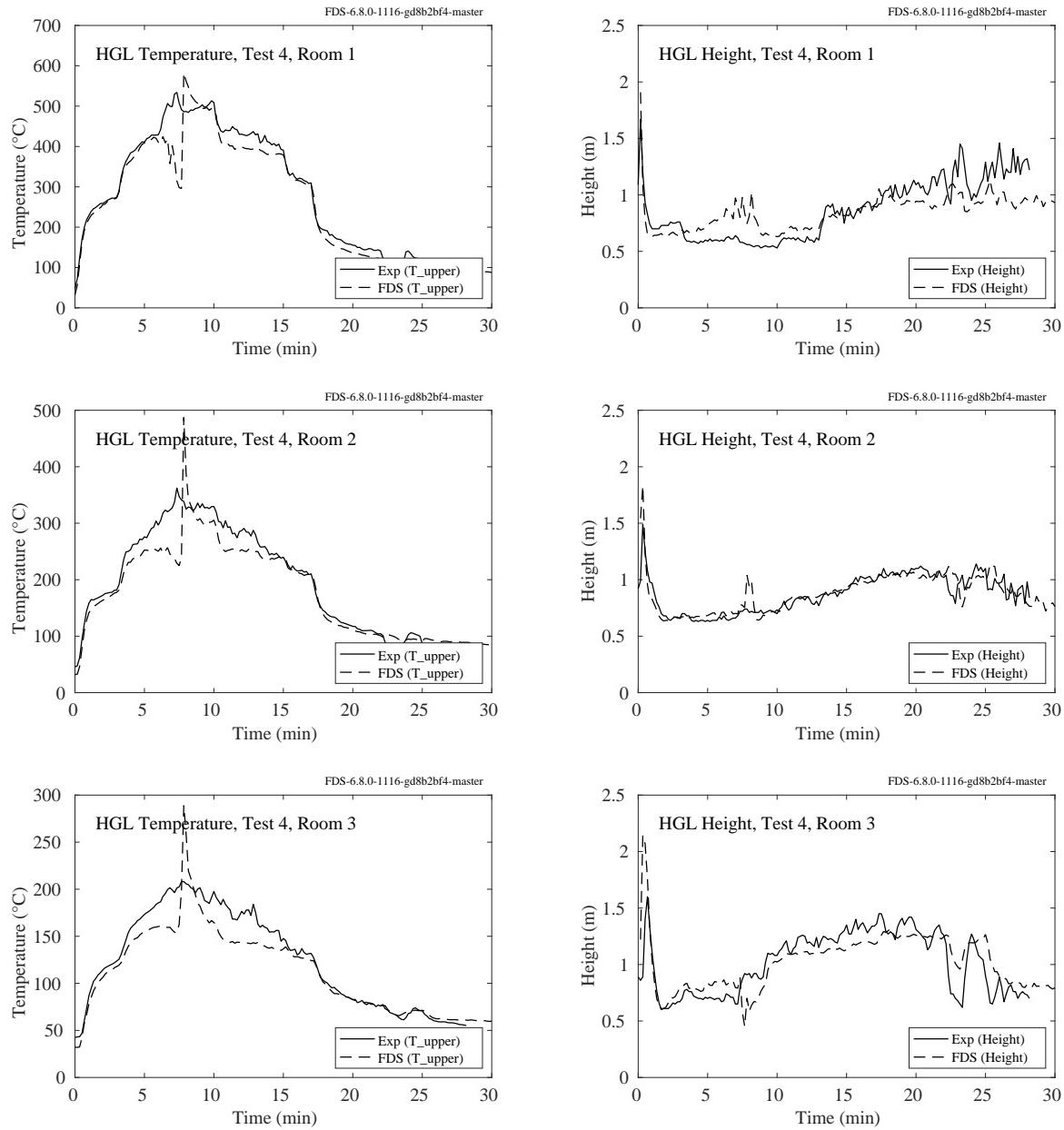


Figure 5.9: DelCo Trainers, HGL Temperature and Height, Test 4.

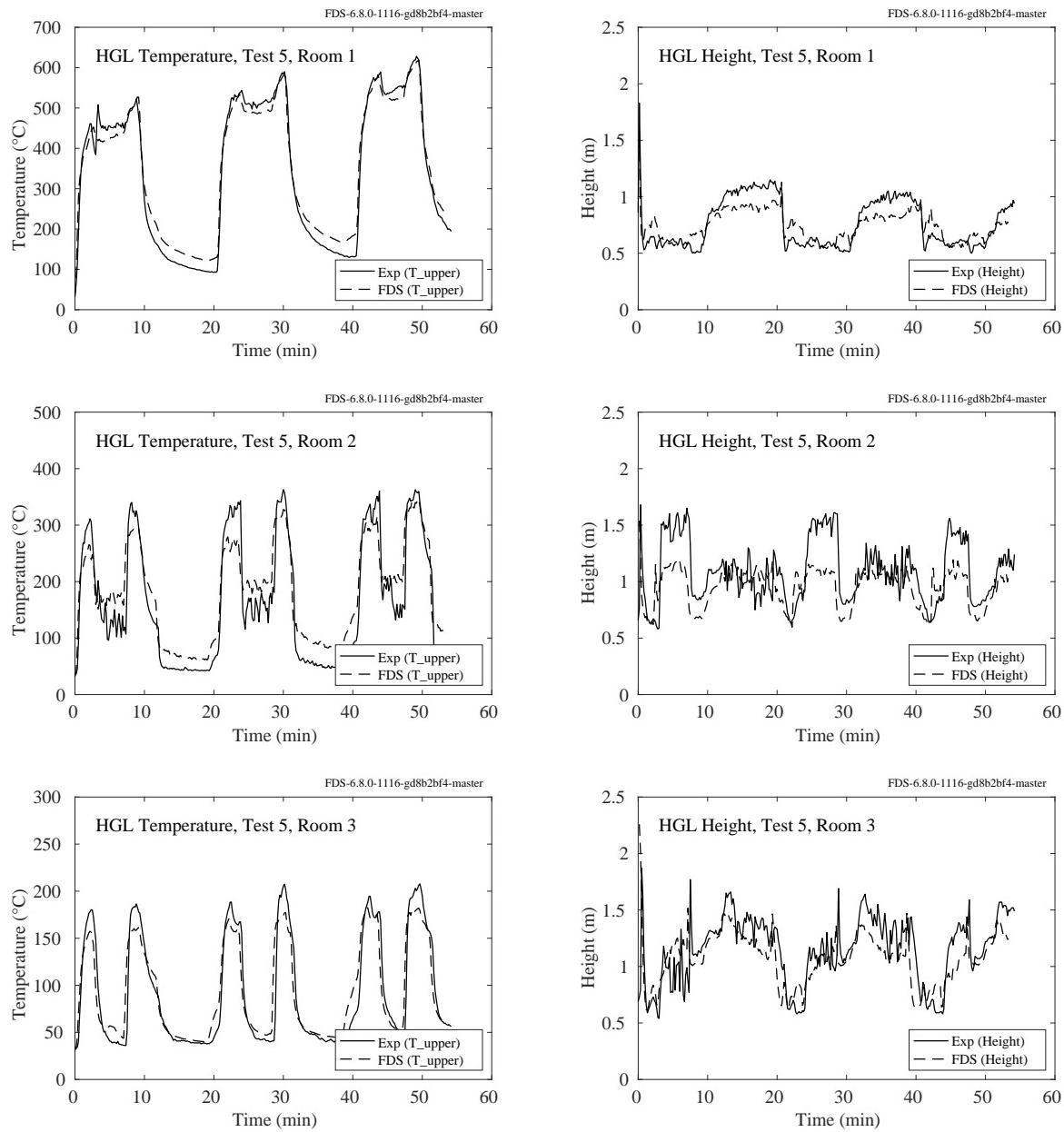


Figure 5.10: DelCo Trainers, HGL Temperature and Height, Test 5.

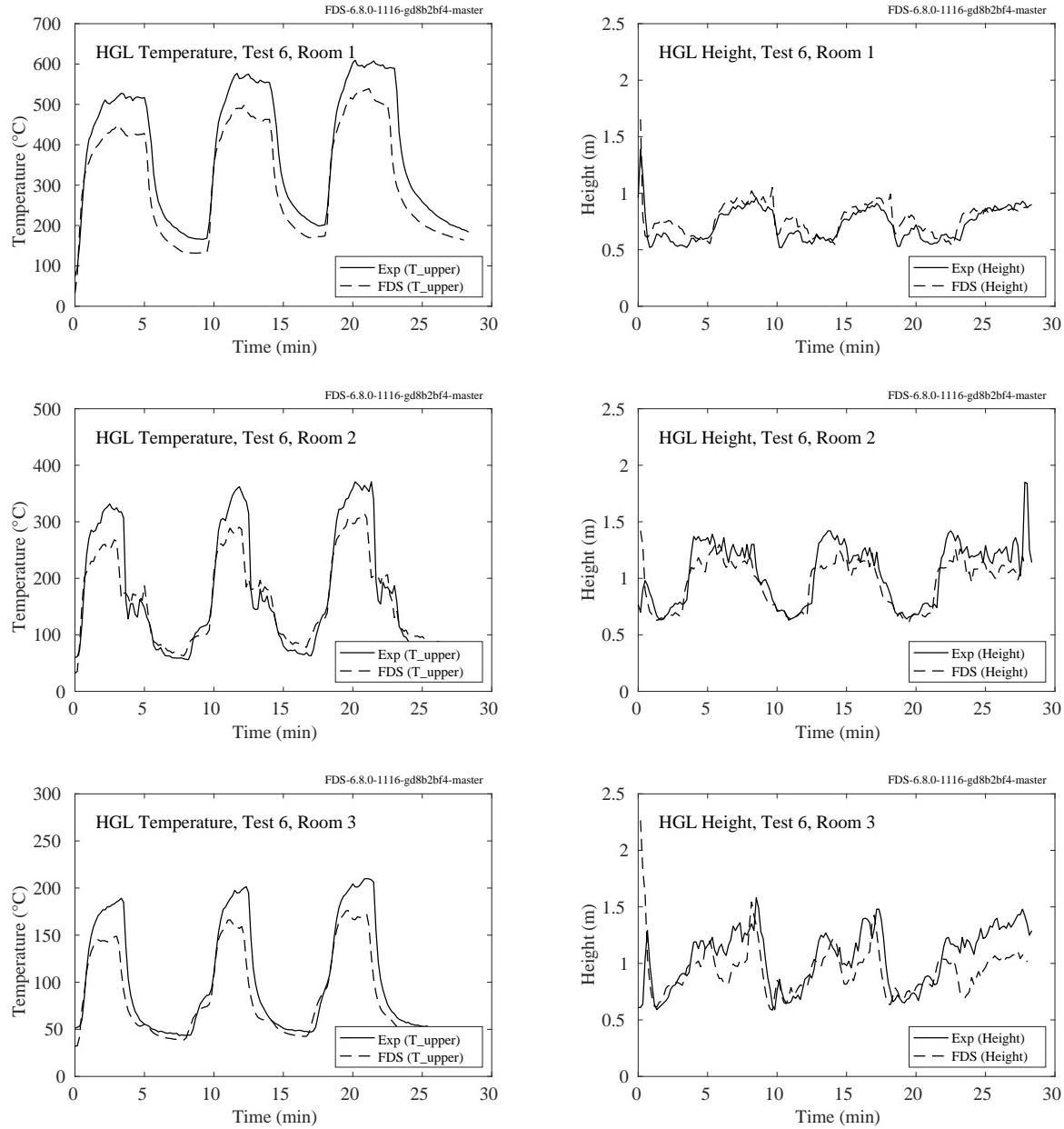


Figure 5.11: DelCo Trainers, HGL Temperature and Height, Test 6.

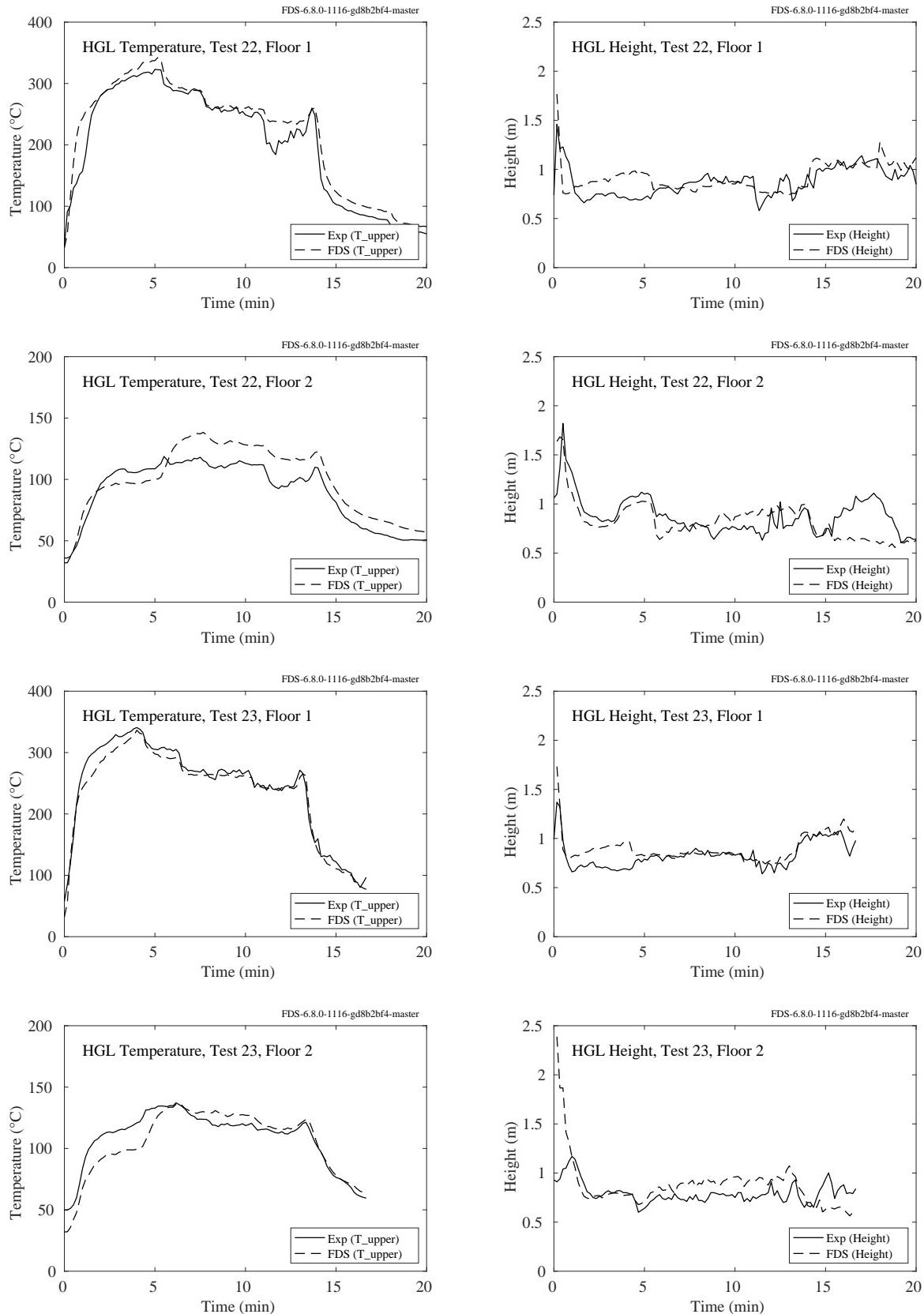


Figure 5.12: DelCo Trainers, HGL Temperature, Tests 22-23.

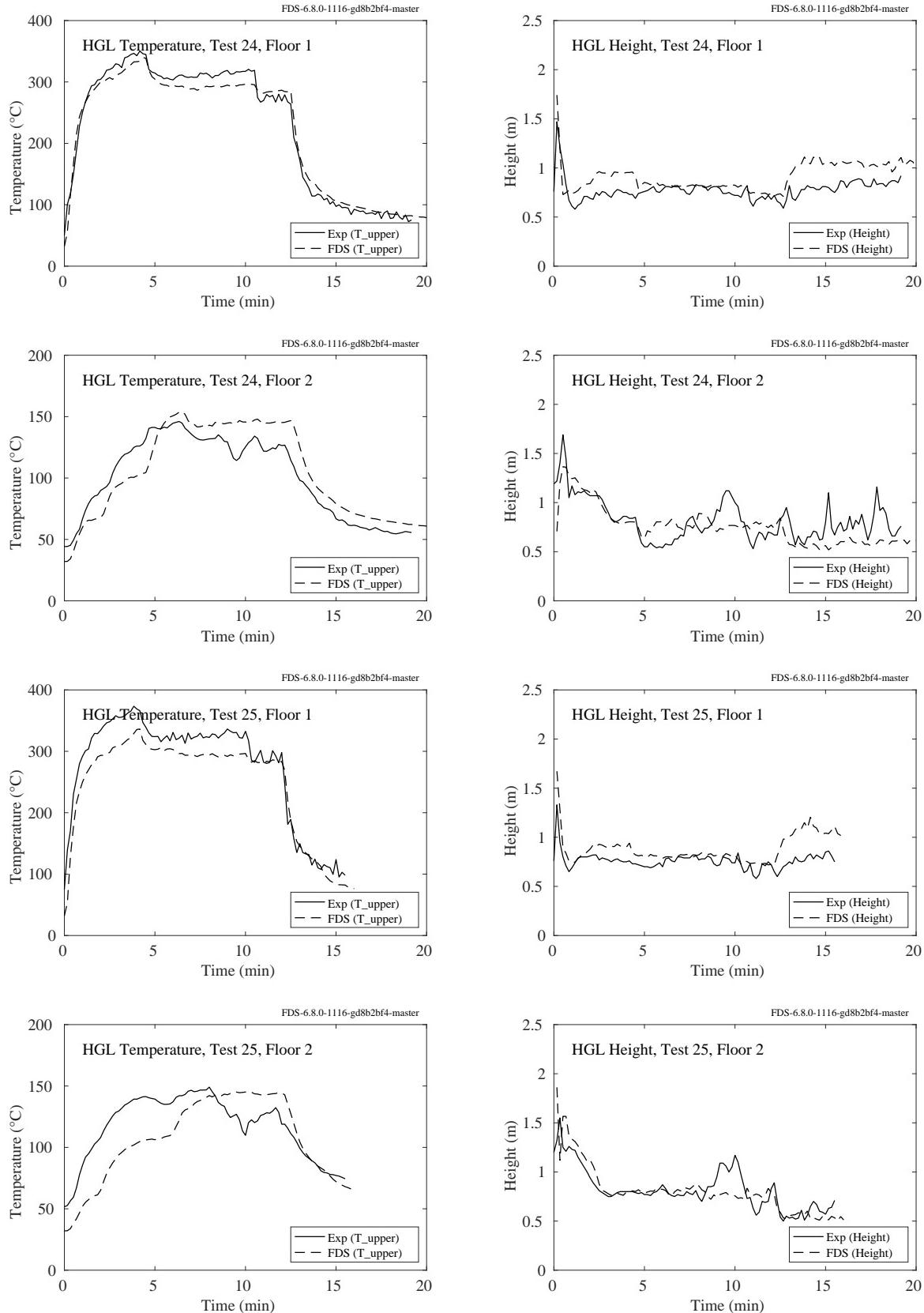


Figure 5.13: DelCo Trainers, HGL Temperature, Tests 24-25.

## 5.5 FM/SNL Test Series

Nineteen tests from the FM/SNL test series were selected for comparison. The HGL temperature and height are calculated using the standard method. The thermocouple arrays that were located in Sectors 1, 2 and 3 are averaged (with an equal weighting for each) for all tests except Tests 21 and 22. For these tests, only Sectors 1 and 3 are used, as Sector 2 falls within the smoke plume. Also, for all but the gas burner experiments, the time history of the HRR is estimated. Only the peak HRR is reported.

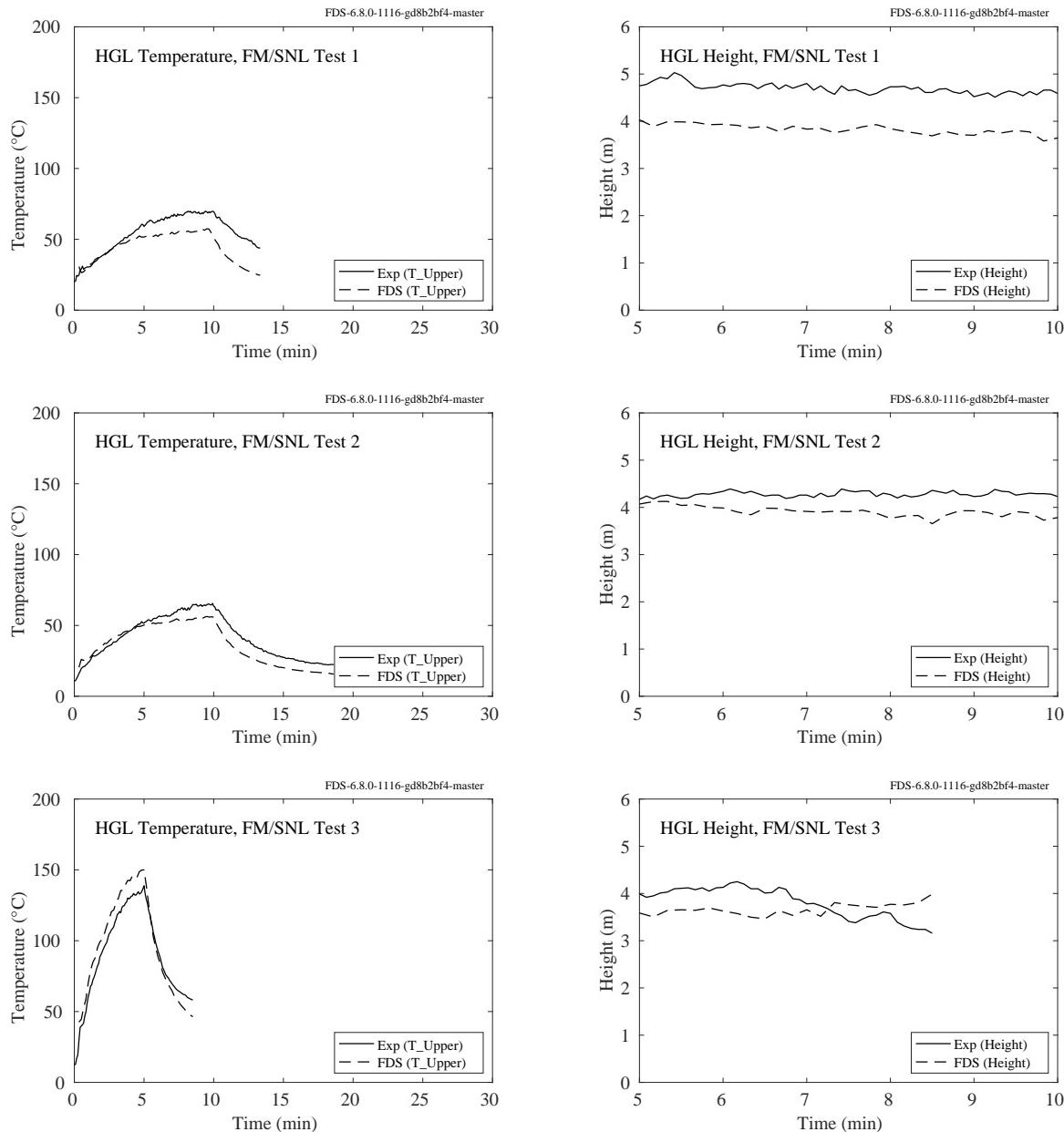


Figure 5.14: FM/SNL experiments, HGL temperature and height, Tests 1, 2, 3.

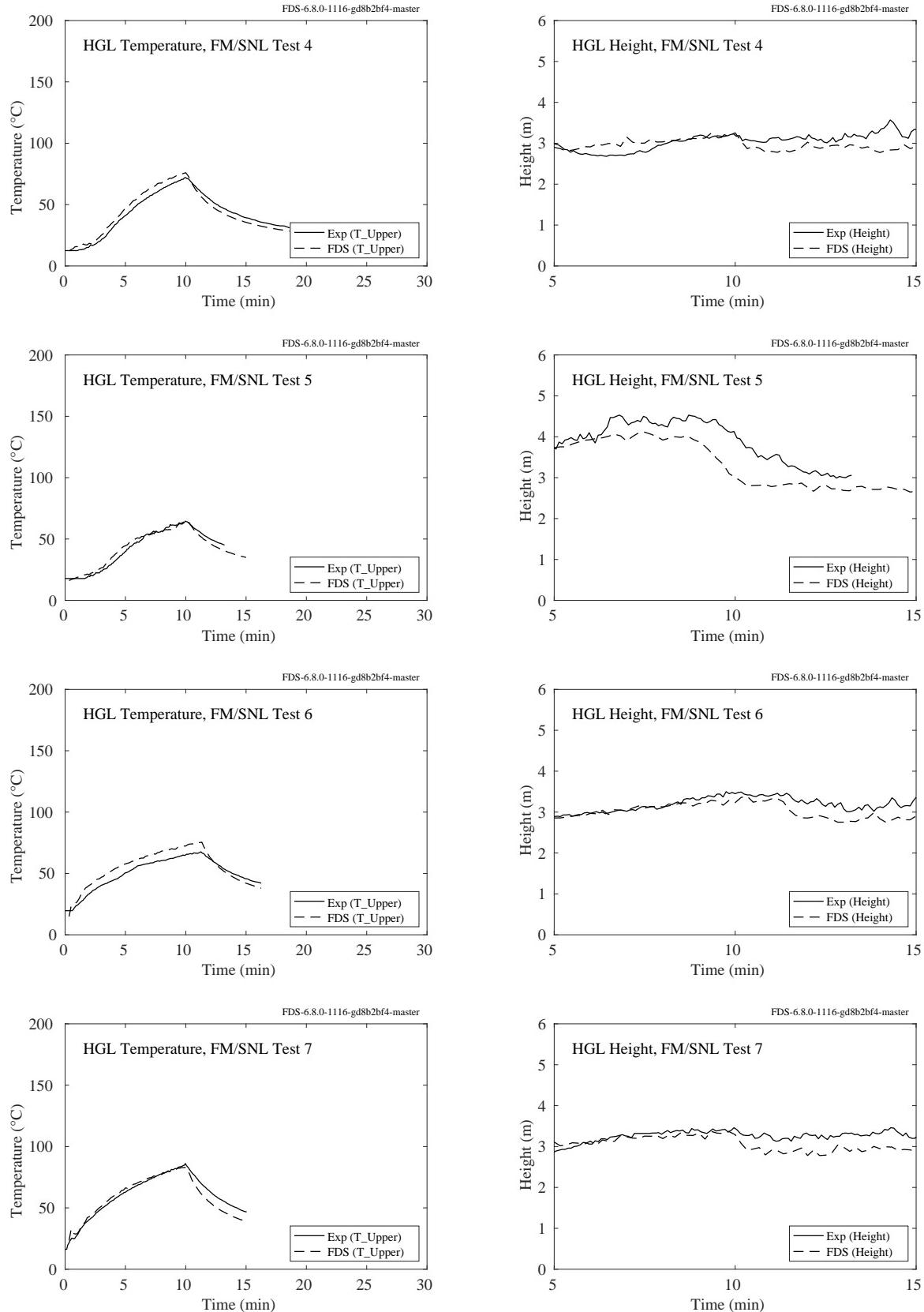


Figure 5.15: FM/SNL experiments, HGL temperature and height, Tests 4, 5, 6, 7.

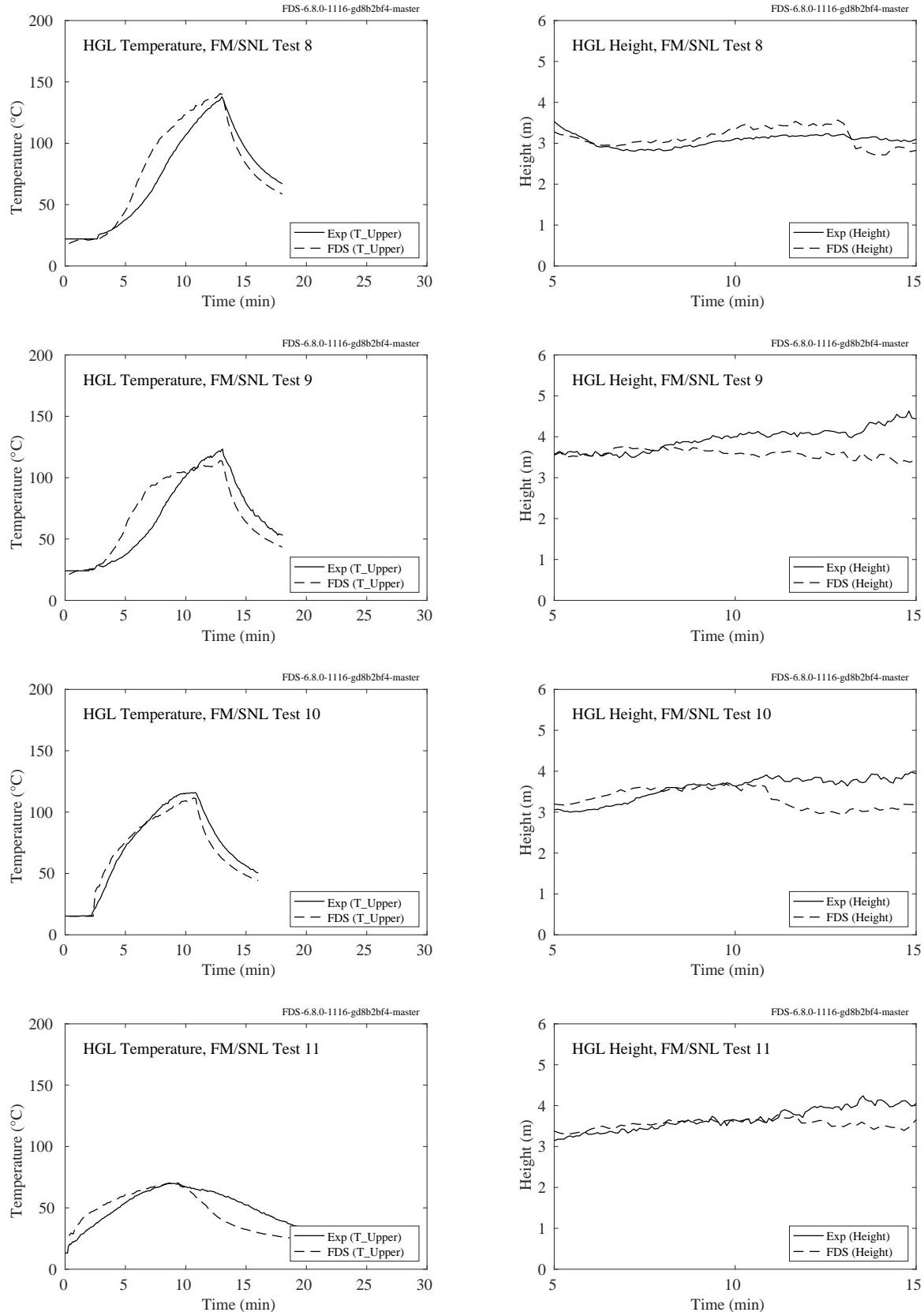


Figure 5.16: FM/SNL experiments, HGL temperature and height, Tests 8, 9, 10, 11.

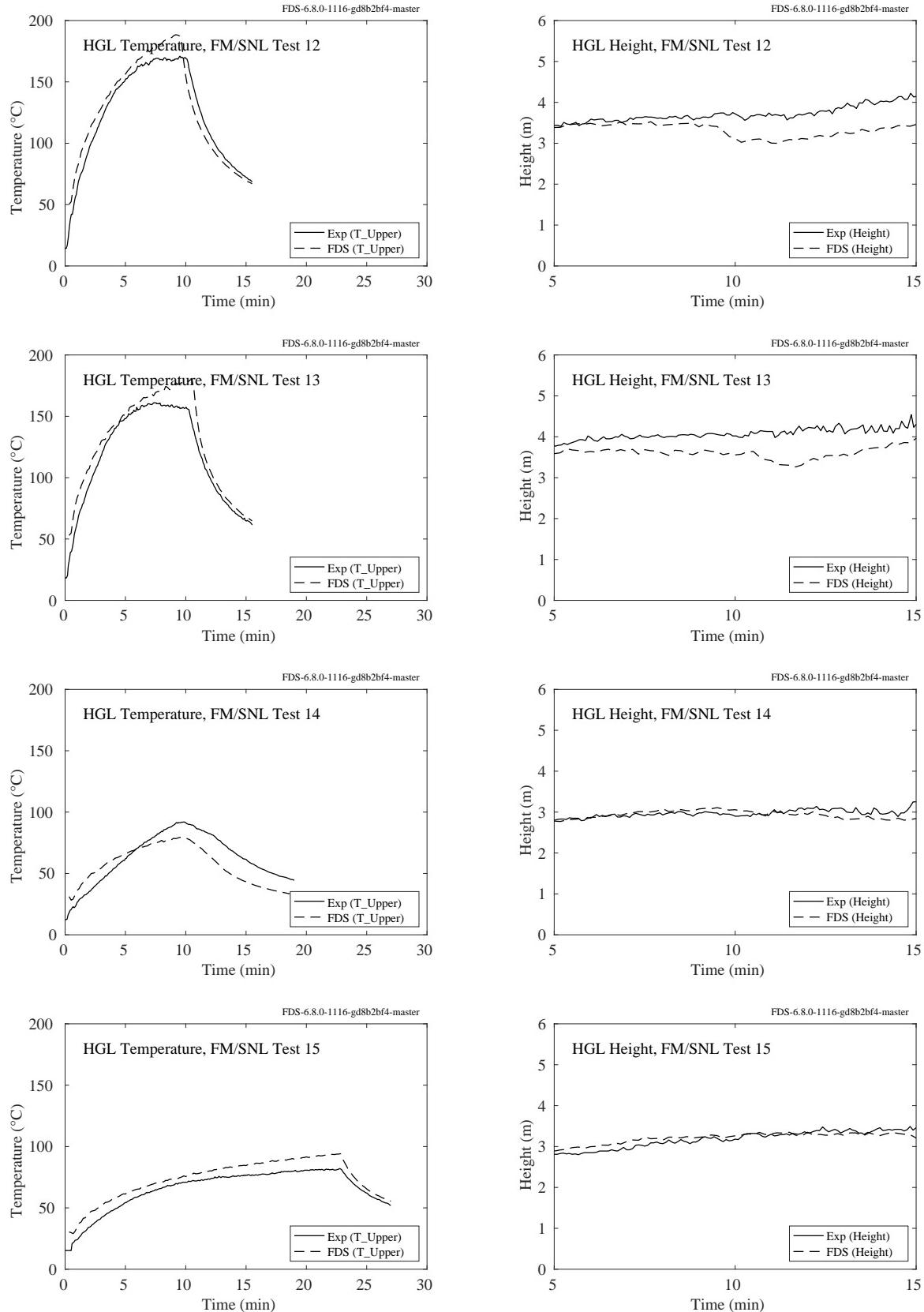


Figure 5.17: FM/SNL experiments, HGL temperature and height, Tests 12, 13, 14, 15.

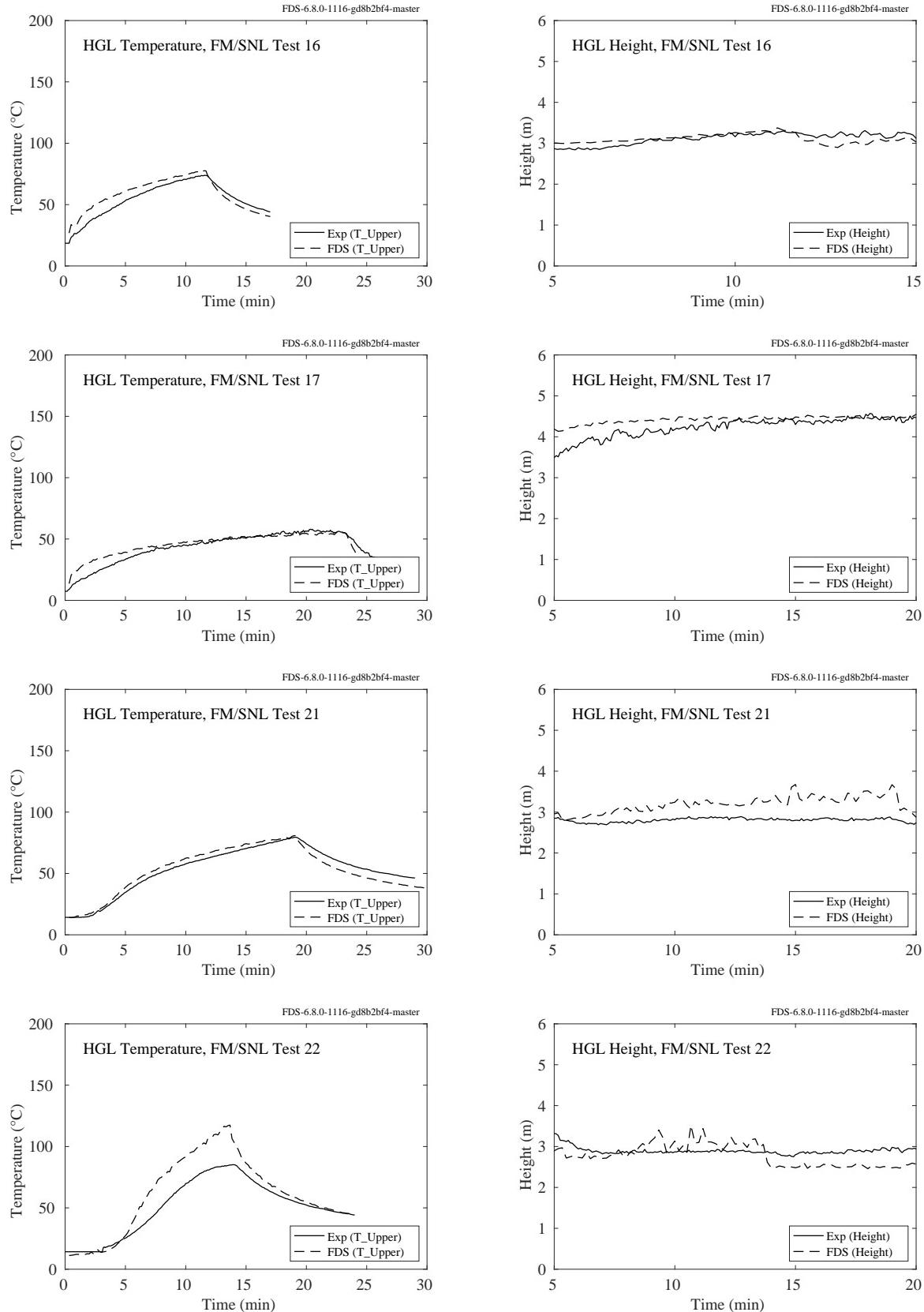


Figure 5.18: FM/SNL experiments, HGL temperature and height, Tests 16, 17, 21, 22.

## 5.6 JH/FRA Experiments

Eight tests from the JH/FRA test series were selected for comparison. The HGL temperature and height are calculated using the standard method. The thermocouple arrays that were located in the north east and south east corners are averaged (with an equal weighting for each) for all tests.

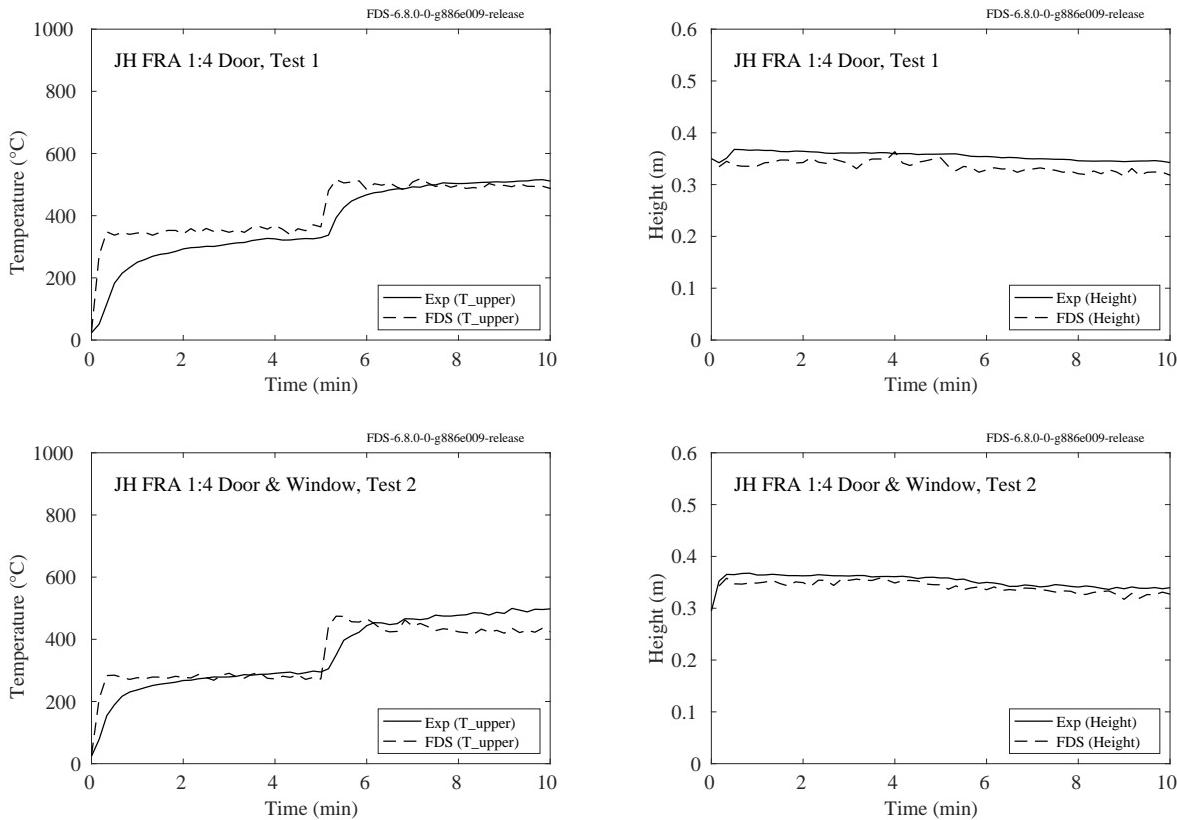


Figure 5.19: JH/FRA experiments, HGL temperature and height, 1:4 scale inert lining configuration.

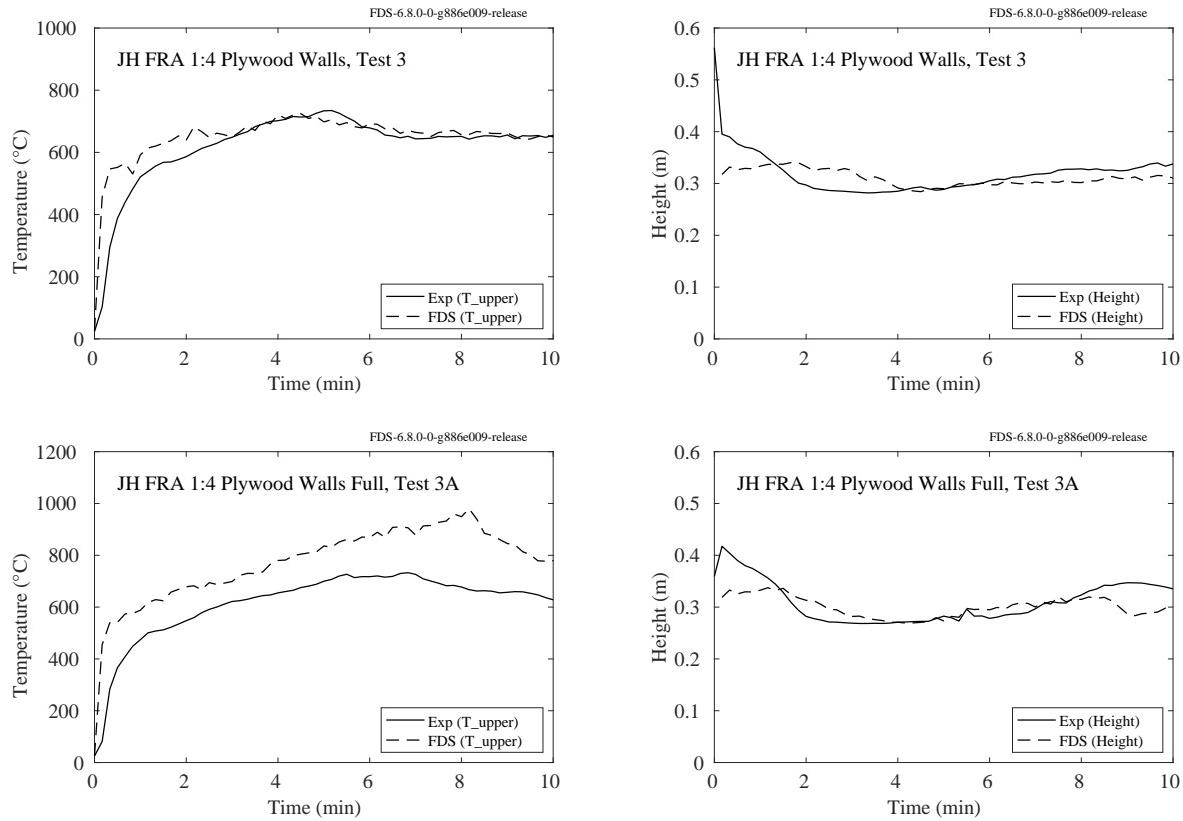


Figure 5.20: JH/FRA experiments, HGL temperature and height, 1:4 scale combustible lining configuration.

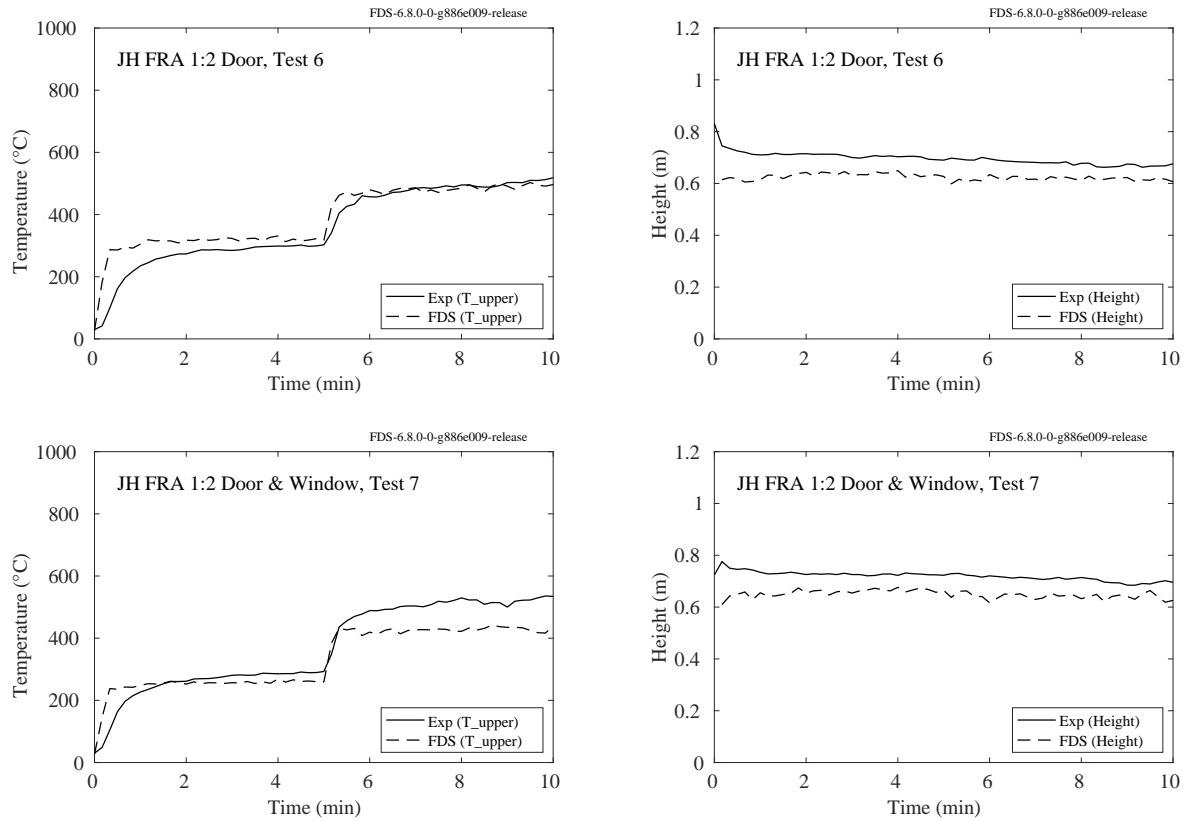


Figure 5.21: JH/FRA experiments, HGL temperature and height, 1:2 scale inert lining configuration.

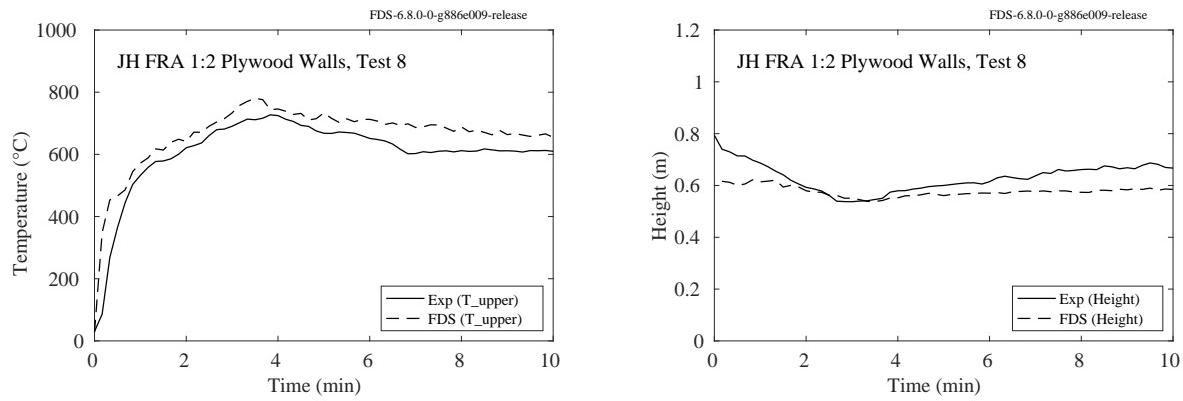


Figure 5.22: JH/FRA experiments, HGL temperature and height, 1:2 scale combustible lining configuration.

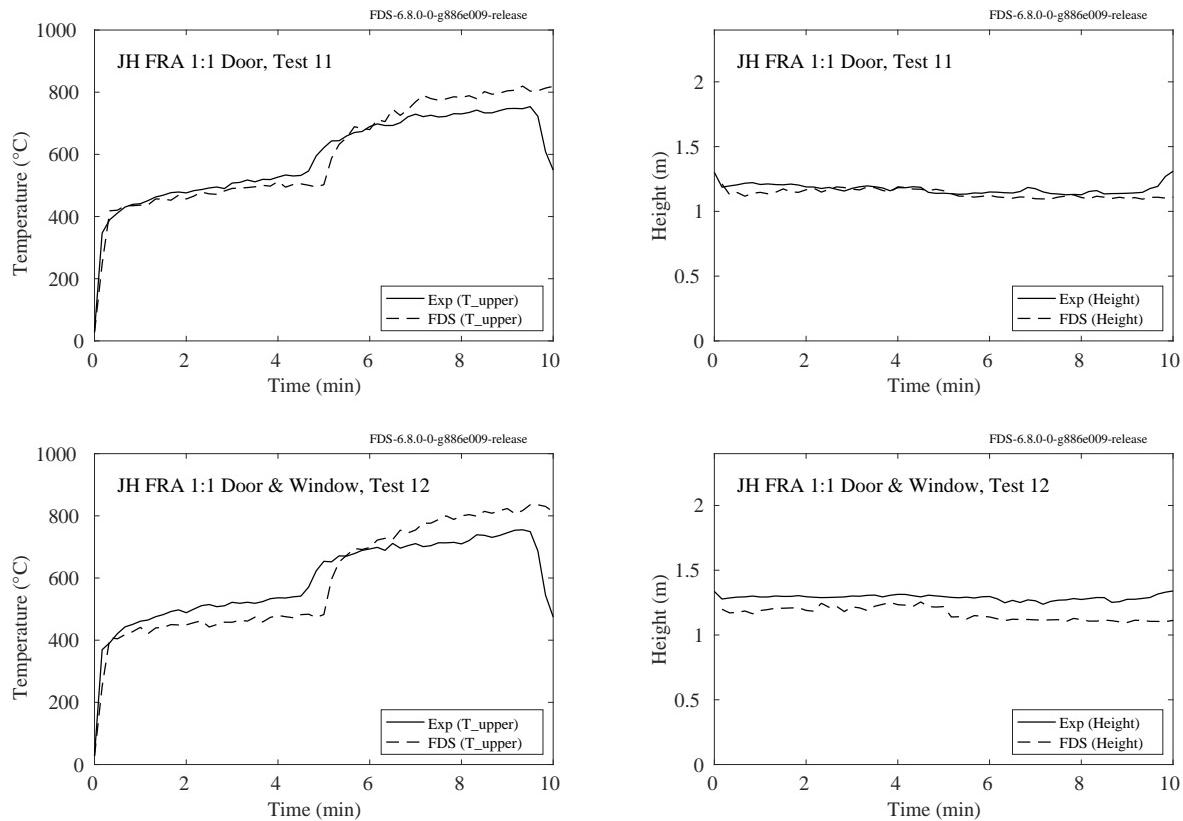


Figure 5.23: JH/FRA experiments, HGL temperature and height, 1:1 scale inert lining configuration.

## 5.7 LLNL Enclosure Series

The figures on the following pages compare predicted and measured hot gas layer temperatures from the LLNL Enclosure experiments. Fifteen thermocouples were evenly spaced from floor to ceiling on either side of the burner. The measured temperatures were reported as averages of the lower, middle, and upper five TCs. Some of the experiments were conducted with a separated plenum space in the top one-third of the overall compartment (Tests 17-60). In these cases, the upper five TCs are a measure of the average plenum temperature.

In the figures, the black circles represent the average of the five upper-most TC measurements. The red circles represent the average of the middle five TC measurements. The corresponding colored curves represent the simulation. For the experiments involving an upper plenum, the middle five TCs are located immediately beneath the plenum and their average temperature is typically greater than that of the upper-most TCs in the plenum. Note that in a number of experiments, the fuel flow was stopped or the fire self-extinguished. The simulations last only as long as the reported measurements.

Details on the experiments and modeling can be found in Sec. 3.43.

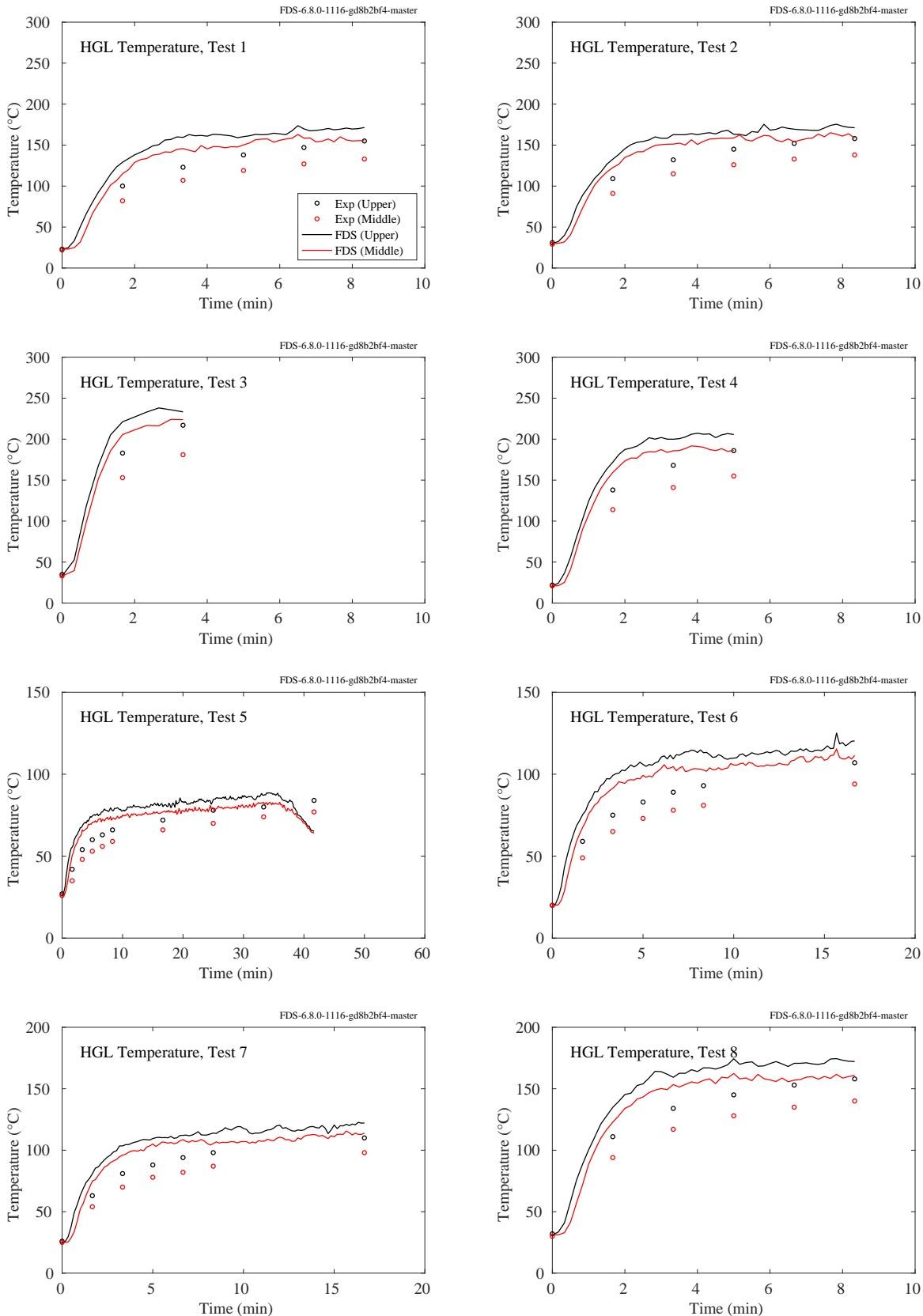


Figure 5.24: LLNL Enclosure experiments, HGL temperature, Tests 1-8.

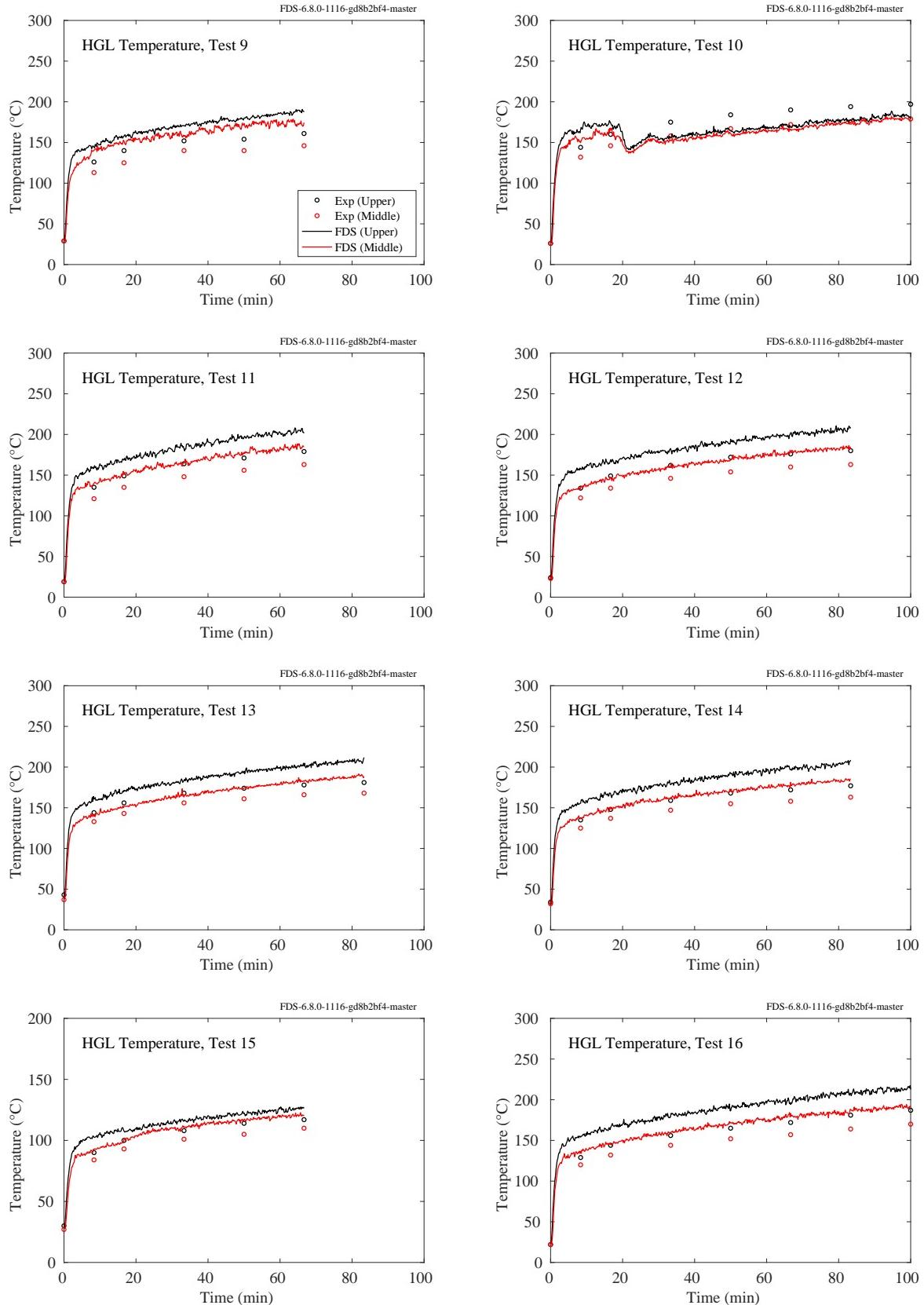


Figure 5.25: LLNL Enclosure experiments, HGL temperature, Tests 9-16.

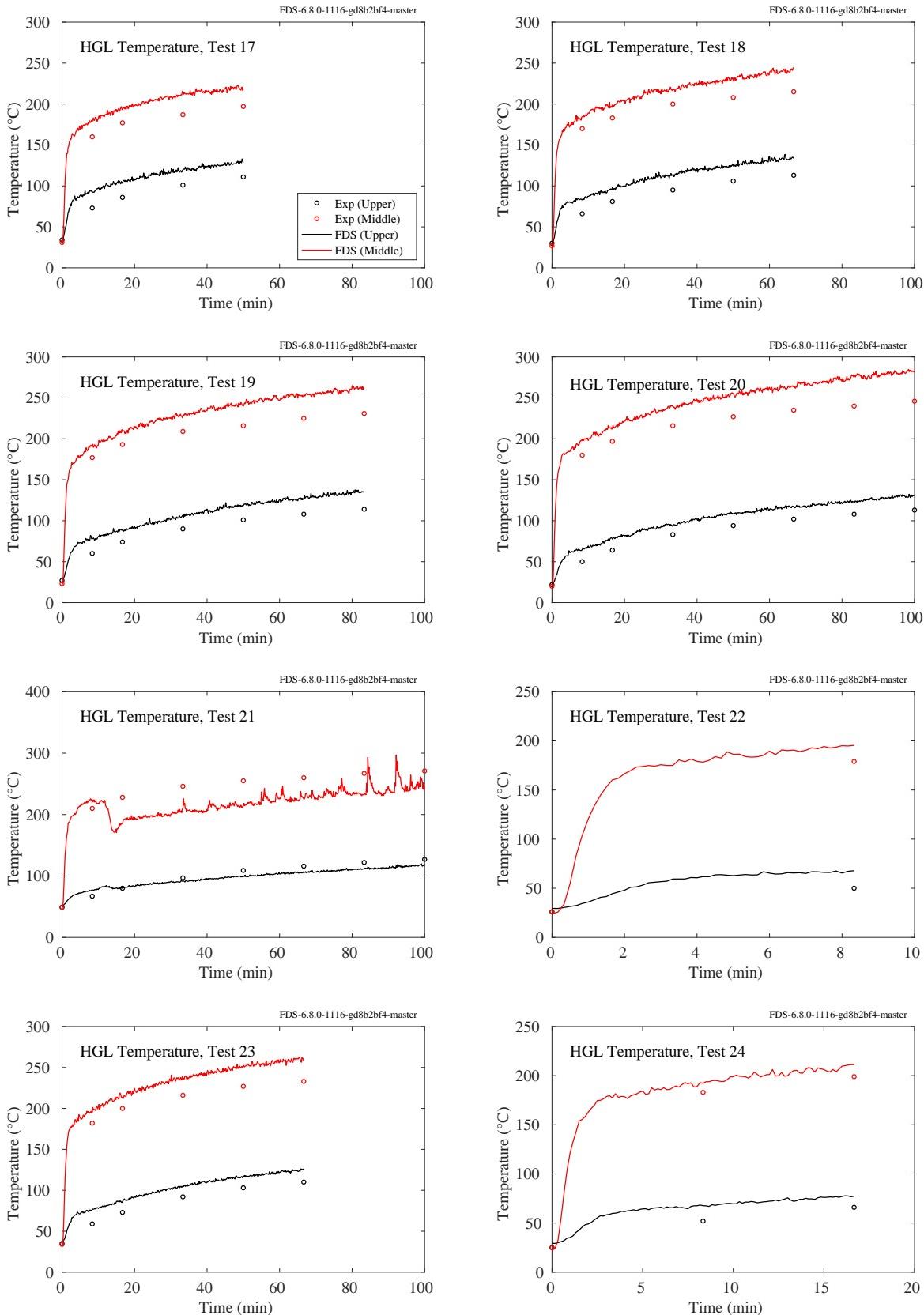


Figure 5.26: LLNL Enclosure experiments, HGL temperature, Tests 17-24.

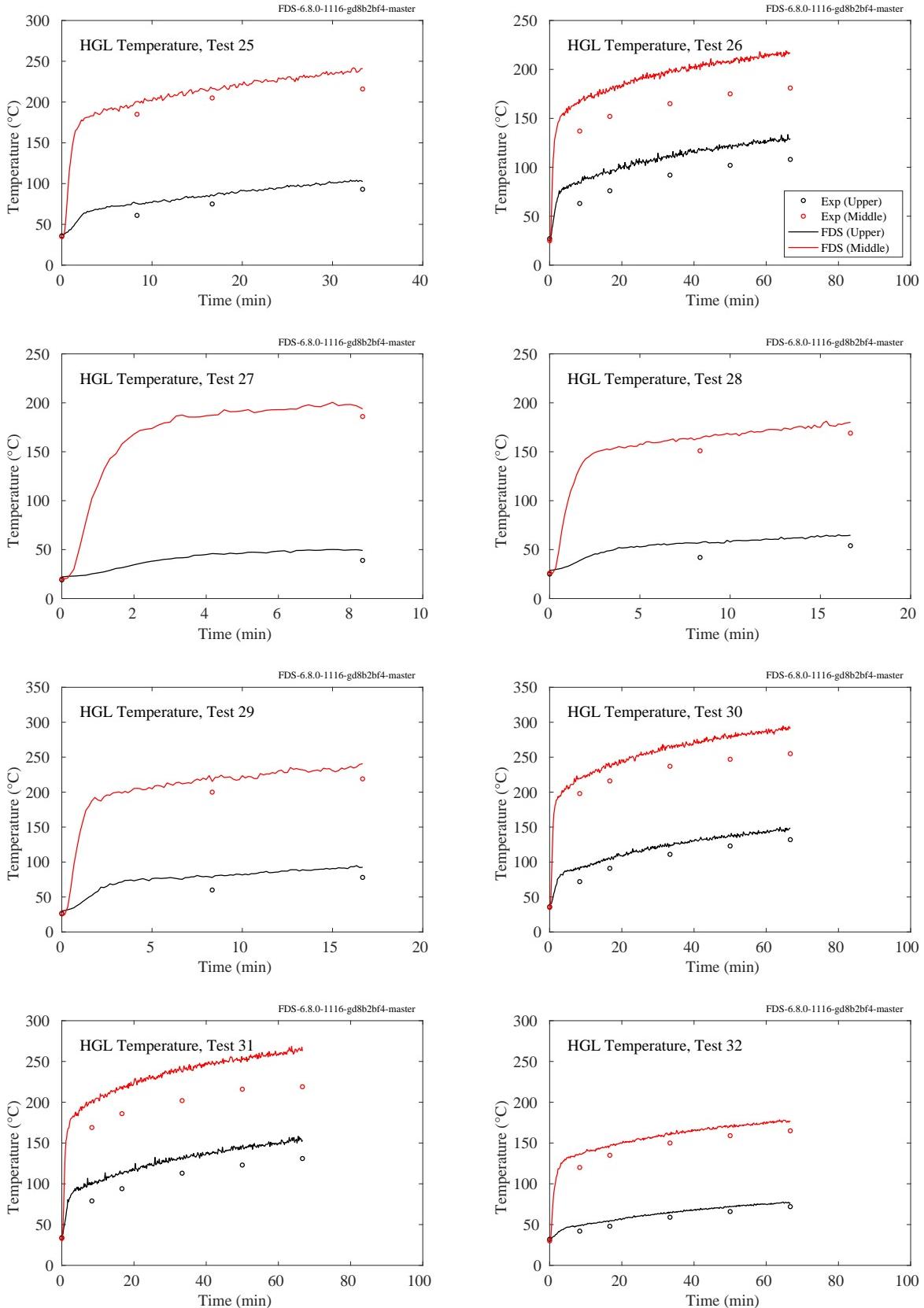


Figure 5.27: LLNL Enclosure experiments, HGL temperature, Tests 25-32.

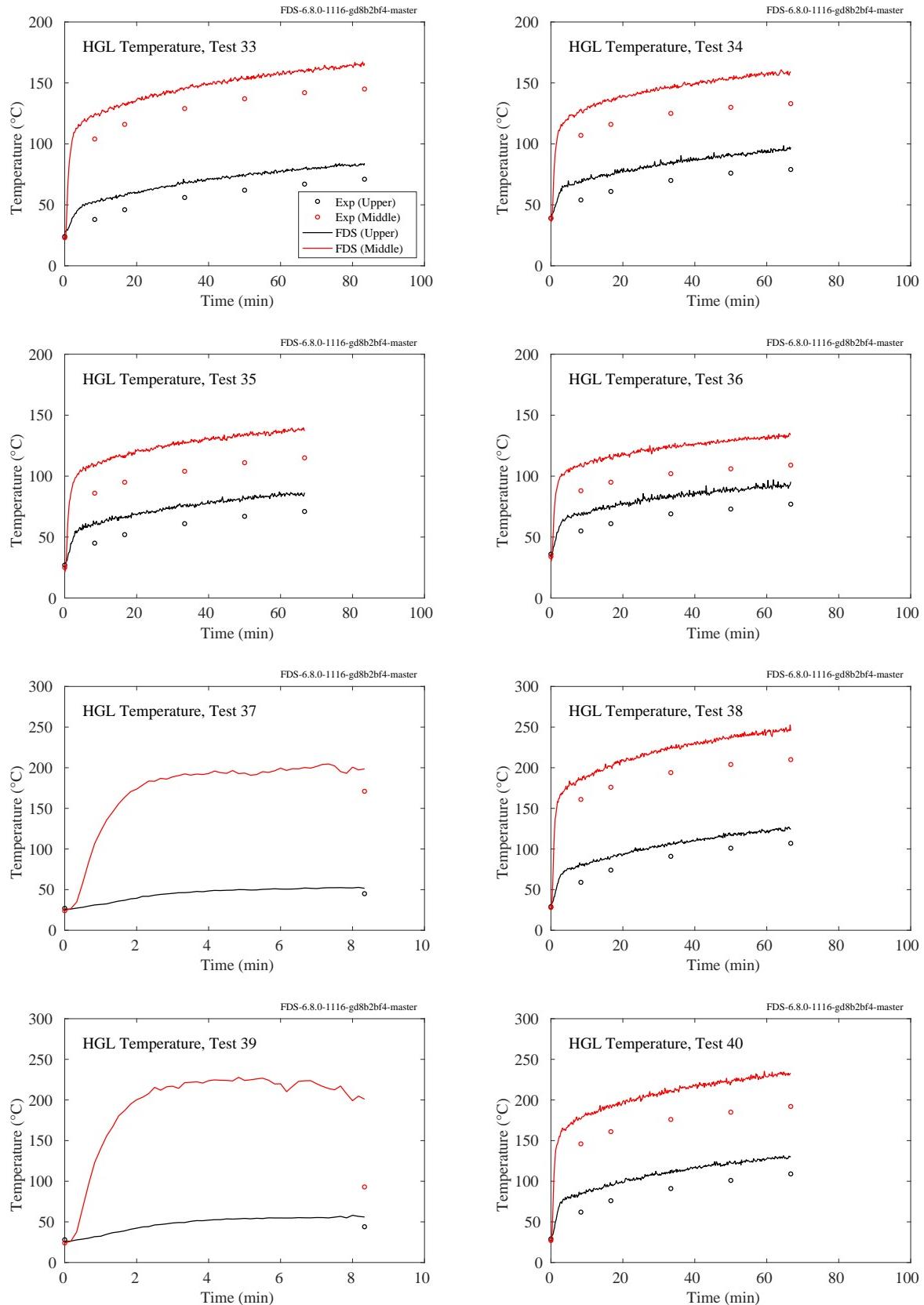


Figure 5.28: LLNL Enclosure experiments, HGL temperature, Tests 33-40.

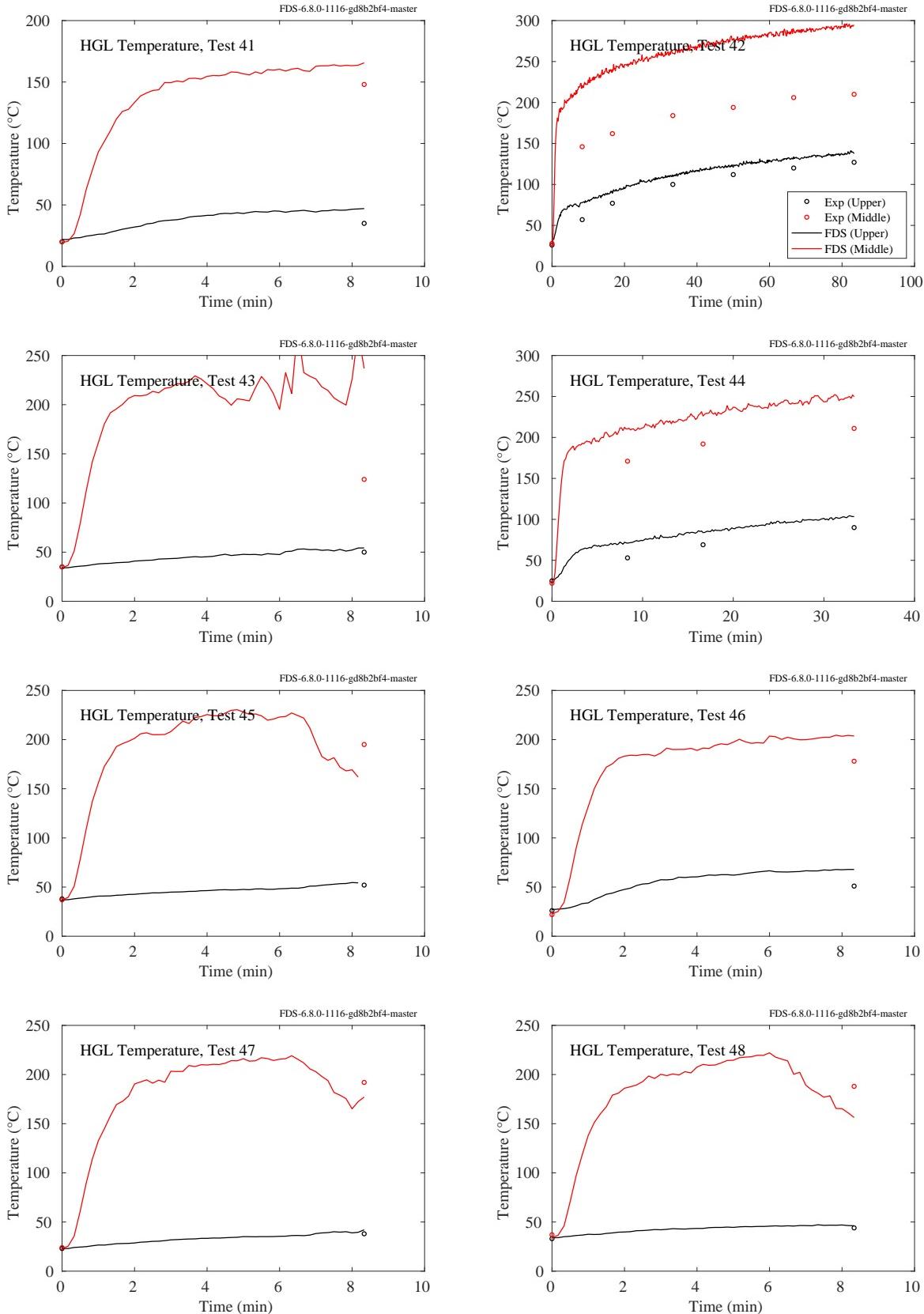


Figure 5.29: LLNL Enclosure experiments, HGL temperature, Tests 41-48.

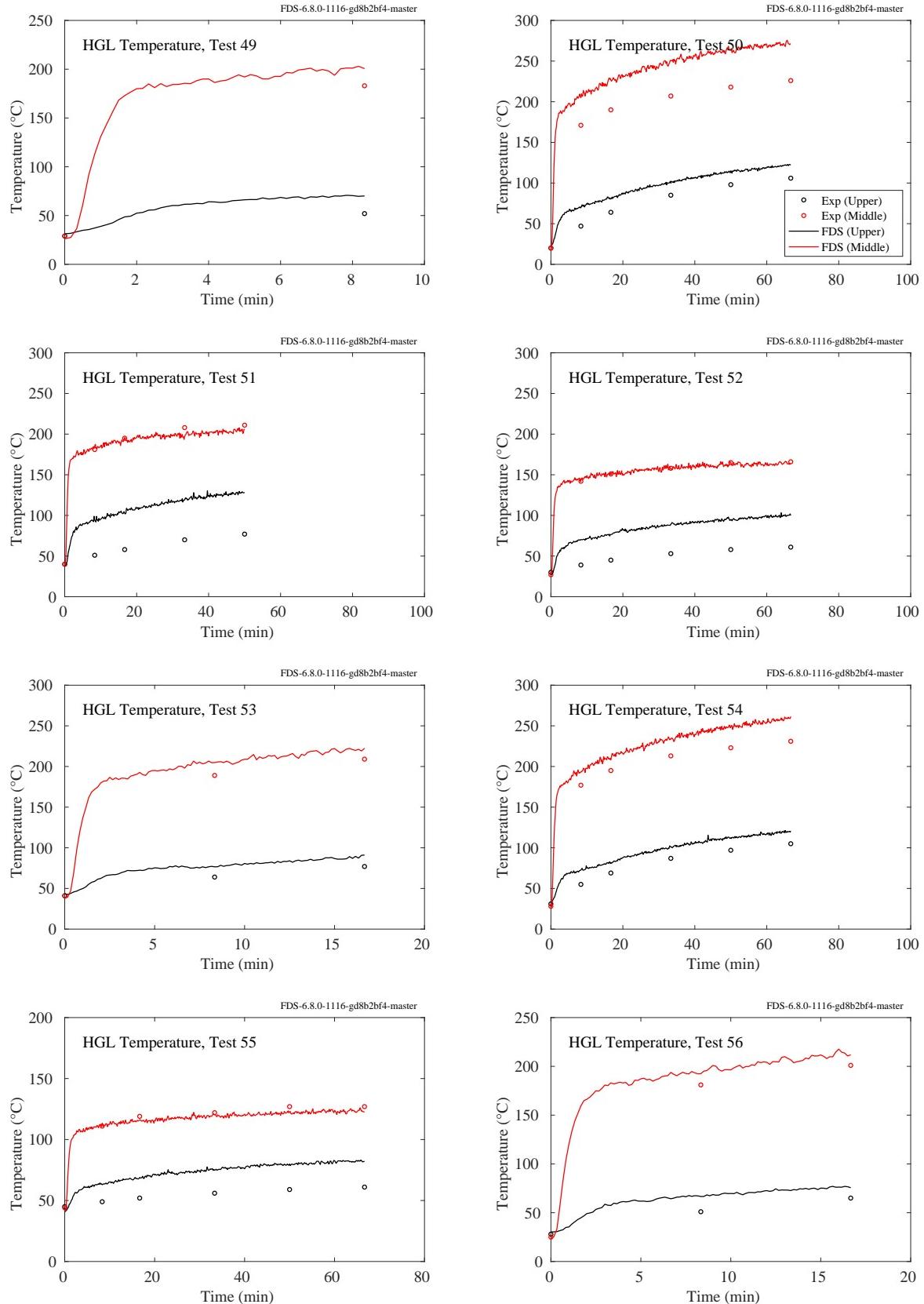


Figure 5.30: LLNL Enclosure experiments, HGL temperature, Tests 49-56.

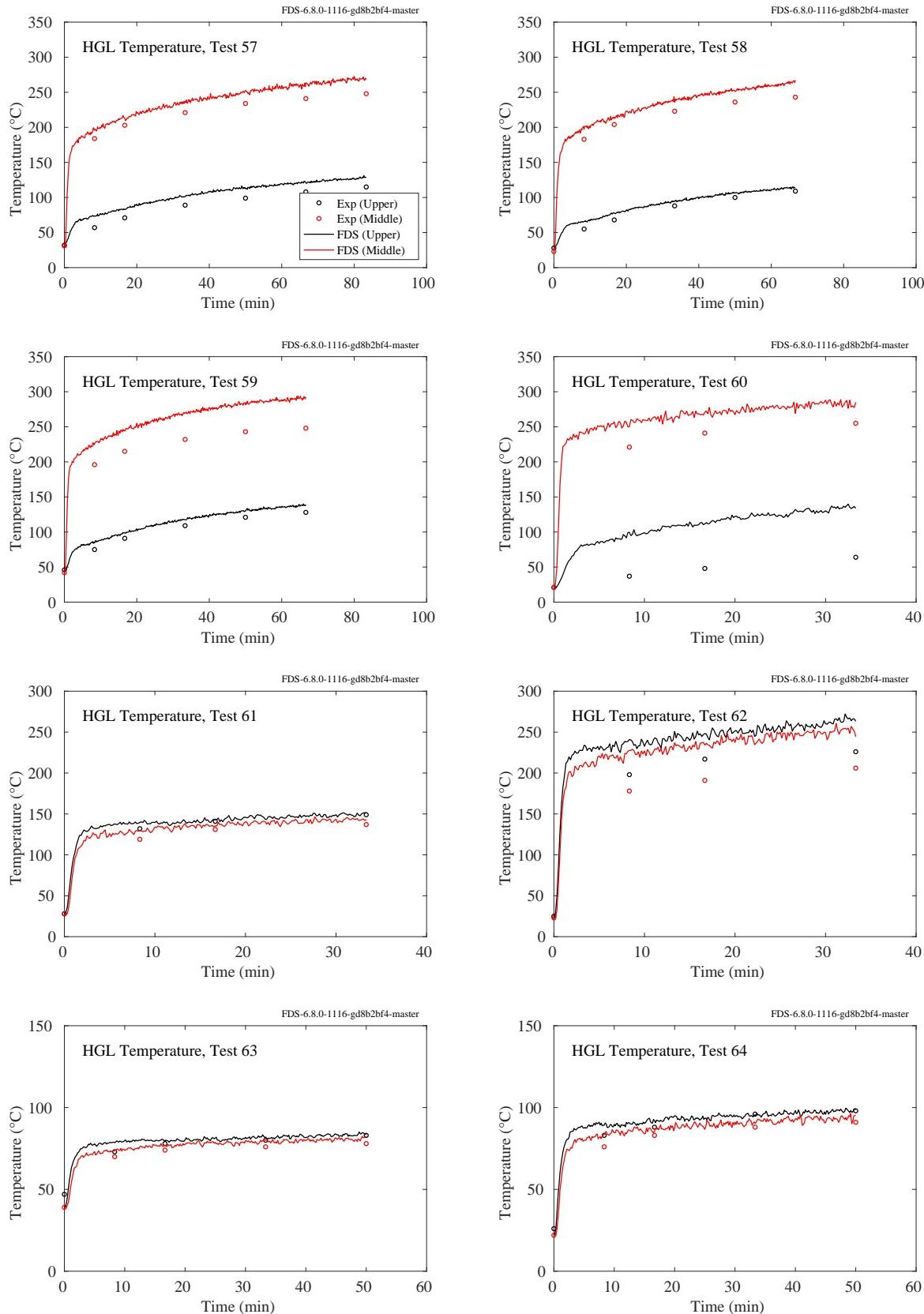


Figure 5.31: LLNL Enclosure experiments, HGL temperature, Tests 57-64.

## 5.8 NBS Multi-Room Test Series

This series of experiments was performed in two relatively small rooms connected by a long corridor. The fire was located in one of the rooms. Eight vertical arrays of thermocouples were positioned throughout the test space: Tree 1 in the burn room, Tree 2 in the doorway of the burn room, Trees 3, 4, and 5 in the corridor, Tree 6 in the exit doorway to the outside at the far end of the corridor, Tree 7 in the doorway of the “target” room, and Tree 8 inside the target room. Four trees have been selected for comparison with model prediction: Tree 1 in the burn room, the trees in the corridor, and Tree 8 in the target room in Test 100Z. In Tests 100A and 100O, the target room was closed. The test director reduced the layer information individually for the eight thermocouple arrays using an alternative method. These results were included in the original data sets. However, in this report the selected TC trees were reduced using the method described in Sec. 5.1.

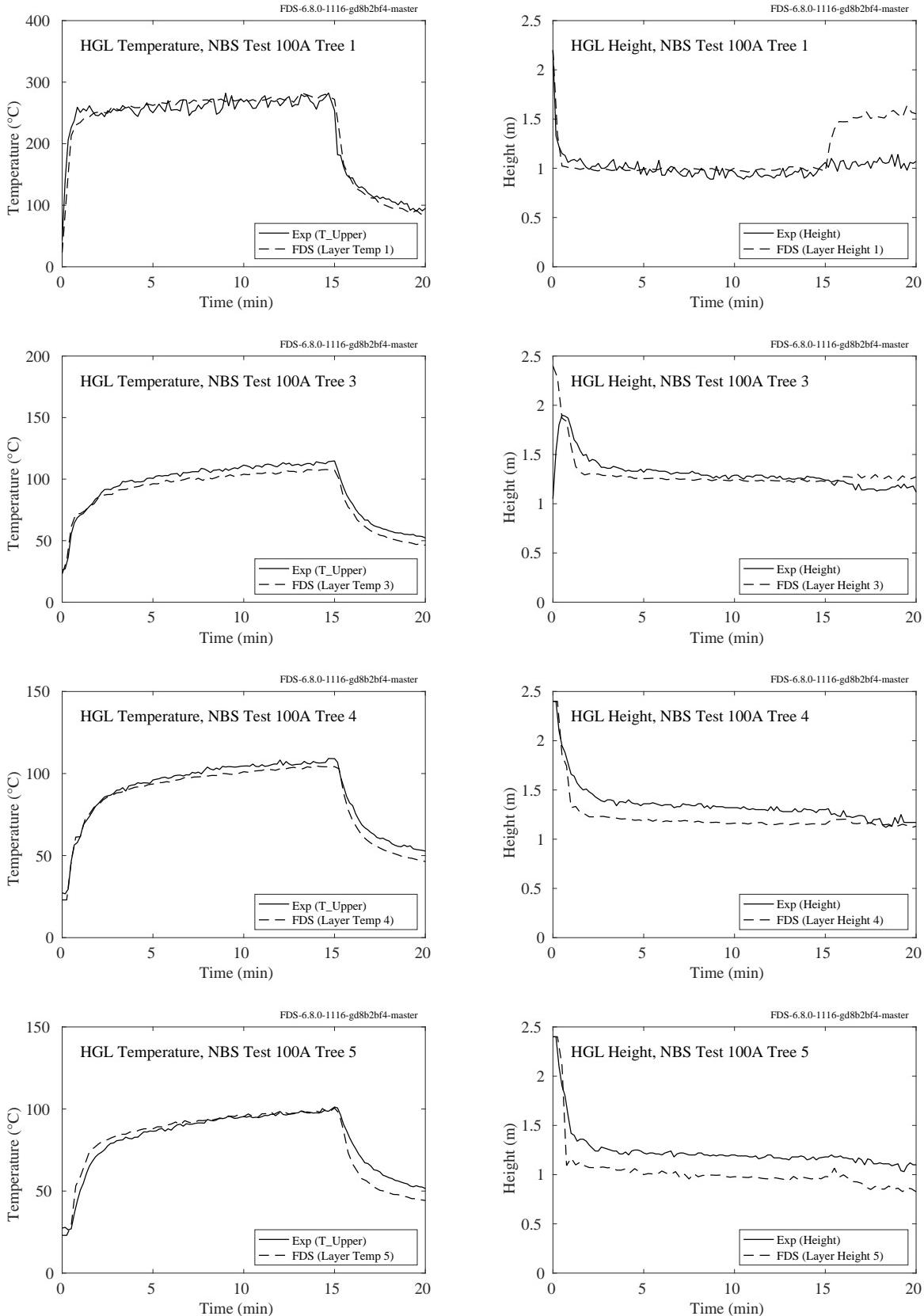


Figure 5.32: NBS Multi-Room experiments, HGL temperature and height, Test 100A.

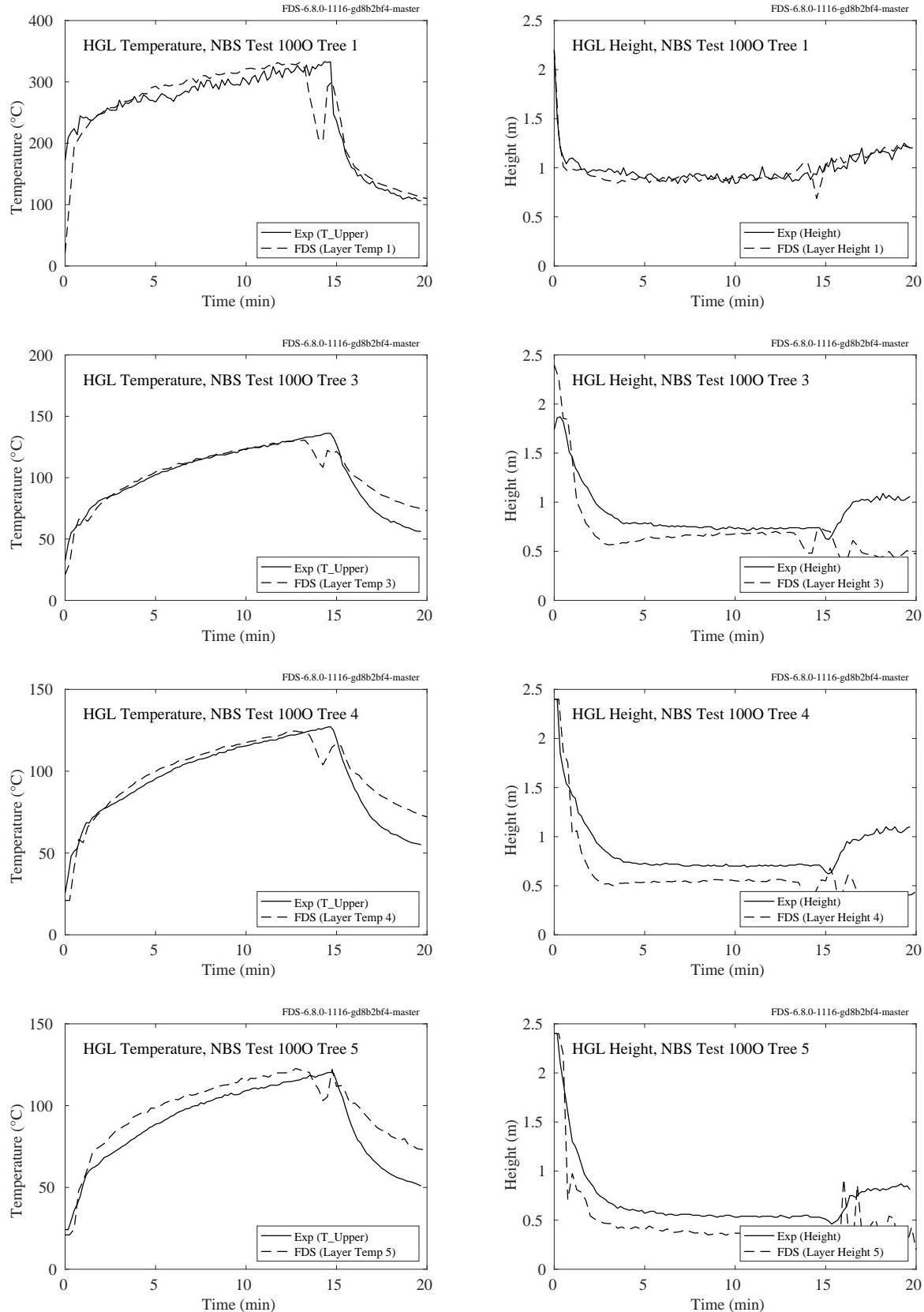


Figure 5.33: NBS Multi-Room experiments, HGL temperature and height, Test 100O.

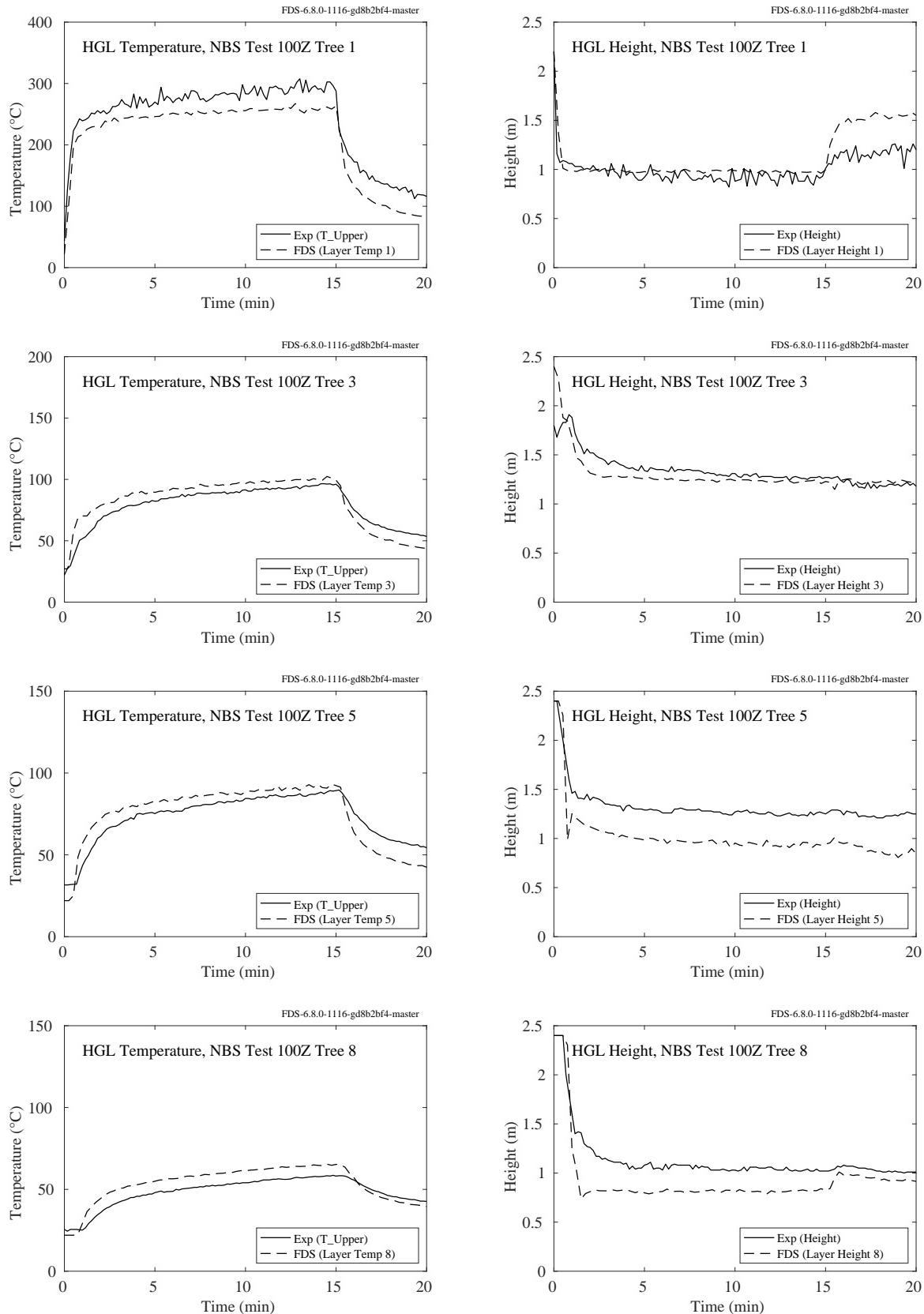


Figure 5.34: NBS Multi-Room experiments, HGL temperature and height, Test 100Z.

## 5.9 NIST Composite Beam

A brief description of the experiments is given in Sec. 3.50. The compartment interior dimensions are 12.4 m long, running east-west, 1.9 m wide, and 3.77 m high. Four experiments with fires were performed, labeled as Tests 2-5. Test 1 did not include a fire.

To measure the hot gas layer in the compartment, stainless steel sheathed thermocouples (Omega TJ36-CAXL-14U-24 and TJ36-CAXL-38U-24) were mounted 0.8 m below the concrete slab, extending out of the compartment walls. Results are shown in Figs. 5.35 and 5.36. TCC1 was mounted 30 cm from the west wall and 46 cm from the north wall. TCC5 was mounted 30 cm from the east wall and 46 cm from the south wall. TCC2, TCC3, and TCC4 were mounted 46 cm from the north wall, and at positions -4.3 m, 0 m, and 4.3 m relative to the line of east-west symmetry, respectively (east is the positive direction). TCC6, TCC7, and TCC8 were mounted 46 cm from the south wall and 4.3 m, 0 m, and -4.3 m from the east-west line of symmetry, respectively.

Because of the symmetry of the experimental configuration, TCC1 and TCC5 are duplicates, TCC3 and TCC7 are duplicates, and TCC2, TCC4, TCC6, and TCC8 are duplicates.

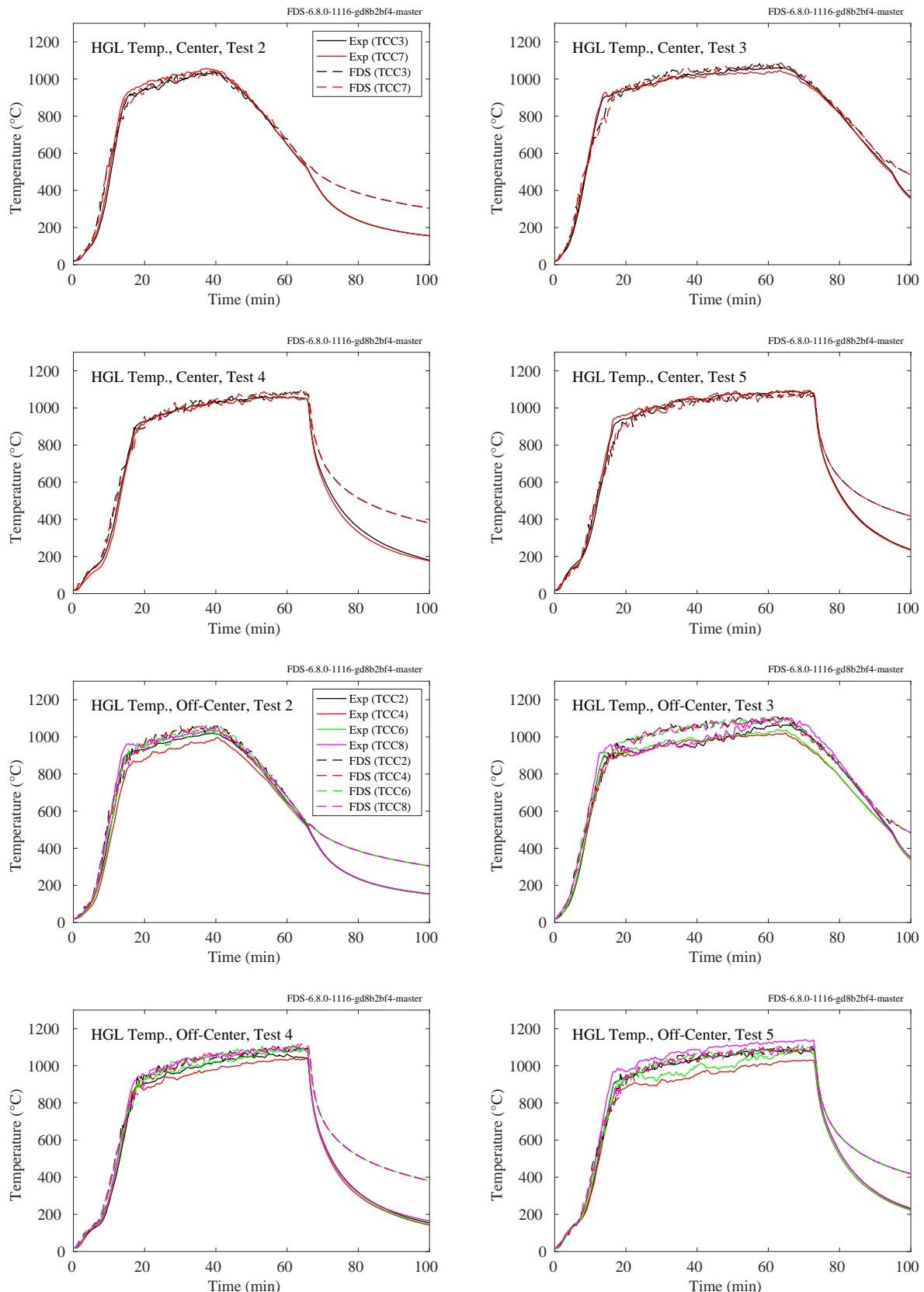


Figure 5.35: NIST Composite Beam, mid-compartment HGL temperatures.

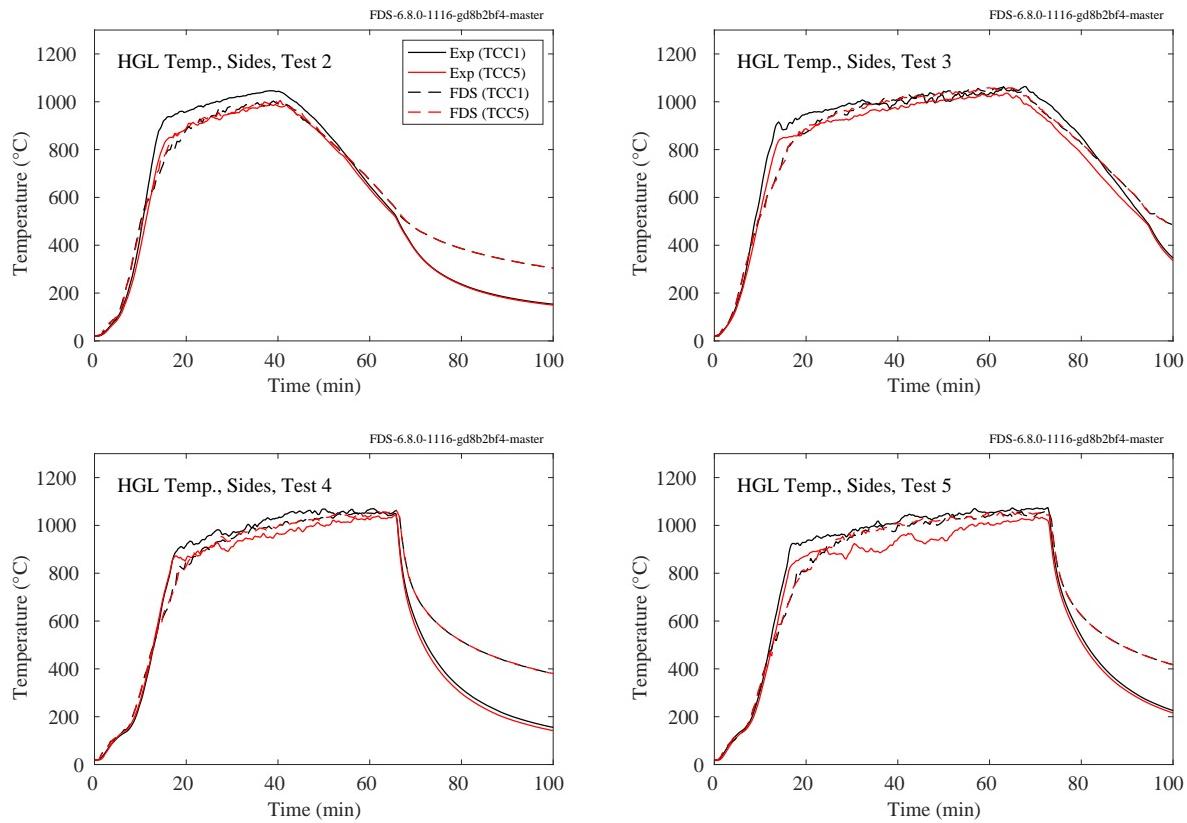


Figure 5.36: NIST Composite Beam, end-compartment HGL temperatures.

## 5.10 NIST E119 Compartment

A brief description of the experiments is given in Sec. 3.51. The compartment interior dimensions are 10.8 m long, running east-west, 7.0 m wide, and 3.8 m high. Three fire experiments were performed, labeled as Tests 1-3.

To measure the upper layer gas temperatures in the compartment, twelve stainless steel sheathed thermocouples (Omega TJ36-CAXL-14U-24) were mounted 0.305 m below the ceiling, extending out of the ceiling slab. Results are shown in Figs. 5.37 through 5.39. Locations of TC1 through TC12 were shown in Fig. 3.27. Because of the symmetry of the experimental configuration, TC1 and TC4 are duplicates, TC2 and TC3 are duplicates, TC9 and TC12 are duplicates, and TC10, TC11 are duplicates.

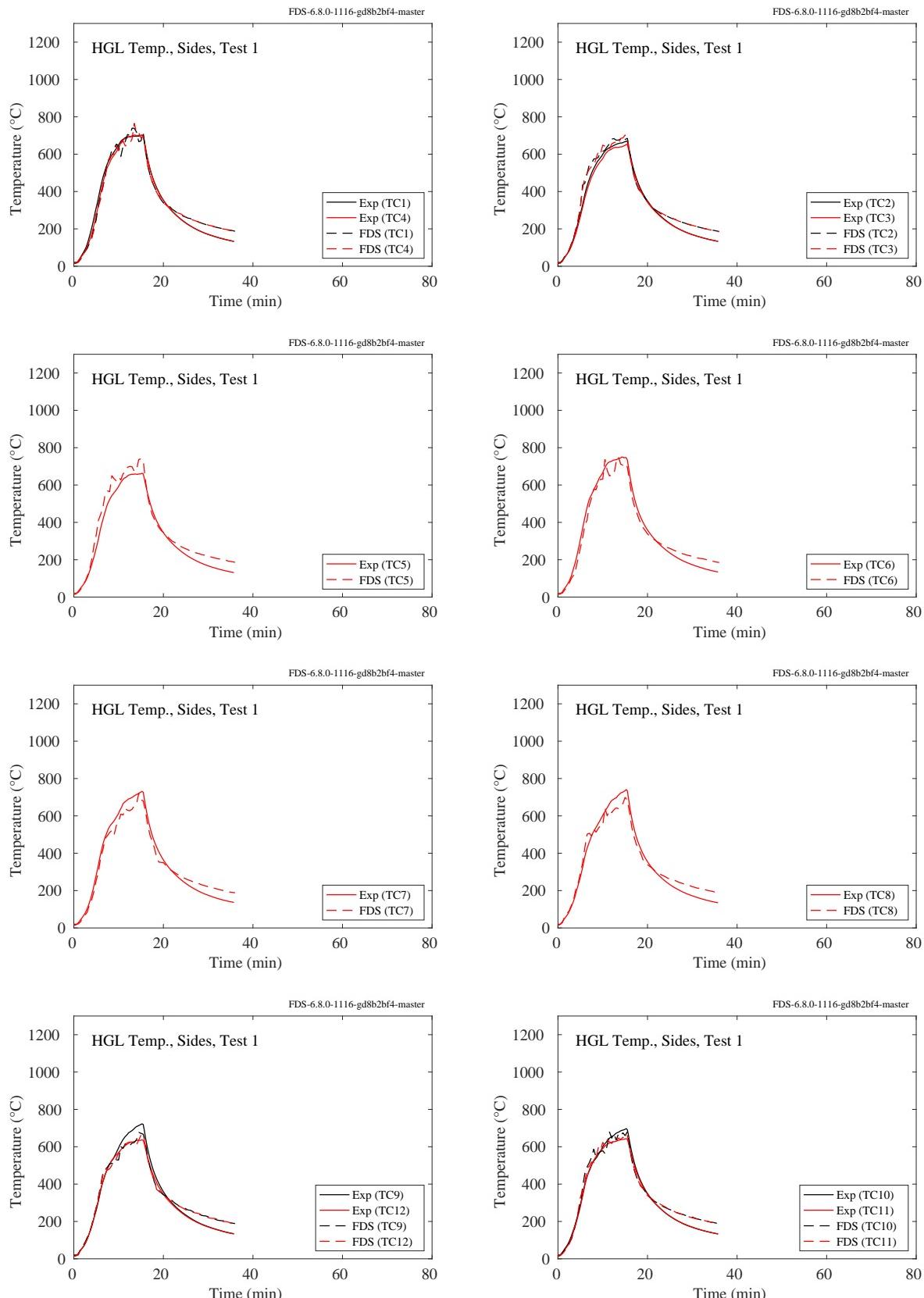


Figure 5.37: NIST E119 Compartment Test 1, upper layer gas temperatures.

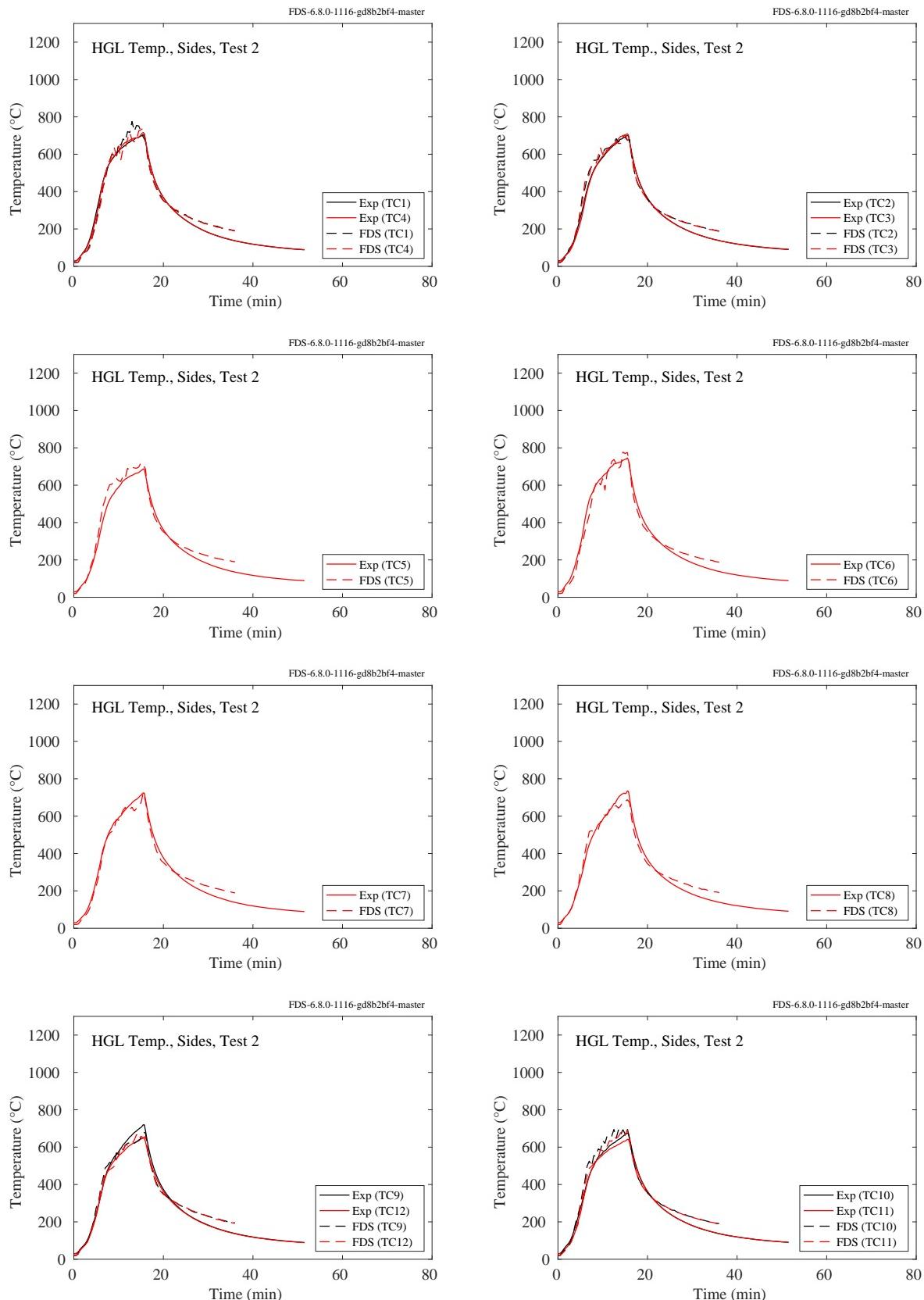


Figure 5.38: NIST E119 Compartment Test 2, upper layer gas temperatures.

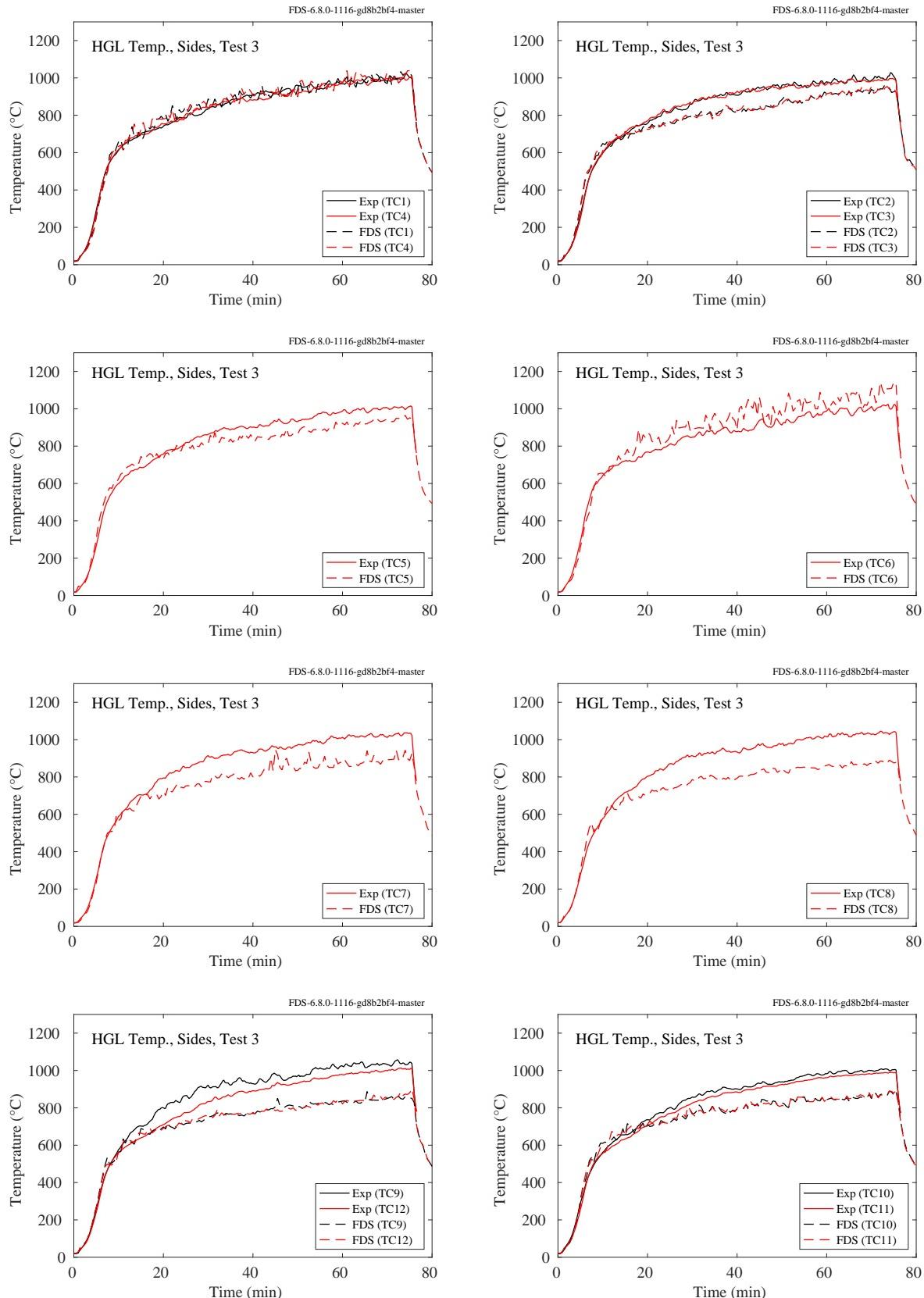


Figure 5.39: NIST E119 Compartment Test 3, upper layer gas temperatures.

## 5.11 NIST Full-Scale Enclosure (FSE), 2008

Thermocouple arrays were suspended from the ceiling at two points along the centerline of the ISO 9705 compartment. The array in the front of the compartment was located 72 cm inside the door, and the array in the rear was 72 cm from the back wall. Each array consisted of 11 TCs positioned at heights of 3 cm, 30 cm, 60 cm, 90 cm, 105 cm, 120 cm, 135 cm, 150 cm, 180 cm, 210 cm, and 2.38 cm. The height of the compartment was 2.4 m. In the plots on the following pages, the average HGL temperature and layer height are shown for experiments 8 through 32. The thermocouple arrays were not installed for experiments labeled ISONG3, ISOHept4, or ISOHept5.

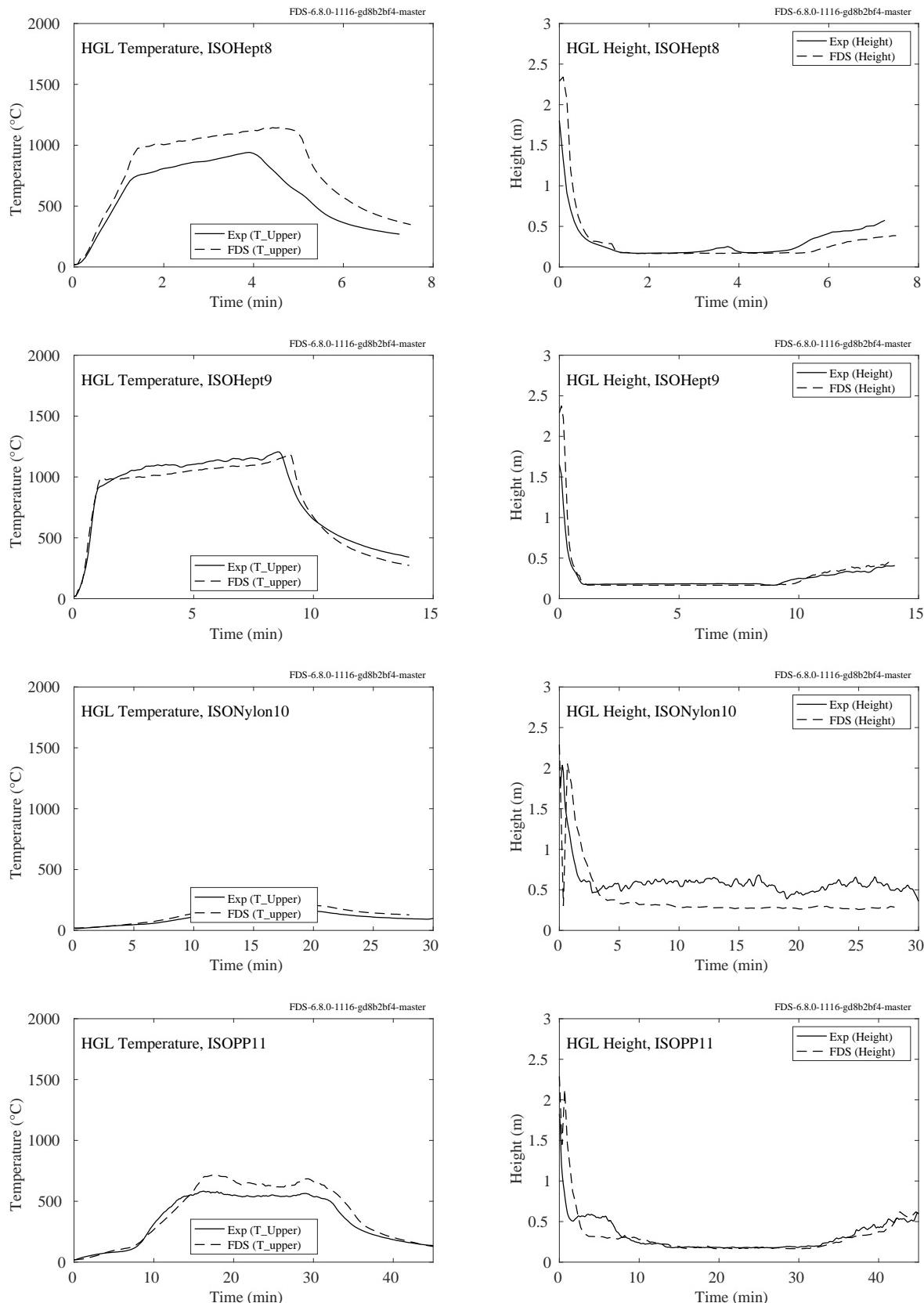


Figure 5.40: NIST FSE, HGL temperature and height, Tests 8-11.

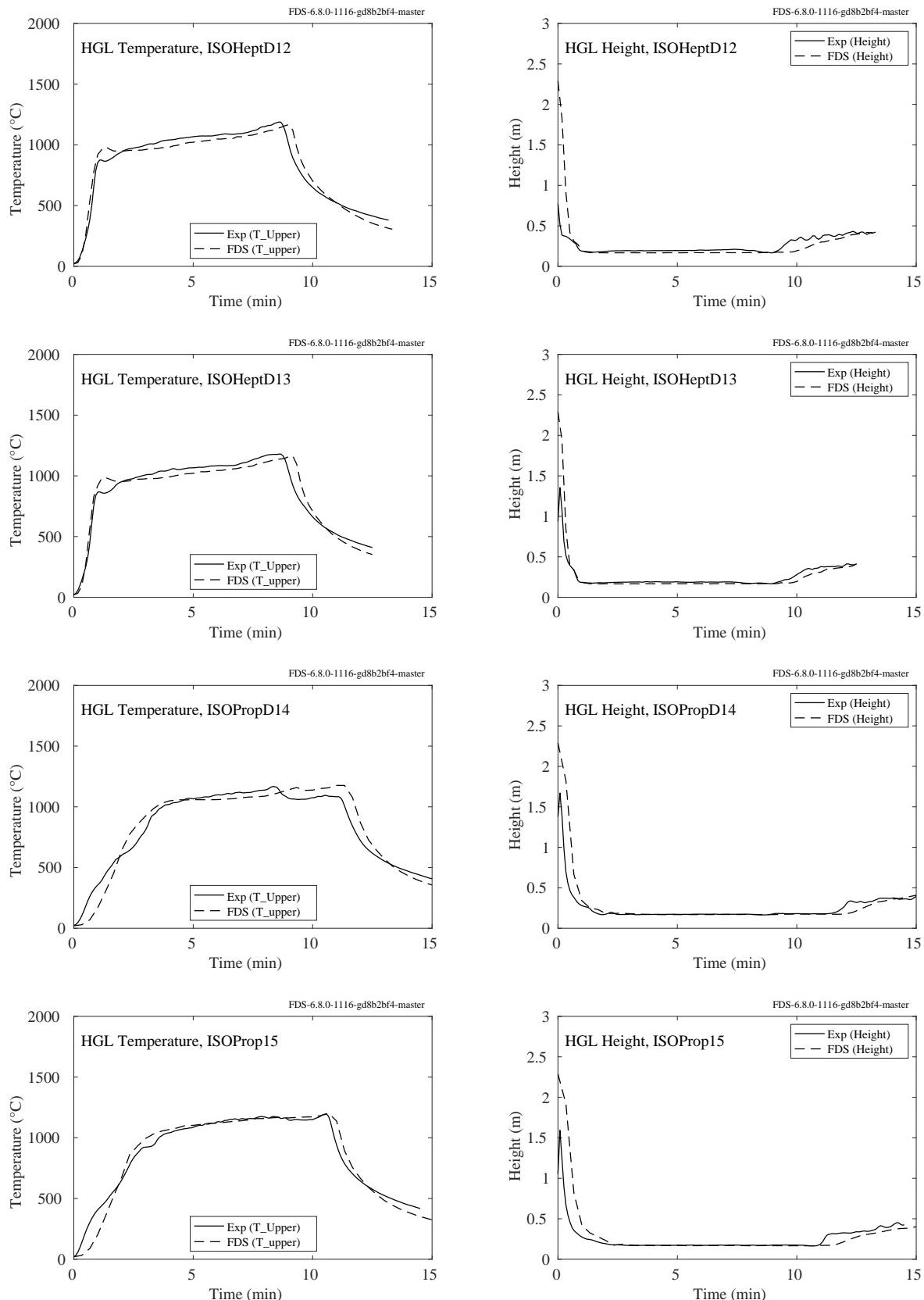


Figure 5.41: NIST FSE, HGL temperature and height, Tests 12-15.

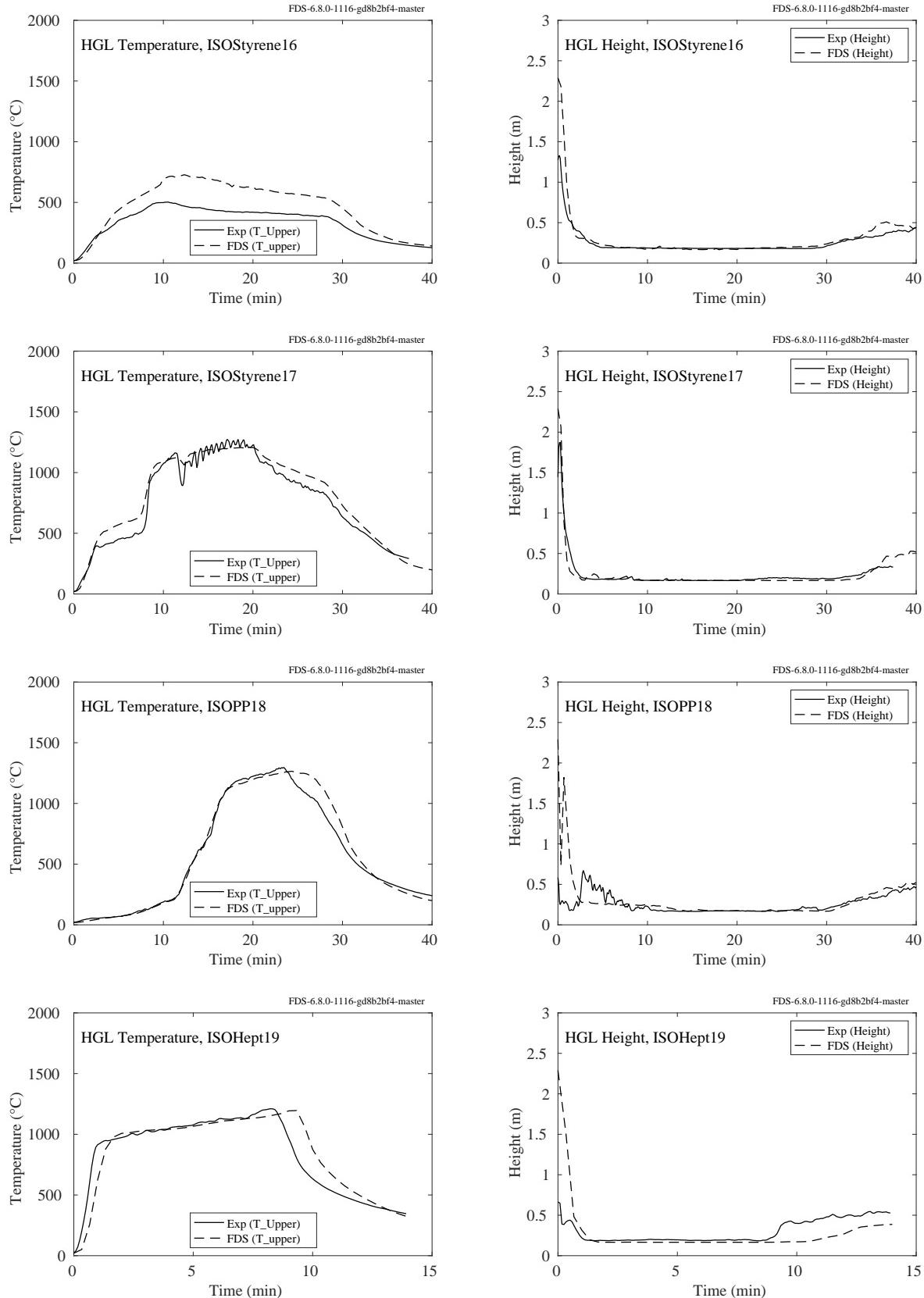


Figure 5.42: NIST FSE, HGL temperature and height, Tests 16-19.

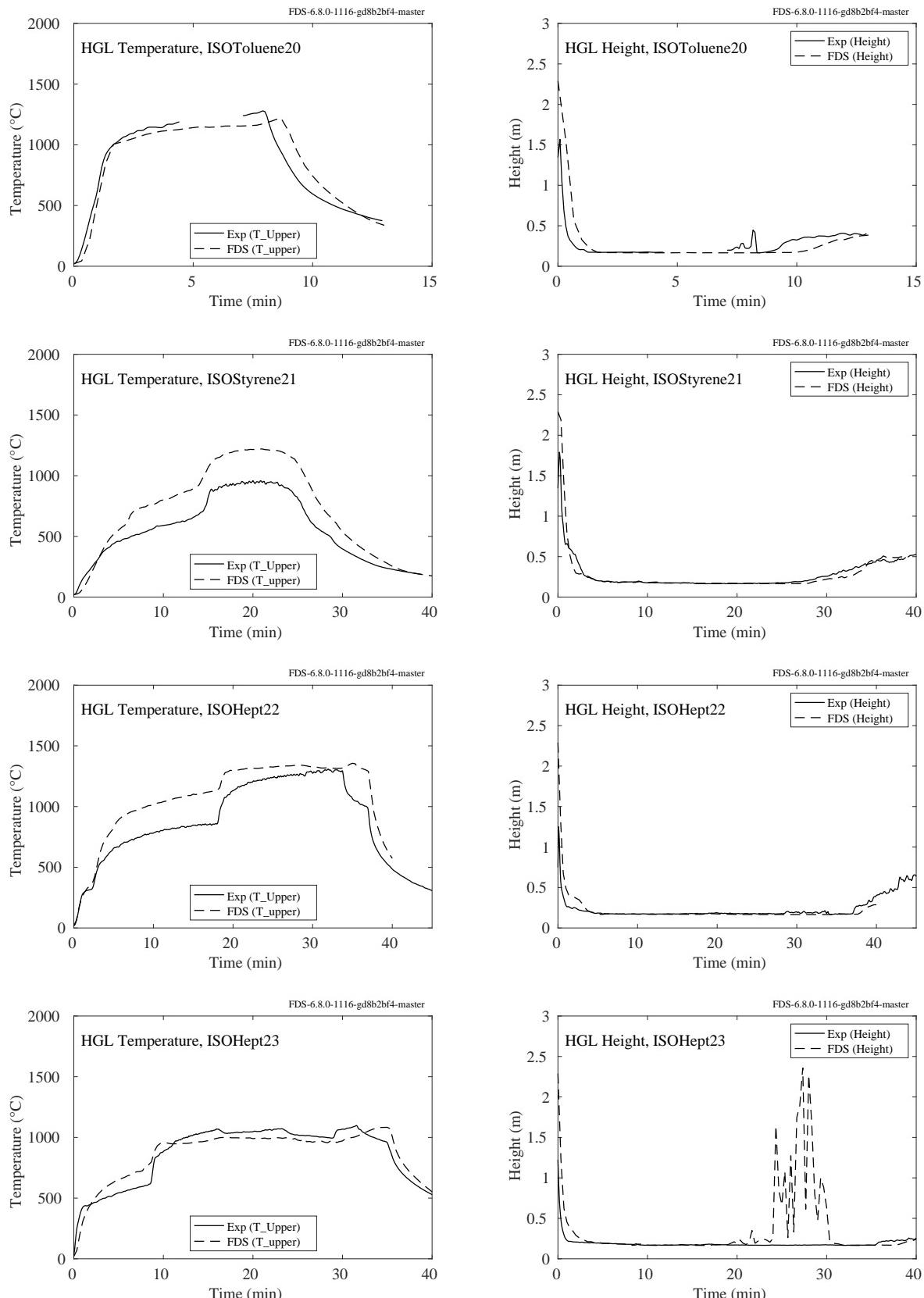


Figure 5.43: NIST FSE, HGL temperature and height, Tests 20-23.

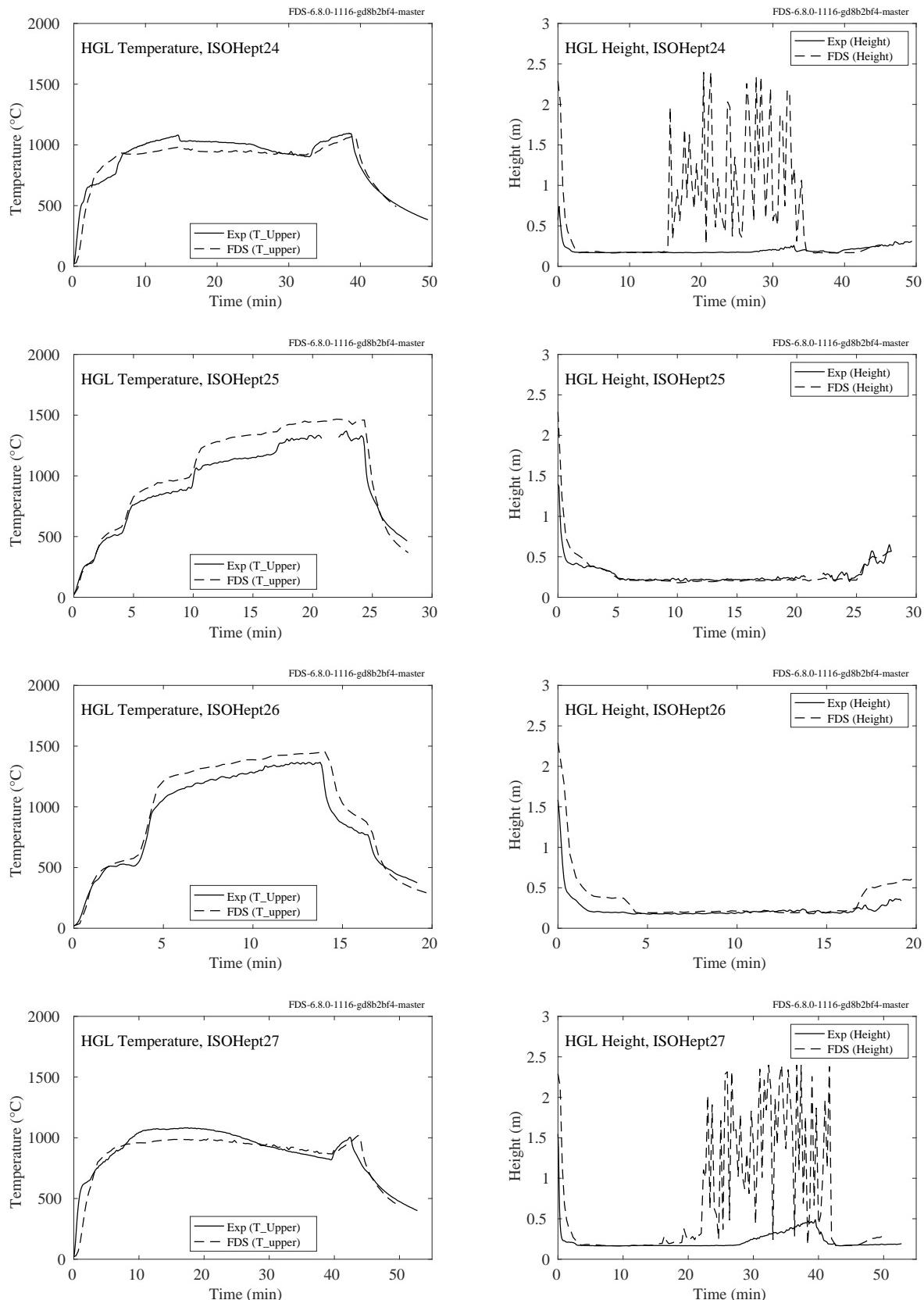


Figure 5.44: NIST FSE, HGL temperature and height, Tests 24-27.

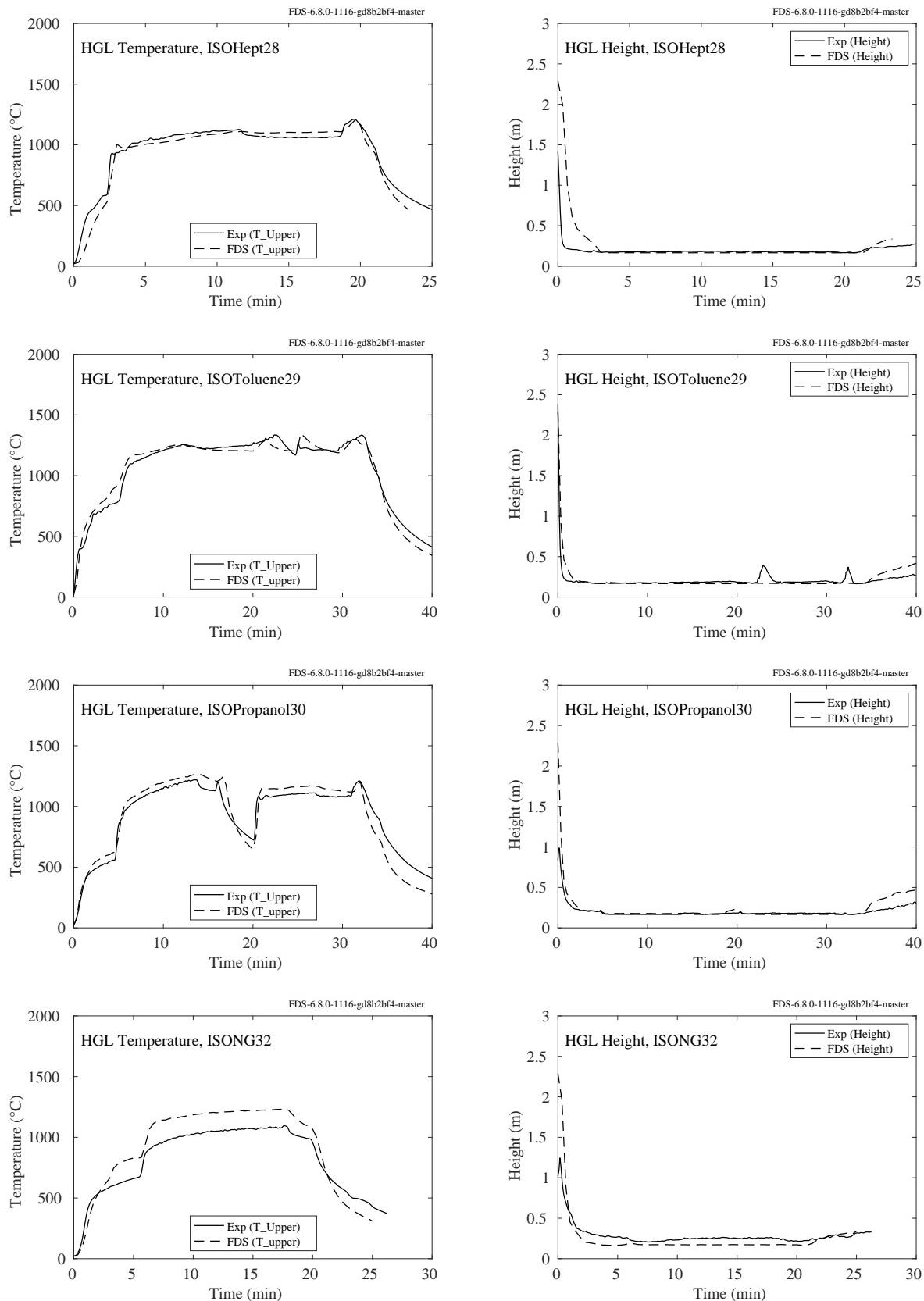


Figure 5.45: NIST FSE, HGL temperature and height, Tests 28-30, 32.

## 5.12 NIST/NRC Test Series

The NIST/NRC series consisted of 15 heptane spray fire experiments with varying heat release rates, pan locations, and ventilation conditions. Gas temperatures were measured using seven floor-to-ceiling thermocouple arrays (or “trees”) distributed throughout the compartment. The average hot gas layer temperature and height are calculated using thermocouple Trees 1, 2, 3, 5, 6 and 7. Tree 4 was not used because one of its thermocouples (TC 4-9) malfunctioned during most of the experiments. A few observations about the simulations:

- During Tests 4, 5, 10 and 16 a fan blew air into the compartment through a vent in the south wall. The measured velocity profile of the fan was not uniform, with the bulk of the air blowing from the lower third of the duct towards the ceiling at a roughly 45° angle. The exact flow pattern is difficult to replicate in the model, thus, the results for Tests 4, 5, 10 and 16 should be evaluated with this in mind. The effect of the fan on the hot gas layer is small, but it does have a some effect on target temperatures near the vent.
- For all of the tests involving a fan, the predicted HGL height increased after the fire was extinguished, while the measured HGL decreased. This appears to be a curious artifact of the layer reduction algorithm. It is not included in the calculation of the relative difference.
- In the closed door tests, the hot gas layer descended all the way to the floor. However, the reduction method, used on both the measured and predicted temperatures, does not account for the formation of a single layer, and therefore does not indicate that the layer drops all the way to the floor. This is neither a flaw in the measurements nor in FDS, but rather in the layer reduction method.
- The HGL reduction method produces spurious results in the first few minutes of each test because no clear layer has yet formed. These early times are not included in the relative difference calculation.

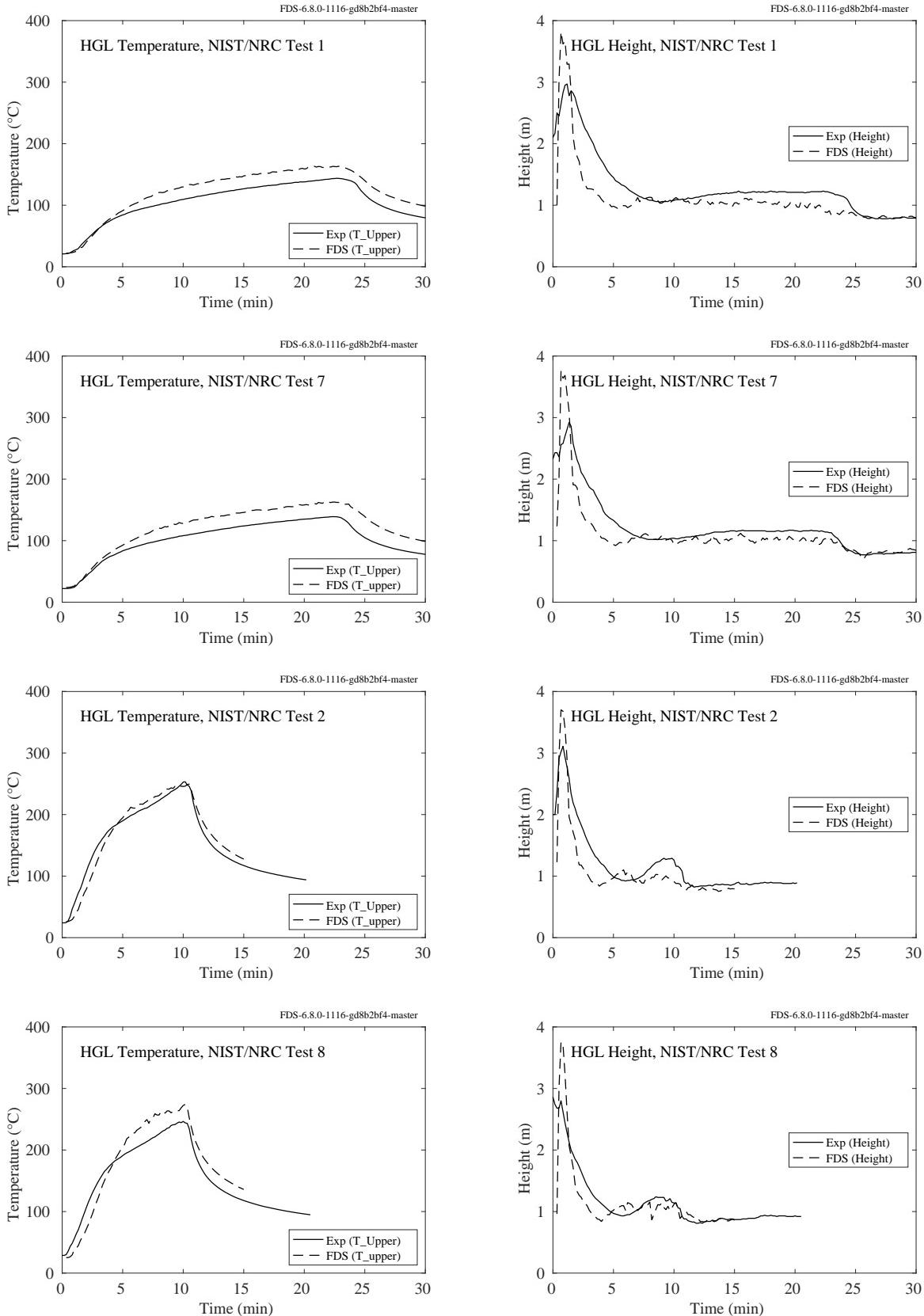


Figure 5.46: NIST/NRC experiments, HGL temperature and height, Tests 1-2, 7-8.

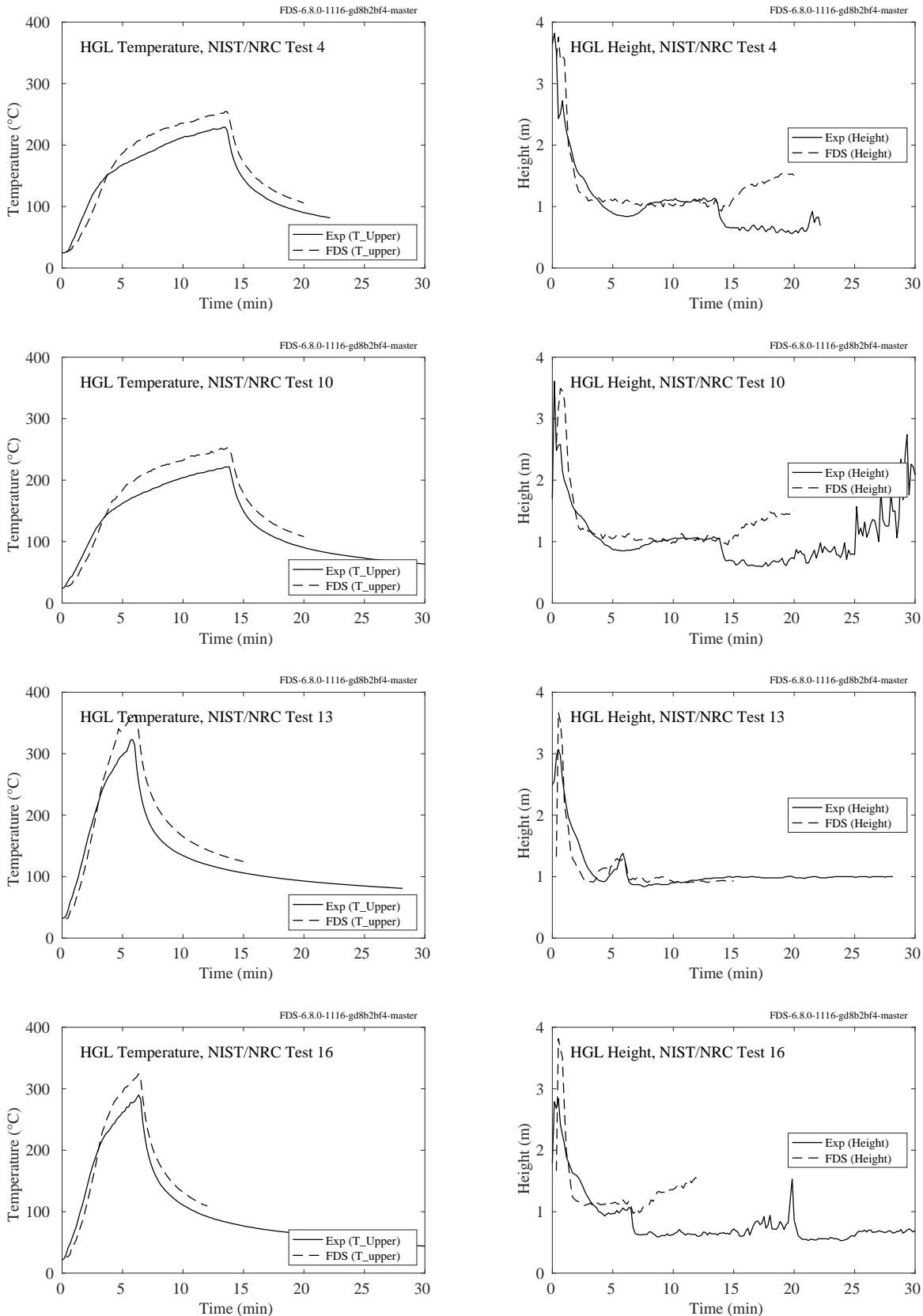
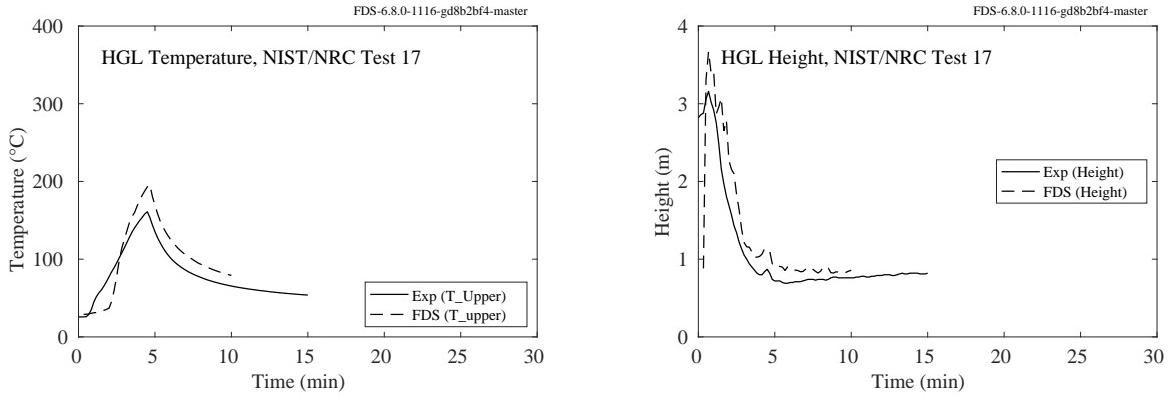


Figure 5.47: NIST/NRC experiments, HGL temperature and height, Tests 4, 10, 13, 16.



Open door tests to follow

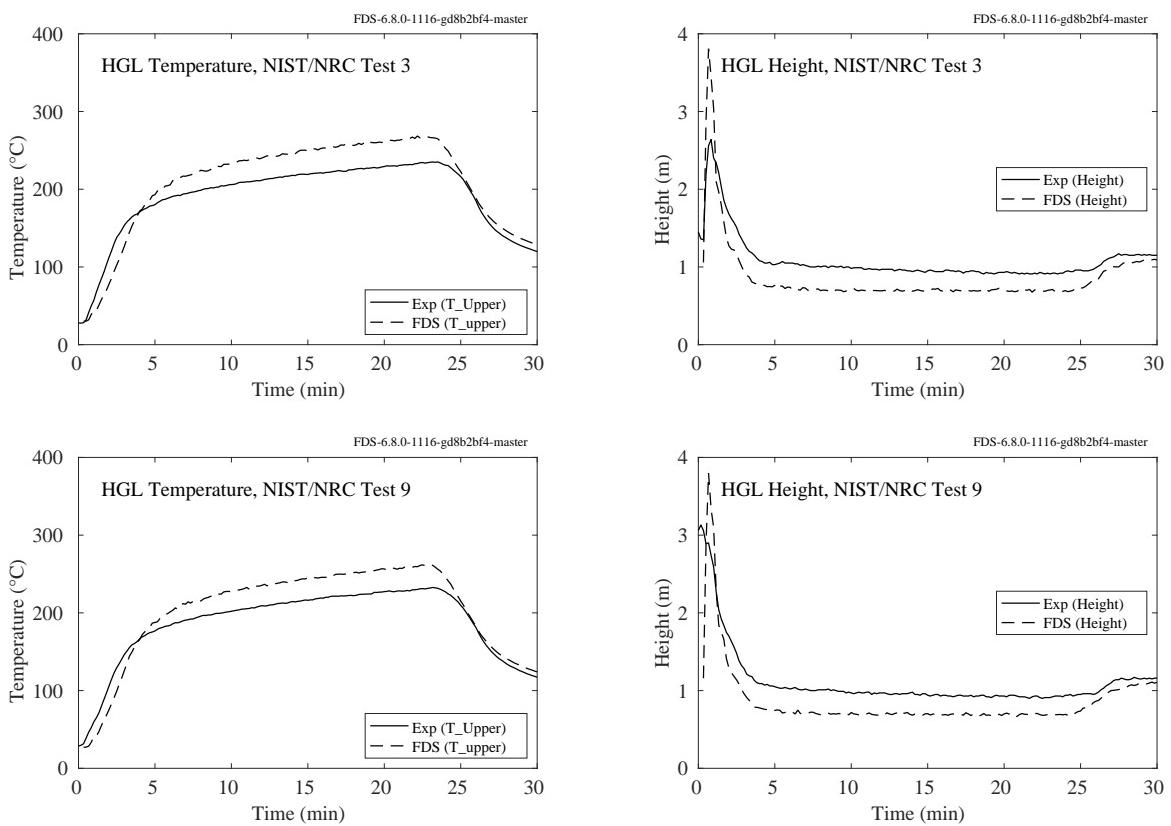


Figure 5.48: NIST/NRC experiments, HGL temperature and height, Tests 3, 9, 17.

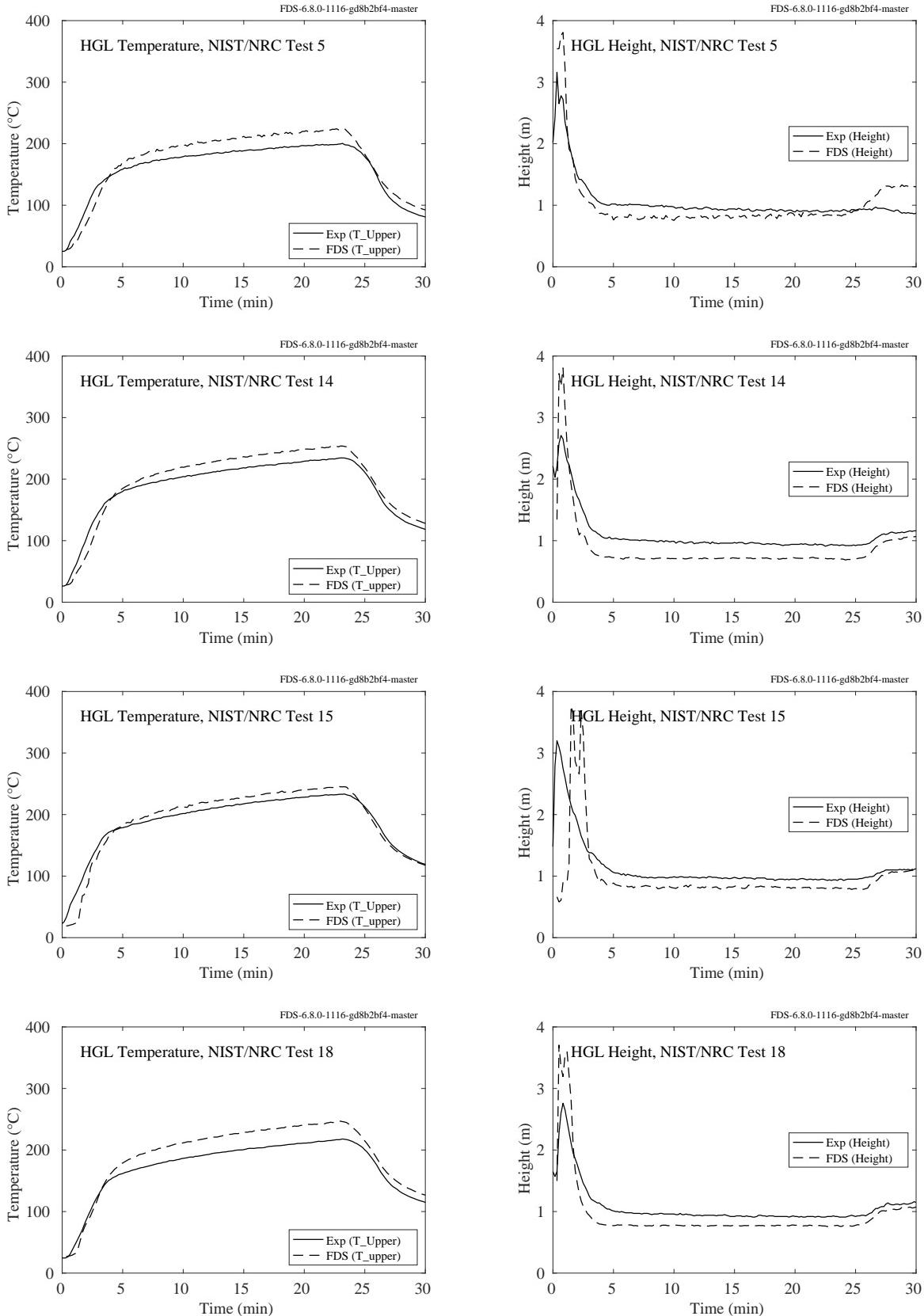


Figure 5.49: NIST/NRC experiments, HGL temperature and height, Tests 5, 14, 15, 18.

## 5.13 NIST/NRC Corner Effects Experiments

The plots on the following pages compare hot gas layer temperatures and heights in a large compartment where corner, wall, and cabinet effects experiments were conducted. The corner and wall experiments involved a 60 cm by 60 cm natural gas burner with heat release rates of 200 kW, 300 kW, and 400 kW. The burner was either set in a corner or against a wall. The cabinet experiments involved gas burners set in one of two mock steel cabinets, with a variety of heat release rates.

In all experiments, two vertical thermocouple arrays were placed along the centerline of the room, each one-third of the room length from each respective short wall. The arrays each had 13 bare-bead thermocouples. The first was 2 cm below the ceiling, and the rest were spaced 30 cm apart.

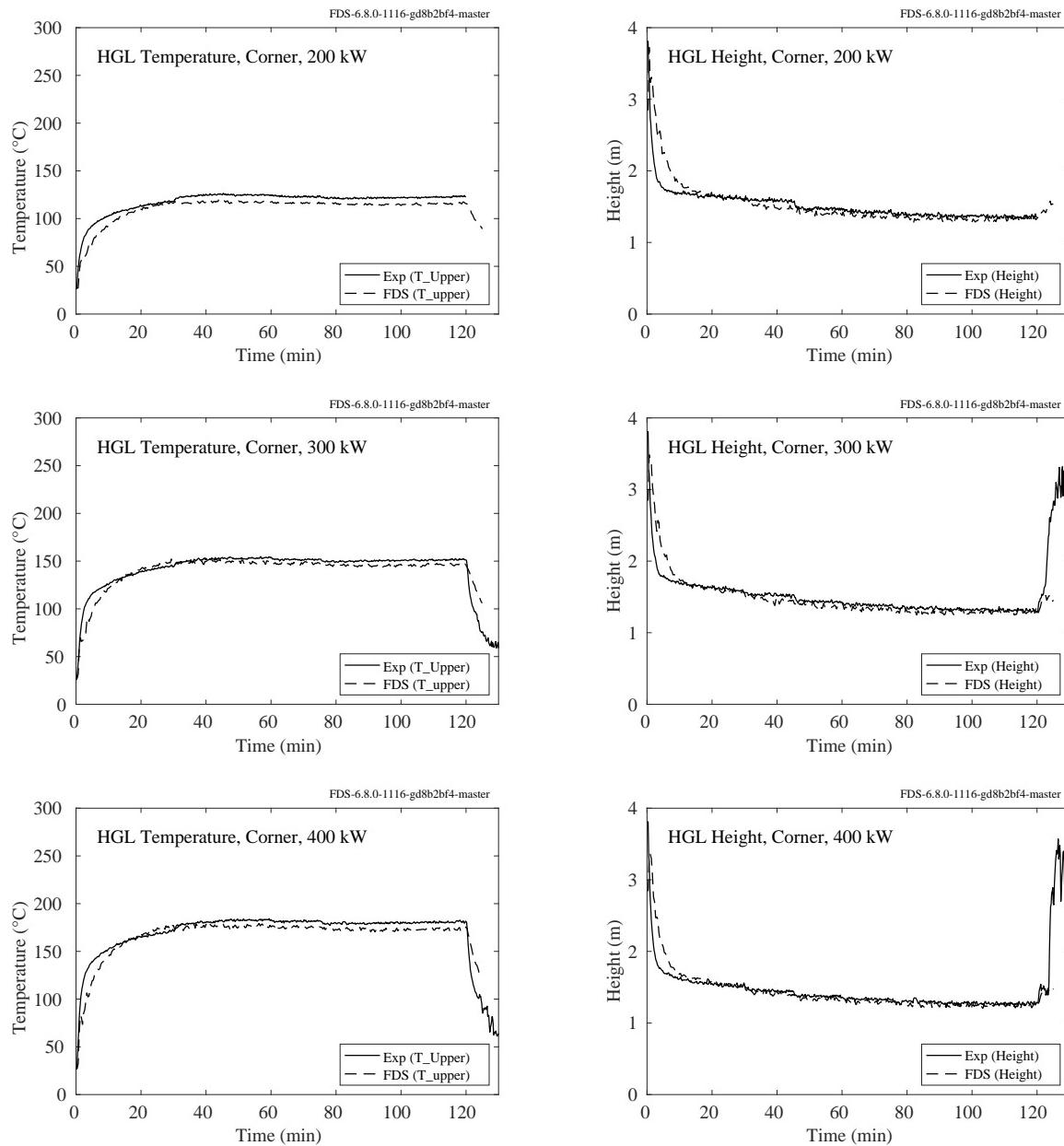


Figure 5.50: NIST/NRC Corner Effects experiments, HGL temperature and height, corner experiments.

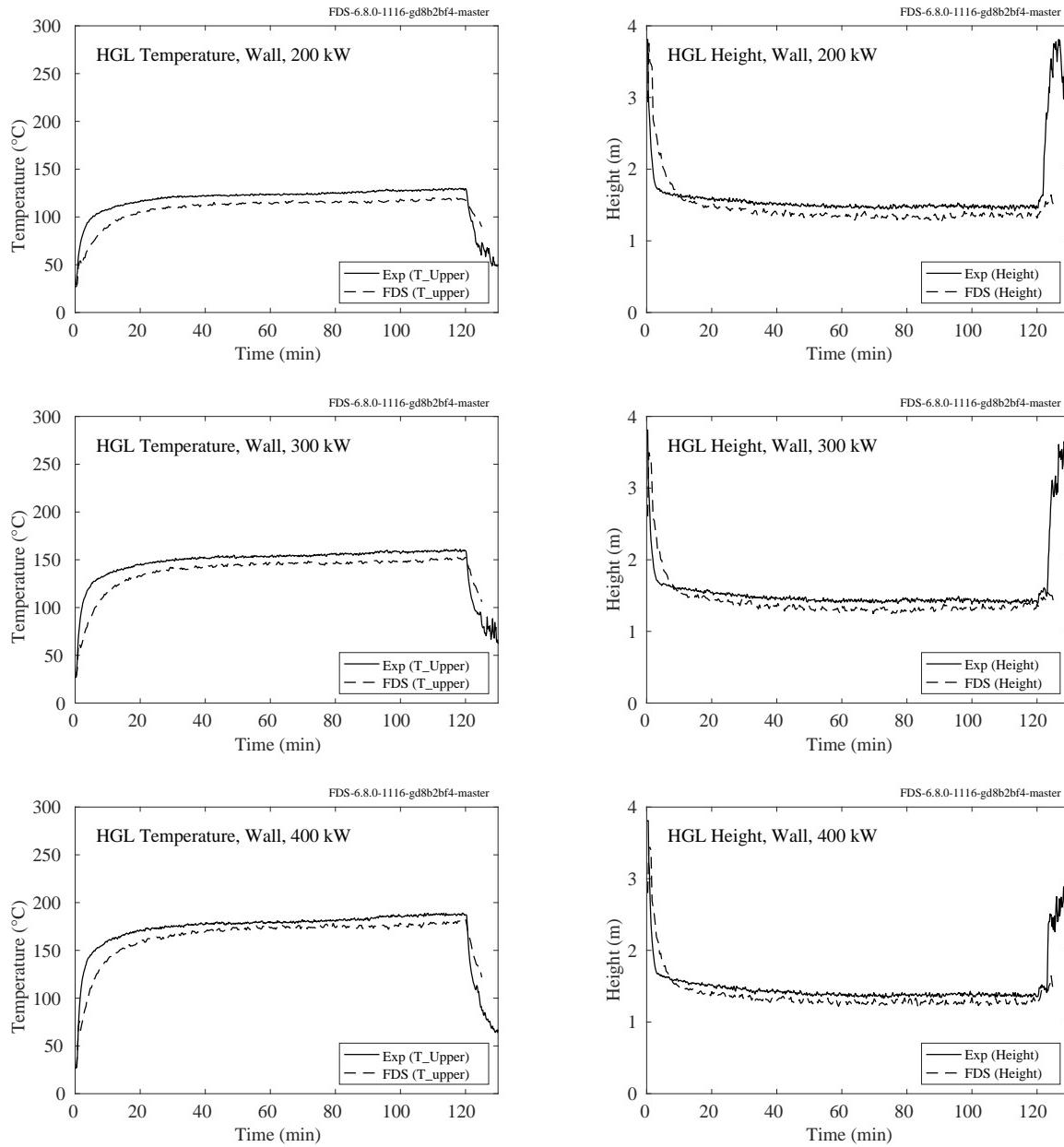


Figure 5.51: NIST/NRC Corner Effects experiments, HGL temperature and height, wall experiments.

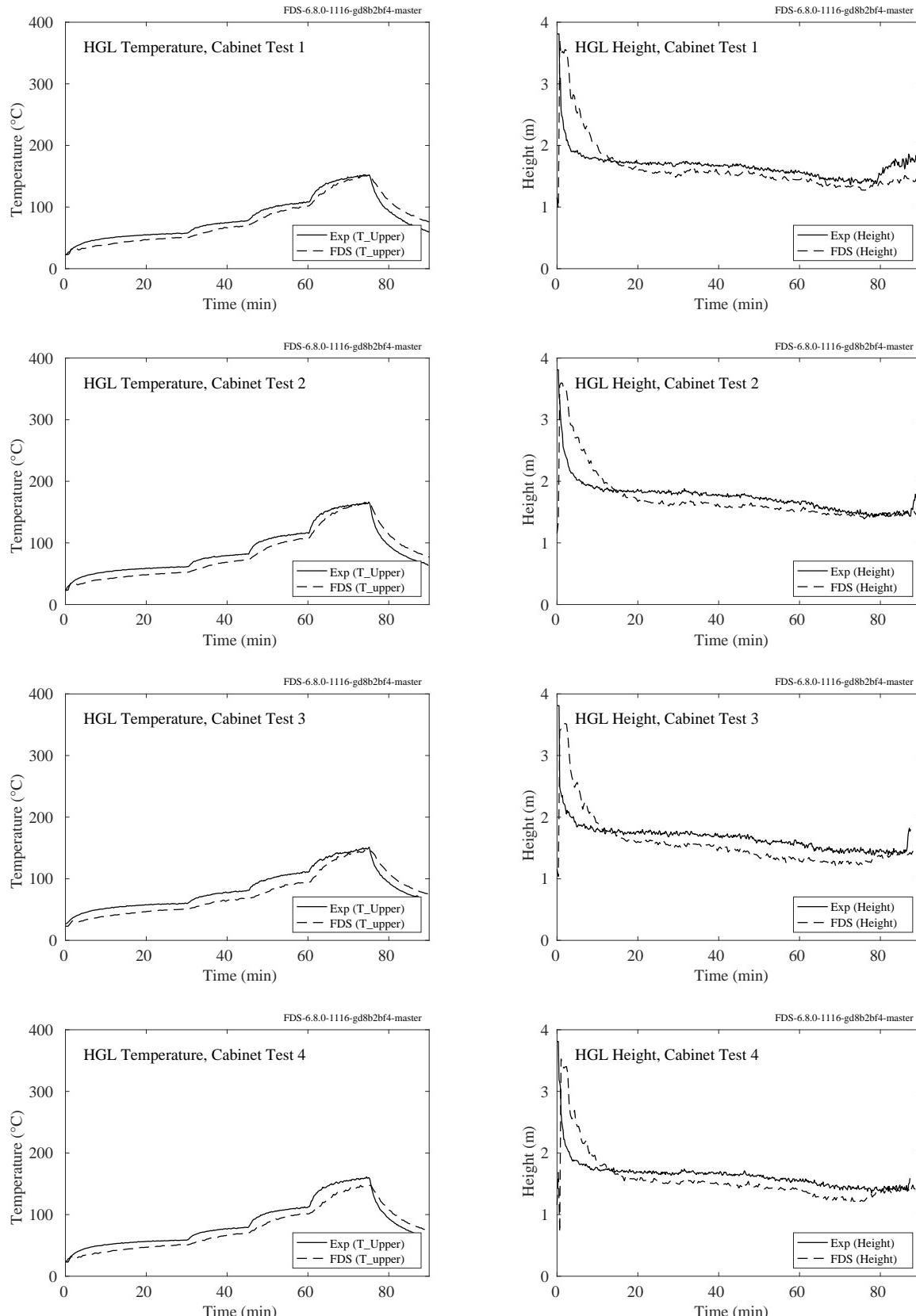


Figure 5.52: NIST/NRC Corner Effects experiments, HGL temperature and height, cabinet experiments 1-4.

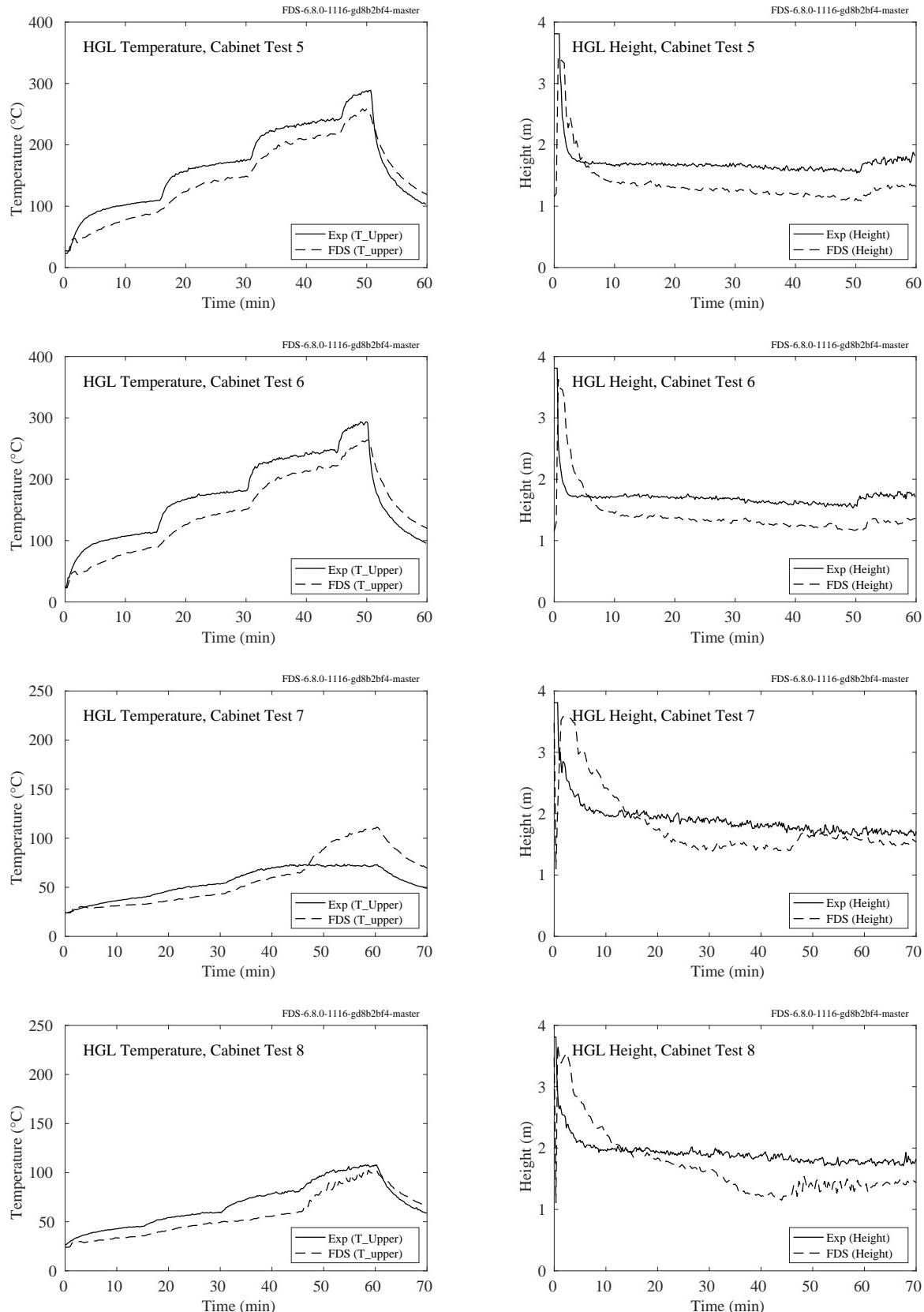


Figure 5.53: NIST/NRC Corner Effects experiments, HGL temperature and height, cabinet experiments 5-8.

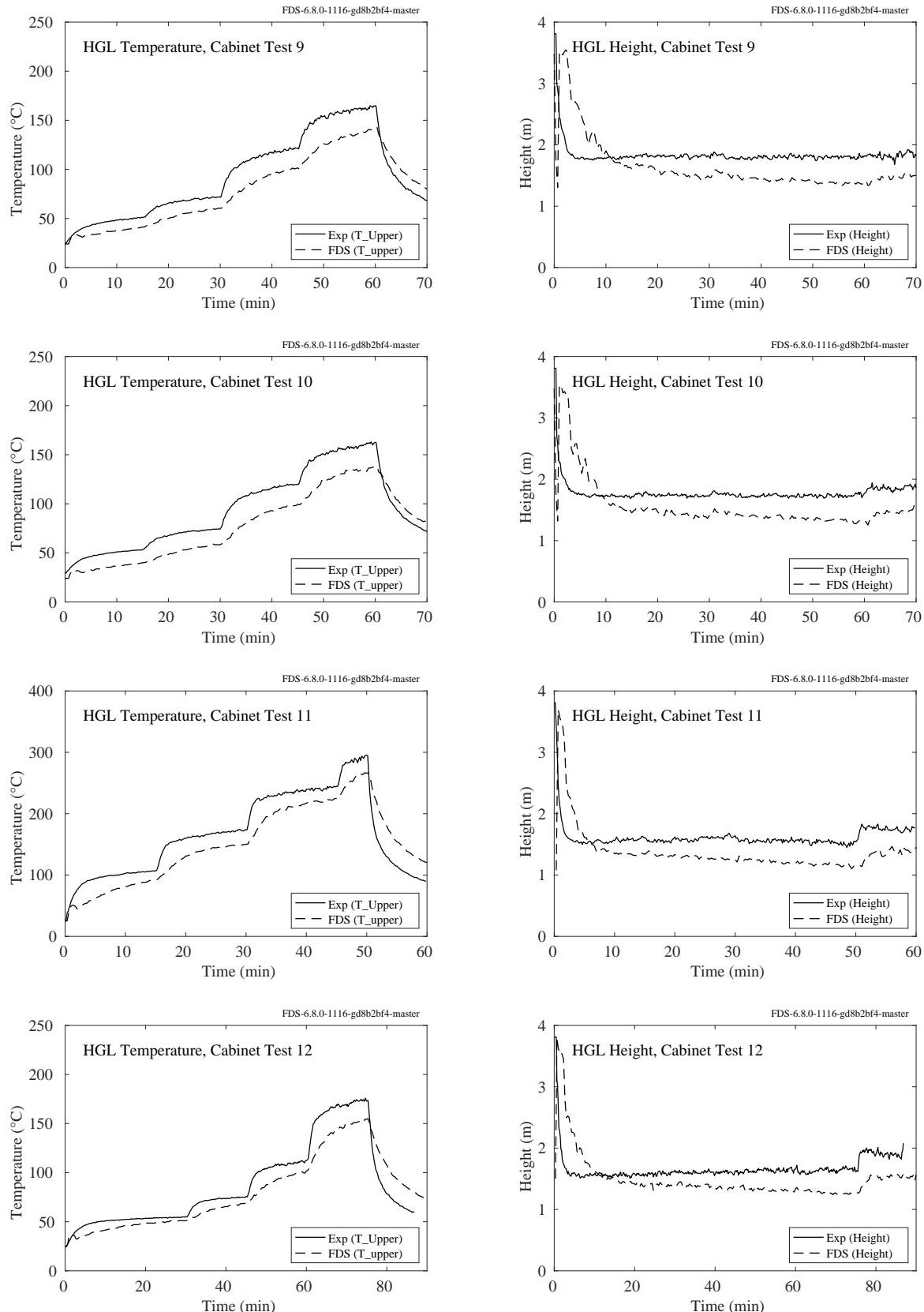


Figure 5.54: NIST/NRC Corner Effects experiments, HGL temperature and height, cabinet experiments 9-12.

## 5.14 NIST Vent Study

These experiments were performed in a small-scale two floor enclosure, with each floor connected by one or two ceiling vents. Each floor contained a vertical array of eight sheathed thermocouples at distances below the ceiling of 5, 10, 15, 20, 25, 30, 40, and 50 cm. Fifteen experiments were performed, but only 12 were modeled because three experiments involved a circular vent rather than square which could not be distinguished in the FDS simulations. The results of these experiments were nearly identical.

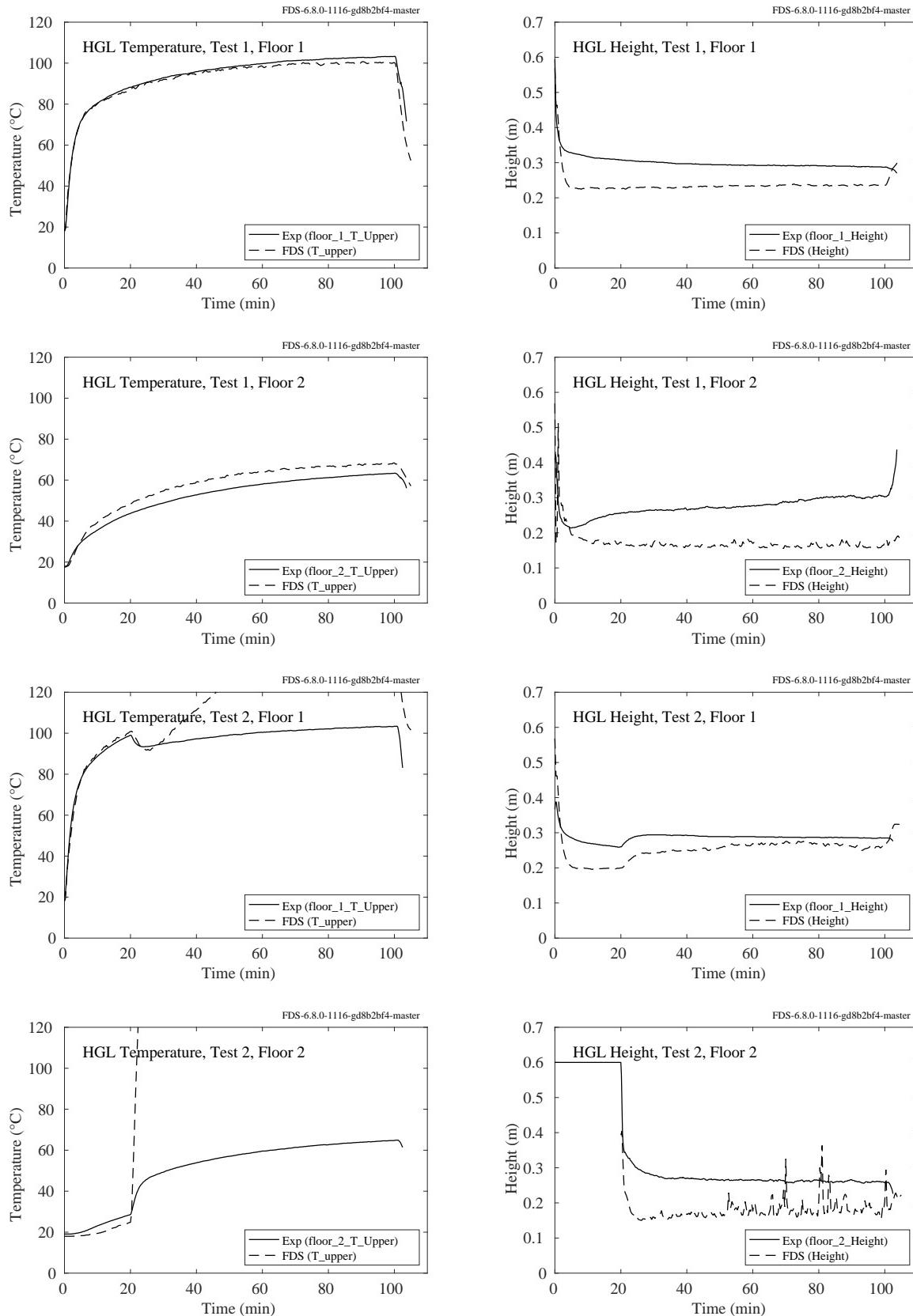


Figure 5.55: NIST Vent Study, HGL temperature and height, Tests 1 and 2.

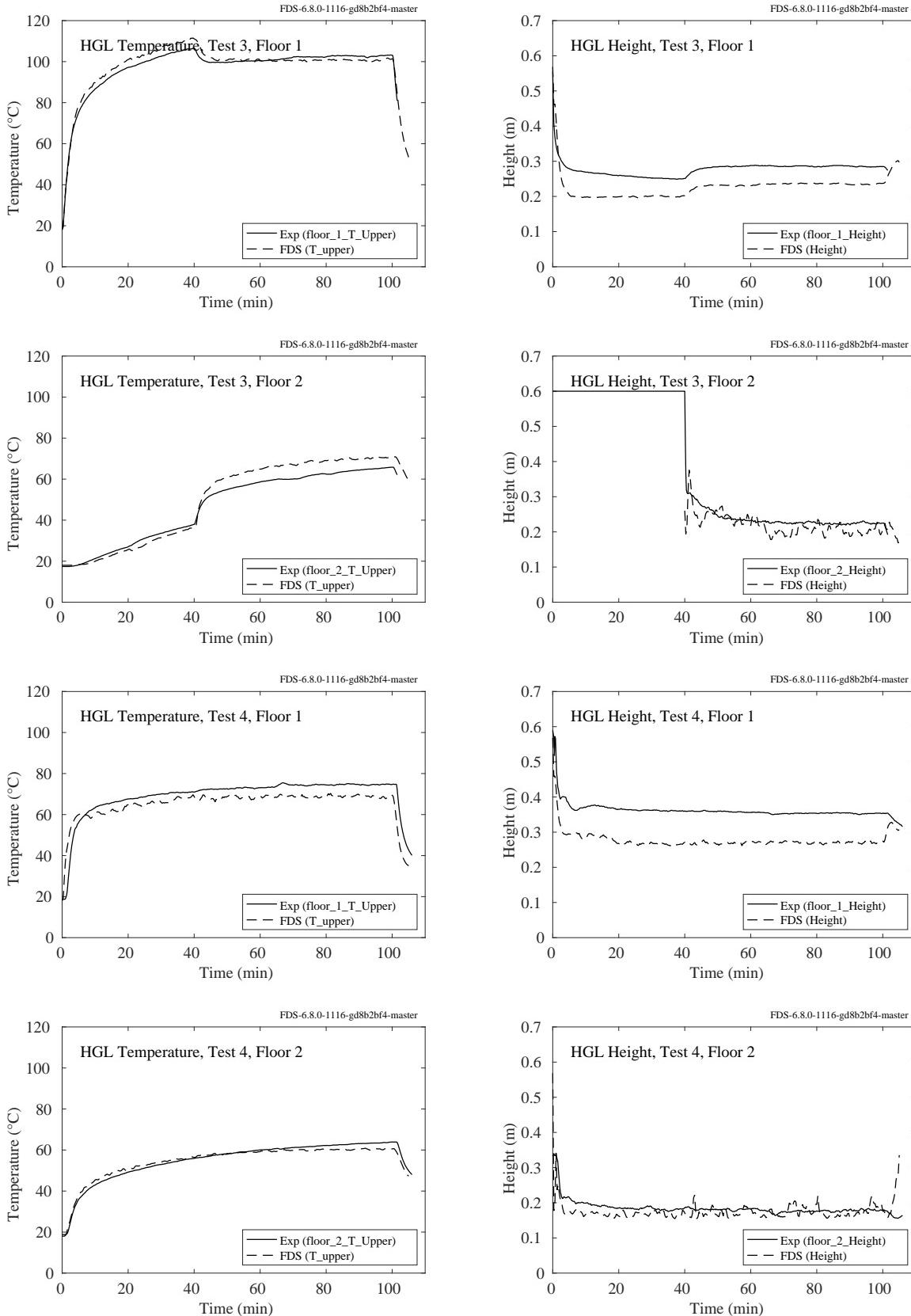


Figure 5.56: NIST Vent Study, HGL temperature and height, Tests 3 and 4.

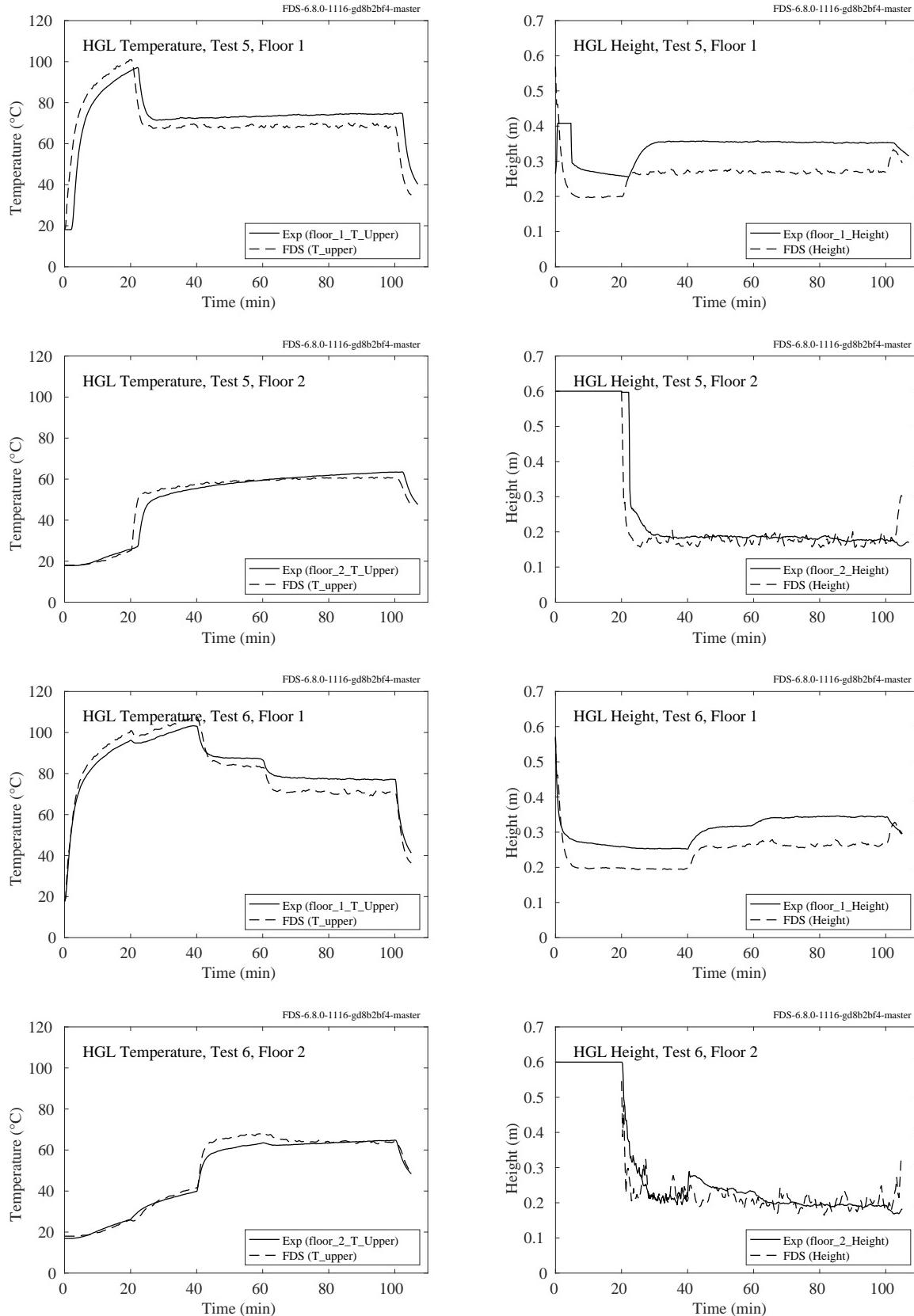


Figure 5.57: NIST Vent Study, HGL temperature and height, Tests 5 and 6.

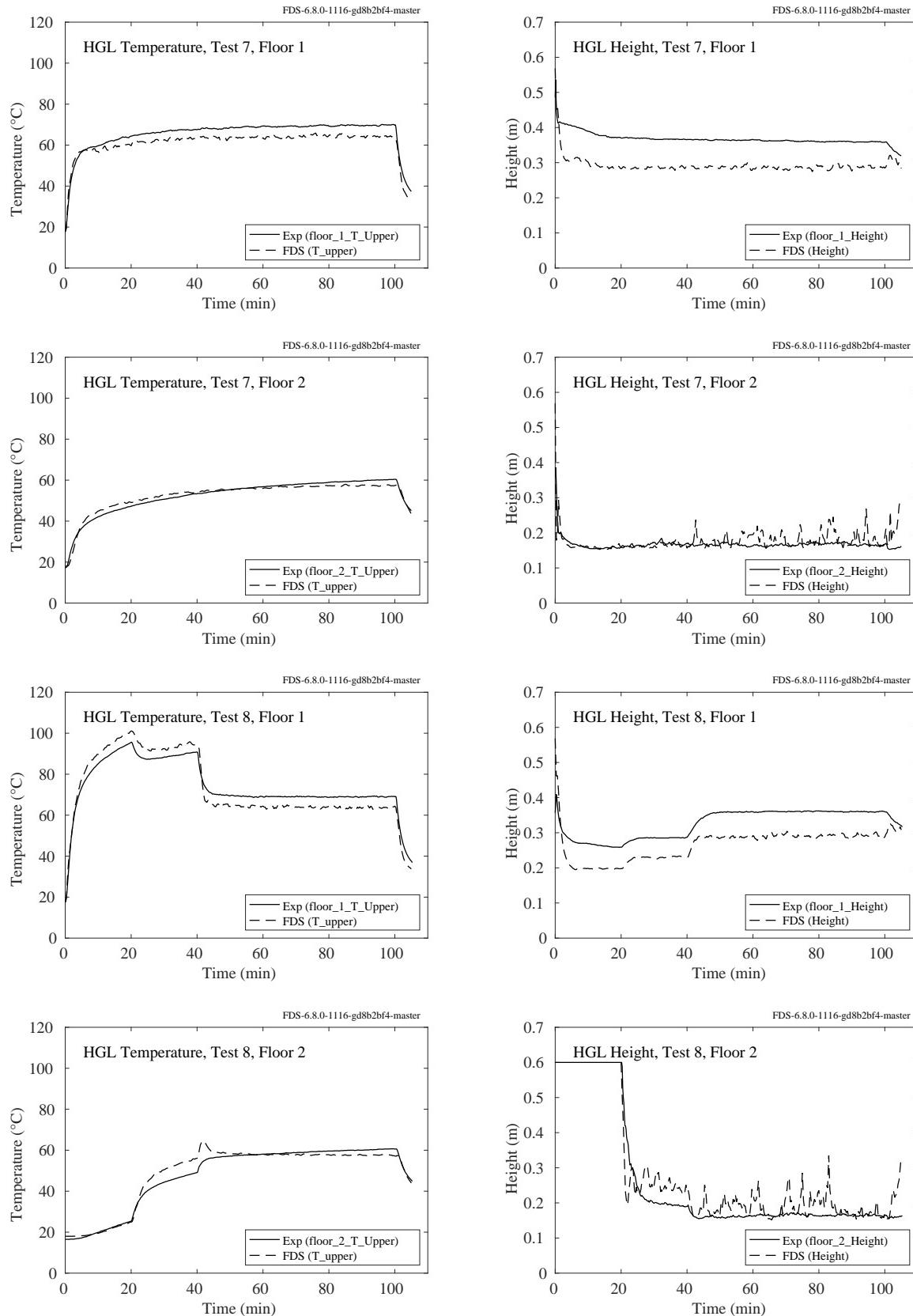


Figure 5.58: NIST Vent Study, HGL temperature and height, Tests 7 and 8.

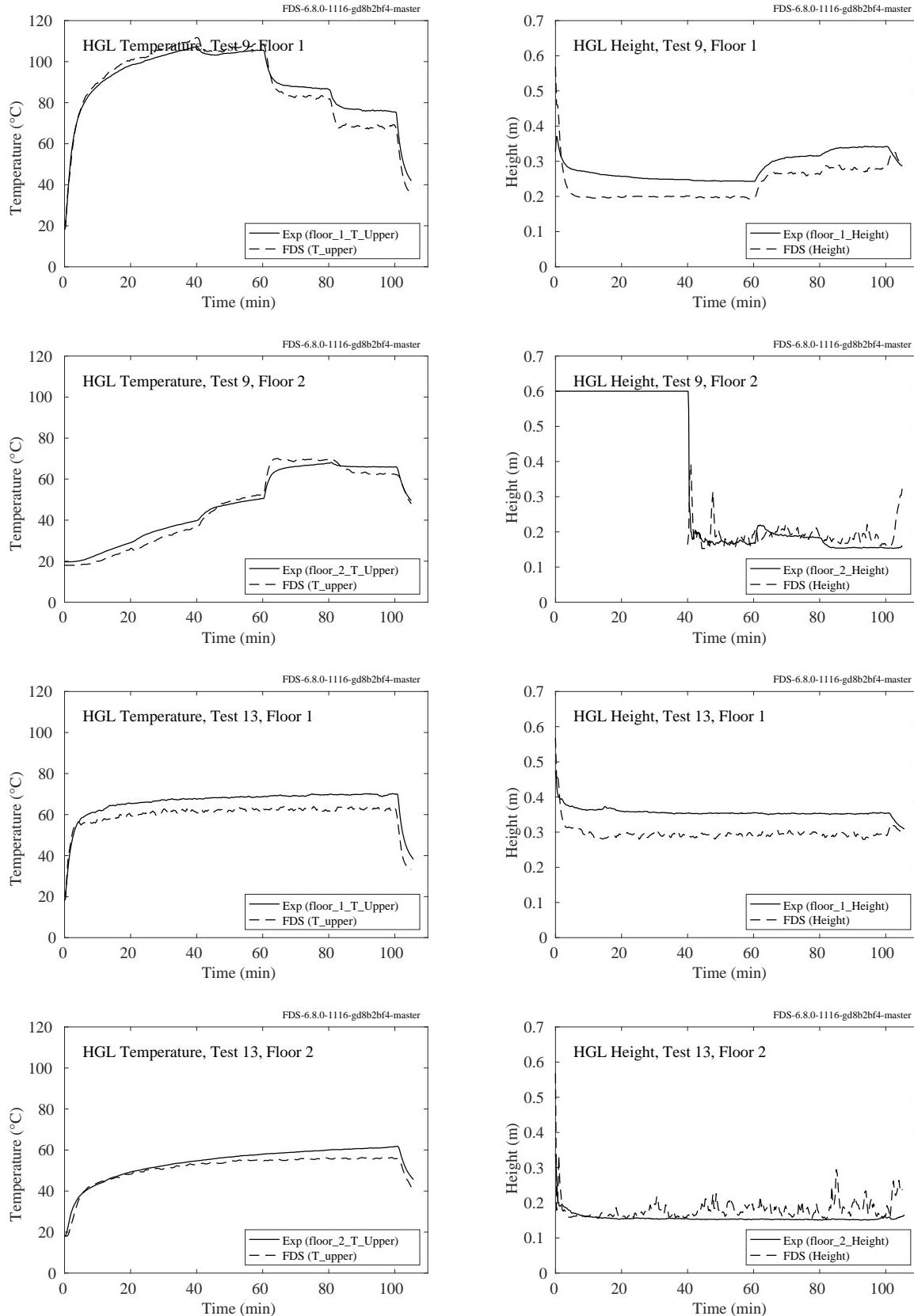


Figure 5.59: NIST Vent Study, HGL temperature and height, Tests 9 and 13.

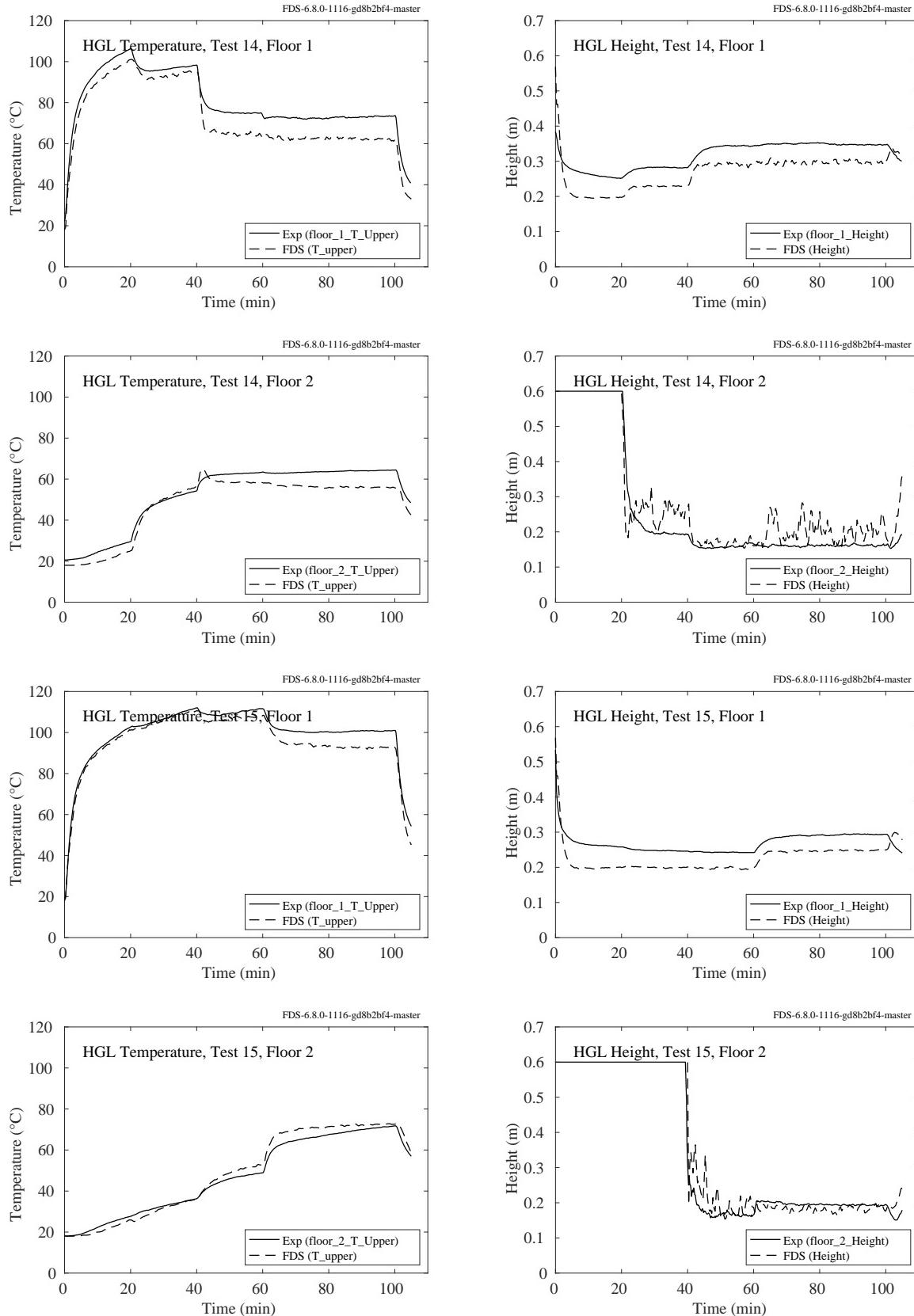


Figure 5.60: NIST Vent Study, HGL temperature and height, Tests 14 and 15.

## 5.15 NRCC Smoke Tower

In the NRCC Smoke Tower experiments, there was a vertical array consisting of thirteen TCs that were installed in the fire compartment on the second floor at the following heights: 0.62 m, 0.92 m, 1.22 m, 1.37 m, 1.52 m, 1.67 m, 1.82 m, 1.97 m, 2.12 m, 2.27 m, 2.42 m, 2.57 m and 2.95 m. Also, five TCs were installed in the doorway between the stair vestibule and stair shaft on the second floor. Figure 5.61 shows the predicted and measured HGL temperature for both vertical arrays.

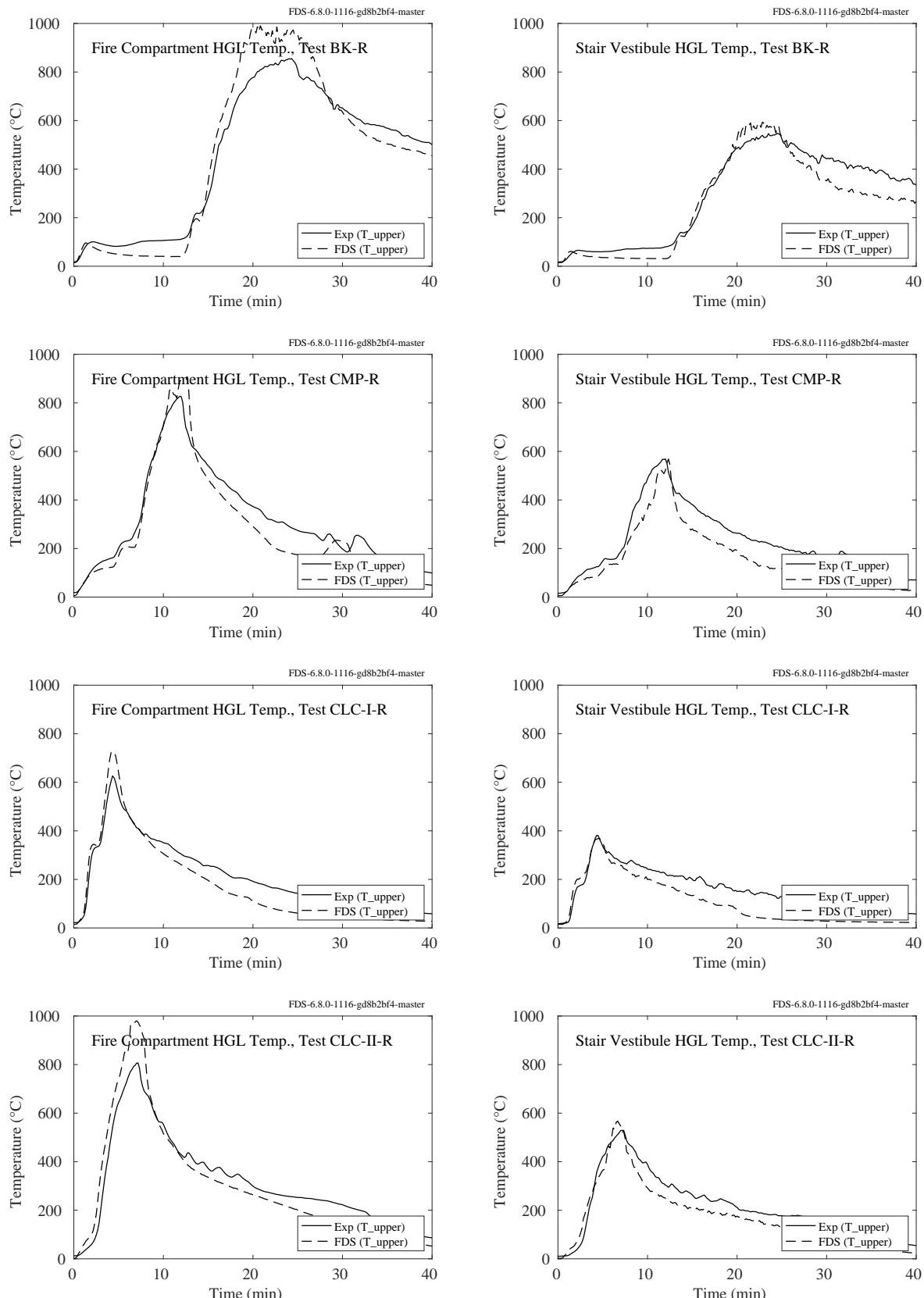


Figure 5.61: NRCC Smoke Tower experiments, HGL temperature in the fire room and stair vestibule.

## 5.16 PRISME DOOR Experiments

The compartments in the PRISME DOOR experiments contained vertical arrays of thermocouples to measure the HGL temperature and depth. Each array contained 18 TCs and each compartment included three arrays. The array above the fire was excluded from the calculation of the HGL temperature and depth.

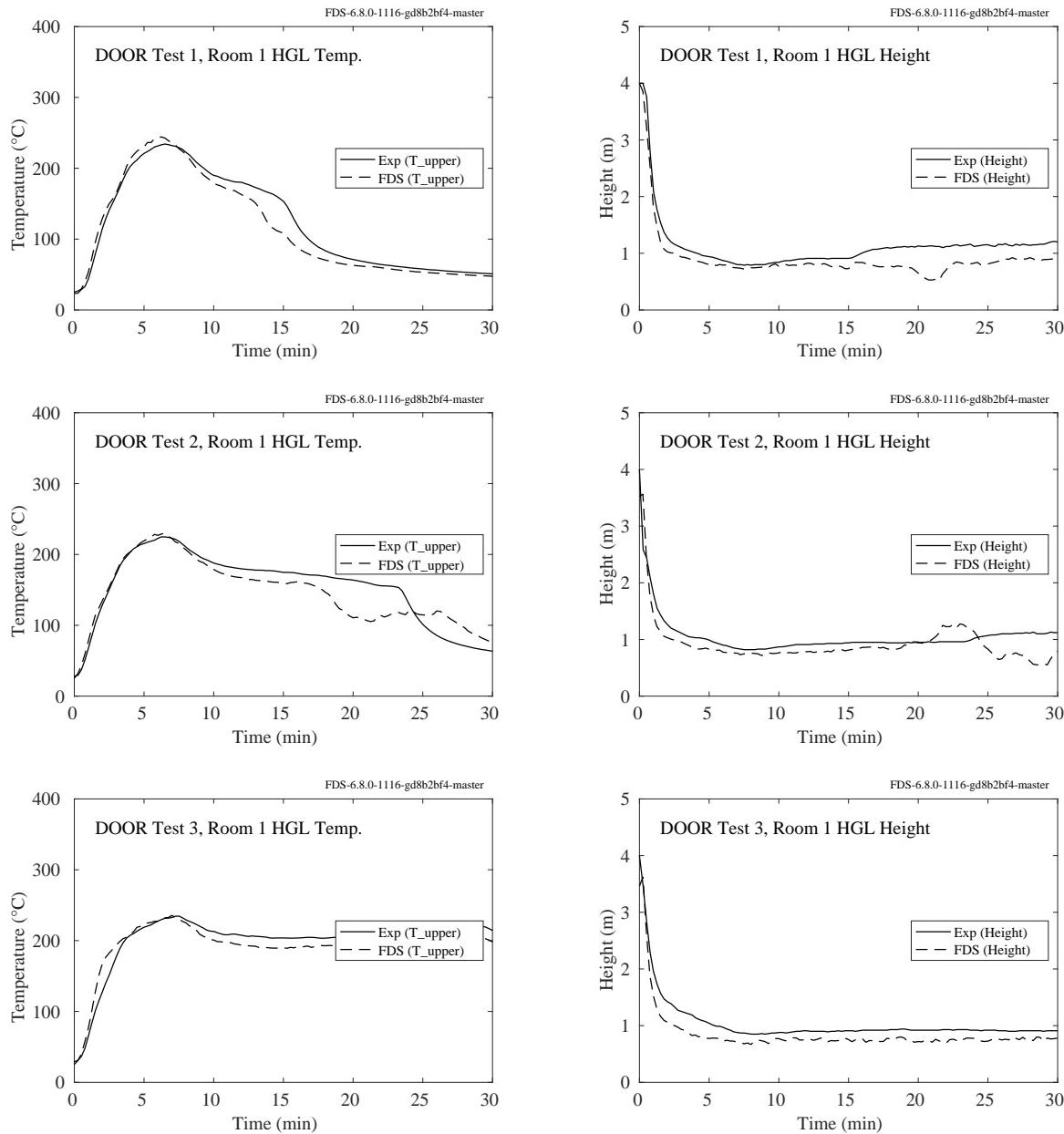


Figure 5.62: PRISME DOOR experiments, HGL temperature and height, Room 1, Tests 1-3.

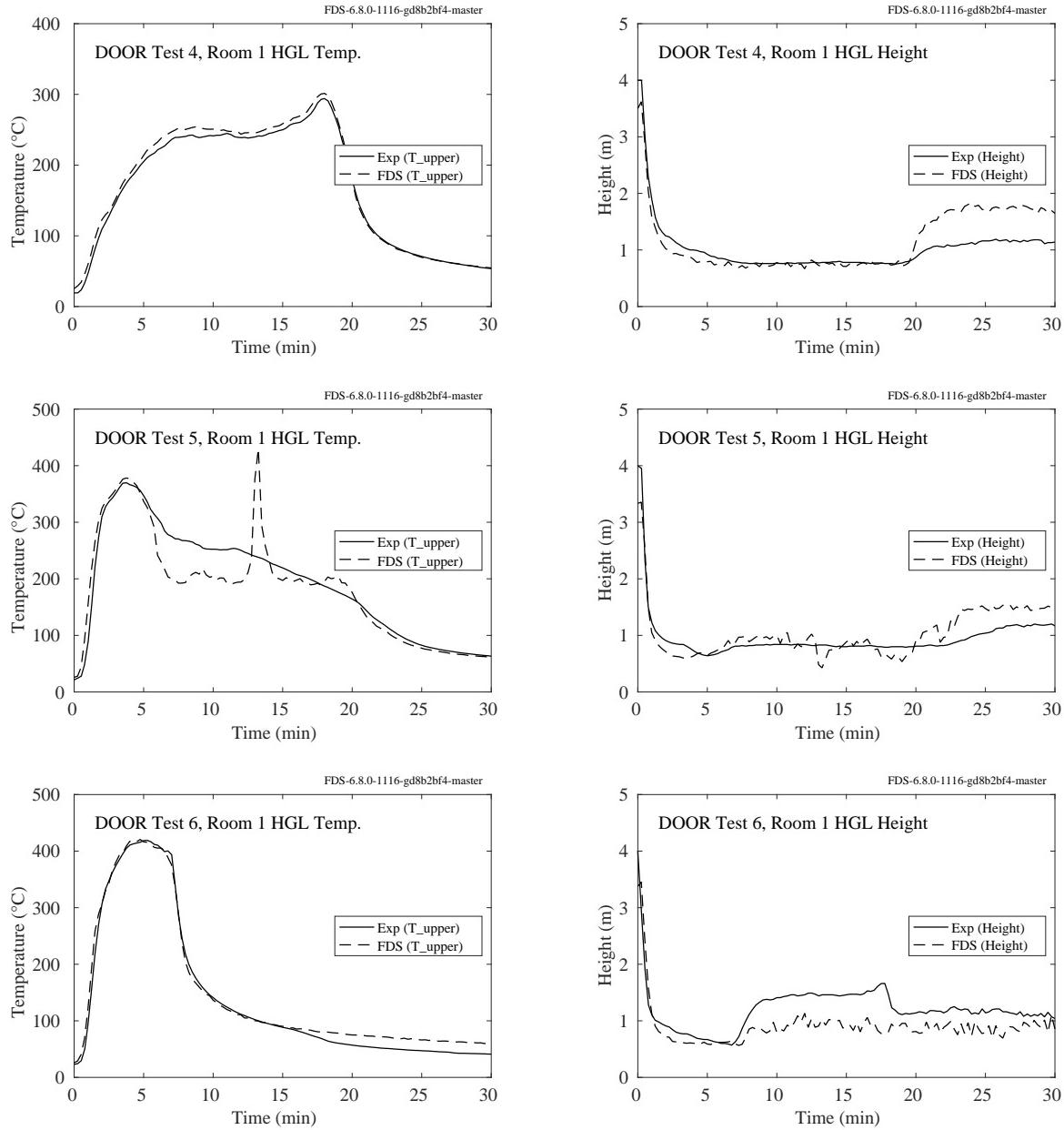


Figure 5.63: PRISME DOOR experiments, HGL temperature and height, Room 1, Tests 4-6.

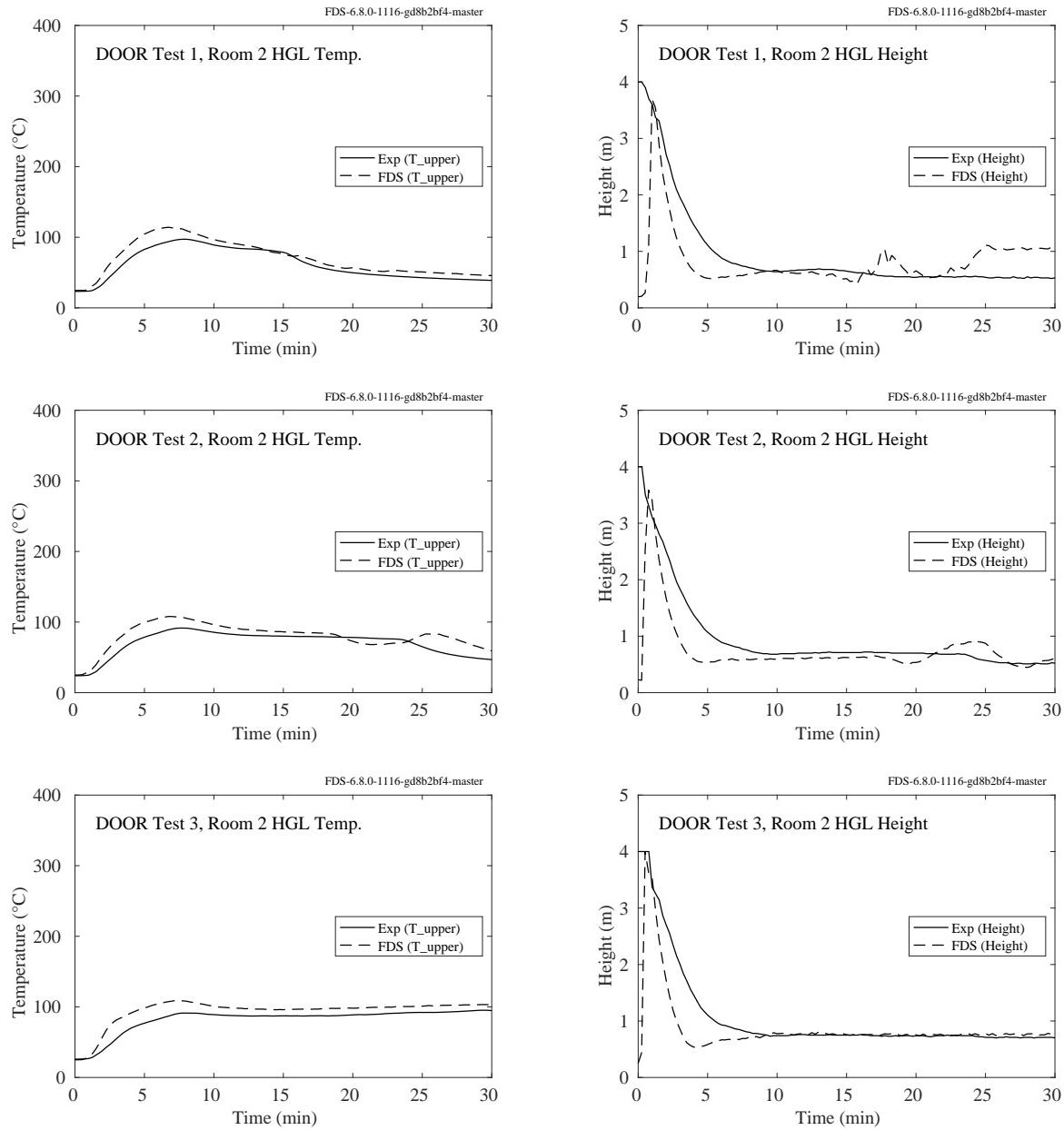


Figure 5.64: PRISME DOOR experiments, HGL temperature and height, Room 2, Tests 1-3.

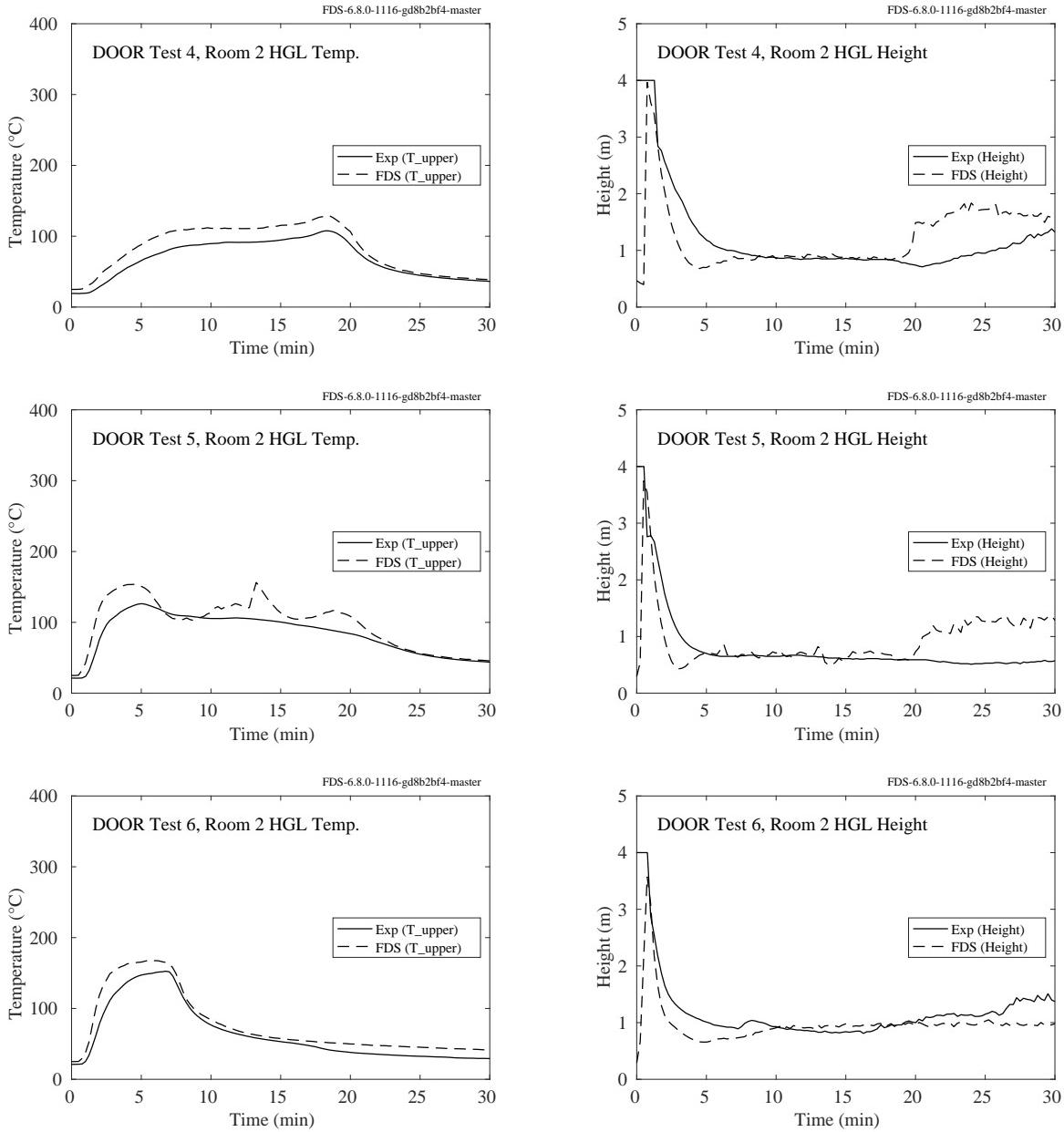


Figure 5.65: PRISME DOOR experiments, HGL temperature and height, Room 1, Tests 4-6.

## **5.17 PRISME SOURCE Experiments**

The PRISME SOURCE experiments were conducted in a single compartment connected to an HVAC network. The compartment was 5 m by 6 m by 4 m high. The HGL temperature was computed from a single vertical thermocouple array located in the northeast quadrant of the compartment. The array contained 18 TCs; the highest one 0.1 m below the ceiling.

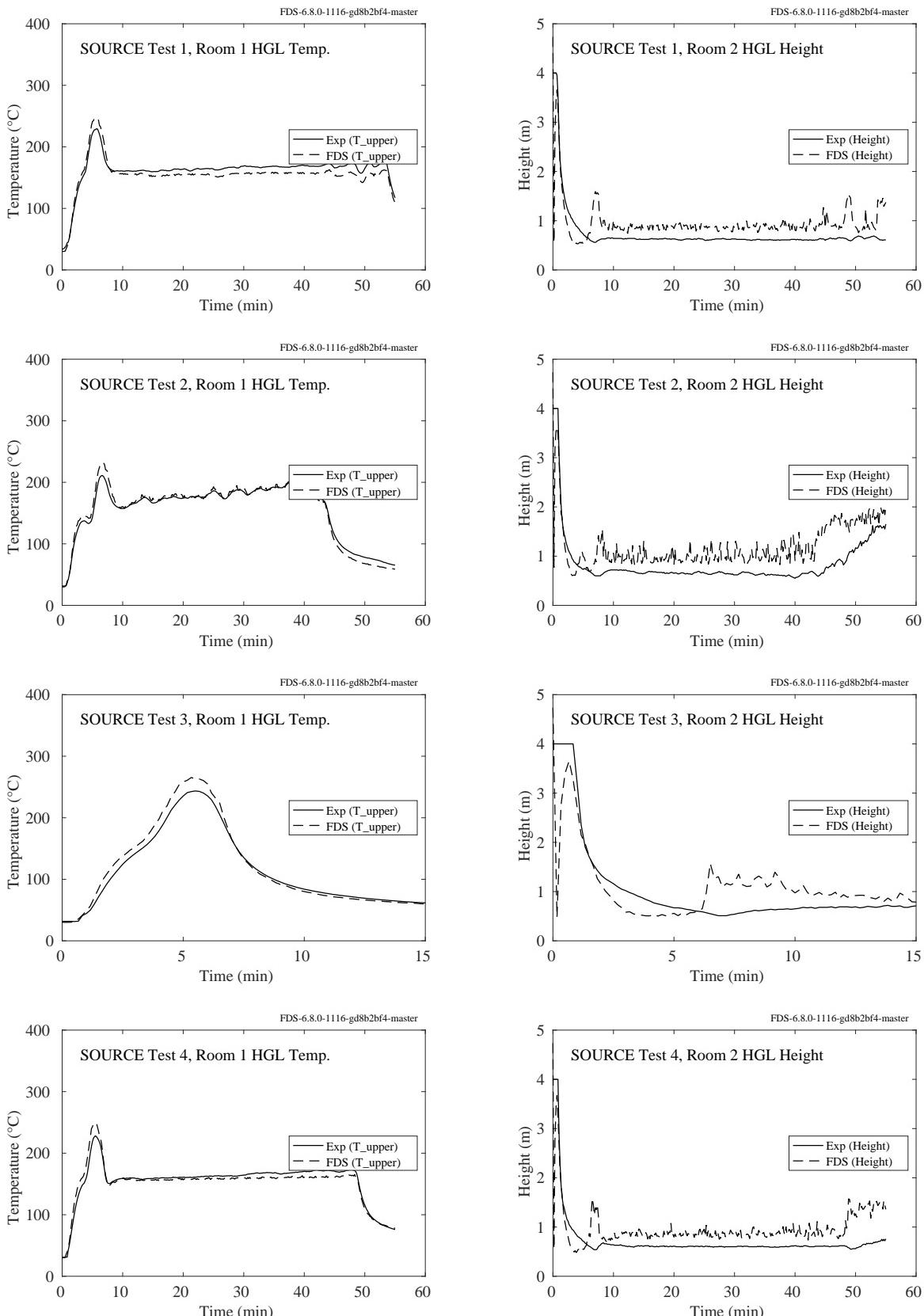


Figure 5.66: PRISME SOURCE experiments, HGL temperature and height, Room 2, Tests 1-4.

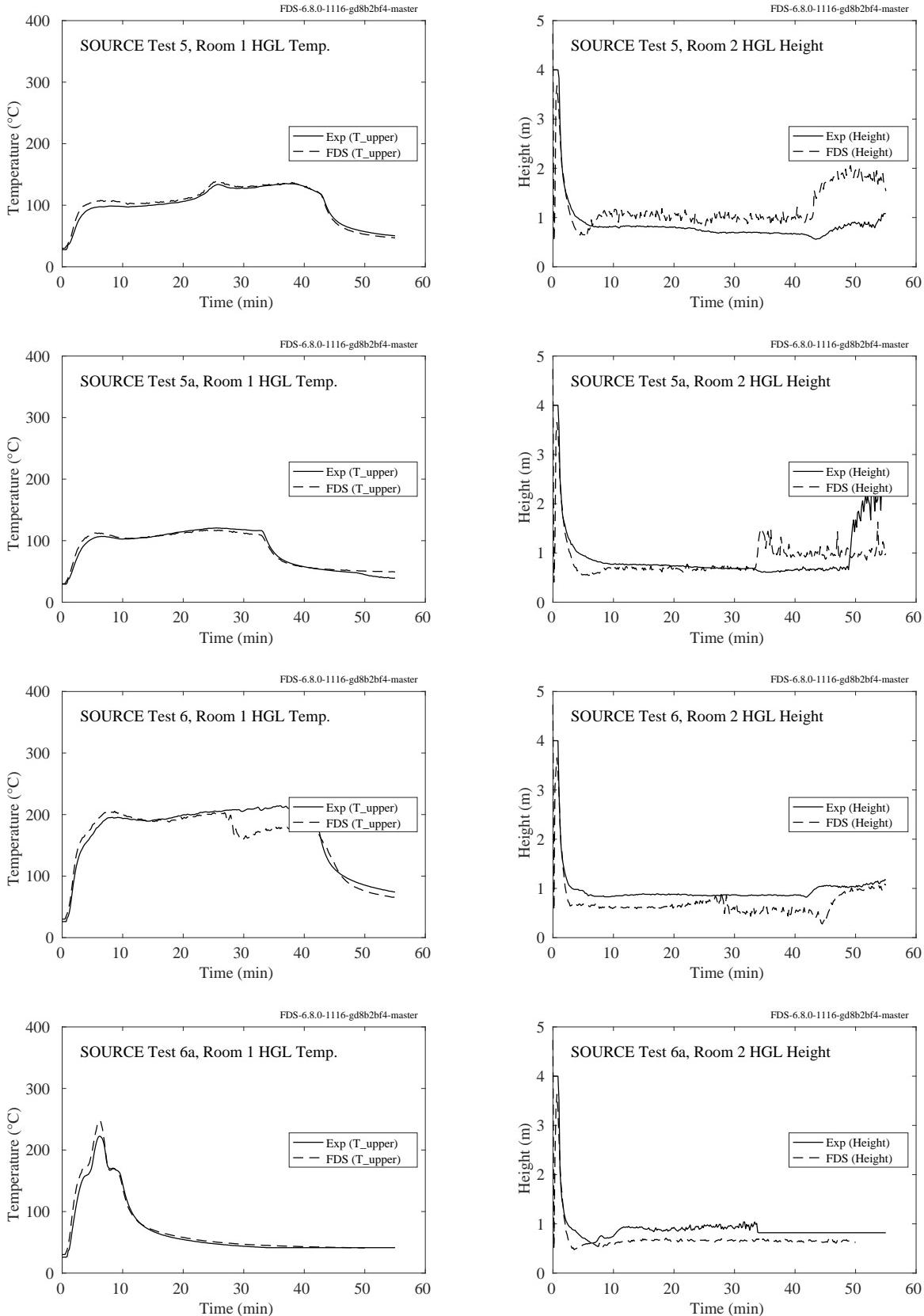


Figure 5.67: PRISME SOURCE experiments, HGL temperature and height, Room 2, Tests 5-6.

## 5.18 Steckler Compartment Experiments

Steckler et al. [319] mapped the doorway/window flows in 55 compartment fire experiments. The test matrix is presented in Table 3.38. Shown on the following pages are the temperature profiles inside the compartment compared with model predictions. To quantify the difference between prediction and measurement, the maximum temperatures were compared.

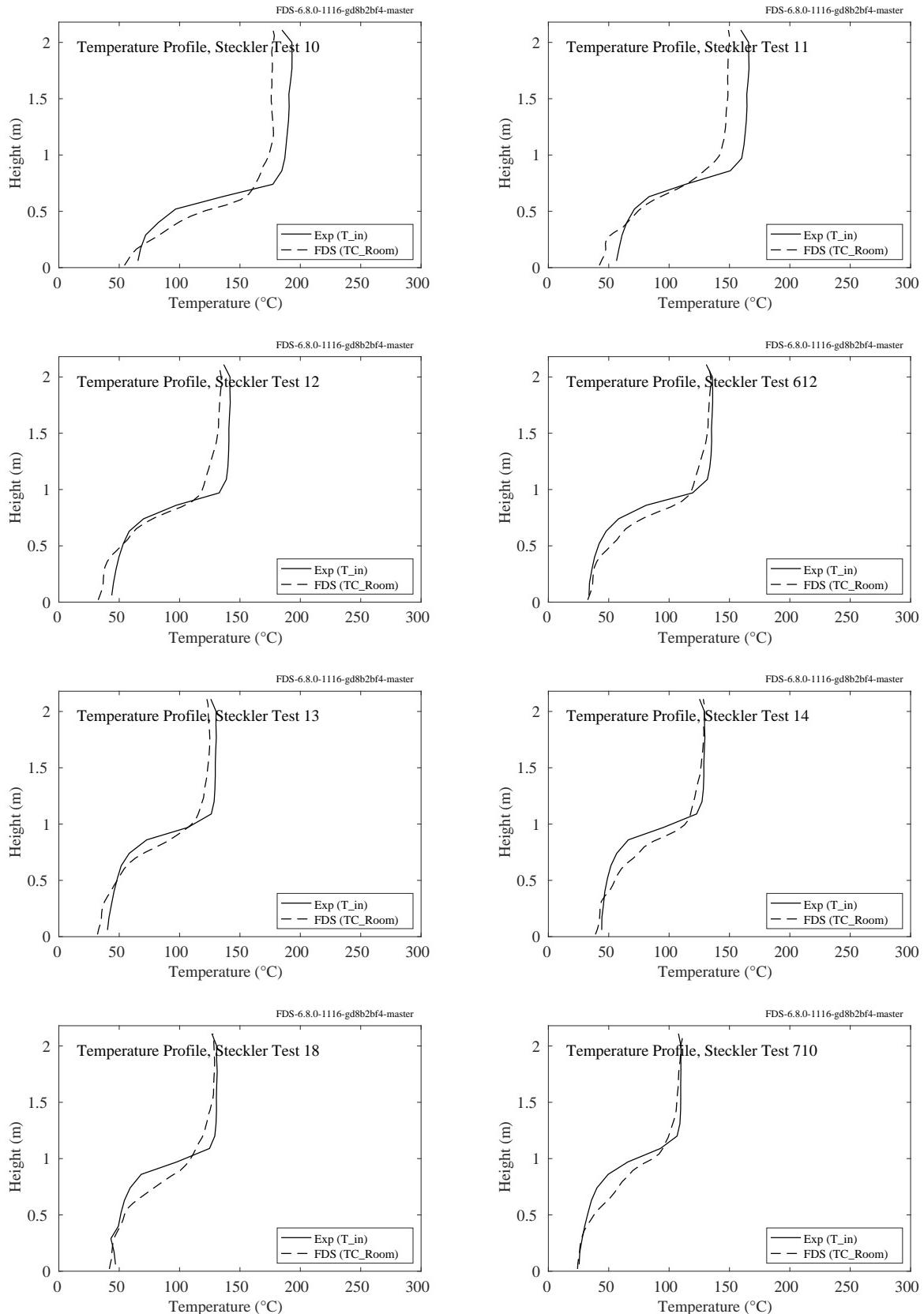


Figure 5.68: Steckler experiments, HGL temperature, Tests 10, 11, 12, 13, 14, 18, 612, 710.

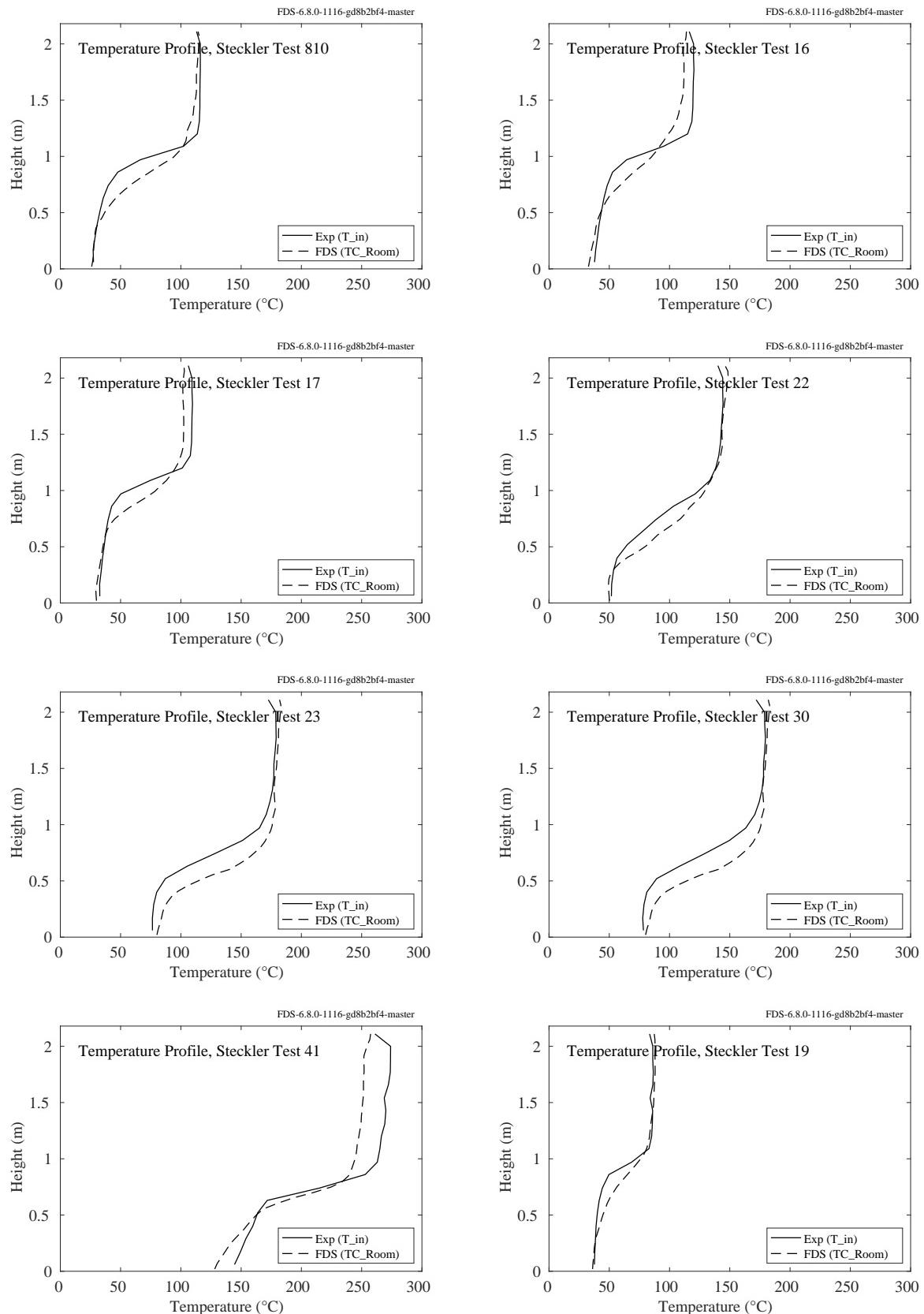


Figure 5.69: Steckler experiments, HGL temperature, Tests 16, 17, 19, 22, 23, 30, 41, 810.

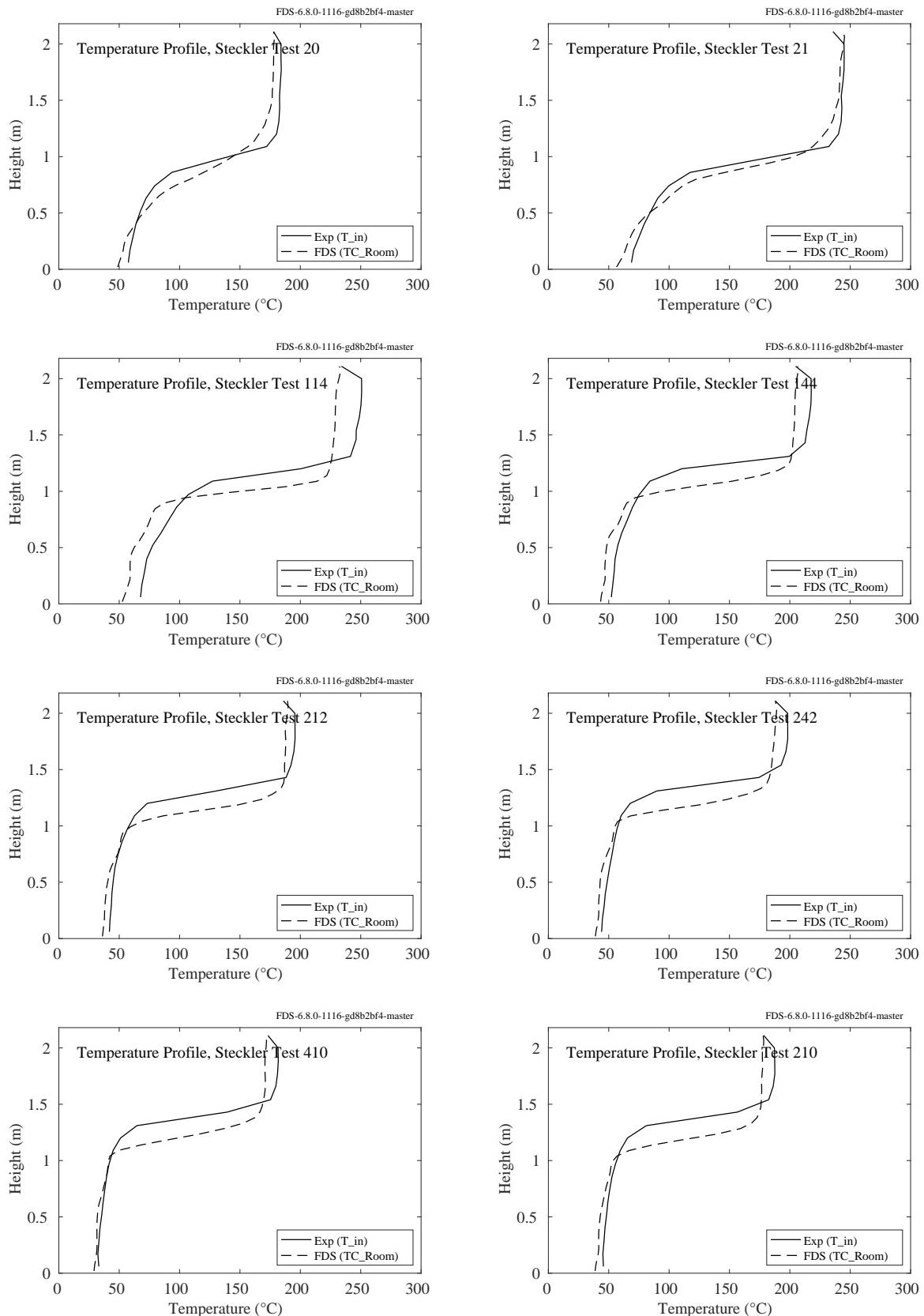


Figure 5.70: Steckler experiments, HGL temperature, Tests 20, 21, 114, 144, 210, 212, 242, 410.

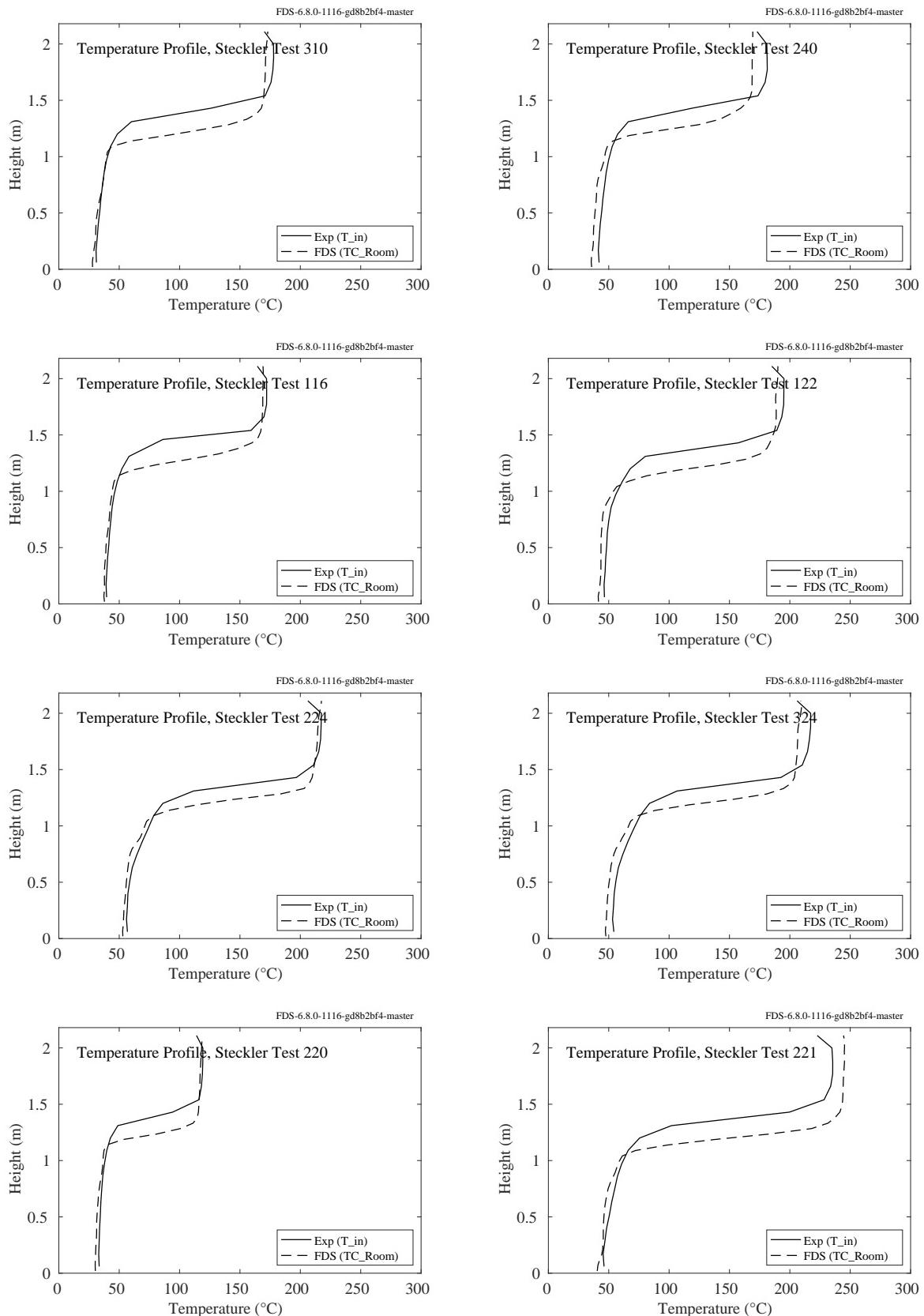


Figure 5.71: Steckler experiments, HGL temperature, Tests 116, 122, 220, 221, 224, 240, 310, 324.

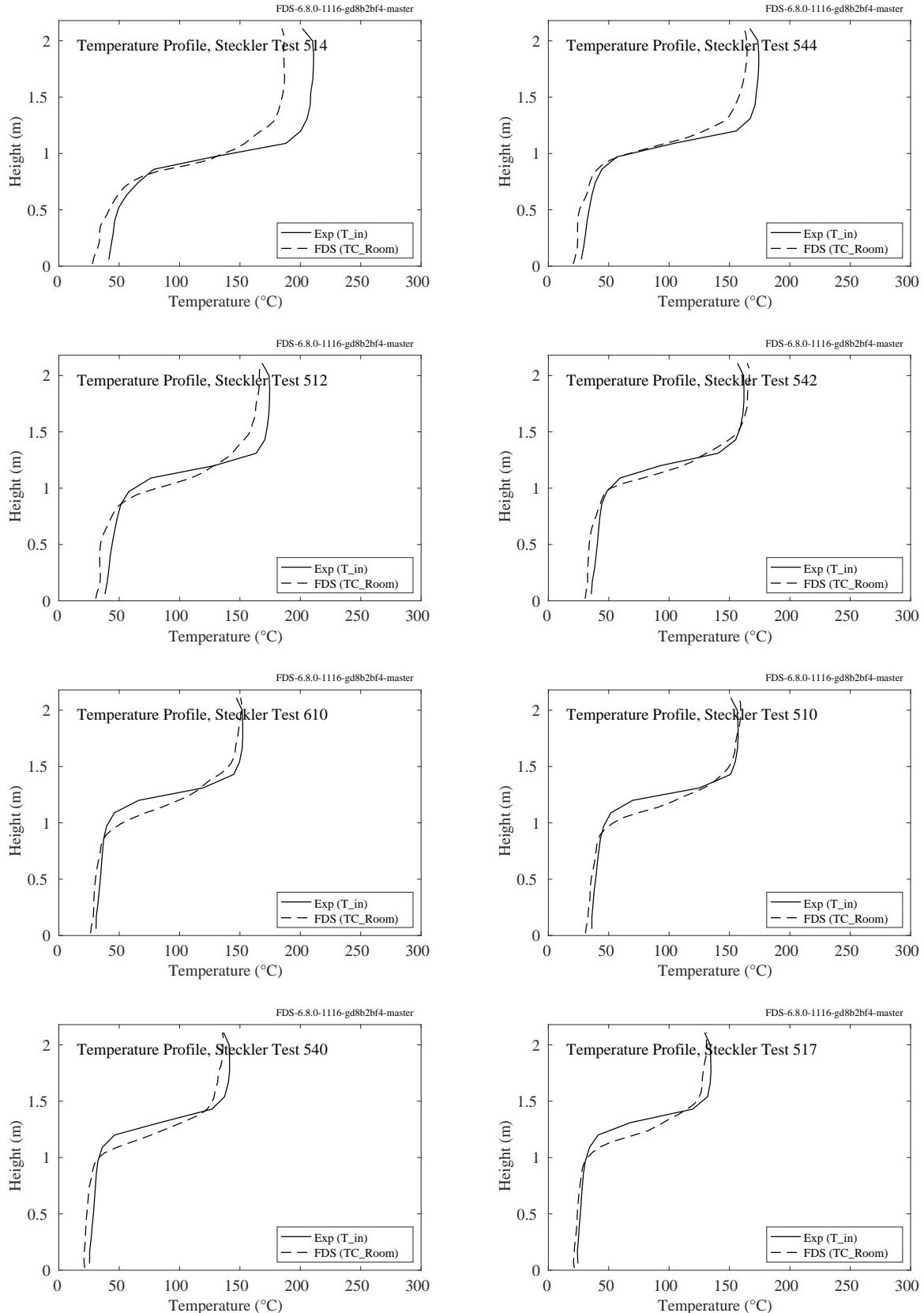


Figure 5.72: Steckler experiments, HGL temperature, Tests 510, 512, 514, 517, 540, 542, 544, 610.

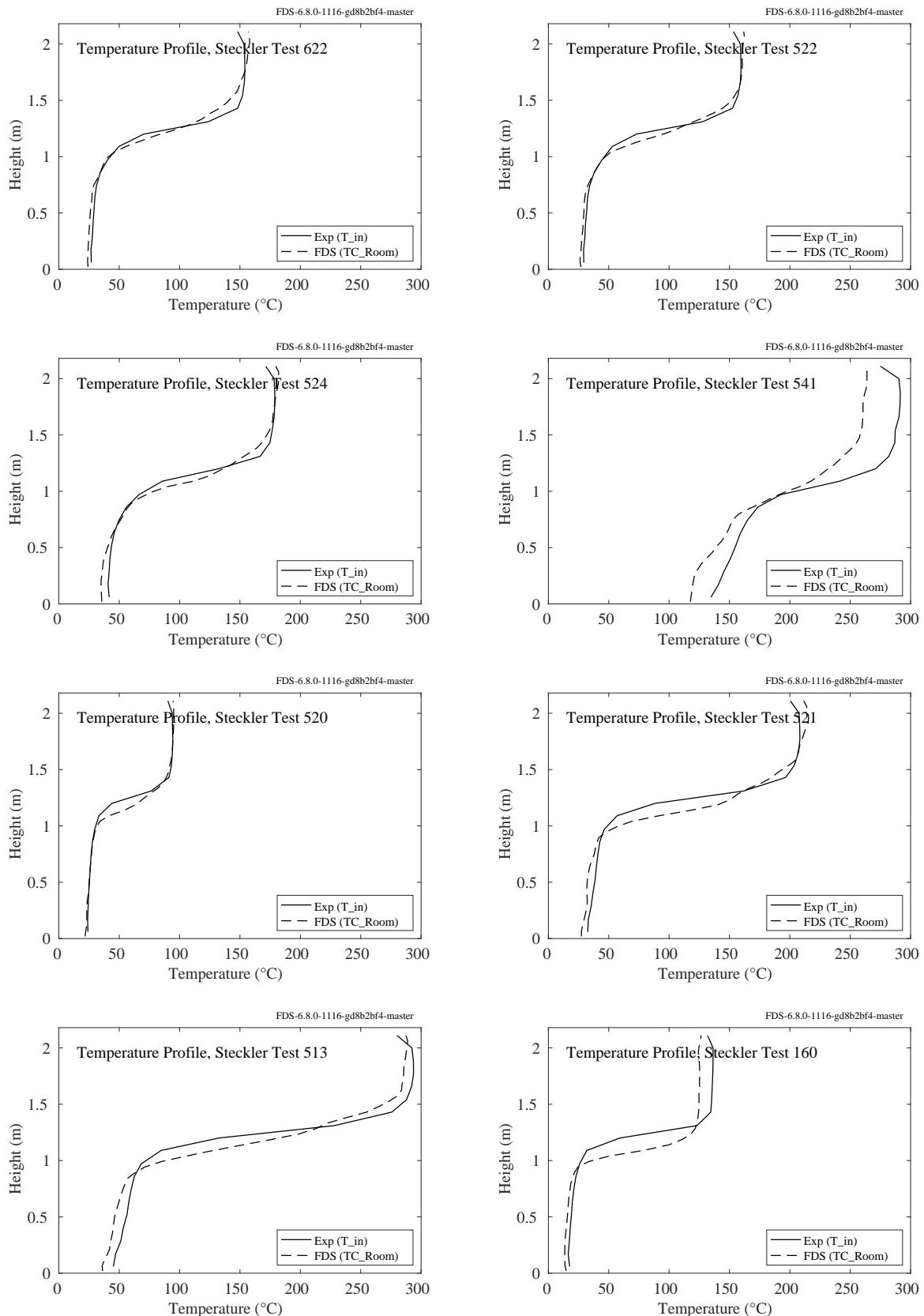


Figure 5.73: Steckler experiments, HGL temperature, Tests 160, 513, 520, 521, 522, 524, 541, 622.

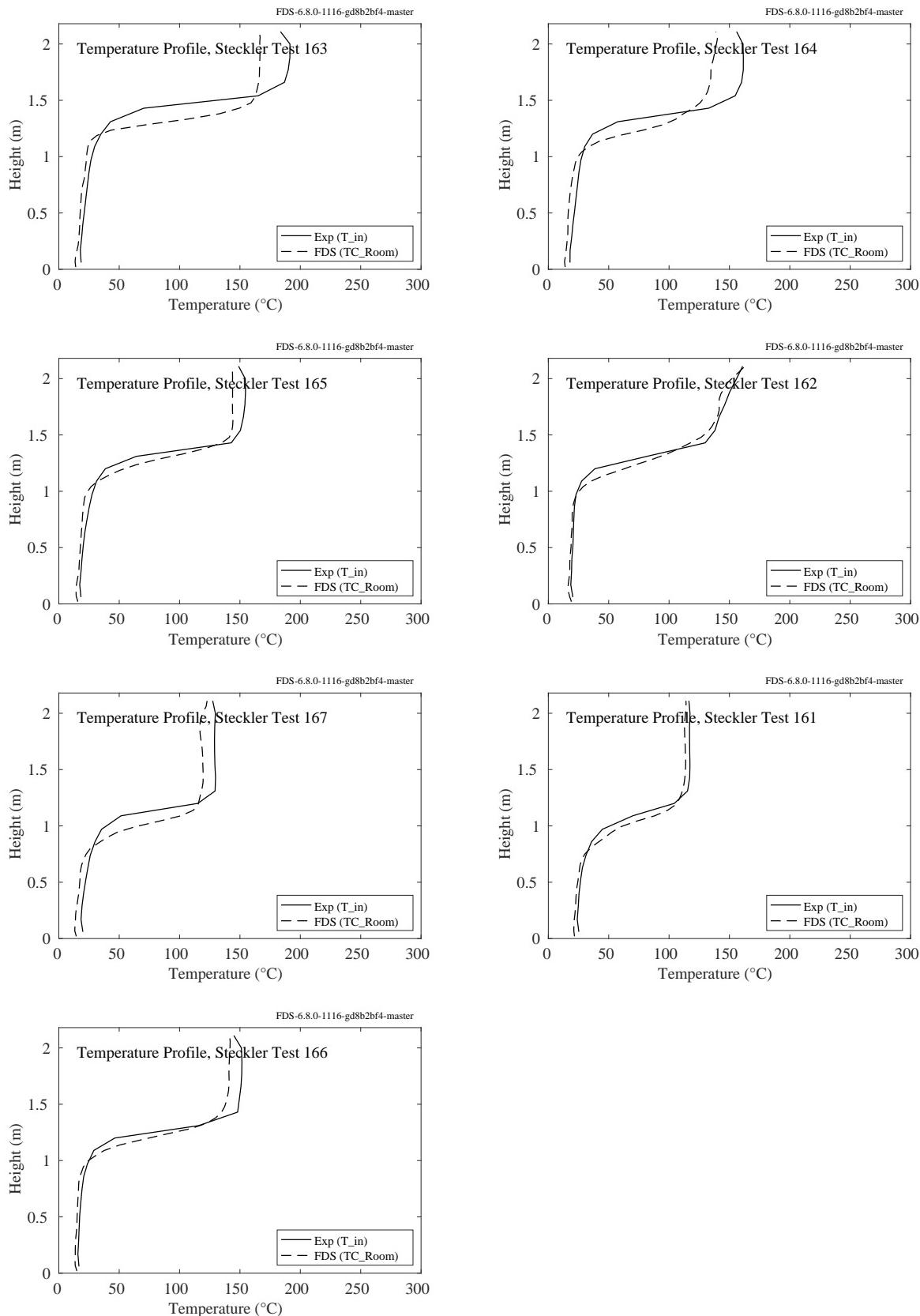


Figure 5.74: Steckler experiments, HGL temperature, Tests 161, 162, 163, 164, 165, 166, 167.

## 5.19 UL/NIST Vent Experiments

The HGL temperature and height for the four experiments was calculated from two vertical arrays of eight thermocouples each. The arrays were centered on the long central axis of the compartment and 90 cm from each short size wall. The 2.4 m by 1.2 m double vent was 90 cm from each array. The uppermost TC was 2.5 cm below the ceiling. The second TC was 30 cm (1 ft) below the ceiling, and the rest were spaced evenly by 1 ft.

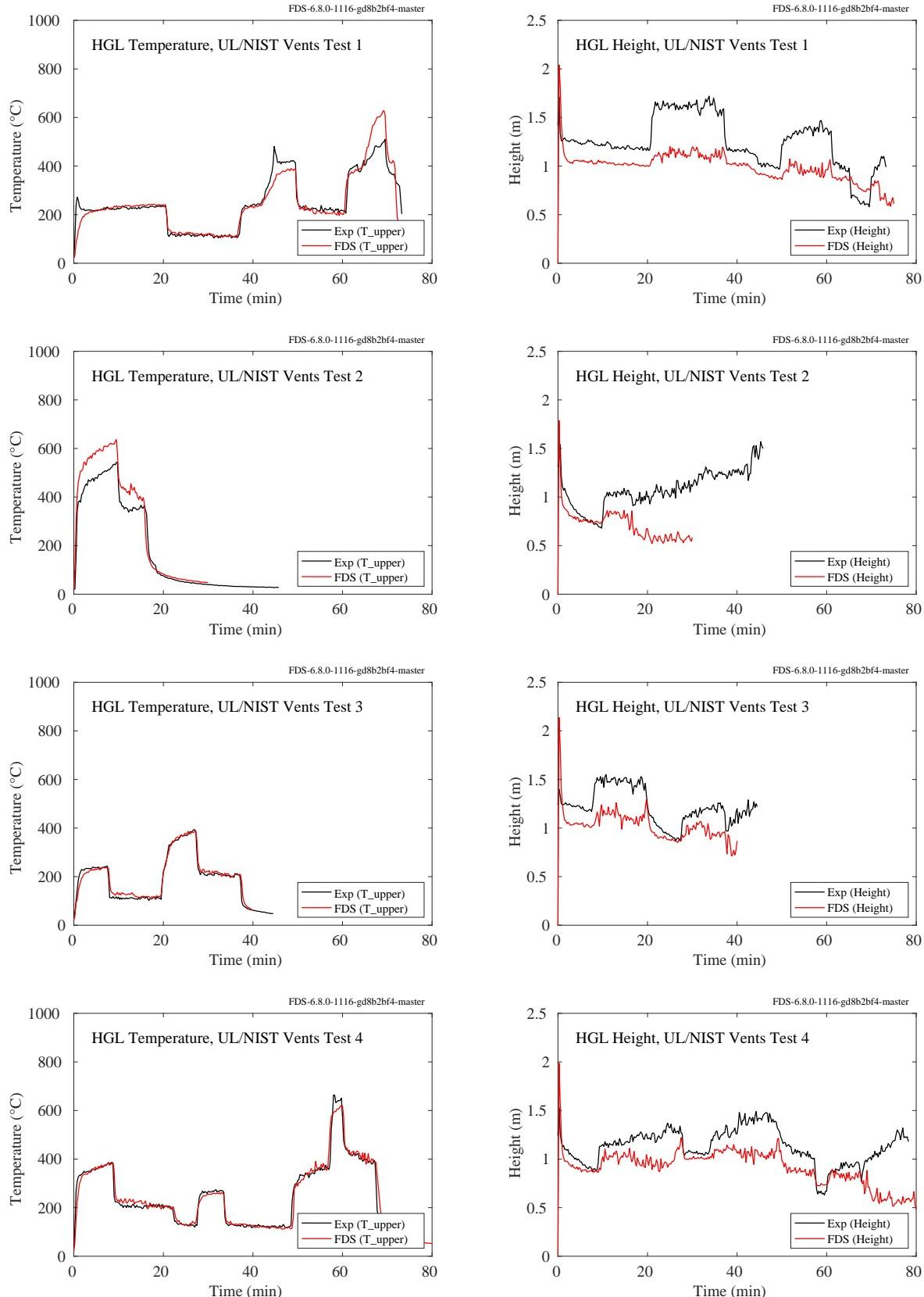


Figure 5.75: UL/NIST experiments, HGL temperature and height, Tests 1-4.

## 5.20 UL/NIJ House Experiments

Details of the experiments can be found in Sec. 3.90

The HGL temperature and height for three experiments conducted in the ranch-style house were calculated from two vertical arrays of eight thermocouples. The thermocouple arrays were located in the hallway (4TC) and in the living room (5TC).

The HGL temperature and height for three experiments conducted in the two-story colonial-style house were calculated from a vertical array of thermocouples in the center of the family room (8TC). The uppermost TC was 2.5 cm below the ceiling. The second TC was 30 cm (1 ft) below the ceiling, and the rest were spaced evenly by 30 cm (1 ft).

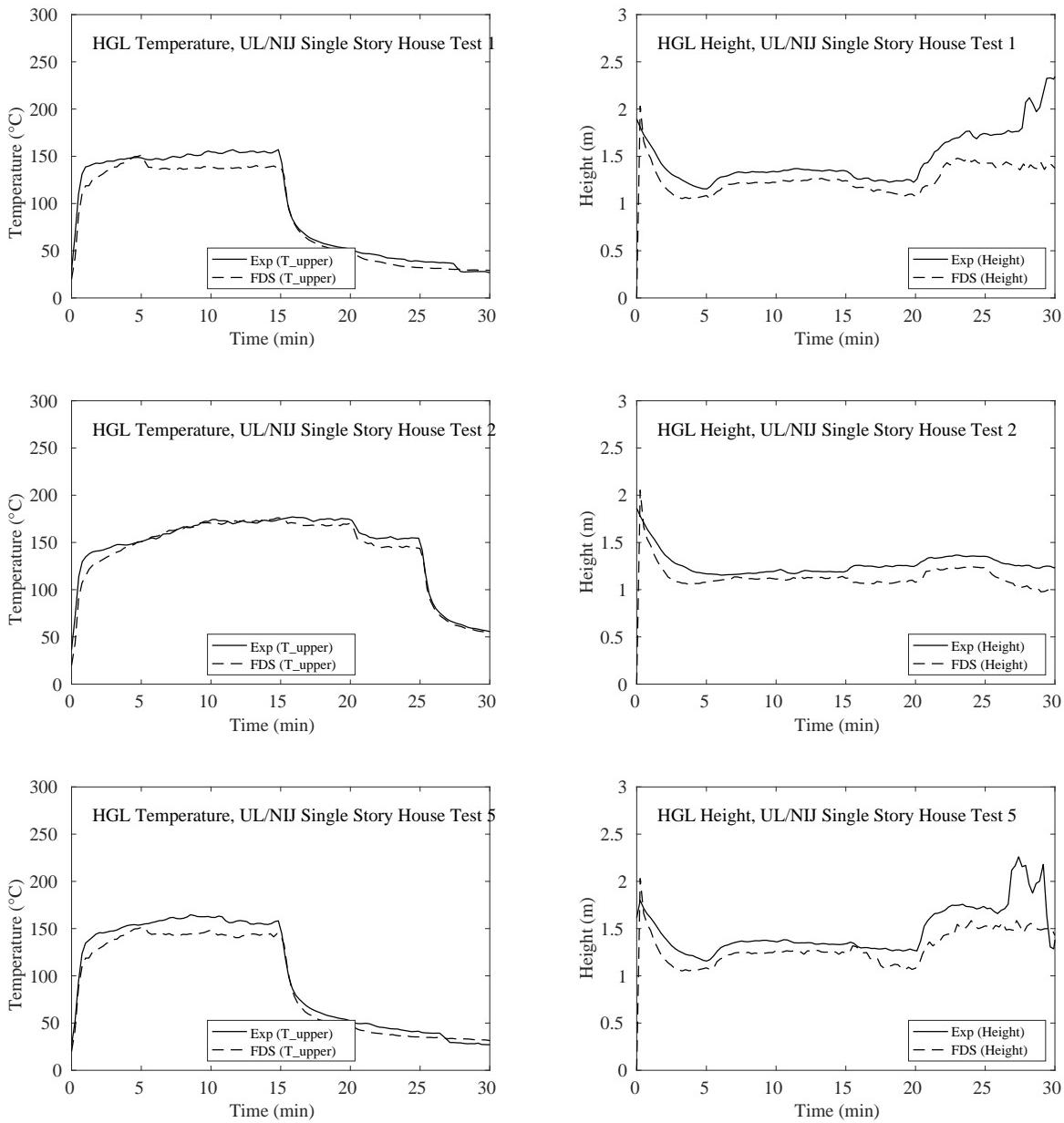


Figure 5.76: UL/NIJ Experiments, HGL temperature and height, single-story ranch-style House Tests 1, 2, and 5

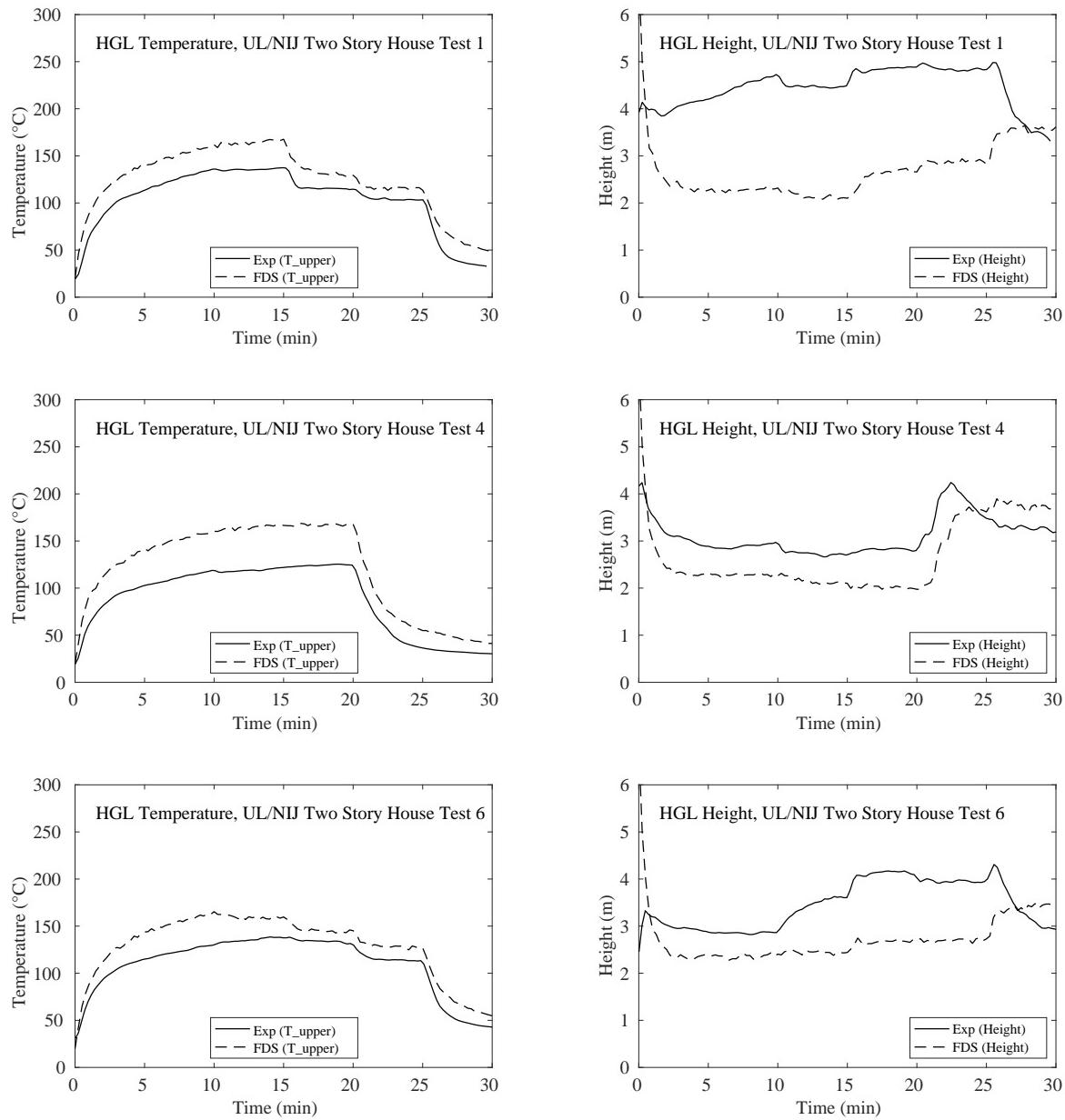


Figure 5.77: UL/NIJ Experiments, HGL temperature and height, two-story colonial-style House Tests 1, 4, and 6

## 5.21 VTT Test Series

The HGL temperature and height are calculated from the (1 min) averaged gas temperatures from three vertical thermocouple arrays using the standard reduction method. There are 10 thermocouples in each vertical array, spaced 2 m apart in the lower two-thirds of the hall, and 1 m apart near the ceiling.

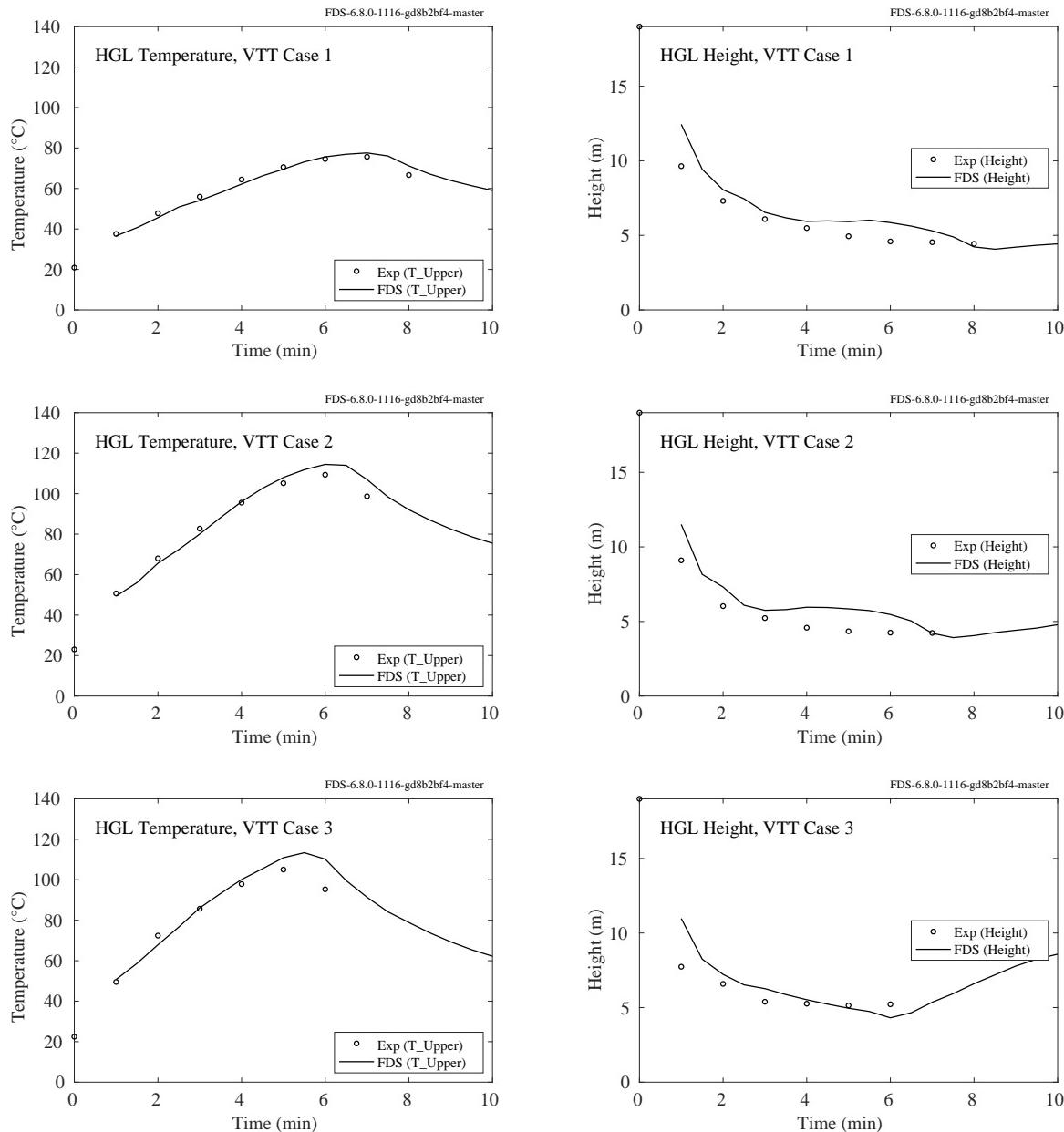


Figure 5.78: VTT experiments, HGL temperature and height, Tests 1-3.

## 5.22 WTC Test Series

The HGL temperature and height for the WTC experiments were calculated from two TC trees, one that was approximately 3 m to the west and one 2 m to the east of the fire pan (see Fig. 3.61). Each tree consisted of 15 thermocouples, the highest point being 5 cm below the ceiling.

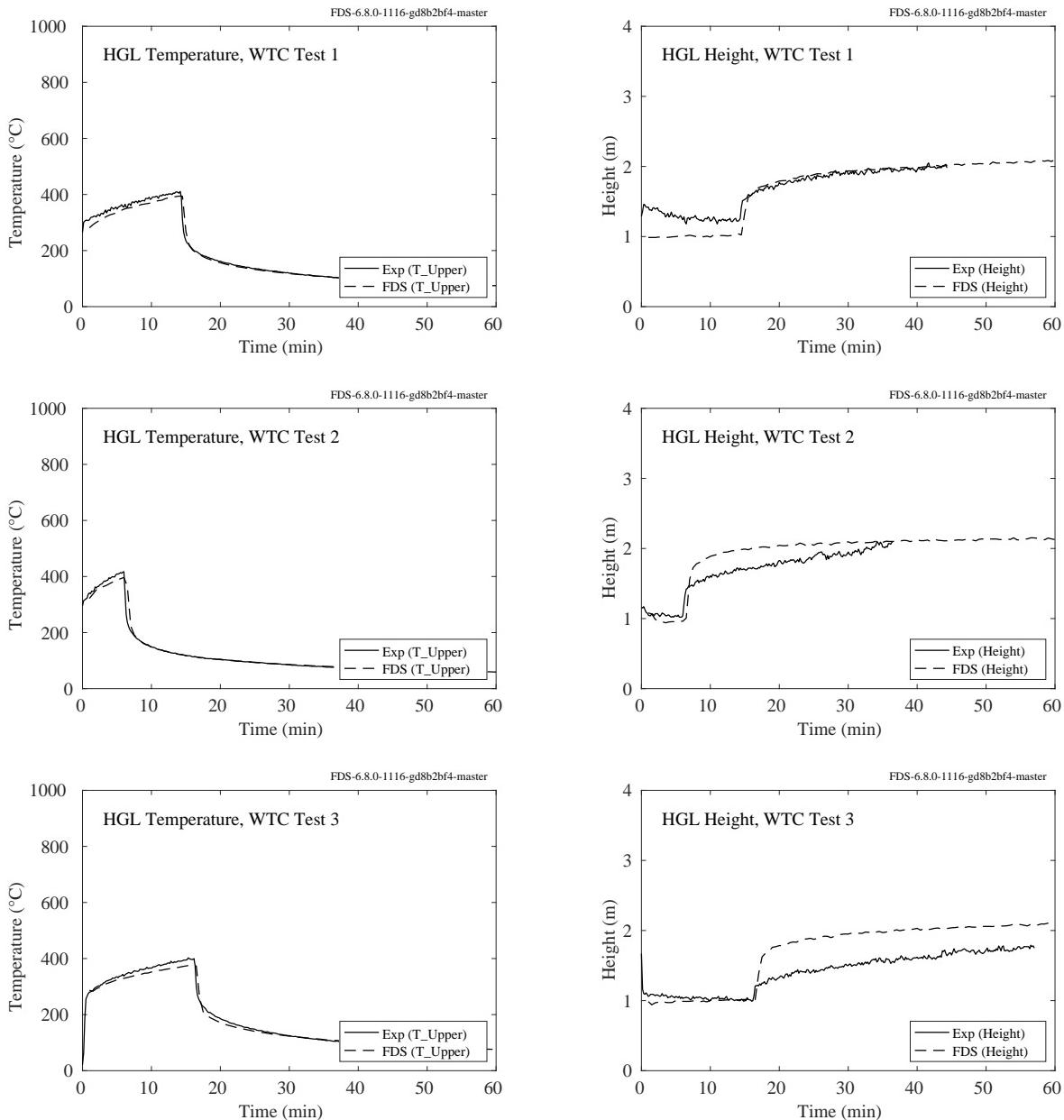


Figure 5.79: WTC experiments, HGL temperature and height, Tests 1-3.

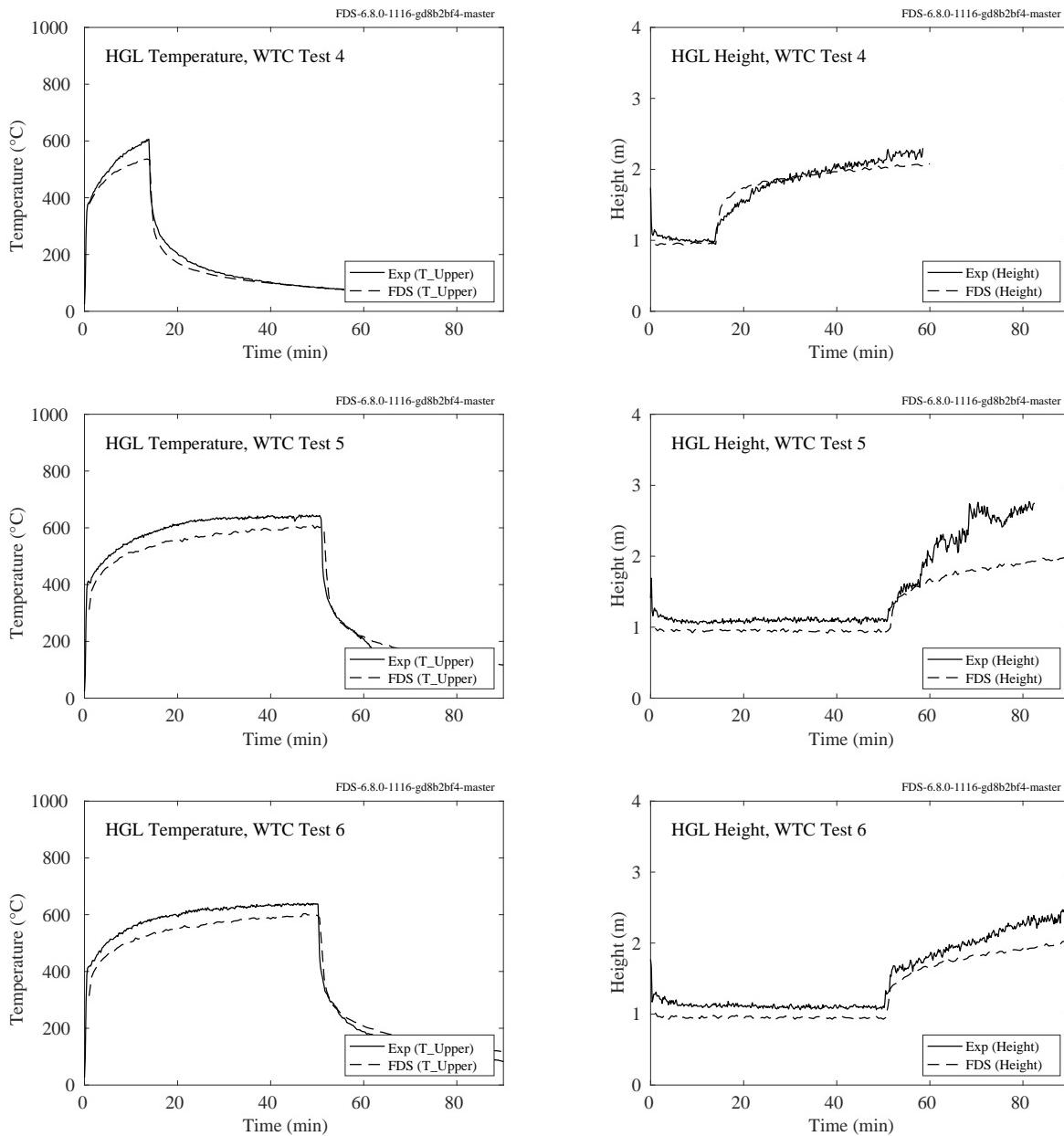


Figure 5.80: WTC experiments, HGL temperature and height, Tests 4-6.

## 5.23 Summary of Hot Gas Layer Temperature and Height

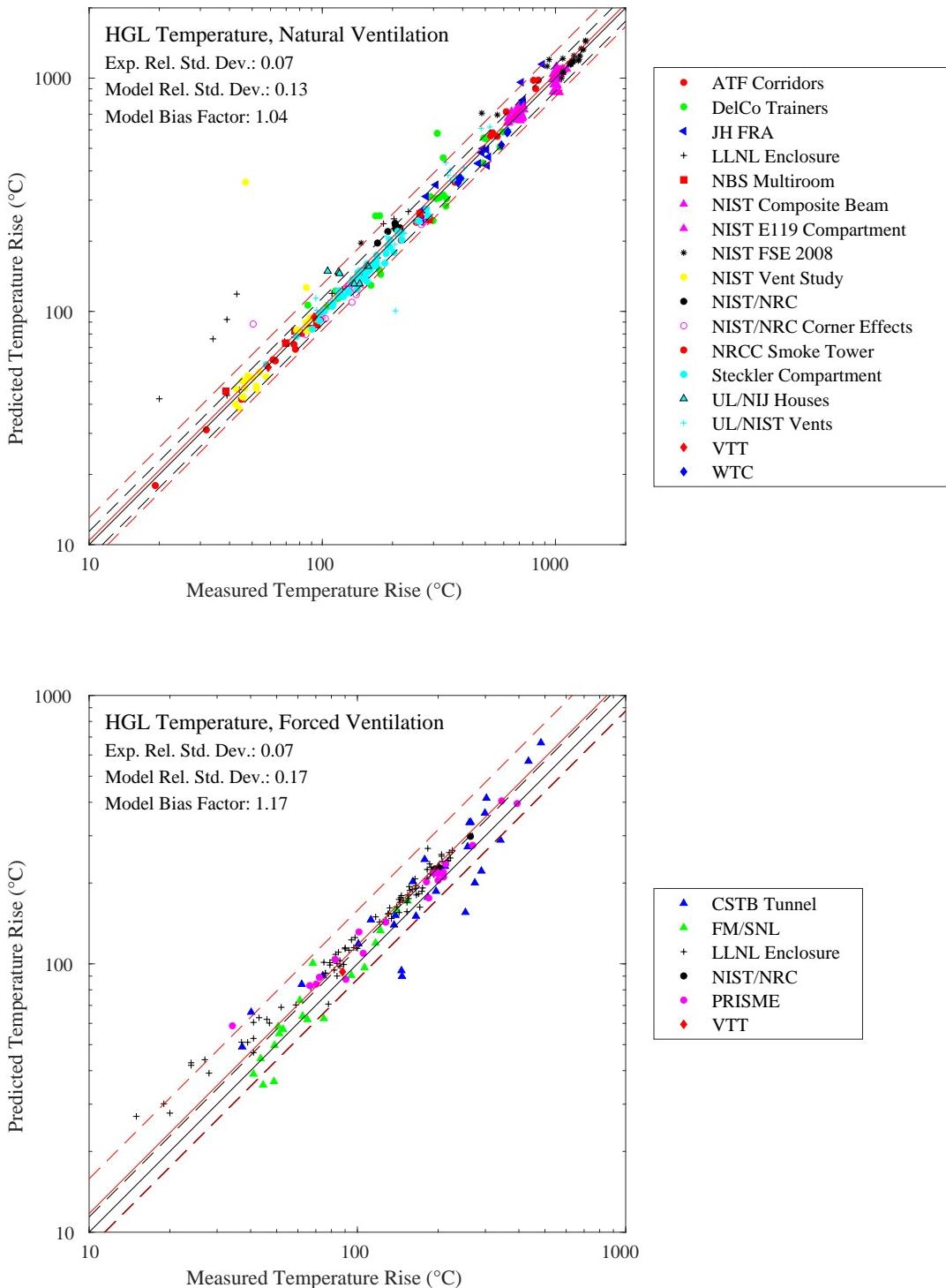


Figure 5.81: Summary, HGL temperature, natural and forced ventilation.

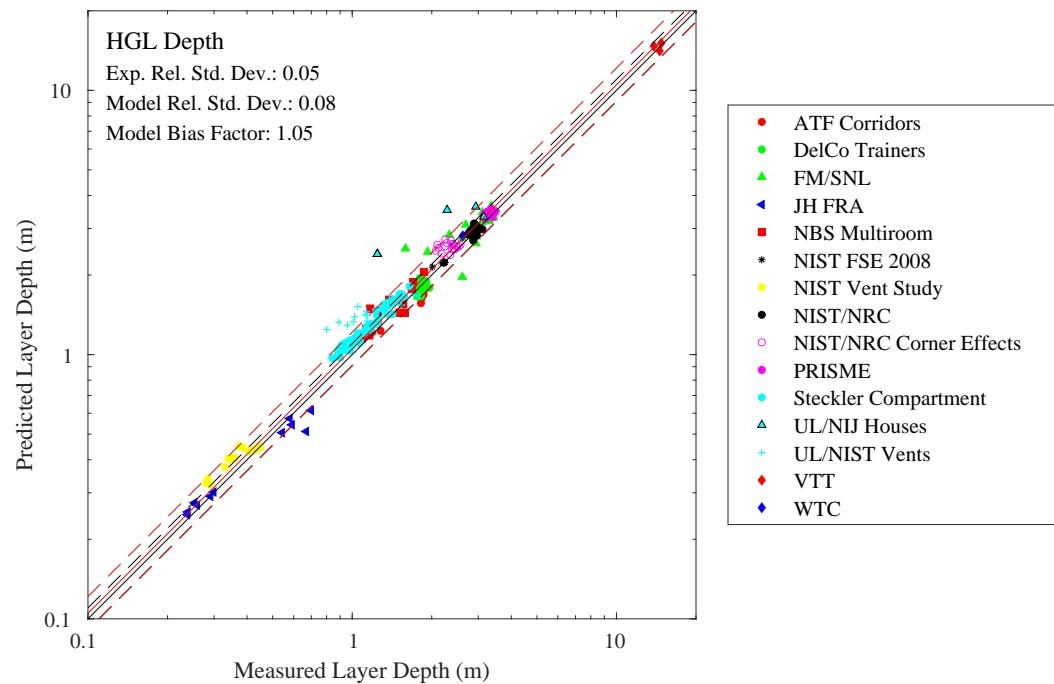
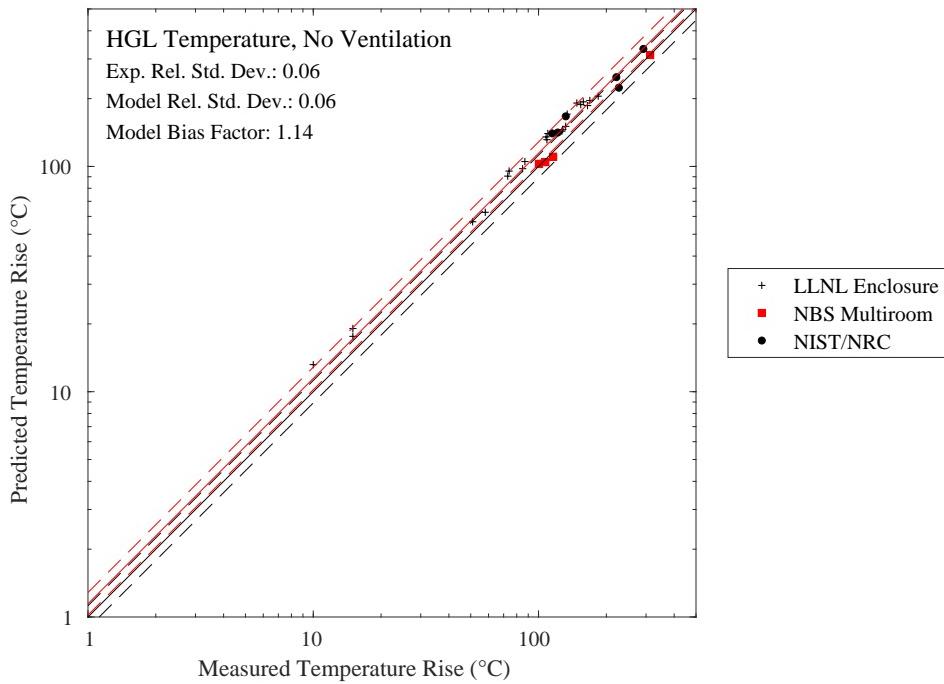


Figure 5.82: Summary, HGL temperature, unventilated compartments; HGL depth.



# Chapter 6

## Fire Plumes

### 6.1 Plume Temperatures

For fire plumes, a measure of how well the flow field is resolved is given by the non-dimensional expression  $D^*/\delta x$ , where  $D^*$  is a characteristic fire diameter

$$D^* = \left( \frac{\dot{Q}}{\rho_\infty c_p T_\infty \sqrt{g}} \right)^{\frac{2}{5}} \quad (6.1)$$

and  $\delta x$  is the nominal size of a mesh cell<sup>1</sup>. The quantity  $D^*/\delta x$  can be thought of as the number of computational cells spanning the characteristic (not necessarily the physical) diameter of the fire. The more cells spanning the fire, the better the resolution of the calculation. It is better to assess the quality of the mesh in terms of this non-dimensional parameter, rather than an absolute mesh cell size. For example, a cell size of 10 cm may be “adequate,” in some sense, for evaluating the spread of smoke and heat through a building from a sizable fire, but may not be appropriate to study a very small, smoldering source. The resolution of all the numerical simulations included in this chapter is given in Table 3.49.

---

<sup>1</sup>The characteristic fire diameter is related to the characteristic fire size via the relation  $Q^* = (D^*/D)^{5/2}$ , where  $D$  is the physical diameter of the fire.

### 6.1.1 FM Burner Experiments

A summary of these experiments can be found in Sec. 3.25.

Mean and rms temperature measurements were made above a 13.7 cm (inner) diameter, 15 kW ethylene burner. The radial profiles are located at heights of 1.0, 1.5, 2.0, 2.5, 3.0, and 3.5 burner diameters,  $D$ . Figure 6.3 displays the probability distributions (PDFs) at the six heights and radii of 0 cm, 1 cm, 2 cm, 3 cm, and 4 cm.

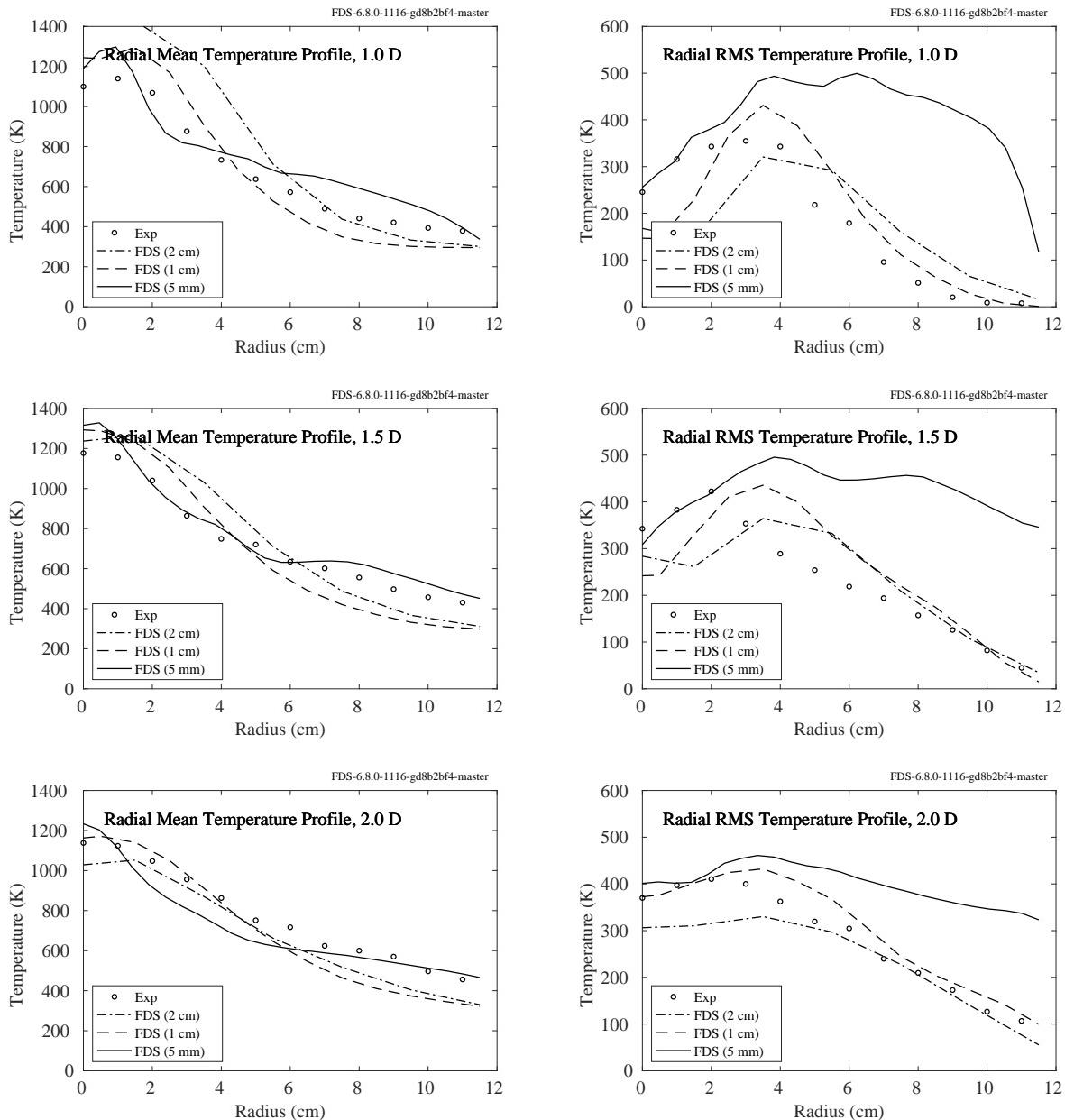


Figure 6.1: FM Burner experiments, plume mean and rms temperatures at heights of 1.0, 1.5, and 2.0 diameters.

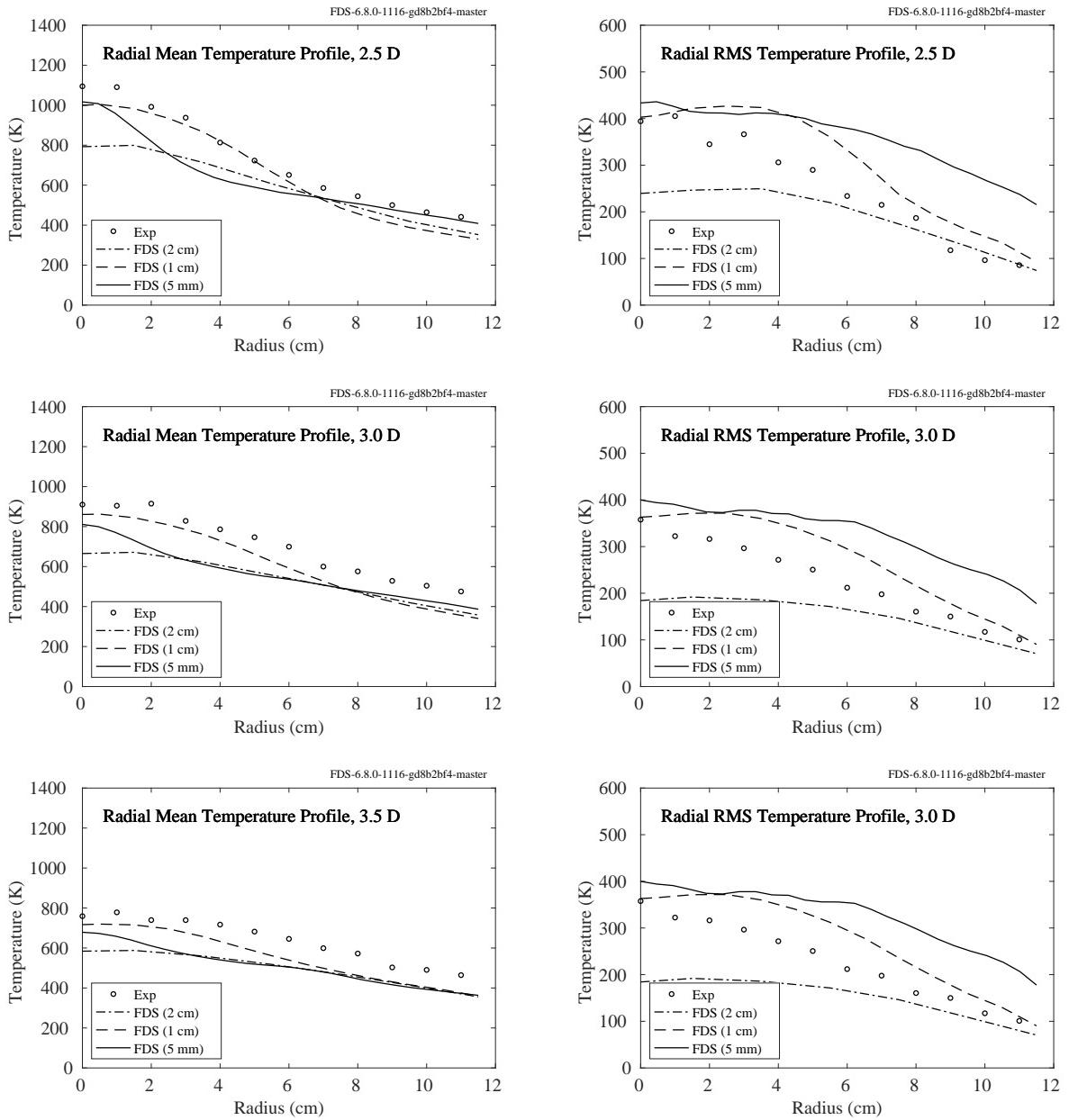


Figure 6.2: FM Burner experiments, plume mean and rms temperatures at heights of 2.5, 3.0, and 2.5 diameters.

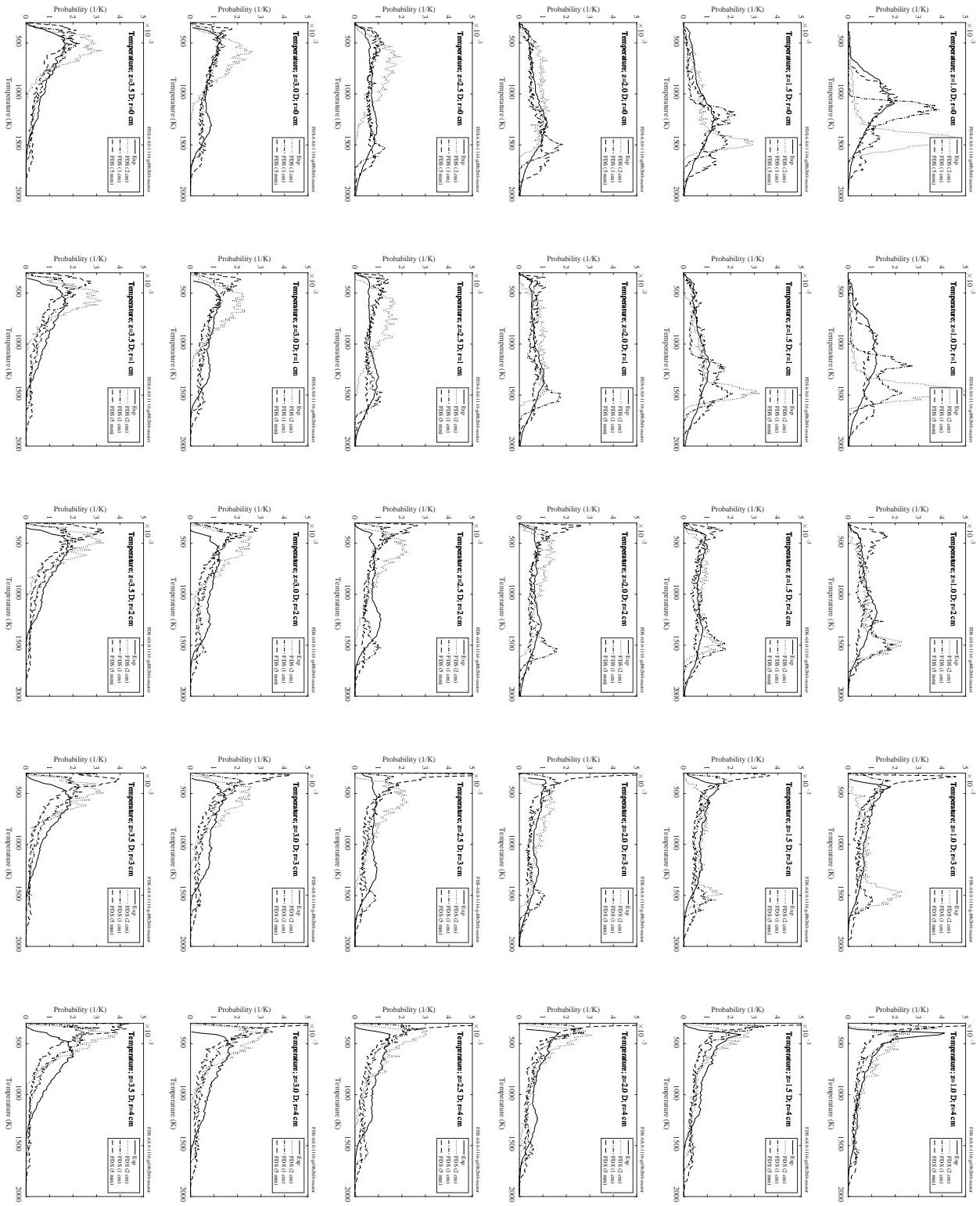


Figure 6.3: FM Burner experiments, temperature PDFs.

## 6.1.2 FM/SNL Experiments

A summary of these experiments can be found in Sec. 3.28.

The FM/SNL tests consisted of propylene gas burners, heptane pools, methanol pools, PMMA solids, as well as qualified and unqualified cables, burned in a large room which, for the first 18 tests, was free of obstructions. Plume Temperatures shown here were measured at approximately 6 m from the floor, or 0.98 times the total ceiling height. For Tests 1-5 and 7-9, the thermocouple station (Station 13) was centered above the fire pan. Tests 6 and 10-15 used an alternate fire location, centered along the south wall. Station 9 was not centered above these fires, but fell within the plume. Tests 16 and 17 had fires located in the south-west corner of the room, too remote from any stations to allow for plume measurements.

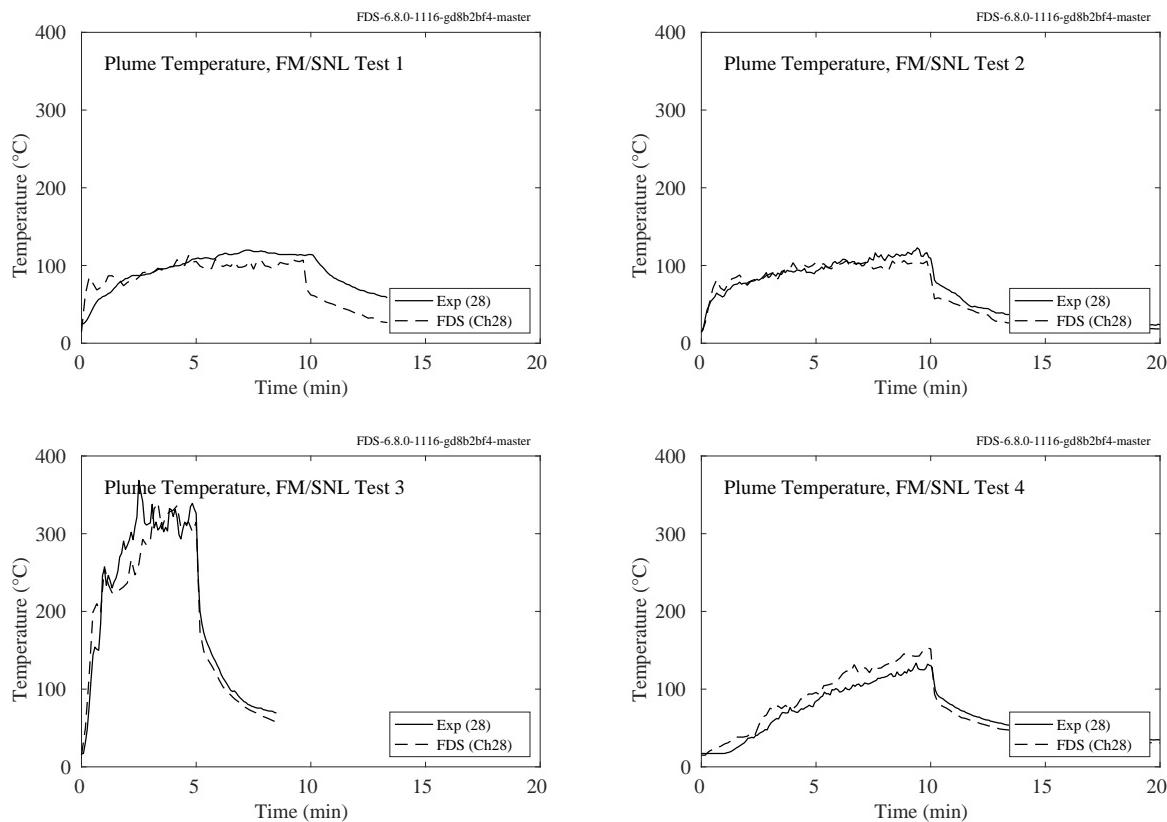


Figure 6.4: FM/SNL experiments, plume temperature, Tests 1-4.

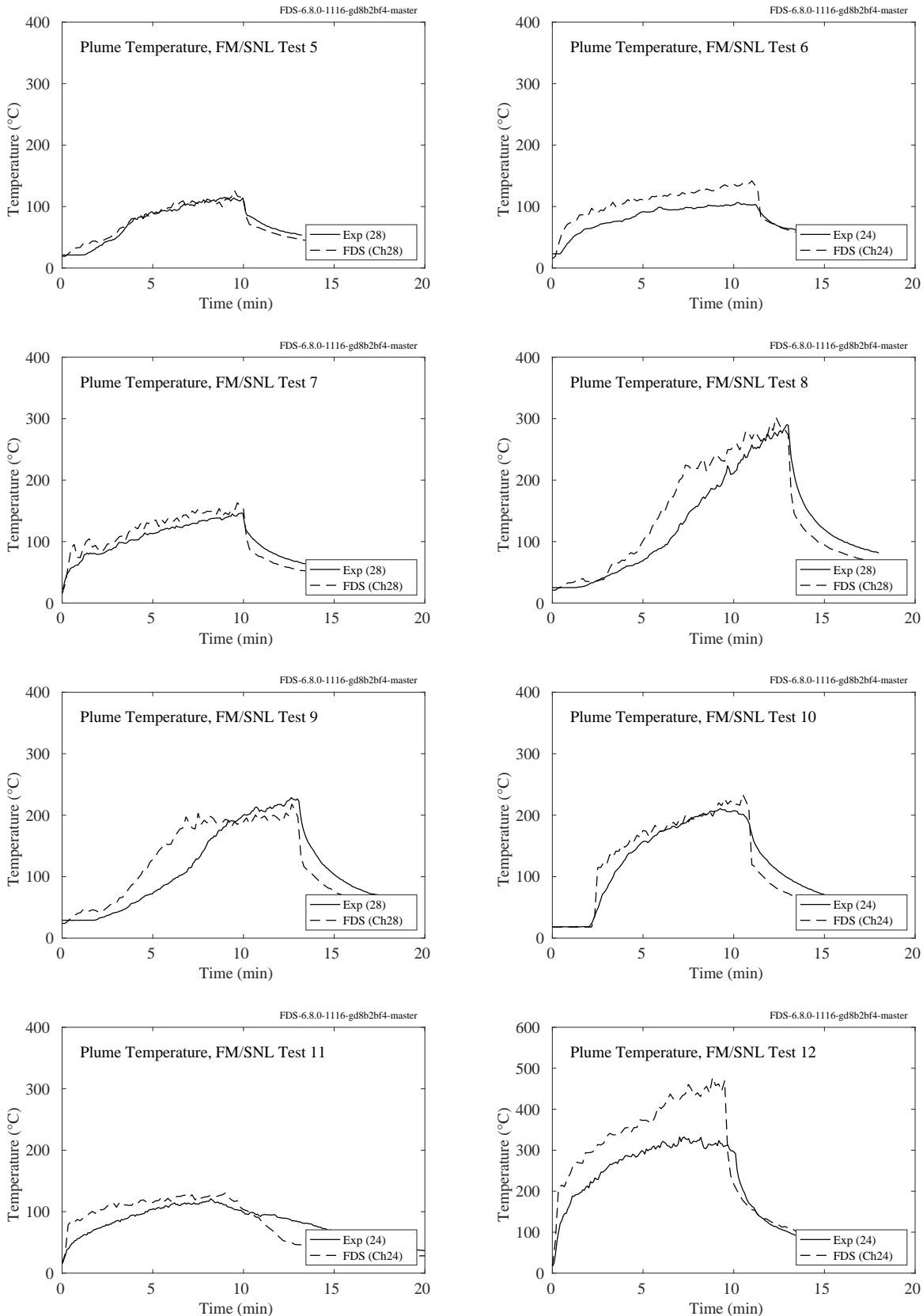


Figure 6.5: FM/SNL experiments, plume temperature, Tests 5-12.

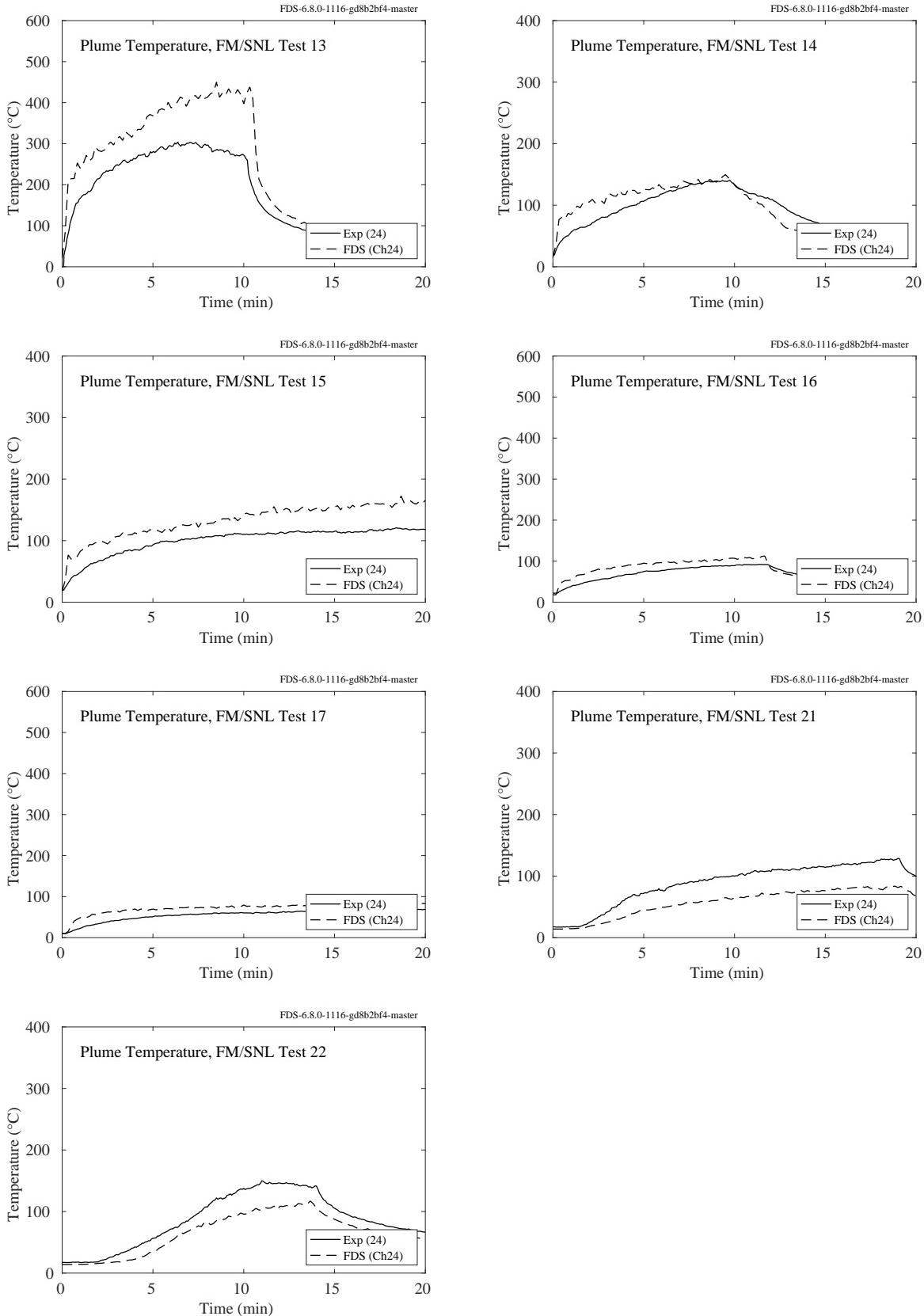


Figure 6.6: FM/SNL experiments, plume temperature, Tests 13-17, 21-22.

### 6.1.3 McCaffrey's Plume Correlation

A summary of these experiments can be found in Sec. 3.46.

The following plots show the results of simulations of McCaffrey's five fires at three grid resolutions, nominally  $D^*/\delta x = [3, 6, 12, 24]$  based on the  $D^*$  of the 14.4 kW burner (respectively, crude, coarse, medium, and fine resolution). Temperature measurements and reported simulation results are for thermocouple temperature.

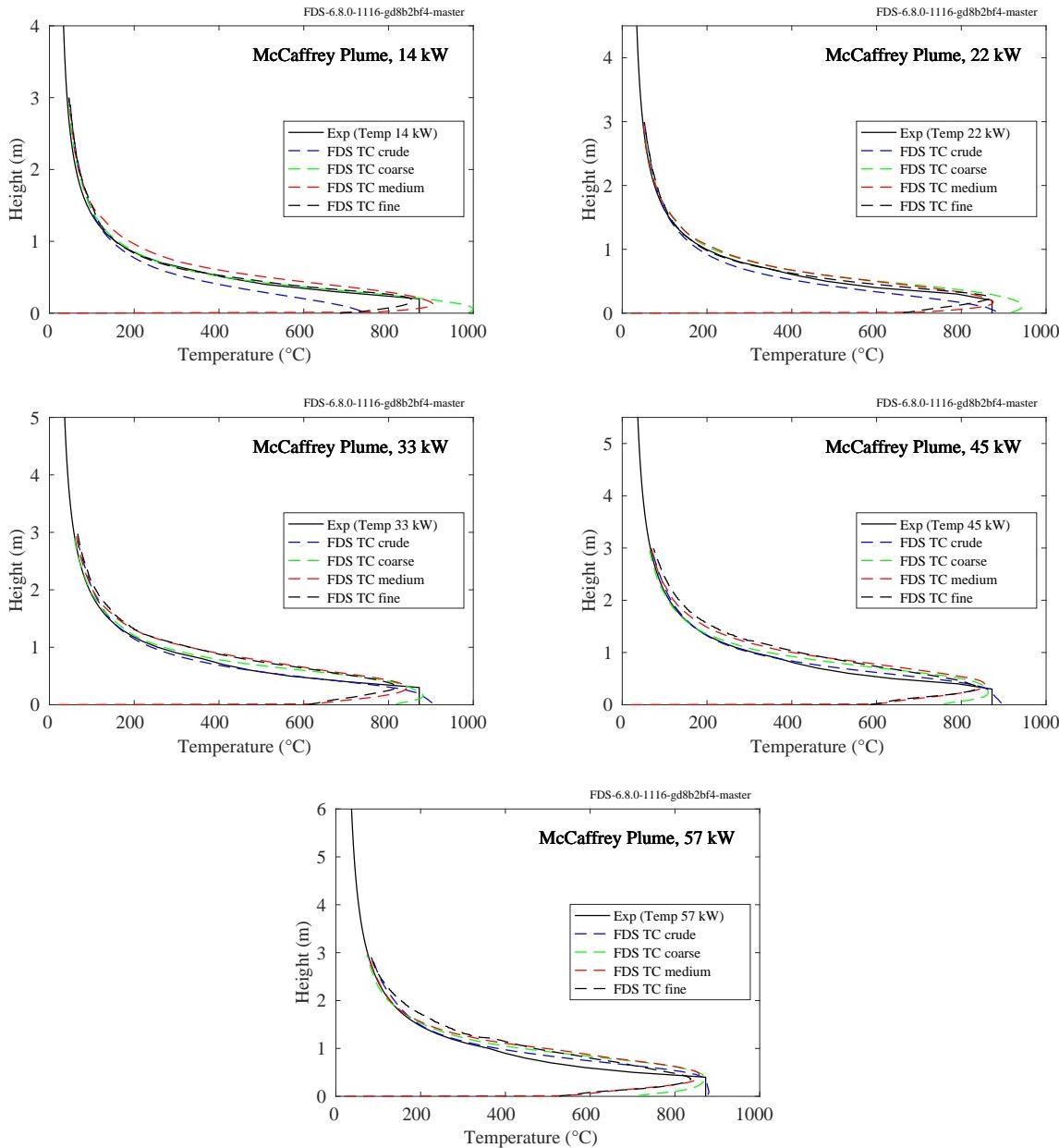


Figure 6.7: McCaffrey experiments, plume temperature.

Below we plot the same results but arranged in a different way. The height dimension is scaled by the fire Froude number and each plot represents nominally the same resolution level.

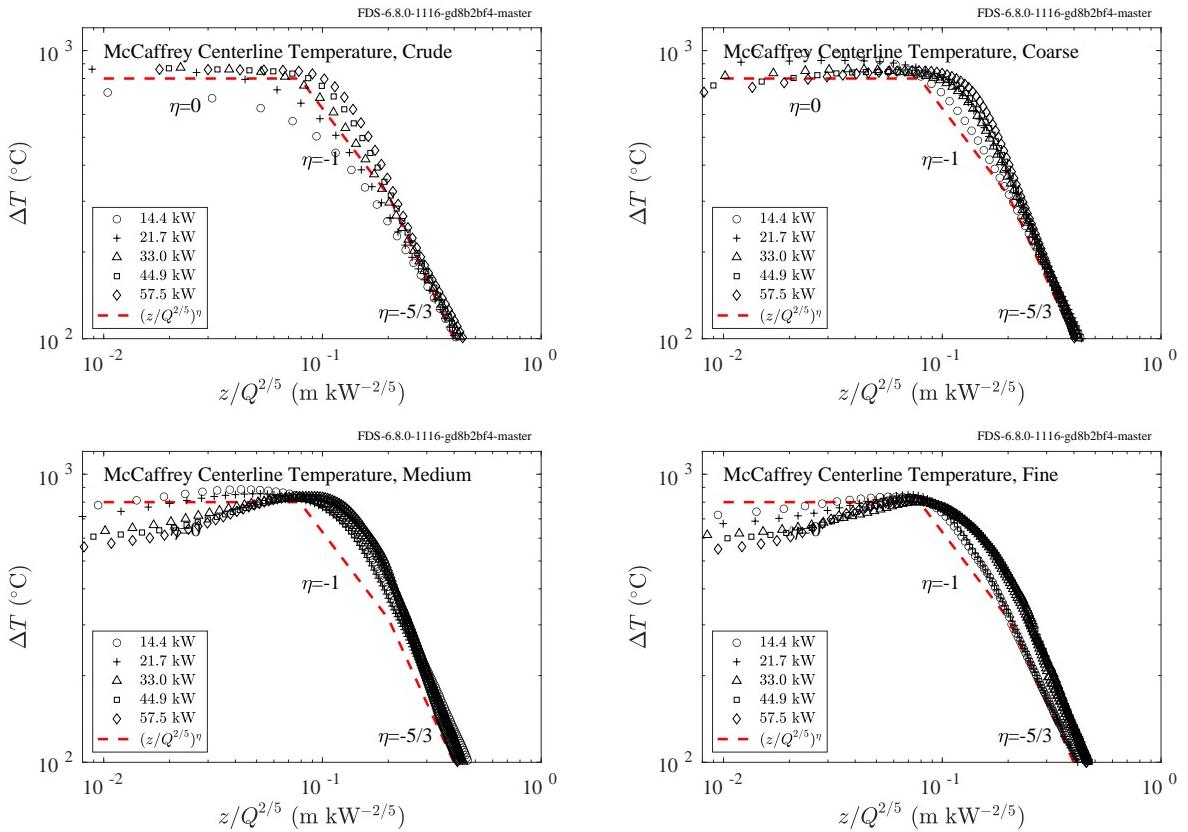


Figure 6.8: McCaffrey experiments, plume temperature, Froude scaling.

### 6.1.4 NIST/NRC Corner/Wall/Cabinet Effects Experiments

A summary of these experiments can be found in Sec. 3.56.

This set of experiments involved a 60 cm by 60 cm natural gas burner with heat release rates of 200 kW, 300 kW, and 400 kW. The burner was initially positioned in a corner or against a wall and then gradually moved away. A three-tiered array of thermocouples was positioned above the burner and moved along with it. Each tier contained 29 bare-bead thermocouples at heights of 2.13 m, 2.74 m, and 3.35 m above the floor. The plots below show the maximum temperature of the 29 thermocouples, time-averaged over 2 min, at each level. Note that FDS does not allow its devices to move; thus the time over which the model and measurement are compared is limited to that time period in the experiment when the center of the burner was underneath the fixed TC array in the corner or against the wall. In short, the last 30 min of the experiments are not considered.

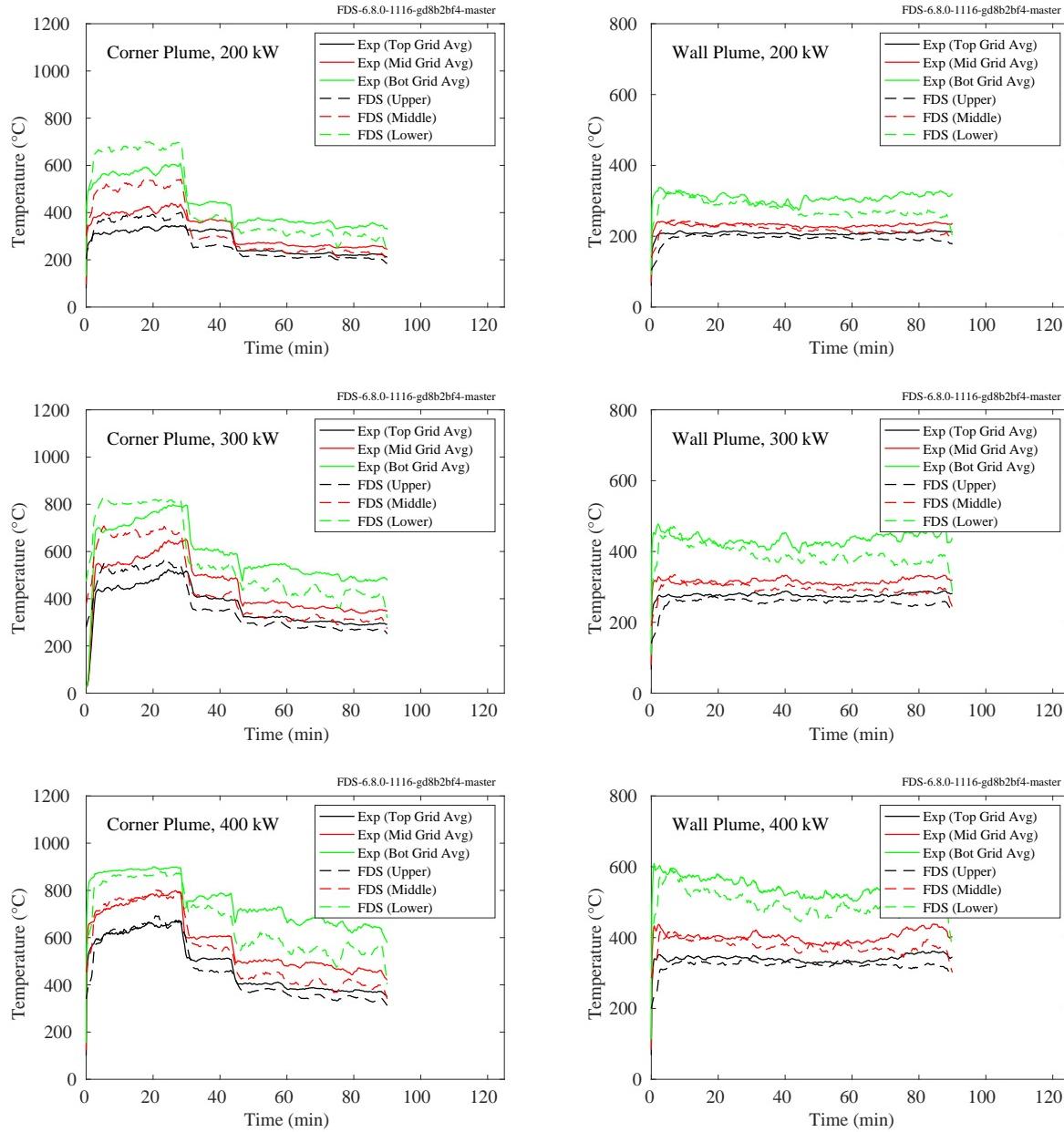


Figure 6.9: NIST/NRC Corner Effects experiments, plume temperature.

### 6.1.5 NIST Pool Fires

Details of the NIST Pool Fires experiments and modeling are found in Sec. 3.61. On the following pages are comparisons of predicted and measured temperatures at various locations in and around liquid and gaseous pool fires.

- Figures 6.10 and 6.11 display centerline profiles of mean and rms temperature for 30 cm diameter acetone, ethanol, and methanol liquid pool fires; and 37 cm methane and propane gaseous fires [362].
- Figure 6.12 displays radial profiles of mean and rms temperature for a 30 cm methanol fire at heights of  $z = 3$  cm (mean only),  $z = 30$  cm (mean only),  $z = 41$  cm,  $z = 51$  cm, and  $z = 61$  cm. The profiles at 3 cm and 30 cm are from Ref. [344] and the others are from Ref. [363].
- Figures 6.13 and 6.14 display centerline and radial profiles of mean and rms temperature for a 100 cm methanol fire. The radial profiles are located at heights of  $z = 20$  cm,  $z = 60$  cm,  $z = 100$  cm,  $z = 140$  cm, and  $z = 180$  cm [364].

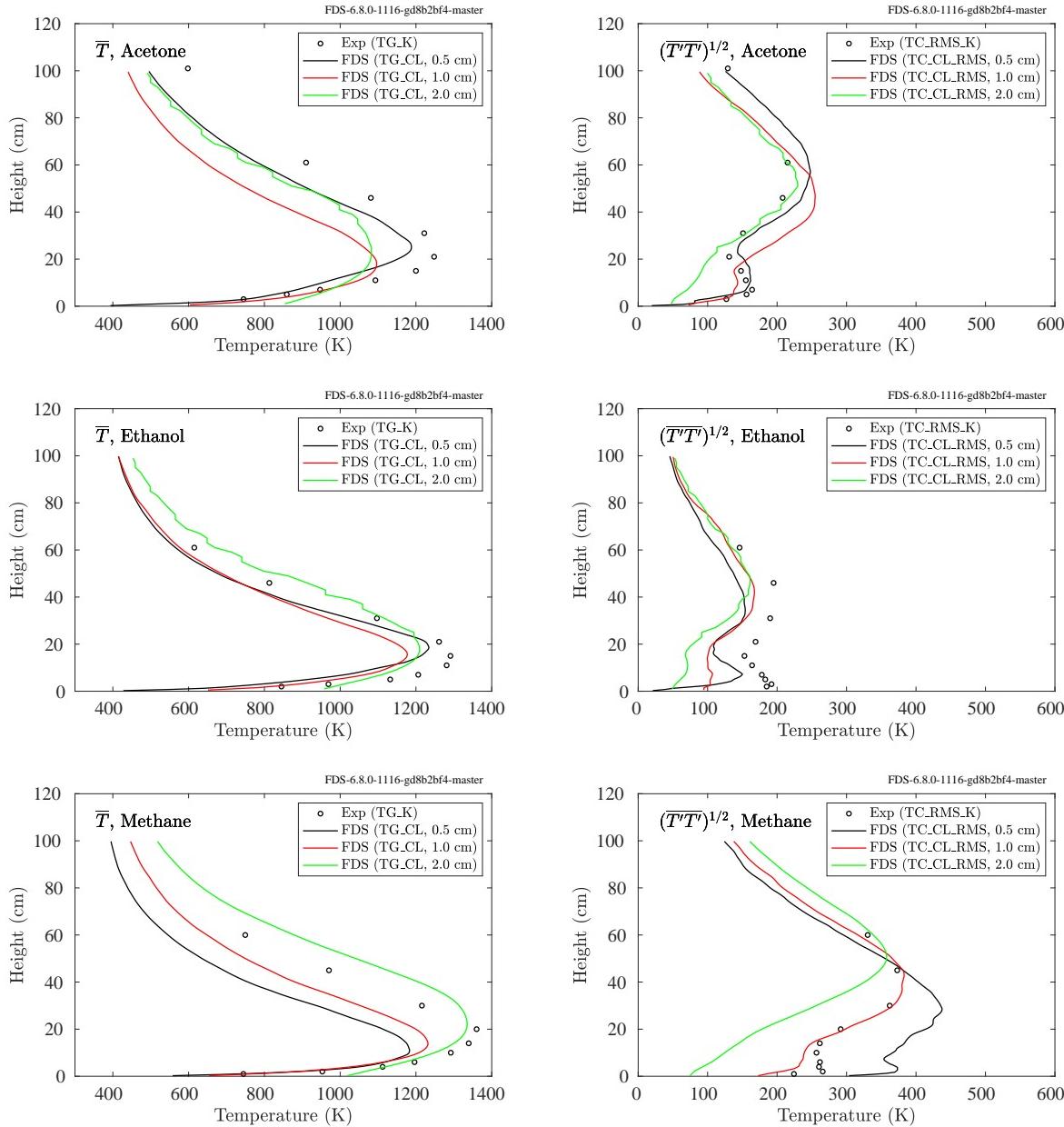


Figure 6.10: NIST Pool Fires, centerline temperature profiles, 30 cm acetone, 30 cm ethanol, 37 cm methane.

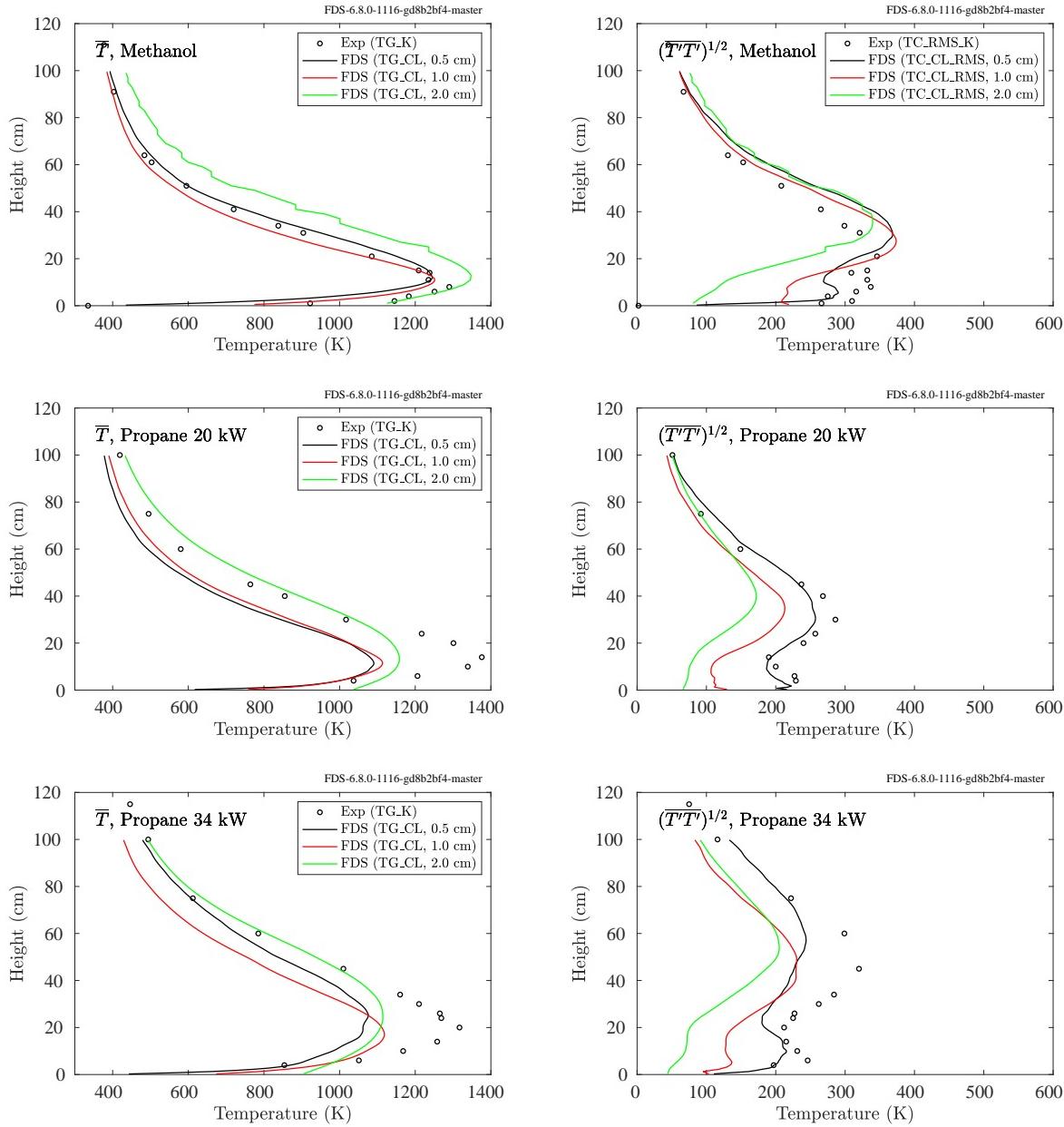


Figure 6.11: NIST Pool Fires, centerline temperature profiles, 30 cm methanol and 37 cm propane.

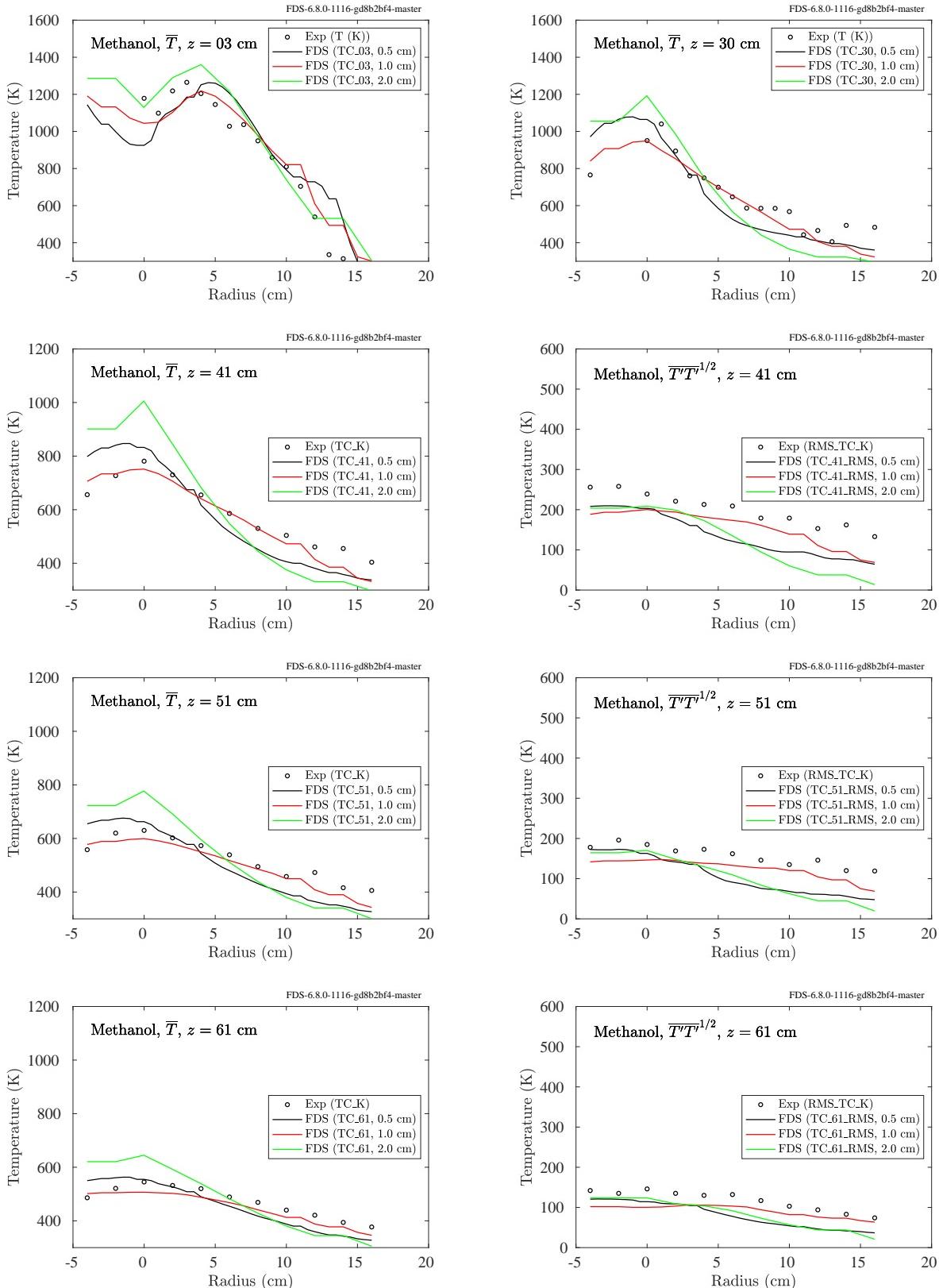


Figure 6.12: NIST Pool Fires, 30 cm methanol, radial profiles of mean and rms temperature.

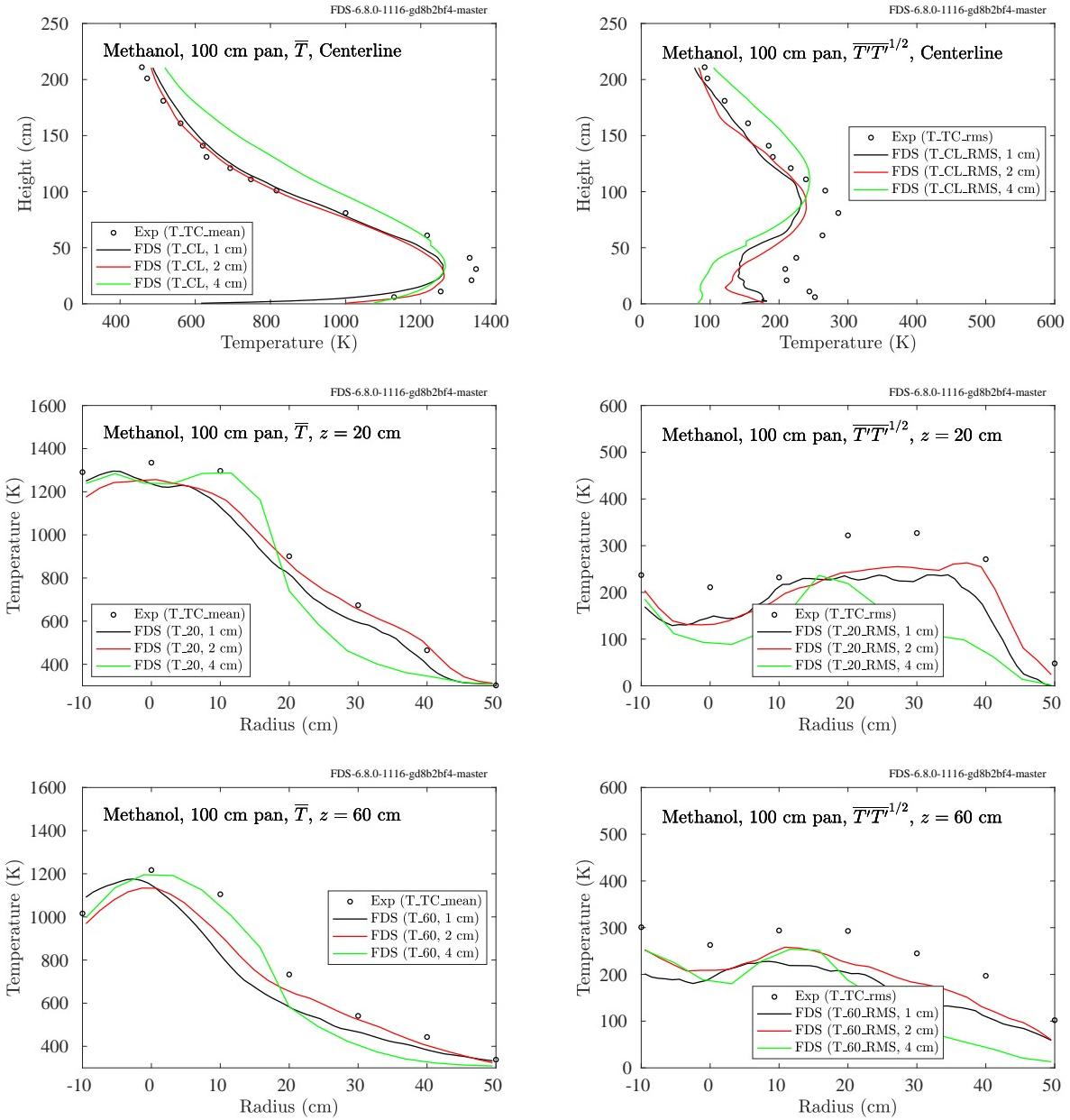


Figure 6.13: NIST Pool Fires, 100 cm methanol fire, centerline profiles of mean and rms temperature (top row), radial profiles at  $z = 20$  cm (middle row) and  $z = 60$  cm (bottom row).

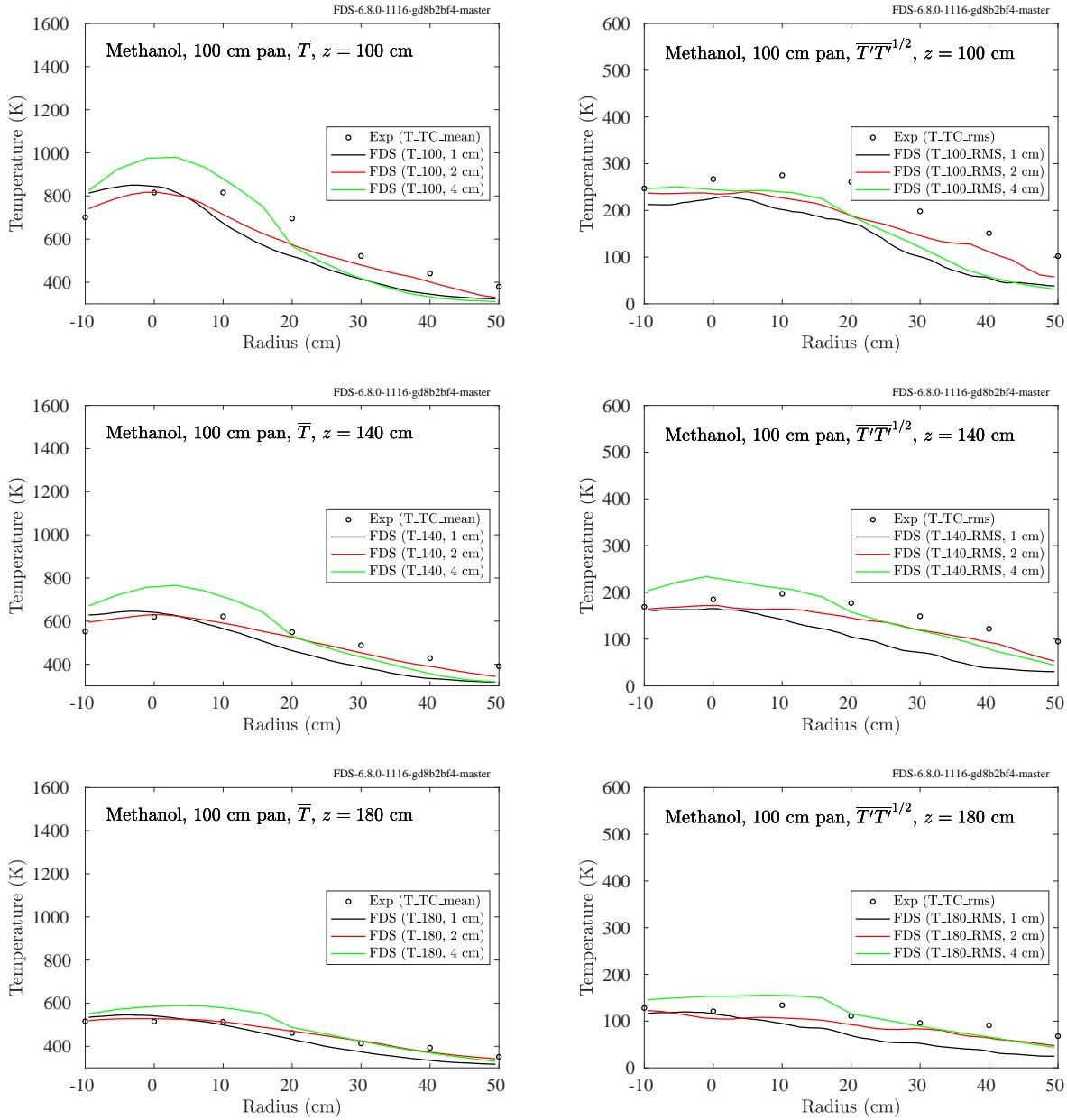


Figure 6.14: NIST Pool Fires, 100 cm methanol fire, radial profiles of mean and rms temperature at  $z = 100 \text{ cm}$  (top row),  $z = 140 \text{ cm}$  (middle row),  $z = 180 \text{ cm}$  (bottom row).

### 6.1.6 NRCC Smoke Tower Experiments, Stairwell Plumes

A summary of these experiments can be found in Sec. 3.67.

The NRCC Smoke Tower experiments include measurements of the temperature of smoke ascending a 10 story stairwell. This data is included here in the chapter on Fire Plumes because smoke movement in a vertical shaft with stairs can be considered an obstructed plume. Shown in Fig. 6.15 are predictions of gas temperature measurements made in the center of the stairwell approximately 1.8 m above the slab at floors 2-10. Note that the plot labels “Slot” refer to the data acquisition system in the experiments only and have no meaning in the present context. It should be clear from the plot title how the various curves ought to be interpreted.

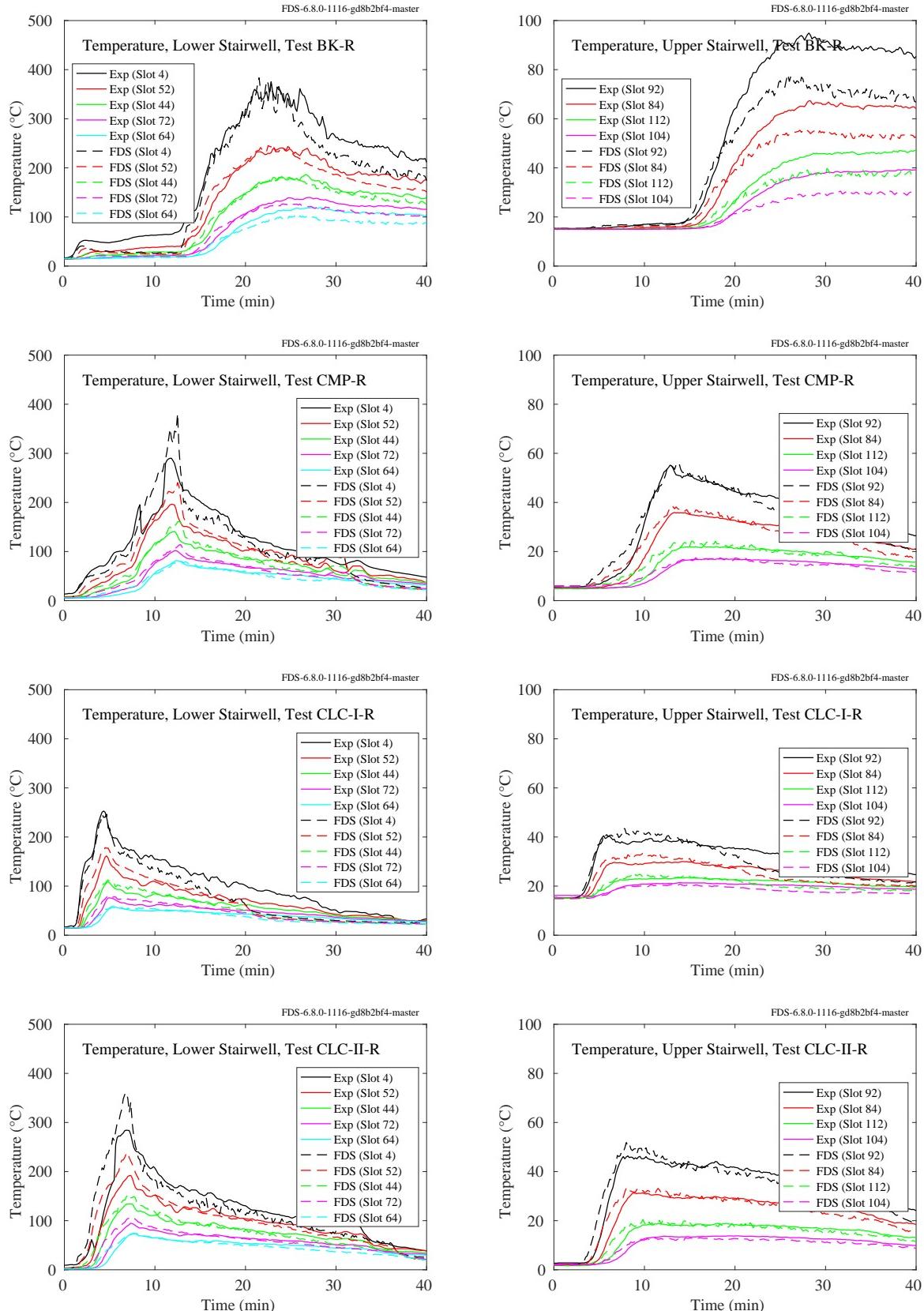


Figure 6.15: NRCC Smoke Tower, stairwell temperatures.

### 6.1.7 Sandia Methane Burner Experiments

A summary of these experiments can be found in Sec. 3.75.

Figures 6.16 through 6.19 compare measured and predicted thermocouple temperatures along the vertical centerline of 3 m methane gas burner fires.

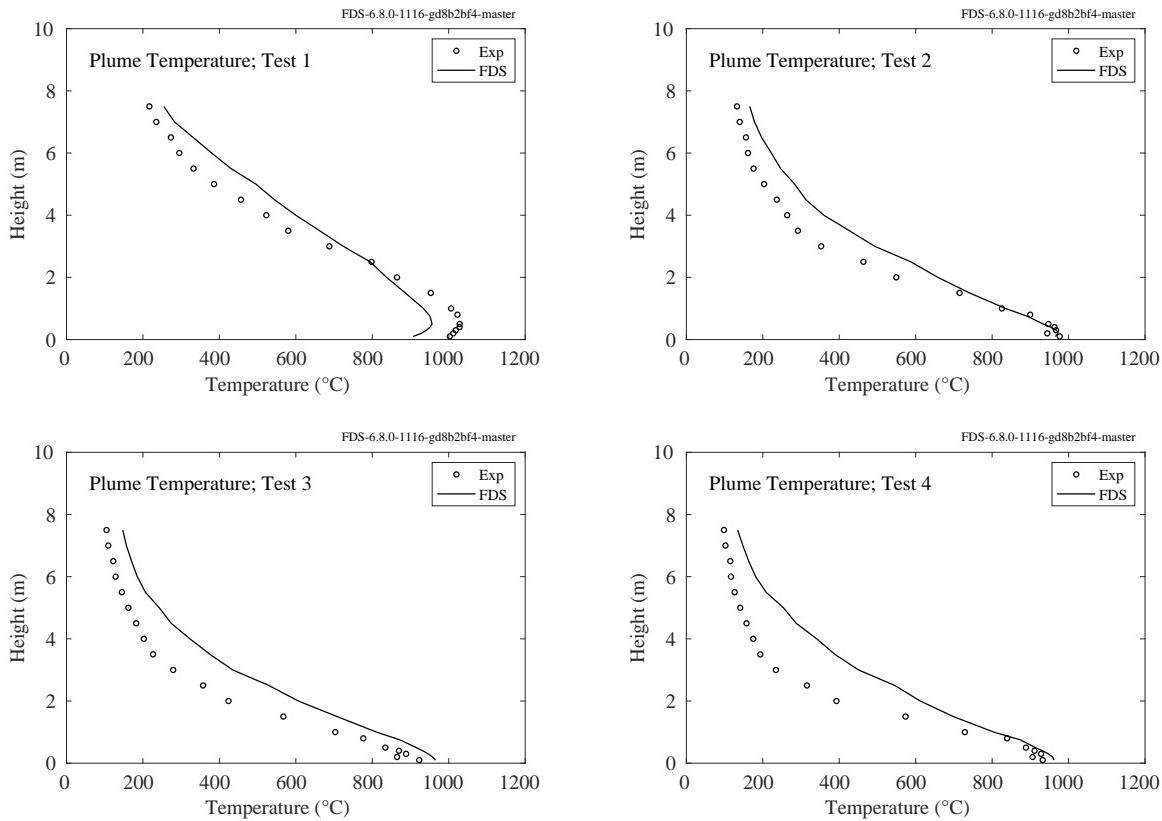


Figure 6.16: Sandia Methane Burner experiments, plume temperature, Tests 1-4.

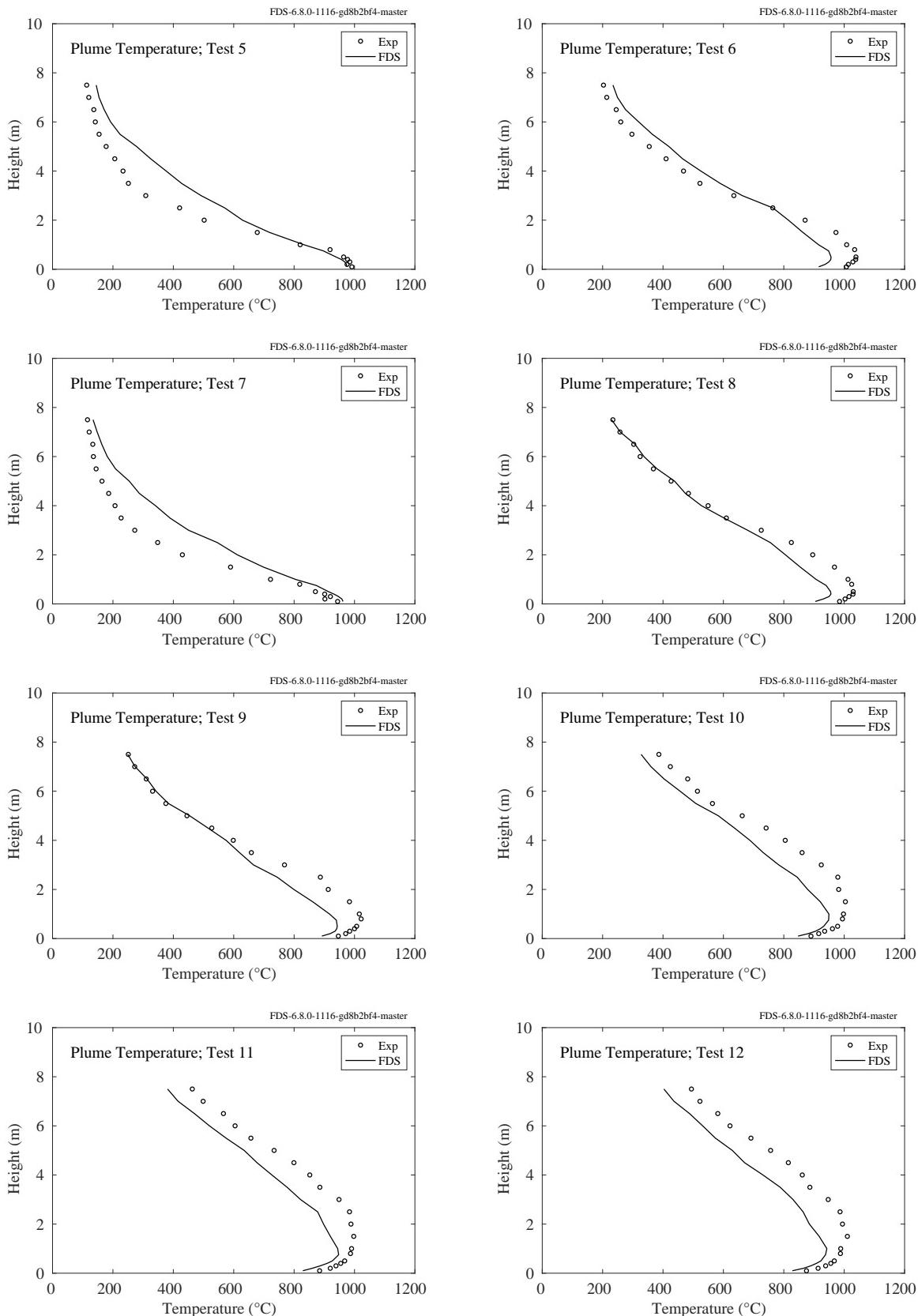


Figure 6.17: Sandia Methane Burner experiments, plume temperature, Tests 5-12.

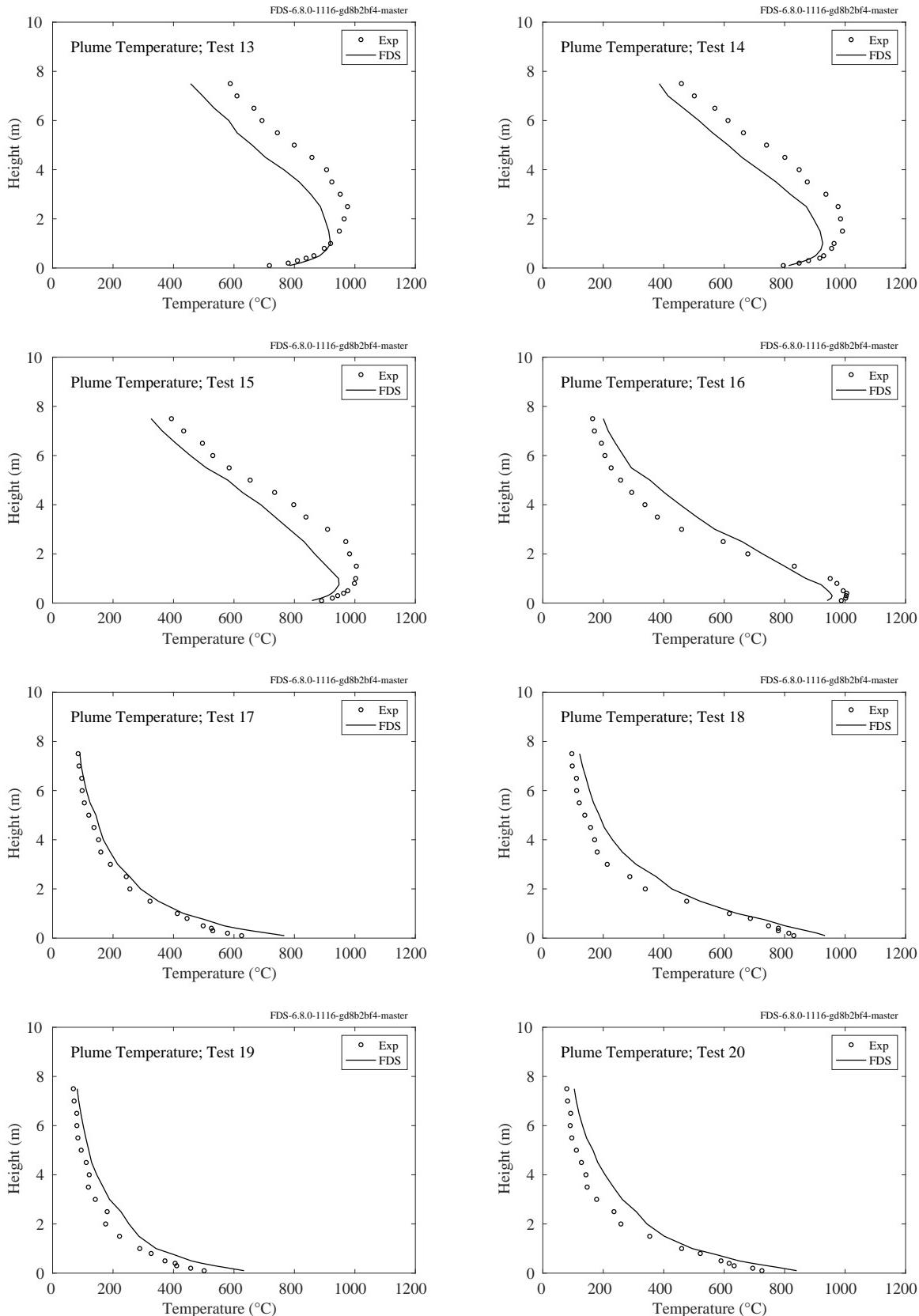


Figure 6.18: Sandia Methane Burner experiments, plume temperature, Tests 13-20.

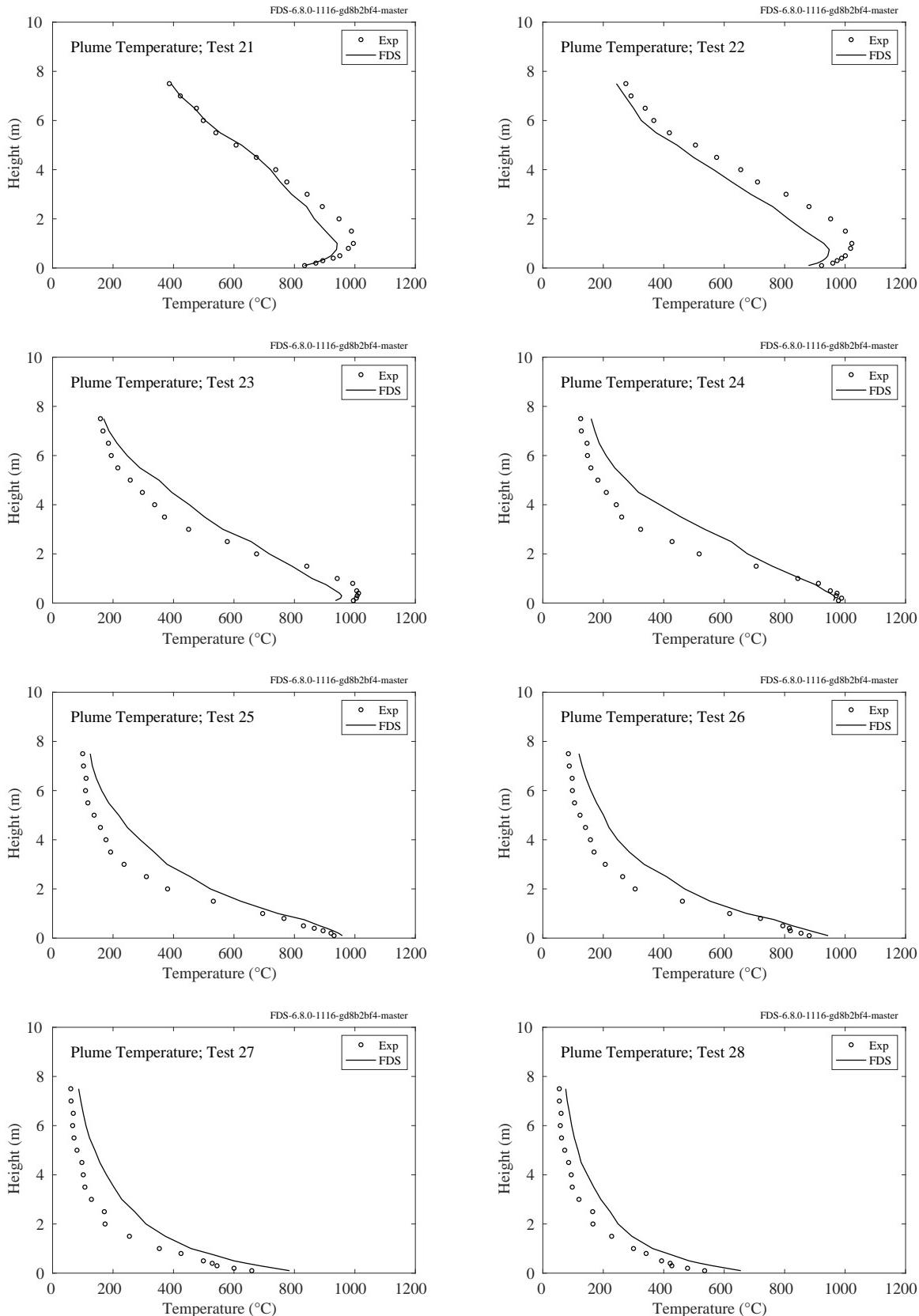


Figure 6.19: Sandia Methane Burner experiments, plume temperature, Tests 21-28.

### 6.1.8 SP Adiabatic Surface Temperature Experiments

A summary of these experiments can be found in Sec. 3.83.

Three experiments were conducted at SP, Sweden, in 2011, in which a 6 m long, 20 cm diameter vertical column was positioned in the middle of 1.1 m and 1.9 m diesel fuel and 1.1 m heptane pool fires [314]. Gas, plate, and steel surface temperature measurements were made at heights of 1 m, 2 m, 3 m, 4 m, and 5 m above the pool surface. Gas temperatures were measured with 0.25 mm and 0.50 mm bead thermocouples. The results are very similar and only the 0.25 mm values are used. In the experiments, the fire was reported to lean. The lean was significant for the 1.9 m diesel fuel fire. In that case, only data from 1 m and 2 m above the pool are used. The average temperature between 10 min and 15 min is the basic of comparison.

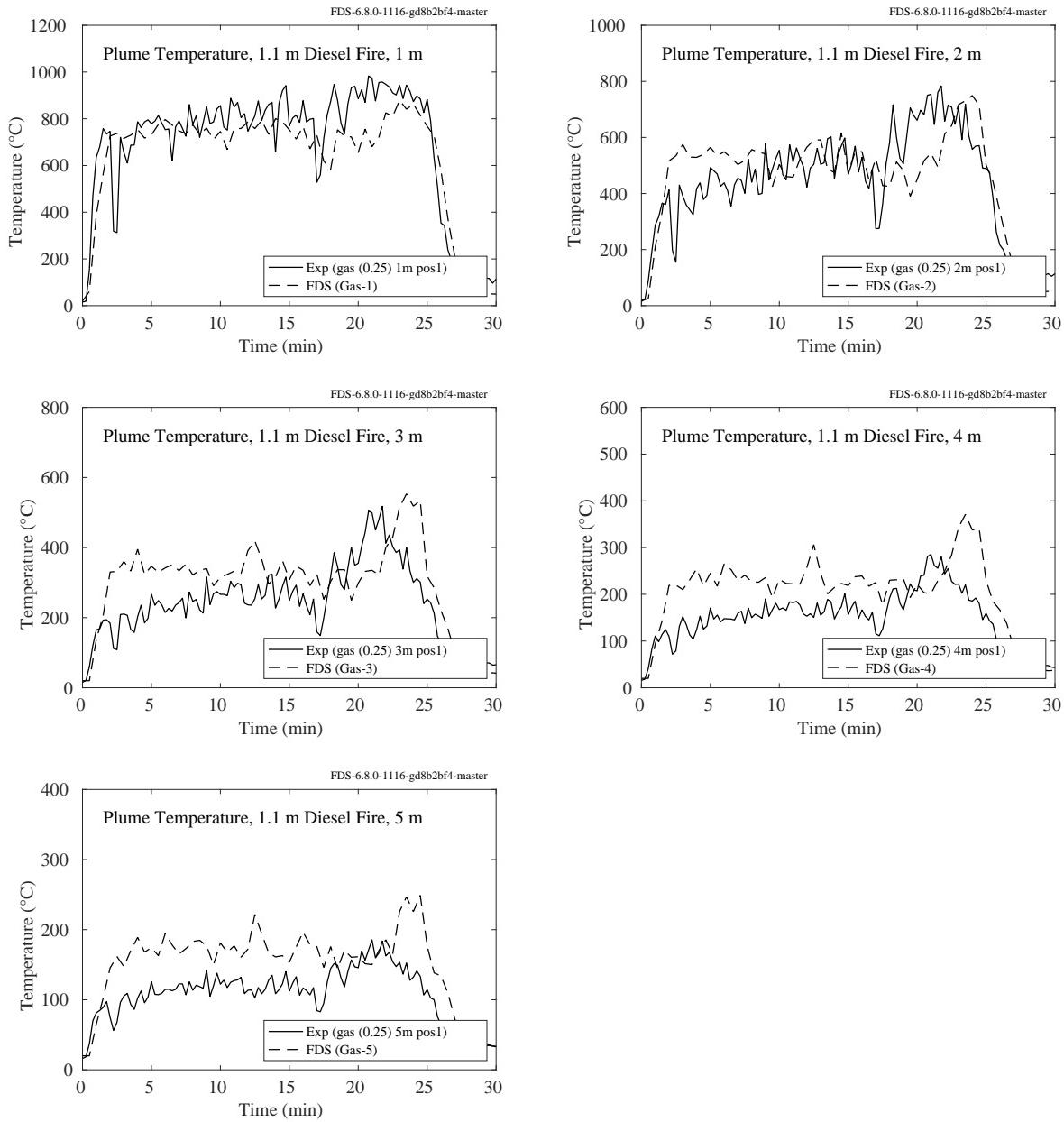


Figure 6.20: SP AST experiments, plume temperature, 1.1 m diesel fire.

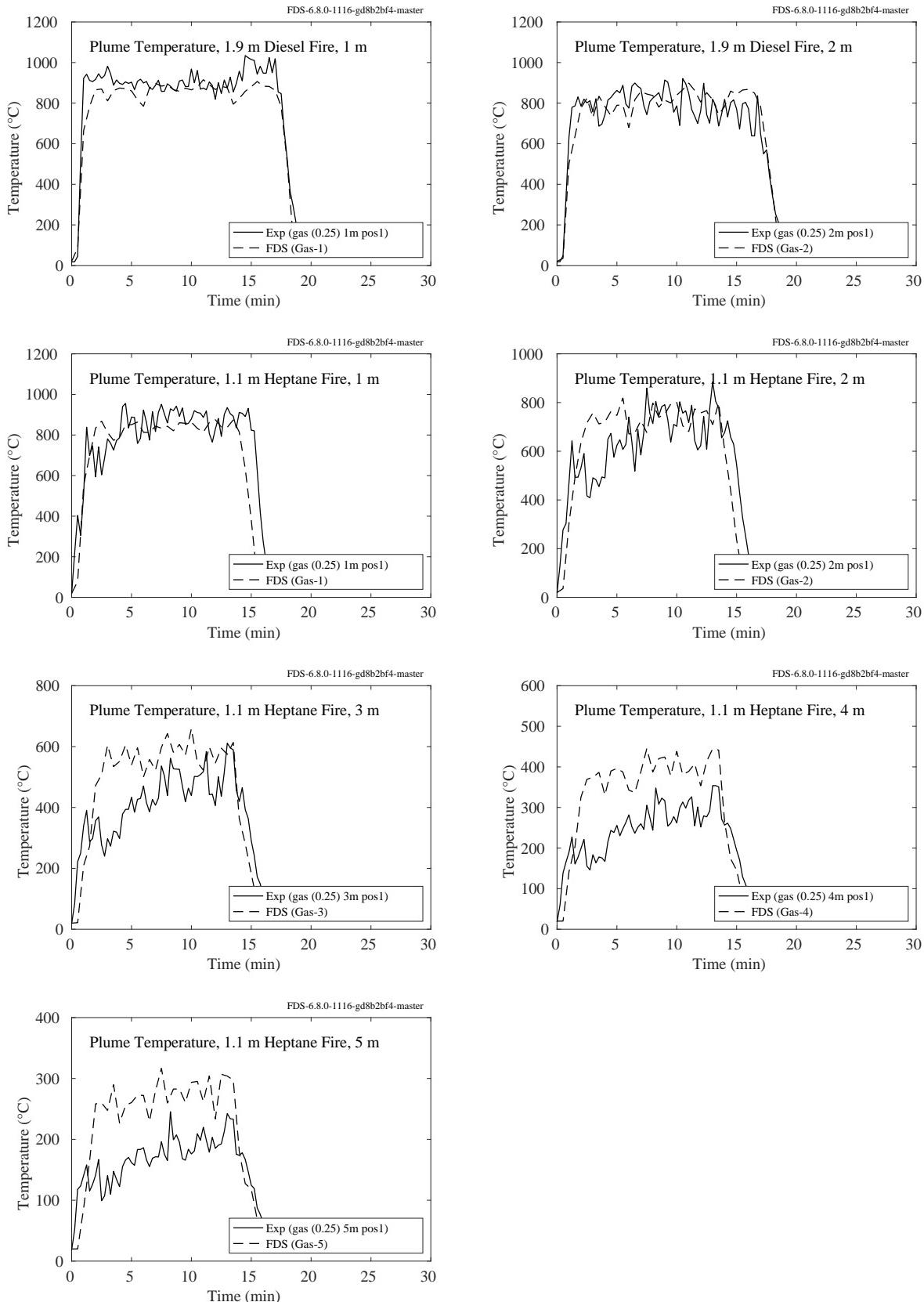


Figure 6.21: SP AST experiments, plume temperature, 1.9 m diesel and 1.9 m heptane fires.

### 6.1.9 UMD Line Burner

A summary of these experiments can be found in Sec. 3.93.

In this section, we present thermocouple temperature measurements and computational results for the UMD Line Burner. Experimental details may be found in White et al. [332]. FDS simulations are performed at three grid resolutions corresponding to  $W/\delta x = 4, 8, 16$ , where  $W = 5 \text{ cm}$  is the width of the fuel slot in the line burner. Fig. 6.22 shows measured and computational results for mean thermocouple temperature across the width of the burner at two heights,  $z$ , above the burner surface. Fig. 6.23 shows a slice of gas temperature for the case with methane fuel and 18 vol. %  $\text{O}_2$  in the coflow stream (nitrogen dilution). The purpose of the image is to provide a qualitative result for the flame.

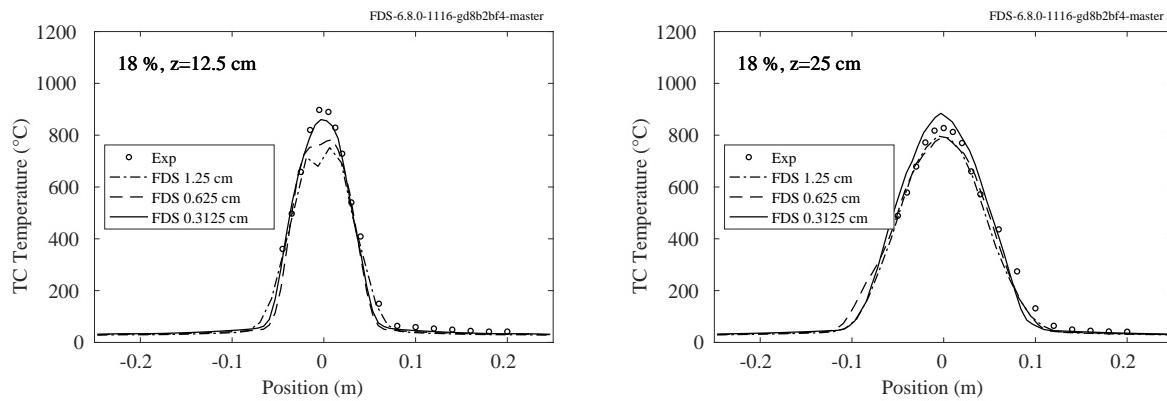


Figure 6.22: Measured and computed mean thermocouple temperature profiles at 18 vol %  $\text{O}_2$ .

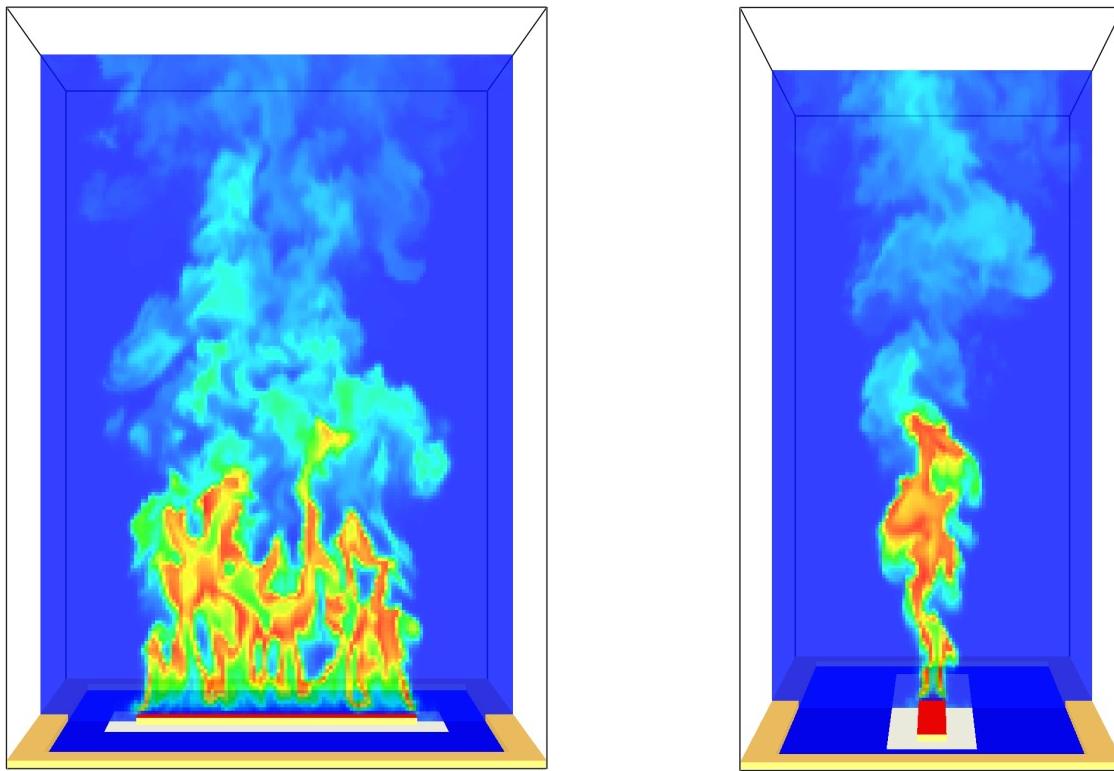


Figure 6.23: UMD Line Burner temperature contours, front (left) and side (right) views for the  $\delta x = 0.625$  cm case. Fuel (natural gas in this case) enters through the red surface. The air with nitrogen dilution (to 18 vol. % O<sub>2</sub> in this case) enters through the blue surface. The white ceramic flame holder is seen surrounding the red burner surface. The right side view corresponds to the profiles shown in Fig. 6.22 through the center of the burner at different heights  $z$  from the red burner surface. Within the slice plane blue represents 20 °C, red 1500 °C.

### 6.1.10 USN High Bay Hangar Experiments

A summary of these experiments can be found in Sec. 3.98.

A large number of plume temperature measurements are available from the US Navy experiments conducted at Keflavik, Iceland, and Barber's Point, Hawaii. The hangars were very large in size (22 m high in Iceland and 15 m high in Hawaii) and the heat release rates varied from 100 kW to 33 MW. All experiments made use of a fuel pan filled with either JP-5 or JP-8 jet fuel, positioned in the center of the hangar.

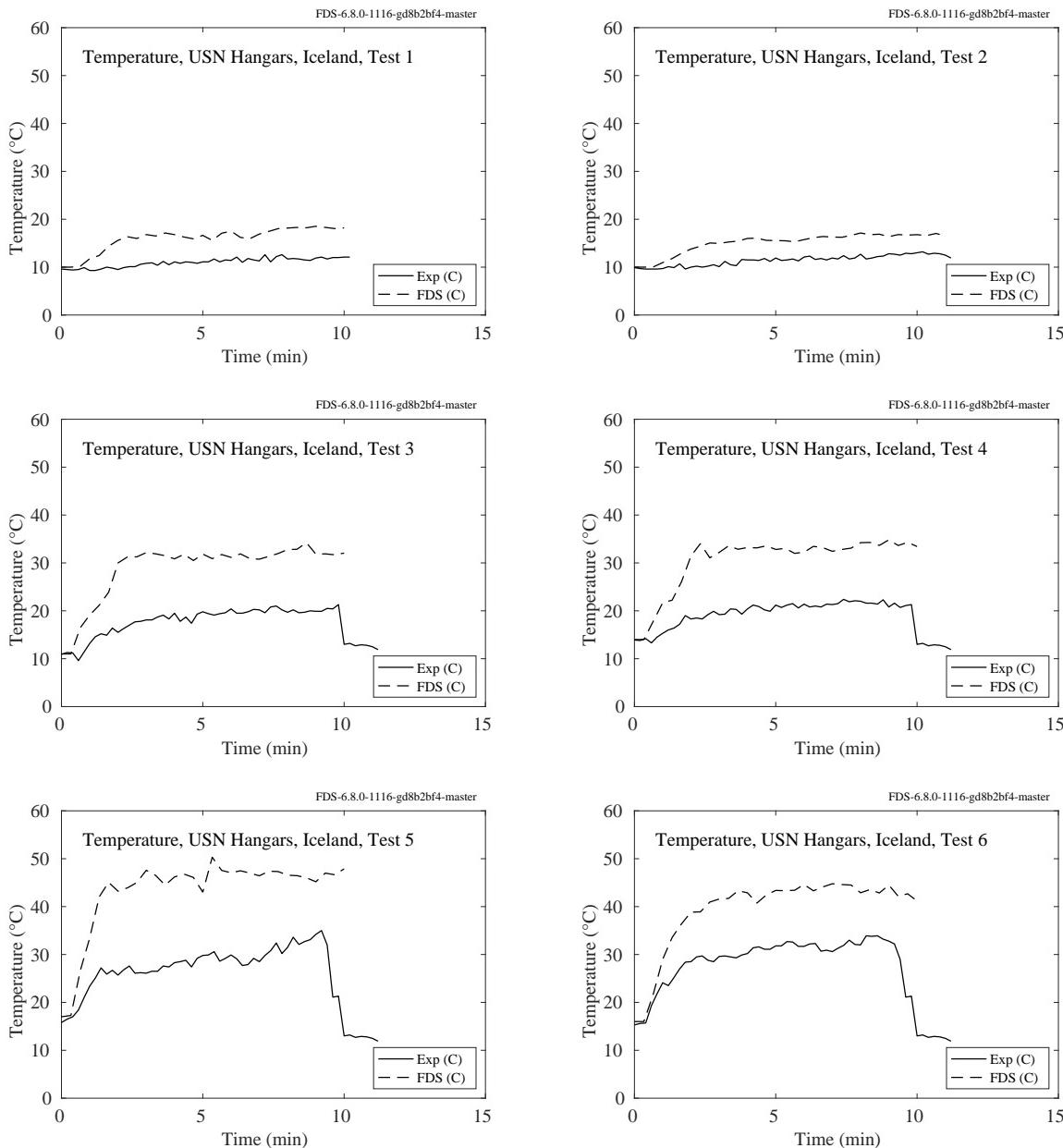


Figure 6.24: USN Hangar experiments, Iceland, plume temperature, Tests 1-6.

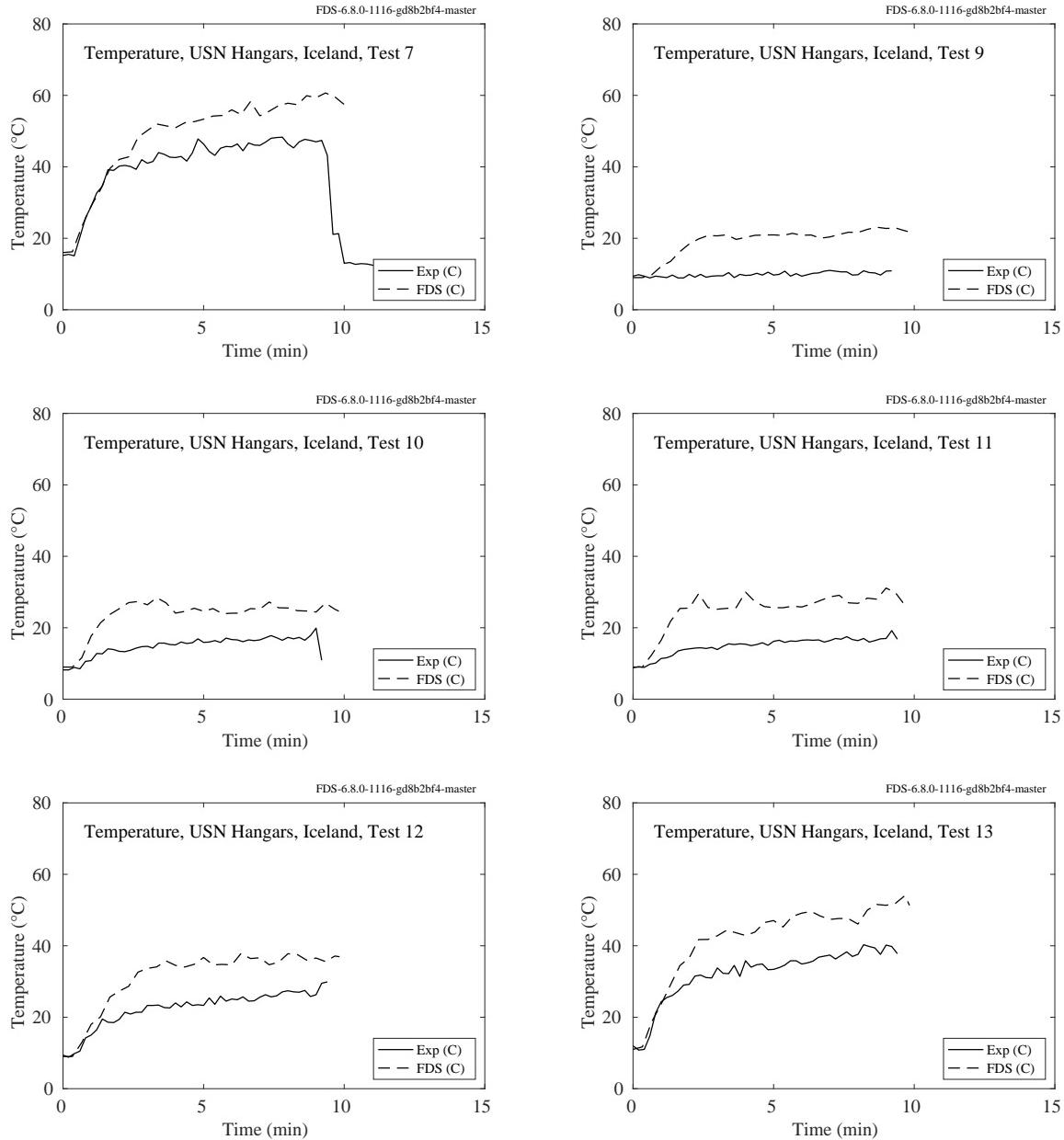


Figure 6.25: USN Hangar experiments, Iceland, plume temperature, Tests 7, 9-13.

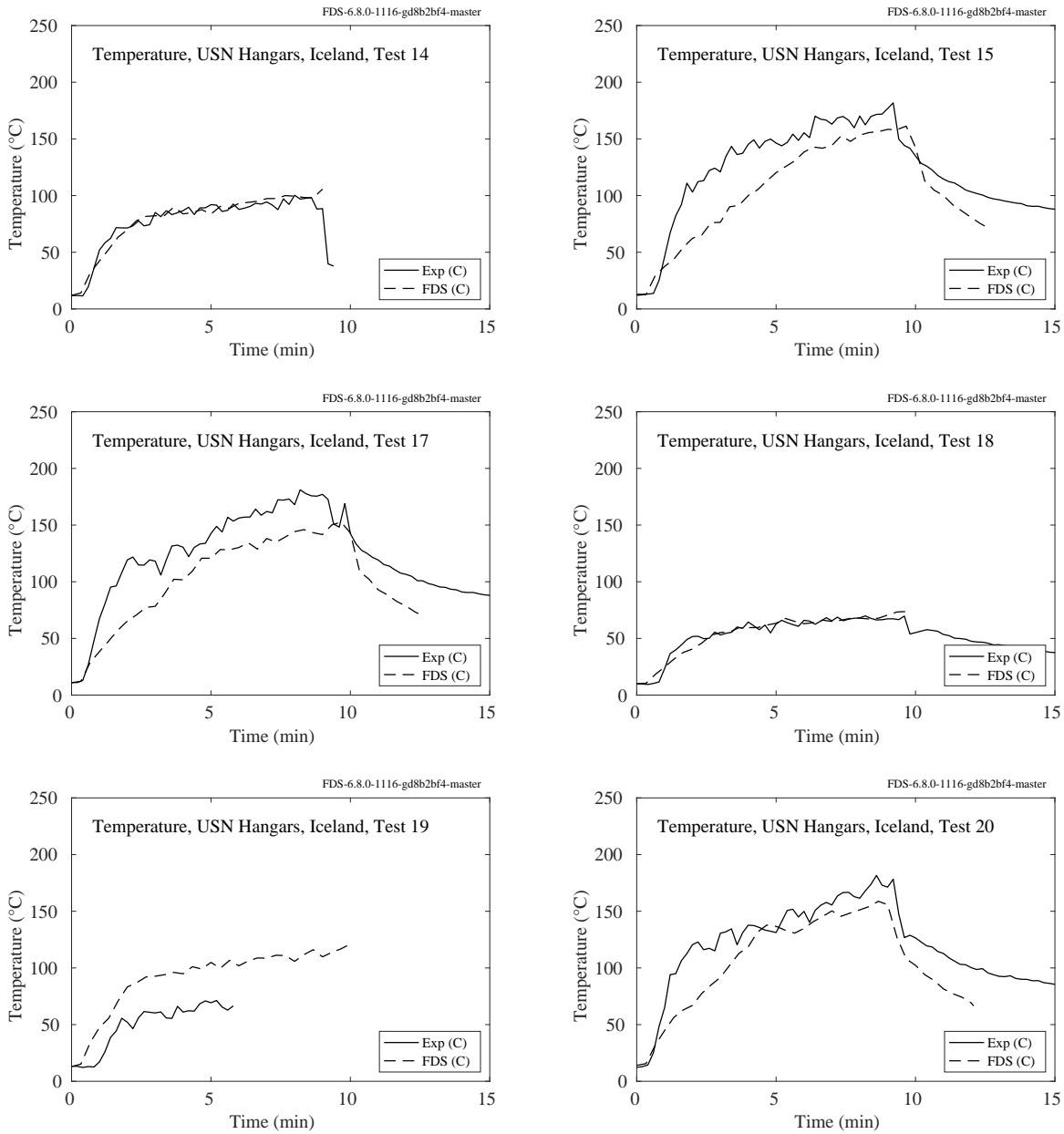


Figure 6.26: USN Hangar experiments, Iceland, plume temperature, Tests 14-15, 17-20.

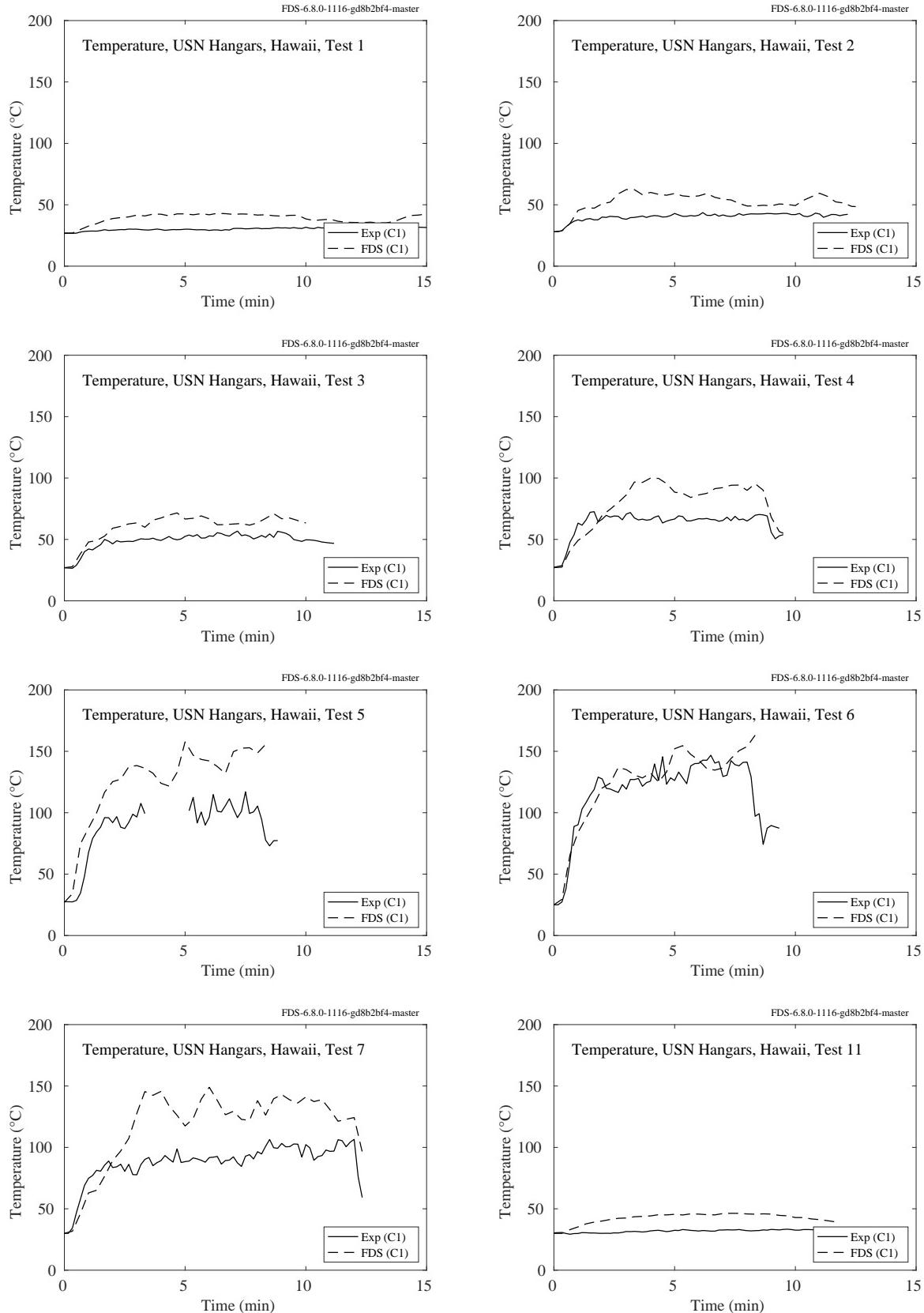


Figure 6.27: USN Hangar experiments, Hawaii, plume temperature, Tests 1-7, 11.

### 6.1.11 VTT Large Hall Experiments

A summary of these experiments can be found in Sec. 3.102.

The VTT experiments consisted of liquid fuel pan fires positioned in the middle of a large fire test hall. Plume temperatures were measured at two heights above the fire, 6 m (T G.1) and 12 m (T G.2). The flames were observed to extend to about 4 m above the fire pan.

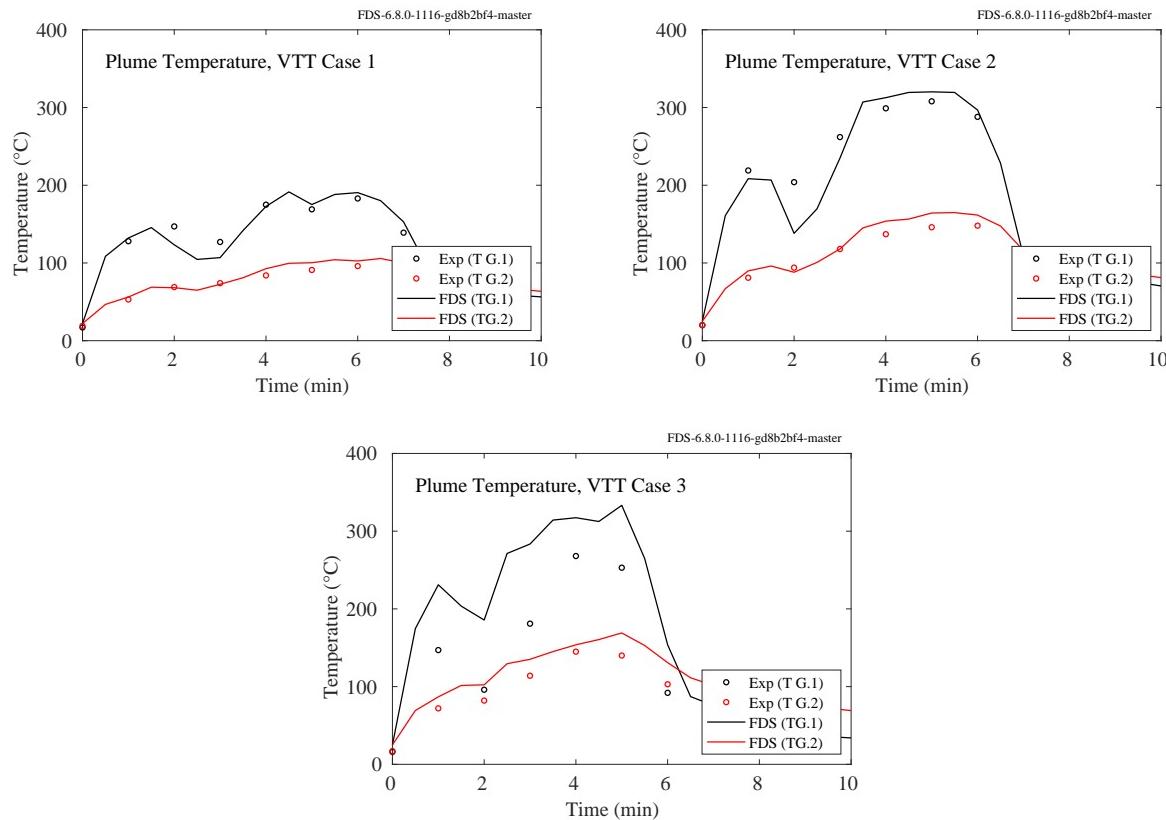


Figure 6.28: VTT experiments, plume temperature.

### 6.1.12 Waterloo Methanol Pool Fire Experiment

A summary of these experiments can be found in Sec. 3.104.

Figure 6.29 displays the centerline profile of measured and predicted mean temperatures above a 30 cm diameter methanol pool fire. These measurements were conducted by Hamins and Lock [344] at NIST, along with radial profiles at 40 cm, 50 cm, and 60 cm. All of the other measurements on the following pages were conducted by Weckman at the University of Waterloo [342].

Figures 6.30 through 6.33 display radial profiles of measured and predicted mean (left hand plots) and root mean square (right hand plots) temperatures. The root mean square of the temperature is given by

$$\overline{(T' T')}^{1/2} = \sqrt{\frac{\sum_{i=1}^n (T_i - \bar{T})^2}{n-1}} \quad (6.2)$$

where  $T_i$  is the instantaneous value of temperature and  $\bar{T}$  is the average value over 50 s. The profile heights range from 2 cm to 30 cm above the pool surface. Time resolved temperature data was measured using 50  $\mu\text{m}$  diameter, bare-wire thermocouples (Pt vs Pt-10% Rh) with known bead diameters in the range of 75  $\mu\text{m}$  to 100  $\mu\text{m}$ .

Figures 6.34 through 6.36 display radial profiles of measured and predicted estimates of temperature-velocity covariances:

$$\overline{w' T'} = \frac{\sum_{i=1}^n (w_i - \bar{w})(T_i - \bar{T})}{n-1} \quad ; \quad \overline{u' T'} = \frac{\sum_{i=1}^n (u_i - \bar{u})(T_i - \bar{T})}{n-1} \quad (6.3)$$

where  $u_i$  and  $w_i$  are instantaneous values of the horizontal and vertical components of velocity and  $\bar{u}$  and  $\bar{w}$  are 50 s time averages.

The FDS results are shown at three grid resolutions, 0.5 cm, 1 cm, and 2 cm.

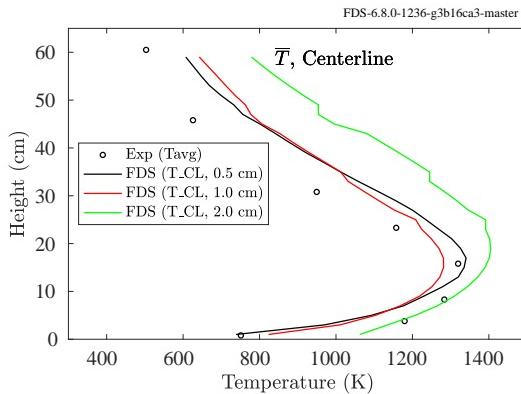


Figure 6.29: Waterloo Methanol, centerline profile of mean temperature, 2 cm to 60 cm above the burner.

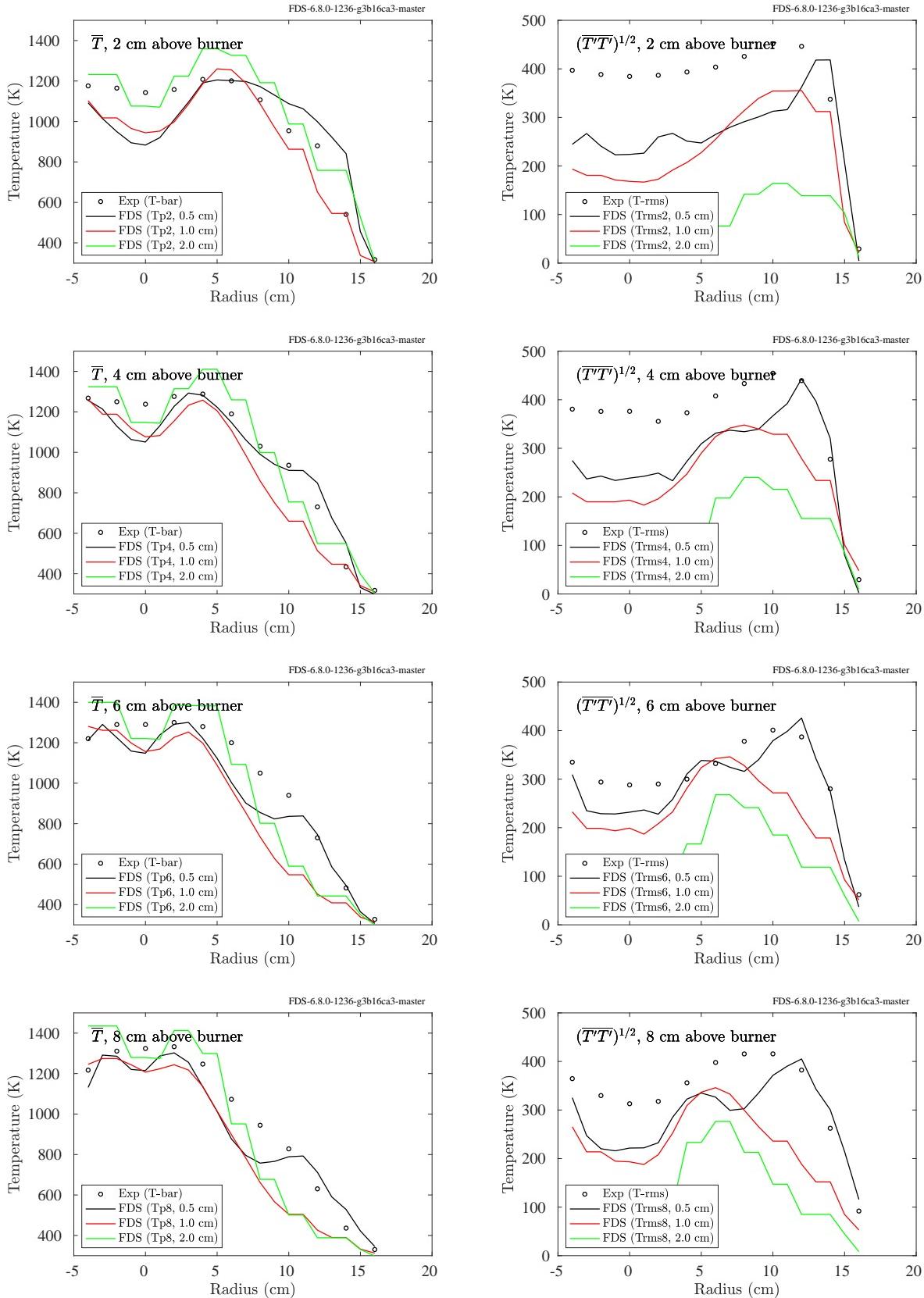


Figure 6.30: Waterloo Methanol, radial profiles of mean (left) and rms (right) temperature, 2 cm to 8 cm above the burner.

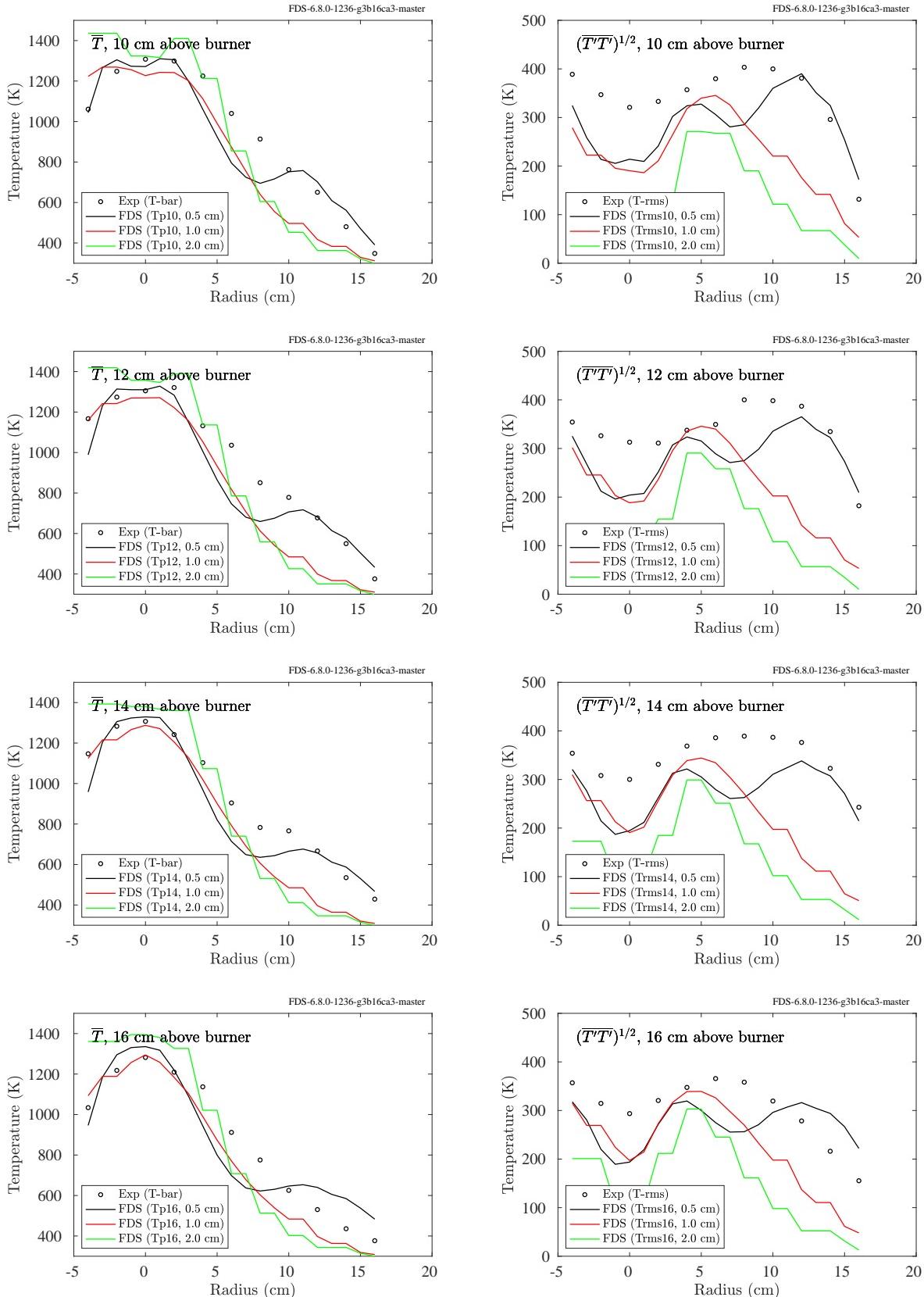


Figure 6.31: Waterloo Methanol, radial profiles of mean (left) and rms (right) temperature, 10 cm to 16 cm above the burner.

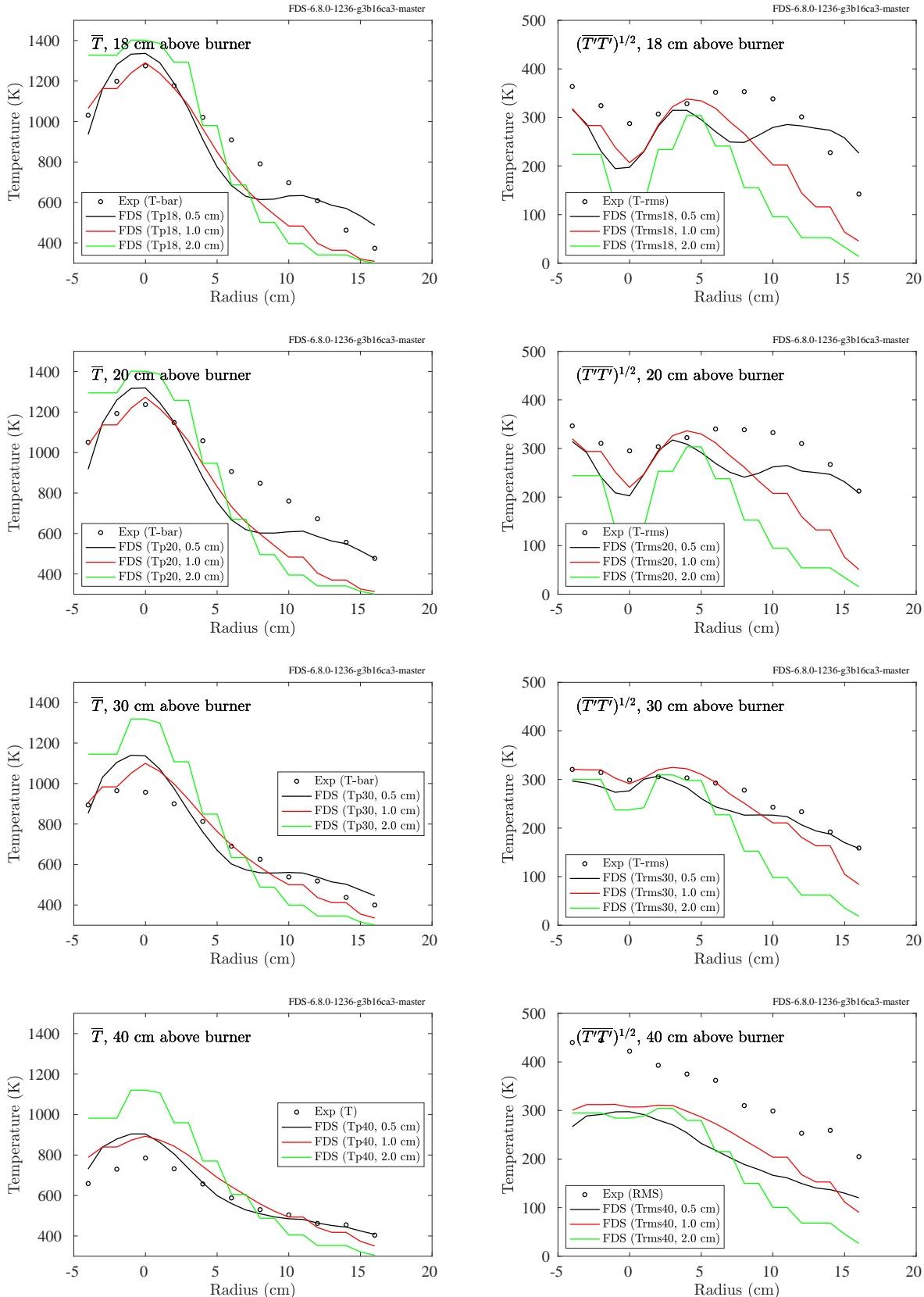


Figure 6.32: Waterloo Methanol, radial profiles of mean (left) and rms (right) temperature, 18 cm to 40 cm above the burner. The measurement at 40 cm was performed by Hamins and Lock [344].

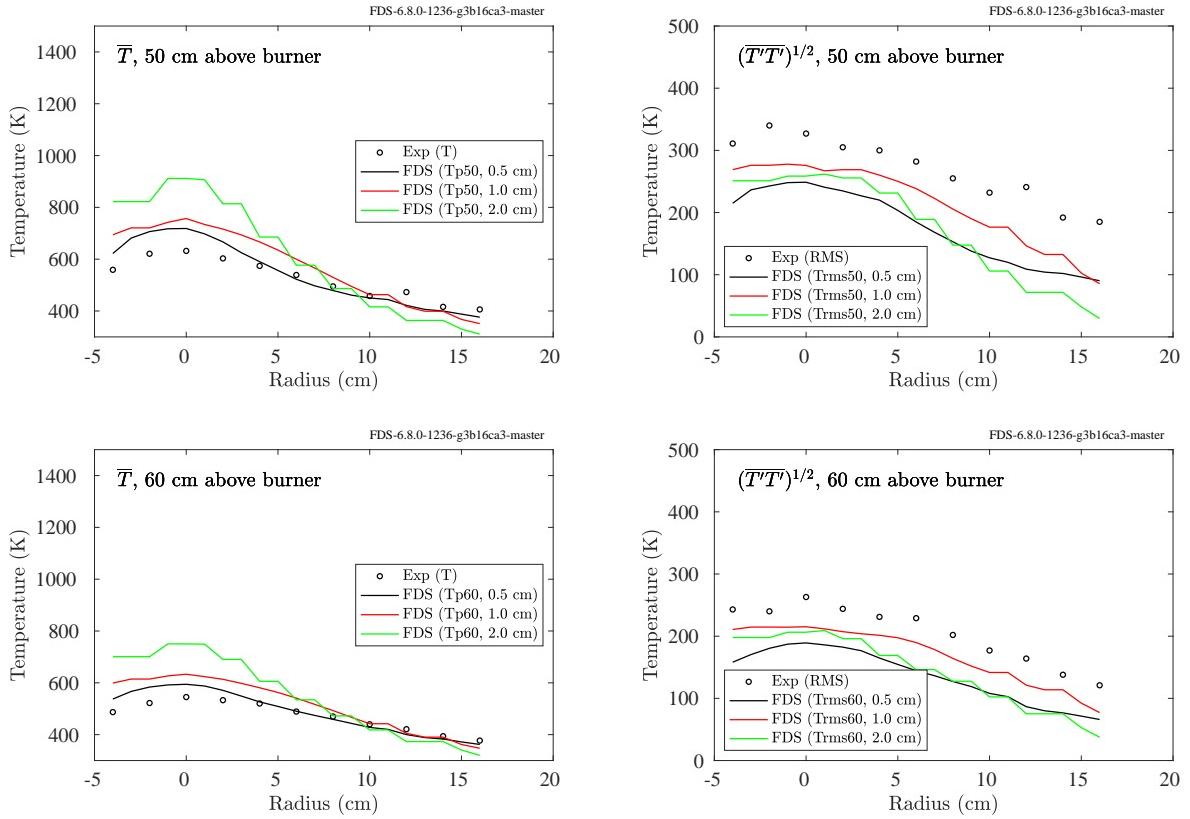
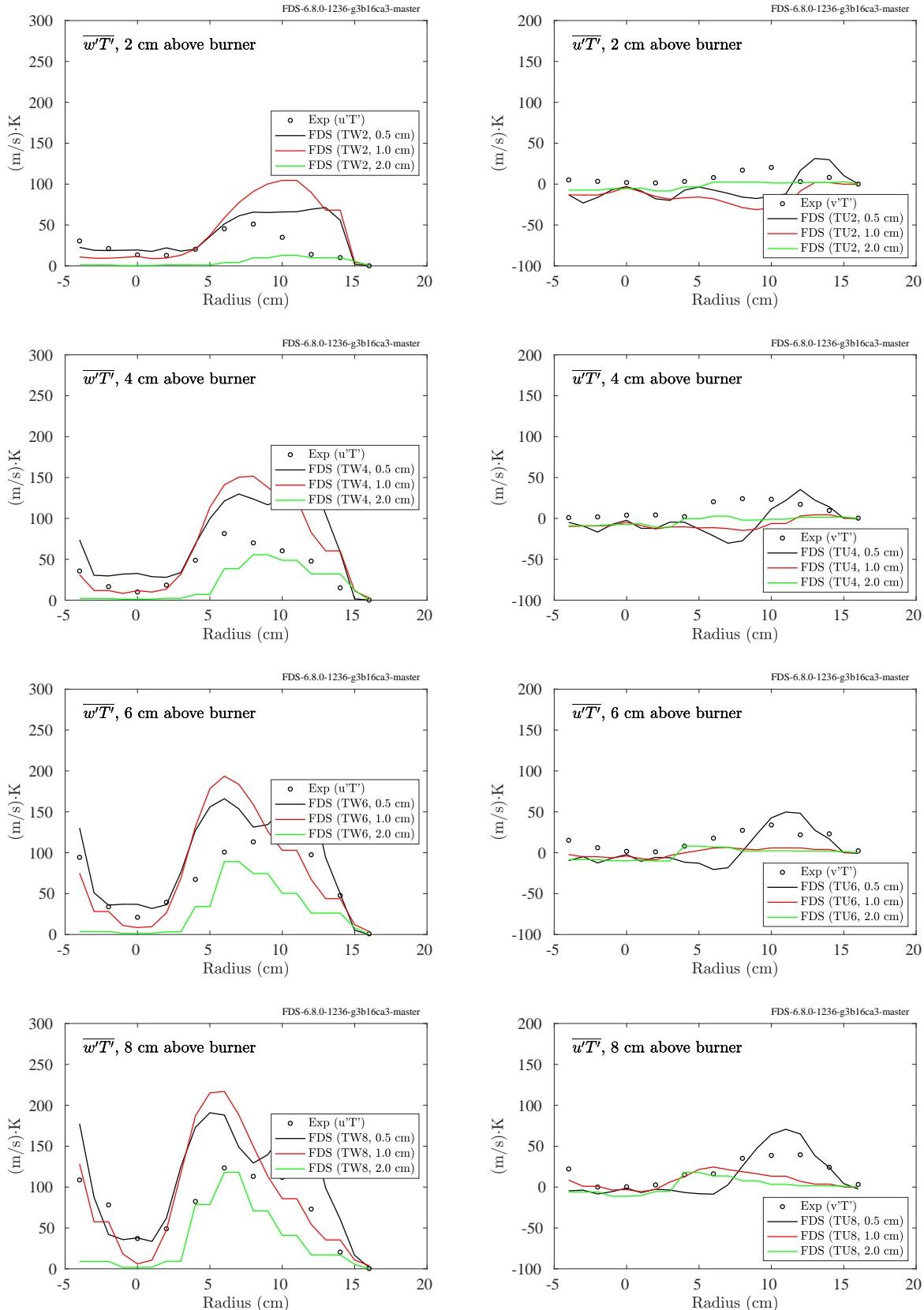
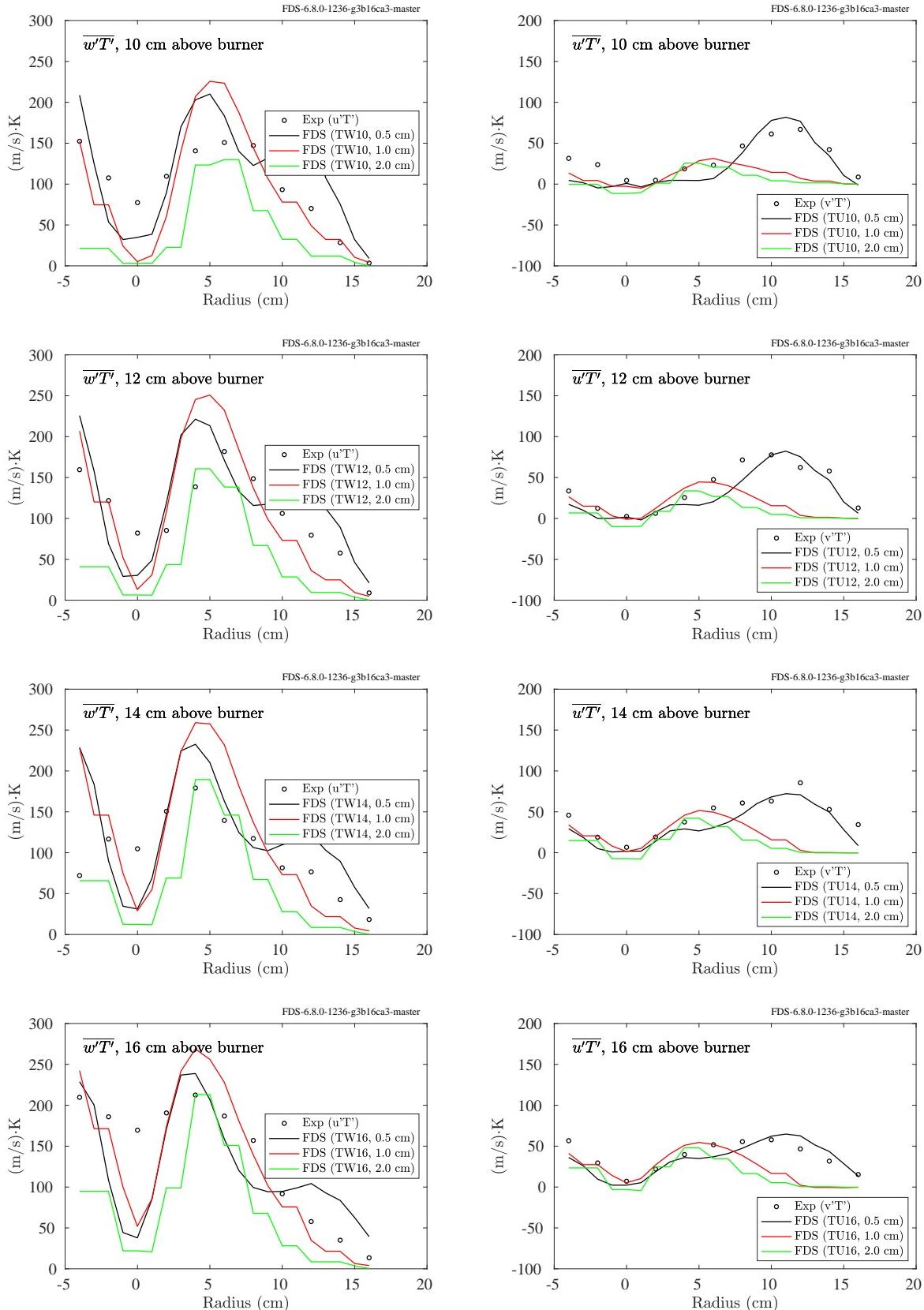


Figure 6.33: Waterloo Methanol, radial profiles of mean (left) and rms (right) temperature, 50 cm to 60 cm above the burner. The measurements were performed by Hamins and Lock [344].

Figure 6.34: Waterloo Methanol, radial profiles of  $\overline{T'w'}$  (left) and  $\overline{T'u'}$  (right), 2 cm to 8 cm above the burner.

Figure 6.35: Waterloo Methanol, radial profiles of  $\overline{T'w'}$  (left) and  $\overline{T'u'}$  (right), 10 cm to 16 cm above the burner.

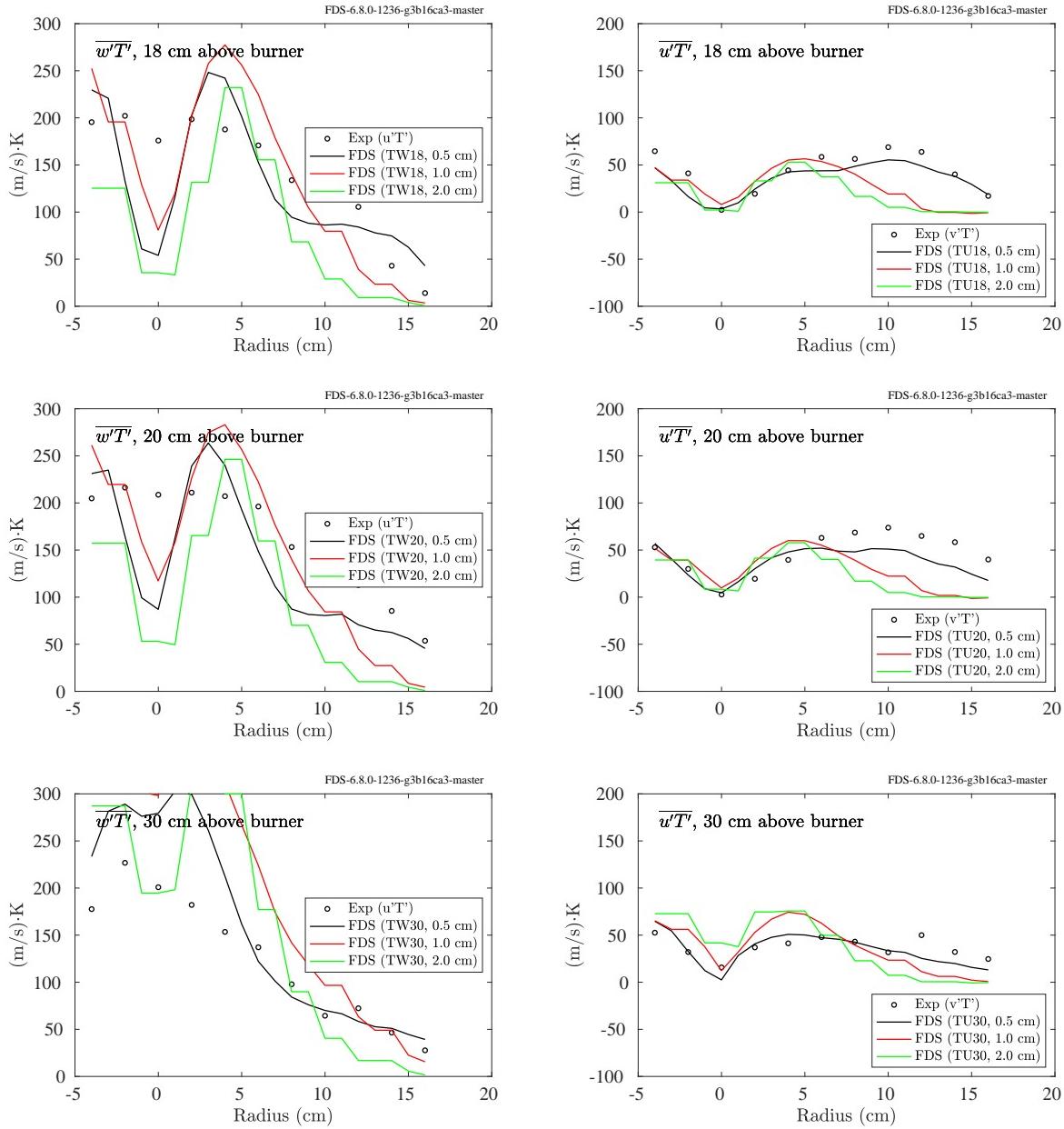


Figure 6.36: Waterloo Methanol, radial profiles of  $\overline{T'w'}$  (left) and  $\overline{T'u'}$  (right), 18 cm to 30 cm above the burner.

### 6.1.13 Summary of Plume Temperature Predictions

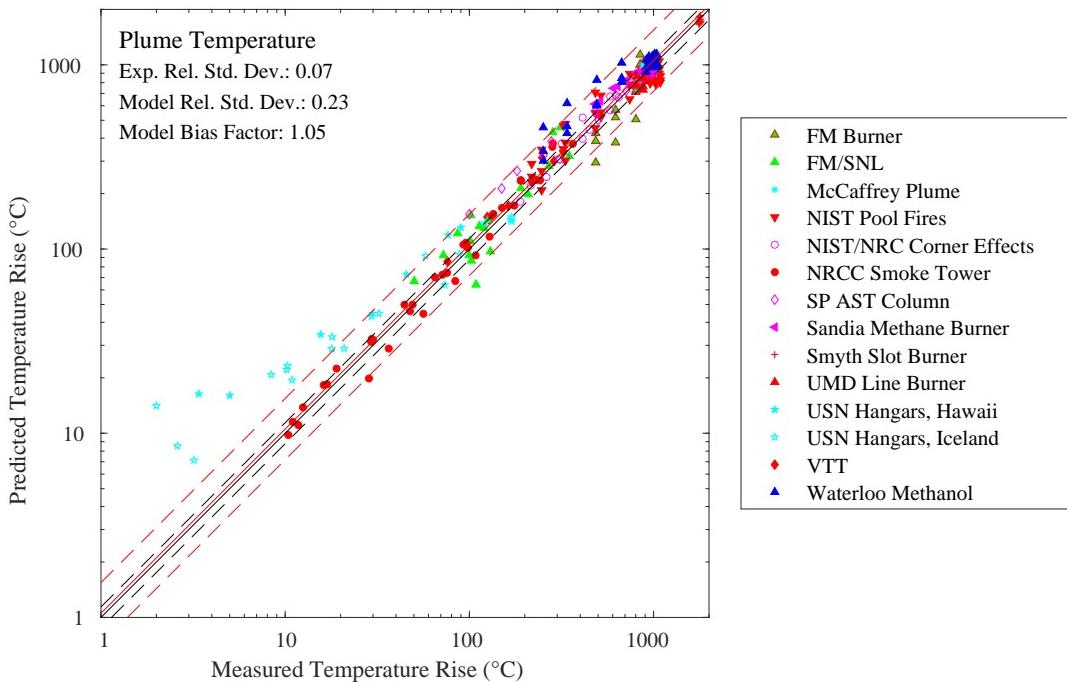


Figure 6.37: Summary of plume temperature predictions.

## 6.2 Flame Height

In fire experiments, the flame height is typically defined as the height at which luminous flame can be seen 50 % of the time. For simulations, the “flame height” can be defined as the height at which most of the fire’s energy has been released. “Most” is taken as some fraction,  $f$ , between 0.95 and 0.99. Mathematically, this is found by considering the heat release rate per unit vertical length,  $z$ :

$$\dot{q}'(z, t) = \int_{-\infty}^{\infty} \int_{-\infty}^{\infty} \dot{q}'''(x', y', z, t) dx' dy' \quad (6.4)$$

where  $\dot{q}'''(x, y, z, t)$  is the instantaneous heat release rate per unit volume at a specific point in the domain. The flame height of the simulated fire is given by  $z_L(t) - z_0$ , where  $z_L(t)$  is the height at which the cumulative heat release rate reaches the fraction,  $f$ , of the total,  $\dot{Q}(t)$ .

$$f \dot{Q}(t) = \int_{z_0}^{z_L(t)} \dot{q}'(z', t) dz' \quad (6.5)$$

$z_0$  is the height of the firebed or burner surface.

### 6.2.1 Heskestad’s Flame Height Correlation

Table 6.1 lists the parameters for FDS simulations of fires in a 1 m by 1 m square pan<sup>2</sup>. Figure 6.38 shows a verification of the heat release rate for each case, and Fig. 6.39 compares the FDS predictions with Heskestad’s empirical correlation. Note that the flame height for the FDS simulations is defined as the distance above the pan, on average, at which 99 % of the fuel has been consumed. Note also that the simulations were run at three different grid resolutions. A convenient length scale is given by

$$D^* = (Q^*)^{2/5} D \quad (6.6)$$

Given a grid cell size,  $\delta x$ , the three resolutions can be characterized by the non-dimensional quantity,  $D^*/\delta x$ , whose values in these cases are 5, 10 and 20.

The flame height definition used in Fig. 6.39 (99 % fuel consumption) is admittedly arbitrary and is often questioned when FDS predictions of flame height are compared with experimental values, which are usually based on luminosity (effectively measuring radiation emission from soot). Further, Heskestad’s flame height correlation is one among many such correlations [25, 365, 366, 367, 368, 369, 370], and the reported variation is significant, especially at low values of  $Q^*$  where the details of the burner configuration (shape of the burner, etc.) become important. To illustrate the uncertainty one can expect from FDS calculations and to test the sensitivity of the reported FDS results to the flame height definition, Fig. 6.40 shows two different FDS flame height predictions, one at 99 % fuel consumption (as in Fig. 6.39)—the red curve—and one using 95 % fuel consumption—the blue curve. Three different grid resolutions were run for each flame height definition. For 99 % fuel consumption, the red dashed line is the maximum flame height from the three resolutions. For 95 % fuel consumption, the blue dashed line is the minimum flame height from the three resolutions. We also overlay several different flame height correlations (colored solid lines).

Figure 6.41 includes comparisons of the predicted HRR as a function of the height of the burner for three different values of  $Q^*$ . The experimental measurements were performed by Tamanini at Factory Mutual [371]. Both the HRR and height above the burner have been non-dimensionalized by the total HRR and the flame height, respectively. These results demonstrate that the predicted spatial distribution of the energy release improves as the numerical grid is refined.

---

<sup>2</sup>The effective diameter,  $D$ , of a 1 m square pan is 1.13 m, obtained by equating the area of a square and circle.

Table 6.1: Summary of parameters for the flame height predictions. The grid cell size,  $\delta x_{10}$ , refers to the case where  $D^*/\delta x=10$ .

| $Q^*$ | $\dot{Q}$ (kW) | $D^*$ (m) | $\delta x_5$ (m) | $\delta x_{10}$ | $\delta x_{20}$ |
|-------|----------------|-----------|------------------|-----------------|-----------------|
| 0.1   | 151            | 0.45      | 0.090            | 0.045           | 0.022           |
| 0.2   | 303            | 0.59      | 0.119            | 0.059           | 0.030           |
| 0.5   | 756            | 0.86      | 0.171            | 0.086           | 0.043           |
| 1     | 1513           | 1.13      | 0.226            | 0.113           | 0.057           |
| 2     | 3025           | 1.49      | 0.298            | 0.149           | 0.075           |
| 5     | 7564           | 2.15      | 0.430            | 0.215           | 0.108           |
| 10    | 15127          | 2.84      | 0.568            | 0.284           | 0.142           |
| 20    | 30255          | 3.75      | 0.749            | 0.375           | 0.187           |
| 50    | 75636          | 5.40      | 1.081            | 0.540           | 0.270           |
| 100   | 151273         | 7.13      | 1.426            | 0.713           | 0.356           |
| 200   | 302545         | 9.41      | 1.882            | 0.941           | 0.470           |
| 500   | 756363         | 13.6      | 2.715            | 1.357           | 0.679           |
| 1000  | 1512725        | 17.9      | 3.582            | 1.791           | 0.895           |
| 2000  | 3025450        | 23.6      | 4.726            | 2.363           | 1.182           |
| 5000  | 7563625        | 34.1      | 6.819            | 3.409           | 1.705           |
| 10000 | 15127250       | 45.0      | 8.997            | 4.499           | 2.249           |

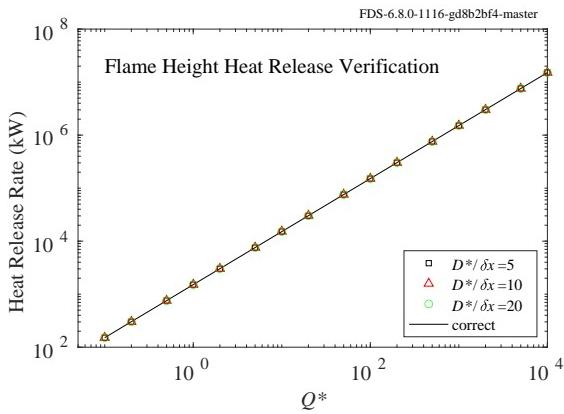


Figure 6.38: Verification of the heat release rate for Heskestad Flame Height cases.

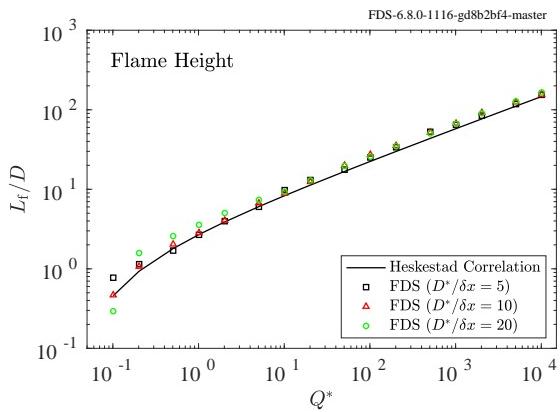


Figure 6.39: Comparison of FDS predictions of flame height from a 1 m square pan fire for  $Q^*$  values ranging from 0.1 to 10000.

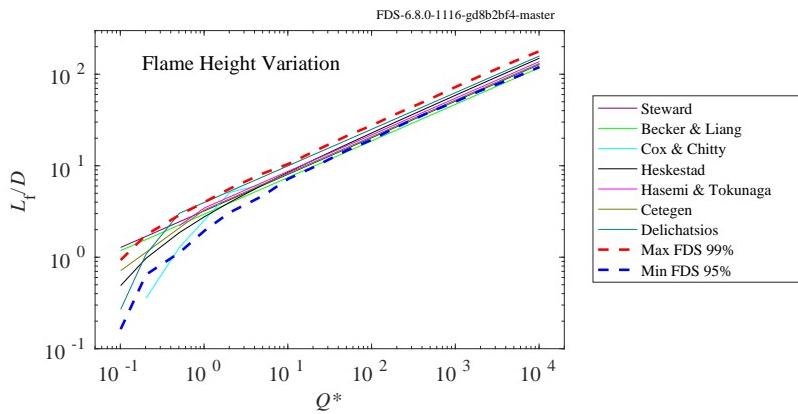


Figure 6.40: Flame height predictions from various correlations compared with FDS predictions using two different flame height definitions. Uncertainty (maximum variation) at  $Q^* > 1$  is  $\pm 15\%$ . At  $Q^* = 0.1$ , the uncertainty is approximately  $\pm 65\%$ . Correlation references: Steward [365], Becker and Liang [366], Cox and Chitty [367], Heskestad [25], Hasemi and Tokunaga [368], Cetegen [369], Delichatsios [370].

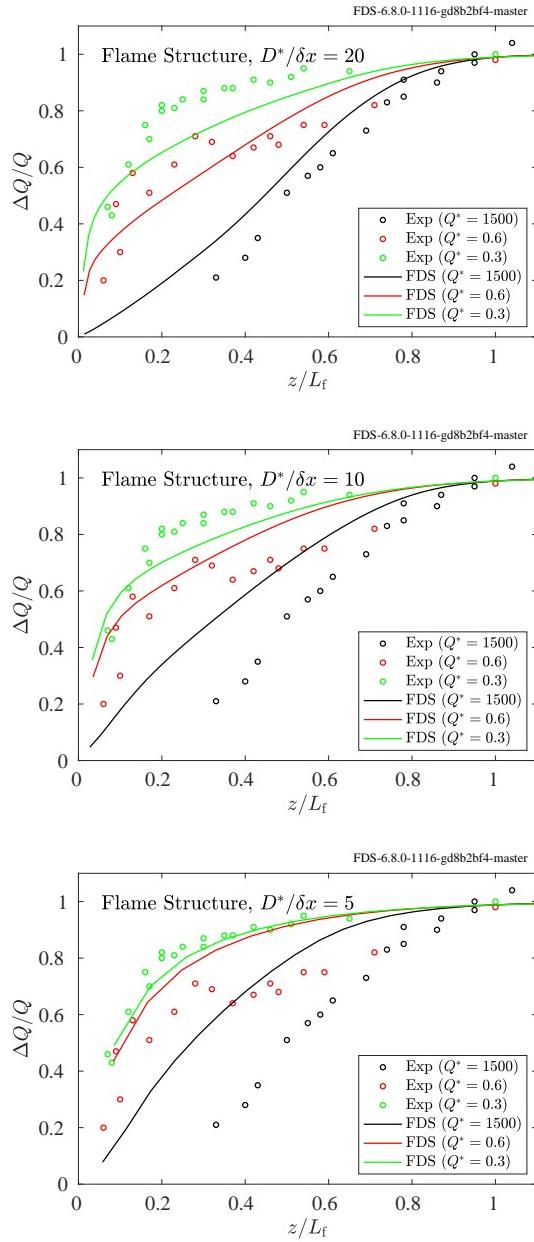


Figure 6.41: Predicted HRR as a function of height above the burner compared to measurements.

## 6.2.2 UMD Line Burner

A summary of these experiments can be found in Sec. 3.93.

FDS simulations are performed at three grid resolutions corresponding to  $W/\delta x = 4, 8, 16$ , where  $W = 5$  cm is the width of the fuel slot in the line burner. Fig. 6.42 shows measured and predicted flame heights of the methane and propane fires as a function of oxygen concentration. For FDS, the flame height is taken as the distance above the burner where 97 % of the fuel gas is consumed, on average.

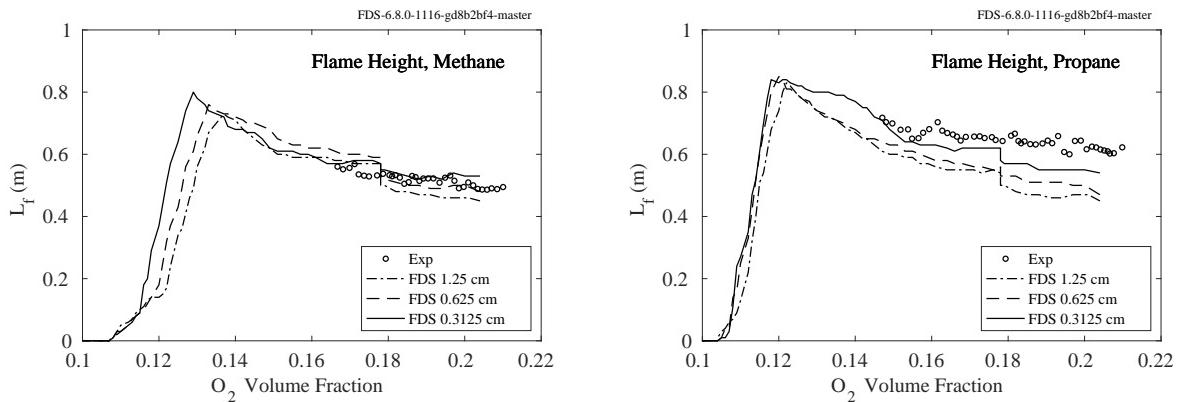


Figure 6.42: Measured and predicted mean flame heights for the methane and propane UMD Line Burner experiments.

### 6.2.3 Flame Height Summary

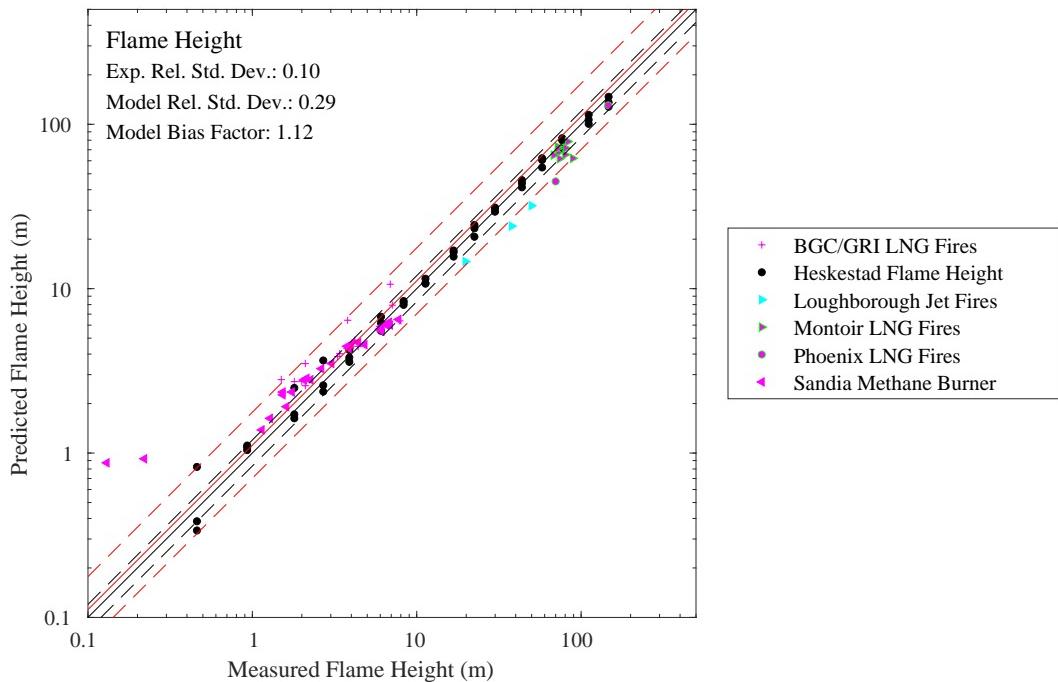


Figure 6.43: Summary of measured and predicted mean flame heights.

### 6.3 Flame Tilt

When assessing the hazards of a large, outdoor fire, not only is flame height a concern, but the flame tilt as well. That is, a fire in the wind tends to tilt in the windward direction. The angle from the vertical is referred to as “flame tilt.” Figure 6.44 presents the results of flame tilt predictions for some large, outdoor pool fire experiments.

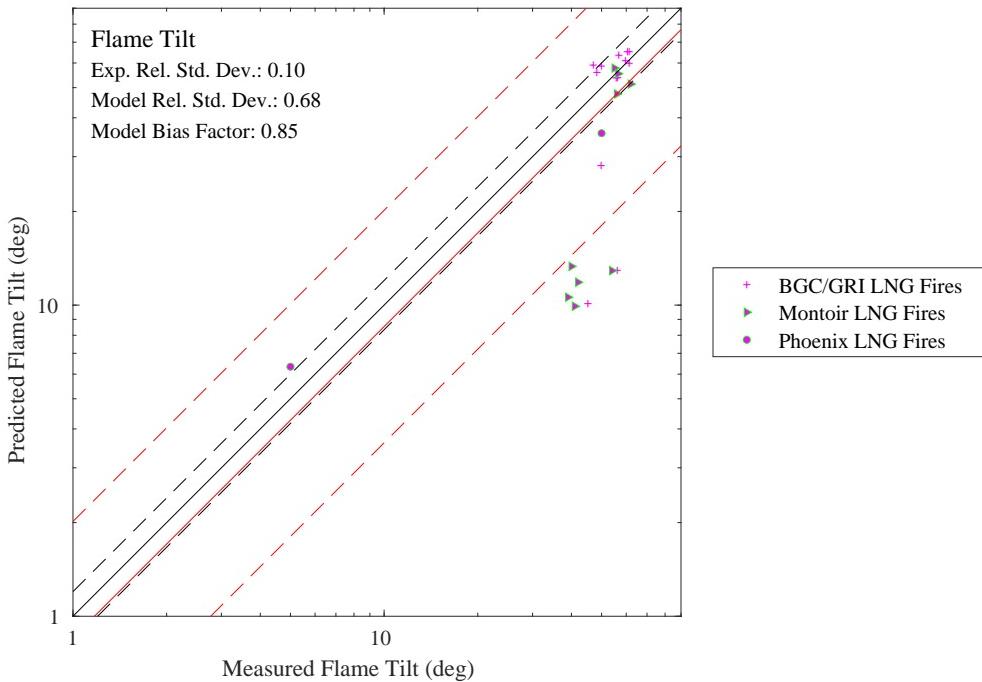


Figure 6.44: Summary of measured and predicted mean flame tilt angle.

## 6.4 Harrison Spill Plumes/Entrainment Experiments

Details of these experiments can be found in Sec. 3.34.

In each of these reduced-scale spill plume experiments, the entrained mass flow rate into the plume was measured at a series of heights by varying the flow through an exhaust hood to maintain a constant smoke layer depth. Figure 6.45 compares measured and predicted entrainment rates at five different elevations for the fire scenarios labelled SE4 through SE21 in Ref. [224]. Two general configurations are considered – one that is intended to mimic a balcony spill plume and one in which the plume adheres to a vertical wall above the compartment opening.

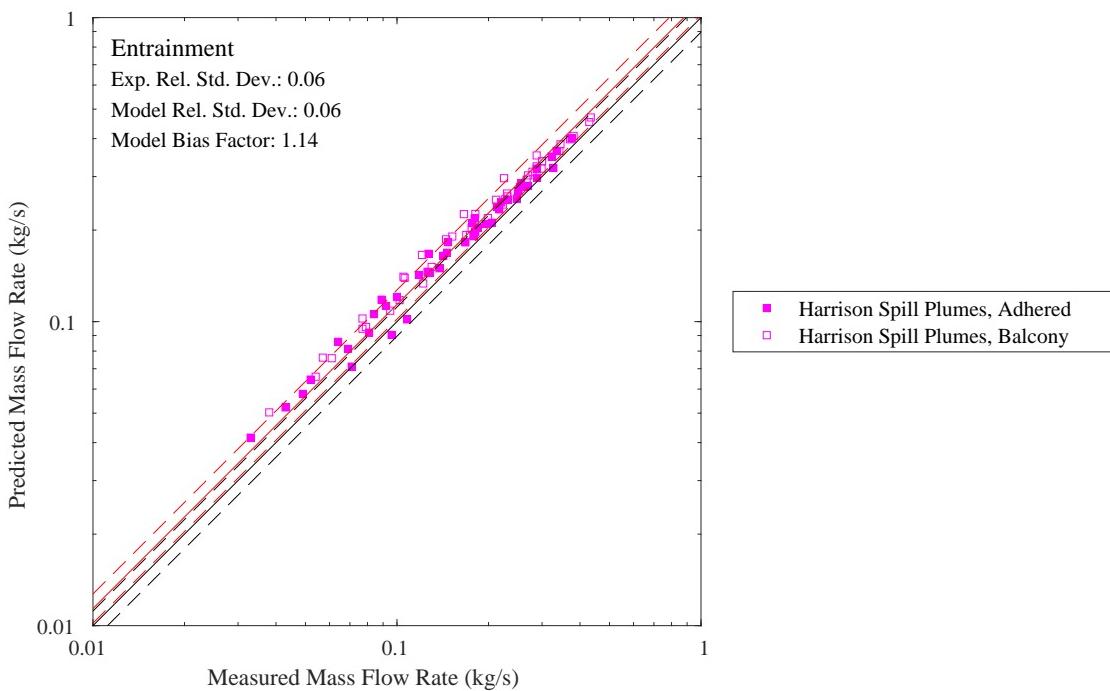


Figure 6.45: A comparison of predicted and measured mass flow rates at various heights for the Harrison Spill Plume experiments.

## 6.5 Sandia Plume Experiments

Details of these experiments can be found in Sec. 3.76.

The Fire Laboratory for Accreditation of Models by Experimentation (FLAME) facility [298, 299] at Sandia National Laboratories in Albuquerque, New Mexico, is designed specifically for validating models of buoyant fire plumes. The plume source is 1 m in diameter surrounded by a 0.5 m steel “ground plane”. Particle Image Velocimetry (PIV) and Planar Laser-Induced Fluorescence (PLIF) techniques were used to obtain instantaneous joint scalar and velocity fields.

### 6.5.1 Sandia 1 m Helium Plume

Calculations of the Sandia 1 m helium plume are run at three grid resolutions: 6 cm, 3 cm, and 1.5 cm. To give the reader with a qualitative feel for the results, Fig. 6.46 provides a snapshot of density contours from the simulation. The calculations are run in parallel on 16 processors; the outlined blocks indicate the domain decomposition. Data for vertical velocity, radial velocity, and helium mass fraction are recorded at three levels downstream from the base of the plume,  $z = [0.2, 0.4, 0.6]$  m, corresponding to the experimental measurements of O’Hern et al. [298]. Results for the mean and root mean square (RMS) profiles are given in Figs. 6.47 - 6.49. The means are taken between  $t = 10$  and  $t = 20$  seconds in the simulation.

The domain is 3 m by 3 m by 4 m. The boundary conditions are open on all sides with a smooth solid surface surrounding the 1 m diameter helium pool. The ambient and helium mixture temperature is set to 12 °C and the background pressure is set to 80900 Pa to correspond to the experimental conditions. The helium/acetone/oxygen mixture molecular weight is set to 5.45 kg/kmol. The turbulent Schmidt and Prandtl numbers are left at the FDS default value of 0.5. The helium mixture mass flux is specified as 0.0605 kg/s/m<sup>2</sup>. This case was studied previously by DesJardin et al. [300].

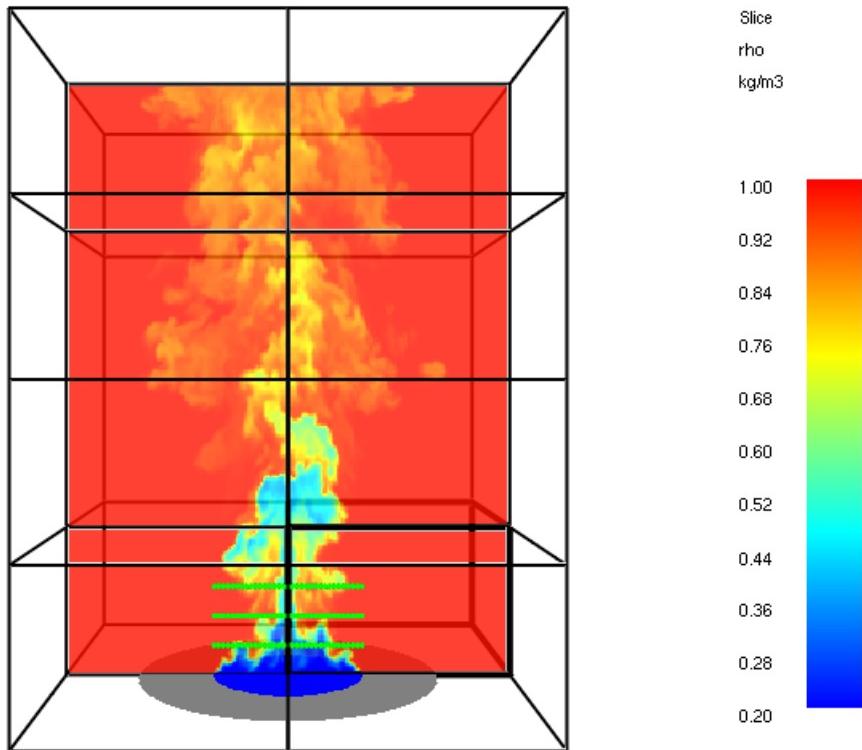


Figure 6.46: A snapshot of FDS results at 1.5 cm resolution for the Sandia 1 m helium plume showing density contours. The rows of measurement devices are visible near the base. The calculations are run in parallel on 16 processors; the outlined blocks indicate the domain decomposition.

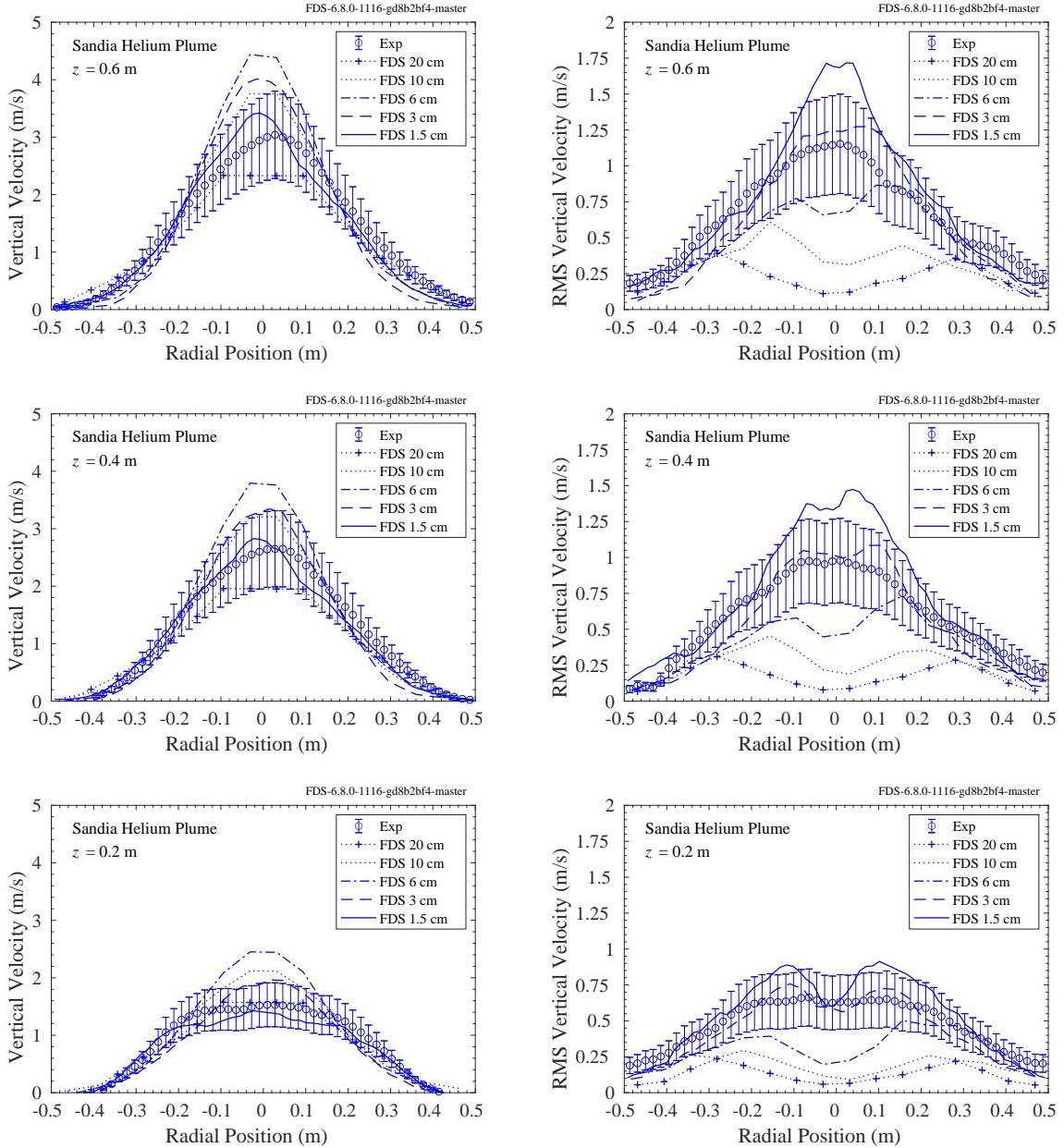


Figure 6.47: FDS predictions of mean and root mean square (RMS) vertical velocity profiles for the Sandia 1 m helium plume experiment. Results are shown for 6 cm, 3 cm, and 1.5 cm grid resolutions. With  $z$  being the streamwise coordinate, the bottom row is at  $z = 0.2 \text{ m}$ , the middle row is at  $z = 0.4 \text{ m}$ , and the top row is at  $z = 0.6 \text{ m}$ .

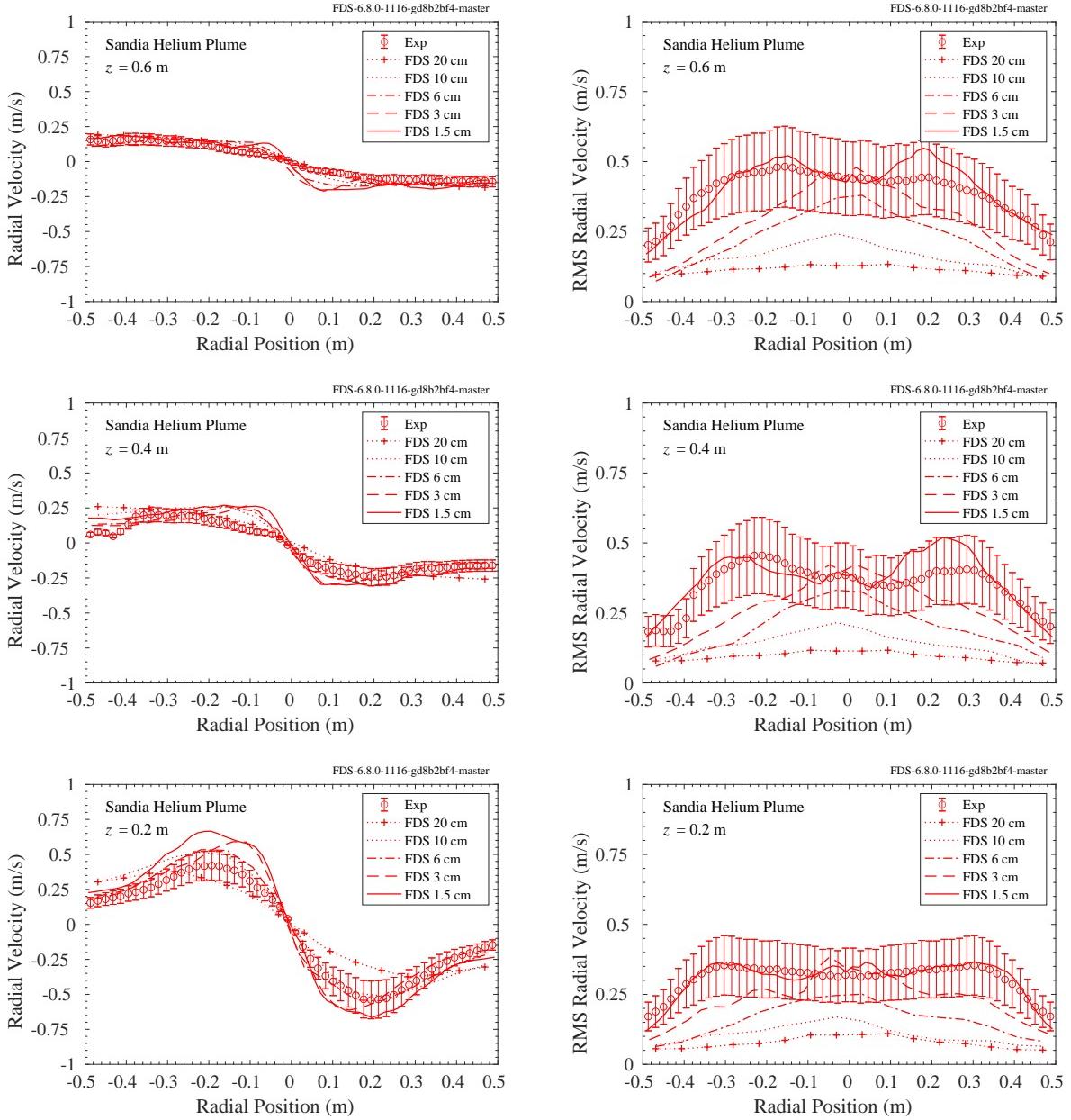


Figure 6.48: FDS predictions of mean and root mean square (RMS) radial velocity profiles for the Sandia 1 m helium plume experiment. Results are shown for 6 cm, 3 cm, and 1.5 cm grid resolutions. With  $z$  being the streamwise coordinate, the bottom row is at  $z = 0.2\text{ m}$ , the middle row is at  $z = 0.4\text{ m}$ , and the top row is at  $z = 0.6\text{ m}$ .

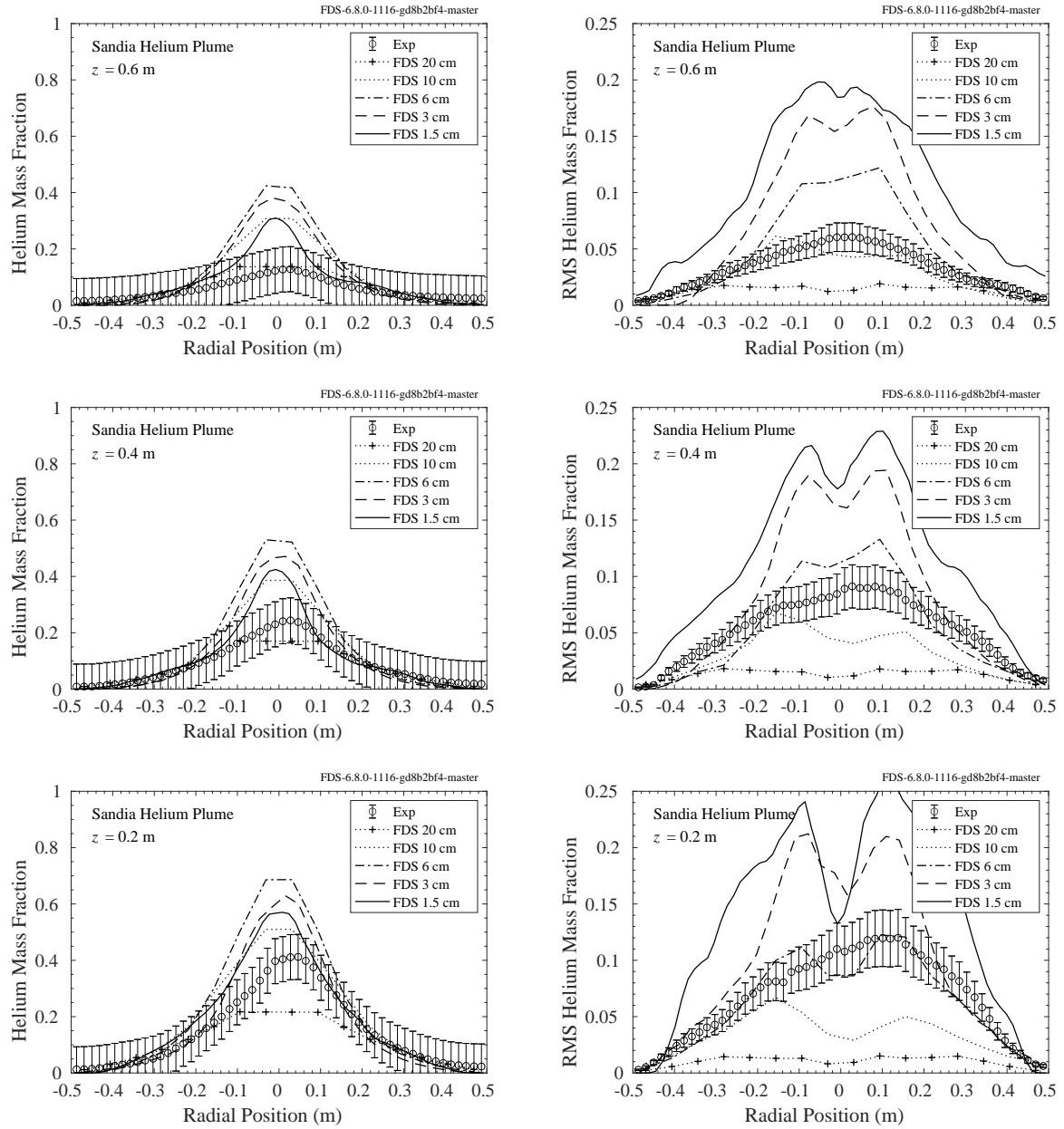


Figure 6.49: FDS predictions of mean and root mean square (RMS) helium mass fraction profiles for the Sandia 1 m helium plume experiment. Results are shown for 6 cm, 3 cm, and 1.5 cm grid resolutions. With  $z$  being the streamwise coordinate, the bottom row shows data at  $z = 0.2 \text{ m}$ , the middle row shows data at  $z = 0.4 \text{ m}$ , and the top row shows data at  $z = 0.6 \text{ m}$ .

## 6.5.2 Sandia 1 m Methane Pool Fire

The Sandia 1 m methane pool fire series provides data for three methane flow rates: Test 14 (low flow rate), Test 24 (medium flow rate), and Test 17 (high flow rate) [301]. The experiments are simulated using three grid resolutions: 6 cm, 3 cm, and 1.5 cm. Fig. 6.50 provides a snapshot of temperature contours from the 1.5 cm Test 17 simulation. The calculations are run in parallel on 16 processors—a similar computational set up as the helium case (the experiments were run in the same facility at Sandia). Data for vertical velocity and radial velocity are recorded at three levels downstream from the base of the plume,  $z = [0.3, 0.5, 0.9]$  m. Results for the mean profiles (and turbulent kinetic energy for Test 24) are given in Figs. 6.51 - 6.54. The means are taken between  $t = 10$  and  $t = 20$  seconds in the simulation.

For Test 17, we recorded the vertical velocity as a time series in four locations in the plume—at two positions along the centerline and at two positions on the edge. The time series from our 1.5 cm simulation at  $x = 0$  m and  $z = 0.5$  m, corresponding to Fig. 6 in [302], is shown in Fig. 6.55 along with the power spectrum from the average of the four time series locations. The FDS results compare well with the experimentally obtained puffing frequency of 1.65 Hz [302].

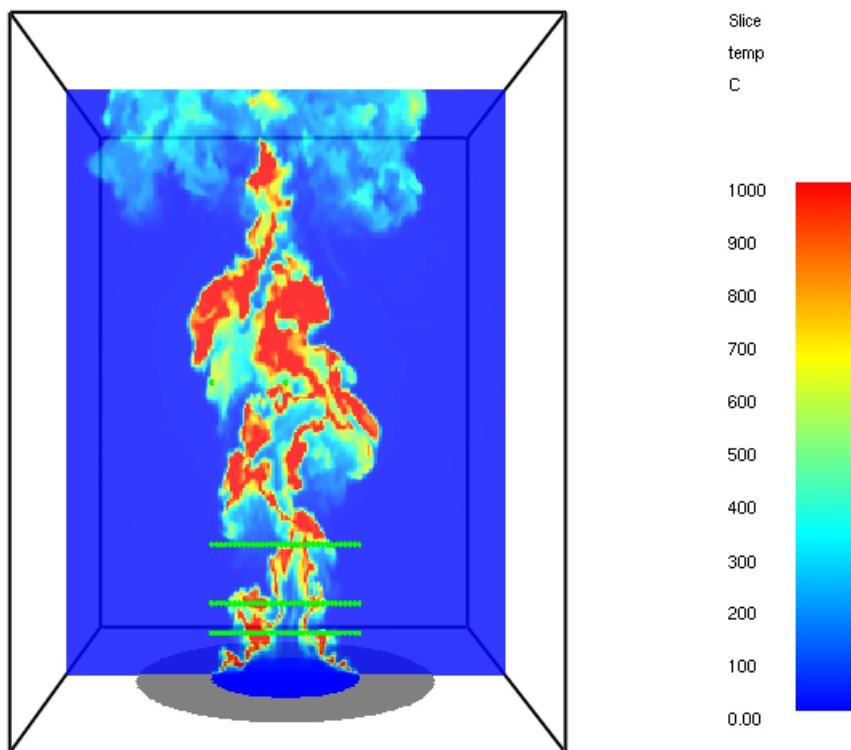


Figure 6.50: A snapshot of FDS results at 1.5 cm resolution for the Sandia 1 m methane pool fire (Test 17 – high flow rate) showing instantaneous contours of temperature. The rows of measurement devices (green) are visible near the base.

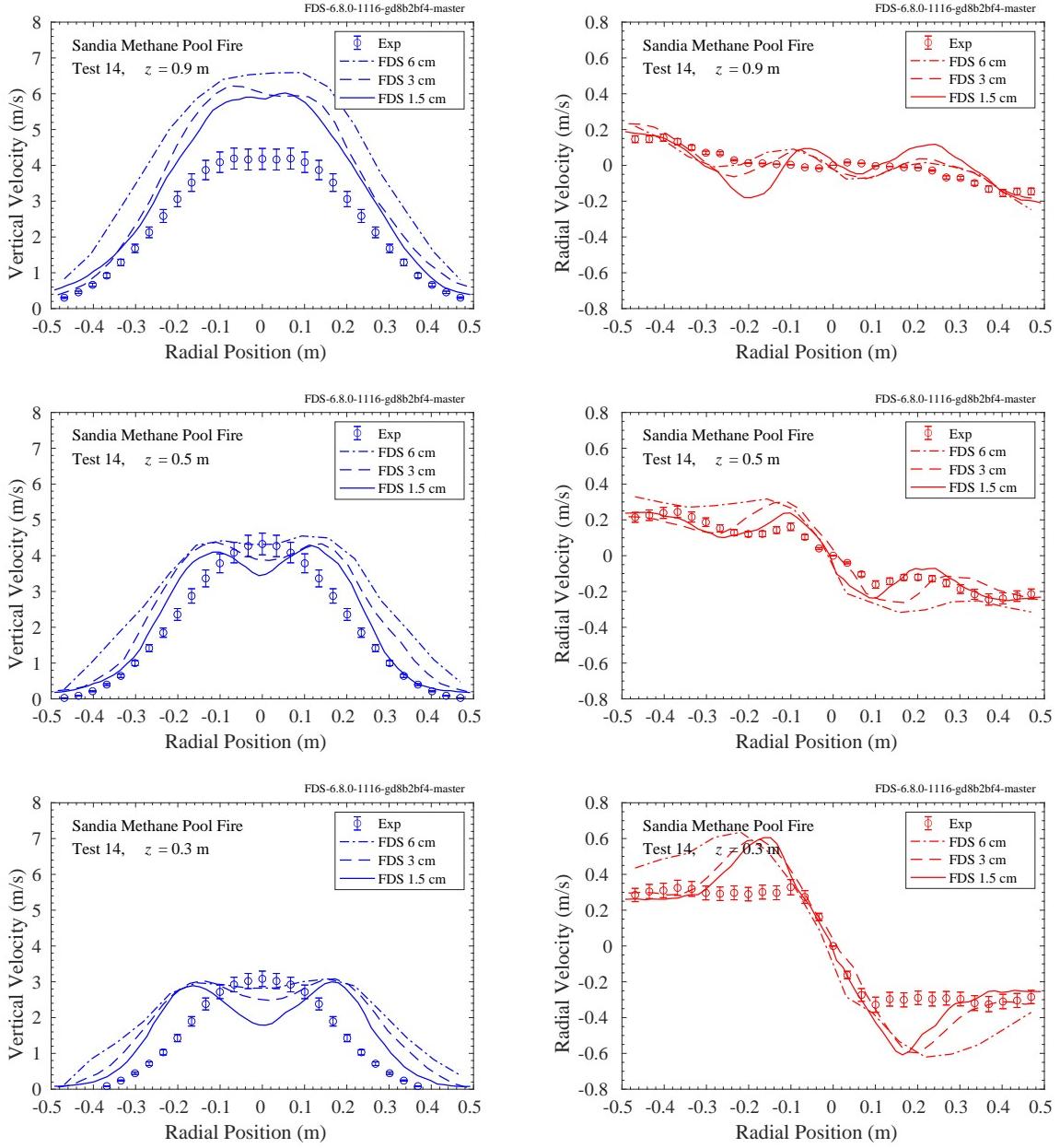


Figure 6.51: FDS predictions of mean velocity profiles for the Sandia 1 m methane pool fire experiment (Test 14 – low flow rate). Results are shown for 6 cm, 3 cm, and 1.5 cm grid resolutions. The  $z$  coordinate represents height above the methane pool; bottom row:  $z = 0.3\text{ m}$ , middle row:  $z = 0.5\text{ m}$ , and top row:  $z = 0.9\text{ m}$ .

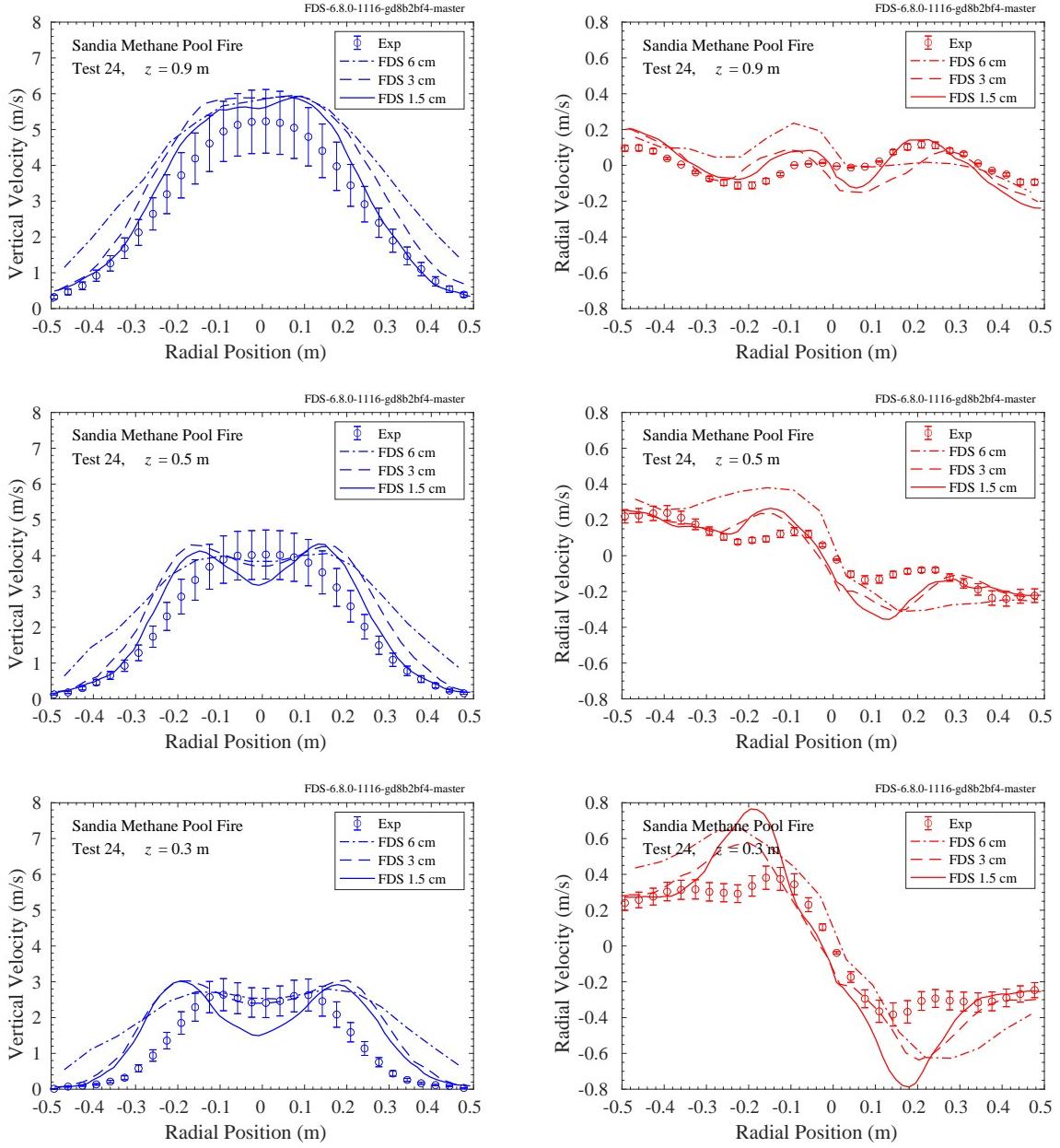


Figure 6.52: FDS predictions of mean velocity profiles for the Sandia 1 m methane pool fire experiment (Test 24 – medium flow rate). Results are shown for 6 cm, 3 cm, and 1.5 cm grid resolutions. The  $z$  coordinate represents height above the methane pool; bottom row:  $z = 0.3\text{ m}$ , middle row:  $z = 0.5\text{ m}$ , and top row:  $z = 0.9\text{ m}$ .

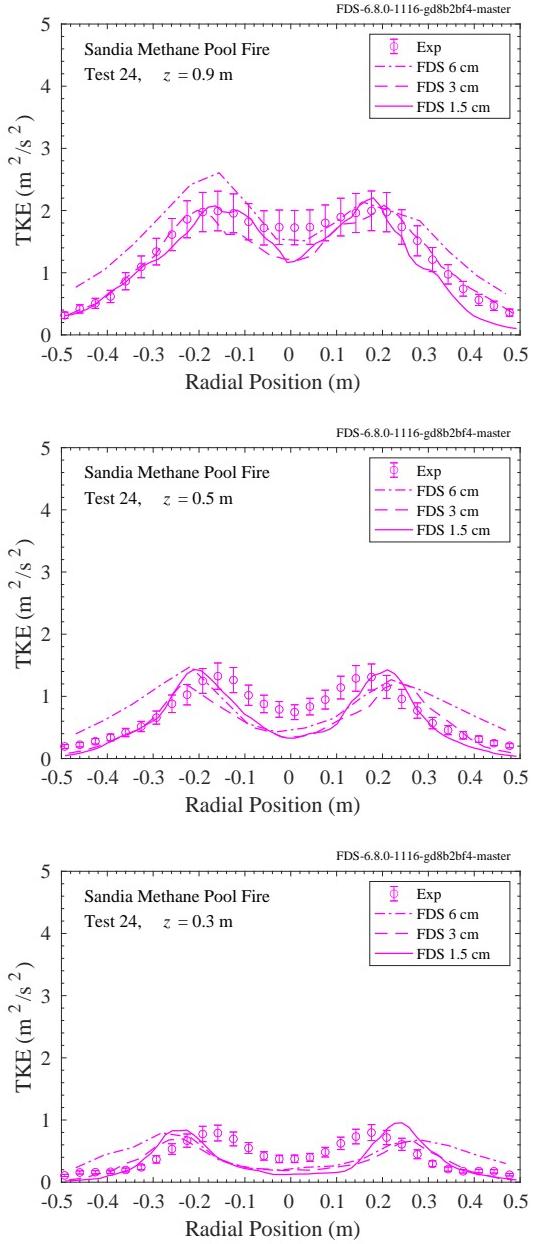


Figure 6.53: FDS predictions of turbulent kinetic energy (TKE) profiles for the Sandia 1 m methane pool fire experiment (Test 24 – medium flow rate). Results are shown for 6 cm, 3 cm, and 1.5 cm grid resolutions. The  $z$  coordinate represents height above the methane pool; bottom row:  $z = 0.3$  m, middle row:  $z = 0.5$  m, and top row:  $z = 0.9$  m.

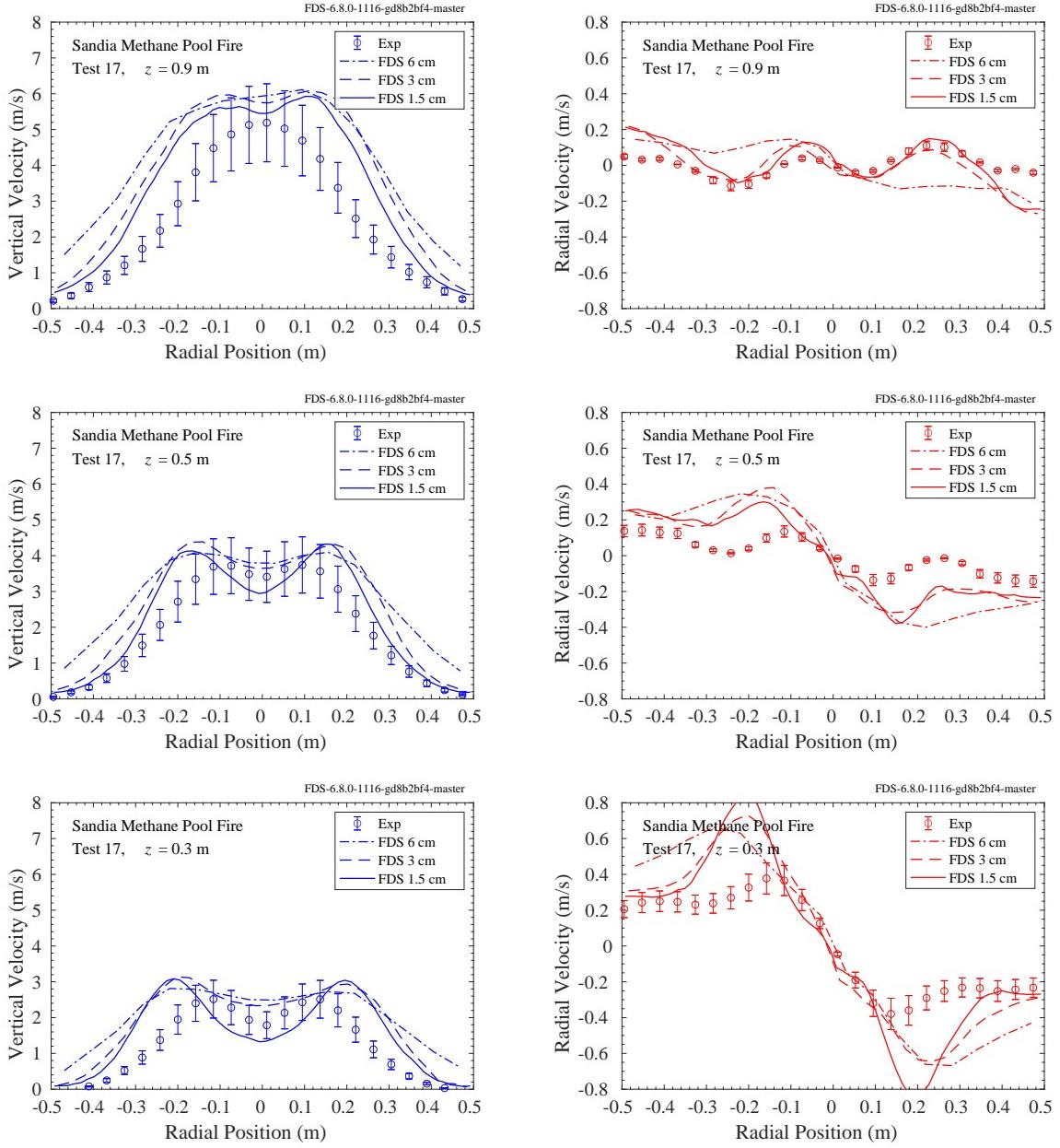


Figure 6.54: FDS predictions of mean velocity profiles for the Sandia 1 m methane pool fire experiment (Test 17). Results are shown for 3 cm and 1.5 cm grid resolutions. The  $z$  coordinate represents height above the methane pool; bottom row:  $z = 0.3\text{ m}$ , middle row:  $z = 0.5\text{ m}$ , and top row:  $z = 0.9\text{ m}$ .

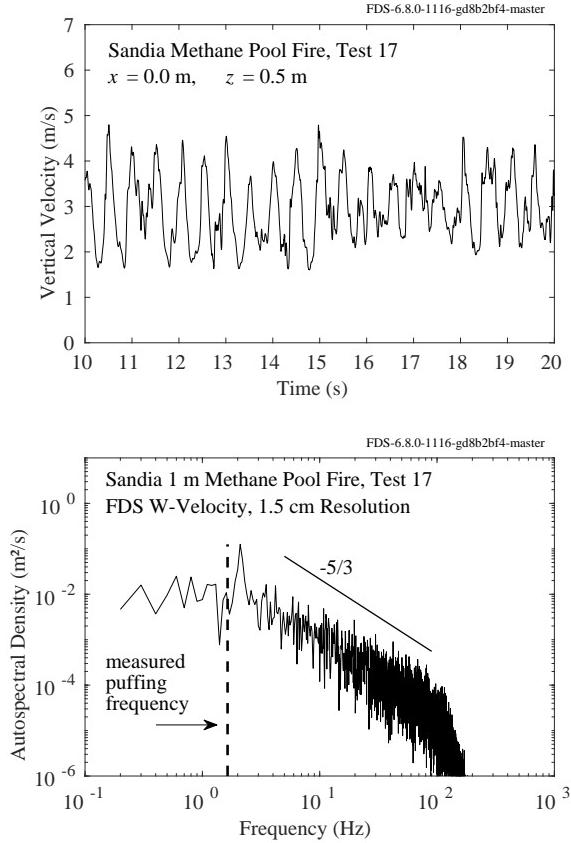


Figure 6.55: FDS velocity signal and power spectrum for the Sandia 1 m methane pool fire experiment (Test 17). The vertical velocity signal (top plot) is output from FDS on the centerline at  $z = 0.5$  m downstream of the fuel source. The power spectrum of vertical velocity is measured at four locations and averaged. Two of the measurement locations are along the centerline, at  $z = [0.5, 2.0]$  m, and two are along the edge of the plume,  $x = 0.5$  m and  $z = [0.5, 2.0]$  m. The measured puffing frequency of the plume is 1.65 Hz [302]. The temporal Nyquist limit of the simulation (the highest resolvable frequency due to the discrete time increment) is  $1/(2\delta t) \approx 1000$  Hz ( $\delta t \approx 0.0005$ ).

### 6.5.3 Sandia 1 m Hydrogen Pool Fire

Sandia Test 35 [301] is simulated at three grid resolutions: 6 cm, 3 cm, and 1.5 cm. The computational set up is nearly identical to the methane cases. Results for mean vertical and radial velocity are given in Figs. 6.57. Results for turbulent kinetic energy are presented in Fig. 6.58. Means are taken from a time average between  $t = 10$  and  $t = 20$  seconds in the simulation.

By examining movies of the simulation results we can see a qualitative difference between the methane and hydrogen cases. The dynamics of the hydrogen case tend to dominated by near total consumption events which create blowback on the pool followed by streaks of accelerating buoyant flow which increase the mean vertical velocity. An example of the consumption event is seen near the end of the case shown in Fig. 6.56. It is possible that we have not run the simulation long enough for accurate statistics and that streaking events early in the time window (between 10-20 seconds) are biasing the mean vertical velocity to be too high, as is clear from the top-left plot in Fig. 6.57.

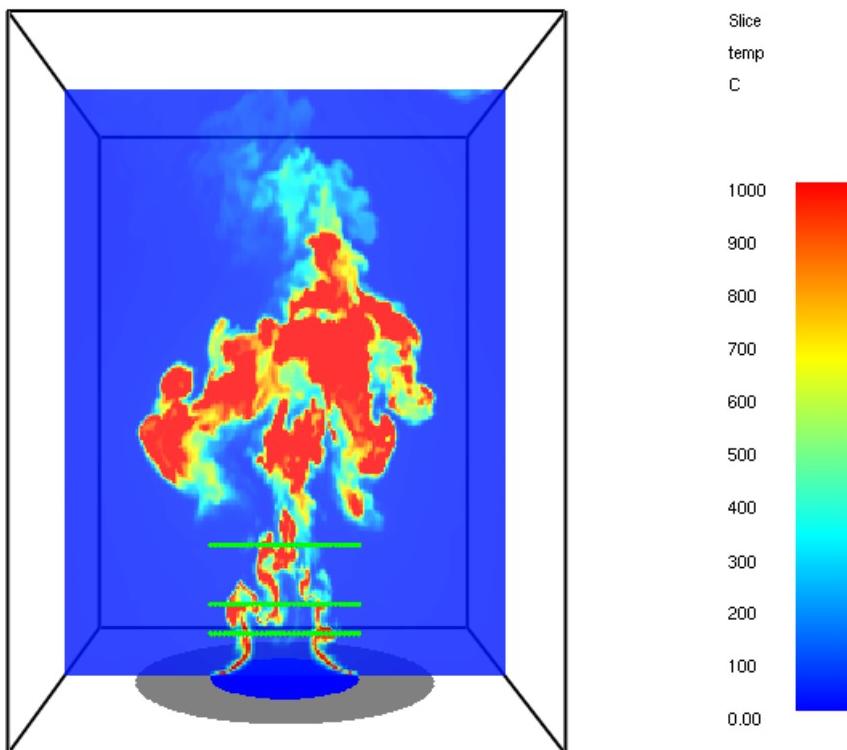


Figure 6.56: A snapshot of FDS results at 1.5 cm resolution for the Sandia 1 m hydrogen pool fire (Test 35) showing instantaneous contours of temperature. The rows of measurement devices (green) are visible near the base.

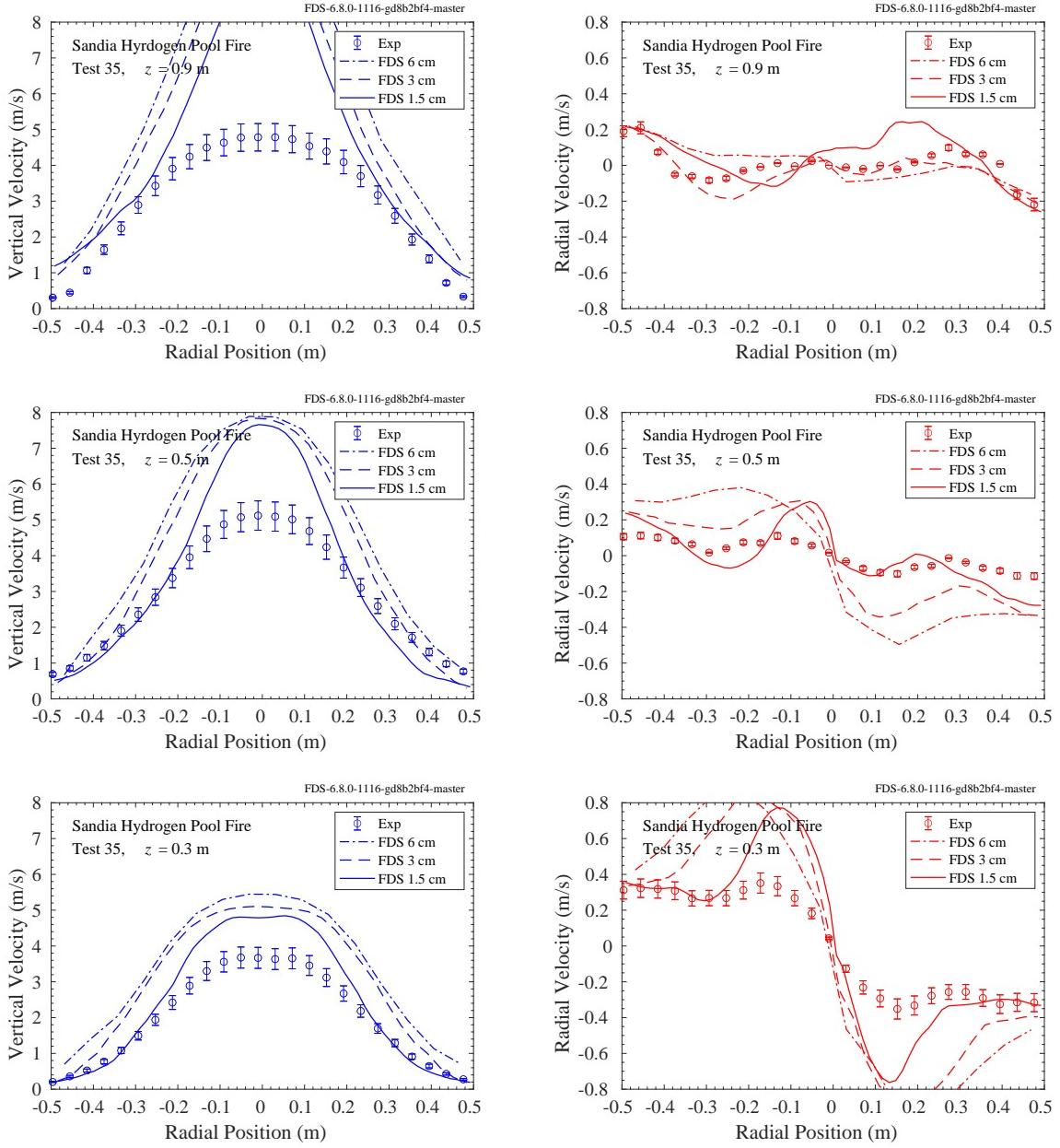


Figure 6.57: FDS predictions of mean velocity profiles for the Sandia 1 m hydrogen pool fire experiment (Test 35). Results are shown for 6 cm, 3 cm, and 1.5 cm grid resolutions. The  $z$  coordinate represents height above the pool; bottom row:  $z = 0.3\text{ m}$ , middle row:  $z = 0.5\text{ m}$ , and top row:  $z = 0.9\text{ m}$ .

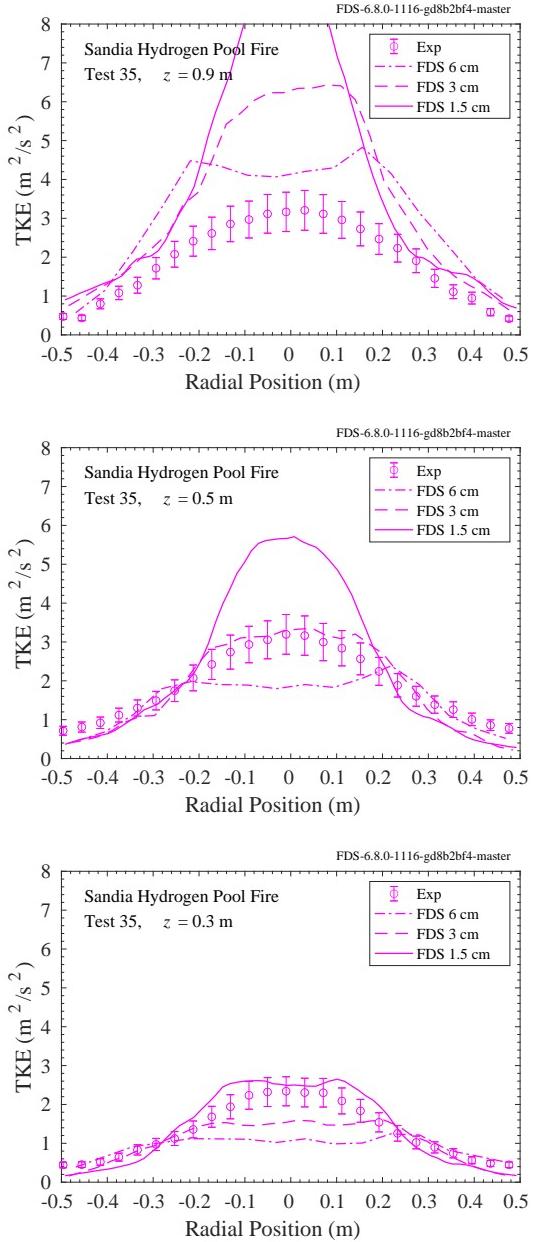


Figure 6.58: FDS predictions of turbulent kinetic energy (TKE) profiles for the Sandia 1 m hydrogen pool fire experiment (Test 35). Results are shown for 6 cm, 3 cm, and 1.5 cm grid resolutions. The  $z$  coordinate represents height above the methane pool; bottom row:  $z = 0.3 \text{ m}$ , middle row:  $z = 0.5 \text{ m}$ , and top row:  $z = 0.9 \text{ m}$ .

## 6.6 Purdue 7.1 cm Methane Flame

Details of these experiments can be found in Sec. 3.72.

Figures 6.59-6.62 show results for the Purdue 7.1 cm methane flame [30]. Three sets of results are presented: two coarse (4 mm) cases and one fine (2 mm) case. The fine mesh case is run with MPI on 16 meshes. The coarse cases are run two ways: a single mesh case (dashed lines) and a 16 mesh case (dotted lines). As should be the case, the single- and multi-mesh cases yield the same results. This gives confidence in the domain decomposition strategy for open plume flows with FDS.

The discrepancy at the centerline for mixture fraction and vertical velocity may be attributed to our not accounting for (1) the slight divergence of the flow at the burner exit ( $7^\circ$  [30]) and (2) the asymmetries and fluctuations in the burner exit and ambient environment. Examination of the FDS output shows the solution remains very symmetric, preventing large gulps of air from penetrating the centerline of the plume, which would tend to smooth out the profiles near the center reducing the bimodal vertical velocity profile and centerline mixture fraction.

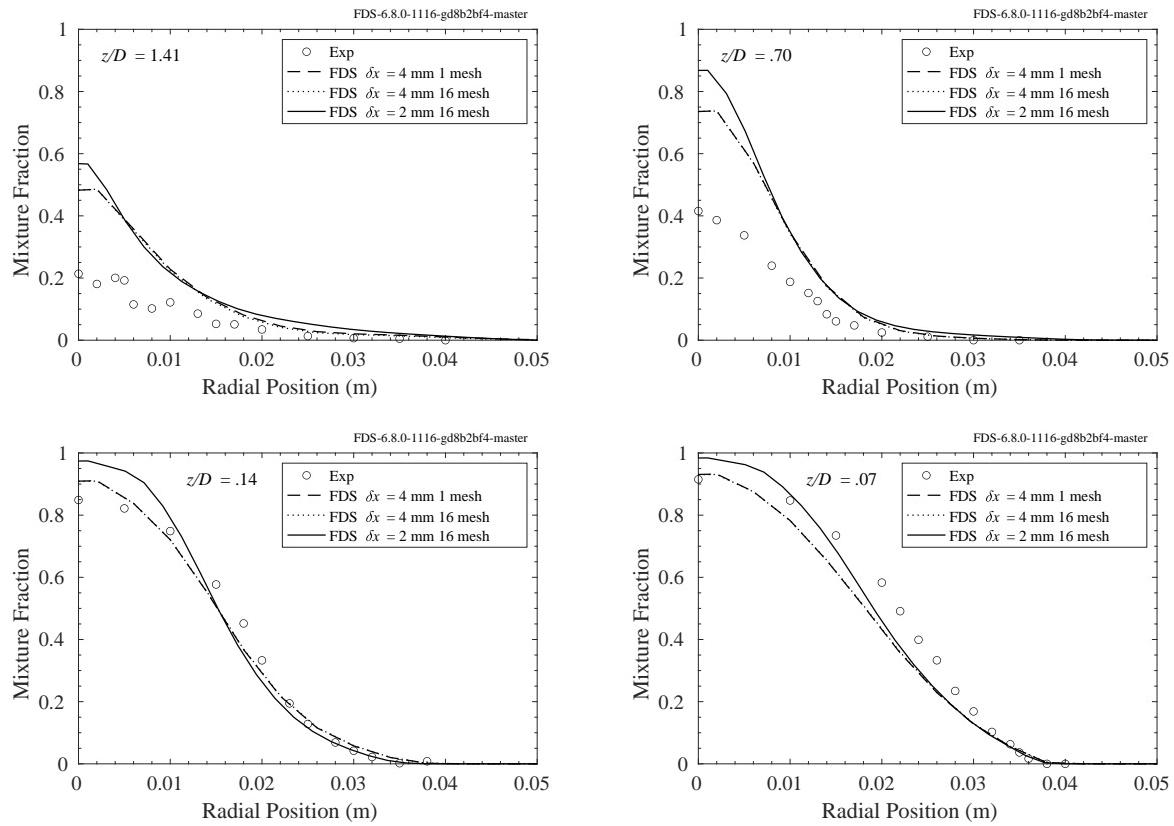


Figure 6.59: Measured [32] and computed radial profiles of the mean mixture fraction at select heights above the burner exit simulated using grids with different spatial resolutions.

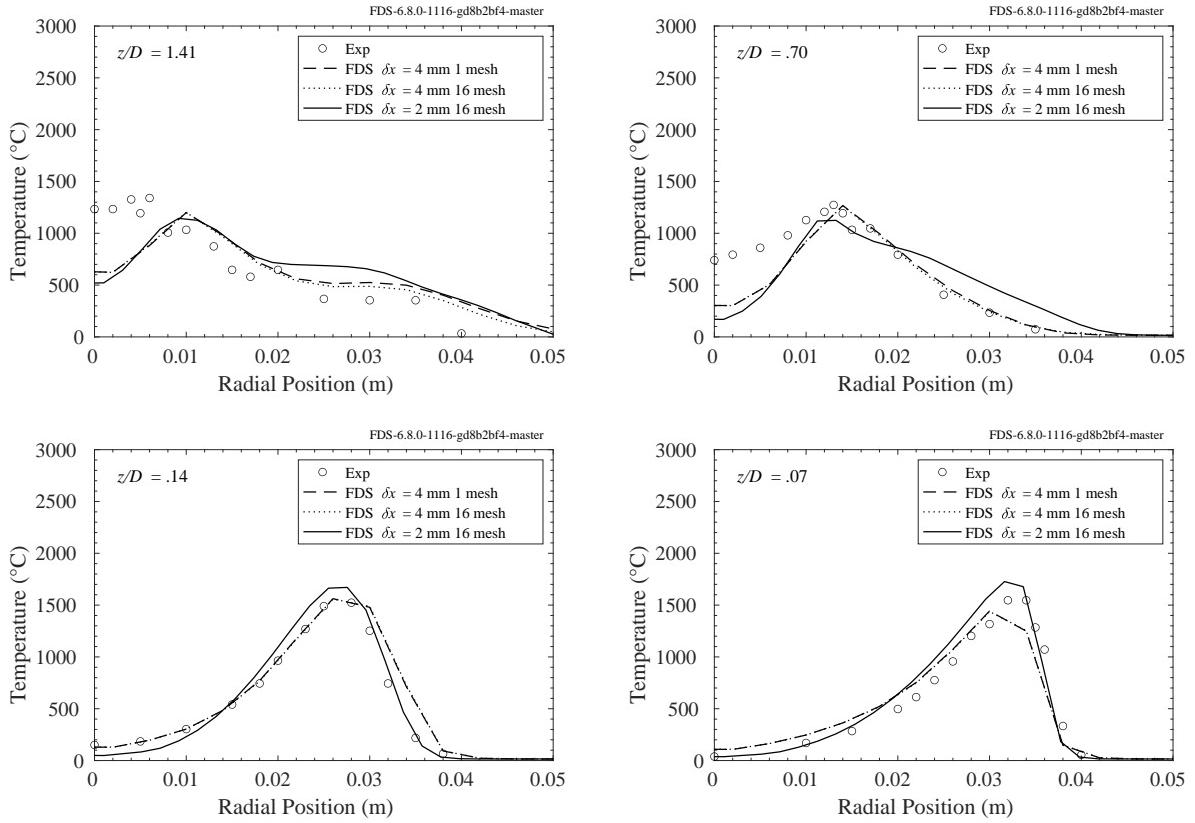


Figure 6.60: Inferred [30] and computed radial profiles of the mean temperature at select heights above the burner exit simulated using grids with different spatial resolutions.

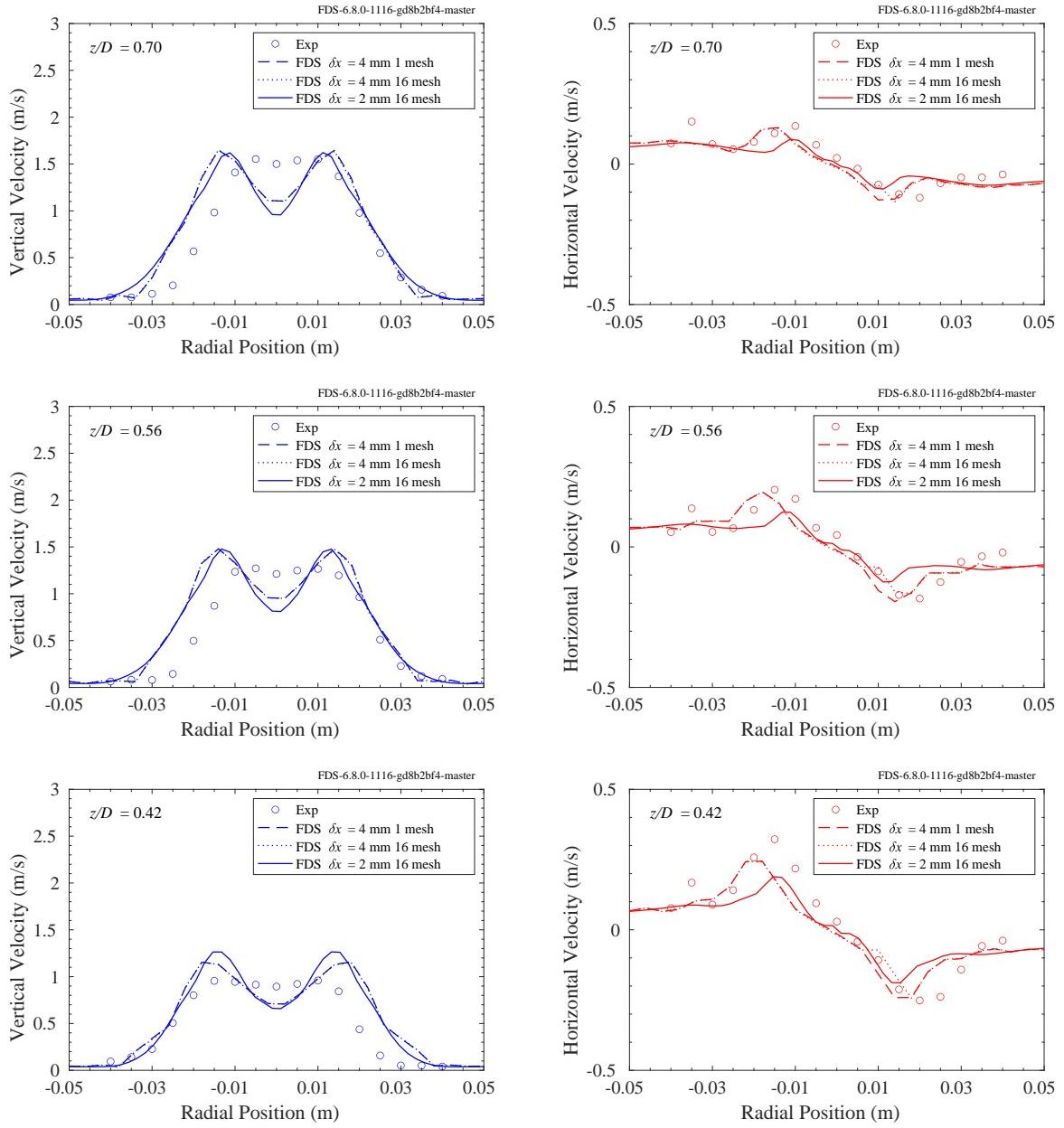


Figure 6.61: Measured [32] and computed radial profiles of the mean vertical and horizontal velocities at select heights above the burner exit simulated using grids with different spatial resolutions.

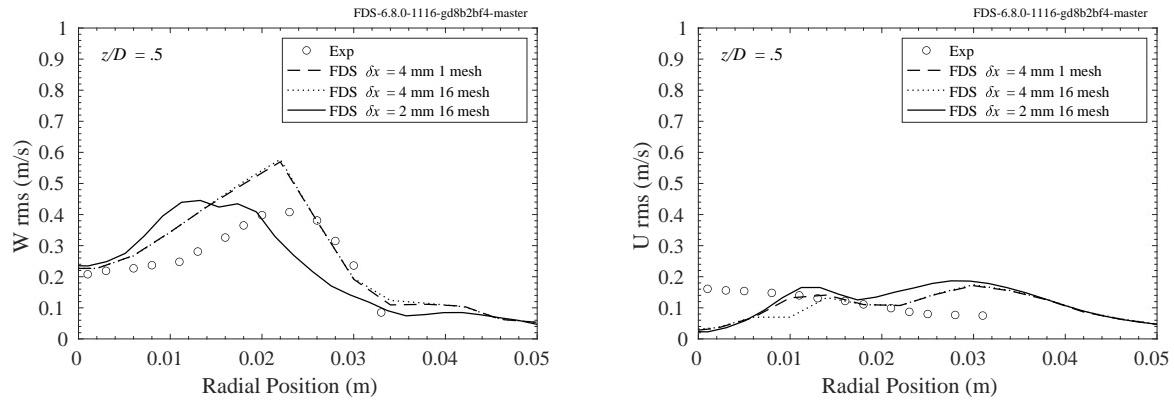


Figure 6.62: Measured and computed profiles of rms vertical (left) and radial (right) velocity profiles at  $z/D = 0.5$ .

## 6.7 FM Vertical Wall Flame Experiments

Details of these experiments can be found in Sec. 3.29.

Figure 6.63 displays the measured and predicted thermocouple (i.e. uncorrected) temperatures as a function of the normal distance,  $y$ , from the surface of a vertical, water-cooled burner. The measurements were made 771 mm from the base of the burner for propylene mass flow rates of 8.75, 11.85, 12.68, 17.05, 22.37, and 22.49 g/m<sup>2</sup>/s.

Figure 6.64 displays the measured and predicted soot depth at heights of 365, 527, 771, 1022, and 1317 mm above the base of the burner for various fuel burning rates. The soot depth was measured by inserting glass rods through the flame, normal to the burner surface, for 2 s. The soot depth is the length of the blackened portion of the rod, taken to represent the average flame depth over the 2 s interval. For the FDS simulations, the soot depth was taken to be the distance from the burner surface where the soot mass fraction drops below 0.0025.

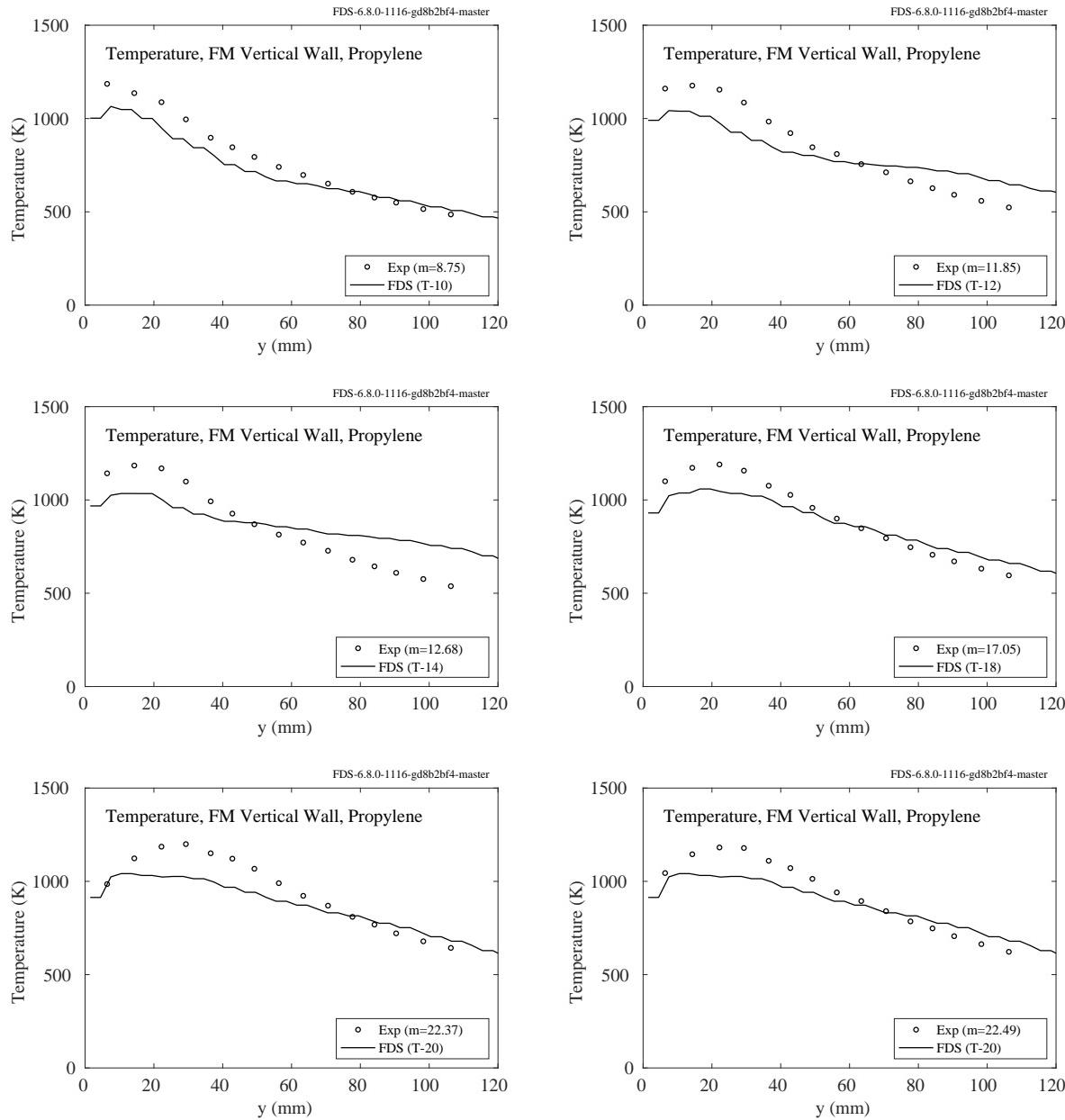


Figure 6.63: Uncorrected horizontal temperature profiles normal to the burner surface for fuel flow rates of 8.75, 11.85, 12.68, 17.05, 22.37, and 22.49 g/m<sup>2</sup>/s.

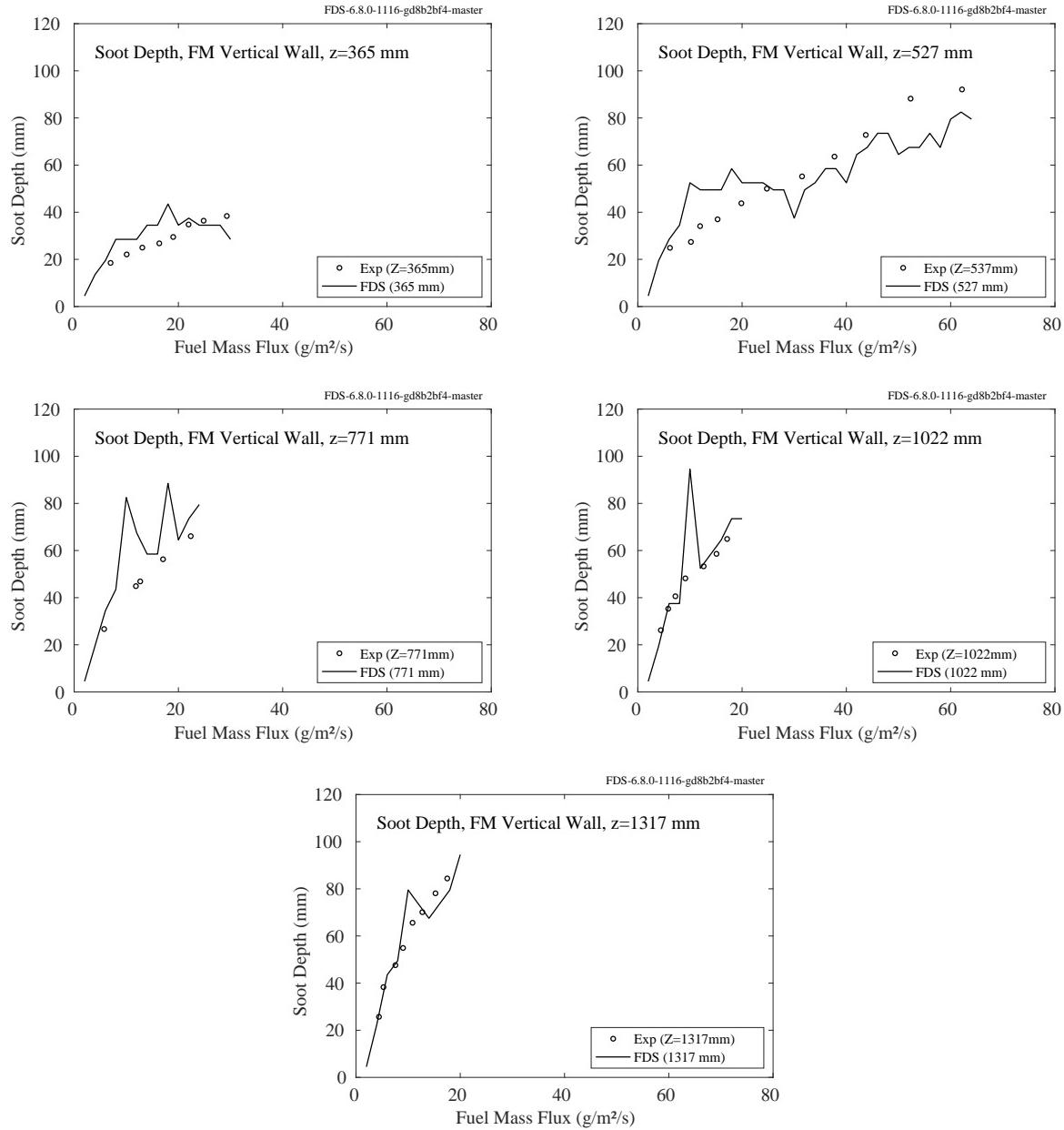


Figure 6.64: Soot depth at heights of 365, 527, 771, 1022, and 1317 mm.

## Chapter 7

# Ceiling Jets and Device Activation

FDS is a CFD-based fire model and has no specific ceiling jet algorithm. Rather, temperatures throughout the fire compartment are computed directly from the governing conservation equations. Nevertheless, temperature measurements near the ceiling are useful in evaluating the model's ability to predict the activation times of sprinklers, smoke detectors, and other fire protection devices. The term "ceiling jet" is used loosely here – it distinguishes a point temperature measurement near the ceiling from an average "hot gas layer" (HGL) temperature.

This chapter first presents comparisons of model predictions and temperature measurements near to the ceiling. Next, predicted sprinkler activation times and the total number of activations are compared with measurements. Finally, predicted smoke detector activation times are compared with measurements.

### 7.1 Ceiling Jet Temperatures

The ceiling jet temperature measurements presented in this section were made for a variety of reasons. Most often, these measurements were simply the upper most thermocouple temperature in a vertical array. Sometimes, these measurements were designed to detect the activation time of a sprinkler. In any case, these measurements are used to evaluate the model's ability to predict the gas temperature at a single point, as opposed to the hot gas layer average.

### 7.1.1 ATF Corridors Experiment

This series of experiments involved two fairly long corridors connected by a staircase. The fire, a natural gas sand burner, was located on the first level at the end of the corridor away from the stairwell. The corridor was closed at this end, and open at the same position on the second level. Two-way flow occurred on both levels because make-up air flowed from the opening on the second level down the stairs to the first. The only opening to the enclosure was the open end of the second-level corridor.

Temperatures were measured with seven thermocouple trees. Tree A was located fairly close to the fire on the first level. Tree B was located halfway down the first-level corridor. Tree C was close to the stairwell entrance on the first level. Tree D was located in the doorway of the stairwell on the first level. Tree E was located roughly along the vertical centerline of the stairwell. Tree F was located near the stairwell opening on the second level. Tree G was located near the exit at the other end of the second-level corridor. The graphs on the following pages show the top and bottom TC from each tree for the given fire sizes of 50 kW, 100 kW, 250 kW, 500 kW, and a mixed HRR “pulsed” fire.

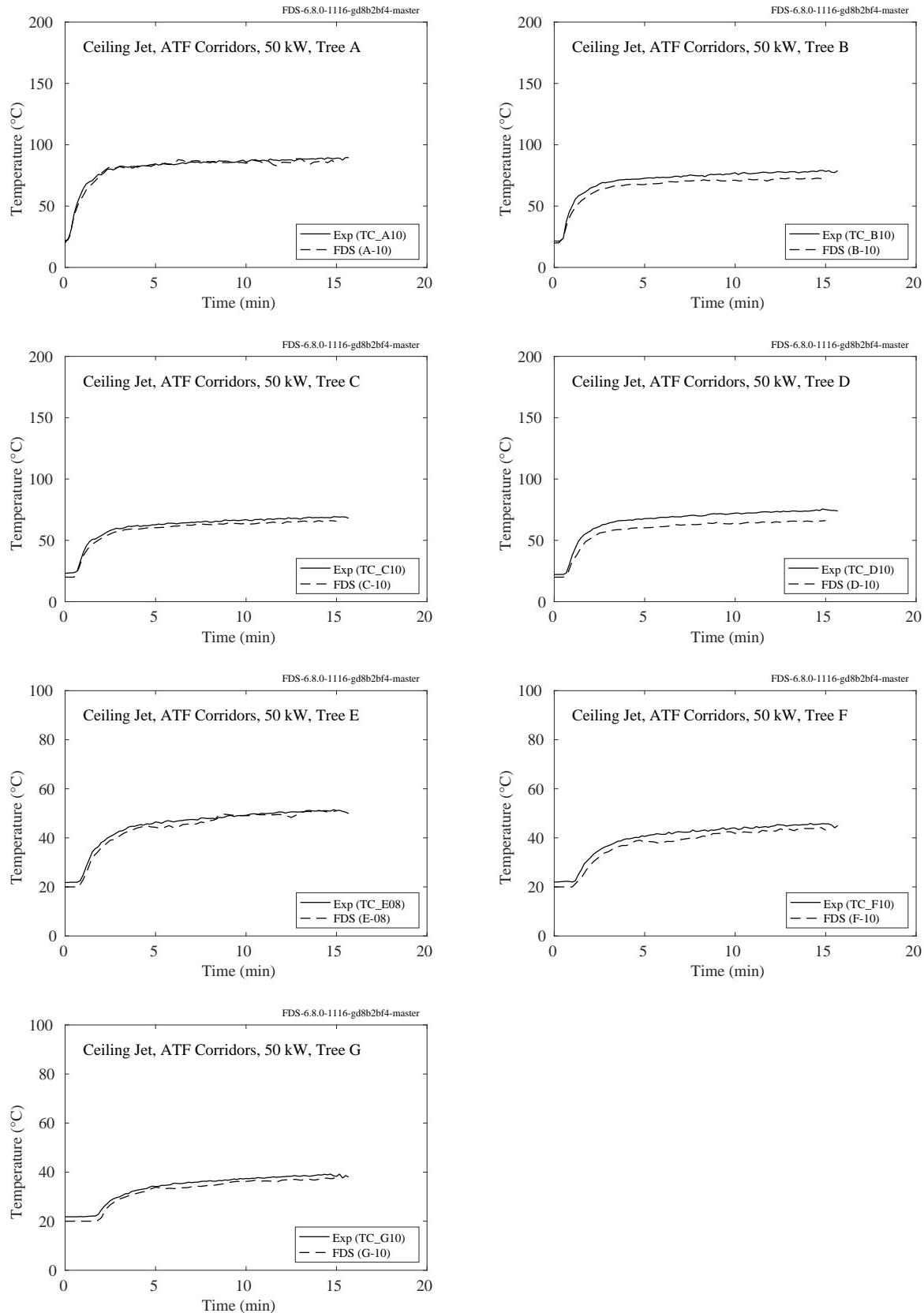


Figure 7.1: ATF Corridors experiments, ceiling jet, 50 kW.

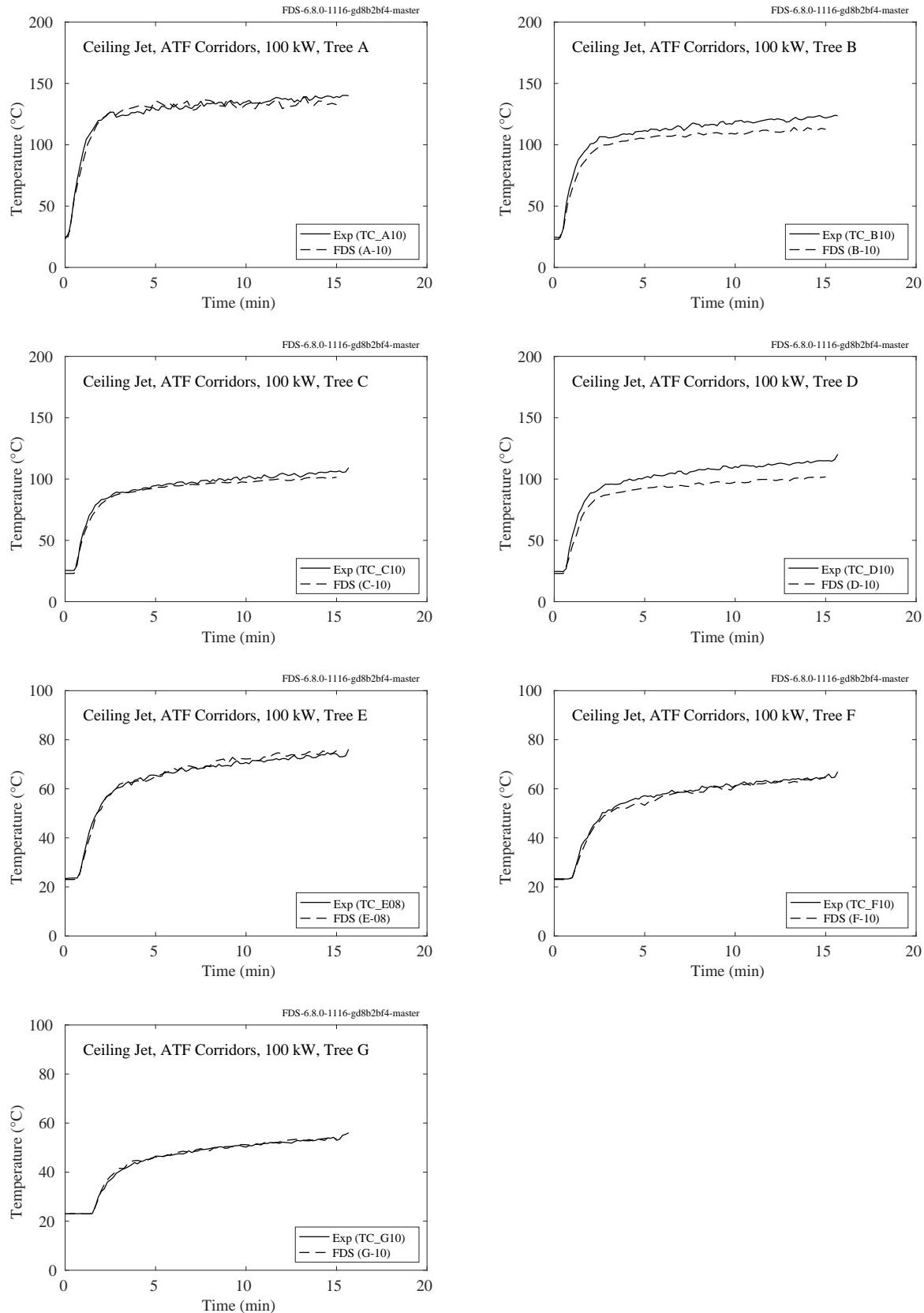


Figure 7.2: ATF Corridors experiments, ceiling jet, 100 kW.

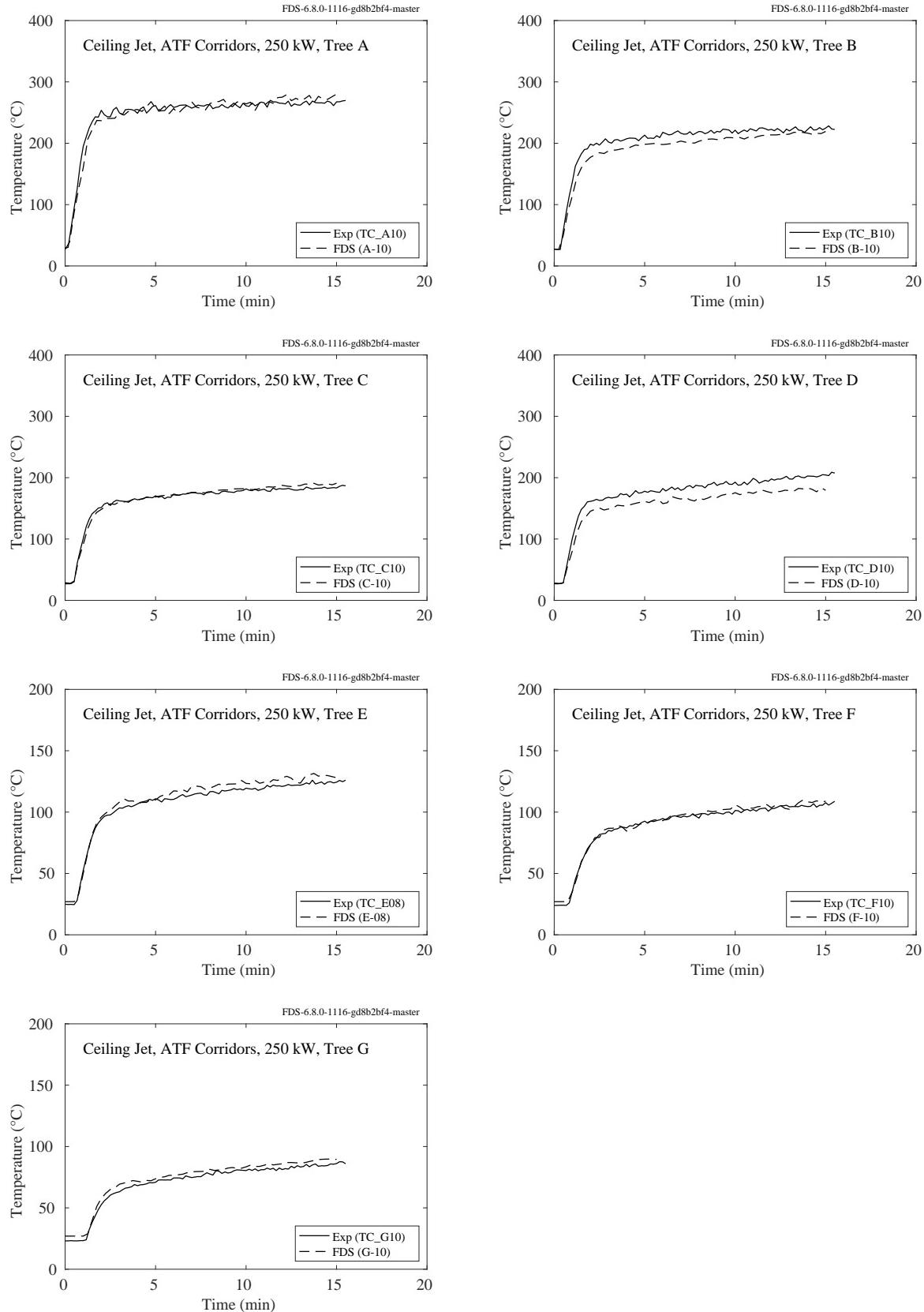


Figure 7.3: ATF Corridors experiments, ceiling jet, 250 kW.

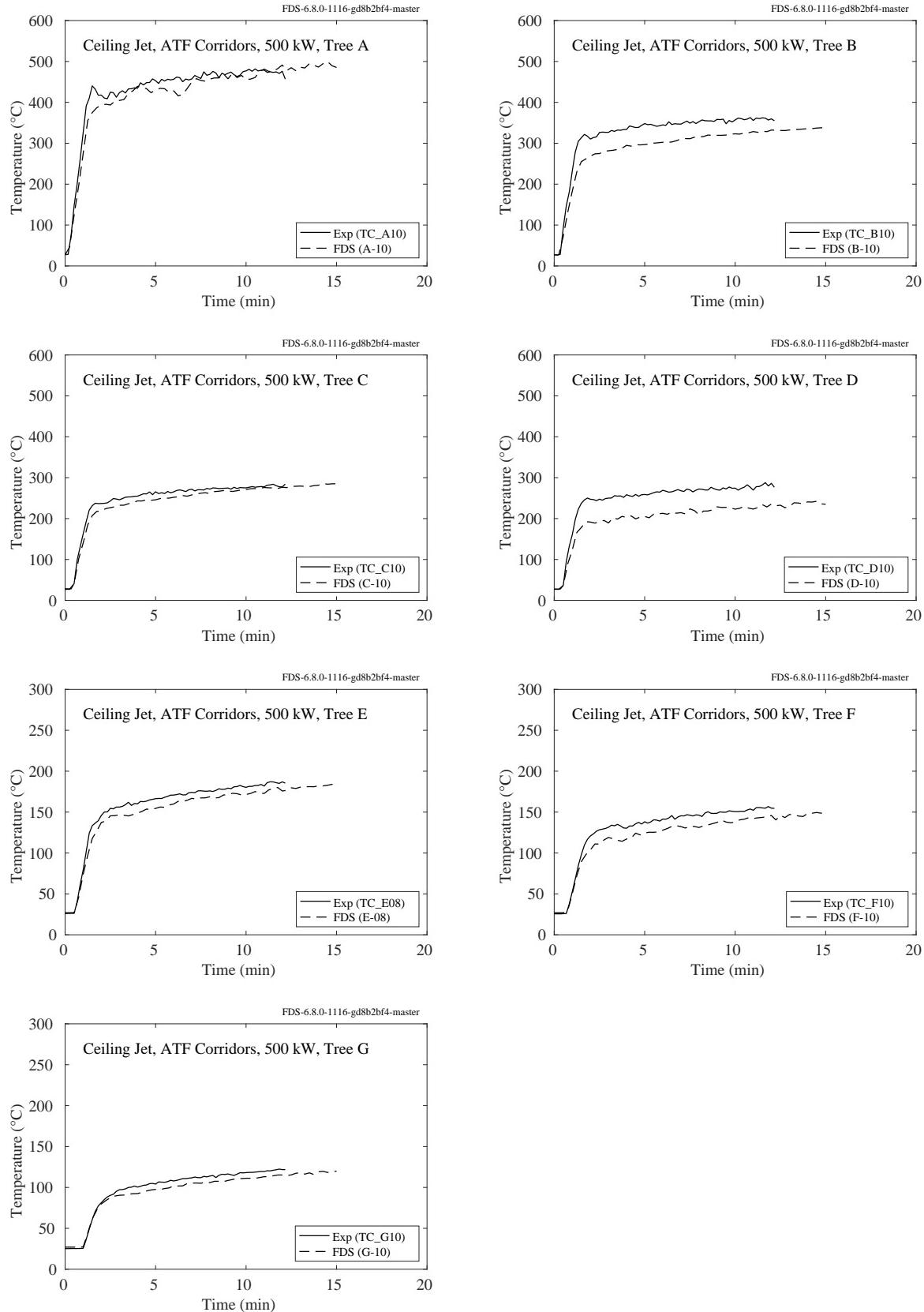


Figure 7.4: ATF Corridors experiments, ceiling jet, 500 kW.

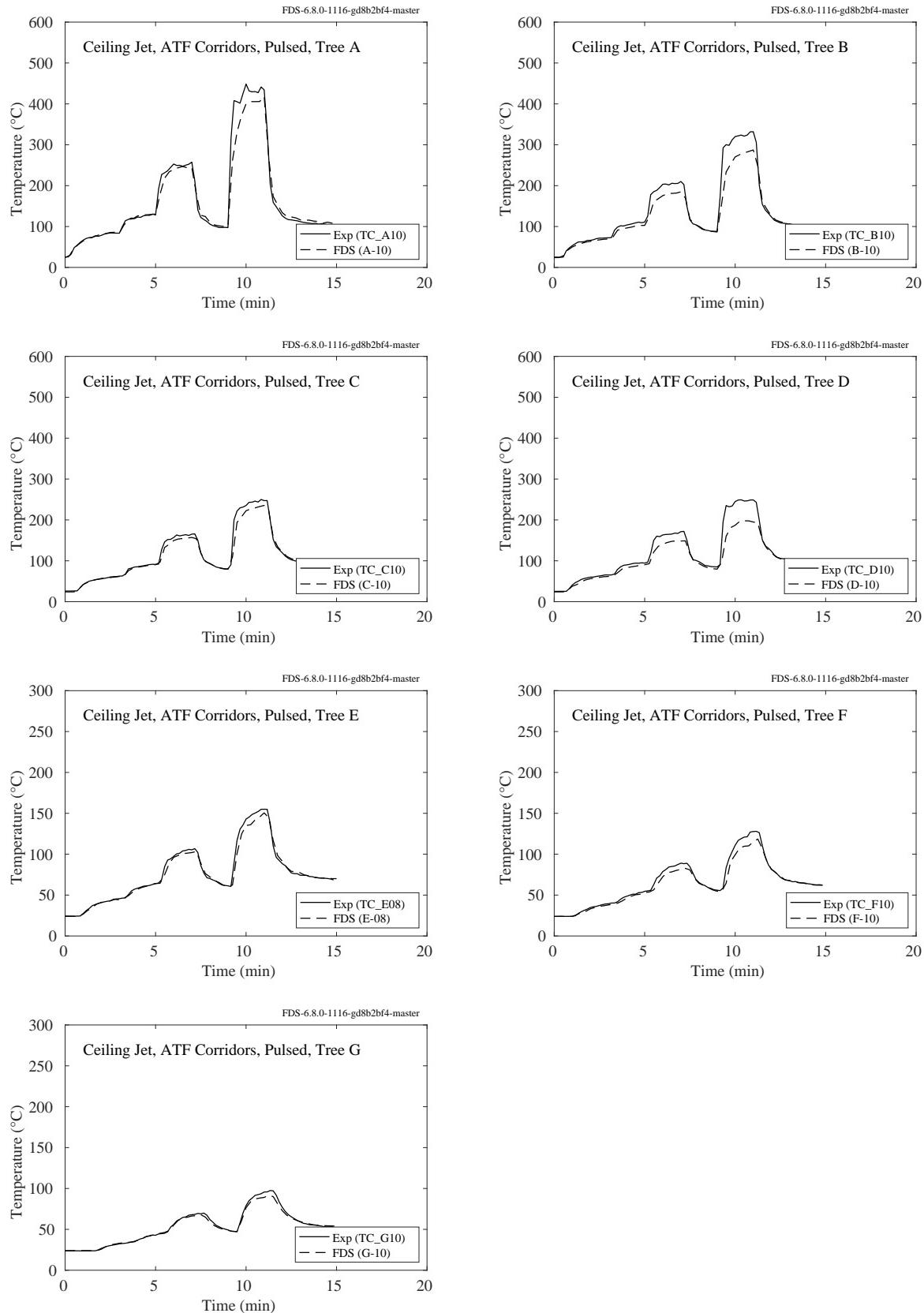


Figure 7.5: ATF Corridors experiments, ceiling jet, mixed HRR.

### 7.1.2 Arup Tunnel Experiments

The plots below show the predicted and measured temperatures from a fire experiment conducted in a tunnel. Near-ceiling temperatures were measured at distances of 2 m, 4 m, 6 m and 8 m from the fire along the centerline of tunnel.

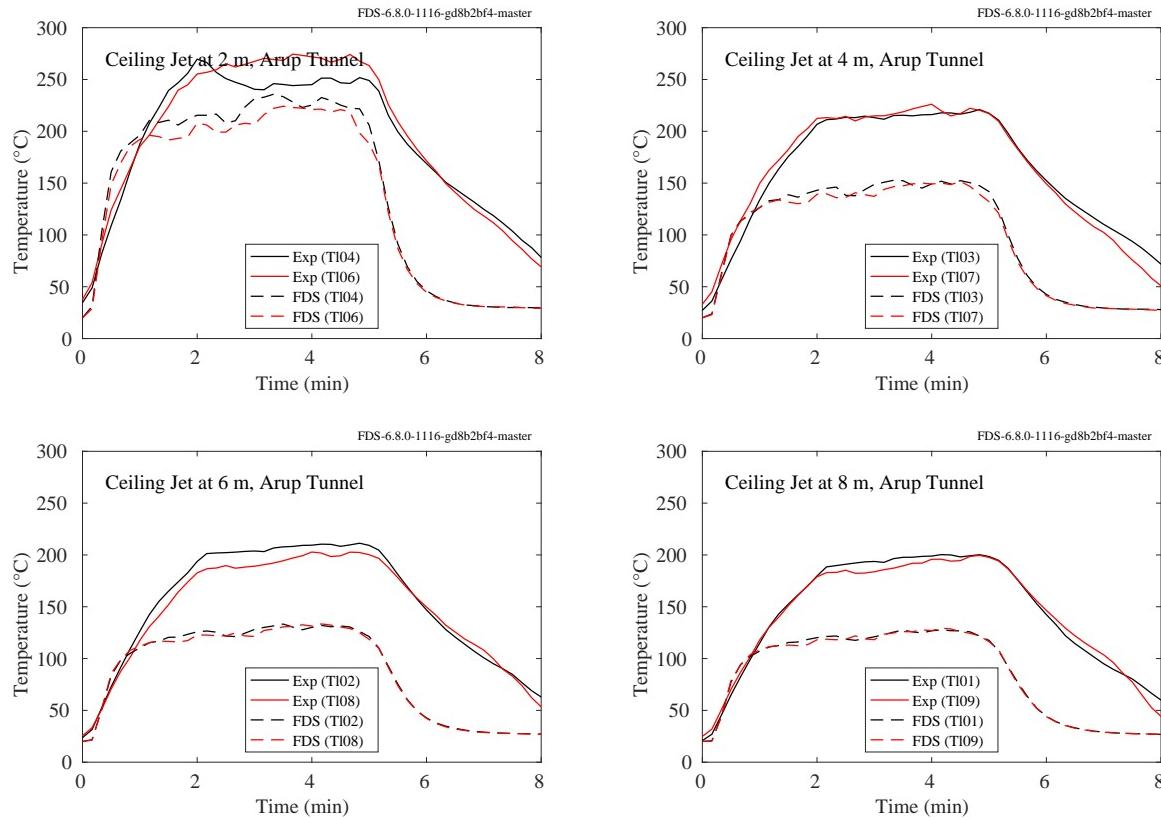


Figure 7.6: Arup Tunnel experiments, ceiling jet.

### 7.1.3 DelCo Trainers

The plots below and on the following pages display comparisons of ceiling jet temperatures for the DelCo Trainer experiments. Tests 2-6 were conducted in a single level house mock-up with three rooms adjacent to one another. Locations A1 and A2 were in the fire room, A3 was in an adjacent room, and A4 and A5 were in a room next to the adjacent room. Tests 22-25 were conducted in a two level house mock-up. Locations A1, A2, and A3 were 2 cm below the ceiling of the first level, and A7, A8, and A9 were 2 cm below the ceiling of the second level. See Sec. 3.18 for their exact locations.

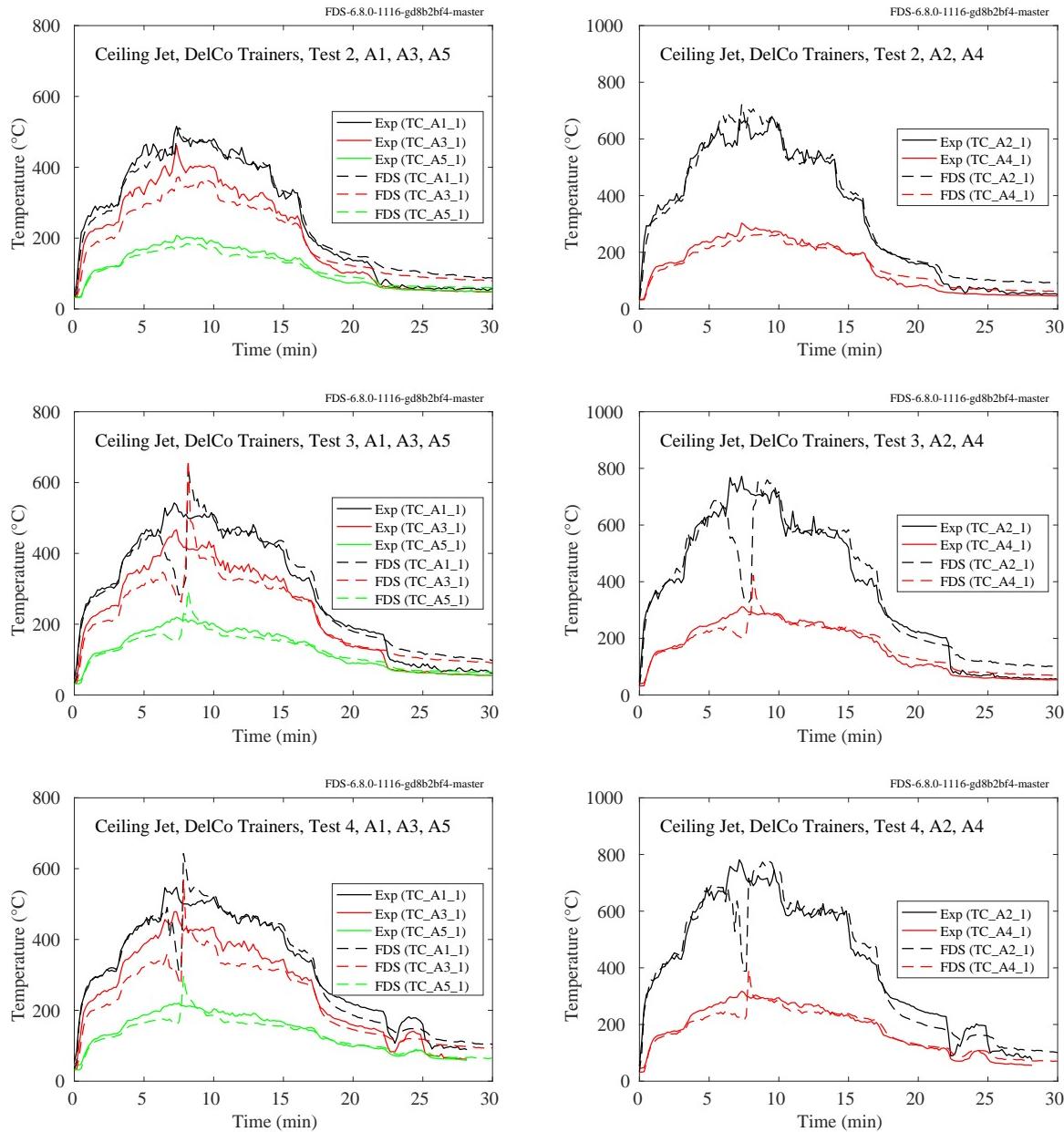


Figure 7.7: DelCo Trainers, ceiling jet temperature, Tests 2-4.

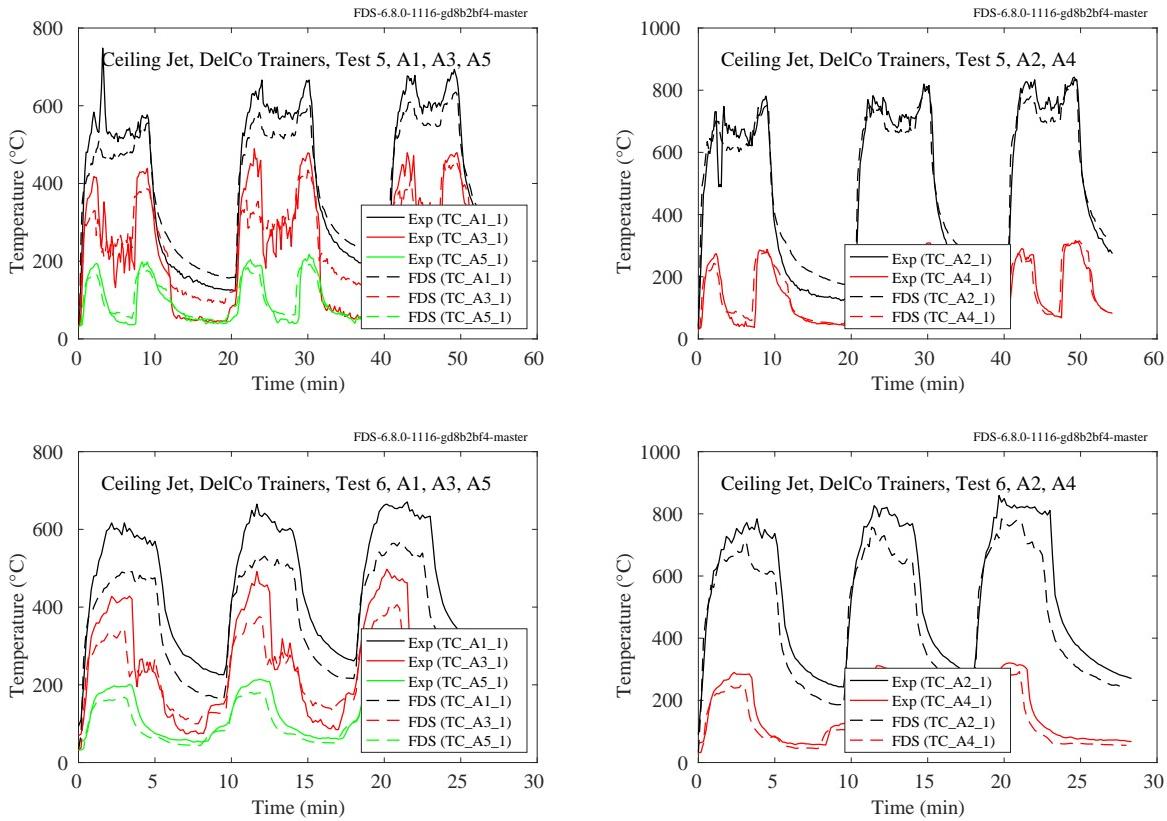


Figure 7.8: DelCo Trainers, ceiling jet temperature, Tests 5 and 6.

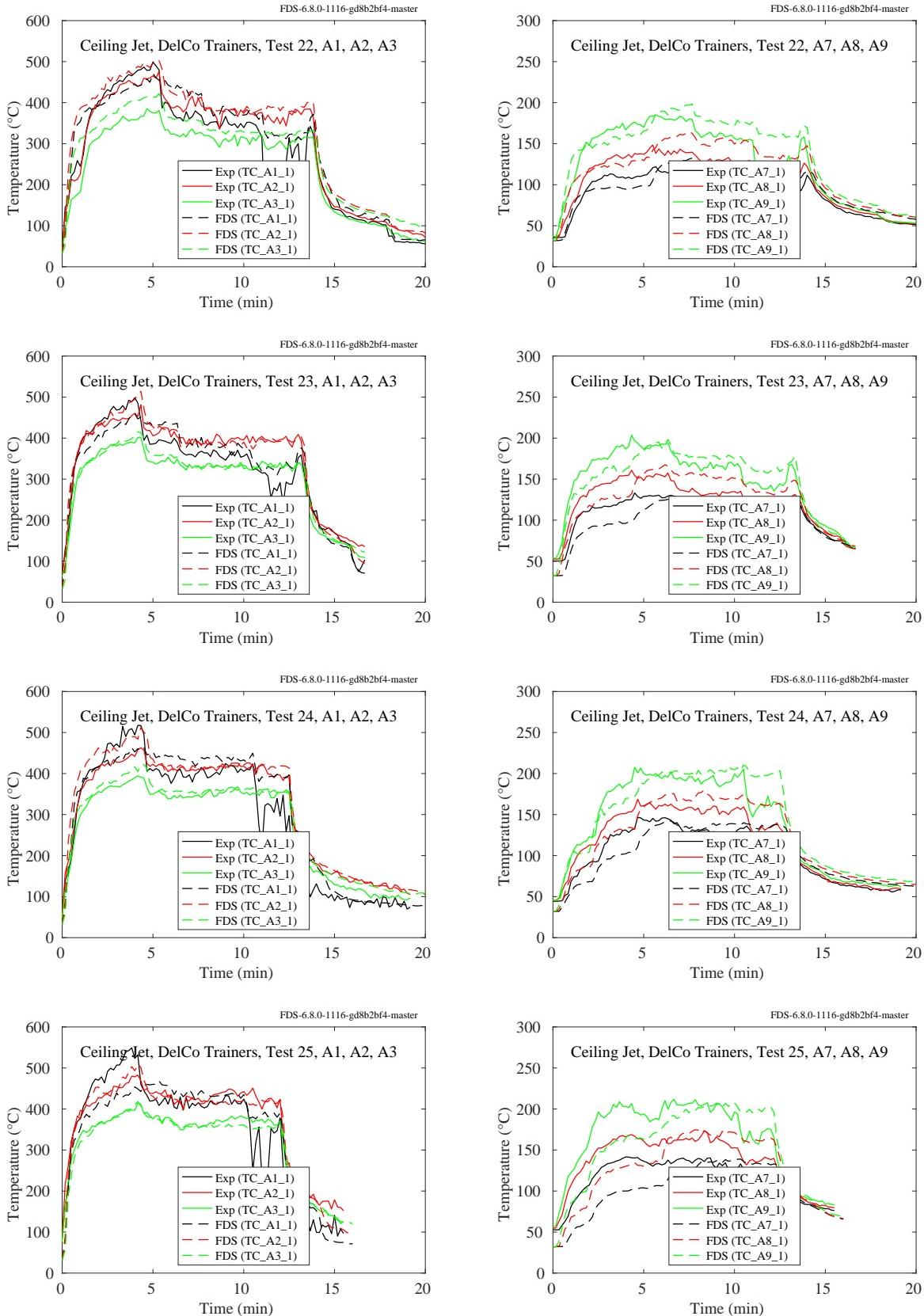


Figure 7.9: DelCo Trainers, ceiling jet temperature, Tests 22-25.

### 7.1.4 FAA Cargo Compartments

Figure 7.10 displays the locations of the near-ceiling thermocouples in the Boeing 707 compartment. The TCs were positioned approximately 4 cm below the ceiling. The small numbered squares indicate the fire locations for Tests 1, 2 and 3.

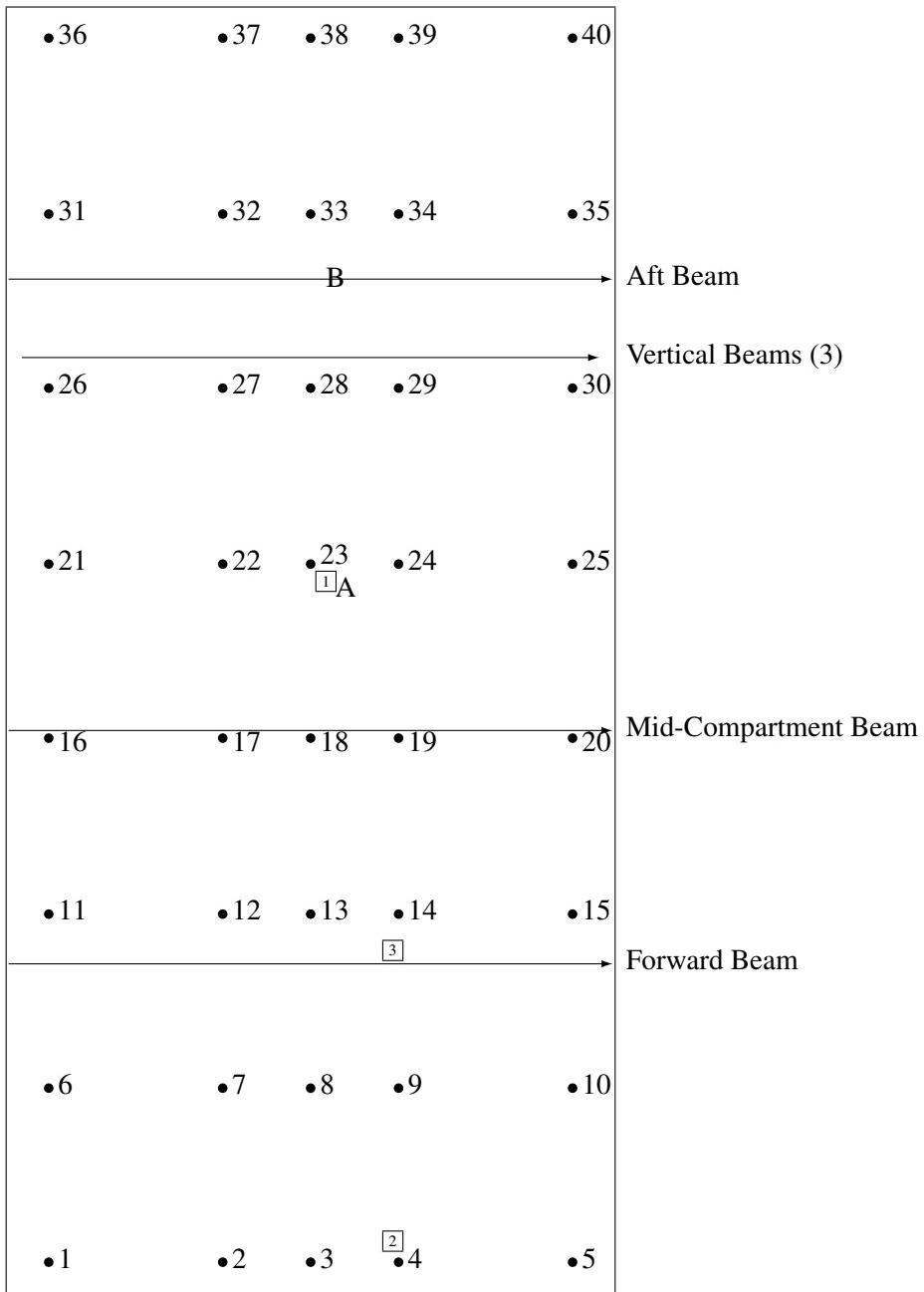


Figure 7.10: Layout of the near-ceiling thermocouples and other instruments, FAA Cargo Compartment Experiments.

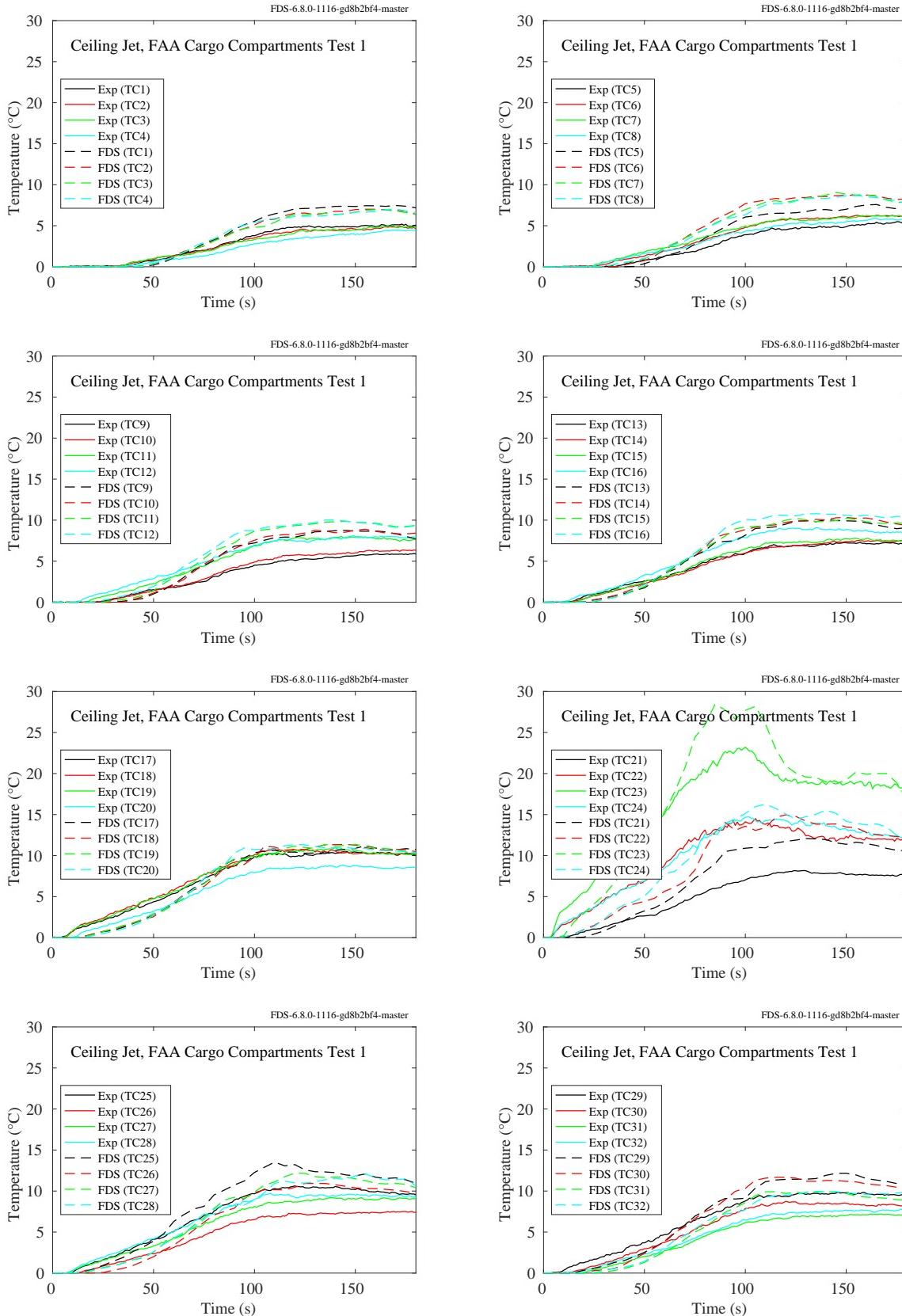


Figure 7.11: FAA Cargo Compartment experiments, ceiling jet, Test 1.

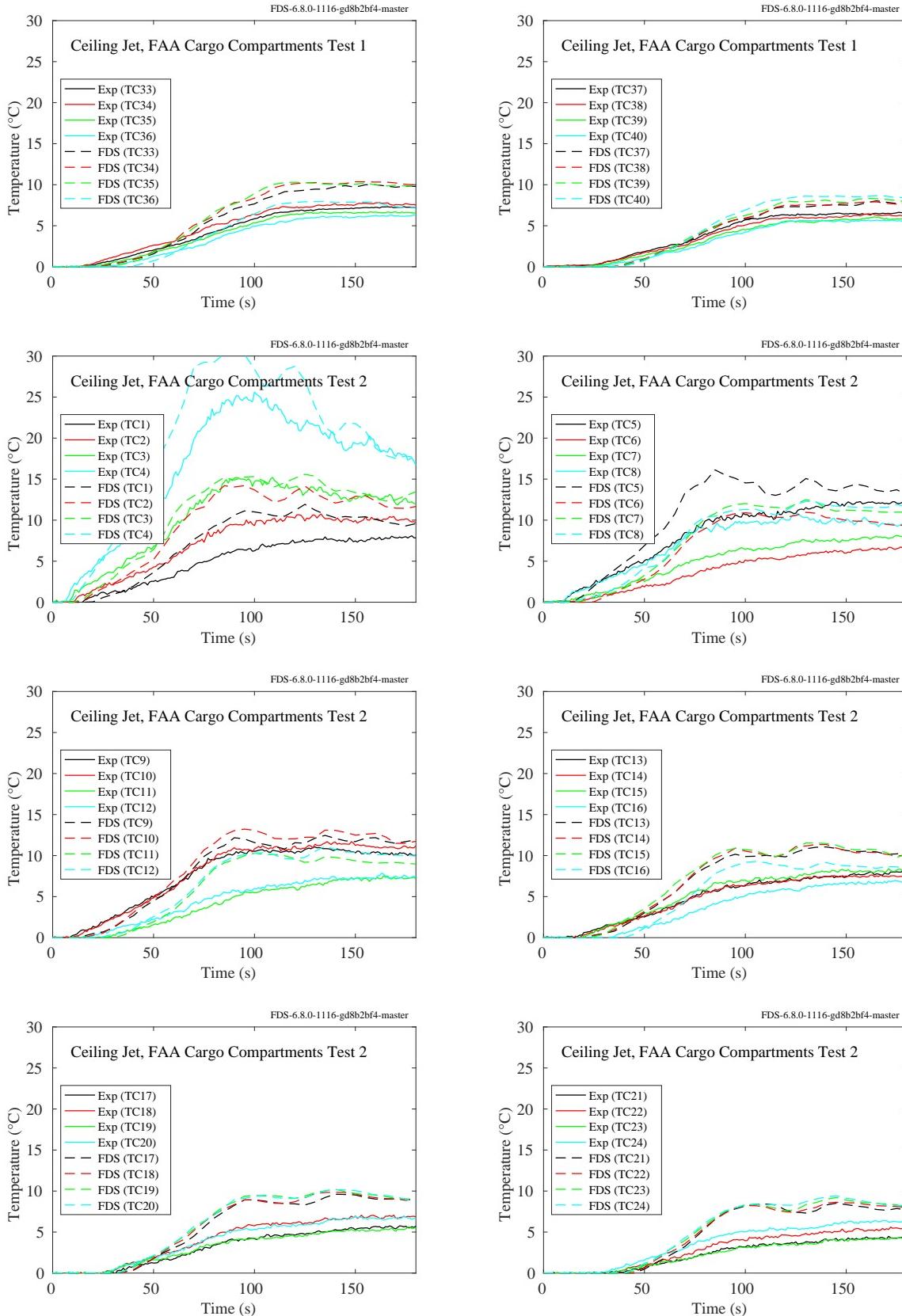


Figure 7.12: FAA Cargo Compartment experiments, ceiling jet, Test 1 and 2.

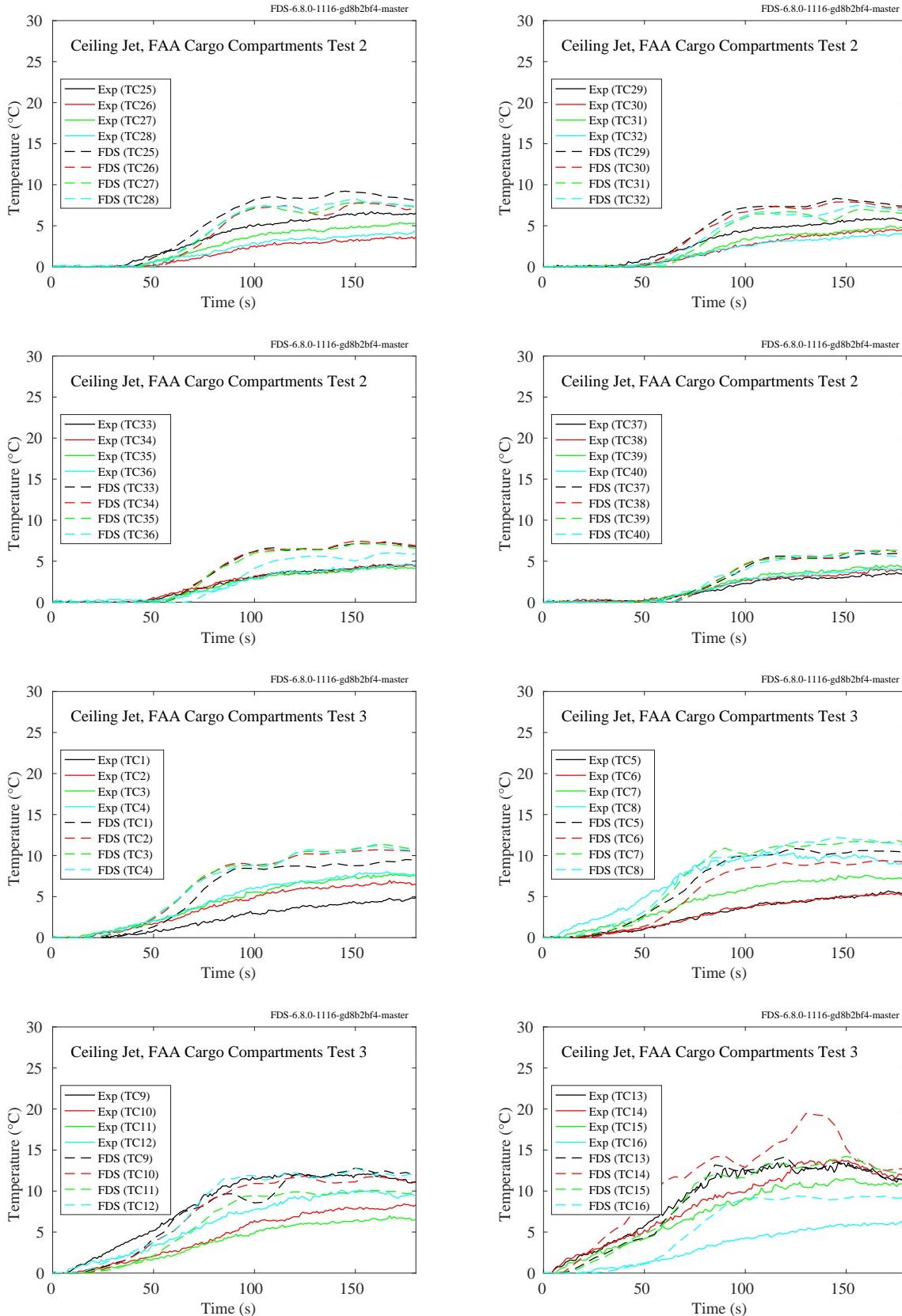


Figure 7.13: FAA Cargo Compartment experiments, ceiling jet, Test 2 and 3.

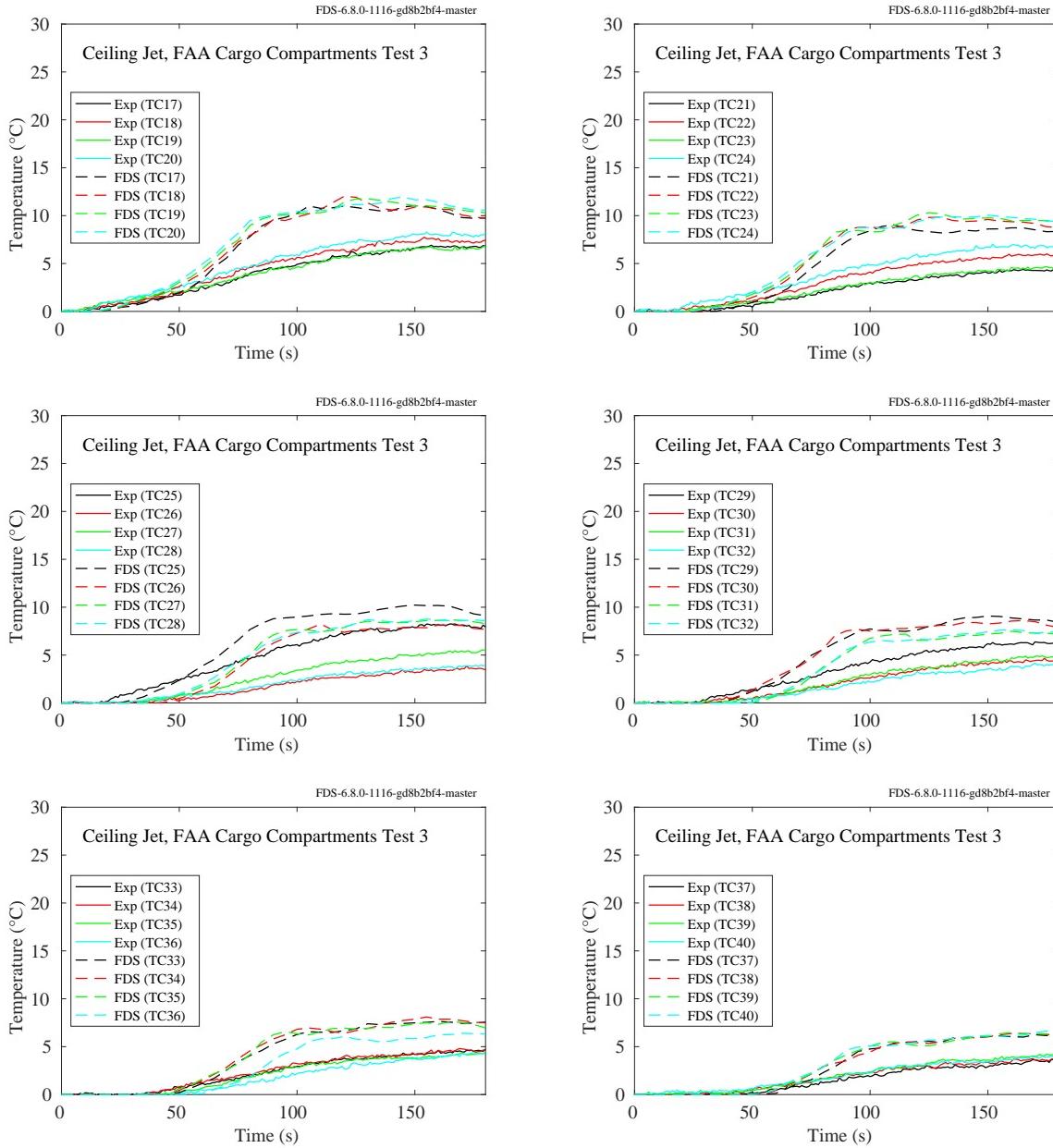


Figure 7.14: FAA Cargo Compartment experiments, ceiling jet, Test 3.

### 7.1.5 FM/SNL Experiments

The near-ceiling thermocouples in Sectors 1 and 3 have been chosen to evaluate the ceiling jet temperature prediction.

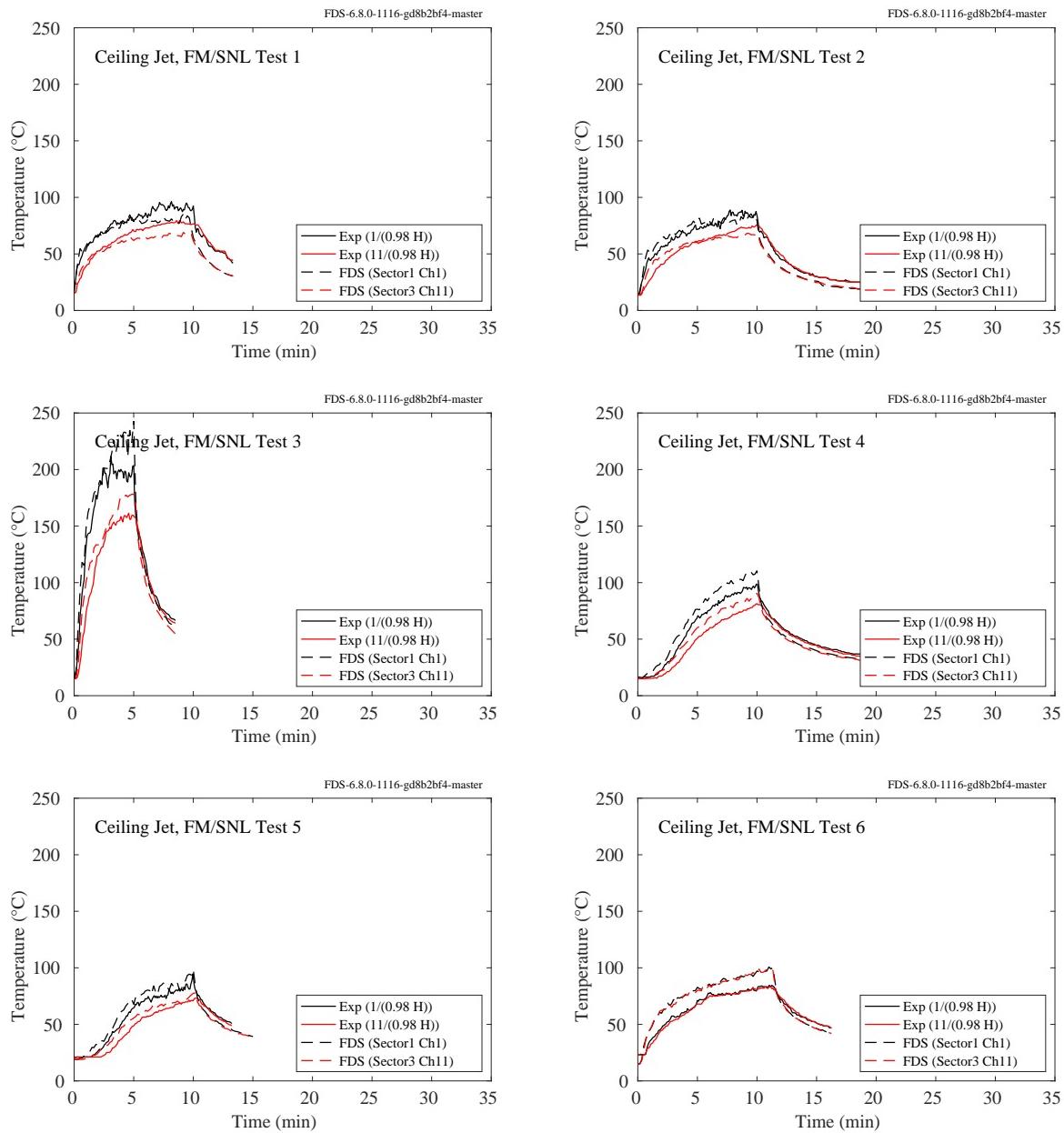


Figure 7.15: FM/SNL experiments, ceiling jet, Tests 1-6.

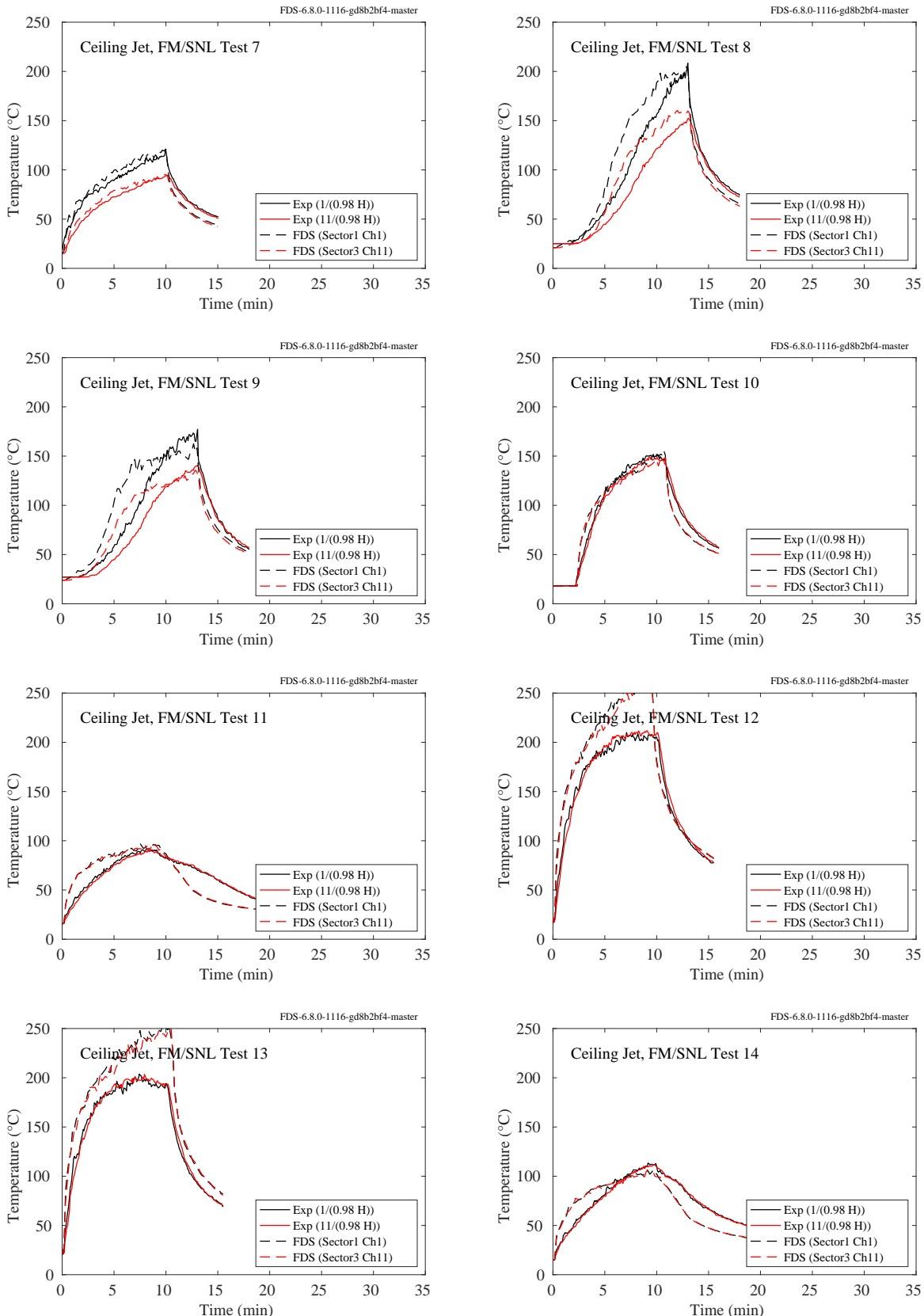


Figure 7.16: FM/SNL experiments, ceiling jet, Tests 7-14.

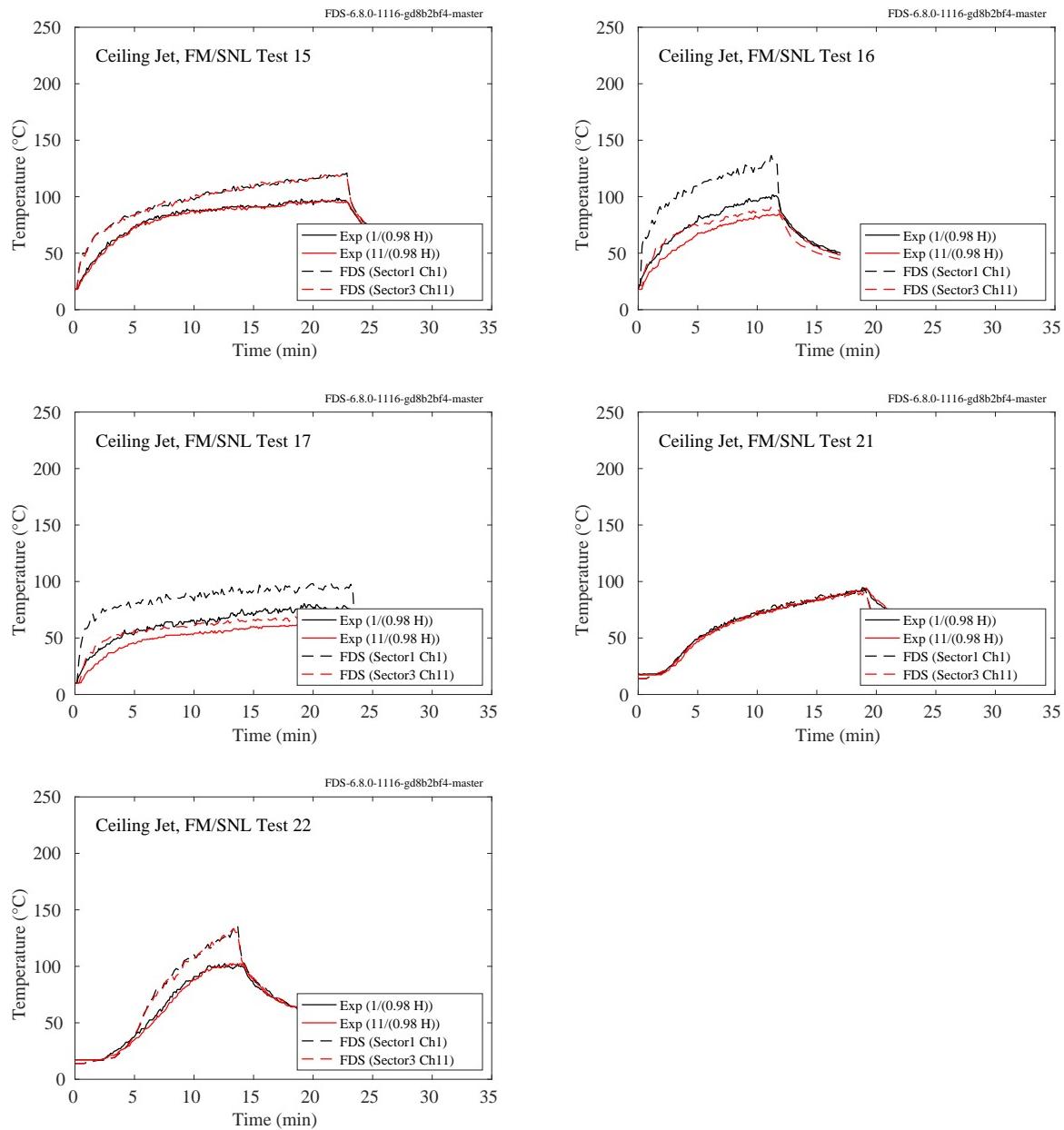


Figure 7.17: FM/SNL experiments, ceiling jet, Tests 15-17, 21-22.

### 7.1.6 NIST Composite Beam

A brief description of the experiments is given in Sec. 3.50. The compartment interior dimensions are 12.4 m long, running east-west, 1.9 m wide, and 3.77 m high. Four experiments with fires were performed, labeled as Tests 2-5. Test 1 did not include a fire.

To measure the ceiling jet temperature in the compartment, stainless steel sheathed thermocouples (Omega TJ36-CAXL-14U-24 and TJ36-CAXL-38U-24) were mounted 2.5 cm and 23 cm below the ceiling, extending through four holes drilled down through the concrete. Two TCs were located at each of the four positions. TCC9 and TCC10 were located 2.6 m west and 0.6 m north of the compartment center. TCC11 and TCC12 were located at the same location east of the center. TCC13 and TCC14 were located at the same relative location, south and east of the center. TCC15 and TCC16 were located west and south of the center.

Because of the symmetry of the experimental configuration, TCC9, TCC11, TCC13, and TCC15, all 2.5 cm below the ceiling are duplicates; as are TCC10, TCC12, TCC14, and TCC16, located 23 cm below the ceiling.

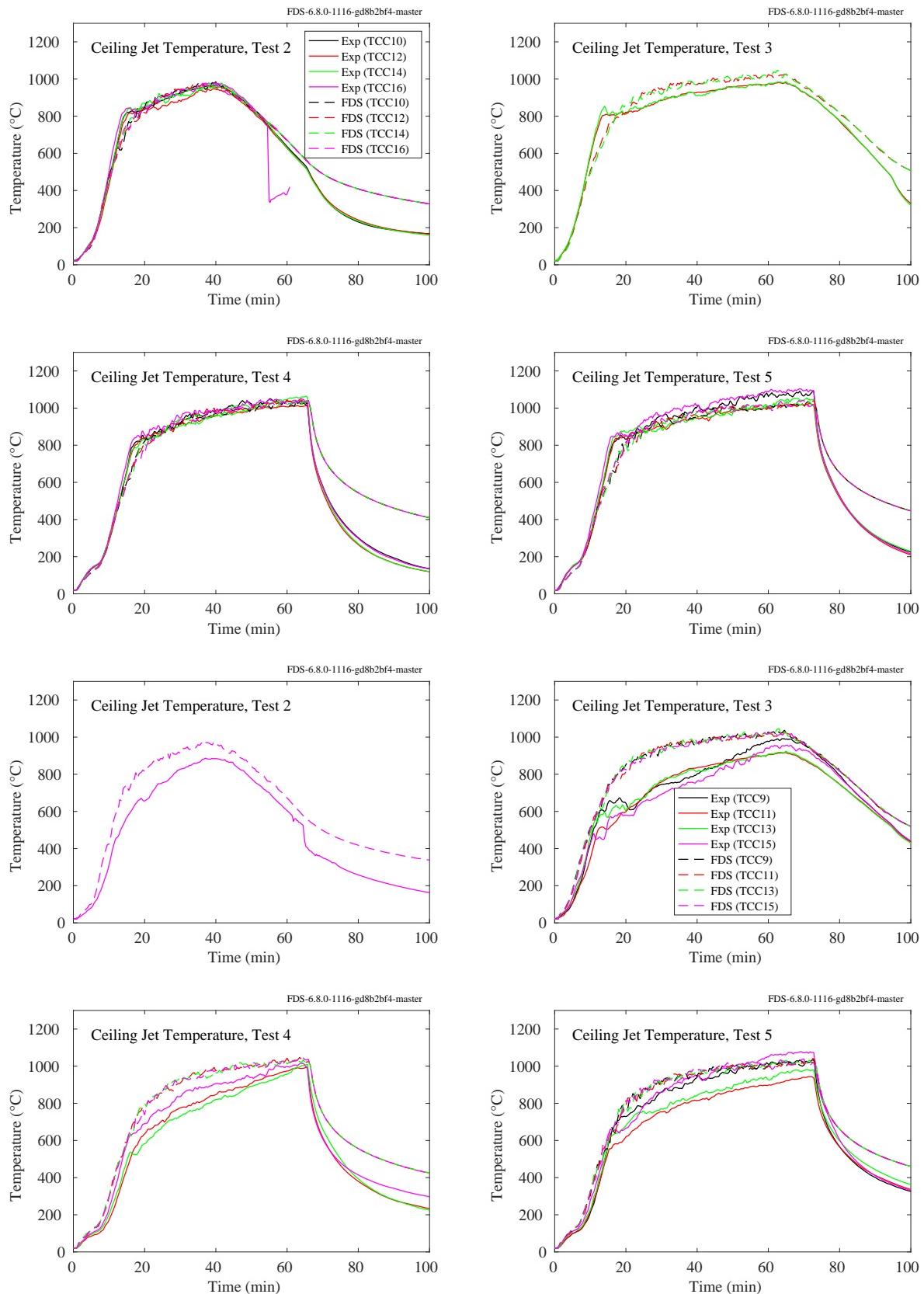


Figure 7.18: NIST Composite Beam, ceiling jet temperatures.

### 7.1.7 NIST Smoke Alarm Experiments

The primary purpose of the NIST Smoke Alarm Experiments was to measure smoke detector activation times in residential settings. In the single-story manufactured home tests that were selected for validation, five smoke detector measurement stations (Station A through Station E) were located in different areas of the manufactured home. Thermocouple trees were also located at each measurement station. The highest thermocouple in the tree can be compared to ceiling jet temperature predictions. The plots on the following page show the measured and predicted ceiling jet temperatures for the five measurement stations in each test.

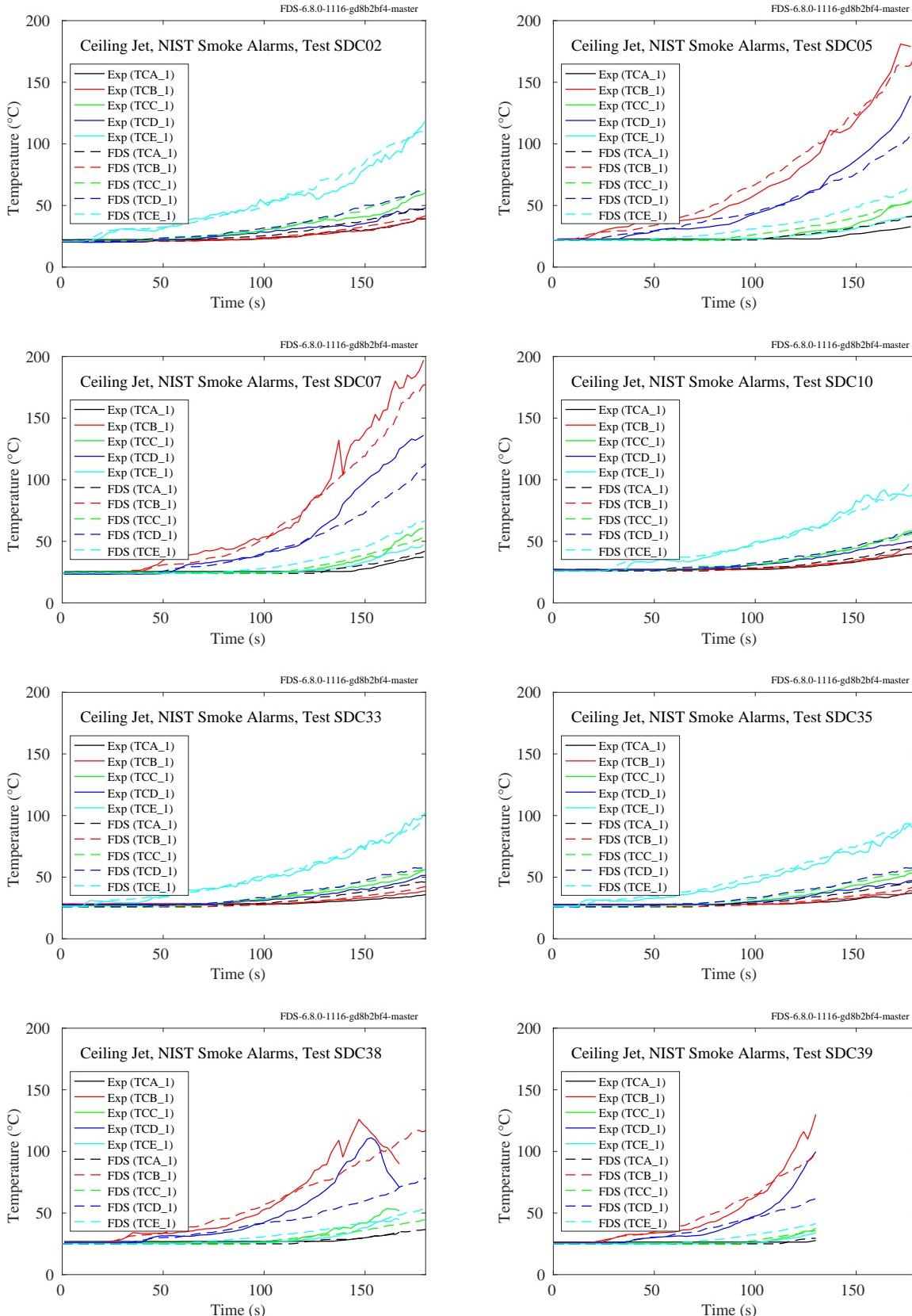


Figure 7.19: NIST Smoke Alarm experiments, ceiling jet.

### **7.1.8 NIST/NRC Experiments**

In the NIST/NRC experiments, seven vertical arrays of thermocouples were positioned throughout the compartment. The thermocouple nearest the ceiling in Tree 7, located towards the back of the compartment away from the door, has been chosen to evaluate the ceiling jet temperature prediction.

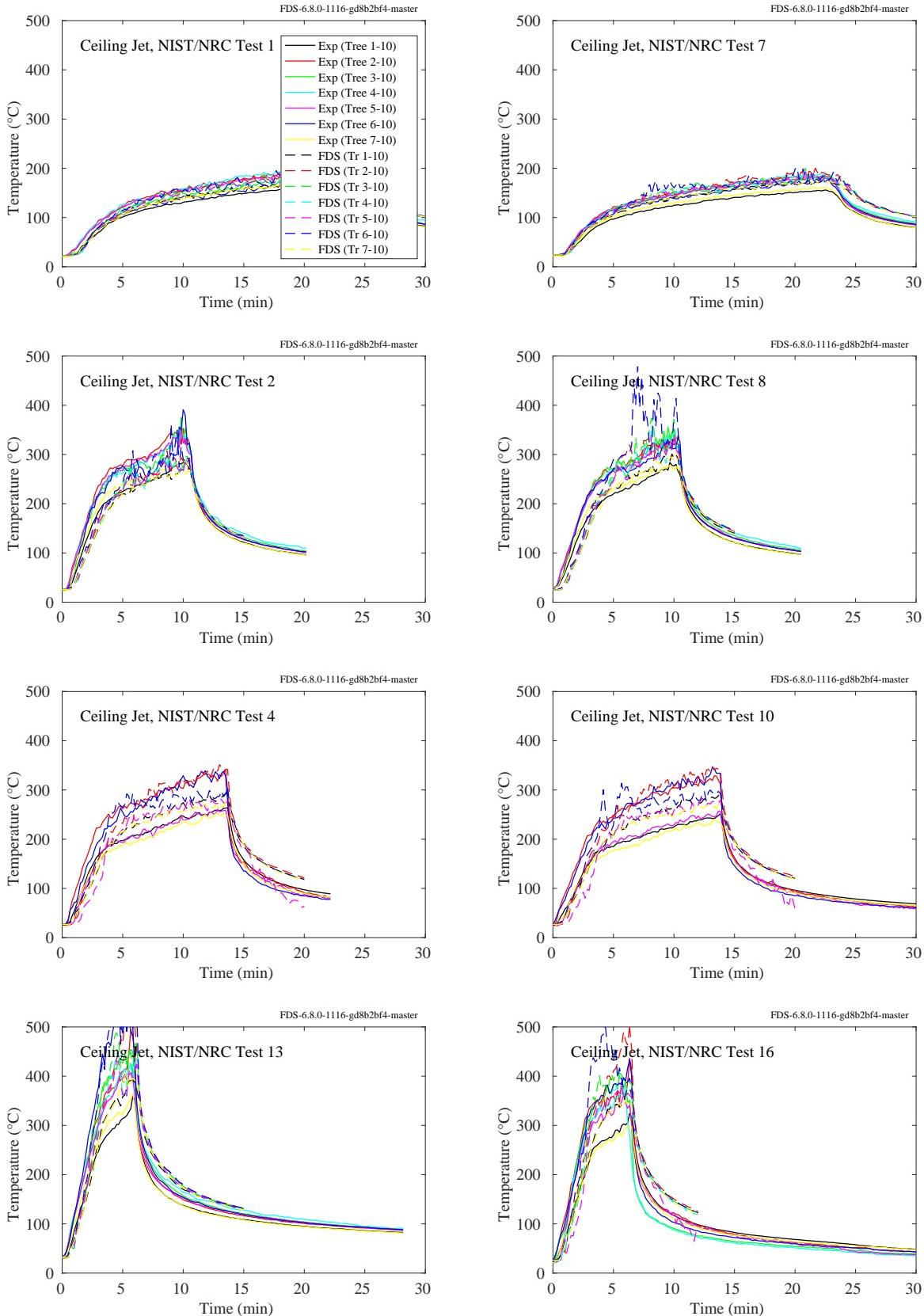


Figure 7.20: NIST/NRC experiments, ceiling jet, Tests 1, 2, 4, 7, 8, 10, 13, 16.

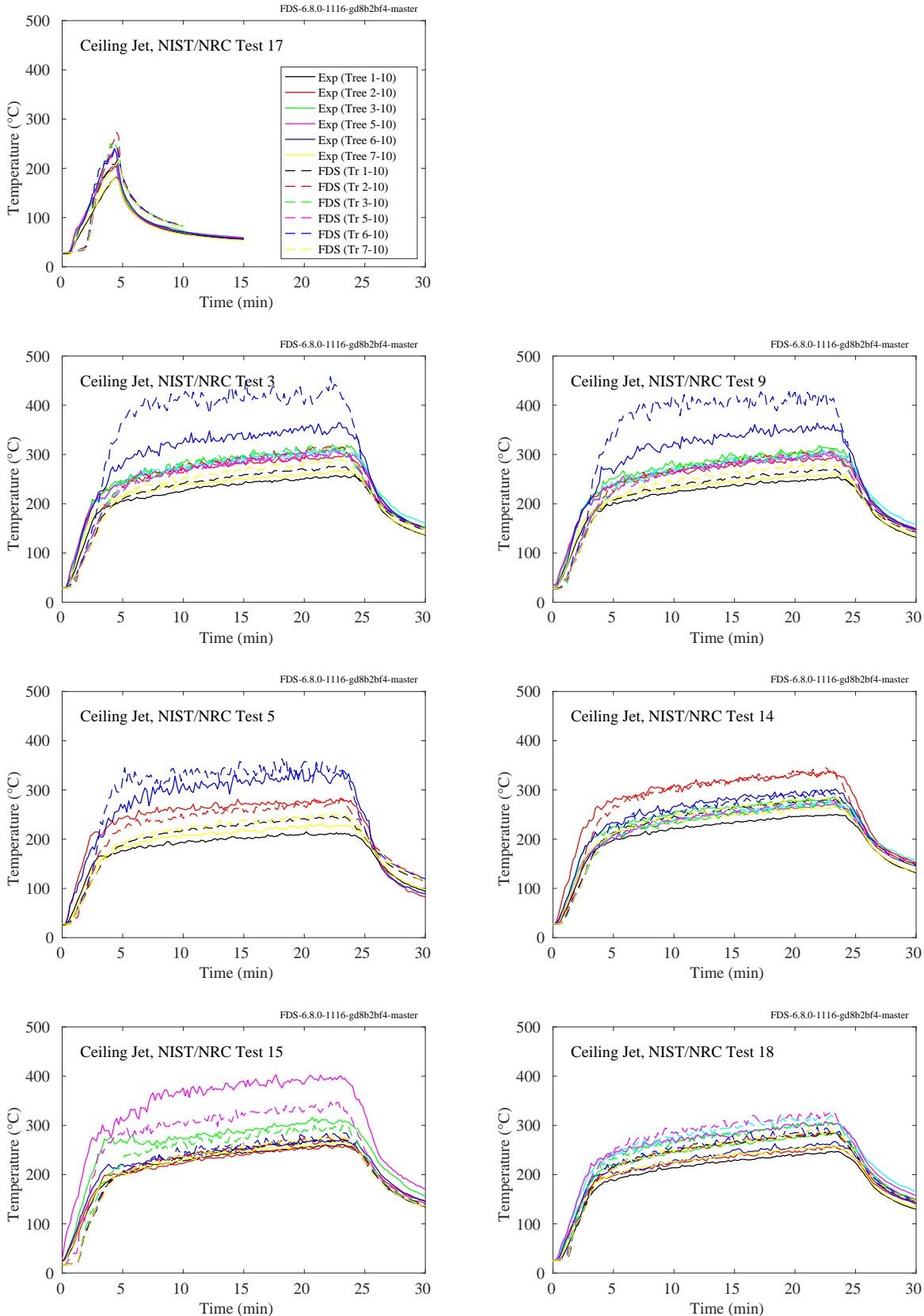


Figure 7.21: NIST/NRC experiments, ceiling jet, Tests 3, 5, 9, 14, 15, 17, 18.

### 7.1.9 NIST/NRC Corner Effects Experiments

The plots on the following pages compare ceiling jet temperatures at two locations in a large compartment where corner, wall, and cabinet effects experiments were conducted. The corner and wall experiments involved a 60 cm by 60 cm natural gas burner with heat release rates of 200 kW, 300 kW, and 400 kW. The burner was either set in a corner or against a wall. The cabinet experiments involved gas burners set in one of two mock steel cabinets, with a variety of heat release rates.

In all experiments, two vertical thermocouple arrays were placed along the centerline of the room, each one-third of the room length from each respective short wall. The arrays each had 13 bare-bead thermocouples. The first was 2 cm below the ceiling, used to measure the ceiling jet temperature.

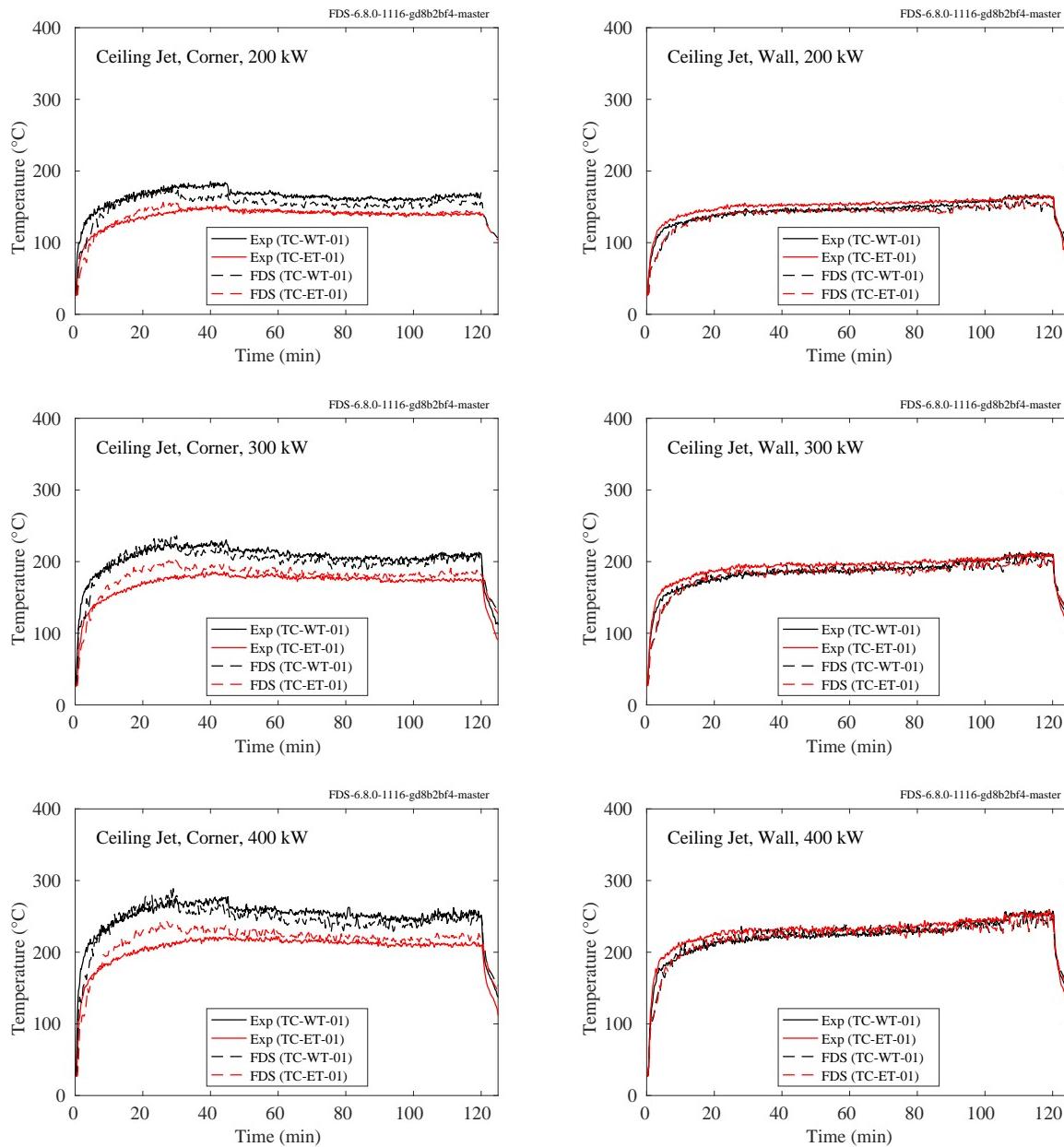


Figure 7.22: NIST/NRC Corner Effects experiments, ceiling jet temperature, wall and corner tests.

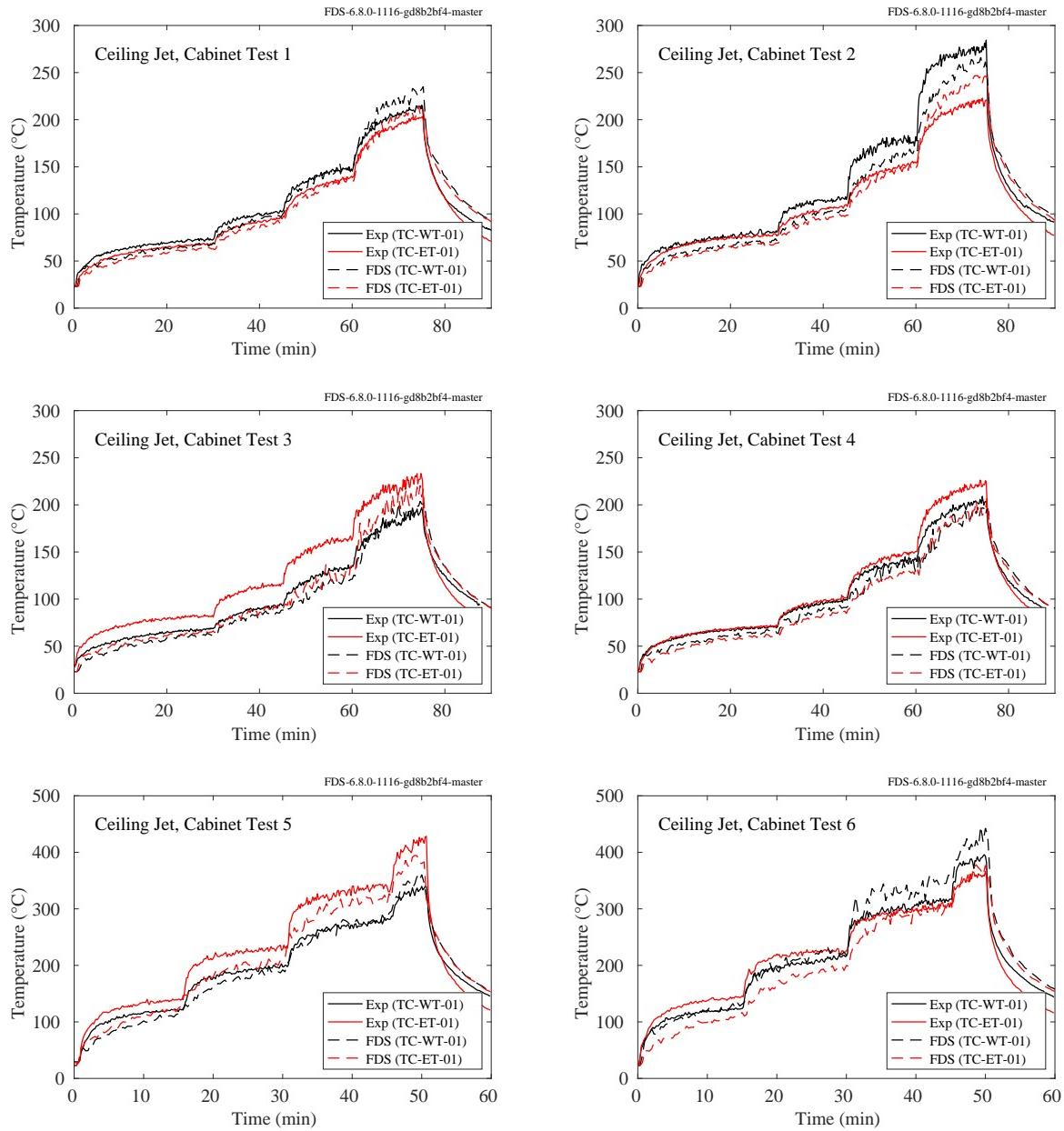


Figure 7.23: NIST/NRC Corner Effects experiments, ceiling jet temperature, large cabinet.

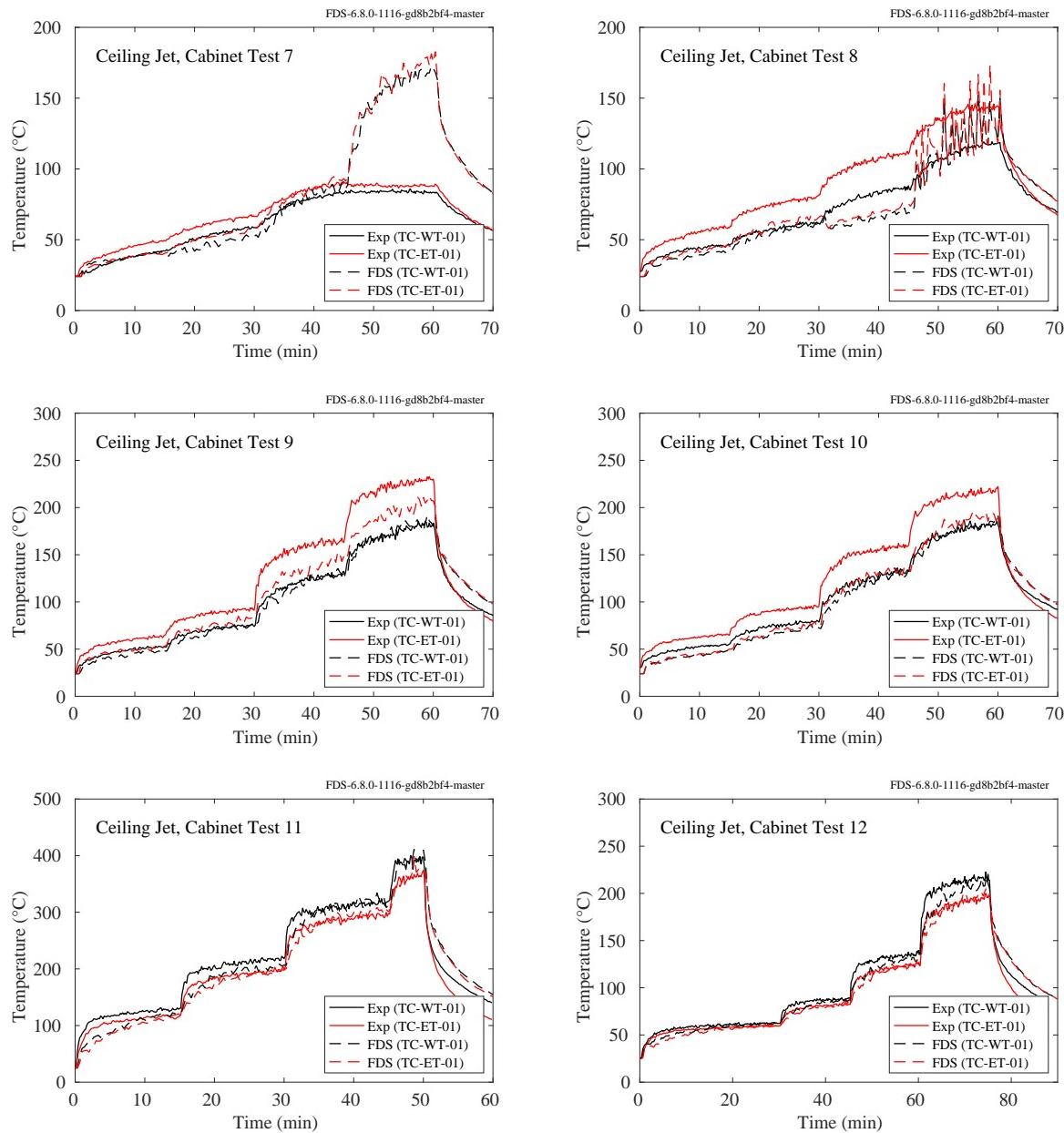


Figure 7.24: NIST/NRC Corner Effects experiments, ceiling jet temperature, medium-sized cabinet.

### 7.1.10 NIST Vent Study

These experiments were performed in a small-scale two floor enclosure, with each floor connected by one or two ceiling vents. Each floor contained a vertical array of eight sheathed thermocouples; the uppermost being 5 cm below the ceiling.

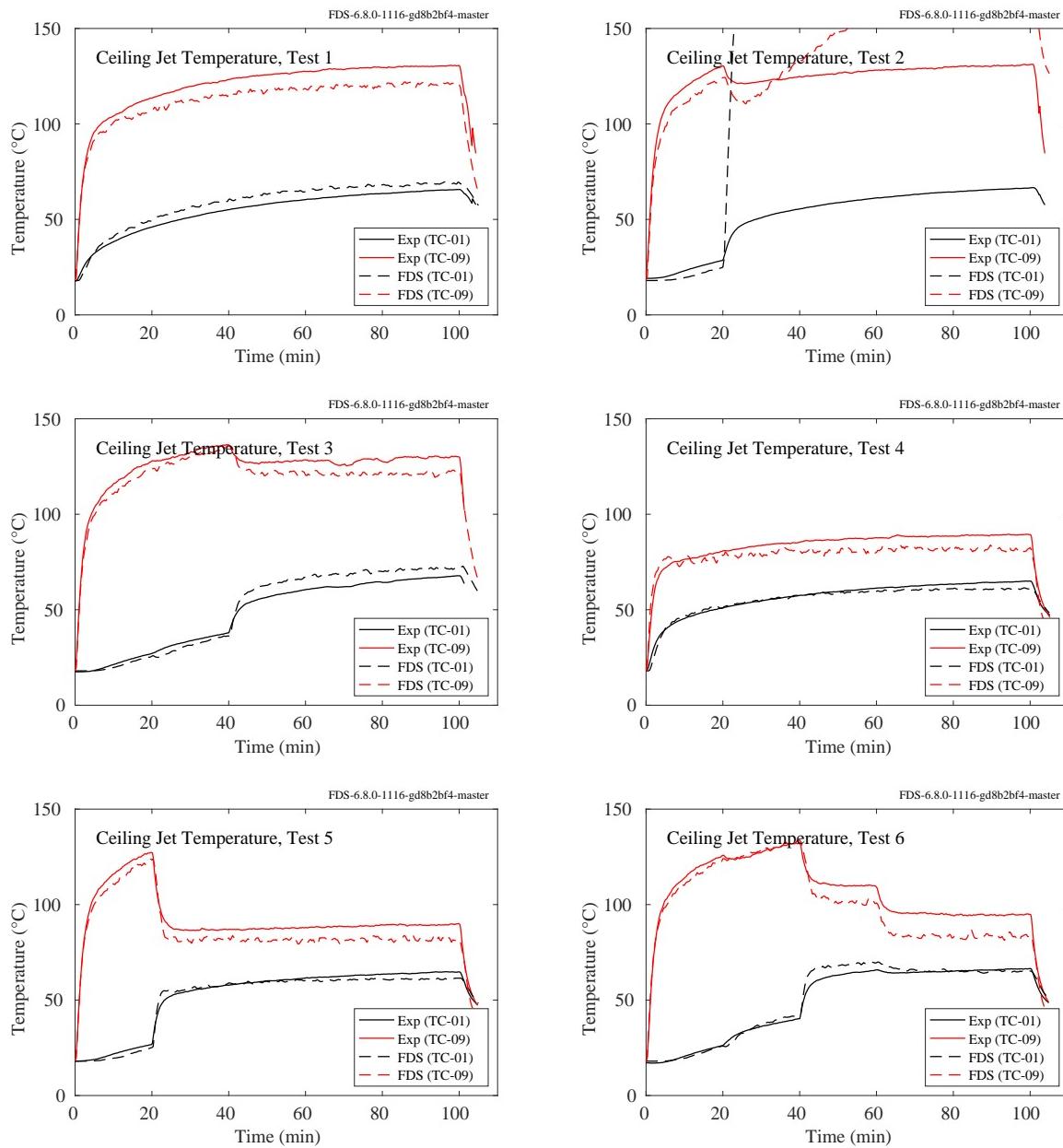


Figure 7.25: NIST Vent Study, ceiling jet temperature, Tests 1-6.

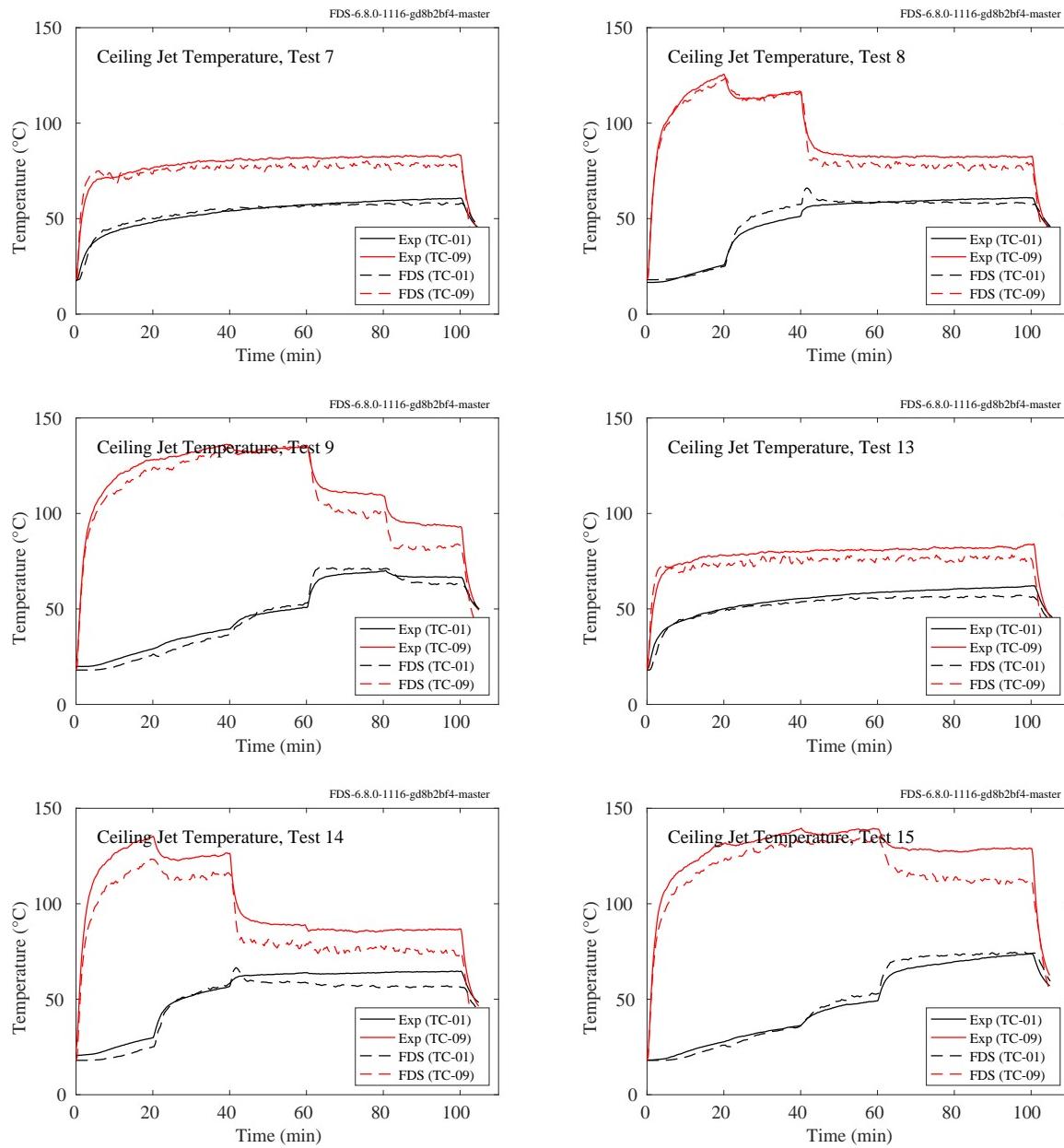


Figure 7.26: NIST Vent Study, ceiling jet temperature, Tests 7-9, 13-15.

### 7.1.11 NRCC Smoke Tower

In the NRCC Smoke Tower experiments, there was a vertical array of 13 TCs and a single near-ceiling TC on the opposite side of the fire compartment. Shown in Fig. 7.27 are the predicted and measured temperatures of the single TC and the uppermost TC of the vertical array in the fire compartment. Shown in Fig. 7.28 are predictions of gas temperature measurements made in the stair vestibule of floors 4, 6, 8, and 10, along with inner compartment temperature measurements made on floors 4, 8, and 10. Note that the plot labels “Slot” refer to the data acquisition system in the experiments only and have no meaning in the present context. It should be clear from the plot title how the various curves ought to be interpreted.

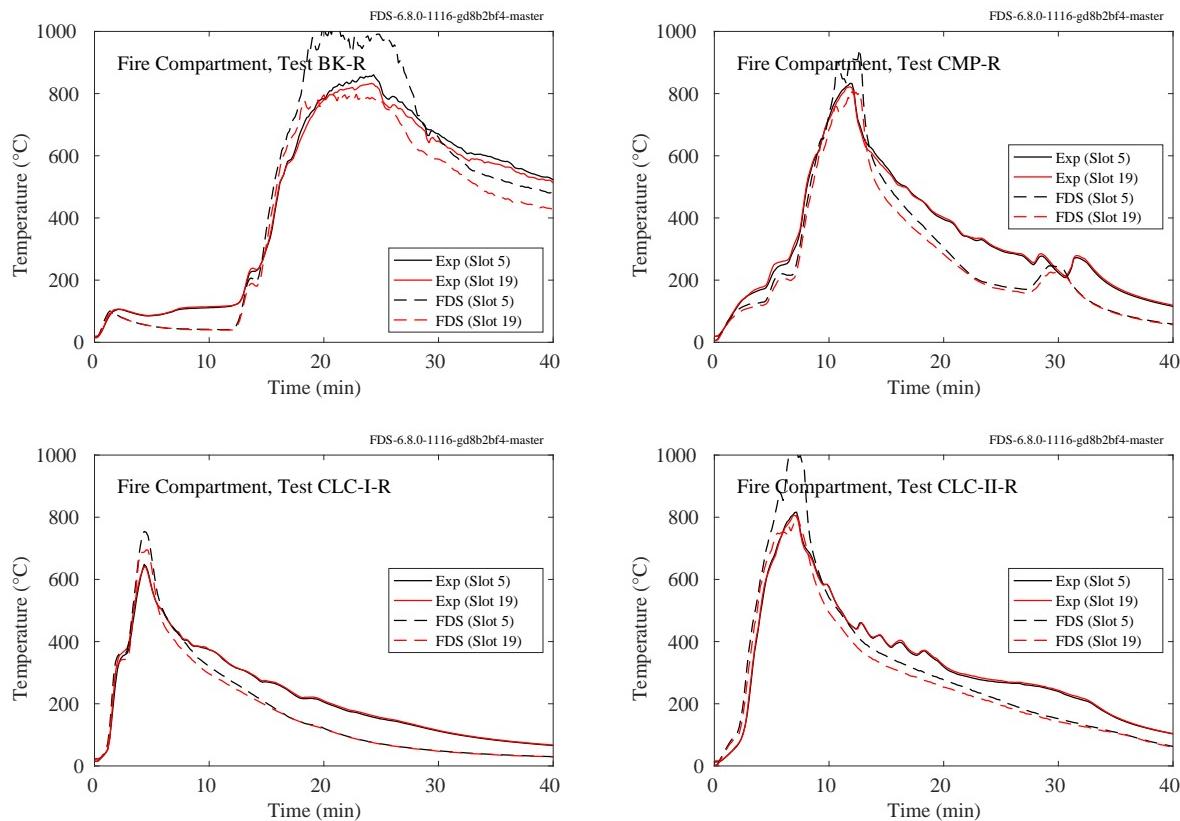


Figure 7.27: NRCC Smoke Tower experiments, ceiling jet.

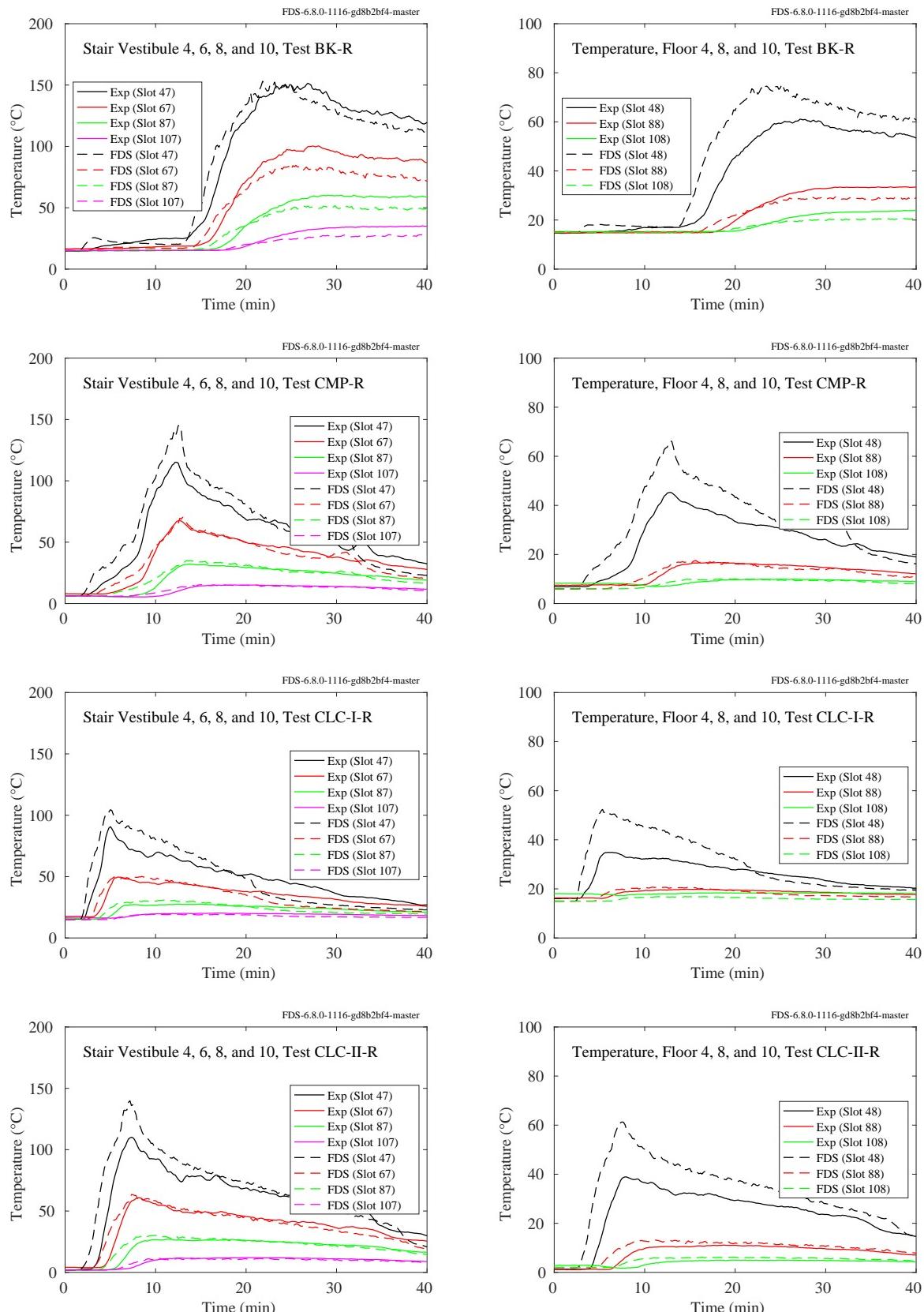


Figure 7.28: NRCC Smoke Tower, upper floor temperatures.

### 7.1.12 PRISME DOOR Experiments

In the PRISME DOOR experiments, the uppermost TC in the vertical arrays were used to measure the ceiling jet temperature. These TCs were approximately 10 cm below the ceiling.

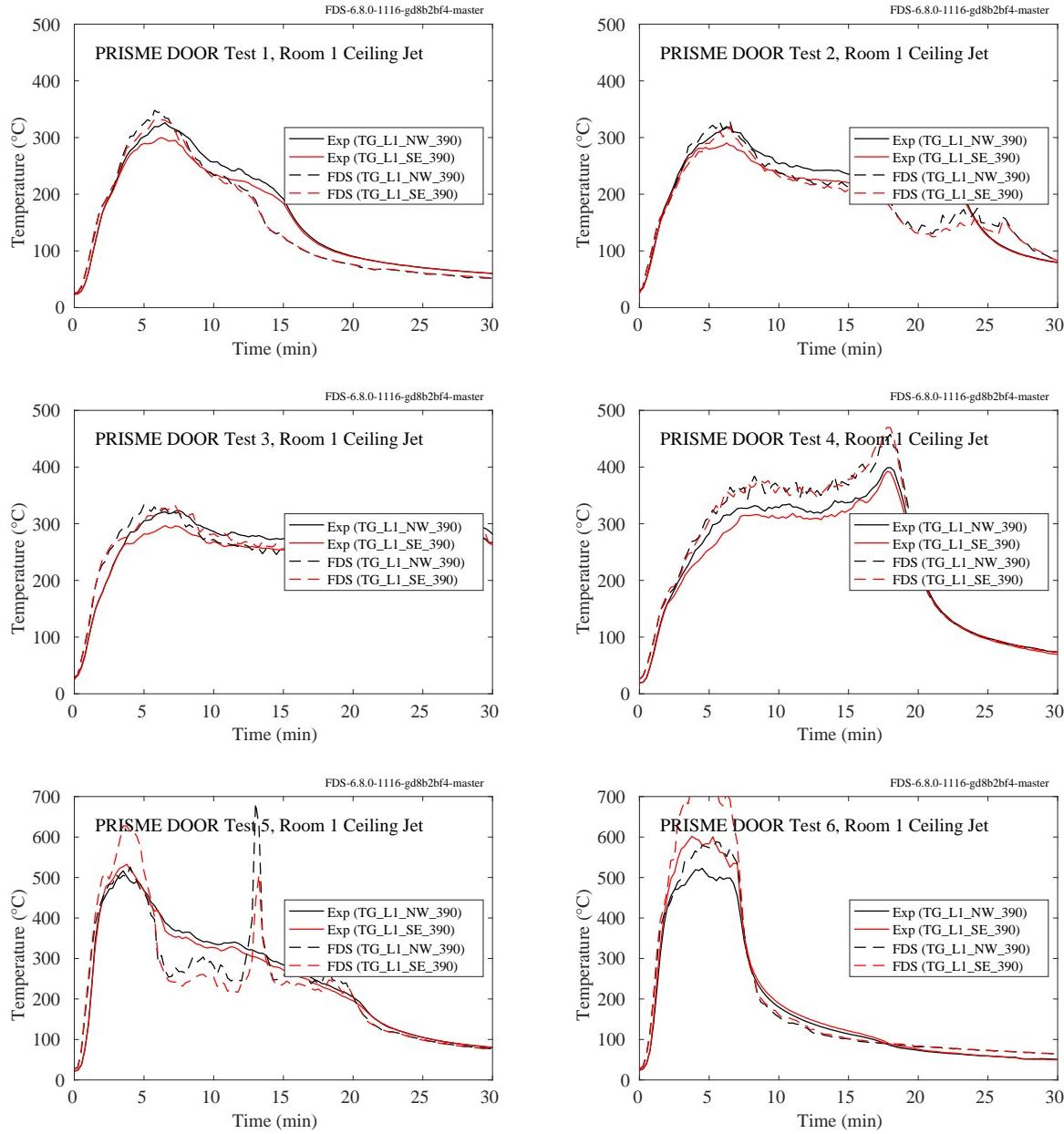


Figure 7.29: PRISME DOOR experiments, ceiling jet, Room 1.

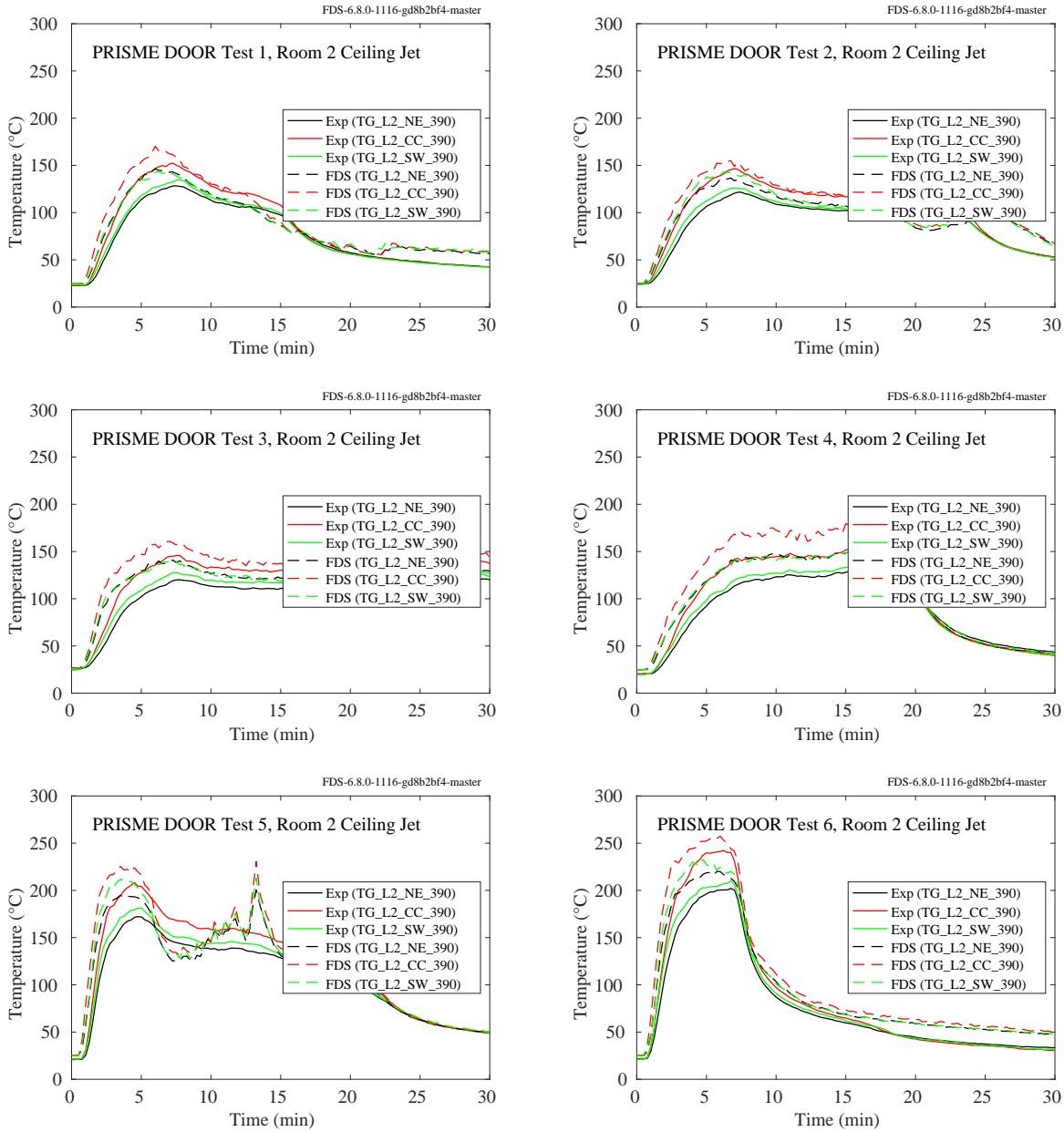


Figure 7.30: PRISME DOOR experiments, ceiling jet, Room 2.

### **7.1.13 PRISME SOURCE Experiments**

In the PRISME SOURCE experiments, the uppermost TC in the vertical array was used to measure the ceiling jet temperature. The thermocouple array was located in the northeast corner of the room. This TC was approximately 10 cm below the ceiling.

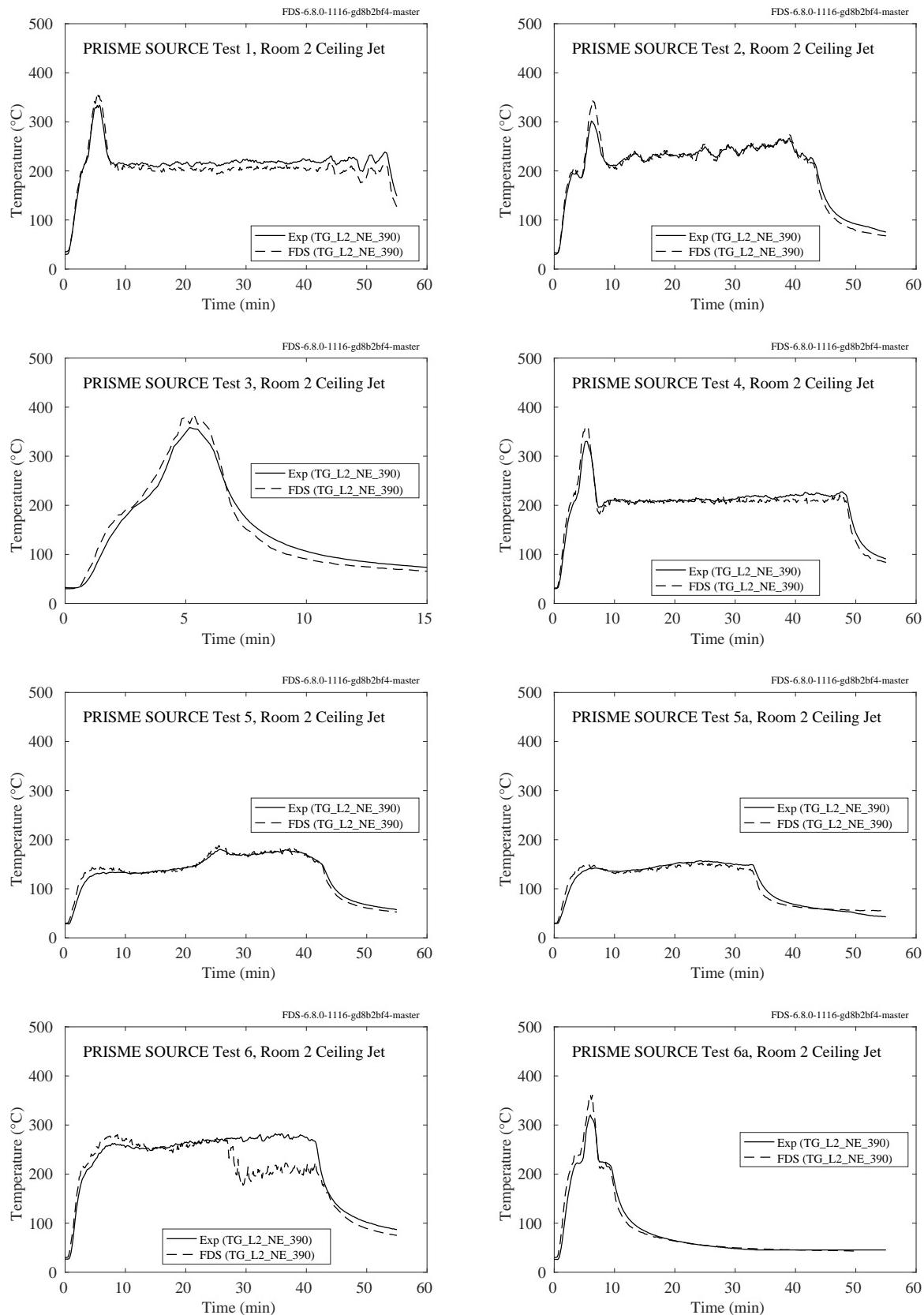


Figure 7.31: PRISME SOURCE experiments, ceiling jet, Room 2.

### 7.1.14 SP Adiabatic Surface Temperature Experiments

Three experiments were conducted in a standard compartment, 3.6 m long by 2.4 m wide by 2.4 m high, with a 0.8 m wide by 2.0 m high door centered on the narrow wall. A single beam was suspended 20 cm below the ceiling lengthwise along the centerline of the compartment. There were three measurement stations along the beam at distances of 0.9 m (Station A), 1.8 m (Station B), and 2.7 m (Station C) from the far wall where the fire was either positioned in the corner (Tests 1 and 2), or the center (Test 3). The gas temperatures reported here were measured 10 cm away from all four sides of the beam at Station A, and 10 cm away from the two lateral sides at Stations B and C. In the figure legends, the measurement station is denoted A, B, or C, and the position is denoted 1, 2, 3, or 4. Position 1 is 10 cm above the beam. Position 2 is 10 cm from the side of the beam facing away from the fire, Position 3 is 10 cm below the beam, and Position 4 is 10 cm away from the side of the beam facing the fire.

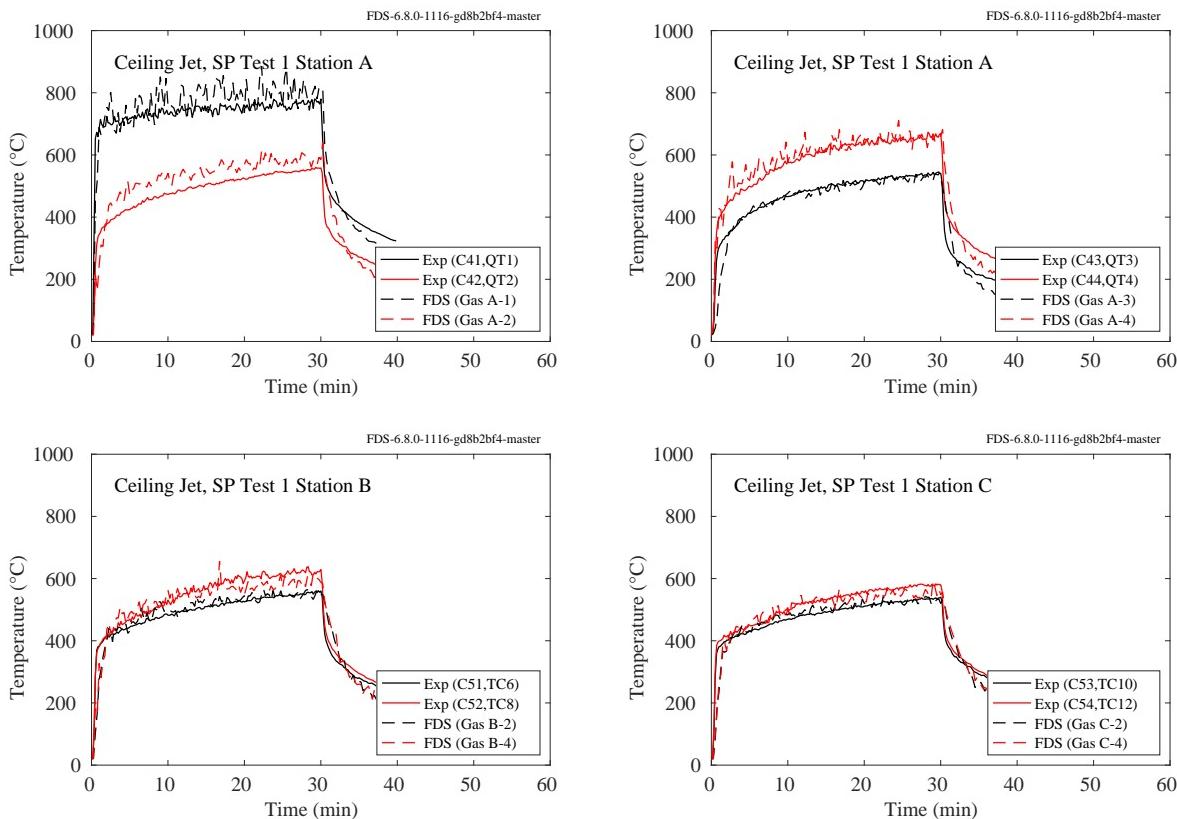


Figure 7.32: SP AST experiments, ceiling jet, Test 1.

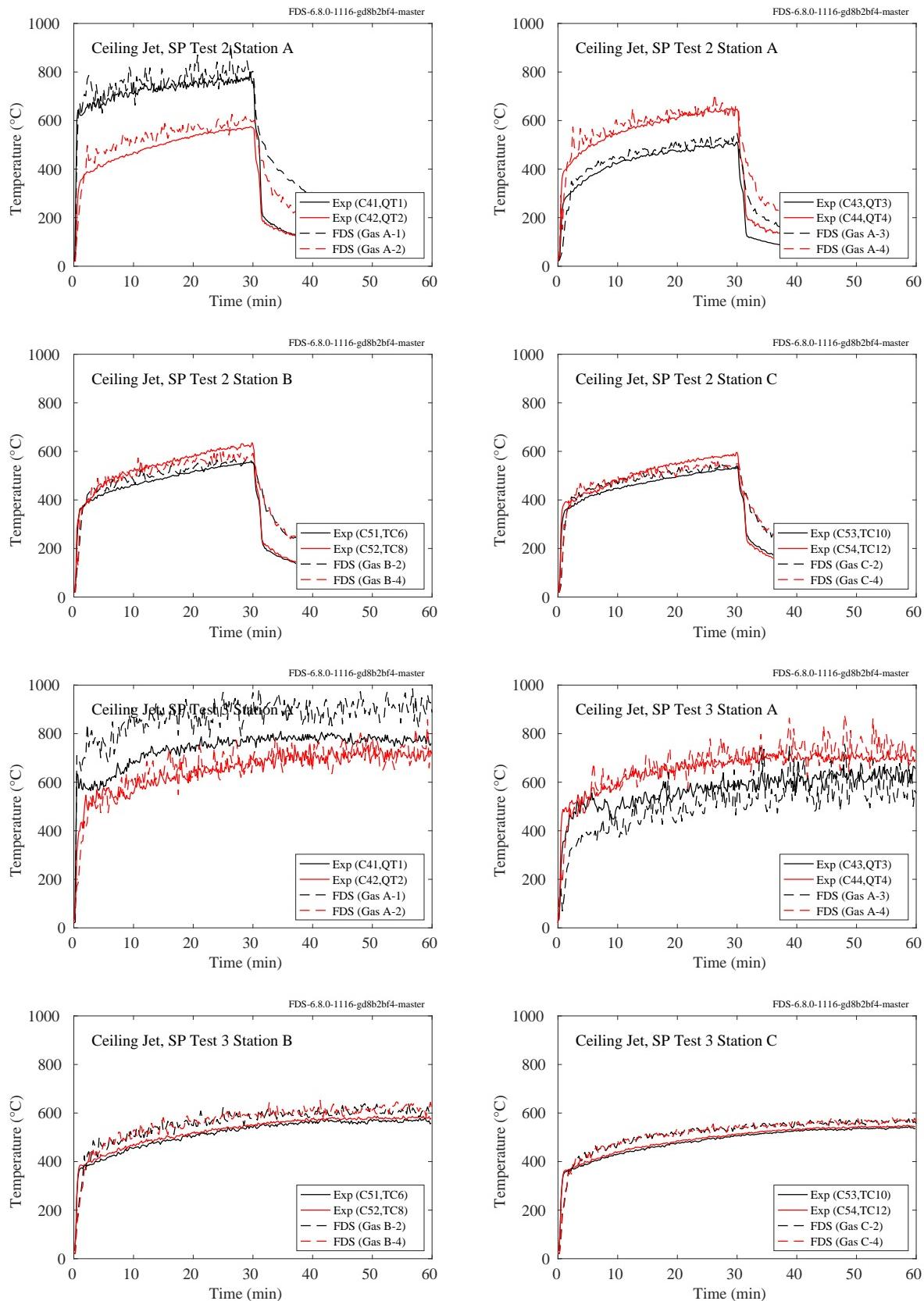


Figure 7.33: SP AST experiments, ceiling jet, Tests 2 and 3.

### 7.1.15 UL/NFPRF Series I Experiments

The primary purpose of the UL/NFPRF experiments was to measure sprinkler activation times for a series of heptane spray burner fires. To determine activation times, thermocouples were affixed to each sprinkler, and a sudden drop in temperature indicated activation. These same thermocouple temperatures (solid lines) can be compared to ceiling jet temperature predictions (dashed lines). Referring to Fig. 3.52, the chosen measurement locations are 56 (black lines), 68 (red lines), 86 (green lines), and 98 (blue lines), providing comparisons as close to, and as far away from, the fire as possible.

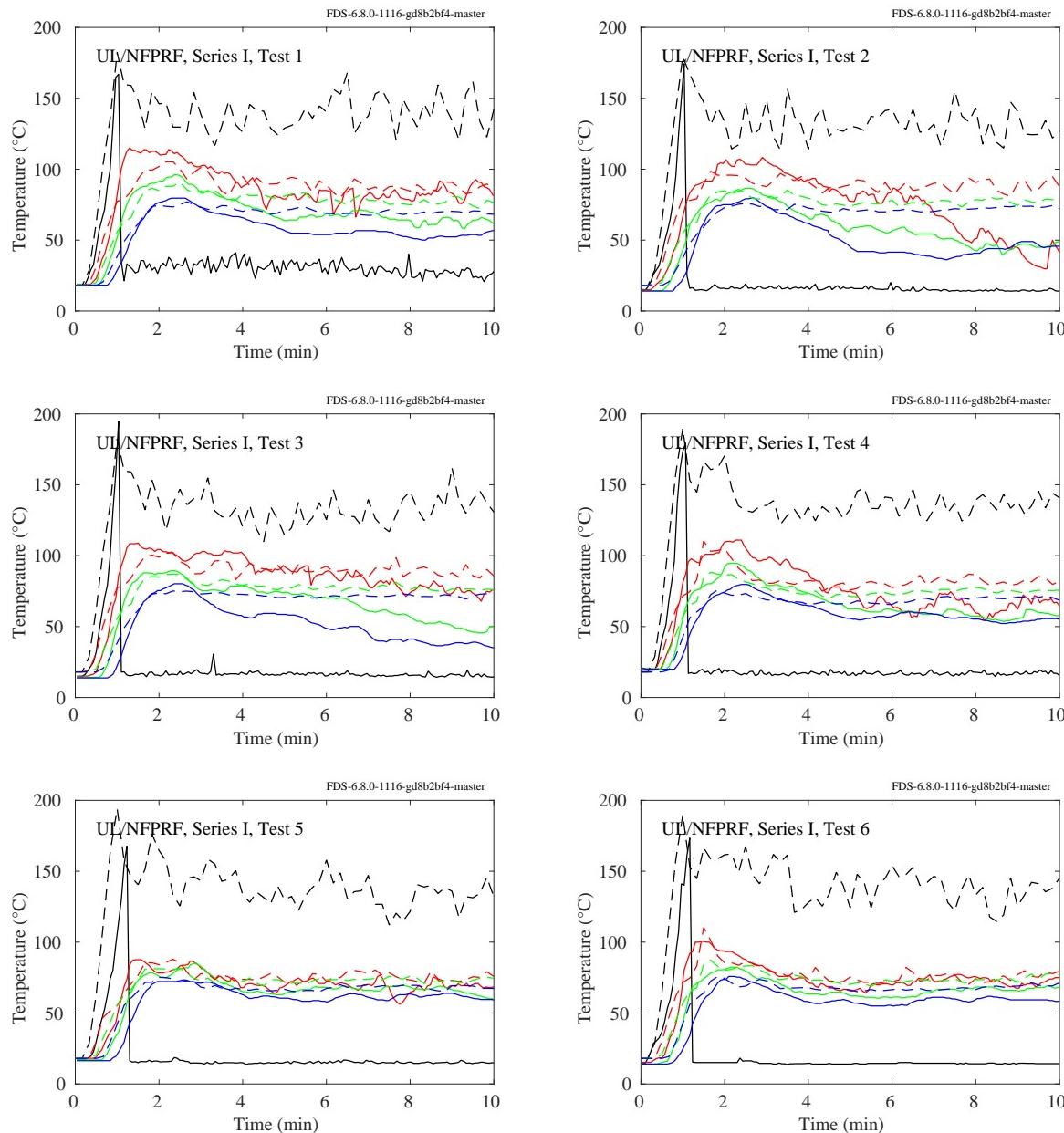


Figure 7.34: UL/NFPRF experiments, ceiling jet, Series I, Tests 1-6.

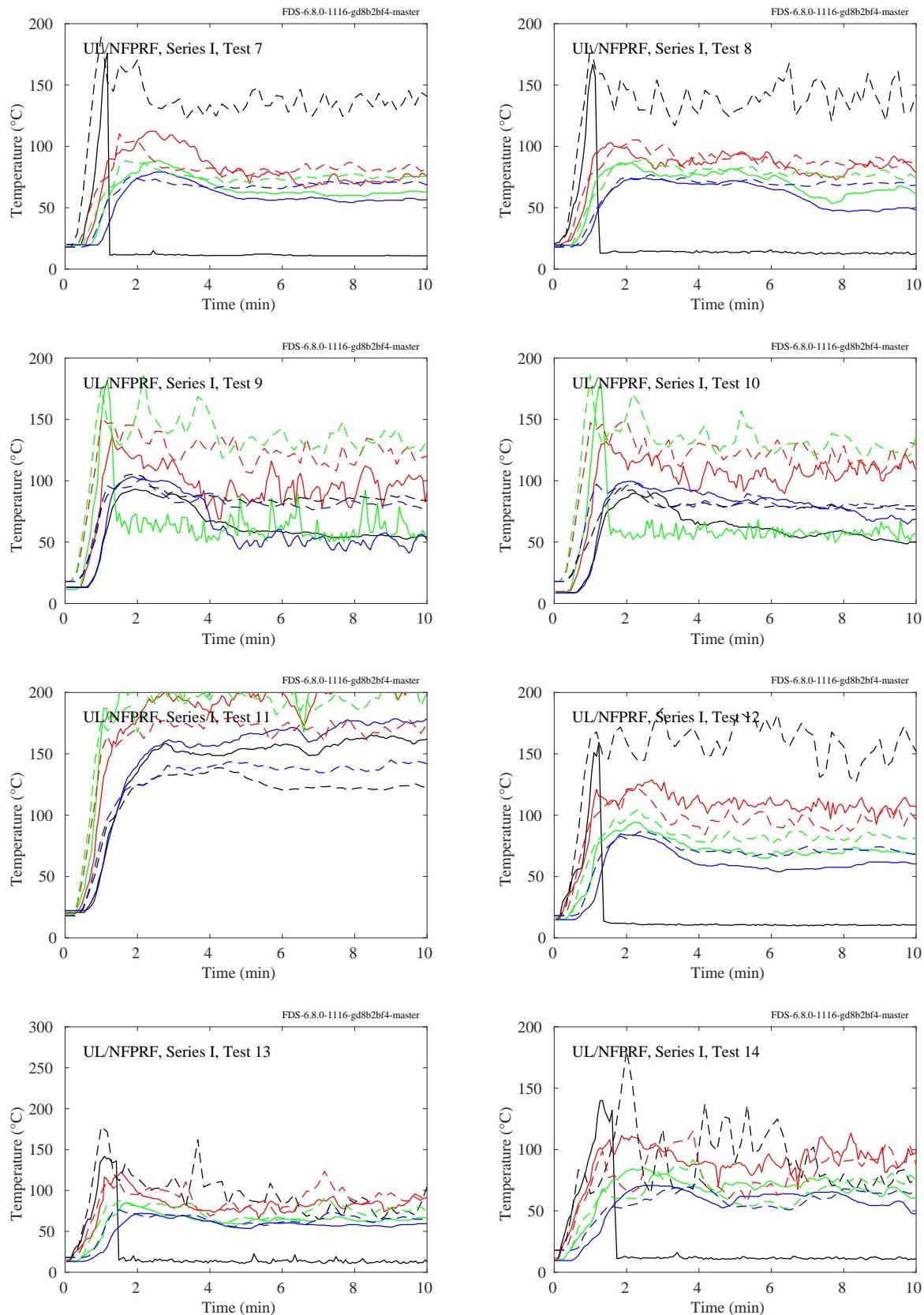


Figure 7.35: UL/NFPPRF experiments, ceiling jet, Series I, Tests 7-14.

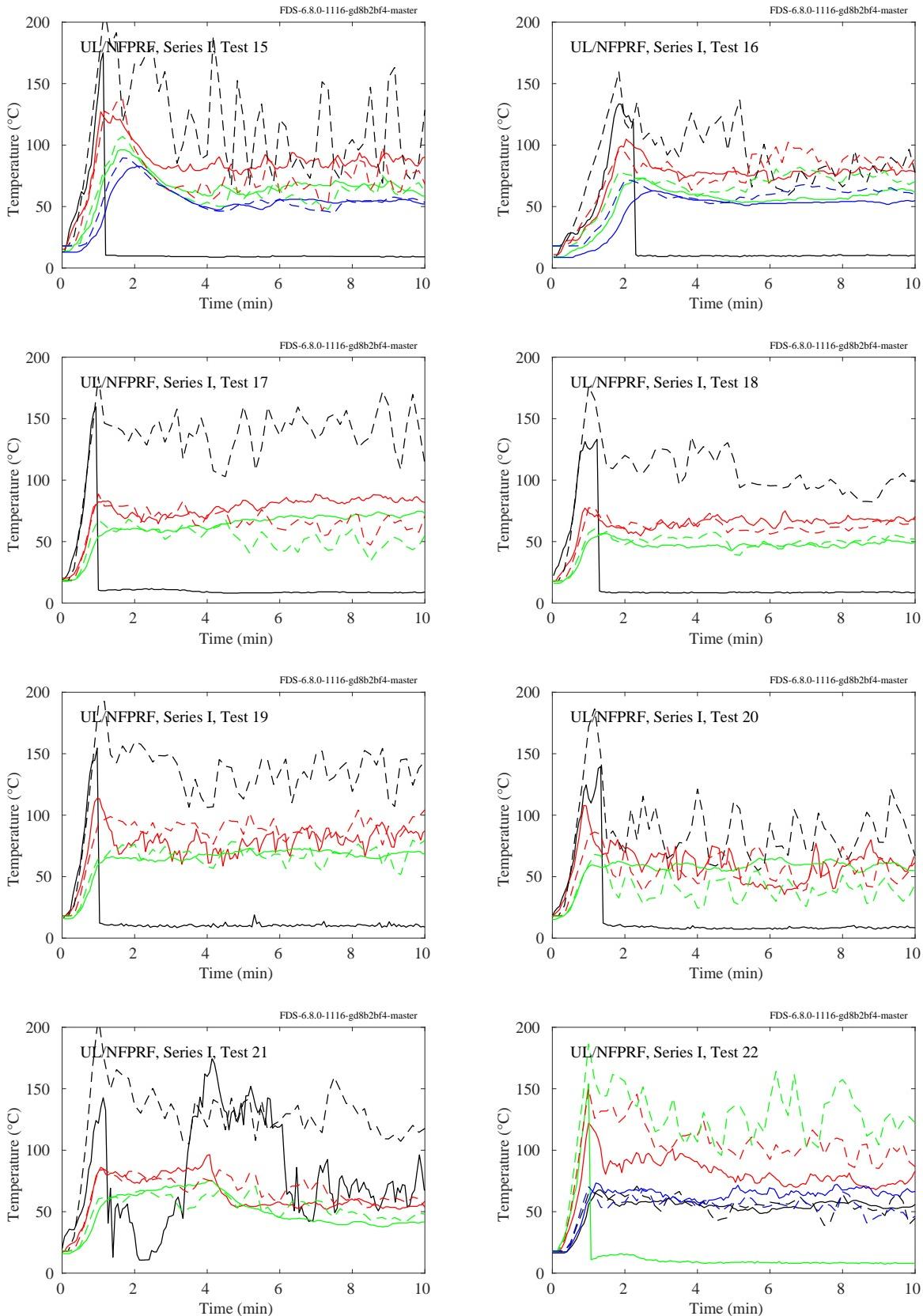


Figure 7.36: UL/NFPPRF experiments, ceiling jet, Series I, Tests 15-22.

### 7.1.16 UL/NIJ House Experiments

The following plots compare the uppermost thermocouple measurements with corresponding model predictions for the ranch-style and colonial-style houses.

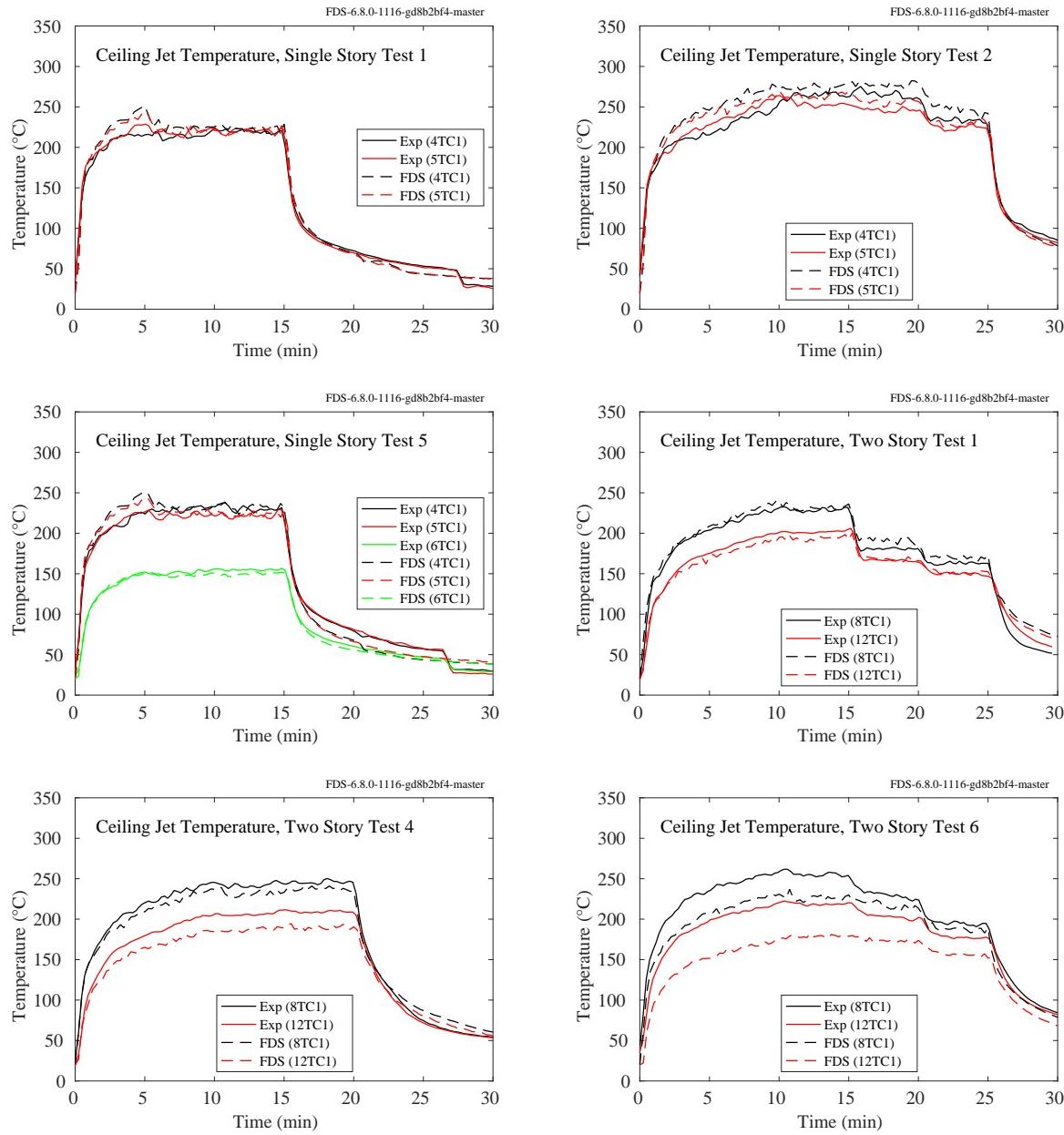


Figure 7.37: UL/NIJ Experiments, ceiling jet temperature

### **7.1.17 UL/NIST Vent Experiments**

The ceiling jet temperatures were measured at two locations, 90 cm from the short ends of the 2.4 m by 1.2 m double vent.

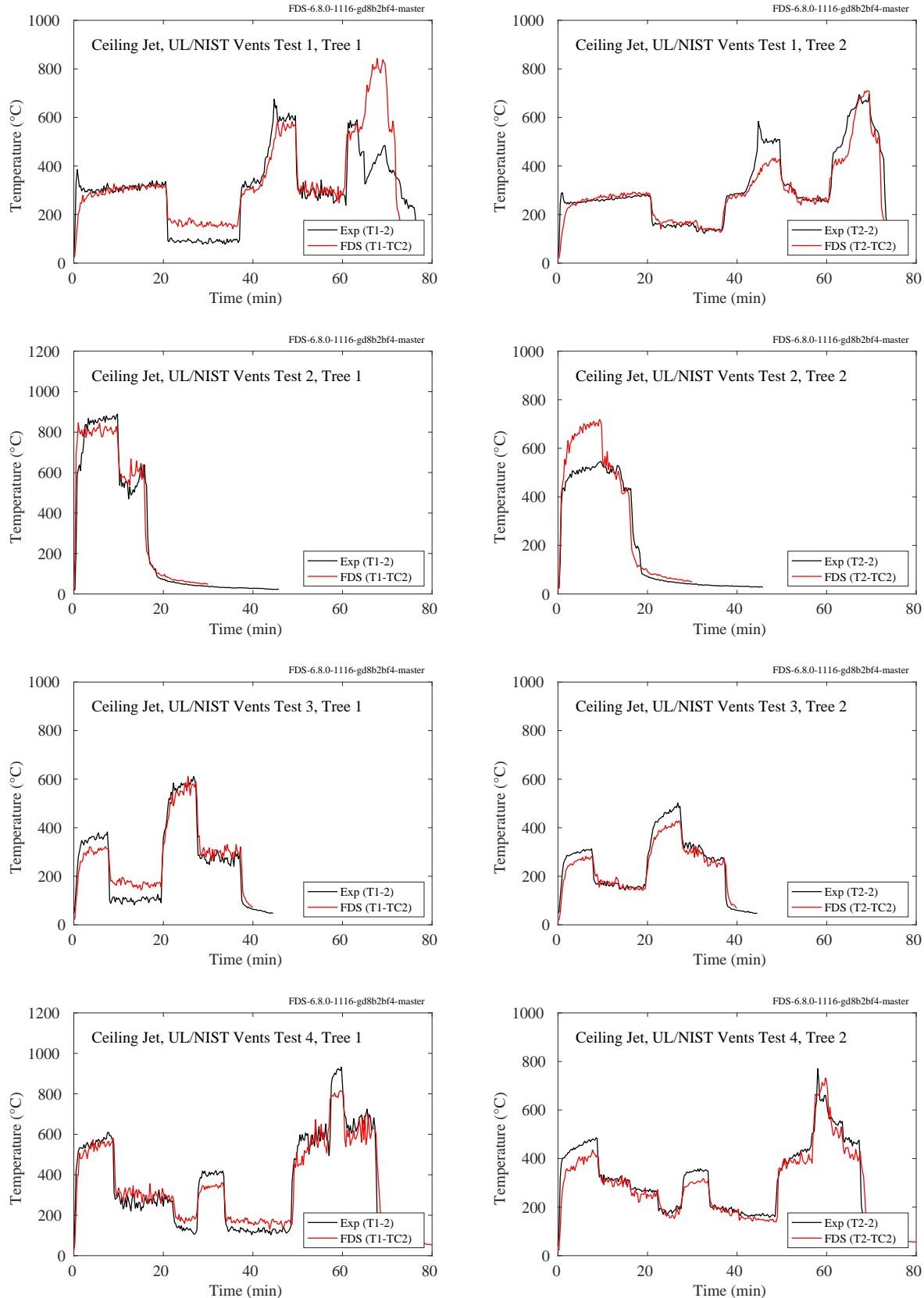


Figure 7.38: UL/NIST Vents experiments, ceiling jet.

### **7.1.18 Vettori Flat Ceiling Experiments**

For these experiments, the measured and predicted thermocouple temperature at the location of the first two activating sprinklers are compared. The experiments consisted of either Smooth or Obstructed ceilings; Slow, Medium or Fast fires; and a burner in the Open, at the Wall, or in the Corner. The experiments included three replicates of each of the smooth ceiling configurations and two replicates of each of the obstructed ceiling configurations.

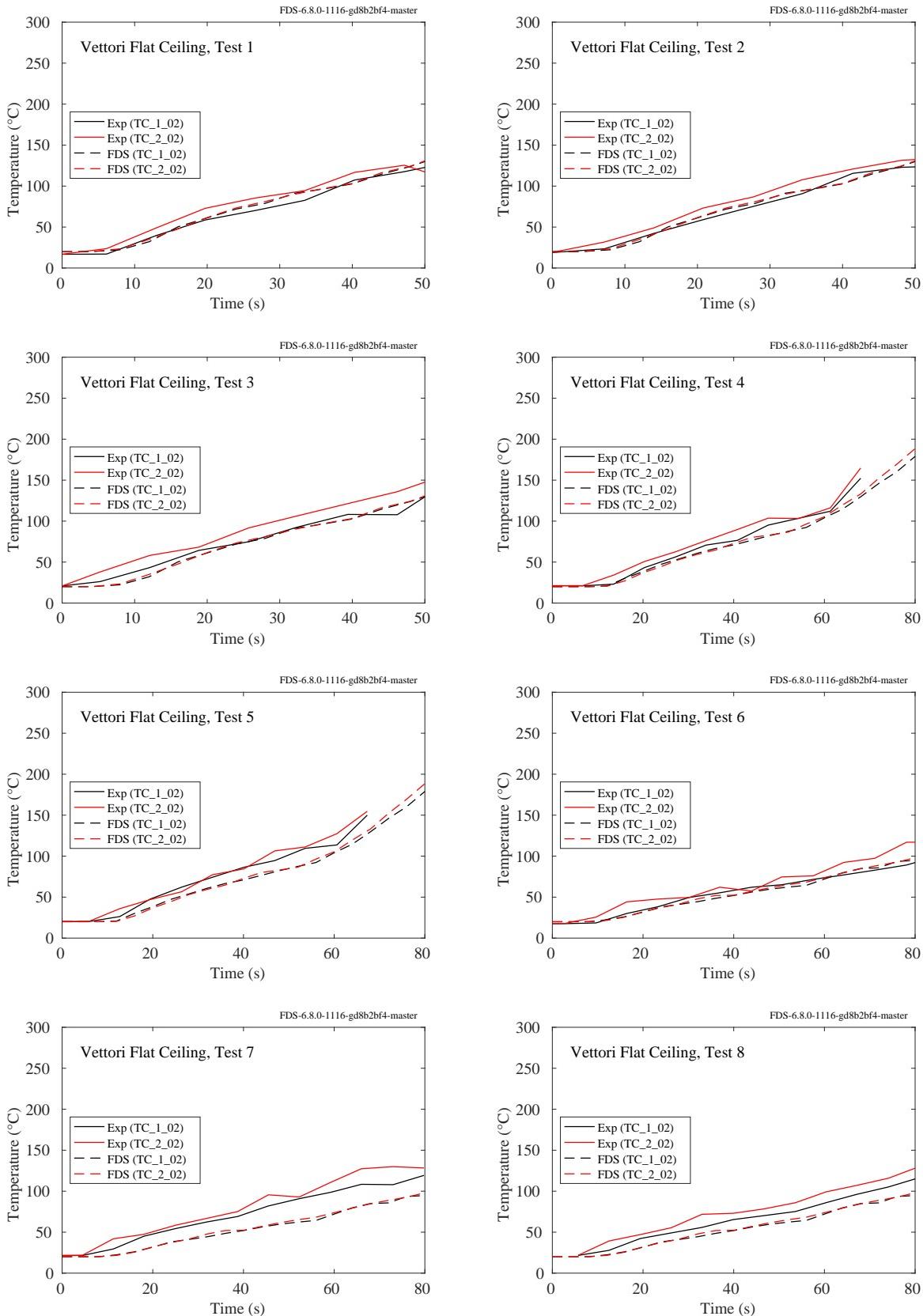


Figure 7.39: Vettori Flat Ceiling experiments, ceiling jet, Tests 1-8.

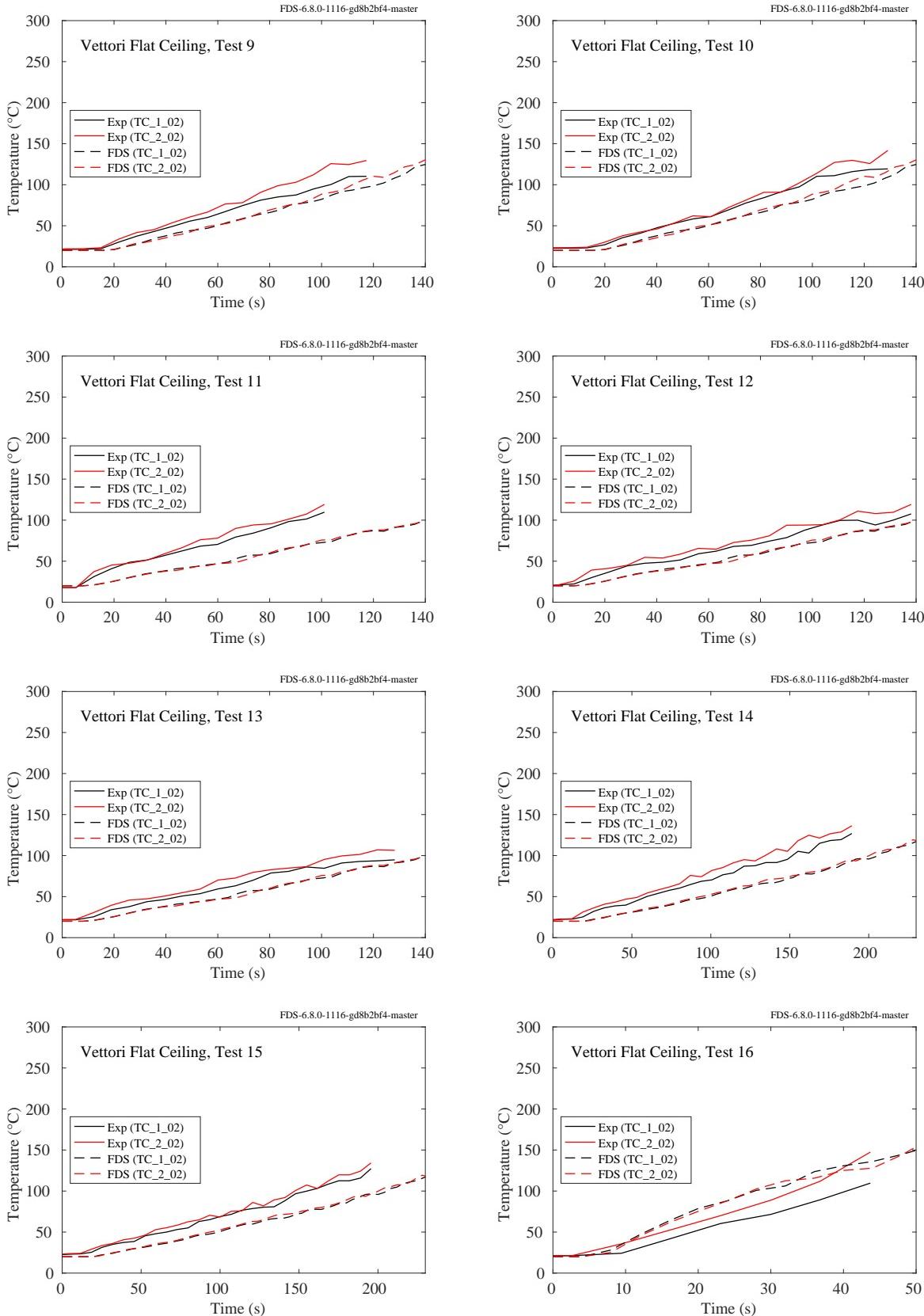


Figure 7.40: Vettori Flat Ceiling experiments, ceiling jet, Tests 9-16.

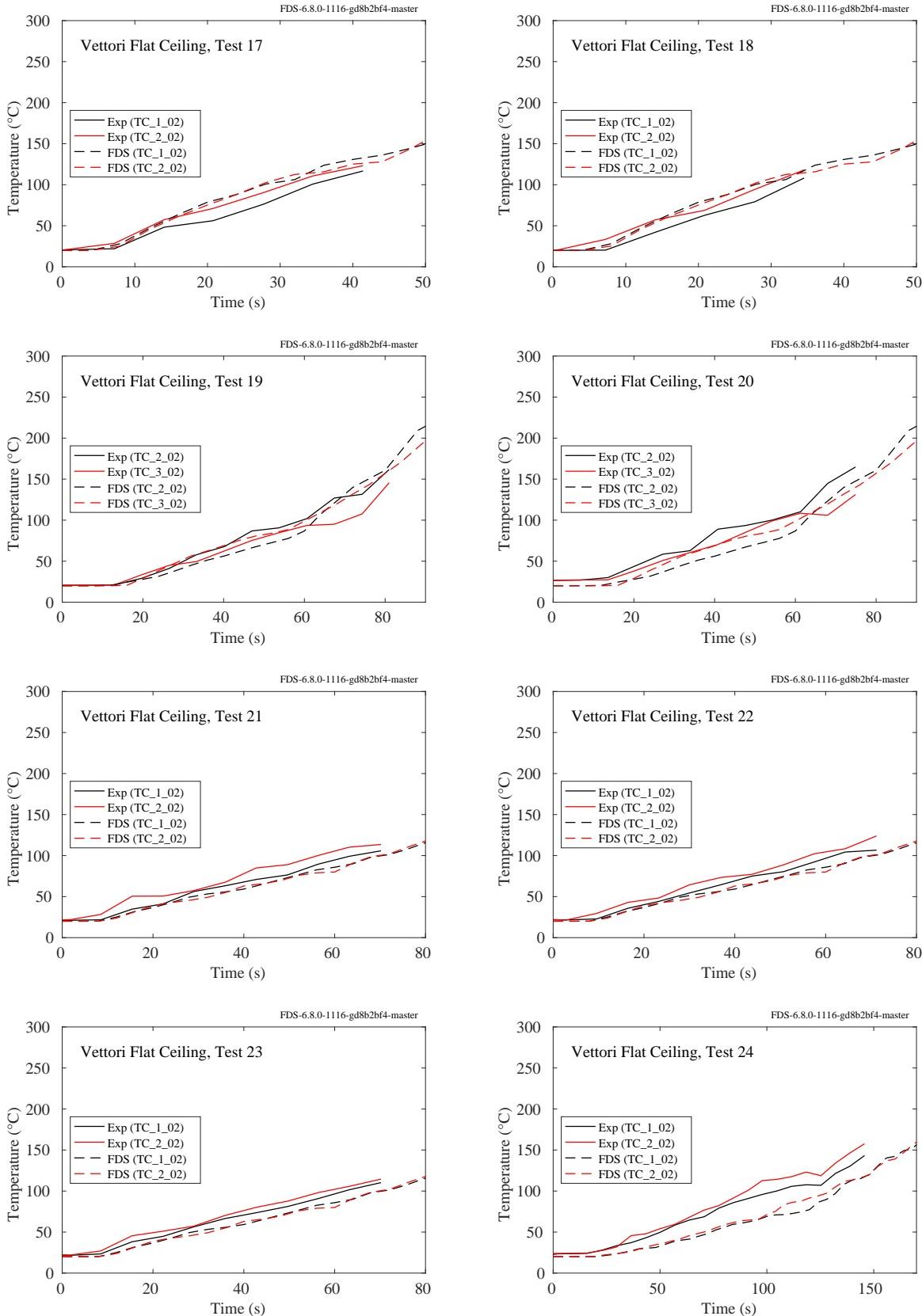


Figure 7.41: Vettori Flat Ceiling experiments, ceiling jet, Tests 17-24.

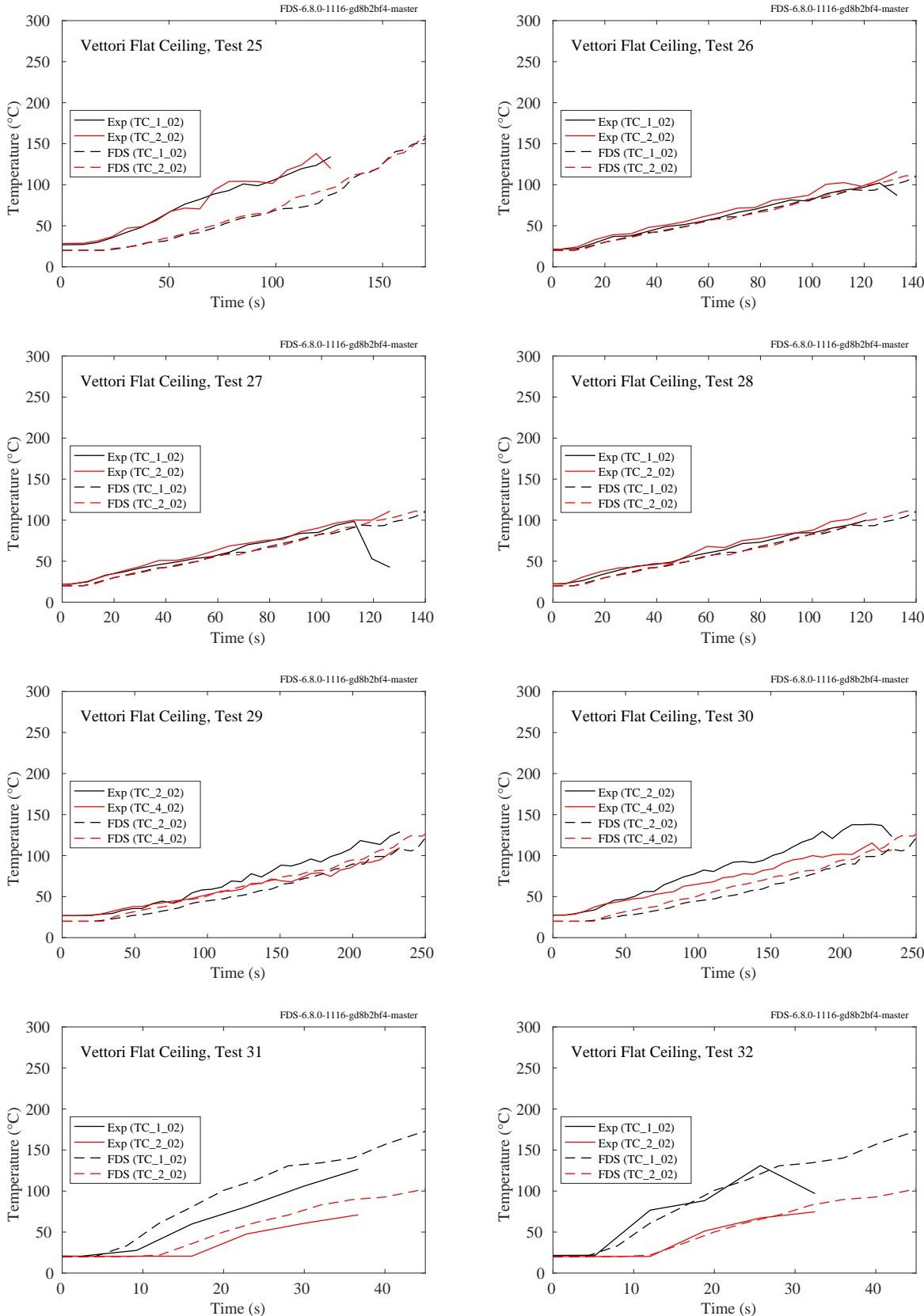


Figure 7.42: Vettori Flat Ceiling experiments, ceiling jet, Tests 25-32.

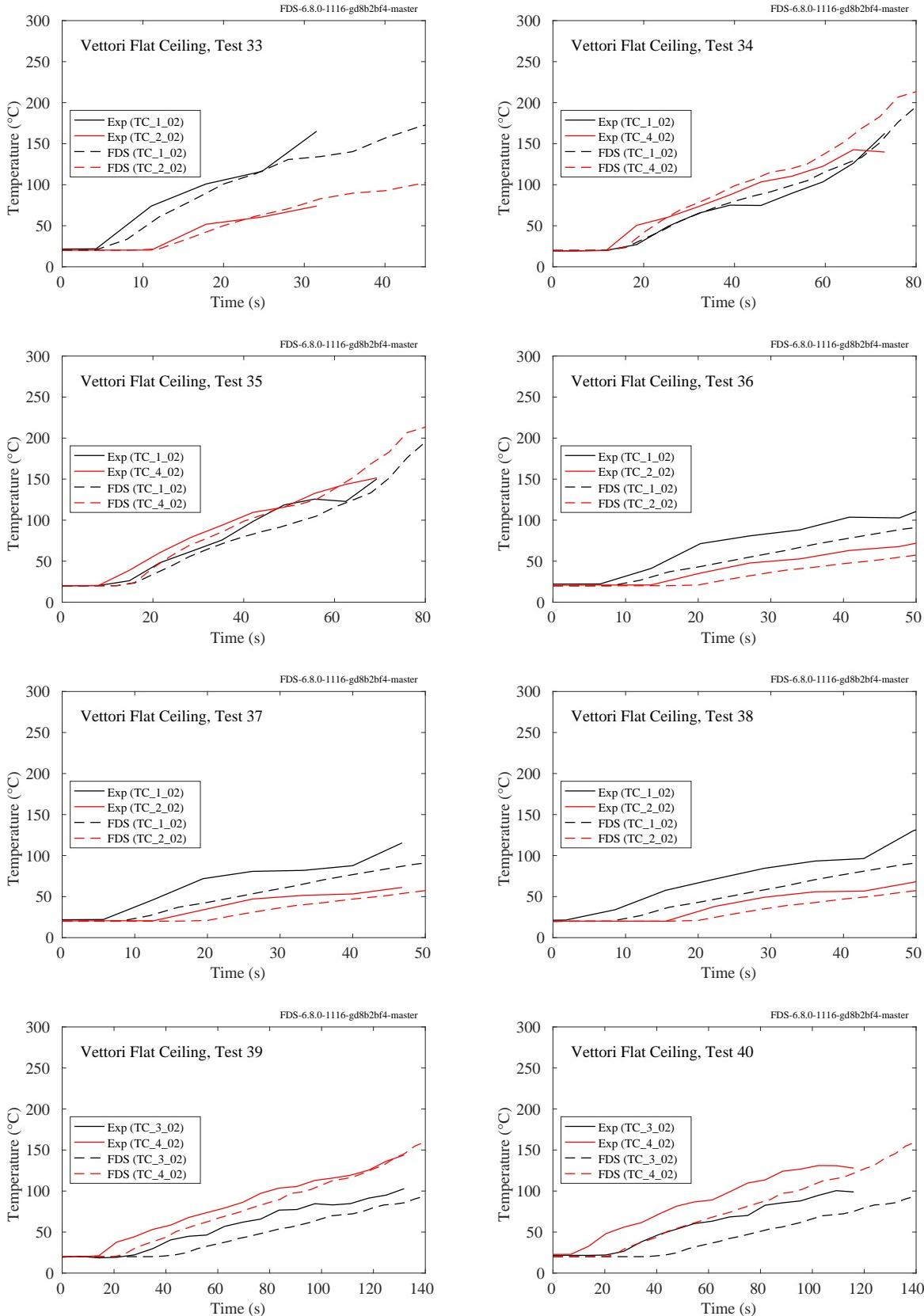


Figure 7.43: Vettori Flat Ceiling experiments, ceiling jet, Tests 33-40.

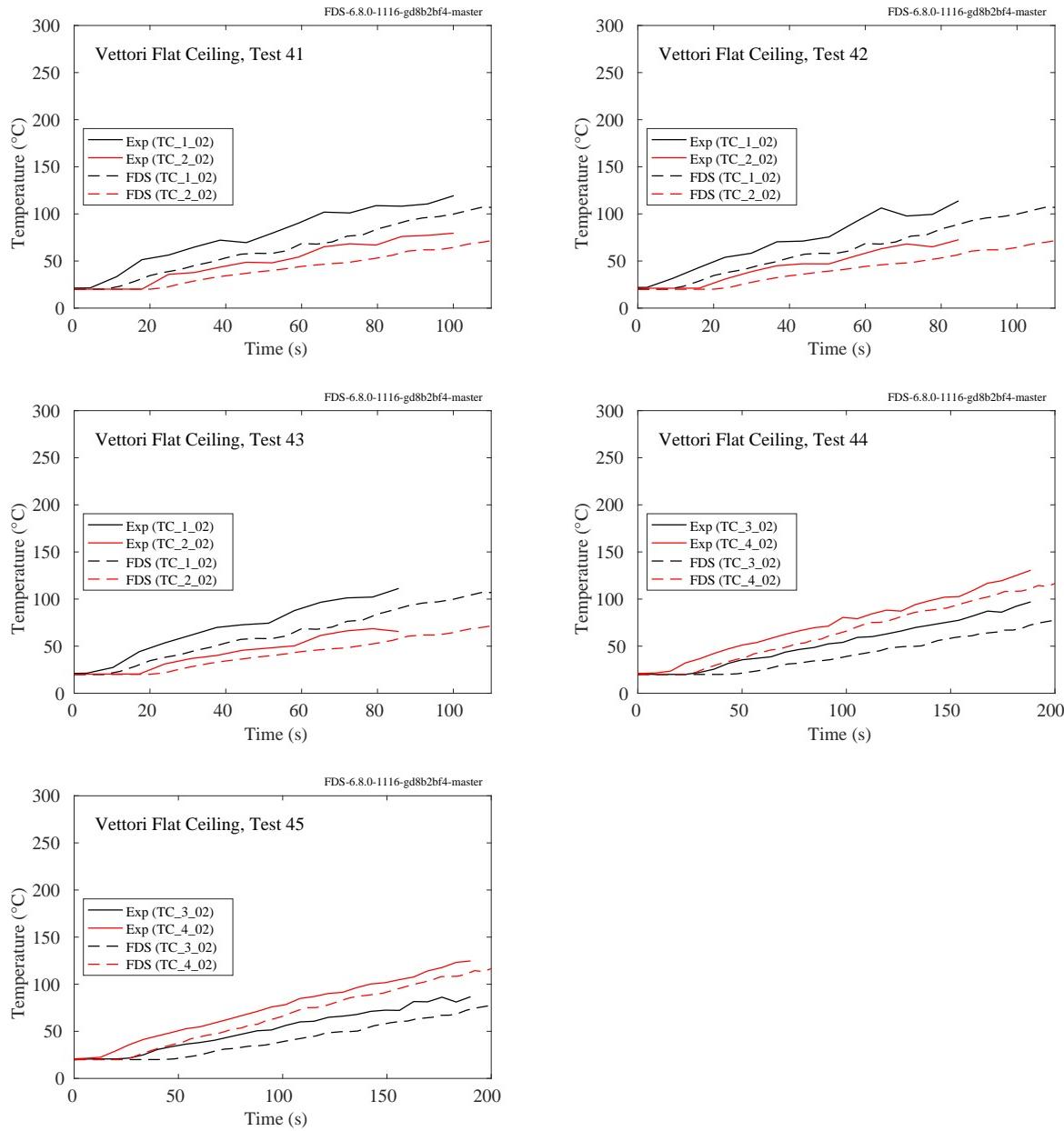


Figure 7.44: Vettori Flat Ceiling experiments, ceiling jet, Tests 41-45.

### 7.1.19 Vettori Sloped Ceiling Experiments

For these experiments, the measured and predicted thermocouple temperature at the locations of the first two activating sprinklers are compared. The thermocouples were located 15 cm below the ceiling. Replicate results are shown side by side, i.e. Test 2 is a replicate of Test 1; Test 4 is a replicate of Test 3, and so on. There were 36 unique configurations (2 replicates of each) combining the following parameters:

- Flat, 13°, or 24° Ceiling Slope
- Smooth or Obstructed Ceiling Surface
- Fast or Slow Growth Fire
- Corner, Wall, or Detached Burner Location

The plots are labelled using this convention. For example, “13SFC” means that the ceiling is sloped 13° from horizontal, the ceiling is Smooth (no beams), the fire growth rate is Fast, and the burner is in the Corner of the room.

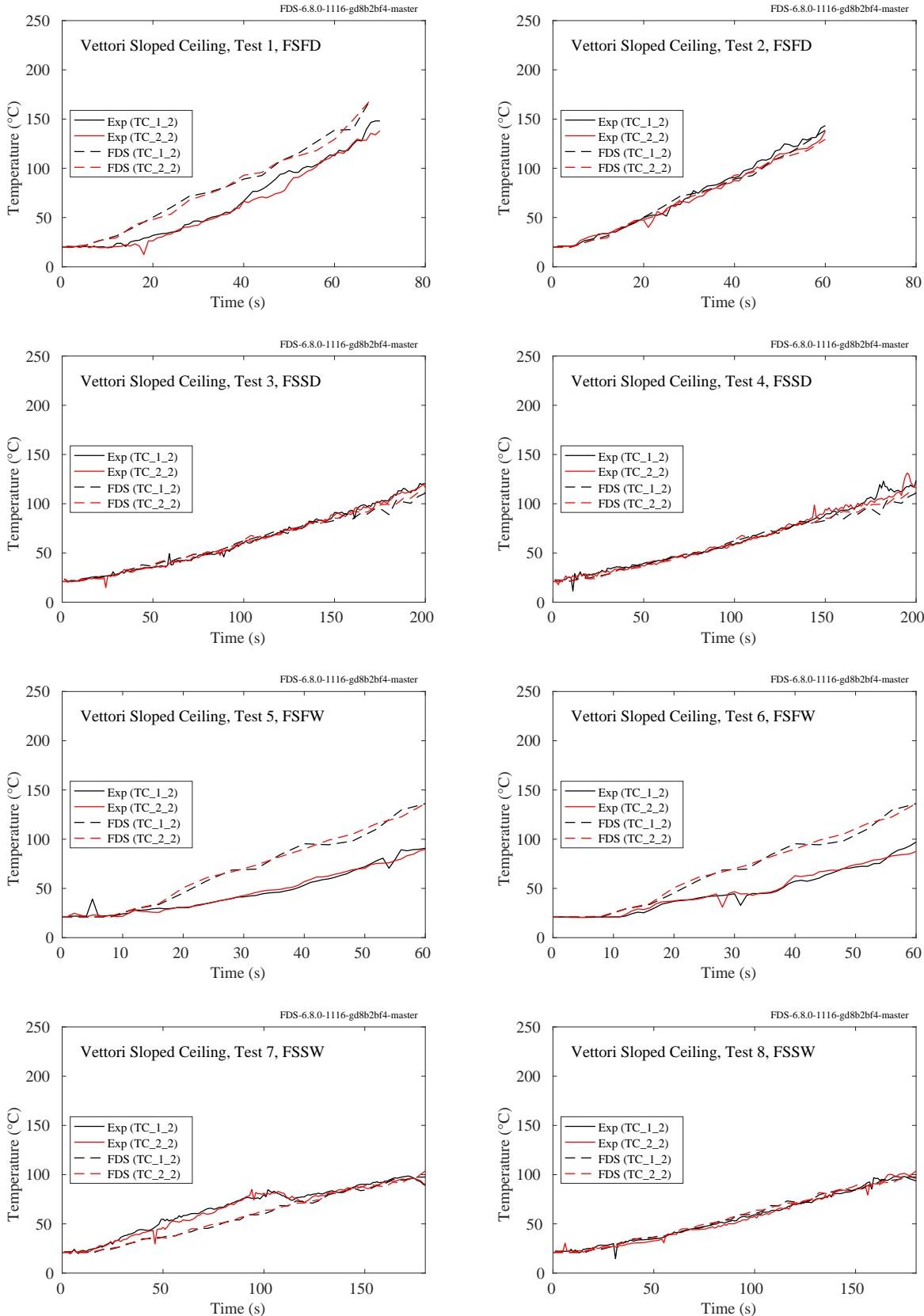


Figure 7.45: Vettori Sloped Ceiling experiments, ceiling jet, Tests 1-8.

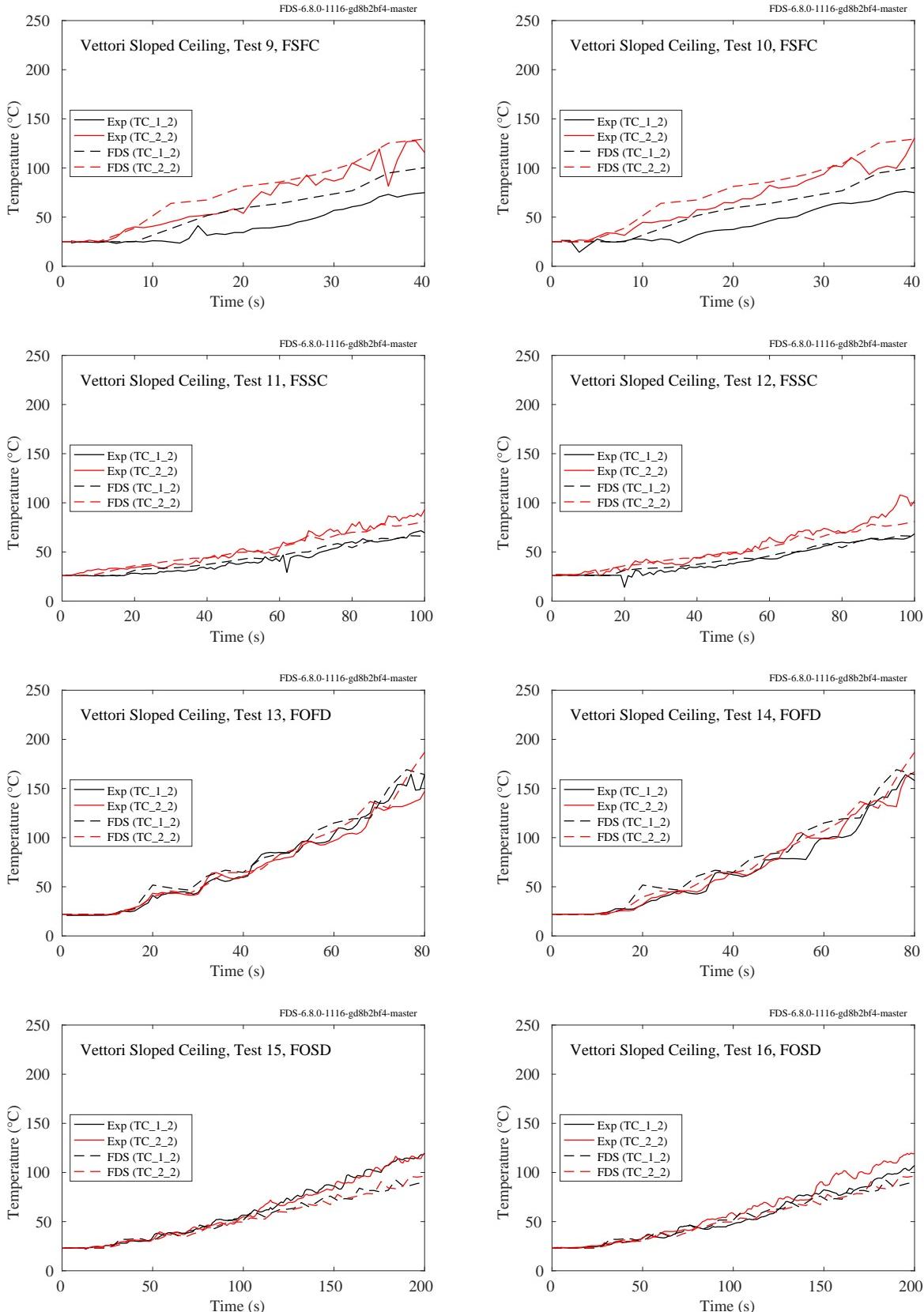


Figure 7.46: Vettori Sloped Ceiling experiments, ceiling jet, Tests 9-16.

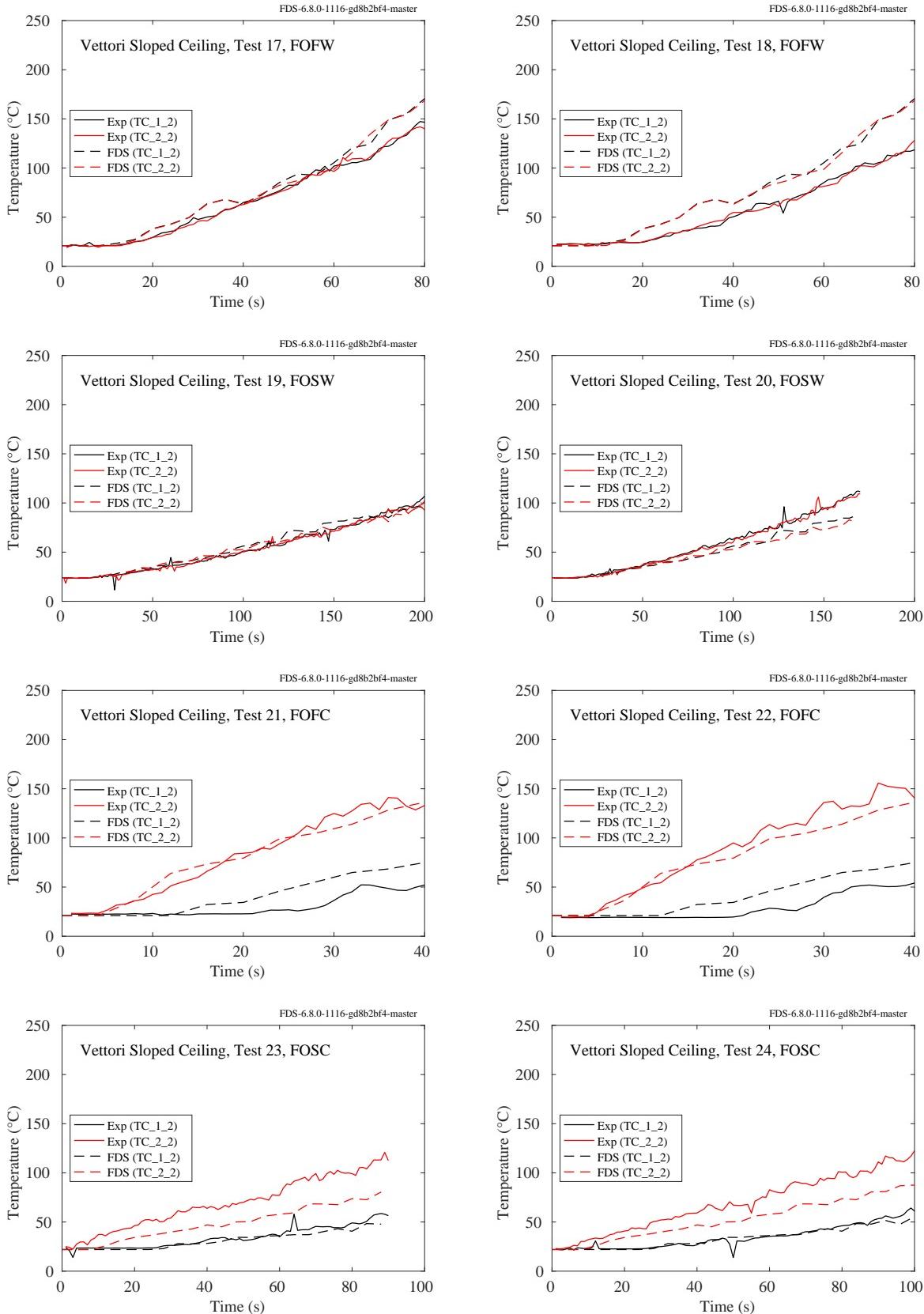


Figure 7.47: Vettori Sloped Ceiling experiments, ceiling jet, Tests 17-24.

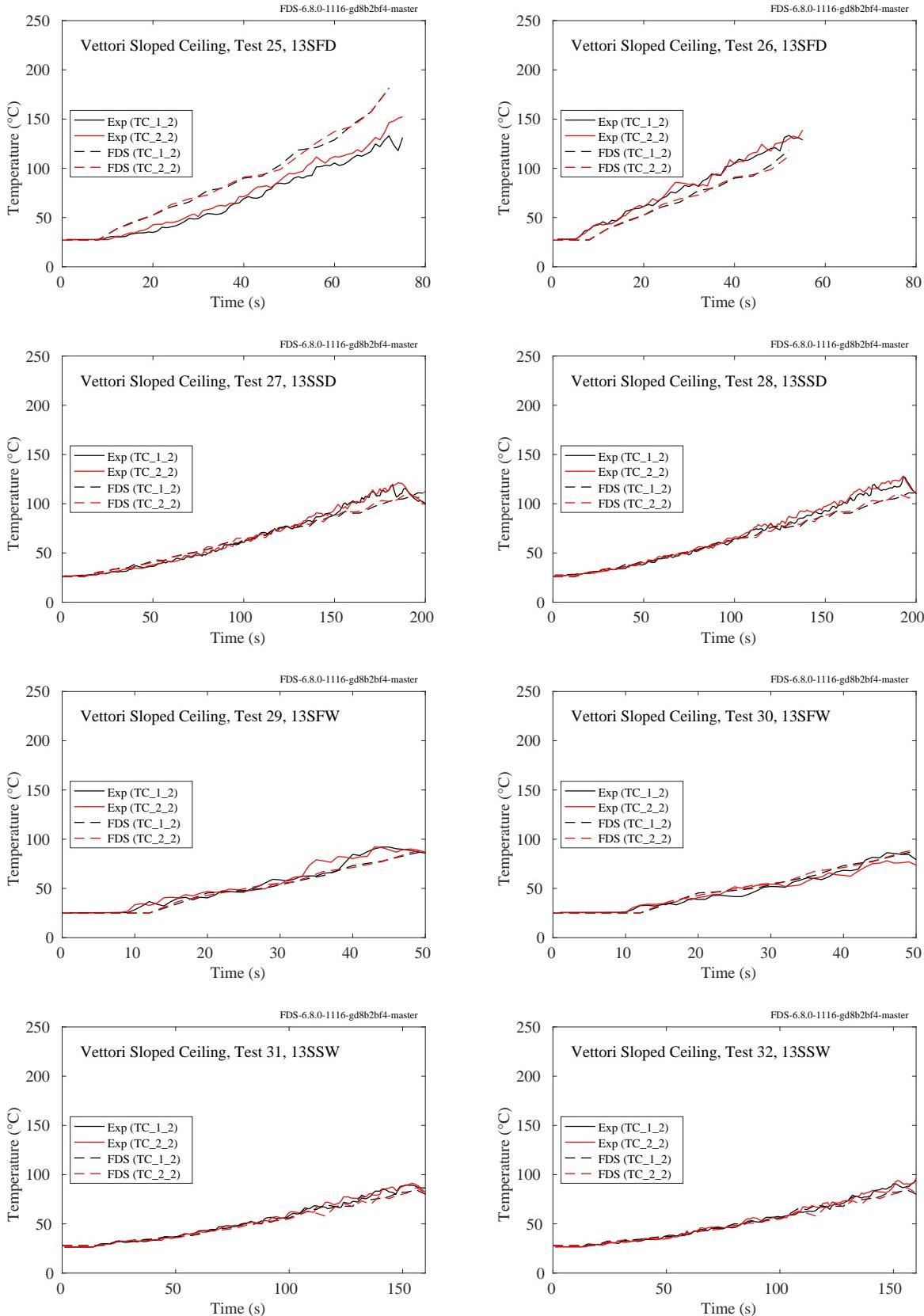


Figure 7.48: Vettori Sloped Ceiling experiments, ceiling jet, Tests 25-32.

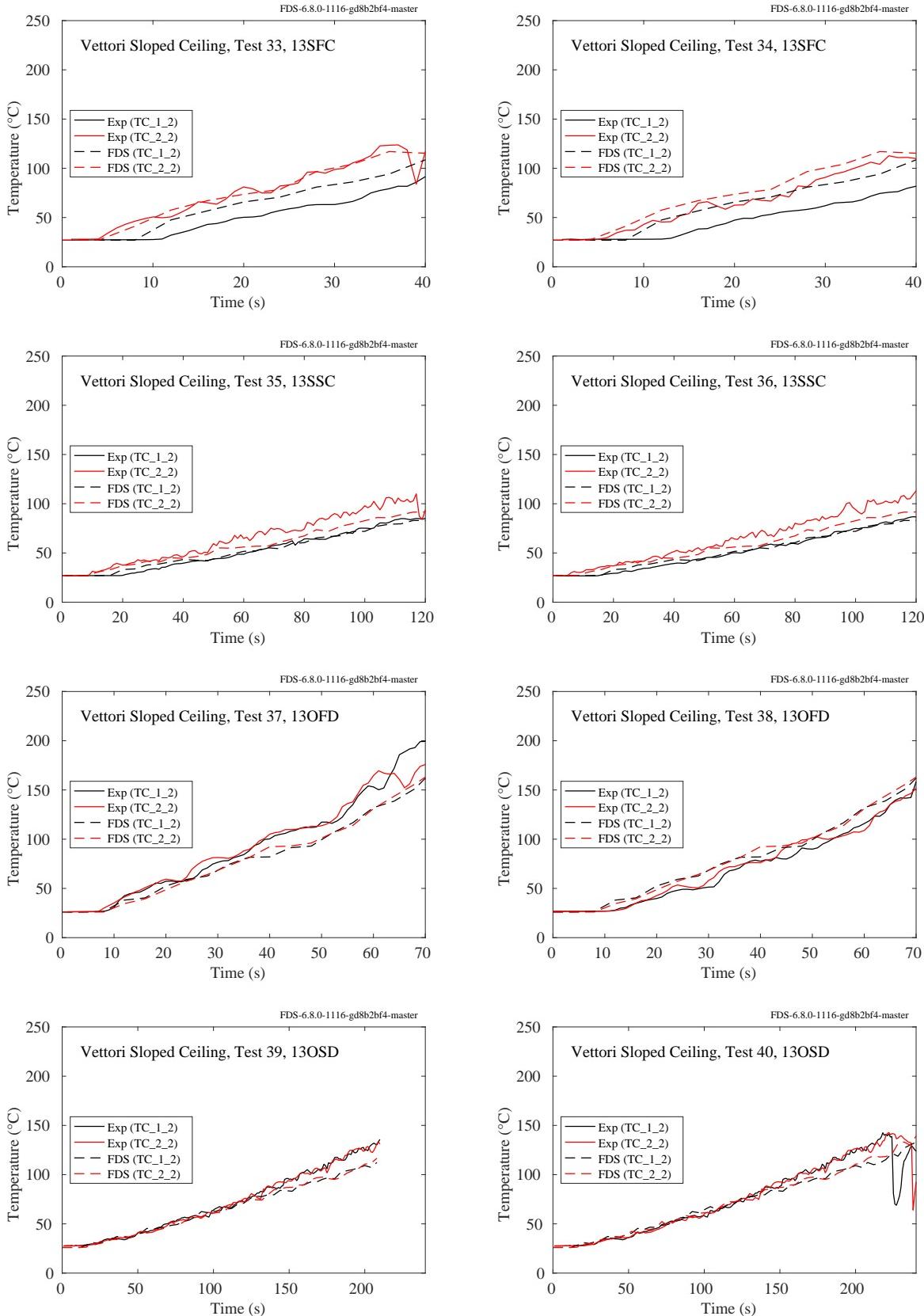


Figure 7.49: Vettori Sloped Ceiling experiments, ceiling jet, Tests 33-40.

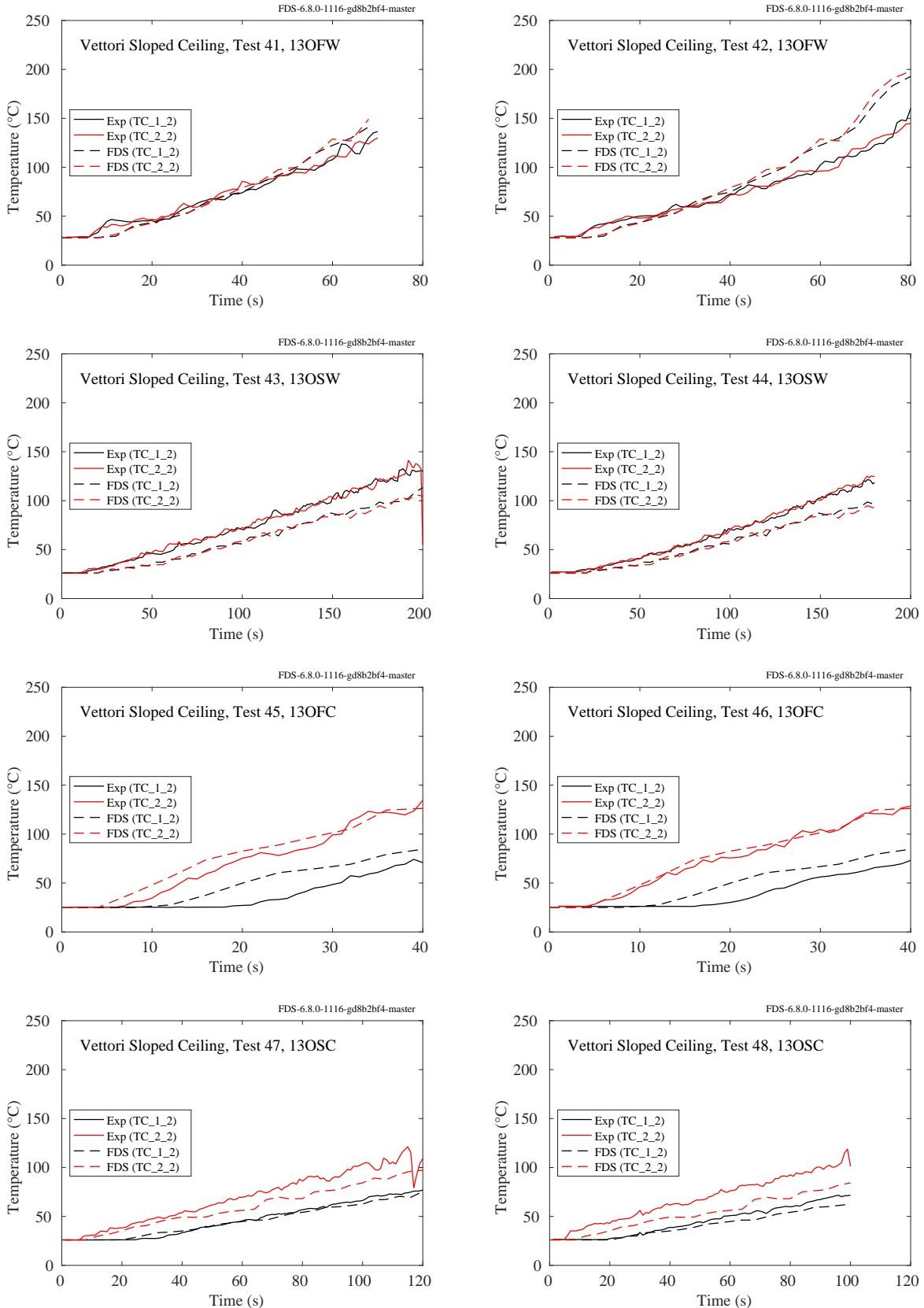


Figure 7.50: Vettori Sloped Ceiling experiments, ceiling jet, Tests 41-48.

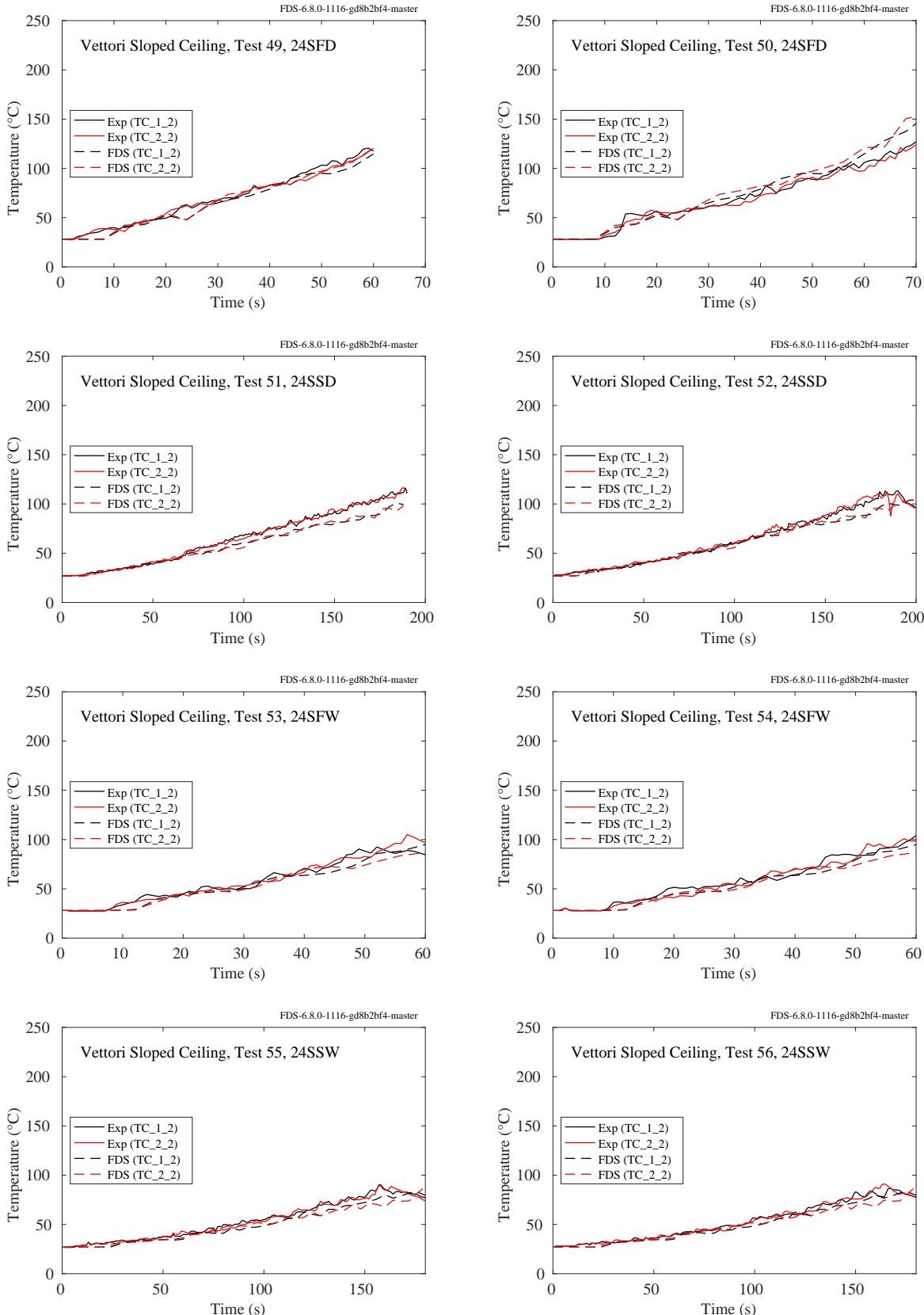


Figure 7.51: Vettori Sloped Ceiling experiments, ceiling jet, Tests 49-56.

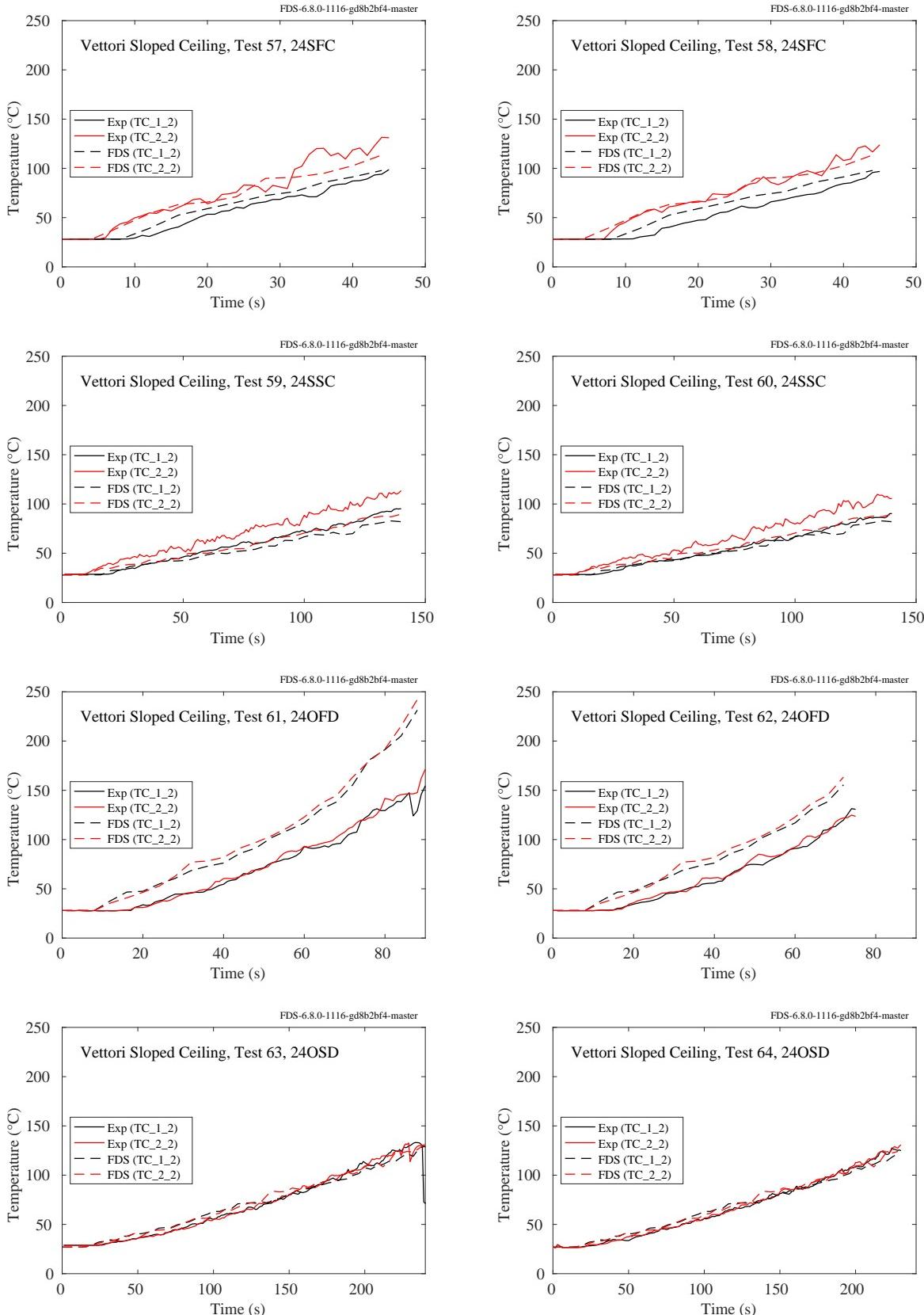


Figure 7.52: Vettori Sloped Ceiling experiments, ceiling jet, Tests 57-64.

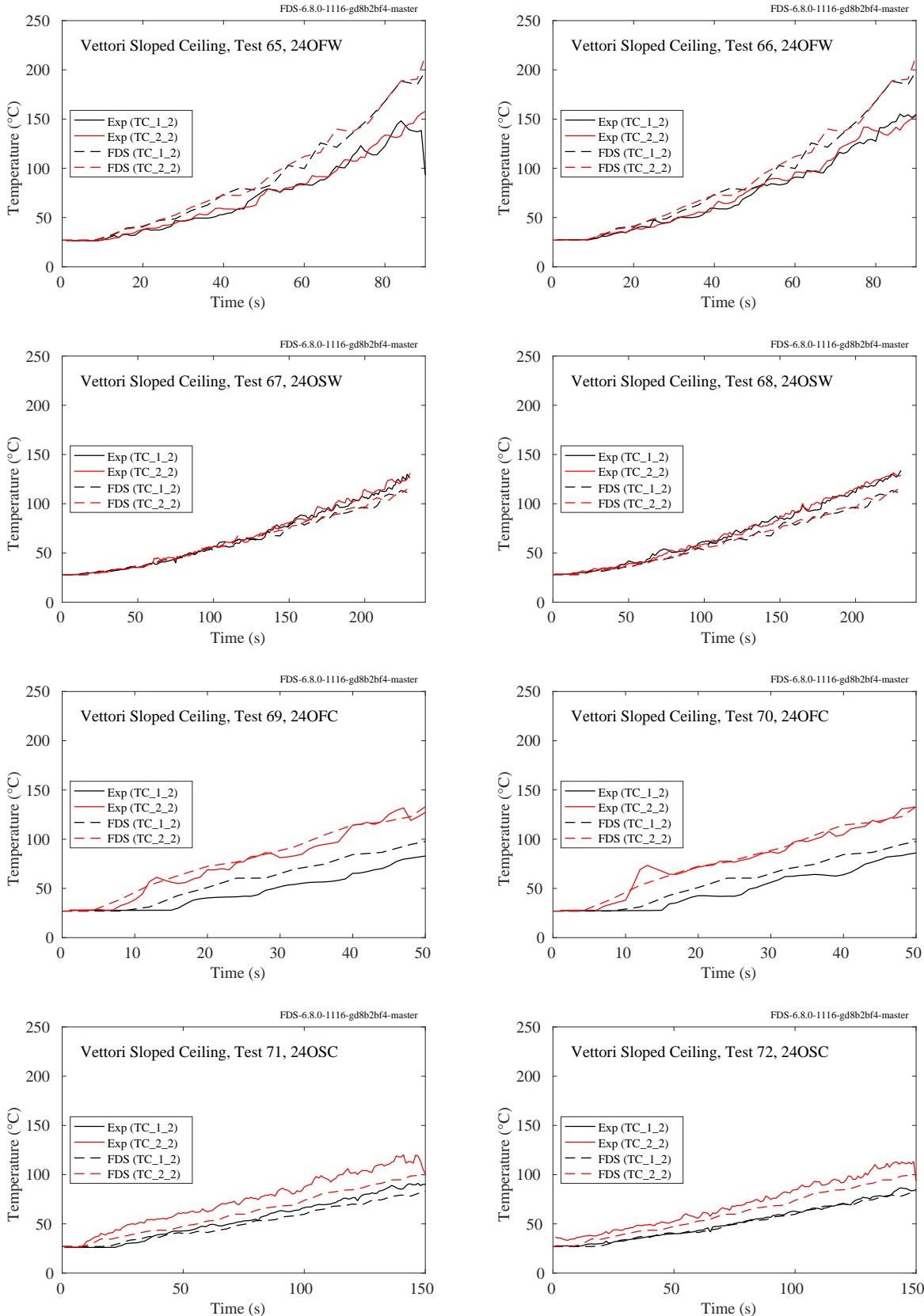


Figure 7.53: Vettori Sloped Ceiling experiments, ceiling jet, Tests 65-72.

### 7.1.20 WTC Experiments

In the WTC experiments, the compartment was 7 m long, 3.6 m wide and 3.8 m high. A 1 m by 2 m pan was positioned close to the center of the compartment. Aspirated thermocouples were positioned 3 m to the west (TTRW1) and 2 m to the east (TTRE1) of the fire pan, 18 cm below the ceiling.

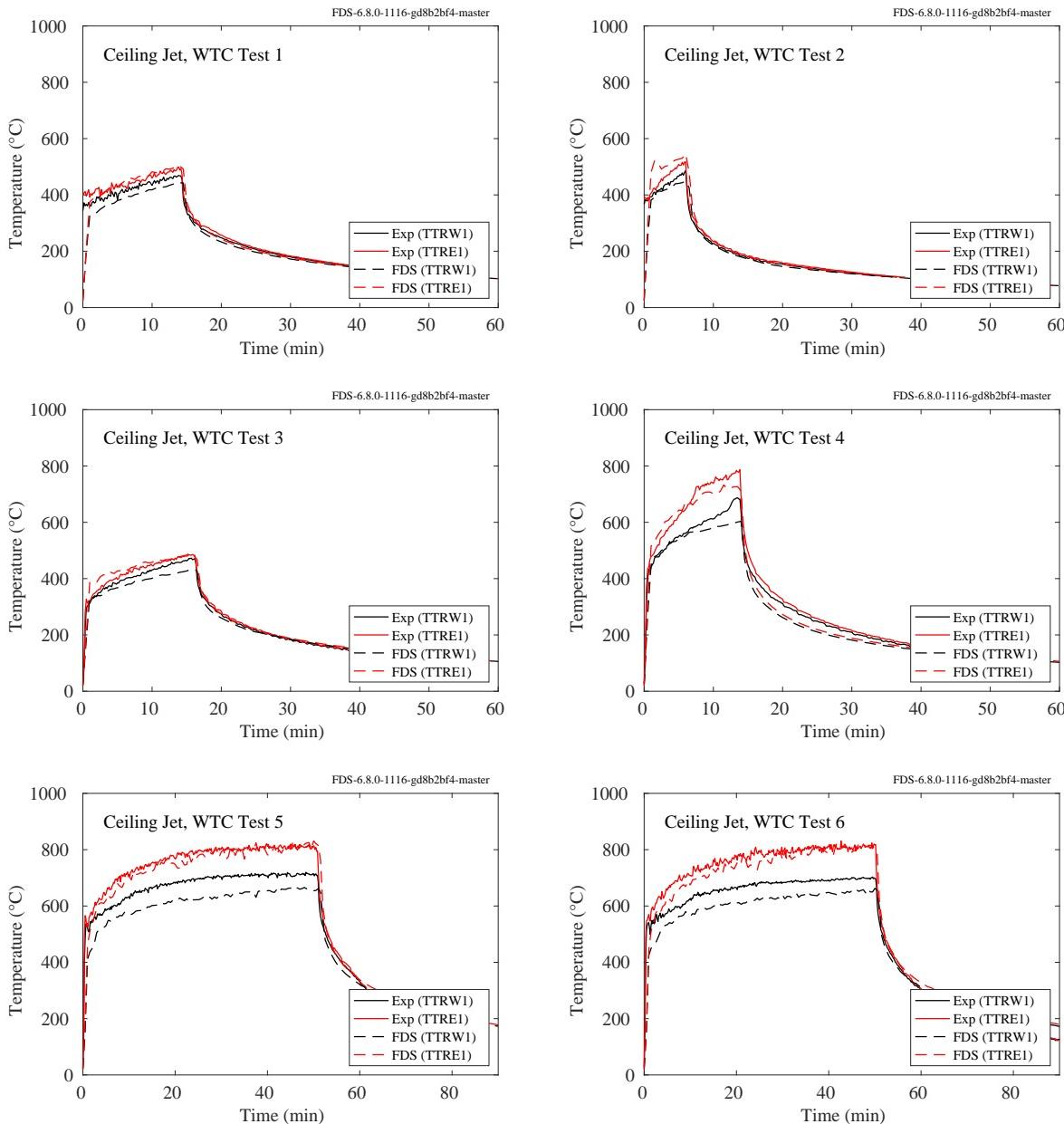


Figure 7.54: WTC experiments, ceiling jet, Tests 1-6.

### 7.1.21 Summary of Ceiling Jet Temperature Predictions

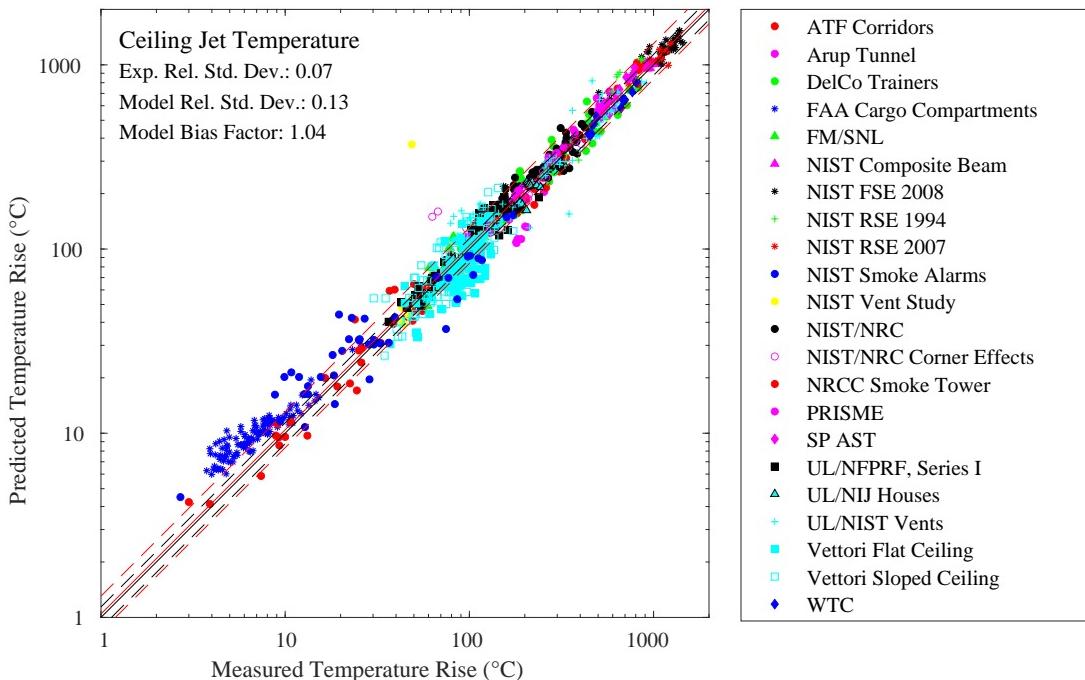


Figure 7.55: Summary of ceiling jet temperature predictions.

## 7.2 Sprinkler Activation Times

There are two ways to evaluate the model's ability to predict sprinkler activation. The first is to simply compare the total number of predicted versus observed activations. The second is to compare the time to first activation. Comparing the total number of activations indirectly indicates if the model accurately predicts the cooling of the hot gases by the water spray. Comparing time to first activation indirectly indicates if the model accurately predicts the velocity and temperature of the ceiling jet.

### 7.2.1 Time to First Sprinkler Activation

Figure 7.56 compares measured and predicted sprinkler activation times. For the UL/NFPRF experiments, only the time to first activation is compared because the resulting water spray sometimes delays the second activation substantially. While the model accounts for the cooling effect of the spray, the disruption of the activation sequence is somewhat random. A better way to check the accuracy of the model is to compare the predicted and measured total number of activation, which is discussed in the next section. For the Vettori experiments, the sprinklers did not flow water; thus, it is possible to consider the activation times of up to four sprinklers.

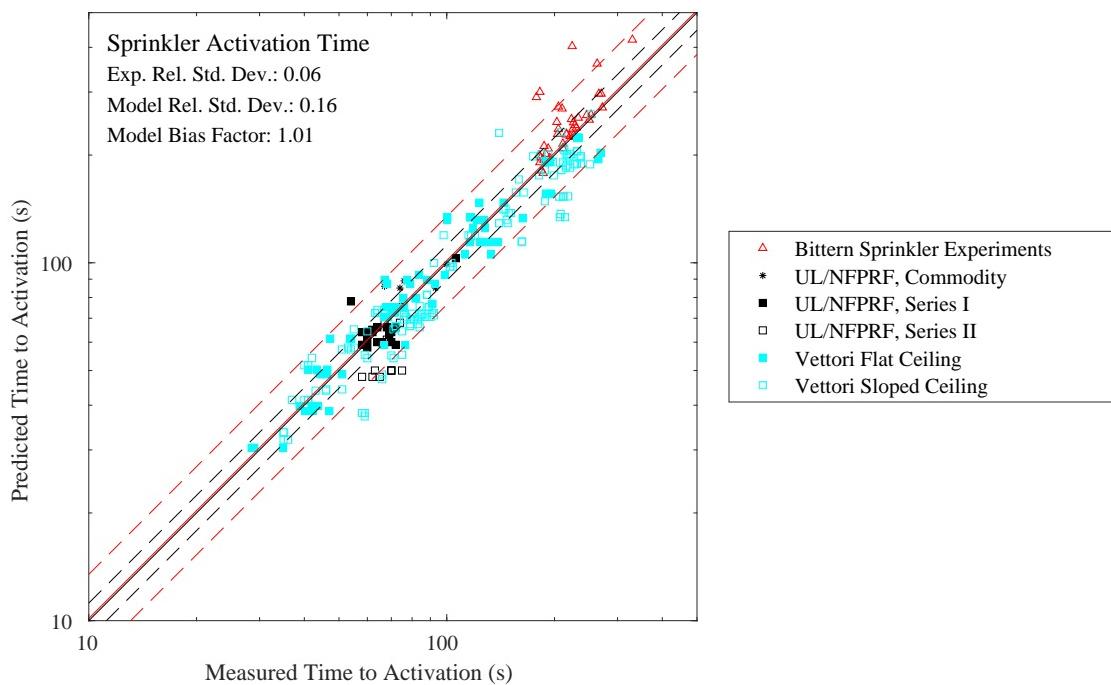


Figure 7.56: Comparison of measured and predicted sprinkler actuation times.

## 7.2.2 Number of Sprinkler Activations

The figures on the following pages display the number of sprinklers actuated as a function of time. The results are summarized in Fig. 7.63. The discussion of the uncertainty for this quantity can be found in Sec. 4.3.2.

Note that no sprinklers were installed for Test 11, Series I.

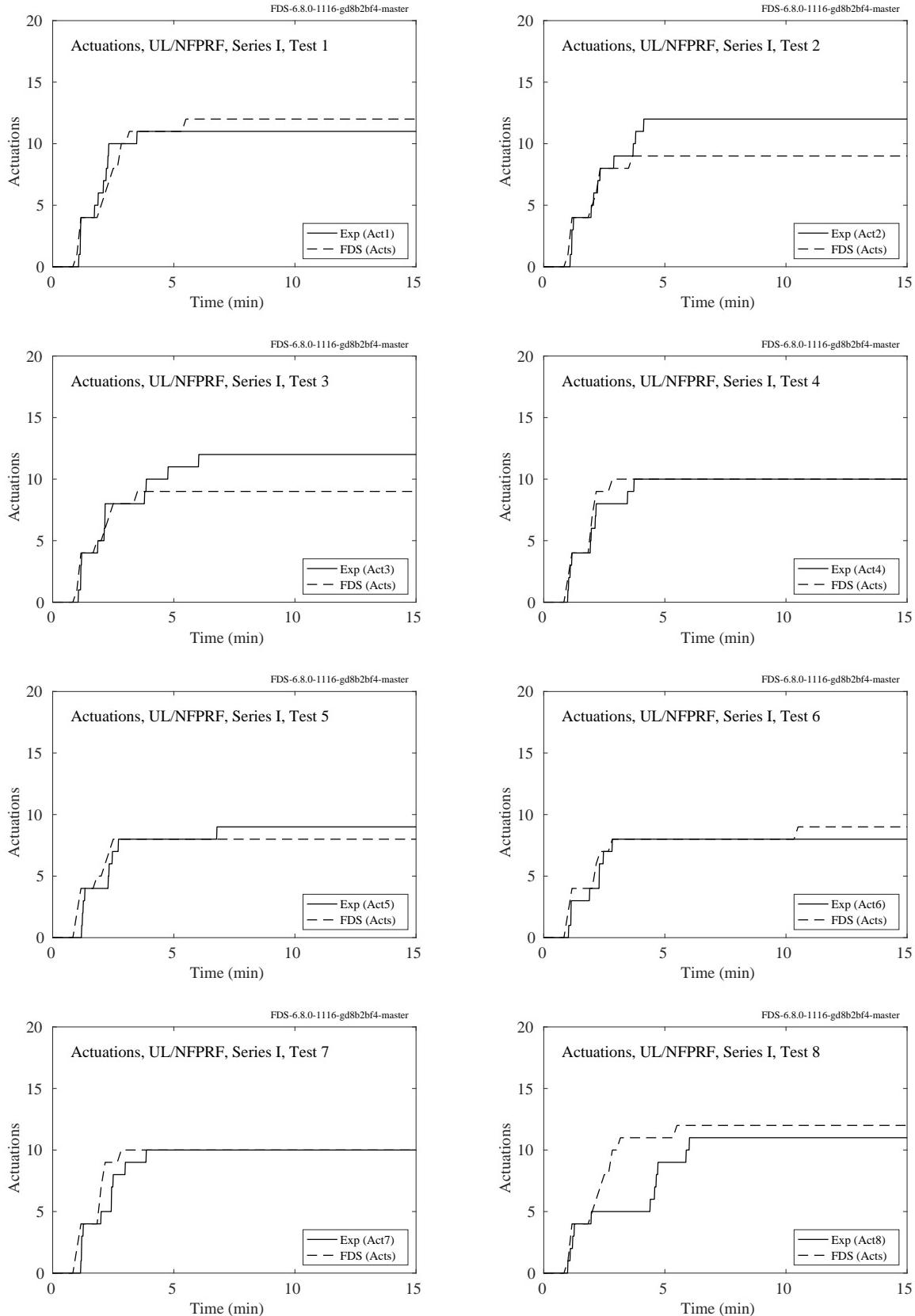


Figure 7.57: UL/NFPRF experiments, number of sprinkler activations, Series I, Tests 1-8.

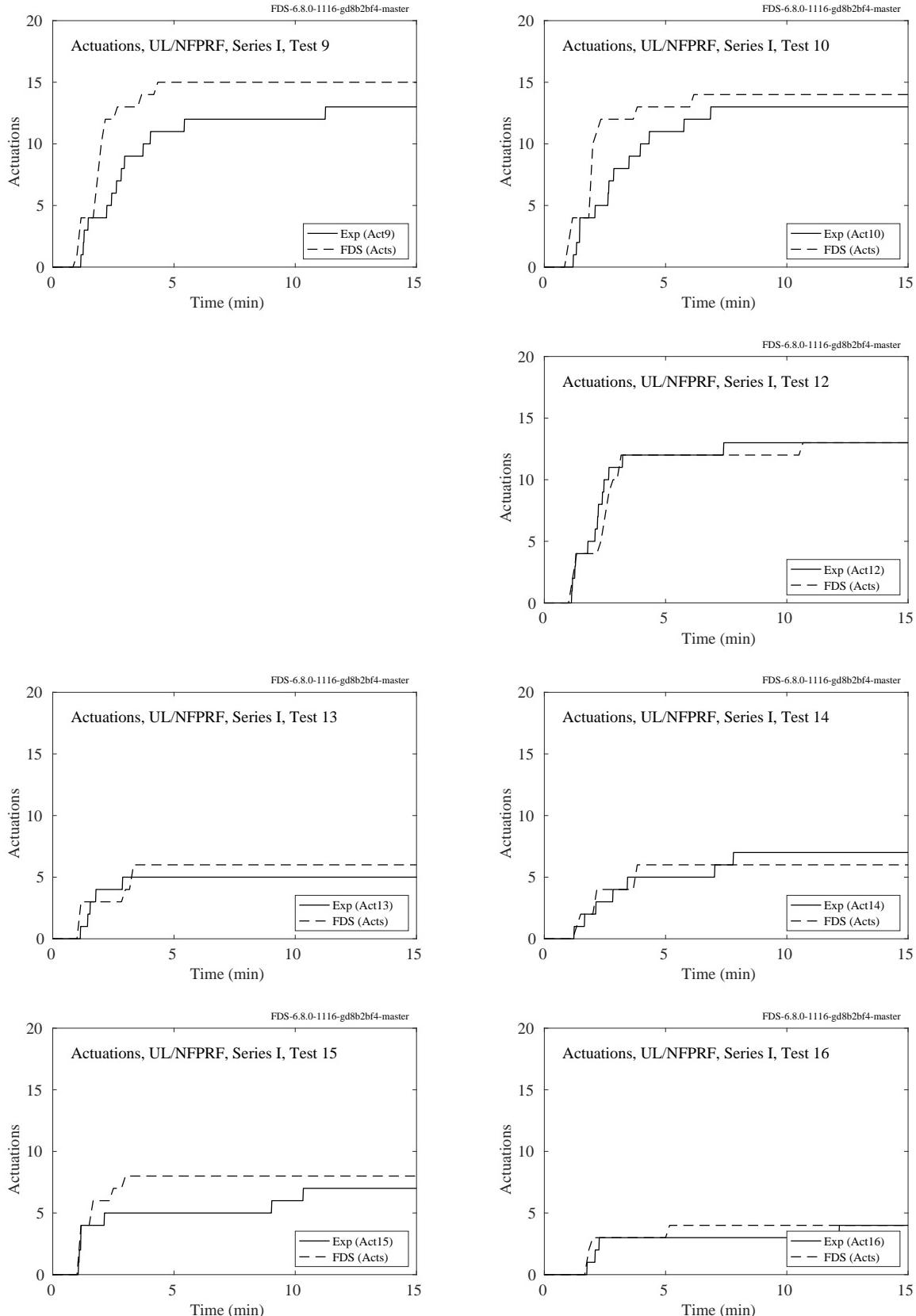


Figure 7.58: UL/NFPRF experiments, number of sprinkler activations, Series I, Tests 9-16.

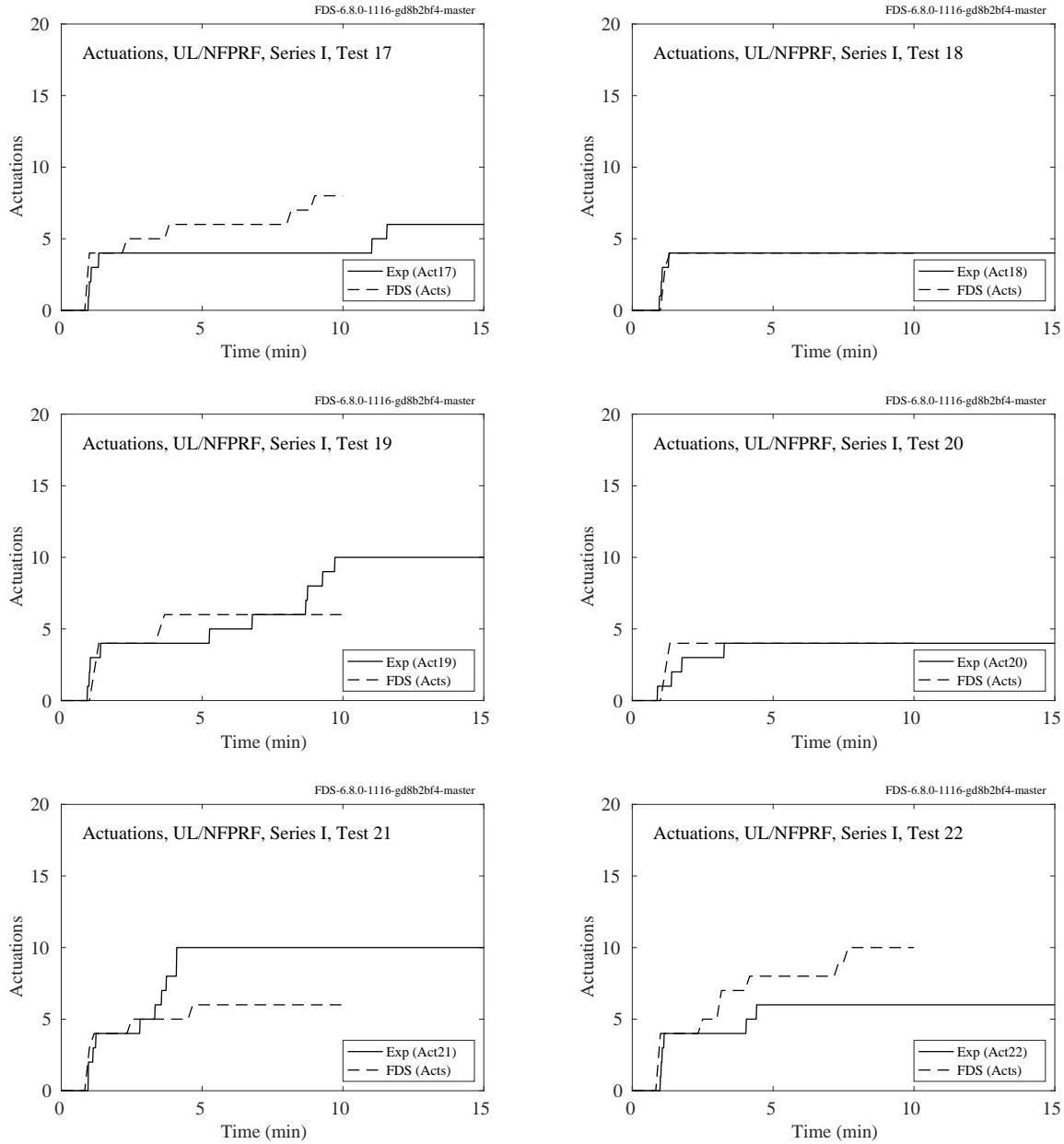


Figure 7.59: UL/NFPRF experiments, number of sprinkler activations, Series I, Tests 17-22.

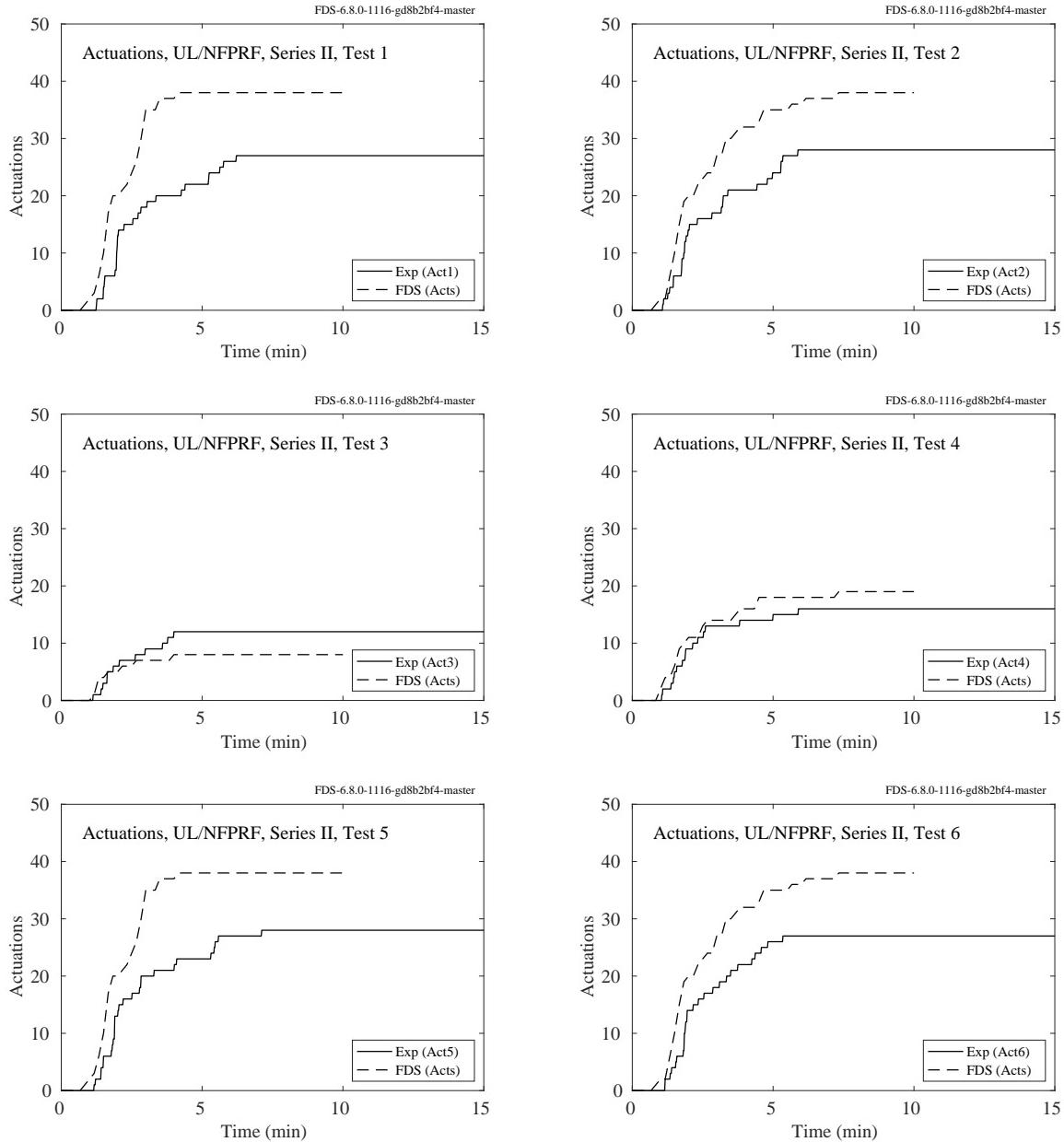


Figure 7.60: UL/NFPRF experiments, number of sprinkler activations, Series II, Tests 1-6.

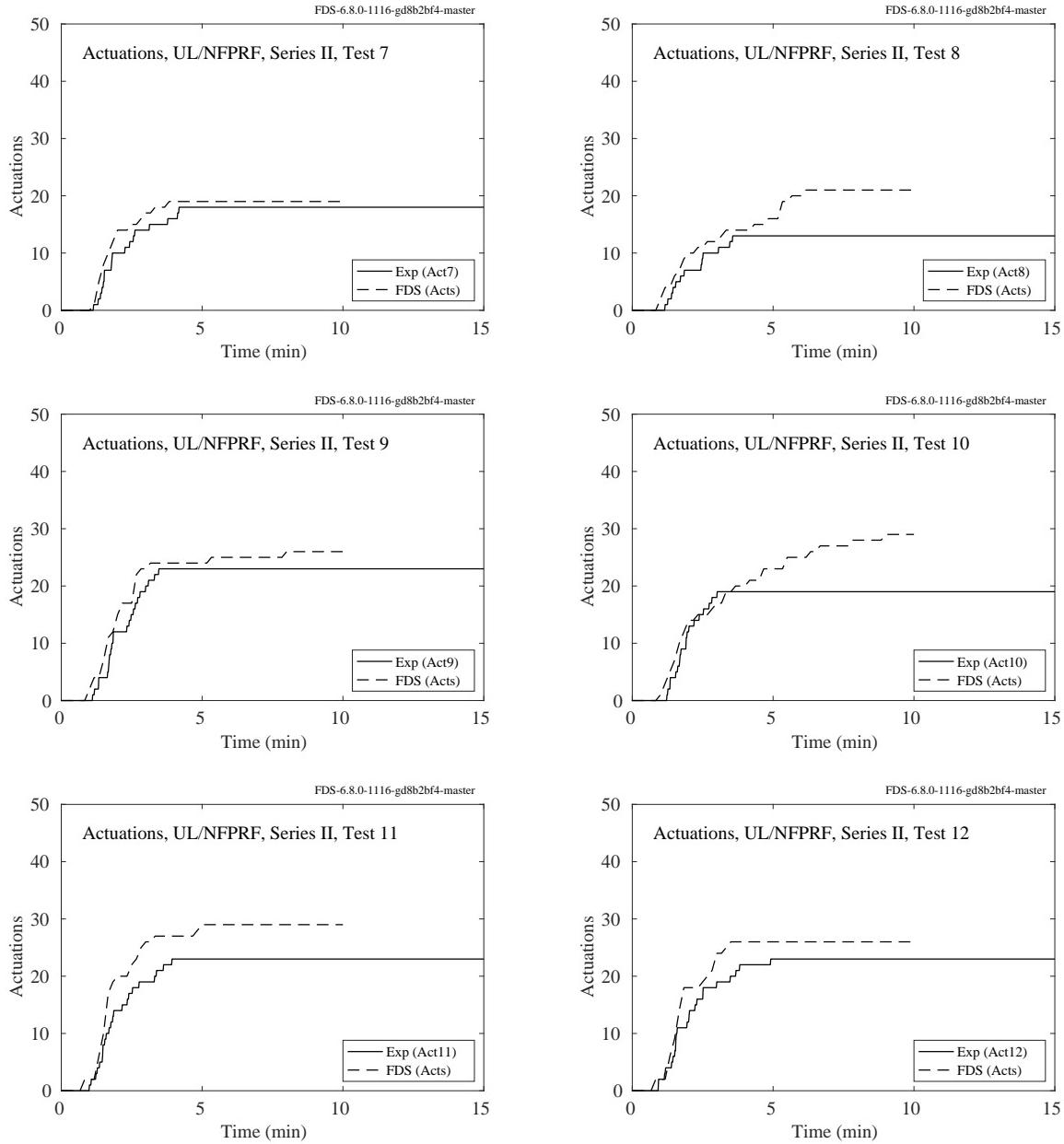


Figure 7.61: UL/NFPRF experiments, number of sprinkler activations, Series II, Tests 7-12.

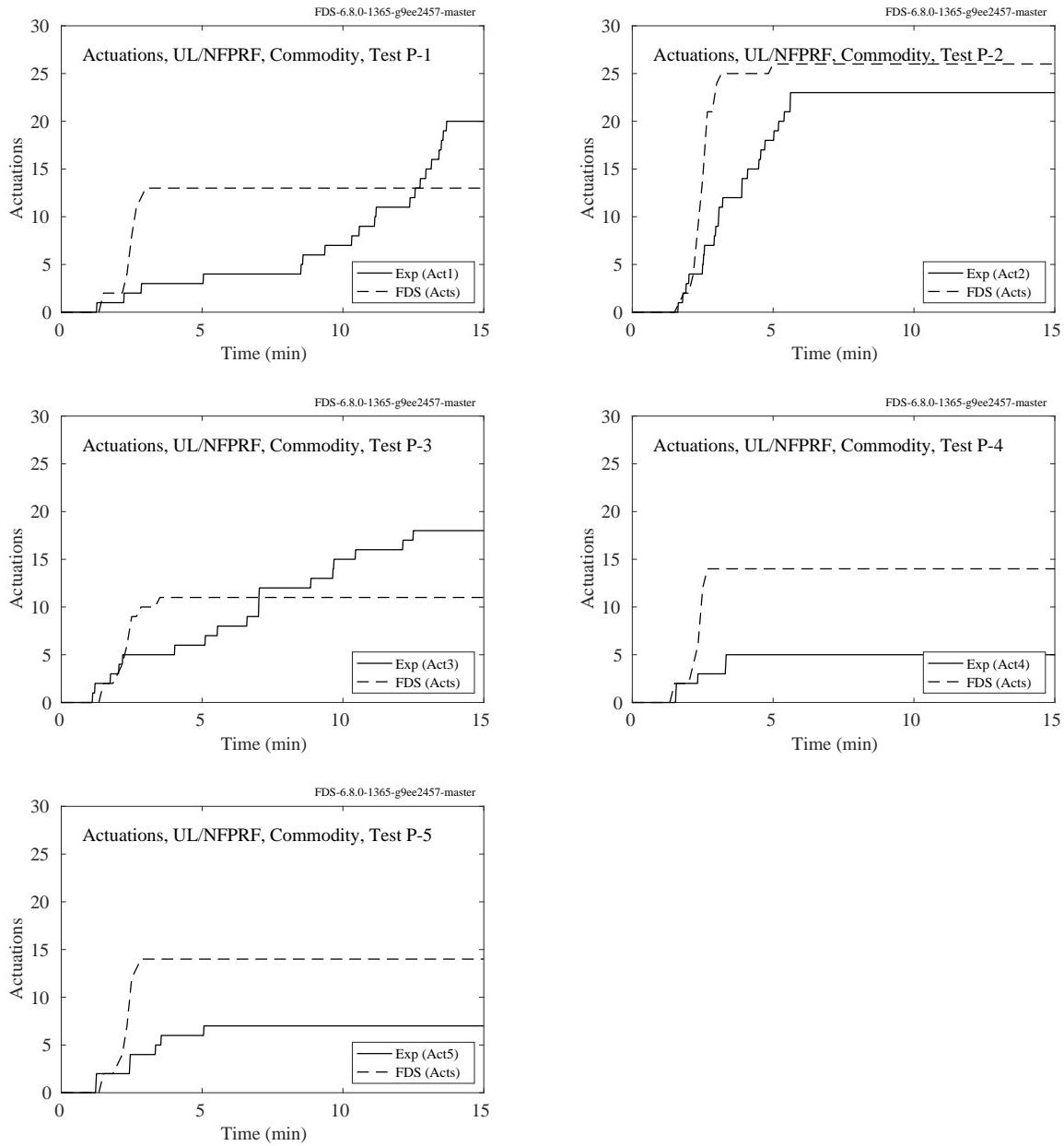


Figure 7.62: UL/NFPRF experiments, number of sprinkler activations, Group A Commodity, Tests 1-5.

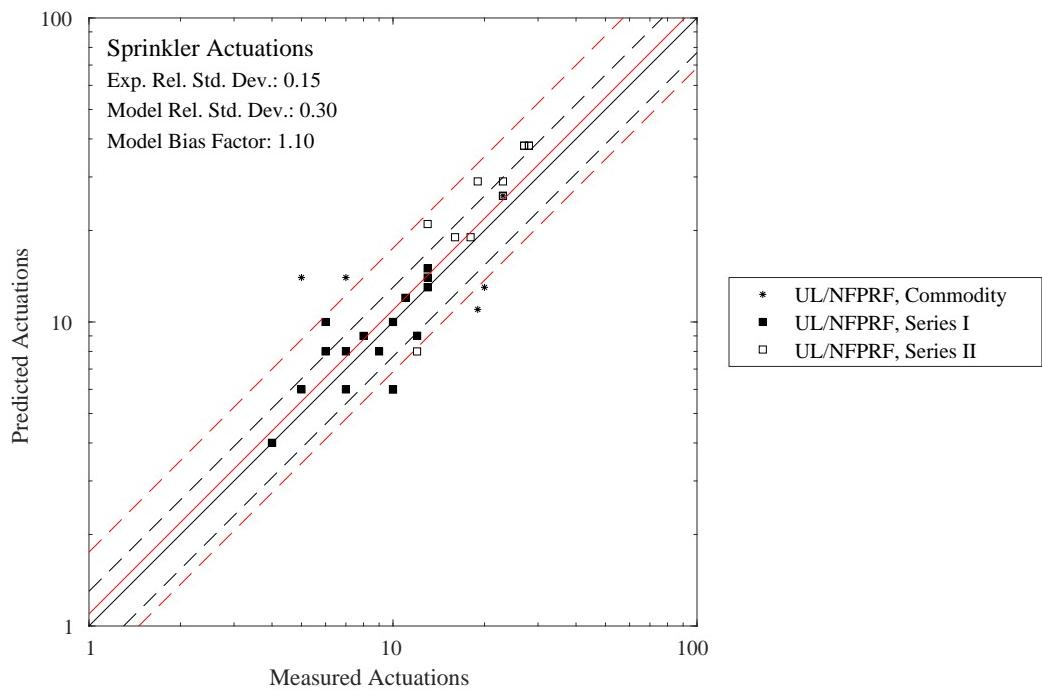


Figure 7.63: Comparison of the number of predicted and measured sprinkler activations.

### 7.3 Smoke Detector Activation Times

FDS can model smoke detector activation in two ways. The first method is based on the assumption that activation occurs when the gas temperature near the detector rises above a given threshold. Essentially this method treats the smoke detector exactly like a heat detector with a relatively low RTI value. Figure 7.64 compares the measured versus predicted smoke detector activation times using a heat detector/temperature rise approach. The heat detectors were set with an RTI of  $5 \sqrt{m \cdot s}$  and an activation temperature of  $5^\circ\text{C}$  above ambient, based on the suggestion of Bukowski and Averill [354].

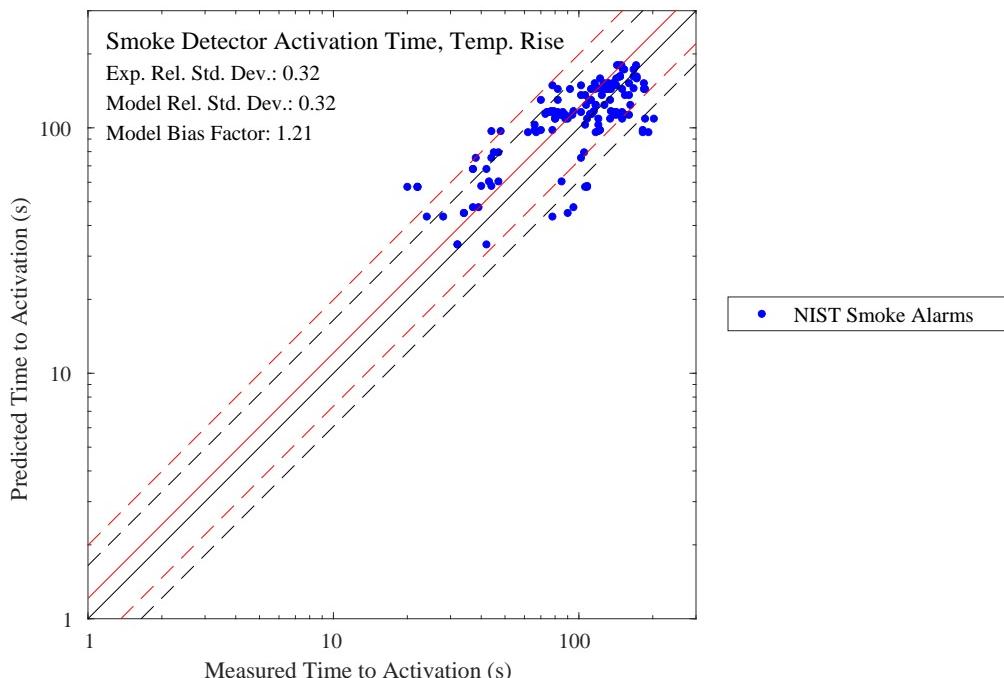


Figure 7.64: Summary of smoke detector activation times (using temperature rise), NIST Smoke Alarms.

The second method of predicting smoke detector activation is to use an empirical model of the smoke transit time within the device to estimate when the smoke concentration will rise above a particular threshold value set by the manufacturer. Figure 7.65 compares the measured versus predicted smoke detector activation times using the smoke detector model. Note that the test report [265] does not provide the parameters that characterize the smoke transit time within the detector. Instead, generic values are used.

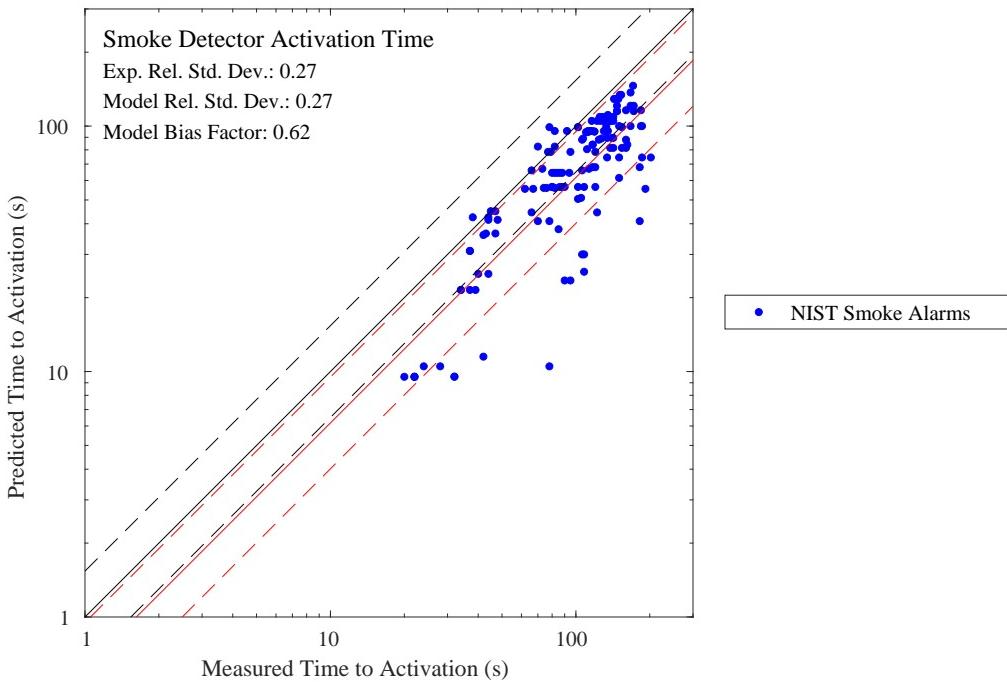


Figure 7.65: Summary of smoke detector activation times (using smoke detector model), NIST Smoke Alarms.

## 7.4 Backlayering of Smoke in Tunnels

This section presents small and large-scale experiments focused on the phenomenon known as “backlayering;” that is, where jet fans are installed near the ceiling of a tunnel to blow smoke from a fire in one direction. Propagation of smoke upwind of the fire is called backlayering.

### 7.4.1 Wu Bakar Tunnel Experiments

This section contains the results of the simulations of the Wu and Bakar experiments described in Sec. 3.106. Five simulations are conducted. In each, the heat release rate is stepped up from its lowest reported value to its highest, each step lasting 20 s. For each of the eight heat release rates, the tunnel velocity is set to the reported critical velocity. Temperature readings along the ceiling indicate where the smoke layer temperature drops below 30 °C, 10 °C above ambient. This is taken as the extent of the back-layer. Using an empirical correlation for the normalized back-layer length,  $L_b^*$ , developed by Li et al. [372]

$$L_b^* = \begin{cases} 18.5 \ln(0.81 Q^{*1/3}/V^*) & Q^* \leq 0.15 \\ 18.5 \ln(0.43/V^*) & Q^* > 0.15 \end{cases} \quad (7.1)$$

where

$$L_b^* = \frac{L_b}{\bar{H}} \quad ; \quad \bar{H} = \frac{4A}{P} \quad ; \quad Q^* = \frac{Q}{\rho_\infty c_p T_\infty \sqrt{g \bar{H}^5}} \quad ; \quad V^* = \frac{V}{\sqrt{g \bar{H}}} \quad (7.2)$$

the FDS-predicted critical velocity,  $V_{FDS}$ , can be estimated from the measured,  $V_{exp}$ , via

$$V_{FDS} \approx V_{exp} \left( 1 + \frac{L_{b,FDS}}{18.5 \bar{H}} \right) \quad (7.3)$$

Note that  $\bar{H}$  is known as the *hydraulic diameter* which takes into consideration the tunnel’s cross-sectional area,  $A$ , and perimeter,  $P$ . For a square cross section, the hydraulic diameter equals the tunnel height.

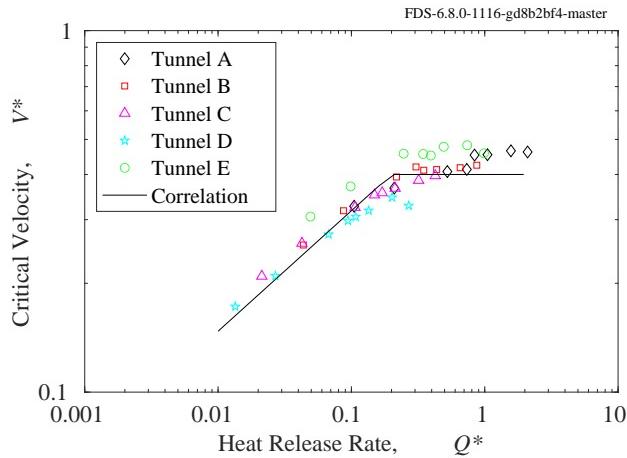


Figure 7.66: Wu and Bakar critical velocity correlation with FDS results added.

The non-dimensionalized critical velocity predictions are plotted against the non-dimensionalized HRR in Fig. 7.66. The solid line in the figure is the correlation developed by Wu and Bakar [347]:

$$V^* = \begin{cases} 0.4(Q^*/0.2)^{1/3} & Q^* \leq 0.2 \\ 0.4 & Q^* > 0.2 \end{cases} \quad (7.4)$$

### 7.4.2 Memorial Tunnel Experiments

A description of the Memorial Tunnel experiments can be found in Sec. 3.47. Figure 7.67 compares predicted and measured volume flow through the tunnel as a function of the number of activated jet fans. Note that the experimental data has been reported in Ref. [373], published in 1999. The original test report, published in 1995 [248], contains a section (8.8) where these cold flow fan tests are discussed. The reported volume flows in the original report are approximately 20 % higher than those reported in the follow-up report. The reason for the discrepancy is that the cross-sectional area was reduced at the measurement locations due to the installation of instrument packages.

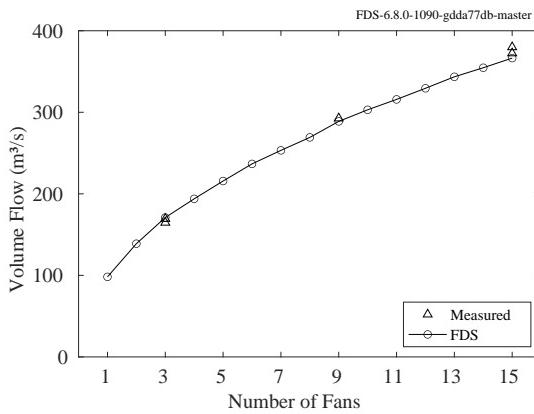


Figure 7.67: Volume flow in Memorial Tunnel as a function of the number of jet fans.

The figures on the following pages summarize the results of 17 simulations of the longitudinal fan experiments (Sequences 15, 17, and 18). For each experiment, the measured heat release rate is shown. The model heat release rate is specified to match, but some deviations between the two are evident. Next, the measured and predicted volume flow through the tunnel is presented. The measured and predicted values are taken at Loop 214, just inside the north (uphill) portal. Next shown are the near-ceiling temperature and velocity at Loop 305, approximately 10 m uphill of the fire. “Backlayering” of smoke is assumed if the temperature at this location rises significantly above ambient. The jet fans were positioned uphill of the fire and usually blew in the downhill direction, except for Tests 23B, 24B, and 25B, where the fans were positioned downhill of the fire, but still blew in the downhill direction. The fan flow direction was reversed during some of the experiments.

The fifth figure indicates where a near-ceiling temperature of 50 °C is located, as interpolated from the measurements made 0.9 m below the ceiling. This position varies in time as the jet fans are activated. The fire location is designated with the letter “F”. In most cases, the fans blew air downhill from the north portal (left) towards the south portal (right). Backlayering is indicated when the location of 50 °C falls to the left of the dashed vertical line.

Finally, the contour plots show comparisons of measured and predicted gas temperature in the vertical centerline plane of the tunnel. The temperature contours are drawn from temperature values obtained along 13 vertical arrays of thermocouples. The fire location is designated with the letter “F”.

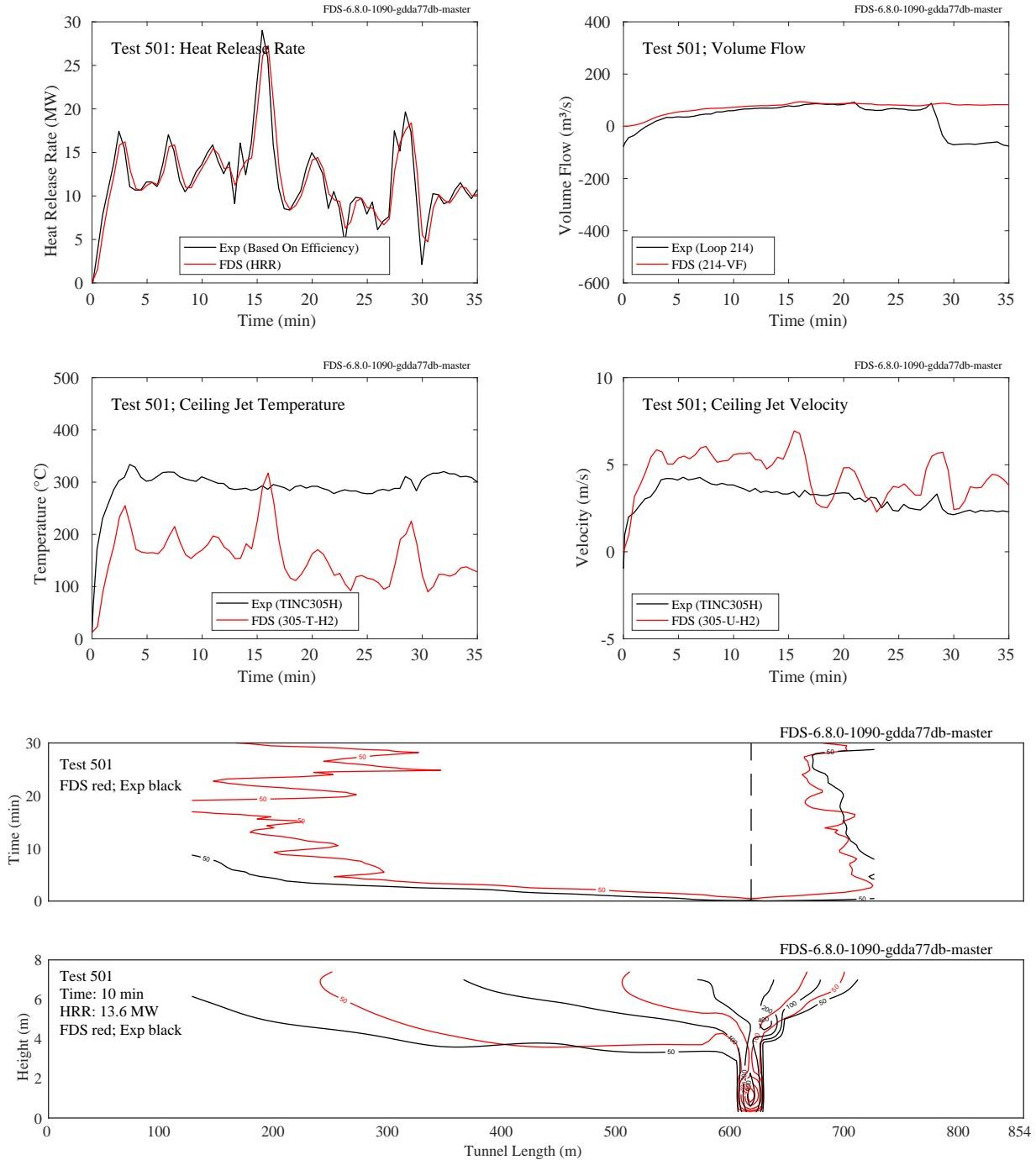


Figure 7.68: Summary of Memorial Tunnel Test 501. The measured and specified heat release rates are shown in the upper left figure. The measured and predicted volume flows through the North Portal are shown in the upper right. Note that a positive value denotes a flow direction from south to north, against the direction of the fan flow. The Ceiling Jet Temperature shown in the left figure of the second row is taken near the ceiling at Loops 305 and 306, 10 m and 30 m uphill of the fire. The Ceiling Jet Velocity, second row right, is taken near the ceiling at Loop 305, 10 m uphill of the fire. The third row figure indicates the location of the 50 °C near-ceiling temperature as a function of time. The last plot displays measured and predicted temperature contours along the vertical centerline plane.

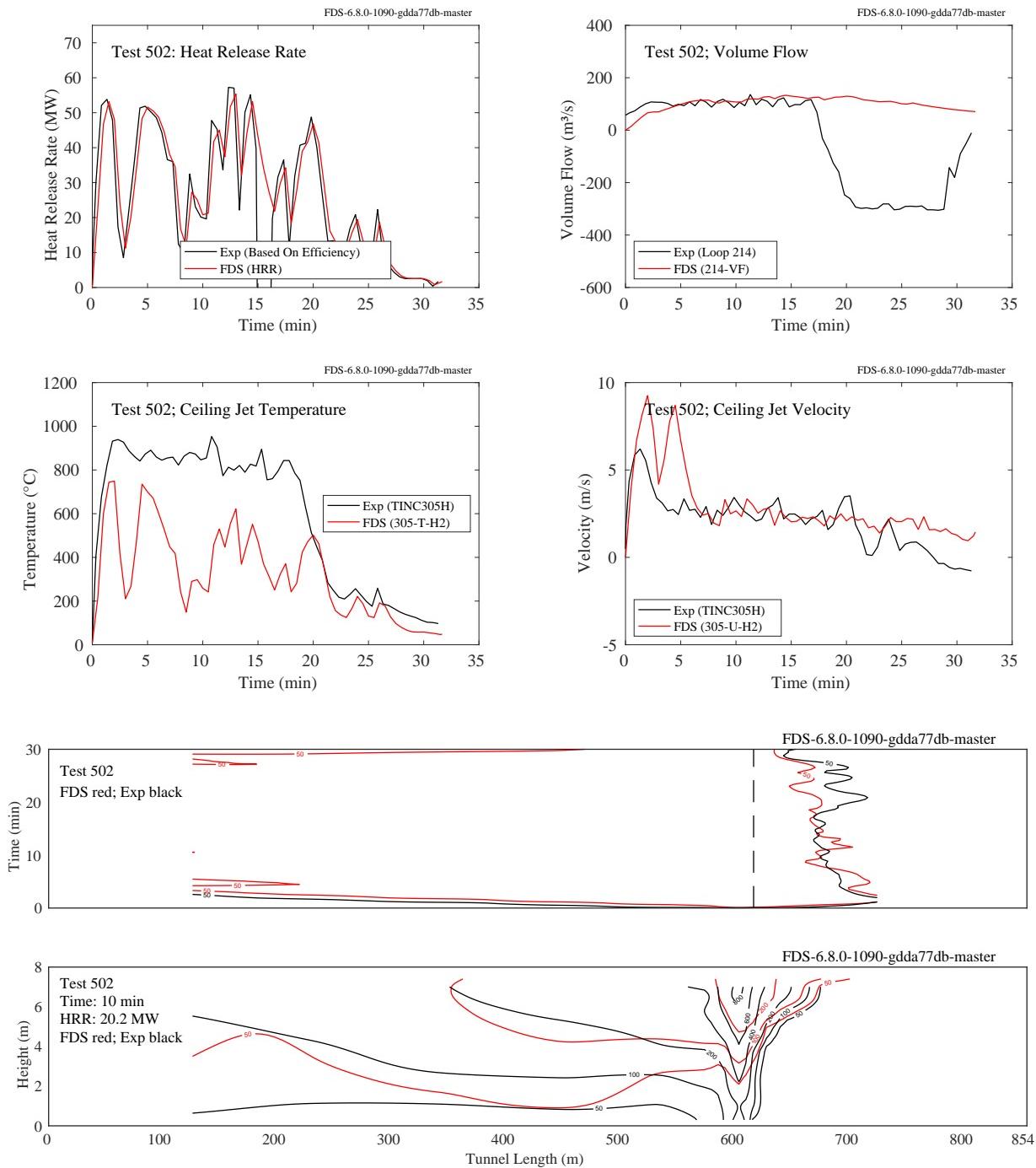


Figure 7.69: Summary of Memorial Tunnel Test 502. The measured and specified heat release rates are shown in the upper left figure. The measured and predicted volume flows through the North Portal are shown in the upper right. Note that a positive value denotes a flow direction from south to north, against the direction of the fan flow. The Ceiling Jet Temperature shown in the left figure of the second row is taken near the ceiling at Loops 305 and 306, 10 m and 30 m uphill of the fire. The Ceiling Jet Velocity, second row right, is taken near the ceiling at Loop 305, 10 m uphill of the fire. The third row figure indicates the location of the  $50^{\circ}\text{C}$  near-ceiling temperature as a function of time. The last plot displays measured and predicted temperature contours along the vertical centerline plane.

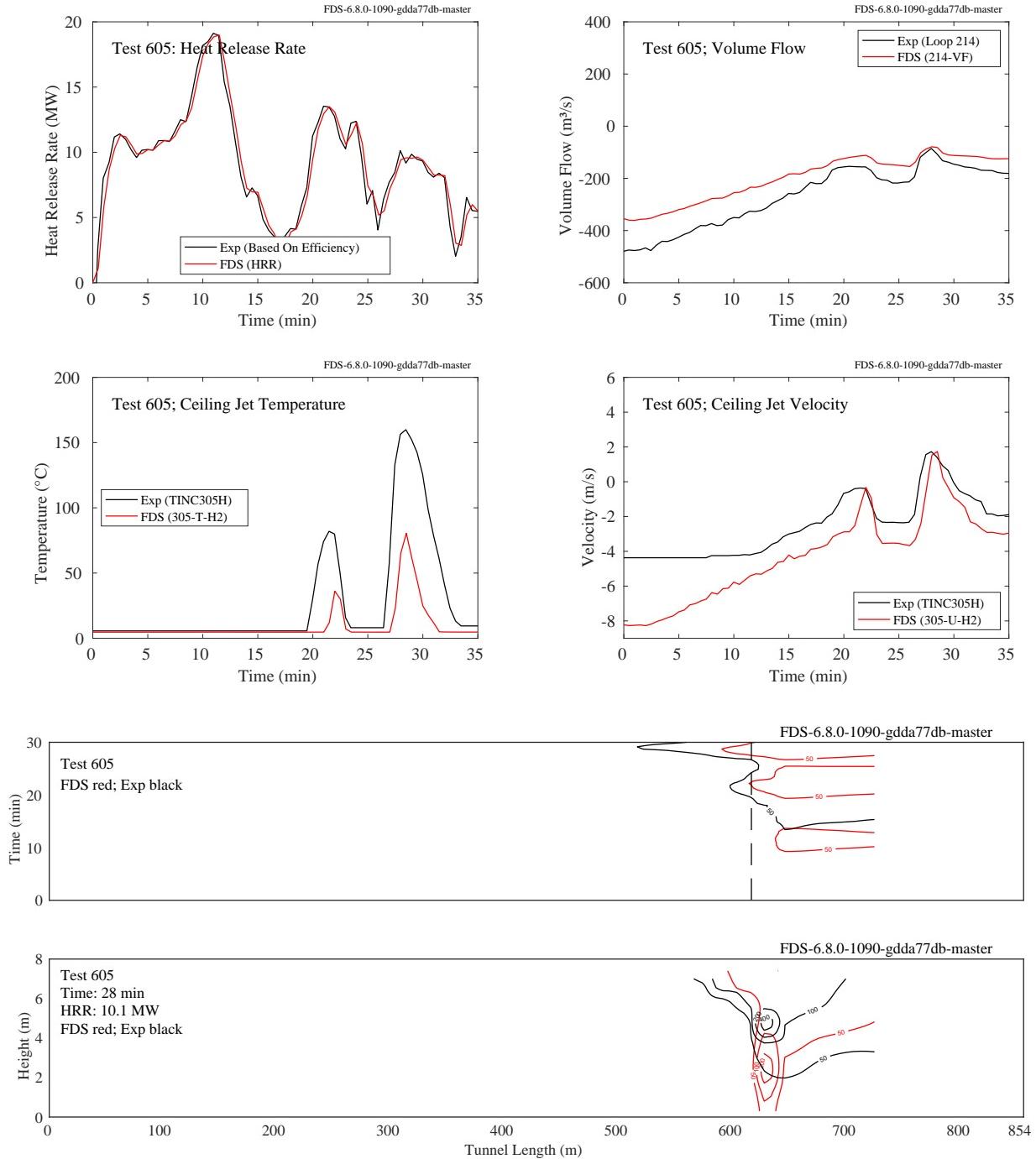


Figure 7.70: Summary of Memorial Tunnel Test 605. The measured and specified heat release rates are shown in the upper left figure. The measured and predicted volume flows through the North Portal are shown in the upper right. Note that a positive value denotes a flow direction from south to north, against the direction of the fan flow. The Ceiling Jet Temperature shown in the left figure of the second row is taken near the ceiling at Loops 305 and 306, 10 m and 30 m uphill of the fire. The Ceiling Jet Velocity, second row right, is taken near the ceiling at Loop 305, 10 m uphill of the fire. The third row figure indicates the location of the 50  $^{\circ}\text{C}$  near-ceiling temperature as a function of time. The last plot displays measured and predicted temperature contours along the vertical centerline plane.

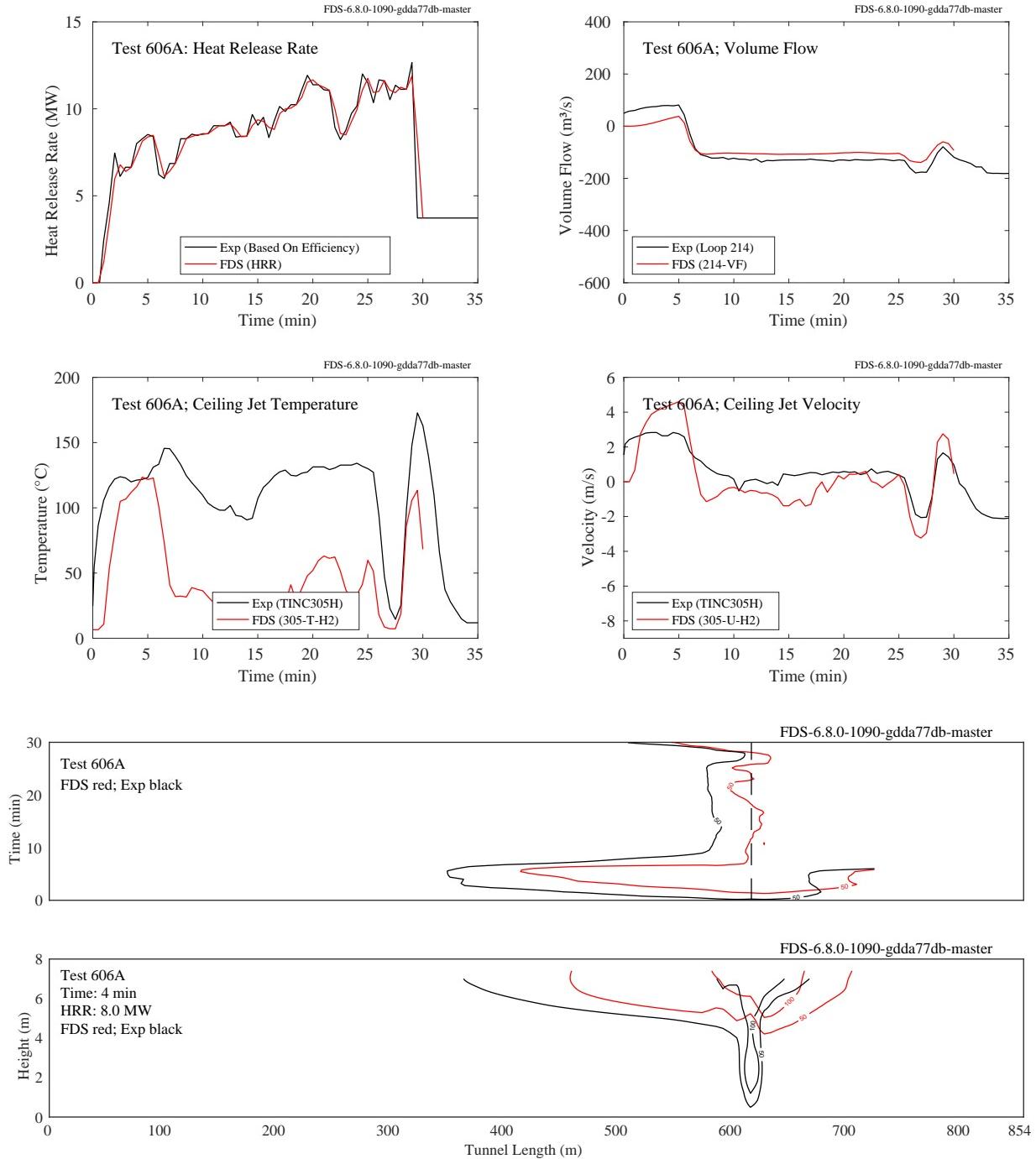


Figure 7.71: Summary of Memorial Tunnel Test 606A. The measured and specified heat release rates are shown in the upper left figure. The measured and predicted volume flows through the North Portal are shown in the upper right. Note that a positive value denotes a flow direction from south to north, against the direction of the fan flow. The Ceiling Jet Temperature shown in the left figure of the second row is taken near the ceiling at Loops 305 and 306, 10 m and 30 m uphill of the fire. The Ceiling Jet Velocity, second row right, is taken near the ceiling at Loop 305, 10 m uphill of the fire. The third row figure indicates the location of the 50 °C near-ceiling temperature as a function of time. The last plot displays measured and predicted temperature contours along the vertical centerline plane.

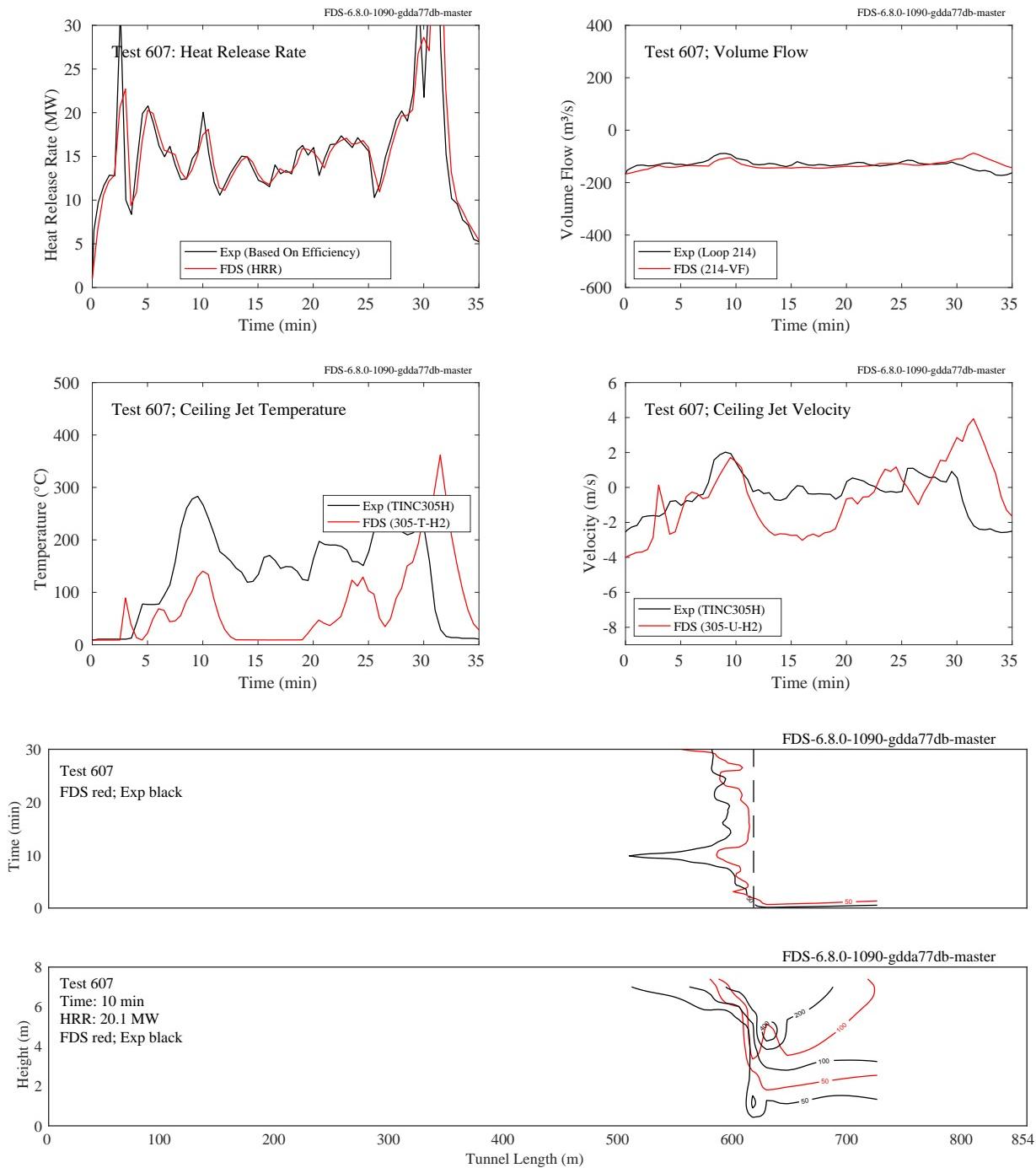


Figure 7.72: Summary of Memorial Tunnel Test 607. The measured and specified heat release rates are shown in the upper left figure. The measured and predicted volume flows through the North Portal are shown in the upper right. Note that a positive value denotes a flow direction from south to north, against the direction of the fan flow. The Ceiling Jet Temperature shown in the left figure of the second row is taken near the ceiling at Loops 305 and 306, 10 m and 30 m uphill of the fire. The Ceiling Jet Velocity, second row right, is taken near the ceiling at Loop 305, 10 m uphill of the fire. The third row figure indicates the location of the 50 °C near-ceiling temperature as a function of time. The last plot displays measured and predicted temperature contours along the vertical centerline plane.

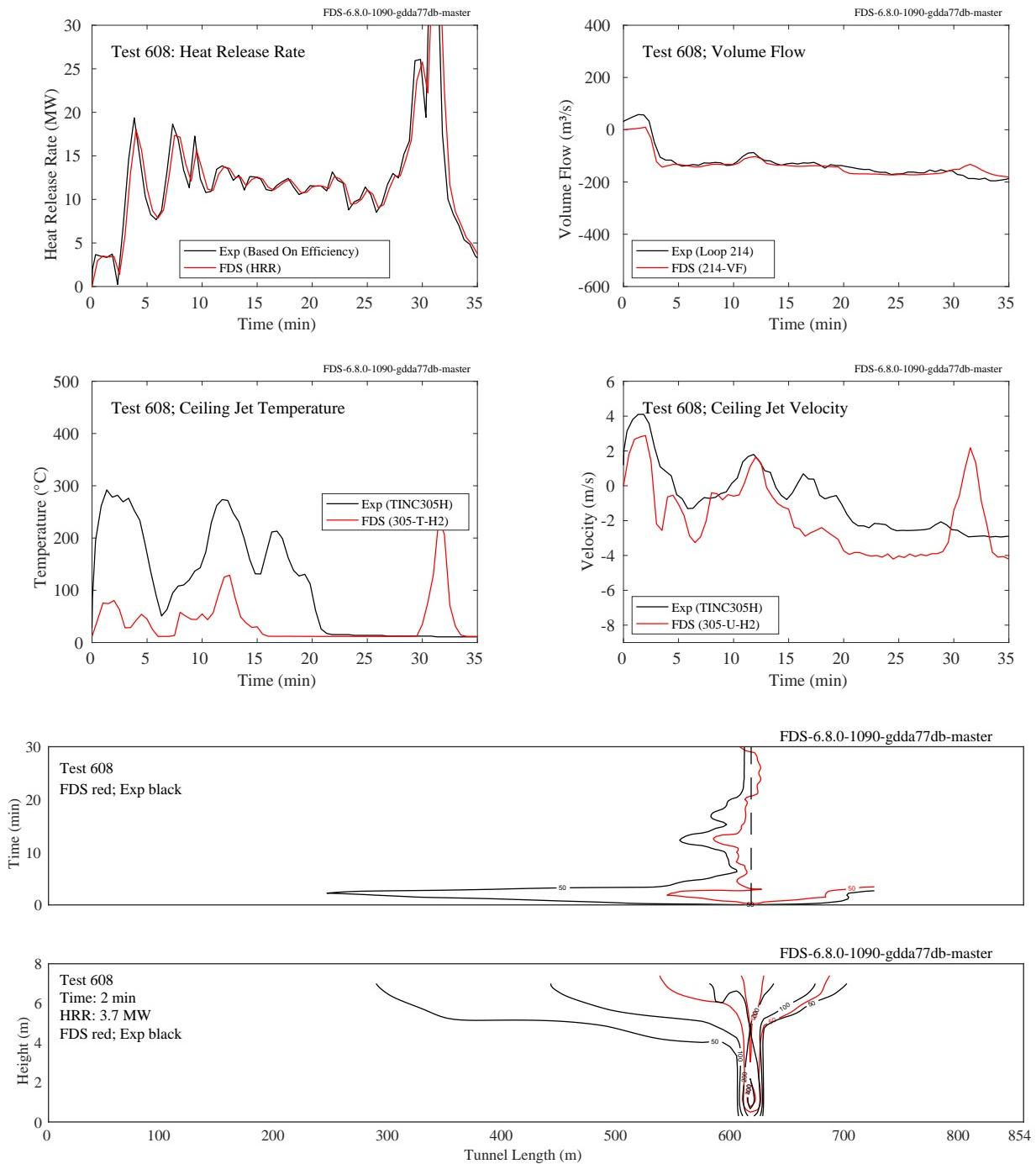


Figure 7.73: Summary of Memorial Tunnel Test 608. The measured and specified heat release rates are shown in the upper left figure. The measured and predicted volume flows through the North Portal are shown in the upper right. Note that a positive value denotes a flow direction from south to north, against the direction of the fan flow. The Ceiling Jet Temperature shown in the left figure of the second row is taken near the ceiling at Loops 305 and 306, 10 m and 30 m uphill of the fire. The Ceiling Jet Velocity, second row right, is taken near the ceiling at Loop 305, 10 m uphill of the fire. The third row figure indicates the location of the 50 °C near-ceiling temperature as a function of time. The last plot displays measured and predicted temperature contours along the vertical centerline plane.

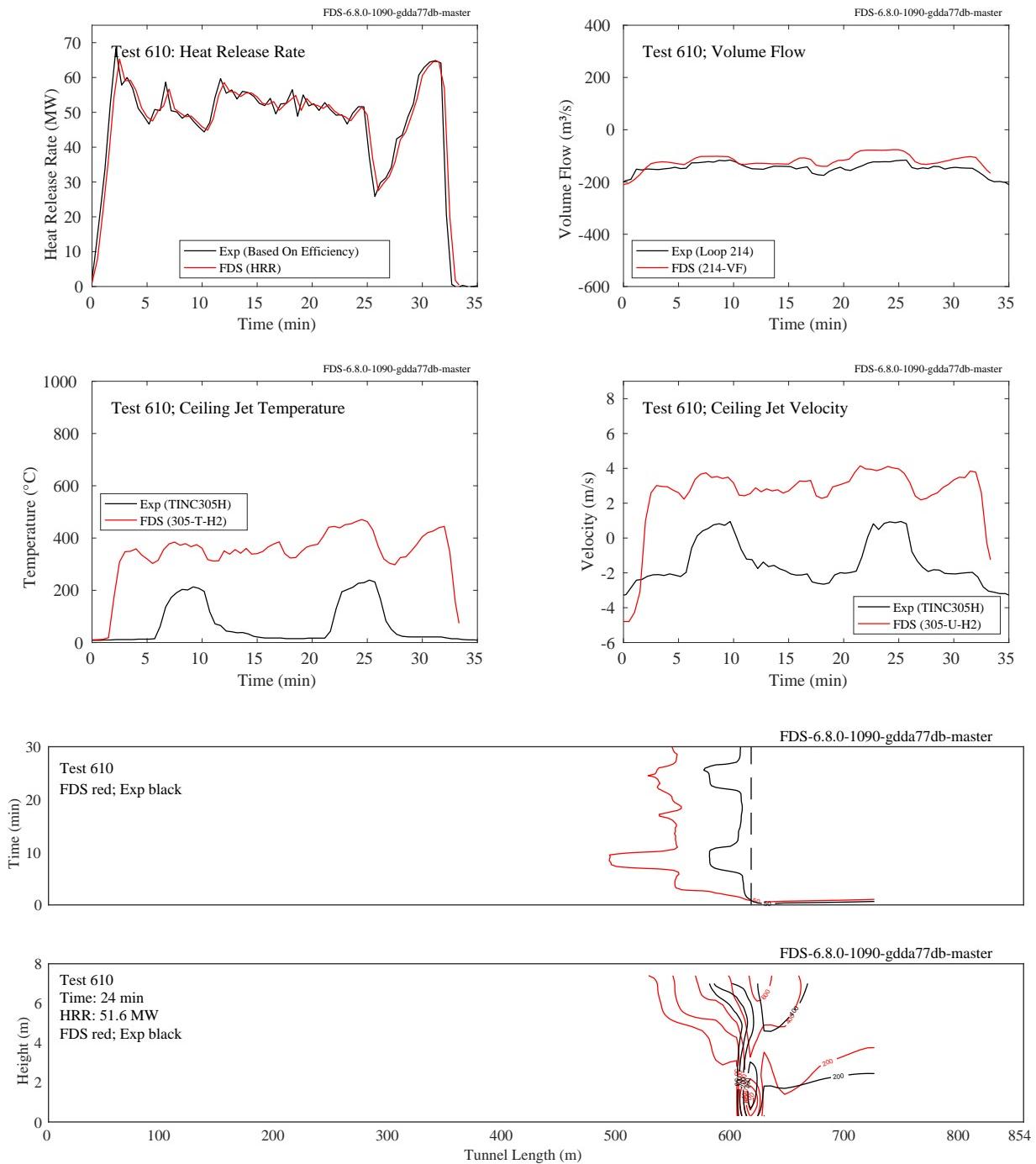


Figure 7.74: Summary of Memorial Tunnel Test 610. The measured and specified heat release rates are shown in the upper left figure. The measured and predicted volume flows through the North Portal are shown in the upper right. Note that a positive value denotes a flow direction from south to north, against the direction of the fan flow. The Ceiling Jet Temperature shown in the left figure of the second row is taken near the ceiling at Loops 305 and 306, 10 m and 30 m uphill of the fire. The Ceiling Jet Velocity, second row right, is taken near the ceiling at Loop 305, 10 m uphill of the fire. The third row figure indicates the location of the 50 °C near-ceiling temperature as a function of time. The last plot displays measured and predicted temperature contours along the vertical centerline plane.

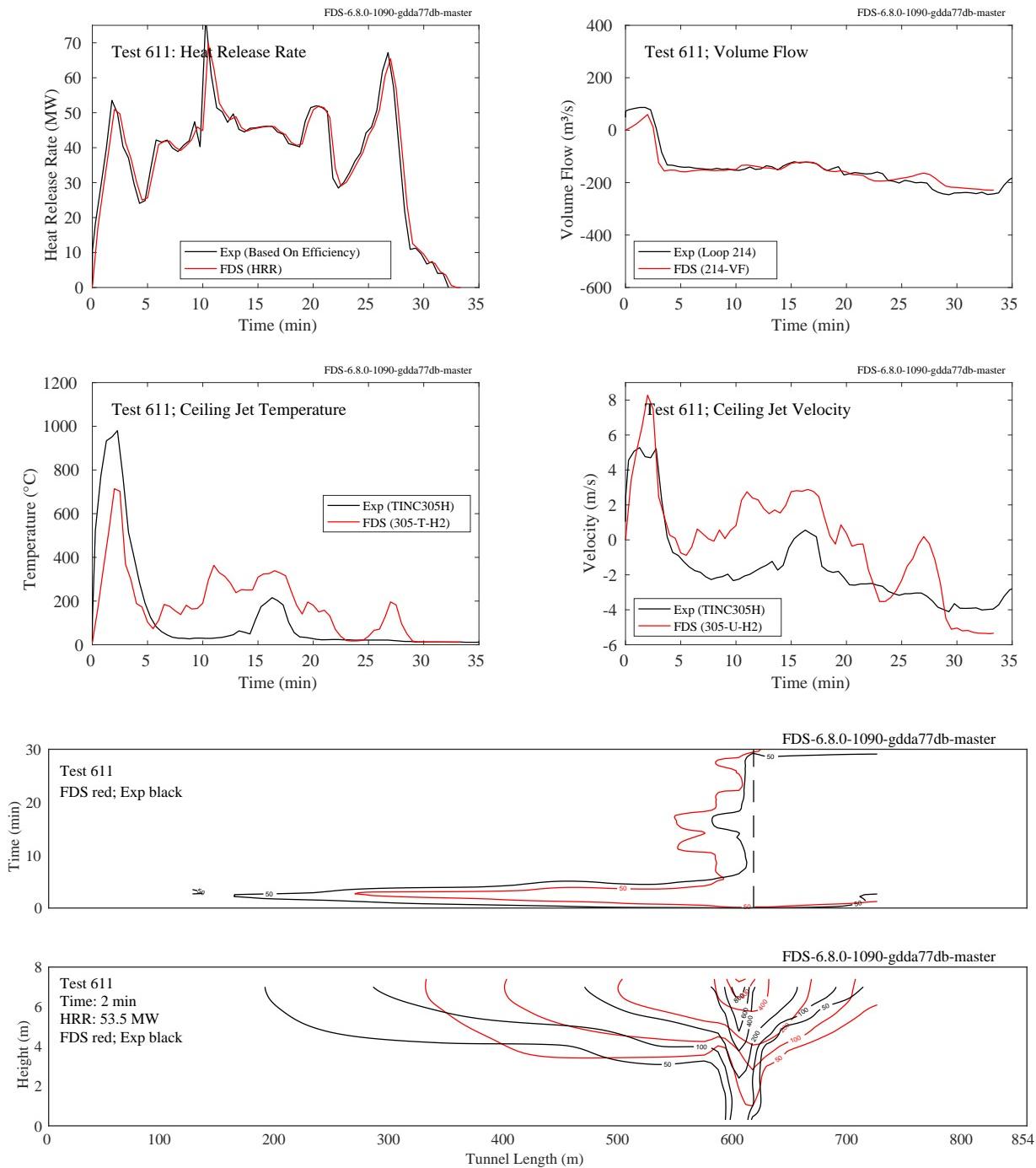


Figure 7.75: Summary of Memorial Tunnel Test 611. The measured and specified heat release rates are shown in the upper left figure. The measured and predicted volume flows through the North Portal are shown in the upper right. Note that a positive value denotes a flow direction from south to north, against the direction of the fan flow. The Ceiling Jet Temperature shown in the left figure of the second row is taken near the ceiling at Loops 305 and 306, 10 m and 30 m uphill of the fire. The Ceiling Jet Velocity, second row right, is taken near the ceiling at Loop 305, 10 m uphill of the fire. The third row figure indicates the location of the 50 °C near-ceiling temperature as a function of time. The last plot displays measured and predicted temperature contours along the vertical centerline plane.

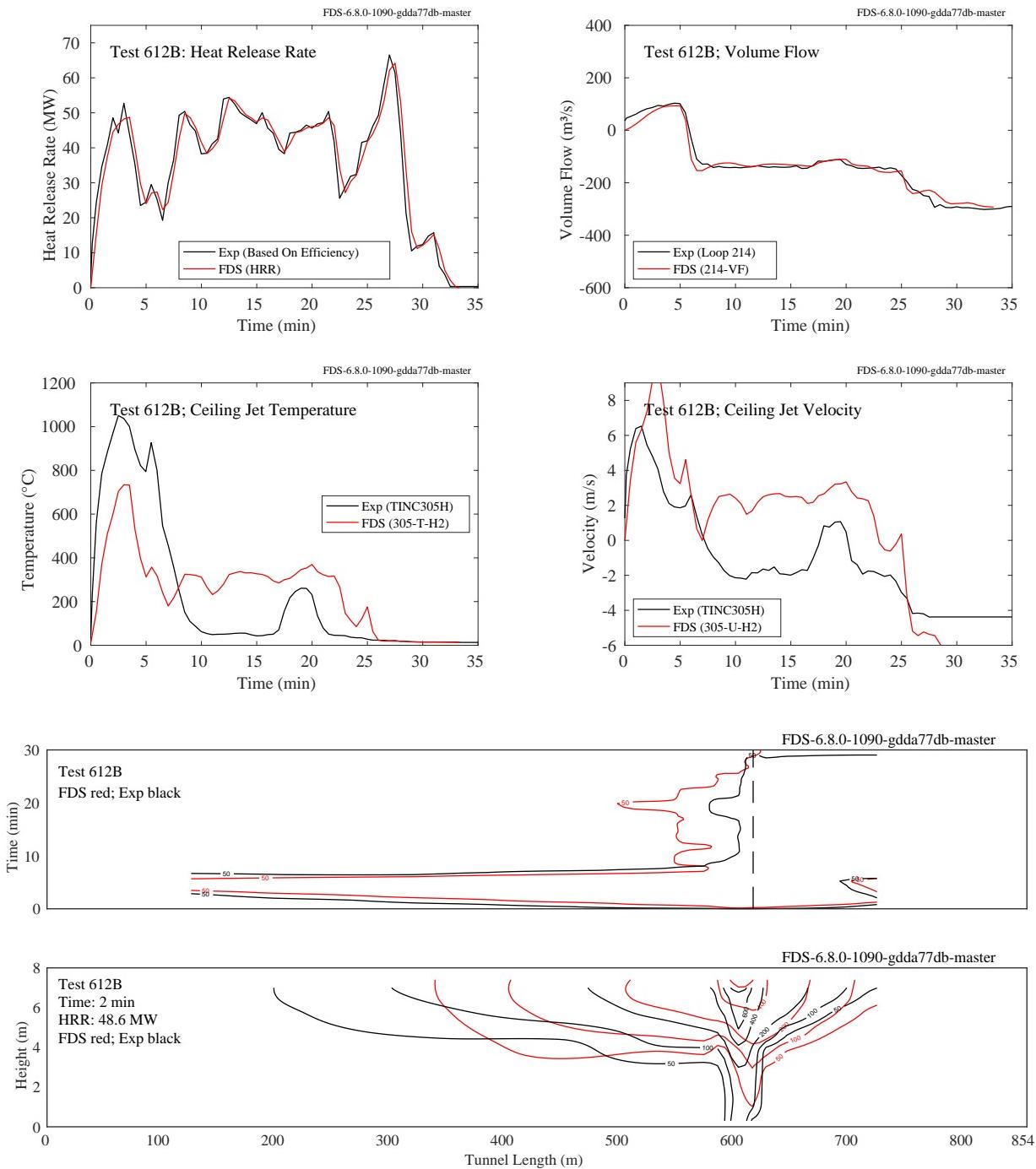


Figure 7.76: Summary of Memorial Tunnel Test 612B. The measured and specified heat release rates are shown in the upper left figure. The measured and predicted volume flows through the North Portal are shown in the upper right. Note that a positive value denotes a flow direction from south to north, against the direction of the fan flow. The Ceiling Jet Temperature shown in the left figure of the second row is taken near the ceiling at Loops 305 and 306, 10 m and 30 m uphill of the fire. The Ceiling Jet Velocity, second row right, is taken near the ceiling at Loop 305, 10 m uphill of the fire. The third row figure indicates the location of the 50 °C near-ceiling temperature as a function of time. The last plot displays measured and predicted temperature contours along the vertical centerline plane.

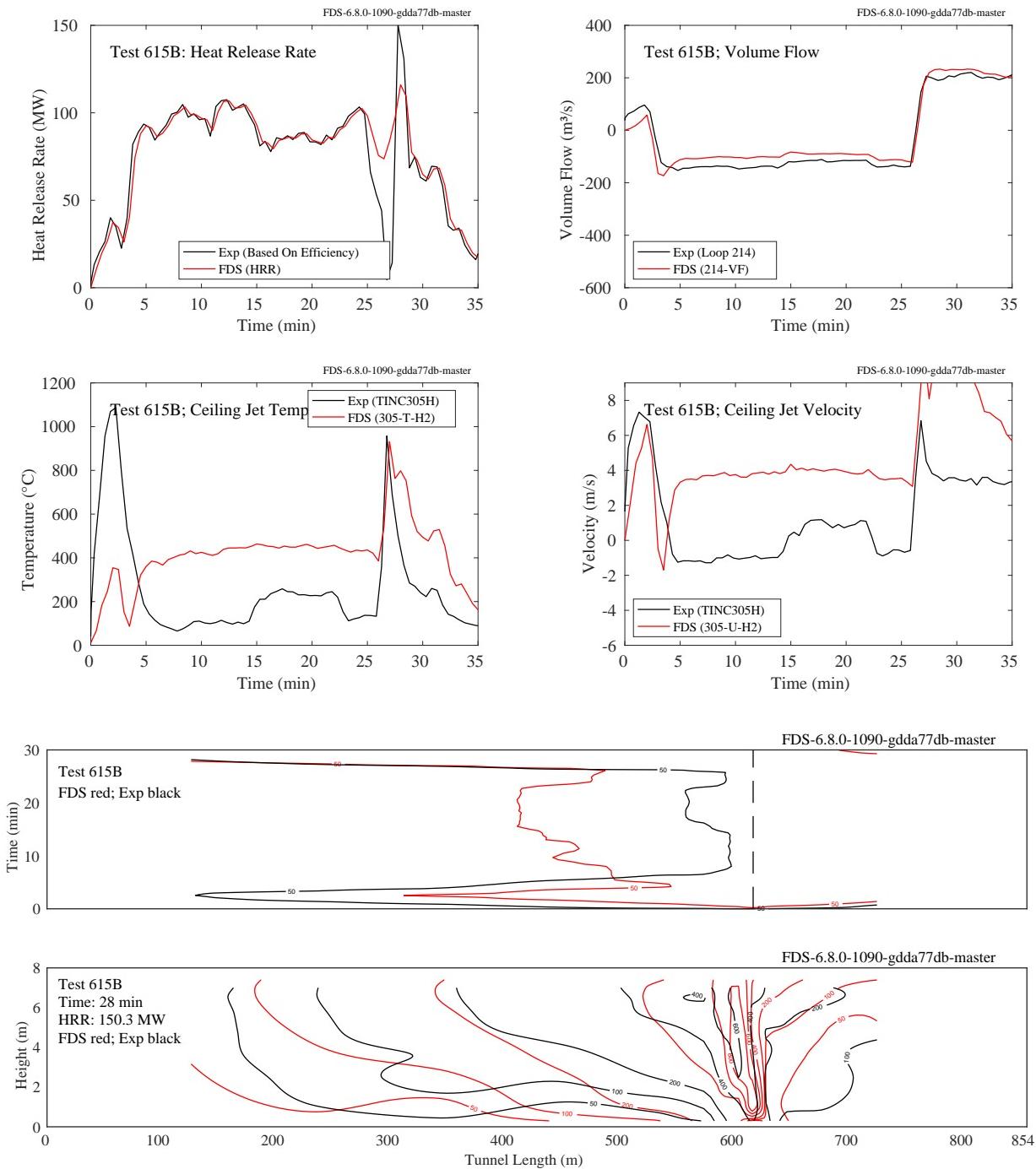


Figure 7.77: Summary of Memorial Tunnel Test 615B. The measured and specified heat release rates are shown in the upper left figure. The measured and predicted volume flows through the North Portal are shown in the upper right. Note that a positive value denotes a flow direction from south to north, against the direction of the fan flow. The Ceiling Jet Temperature shown in the left figure of the second row is taken near the ceiling at Loops 305 and 306, 10 m and 30 m uphill of the fire. The Ceiling Jet Velocity, second row right, is taken near the ceiling at Loop 305, 10 m uphill of the fire. The third row figure indicates the location of the 50 °C near-ceiling temperature as a function of time. The last plot displays measured and predicted temperature contours along the vertical centerline plane.

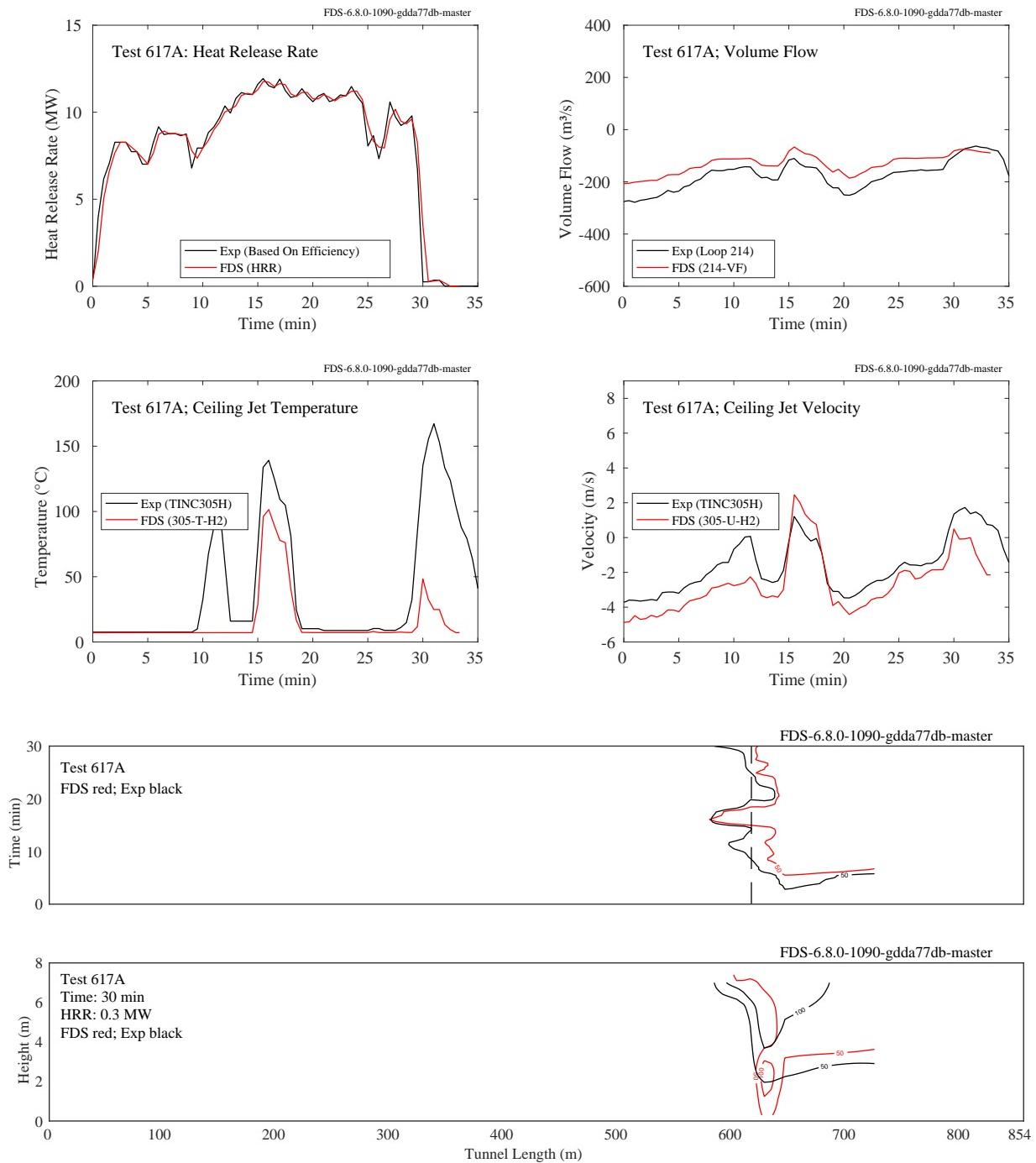


Figure 7.78: Summary of Memorial Tunnel Test 617A. The measured and specified heat release rates are shown in the upper left figure. The measured and predicted volume flows through the North Portal are shown in the upper right. Note that a positive value denotes a flow direction from south to north, against the direction of the fan flow. The Ceiling Jet Temperature shown in the left figure of the second row is taken near the ceiling at Loops 305 and 306, 10 m and 30 m uphill of the fire. The Ceiling Jet Velocity, second row right, is taken near the ceiling at Loop 305, 10 m uphill of the fire. The third row figure indicates the location of the 50 °C near-ceiling temperature as a function of time. The last plot displays measured and predicted temperature contours along the vertical centerline plane.

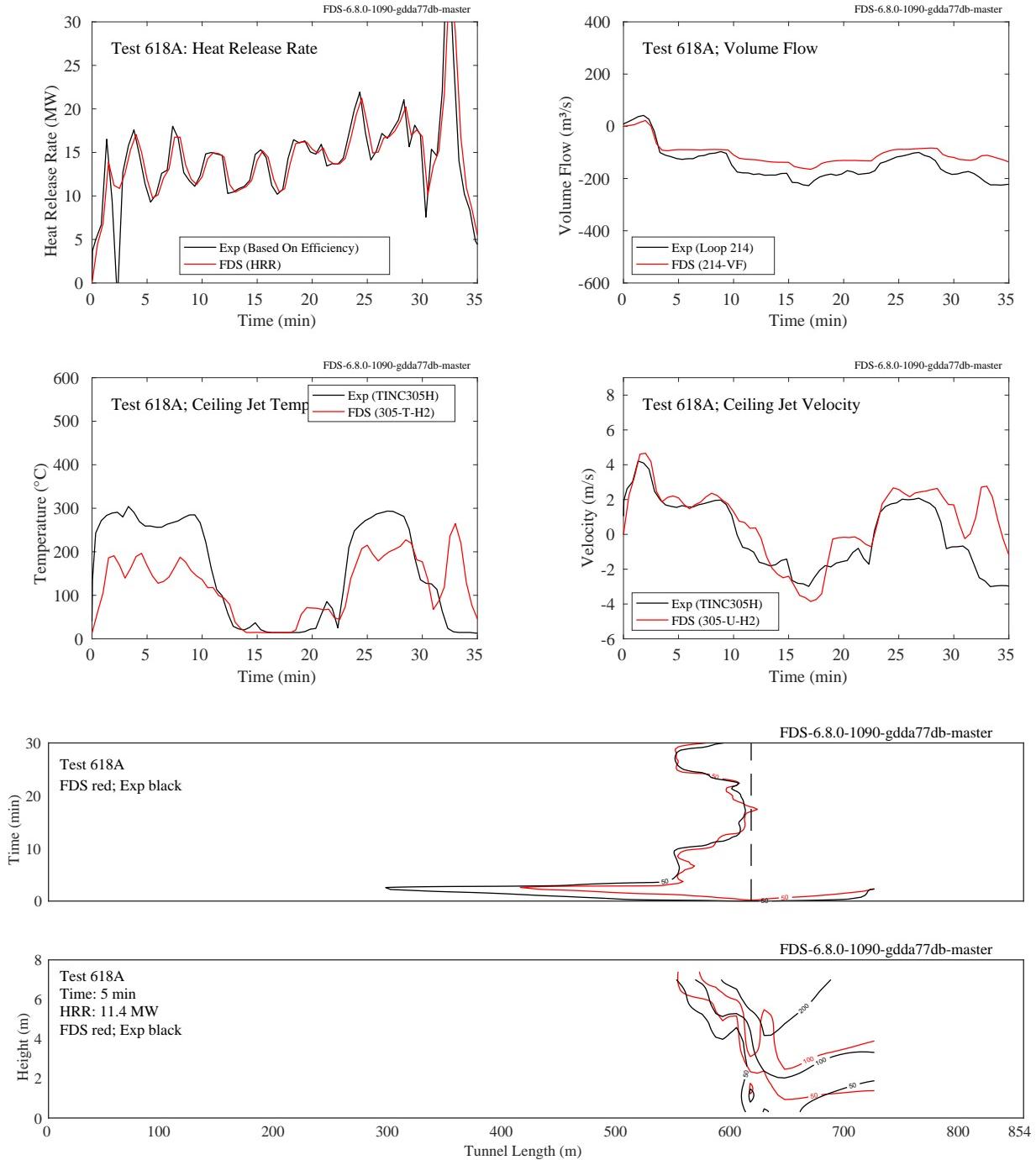


Figure 7.79: Summary of Memorial Tunnel Test 618A. The measured and specified heat release rates are shown in the upper left figure. The measured and predicted volume flows through the North Portal are shown in the upper right. Note that a positive value denotes a flow direction from south to north, against the direction of the fan flow. The Ceiling Jet Temperature shown in the left figure of the second row is taken near the ceiling at Loops 305 and 306, 10 m and 30 m uphill of the fire. The Ceiling Jet Velocity, second row right, is taken near the ceiling at Loop 305, 10 m uphill of the fire. The third row figure indicates the location of the 50 °C near-ceiling temperature as a function of time. The last plot displays measured and predicted temperature contours along the vertical centerline plane.

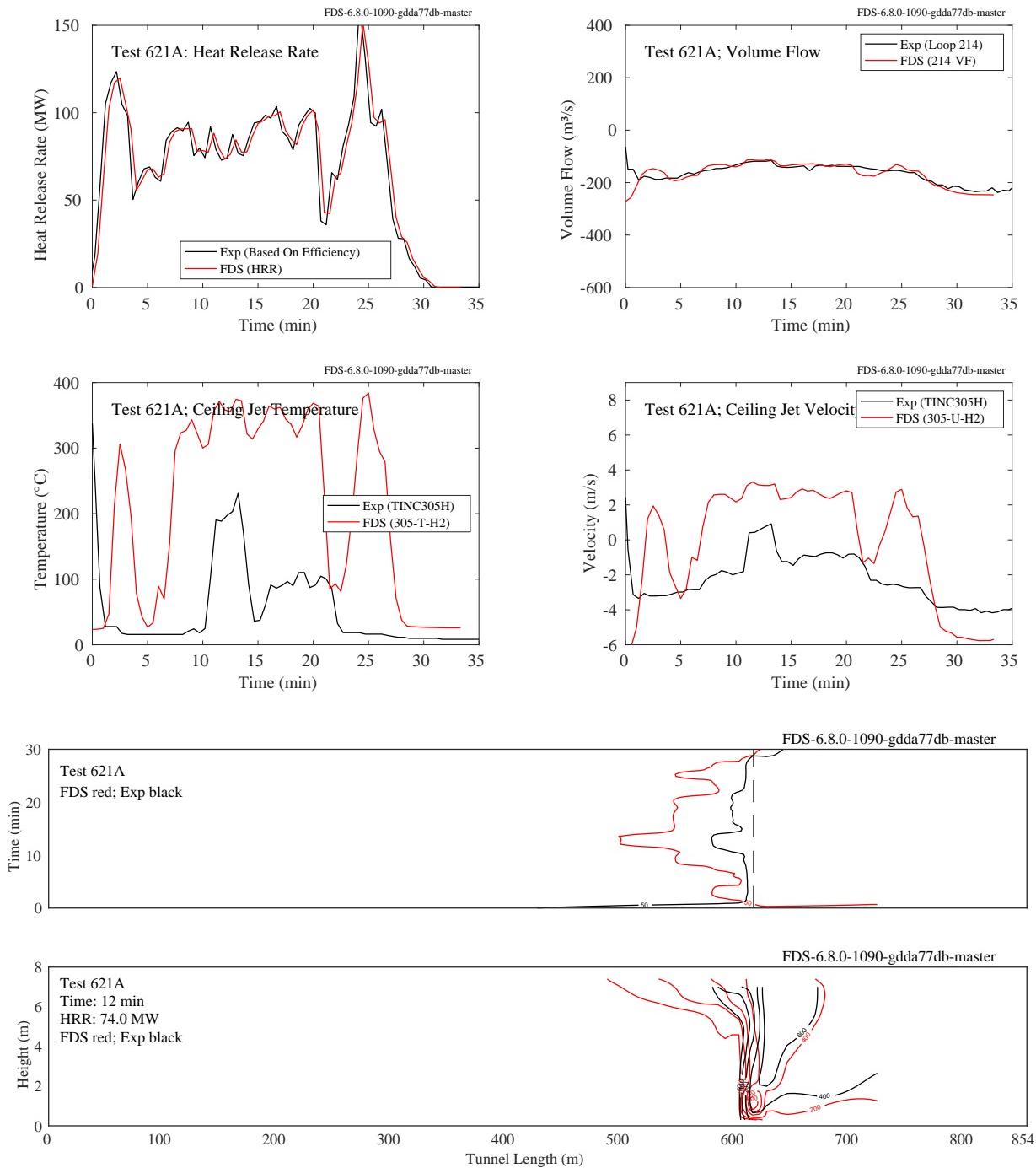


Figure 7.80: Summary of Memorial Tunnel Test 621A. The measured and specified heat release rates are shown in the upper left figure. The measured and predicted volume flows through the North Portal are shown in the upper right. Note that a positive value denotes a flow direction from south to north, against the direction of the fan flow. The Ceiling Jet Temperature shown in the left figure of the second row is taken near the ceiling at Loops 305 and 306, 10 m and 30 m uphill of the fire. The Ceiling Jet Velocity, second row right, is taken near the ceiling at Loop 305, 10 m uphill of the fire. The third row figure indicates the location of the  $50^{\circ}\text{C}$  near-ceiling temperature as a function of time. The last plot displays measured and predicted temperature contours along the vertical centerline plane.

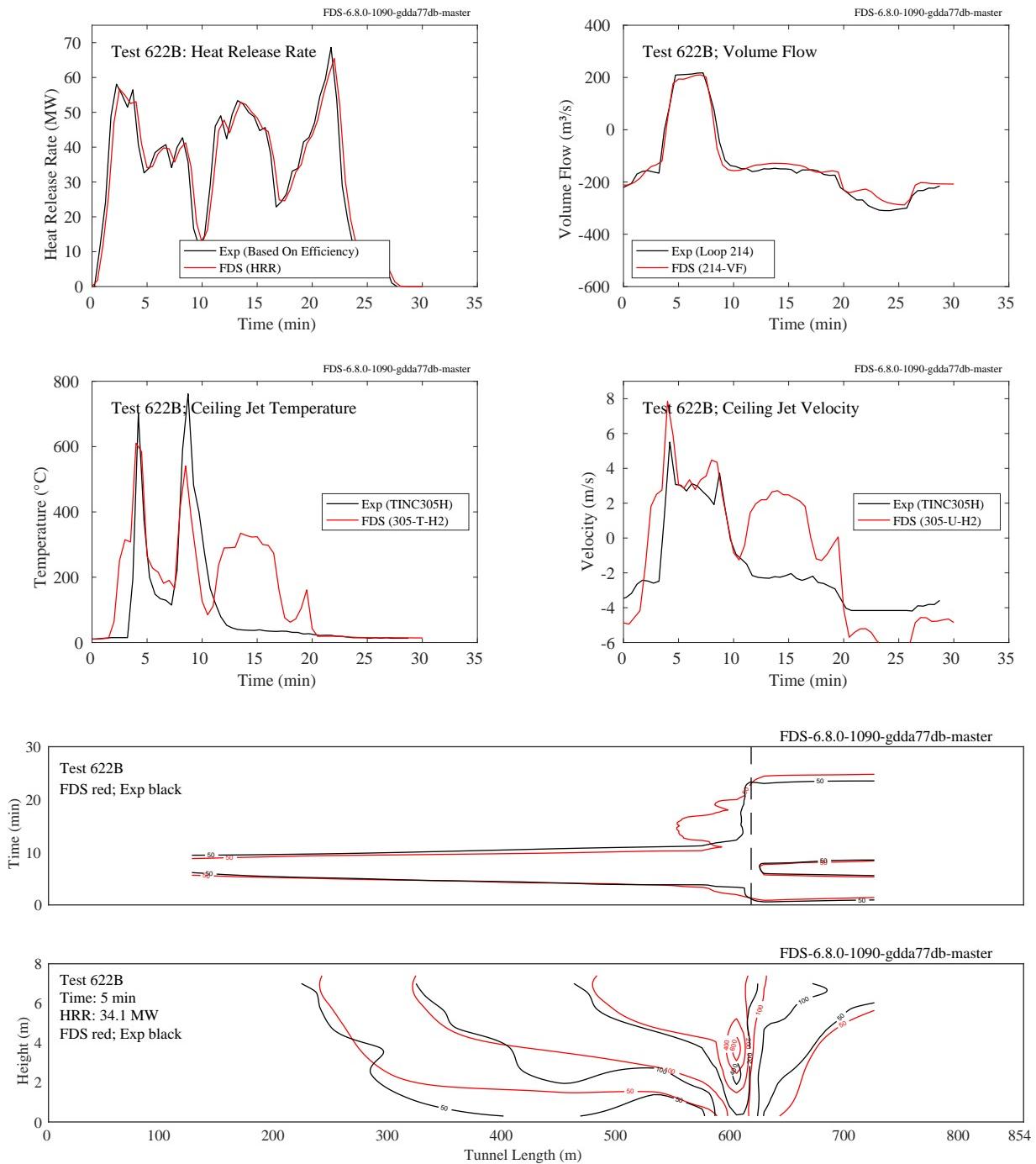


Figure 7.81: Summary of Memorial Tunnel Test 622B. The measured and specified heat release rates are shown in the upper left figure. The measured and predicted volume flows through the North Portal are shown in the upper right. Note that a positive value denotes a flow direction from south to north, against the direction of the fan flow. The Ceiling Jet Temperature shown in the left figure of the second row is taken near the ceiling at Loops 305 and 306, 10 m and 30 m uphill of the fire. The Ceiling Jet Velocity, second row right, is taken near the ceiling at Loop 305, 10 m uphill of the fire. The third row figure indicates the location of the 50 °C near-ceiling temperature as a function of time. The last plot displays measured and predicted temperature contours along the vertical centerline plane.

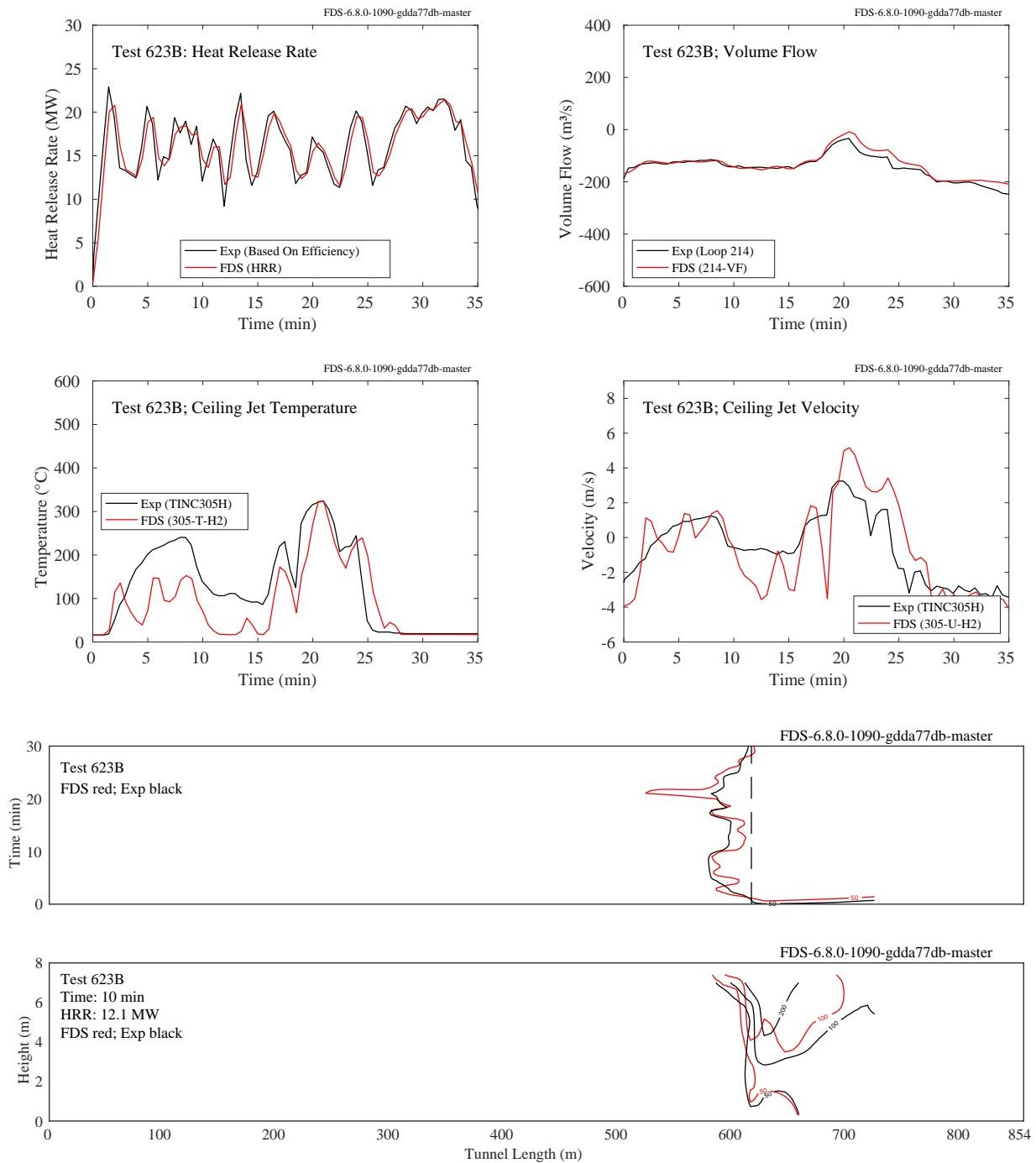


Figure 7.82: Summary of Memorial Tunnel Test 623B. The measured and specified heat release rates are shown in the upper left figure. The measured and predicted volume flows through the North Portal are shown in the upper right. Note that a positive value denotes a flow direction from south to north, against the direction of the fan flow. The Ceiling Jet Temperature shown in the left figure of the second row is taken near the ceiling at Loops 305 and 306, 10 m and 30 m uphill of the fire. The Ceiling Jet Velocity, second row right, is taken near the ceiling at Loop 305, 10 m uphill of the fire. The third row figure indicates the location of the 50 °C near-ceiling temperature as a function of time. The last plot displays measured and predicted temperature contours along the vertical centerline plane.

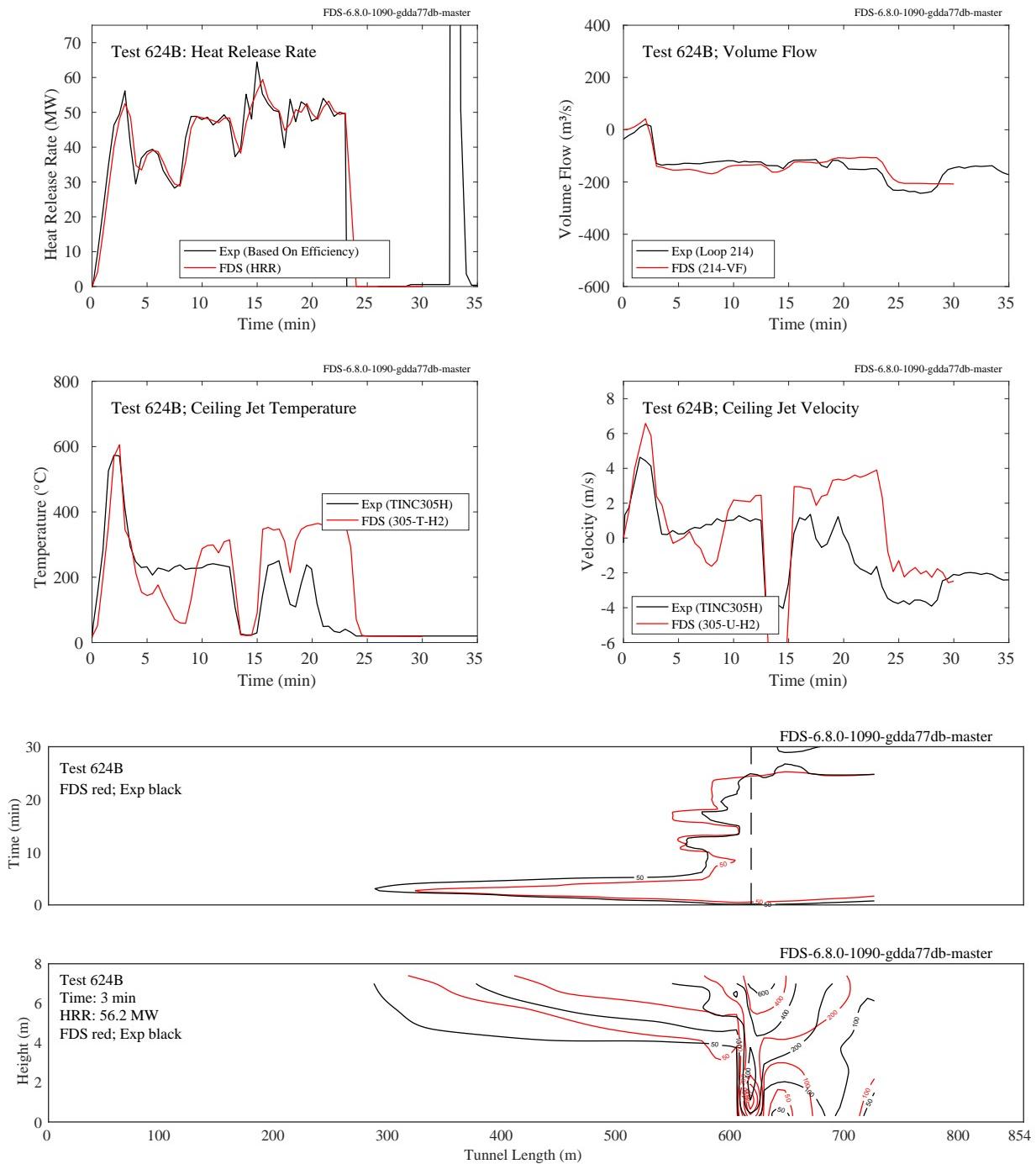


Figure 7.83: Summary of Memorial Tunnel Test 624B. The measured and specified heat release rates are shown in the upper left figure. The measured and predicted volume flows through the North Portal are shown in the upper right. Note that a positive value denotes a flow direction from south to north, against the direction of the fan flow. The Ceiling Jet Temperature shown in the left figure of the second row is taken near the ceiling at Loops 305 and 306, 10 m and 30 m uphill of the fire. The Ceiling Jet Velocity, second row right, is taken near the ceiling at Loop 305, 10 m uphill of the fire. The third row figure indicates the location of the  $50^{\circ}\text{C}$  near-ceiling temperature as a function of time. The last plot displays measured and predicted temperature contours along the vertical centerline plane.

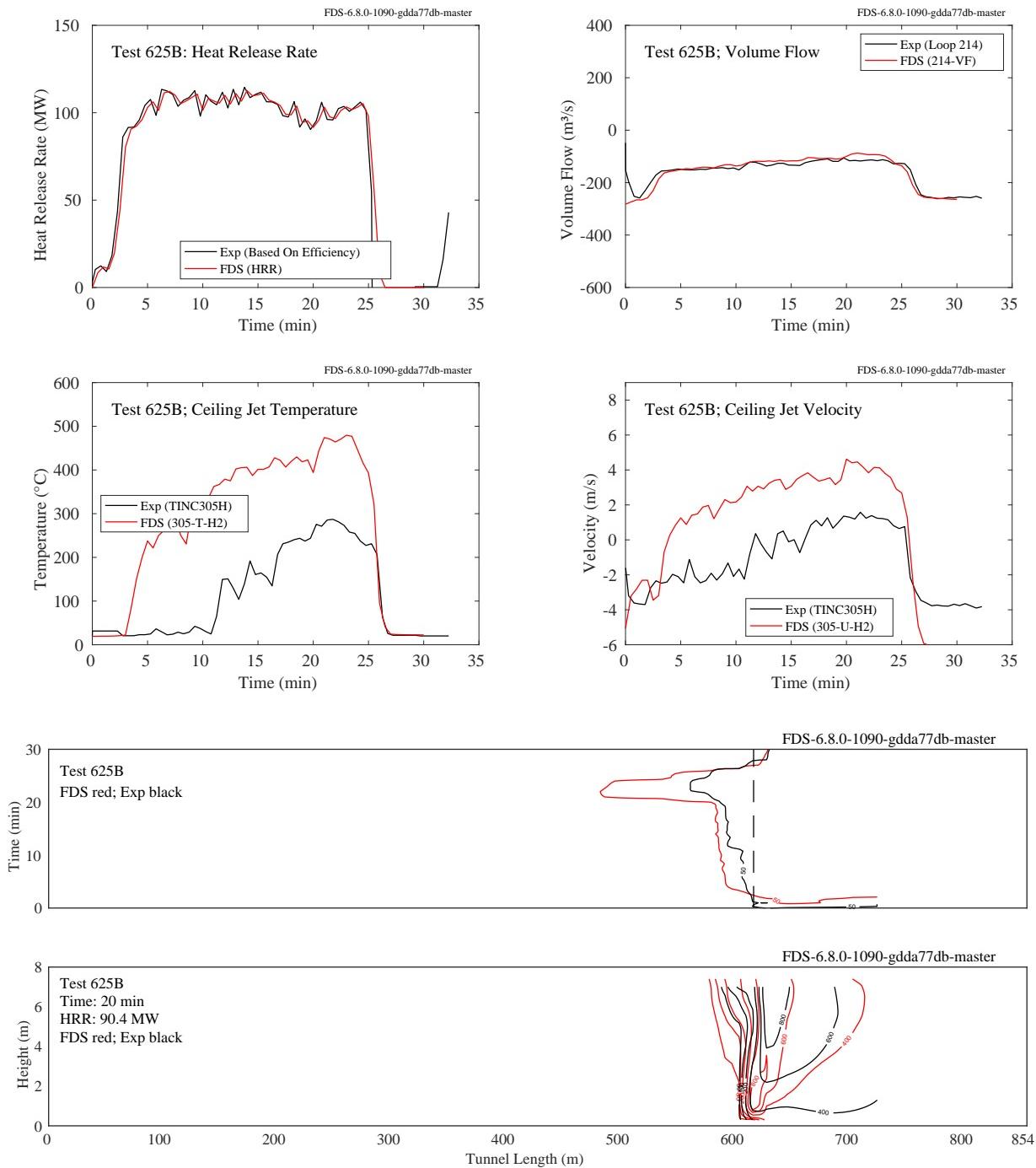


Figure 7.84: Summary of Memorial Tunnel Test 625B. The measured and specified heat release rates are shown in the upper left figure. The measured and predicted volume flows through the North Portal are shown in the upper right. Note that a positive value denotes a flow direction from south to north, against the direction of the fan flow. The Ceiling Jet Temperature shown in the left figure of the second row is taken near the ceiling at Loops 305 and 306, 10 m and 30 m uphill of the fire. The Ceiling Jet Velocity, second row right, is taken near the ceiling at Loop 305, 10 m uphill of the fire. The third row figure indicates the location of the  $50^{\circ}\text{C}$  near-ceiling temperature as a function of time. The last plot displays measured and predicted temperature contours along the vertical centerline plane.

The plots on the following pages show the results of the transverse ventilation cases. Only the extent of the back-layering is shown.

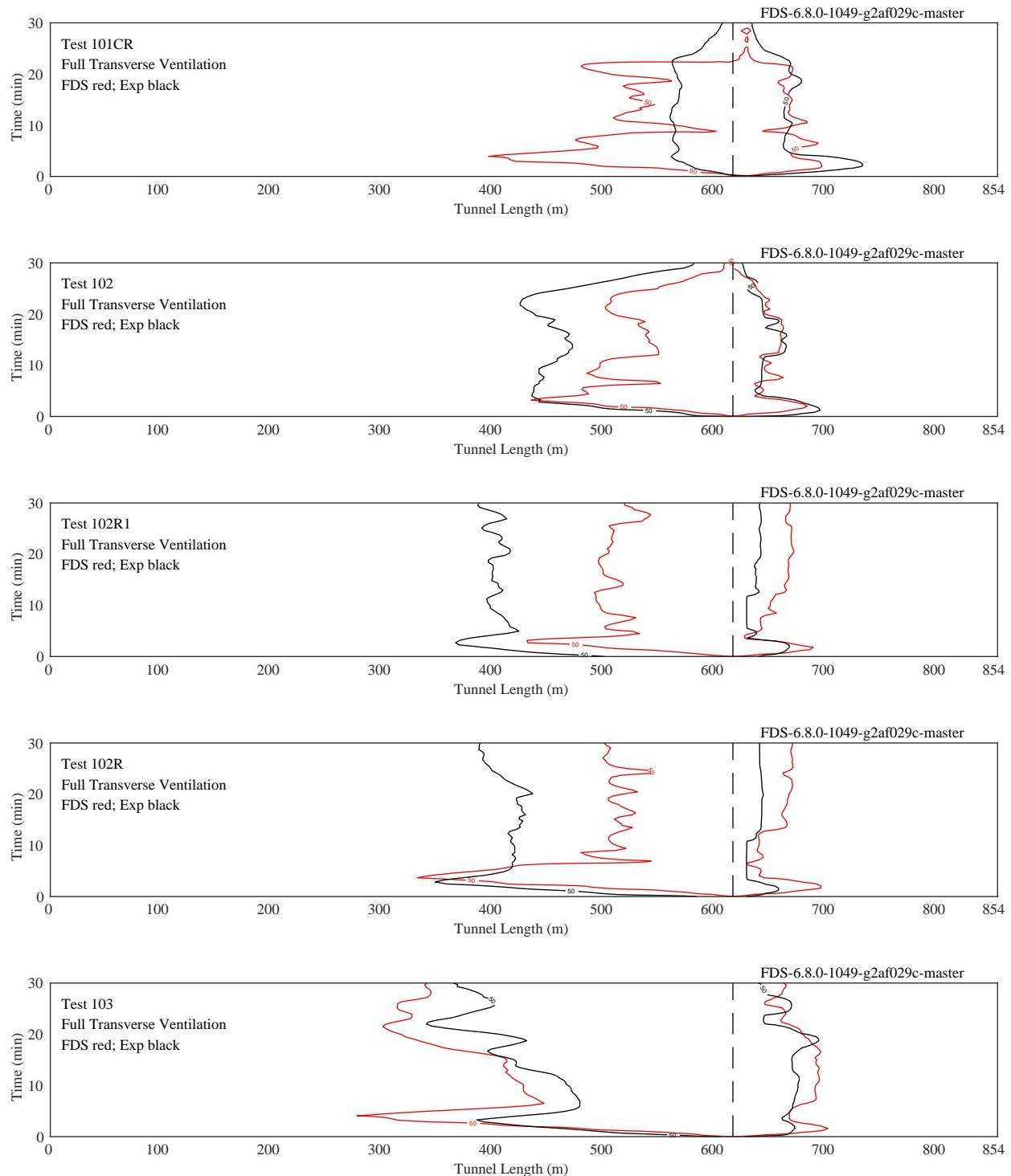


Figure 7.85: Back-layer, Full Transverse Ventilation, Sequence 1. The air is supplied by the south portal fans along the entire length of the tunnel at road level on the west curb. Air is exhausted by the north portal fans along the entire length of the tunnel through the east side ceiling vents.

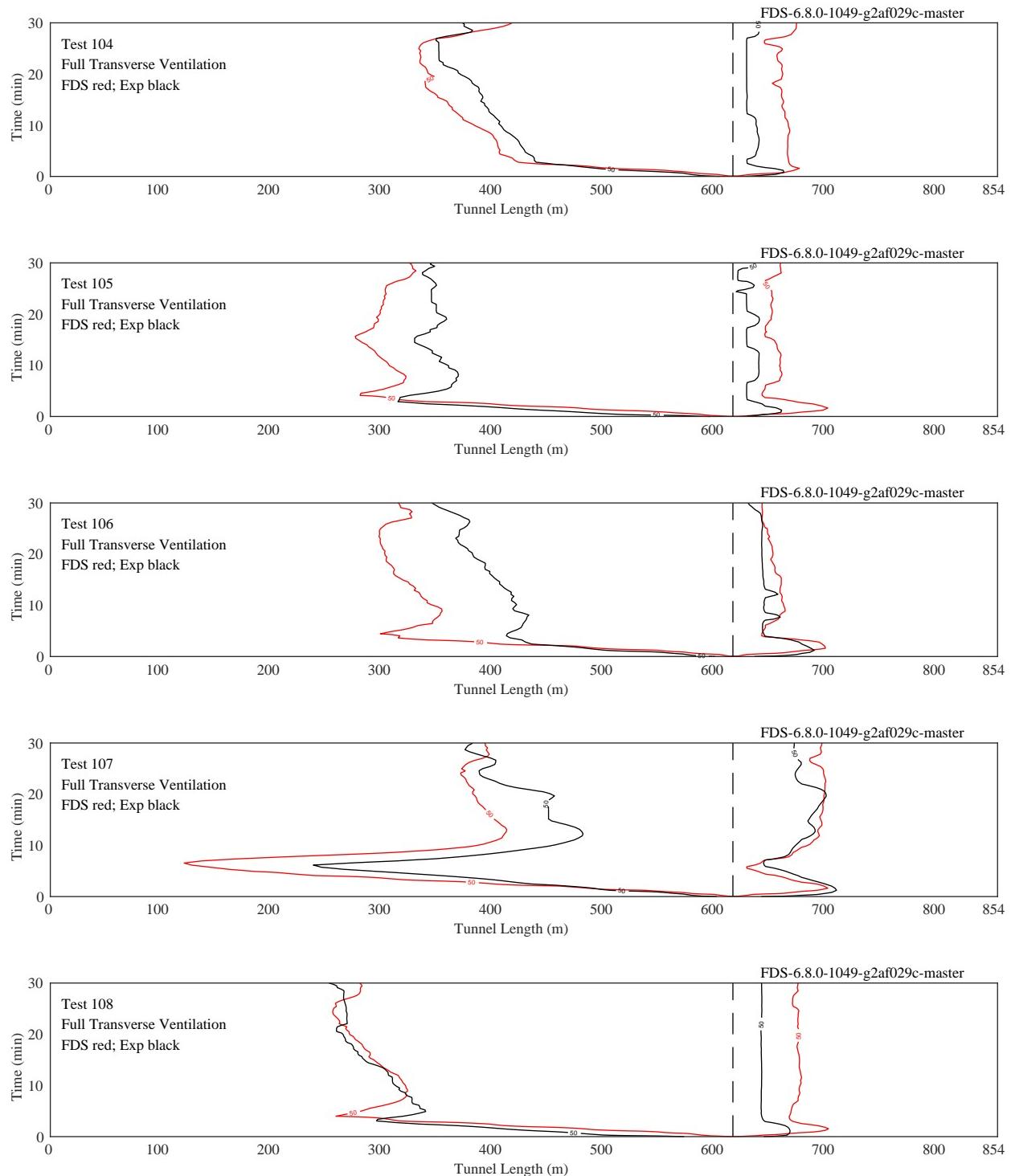


Figure 7.86: Back-layer, Full Transverse Ventilation, Sequence 1. The air is supplied by the south portal fans along the entire length of the tunnel at road level on the west curb. Air is exhausted by the north portal fans along the entire length of the tunnel through the east side ceiling vents.

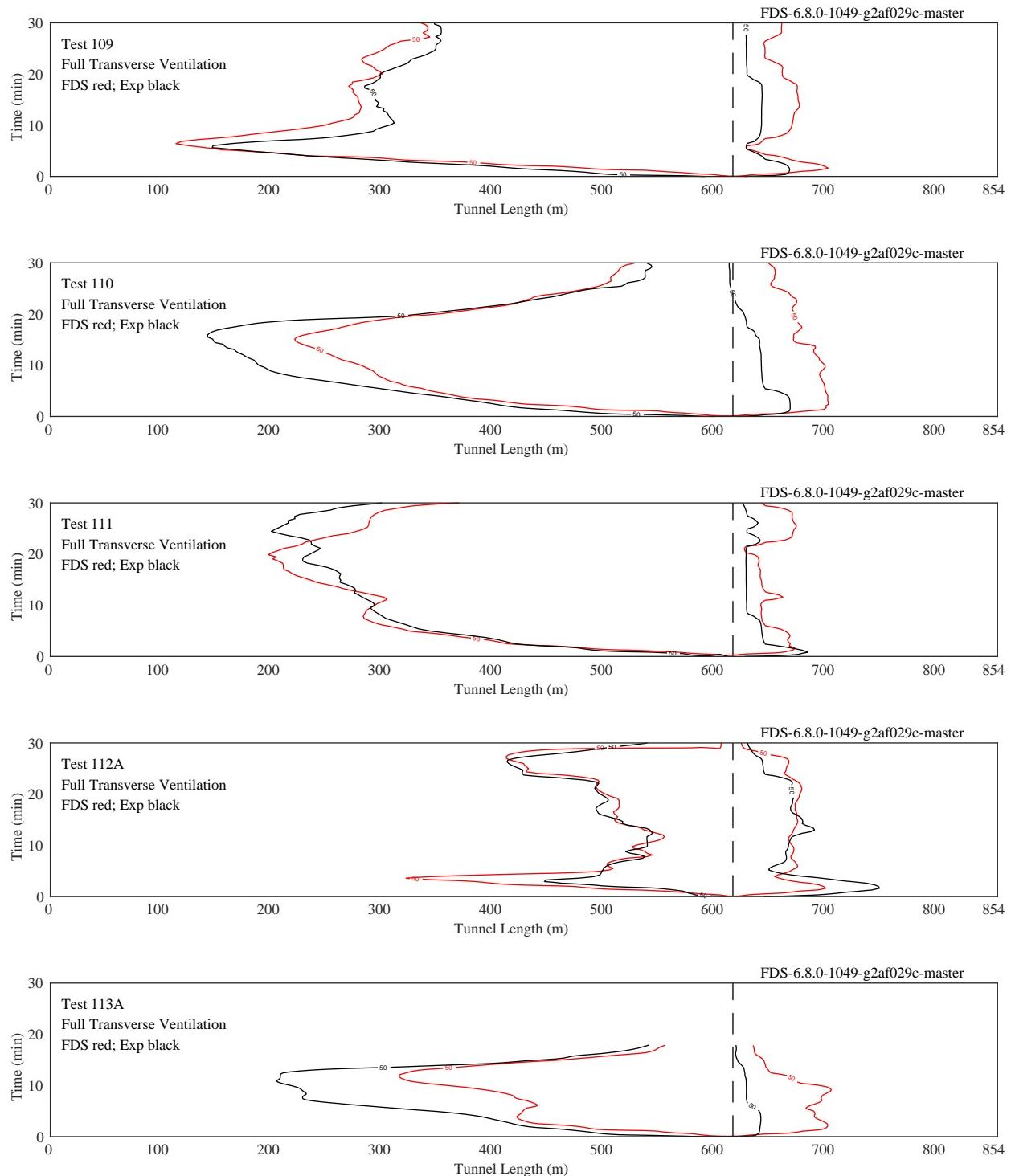


Figure 7.87: Back-layer, Full Transverse Ventilation, Sequence 1. The air is supplied by the south portal fans along the entire length of the tunnel at road level on the west curb. Air is exhausted by the north portal fans along the entire length of the tunnel through the east side ceiling vents.

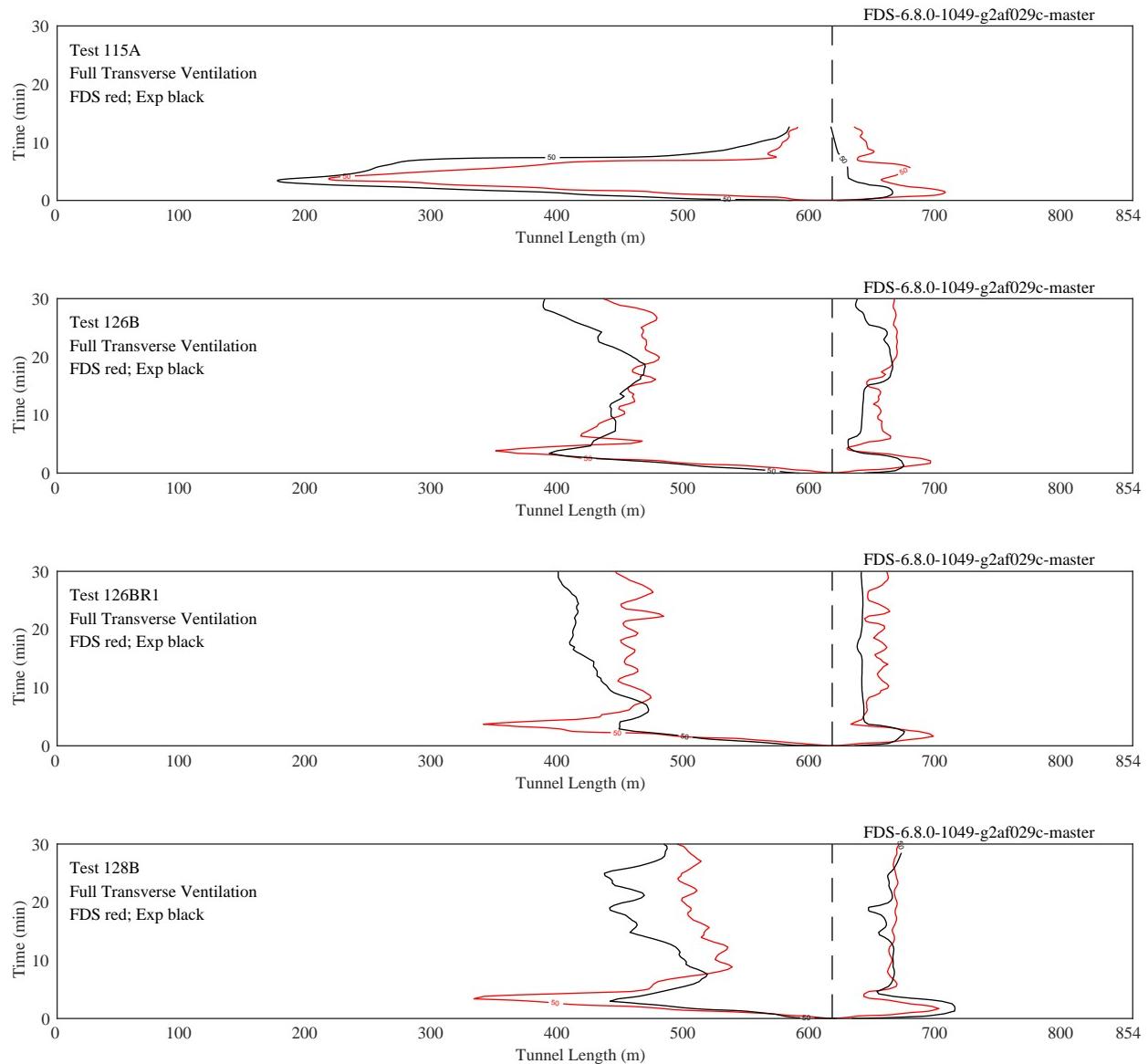


Figure 7.88: Back-layer, Full Transverse Ventilation, Sequence 1. The air is supplied by the south portal fans along the entire length of the tunnel at road level on the west curb. Air is exhausted by the north portal fans along the entire length of the tunnel through the east side ceiling vents.

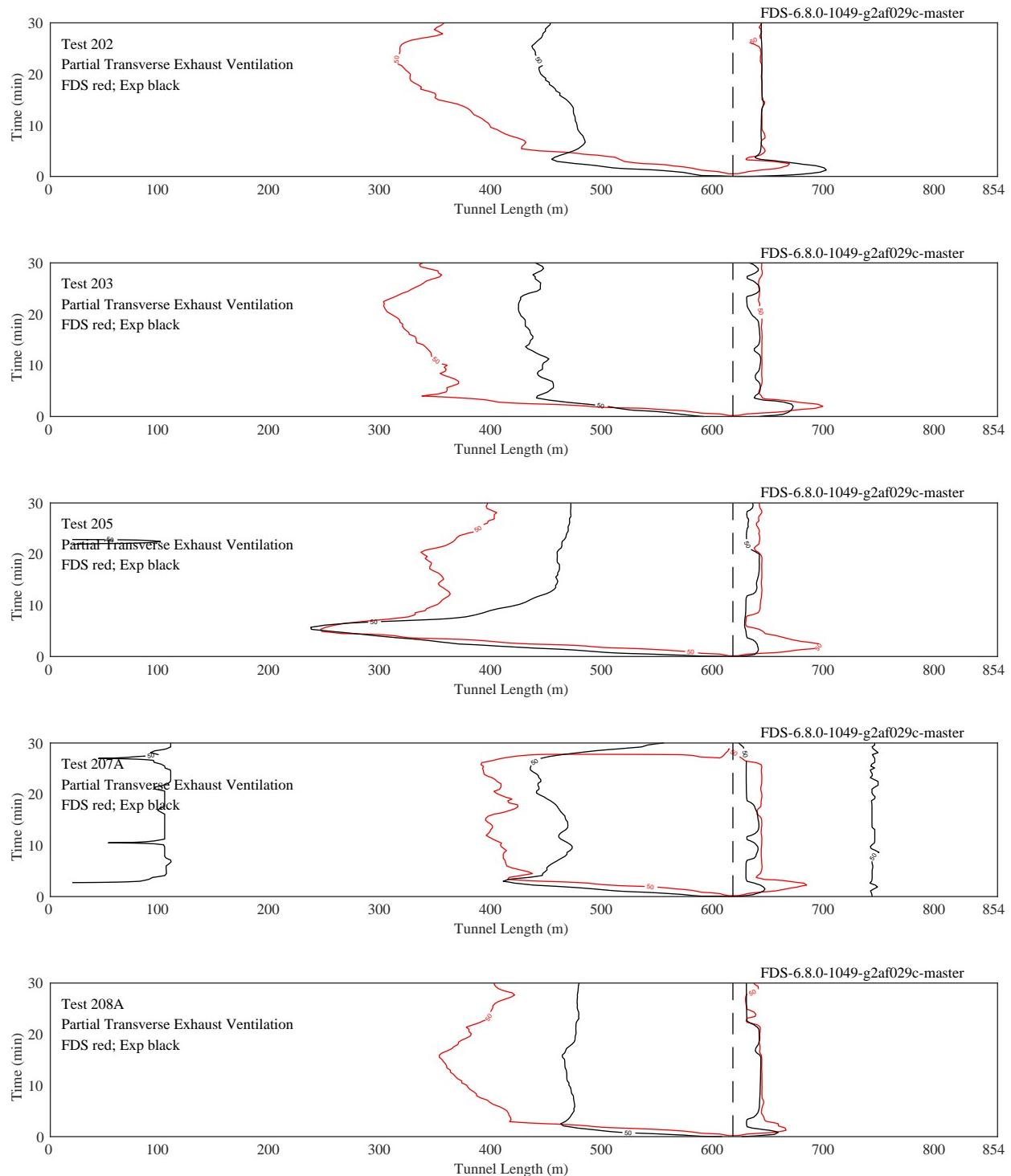


Figure 7.89: Back-layer, Partial Transverse Exhaust Ventilation, Sequence 3. The air is exhausted at the ceiling using both the north and south portal fans.

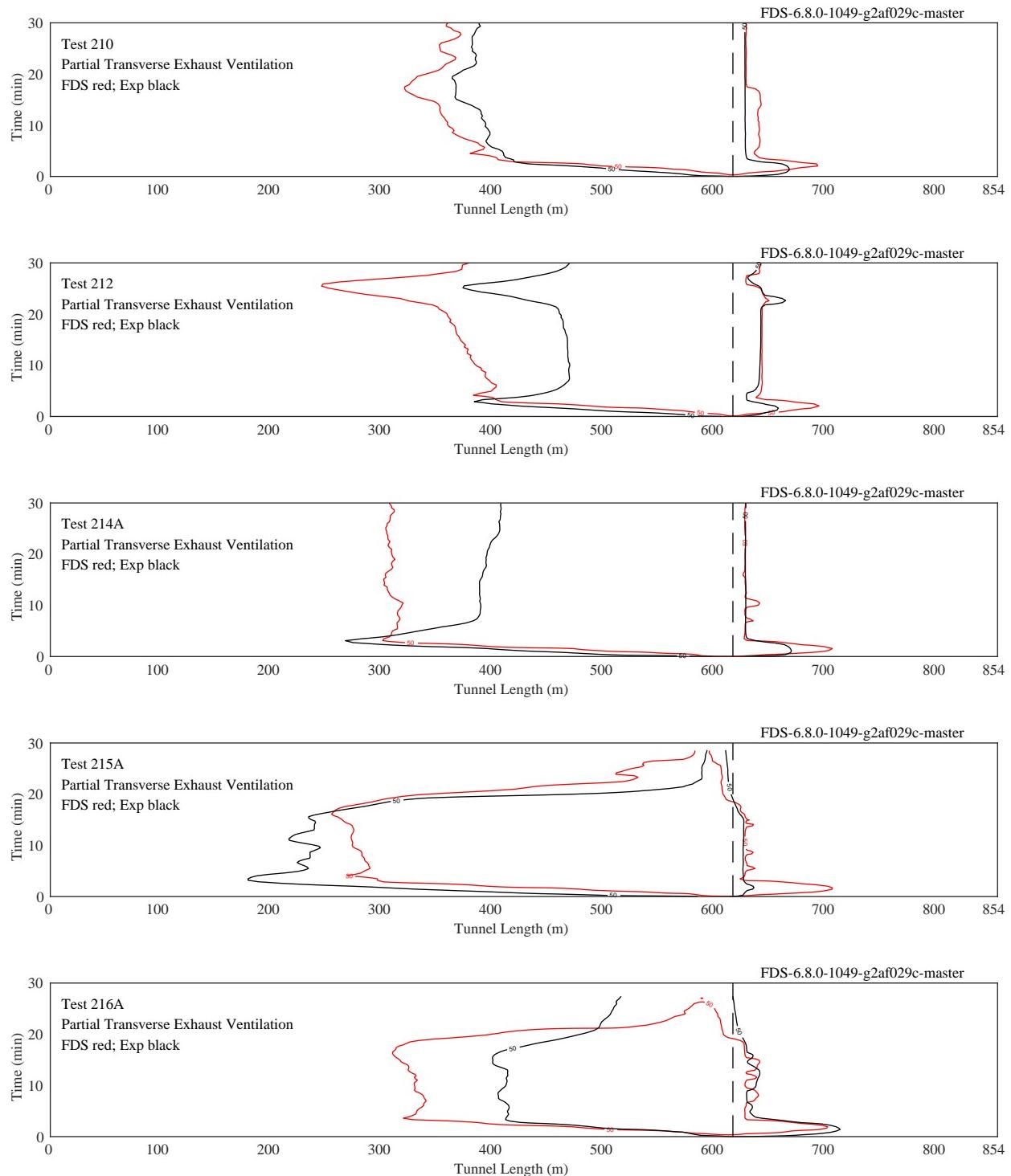


Figure 7.90: Back-layer, Partial Transverse Exhaust Ventilation, Sequence 3. The air is exhausted at the ceiling using both the north and south portal fans.

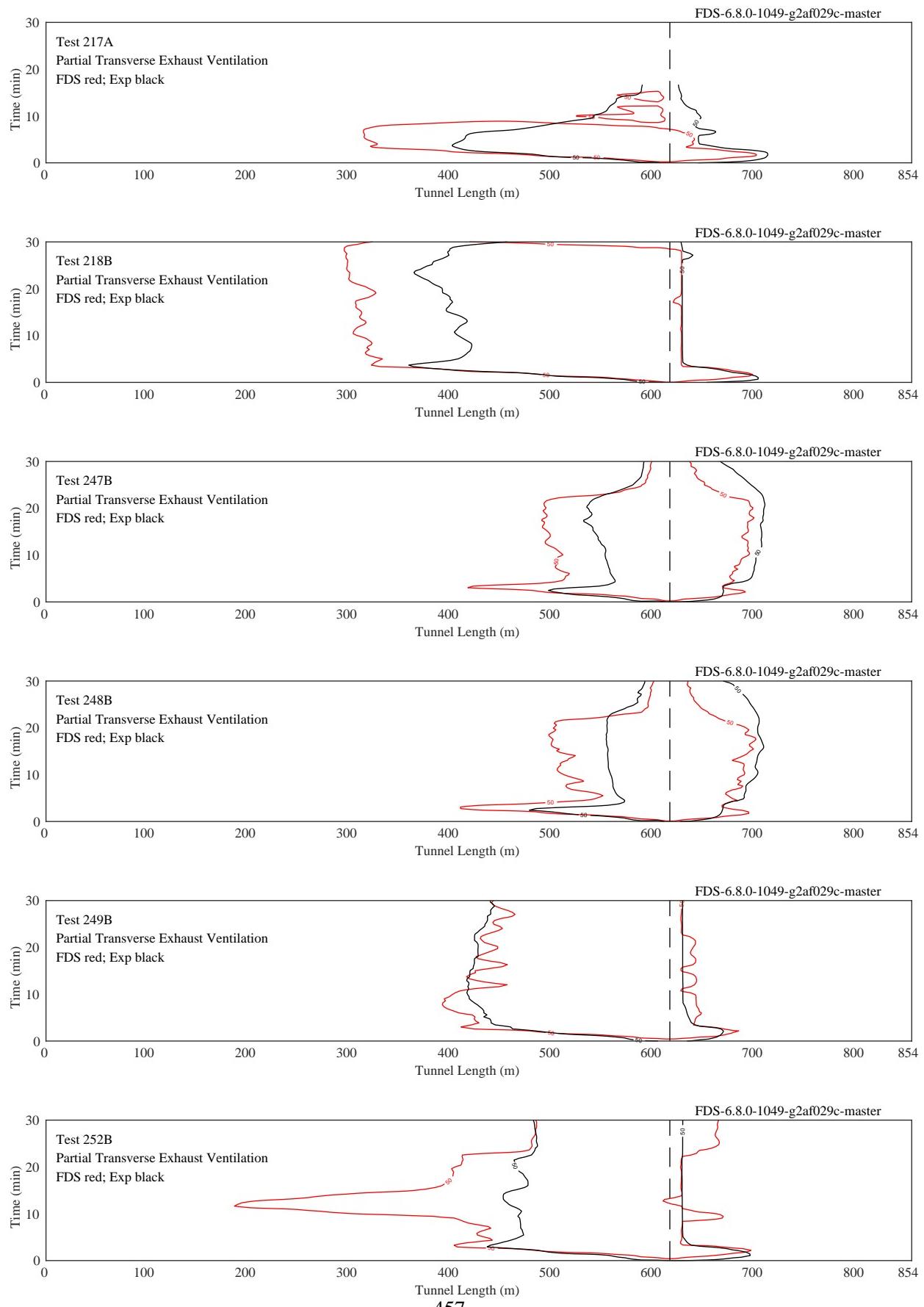


Figure 7.91: Back-layer, Partial Transverse Exhaust Ventilation, Sequence 3. The air is exhausted at the ceiling using both the north and south portal fans.

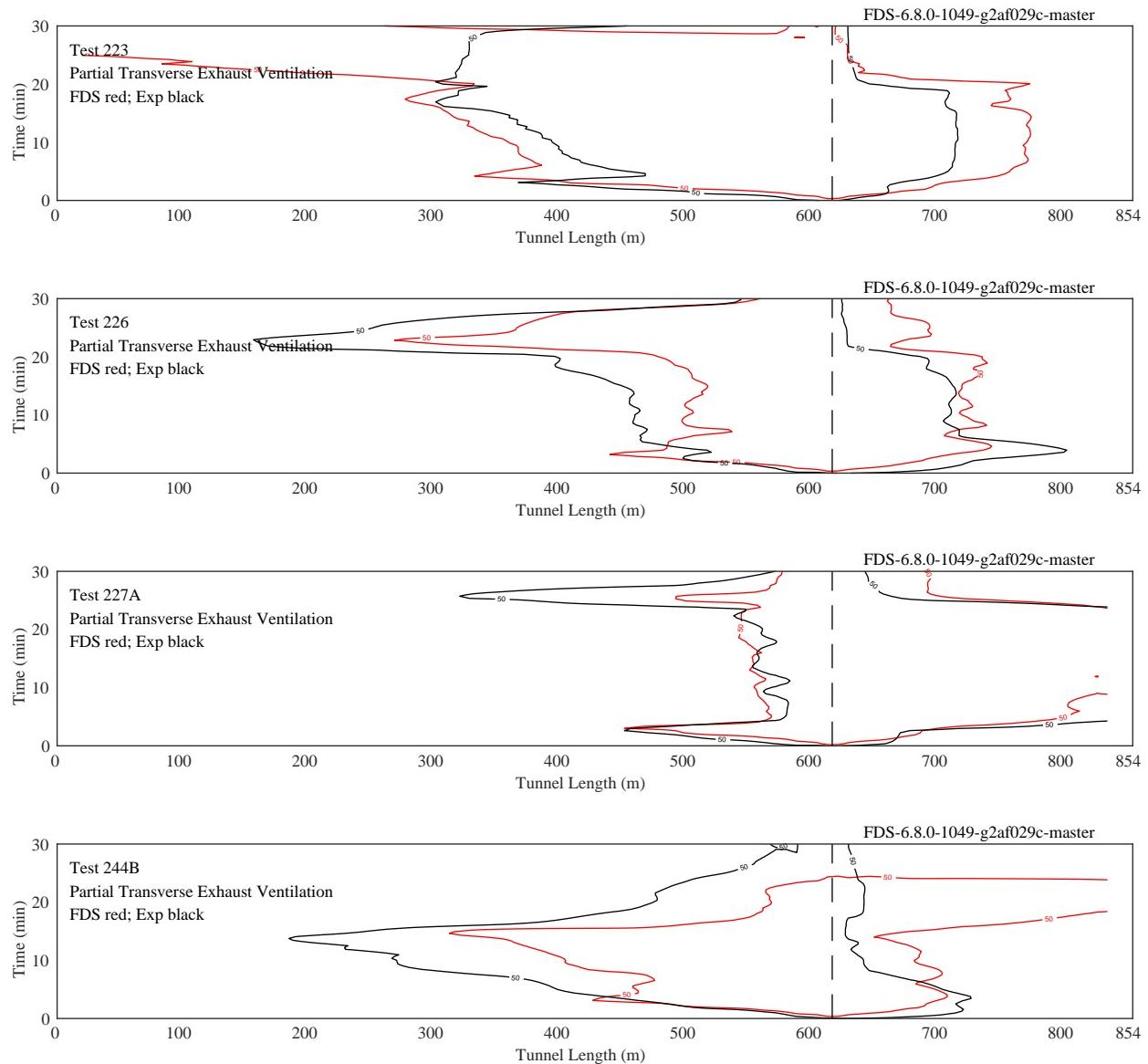


Figure 7.92: Back-layer, Partial Transverse Supply Ventilation, Sequences 4 and 5. For Sequence 4, the air is supplied at the roadway along the west wall. For Sequence 5, the air is supplied at the ceiling.

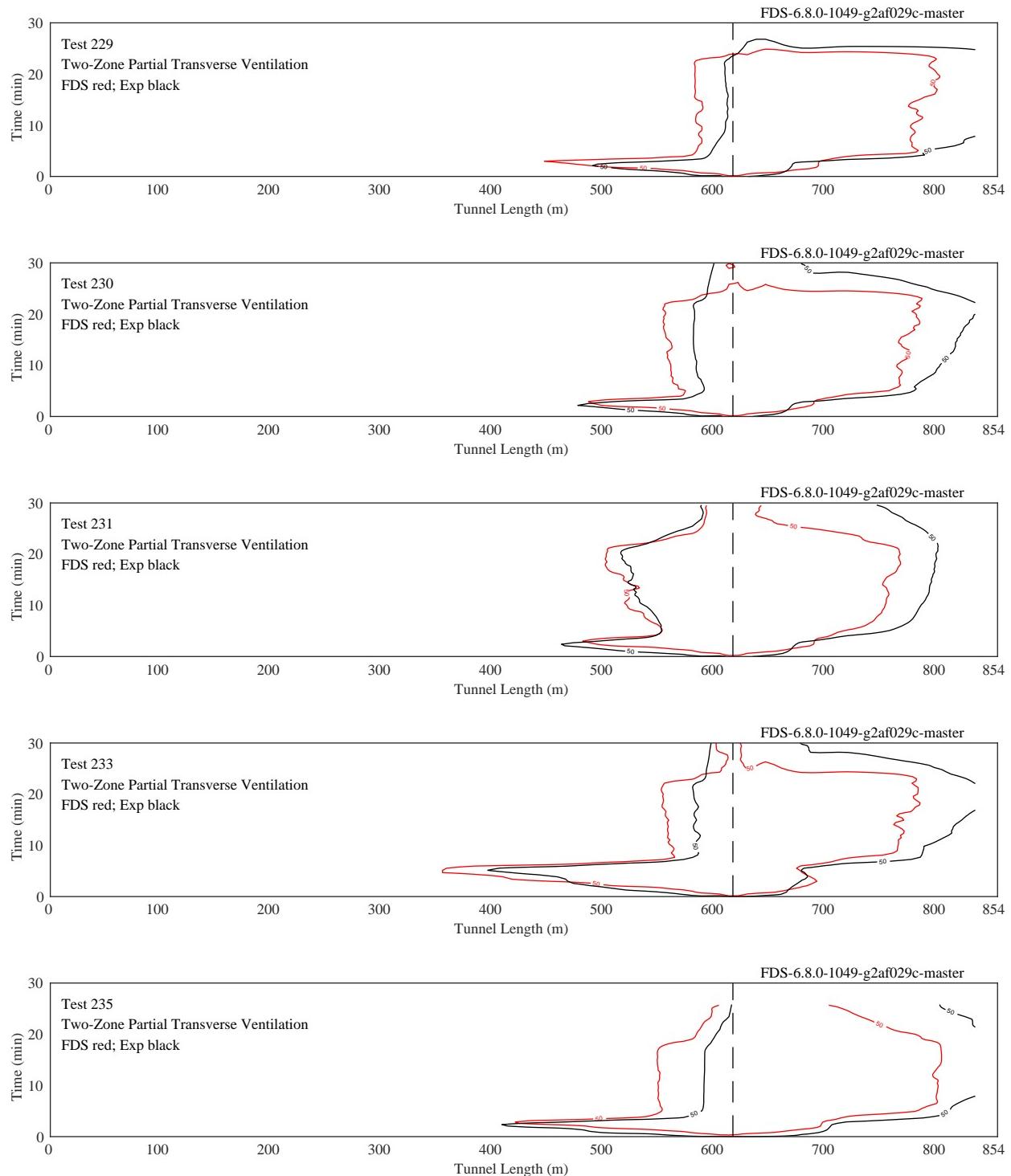


Figure 7.93: Back-layer, Two-Zone Partial Transverse Ventilation, Sequence 6. Air is supplied through the ceiling in the northern half of the tunnel and exhausted through the ceiling in the southern half.

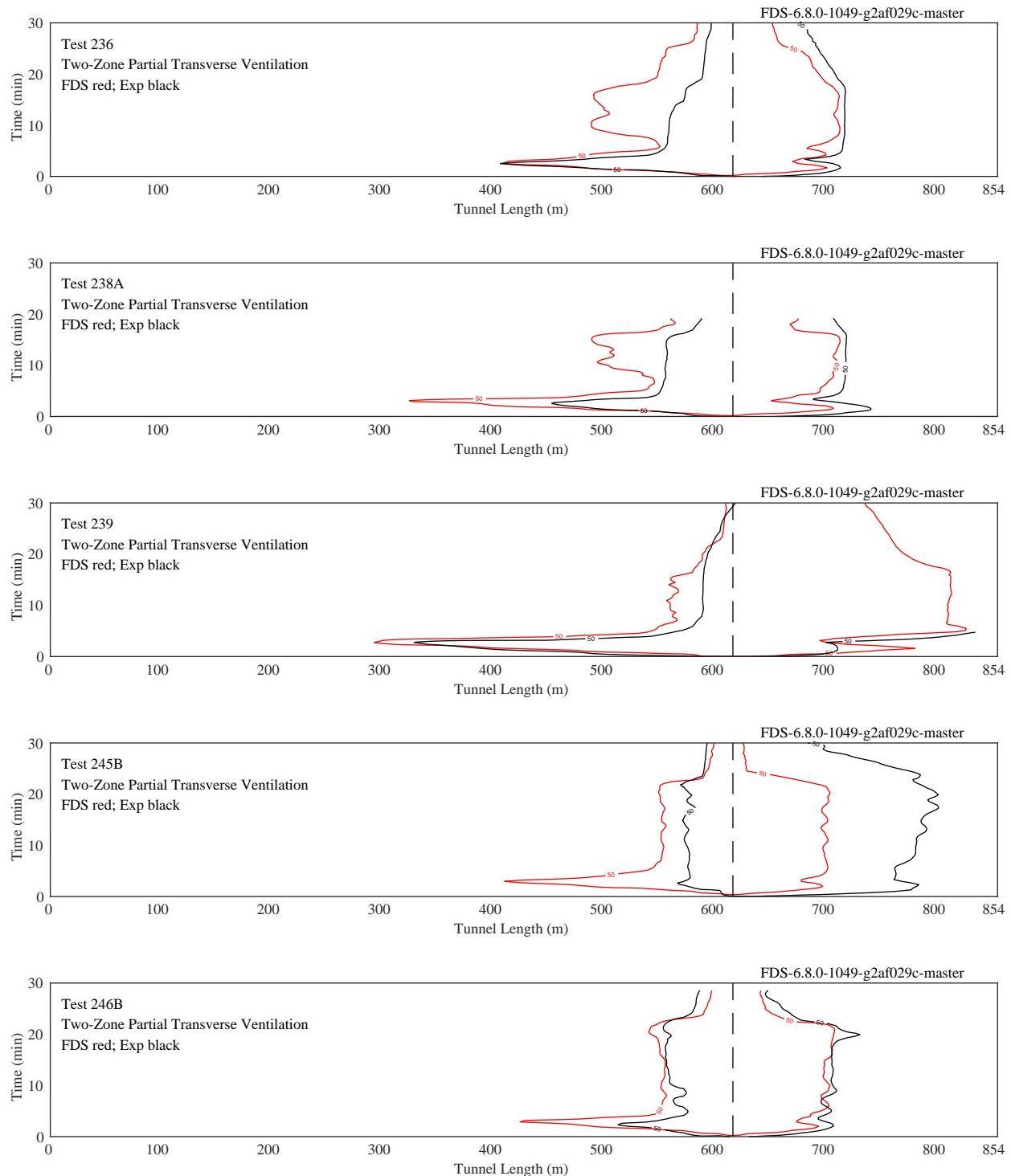


Figure 7.94: Back-layer, Two-Zone Partial Transverse Ventilation, Sequence 6. Air is supplied through the ceiling in the northern half of the tunnel and exhausted through the ceiling in the southern half.

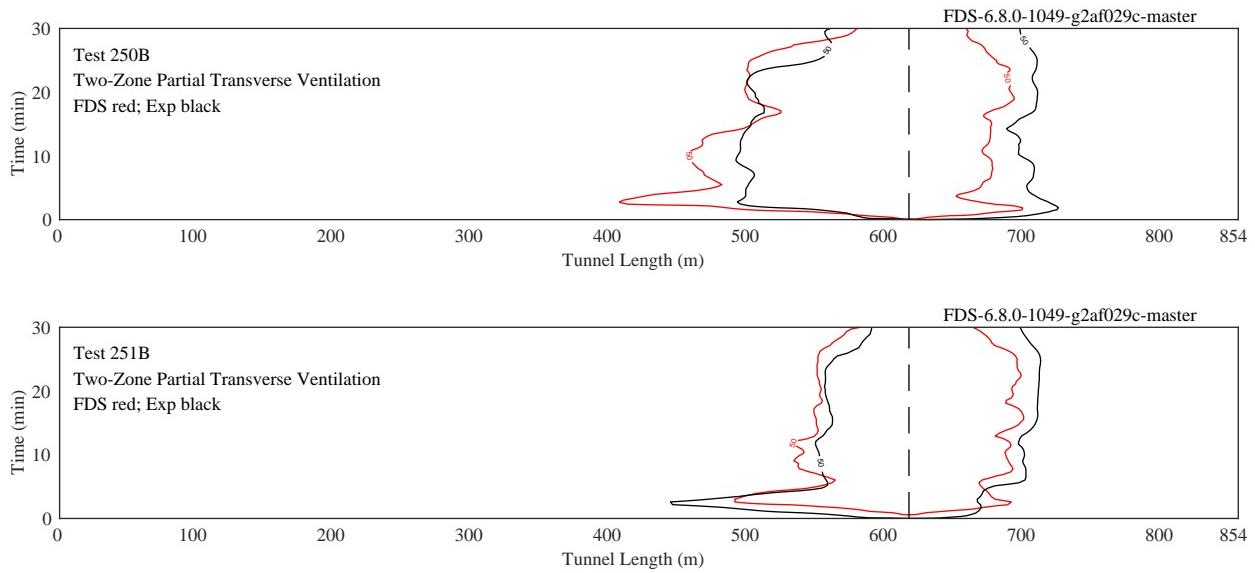


Figure 7.95: Back-layer, Two-Zone Partial Transverse Ventilation, Sequence 6. Air is supplied through the ceiling in the northern half of the tunnel and exhausted through the ceiling in the southern half.

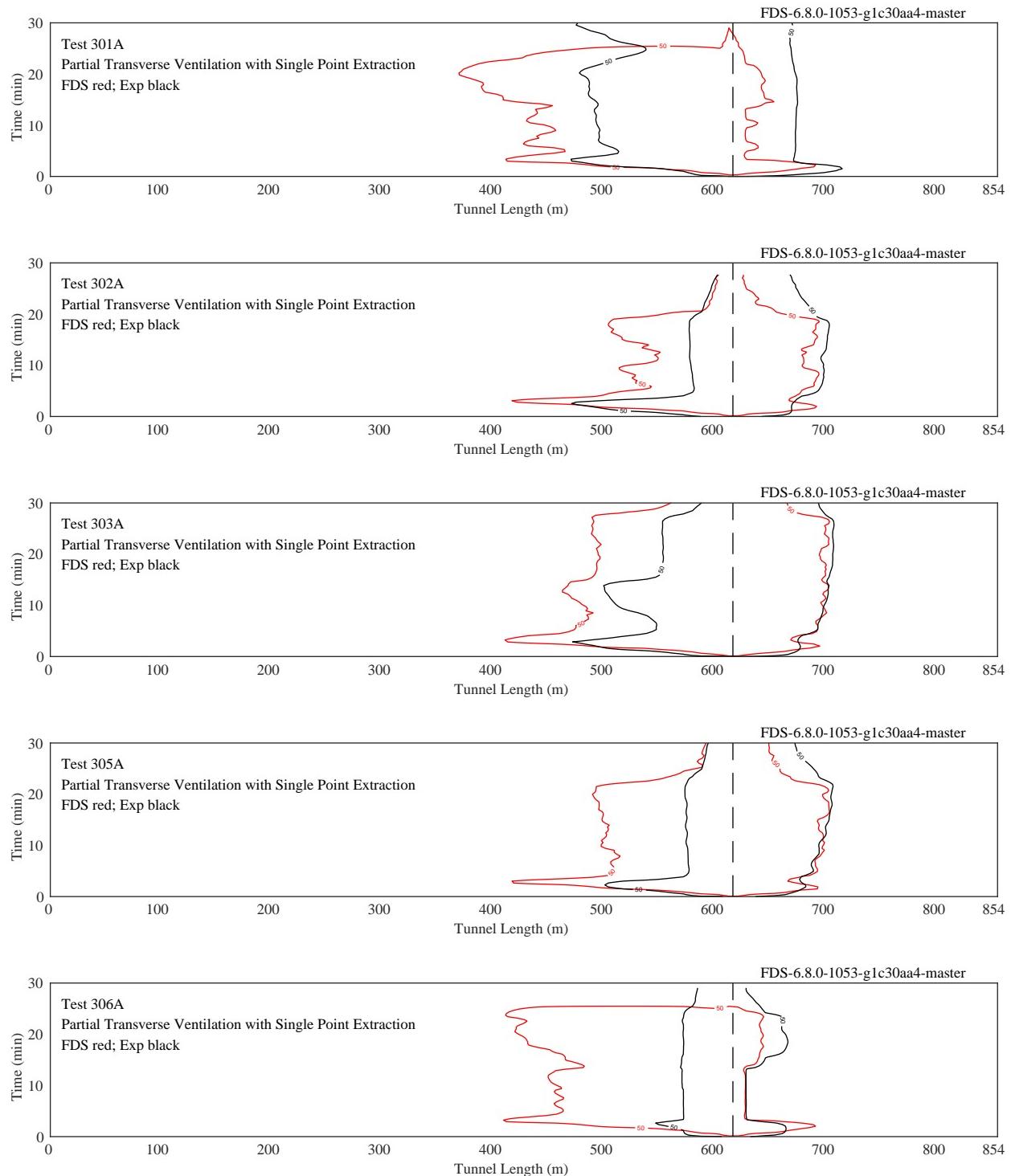


Figure 7.96: Back-layer, Partial Transverse Ventilation with Single Point Extraction, Sequence 8. Air exhausted through the ceiling, which includes an extra large port.

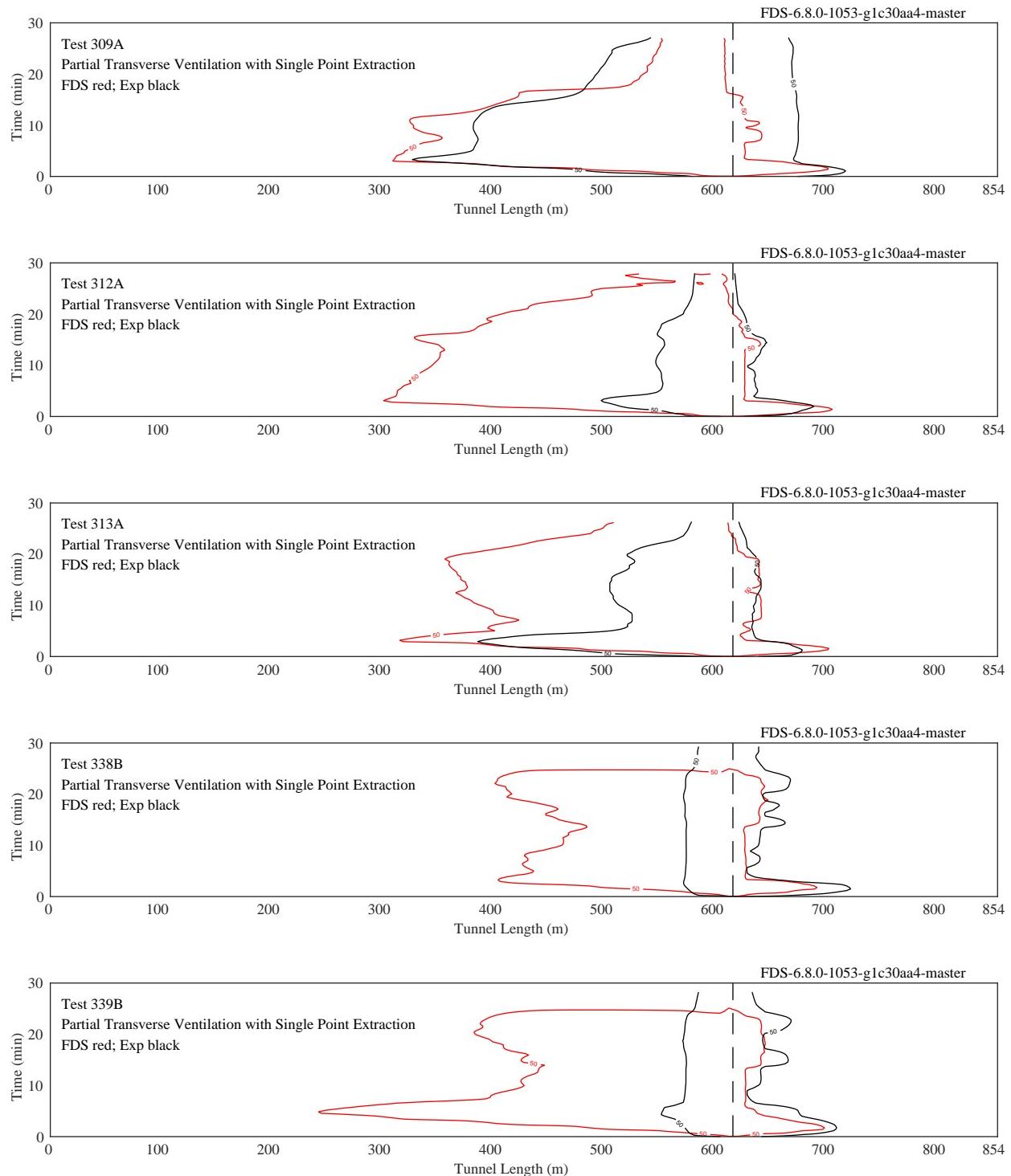


Figure 7.97: Back-layer, Partial Transverse Ventilation with Single Point Extraction, Sequence 8. Air exhausted through the ceiling, which includes an extra large port.

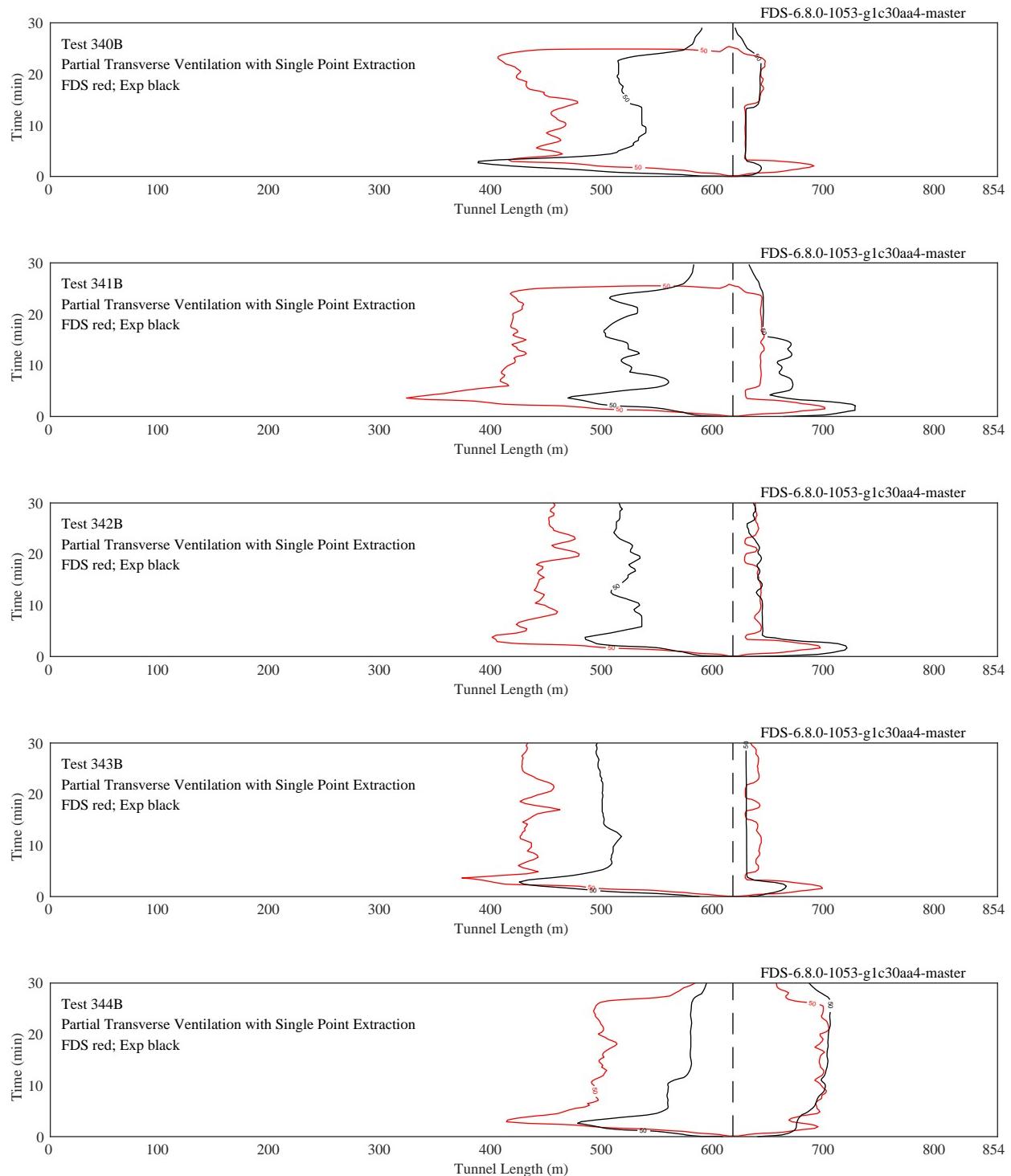


Figure 7.98: Back-layer, Partial Transverse Ventilation with Single Point Extraction, Sequence 8. Air exhausted through the ceiling, which includes an extra large port.

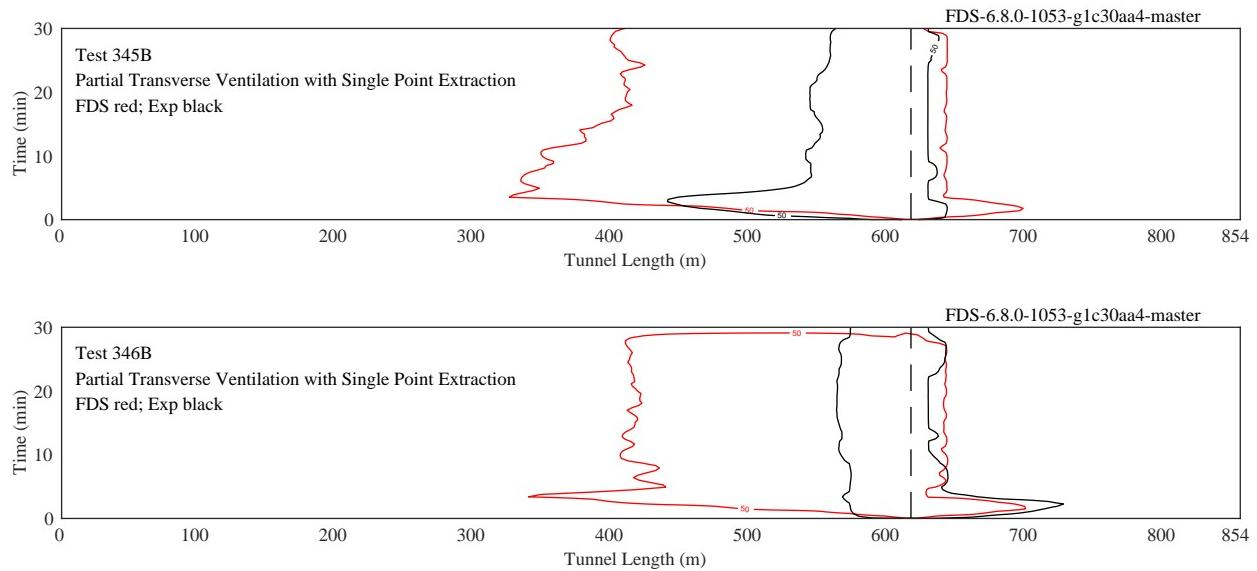


Figure 7.99: Back-layer, Partial Transverse Ventilation with Single Point Extraction, Sequence 8. Air exhausted through the ceiling, which includes an extra large port.

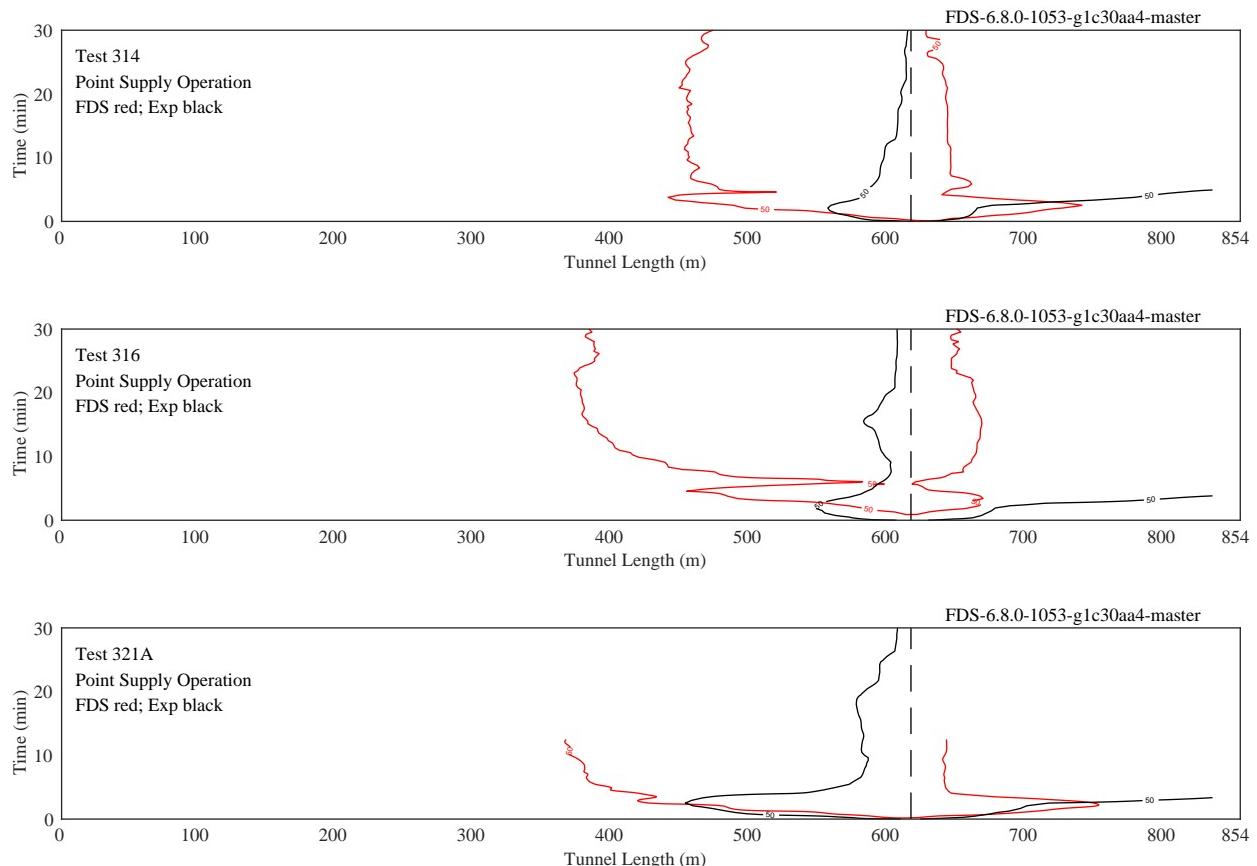


Figure 7.100: Back-layer, Point Supply Operation, Sequence 9. Air is supplied through a single large ceiling vent.

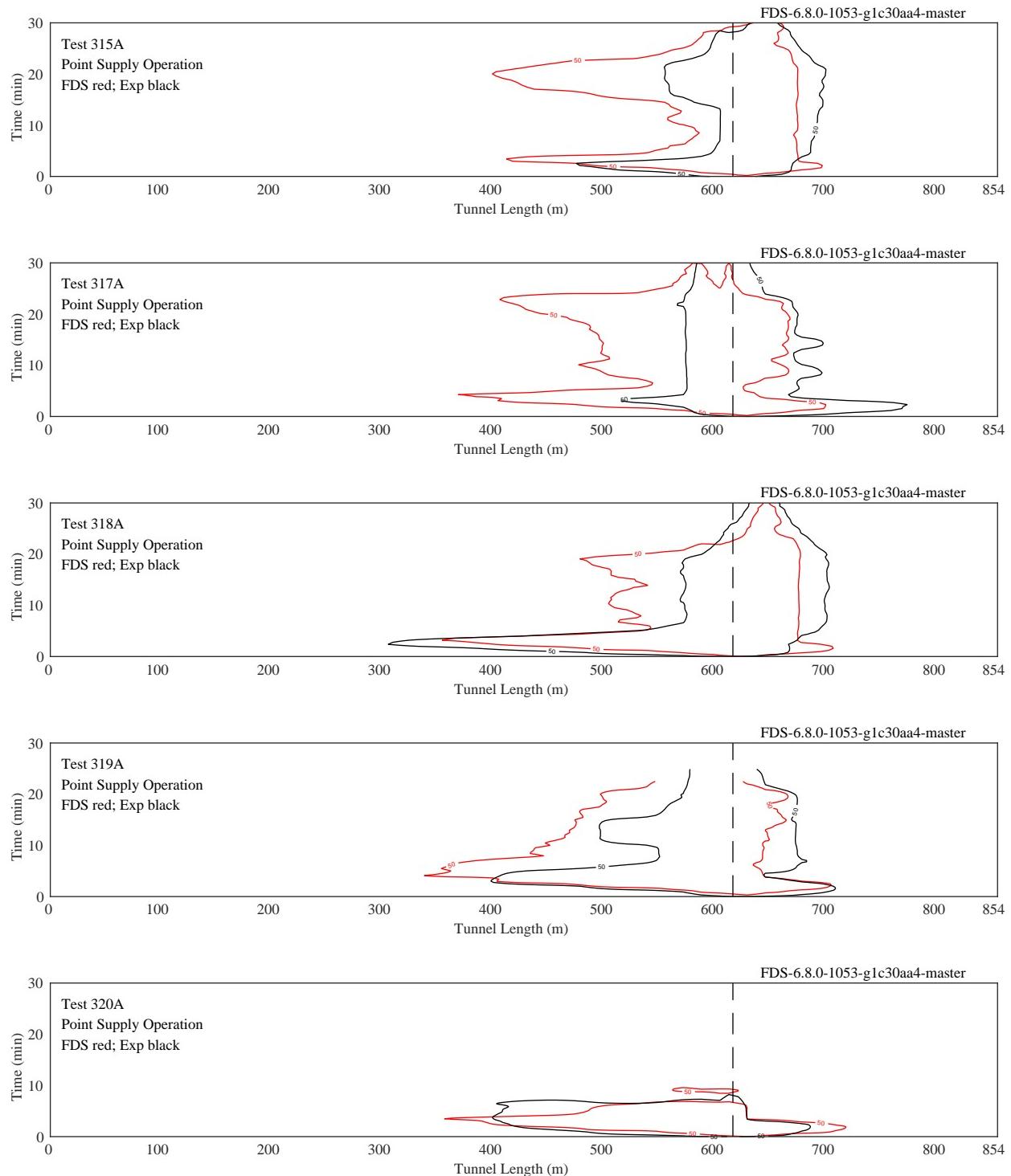


Figure 7.101: Back-layer, Point Exhaust Operation, Sequence 10. Air is exhausted through a single large ceiling vent.

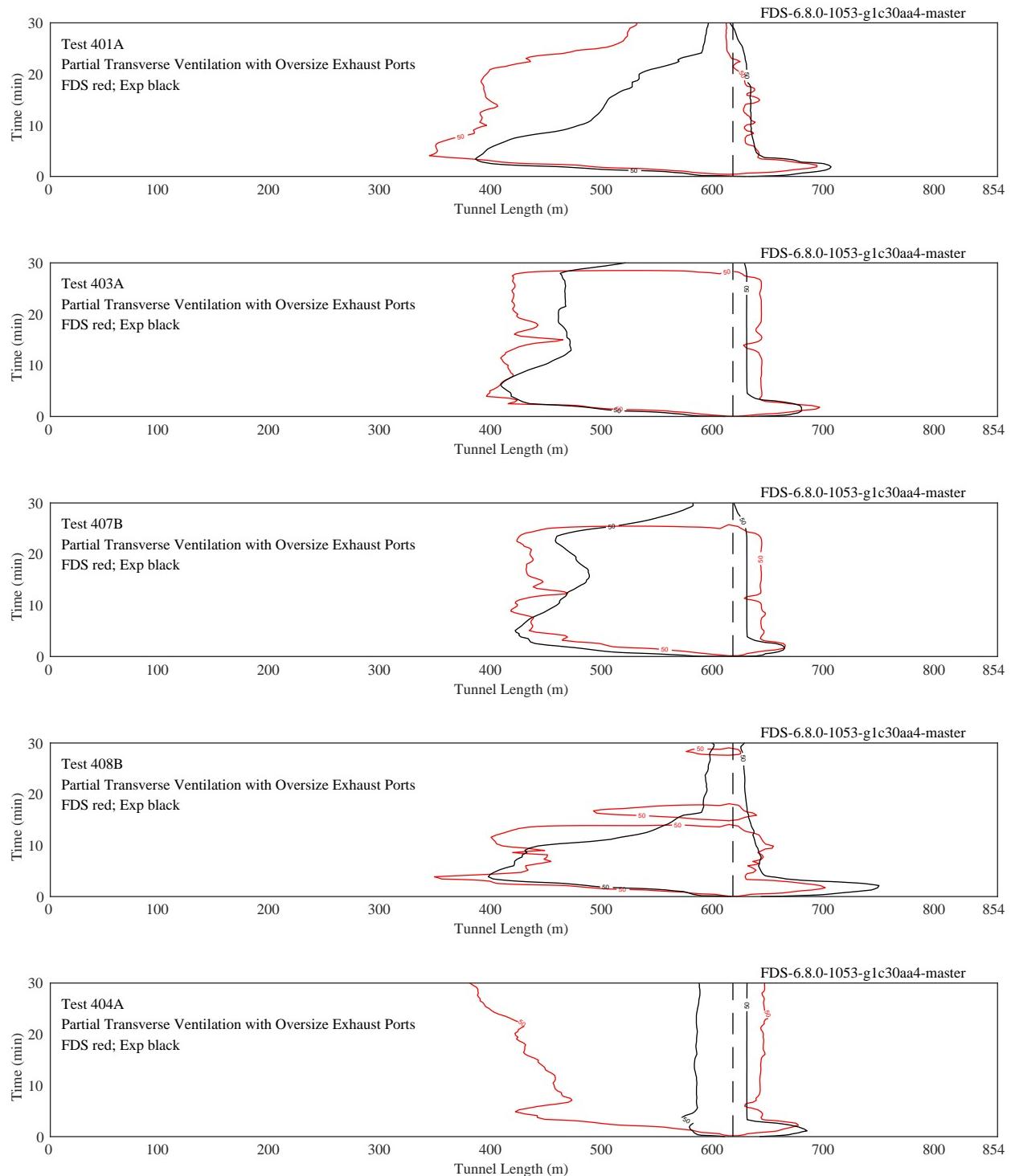


Figure 7.102: Back-layer, Partial Transverse Ventilation with Oversize Exhaust Ports, Sequence 13 and 14. Air is exhausted through ceiling vents and extra large openings.

### 7.4.3 FHWA Tunnel Experiments

The figures on the following pages summarize the results of 11 simulations of reduced-scale tunnel fire experiments conducted at the Institute für Angewandte Brandschutzforschung (IFAB), Germany. For each experiment, the measured heat release rate (HRR) is shown. The HRR was measured using a load cell and using oxygen consumption calorimetry. When available, the load cell data was used in the simulations. The plots make clear which measurement was used.

The plots to the right of each figure indicate where a near-ceiling temperature of 50 °C is located, as interpolated from the measurements made just below the ceiling. The fire location is designated with the vertical dashed line. The ventilation flow is from left to right; thus, backlayering is indicated when the location of the 50 °C contour falls to the left of the dashed vertical line.

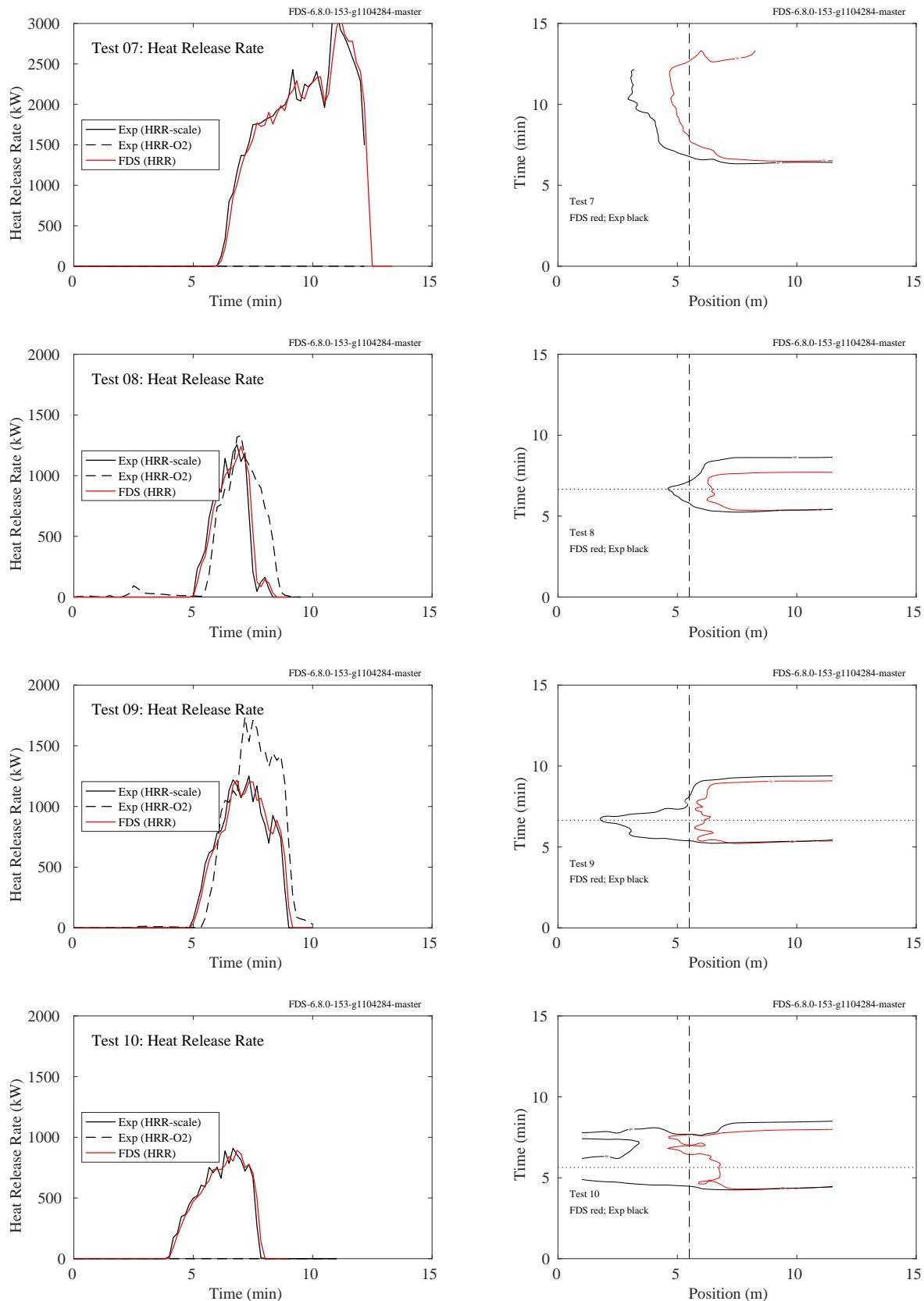


Figure 7.103: Summary of FHWA Tunnel experiments 7, 8, 9 and 10.

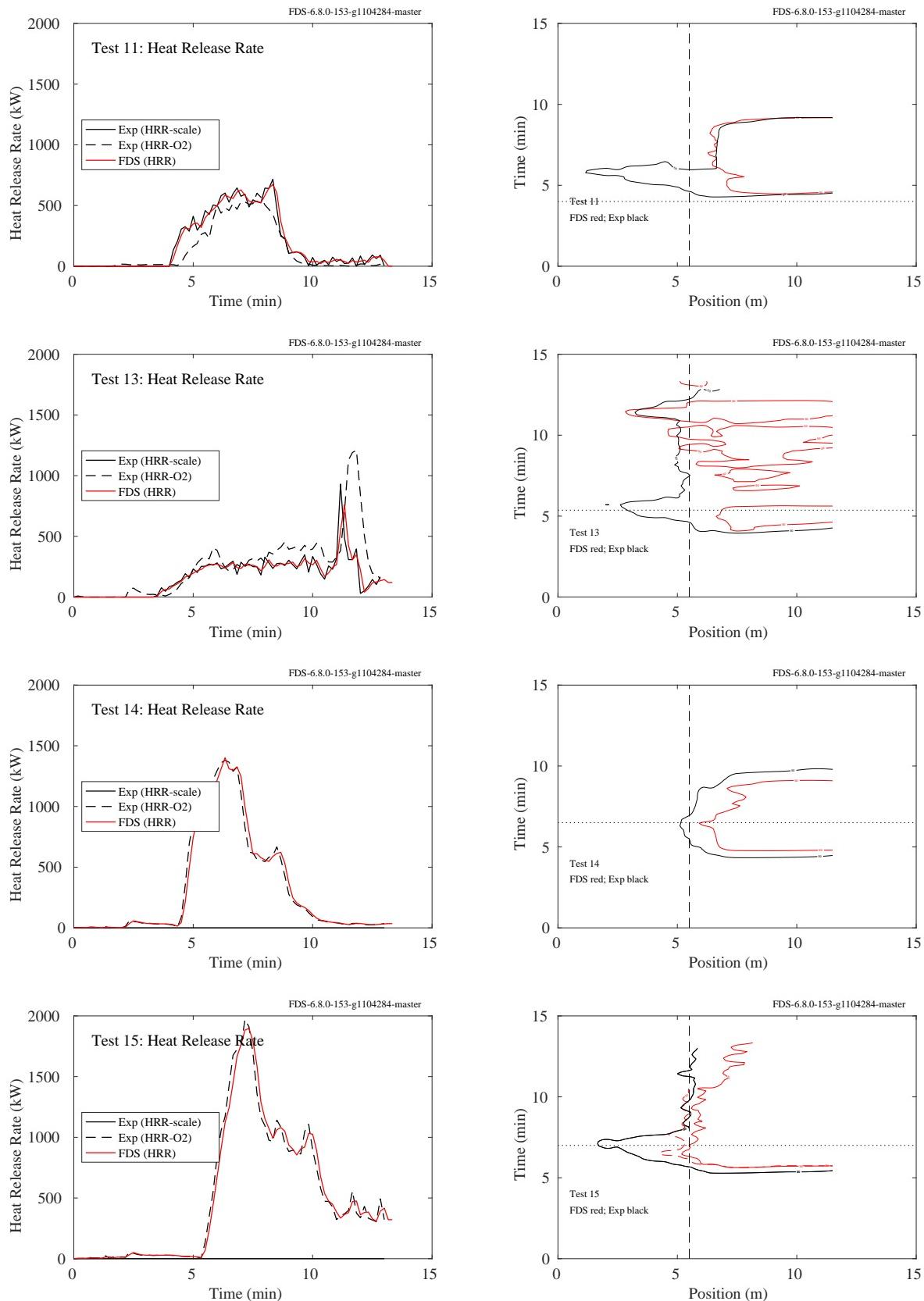


Figure 7.104: Summary of FHWA Tunnel experiments 11, 13, 14 and 15.

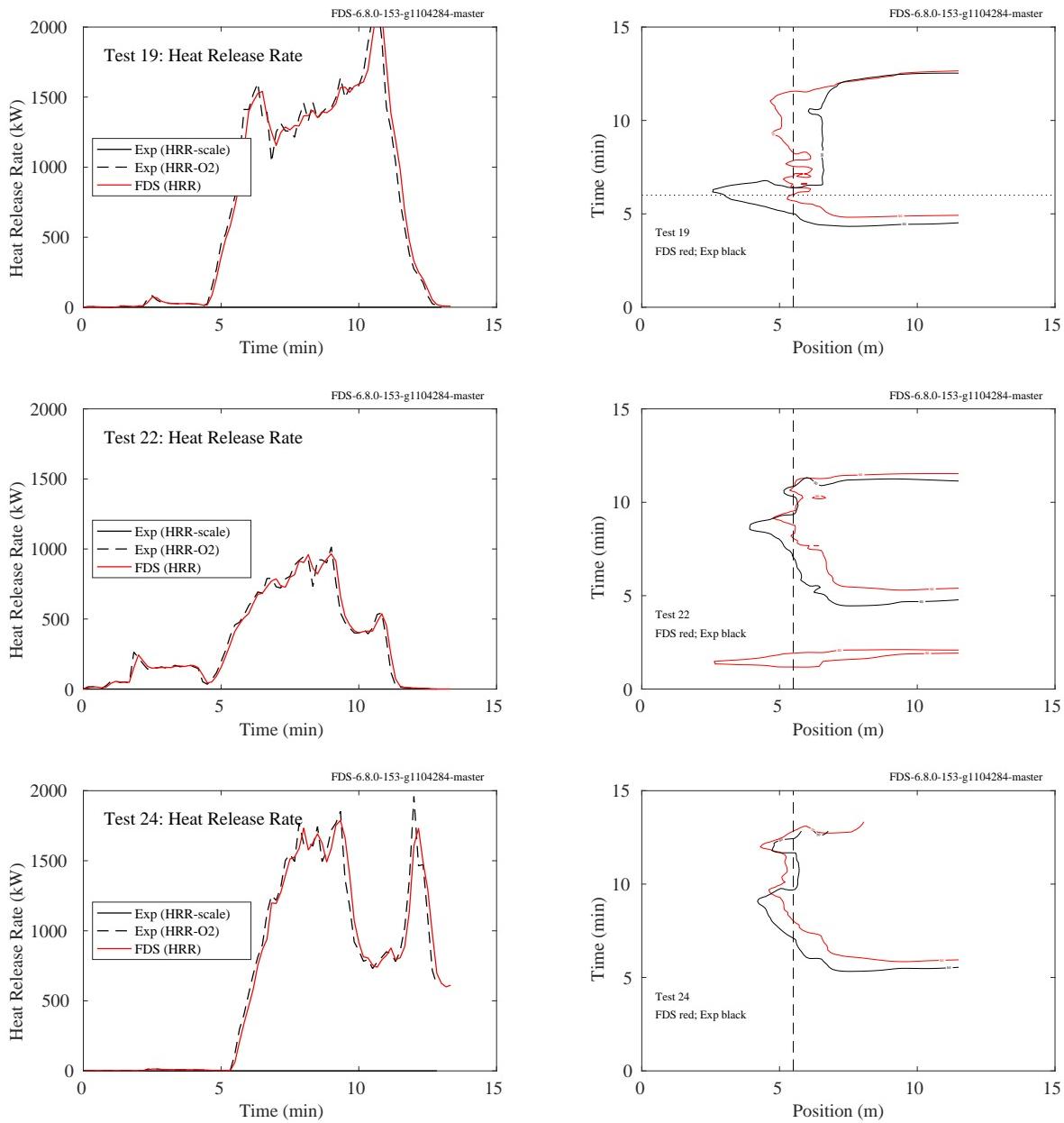


Figure 7.105: Summary of FHWA Tunnel experiments 19, 22 and 24.

## Chapter 8

# Gas Velocity

Gas velocity is often measured at compartment inlets and outlets as part of a global assessment of mass and energy conservation. This chapter contains measurements of gas velocity and related quantities.

### 8.1 ATF Corridor Experiments

Comparisons of bi-directional velocity measurements with FDS predictions for the ATF Corridor experiments are presented on the following pages. Velocity measurements were made at four locations, two on the first level (Trees H and I) and two on the second level (Trees J and K). Shown are the upper-most and lower-most probe for each vertical array. Typically there were four probes per tree, with the number 1 indicating the upper-most probe.

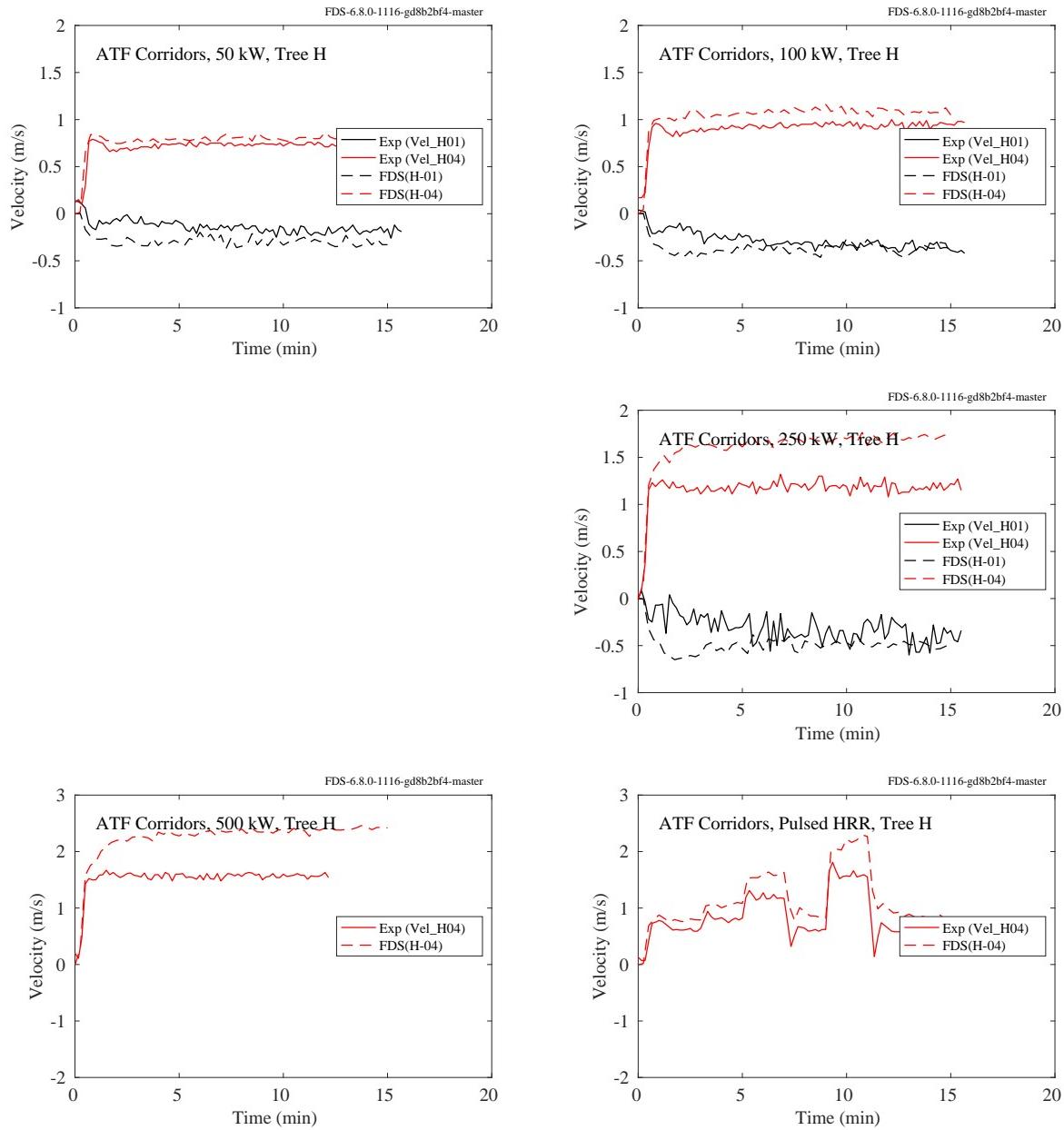


Figure 8.1: ATF Corridors, gas velocity, first level, Location H.

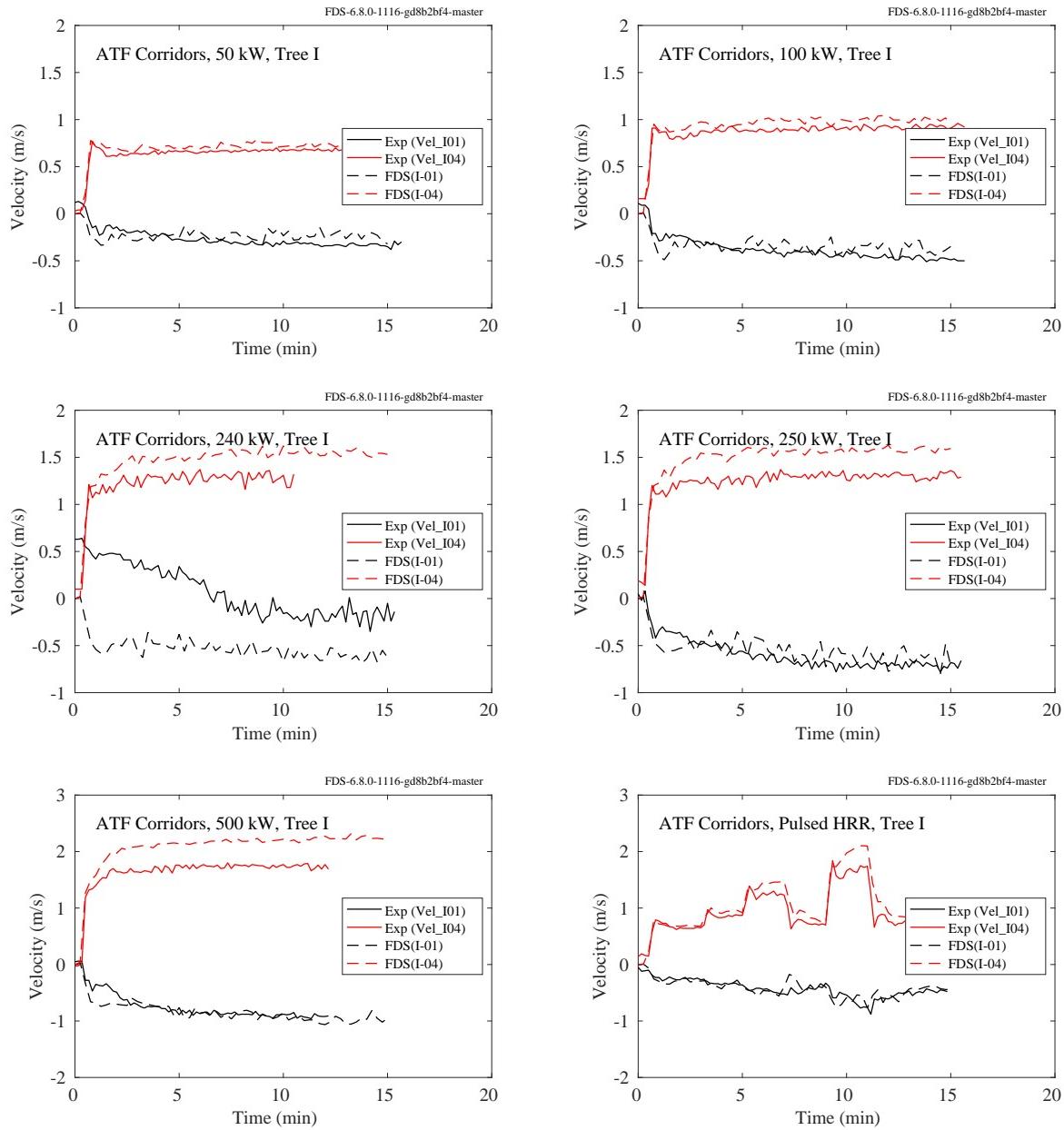


Figure 8.2: ATF Corridors, gas velocity, first level, Location I.

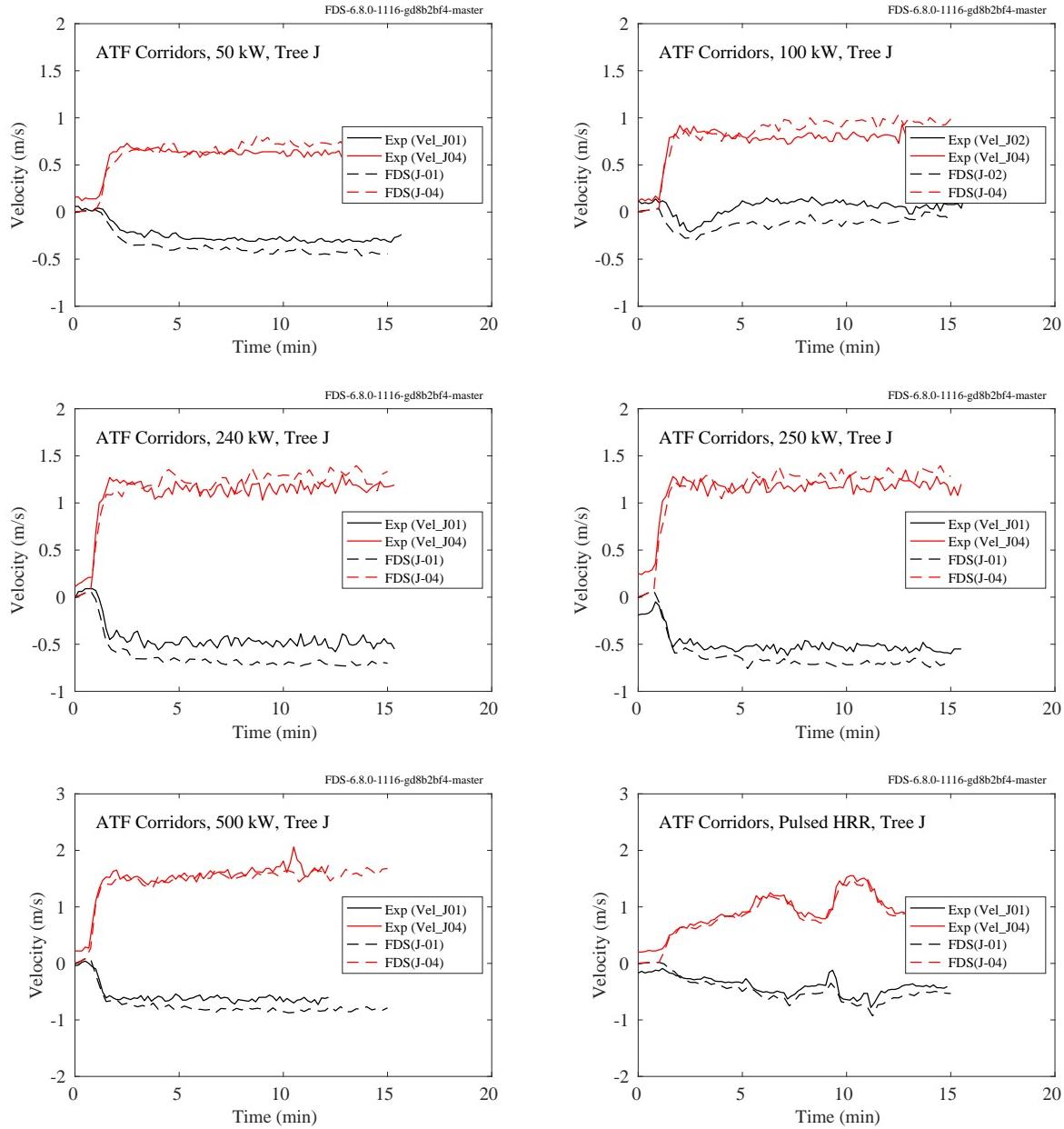


Figure 8.3: ATF Corridors, gas velocity, second level, Location J.

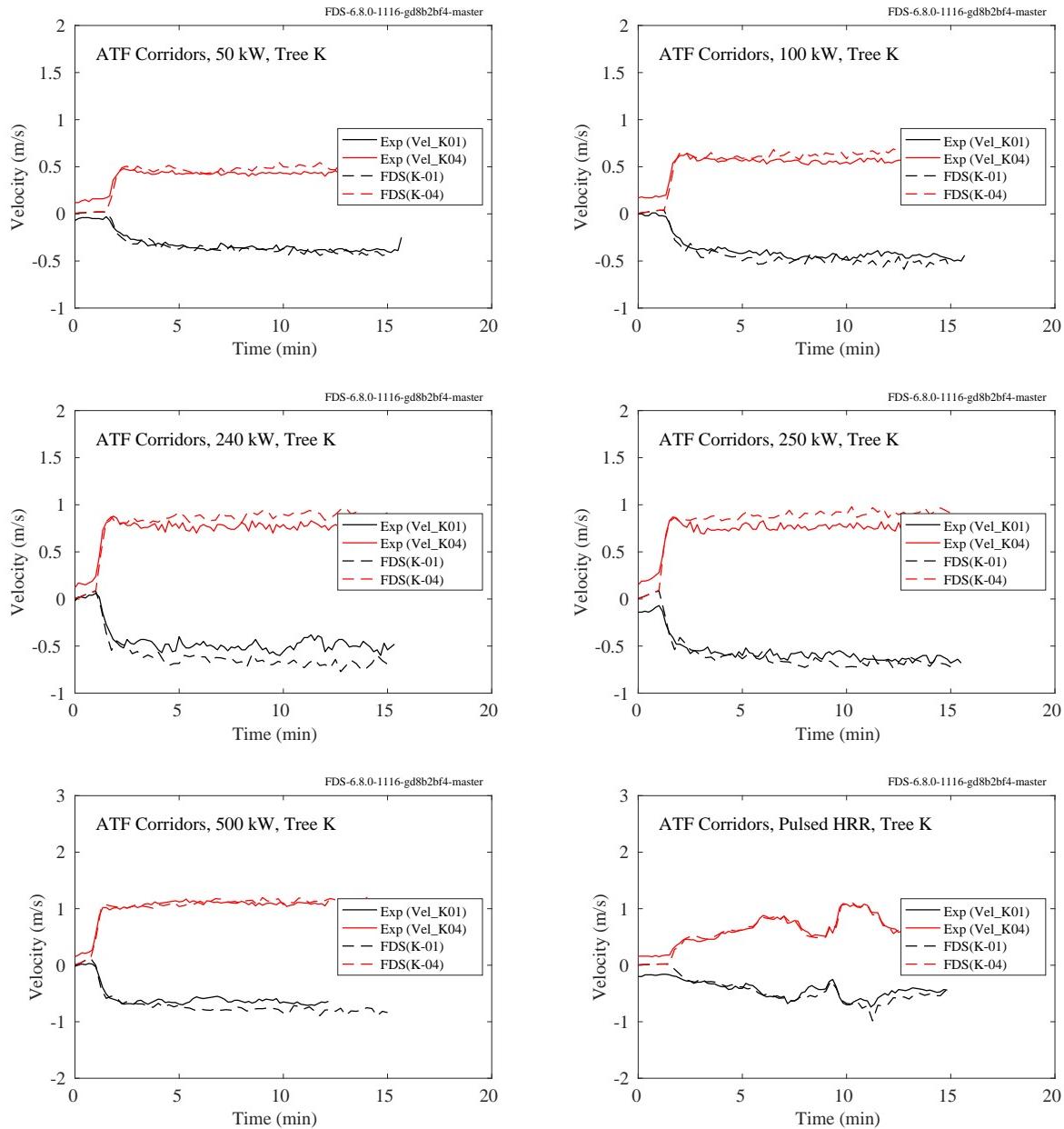


Figure 8.4: ATF Corridors, gas velocity, second level, Location K.

## 8.2 Backward Facing Step

A snapshot the instantaneous velocity contours of the flow over a backward facing step is shown in Fig. 8.5. The dimensions of the tunnel are given in Fig. 3.2. Virtual measurement devices are placed throughout the channel to collect data relating to flow characteristics such as velocity, turbulence RMS velocity, and friction velocity. These virtual measurement devices are placed into lines, four vertical and one horizontal, with a device in the volumetric center of each grid cell. A vertical line device is placed within the inlet region at a location of  $x = -3h$ , and three line devices are placed in the post-step region at locations of  $4h$ ,  $6h$ , and  $10h$ . The post-step vertical line devices are placed accordingly to sample the recirculation, reattachment, and recovery regions. A horizontal line device is used to sample data directly adjacent to the bottom wall of the channel in the post-step region ( $0h$  to  $20h$ ).

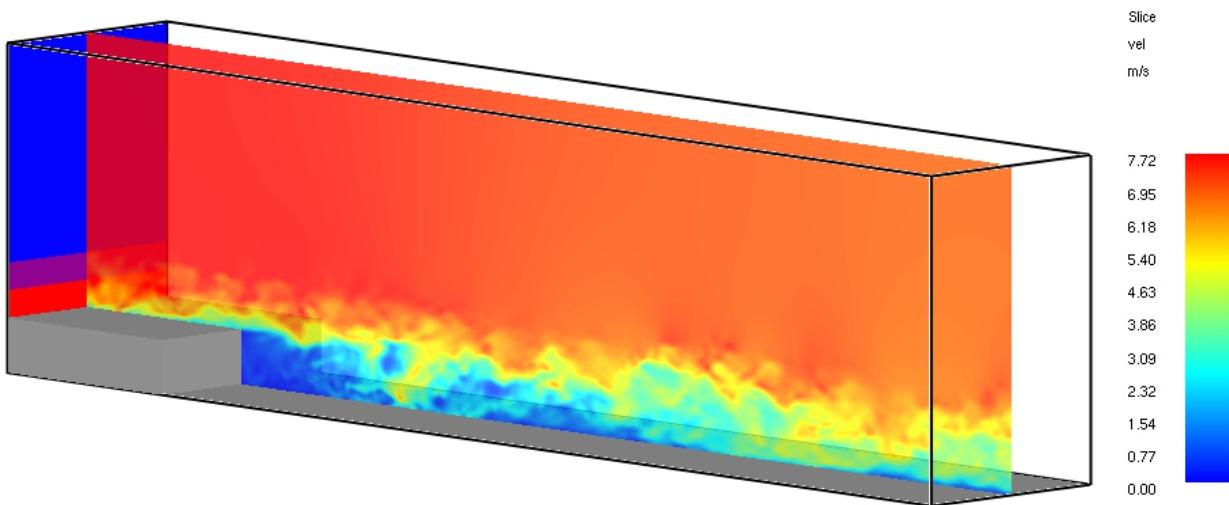


Figure 8.5: Instantaneous contours of velocity magnitude.

The profile of the inlet streamwise velocity component,  $\bar{u}(z)$ , is specified using experimental data provided by Jovic and Driver [50], while the transverse components,  $\bar{v}(z)$  and  $\bar{w}(z)$ , are set to zero. Turbulent eddies are injected using the Synthetic Eddy Method of Jarrin [339]. Eddies are injected at random locations in the bottom two inlets, advected with the flow over a distance equal to the maximum eddy length scale and recycled at the inlet. The inlet maximum eddy length scale is 0.03 m, the number of eddies is 100, and the RMS velocity is set to 0.5 m/s for the middle inlet and 1.0 m/s for the bottom inlet to match the measured inlet data at  $x/h = -3$  as closely as possible.

The boundary conditions for velocity and pressure on the top of the domain are “mirror”, that is, zero gradient. The spanwise boundaries are periodic. The outlet boundary is “open”.

Figure 8.6 shows the longitudinal profiles of the friction coefficient (left) and the pressure coefficient (right). The  $x/h$  location where  $C_f$  crosses zero is the reattachment length, a key validation metric for this flow. The measured value is approximately 6. Figure 8.7 shows the inlet ( $x/h = -3$ ) and downstream mean and covariance profiles.

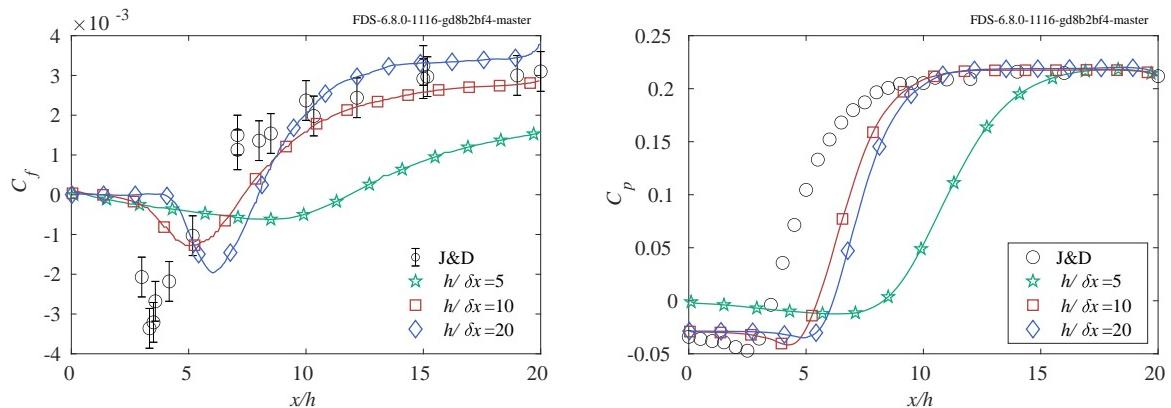


Figure 8.6: Longitudinal profiles of (left) friction coefficient and (right) pressure coefficient.

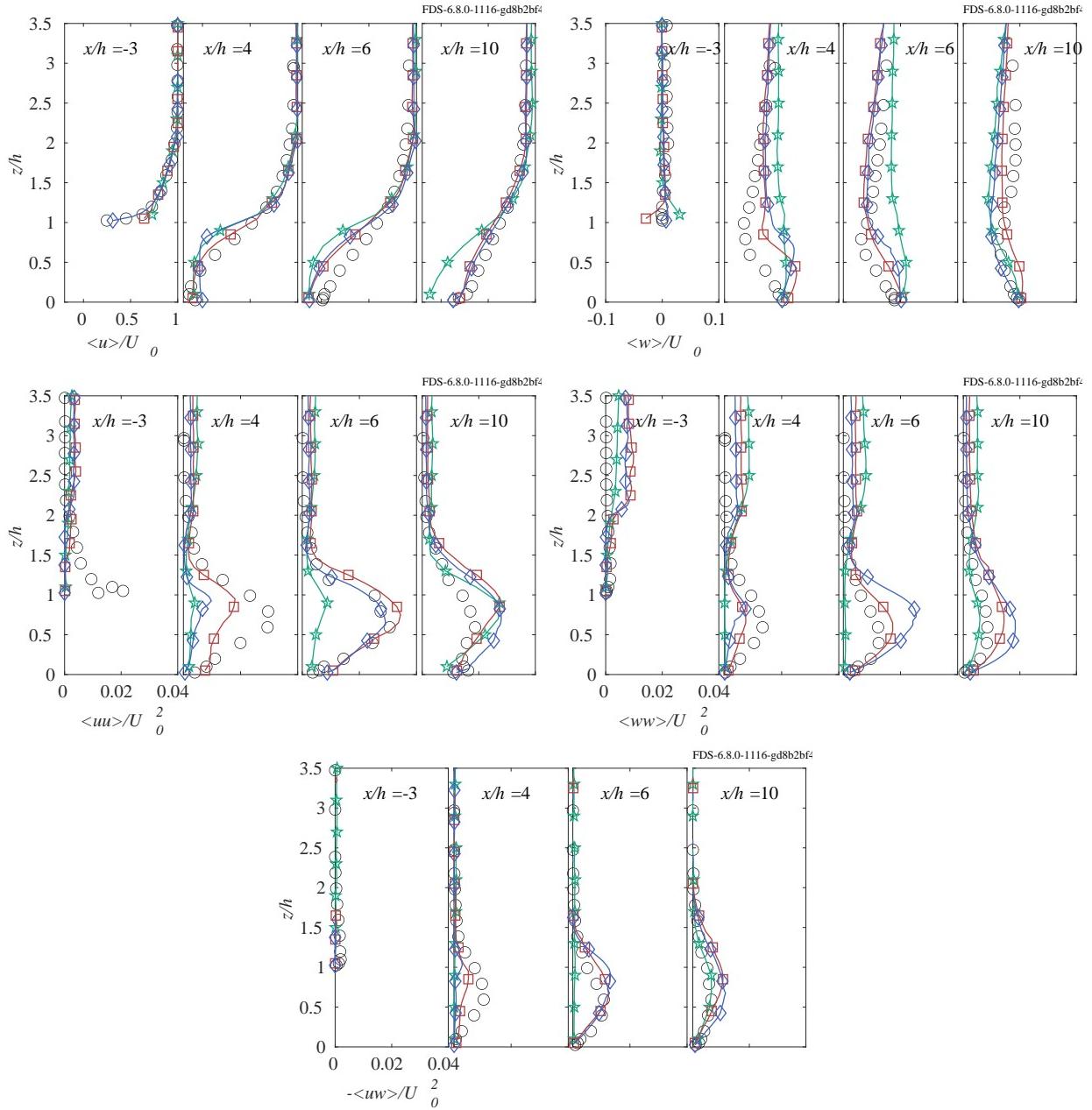


Figure 8.7: Flow profiles for various grid resolutions. Symbols:  $\star$ ,  $h/\delta z=5$ ;  $\square$ ,  $h/\delta z=10$ ;  $\diamond$ ,  $h/\delta z=20$ ;  $\circ$ , J&D experimental data.

### 8.3 Bryant Doorway Experiments

On the following page there are seven plots comparing the predicted and measured centerline velocity<sup>1</sup> profiles in a doorway of a standard ISO 9705 compartment. The measurements shown are based on PIV (Particle Image Velocimetry). Note that some of the measurements do not extend to the top of the doorway (1.96 m above the compartment floor) because the heat from the fire prevented adequate laser resolution of the particles. Velocity measurements were also made using bi-directional probes [159], but these measurements were shown to be up to 20 % greater in magnitude than the comparable PIV measurement.

---

<sup>1</sup>Note that the quantity that is being compared is the total velocity multiplied by the sign of its normal component.

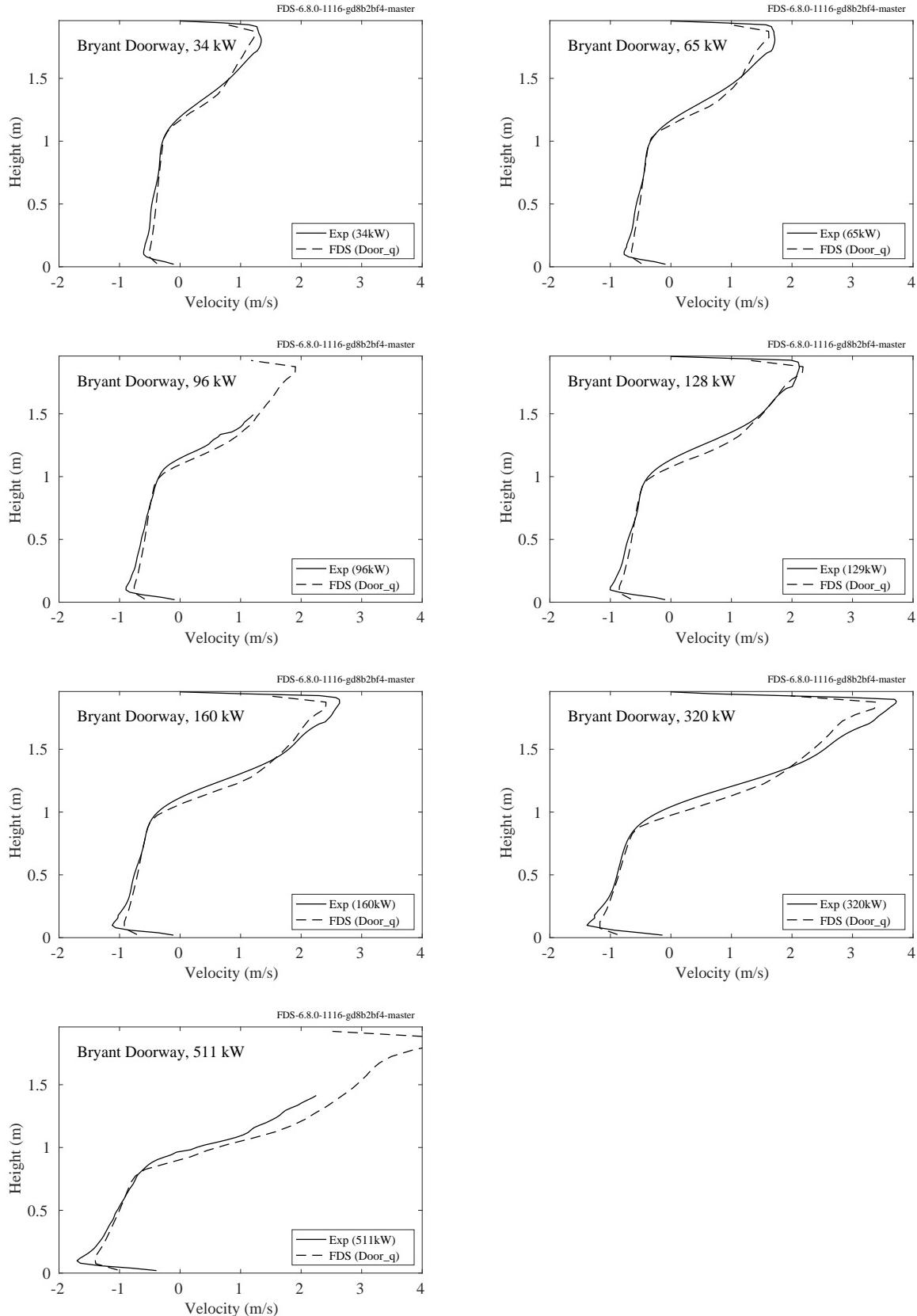


Figure 8.8: Bryant Doorway experiments, gas velocity profiles.

## 8.4 Edinburgh Vegetation Drag

The following figures show average velocities, taken over a 60 s period and obtained 225 mm from the leading edge of the fuel bed, as shown in Figure 3.10. In the case of the simulations, averaging starts after 20 s in order to allow quasi-steady conditions to establish. The experimental points represent an average of two repeats, involving re-packing of the fuel bed.

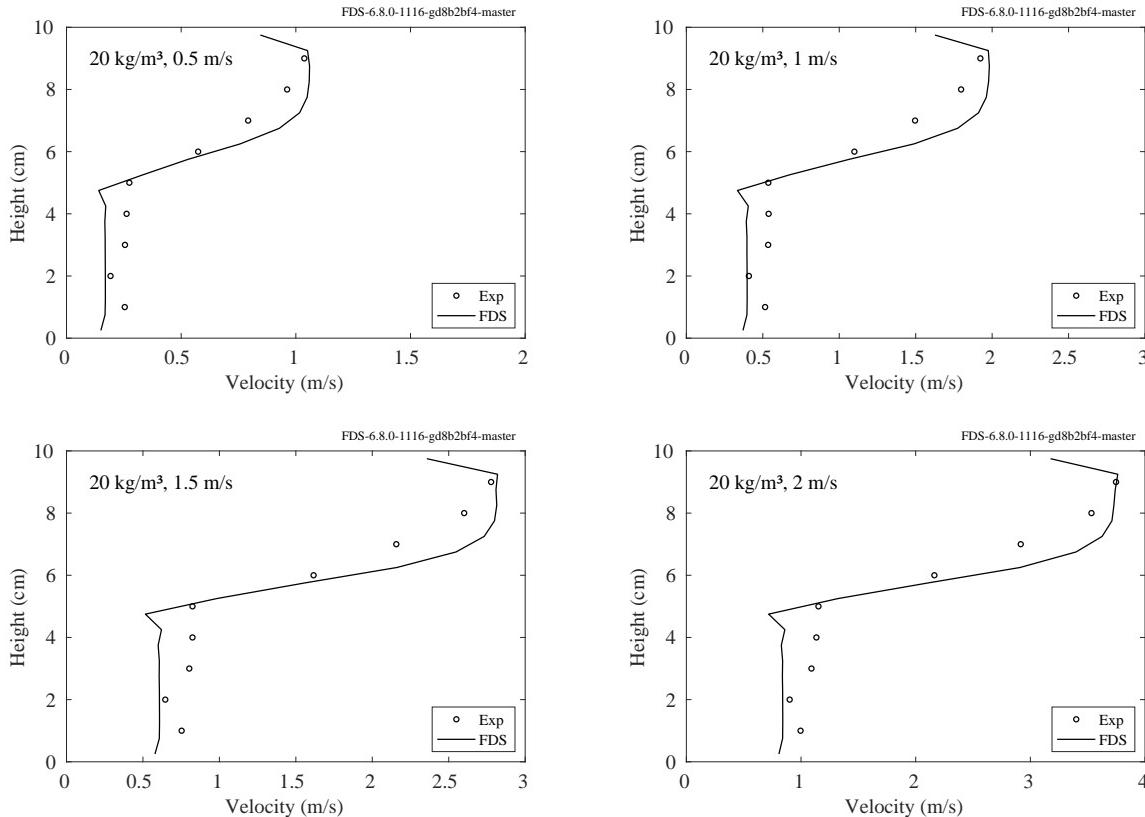


Figure 8.9: Edinburgh Vegetation Drag, gas velocity profiles, low bulk density.

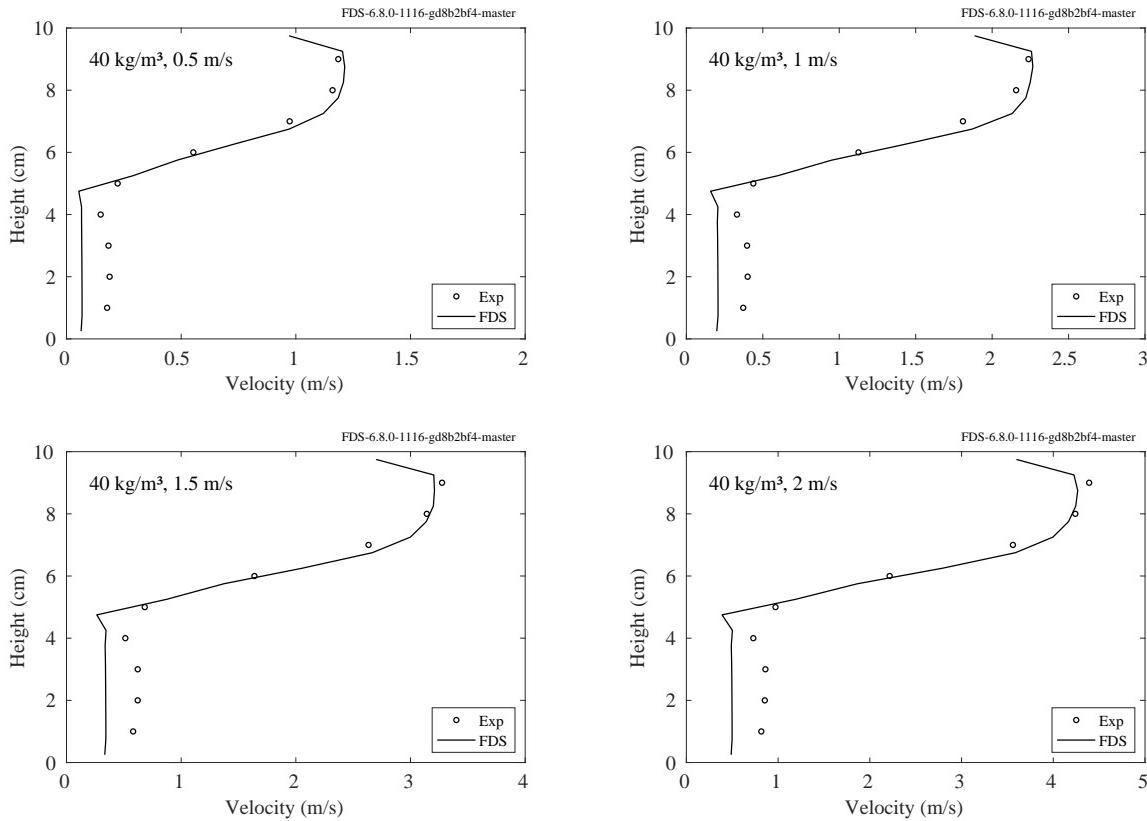


Figure 8.10: Edinburgh Vegetation Drag, gas velocity profiles, medium bulk density.

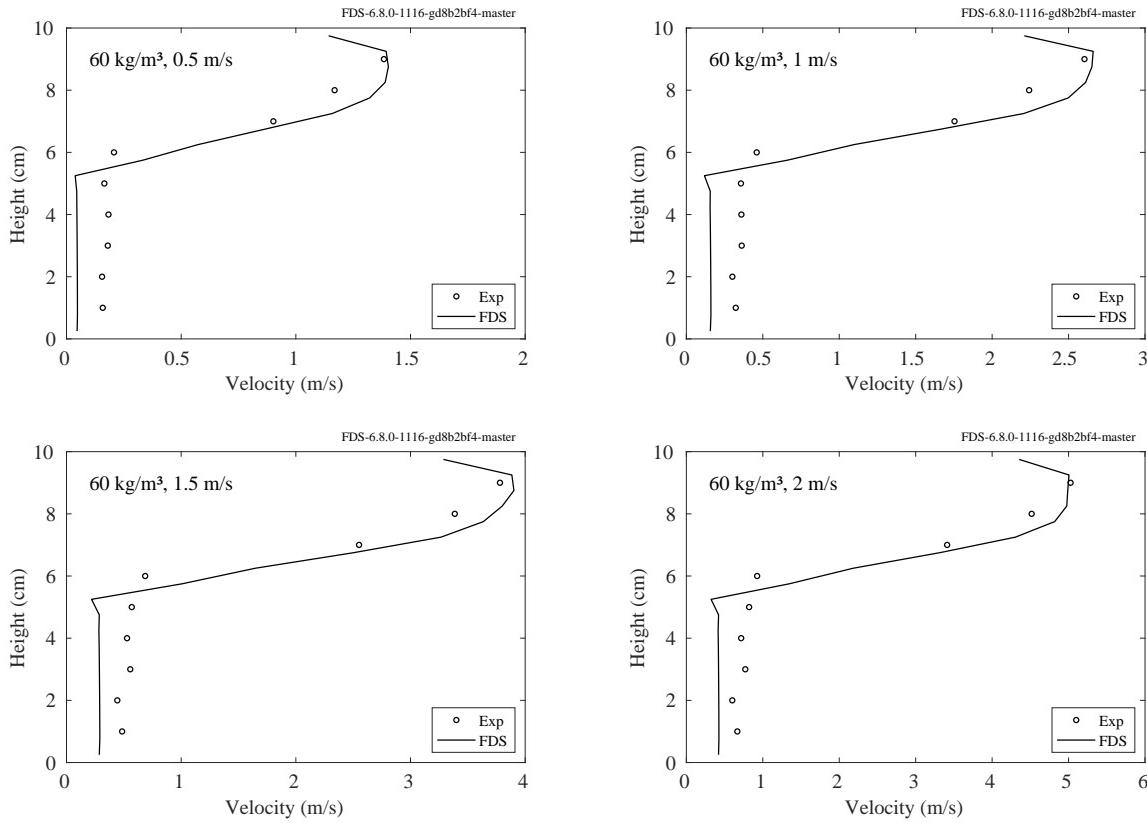


Figure 8.11: Edinburgh Vegetation Drag, gas velocity profiles, high bulk density.

## 8.5 FM/FPRF Datacenter Experiments

On the following page there are eight plots comparing the predicted and measured velocities for the high and low fan speed flow mapping tests in the FM/FPRF datacenter mockup. For each test there are plots for u-velocity, v-velocity, w-velocity and total velocity. Error bars are the measured and predicted RMS values. The dotted lines represent the measurement error. Measurement error was not a simple percentage of the measured value but rather was a propagation of fan flow error (the primary FDS input), sonic anemometer intrinsic error, and an estimate of the error based on the accuracy of placing the anemometer (determined from attempts to make repeat measurements after removing and replacing the probe).

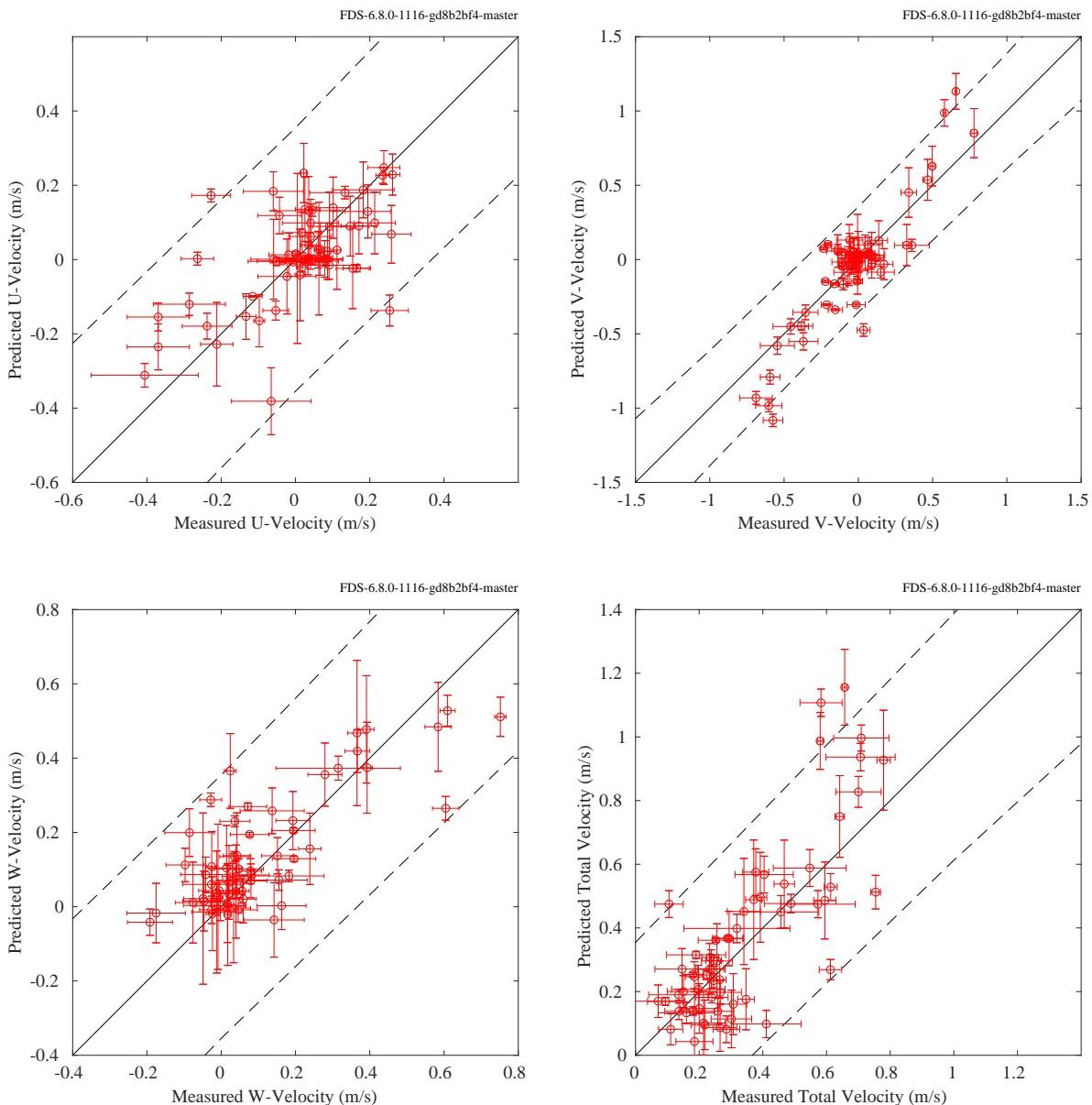


Figure 8.12: FM/FPRF experiments, gas velocity, low fan rate.

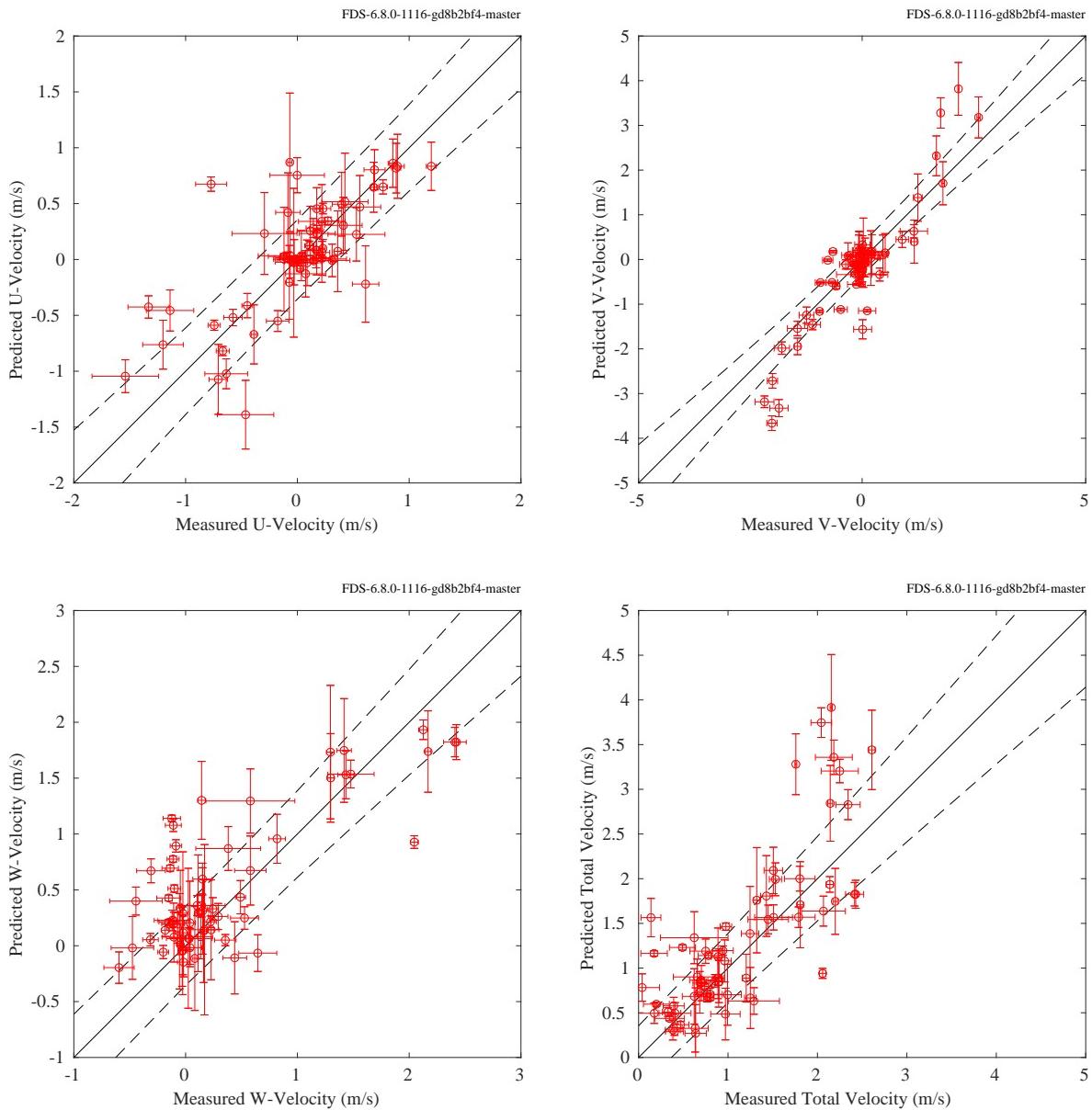


Figure 8.13: FM/FPRF experiments, gas velocity, high fan rate.

## 8.6 JH/FRA Experiments

The following pages compare the predicted and measured velocities through the compartment door in the JH/FRA scaled compartment series. For each test there are plots of the velocity with time at five heights in the door. Each velocity was measured with bi-directional probes. The test with inert lining increased the burner HRR after 5 minutes (see Section 3.37). The velocities in the quarter-scale compartments were generally over predicted by FDS compared with those measured; whereas, the velocities measured in the full-scale compartments were higher than those predicted by FDS.

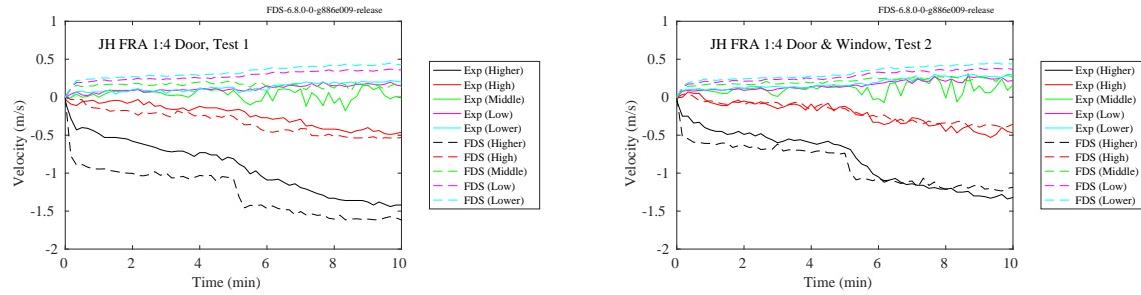


Figure 8.14: JH/FRA experiments, gas velocity, 1:4 scale inert lining configurations.

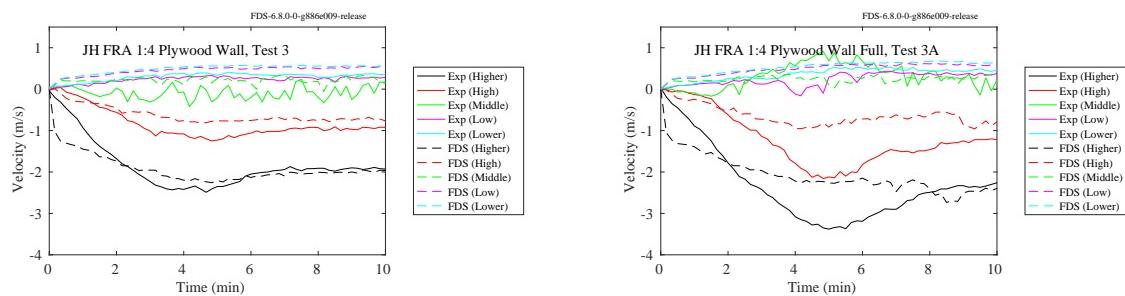


Figure 8.15: JH/FRA experiments, gas velocity, 1:4 scale combustible lining configurations.

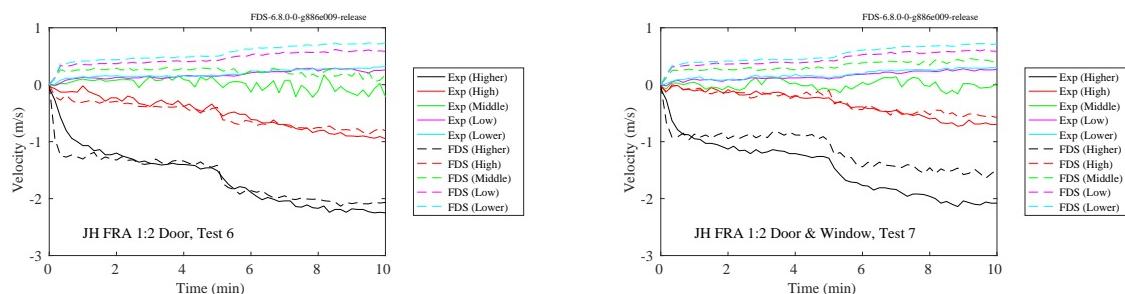


Figure 8.16: JH/FRA experiments, gas velocity, 1:2 scale inert lining configurations.

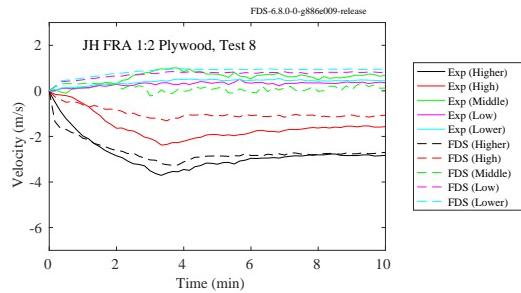


Figure 8.17: JH/FRA experiments, gas velocity, 1:2 scale combustible lining configurations.

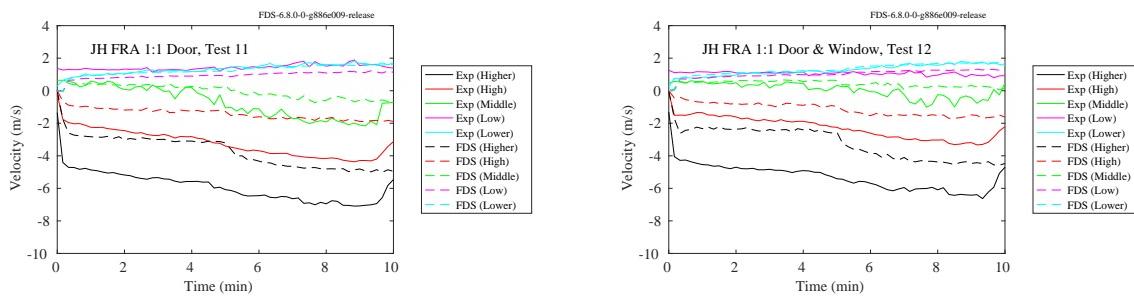


Figure 8.18: JH/FRA experiments, gas velocity, 1:1 scale inert lining configurations.

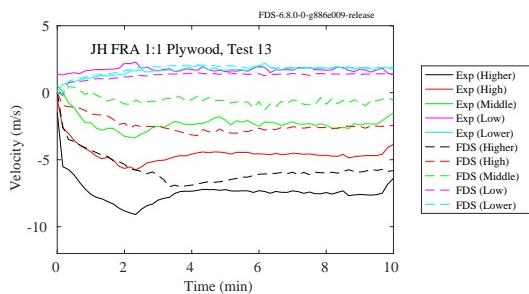


Figure 8.19: JH/FRA experiments, gas velocity, 1:1 scale combustible lining configurations.

## 8.7 McCaffrey's Plume Correlation

The following plots show the results of simulations of McCaffrey's five fires at three grid resolutions, nominally  $D^*/\delta x = [3, 6, 12, 24]$  based on the  $D^*$  of the 14.4 kW burner (respectively, crude, coarse, medium, and fine resolution).

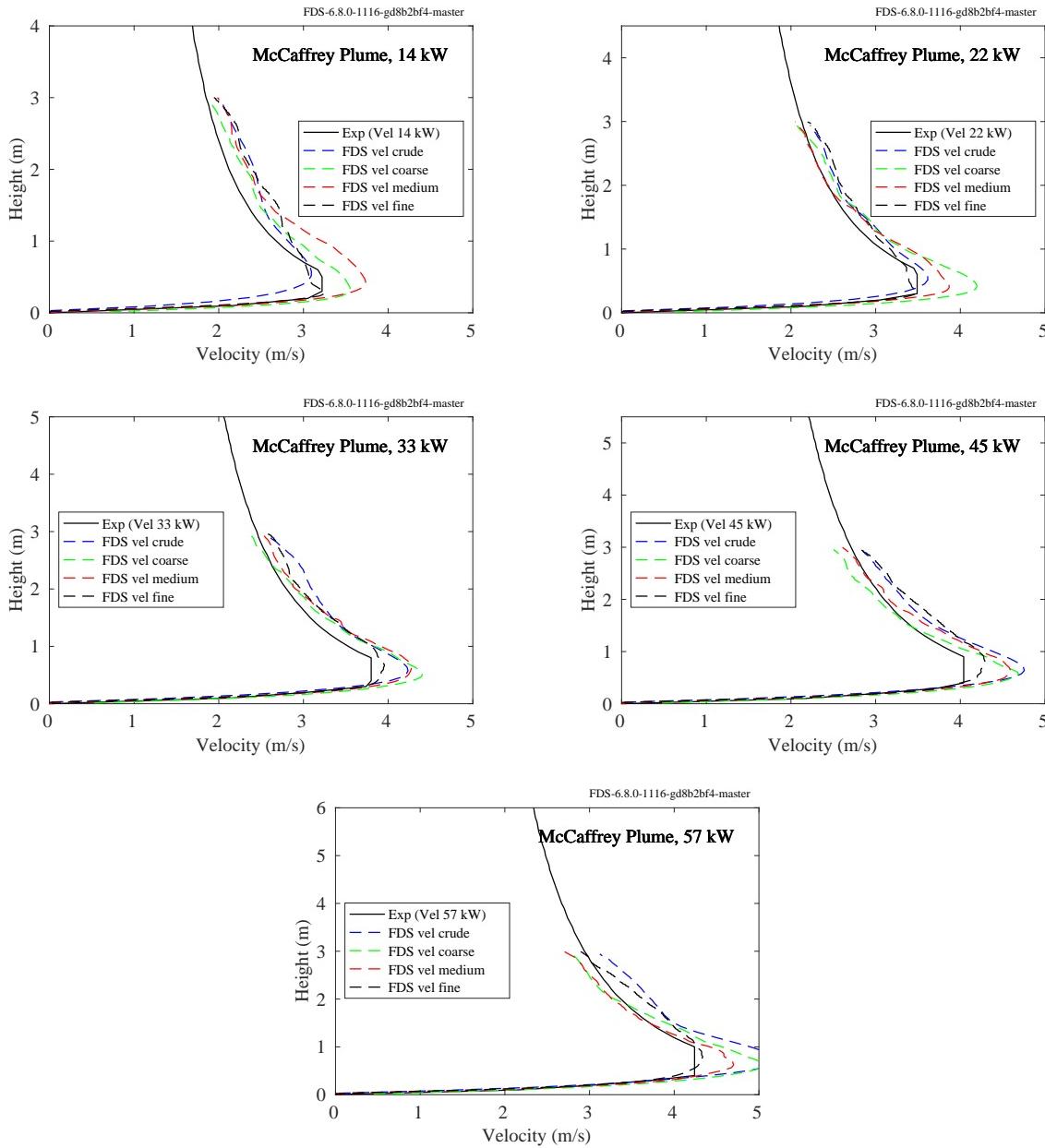


Figure 8.20: McCaffrey Plumes, centerline plume velocity.

Below we plot the same results but arranged in a different way. The height dimension is scaled by the fire Froude number and each plot represents nominally the same resolution level.

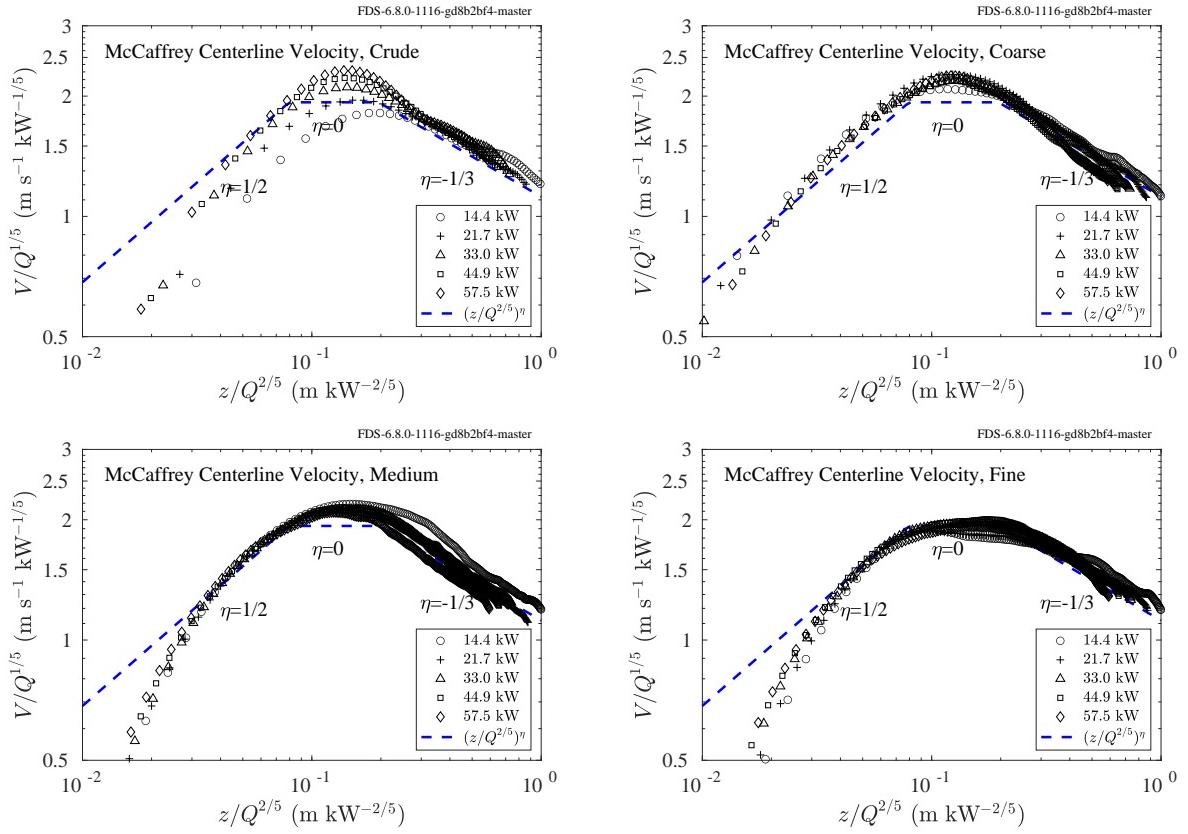


Figure 8.21: McCaffrey Plumes, centerline plume velocity, Froude scaling.